



HAL
open science

On the Design of Steel Members with Open Cross-Sections Subject to Combined Axial Force, Bending and Torsion

André Beyer

► **To cite this version:**

André Beyer. On the Design of Steel Members with Open Cross-Sections Subject to Combined Axial Force, Bending and Torsion. Mechanics of materials [physics.class-ph]. Université de Lorraine, 2017. English. NNT : 2017LORR0204 . tel-01813712

HAL Id: tel-01813712

<https://theses.hal.science/tel-01813712>

Submitted on 12 Jun 2018

HAL is a multi-disciplinary open access archive for the deposit and dissemination of scientific research documents, whether they are published or not. The documents may come from teaching and research institutions in France or abroad, or from public or private research centers.

L'archive ouverte pluridisciplinaire **HAL**, est destinée au dépôt et à la diffusion de documents scientifiques de niveau recherche, publiés ou non, émanant des établissements d'enseignement et de recherche français ou étrangers, des laboratoires publics ou privés.



AVERTISSEMENT

Ce document est le fruit d'un long travail approuvé par le jury de soutenance et mis à disposition de l'ensemble de la communauté universitaire élargie.

Il est soumis à la propriété intellectuelle de l'auteur. Ceci implique une obligation de citation et de référencement lors de l'utilisation de ce document.

D'autre part, toute contrefaçon, plagiat, reproduction illicite encourt une poursuite pénale.

Contact : ddoc-theses-contact@univ-lorraine.fr

LIENS

Code de la Propriété Intellectuelle. articles L 122. 4

Code de la Propriété Intellectuelle. articles L 335.2- L 335.10

http://www.cfcopies.com/V2/leg/leg_droi.php

<http://www.culture.gouv.fr/culture/infos-pratiques/droits/protection.htm>

THÈSE

Pour l'obtention du titre de

DOCTEUR DE L'UNIVERSITÉ DE LORRAINE

Spécialité :

Sciences des Matériaux – Matériaux pour le génie civil

Présentée par
André BEYER

Résistance des barres en acier à section ouverte soumises à une combinaison d'effort normal, de flexion et de torsion

Thèse soutenue publiquement le 2 Novembre 2017 à Nancy devant le jury composé de :

Rapporteurs :	Prof. D. CAMOTIM	Professeur, Universidade Técnica de Lisboa, Portugal
	Prof. A. TARAS	Professeur, Universität der Bundeswehr München, Allemagne
Examineurs :	Prof. L. GARDNER	Professeur, Imperial College London, United Kingdom
	Prof. N. BOISSONNADE	Professeur, Laval University, Canada
	Prof. M. MARTINY	Professeur, Université de Lorraine, France
	M. A. BUREAU	Chef du Service Recherche Construction Métallique - CTICM, France
Directeur de thèse :	Prof. A. KHELIL	Professeur, Université de Lorraine, France

Institut Jean Lamour (IJL) – UMR 7198 - Département CP2S – Equipe 207

Université de Lorraine – Pôle M4 : matière, matériaux, métallurgie, mécanique

ACKNOWLEDGEMENTS

First, I would like to express my special thanks to the executive committee of CTICM. Indeed, without their trust in me, this project would never have been initiated in the first place. I hope, that the result of this thesis shows that I have been worthy of their confidence.

I like to thank Mr. Alain BUREAU, head of the Steel Construction Research Division of CTICM, for his confidence and the time he spent during these last three years to discuss the advancement of the research work with me.

I also want to thank Prof. Abdelouahab KHELIL, director of this thesis, for his personal dedication to this work and all the help he could provide me for solving technical and administrative questions.

I would like to express my gratitude to Prof. Nicolas BOISSONNADE who has accompanied this work during the last three years. The thesis advanced thanks to our intensive discussions and the resulting input for my work. This thesis contains more than 600 pages and this is, at least, partially due to the fact, you pushed me forward to investigate all details that influence the problem I have studied.

Obviously, I have to thank the reporters of this thesis, Prof. Dinar CAMOTIM and Prof. Andreas TARAS. Thank you that you did not revoke your decision to be reporters when you see the thickness of the manuscript for the first time. I am aware that reading and commenting this thesis has been a lot of work for you. I would like to thank for these comments and for the interesting discussions, we had during the PhD defence. I am also grateful that Prof. Leroy GARDNER and Prof. Marion MARTINY accepted to be part of the jury and dedicated their time to discuss the outcomes of my work.

Last, but most evidentially I would like to express my gratitude to my wife, Marie, and my two daughters, Léonie and Léna, who supported me during the three years of my PhD thesis. I love you.

ABSTRACT

Structural steel members with open cross-section are, in the majority of cases, subject to a combination of axial force and mono- or bi-axial bending. Nonetheless, owing to specific use, they may be subject to torsion as well. Indeed, crane girders are subject to torsion as the crane, circulating at the upper or lower flange, induces horizontal loads applied outside of the shear centre of the girder. Also, members with U section, sometimes used as edge girders, are generally subject to torsion as the vertical load acts through the web and it is consequently applied outside of the shear centre. Even if torsional loads are of practical interest for steel members of open section, the European standard for the design of steel structures, Eurocode 3, does not contain a generally accepted design method addressing the resistance of these members. Consequently, the main objective of this thesis is to fill the gap in the current standard. So as to attain this objective the behaviour of members of open section subject to complex load combinations is studied theoretically, experimentally and numerically.

First, a finite element model is developed. In particular, the influence of the fillets of hot-rolled members and the influence of the calculation imperfections are studied. This study helped to complete the recommendations for numerical simulations that have been developed especially for members with double symmetric I sections and that may consequently not be applied directly to U-shaped members.

In a second step, the plastic cross-section resistance is studied based on ten laboratory tests and an extensive numerical simulation campaign. The laboratory tests have been performed in order to characterise the interaction between the major-axis bending moment and the shear force. Indeed, it appeared that existing design models for this load configuration may yield highly different results. The tests together with supplementary numerical simulations highlight the influence of strain hardening on the shear resistance. It is shown that only a design model, which explicitly considers the level of strain hardening in a given section, may reliably predict the shear resistance. An example of such a design model is the "Continuous Strength Method". The study is then extended to plastic interaction for mono-symmetric sections and to plastic interaction including the effect of torsion. In case of applied torsion, the member generally possesses a non-negligible plastic torsional system reserve that cannot be accounted for by simple elastic analysis. In order to overcome this limitation, a two-step elastic analysis method is proposed that should, however, only be applied in practice if no specific "Serviceability Limit State" criteria are formulated for the studied members. Based on an extensive parametric study simplified interaction equations are proposed for the plastic cross-section resistance. Yet, as these interaction equations become very complex in some cases, it appeared more straightforward to adapt the "Partial Internal Force Method" to the results obtained by the numerical simulations and the laboratory tests. The resulting design method is shown to be sufficiently precise.

The last part of this thesis is dedicated to the resistance of the member including second order effects and the effect of elasto-plastic instability. Existing design methods for members with or without torsion are discussed and compared to selected numerical simulations. Resulting

limitations and inconsistencies in these methods are then analysed. In order to get more insights into the behaviour of members subject to torsion, a theoretical study is performed based on the assumption of elastic material behaviour. The critical elastic loads are determined and it is shown that in some cases pre-buckling displacements should be considered. Indeed, for U-shaped members under minor-axis bending or bi-axial bending critical loads not considering the influence of pre-buckling displacements are not representative of the member behaviour. Subsequently to the investigations concerning elastic instability, the elastic second order equilibrium of the member is studied to redevelop the analytical background of available design methods addressing the resistance of members subject to a compression axial force and bi-axial bending. These investigations are also used to highlight the parameters that should be additionally accounted for if the member is also subject to torsion. Based on the theoretical developments and a second extensive numerical study covering more than 10 000 configurations (form of the section + load case) an extension of the Eurocode 3 Part 1-1 interaction equations for the member resistance is proposed. It is shown that the approach is sufficiently precise for member with compact and slender double symmetric I section. The proposal becomes more conservative for short U-shaped members due to the simple approximation of the plastic cross-section interaction. Finally, it appears that the interaction equations are very conservative for members with mono-symmetric I section due to their high plastic torsional system reserve.

A second design approach is developed in the format of the “Overall Interaction Concept” (OIC) for members with compact double symmetric I section in order to overcome the conservatism of the interaction equations linked to the approximation of the plastic cross-section interaction. The OIC proposal is shown to be at least as precise as the Eurocode 3 interaction equations (even in their initial field of application) and it is even more precise for members with short to intermediate lengths.

RÉSUMÉ ÉTENDU

Les barres en acier à section ouverte sont généralement soumises à une combinaison de flexion bi-axiale et d'effort normal. Cependant, dans certain cas, ces barres sont également soumises à un moment de torsion. En effet, les poutres de roulement sont sollicitées par de la torsion en raison du fonctionnement de l'appareil de levage qui induit des charges horizontales appliquées en dehors du centre de cisaillement de la section de la poutre. Aussi, les barres en U, souvent utilisées comme poutres de rive, sont sollicitées en torsion étant donné que les charges sont généralement appliquées dans le plan moyen de l'âme de la section et donc en dehors du centre de cisaillement.

Actuellement, la résistance des barres soumises à de la torsion ne peut pas être vérifiée sauf par une analyse numérique complexe. Mais, dans la pratique des bureaux d'étude, ce type d'analyse n'est pas facilement réalisable à cause d'un manque des logiciels adaptés. C'est pourquoi, cette thèse a pour objectif de définir un modèle de résistance qui peut facilement être utilisé dans les bureaux d'étude. En particulier, il est envisagé:

- D'étudier le comportement des barres soumises à une combinaison complexe d'effort par voies théorique, expérimentale et numérique ;
- De développer un modèle de résistance fiable pour déterminer la résistance plastique de la section ;
- De développer un modèle de résistance fiable pour déterminer la résistance de la barre prenant en compte l'effet de l'instabilité élasto-plastique.

Afin d'atteindre ces objectifs, la théorie nécessaire pour comprendre le comportement des barres à section ouverte soumises à de la torsion est présentée. Il est montré qu'en élasticité le comportement est équivalent à celui des barres soumises à une combinaison d'effort axial de traction et d'un moment de flexion. Dans la suite de cette thèse, nous démontrons que cette équivalence peut être étendue dans le domaine plastique.

Avant l'étude proprement dite du comportement des barres en acier soumises à de la torsion, un modèle numérique par éléments finis est établi. Il est apparu nécessaire d'étudier en détail la modélisation des congés de raccordement des barres en acier laminées à chaud. En effet, les congés ont une influence non négligeable sur la distribution des contraintes de cisaillement créées par le moment de torsion de Saint-Venant. En plus, on leur attribue généralement un effet favorable pour la résistance à l'effort tranchant. L'étude numérique a révélé que seule une modélisation par éléments finis volumiques est capable de représenter fidèlement la distribution des contraintes provoquées par la torsion sur des sections laminées à chaud et ainsi seule une modélisation volumique peut précisément prédire la résistance de la section. Les congés possèdent également une influence sur la résistance des barres si une configuration particulière est étudiée (configuration = combinaison entre section de la barre et chargement). En revanche, nous avons pu montrer que l'influence des congés disparaît lorsque la résistance est représentée dans un diagramme de type χ - λ (facteur de réduction – élancement réduit). De plus, il est possible de démontrer qu'une modélisation par éléments finis de type coque est capable de reproduire le

comportement en torsion des barres sans congés. Ses deux conclusions seulement ont permis d'établir une base de données de résultats numériques contenant plus que dix milles cas de barres. Ce grand nombre de cas, nécessaire pour étudier tous les paramètres qui influencent le problème traité, n'a pas pu être simulé avec une modélisation volumique en raison de la durée du calcul numérique. Afin d'assurer la fiabilité des résultats, les deux modèles numériques (modélisation volumique et modélisation en coque) ont été validés par rapport à des résultats expérimentaux publiés dans le passé.

Ensuite, la résistance plastique de la section est étudiée. Cette résistance représente le cas limite de la résistance de la barre dans son ensemble si sa sensibilité à l'instabilité élasto-plastique devient négligeable (par exemple pour les barres courtes). C'est pourquoi il est indispensable de porter une attention particulière à la caractérisation du comportement plastique de la section.

Tout d'abord, nous avons analysé les modèles de résistance disponibles dans la littérature. Il a alors été mis en évidence que :

- Les équations d'interaction plastique proposées dans l'Eurocode 3 Partie 1-1 pour le cas d'une combinaison d'effort normal et de flexion bi-axiale sont plus précises que les formules d'interaction données par la norme Américaine AINSI/AISC 360-10 et que celles données par la norme Australienne AS 4100 ;
- La définition de l'aire de cisaillement des sections laminées à chaud diffère largement dans les trois normes citées, ce qui conduit à des résistances à l'effort tranchant très différentes ;
- Ces trois normes ne contiennent pas de modèle de résistance satisfaisant pour les sections soumises aux effets de torsion.

Afin de franchir les limitations observées, nous avons présenté deux autres modèles de résistance. Le premier est basé sur une distribution prédéfinie des contraintes. Ces contraintes sont ensuite augmentées itérativement jusqu'à ce que la section soit entièrement plastifiée. Ce modèle nécessite une implémentation numérique. Le second modèle est basé sur la méthode « Partial Internal Force Method » (PIFM) introduite dans la référence (Kindmann et al. 1999a). Les limitations de la version initiale de cette méthode ont été analysées et nous avons proposé des adaptations qui améliorent la précision de cette méthode pour les sections soumises à une combinaison d'effort axial et de flexion bi-axiale. Toutefois, ces deux dernières méthodes sont basées sur certaines hypothèses, notamment concernant l'aire de cisaillement des sections laminées à chaud. Par conséquent, il est apparu nécessaire de valider l'hypothèse concernant l'aire de cisaillement par voie expérimentale. En tout, dix barres en acier laminées à chaud ont été testées en laboratoire. Ensuite, nous avons complété les résultats par des analyses numériques avec le modèle volumique prenant en compte l'effet supposé des congés. Ces simulations supplémentaires ont porté sur une plus grande variété de géométries de section et de nuances d'acier. Cette étude a permis de montrer que :

- Le modèle de résistance à l'effort tranchant (et ainsi la définition de l'aire de cisaillement) donné dans l'Eurocode 3 Partie 1-1 est satisfaisant pour les sections compactes (faible rapport hauteur/largeur) ;
- L'effet des congés sur la résistance à l'effort tranchant des sections en I est cependant faible. En effet, les sections sans congés de raccordement atteignent pratiquement la même résistance à l'effort tranchant que les mêmes sections possédant des congés ;
- La résistance à l'effort tranchant est en effet lié à l'écroûissage de l'acier. Par conséquent, le modèle de résistance de l'Eurocode 3 Partie 1-1 peut devenir insécuritaire dans certains cas si le niveau d'écroûissage atteignable par la section n'est pas suffisant ;
- Un modèle de résistance qui tient spécifiquement compte du niveau d'écroûissage possible dans une section donnée, comme la « Continuous Strength Method », est capable de prédire plus fidèlement la résistance à l'effort tranchant des sections avec ou sans congés de raccordement.

L'étude est ensuite élargie sur l'interaction plastique entre effort tranchant V_z et moment de flexion autour de l'axe de forte inertie pour les sections en U et en I mono-symétrique et sur l'interaction plastique entre effort tranchant V_y et moment de flexion autour de l'axe de faible inertie pour les sections en I mono-symétrique et doublement symétrique ainsi que pour les sections en U. Pour chaque cas, une formule d'interaction est proposée. A la suite de ces investigations, l'impact de la torsion sur la résistance plastique est étudié. D'abord, l'influence du type d'analyse (élastique ou plastique) est discutée. Nous avons montré que la résistance plastique des barres à section ouverte est fortement influencée par la réserve plastique en torsion de la barre. En effet, l'étude numérique révèle que la rigidité en gauchissement de la barre diminue à l'endroit de la plastification de la section la plus chargée jusqu'à la formation d'une « rotule en gauchissement ». Après la formation de cette rotule plastique, les charges peuvent continuer d'augmenter alors que la torsion est reprise uniquement par les contraintes de cisaillement associées au moment de torsion de Saint-Venant tandis qu'elle était reprise majoritairement par la torsion non-uniforme et en particulier par le bi-moment avant l'apparition de la rotule. Ainsi, la ruine plastique de la barre dans son ensemble n'est pas provoquée par une interaction d'efforts internes à l'endroit le plus chargé (selon une analyse élastique) mais cette ruine est provoquée par la plastification de la barre sur toute sa longueur due à l'interaction du moment de torsion de Saint-Venant avec les autres efforts internes. L'augmentation de l'importance relative des moments de torsion de Saint-Venant ne peut pas être prédite par une simple analyse élastique de la barre. Cependant, l'habitude actuelle qui consiste à vérifier la résistance de la section (ou de la barre) en se basant sur une analyse élastique pour la détermination des efforts internes et en négligeant le moment de torsion de Saint-Venant dans l'interaction plastique reste acceptable parce que cette approche donne, pour les cas pratiques, toujours une estimation de résistance plus faible que si la réserve plastique en torsion est considérée. Toutefois, il peut être économiquement intéressant de prendre en compte la réserve plastique en torsion. C'est pourquoi nous avons proposé une méthode d'analyse élastique en deux étapes qui est capable de représenter le

comportement plastique des barres à sections ouvertes en torsion. Cette méthode doit être limitée aux barres courtes, non sensibles aux effets d'instabilité élasto-plastique et aux barres non soumises à des critères particuliers d'Etat Limite de Service étant donné que la mobilisation de la réserve plastique en torsion implique aussi une augmentation non négligeable de la rotation en torsion qui ne peut pas être déterminée fidèlement par le modèle d'analyse simplifié.

A la suite de l'examen du comportement plastique des barres, l'interaction plastique d'une section sous effet combiné du bi-moment, des moments de flexion et de l'effort tranchant V_z est étudiée. Nous avons proposé des formules d'interaction « simplifiées » pour les sections en I mono et doublement symétrique et pour les sections en U. Cependant, la complexité des expressions développées augmente considérablement avec la mono-symétrie de la section et avec le cas d'interaction considéré. Nous avons montré qu'une seule formule ou même un nombre limité de formules d'interaction ne peut pas être développé pour couvrir une interaction entre l'effort axial, la flexion bi-axiale et le bi-moment. Il est apparu plus prometteur d'adapter davantage la méthode PIFM aux résultats obtenus par l'étude paramétrique concernant la résistance plastique de la section. Les adaptations ont été validées par rapport aux résultats numériques et nous avons pu démontrer la bonne précision de l'approche proposée.

Après avoir mis au point un modèle de résistance pour les barres (courtes) qui peuvent atteindre leur résistance plastique théorique, nous avons abordé la résistance des barres sensibles à l'instabilité élasto-plastique. Afin de caractériser leur comportement une large campagne de simulations numériques a été réalisée avec l'objectif de couvrir au maximum la globalité des paramètres qui étaient susceptibles d'influencer le problème. Ainsi, une totalité d'environ 10 000 configurations (section + cas de charge) a été traitée. Cependant, avant de commencer cette campagne numérique, il a été indispensable d'étudier l'influence des imperfections de calcul sur le résultat numérique obtenu. En effet, les barres en acier possèdent des imperfections physiques concernant leur géométrie (imperfections géométriques) et concernant leur matériau (imperfections matérielles). Ces imperfections sont en réalité de nature arbitraire et ne peuvent donc pas être reproduites directement lors des simulations numériques. Il est alors nécessaire de les remplacer par des imperfections équivalentes afin d'obtenir une limite basse sécuritaire qui couvre l'effet le plus défavorable des imperfections réelles. Dans la littérature, il existe des études détaillées concernant les imperfections équivalentes pour les barres à section en I doublement symétrique. En revanche, pour les sections en I mono-symétriques et particulièrement pour les sections en U, certaines informations ou recommandations ne sont pas détaillées et d'autres sont contradictoires. Nous avons alors réalisé une étude spécifique pour caractériser l'influence des imperfections sur les résultats des simulations numériques. Cette étude a permis d'obtenir les résultats suivants :

- Les recommandations concernant les imperfections géométriques appliquées aux sections en I doublement symétriques ne peuvent pas être transposées directement aux sections en U. Il est absolument nécessaire de vérifier que les imperfections amplifient l'effet des charges, ce qui n'est pas évident en raison de

l'influence du bi-moment résultant de la distribution des contraintes internes (à ne pas confondre avec le bi-moment généré par des charges de torsion).

- Les imperfections géométriques locales (de plaque) doivent être appliquées avec une longueur d'onde (dans le sens de la barre) identique pour les semelles et l'âme de la section sinon la charge ultime obtenue numériquement ne correspond pas à une limite basse.
- Une distribution auto-équilibrée de contraintes résiduelles (due au processus de fabrication de la barre en acier – ici laminage à chaud) a été déterminée pour les sections en U à l'aide des conditions d'équilibre interne et par simulation thermomécanique. Les deux approches donnent des résultats proches.

A l'issue de l'étude concernant les imperfections de calcul, nous avons discuté différents modèles de résistance disponibles dans la littérature pour les barres à section ouverte soumises à un chargement complexe incluant des charges de torsion. A l'aide du modèle numérique validé, il a été possible de mettre en évidence certaines limitations des approches étudiées. Afin d'obtenir une connaissance plus détaillée du comportement théorique des barres en torsion une étude analytique est ensuite réalisée.

L'instabilité élastique (supposant un comportement élastique du matériau) est la base d'un grand nombre de modèles de résistance à l'instabilité des barres en acier. C'est pourquoi, nous l'avons étudiée en détail. En particulier, nous avons montré que les déplacements de pré-flambage (généralement négligés) ont une influence majeure sur la charge critique des barres en U fléchies autour de leur axe de faible inertie et en flexion bi-axiale. Pour ces cas-là, la charge critique n'est pas représentative du comportement élasto-plastique de la barre si elle ne tient pas compte des déplacements de pré-flambage. Aussi, nous avons pu identifier les cas dans lesquels une barre en U peut être sensible à l'instabilité élastique si elle est soumise à un moment M_z agissant autour de l'axe de faible inertie. L'étude analytique a également permis de déterminer les modes propres d'instabilité élastique qui sont ensuite utilisés comme imperfection équivalente lors de l'étude analytique de l'équilibre élastique au second ordre de la barre. Nous avons étudié l'équilibre élastique pour différent cas de charge, y compris des charges de torsion, avec l'objectif :

- De (re-) démontrer la base théorique du modèle de résistance proposé actuellement dans l'Eurocode 3 Partie 1-1 pour la résistance des barres en acier à section doublement symétrique soumises à une combinaison d'effort axial et de flexion bi-axiale ;
- D'obtenir des paramètres supplémentaires nécessaires pour décrire le comportement théorique des barres soumises, en plus, à un moment de torsion.

Cette étude théorique a mis en évidence qu'il n'est pas possible de développer un modèle entièrement analytique décrivant la résistance des barres soumises à un chargement complexe. En effet, les hypothèses nécessaires pour obtenir des solutions analytiques sont en partie contradictoires (par exemple pour l'approximation de la déformée et de la distribution des

moments de flexion et de torsion). C'est pourquoi, certaines approximations doivent être acceptées lors du développement du modèle de résistance.

Ce modèle de résistance est développé dans la dernière partie de la thèse. Tout d'abord, le modèle existant pour les barres soumises à un effort axial et à de la flexion bi-axiale est étendu au cas de la torsion. Aussi, nous avons élaboré des extensions nécessaires pour couvrir entièrement des sections mono-symétriques. Les extensions proposées sont :

- Suffisamment précises pour couvrir les barres à section doublement symétrique, sensibles ou non à l'instabilité locale de voilement. La perte de précision du modèle de résistance par rapport au cas des barres soumises uniquement à un effort axial et à de la flexion bi-axiale est négligeable pour la pratique ;
- Sécuritaires pour les barres à section en U courtes en raison de l'approximation nécessaire de l'interaction plastique complexe pour ce type de section. Seul une complexification considérable pourrait améliorer la précision des formules d'interaction pour les barres en U ;
- Très sécuritaires pour les barres à section en I mono-symétrique en raison de la réserve plastique en torsion très prononcée. Cette réserve plastique ne peut pas être prise en compte dans le cadre de la proposition mais elle influence la résistance des barres, même celles de longueur intermédiaire. Il pourrait être envisagé de prendre en compte la réserve plastique à l'aide du modèle d'analyse élastique en deux étapes proposé dans le cadre de cette thèse. Cependant, ce type d'analyse n'est pas recommandé ici pour les barres à section mono-symétrique étant donné que la rotation de torsion obtenue au niveau de charge « Etat Limite de Service » (ELS) ne correspond pas à la rotation de torsion réelle de la barre à ce niveau de charge (déterminée par une analyse plus précise – analyse plastique). Par conséquent, il ne peut pas être assuré que les critères ELS sont réellement respectés.

L'imprécision observée pour le modèle de résistance basé sur des formules d'interaction est partiellement due à l'approximation de l'interaction plastique. Afin de franchir cette limite propre aux formules d'interaction, des modèles de résistance plus globaux comme le « Overall Interaction Concept » (OIC) ont été développés dans le passé. Cette approche exprime la résistance d'une barre dans le format χ - λ et peut ainsi lier de façon continue la résistance plastique exacte d'une barre courte avec la résistance à l'instabilité élasto-plastique d'une barre longue. L'OIC a fait ses preuves pour les profils creux. Par conséquent, il semblait intéressant d'étudier si cette approche était également capable de représenter fidèlement la résistance des barres à section ouverte. A l'aide du développement théorique et de la base de données de résultats numériques, une approche simple dans le format OIC a été proposée pour les barres en I doublement symétrique soumises à une combinaison d'effort axial, de flexion bi-axiale et de torsion. Nous avons pu montrer que cette proposition est au moins aussi précise que les formules d'interaction et elle est plus précise que celles-ci pour les barres de longueur faible ou intermédiaire.

NOTATIONS, ACRONYMS AND DEFINITIONS

Definitions:

Hereafter, several terms that are referred to throughout this thesis are defined.

Equivalent structural geometric imperfection:

Geometric imperfection included in the analysis influencing the behaviour and resistance of a structure as a whole like out-of-straightness of columns.

Equivalent geometric member imperfection:

Geometric imperfection included in the analysis of a given member generally not influencing the behaviour of a structure as a whole (in specific cases an influence may exist). This imperfection is applied to replace the influence of arbitrary physical geometric imperfections of members (for example: initial curvature of the member) and to induce member instability modes during numerical simulations (lateral-torsional buckling, flexural buckling, etc.).

Equivalent geometric (local) plate imperfection:

Geometric imperfection included in the analysis of a given member and applied to its constituting plates (flanges and web of the section) generally not influencing the behaviour of a structure as a whole (in specific cases an influence may exist). This imperfection is applied to replace the influence of arbitrary physical geometric imperfections of the cross-section (for example: initial curvature of the web) and to induce local plate instability modes during numerical simulations (local buckling.).

Internal forces and moments:

Forces and moments transiting through a member or a structure necessary to equilibrate the effect of the applied loads (for example: axial force, bending moments, shear force, etc.).

Internal moments:

For simplicity, the term of internal moments is used if only moments transit through a member (including bending moments, torsional moments and the bi-moment but excluding the axial force and the shear forces).

Serviceability Limit State:

State beyond which specified service requirements for a structure or a structural member are no longer met.

Plastic Limit State:

State associated with plastic failure of a member or a section without considering imperfections or geometric non-linearity.

Plastic resistance factor:

Load factor associated with the Plastic Limit State.

Ultimate Limit State:

State associated with collapse or with other similar forms of structural failure.

Ultimate resistance curve:

Curve presented in the λ - χ format linking the relative slenderness λ with the ultimate resistance represented by the ratio R_{ult} (ultimate resistance factor) to R_{pl} (plastic resistance factor).

Ultimate resistance factor:

Load factor associated with the ultimate resistance of a member (or structure).

Acronyms:

The following abbreviations are used in this thesis:

CSM:	Continuous Strength Method
DSM:	Direct Strength Method
FEM:	Finite Element Method
FOSTA:	Forschungsvereinigung für Stahlanwendung (German steel research association)
GMNIA:	Geometrical and Material Non-linear Analysis including imperfections
LA:	Linear (elastic) analysis
LBA:	Linear buckling analysis
MNA:	Material Non-linear Analysis (not including imperfections and the effect of geometric non-linearity)
OIC:	Overall Interaction Concept

Notations

It should be noted that Eurocode 3 notations are used as far as possible in the framework of this thesis. The main notations used here are defined below:

Capital Latin letters:

A:	Area
A_p :	Area contained in the contour of the mid-line of a hollow section
B:	Bi-moment
B_{pl} :	Plastic resistance to the bi-moment
B_R :	Resistance to the bi-moment
C:	Centroid of the cross-section
C_{mLT} :	Moment factor according to Eurocode 3 Part 1-1
C_{my} :	Moment factor according to Eurocode 3 Part 1-1
C_{mz} :	Moment factor according to Eurocode 3 Part 1-1
E:	Young's modulus (of steel)
F_y :	Lateral point load (along y-axis)
F_z :	Vertical point load (along z-axis)

G :	Shear modulus (of steel)
I_0 :	Polar second moment of area
I_y :	Major-axis second moment of area
I_z :	Minor-axis second moment of area
I_t :	Torsion constant
I_w :	Warping constant
L :	Member length
$L_{th,ltbMz}$:	Threshold length for elastic instability of U-shaped members subject to minor-axis bending
M_h :	Bending moment at member ends according to Eurocode 3 Part 1-1
M_s :	Bending moment at mid-span of the member according to Eurocode 3 Part 1-1
M_T :	Applied torsional moment
M_x :	Internal total torsional moment
$M_{x,St,V}$:	Saint Venant's torsional moment
$M_{x,St,V,R}$:	Resistance to the Saint Venant's torsional moment
$M_{x,w}$:	Warping torsional moment
$M_{x,w,R}$:	Resistance to the warping torsional moment
M_y :	Major-axis bending moment
$M_{y,Ed}$:	Design value of the major-axis bending moment
$M_{y,cr}$:	Critical major-axis bending moment for lateral-torsional buckling
$M_{y,cr,I}$:	Critical major-axis bending moment explicitly not considering pre-buckling displacements
$M_{y,cr,II}$:	Critical major-axis bending moment explicitly considering pre-buckling displacements
$M_{y,MNA}$:	Major-axis bending moment at plastic limit state obtained through MNA simulation
$M_{y,pl}$:	Plastic resistance to the major-axis bending moment
$M_{y,R}$:	Major-axis bending moment resistance
$M_{y,Rk}$:	Characteristic value of the major-axis bending moment resistance
$M_{y,ult}$:	Major-axis bending at ultimate limit state (generally obtained by laboratory test or GMNIA analysis)

M_z :	Minor-axis bending moment
$M_{z,Ed}$:	Design value of the minor-axis bending moment
$M_{z,cr}$:	Critical minor-axis bending moment
$M_{z,cr,I}$:	Critical minor-axis bending moment explicitly not considering the effect of pre-buckling displacements
$M_{z,cr,II}$:	Critical minor-axis bending moment explicitly considering the effect of pre-buckling displacements
$M_{z,MNA}$:	Minor-axis bending moment at plastic limit state obtained through MNA simulation
$M_{z,pl}$:	Plastic resistance to the minor-axis bending moment
$M_{z,R}$:	Minor-axis bending moment resistance
$M_{z,Rk}$:	Characteristic value of the minor-axis bending moment resistance
$M_{z,ult}$:	Minor-axis bending moment at ultimate limit state (generally obtained by laboratory test or GMNIA analysis)
N :	Axial force
N_{Ed} :	Design value of the axial force
$N_{cr,y}$:	Critical axial force for flexural buckling about the major-axis
$N_{cr,z}$:	Critical axial force for flexural buckling about the minor-axis
$N_{cr,t}$:	Critical axial force for torsional buckling
N_{MNA} :	Axial force at plastic limit state obtained through MNA simulation
N_{pl} :	Plastic resistance to the axial force
N_R :	Resistance to the axial force
N_{Rk} :	Characteristic value of the resistance to the axial force
N_{ult} :	Axial force at ultimate limit state (generally obtained by laboratory test or GMNIA analysis)
$R_{b,L}$:	Load factor associated with the cross-section resistance (including the effect of local buckling) according to OIC
$R_{b,L+G}$:	Load factor associated with the ultimate member resistance (including the effect of local buckling and member buckling modes) according to OIC
$R_{cr,G}$:	Load amplification factor to attain the critical load for member instability according to OIC (also denoted as α_{cr})

$R_{cr,G}^*$:	Load amplification factor to attain the critical load for member instability considering that the torsion constant I_t equals 0 (=neglecting the Saint-Venant's torsional stiffness of the member – also denoted as α_{cr}^*)
$R_{cr,L}$:	Load amplification factor to attain the critical load for cross-section instability according to OIC
$R_{el,ov}$:	Load amplification factor to attain the elastic cross-section resistance considering all internal forces and moments
$R_{el,MyN}$:	Load amplification factor to attain the elastic cross-section resistance only considering the major-axis bending moment and the axial force
R_{pl} :	Load amplification factor to attain the plastic cross-section resistance according to OIC
$R_{pl,MNA}$:	Numerically determined load factor associated with the plastic limit state (determined through MNA simulations)
$R_{pl,ov}$:	Load amplification factor to attain the plastic cross-section resistance considering all internal forces and moments
$R_{pl,MyN}$:	Load amplification factor to attain the plastic cross-section resistance only considering the major-axis bending moment and the axial force
R_{ult} :	Numerically determined load factor associated with the ultimate member resistance
S:	Shear centre of the cross-section
T:	Temperature
V_z :	Transverse shear force (associated with M_y)
$V_{z,Ed}$:	Design value of transverse shear force
$V_{z,MNA}$:	Transverse shear force at plastic limit state obtained through MNA simulation
$V_{z,pl}$:	Plastic resistance to the transverse shear force
$V_{z,pl,w}$:	Plastic resistance of the web to the transverse shear force
$V_{z,R}$:	Resistance to the transverse shear force
$V_{z,Rk}$:	Characteristic value of the transverse shear force resistance
$V_{z,ult}$:	Transverse shear force at ultimate limit state (generally obtained by laboratory test or GMNIA analysis)
V_y :	Horizontal shear force (associated with M_z)
$V_{y,Ed}$:	Design value of horizontal shear force
$V_{y,MNA}$:	Horizontal shear force at plastic limit state obtained through MNA simulation

$V_{y,pl}$:	Plastic resistance to the horizontal shear force
$V_{y,R}$:	Resistance to the horizontal shear force
$V_{y,Rk}$:	Characteristic value of the horizontal shear force resistance
$V_{y,ult}$:	Horizontal shear force at ultimate limit state (generally obtained by laboratory test or GMNIA analysis)

Notations - Small Latin letters:

a:	Horizontal dimension (used for rectangular hollow sections)
b:	Width
b_f :	Width of the flange
e:	Eccentricity of a load
e_0 :	Amplitude of an equivalent geometric imperfection
e_z :	Eccentricity of a load along the z-axis
e_y :	Eccentricity of a load along the y-axis
f_y :	Yield strength
f_u :	Ultimate strength
h:	Total height of a section (also used for Convection coefficient in paragraph 5.2.5.1)
h_w :	Height of the web
i_0 :	Polar radius of gyration
k_{yz} :	Interaction factor according to Eurocode 3 Part 1-1
k_{yy} :	Interaction factor according to Eurocode 3 Part 1-1
k_{zy} :	Interaction factor according to Eurocode 3 Part 1-1
k_{zz} :	Interaction factor according to Eurocode 3 Part 1-1
$l_{wave/2}$:	Half wavelength of local plate imperfections
m_x :	Distributed torsional load
m_y :	Ratio between the major-axis bending moment M_y and the plastic major-axis bending moment resistance $M_{y,pl}$
m_z :	Ratio between the minor-axis bending moment M_z and the plastic minor-axis bending moment resistance $M_{z,pl}$

- n: Ratio between the axial force N and the plastic resistance N_{pl}
- p: Circumference associated with the mid-line of a hollow section
- r: Radius of the fillets of hot-rolled sections
- r_i : Inner corner radius of a rectangular hollow section (RHS)
- r_o : Outer corner radius of a rectangular hollow section (RHS)
- t: Thickness of a plate
- t_f : Thickness of the flanges
- t_w : Thickness of the web
- u: Longitudinal displacement of the centroid (along the x-axis)
- v: Lateral displacement of the centroid (along the y-axis)
- $v_{,x}$: First derivative of v with respect to x
- $v_{,xx}$: Second derivative of v with respect to x
- w: Vertical displacement of the centroid (along the z-axis)
- $w_{,x}$: First derivative of w with respect to x
- $w_{,xx}$: Second derivative of w with respect to x
- x: Abscissa
- y_c : Position of the centroid of a section along the y-axis
- y_s : Distance between the shear centre and the centroid of a section along the y-axis
- $y_{s,w}$: Distance between the shear centre and the web of a section along the y-axis (used for U sections)
- z_c : Position of the centroid of a section along the z-axis
- z_s : Distance between the shear centre and the centroid of a section along the z-axis

Notations - Greek letters:

- α : Imperfection factor
- $\alpha_{ult,k}$: Minimum load amplifier of the design loads to reach the characteristic resistance of the most critical cross-section according to Eurocode 3 Part 1-1

- α_{cr}^* : Load amplification factor to attain the critical load for member instability considering that the torsion constant I_t equals 0 (=neglecting the Saint-Venant's torsional stiffness of the member – also denoted as $R_{cr,G}^*$ in OIC notations)
- α_{cr} : Load amplification factor to attain the critical load for member instability according to (also denoted as $R_{cr,G}$ in OIC notations)
- $\alpha_{cr,I}$: Load amplification factor to attain the critical load for member instability explicitly not considering the effect of pre-buckling displacements
- $\alpha_{cr,II}$: Load amplification factor to attain the critical load for member instability explicitly considering the effect of pre-buckling displacements
- $\alpha_{cr,op}$: Load amplification factor to attain the critical load for out-of-plane instability of a member without considering the effect of flexural buckling about the major-axis (according to Eurocode 3 Part 1-1)
- β_y : Wagner constant considering the asymmetry of a section with respect to the z-axis
- β_z : Wagner constant considering the asymmetry of a section with respect to the y-axis
- χ : Reduction factor
- χ_L : Reduction factor considering the effect of local buckling according to OIC
- χ_{L+G} : Reduction factor considering the effect of local buckling and member buckling modes according to OIC
- χ_{LT} : Reduction factor associated with lateral-torsional buckling
- χ_{op} : Reduction factor of a structural component for out-of-plane buckling according to Eurocode 3 Part 1-1
- χ_{TF} : Reduction factor associated with torsional-flexural buckling
- χ_y : Reduction factor associated with flexural buckling about the major-axis
- χ_z : Reduction factor associated with flexural buckling about the minor-axis
- ε : Emissivity used in thermal analyses
- ε_y : Yield strain
- ε_{st} : Strain associated with the start of strain hardening
- ε_t : Warping decay factor
- ε_u : Ultimate strain
- φ : Torsional twist

$\varphi_{,x}$:	First derivative of the torsional twist
$\varphi_{,xx}$:	Second first derivative of the torsional twist
γ_{M1} :	Partial (safety) factor for failure modes linked to stability
η :	Generalized imperfection
$\bar{\lambda}$:	Relative slenderness (denoted as λ throughout the text)
$\bar{\lambda}_L$:	Local relative slenderness of a member according to OIC (denoted as λ_L throughout the text)
$\bar{\lambda}_{L+G}$:	Global relative slenderness of a member according to OIC (denoted as λ_{L+G} throughout the text)
$\bar{\lambda}_{LT}$:	Relative slenderness with respect to lateral-torsional buckling (denoted as λ_{LT} throughout the text)
$\bar{\lambda}_{op}$:	Global relative slenderness of a structural component for out-of-plane buckling according to Eurocode 3 Part 1-1 (denoted as λ_{op} throughout the text)
$\bar{\lambda}_t$:	Relative slenderness with respect to torsional buckling (denoted as λ_t throughout the text)
$\bar{\lambda}_{TF}$:	Relative slenderness with respect to torsional-flexural buckling (denoted as λ_{TF} throughout the text)
$\bar{\lambda}_y$:	Relative slenderness with respect to flexural buckling about the major-axis (denoted as λ_y throughout the text)
$\bar{\lambda}_z$:	Relative slenderness with respect to flexural buckling about the minor-axis (denoted as λ_z throughout the text)
ν :	Poisson's ratio
σ :	Stress
ω :	Warping function

TABLE OF CONTENTS

ACKNOWLEDGEMENTS	II
ABSTRACT	III
RESUME ETENDU	V
NOTATIONS, ACRONYMS AND DEFINITIONS	XI
1 INTRODUCTION	1
1.1 Context	2
1.2 Objectives and scope of the thesis	10
1.3 Structure of the thesis	10
1.4 Assumptions and definitions	12
2 BASIC THEORY OF TORSION	15
2.1 General	16
2.2 Stresses and internal forces and moments resulting from torsional loads	16
2.3 Amplitude of Saint-Venant's and warping torsion for open cross-sections	21
2.4 Equivalence between members subject to torsion and members subject to bending and tension axial force	24
2.5 Warping function for open cross-sections	28
2.6 Summary	31
3 FINITE ELEMENT MODEL	33
3.1 General	35
3.2 General description of the finite element model	35
3.2.1 Material law and equivalent imperfections	35
3.2.2 Finite elements used in this thesis	36
3.2.2.1 General	36
3.2.2.2 Beam 4	36
3.2.2.3 Beam 188	36
3.2.2.4 Shell 181	37
3.2.2.5 Solid 185	37
3.2.3 Boundary conditions and loading	38
3.2.3.1 General	38

3.2.3.2 End supports for I sections	38
3.2.3.3 End supports for U sections	39
3.2.3.4 Load introduction	40
3.3 Section modelling	41
3.3.1 Different possibilities to model fillets	41
3.3.2 Study on the influence of meshing density	44
3.3.2.1 General	44
3.3.2.2 Element width for stocky and medium slender cross-sections	45
3.3.2.3 Element aspect ratio	50
3.3.2.4 Element width for slender cross-sections	53
3.3.2.5 Summary on meshing density	56
3.3.3 Evaluation of the stiffness of the different modelling techniques	57
3.3.3.1 General	57
3.3.3.2 Major-axis flexural buckling	58
3.3.3.3 Minor-axis flexural buckling	60
3.3.3.4 Torsional buckling	62
3.3.3.5 Lateral torsional buckling	64
3.3.3.6 Conclusions	66
3.3.4 Plastic section resistance	66
3.3.4.1 General	66
3.3.4.2 Mono-axial bending and axial force	66
3.3.4.3 Torsion	68
3.3.4.4 Interaction between major-axis bending and shear force	76
3.3.4.5 Conclusions	80
3.3.5 Influence of fillets on the member resistance	82
3.3.6 Choice of the numerical model	86
3.4 Comparison of the numerical model to physical tests	87
3.4.1 General	87
3.4.2 Tests performed at TU Berlin	87
3.4.2.1 Numerical model	87
3.4.2.2 Results for I sections	89
3.4.2.3 Results for U sections	91
3.4.2.4 Summary of the results	93
3.4.2.5 Influence of the fillets on the test results	94
3.4.3 Conclusions	96
4 PLASTIC CROSS-SECTION RESISTANCE	99
4.1 Introduction	101
4.2 Assessing the plastic cross-section resistance	102
4.2.1 Plastic interaction in various standards	102
4.2.1.1 Internal forces and moments creating only axial stresses	102
4.2.1.2 Interaction between shear and axial stresses	108

4.2.2 Numerical tools for the cross-section interaction	116
4.2.2.1 General	116
4.2.2.2 Iterative calculation based on predefined elastic stress distribution	116
4.2.2.3 Partial internal force method	120
4.2.3 Conclusions	131
4.3 Laboratory tests performed at University of Applied Sciences of Western Switzerland	133
4.3.1 Motivation	133
4.3.2 Choice of the test specimen and test program	133
4.3.3 Test set-up	137
4.3.4 Preparatory measurements	139
4.3.4.1 General	139
4.3.4.2 Dimensions of the cross-sections	139
4.3.4.3 Tensile tests characterising the material behaviour	141
4.3.5 Three point bending tests	143
4.3.6 Numerical simulations of the laboratory tests	145
4.3.6.1 Presentation of the numerical model	145
4.3.6.2 Comparison between numerical model and laboratory tests	146
4.3.6.3 Comparison between laboratory tests and resistance models	150
4.3.7 Complementary numerical simulations and comparison to resistance models	155
4.3.8 Conclusions	162
4.4 Parametric study and resistance model	163
4.4.1 General remarks	163
4.4.1.1 Studied cross-sections	163
4.4.1.2 Load cases	165
4.4.1.3 Material model	167
4.4.2 Interaction between major-axis bending and shear force	169
4.4.2.1 Double symmetric I sections	169
4.4.2.2 U sections	173
4.4.2.3 Mono-symmetric I sections	177
4.4.3 Interaction between minor-axis bending and shear force	184
4.4.3.1 Double symmetric I sections	184
4.4.3.2 U sections	186
4.4.3.3 Mono-symmetric I sections	188
4.4.3.4 Conclusions	190
4.4.4 Interaction between bending, shear force and torsion	191
4.4.4.1 Influence of the plastic torsional system reserve of the member	191
4.4.4.2 Double symmetric I sections	205
4.4.4.3 Mono-symmetric I sections	219
4.4.4.4 U sections	228
4.4.5 Other selected cases	238
4.4.5.1 General	238
4.4.5.2 Combined axial force, bending and torsion for double symmetric I sections	238
4.4.5.3 Combined axial force and major-axis bending for U sections	241

4.4.5.4 Conclusions	245
4.5 Proposed resistance model	246
4.6 General conclusions concerning the plastic cross-section resistance	255
5 MEMBER RESISTANCE	257
5.1 Introduction	260
5.2 Numerical study – Particular modelling aspects	262
5.2.1 Influence of assumed imperfections on the ultimate member resistance	262
5.2.1.1 General	262
5.2.1.2 Residual stresses for double symmetric I sections	262
5.2.1.3 Residual stresses for welded mono-symmetric I sections	267
5.2.1.4 Equivalent geometric member imperfection for I sections	270
5.2.1.5 Residual stresses for U sections	271
5.2.1.6 Equivalent geometric member imperfection for U sections	285
5.2.1.7 Equivalent geometric plate imperfection	300
5.2.2 Influence of loading sequence	305
5.2.3 Influence of local plate instability on ultimate member resistance	308
5.2.3.1 General	308
5.2.3.2 Calibration of rigid beam elements	309
5.3 Design proposals for the resistance of members subject to combined axial force and bi-axial bending without torsion	314
5.3.1 General	314
5.3.2 Double symmetric members	314
5.3.3 Extension of the Eurocode 3 Part 1-1 interaction equations to mono-symmetric I and U sections	318
5.4 Review of design proposals for members with open section subject to combined axial compression, bending and torsion	321
5.4.1 General	321
5.4.2 Great Britain: BS 5950-1;2000 and SCI Publication 057	322
5.4.3 Design rules proposed at RWTH Aachen	326
5.4.3.1 General	326
5.4.3.2 Proposal RWTH Aachen I	326
5.4.3.3 Proposal RWTH Aachen II	331
5.4.3.4 Proposal RWTH Aachen III	340
5.4.3.5 Summary of design proposals made at RWTH Aachen	344
5.4.4 Design rule proposed at TU Berlin	345
5.4.5 Design rule proposed at Eindhoven University of Technology	347
5.4.6 Summary of the proposals and comparison to physical tests	352
5.4.7 Conclusions	358

5.5 Analytical solutions	359
5.5.1 General	359
5.5.2 Assumptions	359
5.5.3 System of axis and kinematics	360
5.5.4 Energy method, equilibrium of the member and critical loads	361
5.5.4.1 General	361
5.5.4.2 Energy method	363
5.5.4.3 Differential equations characterizing the second order static equilibrium of the member	365
5.5.4.4 Elastic stability and state of indifferential equilibrium	367
5.5.5 Determination of critical loads for I-shaped members	372
5.5.5.1 Common approach neglecting pre-buckling displacements	372
5.5.5.2 Influence of pre-buckling displacements	376
5.5.5.3 Conclusions	381
5.5.6 Determination of critical loads for U-shaped members	382
5.5.6.1 Common approach neglecting pre-buckling displacements	382
5.5.6.2 Influence of pre-buckling displacements	384
5.5.7 Elastic second order equilibrium of the member	400
5.5.7.1 General	400
5.5.7.2 Members of double symmetric I section subject to constant major-axis bending	402
5.5.7.3 Members of double symmetric I section subject to major-axis bending and axial force	407
5.5.7.4 Members subject to bending and torsion	416
5.5.7.5 Members subject to combined bi-axial bending, axial force and torsion	430
5.5.7.6 Conclusions	433
5.6 Numerical parametric study	435
5.6.1 General	435
5.6.2 Scope of the parametric study	436
5.6.2.1 Representation of the results	436
5.6.2.2 Cross-sections	438
5.6.2.3 Load cases	439
5.6.2.4 Influence of steel grade on the ultimate member resistance	444
5.6.3 Overall results	447
5.6.4 Design based on interaction formulae	452
5.6.4.1 General	452
5.6.4.2 Members with double symmetric I sections	455
5.6.4.3 Members with mono-symmetric I sections	491
5.6.4.4 Members with U sections	500
5.6.4.5 Summary of the design of members subject to torsion based on interaction equations	518
5.6.5 Design based on OIC approach – Double symmetric I sections	523
5.6.5.1 General requirements for the OIC approach to be developed	523
5.6.5.2 OIC approach for lateral-torsional buckling	525

5.6.5.3 OIC approach for flexural buckling under combined minor-axis bending and axial force	535
5.6.5.4 OIC approach for lateral-torsional buckling under combined major- and minor-axis bending	543
5.6.5.5 OIC approach for combined major-axis bending and axial force	551
5.6.5.6 OIC approach for combined bi-axial bending and axial force	559
5.6.5.7 Extension of the OIC approach to torsion	568
5.6.5.8 Summary of the OIC approach for the resistance of members of double symmetric I section	578
5.7 Conclusions	582
6 GENERAL CONCLUSIONS	585
6.1 Summary and conclusions	586
6.2 Original contributions of the present thesis	591
6.3 Future research	593
6.4 Publications	595
7 REFERENCES	597
8 ANNEXES	603
8.1 Annex A: Recall of Annex A of EN 1993-1-1:2005	604
8.2 Annex B: Measured geometry and material law for the laboratory tests performed at University of Applied Sciences of Western Switzerland	606
8.3 Annex C: Sections used for the parametric study concerning the member resistance	614

1 INTRODUCTION

1.1	Context	2
1.2	Objectives and scope of the thesis	10
1.3	Structure of the thesis	10
1.4	Assumptions and definitions	12

1.1 Context

In practice, steel members are mainly subject to a combination of axial force and major-axis or bi-axial bending. Especially, for members of open-cross section, torsional loads should be avoided as much as possible. Yet, in some cases, the application of torsion is **inevitable**. For example, crane girders (see beams painted in blue of Figure 1-1), i.e. girders supporting moveable cranes, experience torsion as the loads resulting from the braking of the carriage are generally introduced in the upper flange and therefore above the shear centre. Sometimes, the erection process leads to loads applied outside the shear centre, too. A typical example is a girder supporting a pre-cast slab that is typically supported by the flange of the cross-section. The torsional load may even increase if it is not possible to cast the additional part of the slab symmetrically. This situation should obviously be avoided. Also, U-shaped members are generally subject to torsional moments as the loads are introduced through the web and consequently with an eccentricity to the shear centre. In some cases, U sections may also be used for architectural reasons as shown in Figure 1-2. Hence, even if members of open cross-sections are less frequently used in case of torsion, this load case is of practical interest and should be treated in design standards. However, the major international steel design standards do not include explicit and practical recommendations for the design of steel members subject to combined axial force, bending and torsion.



Figure 1-1: Example of a crane girder



Figure 1-2: Example of U-shaped member used for architectural reasons

The European standard for the design of steel structures, EN 1993-1-1 – Eurocode 3: Design of steel structures – Part 1-1: General rules and rules for buildings (CEN 2005a) only addresses the design of members subject to combined axial force and bi-axial bending on behalf of the well accepted interaction equations reproduced in Eq. (1.1).

$$\frac{N_{Ed}}{\chi_y \frac{N_{Rk}}{\gamma_{M1}}} + k_{yy} \frac{M_{y,Ed} + \Delta M_{y,Ed}}{\chi_{LT} \frac{M_{y,Rk}}{\gamma_{M1}}} + k_{yz} \frac{M_{z,Ed} + \Delta M_{z,Ed}}{\frac{M_{z,Rk}}{\gamma_{M1}}} \leq 1,0$$

$$\frac{N_{Ed}}{\chi_z \frac{N_{Rk}}{\gamma_{M1}}} + k_{zy} \frac{M_{y,Ed} + \Delta M_{y,Ed}}{\chi_{LT} \frac{M_{y,Rk}}{\gamma_{M1}}} + k_{zz} \frac{M_{z,Ed} + \Delta M_{z,Ed}}{\frac{M_{z,Rk}}{\gamma_{M1}}} \leq 1,0$$

(1.1)

One notices that two distinct design criteria have to be fulfilled. The first design criterion considers the second order effects created by the axial force and the influence of equivalent imperfection about the major-axis (mainly considered in χ_y) and the second criterion considers the second order effects of the axial force and the equivalent imperfection about the minor-axis (mainly considered in χ_z). The second order effects arising from lateral torsional buckling are mostly accounted for through the reduction factor χ_{LT} . The interaction factors k_{ij} account for possible plasticity (in case of compact sections – sections of class 1 and 2 following (CEN 2005a)) and consequently non-linear interaction between the internal forces. Additionally, they consider partially the second order effects arising from the axial force and the major-axis bending moment. The theoretical derivation of the interaction formulae is discussed extensively in references

(Boissonnade et al. 2002), (Boissonnade et al. 2004), (Villette 2004), (Greiner et al. 2006) and (ECCS 2006). Here it is not be discussed in detail.

The interaction factors may be determined by Annex B of EN 1993-1-1 as shown in Figure 1-3 and Figure 1-4. A second method for the determination of the interaction factors k_{ij} is proposed in Annex A of the same standard. However, this method is not represented here as it is applied less frequently in the practice due to its complexity (see Annex A of this thesis).

It should be noted that independently from the method used for the determination of the interaction factors, the field of application of the interaction formulae represented in Eq. (1.1) is limited to:

- Members with constant cross-section along their length;
- Members with double symmetric cross-section;
- Members possessing cross-sections not sensitive to distortional buckling;
- Members without any intermediate lateral restraint;
- Members not subject to applied torsional moments.

In recent years, several research projects aimed at closing some of the gaps listed above. In particular, one may cite references (Kaim 2004) and (Kalameya 2008) proposing an extension to mono-symmetric I and U sections respectively. In reference (Aswandy 2007) the extension of the interaction equations to members with intermediate lateral restraints is investigated. Finally, the extension of the interaction equations to tapered members (members with non-constant cross-section over their length) is studied in (Marques et al. 2014). It should be mentioned that all of the research works cited here before concentrate on extensions based on Annex B interaction factors as these possess a wider practical application. One should also note that the proposals given to overcome the limits of the interaction Eurocode 3 Part 1-1 interaction formulae have not been integrated into the current version of this design standard.

Interaction factors	Type of sections	Design assumptions	
		elastic cross-sectional properties class 3, class 4	plastic cross-sectional properties class 1, class 2
k_{yy}	I-sections RHS-sections	$C_{my} \left(1 + 0,6 \bar{\lambda}_y \frac{N_{Ed}}{\chi_y N_{Rk} / \gamma_{M1}} \right)$ $\leq C_{my} \left(1 + 0,6 \frac{N_{Ed}}{\chi_y N_{Rk} / \gamma_{M1}} \right)$	$C_{my} \left(1 + (\bar{\lambda}_y - 0,2) \frac{N_{Ed}}{\chi_y N_{Rk} / \gamma_{M1}} \right)$ $\leq C_{my} \left(1 + 0,8 \frac{N_{Ed}}{\chi_y N_{Rk} / \gamma_{M1}} \right)$
k_{yz}	I-sections RHS-sections	k_{zz}	$0,6 k_{zz}$
k_{zy}	I-sections RHS-sections	$0,8 k_{yy}$	$0,6 k_{yy}$
k_{zz}	I-sections	$C_{mz} \left(1 + 0,6 \bar{\lambda}_z \frac{N_{Ed}}{\chi_z N_{Rk} / \gamma_{M1}} \right)$ $\leq C_{mz} \left(1 + 0,6 \frac{N_{Ed}}{\chi_z N_{Rk} / \gamma_{M1}} \right)$	$C_{mz} \left(1 + (2\bar{\lambda}_z - 0,6) \frac{N_{Ed}}{\chi_z N_{Rk} / \gamma_{M1}} \right)$ $\leq C_{mz} \left(1 + 1,4 \frac{N_{Ed}}{\chi_z N_{Rk} / \gamma_{M1}} \right)$
	RHS-sections	$C_{mz} \left(1 + 0,6 \bar{\lambda}_z \frac{N_{Ed}}{\chi_z N_{Rk} / \gamma_{M1}} \right)$ $\leq C_{mz} \left(1 + 0,6 \frac{N_{Ed}}{\chi_z N_{Rk} / \gamma_{M1}} \right)$	$C_{mz} \left(1 + (\bar{\lambda}_z - 0,2) \frac{N_{Ed}}{\chi_z N_{Rk} / \gamma_{M1}} \right)$ $\leq C_{mz} \left(1 + 0,8 \frac{N_{Ed}}{\chi_z N_{Rk} / \gamma_{M1}} \right)$

For I- and H-sections and rectangular hollow sections under axial compression and uniaxial bending $M_{y,Ed}$ the coefficient k_{zy} may be $k_{zy} = 0$.

a) Members without lateral-torsional buckling

Interaction factors	Design assumptions	
	elastic cross-sectional properties class 3, class 4	plastic cross-sectional properties class 1, class 2
k_{yy}	k_{yy} from Table B.1	k_{yy} from Table B.1
k_{yz}	k_{yz} from Table B.1	k_{yz} from Table B.1
k_{zy}	$\left[1 - \frac{0,05 \bar{\lambda}_z}{(C_{mLT} - 0,25) \chi_z N_{Rk} / \gamma_{M1}} \frac{N_{Ed}}{\gamma_{M1}} \right]$ $\geq \left[1 - \frac{0,05}{(C_{mLT} - 0,25) \chi_z N_{Rk} / \gamma_{M1}} \frac{N_{Ed}}{\gamma_{M1}} \right]$	$\left[1 - \frac{0,1 \bar{\lambda}_z}{(C_{mLT} - 0,25) \chi_z N_{Rk} / \gamma_{M1}} \frac{N_{Ed}}{\gamma_{M1}} \right]$ $\geq \left[1 - \frac{0,1}{(C_{mLT} - 0,25) \chi_z N_{Rk} / \gamma_{M1}} \frac{N_{Ed}}{\gamma_{M1}} \right]$ for $\bar{\lambda}_z < 0,4$: $k_{zy} = 0,6 + \bar{\lambda}_z \leq 1 - \frac{0,1 \bar{\lambda}_z}{(C_{mLT} - 0,25) \chi_z N_{Rk} / \gamma_{M1}} \frac{N_{Ed}}{\gamma_{M1}}$
k_{zz}	k_{zz} from Table B.1	k_{zz} from Table B.1

b) Members with lateral torsional buckling

Figure 1-3: Annex B of EN 1993-1-1 - Determination of interaction factors k_{ij} for a) members not susceptible to lateral torsional buckling and b) members susceptible to lateral torsional buckling

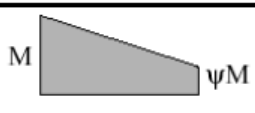
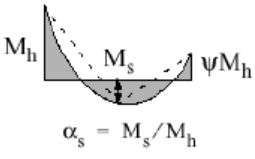
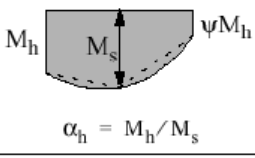
Moment diagram	range		C_{my} and C_{mz} and C_{mLT}	
			uniform loading	concentrated load
	$-1 \leq \psi \leq 1$		$0,6 + 0,4\psi \geq 0,4$	
	$0 \leq \alpha_s \leq 1$	$-1 \leq \psi \leq 1$	$0,2 + 0,8\alpha_s \geq 0,4$	$0,2 + 0,8\alpha_s \geq 0,4$
	$-1 \leq \alpha_s < 0$	$0 \leq \psi \leq 1$	$0,1 - 0,8\alpha_s \geq 0,4$	$-0,8\alpha_s \geq 0,4$
$-1 \leq \psi < 0$		$0,1(1-\psi) - 0,8\alpha_s \geq 0,4$	$0,2(-\psi) - 0,8\alpha_s \geq 0,4$	
	$0 \leq \alpha_h \leq 1$	$-1 \leq \psi \leq 1$	$0,95 + 0,05\alpha_h$	$0,90 + 0,10\alpha_h$
	$-1 \leq \alpha_h < 0$	$0 \leq \psi \leq 1$	$0,95 + 0,05\alpha_h$	$0,90 + 0,10\alpha_h$
		$-1 \leq \psi < 0$	$0,95 + 0,05\alpha_h(1+2\psi)$	$0,90 - 0,10\alpha_h(1+2\psi)$
For members with sway buckling mode the equivalent uniform moment factor should be taken $C_{my} = 0,9$ or $C_{Mz} = 0,9$ respectively.				
C_{my} , C_{mz} and C_{mLT} should be obtained according to the bending moment diagram between the relevant braced points as follows:				
moment factor	bending axis	points braced in direction		
C_{my}	y-y	z-z		
C_{mz}	z-z	y-y		
C_{mLT}	y-y	y-y		

Figure 1-4: Annex B of EN 1993-1-1 - Equivalent uniform moment factors

Additionally to the interaction formulae, the current version of Eurocode 3 Part 1-1 proposes the general method for lateral and lateral torsional buckling of structural components in order to overcome some of the limits of the interaction formulae. This method may be represented by Eq. (1.2)

$$\frac{\chi_{op} \alpha_{ult,Rk}}{\gamma_{M1}} \geq 1,0 \tag{ 1.2 }$$

Conversely to the interaction equations, the general method may be applied to members of non-constant cross-section and intermediate lateral restraints. However, it is limited to combined major-axis bending and axial force. Consequently, members subject to an additional minor-axis bending moment or torsional moments cannot be treated. Therefore, this method seems even more limited than the interaction formulae represented in Eq. (1.1) if their extensions proposed in (Kaim 2004), (Aswandy 2007), (Kalameya 2008) and (Marques et al. 2014) are considered. Also, the general method is limited to sections symmetric about their minor-axis. Hence, the stability of U-shaped members cannot be verified using this method.

The two methods mentioned before should be applied to verify the resistance of the member including member second order effects and member imperfection. This verification becomes relevant when the members are slender and fail before they attain the resistance of the most loaded cross-section. However, even for the **cross-section** resistance, i.e. the resistance of short members that do not fail by member instability, Eurocode 3 Part 1-1 does not give clear design rules for compact sections likely to attain full yielding in case of combined internal forces including torsion. Due to this lack of provisions, the cross-section design is limited to the elastic

resistance. For I sections a proposal has been made by Mirambel in reference (Mirambel et al. 2016) to close this gap. This proposal is discussed in detail in Chapter 4 of this thesis. Anyhow, it is not applicable to U sections and therefore cannot completely eliminate the restrictions of Eurocode 3 Part 1-1.

Consequently, it may be concluded that even if some research effort has been spent to extend the field of application of the Eurocode 3 Part 1-1 methods, up to date there exists no practical approach for the design of members of open cross-section subject to torsion.

Other major international standard propose different interaction formulae. Nevertheless, the field of application is very close to the European interaction equations. As an example, the American national standard ANSI/AISC 360-10 may be cited. For double symmetric cross-sections, it proposes the following interaction equation for combined axial compression and bi-axial bending (the notations of Eurocode 3 Part 1-1 are used as far as possible):

$$\frac{N_{Ed}}{2 \times 0,9N_{c,Rk}} + \left(\frac{M_{y,Ed}}{0,9\chi_{LT}M_{y,Rk}} + \frac{M_{z,Ed}}{0,9M_{z,Rk}} \right) \leq 1,0 \quad \text{for } \frac{N_{Ed}}{0,9N_{c,Rk}} < 0.2$$

$$\frac{N_{Ed}}{0,9N_{c,Rk}} + \frac{8}{9} \left(\frac{M_{y,Ed}}{0,9\chi_{LT}M_{y,Rk}} + \frac{M_{z,Ed}}{0,9M_{z,Rk}} \right) \leq 1,0 \quad \text{for } \frac{N_{Ed}}{0,9N_{c,Rk}} \geq 0.2 \quad (1.3)$$

$$\text{And : } N_{c,Rk} = \text{Min}(\chi_y, \chi_z, \chi_T)N_{Rk}$$

It should be noted that the moments $M_{y,Ed}$ and $M_{z,Ed}$ should include global and member second order effects. The effect of local instability is considered through a reduction of the plastic cross-section resistances N_{Rk} , $M_{y,Rk}$ and $M_{z,Rk}$. In case of mono-symmetric or unsymmetrical cross-sections the maximum resulting von Mises stress, including second order effects, should be less than the yield strength. Hence, a possible plastic resistance is not accounted for leading to very safe-sided results for compact sections. Moreover, the case of applied torsional loads is not treated explicitly.

Only two major international design standards have been rapidly presented here. However, it appears that the resistance of members subject to torsion is not satisfactorily addressed in any major steel design standards.

In the past, several design approaches were proposed for the resistance of members subject to torsion as summarized in Table 1-1. Yet, except the proposal entitled "Berlin" none of them has been incorporated in Eurocode 3. The proposal entitled "BSI and Nethercott" was recommended in the former British standard BS 5950-1 (BSI 2000). Nonetheless, it was not considered for Eurocode 3. In Chapter 5 of this thesis, the proposals will be analysed in detail. Still, even without detailing these approaches further on, it may be seen that none of them possesses a field of application sufficiently wide to be applied to I- and U-shaped members subject to combined axial force, bi-axial bending and torsion.

Table 1-1: Summary of available design approaches for the resistance of members subject to torsion

Proposal (reference)	Field of application		Limitations
	Shape of the section	Load case	
BSI and Nethercott (Nethercott et al. 1989)	I and U sections	M_y, M_z, M_T	No axial force N
Aachen I (FOSTA 2004)	I sections	N, M_y, M_z, M_T	Not applicable to U sections
Aachen II (Stangenberg 2007)	I and U sections	N (for I sections), M_y, M_z, M_T	No axial force in case of mono-symmetric sections
Aachen III (Naumes 2009)	I sections	N, M_y, M_z, M_T	Not applicable to U sections
Berlin* (Glitsch 2008)	I sections	M_y, M_z, M_T	No axial force Not applicable to U sections
Eindhoven (de Louw 2007)	U sections	M_y, M_T – loads applied in the web plane	No axial force and minor axis bending Not applicable to I sections

*included in Annex A of EN 1993-6 (CEN 2007b)

Last, it seems interesting to mention that “global design methods”, as the Direct Strength Method DSM and the Overall Interaction Concept OIC, have become more and more popular in the last decade compared to interaction formulae as the ones proposed in Eurocode 3 Part 1-1 or ANSI/AISC 360. These global design approaches generally promise:

- Full continuity between cross-section and member resistance;
- Mechanically consistent and comprehensible resistance predictions;
- Simple and direct design equations.

Recently, several research projects promoted OIC especially for tubular cross-sections as illustrated in references (Taras 2011), (Boissonnade et al. 2013), (Li 2014), (Nseir 2015), (Boissonnade et al. 2017). Thanks to these studies a fully continuous and consistent design approach for the resistance of rectangular and circular hollow sections under combined axial force and bi-axial bending has been developed. The principle of OIC is illustrated in Figure 1-5.

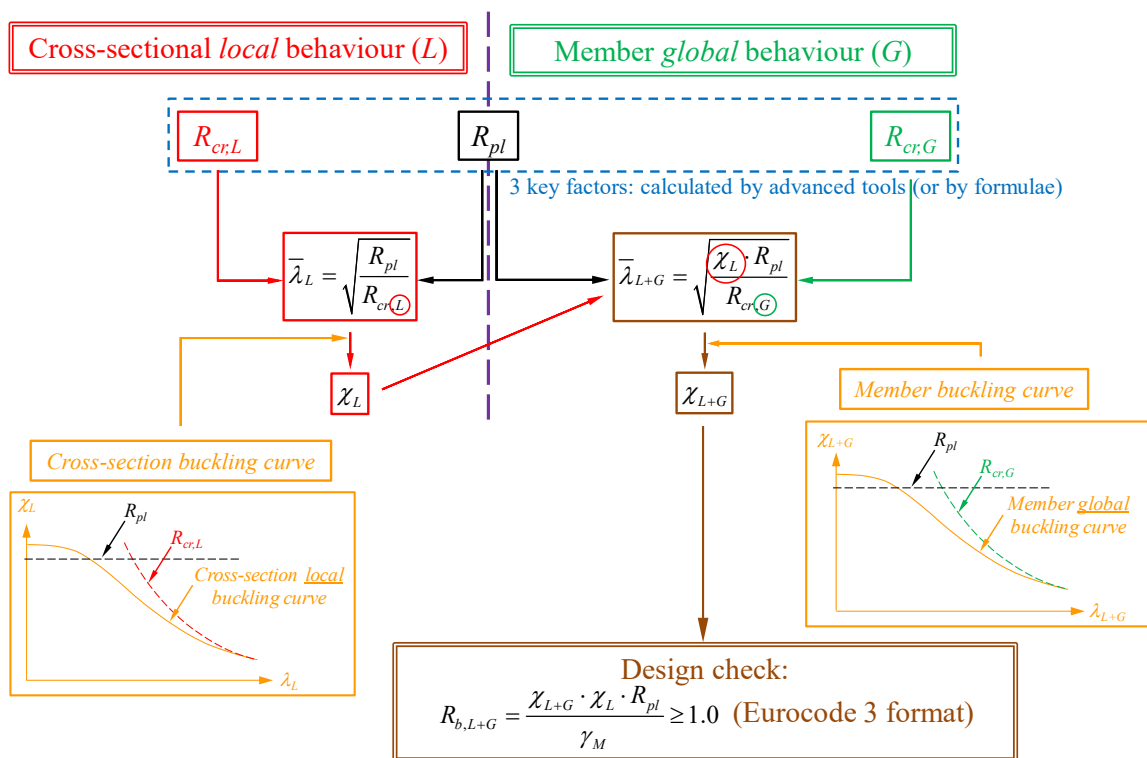


Figure 1-5: Main principle of OIG

As shown in Figure 1-5, OIG is based on 7 steps that are:

- Determination of the load amplification factor leading to the plastic limit state of the cross-section: R_{pl}
- Determination of load amplification factor leading to local instability of the cross-section: $R_{cr,L}$
- Determination of the cross-section slenderness: λ_L
- Determination of the cross-section resistance reduction depending on the cross-section slenderness: χ_L
- Determination of load amplification factor leading to member instability: $R_{cr,G}$
- Determination of the member slenderness: λ_{L+G}
- Determination of the member resistance reduction depending on the cross-section slenderness: χ_{L+G}

Even if the OIG seems promising, up to date open cross-section have been treated in a rather limited extend in references (Kettler 2008) and (Taras 2011) addressing the cross-section and in-plane member resistance of double symmetric I sections. In particular, applied torsion and out-of-plane instability including torsional twist (flexural torsional buckling, lateral torsional) have not been in the centre of OIG research yet. Also, the resistance of members of mono-symmetric

cross-sections has not been treated. Therefore, it seems that an important research effort is still necessary to extend OIC to open cross-sections and complex combination of internal forces and moments as well as interaction between different modes of instability.

1.2 Objectives and scope of the thesis

The three main objectives of this thesis directly result from the limitations of the steel design standards outlined before:

- Study of the behaviour of members subject to combined axial compression, bi-axial bending and torsion.
- Derive design provisions addressing the plastic cross-section **resistance of open sections** subject to combined axial compression, bi-axial bending and torsion.
- Derive design provisions addressing the **resistance of members** subject to combined axial compression, bi-axial bending and torsion.

Moreover, it is intended to propose rules that represent an extension of the well-accepted design provisions given in Eurocode 3 Part 1-1 in order to facilitate the acceptance for practical design engineers. Yet, the possibility of design rules based on a global design concept as the OIC is studied as this approach may contribute to the simplification and unification of the design provisions currently available in steel design standards.

However, due to the large field of parameters that will be included in the study performed to achieve the objectives of this thesis the scope of the research presented hereafter had to be limited to:

- **Double symmetric I** sections whose cross-section may be sensitive to local plate buckling or not (class 1 to class 4 sections in the terminology of Eurocode 3 Part 1-1). I sections may be fabricated from hot rolling or welding.
- **Compact welded mono-symmetric I sections** and **hot-rolled U sections of type UPE** always attaining their theoretical plastic cross-section resistance if member instability becomes negligible (class 1 or class 2 in the terminology of Eurocode 3 Part 1-1).

1.3 Structure of the thesis

This first chapter has given a short introduction showing that the resistance of members subject to torsion in addition to axial compression and bending is not treated satisfactorily in the current design standards. In consequence, three main objectives for this thesis are formulated.

Chapter 2 addresses briefly the theory of torsion necessary to understand the behaviour of members with open cross-section. The difference to members with closed sections is highlighted and it is shown why open cross-sections may be sensitive to torsion.

In order to develop a comprehensive design approach covering the resistance of I- and U-shaped members, an extensive numerical study is necessary. The Finite Element model used for this purpose is presented in detail in *Chapter 3*. Different modelling techniques are investigated in order to represent as precisely as possible the physical member. The Finite Element model is then validated with reference to analytical results and physical tests found in the literature.

Chapter 4 is dedicated to the plastic cross-section resistance and interaction relevant for the design of short and compact members. Especially global design methods (for example OIC) employ the plastic cross-section resistance also as key parameter for the design of long and slender members. Consequently, the plastic **cross-section resistance** under combined loading is of importance when the **member resistance** is addressed. In a first step design approaches found in standards and in the literature are reviewed and discussed. This analysis leads to several questions. In order to obtain the elements necessary to give satisfactory answers, a campaign of physical tests as well as an extensive numerical study are performed and the results are presented. Finally, a practical design approach is proposed and validated.

Chapter 5 then addresses the member resistance including second order effects and the effect of elasto-plastic instability. The design proposal developed in this chapter is based on an extensive numerical study. In order to ensure the reliability of the numerical simulations the influence of assumed calculation imperfection on the obtained results is studied. After this, the design proposals given in Table 1-1 are discussed in detail. With the help of the validated finite element model, limitations and inconsistencies of these design approaches are highlighted.

So as to develop a design approach covering members of open cross-section under a complex load combination including torsion, it appears necessary to study their behaviour theoretically. In a first step, analytical solutions for the elastic critical loads of I- and U-shaped members are recalled and extended. After this an analytical study derives second order internal forces and moments for members in combined axial force, bi-axial bending and torsion. These analytical solutions are helpful to identify which parameters are essential to describe the member stability. Thereafter, the data basis of numerical simulations, covering more than 10 000 cases, is used for the development of a **simple** design model. Indeed, so as to facilitate the acceptance of the design model in practice, it is intended to propose an extension of the Eurocode 3 Part 1-1 interaction equations addressing the member instability. This extension should not significantly increase the complexity of the interaction equations in their current field of application. Consequently, a certain loss of precision is explicitly accepted. Nonetheless, a second design approach is elaborated in the OIC format so as overcome some limitations of the Eurocode 3 Part 1-1 interaction equations.

Finally, *Chapter 6* summarizes the original contributions of this thesis and details future research needs required to extend the results of this thesis.

1.4 Assumptions and definitions

The developments presented in the framework of this thesis are based on the system of axis shown in Figure 1-6.

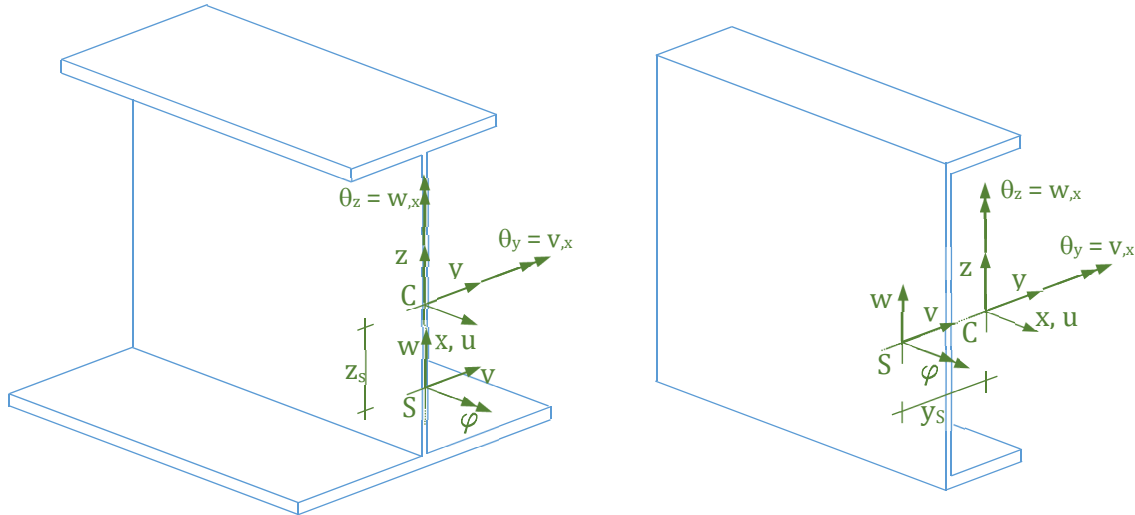


Figure 1-6: Reference system

It has to be insisted on the definition of positive displacement and internal forces and moments as the sign convention is of high importance for non-symmetric cross-sections. Hereafter it is assumed that:

- Compression stresses are negative and tension stresses are positive;
- A negative axial force creates tension stresses in the section;
- A positive major-axis bending moment creates compression stresses in the upper flange ($z > 0$);
- A positive minor-axis bending moment creates compression stresses for positive y -coordinates (tips of the flanges for U section and right part of the flange for I sections – see Figure 1-6);
- A positive bi-moment (see Chapter 2) creates compression stresses if both coordinates y and z are positive, i.e. at the right tip of the upper flange, or negative, i.e. at the left tip of the lower flange.

Figure 1-7 represents the positive directions of the bending moments and the bi-moment. It has to be noted that the web of the U section is always supposed to be situated on the left of the centroid ($y < 0$).

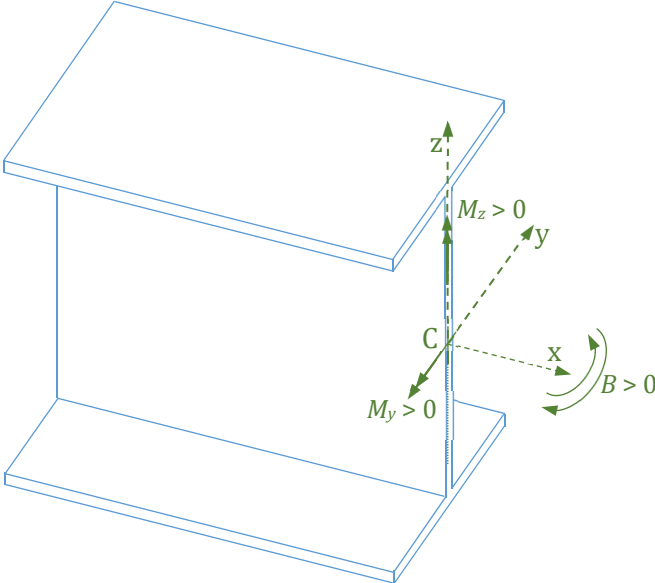


Figure 1-7: Definition of positive moments

2 BASIC THEORY OF TORSION

2.1	General	16
2.2	Stresses and internal forces and moments resulting from torsional loads	16
2.3	Amplitude of Saint Venant's and warping torsion for open cross-sections	22
2.4	Equivalence between members subject to torsion and members subject to bending and tension axial force	24
2.5	Warping function for open cross-sections	28
2.6	Summary	32

2.1 General

The present Chapter provides a brief review of the elastic theory of torsion. However, the discussion represented hereafter concentrates on points that necessary to understand the results presented in Chapters 4 and 5. Very detailed presentations on the theory of torsion may be found in many publications as for example in (Vlasov 1962), (Tmoshenko et al. 1970) (de Ville de Goyet 1989), (Friemann et al. 2005) and (Bazant et al. 2010).

2.2 Stresses and internal forces and moments resulting from torsional loads

The two main terms to be distinguished in the following are twisting and warping. Figure 2-1 represents both for the example of an I section.

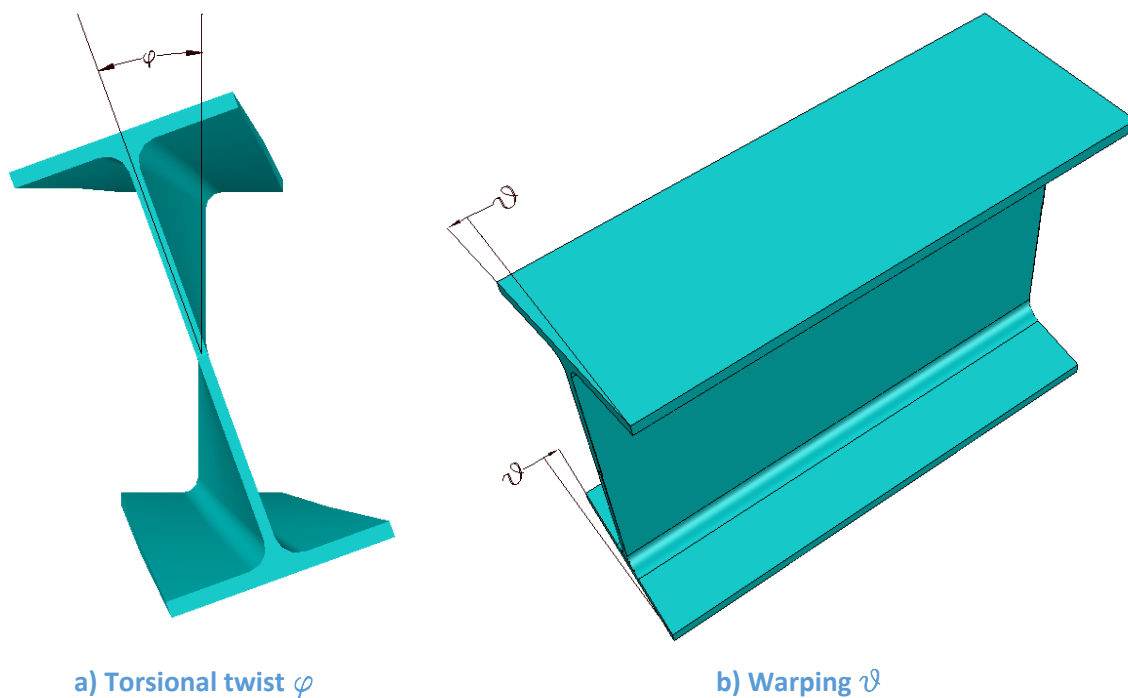


Figure 2-1: Representation of a) torsional twist and b) warping

For a double symmetric I section warping generates axial displacements of the flanges (associated to rotation ϑ in Figure 2-1). Members loaded by constant torsional moment and possessing no restraint to these axial displacements, or warping, along their length and at their ends are exclusively subject to “pure” or “Saint Venant’s” torsion, denoted as $M_{x,St.V}$ hereafter. In this case the cross-sections along the member are only subject to shear stresses. The associated stress pattern depends on the cross-section shape as recalled in Figure 2-2. It may be observed that the shear stresses are practically uniformly distributed over the thickness of a thin walled closed cross-sections. Indeed, there is a small variation of the shear stresses through the thickness. In case of open cross-section, the shear stresses resulting from Saint Venant’s torsion vary linearly over the thickness. Consequently, the lever arm of the stress resultants is only of about half of the

plates thickness whereas it is equal to the distance between the plates of the rectangular hollow section (a and b in Figure 2-3) leading to a much higher resistance to Saint Venant's torsion this type of section (see Table 2-1).

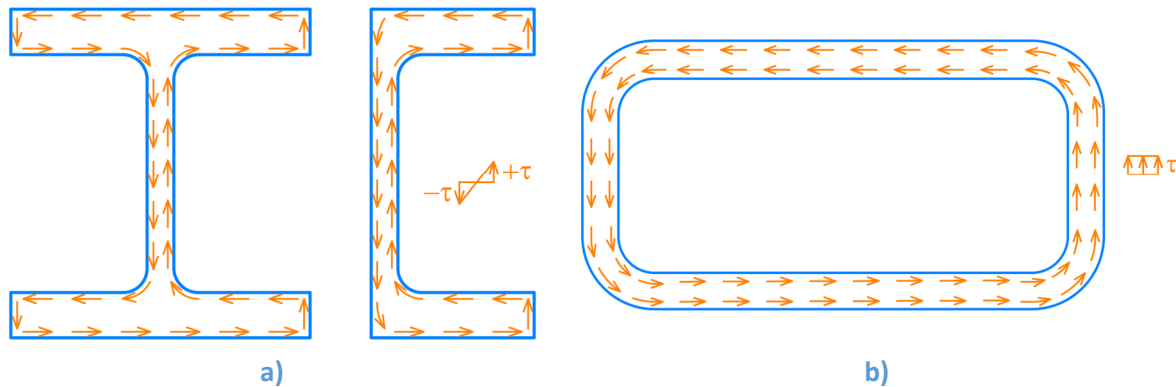


Figure 2-2: Shear stress distribution in open and closed cross-sections

As mentioned the Saint Venant's torsional moment that can be resisted by a rectangular hollow section (RHS) may be calculated in a simplified manner by multiplying the resulting forces in each plate with the lever arm accordingly to Figure 2-3 and Eq. (2.1).

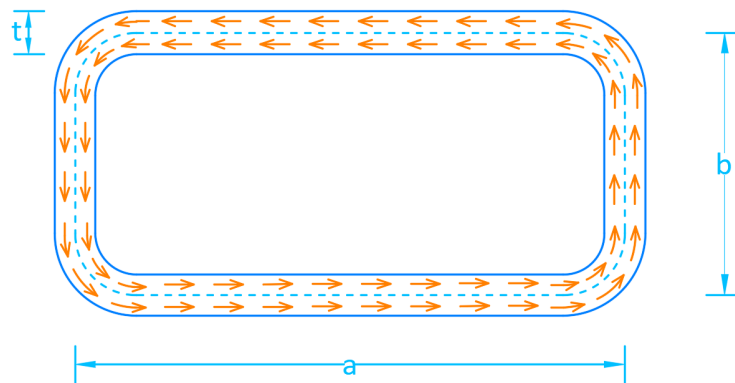


Figure 2-3: Calculation of the Saint Venant's torsional moment resistance for RHS

$$M_{x,St.V,R} = \frac{f_y}{\sqrt{3}} \times a \times b \times t + \frac{f_y}{\sqrt{3}} \times b \times a \times t = 2A_p t \frac{f_y}{\sqrt{3}} \quad (2.1)$$

and

$$A_p = a \times b \quad (2.2)$$

The product standard for structural hollow sections EN 10210-2 (CEN 2006) gives the following expression considering the through thickness variation of the shear stresses. In Eq. (2.4), r_o and r_i are the outer and the inner corner radius, respectively.

$$M_{x,St.V,R} = \frac{f_y}{\sqrt{3}} W_t = \frac{f_y}{\sqrt{3}} \frac{4A_p^2 \frac{t}{p} + \frac{pt^3}{3}}{t + 2\frac{A_p}{p}} \quad (2.3)$$

and

$$p = 2[(b - t) + (h - t)] - \left[\frac{(r_o - r_i)}{2} \right]^2 (4 - \pi) \quad (2.4)$$

For a double symmetric I sections one may obtain a simplified expression of the plastic Saint Venant’s torsional moment neglecting the fillets as given in Eq. (2.5) (see also reference (Ludwig 2014)).

$$M_{x,St.V,R} = \frac{f_y}{\sqrt{3}} \frac{1}{3} t_f^2 (3b - t_f) + \frac{f_y}{\sqrt{3}} \frac{1}{6} t_w^2 (3h_w + t_w) \quad (2.5)$$

The exact plastic Saint Venant’s torsional moment resistance of hot-rolled I sections may be determined based on Finite Element calculations or with reference (Naida 1923). Figure 2-4 represents a comparison for the most commonly used European I profiles. For cross-sections of type HEAA, the fillets may increase the Saint Venant’s torsional moment resistance by up to 30% as the contribution of the slender webs to the plastic Saint Venant’s torsional moment resistance is rather low. Inversely, for the very compact sections of type HEM the relative contribution of the fillets is only of about 7% because the compact web contributes in a greater amount as for the other section series.

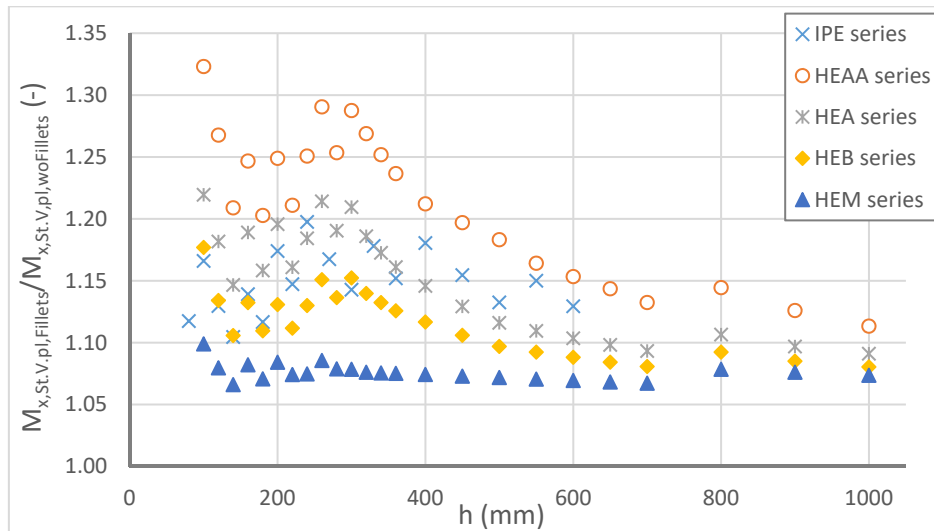


Figure 2-4: Contribution of the fillets to the plastic St. Venant's torsional moment resistance

Even if the fillets may have a non-negligible influence on the plastic Saint Venant’s torsional moment (and on the torsional constant I_t) of hot-rolled open cross-sections, their Saint Venant’s torsional stiffness is much less than those of closed cross-sections as shown in Table 2-1. This table compares selected hot-rolled I sections and rectangular hollow sections possessing

approximatively the same major-axis second moment of area I_y . Obviously, rectangular hollow sections are much more efficient to resist torsion as demonstrated by the ratio of the plastic Saint Venant's torsional moment resistances $M_{x,St.V,pl,RHS}/M_{x,St.V,pl,L}$. In case of pure Saint Venant's torsion, the torsional constant I_t also highly influences the behaviour of the member as the torsional twist φ only depends on its value, the value of the torsional moment and the member length as represented in Eq. (2.6) and Eq. (2.7).

$$\varphi_{,x} = \frac{M_{x,St.V}}{GI_t} \quad (2.6)$$

$$\varphi = \frac{M_{x,St.V}}{GI_t} L \quad (2.7)$$

Here before, it has been insisted on the case of Saint Venant's torsion. However, in general, Saint Venant's torsion is of theoretical nature as it supposes that cross-section warping is not restrained along the member or at its ends and that the torsional moment is constant along the member. In practice, load introduction or boundary conditions (fixed end of cantilevers) always represent a certain degree of warping restraint. Yet, as warping displacements are very low for closed cross-sections or T sections, pure torsion may be considered in these cases. Conversely, warping displacements may not be neglected for I or U sections. In Figure 2-1, it may be observed that warping can be associated to differential longitudinal displacements of the parts of the cross-section. A warping restraint therefore induces axial stresses into the cross-section. In this situation torsion is carried partly through the shear stresses arising from Saint Venant's torsion and by axial stresses (and shear stresses resulting from the variation of these axial stresses over the member length) resulting from warping torsion (also referred to as restrained torsion). The distribution of the axial and shear stresses resulting from warping torsion are schematically represented in Figure 2-5 for an I section and Figure 2-6 for a U section. Yet, it may be noted that the shear stresses resulting from restrained torsion are rather low and may be neglected in practice when the cross-section resistance under combined bending, axial force and torsion is studied (see Chapter 4). Inversely, the axial stresses have to be accounted for in the interaction. They may be determined with Eq. (2.8). The concept of the warping function ω , necessary for the determination of the warping constant I_w and the stress distribution in the cross-section is recalled in paragraph 2.5.

$$\sigma_x = \frac{B}{I_w} \omega \quad (2.8)$$

$$\text{and } I_w = \int \omega^2 dA \quad (2.9)$$

Table 2-1: Comparison of I and RHS sections

I profiles					Rectangular hollow sections RHS							Differences		
Name	I_y (cm ⁴)	I_t [cm ⁴]	$M_{x,se,v,pl}$ (S235) (kNm)	W_I (kg/m)	Name	I_y (cm ⁴)	I_t (cm ⁴)	$M_{x,se,v,pl}$ (S235) (kNm)	W_{RHS} (kg/m)	$I_{t,RHS}/I_{t,I}$	$M_{x,se,v,pl,RHS}/M_{x,se,v,pl,I}$	W_{RHS}/W_I		
IPE 200	1943	6.98	1.58	22.4	200x100x6.3*	1829	1475	28.3	28.1	211	17,9	1,25		
IPE 550	67120	123	14.42	106	500x300x12.5*	65813	64388	445	151	523	30,9	1,42		
HEA 300	18260	85.17	11.07	88.3	350x150x14.2*	17254	19189	154	103	225	13,9	1,17		
HEA 900	422100	736.8	54.75	252	800x350x25**	429183	294730	1544	426	400	28,2	1,69		
HEB 240	11260	102.7	11.99	83.2	400x100x6.3*	10813	3565	58.3	47.9	34.7	4,87	0,58		
HEB 700	256900	830.9	57.04	241	700x350x20**	253053	203311	1119	314	244	19,6	1,30		
HEM 220	14600	315.3	24.79	117	300x200x12.*	14273	15675	172.46	91.9	49.7	6,96	0,79		
HEM 600	237400	1564	85.21	285	750x350x15**	232084	172392	942	250	110	11,1	0,88		

*see reference (CEN 2006)

**Free profiles not included in cross-section catalogues

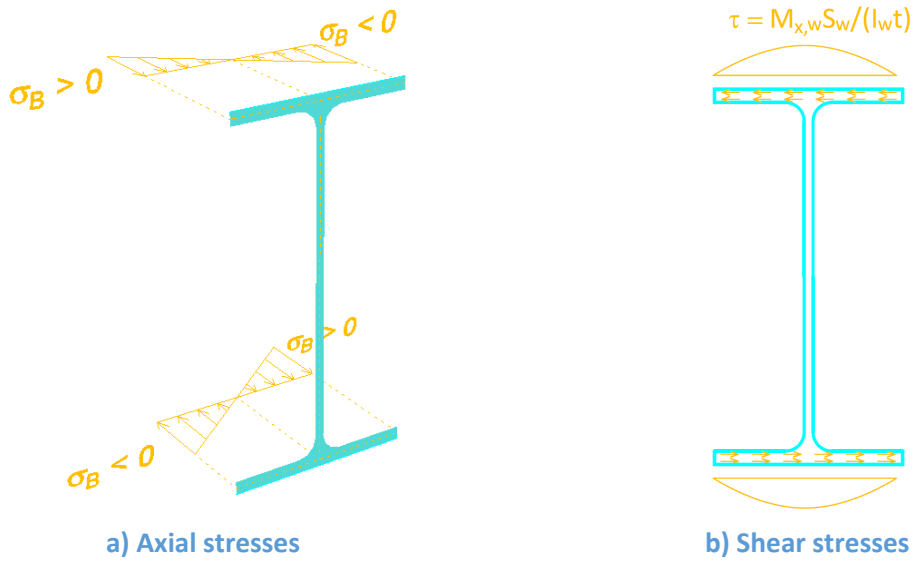


Figure 2-5: Distribution resulting from restrained torsion for an I section

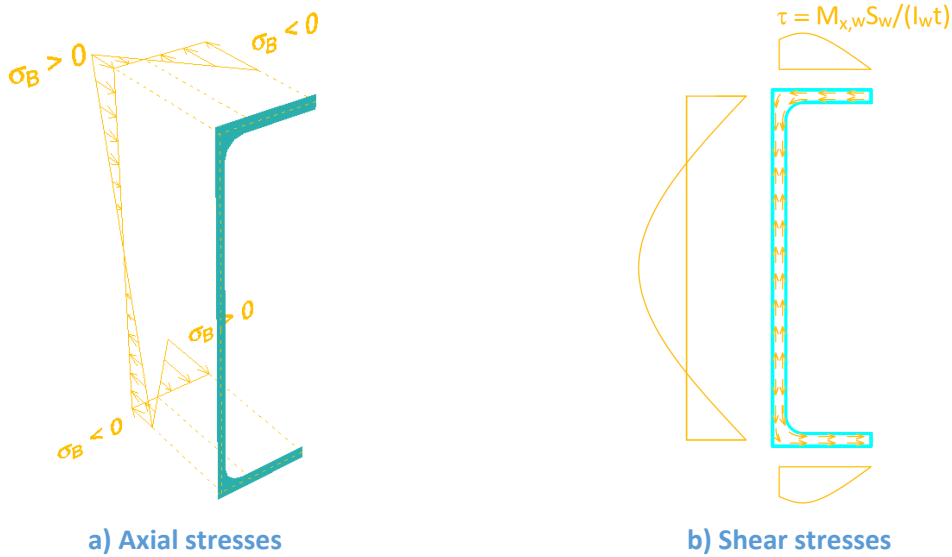


Figure 2-6: Distribution stresses resulting from restrained torsion for a U section

Figure 2-5 shows that the axial stresses resulting from restrained torsion mostly transit through the flanges of I sections. The web is not subject to these axial stresses and may consequently always carry additional stresses generated by a supplementary axial force or major-axis bending moment. Inversely, the stresses resulting from warping torsion transit through the flanges **and** the web of U sections. Therefore, if these sections are subject to a bi-moment equal to the plastic bi-moment, no additional axial force or bending may be resisted. Obviously, the stress distribution directly influences the plastic cross-section resistance studied in Chapter 4 of this thesis.

2.3 Amplitude of Saint Venant's and warping torsion for open cross-sections

Through the previous paragraph, the two concepts of Saint Venant's and warping torsion have been recalled. Eq. (2.10) shows that the total torsional moment may be expressed as the sum of both torsional moments.

$$M_{x,tot} = M_{x,St.V} + M_{x,w} \quad (2.10)$$

Eq. (2.10) may also be expressed in terms of the derivatives of the torsional twist:

$$M_{x,tot} = GI_t \varphi_{,x} - EI_w \varphi_{,xxx} \quad (2.11)$$

As in Eq. (2.10) the first term of the right hand side of Eq. (2.11) corresponds to the Saint Venant's torsional moment and the second term corresponds to the warping torsional moment. By rearranging Eq. (2.11) as shown in Eqs. (2.12) and (2.13), it is possible to derive the parameter ε_t indicating the relative importance of warping torsion to the total torsional moment as represented in the Figure 2-8 and Figure 2-9. It should be noted that the parameter ε_t is specific for a member of a given cross-section and length.

$$\frac{M_{x,tot}}{GI_t} = \varphi_{,x} - \frac{L^2}{\varepsilon_t^2} \varphi_{,xxx} \quad (2.12)$$

$$\varepsilon_t = L \sqrt{\frac{GI_t}{EI_w}} \quad (2.13)$$

So as to illustrate the influence of ε_t , we consider the example of a member of HEB 400 cross-section. The length of the member is varied in order to vary the parameter ε_t . It is supposed that the member possesses fork end supports and is loaded by a torsional moment M_T of 10 kNm applied at mid-span as represented schematically in Figure 2-7.

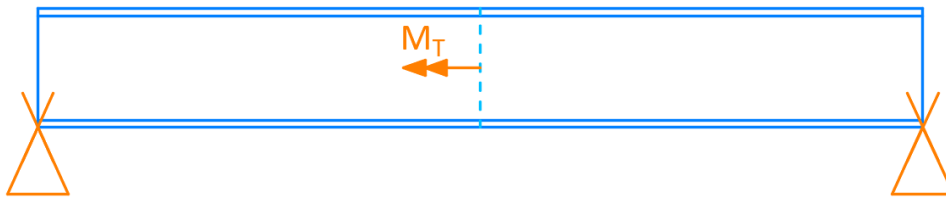


Figure 2-7 : Studied member subject to an applied torsional moment

Figure 2-8 and Figure 2-9 show the distribution of the torsional moments and the distribution of bi-moments depending on the member length and consequently depending on the parameter ε_t . Obviously, the distribution and the value of the **total** torsional moment $M_{x,tot}$, composed of the Saint Venant's torsional moment $M_{x,St.V}$ and the warping torsional moment $M_{x,w}$, does not depend on the member length. On the contrary, Figure 2-8 clearly demonstrates that the relative importance of the warping torsional moment decreases with increasing member length (and increasing parameter ε_t). For short members ($L = 200$ cm for $\varepsilon_t = 1,20$) the warping torsional moment attains nearly 90% of the total torsional moment at the member ends. For longer

members the warping torsional moment vanishes near the fork supports. At mid-span, where warping is restrained (warping has to vanish due to symmetry conditions), the warping torsional moment equals the total torsional moment in all cases.

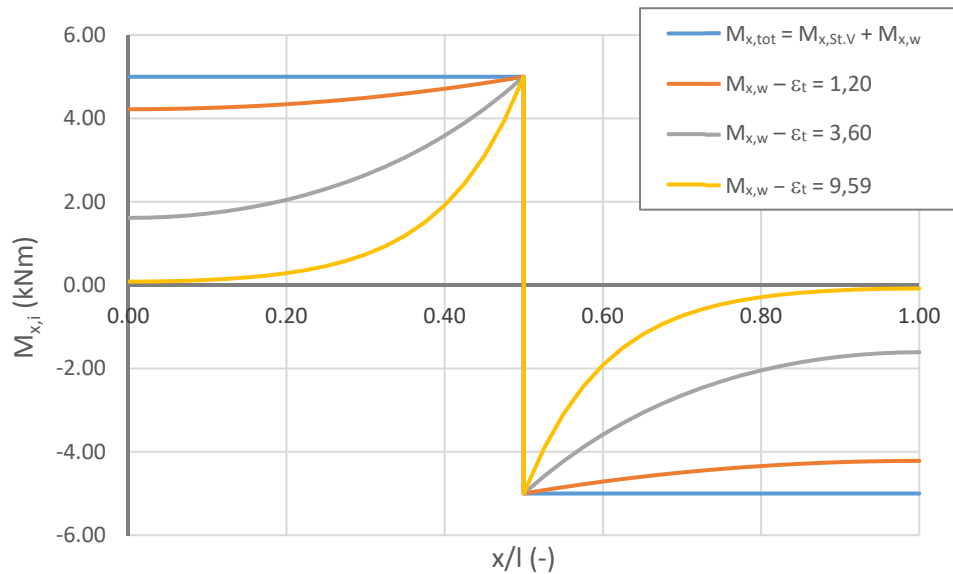


Figure 2-8: Distribution of warping torsional moment and the total torsional moment depending on parameter ϵ_t

Figure 2-9 represents the distribution of the bi-moment along the member length. As expected, the bi-moment vanishes at the member ends because the fork supports do not generate a warping restraint. At mid-span the bi-moment attains its maximum. The exact distribution of the bi-moment between the member ends and mid-spans depends on the parameter ϵ_t again. With increasing ϵ_t the variation of the bi-moment becomes more and more non-linear. For a value of ϵ_t close to 10 ($L = 1600$ cm), the bi-moment is concentrated at mid-span near the warping restraint and the other parts of the member are only subject to low bi-moments.

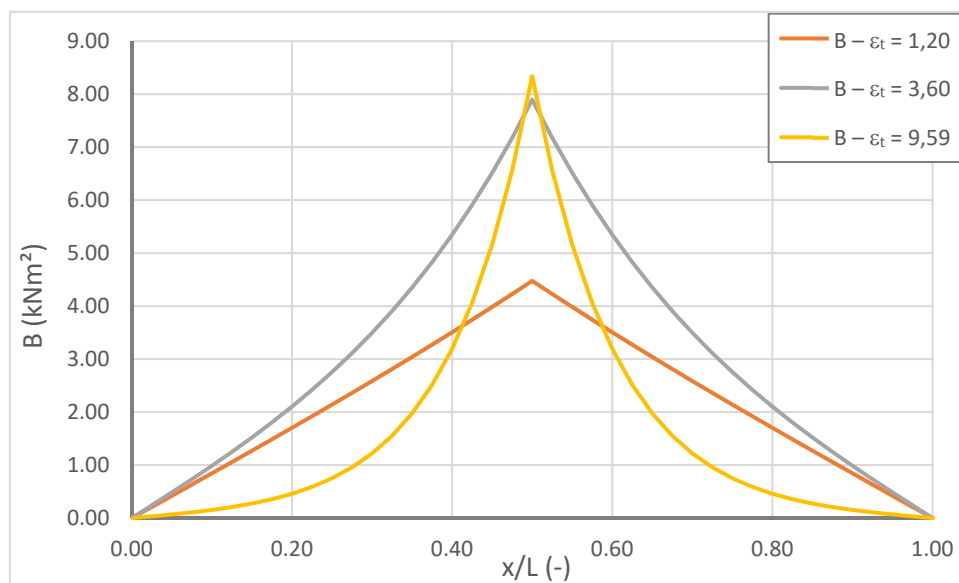


Figure 2-9: Distribution of bi-moment depending on parameter ϵ_t

As an increasing value of parameter ϵ_t indicates decreasing influence of warping torsion, ϵ_t is referred to as warping decay factor hereafter. For practical lengths, members with open cross-section generally possess rather low values of the warping decay factors (between 1 and 10). Consequently, they are always subject to mixed torsion, i.e. a combination between Saint Venant's and warping torsion whose relative magnitude results from the exact value of the warping decay factor. Contrariwise, due to their high Saint Venant's torsional stiffness, members with closed cross-sections possess warping decay factors highly exceeding 10. Warping torsion may therefore be neglected in general. The same is true for T sections as their warping constant is very low (see paragraph 2.5).

2.4 Equivalence between members subject to torsion and members subject to bending and tension axial force

First, the member represented in Figure 2-10 is considered. It is assumed that this member possesses fork end supports and that it is subject to a distributed torsional load m_x . Admittedly, this loading condition is of pure theoretical nature but it is used to highlight an important point concerning the behaviour of members subject to torsion.

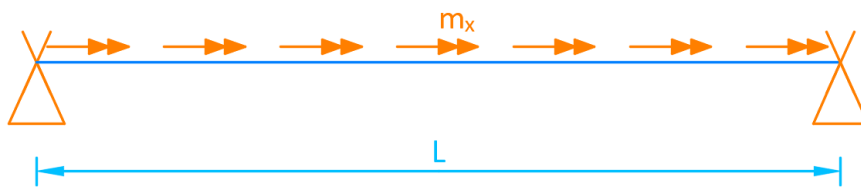


Figure 2-10: Member on fork end supports subject to a distributed torsional load

For the given loading and support conditions, the behaviour of the member may be characterised with the differential equation provided hereafter:

$$EI_w \varphi_{,xxxx} - GI_t \varphi_{,xx} = m_x \quad (2.14)$$

It appears that Eq. (2.15) is of the same format as the differential equation characterising the member subject to a distributed vertical load represented in Figure 2-11.

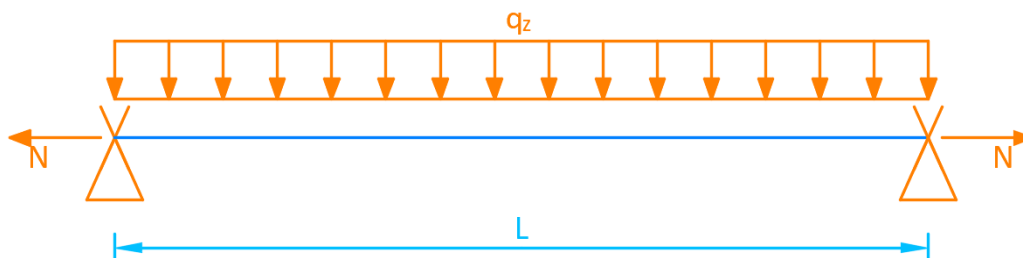


Figure 2-11 : Member on point supports subject to a distributed vertical load

The differential equation characterising the in-plane **second order equilibrium** of the member of Figure 2-11 is recalled in Eq. (2.15).

$$EI_y w_{,xxx} + Nw_{,xx} = q_z \quad (2.15)$$

Similarly to the case of members in torsion, it is possible to define the parameter ε_M specific for a given member (it is recalled that an axial compression force is defined as positive here):

$$\varepsilon_M = L \sqrt{\frac{-N}{EI_y}} \quad (2.16)$$

By comparing Eqs. (2.14) and (2.15), one may remark that the vertical load corresponds to the torsional load, the axial tension force corresponds to the Saint Venant's torsional stiffness of the member and the bending stiffness corresponds to the warping stiffness of the member. Moreover, it is possible to develop an equivalence between the internal forces and moments as shown in Table 2-2.

Table 2-2 : Internal forces and moments resulting from bending and torsion

Member in bending	Member under torsion
Bending moment: $M_y = EI_y w_{,xx}$	Bi-moment: $B = -EI_w \varphi_{,xx}$
Shear force: $V_z = EI_y w_{,xxx}$	Warping torsional moment: $M_{x,w} = -EI_w \varphi_{,xxx}$
Resulting vertical force (in the global coordinate system): $V_{z,Glob} = EI_y w_{,xxx} - Nw_{,x}$	Total torsional moment: $M_{x,tot} = -EI_w \varphi_{,xxx} + GI_t \varphi_{,x} = M_{x,w} + M_{x,St.V}$

So as to illustrate the results of Table 2-2, it is proposed to study the example of a member of IPE 500 section. Two cases are distinguished:

- 1) The member is subject to a uniformly distributed torsional load m_x of 1 kNm/m generating a combination of bi-moment B, warping torsional moment $M_{x,w}$ and Saint Venant's torsional moment $M_{x,St.V}$.
- 2) The member is subject to a uniformly distributed vertical load q_z generating a combination of major-axis bending moment and a shear force. Additionally, the member is subject to an axial tension force N.

The behaviour of these two members is similar if the two specific parameters ε_t and ε_M are equal. Consequently, the axial tension force necessary to equalize ε_t and ε_M is determined as follows:

$$\varepsilon_M = L \sqrt{\frac{-N}{EI_y}} = \varepsilon_t = L \sqrt{\frac{GI_t}{EI_w}} \quad (2.17)$$

and:

$$N = -GI_t \frac{I_y}{I_w} \quad (2.18)$$

For the studied member of IPE 500 section the axial tension force is equal to $N = -28297,6$ kN. The two members are studied for different member lengths so as to highlight the influence of the parameters ε_t and ε_M . The studied lengths and the corresponding values of ε_t and ε_M are given in Table 2-3.

Table 2-3: Studied lengths

Length (mm)	Factors ε_t and ε_M
200	1,057
500	2,642
1000	5,283
2000	10,566

Both members are calculated through an elastic analysis to obtain the resulting internal forces and moments. It should be noted that the member subject to torsion is analysed without considering second order effects (not existing for this case) whereas the second order effects are accounted for for the member in bending. The obtained distribution of the bi-moment and the major-axis bending moment are represented in Figure 2-12. As in paragraph 2.3, Figure 2-12 clearly shows the influence of the warping decay factor ε_t . Again, the relative influence of the bi-moment decreases with the length of the given member (and hence with increasing ε_t). For the shortest member the distribution is nearly parabolic and the maximum bi-moment can be estimated with $m_x L^2/8$. The difference between the obtained value and the value calculated precisely is only of about 10%. Inversely, the relative value of maximum bi-moment (with reference to $m_x L^2/8$) decreases rapidly and it attains only approximately 7% of the value $m_x L^2/8$ for the longest member. Also, one observes that the flatness of the curves increases with increasing warping decay factor. The observed torsional behaviour of the member has already been described in paragraph 2.3. Figure 2-12 reveals that the second order behaviour of members subject to tension axial forces and bending is identical to the behaviour of members under torsion. Indeed, the relative value of the major-axis bending moment is exactly equal to the relative value of the bi-moment. The major-axis bending moment is normalised with reference to $q_z L^2/8$ representing the maximum first order moment M_y . The flattening of the curves is linked to the major-axis bending moment created by the axial tension force. Understandingly, this moment is lower near the end supports as the vertical displacement is low. Inversely, the effect of this second order moment is very high at mid-span as the vertical displacement obviously attains its maximum there.

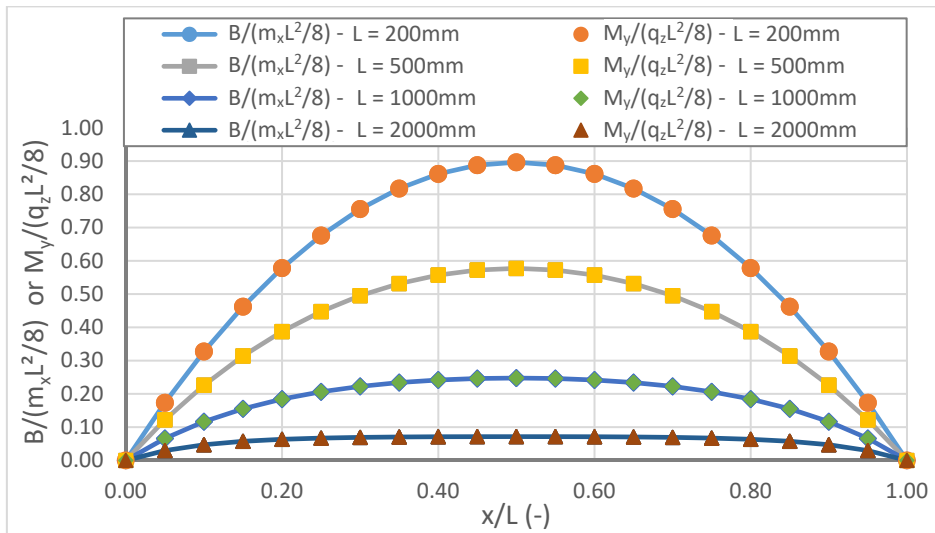


Figure 2-12: Distribution of the bi-moment and the major-axis bending moment along the members

It seems also interesting to study the evolution of the Saint-Venant’s torsional moment along the members of different lengths. The results are represented in Figure 2-13. Again, it is clear that the relative influence of the torsional moment increases with increasing member length and increasing warping decay factor ε_t . It is shown that the Saint-Venant’s torsional moment can be linked to the axial tension force and more precisely to the resulting vertical force (in the global coordinate system) generated by the vertical displacement and the axial force. The equivalence between the in-plane second order equilibrium of member in bending and the equilibrium of members subject to torsion has been established in elasticity for a long time. In paragraph 5.6.4 it is shown that the equivalence may also be applied in the plastic domain.

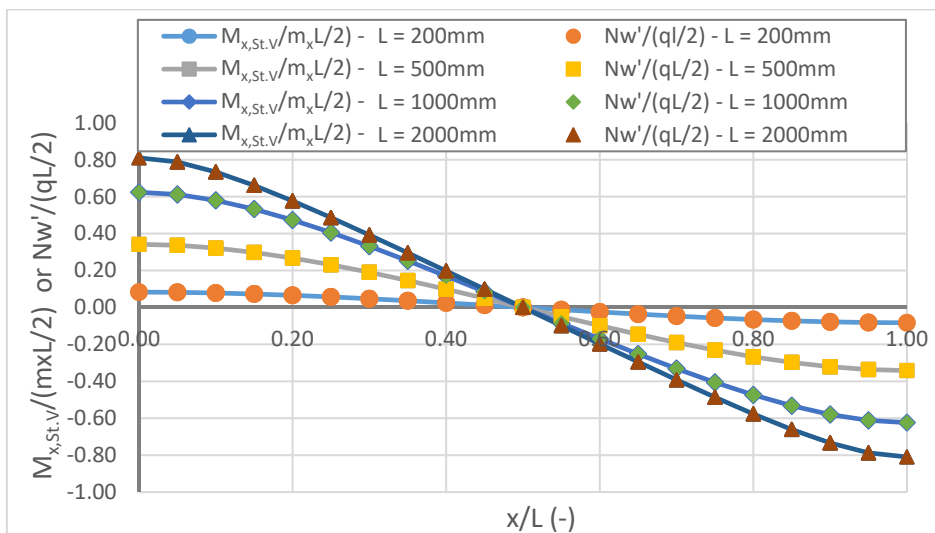


Figure 2-13: Distribution of the Saint-Venant’s torsional moment and Nw_x along the members

In the previous paragraphs, the warping stiffness has been referred to several times. The warping stiffness and the warping function are also important terms in Chapters 4 and 5 addressing the

cross-section and member resistance for members of I and U sections. Consequently, it seems interesting to recall the derivation of the warping function in the next paragraph.

2.5 Warping function for open cross-sections

Let us consider the open cross-section of arbitrary shape represented in Figure 2-14. The centroid of the cross-section is denoted as C and its shear centre is denoted S. Also, the distance r_s between the shear centre and the tangent to the cross-section passing through the point P is represented. Along the cross-section the position of the point P is measured with the length coordinate s . Additionally, the point P may move axially along the x axis and perpendicular to the mid-line of the cross-section. The axial displacement is denoted as “ u ” and the displacement perpendicular to the sections mid-line is denoted as ξ .

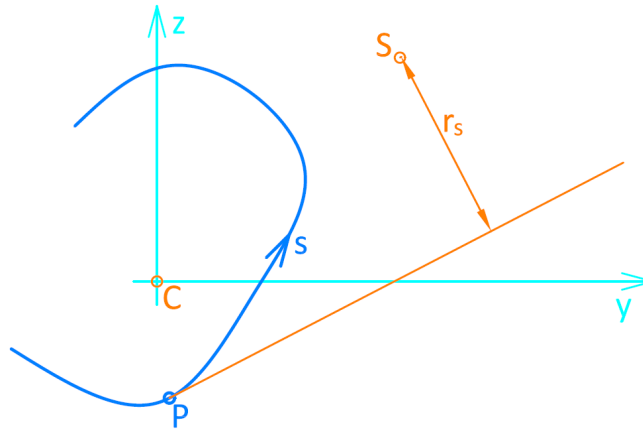


Figure 2-14: Definition of warping function

It is assumed that the shear strains in the middle surface of the walls of the cross-section is negligible (Wagner’s assumption). This may be expressed by:

$$\gamma_{sx} = 0 = \frac{\partial u}{\partial s} + \frac{\partial \xi}{\partial x} \quad (2.19)$$

Let us now consider that the cross-section is subject to a torsional rotation φ . It is assumed that the cross-section shape does not change after deformation (cross-section is rigid but free to warp). Consequently, the displacement ξ may be expressed as shown in Eq. (2.20).

$$\xi = \varphi r_s \quad (2.20)$$

In order to obtain the longitudinal displacement of the point P, Eq. (2.19) is rearranged and integrated with respect to s .

$$u = -\int \xi_{,x} ds + u_a \quad (2.21)$$

In Eq. (2.20), u_a is an integration constant and physically represents the axial displacement at the origin of the length coordinate s .

Eq. (2.20) is now introduced into Eq. (2.21) to obtain:

$$u = -\int r_s ds \varphi_{,x} + u_a \quad (2.22)$$

At this point the warping function is introduced and defined as:

$$\omega = \int r_s ds \quad (2.23)$$

It has been considered that the cross-section is only subject to a torsional rotation. As no axial force is applied, the resultant of axial stresses has to be equal to zero. Based on this condition, the integration constant u_a can be assimilated to the mean value of the warping function over the cross-section as demonstrated in reference (Vlassov 1962). One obtains:

$$u_a = \frac{1}{A} \int \int r_s ds dA = \frac{1}{A} \int \int r_s t ds ds \quad (2.24)$$

A generalized form of the warping function may be introduced as:

$$\bar{\omega} = \int r_s ds - \frac{1}{A} \int \int r_s t ds ds \quad (2.25)$$

For simplicity the generalized warping function is denoted as ω hereafter. Also, it has been shown in reference (Vlassov 1962) that the integration constant vanishes if the origin of the length coordinate s is chosen at the centre of torsion and therefore, following the theorem of Maxwell-Betti, at the shear centre of the cross-section.

The generalized warping function is represented in Figure 2-15 for I and U sections studied in the framework of the present thesis.

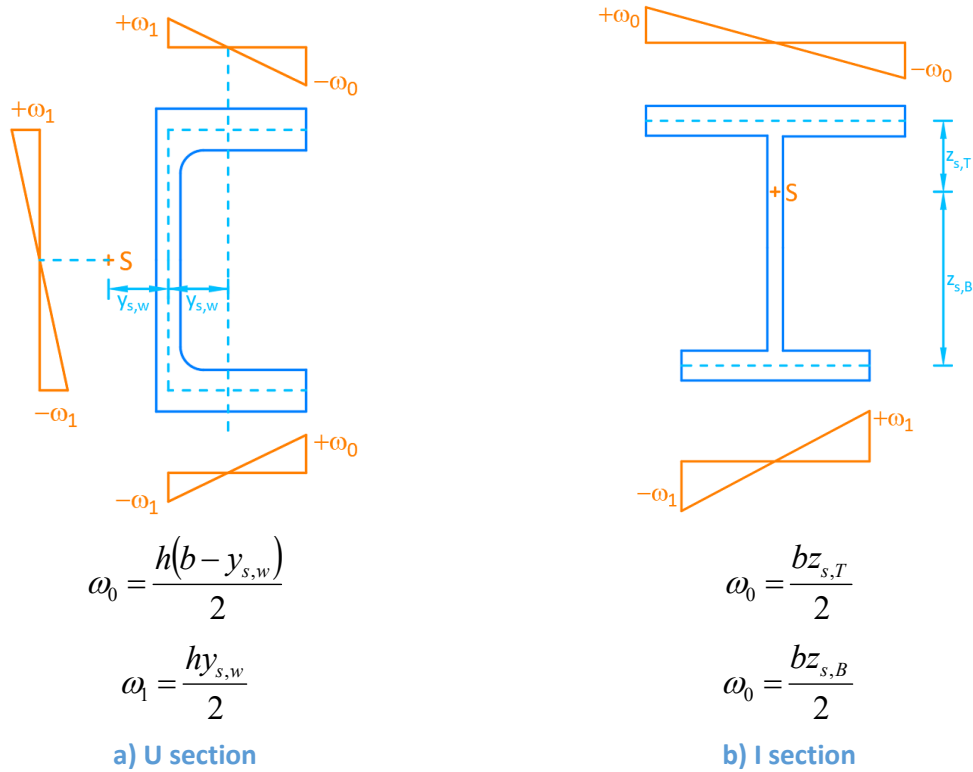


Figure 2-15: Warping function for I and U sections

Here before it has been implicitly assumed that the cross-section may be assimilated to its mid-line in order to derive the warping function. For the majority of practically used cross-sections, as for I and U sections, this is sufficiently precise. Nevertheless, in some cases this assumption may lead to non-negligible errors. In fact, in reference (de Ville de Goyet 1989), it is shown that the complete warping function may be expressed as the sum of global warping (first term in Eq. (2.26)) and local or secondary warping (second and third term in Eq. (2.26)), i.e. differential longitudinal displacements over the thickness of a cross-section's plate.

$$\omega = \int r_s ds + (s - r_t)s_t + s_t \left(\frac{2 \sinh(\mu s)}{\mu \cosh\left(\frac{\mu b}{2}\right)} - s \right) \quad (2.26)$$

$$\text{and } \mu^2 = \frac{12}{t^2} \quad (2.27)$$

Figure 2-16 illustrates global and local warping of an I section.

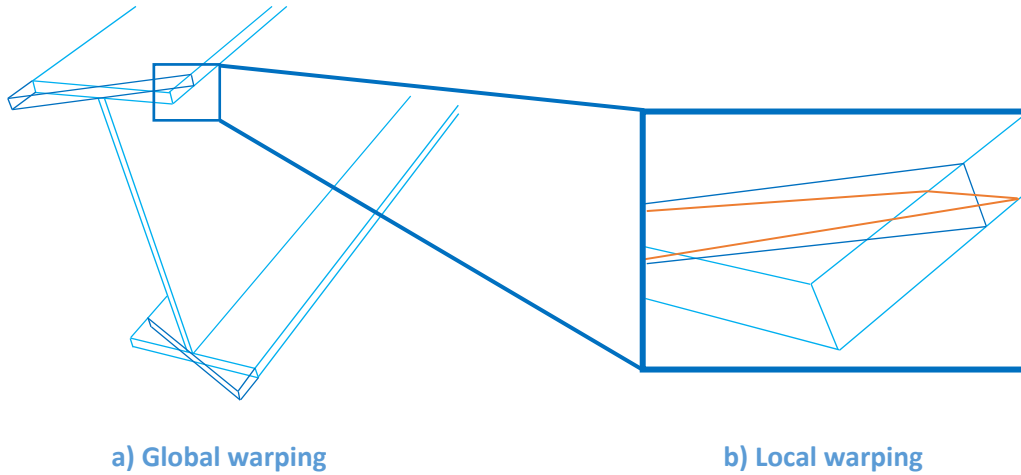


Figure 2-16: Global and local warping of an I section

In particular, local warping has to be accounted for when the warping constant calculated based on the global warping functions vanishes as for T or L sections. The influence of local warping is quantified in Table 2-4 (see also (de Ville de Goyet 1989) and (Boissonnade 2002)).

Table 2-4: Influence of local warping

Cross-section		I_w local
T		$\frac{t_f^3 b^3}{144} + \frac{t_w^3 (h - t_f)^3}{36}$
L		$\frac{t^3}{36} [(h - t)^3 + (b - t)^3]$

2.6 Summary

The present chapter gave a short review about the theory of torsion especially for members with open cross-section. The developments discussed before have been presented in many publications in the past and should not be considered as an original contribution of this thesis. In particular, it has been recalled that:

- The torsional behaviour of members with open cross-section is equivalent to the second order equilibrium of members subject to an axial tension force and bending;
- Members with open cross-section are always subject to mixed torsion, i.e. a combination of Saint-Venant's and warping torsion;
- The relative magnitude of these two types of torsional moments can be estimated based on the warping decay factor ε_t ;
- Saint-Venant's torsion generates shear stresses that vary linearly over the thickness of the plates of the cross-section;
- Warping torsion generates shear and axial stresses. Both may be considered as constant over the thickness of the plates of the I and U sections;
- The distribution of axial stresses resulting from the bi-moment is affine to the warping function ω that is cross-section specific;
- In general only global warping has to be considered for open cross-sections apart from cross-sections composed of plates crossing each other in one point (L, T sections).

3 FINITE ELEMENT MODEL

3.1	General	35
3.2	General description of the finite element model	35
3.2.1	Material law and equivalent imperfections	35
3.2.2	Finite elements used in this thesis	36
3.2.2.1	General	36
3.2.2.2	Beam 4	36
3.2.2.3	Beam 188	36
3.2.2.4	Shell 181	37
3.2.2.5	Solid 185	37
3.2.3	Boundary conditions and loading	38
3.2.3.1	General	38
3.2.3.2	End supports for I sections	38
3.2.3.3	End supports for U sections	39
3.2.3.4	Load introduction	40
3.3	Section modelling	41
3.3.1	Different possibilities to model fillets	41
3.3.2	Study on the influence of meshing density	44
3.3.2.1	General	44
3.3.2.2	Element width for stocky and medium slender cross-sections	45
3.3.2.3	Element aspect ratio	49
3.3.2.4	Element width for slender cross-sections	52
3.3.2.5	Summary on meshing density	55
3.3.3	Evaluation of the stiffness of the different modelling techniques	57
3.3.3.1	General	57
3.3.3.2	Major-axis flexural buckling	58
3.3.3.3	Minor-axis flexural buckling	60
3.3.3.4	Torsional buckling	62
3.3.3.5	Lateral-torsional buckling	64
3.3.3.6	Conclusion	65
3.3.4	Plastic section resistance	66
3.3.4.1	General	66
3.3.4.2	Mono-axial bending and axial force	66
3.3.4.3	Torsion	68
3.3.4.4	Interaction between major-axis bending and shear force	76
3.3.4.5	Conclusion	80
3.3.5	Influence of the fillets on the member resistance	82
3.3.6	Choice of the numerical model	86

3.4	Comparison of the numerical model to physical tests	87
3.4.1	General	87
3.4.2	Tests performed at TU Berlin	87
3.4.2.1	Numerical Model	87
3.4.2.2	Results for I sections	89
3.4.2.3	Results for U sections	91
3.4.2.4	Summary of the results	93
3.4.2.5	Influence of the fillets on the test results	94
3.4.3	Conclusions	96

3.1 General

Chapter 3 presents in detail the finite element model that is used throughout this thesis to study the behaviour of members with open cross-section subject to torsion. First, the general modelling choices concerning boundary conditions and load introduction are explained. Then, the modelling of the member itself is investigated. In particular, paragraph 3.3 discusses the numerical modelling of hot-rolled sections including their fillets. Different modelling techniques are investigated and validated with reference to theoretical results and laboratory tests. Based on these comparisons a numerical model is chosen for the use in Chapters 4 and 5.

3.2 General description of the finite element model

3.2.1 Material law and equivalent imperfections

Depending on the type of analysis, different material laws are applied in the framework of this thesis. They are defined in Table 3-1.

Table 3-1: Material laws used for different types of analysis

Type of analysis	Objective	Material law
Linear Analysis (LA)	Determination of elastic distribution of internal forces and moments	Elastic
Linear Buckling Analysis (LBA)	Determination of critical loads	Elastic
Material non-linear analysis (without imperfection and second order effects - MNA)	Determination of the plastic cross-section resistance	Elastic - perfectly plastic
Geometrical and Material Non-linear Analysis of the Imperfect member (GMNIA)	Determination of the ultimate member resistance	Multi-linear (see Figure 3-1)

Table 3-1 also defines the objective that is associated with the different types of analysis. It should be noted that the MNA simulations are performed without equivalent geometric imperfections because they are used to determine the theoretical plastic cross-section resistance without considering the influence of instability. Therefore, geometric non-linearity is not included neither in this type of analysis. Conversely, the GMNIA simulations are performed to characterize the member behaviour and the member resistance. Consequently, they should include the effect of imperfections and the second order effects. If not otherwise indicated, the member imperfections are applied affine to the first (member) eigenmode obtained through the LBA simulations with an amplitude of $L/1000$ in this type of analysis. For members of slender section, local plate imperfections are also included. They are defined by sine-waves of amplitude $h_w/200$ for the web

and $b_f/400$ for the flanges (as recommended in (CEN 2007a)). The influence of the wave length is studied in paragraph 5.2.1.7. Additionally to the equivalent geometric imperfections, residual stresses are introduced for the GMNIA simulations accordingly to reference (ECCS 1984). It is to be noted that a deeper investigation on the influence of assumed imperfections (geometric imperfections and residual stresses) on the member resistance is presented in paragraph 5.2. This paragraph is only intended to give the general information necessary for the simulations performed in Chapter 3.

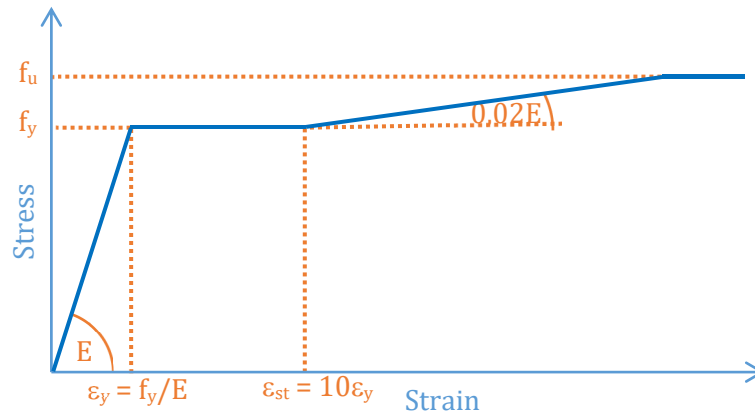


Figure 3-1 : Multi-linear material law

3.2.2 Finite elements used in this thesis

3.2.2.1 General

In the framework of this thesis, the commercial finite element program ANSYS v17.0 is used. In the following, a short presentation is given for all types of finite elements employed here. Detailed information may be obtained in reference (ANSYS 2016).

3.2.2.2 Beam 4

Beam 4 is a uniaxial finite element with two nodes at its ends and six degrees of freedom for each of these nodes. A third optional node is used for the element orientation. The cross-section characteristics (Area, second moments of area, torsional constant, etc.) are not defined by its geometry but directly by entering the numerical values of these characteristics. This type of beam element is only used in order to simulate stiff cross-sections along the member and rigid links between different types of elements (see paragraph 5.3).

3.2.2.3 Beam 188

As Beam 4, the finite element Beam 188 is defined by two nodes at the element ends and a third node defining the element orientation. Beam 188 has seven degrees of freedom at the nodes including warping. The cross-section is defined by its geometry and the corresponding cross-section characteristics are calculated by ANSYS. Beam 188 is suited for plastic analysis. In order to obtain a smooth stress distribution and to respect the zero shear stress condition at the cross-section boundaries, the section has to be discretised in a sufficient number of cells. Each cell

contains four section integration points as shown in Figure 3-2. It should also be noted that Beam 188 is based on Timoshenko beam theory including shear-deformation effects relevant for short beams.

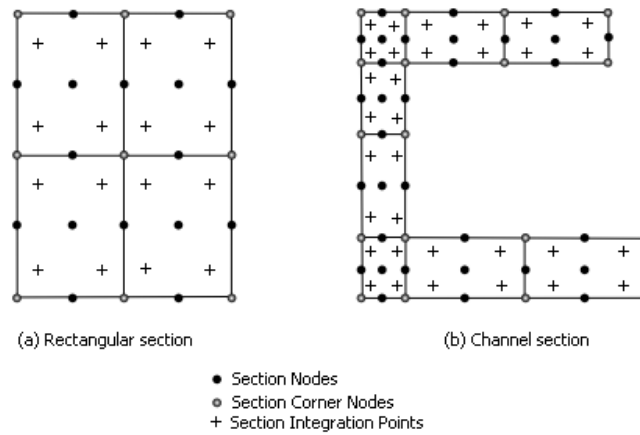


Figure 3-2: Discretization of the cross-section of element Beam 188 – Figure188.3 of reference (ANSYS 2016)

3.2.2.4 Shell 181

Shell 181 is a four-node shell element with six degrees of freedom at each node. The number of integration points may be defined by the user. However, an odd number has to be chosen. At least three integration points through the thickness are applied: one at the centre and one at each boundary surface. For all shell elements ANSYS uses the Simpson integration rule. In case of non-linear stress distribution at least 5 integration points through the thickness should be used. Here, 9 integration points are used in order to represent precisely the distribution of shear stresses due to the Saint Venant's torsional moment. Also, one may note that the element Shell 181 is based on the Mindlin-Reissner theory (first order shear-deformation theory) considering shear deformations through the thickness of the plate. This element is suited for thin to moderately thick shell structures and it may therefore be used to model steel members.

3.2.2.5 Solid 185

Solid 185 is an eight node volume finite element. It possesses three degrees of freedom at each node (3 translations). The rotational degrees of freedom are not accounted for. Enhanced strain formulations are used so as to handle shear locking and volumetric locking recommended for bending-dominated problems.

3.2.3 Boundary conditions and loading

3.2.3.1 General

In case of finite beam elements, the application of boundary conditions and loading is rather trivial as both may be applied directly at the nodes defining the element as only **one node** is associated to a given section along the member length. However, when the physical member is modelled with shell or solid finite elements, the application of boundary conditions and loading is much more delicate as a given cross-section along the member length is defined by a **certain number of nodes** (depending on the mesh density). Also, the application of loads or boundary conditions are applied at only one node may lead to numerical convergence problems and unphysical high strains and stresses as well as local instabilities in the vicinity of the application node. Therefore, some precaution must be taken in order to apply loads and boundary conditions to shell or solid model.

3.2.3.2 End supports for I sections

In paragraph 3.3, several techniques are presented to model the cross-section. However, for all models (except the beam model) the same principles are employed to model the theoretical boundary conditions (e.g. fork end supports) and load introduction. Figure 3-3 represents schematically the end supports of two models, one consisting of shell elements and the other consisting of solid elements.

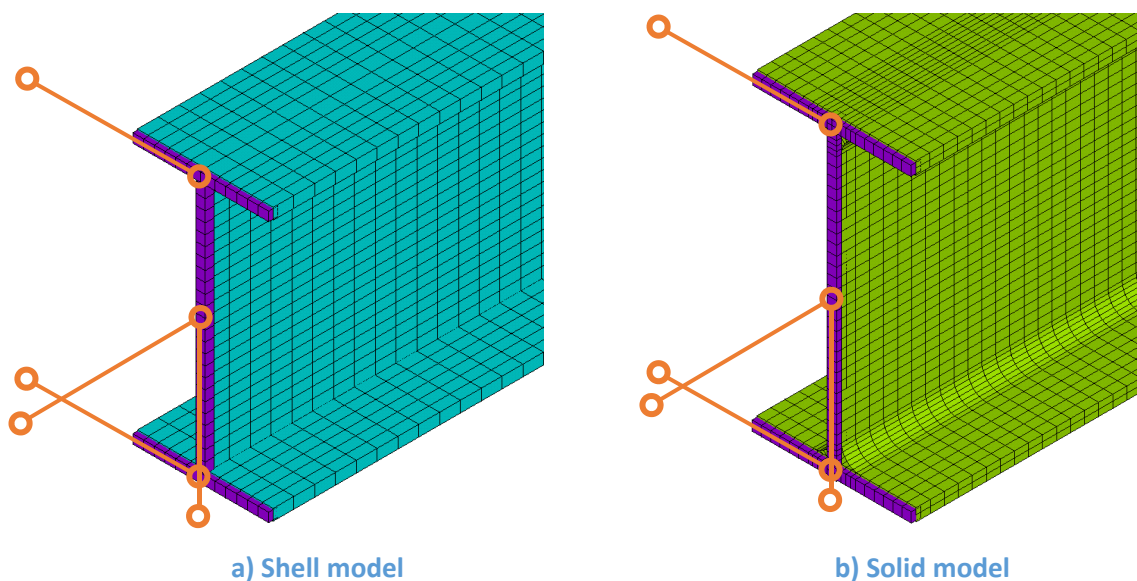


Figure 3-3: Rigid Beam elements to prevent local instability at the support location

In order to prevent local instability at the end section and to avoid the previously mentioned problem of unphysical high stresses at the end sections, the mid-line of the two models is meshed with rigid beam elements of type Beam 4 represented in violet in the following figures. In some references as (Boissonnade 2012) and (Hayeck 2017), the rigid beam elements are replaced by kinematic conditions. Here, it is preferred to introduce beam elements as the kinematic conditions

used in ANSYS are linearized and therefore not suited in case of large deformations (see “cerig” command in (ANSYS 2016)).

3.2.3.3 End supports for U sections

In case of U sections, neither the centroid nor the shear centre is located in the section itself. Consequently, the application of boundary conditions may seem more delicate than for I sections. The real physical boundary condition depend on the design of the joints of the (U-shaped) member with the connected structural elements. Obviously, there is a rather important variety of possible designs (end plats, angle sections ...) and, depending on the design, the physical boundary conditions may be more or less close to idealised boundary conditions considered in the numerical model. In particular, it may be noted that a complete fork support may not be realised physically as the warping function does not vanish neither over the whole web nor over the whole flanges of U sections (see Chapter 2). If for example the web of the U section is connected by angle sections or partial depth endplates to a column, the warping displacements are always restrained at a certain degree. For I sections, this is not the case because the warping function vanishes over the whole web. Consequently, connecting the web of an I-shaped beam to a column does not restrain warping. Admittedly, it would be desirable to represent as precisely as possible the physical boundary conditions in the numerical model to capture their (beneficial) effect. Still, this seems delicate due to the variety of possible design. Rather, it is proposed to determine lower bound results for U-shaped members based on the assumption of ideal fork end supports. In order to allow free warping the axial displacements is restrained at one member end at the mid-height of the web (level of the centroid and the shear centre). At this point, the warping function vanishes and warping may therefore freely develop if necessary. In order to prevent lateral displacements and torsional twist, lateral restraints are applied at the upper and lower flange at the intersection with the web. Figure 3-4 illustrates the application of the boundary conditions for U-shaped members.

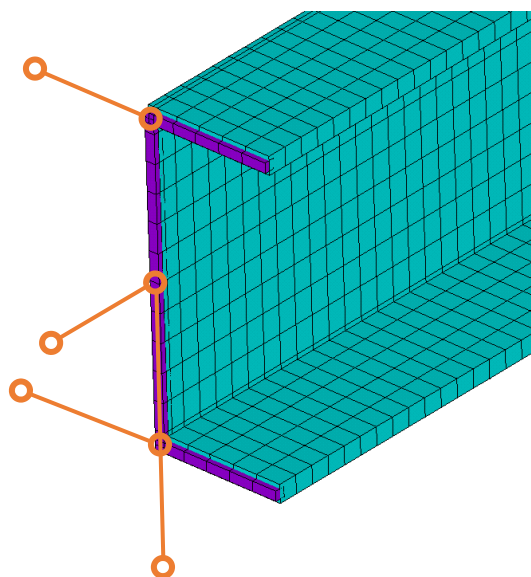


Figure 3-4: End fork condition applied at a U-shaped member

3.2.3.4 *Load introduction*

Point loads introduced in the span are applied as nodal forces. In order to prevent the cross-section from local buckling, a stiffener is created at the point of load introduction as shown in Figure 3-5. This represents the practical habit. Otherwise, it would have been possible to introduce rigid beam elements as done for the application of the boundary conditions.

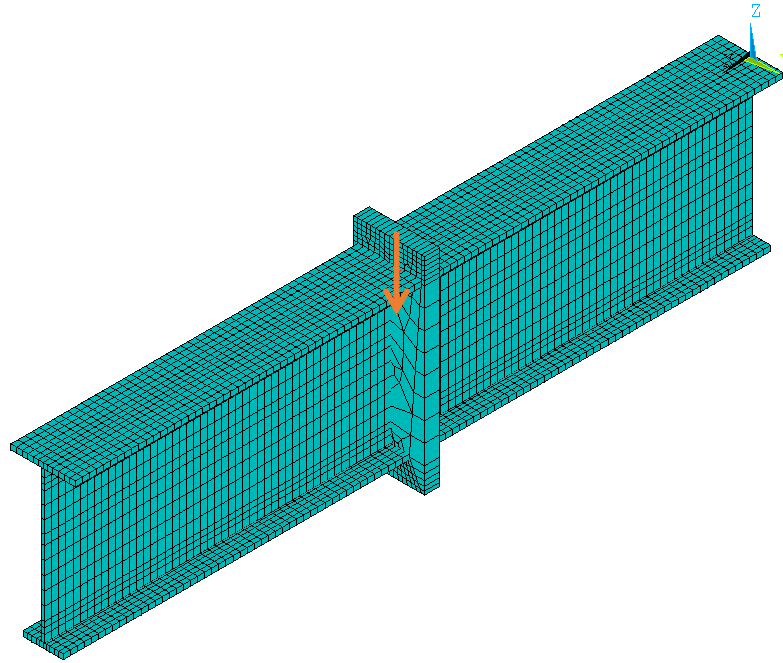


Figure 3-5: Introduction of point load at mid-span

Applied major- and minor-axis bending moments and axial forces are introduced by nodal forces distributed over the cross-section following a plastic stress distribution as represented for the case of major-axis bending in Figure 3-6. Consequently, the values of the nodal forces depend on the width of the neighbouring elements and the node location.

Obviously, the plastic stress distribution only represents a limit case. Sometimes, it is preferred to introduce point loads at the member ends based on an elastic stress distribution. Nonetheless, this also represents only a limit case. Physically the stress distribution changes with ongoing yielding and evolves between elastic distribution and plastic distribution. Additionally, in the real structure, end moments are only introduced in a given member if this member is continuous or possesses moment-resisting connections providing a certain level of (warping) restraint. As it is intended to obtain lower bound resistances, the members are analysed supposing fork end supports as detailed in paragraph 3.2.3. Therefore, a simplification has to be accepted for the introduction of end moments. Also, it may be shown that the distributions of forces (based on elastic or plastic stress distribution) does not significantly influence the obtained member resistance.

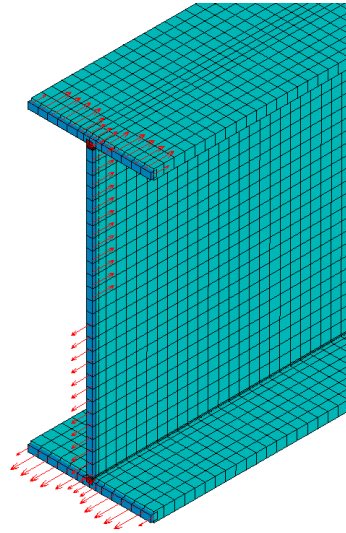


Figure 3-6: Introduction of an applied major-axis bending moment

3.3 Section modelling

3.3.1 Different possibilities to model fillets

In order to account for the influence of the fillets on the cross-section and member resistance of hot-rolled sections, different techniques may be applied. They are presented hereafter and evaluated in the following paragraphs.

A first approach consists in the use of shell elements with modified thickness (see for example (Kettler 2008)). Here, it is proposed to modify the thickness of shell elements in the web in the zone of the fillets. Figure 3-7 shows an IPE 200 section modelled by the “modified thickness technique”. This model is referred to as “Shell var” (var = variable thickness) in paragraph 3.3.2.

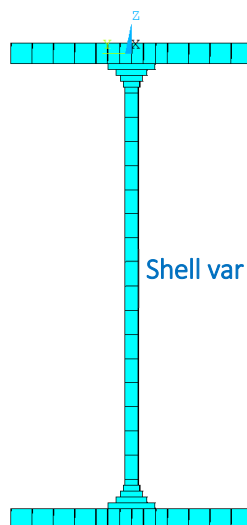


Figure 3-7: Modelling the fillets by shell elements of variable thickness

In (Taras 2011), the fillets are modelled by beam elements of rectangular hollow sections. The height and width of the hollow section as well as the thickness of its walls are chosen here to obtain the same torsion constant and area for the numerical I section as for the physical section. The out-of-plane and in plane bending stiffness are well approximated. The nodes of the beam elements are common with the shell elements and situated at the theoretical centroid of the fillets. Figure 3-8, shows the IPE 200 section whose fillets are modelled by rectangular hollow sections. This model is referred to as “Shell-Beam 1” in paragraph 3.3.2.

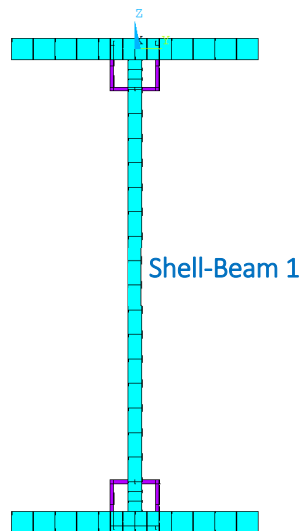


Figure 3-8: Modelling the fillets by rectangular hollow section beam elements

Similarly to the previous approach, the fillets may be modelled by beam elements possessing the exact geometry of the fillets. Additional nodes are created at the centroid of each fillet. These nodes are then attached to the shell model (at nodes A and B of Figure 3-9) by rigid beam elements as shown in Figure 3-9. Again an IPE 200 section is shown to demonstrate this approach. This model is referred to as “Shell-Beam 2” in paragraph 3.3.2.

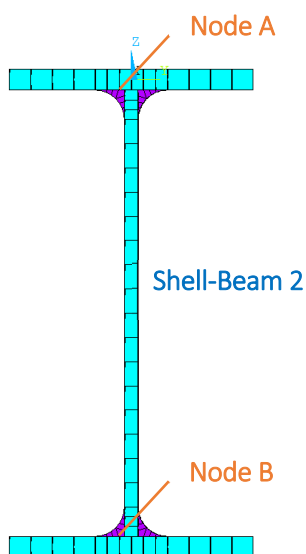


Figure 3-9: Modelling fillets by beam elements of identical geometry

The next approach evaluated here consists of a combination of shell and solid elements. The zone of the section that can be assimilated to plates is modelled by the shell elements and the fillet zone is modelled by solid elements as shown in Figure 3-10. The shell elements are attached to the solid elements by non-flexible contact (always bounded – MPC technology of ANSYS; see reference (ANSYS 2016)). A full continuity between the different elements can therefore be considered. This approach is advantageous as the fillet geometry can, depending on the solid element density, be modelled perfectly. The real stiffness of the fillet zone, offering the restraint to the flanges and the web, is accounted for. This model is referred to as “Shell-Solid” in paragraph 3.3.2.

A clear inconvenient of this technique is the longer calculation time as the model possesses more degrees of freedom as a simple shell model or a model consisting of a combination of shell and beam elements (the calculation times are evaluated at the end of this paragraph).

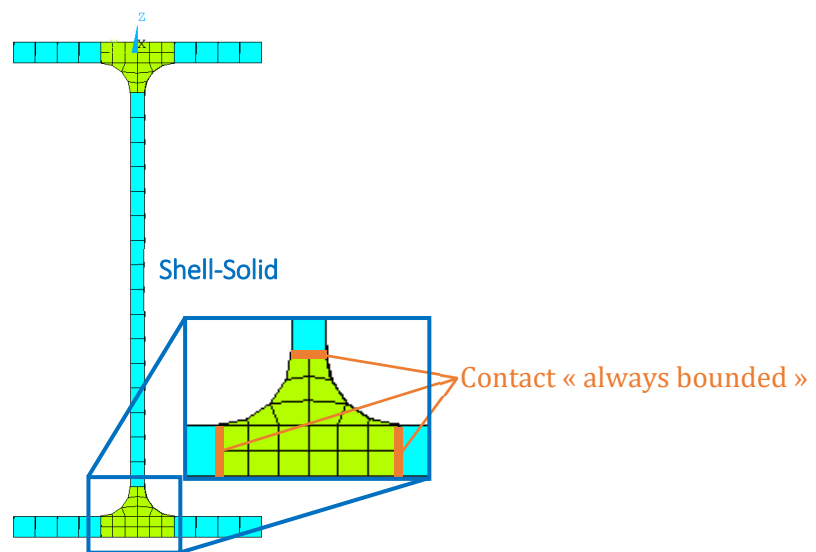


Figure 3-10: Modelling the fillet zone with solid elements

Last, the member is modelled entirely with solid elements. As no interface between different element types exists, full continuity between the finite elements can be ensured. Additionally, the section geometry is most reliably approximated. However, the use of solid elements implies longer calculation time as mentioned before. Figure 3-11 shows the solid model of an IPE 200 section. This model is referred to as “Solid” in paragraph 3.3.2.

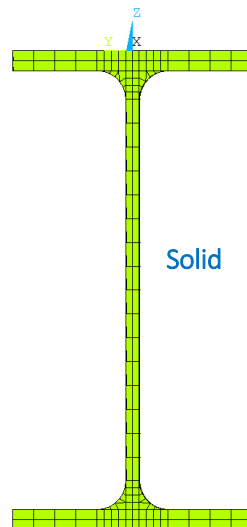


Figure 3-11: Modelling the section entirely with solid elements

3.3.2 Study on the influence of meshing density

3.3.2.1 General

Hereafter, the influence of the meshing density is studied. In particular three points need to be taken into special consideration:

- The element width: If the mesh is too coarse, the numerical result may be unreliable as the distribution of stresses and displacements are less well approximated. Also, as the distribution of residual stresses is not uniform over the cross-section but linear or quadratic (see paragraph 5.3), the number of elements over the cross-section and consequently their width has to be calibrated in order to represent the residual stresses (in particular as the residual stresses are generally introduced as constant per finite element).
- The element aspect ratio: Here, the aspect ratio is defined as ratio between element length and element width (here the element length refers to the element dimension along the x-axis of the member and the element width refers to the dimension of the element in the plane of the cross-section; i.e. the y-z plane of the flanges). The use of finite elements of quadratic shape (element length = element width; aspect ratio = 1) generally yields the most reliable results. However, for long members, using finite elements of quadratic shape leads to an important number of elements and therefore excessive calculation times. Hence, it seems interesting to study the influence of the aspect ratio of the element in order to optimize the meshing density with reference to calculation time.
- The number of elements to represent local buckling: A special issue arises for slender (class 4 in the terminology of Eurocode 3 Part 1-1 (CEN 2005a)) sections. Indeed, a minimum number of elements is necessary to represent the formation of

local buckles. If too few elements are used, the curvature of the buckle may not be sufficiently approximated and the numerical result may be less precise.

The mentioned topics are studied in the following paragraphs.

3.3.2.2 Element width for stocky and medium slender cross-sections

In the following, the influence of the element width is studied for stocky and medium slender sections whose ultimate resistance is not influenced by local plate instability. The influence of the element width is studied for several examples through GMNIA simulations including the residual stress pattern represented in Figure 3-14 and Figure 3-15 as well as a geometric member imperfection affine to the first member (or global) Eigen mode with an amplitude of $L/1000$. The material behaviour is supposed multi-linear including strain hardening (see Figure 3-1) . All studied members are fabricated from steel S235.

The first example is a member of IPE 240 section without fillets (the modelling of the fillets is addressed in paragraph 3.3.3) subject to a constant bending moment of 56,92 kNm and a compression axial force of 379,3 kN (this load combination leads to full yielding of the section). The length of the member is varied between 800 mm and 7000 mm. For the second example the same configuration is studied but the section is supposed to be welded. The meshing density is characterised by the number of elements per flange. The element width of the finite elements in the web is the same as the one in the flanges. For all cases, the element aspect ratio is 1 (elements width = element length).

Figure 3-12 shows the results obtained for the member made of hot-rolled IPE 240 section. The reference value is the result obtained with a meshing density of 20 elements per flange (as being the mesh with the highest density). As can be seen the results for the different densities are rather close. If at least 8 elements are used along the width of the flange, the difference to the reference value is less than 1%.

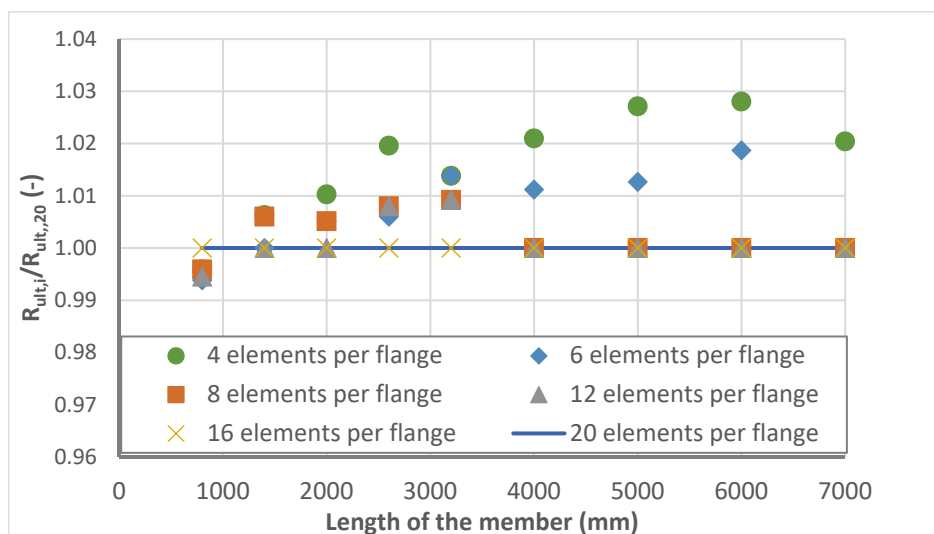


Figure 3-12: Ultimate resistance as a function of the meshing density for a hot-rolled section

Figure 3-13 presents the results for the member made of a welded “IPE 240” section (the reference results are those obtained for 26 elements per flange). Here, it may be observed that the meshing density is of more importance than for hot-rolled sections. In fact, at least 12 to 16 elements per flange are needed in order to converge to the reference value. Also, it can be seen that the difference between the coarse meshes (4 and 6 elements per flange) and the finest meshing densities increases with the member length. This observation seems somewhat surprising because the effect of the imperfections generally vanishes for members of high length and high member slenderness. Figure 3-12 represents a similar tendency but much less pronounced. The problem of the coarser meshes is not studied further in here. Rather, a sufficiently fine mesh is chosen to ensure reliable results.

It may be understood why a denser mesh is necessary for welded sections than for hot-rolled sections if the specific residual stress patterns of Figure 3-14 and Figure 3-15 are studied. It can be seen that the variation of the residual stresses is much higher and much more concentrated for welded sections than for hot-rolled sections. Indeed, Figure 3-15 shows that the residual stresses for welded sections varies from $+f_y$ to $-0,25f_y$ on a distance representing only 5% of the panel width (web height or flange width). Obviously, a smaller element width is necessary to represent this variation.

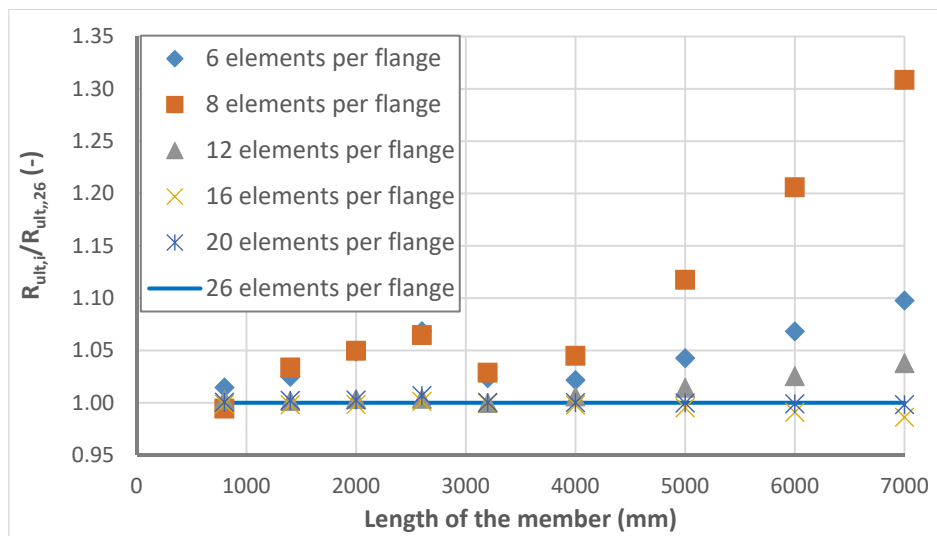


Figure 3-13: Calculated ultimate resistance as a function of the meshing density for a welded section

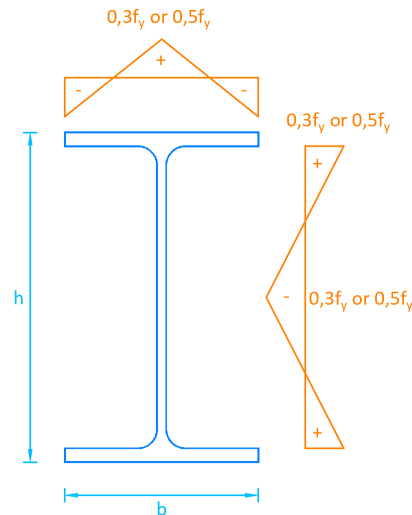
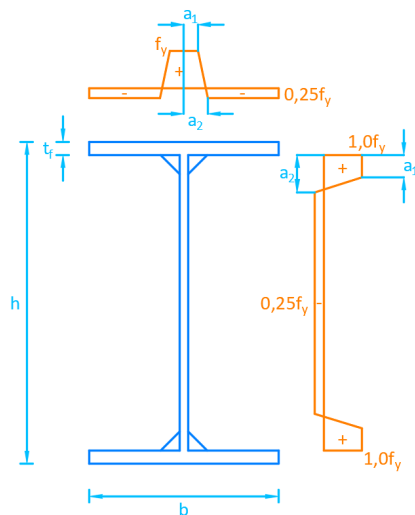


Figure 3-14: Residual stress distribution for a hot-rolled section



	Flange	Web
a_1	$0,075b_f$	$0,075(h-2t_f)$
a_2	$0,125b_f$	$0,125(h-2t_f)$

Figure 3-15: Residual stress distribution for a welded section

In order to confirm the previous findings, the meshing density is evaluated next for the more complex load case of Figure 3-16. The member is made of an IPE 300 section without fillets. It is subject to axial compression and to a lateral and vertical point load applied on the upper flange at mid-span as represented in Figure 3-16.

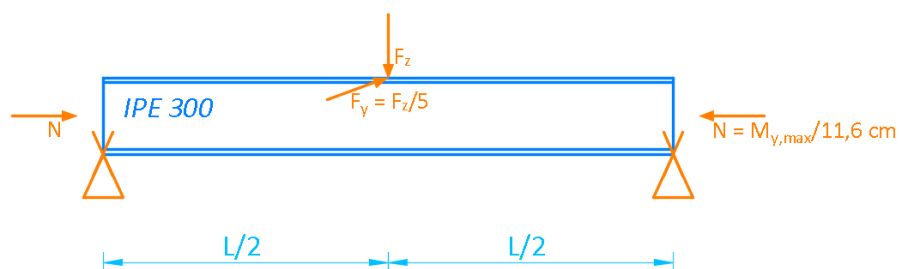


Figure 3-16: Member subject to compression, bi-axial bending and torsion

The results obtained for this most complex load combination are given in Figure 3-17 to Figure 3-19. Additionally to the cases of hot-rolled and welded residual stress pattern, the case of a section without residual stresses is represented in Figure 3-17. It can be observed that if the member is not subject to any residual stresses, the meshing density seems not to be of importance. Indeed, the differences between the different meshing are much less than 1% and consequently negligible.

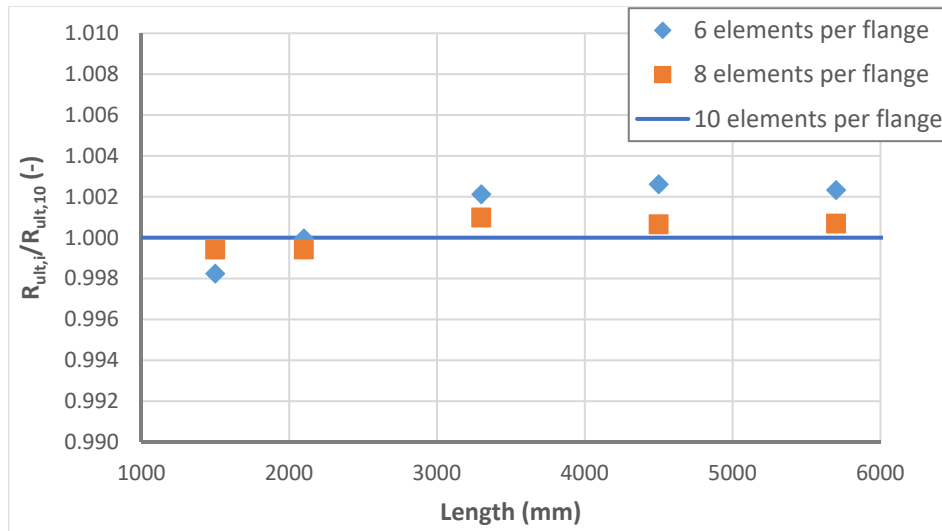


Figure 3-17: IPE 300 section without residual stresses

In case of residual stresses corresponding to hot-rolled sections, one may again remark that 8 elements per flange are sufficient to obtain reliable results. Inversely, the mesh should be rather dense for the case of welded sections. Figure 3-19 shows again that at least 12 to 16 elements along the flange are necessary in order to converge to the reference results. As before, one may observe the surprising behaviour of longer members with the coarsest mesh of 8 elements per flange. In order to obtain reliable results 16 elements per flange are consequently used for members of welded sections in the following.

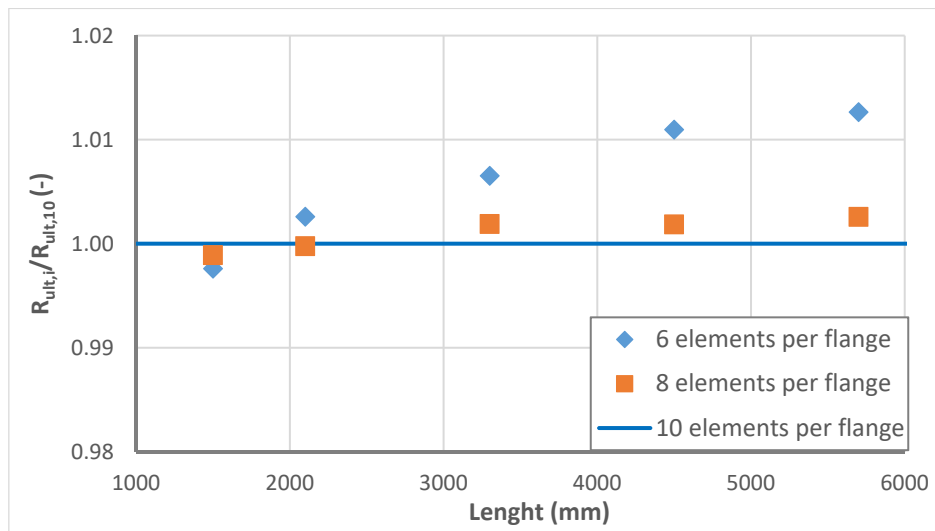


Figure 3-18 : IPE 300 section with residual stresses of hot-rolled sections

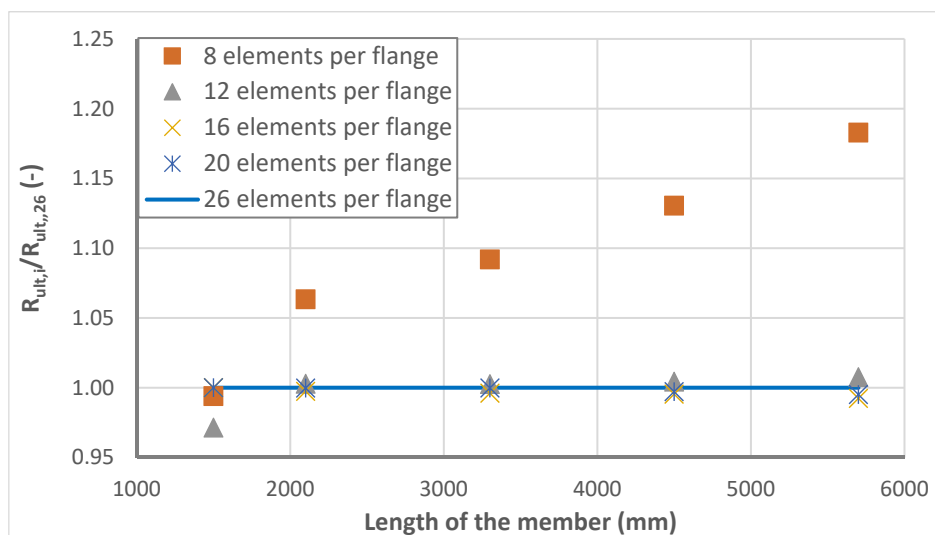


Figure 3-19 : IPE 300 section with residual stresses of welded sections

3.3.2.3 Element aspect ratio

As mentioned previously, the second point that has to be discussed is the aspect ratio of the finite elements. In Figure 3-21, the results of the member used in the first example of paragraph 3.3.2.2 (equivalent IPE 240 section subject to $M_y = 56,92$ kNm and $N = 379,3$ kN) are represented. In every case the element width corresponds to a number of 8 elements per flange (residual stresses according to hot-rolled sections).

As can be seen, up to an aspect ratio of 7, the results differ very few from the reference (aspect ratio = 1). The sole remarkable difference is obtained for the member of 7 m length meshed with elements of an aspect ratio of 10.

However, the load case of constant internal forces, creating uniformly distributed stresses along the member, may be favourable when the aspect ratio is studied. Therefore, the case of the

member shown in Figure 3-20 is studied. The member is consequently subject to a combination of major-axis bending and torsion (and shear forces for the shortest specimen).

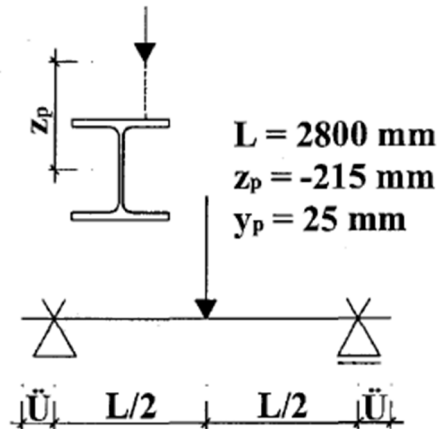


Figure 3-20: Member subject to non-uniform bending and torsion (Figure from reference (FOSTA 2004))

The element width corresponds to a number of 8 elements per flange.

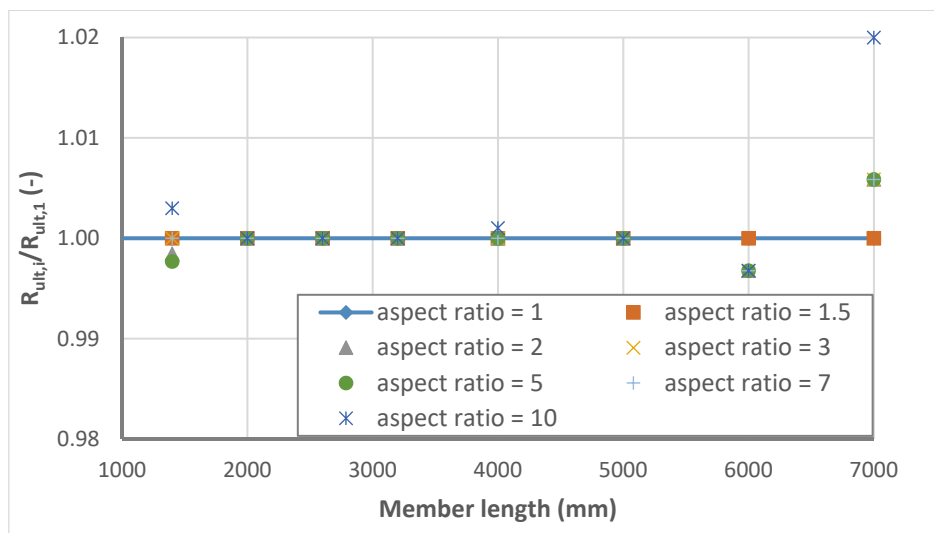


Figure 3-21: Calculated ultimate resistance as a function of the aspect ratio of the finite element

Figure 3-22 shows that the aspect ratio seems to have more influence on the calculated ultimate resistance in case of variable internal forces. It is to be noted that the maximum difference is obtained for short members. In case of longer members, the difference becomes negligible (less than 0,5%). Hence, one might also argue that it is not the aspect ratio that needs to be calibrated but the number of elements along the member length. The results depending on the number of elements are represented in Figure 3-23.

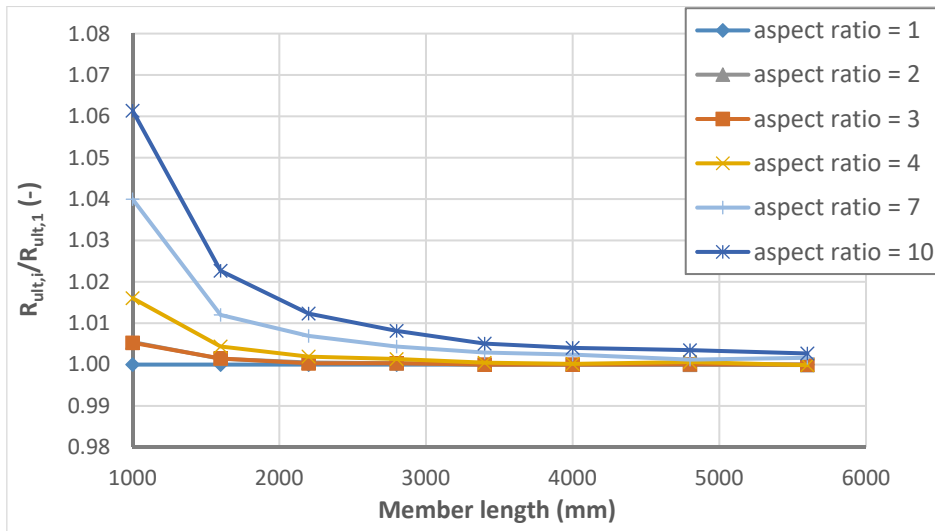


Figure 3-22: Calculated ultimate resistance as a function of the aspect ratio of the finite element for a hot-rolled section under non-uniform bending and torsion

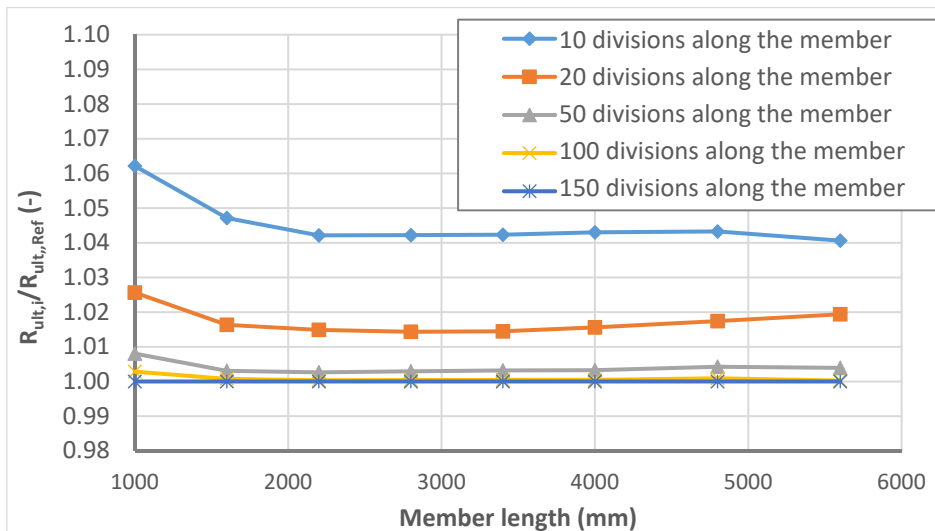


Figure 3-23: Calculated ultimate resistance as a function of the element division along the member for a hot-rolled section under non-uniform bending and torsion

It can be seen in Figure 3-23 that the element division along the member length seems to be a more meaningful parameter to assess the quality of the finite element model. In fact, the error of each model with respect to the reference (8 elements per flange and 150 divisions along the member) varies much less than the error represented in Figure 3-22 (error as a function of the element aspect ratio). It can be concluded that it is not the aspect ratio of the finite element that is at the origin of the error but a too small element division along the member. As the internal forces acting in the member are non-uniform and hence the stresses are also non-uniform along the member, a minimum number of elements is needed to represent this non-uniform stress distribution. Figure 3-23 also shows that the maximum error is always obtained for the shortest member. As the cross-section is compact (IPE 200: class 1 following Eurocode 3 terminology), the stockiest member of 1 m of length is susceptible to attain a certain amount of its plastic resistance. Therefore, the finite element mesh should be fine enough to represent the extent of plasticity. In

Figure 3-24, one may see that, depending on the element division along the member, the yielded zone on the top flange differs. In fact, the model possessing the coarsest mesh (Figure 3-24 a) predicts the greatest plastic zone. However, the peak plastic strain is much smaller than the peak plastic strain calculated by the model with the finest mesh (Figure 3-24 d). One may also remark that the continuity of the plastic strain between the finite elements is not entirely respected in the model represented in Figure 3-24 a) and Figure 3-24 b), whereas the plastic strain spreads continuously over the elements in Figure 3-24 c) and Figure 3-24 d) (it is to be noted that the results determined at the integration points are represented and not the averaged results over the element).

Therefore, in the following at least 100 element divisions along the member is used for the finite element model.

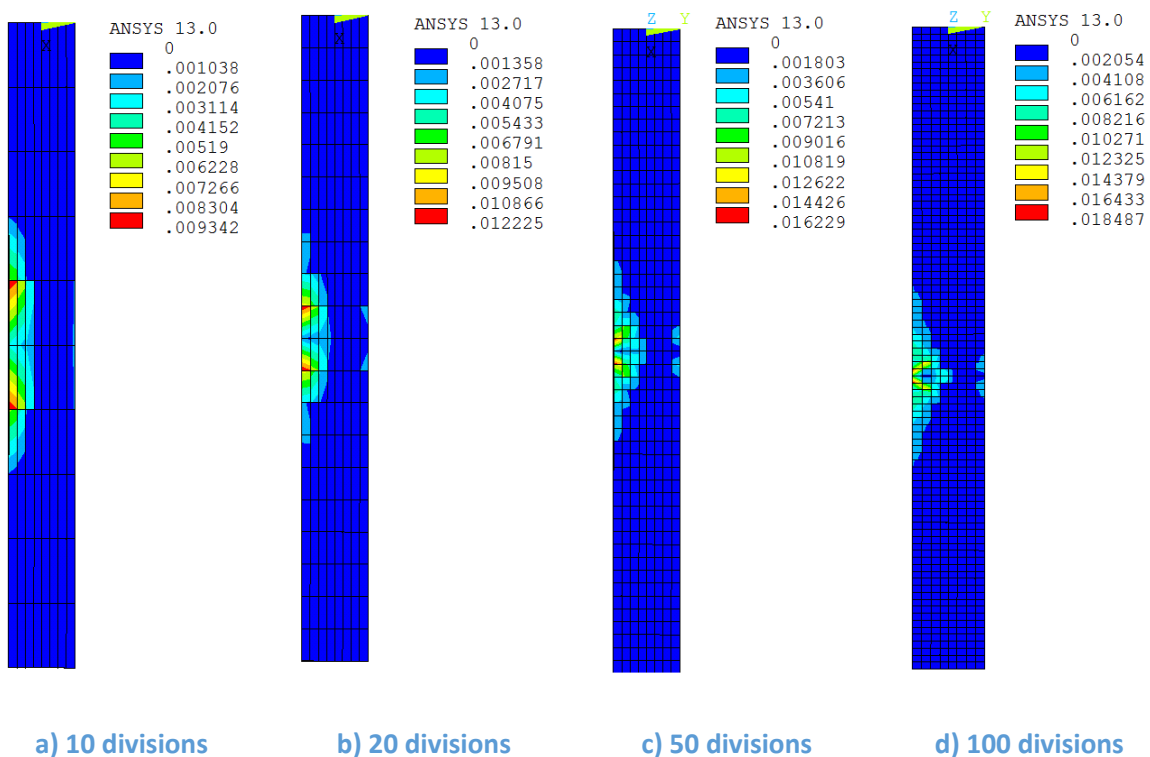


Figure 3-24: Plastic strain distribution on the top flange for the member of 1 m of length depending on the element division along the member

3.3.2.4 Element width for slender cross-sections

Hereafter, cross-sections that are sensitive to local buckling are referred to as slender cross-sections (class 4 section in the terminology of Eurocode 3). For these sections the meshing has to be capable of reproducing local instability. Obviously, the mesh would be too coarse if there is only one finite element along the presumed local buckle. Conversely, a very fine mesh would again lead to longer calculation time. Hence, it is of interest to study the influence of the number of finite elements along the local buckle on the calculated ultimate resistances. Here, two welded sections are studied. They are noted as $W.h.t_w.b_f.t_f$:

- W.500.9,5.200.12,5 (web is sensitive to local buckling – class 4 web)

- W.500.7.200.5,36 (flange is sensitive to local buckling – class 4 flange)

The studied members are subject to constant major-axis bending. The Figure 3-27 and Figure 3-28 compare the results obtained through GMNIA calculations. These calculations include the typical residual stress pattern for welded sections (see Figure 3-15), a member imperfection affine to the first Eigen-mode for lateral-torsional buckling with an amplitude of $L/1000$ and a local imperfection. It is chosen to apply a local imperfection of sinusoidal shape. The longitudinal extension of one half wave of the local imperfection (see Figure 3-25) is chosen to be the mean value of the sum of half the flange width and the web height (twice the medium length of half the flange width and the web height) as shown in Eq. (3.1). In the perpendicular direction the local imperfection extends over the width of the considered plate (over $b_f/2$ for the flanges and over h_w for the web – see Figure 3.2).

$$l_{wave / 2} = \frac{\frac{b_f}{2} + h_w}{2} \quad (3.1)$$

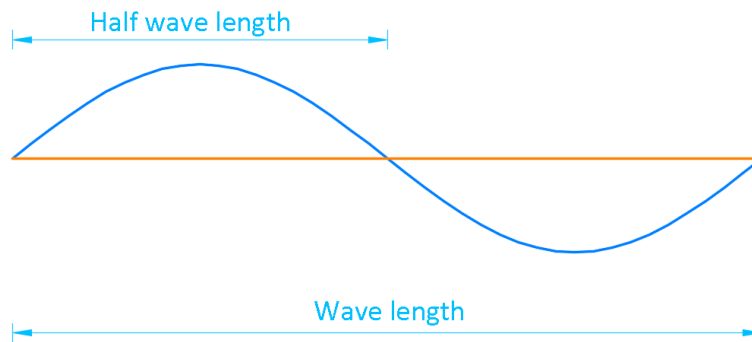


Figure 3-25: Definition of wave length for the sinusoidal imperfection

The amplitude of the imperfection is chosen to be equal to $h_w/200$ for the web and $b_f/400$ for the flanges (a deeper investigation on the influence of the local imperfection on the member resistance is presented in paragraph 5.2.1.7). Figure 3-26 shows the applied local imperfection for one example with an increased amplitude for a better representation. It should be noted that the number of elements per quarter wave (half of the local buckle) is 10 for the given example.

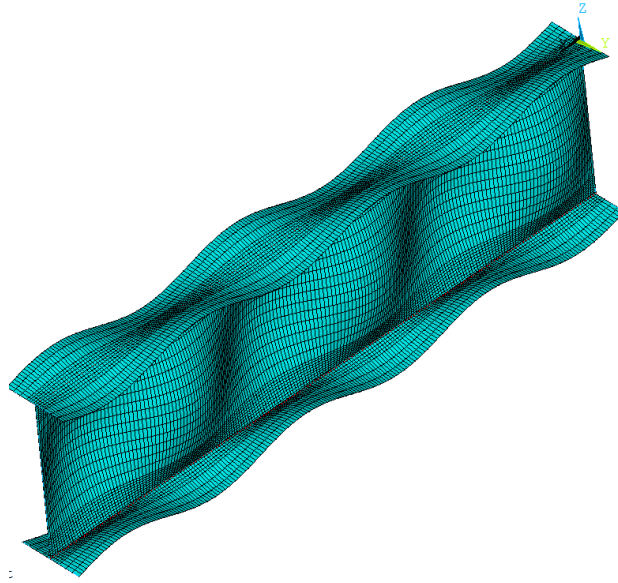


Figure 3-26: Local imperfection applied to an I-shaped member

Figure 3-27 and Figure 3-28 compare the ultimate load factors obtained based on different numbers of elements per quarter wave. In order to facilitate the comparison between both members, the scale of the ordinate axes (representing the ratio $R_{ult,i}/R_{ult,10}$) is the same.

As expected, the figures clearly show that the coarsest mesh yields the least reliable results. Also, one may observe that a coarser mesh leads to unsafe results (up to 5% for W.500.7.200.5,36 – see Figure 3-28). This may be explained by the fact that curvature of the plate due to local buckling is less well approximated by a coarse mesh. Consequently, the stresses resulting from local buckling are lower in this case (again it is referred to paragraph 5.2.1.7 giving details on the influence of the local imperfection). Finally, the figures show that the differences between the mesh densities decrease with the member length. Here the interaction between member instability (lateral-torsional buckling) and section instability is the probable reason. In fact, the sensitivity of the member to lateral torsional buckling increases with the member length. Therefore, the stresses are lower at the Ultimate Limit State and hence the cross-section is less sensitive to local buckling.

However, the tendencies discussed above are much more pronounced in case of the section with slender flanges. As the flanges contribute much more to the bending resistance of the section than the web, local buckling of the flanges has a greater influence on the section and member resistance than local buckling of the web. Consequently, the differences between a coarse mesh and a fine mesh are less pronounced for the section with a slender web.

On the basis of the results presented in Figure 3-27 and Figure 3-28, it is concluded that at least 4 elements per quarter wave seem to be necessary to obtain reliable results.

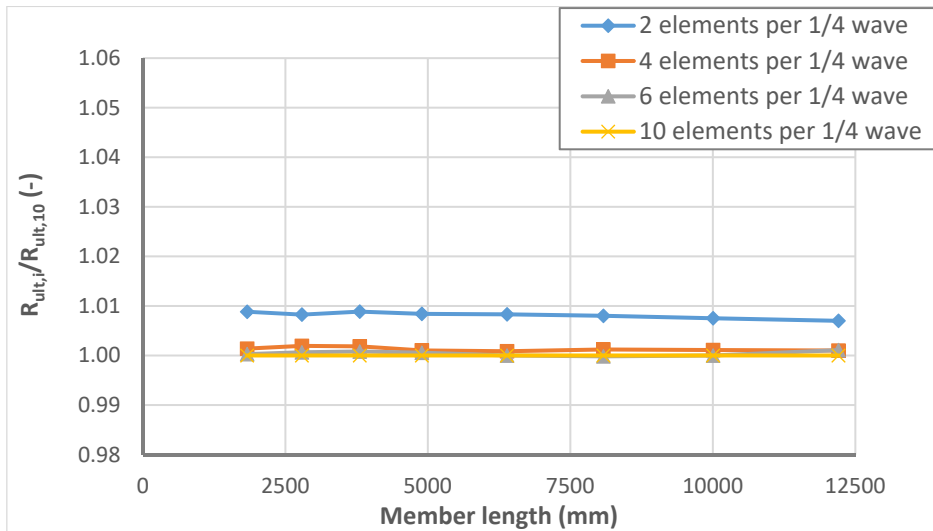


Figure 3-27: Influence of element number along the local buckle – W500.9,5.200.12,5

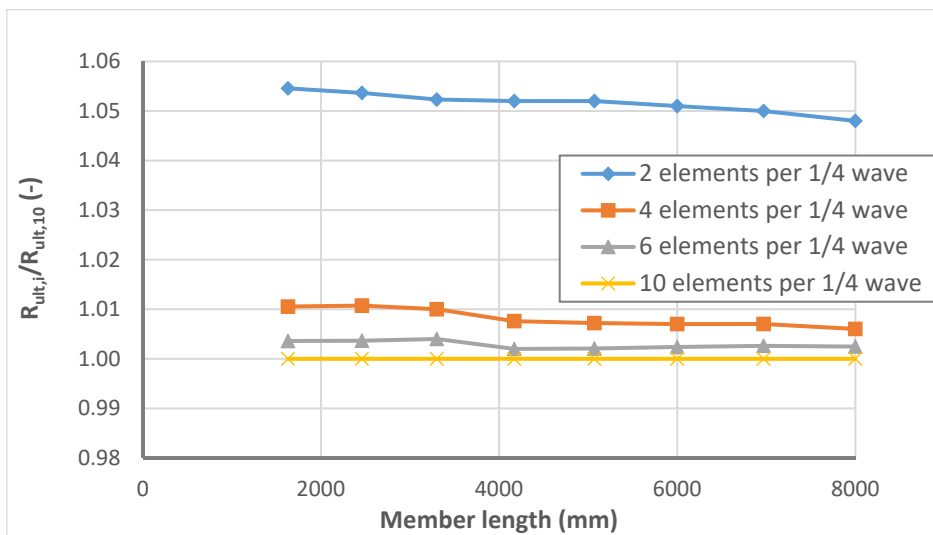


Figure 3-28: Influence of element number along the local buckle – W.500.7.200.5,36

3.3.2.5 Summary on meshing density

Through paragraph 3.3.2, the influence of the meshing density on the ultimate resistance has been analysed. This study permits to conclude on the following points:

- For hot-rolled sections, 8 finite elements of constant width per flange are sufficient to obtain reliable results;
- For welded sections, at least 16 finite elements of constant width per flange are necessary to account for the residual stress distribution;
- For stocky and medium slender sections (not sensitive to local buckling), the member should be divided into at least 100 elements along its length;
- For slender sections (sensitive to local buckling), the element division along the length depends on the wave length of the presumed local buckle; it seems necessary to use at least 4 elements along one quarter wave;

- The aspect ratio of the finite element is not of primary importance for the numerically determined ultimate resistance of the member; however the number of elements along the member should respect the prescription given above. Also, in order to avoid excessively long elements, the aspect ratio is limited to 3 hereafter.

3.3.3 Evaluation of the stiffness of the different modelling techniques

3.3.3.1 General

In Chapter 2, it has been recalled that the fillets of hot-rolled sections may have a non-negligible influence to the cross-section characteristics, especially to those linked to Saint Venant's torsion as the torsion constant I_t and the Saint Venant's torsional moment resistance $M_{x,St,V,R}$. It seems therefore interesting to study how the influence of the fillets may be precisely accounted for. In paragraph 3.3.1, different modelling techniques have been presented. They are evaluated hereafter in two steps:

- First, elastic critical loads are calculated for different load cases in order to evaluate the precision of the bending, torsional and warping stiffness obtained with the different modelling techniques.
- In a second step (see paragraph 3.3.4) the plastic cross-section resistances obtained with the different models are compared for simple and combined load cases.

The sections used for this sub study as well as their geometric and mechanical characteristics are given in Table 3-2.

In order to evaluate the quality of the approximation of the mechanical characteristics by the different modelling techniques, the elastic critical loads are calculated for the following modes:

- Major-axis flexural buckling;
- Minor-axis flexural buckling;
- Torsional buckling;
- Lateral-torsional buckling.

Different lengths are studied for each member so that the relative slenderness is varied between approximately 0,1 and 2 supposing that the member is made of S235.

For the following comparisons the reference value is obtained with the analytical expressions based on the theoretical values of the cross-section constants I_y , I_z , I_w et I_t . In fact, in order to validate the numerical model in a last step with reference to physical tests, it is necessary to reproduce as precisely as possible the physical cross-section and its mechanical characteristics. Hereafter only selected results are presented. Nevertheless, they are representative of the totality of results.

Table 3-2: Sections used to evaluate different techniques for the modelling of the fillets

Section	Geometry		Mechanical characteristics	
IPE 200	h [mm]	200	A [cm ²]	28,484
	t _w [mm]	5,5	I _y [cm ⁴]	1943,2
	b [mm]	100	I _z [cm ⁴]	142,37
	t _f [mm]	8,5	I _t [cm ⁴]	6,884
	r [mm]	12	I _w [cm ⁶]	13052
IPE 550	h [mm]	550	A [cm ²]	134,42
	t _w [mm]	11,1	I _y [cm ⁴]	67117
	b [mm]	210	I _z [cm ⁴]	2667,6
	t _f [mm]	17,2	I _t [cm ⁴]	122,16
	r [mm]	24	I _w [cm ⁶]	1,893.10 ⁶
HEM 160	h [mm]	180	A [cm ²]	97,051
	t _w [mm]	14	I _y [cm ⁴]	5098,3
	b [mm]	166	I _z [cm ⁴]	1758,8
	t _f [mm]	23	I _t [cm ⁴]	163,63
	r [mm]	15	I _w [cm ⁶]	108380
HEB 300	h [mm]	300	A [cm ²]	149,08
	t _w [mm]	11	I _y [cm ⁴]	25166
	b [mm]	300	I _z [cm ⁴]	8562,8
	t _f [mm]	19	I _t [cm ⁴]	185,87
	r [mm]	27	I _w [cm ⁶]	1,69.10 ⁶
HEA 800	h [mm]	790	A [cm ²]	285,83
	t _w [mm]	15	I _y [cm ⁴]	303443
	b [mm]	300	I _z [cm ⁴]	12639
	t _f [mm]	28	I _t [cm ⁴]	606,77
	r [mm]	30	I _w [cm ⁶]	18,35.10 ⁶

3.3.3.2 Major-axis flexural buckling

Hereafter, the results for the different models are compared for the case of major-axis flexural buckling. In addition to the models presented in paragraph 3.3.1 the results of two beam models, noted as Timoshenko and Bernoulli, are included in the following figures in order to illustrate the influence of shear deformations on the critical load for small values of the relative slenderness (short members). In fact, the difference between both beam models can be directly linked to shear deformation, not considered by the Bernoulli beam model, as both beam models are identical in all other points.

The reference value is the result obtained by the Timoshenko beam elements considering the influence of shear deformations. The results are represented as function of the relative

slenderness λ_y defined by (it may be noted that all sections can be considered as compact, i.e. susceptible to attain the plastic resistance N_{pl} if second order effects are negligible):

$$\bar{\lambda}_y = \sqrt{\frac{N_{pl}}{N_{cr,y}}} \quad (3.2)$$

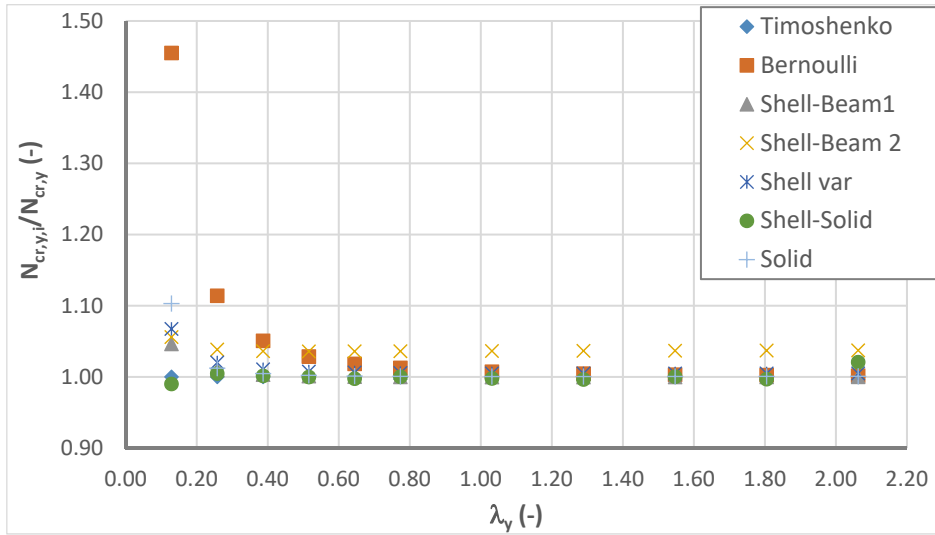


Figure 3-29: Comparison of the critical loads obtained by the different models – IPE 200

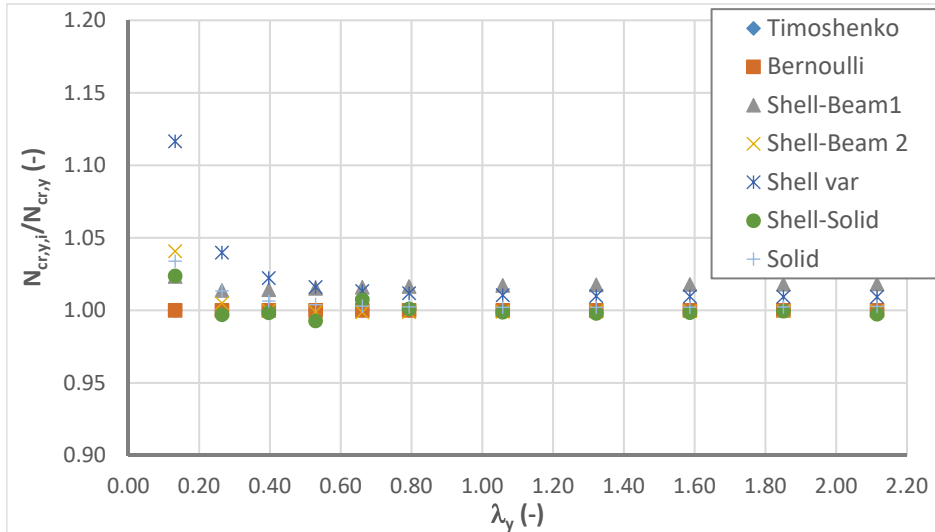


Figure 3-30: Comparison of the critical loads obtained by the different models – HEM 160

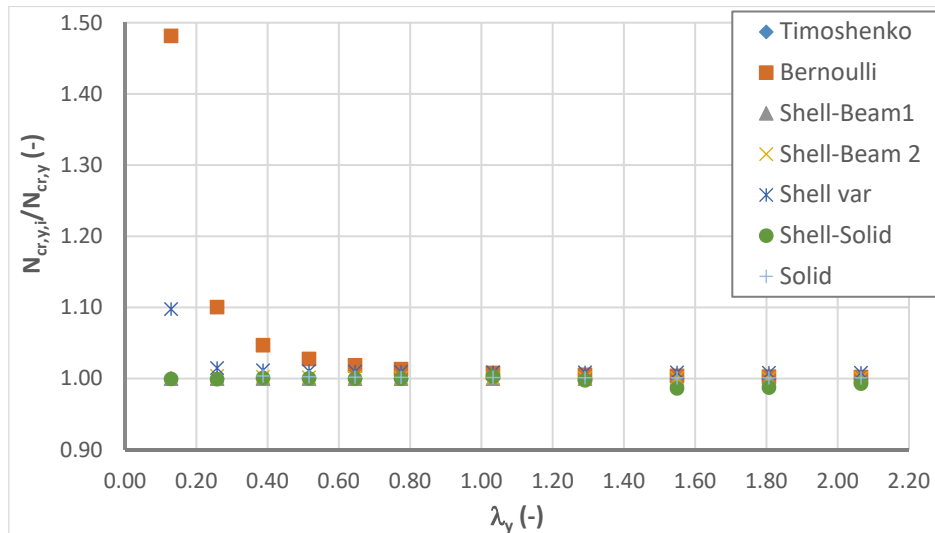


Figure 3-31: Comparison of the critical loads obtained by the different models – HEA 800

The influence of shear deformation on the critical axial force for major-axis buckling can be identified easily in the previous figures. For a relative slenderness of approximately 0,1 the difference attains 40 to 90%. Between models considering the shear deformations (all but beam model Bernoulli) and the Bernoulli beam model. Even for more realistic values of the relative slenderness (between 0,4-0,6) the influence of shear deformation does not completely disappear, yet it is much less pronounced (3-10%).

The results obtained by the other models correspond very well to the reference result. The differences are in most cases lower than 1% and consequently negligible.

3.3.3.3 Minor-axis flexural buckling

As for the case of major-axis buckling, the models are compared hereafter. The reference value is again the result obtained with the Timoshenko beam model considering the influence of shear deformations. The results presented next are again given as a function of the relative slenderness following the definition of Eq. (3.3).

$$\bar{\lambda}_z = \sqrt{\frac{N_{pl}}{N_{cr,z}}} \quad (3.3)$$

Figure 3-32 to Figure 3-34 highlight the influence of shear deformation for a small relative slenderness again. Additionally, the results confirm that all studied models represent well the major- and minor-axis bending stiffness of the member. The results are even closer to each other than in the case of major-axis buckling.

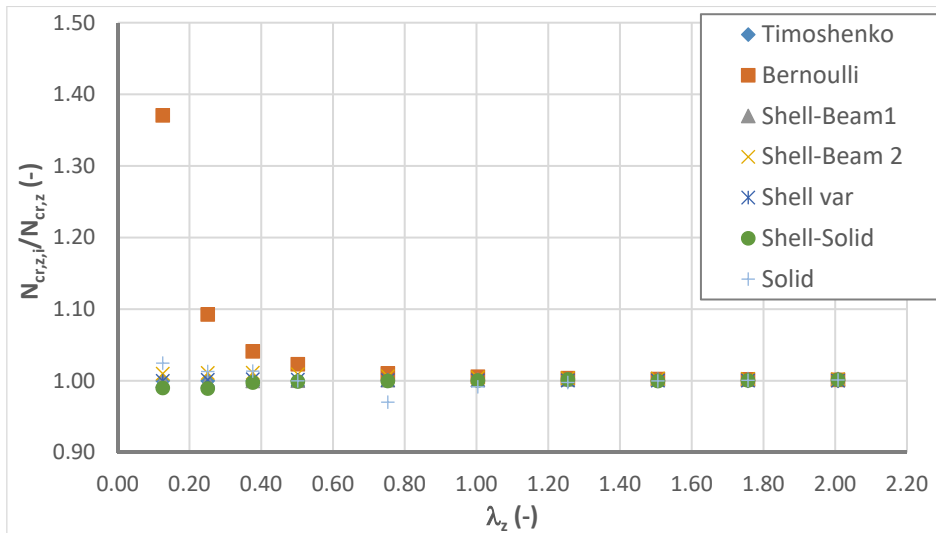


Figure 3-32: Comparison of the critical loads obtained by the different models – IPE 550

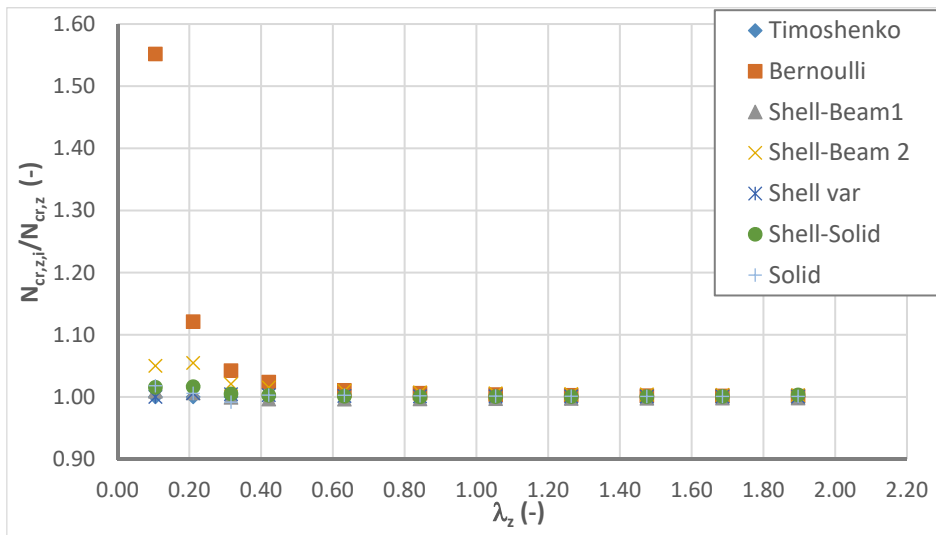


Figure 3-33: Comparison of the critical loads obtained by the different models – HEB 300

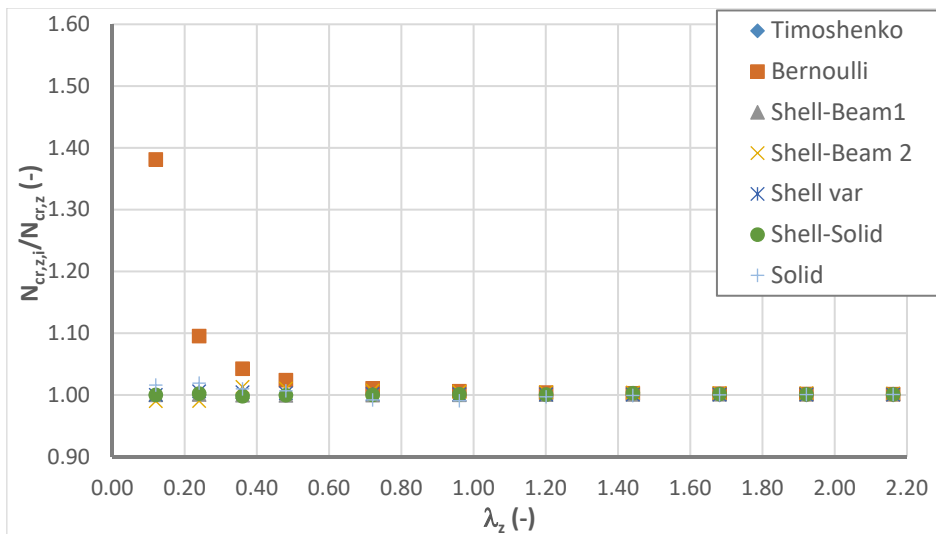


Figure 3-34: Comparison of the critical loads obtained by the different models – HEA 800

3.3.3.4 Torsional buckling

Figure 3-35 to Figure 3-37 compare the quality of the models to predict the critical load for torsional buckling. The reference result may be obtained with Eq. (3.4).

$$N_{cr,t} = \frac{1}{i_p^2} \left(GI_t + EI_w \frac{\pi^2}{L^2} \right) \quad (3.4)$$

and

$$\bar{\lambda}_t = \sqrt{\frac{N_{pl}}{N_{cr,t}}} \quad (3.5)$$

In the case of torsional buckling, the difference between the two beam models is negligible. However, it seems that the representation of the torsional stiffness of the member is more delicate than the modelling of the bending stiffness. In fact, the differences between the studied models are much more pronounced than before. The model giving the results the closest to the reference is the one combining shell and solid elements; the difference is generally less than 1%. The model combining shell and rectangular beam elements also yields very satisfactory results. The models “Shell var” and “Shell-Beam 2” give similar but generally the least exact results. For these two models, it may be observed that the difference to the reference result increases with the member length. It should be recalled that for high member lengths the critical load is mainly influenced by the Saint Venant’s torsional stiffness of the member as shown in Eq. (3.4). In fact, with increasing length the value of the critical axial force for torsional buckling attains a limit value as the term $EI_w\pi^2/L^2$ tends to zero. Based on the results, one may therefore conclude that the warping stiffness is predicted satisfactorily by models “Shell var” and “Shell-Beam 2” (small differences to the reference value for small lengths) whereas the torsional stiffness is poorly approximated. This discrepancy may be attributed to the fact that the continuity of material is not respected in the zone of the fillets. Indeed, for both models, “Shell var” and “Shell-Beam 2”, the geometry of the fillets is precisely modelled but the fillets are not in continuous contact with the web and the flange and consequently, the continuity of material is not ensured (continuity of the warping function). The model combining shell and beam elements of rectangular hollow section does not possess the mentioned continuity, either, as the geometry of the fillets is not modelled directly. However, as the geometry of the rectangular hollow section is calibrated so that the torsional constant and the area of the section are equivalent to the real section, the torsional stiffness as well as the flexural stiffnesses are well approached. The “Solid” model and the “Shell-Solid” model perfectly respect the continuity of the material and consequently yield very satisfactory results.

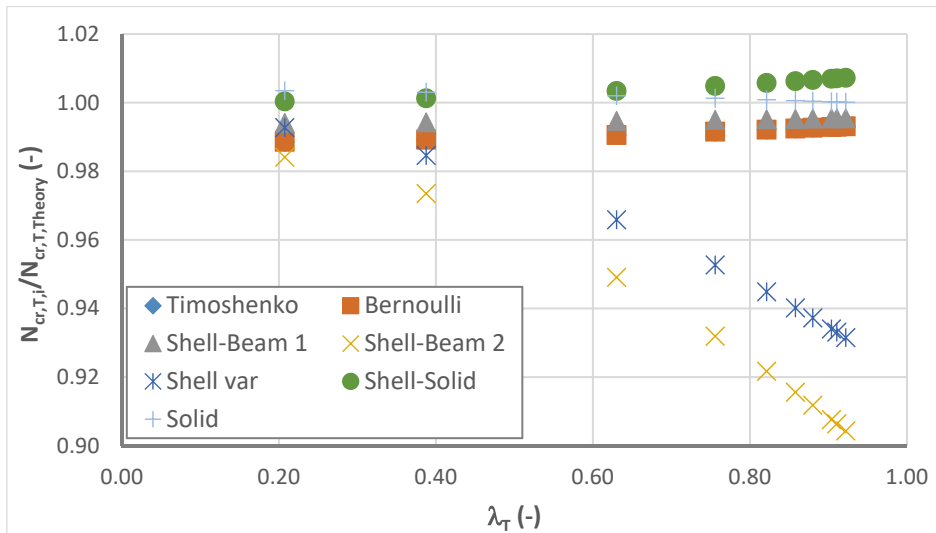


Figure 3-35: Comparison of the critical loads obtained by the different models – IPE 200

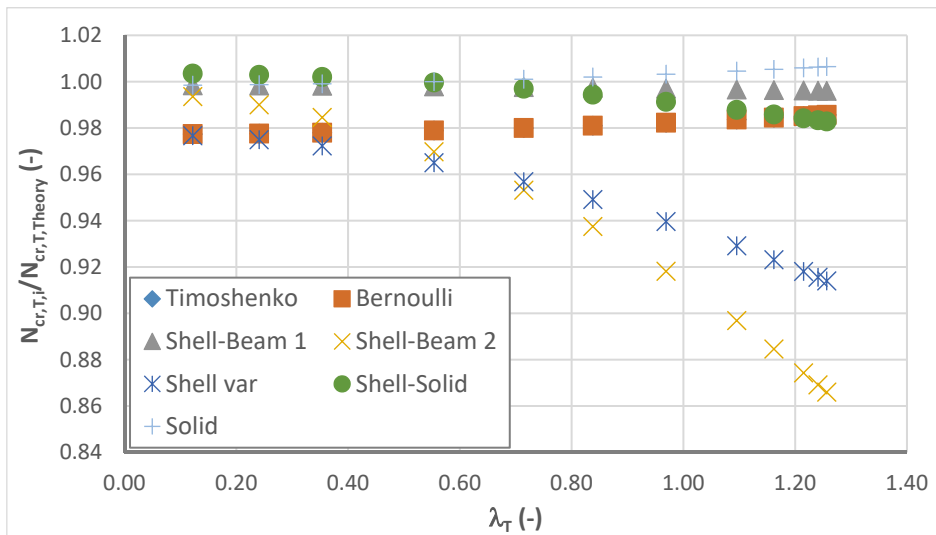


Figure 3-36: Comparison of the critical loads obtained by the different models – IPE 550

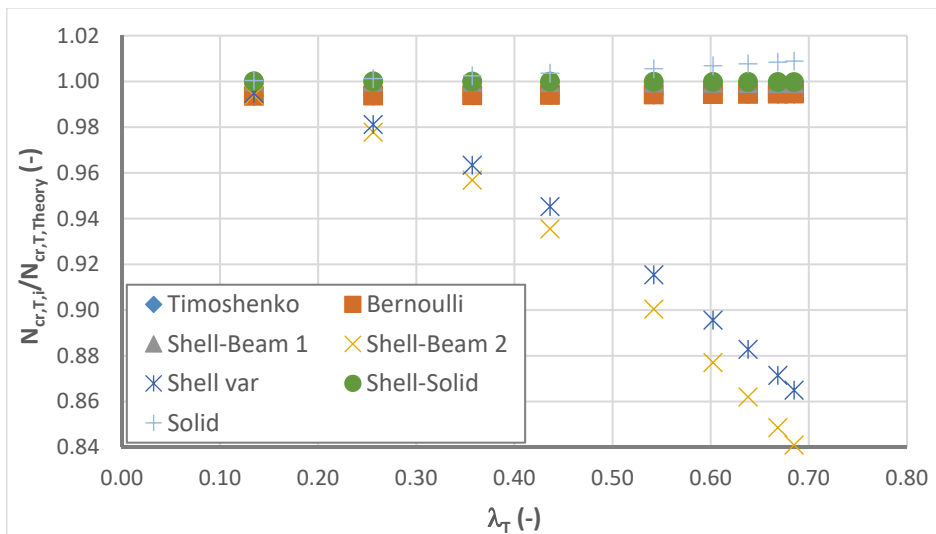


Figure 3-37: Comparison of the critical loads obtained by the different models – HEB 300

3.3.3.5 Lateral-torsional buckling

Last, the influence of the fillet modelling is evaluated for the case of lateral-torsional buckling. As for the case of torsional buckling, the differences between the studied models cannot be overseen in Figure 3-38 to Figure 3-40. The “Solid” model and the model combining shell and solid elements yield the best results. Since the continuity between the different zones of the section is best represented (besides the case of beam models), the quality of the models is not surprising.

Again, the models “Shell-Beam 2” and “Shell-var” represent the stiffness the least well. The differences with respect to the reference attain 5 to 10%. Yet, the model “Shell var” gives slightly more accurate results. Nonetheless, it appears that the differences between these two models and the other models are much less pronounced than for the case of torsional buckling. This may be understood because, additionally to the torsion constant and to the warping constant, the second moment of area about the minor-axis highly influences the value of the critical moment M_{cr} (more than the critical axial force for torsional buckling). This is recalled by the analytical expression represented in Eq. (3.6) (applicable for the case of constant major-axis bending). Eq. (3.6) also shows that the influence of the torsional constant of the section is reduced as it is divided by I_z .

$$M_{y,cr} = EI_z \frac{\pi^2}{L^2} \sqrt{\frac{I_w}{I_z} + \frac{GI_T}{EI_z} \frac{L^2}{\pi^2}} \quad (3.6)$$

and

$$\bar{\lambda}_{LT} = \sqrt{\frac{M_{y,pl}}{M_{y,cr}}} \quad (3.7)$$

Finally, one may observe that the model “Shell-Beam 1” confirms its good quality to represent the torsional stiffness of the member. In most cases, the results are comparable to the more complex “Solid” and “Shell-Solid” models.

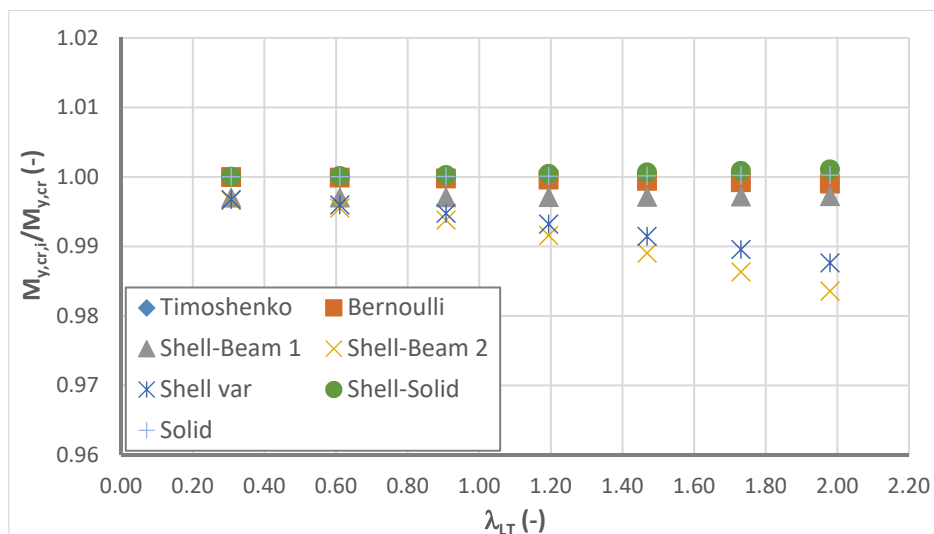


Figure 3-38: Comparison of the critical loads obtained by the different models – IPE 200

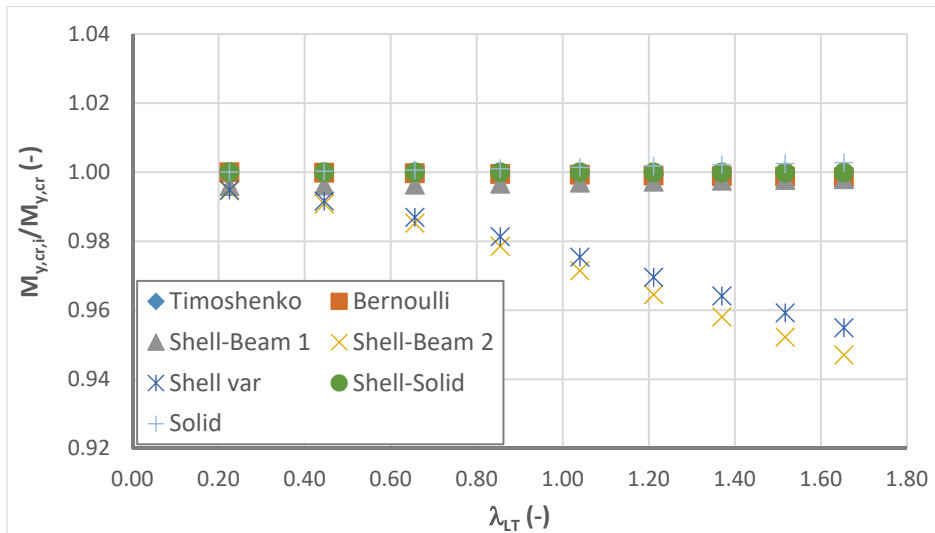


Figure 3-39: Comparison of the critical loads obtained by the different models – HEB 300

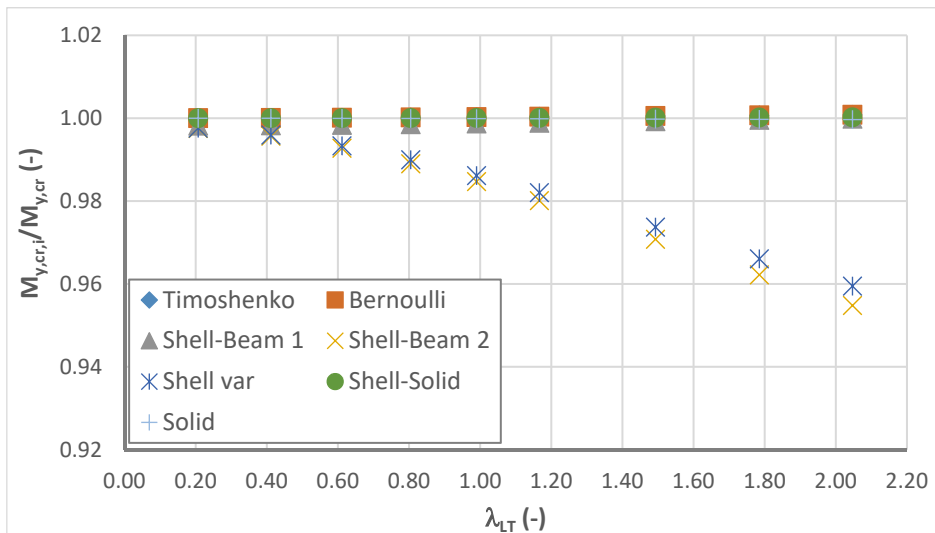


Figure 3-40: Comparison of the critical loads obtained by the different models – HEA 800

3.3.3.6 Conclusion

Here before various numerical investigations were performed with the objective to evaluate the different models with respect to their quality to represent the real stiffness of the member, especially for the case of hot-rolled cross-sections whose fillets have a considerable influence on the torsional stiffness of the beam. The results permit to conclude that:

- All models represent very well the major- and minor-axis bending stiffness;
- The “Solid” model and the model “Shell-Solid” represent best the torsional stiffness of the section;
- The model “Shell-Beam 1”, combining shell and beam elements of rectangular hollow section also represent very well the torsional stiffness of the section;

- The models “Shell-Beam 2” and “Shell var” are the least well suited to represent the torsional stiffness of the section.

As it has been shown that the models “Shell-Beam 2” and “Shell var” are not capable to reproduce satisfactorily the torsional stiffness of the member, they is not be considered in the following.

It should be recalled that the reference values are obtained based on analytical expressions using the theoretical mechanical cross-section characteristics. This is justified as the goal of the comparison is to conclude on what modelling technique may be used to reproduce most precisely the cross-section characteristics of a physical member so as to recalculate laboratory tests used in a last step for the final validation of the numerical model.

3.3.4 Plastic section resistance

3.3.4.1 *General*

The sections of Table 3-2 are used hereafter in order to evaluate whether the different types of section modelling are capable to represent well the plastic distribution of the stresses over the cross-section and consequently the plastic cross-section resistance. In order to obtain the plastic limit load, material non-linear analyses (MNA) are performed supposing an **elastic-perfectly plastic** material behaviour. It is recalled that this type of analysis only includes material non-linear effects. Geometric non-linearity as well as imperfections are not included. Also, it should be noted that residual stresses are not introduced here. In general, their influence on the plastic limit state is negligible owing to the ductility of steel. Nonetheless, if instability (local buckling or member buckling) was studied, residual stresses should be accounted for.

3.3.4.2 *Mono-axial bending and axial force*

The members studied hereafter are supposed to be subject to a constant distribution of major-axis bending, minor-axis bending or the axial force. Also, they are supposed to possess fork end supports. Figure 3-41, Figure 3-42 and Figure 3-43 show the results for the cases of major-axis bending, minor-axis bending and axial force, respectively. One may observe that all models yield results very close to the reference values for all cross-sections and member lengths. The results are slightly conservative compared to the theoretical plastic cross-section resistance but the differences are negligible. It should also be mentioned that the results do not depend on the length as second order effects (geometric non-linearity) are excluded from the numerical simulations (MNA).

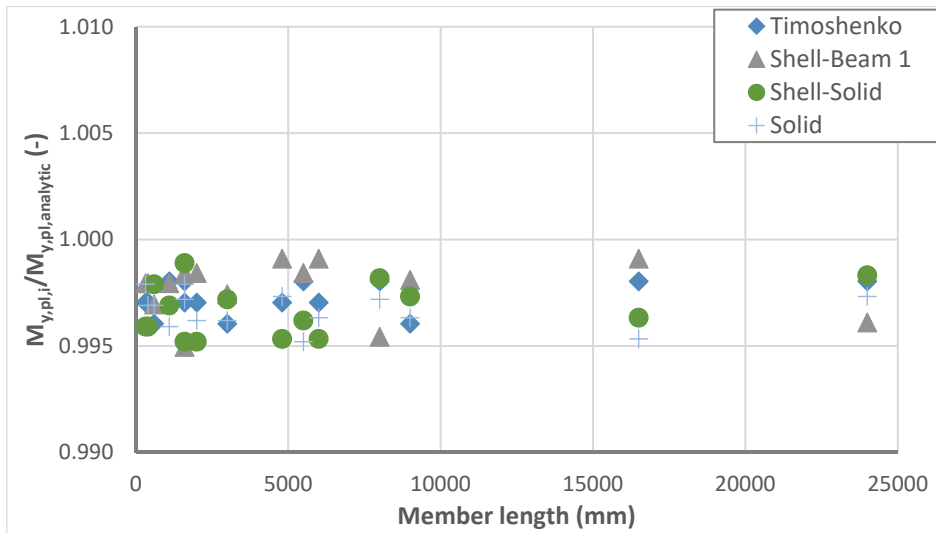


Figure 3-41: Comparison of different models regarding the plastic major-axis bending resistance

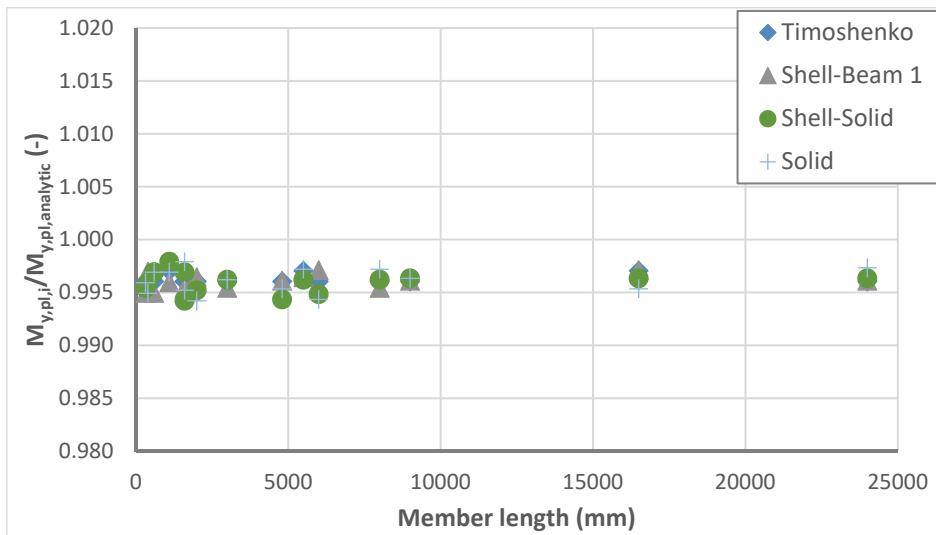


Figure 3-42: Comparison of different models regarding the plastic minor-axis bending resistance

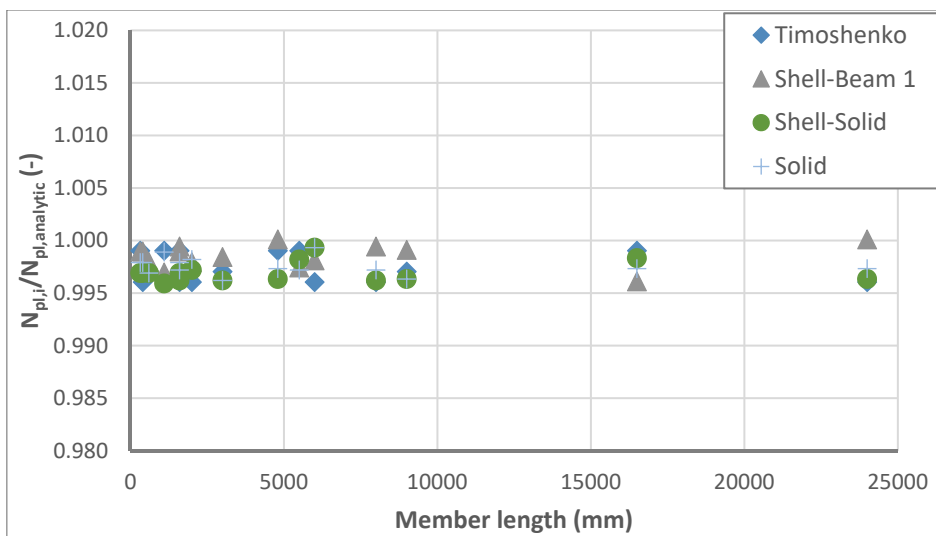


Figure 3-43: Comparison of different models regarding the plastic axial force resistance

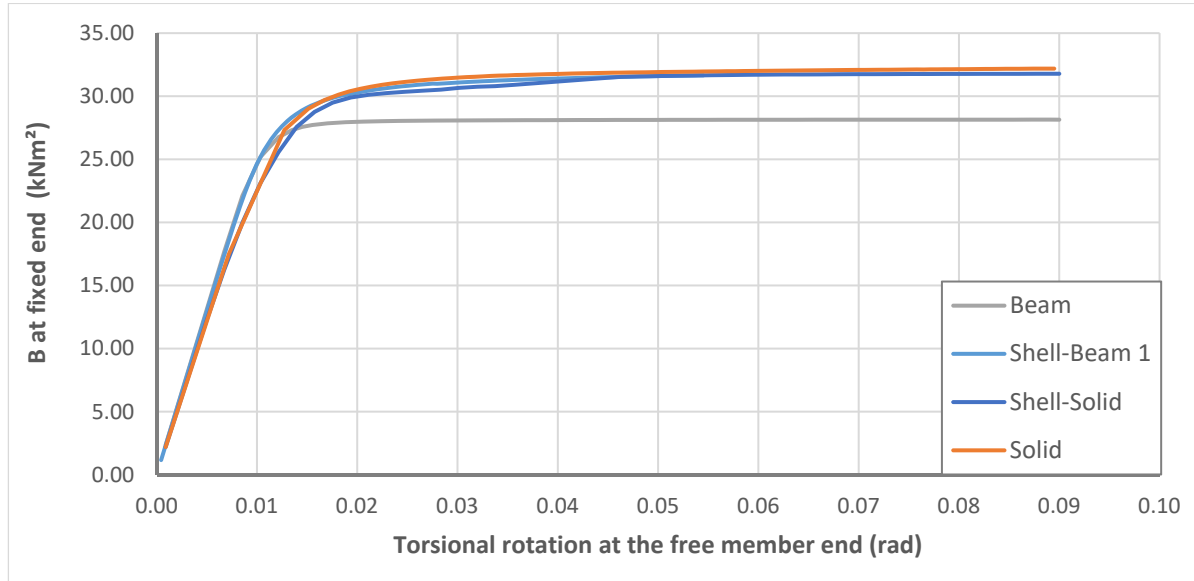
3.3.4.3 Torsion

The case of applied torque differs from the cases treated before. In fact, an applied torsional moment generally creates a combination of bi-moments, warping torsional moments and Saint Venant's torsional moments. Hence, for a section subject to an applied torque, the numerically obtained section resistance corresponds to an interaction between several internal moments. The importance of each component (B , $M_{x,St.V}$, $M_{x,w}$) depends on the length of the member and on the torsional characteristics of the section, i.e. on the warping decay factor ε_T (see Chapter 2).

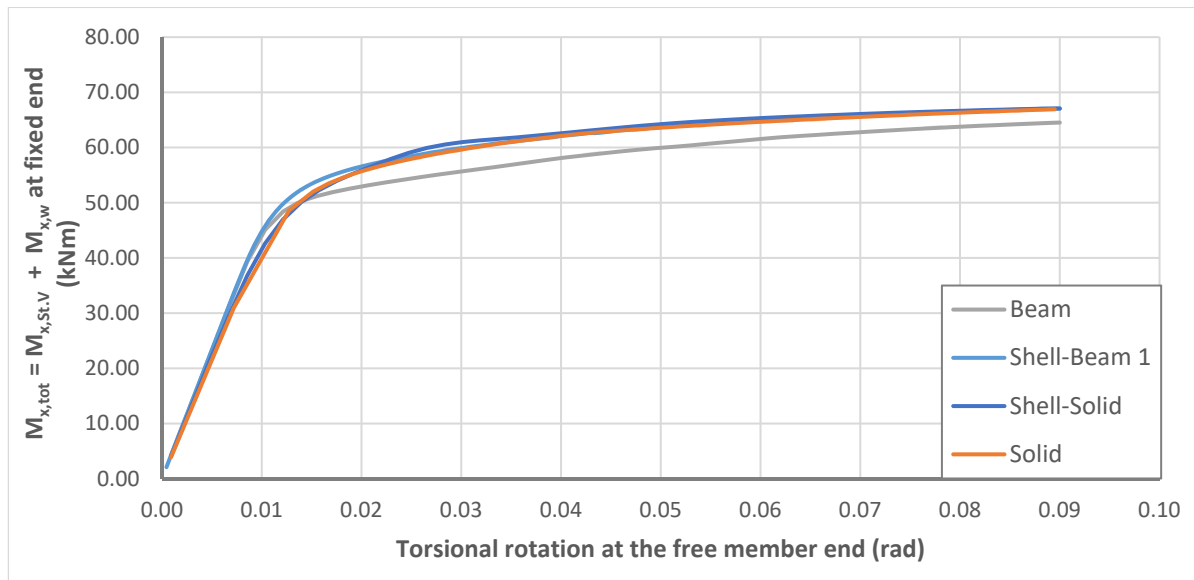
Hereafter, the case of a member made of a HEB 300 cross-section is considered. Conversely to the cases studied before, it is assumed that the member is fixed at one end (all degrees of freedom blocked including warping) and entirely free at the other end. At the free end, a torsional moment is applied. The resulting rotation-bi-moment and rotation-total torsional moment diagrams are given next for different member lengths and therefore different warping decay factors ε_T .

It is interesting to observe in the following figures that:

- The "Solid" model as well as the "Shell-Solid" and the "Shell-Beam 1" model yield very similar results; the "Beam" model shows some differences to the other models;
- Independently of the member lengths, the maximum bi-moment is constant and equal to approximately 30 kNm². However, the plastic bi-moment obtained for the "Solid" and the "Shell" models varies slightly between 32 kNm² and 30 kNm² whereas the plastic bi-moment is always equal to 28,8 kNm² in case of the beam model;
- Conversely to the observation mentioned above, the maximum total torsional moment depends highly on the member length and varies between approximately 69 kNm for the shortest member and about 25 kNm for the longest one;
- Additionally, it may be seen that when the member attains its plastic bi-moment resistance, the total torsional moment continues to increase;
- The plastic bi-moment resistance may be attained for small torsional twists if the member is rather short. Contrariwise, for longer members, the torsional twist necessary to attain the full plastic bi-moment seems excessive (0,40 rad for a member length of 12h = 3600 mm).

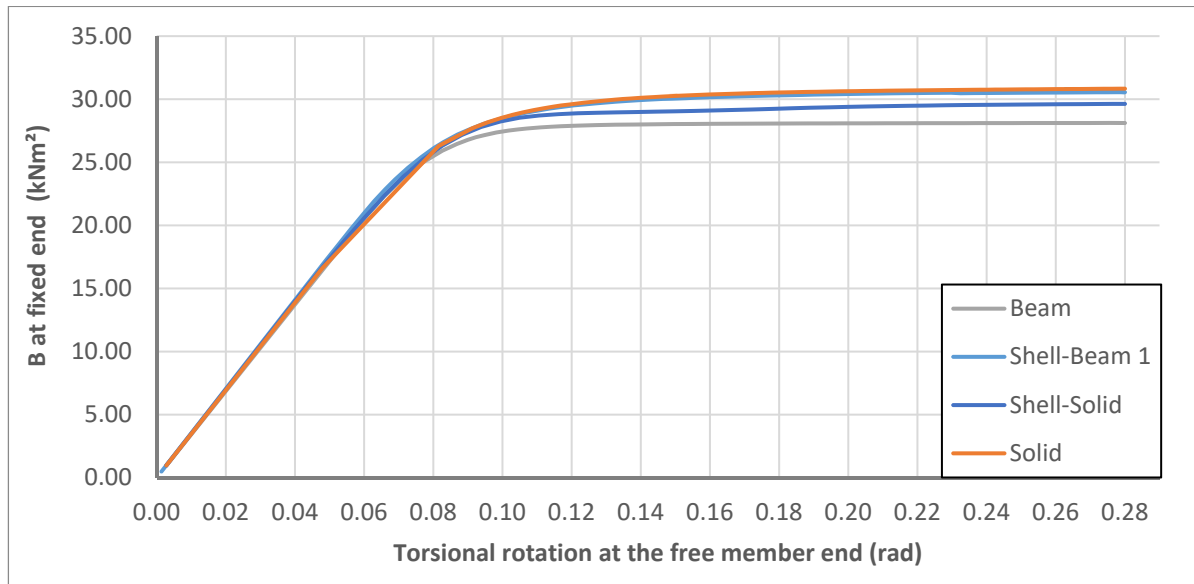


a) Bi-moment

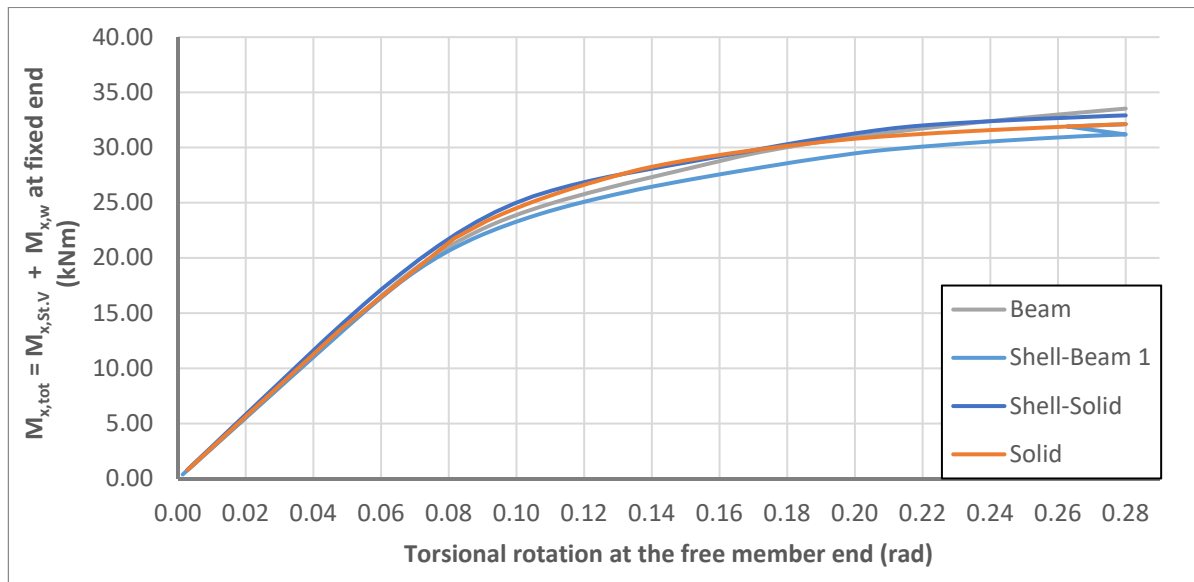


b) Torsional moments

Figure 3-44: Relation between torsional rotation at free end and a) bi-moment B at fixed end and b) torsional moments $M_{x,i}$ at fixed end for a member length of 600 mm ($\varepsilon_T = 0,40$)

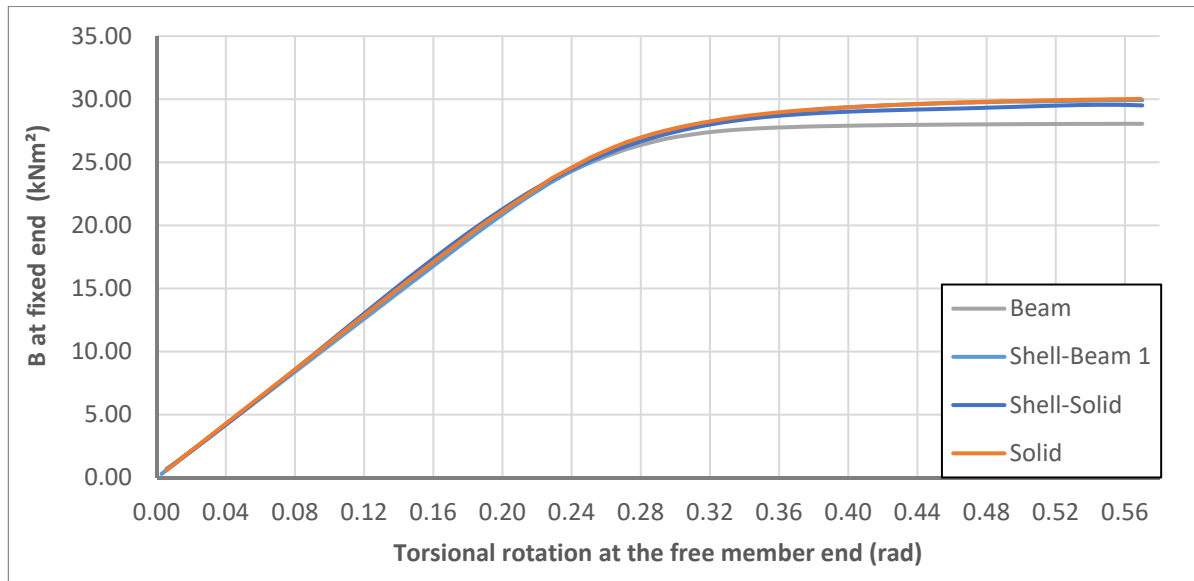


a) Bi-moment

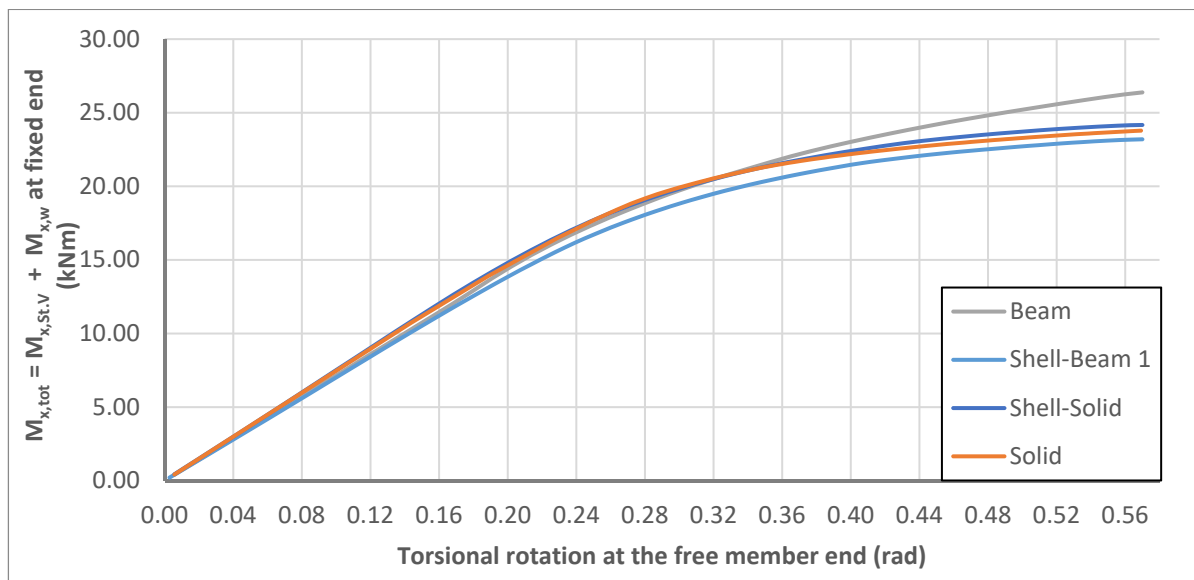


b) Torsional moments

Figure 3-45: Relation between torsional rotation at free end and a) bi-moment B at fixed end and b) torsional moments $M_{x,i}$ at fixed end for a member length of 1800 mm ($\epsilon_T = 1,19$)



a) Bi-moments



b) Torsional moments

Figure 3-46: Relation between torsional rotation at free end and a) bi-moment B at fixed end and b) torsional moments $M_{x,i}$ at fixed end for a member length of 3600 mm ($\epsilon_T = 2,39$)

In order to explain the previous observations, it seems interesting to recall the theoretical distribution of internal moments obtained by an elastic analysis for the studied member as shown in Figure 3-47 and Figure 3-48. One may observe that the torsional moment is nearly completely carried through warping torsion (see Figure 3-47). Conversely, for the member length of 3600 mm (Figure 3-48), the Saint Venant’s torsional moment exceeds the warping torsional moment apart from the zone near the fixed end. Consequently, the total torsional moment may attain higher values for short members as the shear stresses resulting from the warping torsional moment may be neglected (see also Chapter 4). The plastic warping torsional moment resistance of the HEB 300 section is about 217,31 kNm whereas the plastic Saint Venant’s torsional moment resistance is only of 19,0 kNm (see Chapter 2 – Eqs. (2.1) and (2.3)).

It has also been observed in Figure 3-44 to Figure 3-46 that even if the plastic bi-moment is attained the total torsional moment continues to increase. This can be explained as follows: the bi-moment is exclusively carried by the flanges of the cross-section. When they have completely yielded (or nearly) a warping hinge is created as the effective warping stiffness of the member nearly vanishes at the member end. Yet, supplementary torsional moments may be carried through shear stresses resulting from Saint Venant's torsional moment. As the flange has yielded, these shear stresses transit through the web until it has entirely yielded. A deeper discussion on the plastic behaviour of members in torsion is given in paragraphs 4.4.4.1 and 5.6.4.2.

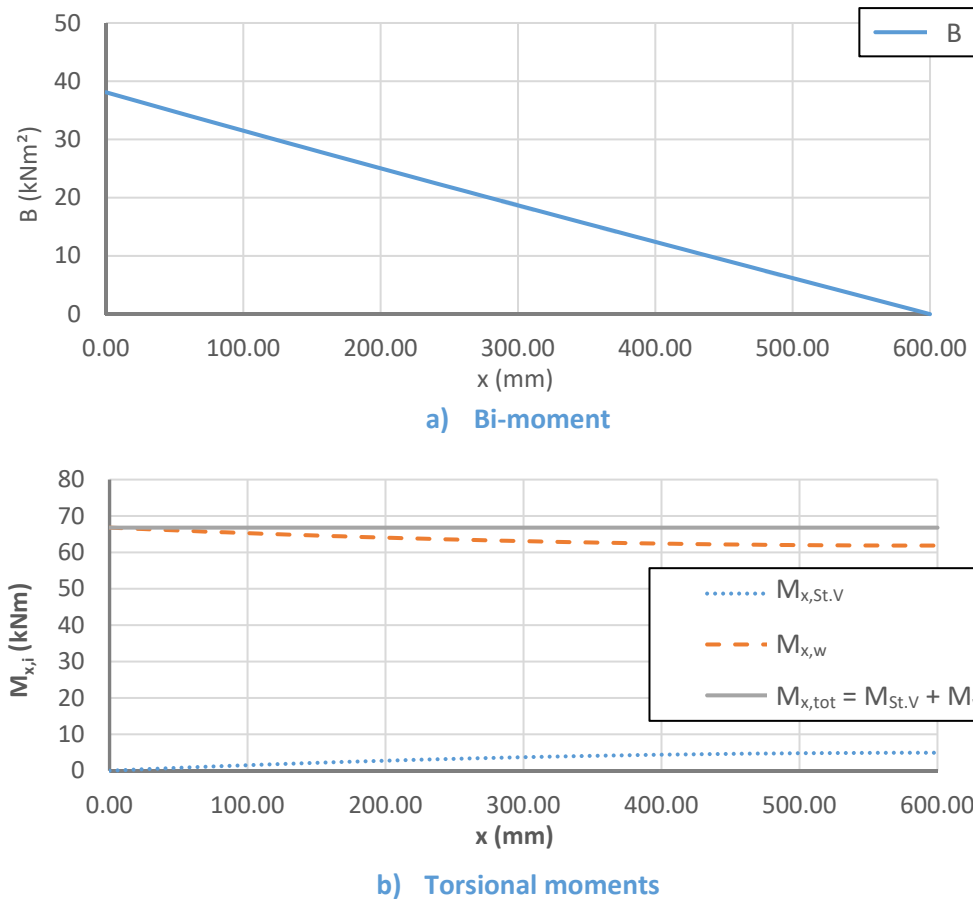
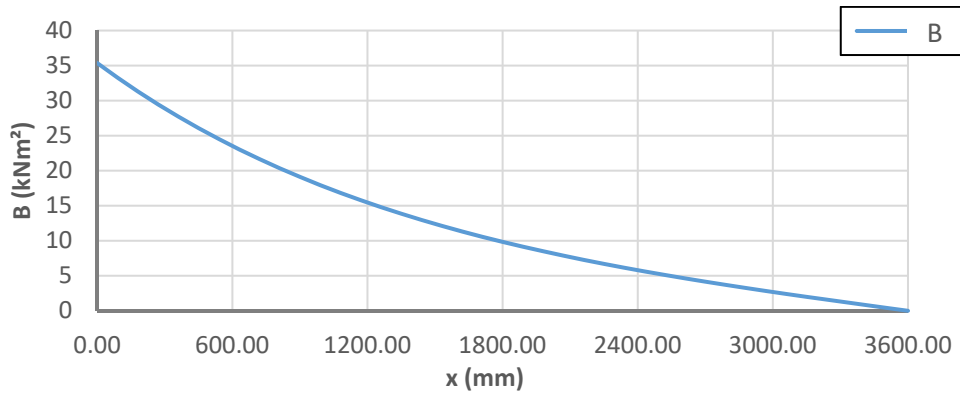
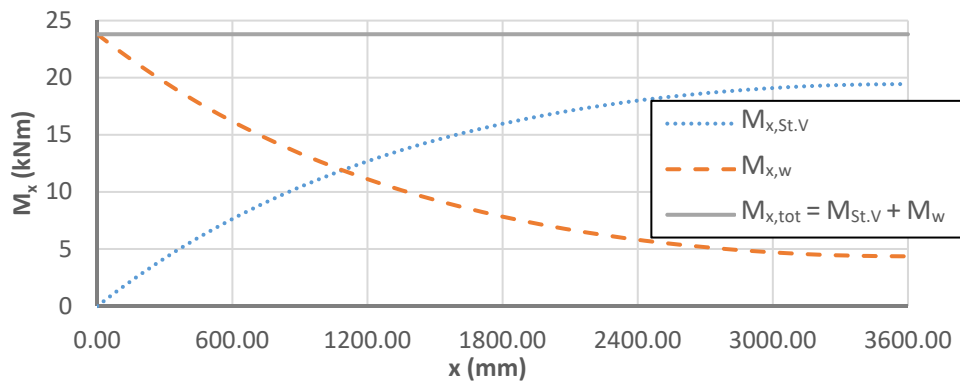


Figure 3-47: Distribution of bi-moment and torsional moments – short member L = 600 mm



a) Bi-moment

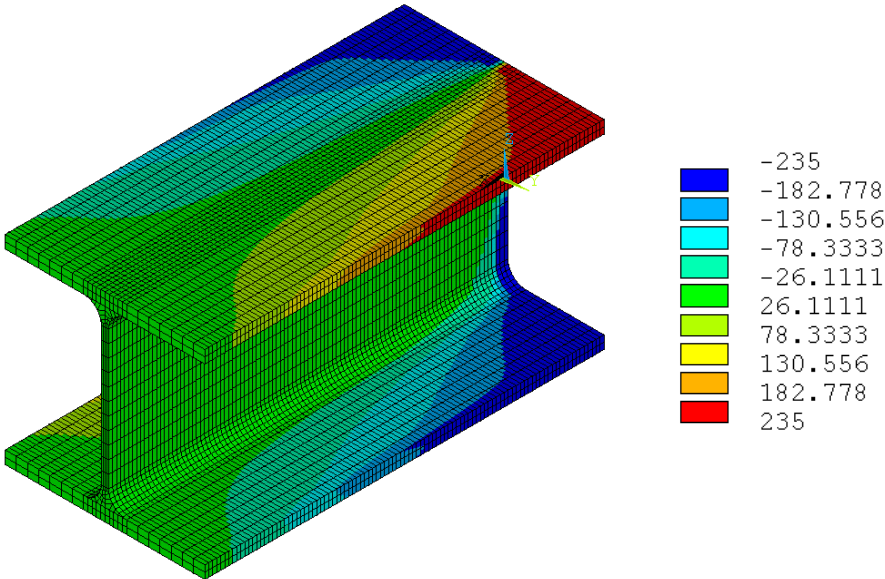


b) Torsional moments

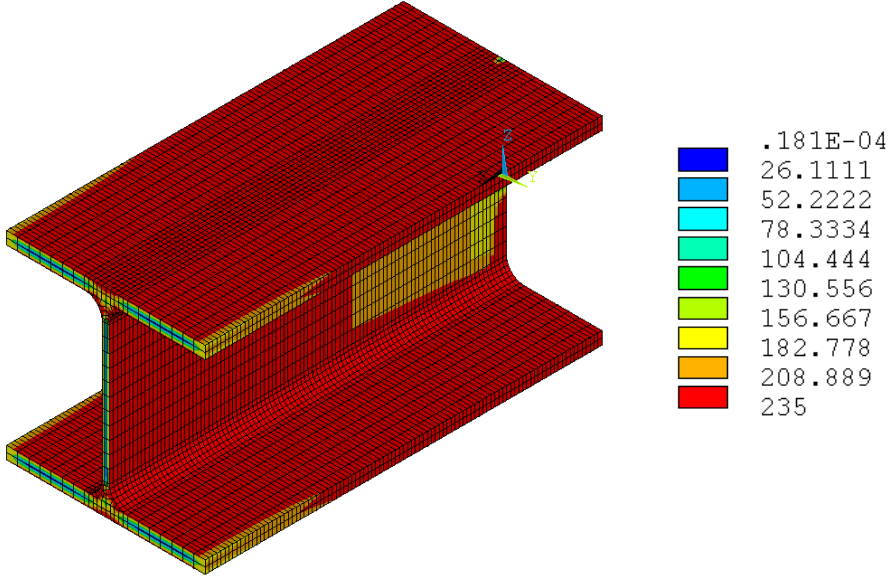
Figure 3-48: Distribution of bi-moment and torsional moments – long member L = 3600 mm

Last, the difference between the beam model and the models containing solid and/or shell elements is of interest. As before a mechanical explanation may be given. In fact, it may be observed in Figure 3-49 and Figure 3-50 that the axial stresses attain the yield stress of 235 MPa in case of the beam model whereas they attain 271,2 MPa in case of model “Shell-Beam 1”. However, for both models, the maximum von Mises stress is equal to the yield stress. Figure 3-51 shows why the axial stresses exceed the yield stress in case of the shell model. Indeed, stresses in the z and y directions develop at the fixed end and allow the axial stresses σ_x to exceed the yield stress according to the von Mises yield criterion. A similar result has been highlighted in reference (Gonçalves et al. 2014) for the bending moment shear force interaction (see also paragraph 3.3.4.4). As the beam model only considers axial stresses σ_x and shear stresses τ_{xy} and τ_{xz} , the effect of a multi-axial stress interaction in the von Mises yield criterion is obviously not considered. Therefore, the maximum bi-moment obtained with the beam model equals the theoretical plastic bi-moment whereas the maximum bi-moment obtained with the shell and solid model may exceed the theoretical plastic bi-moment resistance. It is recalled that the bi-moment acting in the cross-section is obtained by integrating the axial stresses following Eq. (3.8).

$$B = \int \sigma \omega dA \tag{ 3.8 }$$

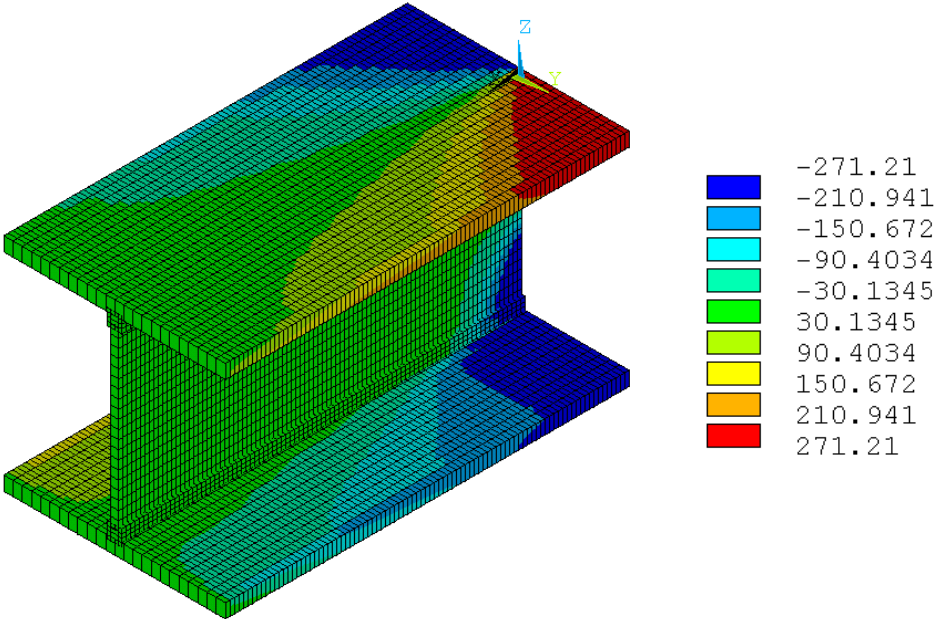


a) Axial stresses

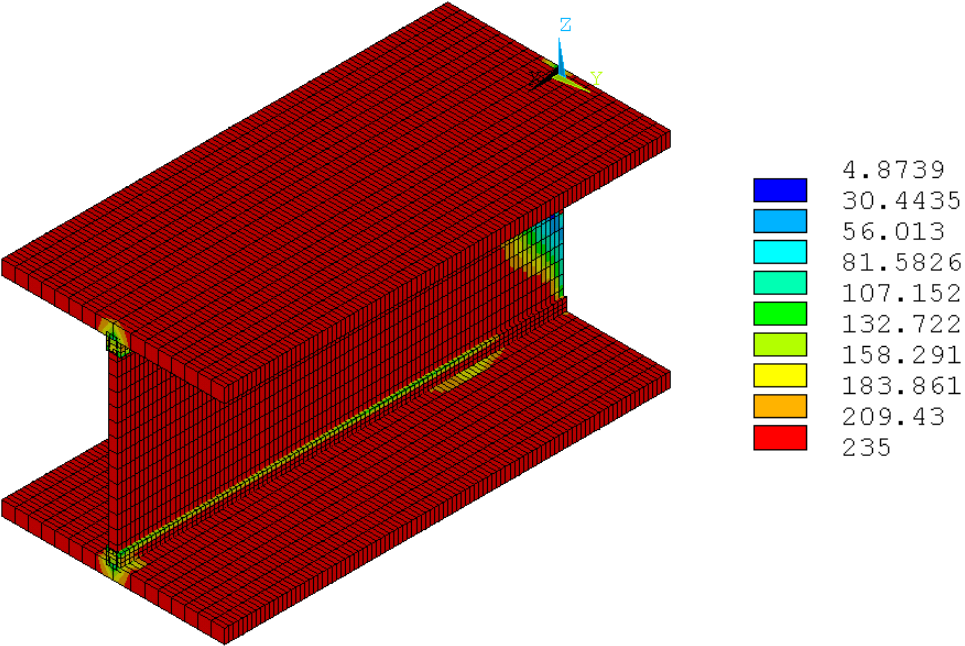


b) Von Mises stresses

Figure 3-49: Beam model - L = 600 mm - Distribution of a) axial stresses and b) von Mises stresses



a) Axial stresses



b) Von Mises stresses

Figure 3-50: Model Shell-Beam 1 - L = 600 mm - Distribution of a) axial stresses and b) von Mises stresses

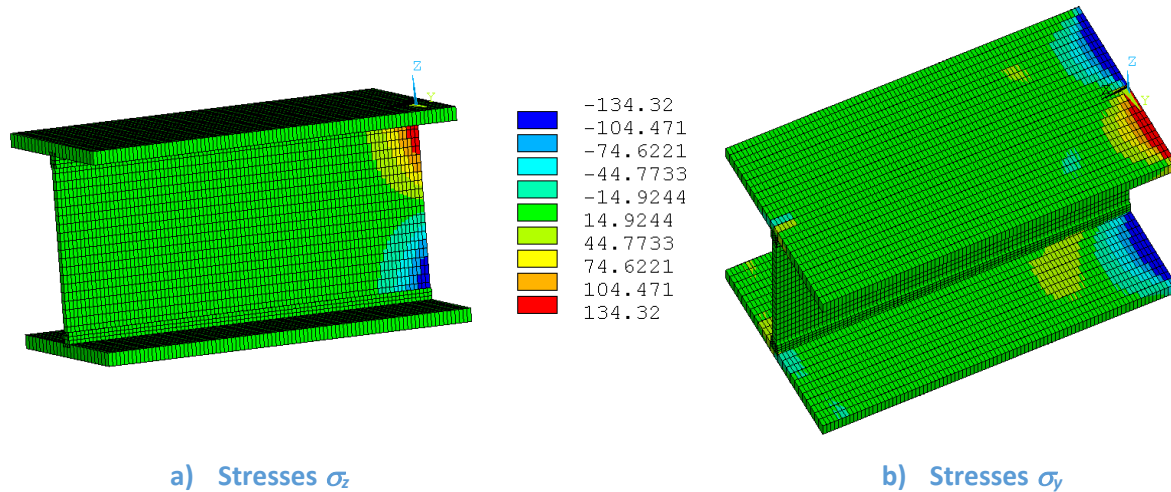


Figure 3-51: Model Shell-Beam 1 - L = 600 mm - Distribution of stresses a) σ_z and stresses b) σ_y

Up to this point, it has been shown that the studied models are very close and may therefore be used to determine the plastic resistance of hot-rolled sections including the influence of the fillets. Eurocode 3 Part 1-1 (CEN 2005a) attributes a rather important influence to the fillets concerning the shear resistance. Consequently, it seems interesting to validate the different modelling techniques also for the bending moment-shear interaction.

3.3.4.4 Interaction between major-axis bending and shear force

Last, the interaction between major-axis bending and shear force is studied. It is supposed that the members possess fork end conditions and that they are subject to bending moments varying linearly from $+M_y$ to $-M_y$ leading to a constant distribution of the shear force over the member length. Hereafter, the case of a HEB 300 cross-section is treated again. Figure 3-52 shows the interaction curve obtained by the different models as well as the interaction curve predicted by Eurocode 3 Part 1-1 (CEN 2005a). It should be noted that only the area of the web is considered as shear area (excluding the fillets). A detailed discussion on the plastic shear resistance and the corresponding shear area is given in chapter 4.

Figure 3-52 clearly shows the difference between the results obtained on the basis of beam elements and the results obtained by the other models. Independently of the applied shear force, the beam model always attains the plastic major-axis bending moment resistance. In order to understand these somewhat surprising results, the stress distribution at the plastic limit state deserves being studied.

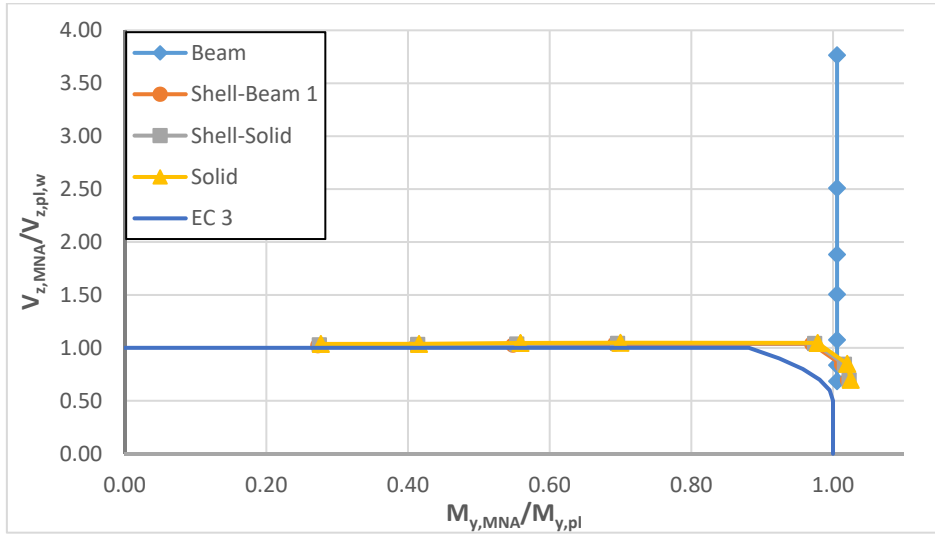


Figure 3-52: Numerical determined interaction between major-axis bending and vertical shear force

Figure 3-53 shows the stress distribution obtained with the beam model. It may be observed that the axial stresses reach the yield stress of 235 MPa at the supports. It seems that there is no interaction between these stresses and the shear stresses. Also, one may observe that the shear stresses greatly exceed the yield stress in shear. It is obvious that the beam model is not suited if the interaction between shear force and bending moments are studied. Here, one may suppose that the interaction between shear stresses resulting from the shear force and the axial stresses is not correctly considered in the von Mises yield criterion.

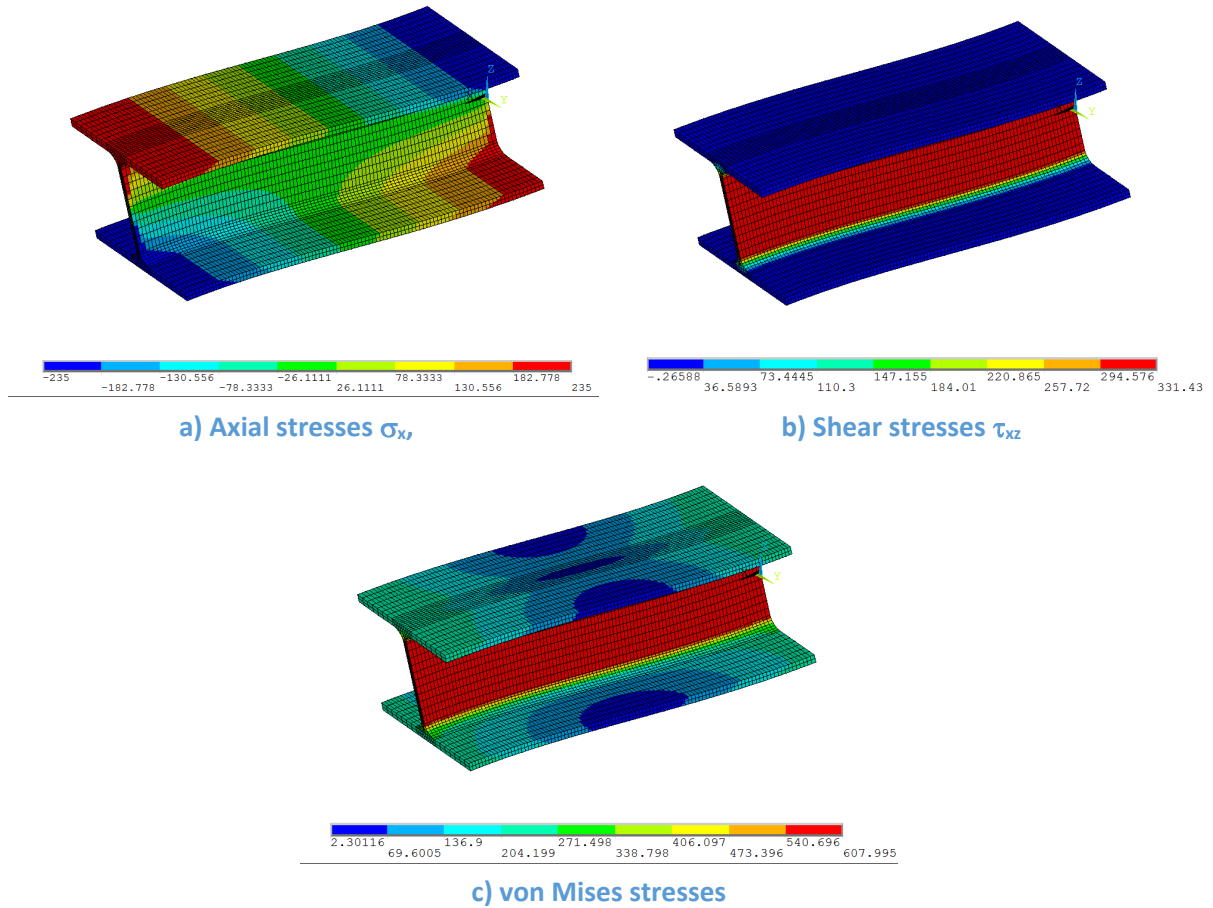


Figure 3-53: Distribution of a) axial stresses σ_x , b) shear stresses τ_{xz} and c) von Mises stresses for a member length of 1800 mm obtained by beam model

In order to compare the results obtained with the other models Figure 3-54 shows the interaction curve again. Obviously, the models “Shell-Beam 1”, “Shell-Solid” and “Solid” yield very similar results. The differences are negligible. As for the beam model, the plastic stress distributions at the ultimate limit state are given for a member of 1800 mm of length in Figure 3-55 and Figure 3-56 for the model “Shell-Beam 1” and the “Solid” model.

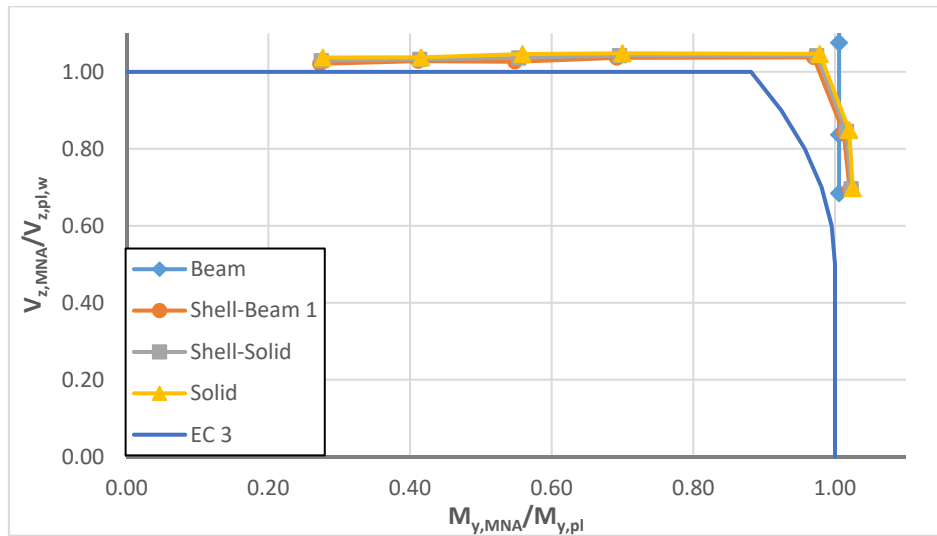


Figure 3-54: Numerically determined interaction curves between major-axis bending and vertical shear force

The following two figures show that both models, “Shell-Beam 1” and “Solid”, yield nearly identical stress distributions at the ultimate limit state. As the continuity of the material in the fillet zone is better represented by the “Solid” model, the stress distribution is smoother, too.

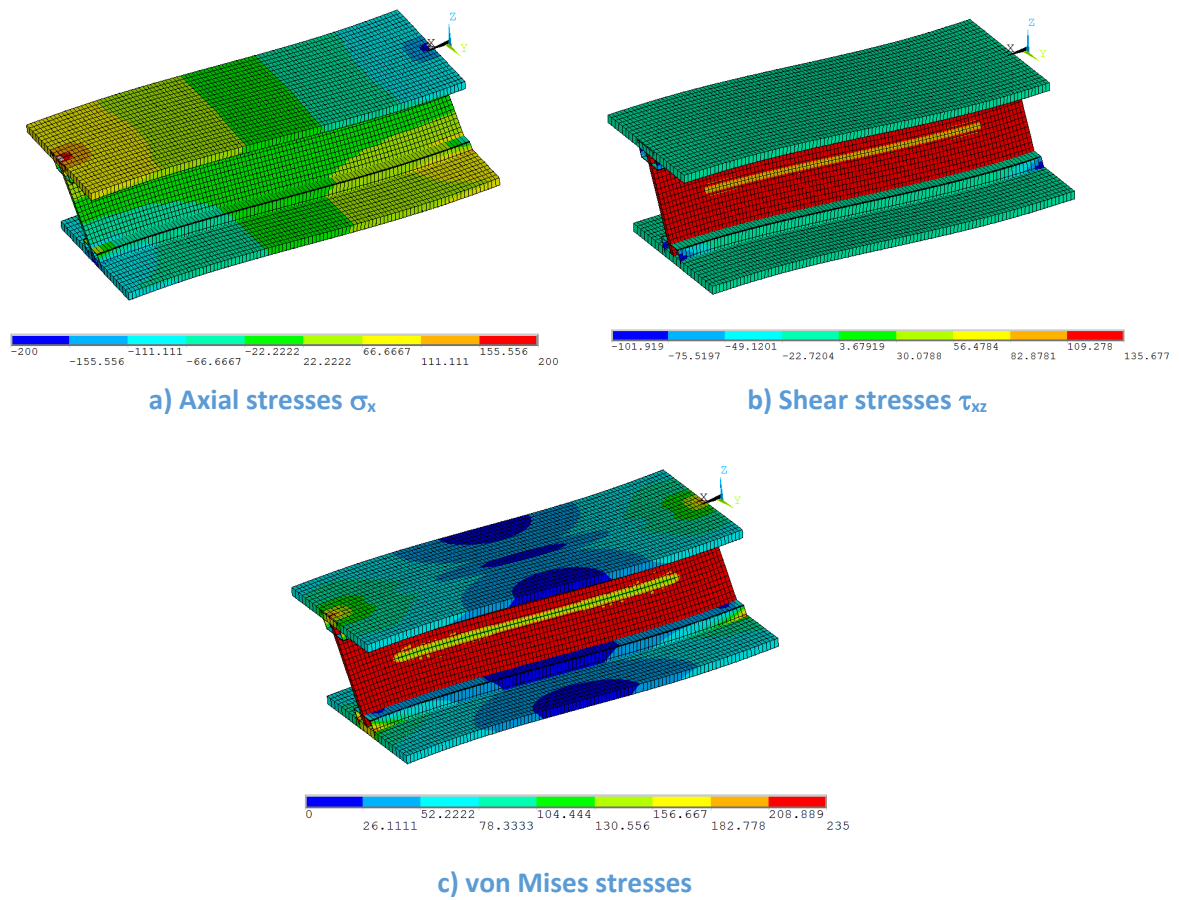


Figure 3-55: Distribution of a) axial stresses σ_x , b) shear stresses τ_{xz} and c) von Mises stresses for a member length of 1800 mm obtained from Shell-Beam 1 model

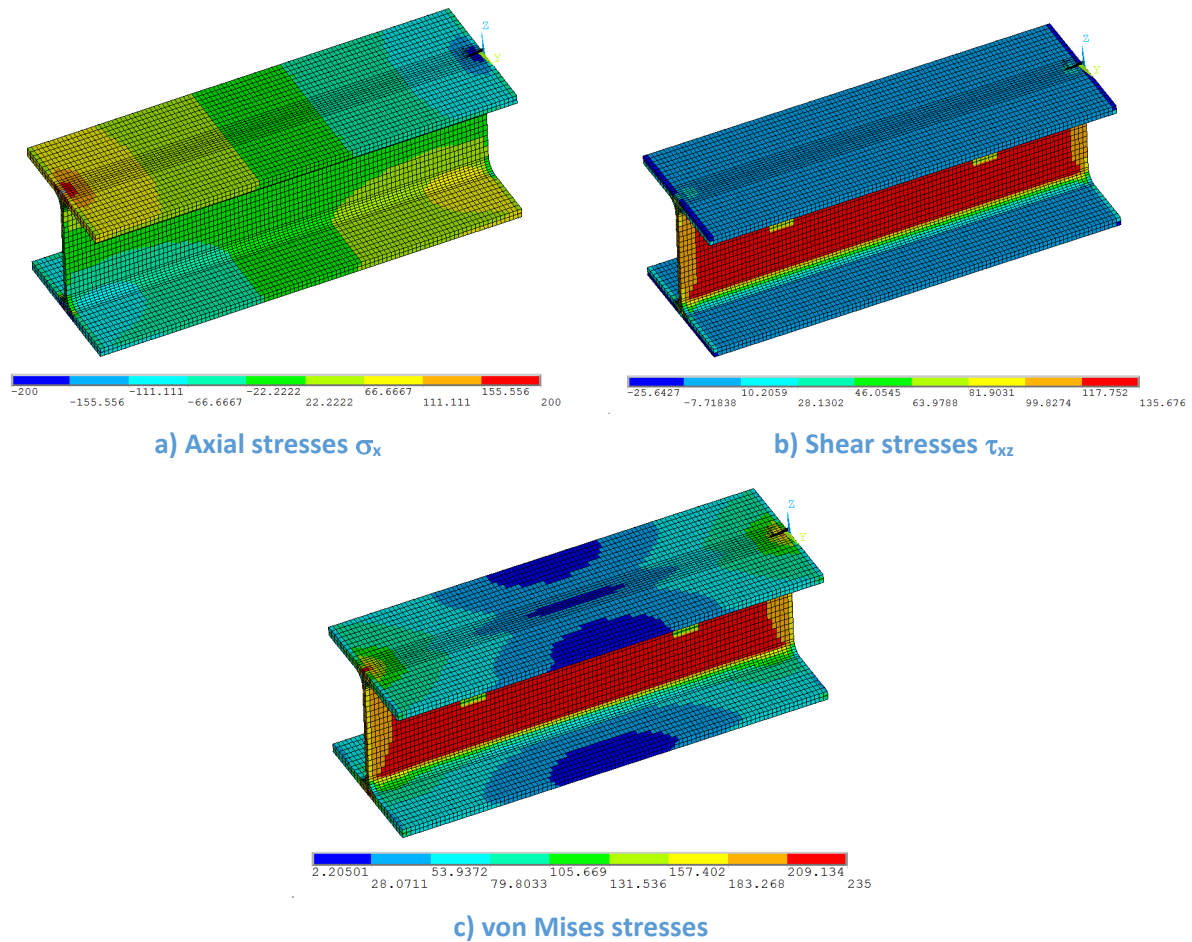


Figure 3-56: Distribution of a) axial stresses σ_x , b) shear stresses τ_{xz} and c) von Mises stresses for a member length of 1800 mm obtained from solid model

The present paragraph has shown that the “Beam” model is not suited to study the bending moment-shear forces interaction. Conversely, models “Shell-Beam 1”, “Shell-Solid” and “Solid” predict nearly identical results and can therefore be used in the following.

3.3.4.5 Conclusion

Paragraph 3.3.4 presented a comparison of different modelling techniques for hot-rolled cross-sections. The objective was to determine whether or not the models are capable to represent the theoretical plastic cross-section resistance. It has been shown that:

- All models yield very similar results for the case of applied bending moments and axial forces;
- For the case of an applied torsional moment and especially for the case of bending moment-shear force interaction the beam model yields poor results as the interaction between shear stresses and axial stresses does not seem to be well represented;

- Models “Solid”, “Shell-Solid” and “Shell-Beam 1” yield very similar results including for the case of applied torsion and bending-shear force interaction.

It has been shown that the models “Solid”, “Shell-Solid” and “Shell-Beam 1” (combining Shell elements and beam elements of rectangular hollow section to model the fillets) yield very similar results for all studied cases. However, as the model “Shell-Beam 1” contains beam elements not capable to correctly represent the interaction between shear and axial stresses, it may not be excluded that the results are affected in certain situations and complex load interactions. Therefore, this model is not used to study the influence of fillets. As the calculation time is nearly identical for both models, “Solid” and “Shell-Solid”, the “Solid” model is used to study the influence of the fillets of hot-rolled sections.

Paragraphs 3.3.3 and 3.3.4 studied the influence of different modelling techniques for the modelling of hot-rolled cross-section and in particular the modelling of their fillets. Eurocode 3 Part 1-1 accepts, conversely to other international standards as (ANSI 2010) and (Standard Australia 1998), that the fillets increase the shear resistance of hot-rolled cross-sections compared to welded cross-sections. Consequently, the fillets have to be included explicitly in numerical simulations so as to quantify their influence on the **plastic section resistance**. However, the use of solid elements implies longer calculation times, that may be acceptable for the study of the plastic cross-section resistance. It should be noted a typical MNA simulation performed in the framework of this paragraph takes about 30 min to 60 min depending on the member length if it is performed with models “Solid” and “Shell-Solid”. Conversely, the same simulations take only about 5 min to 15 min if they are performed with model “Shell-Beam 1”. Therefore, an extensive parametric study concerning the **member resistance** including second order effects does not seem feasible with a solid model because the length of the member enters as supplementary parameter leading to a greater number of cases to be studied. Also, it has been shown several times for simple load cases not including torsion, for example in reference (Taras 2011), that the fillets do not influence the general behaviour of a member. In fact, if the member resistance is given in relative terms in a λ - χ diagram the results are practically identical whether or not the fillets are included into the simulation. Consequently, it seems interesting to study if these conclusions may be extended to the case of members subject to applied torsional moments.

3.3.5 Influence of the fillets on the member resistance

In order to study the influence of the fillets on the behaviour of members subject to combined bending and torsion, the example represented in Figure 3-57 is treated. The member is made of IPE 500 cross-section fabricated from steel grade S235. It is subject to constant major-axis bending and to a torsional moment applied at mid-span. The value of the torsional moment is calculated as a function of the member length by:

$$M_T = M_y \frac{b}{L} \tag{3.9}$$

Eq. (3.9) accounts for the fact that torsional moments are generally introduced by loads applied with an eccentricity to the shear centre. In fact, the torsional moment applied here is equal to a torsional moment that would be introduced by a vertical point load applied at mid-span half way between the web and the flange's tip and creating the maximum bending moment M_y (that is applied at the member ends for studied example).

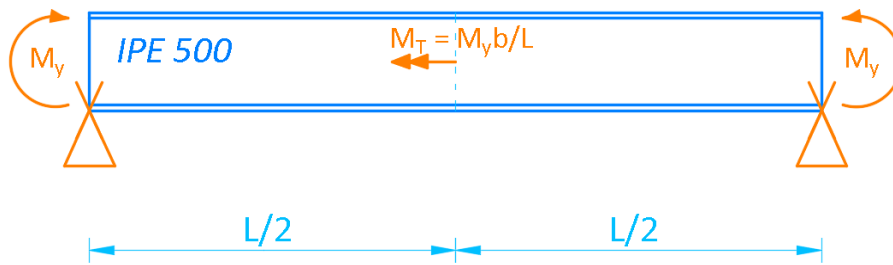


Figure 3-57: IPE500 subject to combined bending and torsion

The three different cases represented in Figure 3-58 are studied. Here the torsional characteristics as well as the plastic major-axis bending moment are of special interests. The cross-section characteristics are given in Table 3-3 for each model. Obviously, the characteristics are identical for the models not considering the fillets. Table 3-3 also shows that the fillets contribute to about 4% to the major-axis bending moment, 28% to the torsion constant, 36% to the plastic Saint Venant's torsional moment and 1% to the warping constant. Obviously, the fillets especially influence the cross-section characteristics related to Saint Venant's torsion.

Table 3-3: Cross-section characteristics for the three models

Characteristic	Solid model with fillets	Solid model without fillets	Shell model without fillets
Plastic bending moment $M_{y,pl}$	515,6 kNm	495,2 kNm	495,2 kNm
Plastic St. Venant's torsional moment $M_{x,St.V,pl}$	11,4 kNm	8,41 kNm	8,41 kNm
Torsional constant I_t	89,37 cm ⁴	69,94 cm ⁴	69,94 cm ⁴
Warping constant I_w	1248658 cm ⁶	1235064 cm ⁶	1235064 cm ⁶

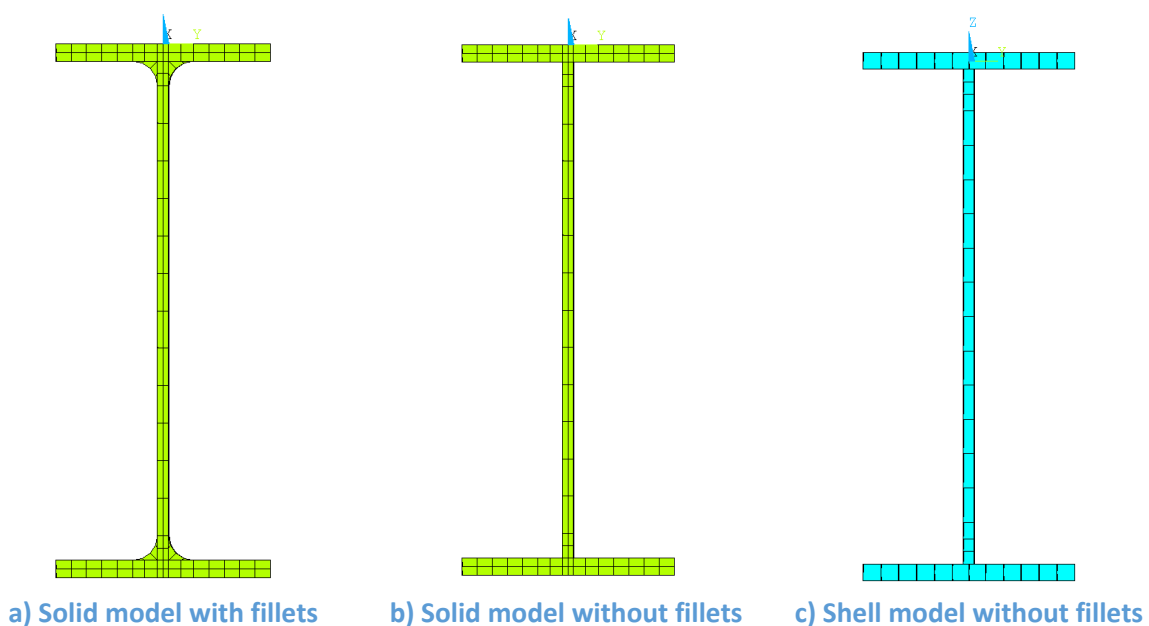


Figure 3-58: Modelling of the IPE 500 section

Figure 3-59 represents the results obtained by GMNIA calculations of the three models for different member lengths. The resistance is represented with reference to the plastic bending moment resistance. As the member is subject to combined bending and torsion (creating a bi-moment, a warping torsional moment and a Saint Venant's torsional moment), the plastic bending moment is not attained even for short members, whatever the model is. It can be seen that, both the solid model not considering the fillets and the shell model yield quasi identical results. This observation confirms the quality of the shell model for the case of applied torsion. Additionally, it may be seen that the influence of the fillets is nearly negligible, especially for short members (attaining the plastic cross-section resistance under combined bending and torsion) and long members ($\lambda_{LT} > 1,4$ - failure characterized by elastic instability). Some differences may be identified for members of medium length. This may be attributed to the contribution of the fillets to the torsional stiffness of the member (see Figure 3-60 and Figure 3-61).

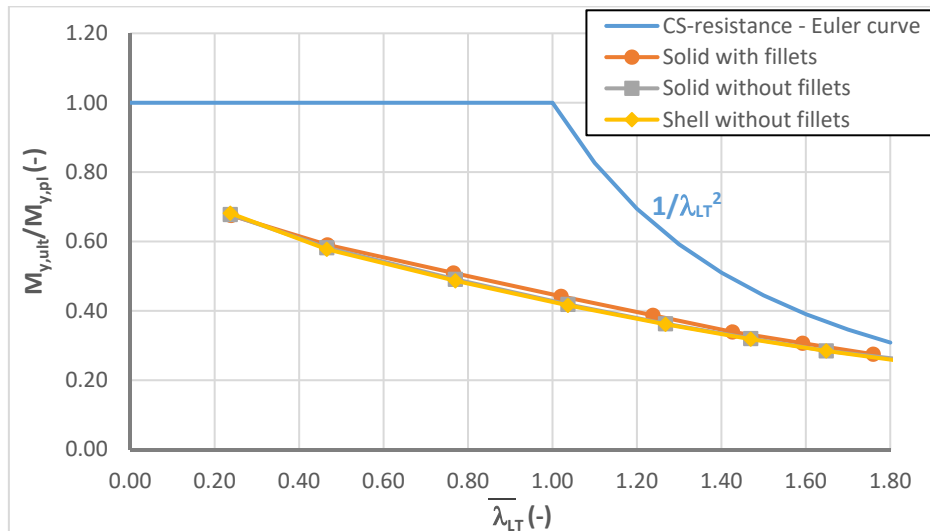


Figure 3-59: Reduction of the ultimate bending moment with the relative lateral-torsional buckling slenderness

Figure 3-60 and Figure 3-61 show the evolution of the torsional twist and the lateral displacement at mid-span with the applied major-axis bending moment for the member possessing a lateral-torsional buckling slenderness of about 1,0 ($L=5400$ mm). The negative sign for the lateral displacement directly results from the sign conventions (positive torsional twist leads to negative lateral displacement). Nonetheless, as the section is double symmetric, the sign is not of primary importance.

It may note that the shell model and the solid model not including the fillets yield identical results again. Owing to higher torsional stiffness of the member with the fillets, the torsional twist and the lateral displacement at a given load level are lower than for the members without fillets. Consequently, the resulting second order internal forces, in particular bi-moment and minor-axis bending moment, are lower too. Thus, the member possessing fillets may resist a higher applied major-axis bending moment. The difference is of about 8%. Nevertheless, it has to be noted that the fillets do not modify the general behaviour of the member. In fact, due to the higher Saint Venant's torsional stiffness, the critical load is higher and the relative slenderness is lower for the member with fillets. Consequently, it is not surprising that its resistance is slightly higher than the resistance of the member with the same dimensions not possessing the fillets. Nonetheless, a single ultimate resistance curve is capable of describing the behaviour of both members. Therefore, a design model may be developed based on a numerical study of members without fillets. If the torsional characteristics are included into this design model, it is able to predict the ultimate resistance of members made of hot-rolled sections as reliably as the resistance of members made of welded sections.

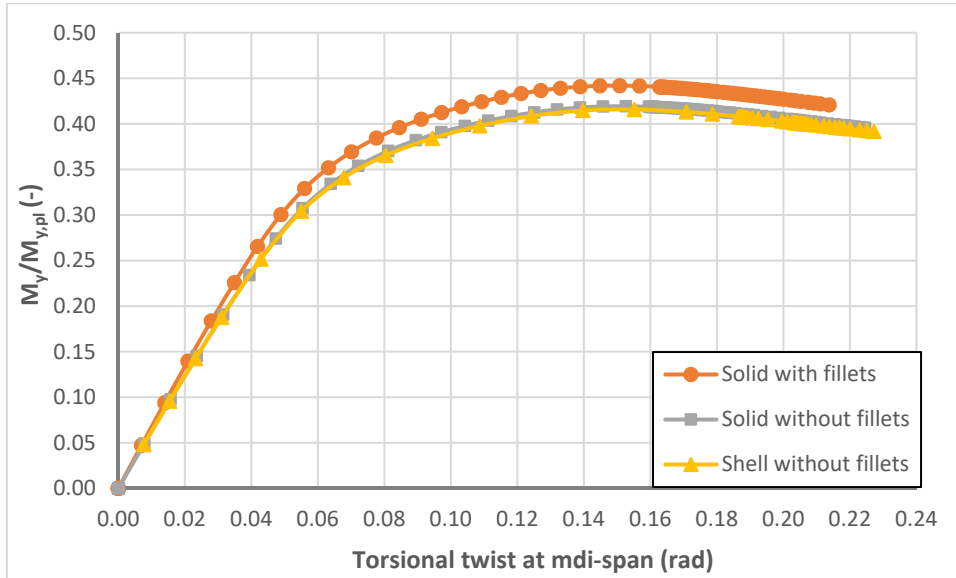


Figure 3-60: Evolution of the torsional twist at mid span with the applied bending moment

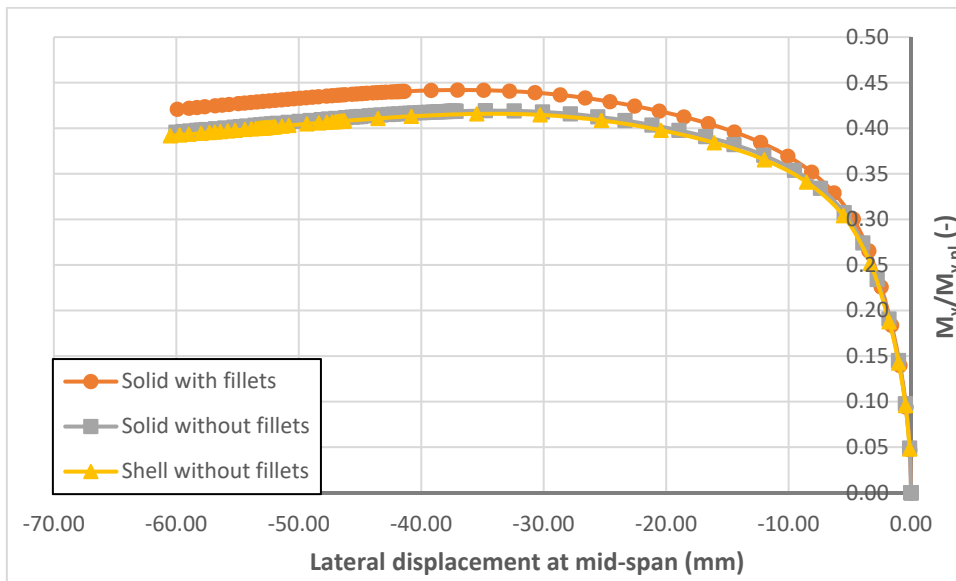


Figure 3-61: Evolution of the lateral displacement of the centroid at mid span with the applied bending moment

3.3.6 Choice of the numerical model

The present paragraph aimed at comparing different types of numerical models with respect to the stiffness of the member and the plastic resistance for elementary load cases (mono-axial bending, axial force or torsion) and combined major-axis bending and shear force. The modelling of the fillets of hot-rolled sections was of special interest. It has been shown that, depending on the type of modelling, the results may vary. Indeed, the first part of this paragraph, concerning the elastic member buckling loads, has shown that even if model “Shell-Beam 2” and the model “Shell var” represent very closely the real geometry of the section, these models represent the least precisely the torsional stiffness of the member. The models containing solid elements in the zone of the fillets and the beam model represent best the torsional stiffness as they not only represent perfectly the section geometry but also model the closest the continuity of the material (representation of the warping function over the fillets!). This continuity can only be approximated very roughly by the models “Shell var” and “Shell-Beam 2”. Hence, these two models are not capable to represent the real torsional stiffness of the member. As the models “Shell-Beam 2” and “Shell var” yield poor results for the torsional stiffness, they have been excluded from the subsequent comparisons. Model “Shell-Beam 1” does not represent the continuity of the material neither, but the geometry of the rectangular hollow section, representing the fillets, is specifically calibrated so as to obtain the exact torsion constant and area of the physical section that is modelled. Therefore, model “Shell-Beam 1” is capable to represent precisely the stiffness of the studied hot-rolled member.

The second part of this paragraph has compared the quality of the different models to attain the full plastic resistance of the section. It has been demonstrated that the models yield similar results for the elementary load cases of major- and minor-axis bending, axial force and applied torque. Conversely, in case of interaction between major-axis bending and shear force, it has been shown that the beam model does not consider the interaction between shear stresses resulting from the shear force and axial stresses. Consequently, the beam model may not be used for the parametric studies. Models “Shell-Beam 1”, “Shell-Solid” and “Solid” yield again very close results. Yet, obviously, the model “Shell-Beam 1” does not perfectly represent the continuity of the material and therefore leads to stress distribution that are less smooth than for the solid model. Also, as this model contains beam elements to model the fillet zone, the shear stress-axial stress interaction is not well represented as shown for the beam model. Since it is intended to study the influence of the fillets of hot-rolled cross-sections on their plastic cross-section resistance, it seems necessary to base the corresponding numerical simulations on a model that represents the best the continuity of the material and the stress distribution. As the model “Shell-Solid” does not reduce the calculation time compared to the solid model, this last is used in the mentioned study. Yet, it has to be noted that the calculation time necessary for the solid model is up to ten times higher than for the shell model. Hence, it is not possible to perform a parametric study on the member resistance based on the solid model. Therefore, the last section of this paragraph studied the influence of the fillets on the member resistance. It has been confirmed that the fillets do not influence the general behaviour of the member but only increase the torsional stiffness and the

cross-section resistance. These observations allows the parametric study concerning the member resistance to be performed based on the shell model not considering the fillets. The difference between hot-rolled sections and welded section is introduced exclusively through the residual stress pattern.

3.4 Comparison of the numerical model to physical tests

3.4.1 General

The numerical model should well represent the reality. Therefore, the best way to validate the numerical model is to compare it to results from physical tests. In reference (FOSTA 2004), a total number of 74 tests on I- and U-shaped sections are documented. The tests have been performed at the three German universities: TU Berlin, RWTH Aachen and RU Bochum. The tests realised at TU Berlin are recalculated hereafter using the model described in the previous paragraphs. A selection of results is given next. Supplementary comparisons to laboratory tests performed in the framework of the present research project are detailed in Chapters 4.

In order to capture the behaviour of the member precisely, the geometrical imperfections measured in (FOSTA 2004) are introduced in the model. Also, the measured stress-strain curve of the steel is used.

3.4.2 Tests performed at TU Berlin

3.4.2.1 Numerical Model

So as to reproduce the conditions of the physical tests, the load introduction and support conditions should be as close as possible to the conditions chosen in the laboratory. The two following figures show the load introduction and support configuration used in the physical tests.

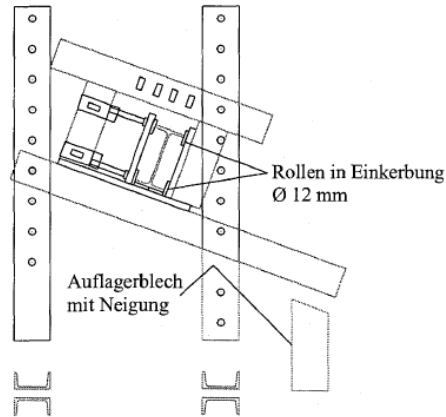


Figure 3-62: Support configuration used for the physical test (figure from (FOSTA 2004))

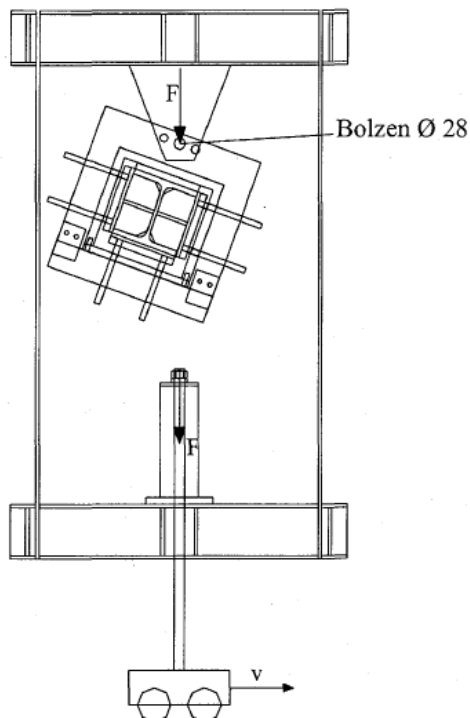


Figure 3-63: Load introduction used for the physical test (figure from (FOSTA 2004))

As can be seen in Figure 3-63, the load is introduced through a frame fixed to the member. This frame is also considered for the numerical model as shown in Figure 3-64. The support conditions are kept as described in paragraph 3.2.3.2 of this report.

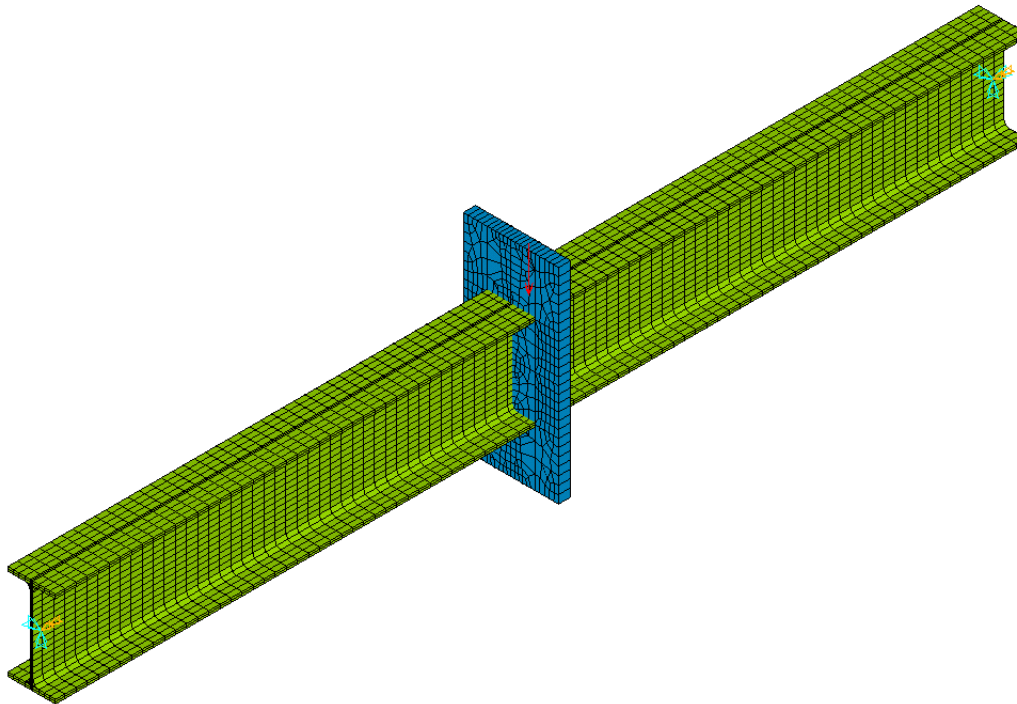


Figure 3-64: Numerical model of the physical tests performed at TU Berlin

Hereafter, the tests are recalculated with a solid model. In paragraph 3.4.2.5 the results obtained by the shell model are compared to the results of the solid model.

3.4.2.2 Results for I sections

First, the test shown in Figure 3-65 is considered. The member is fabricated from an IPE 200 section and it is loaded by a point load applied with a vertical and horizontal eccentricity with respect to the shear centre. Consequently, the member is subject to combined major-axis bending, shear force and torsion. Figure 3-66 to Figure 3-68 provide the load displacement plots. The lateral and vertical displacements are measured at the centroid of the cross-section at mid-span. The vertical displacement is directed downwards. For the torsional twist and the vertical displacement, the sign conventions used in the framework of this thesis are applied.

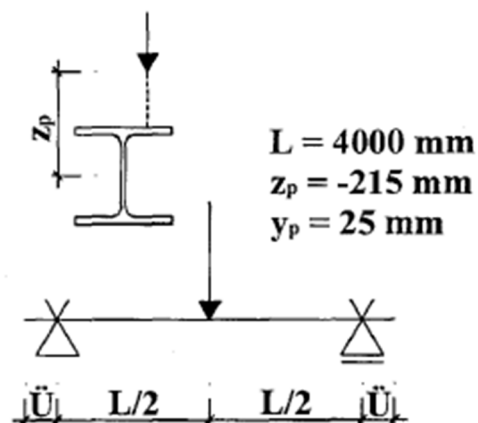


Figure 3-65: Physical test BE-1-4 (from (FOSTA 2004))

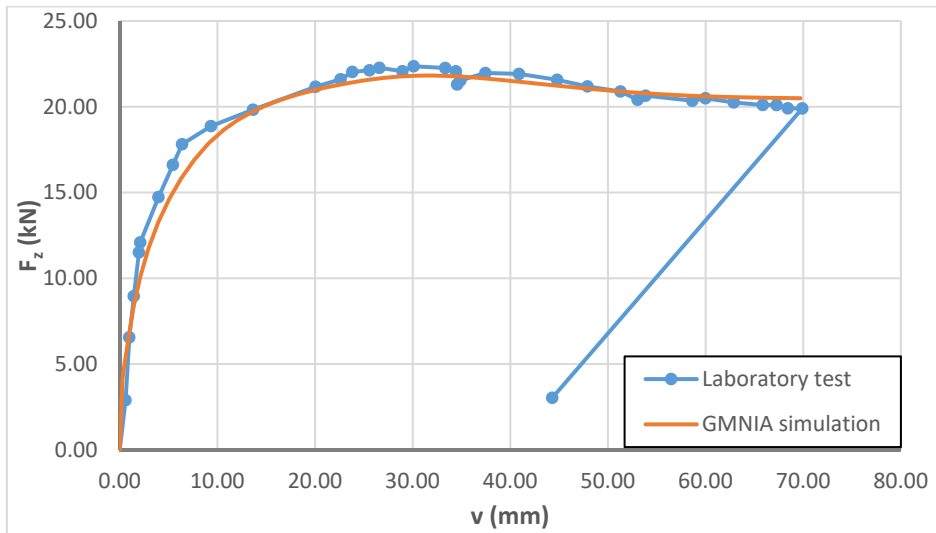


Figure 3-66: Lateral displacement of the centroid at mid-span

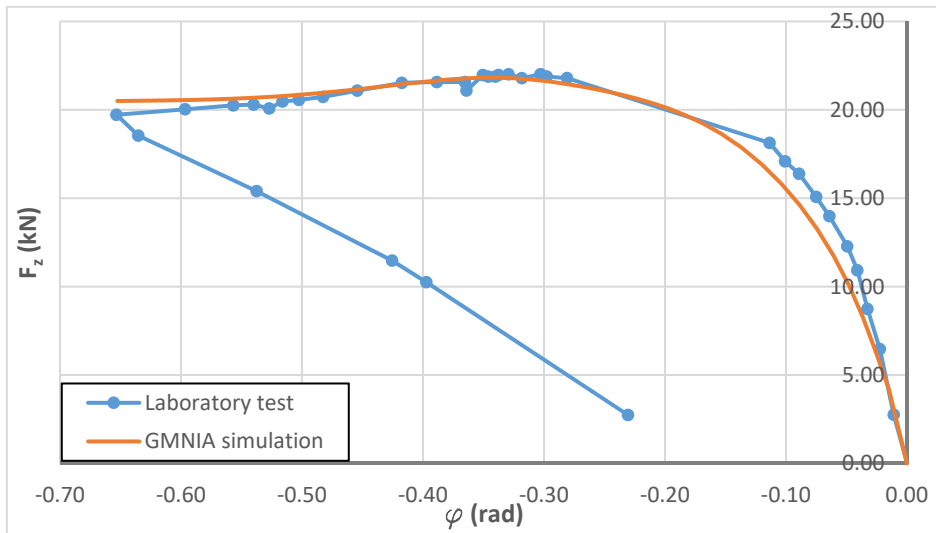


Figure 3-67: Torsional rotation of the centroid at mid-span

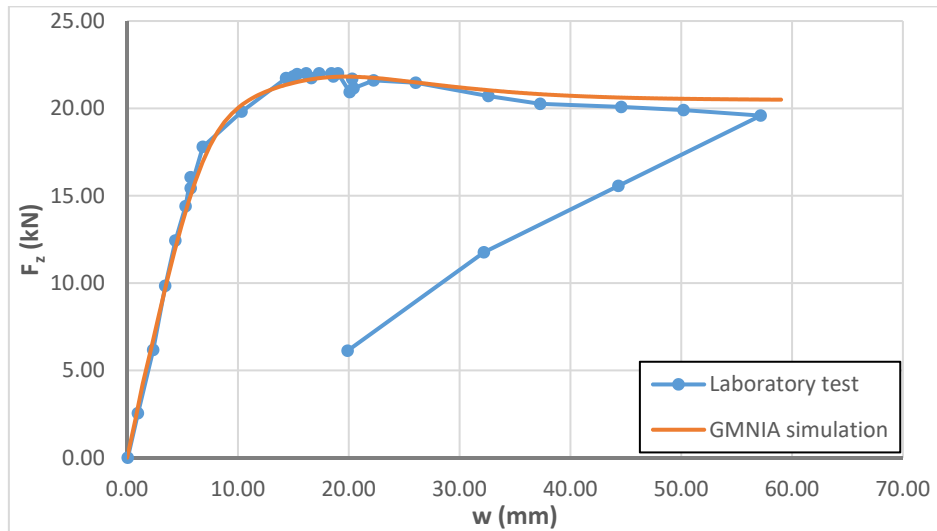


Figure 3-68: Vertical displacement of the centroid at mid-span

Figure 3-66 to Figure 3-68 clearly indicated that:

- The numerical simulation and the laboratory test attain practically the same peak load. Indeed, the member reaches a maximum load of 21,9 kN in the physical test. The numerically obtained value is 21,8 kN. Obviously, the difference is negligible.
- The initial stiffness of the member is also very well approximated by the numerical model. Nonetheless, it appears that the load-displacements curve slightly diverge starting from a load of approximately 10 kN. Near the peak load, the load displacement curves approach again.
- The load-displacement curves are also very close after the peak load level.

It may be concluded that the numerical model precisely predicts the behaviour of the studied member. A more global evaluation is given in paragraph 3.4.2.4. The next paragraph represents the results obtained for a U-shaped member.

3.4.2.3 Results for U sections

Hereafter, the results obtained for the test shown in Figure 3-69 are presented. The cross-section of the member is a UPE 200. The member is subject to a point load applied through the plane of the web with a vertical eccentricity of 215 mm with respect to the shear centre. Consequently, it is again subject to combined major-axis bending, shear force and torsion. The load displacement plots are given in Figure 3-70 to Figure 3-72.

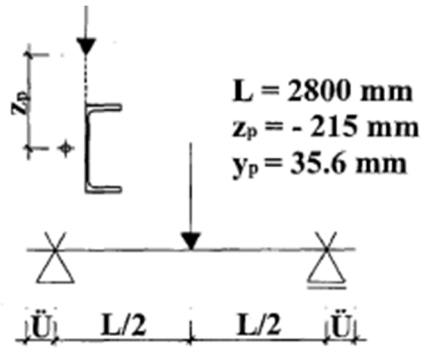


Figure 3-69: Physical test BE-3-22 (from FOSTA 2004))

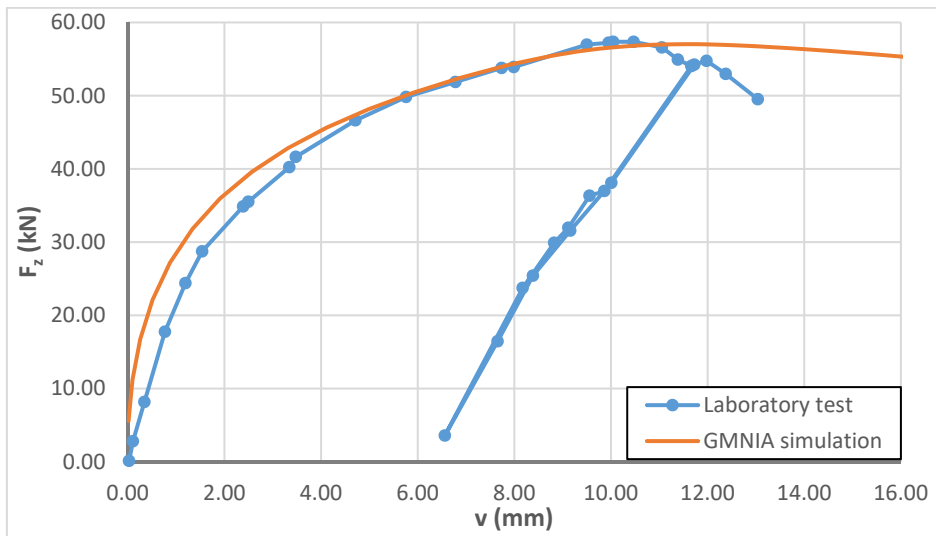


Figure 3-70: Lateral displacement of the centroid at mid-span

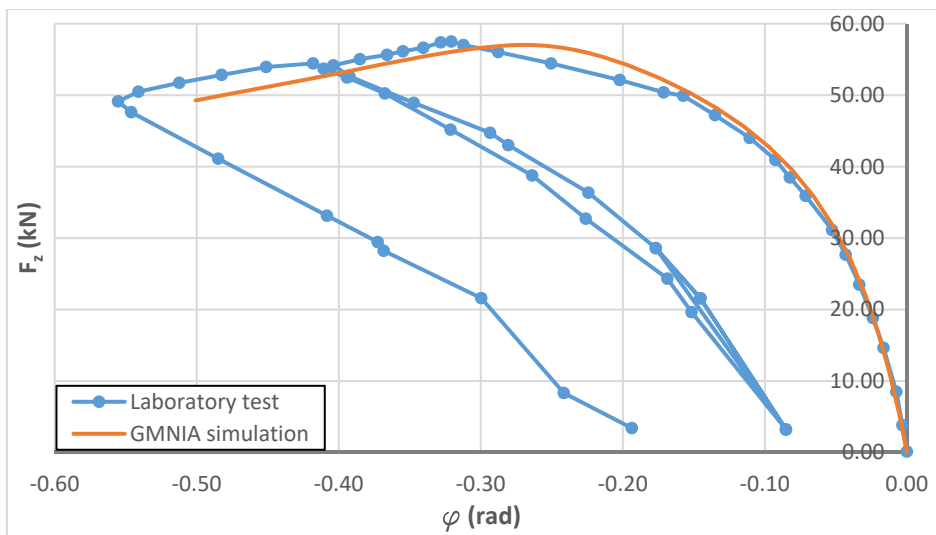


Figure 3-71: Torsional rotation of the centroid at mid-span

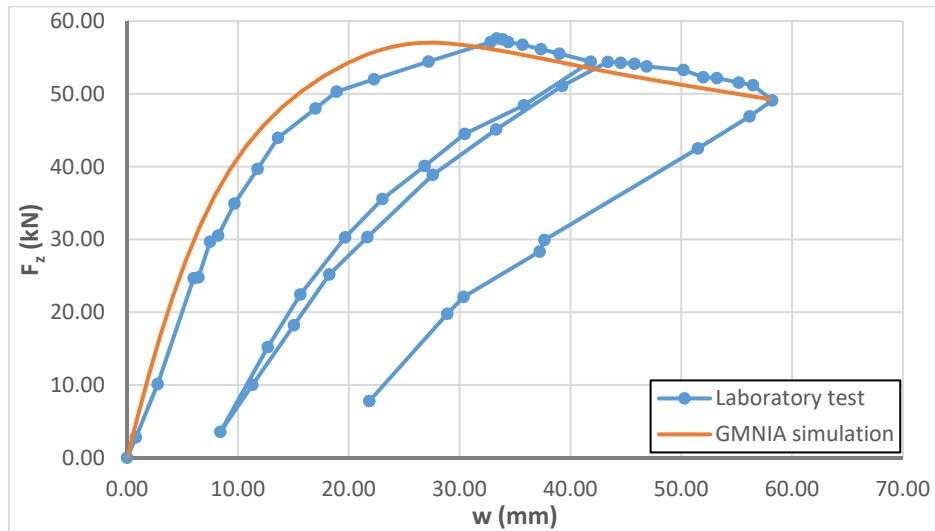


Figure 3-72: Vertical displacement of the centroid at mid-span

In Figure 3-70 to Figure 3-72, one may observe in particular;

- The peak load is quasi identical for the laboratory test and the numerical simulation. Again, the difference is approximatively equal to 1%.
- The initial stiffness of the member with reference to the lateral and the vertical displacement seems to be less well represented than for the IPE 200 section. The torsional twist is however extremely well represented. It is recalled again that the lateral and the vertical displacement have been calculated at the centroid based on the torsional twist and a reference displacement in (FOSTA 2004). This may result in certain imprecision that complicate the comparison.
- The numerical load-displacement curves are also rather close to the laboratory tests after the peak load. Only the lateral displacement is not well represented. Yet, in general the load-displacement curves correspond very well.

As for the double symmetric I section, the numerical simulation represents precisely the physical test for the member of UPE 200 section. A global evaluation of the numerical model with reference to the physical tests is given next.

3.4.2.4 Summary of the results

Figure 3-73 gives an overview of the totality of the tests. As can be seen the numerical model gives very satisfactory results. In fact the maximum difference is about 4%. Also, it can be noted that the GMNIA results are safe-sided for all I-shaped members (tests 1-13). However, for U-shaped members one numerical result is unsafe. Nonetheless, the maximum unsafe difference is only of about 4%. Yet, for test 15, noted as BE-3-21 in reference (FOSTA 2004), local buckling at the supports has been observed in the laboratory. This explains, at least partly, the over-estimation of the GMNIA resistance.

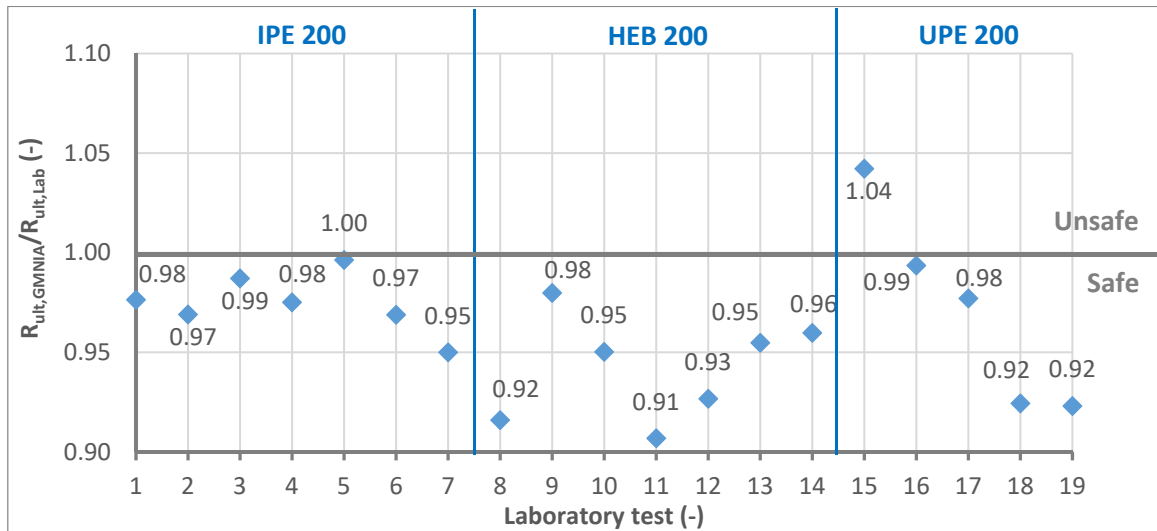


Figure 3-73: Comparison of all physical tests performed at TU Berlin

3.4.2.5 Influence of the fillets on the test results

In paragraph 3.3.5 it has been shown that the fillets do not influence **the general behaviour** of the member (represented in the λ - χ format). Hereafter, this is confirmed again for the case of the physical tests. For this objective, the results obtained for the test BE-1-1 are represented for the case of:

- “Shell model” without fillets;
- “Solid” model without fillets;
- “Solid” model with fillets.

Figure 3-74 represents the test setup. The numerical simulations are performed including the classical residual stress pattern, measured geometric imperfections as well as the measured material law.

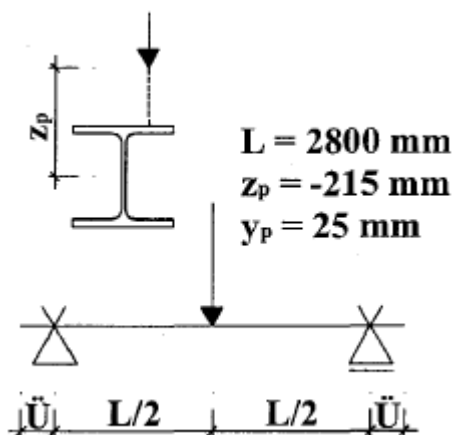


Figure 3-74: Physical test BE-1-1 (from FOSTA. 2004))

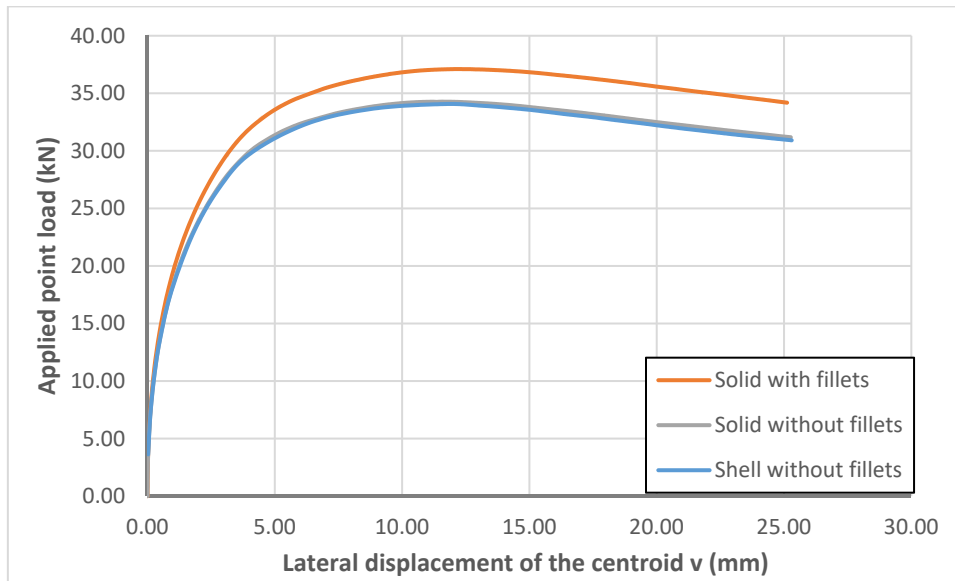


Figure 3-75: Evolution of the applied load with the lateral displacement of the centroid at mid span for test BE-1-1

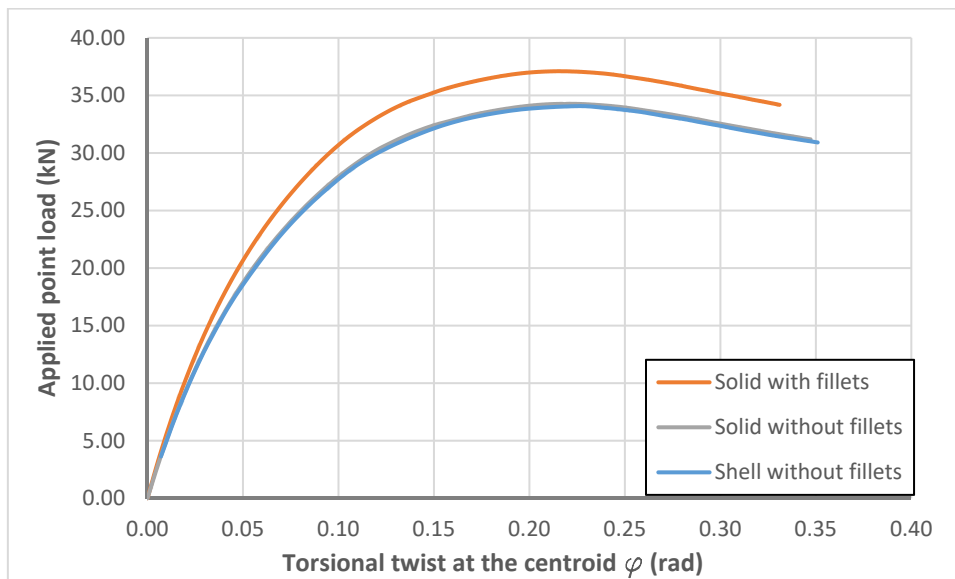


Figure 3-76: Evolution of the applied load with the torsional twist at mid span for test BE-1-1

Figure 3-75 and Figure 3-76 show that the “Shell” and the “Solid” model yield practically identical results if the fillets are not modelled. Conversely, it may be observed that the “Solid” model with fillets leads to a higher ultimate resistance for this individual case. This is not surprising as the fillets add torsional stiffness to the member leading to a lower torsional twist and a lower lateral displacement for a given load level. Hence, second order internal moments are also lower and yielding of the cross-section starts at a higher load level.

The example treated above allows the conclusions of paragraph 3.3.5 to be confirmed. It is shown that the “Shell” model is equivalent to the “Solid” model if the fillets are not considered. Additionally, paragraph 3.3.5 has shown that the influence of the fillets vanish when the resistance is represented in the λ - χ format, i.e. with reference to the real cross-section characteristics.

Consequently, the parametric study concerning the ultimate **member resistance** may be performed based on the less time consuming shell model.

3.4.3 Conclusions

Throughout the present chapter the numerical model used in the framework of this thesis was presented, discussed and validated extensively. This preparatory work was absolutely necessary in order to ensure that the numerical model is capable to predict reliably the resistance of members subject to complex load combinations creating interaction between axial force, bi-axial bending and torsion. Moreover, due to the complexity of the problem treated here, a very high number of parametric calculations has to be performed in order to develop a resistance model in Chapters 4 and 5. Therefore, the numerical model should be sufficiently efficient to perform the parametric studies in a reasonable amount of time.

In particular, the following points were of special interest and have been studied:

- Meshing density of hot-rolled and welded cross-sections for different load cases and for different values of the section slenderness (cross-section classes);
- Modelling techniques for the fillets of hot-rolled cross-sections;
- Influence of fillets on the member resistance;
- Choice and validation of the numerical model.

The different studies presented in the present chapter concerning the points mentioned above made it possible to conclude that:

- The meshing density should be different for hot-rolled and welded sections in order to represent the distribution of different residual stress pattern;
- In the longitudinal direction, at least 100 finite elements should be used to precisely account for the spread of plasticity in material non-linear calculations;
- For slender cross-sections sensitive to local buckling, a higher element density is necessary in the longitudinal direction in order to represent the presumed local buckle reliably;
- The influence of the fillets on the plastic cross-section resistance may only be studied with a solid model due to the limitations of the shell and beam finite elements concerning the interaction between axial and shear stresses. Also, only the solid elements are capable of representing the continuity of material in the fillet zone;
- The fillets do influence the resistance of members fabricated from hot-rolled cross-sections as they increase notably the torsion constant I_t ; yet the general member behaviour is not modified;
- The comparisons between the numerical model and physical tests performed in the framework of a previous research project have shown that the numerical

model is reliable and capable to predict the resistance of members under complex load combinations including cases with torsional loads.

The present chapter only consisted in a general presentation and validation of the numerical model. Specific questions resulting from the study of the member resistance, as for example the sensitivity to loading path and assumed imperfections are studied in Chapter 5. Also, supplementary validations of the numerical models used here are given in Chapter 4, concerning the cross-section resistance and Chapter 5 concerning the member resistance.

Obviously, the numerical simulations as well as the real behaviour of the member always contain a certain amount of uncertainty. Therefore, the numerical simulations can only approach the reality with a given tolerance. Based on the investigations presented in this chapter and in particular the comparisons to physical tests, it may be concluded that the precision of the model used here is of about $\pm 5-10\%$. In the following, extensive parametric studies are performed to characterize the behaviour of members of open cross-section subject to a combination of internal forces and moments including torsion. Therefore, a very high number of parameters is susceptible to have a certain influence. Nonetheless, only parameters possessing an influence of more than 5% percent may be characterised owing to the natural scatter of the numerical results. Yet, this "limitation" seems to be completely acceptable. Additionally, it should be noted that the practical design of the ideal numerically modelled boundary conditions may also possess an influence that could be even higher than 5%. However, the influence of the design of supports and restraints on the member resistance cannot be studied in the framework of this thesis. Hereafter, it is intended to develop lower bound solutions based on idealised boundary conditions.

4 PLASTIC CROSS-SECTION RESISTANCE

4.1	Introduction	101
4.2	Assessing the plastic cross-section resistance	102
4.2.1	Plastic interaction in various standards	102
4.2.1.1	Internal forces and moments creating only axial stresses	102
4.2.1.2	Interaction between shear and axial stresses	108
4.2.2	Numerical tools for the cross-section interaction	116
4.2.2.1	General	116
4.2.2.2	Iterative calculation based on predefined elastic stress distribution	116
4.2.2.3	Partial internal force method – PIFM	120
4.2.3	Conclusions	131
4.3	Laboratory tests performed at University of Applied Sciences of Western Switzerland	133
4.3.1	Motivation	133
4.3.2	Choice of the test specimen and test program	133
4.3.3	Test set-up	137
4.3.4	Preparatory measurements	139
4.3.4.1	General	139
4.3.4.2	Dimensions of the cross-sections	139
4.3.4.3	Tensile tests characterizing the material behaviour	141
4.3.5	Three point bending laboratory tests	143
4.3.6	Numerical simulations of the laboratory tests	145
4.3.6.1	Presentation of the numerical model	145
4.3.6.2	Comparison between numerical model and laboratory tests	146
4.3.6.3	Comparison between laboratory tests and resistance models	150
4.3.7	Complementary numerical simulations and comparison to resistance models	155
4.3.8	Conclusions	161
4.4	Parametric study and resistance model	162
4.4.1	General remarks	162
4.4.1.1	Studied cross-sections	162
4.4.1.2	Load cases	164
4.4.1.3	Material model	166
4.4.2	Interaction between major-axis bending and shear force	168
4.4.2.1	Double symmetric I sections	168
4.4.2.2	U sections	172
4.4.2.3	Mono-symmetric I sections	176
4.4.3	Interaction between minor-axis bending and shear force	183
4.4.3.1	Double symmetric I sections	183
4.4.3.2	U sections	185

On the Design of Steel Members with Open Cross-Sections Subject to Combined Axial Force, Bending and Torsion	Plastic Cross-Section Resistance
4.4.3.3 Mono-symmetric I sections	187
4.4.3.4 Conclusions	189
4.4.4 Interaction between bending, shear force and torsion	190
4.4.4.1 Influence of the plastic torsional system reserve of the member	190
4.4.4.2 Double symmetric I sections	204
4.4.4.3 Mono-symmetric I sections	218
4.4.4.4 U sections	227
4.4.5 Other selected load cases	237
4.4.5.1 General	237
4.4.5.2 Combined axial force, bending and torsion for double symmetric I sections	237
4.4.5.3 Combined axial force and major-axis bending for U sections	240
4.4.5.4 Conclusions	244
4.5 Proposed resistance model	245
4.6 General conclusions concerning the plastic cross-section resistance	254

4.1 Introduction

The ultimate resistance of an arbitrary member subject to an arbitrary combination of loads may be represented by a characteristic curve linking the resistance to the relative slenderness λ . Hereafter, this curve is referred to as ultimate resistance curve of the member. Its form is schematically represented by the dots in Figure 4-1. In this figure the resistance is given by the ratio R_{ult} to $R_{b,L}$, designating the load amplification factor leading to the failure of the **member** and the load amplification factor leading to the failure of the most loaded **cross-section**, respectively.

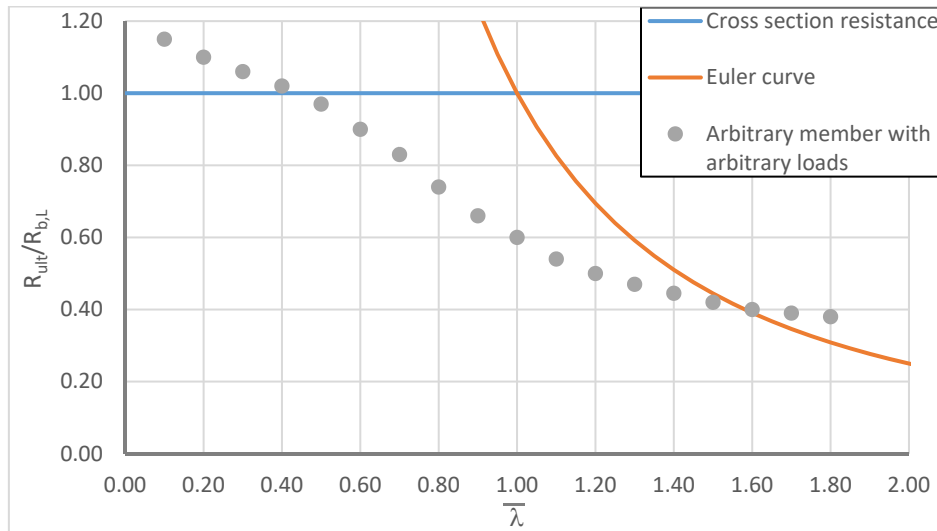


Figure 4-1: Ultimate resistance curve of an arbitrary member subject to an arbitrary combination of loads

The reduced slenderness used as abscissa in Figure 4-1 may be expressed by Eq. (4.1).

$$\bar{\lambda} = \sqrt{\frac{R_{b,L}}{R_{cr,G}}} \quad (4.1)$$

The form of the ultimate resistance curve is not specific to any design model but describes the behaviour of a member in a general way. Two main regions may be distinguished in Figure 4-1:

- 1) Failure of the member is mainly characterized by the failure of the most loaded cross-section;
- 2) Failure of the member is characterized by elasto-plastic (member) instability.

Depending on the cross-section and the load combination, the width of the two regions may vary. Anyhow, the member always attains at least the full cross-section resistance of its most loaded section in region 1). Depending on the compactness of the cross-section, this resistance may be plastic, elastic or even less if the section is sensitive to local buckling before it attains its elastic resistance. For very short members, the resistance may, in some cases, exceed the cross-section resistance due to the spread of plasticity through the member and through the cross-section even for slender sections with limited plastic reserve.

In region 2) the member suffers from a strength reduction ($R_{ult}/R_{b,L} < 1,0$) due to the effect of member imperfection and member instability. For long members the ultimate resistance curve may cross the Euler curve associated with pure elastic instability. However, this is generally linked to excessive displacements as shown in (Taras 2011). Consequently, this post-critical resistance reserve should be neglected for members.

In order to predict the ultimate member resistance with sufficient precision, both regions of the ultimate resistance curve have to be studied and characterized. The present Chapter concentrates on region 1) characterized by cross-section failure. Moreover, hereafter, the plastic cross-section resistance is of special interest due to the lacks in Eurocode 3 Part 1-1. Indeed, the resistance of slender cross-sections may be treated with the effective width method (EWM) proposed in (CEN 2005a). Yet, it may be noted that the EWM was in the centre of criticism due to its complexity (see for example (Nseir 2015) and (Boissonnade et al. 2017)). However, it is still widely accepted as it possesses an extensive range of application. Also, the resistance of semi-compact cross-sections can be treated with the methods proposed in the current version of Eurocode 3 Part 1-1. Additionally, in order to close the discontinuity between compact (or class 2) and semi-compact (or class 3) sections a continuous design method has been proposed in the framework of the RFCS project SEMI-COMP in reference (RFCS 2009).

Conversely to the resistance of slender and semi compact sections, the plastic resistance of compact sections subject to complex combination of internal forces and moments, including torsion, has not been sufficiently investigated and may not be treated neither with the provisions of Eurocode 3 Part 1-1 nor with other international standards as is shown in paragraph 4.2. Therefore, the plastic interaction is studied in the present Chapter based on laboratory tests (see paragraph 4.3) and an extensive numerical study (see paragraph 4.4).

4.2 Assessing the plastic cross-section resistance

4.2.1 Plastic interaction in various standards

4.2.1.1 *Internal forces and moments creating only axial stresses*

In the past, many proposals have been made to assess the plastic cross-section interaction. In Europe the works of (Djalaly 1975), (Rubin 1978), (Rubin 2000), (Rubin 2005), (Kindmann et al. 1999), (Vilette 2004) and (Ludwig 2014) may be cited. This long, but incomplete list shows that the plastic section resistance has been studied for a long time and is still of interest for current researchers.

Hereafter, it is proposed to review only the methods included in major current design standards. Also, the review is limited to open sections (I and U). A more detailed review is given for example in (Vilette 2004).

The following tables summarise the interaction formulae for combined bending and compression given in (ANSI 2010), (Standard Australia 1998) and (CEN 2005a).

Table 4-1: Interaction criterion given in the North American steel building design standard – ANSI/AISC 360-10

Load case	Criterion
N+M _y +M _z	$\frac{N_{Ed}}{N_{Rd}} + \frac{8}{9} \left(\frac{M_{y,Ed}}{M_{y,Rd}} + \frac{M_{z,Ed}}{M_{z,Rd}} \right) \leq 1,0$ for $\frac{N_{Ed}}{N_{Rd}} \geq 0,20$
	$\frac{N_{Ed}}{2N_{Rd}} + \left(\frac{M_{y,Ed}}{M_{y,Rd}} + \frac{M_{z,Ed}}{M_{z,Rd}} \right) \leq 1,0$ for $\frac{N_{Ed}}{N_{Rd}} < 0,20$

Table 4-2: Interaction criterion given in the Australian steel building design standard – AS 4100:1998

Cross-section	Load case	Criterion
General	N+M _y	$\frac{M_{y,Ed}}{M_{N,y,Rd}} \leq 1,0$ and $M_{N,y,Rd} = M_{y,Rd}(1-n)$
	N+M _z	$\frac{M_{z,Ed}}{M_{N,z,Rd}} \leq 1,0$ and $M_{N,z,Rd} = M_{z,Rd}(1-n)$
	N+M _y +M _z	$\frac{N_{Ed}}{N_{Rd}} + \frac{M_{y,Ed}}{M_{y,Rd}} + \frac{M_{z,Ed}}{M_{z,Rd}} \leq 1,0$
Double symmetric I section	N+M _y	$\frac{M_{y,Ed}}{M_{N,y,Rd}} \leq 1,0$ and $M_{N,y,Rd} = 1,18M_{y,Rd}(1-n) \leq M_{y,Rd}$
	N+M _z	$\frac{M_{z,Ed}}{M_{N,z,Rd}} \leq 1,0$ and $M_{N,z,Rd} = 1,19M_{z,Rd}(1-n^2) \leq M_{z,Rd}$
	N+M _y +M _z	$\left(\frac{M_{y,Ed}}{M_{y,N,Rd}} \right)^\gamma + \left(\frac{M_{z,Ed}}{M_{z,N,Rd}} \right)^\gamma \leq 1,0$ and $\gamma = 1,4 + (n) \leq 2,0$

Table 4-3: Interaction criterion given in the European steel building design standard – Eurocode 3 Part 1-1

Cross-section	Load case	Criterion
Double symmetric I section	N+M _y	$\frac{M_{y,Ed}}{M_{N,y,Rd}} \leq 1,0 \text{ and}$ $M_{N,y,Rd} = M_{y,Rd} \text{ if } N_{Ed} \leq \text{Min} \left(0,25N_{Rd}; \frac{0,5h_w t_w f_y}{\gamma_{M0}} \right)$ $M_{N,y,Rd} = M_{y,Rd} \frac{1-n}{1-0,5a} \leq M_{y,Rd} \text{ otherwise}$
	N+M _z	$\frac{M_{z,Ed}}{M_{N,z,Rd}} \leq 1,0 \text{ and}$ $M_{N,z,Rd} = M_{z,Rd} \text{ if } N_{Ed} \leq \frac{h_w t_w f_y}{\gamma_{M0}}$ $M_{N,z,Rd} = M_{z,Rd} \left(1 - \left(\frac{n-a}{1-a} \right)^2 \right) \text{ otherwise}$
	N+M _y +M _z	$\left(\frac{M_{y,Ed}}{M_{N,y,Rd}} \right)^\alpha + \left(\frac{M_{z,Ed}}{M_{N,z,Rd}} \right)^\beta \leq 1,0 \text{ and}$ $\alpha = 2, \beta = 5 \frac{N_{Ed}}{N_{Rd}} \geq 1,0$

By comparing Table 4-1, Table 4-2 and Table 4-3, one may note that the North American design standard proposes certainly the simplest design approach. Also, as the same formulae are used for the cases of mono-axial bending and axial force and bi-axial bending, full continuity of the interaction space is guaranteed. However, one might wonder if the North American interaction formulae are not overly safe-sided for common cases like double symmetric I sections (see Figure 4-2, Figure 4-3 and Figure 4-4).

Both, the Australian and European design standards propose a set of formulae applicable for a given combination of internal forces and moments. However, Eurocode 3 is the only standard presented here considering the influence of the cross-section proportions by introducing the factor “a” (ratio between area of web area and the total area of the cross-section). In order to compare the three approaches in more detail, the following figures give the resulting interaction curves M_y-M_z for three values of the axial force: 0,0; 0,3 N_{pl} and 0,6 N_{pl}. For Eurocode 3 two curves are shown corresponding to the upper and lower bound of European profiles (HEM 100 – a = 0,16 and HEAA 800 – a = 0,51). Finally, the analytical interaction curve, based on a theoretical plastic stress distribution for the combination of axial force and bi-axial bending is represented.

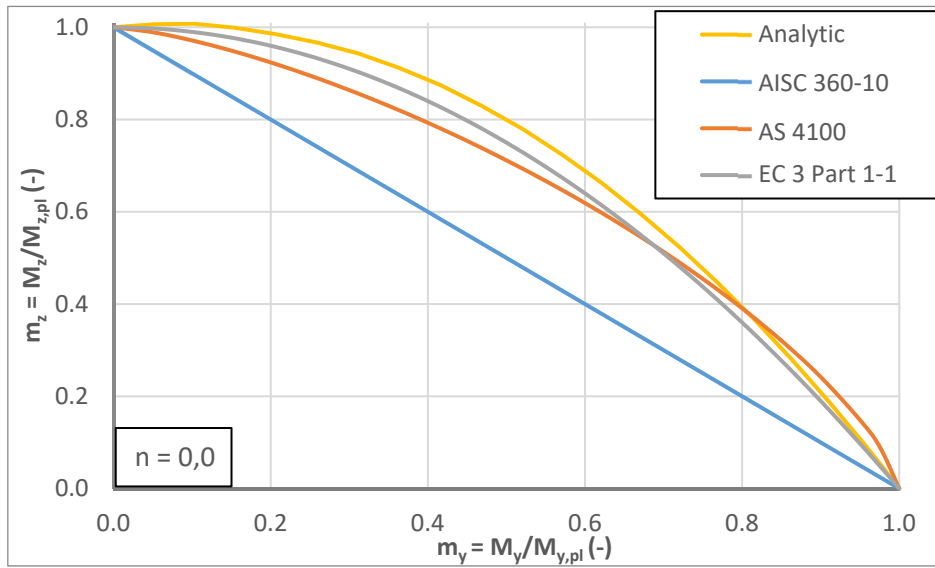


Figure 4-2: M_y - M_z Interaction curve without axial force $N/N_{pl} = 0$

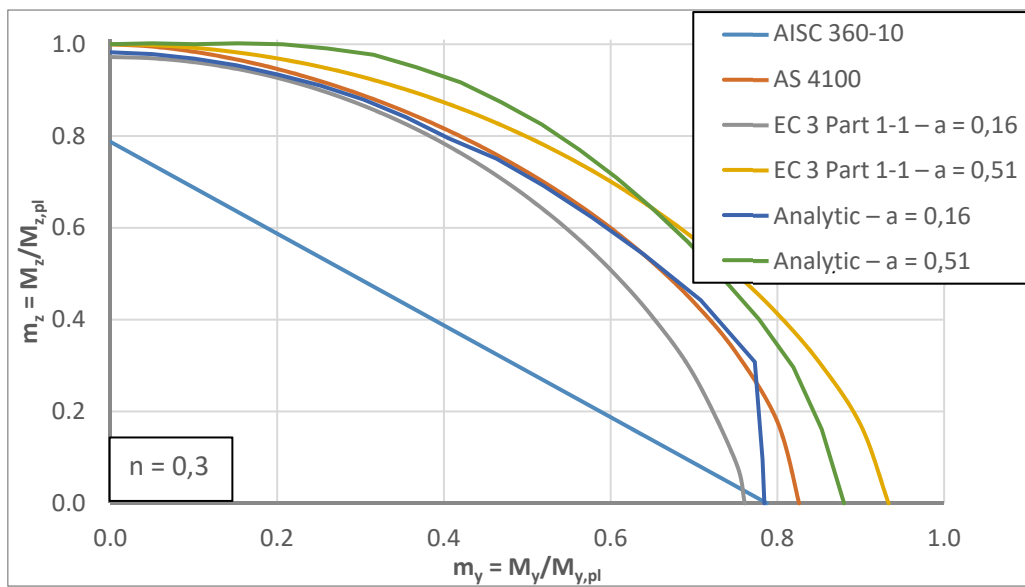


Figure 4-3: M_y - M_z Interaction curve with $N/N_{pl} = 0,30$

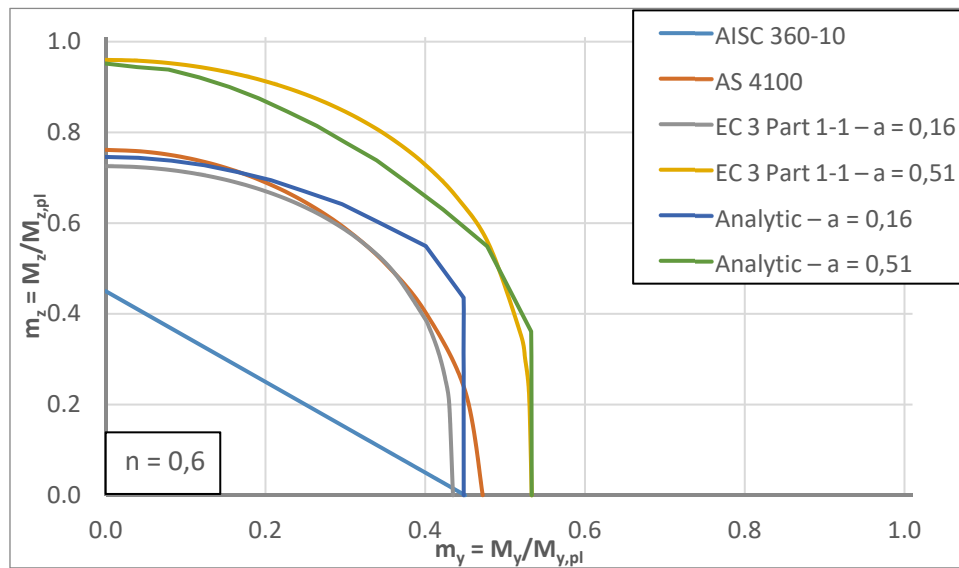


Figure 4-4: My-Mz Interaction curve with $N/N_{pl} = 0,60$

The previous figures clearly show that the design provisions of the North American standard are very safe-sided. Moreover, the conservatism increases with increasing axial force. Nevertheless, it can be noted that in case of combined major-axis bending and axial force ($m_z = 0$), very good agreement with the analytical result is obtained. Both, AS 4100 and Eurocode 3 Part 1-1 capture very well the form of the cross-section interaction. However, as the Australian standard does not include any parameter accounting for the exact proportions of the cross-section, the proposed interaction curve may be far away from the analytical result, especially in case of cross-sections with high values of the coefficient a (a tending to 0,50). It appears that the Australian provisions yield satisfactory results for cross-sections possessing an a value of approximately 0,15-0,25. Yet, one may also see that the provisions given for combined axial force and major-axis bending are unsafe for the given examples.

Eurocode 3 Part 1-1 seems to approximate the best the interaction behaviour of double symmetric I sections subject to a combination of axial force and bi-axial bending even if the interaction formulae are not excessively more complex than the ones proposed in AS 4100. As Eurocode 3 Part 1-1 accounts for the cross-section proportions by introducing the factor a , the results are in better agreement with the analytical results. Nevertheless, the European provisions may also lead to unsafe results in some cases. In Figure 4-3 and Figure 4-4, it can be seen that the results are (too) unsafe for the cross-section of high a value ($a = 0,51$) and values of m_z in the range between 0,7 and 0,9. Admittedly, the double symmetric I sections are rarely subject to such high minor-axis bending moments.

Last, Figure 4-5 shows the interaction curves for the current case of combined axial force and major-axis bending. It is seen that the bi-linear approximation of AISC 360-10 fits very well the lower bound interaction curve. For cross-section with higher a values, it may however be very conservative. As before, the provisions of AS 4100 seem to be calibrated to cross-sections possessing medium values of a . Also, as a cut-off value for the axial force of approximately $0,15N_{pl}$ has been defined, the provisions can be unsafe for low values of axial forces. The same

tendency can be seen for the European provisions. Especially, for cross-sections with high a values, this may lead to unacceptable unsafe results. Conversely, the European interaction curve fits very well the analytical results for high axial forces. Again the cross-section proportion factor a is very beneficial.

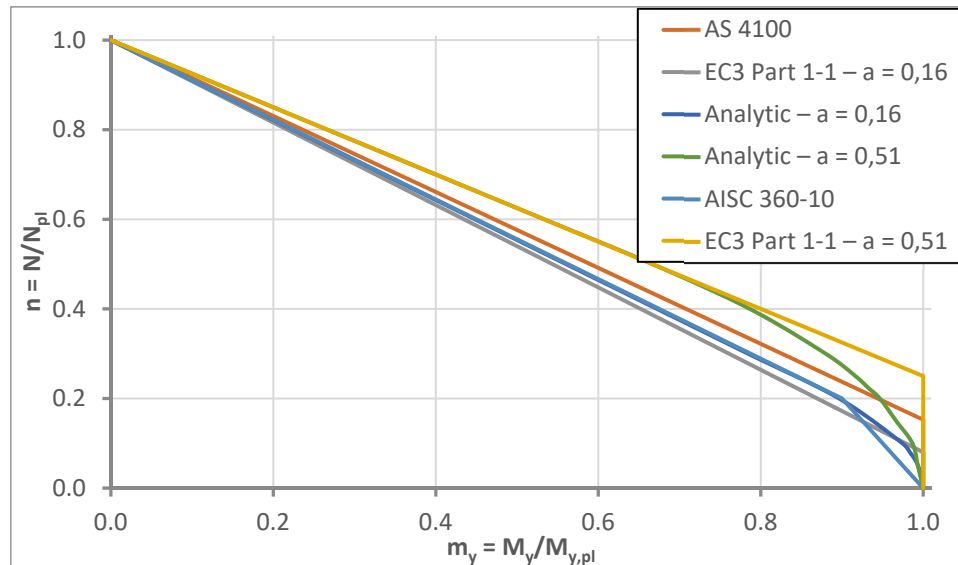


Figure 4-5: M_y - N interaction diagram ($m_z = 0$)

Here before, the N - M_y - M_z cross-section interaction curves provided in three major international standards have been compared. It should be noted that none of the standards provides specific rules for other open cross-sections, as U sections or mono-symmetric I sections. The American provisions are explicitly applicable to all shapes of cross-sections, a reason why these rules may be very conservative for double symmetric I sections. The Australian standard proposes a linear interaction that certainly leads to very conservative results for compact U sections. Finally, the European standard silently omits other open cross-sections. It is implicitly mentioned that an elastic cross-section interaction may always be applied to sections not sensitive to local buckling. Also, it should be noted that none of the mentioned design provisions considers the influence of axial stresses due to the bi-moment in case of plastic interaction (see paragraph 4.2.1.2.2 for more details). The North American design standard as well as Eurocode 3 Part 1-1 propose an elastic interaction that, obviously, leads to very conservative results if only few torsion is applied to the member. Paragraph 4.2.1.2 gives more details on the influence of torsion on the cross-section interaction.

Based on the comparison presented here before, it may be concluded that:

- Very simple design provisions may be over conservative for the specific case of double symmetric I sections, as observed for AISC 360-10.
- More complex design provisions, as given in Eurocode 3 Part 1-1 and AS 4100:1998 may approximate more precisely the real cross-section interaction.

- Specific design provisions for other open sections are not included in the studied design standards.

The last point listed above may be very well understandable. Obviously, including specific rules for other than double symmetric I sections would lead to an even more extended set of interaction formulae that would be more or less complex depending on the desired precision.

4.2.1.2 Interaction between shear and axial stresses

4.2.1.2.1 Cross-section resistance under pure shear

As before the provisions given in AS 4100, AISC 360-10 and Eurocode 3 Part 1-1 are compared for the shear resistance. All three standards define a plastic shear resistance equal to:

$$V_{pl,Rd} = \tau_{Rd} A_v \quad (4.2)$$

The aspect of the plastic shear resistance is equal. However, for the yield shear stress τ_{Rd} and the shear area, different definitions are used. The North American and the Australian design standard define τ_{Rd} as $0,6f_y$. Eurocode 3 uses a more precise definition based on the von Mises yield criterion of (omitting the partial factor γ_{M0} equal to 1,0):

$$\tau_{Rd} = \frac{f_y}{\sqrt{3}} \approx 0,57f_y \quad (4.3)$$

The difference is about 5% and may be neglected. Yet, the difference in the definition of the shear area is much more pronounced. Figure 4-6 illustrates the shear areas used in the different codes.

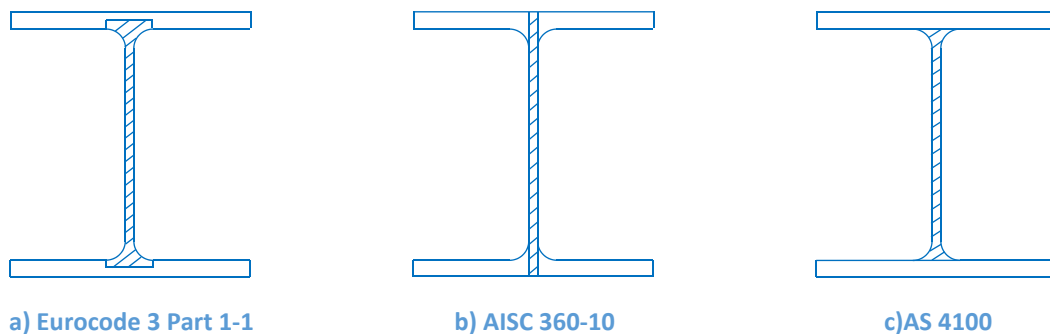


Figure 4-6: Shear areas for double symmetric hot-rolled I sections and shear parallel to the web

For a better visualization, Figure 4-7 shows the relative difference between the shear areas for the two European steel profile series, IPE and HEA, representing approximatively the lower and the upper bound.

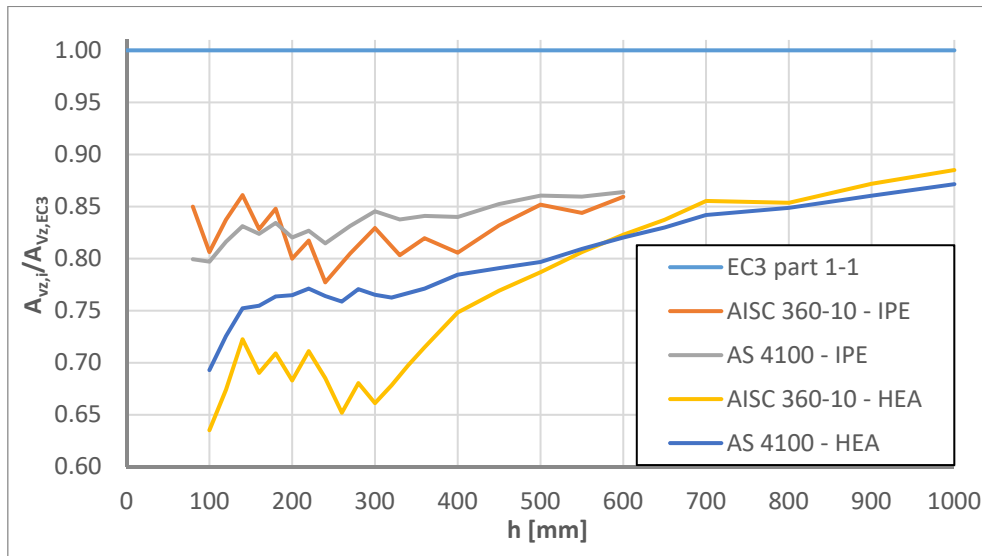


Figure 4-7: Comparison between shear areas A_{vz} defined in different standards

It can be seen that Eurocode 3 may be very economic compared to ANSI/AISC 360-10 and AS 4100. Especially for H sections the difference may attain 25%-30% compared to the North American standard and up to 35% compared to the Australian standard. These last give very similar results apart from H sections with small fillets and thick flanges (HEA 100 – HEA 330). For hot-rolled U-sections the results are similar.

In case of welded sections, Eurocode 3 allows (optionally) the use of $\eta = 1,2$ (=overstrength factor for shear) times the web area as shear area. Hence, the difference between the standard is in the same range as for hot-rolled sections (IPE, HEA 600 and wider). It should be noted, that only AS 4100 introduces a particular formula for mono-symmetric I sections given in Eq. (4.4).

$$V_{z,Rd} = \frac{2V_{z,pl}}{0,9 + \frac{\tau_{max,el}}{\tau_{med,el}}} \quad (4.4)$$

Where:

$\tau_{max,el}$: is the maximum elastic shear stress

$\tau_{med,el}$: is the average elastic shear stress

Finally, it should be noted that the plastic shear resistance might be used up to a limit web slenderness defined in Table 4-4. For more slender webs, shear buckling has to be accounted for. For a better comparison, the values provided in AISC 360-10 and AS 4100 are presented with Eurocode 3 notation. If the overstrength factor η is used with a value greater than 1,0, the limit slenderness for shear buckling has to be decreased in Eurocode 3. It can be observed that the limit slenderness is in the same range.

Table 4-4: Limit slenderness for shear buckling

Eurocode 3 Part 1-1	AISC 360-10	AS 4100
$72\varepsilon/\eta$	67ε	77ε

In practice, the shear force is not acting alone in the section, but it is accompanied by a bending moment. The interaction equations provided in different standards are discussed in the next paragraph.

4.2.1.2.2 Combination of major-axis bending and shear force

AISC 360-10 gives a very simple design provision as the interaction needs not to be accounted for. It should only be checked that:

- The maximum normal stress is less than the yield stress f_y and;
- The maximum shear stress is less than $0,6f_y$.

As plasticity is not accounted for, these design rules may, however, be very conservative, especially for low shear forces. It may be noted that these provisions are applicable for all load combinations creating shear and axial stresses (including the load case of combined bending and torsion).

Eurocode 3 Part 1-1 specifies a set of interaction formulae. The principle is to reduce the bending moment resistance due to the influence of shear as given in Eqs. (4.5) and (4.6) for the M_y - V_z interaction.

$$M_{y,Rd} = M_{y,c,Rd} \quad \text{if } \frac{V_{Ed}}{V_{pl,Rd}} \leq 0,5 \quad (4.5)$$

$$M_{y,Rd} = \left[W_{pl,y} - \frac{\rho A_w^2}{4t_w} \right] f_y \leq M_{y,c,Rd} \quad \text{elsewise}$$

and

$$\rho = \left[\frac{2V_{Ed}}{V_{pl,Rd}} - 1 \right]^2 \leq 1,0 \quad (4.6)$$

It can be seen that the interaction between major-axis bending and shear is neglected up to a value of $V_{z,Ed}/V_{z,pl,Rd} = 0,5$. For higher values of the shear force, a parabolic reduction is applied (see Figure 4-8).

AS 4100 proposes the following interaction:

$$V_{z,m,Rd} = V_{pl,Rd} \left[2,2 - \left(1,6 \frac{M_{y,Ed}}{M_{y,Rd}} \right) \right] \quad (4.7)$$

In order to compare to Eurocode Eq (4.7) is reorganised to obtain:

$$M_{y,V,Rd} = \left(\frac{11}{8} - \frac{V_{z,m,Rd}}{1,6V_{pl,Rd}} \right) M_{y,Rd} \leq M_{y,Rd} \quad (4.8)$$

Eq. (4.8) shows that the interaction between the shear force and the major-axis bending moment can be omitted up to a value of $0,6V_{z,pl}$ for the shear force. For higher shear forces, a linear reduction of the major-axis bending moment should be adopted. The minimum value of the resistance moment obtained for $V_{Ed}/V_{z,pl} = 1$ is equal to $0,75M_{Rd}$. The two proposals are compared in Figure 4-8 and Figure 4-9 for a HEA 280 and a HEAA 1000 cross-section. Also, a numerical interaction curves, noted as “Solid model”, is included (see paragraph 4.4.1). The numerical calculation is based on an elastic-perfectly plastic material law without strain hardening performed on a solid model of a beam subject to a point load at mid-span.

The two figures indicate that the Eurocode 3 interaction curve based on the shear area given in Figure 4-6 yields unsafe results compared to the numerical results not considering strain hardening. Especially, in the case of the compact HEA 280 section, (area of the fillets is rather important), the Eurocode provisions seem to be up to 40% unsafe. Conversely, if only the web area is considered as shear resisting, the Eurocode provisions are closer to the numerical solution, especially in case of the compact section. The provisions given in the Australian standard are also unsafe compared to the numerical results, yet, less than the Eurocode 3 interaction. The unsafe nature of both proposals may be explained by the shear area that is used. As mentioned, if only the area of the web is considered as shear area, the Eurocode provisions are safe-sided for the studied cross-sections. A detailed study on the shear force-bending moment interaction is presented in paragraphs 4.3 and 4.4.

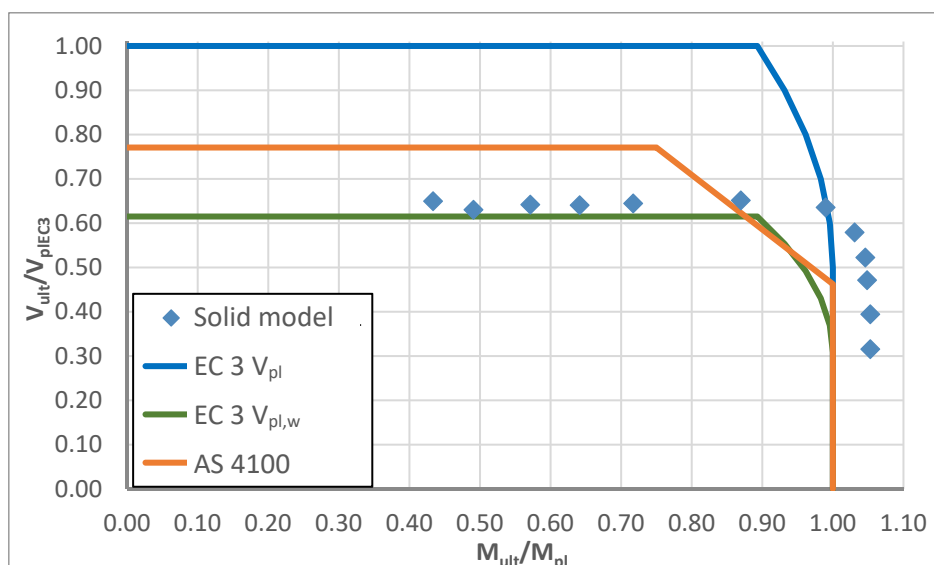


Figure 4-8 : Interaction between shear force V_z and bending moment M_y for a HEA 280 cross-section

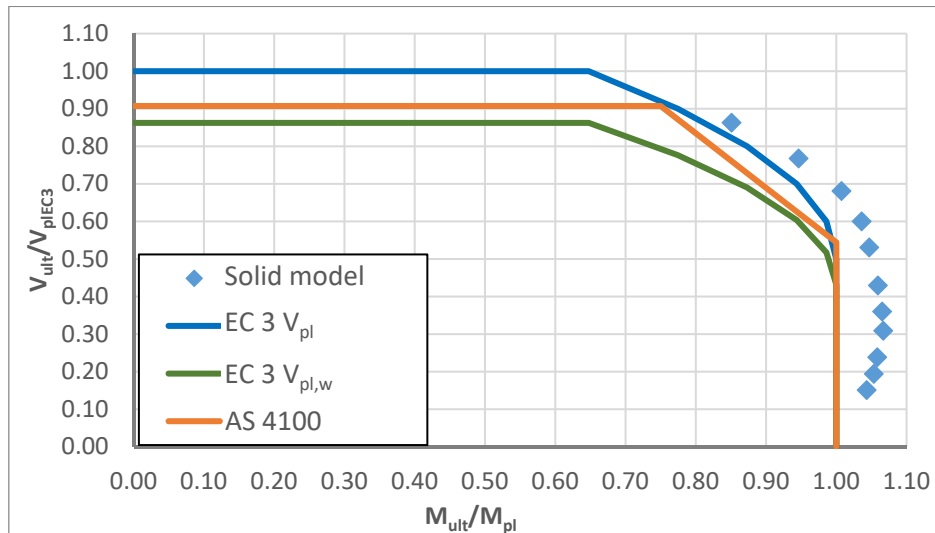


Figure 4-9 : Interaction between shear force V_z and bending moment M_y for a HEAA 1000 cross-section

4.2.1.2.3 Combination of bending, shear force and torsion

Last, it is interesting to study the interaction between bending, torsion and shear force defined in different standards. Yet, neither AISC 360-10 nor AS 4100 provide an interaction rule for this load case (for open sections). As stated previously, AISC 360-10 imposes explicitly an elastic calculation without interaction. In AS 4100 no specific provisions are given. Conversely, Eurocode 3 Part 1-1 provides a specific paragraph on torsion and interaction between torsion and shear. It is stated that for open section the shear resistance $V_{z,pl}$ should be reduced by the influence of shear stresses resulting from torsion. For U and I sections, two different interaction formulae are given:

For I sections:

$$V_{pl,T,Rd} = \sqrt{1 - \frac{\tau_{t,Ed}}{1,25\tau_{Rd}}} V_{pl,Rd} \quad (4.9)$$

For U sections:

$$V_{pl,T,Rd} = \left(\sqrt{1 - \frac{\tau_{t,Ed}}{1,25\tau_{Rd}} - \frac{\tau_{w,Ed}}{\tau_{Rd}}} \right) V_{pl,Rd} \quad (4.10)$$

The stress $\tau_{t,Ed}$ corresponds to the shear stress created by Saint Venant's torsional moments, and the shear stress $\tau_{w,Ed}$ corresponds to shear created by warping torsional moments. Obviously, for I sections, these last are neglected in the interaction as they only affect the flange (see Chapter 2). However, it may be noted that the axial stresses resulting from the bi-moment are not included in the interaction equations. As has been recalled in Chapter 2, an open cross-section carries torsion mainly by warping torsion. Consequently, the axial stresses induced by the bi-moment are not negligible in many cases (see paragraph 4.4).

In order to eliminate the possible insecurity, Mirambell recently proposed an amendment to Eurocode 3 Part 1-1 introducing specific plastic interaction formulae for combined major-axis bending, bi-moments and shear forces for double symmetric I sections (Mirambell 2016). His proposition is based on a predefined plastic stress distribution. It is supposed that the bending moment creates an axial force in the flanges and the bi-moment creates a flange bending moment. Consequently, the interaction between major-axis bending and the bi-moment of the sections is replaced by an interaction between bending moment and axial force of the flange that may be considered as a rectangle. The theoretical considerations of Mirambell are illustrated through Figure 4-10.

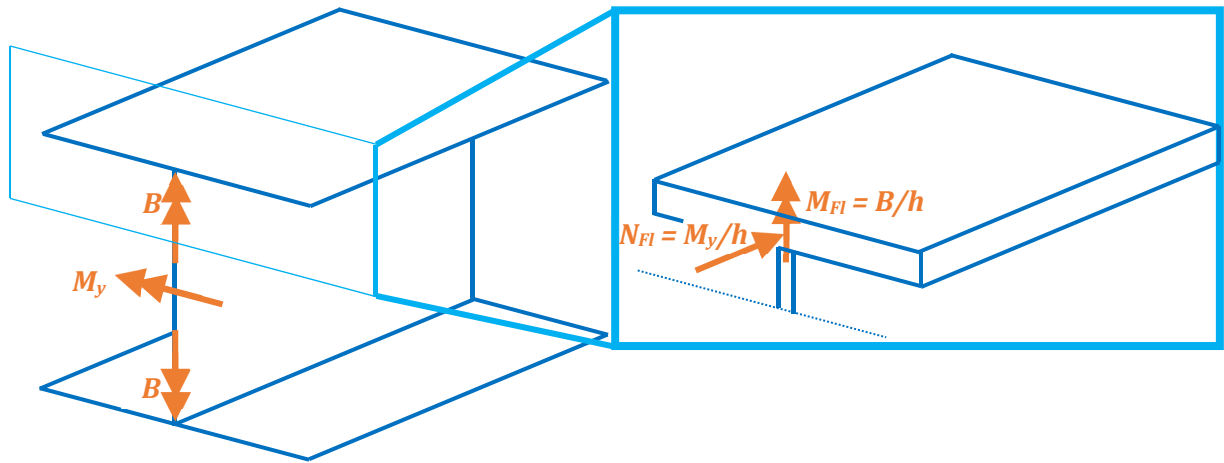


Figure 4-10: Interaction between major-axis bending and bi-moment for a double symmetric I section

Hence, one may express the moment resistance of the flanges by:

$$M_{f,B,Rd} = \sqrt{\left(1 - \frac{B_{Ed}}{B_{Rd}}\right)} M_{f,Rd} \quad (4.11)$$

By introducing the axial stress σ_w due to the bi-moment, given in Eq. (4.12), Mirambell transforms Eq. (4.11) into Eq. (4.13).

$$\sigma_{w,Ed} = \frac{M_w}{M_{w,el,Rd}} f_y \quad (4.12)$$

$$M_{c,B,Rd} = \rho_B M_{c,Rd} = \sqrt{\left(1 - \frac{\sigma_{w,Ed}}{\alpha f_y}\right)} M_{c,Rd} \quad (4.13)$$

He introduces the factor α in order to account for plasticity. If full plasticity is accounted for, this factor should be equal to 1,5. If the resistance to the bi-moment is limited to the elastic resistance, the factor α is obviously equal to 1,0. Mirambell proposes a factor of 1,25 in order to account only partially for the plastic reserve. One might argue that this ensures that the torsional twist does not increase excessively. However, it should be noted that for practical cases, high values of the bi-moment may only be attained for very short members. In these cases, the member may yield

without attaining an unreasonable torsional twist. Inversely, longer members only yield in presence of high torsional twist and consequently the Serviceable Limit State may become relevant for the design. Also, the relative part of the bi-moment in the total load carried by the member reduces (see Chapter 2). Hence, a value of 1,5 for the factor α would certainly be acceptable (see paragraph 4.4.4). Last, it should be noted that following Eq. (4.13), the resistance of the whole cross-section is reduced. The proposal is therefore safe-sided as the stresses due to the bi-moment do not transit through the web. In presence of a bi-moment, the major-axis bending moment resistance should thus be at lowest the bending moment resistance of the web.

In presence of a vertical shear force V_z , Mirambell proposes to reduce the major-axis bending moment resistance as indicated in Eurocode 3 Part 1-1 and shown in Eqs. (4.14), (4.15) and (4.16).

$$\begin{aligned} M_{y,B,V,Rd} &= M_{web,Rd} (1 - \rho_{Vz}) \rho_B + \rho_B M_{f,Rd} \\ &= [1 - \rho_{Vz}] \rho_B \frac{h_w^2 t_w}{4} f_y + \rho_B b t_f (h_w + t_f) f_y \end{aligned} \quad (4.14)$$

$$\rho_{Vz} = \left(\frac{2V_{Ed}}{V_{pl,T,Rd}} - 1 \right)^2 \quad (4.15)$$

$$\rho_B = \sqrt{\left(1 - \frac{\sigma_{w,Ed}}{1,25 f_y} \right)} \quad (4.16)$$

Regarding Eqs. (4.14) to (4.16), one might wonder why the resistance of the web should be reduced due to the influence from Saint Venant's torsion (reduced shear force resistance $V_{pl,T,Rd}$) whereas the resistance of the flanges is supposed to be affected only by the influence of the bi-moment. In order to underline this remark, it may be recalled that for practical cases of I sections whose flanges are thicker than the web, the Saint Venant's torsional shear stresses are higher in the flanges than in the web. Therefore, one might suppose that the resistance of the flanges should be reduced as well, at least for high Saint Venant's torsional moments. A detailed study concerning the plastic cross-section interaction including the effect of torsion is presented in paragraph 4.4.

Through this paragraph, it has been shown that Eurocode 3 contains some provisions for the interaction between the shear force V_z and shear stresses due to Saint-Venant's and warping torsion (for U sections). However, the European standard does not contain any provision for the interaction between the shear force V_y and shear stresses due to torsion. It is recalled that the shear stresses due to V_y and due to warping torsion are affine in the flanges of I sections. Therefore, one might expect a reduction of the shear force resistance. Moreover, the current version of Eurocode 3 Part 1-1 does not include any plastic interaction formula for major-axis bending and the bi-moment. In order to close this lack, Mirambell proposes interaction formulae based on a predefined plastic stress distribution. Yet, some questions remain in particular concerning the interaction with shear stresses arising from Saint-Venant's and warping torsion. Additionally, it should be noted that the proposal may not be applied to U sections as the bi-

moment also transits through their web. Consequently, the interaction behaviour is more complex (see paragraph 4.4.2).

4.2.1.2.4 Conclusion

The previous paragraph has compared rules on plastic section resistance and interaction given in three major steel design standards. It has been shown that:

- AISC 360-10 may be very conservative for the interaction between axial force and bi-axial bending;
- AS 4100 and Eurocode 3 predict rather well the interaction between axial force and bi-axial bending. However, by introducing the cross-section proportion factor “a”, Eurocode 3 yields more precise results;
- AISC 360-10 neglects the interaction between shear and axial stresses. However, only the elastic resistance of the section may be exploited;
- The shear resistance $V_{z,pl}$ provided in AS 4100 and Eurocode 3 Part 1-1 seems to be too optimistic, when compared to numerical simulations (elastic-perfectly plastic material). The influence of strain hardening is studied in paragraph 4.3;
- Only Eurocode 3 Part 1-1 explicitly includes a reduction for the **plastic** section resistance due to shear stresses created by Saint Venant’s and warping torsional moments. However, the interaction between the shear force V_y and shear stresses due to (in particular warping) torsional moments is neglected;
- None of the cited standards includes the axial stresses created by the bi-moment for the reduction of the plastic section resistance;
- The amendment proposal by Mirambell introducing the interaction mentioned in the previous point closes a lack in Eurocode 3 Part 1-1 concerning the interaction between major-axis bending and torsion but this proposal does not close all inconsistencies.

It has also been shown that the more or less complex interaction formulae can only predict approximatively the interaction behaviour between internal forces and moments. Especially, the case of combined bending, shear force and torsion is approximated very roughly. Obviously, formulae yielding more precise results are certainly far more complex (see for example (Ludwig 2014) and (Kindmann et al. 1999)). In the following, two methods implemented by programming are presented. The first method consists in step-by-step calculation of yielding of the cross-section. The second approach corresponds to the design method proposed by Kindmann in reference (Kindmann et al. 1999). The use of numerical tools for the plastic cross-section interaction certainly changes the habit of the vast majority of design engineers. However, a fast and precise determination of the plastic cross-section resistance may contribute to the acceptance of numerical automatized tools. Yet, simple interaction equations that may be applied by hand-calculation should always be proposed, at least for some cases (simple cross-section form, simple interaction cases between two or three internal forces), in order to verify the consistency of the obtained numerical results.

4.2.2 Numerical tools for the cross-section interaction

4.2.2.1 *General*

Sophisticated numerical simulations based on the finite element method can obviously determine the plastic resistance of an arbitrary cross-section subject to an arbitrary combination of internal forces and moments. However, this approach is certainly not suited for the current practice of engineering offices. Nevertheless, practical engineers do increasingly use numerical tools to establish calculation notes and to check the resistance of the studied sections and members, as for the simplest case Excel spread sheets. Therefore, it seems of interest to investigate the possibility of simple numerical tools determining the plastic cross-section resistance. In the following paragraphs, two procedures are presented.

4.2.2.2 *Iterative calculation based on predefined elastic stress distribution*

The first procedure proposed here is based on a step-by-step increase of the loads. The cross-section is discretised in a certain number of cells as shown in Figure 4-11.

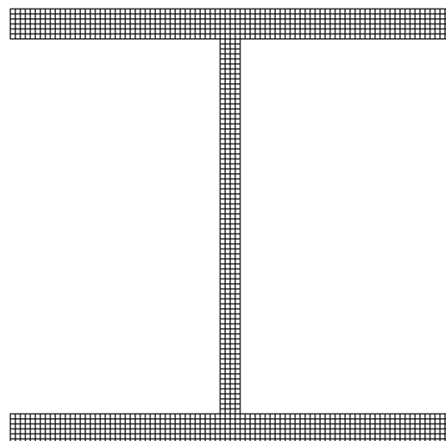


Figure 4-11: Discretisation of the cross-section into cells

Based on a predefined elastic stress distribution the load factor that leads to yielding of the first cell of the section is determined iteratively. For double symmetric I sections the elastic stress distribution is recalled in Figure 4-12 for the different internal forces and moments.

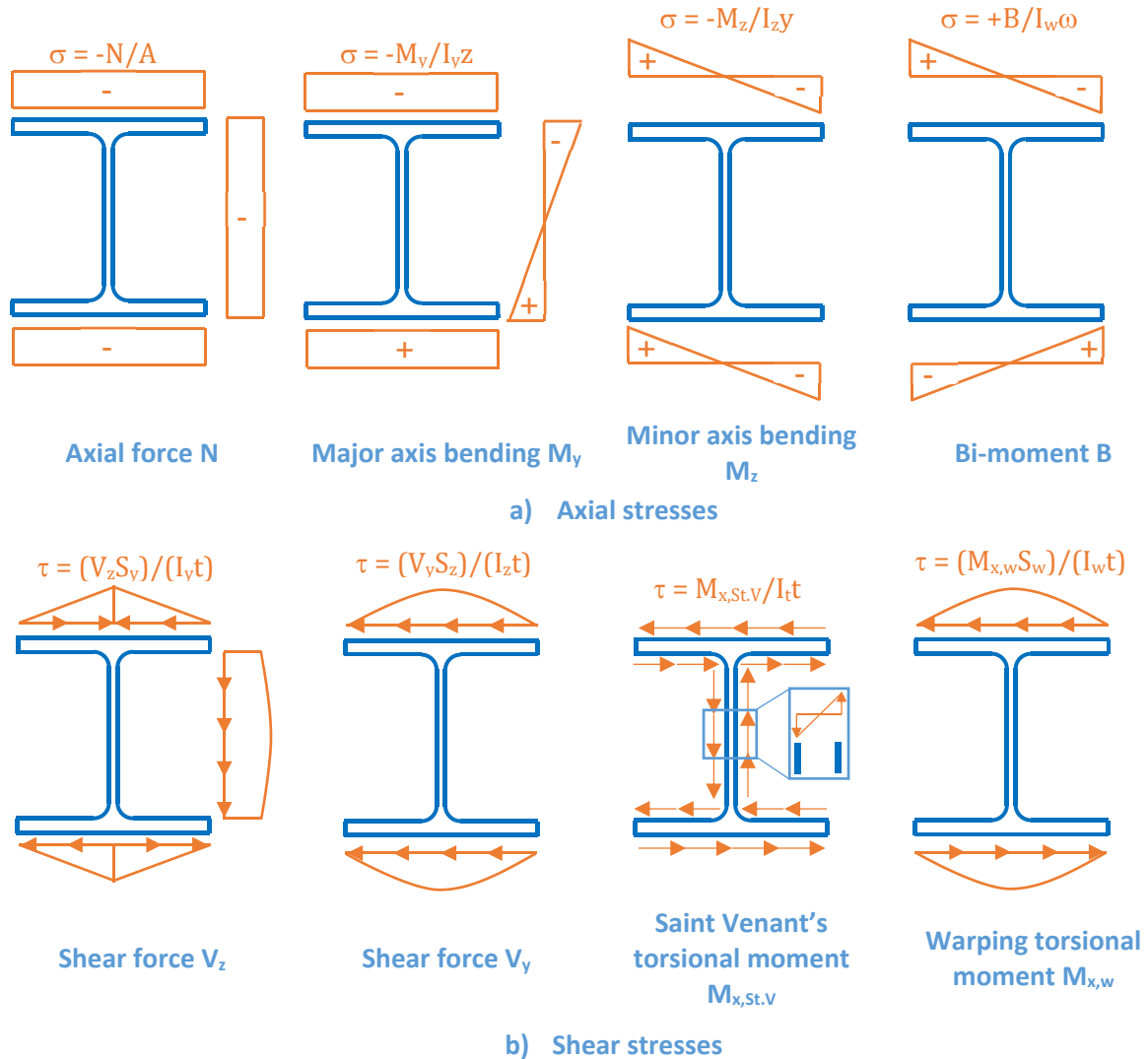


Figure 4-12: Elastic stress distribution for a double symmetric I section

Starting from the point of first yield the load factor is increased stepwise. At each step the load increment, which leads to yielding (based on the von Mises yield criterion) of the next cell of the cross-section, is estimated. Then, the yielded cells are deactivated and the cross-section characteristics are recalculated for the section composed of non-yielded cells. Again, the stresses are distributed elastically over the non-yielded section. The procedure is illustrated in Figure 4-13 and Figure 4-14 for the example of a HEB 200 section without fillets subject to an axial force of 600 kN, a major-axis bending moment of 20 kNm and a minor-axis bending moment of 40 kNm. The section is supposed to be fabricated from steel S235. Green zones indicate that the cells do not have reached the yield stress, blue zones indicate yielding in compression and red zones indicate yielding in tension. Figure 4-13 also represents the principal system of axis that changes its position and orientation with ongoing yielding.

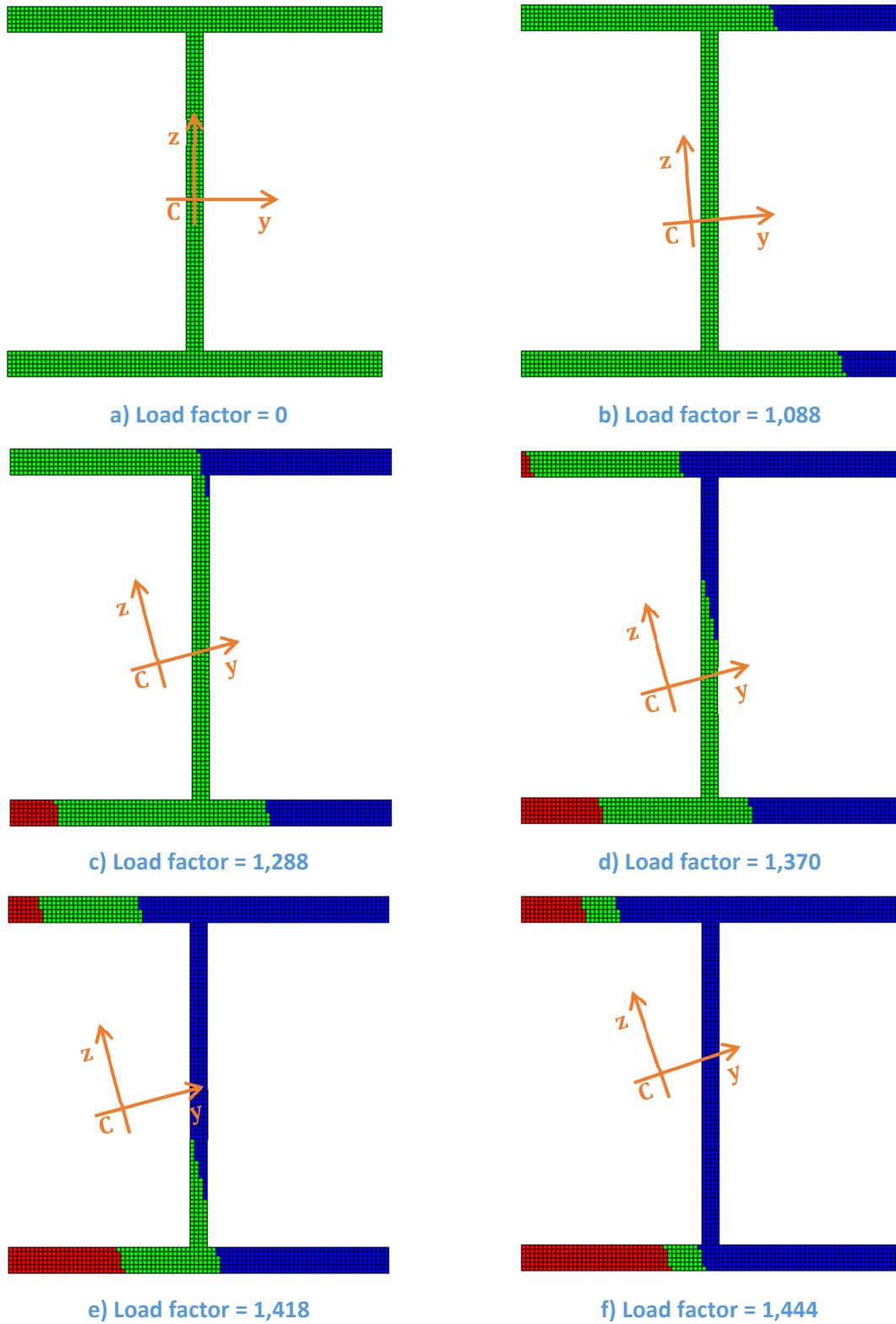


Figure 4-13: Spreading of yielding through the cross-section with increasing load factor

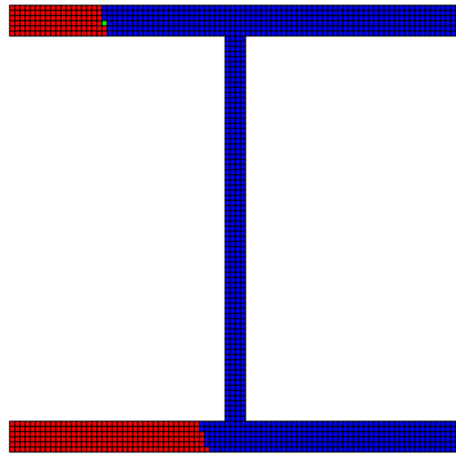


Figure 4-14: Plastic stress distribution the end of the calculation – $R_{pl} = 1,449$

The procedure described above may be applied to an arbitrary combination of internal forces and moments. It should be noted that it is supposed that the distribution of the shear stresses does not depend on the orientation of the principal system of axis, i.e. for example shear stresses due to V_y and due the warping torsional moment $M_{x,w}$ are always supposed to transit through the flanges in case of an I section.

The presented iterative procedure is precise compared to theoretical results. However, it should be noted that it is based on a presumed elastic distribution of stresses that has to be determined previously. Additionally, the plastic shear resistance cannot be determined directly but it has to be based on the assumption of a shear area. Due to the two problems mentioned just before, it is obvious that this approach cannot be applied for arbitrary forms of cross-sections. Yet, for commonly used steel sections, the elastic distribution of the stresses is known and may be included.

The calculation time depends on the number of cells necessary to obtain sufficiently precise results. In particular, in case of complex load combinations, as the one studied here before, and even more in presence of a Saint Venant's torsional moment, an important number of cells may be necessary. As the shear stress varies through the thickness of the plate (web or flange), at least 6 to 8 cells through the thickness are necessary to obtain satisfactory results. Therefore the calculation is slowed down. Nevertheless, it is still faster than a rigorous plastic finite element analysis.

In the next paragraph the method proposed by Kindmann in reference (Kindmann et al. 1999a) is presented.

4.2.2.3 Partial internal force method – PIFM

4.2.2.3.1 Initially proposed version of PIFM

For open cross-sections composed of three plates perpendicular to each other, a quasi-analytical method for the plastic interaction between all eight internal forces and moments has been proposed by Frickel and Kindmann in references (Kindmann et al. 1999a) and (Kindmann et al. 1999b). The so-called “Partial Internal Force Method” is based on the principle that the internal forces may be distributed to the three constituting plates depending on their stiffness and location in the reference system. The reference system is located at the mid-height of the web and oriented as shown in Figure 4-15. It should be noted that the reference system represented in Figure 4-15 is rotated by 180° compared to the system used in the framework of the present thesis.

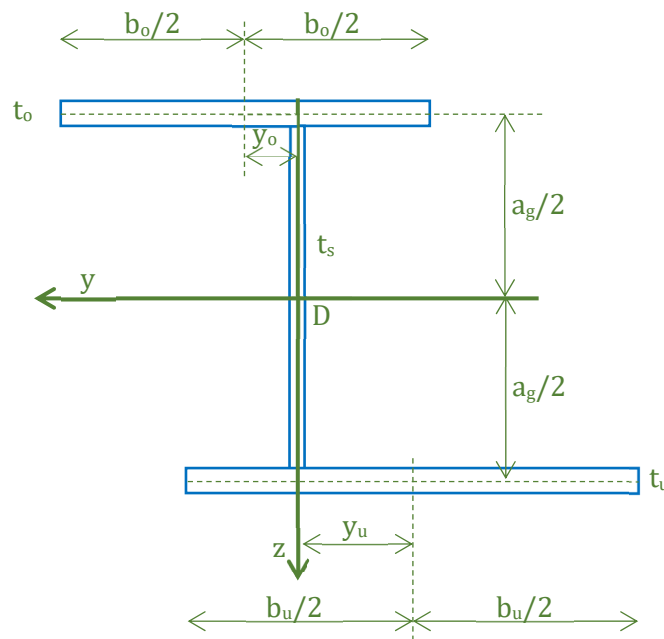


Figure 4-15: Cross-section definition for PIFM

Obviously, the reference system yDz is generally not coincident with the principal axis of the section (this would only be the case for double symmetric I sections). Hence, the internal forces and moments have to be transformed in the reference system first. It yields:

$$N = N \quad (4.17)$$

$$M_y^- = M_y \cos\alpha - M_z \sin\alpha + Nz_G \quad (4.18)$$

$$M_z^- = M_z \cos\alpha + M_y \sin\alpha - Ny_G \quad (4.19)$$

$$B^- = B + M_y(y_S - y_D) + M_z(z_S - z_D) + N\bar{\omega}_k \quad (4.20)$$

$$V_y^- = V_y \cos\alpha - V_z \sin\alpha \quad (4.21)$$

$$V_z^- = V_z \cos\alpha + V_y \sin\alpha \quad (4.22)$$

$$M_{x,w} = M_{x,w} - V_y(z_S - z_D) + V_z(y_S - y_D) \quad (4.23)$$

$$M_{x,St.V} = M_{St.V} \quad (4.24)$$

It should be noted that the Saint Venant’s torsional moment and the axial force are independent from the cross-section system of coordinates.

After the transformation to the reference system, the internal forces and moments creating shear are distributed to the three plates. One obtains:

$$V_{uf} = \frac{V_y}{2} + \frac{M_{x,w}}{a_g} \quad (4.25)$$

$$M_{x,St.V,uf} = M_{x,St.V} \frac{I_{t,uf}}{I_t} \quad (4.26)$$

$$V_{web} = V_z \quad (4.27)$$

$$M_{x,St.V,w} = M_{x,St.V} \frac{I_{t,w}}{I_t} \quad (4.28)$$

$$V_{lf} = \frac{V_y}{2} - \frac{M_{x,w}}{a_g} \quad (4.29)$$

$$M_{x,St.V,lf} = M_{x,St.V} \frac{I_{t,lf}}{I_t} \quad (4.30)$$

It is recalled that the indices “uf” and “lf” refer to the upper flange, the lower flange and the web, respectively.

For each plate, an interaction between the plate’s shear force and the plate’s torsional moment is introduced as given in Eq. (4.31).

$$\frac{1}{2} \frac{M_{x,St.V}}{M_{pl,x,St.V}} + \sqrt{\left(\frac{M_{x,St.V}}{2M_{pl,x,St.V}}\right)^2 + \left(\frac{V}{V_{pl}}\right)^2} = \rho \leq 1 \quad (4.31)$$

This interaction formula assumes a shear stress distribution in the plate as shown in Figure 4-16.

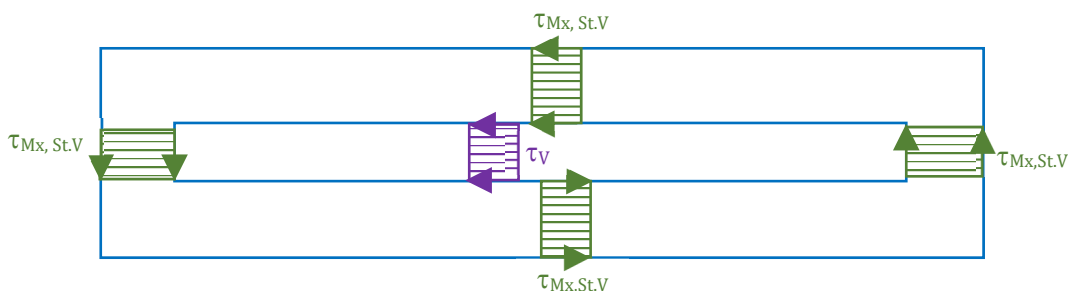


Figure 4-16: Assumptions of the shear stress distribution in a plate (Kindmann et al. 1999a)

If the factor ρ is less than 1,0, the corresponding plate may carry additional axial stresses. In order to account for the interaction between shear and normal stresses, the yield stress of the plate is reduced to:

$$f_{y,red} = f_y \sqrt{1 - \rho^2} \quad (4.32)$$

One may note that Eq. (4.32) is in accordance with the von Mises yield criterion. The reduction can be neglected if the factor ρ is less than 0,25 (Kindmann et al. 1999b). This may however lead to a certain discontinuity for the resistance model. It would be preferable to adopt continuous conditions as for example given in (CEN 2005a) and (Standard Australia 1998).

Based on the reduced yield stress, the plastic resistance of each plate is calculated by:

$$N_{pl,\tau,uf} = b_{uf} t_{uf} f_{y,red} \quad (4.33)$$

$$M_{pl,\tau,uf} = \frac{b_{uf}^2 t_{uf}}{4} f_{y,red} = N_{pl,\tau,uf} \frac{b_{uf}}{4} \quad (4.34)$$

$$N_{pl,\tau,web} = h_w t_w f_{y,red} \quad (4.35)$$

$$M_{pl,\tau,web} = \frac{h_w^2 t_w}{4} f_{y,red} = N_{pl,\tau,web} \frac{h_w}{4} \quad (4.36)$$

$$N_{pl,\tau,lf} = b_{lf} t_{lf} f_{y,red} \quad (4.37)$$

$$M_{pl,\tau,lf} = \frac{b_{lf}^2 t_{lf}}{4} f_{y,red} = N_{pl,\tau,lf} \frac{b_{lf}}{4} \quad (4.38)$$

In a next step, the internal forces and moments creating axial stresses have to be distributed over the three plates. Based on equilibrium considerations, Kindmann obtains the following four equations:

$$N = N_{uf} + N_{web} + N_{lf} \quad (4.39)$$

$$M_y = (N_{lf} - N_{uf}) \frac{a_g}{2} + M_{y,web} \quad (4.40)$$

$$M_z = M_{uf} + M_{lf} - N_{uf} y_{uf} - N_{lf} y_{lf} \quad (4.41)$$

$$B = (M_{lf} - M_{uf}) \frac{a_g}{2} + (N_{uf} y_{uf} - N_{lf} y_{lf}) \frac{a_g}{2} \quad (4.42)$$

It should be noted that the axial forces N_{uf} , N_{lf} and N_{web} as well as the bending moments M_{uf} , M_{lf} and M_{web} refer to the centroid of the corresponding plate. Up to this step they are not known. For the flanges, however, it is possible to write the following condition:

$$M_{uf,wc} = \frac{M_z}{2} - \frac{B}{a_g} = M_{uf} - N_{uf} y_{uf} \quad (4.43)$$

$$M_{lf,wc} = \frac{M_z}{2} + \frac{B}{a_g} = M_{lf} - N_{lf} y_{lf} \quad (4.44)$$

$M_{uf,wc}$ and $M_{lf,wc}$ are the bending moments in the upper and lower flange calculated in the reference system. At the plastic limit state, a quadratic interaction between the moments and the axial force in the flanges can be considered. It yields:

$$\begin{aligned} \frac{M_{uf}}{M_{pl,\tau,uf}} + \left(\frac{N_{uf}}{N_{pl,\tau,uf}} \right)^2 &= \left| \frac{M_{uf,wc} + N_{uf} y_{uf}}{M_{pl,\tau,uf}} \right| + \left(\frac{N_{uf}}{N_{pl,\tau,uf}} \right)^2 \\ &= \left| \frac{M_{uf,wc}}{M_{pl,\tau,uf}} + 2\delta_{uf} \frac{N_{uf}}{N_{pl,\tau,uf}} \right| + \left(\frac{N_{uf}}{N_{pl,\tau,uf}} \right)^2 \leq 1,0 \end{aligned} \quad (4.45)$$

$$\begin{aligned} \frac{M_{lf}}{M_{pl,\tau,lf}} + \left(\frac{N_{lf}}{N_{pl,\tau,lf}} \right)^2 &= \left| \frac{M_{lf,wc} + N_{lf} y_{lf}}{M_{pl,\tau,lf}} \right| + \left(\frac{N_{lf}}{N_{pl,\tau,lf}} \right)^2 \\ &= \left| \frac{M_{lf,wc}}{M_{pl,\tau,lf}} + 2\delta_{lf} \frac{N_{lf}}{N_{pl,\tau,lf}} \right| + \left(\frac{N_{lf}}{N_{pl,\tau,lf}} \right)^2 \leq 1,0 \end{aligned} \quad (4.46)$$

with:

$$\delta_{uf} = \frac{2y_{uf}}{b_{uf}} \quad (4.47)$$

$$\delta_{lf} = \frac{2y_{lf}}{b_{lf}} \quad (4.48)$$

As the moments $M_{uf,wc}$ and $M_{lf,wc}$ are known, Eqs. (4.45) and (4.46) can be solved for the unknown axial forces N_{uf} and N_{lf} . One obtains:

$$N_{uf,\min} = N_{pl,\tau,uf} \left(-\delta_{uf} - \sqrt{\delta_{uf}^2 + 1 - \frac{M_{uf,wc}}{M_{pl,\tau,uf}}} \right) \quad \text{for} \quad \frac{M_{uf,wc}}{M_{pl,\tau,uf}} \geq 2\delta_{uf} \quad (4.49)$$

$$N_{uf,\min} = N_{pl,\tau,uf} \left(-\delta_{uf} - \sqrt{\delta_{uf}^2 + 1 + \frac{M_{uf,wc}}{M_{pl,\tau,uf}}} \right) \quad \text{for} \quad \frac{M_{uf,wc}}{M_{pl,\tau,uf}} < 2\delta_{uf} \quad (4.50)$$

$$N_{uf,\max} = N_{pl,\tau,uf} \left(\delta_{uf} + \sqrt{\delta_{uf}^2 + 1 + \frac{M_{uf,wc}}{M_{pl,\tau,uf}}} \right) \quad \text{for} \quad -\frac{M_{uf,wc}}{M_{pl,\tau,uf}} \geq 2\delta_{uf} \quad (4.51)$$

$$N_{uf,max} = N_{pl,\tau,uf} \left(-\delta_{uf} + \sqrt{\delta_{uf}^2 + 1 - \frac{M_{uf,wc}}{M_{pl,\tau,uf}}} \right) \quad \text{for} \quad -\frac{M_{uf,wc}}{M_{pl,\tau,uf}} < 2\delta_{uf} \quad (4.52)$$

The solution for the axial force in the lower flange may be obtained by simply changing the indices “uf” to “lf” in Eqs. (4.49) to (4.52). Obviously, Eqs. (4.49) to (4.52) can only be solved numerically if the radicand is positive. Therefore, it is possible to determine a condition for the bending moment in the flanges:

$$\left| \frac{M_{uf,wc}}{M_{pl,\tau,uf}} \right| = \left| \frac{M_z^-}{2M_{pl,\tau,uf}} - \frac{B^-}{a_g M_{pl,\tau,uf}} \right| \leq \delta_{uf}^2 + 1 \quad (4.53)$$

$$\left| \frac{M_{lf,wc}}{M_{pl,\tau,lf}} \right| = \left| \frac{M_z^-}{2M_{pl,\tau,lf}} + \frac{B^-}{a_g M_{pl,\tau,lf}} \right| \leq \delta_{lf}^2 + 1 \quad (4.54)$$

As can be seen, Eqs. (4.53) and (4.54) allow checking whether the cross-section is able to resist the applied minor-axis bending moment and bi-moment (transformed to the reference system). At this point, it is still necessary to check the resistance to the applied axial force and major-axis bending moment. Both can be resisted by the full web of the cross-section and the part of the flanges not fully utilized by the minor-axis bending and the bi-moment.

It is shown in Eqs. (4.55) to (4.56), that the axial force in the flanges has to be included in the interval:

$$N_{uf,min} \leq N_{uf} \leq N_{uf,max} \quad (4.55)$$

$$N_{lf,min} \leq N_{lf} \leq N_{lf,max} \quad (4.56)$$

As the web is not utilized yet, the web’s axial force has to be included in the interval:

$$-N_{pl,\tau,w} \leq N_{web} \leq N_{pl,\tau,w} \quad (4.57)$$

Consequently, the total axial force has to respect the conditions expressed by Eq. (4.58).

$$N_{min} \leq N \leq N_{max} \quad (4.58)$$

and:

$$N = N_{web} + N_{lf} + N_{uf} \quad (4.59)$$

$$N_{\min} = N_{lf,\min} + N_{uf,\min} - N_{pl,\tau,web} \quad (4.60)$$

$$N_{\max} = N_{lf,\max} + N_{uf,\max} + N_{pl,\tau,web} \quad (4.61)$$

Similarly, the major-axis bending moment should respect the following condition:

$$M_{y,\min}^- \leq M_y^- \leq M_{y,\max}^- \quad (4.62)$$

Finally, depending on the value of the axial force, the minimum and maximum values of the bending moment are given in Table 4-5.

Table 4-5: Expressions for $M_{y,\min}$ and $M_{y,\max}$

$M_{y,\min}^- =$	$-(N + N_{pl,\tau,w} - 2N_{lf,\min}) \frac{a_g}{2}$	for	$N_{\min} \leq N$ and $N < N_{uf,\max} + N_{lf,\min} - N_{pl,\tau,w}$
	$-(N_{uf,\max} - N_{lf,\min}) \frac{a_g}{2}$ $-\frac{h_w}{4N_{pl,\tau,w}} [N_{pl,\tau,w}^2 - (N_{uf,\max} + N_{lf,\min} - N)^2]$	for	$N_{uf,\max} + N_{lf,\min} - N_{pl,\tau,w} \leq N$ and $N < N_{uf,\max} + N_{lf,\min} + N_{pl,\tau,w}$
	$-(2N_{uf,\max} + N_{pl,\tau,w} - N) \frac{a_g}{2}$	for	$N_{uf,\max} + N_{lf,\min} + N_{pl,\tau,w} \leq N$ and $N < N_{\max}$
$M_{y,\max}^- =$	$(N + N_{pl,\tau,w} - 2N_{uf,\min}) \frac{a_g}{2}$	for	$N_{\min} \leq N$ and $N < N_{uf,\min} + N_{lf,\max} - N_{pl,\tau,w}$
	$(N_{lf,\max} - N_{uf,\min}) \frac{a_g}{2}$ $+\frac{h_w}{4N_{pl,\tau,w}} [N_{pl,\tau,w}^2 - (N_{uf,\min} + N_{lf,\max} - N)^2]$	for	$N_{uf,\min} + N_{lf,\max} - N_{pl,\tau,w} \leq N$ and $N < N_{uf,\min} + N_{lf,\max} + N_{pl,\tau,w}$
	$(2N_{lf,\max} + N_{pl,\tau,w} - N) \frac{a_g}{2}$	for	$N_{uf,\min} + N_{lf,\max} + N_{pl,\tau,w} \leq N$ and $N < N_{\max}$

The plastic resistance conditions redeveloped here before have been derived in reference (Kindmann et al. 1999b). They are summarized hereafter:

$$\frac{1}{2} \frac{M_{x,St.V,uf}}{M_{pl,x,St.V,uf}} + \sqrt{\left(\frac{M_{x,St.V,uf}}{2M_{pl,x,St.V,uf}}\right)^2 + \left(\frac{V_{uf}}{V_{pl,uf}}\right)^2} = \rho \leq 1 \quad (4.63)$$

$$\frac{1}{2} \frac{M_{x,St.V,w}}{M_{pl,x,St.V,w}} + \sqrt{\left(\frac{M_{x,St.V,w}}{2M_{pl,x,St.V,w}}\right)^2 + \left(\frac{V_w}{V_{pl,w}}\right)^2} = \rho \leq 1 \quad (4.64)$$

$$\frac{1}{2} \frac{M_{x,St.V,lf}}{M_{pl,x,St.V,lf}} + \sqrt{\left(\frac{M_{x,St.V,lf}}{2M_{pl,x,St.V,lf}}\right)^2 + \left(\frac{V_{lf}}{V_{pl,lf}}\right)^2} = \rho \leq 1 \quad (4.65)$$

$$\left| \frac{M_{uf,wc}}{M_{pl,\tau,uf}} \right| = \left| \frac{M_z^-}{2M_{pl,\tau,uf}} - \frac{B^-}{a_g M_{pl,\tau,uf}} \right| \leq \delta_{uf}^2 + 1 \quad (4.66)$$

$$\left| \frac{M_{lf,wc}}{M_{pl,\tau,lf}} \right| = \left| \frac{M_z^-}{2M_{pl,\tau,lf}} + \frac{B^-}{a_g M_{pl,\tau,lf}} \right| \leq \delta_{lf}^2 + 1 \quad (4.67)$$

$$N_{\min} \leq N \leq N_{\max} \quad (4.68)$$

$$M_{y,\min}^- \leq M_y^- \leq M_{y,\max}^- \quad (4.69)$$

It should be recalled that the internal forces and moments used in Eqs. (4.63) to (4.69) are not the ones calculated in the principal axes system of the section. This may be confusing for the use in practice as the interaction formulae given in most current standards refer to internal forces and moments in the principal system of the cross-section. However, it seems very interesting to verify the resistance of a great number of practically used sections by only seven interaction criteria. Obviously, the number of interaction criteria to be used decreases if the section is not subject to all eight internal forces and moments. Nevertheless, the described procedure seems somewhat too complicated for practical use by hand-calculation. An implementation in a numerical tool seems necessary as has been done by Kindmann and Wolf (see reference (Wolf et al. 2014)).

Even if the PIFM is of quasi-analytical nature, it has been highly criticised several times for example in (Krüger 1999), (Werner 1999), (Rubin 1999), (Rubin 2000), (Rubin 2005). The reasons for the different critical remarks are presented hereafter based on two examples.

It is proposed to compare the plastic major-axis bending moments obtained with PIFM for the two sections of Figure 4-17 with analytical results based on the plastic stress distribution also given in Figure 4-17. It is supposed that the section is made of steel S235. The analytical results and the PIFM plastic moments are compared in Table 4-6. Based on the supposed axial stress distribution, the analytical major-axis plastic moments are identical. Conversely, the PIFM method predicts a plastic moment of about 5% less for the U section. At a first look, this result seems astonishing.

Before this result is explained, it is proposed to compare the results for a second example.

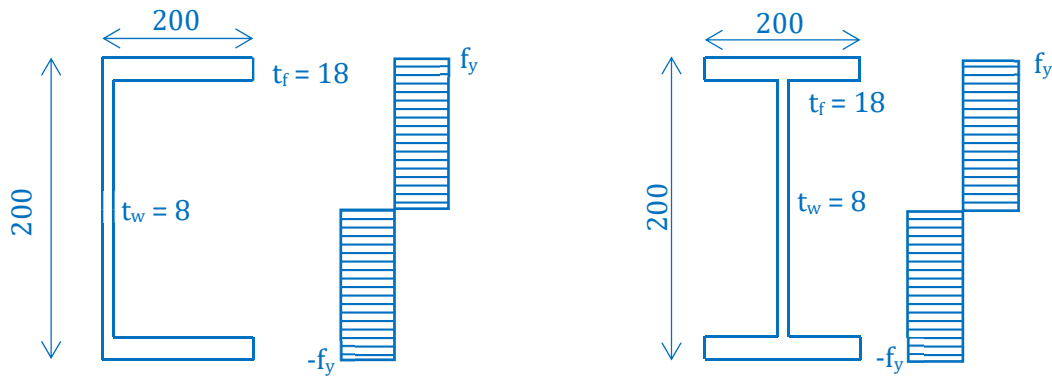


Figure 4-17: U and I cross-section and supposed plastic stress distribution under major axis bending only

Table 4-6: Comparison of plastic major axis bending moment for an I and U section

	Analytic $M_{y,pl}$ [kNm]	PIFM $M_{y,pl}$ [kNm]	$M_{y,pl,PIFM}/M_{y,pl,analytic}$
I section	89,63	89,63	1,000
U section	89,63	84,86	0,947

The section represented in Figure 4-18 is considered and studied under combined bi-axial bending and axial compression.

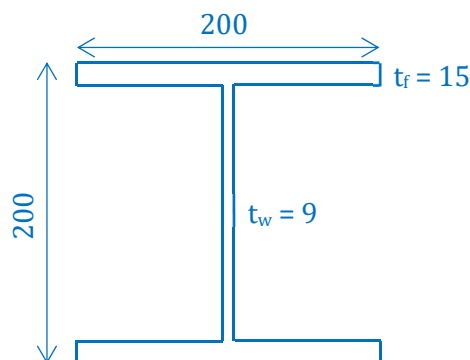


Figure 4-18: HEB 200 cross-section without fillets

It is again supposed that the section is made of steel S235. It is subject to an axial force of 1125 kN, a major-axis bending moment of 60,84 kNm and a minor-axis bending moment of 29,77 kNm. This combination of internal forces and moments leads to full yielding of the cross-section, as shown in Figure 4-19. The stress distribution is obtained by a numerical calculation of the cross-section discretised into cells with the method presented in paragraph 4.2.2.2.

In Figure 4-19 the blue zones correspond to compression axial stresses and the red zone corresponds to tension axial stresses. The neutral axis is represented in green. As the section has (nearly) entirely yielded under the applied loads, the plastic load amplification factor for the given loading is equal to 1,0. If, however, the PIFM method is applied iteratively, the obtained plastic load amplification factor is equal to 0,838. Consequently, PIFM is nearly 20% safe-sided.

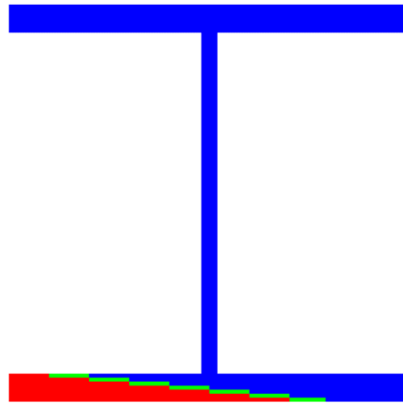


Figure 4-19: Plastic stress distribution for the section of Figure 4-18 under the applied internal forces and moments

In order to understand this difference, it is interesting to determine the internal forces and moments associated with the stress distribution shown in Figure 4-19. Obviously, one obtains an axial force of 1125 kN, a major-axis bending moment of 60,48 kNm and a minor-axis bending moment of 29,77 kNm. **However, one also obtains a bi-moment of 2,74 kNm².** Hereafter this bi-moment is referred to as “stress induced bi-moment” B_{SI} as it directly results from the axial stress distribution and not from an externally applied load.

The stress induced bi-moment also explains the differences noted for the example of the U section. In fact, in order to obtain a full plastic stress distribution, a bi-moment is necessary. As the stress induced bi-moment is not considered in the derivation of PIFM, as already highlighted in (Kindmann 1999b), (Rubin 2000), (Rubin 2005) and (Kettler 2008), the PIFM may be very safe-sided, especially for U-shaped sections and I sections under combined bi-axial bending and compression.

However, despite the safe-sided nature of the proposed method, it may be concluded that the PIFM presents several advantages:

- It gives a small number of interaction formulae treating a great variety of cross-section shapes and combination of internal forces and moments;
- The treatment of the interaction between shear and axial stresses is of special interest as it is not treated satisfactorily in Eurocode 3 and other standards, especially for torsion;
- If PIFM is implemented numerically, its application is easy and yields rapidly results.

Nevertheless, it has also been shown that PIFM presents some disadvantages. In particular, it should be noted that:

- The complexity of PIFM disables it from being used manually,

- For certain load cases, the initially proposed PIFM may be highly conservative compared to results obtained based on a generally accepted presumed plastic stress distribution,
- For compact hot-rolled sections, the fillets may have a non-negligible influence on the plastic resistance but they are not included in PIFM that, consequently, yield conservative results.

The present paragraph has shown that it is possible to derive a design model that, based on theoretical developments, is able to predict the resistance of open cross-sections subject to an arbitrary combination of internal forces and moments. Also, the design expressions ensure a complete continuity in the interaction space between all eight internal forces and moments. However, the resulting design expressions are complex and cannot be applied by “hand” in practice. Therefore, a numerical implementation is necessary. Additionally, PIFM cannot take into account all phenomena necessary to predict the “real” cross-section resistance (in particular the stress induced bi-moment). Consequently, it seems that PIFM is promising; however it needs some adaptations in order to predict economically the plastic cross-section resistance.

4.2.2.3.2 Adaptation of PIFM

In paragraph 4.2.2.3.1, it has been shown that the PIFM is a very promising method to assess the plastic cross-section resistance of complex sections. Nevertheless, it has also been shown, that due to the hypothesis concerning zero stress induced bi-moments, PIFM may lead to very conservative results. It has to be noted, that for an arbitrary combination of loads and an arbitrary cross-section, the stress induced bi-moment necessary for full yielding cannot be determined analytically. In order to allow a more economic design, it seems interesting to adapt PIFM in the following way:

- Introduction of the stress induced bi-moments: First, an initial load amplification factor $\alpha_{pl,0}$ is determined not considering the bi-moment necessary for full yielding. In a second step, the stress induced bi-moment leading to the maximum load amplification factor α_{pl} is calculated iteratively.
- Introduction of the fillets for hot-rolled sections: Due to the position of the fillets, it is considered that they yield in priority under major-axis bending. If the major-axis bending moment carried by the fillets is less than the resistance of the fillets they may be utilized by the minor-axis bending moment (if present). If the fillets may carry additional loads, it is used to resist the axial force (if present).

Obviously, the proposed adaptations absolutely need a numerical implementation. However, this seems not to be disadvantageous, as already the initially proposed PIFM has to be implemented numerically.

The proposed procedure is applied hereafter. First, the example of the previous paragraph is considered again (HEB 200 without fillets, $N = 1125$ kN, $M_y = 60,84$ kNm, $M_z = 29,77$ kNm, S235).

The plastic load factor obtained by the modified PIFM is equal to 0,992. Hence, the difference to the iterative procedure given in paragraph 4.2.2.2 is negligible. Finally, the iteratively determined stress induced bi-moment necessary for full yielding of the cross-section is equal to 2,736 kNm² and consequently, it is equal to the one determined based on the Step-by-Step procedure presented in the previous paragraph.

In order to validate the adaptations further on, the M_y - M_z interaction curves for a HEB 180 (including the fillets) section are determined for three values of the axial force. The reference results are obtained with the Step-by-Step procedure presented in the previous paragraph. Figure 4-20 shows that both methods yield very close results.

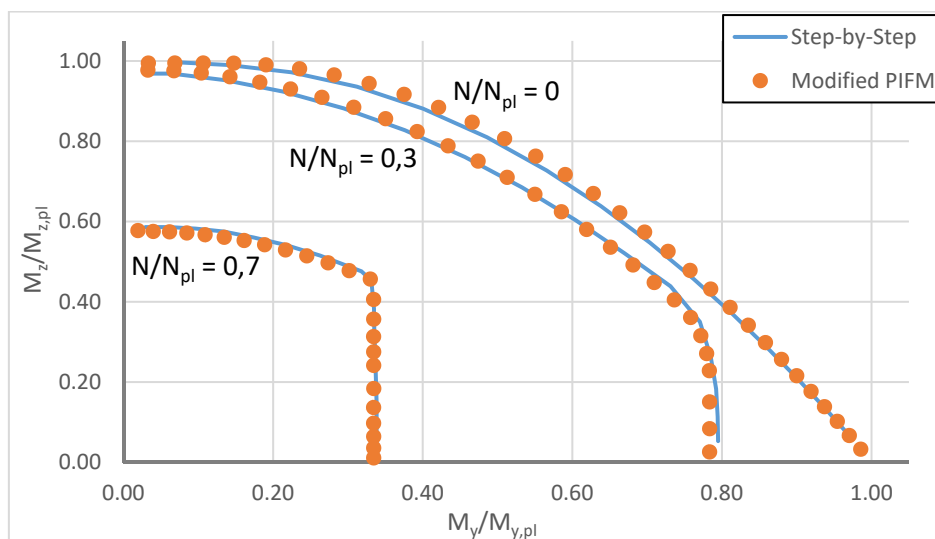


Figure 4-20: Interaction curve M_y - M_z for HEB 180

In order to quantify the influence of the proposed adaptations of PIFM, Figure 4-21 shows interaction curves for the previous example again. Obviously, if no axial force is applied, the results are rather close. Yet, the initially proposed PIFM is slightly safe-sided for high major-axis bending moments as the influence of the fillets is neglected. The difference is of about 3%. It should be noted that for combined major- and minor-axis bending without axial force the stress induced bi-moment is not necessary to yield the section entirely. Conversely, if an axial force is applied to the section in addition to bi-axial bending, yielding of the section is accompanied by a stress induced bi-moment that is not considered in the initially proposed PIFM. In Figure 4-21 the influence of this bi-moment may be clearly identified and it is confirmed that the results may be very conservative and non-economic if the PIFM is applied as proposed by Kindmann (not considering stress induced bi-moments).

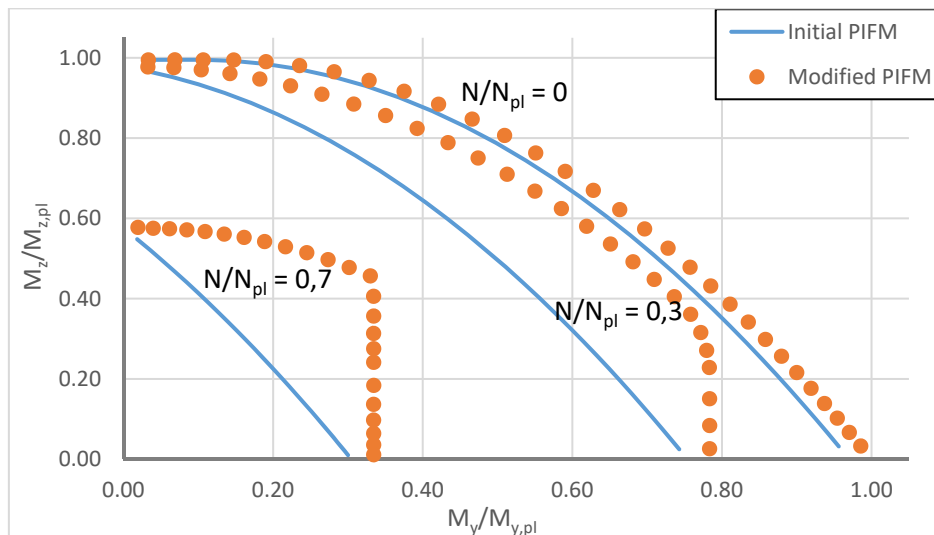


Figure 4-21: Interaction curve M_y - M_z for HEB 180 - Comparison between initially proposed and modified PIFM

The present paragraph presented and validated several adaptations of the Partial Internal Force method proposed by Kindmann in references (Kindmann et al. 1999a) and (Kindmann et al. 1999b). The introduction of the influence of the fillets and, especially, the introduction of stress induced bi-moments lead to precise and more economic results. Nevertheless, further investigations are still necessary, especially for the interaction between internal forces and moment creating axial stresses and internal forces and moments creating shear stresses. Indeed, in this case the interaction behaviour is based on several key assumptions as the shear area. These key assumptions absolutely need validation. Consequently, a specific experimental and a numerical study are presented in paragraph 4.3 with the objective to characterize the bending shear interaction.

4.2.3 Conclusions

Paragraph 4.2 has presented several approaches to assess the plastic cross-section resistance. First, approaches proposed in current design standards have been compared. It has been shown that:

- Eurocode 3 Part 1-1 yields satisfactory results for the cases of combined bi-axial bending and axial force (including the extreme cases if one of the internal forces and moments is zero). Nevertheless, the current provisions may be too optimistic for low axial force and applied major-axis bending (especially for sections with high ratio h/b). It seems that Eurocode 3 provisions may be unsafe for the major-axis bending-shear force interaction (compared to elastic-perfectly plastic analysis), as the shear area for V_z seems to be overestimated;
- The interaction formulae provided in the Australian standard AS 4100:1998 also yield satisfactory results. However, it seems that they have been calibrated for rather compact sections (ratio h/b is small). In case of interaction between major-axis bending and transversal shear force, AS 4100 also seems to yield unsafe

results due to a too optimistic definition of the shear area; however, AS 4100 is less unsafe than Eurocode 3;

- The North American standard AISC 360-10, yields safe-sided results for the interaction between axial force and mono-axial bending. In case of bi-axial bending the results may be even considered as too safe-sided. AISC 360-10 considers that interaction between shear and axial stresses may be neglected for open sections. However, for the individual internal force or moment only the elastic resistance may be exploited;
- None of the cited standards introduces a specific plastic interaction between torsion and other internal forces. Only Eurocode 3 roughly addresses this interaction problem, however the sole influence of shear stresses due to the Saint Venant's torsional moment and the warping torsional moment (for U sections) is introduced. Neither the axial stress due to the bi-moment nor the interaction between shear stresses due to the warping torsional moment and the shear force V_y are accounted for;
- An amendment to Eurocode 3 Part 1-1 has been proposed recently in order to (partially) close the lack observed concerning plastic interaction including torsion. Yet, the proposal seems to be inconsistent in certain points.

Based on the previous remarks, one may summarize that empirical formulations, even rather complex as in case of a combination between bi-axial bending and shear, always possess certain limitations. Therefore, analytical and numerical methods describing the plastic interaction have been studied in the second part of paragraph 4.2. The Partial Internal Force method has been presented and an adaptation has been proposed in order to account for the influence of the fillets and of the stress induced bi-moments, necessary for the full yielding of the cross-section in case of combined bi-axial bending and compression. Also, a Step-by-Step procedure based on a presumed elastic stress distribution has been presented. Both methods yield practically identical results. However, the modified Partial Interaction Method possesses the advantage to be very time efficient. Even if both methods are very precise, they are based on key assumptions especially for the shear resistance. Consequently, the following points of interrogation remain:

- Which definition of the shear area yields safe-sided but economic results?
- What cut-off value of the shear force should be used in combination with major-axis bending?
- Is it safe-sided to neglect the interaction between shear stresses resulting from warping torsion and from the horizontal shear force?
- Is it safe-sided to neglect the interaction between axial stresses resulting from the bi-moment and from other internal forces and moments or should an interaction be included as proposed in reference (Mirambel et al. 2016)?
- Is it possible to develop a safe-sided, economic and simple design method that continuously predicts the plastic cross-section resistance of open section (in particular I and U sections)?

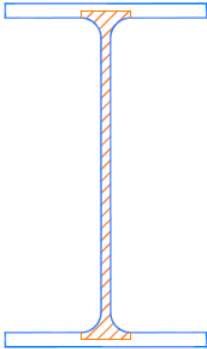
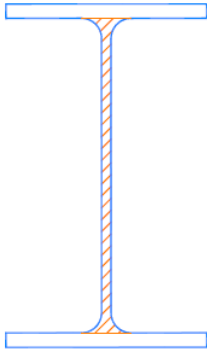
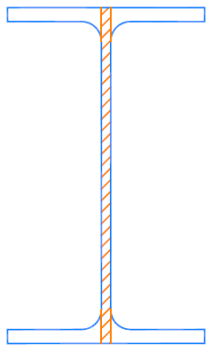
In order to find appropriate solutions to these questions, the following two paragraphs present the results of a series of laboratory tests (paragraph 4.3) and of an extensive numerical study (paragraph 4.4).

4.3 Laboratory tests performed at University of Applied Sciences of Western Switzerland

4.3.1 Motivation

Paragraph 4.2 has shown that the definition of the shear area and consequently the shear resistance for hot-rolled I sections may be very different in the major international design codes as recalled in Table 4-7. Also, the interaction between bending and shear forces is treated differently. This may lead to rather important discrepancies between the code predicted resistances. Therefore, it seems interesting to evaluate the resistance models proposed in the studied standards. Hereafter, the cross-section resistance is studied based on laboratory tests. Furthermore, the laboratory tests serve to validate the numerical model used in the extensive numerical study presented in paragraph 4.4.

Table 4-7: Definition of shear area in different standards

EN 1993-1-1	AS 4100	AISC 360-10
		

4.3.2 Choice of the test specimen and test program

In order to explain the choice of the specimen tested in the laboratory, it seems interesting to recall the general form of the major-axis bending shear force interaction curve proposed in EN 1993-1-1. Figure 4-22 shows that the Eurocode 3 interaction curve is characterized by 4 special features:

- Cut-off limit linked to $0,5V_{pl}$: If the shear force does not exceed 50% of the plastic shear resistance of the cross-section, the major-axis bending moment resistance is not reduced;
- Cut-off limit linked to $M_{y,pl,F}$: If the major-axis bending moment does not exceed the bending moment resistance associated with the flanges only, the shear resistance of the cross-section is not reduced;

- A quadratic interaction is proposed between the two cut-off limits;
- The plastic shear resistance proposed by Eurocode 3 exceeds the plastic shear resistance of the web by approximately 15% to 30% depending on the dimensions of the fillets and the thickness of the flanges.

The supplementary shear resistance mentioned in point 4 is sometimes attributed to the influence of strain hardening. However, it seems that there is no comprehensive numerical, theoretical or experimental study that justifies the shear area defined in Eurocode 3. Therefore, the laboratory tests are designed in particular to investigate the validity of the Eurocode 3 shear resistance reserve.

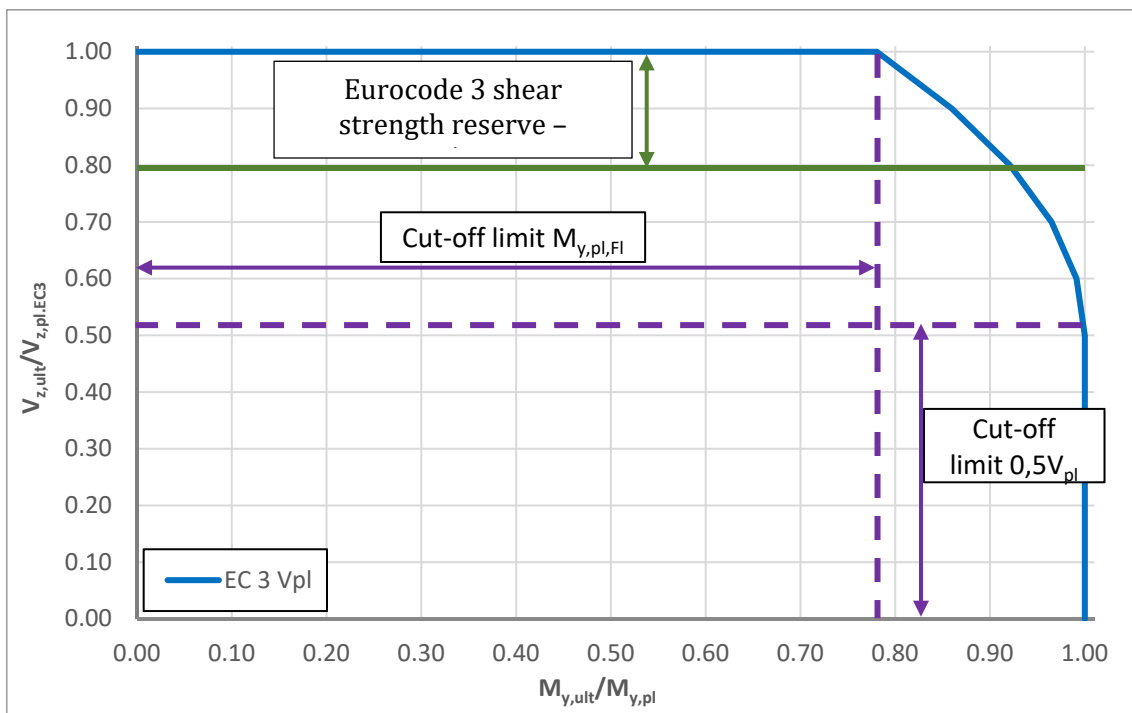


Figure 4-22: M_y - V_z interaction curve proposed in EN 1993-1-1

In order to study members subject to high shear forces, three point bending tests are performed. The cross-sections are chosen so as to maximize the Eurocode 3 shear strength reserve as shown in Table 4-8.

Table 4-8: Studied cross-sections

Cross-section	Shear strength reserve
HEA 220	36%
HEB 180	36%
IPE 270	25%

The three studied cross-sections are tested with two member lengths in order to vary the ratio between the shear force and the bending moment. The following figures represent the tests in the corresponding interaction diagrams. As can be seen in Figure 4-23 the shortest length for each

member is chosen so as to attain the plastic shear resistance of the member without interaction with the bending moment. The resistances of the longer specimen are situated in the interaction zone of the diagrams. It should be noted that for the IPE 270 cross-section, the shortest member is also situated in the interaction zone of the diagram in order to avoid excessively short members.

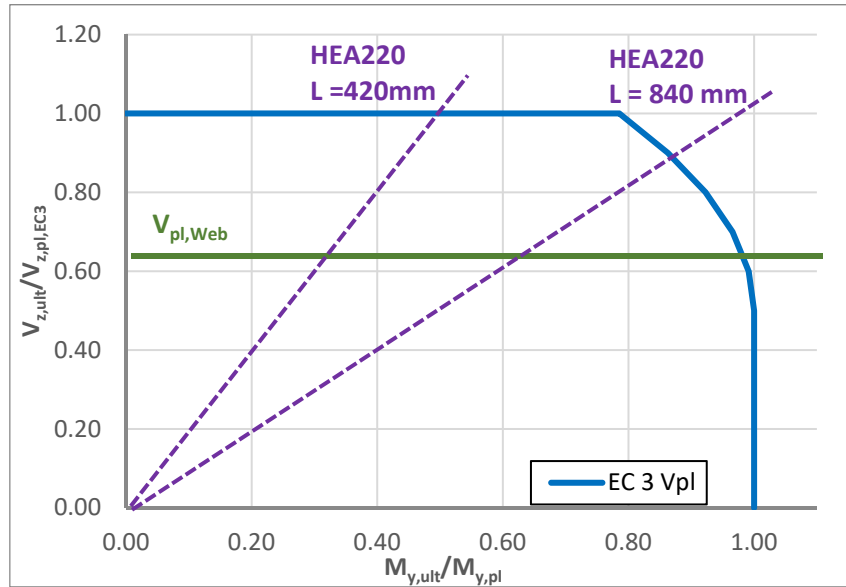


Figure 4-23: Laboratory tests for HEA 220 in the interaction diagram

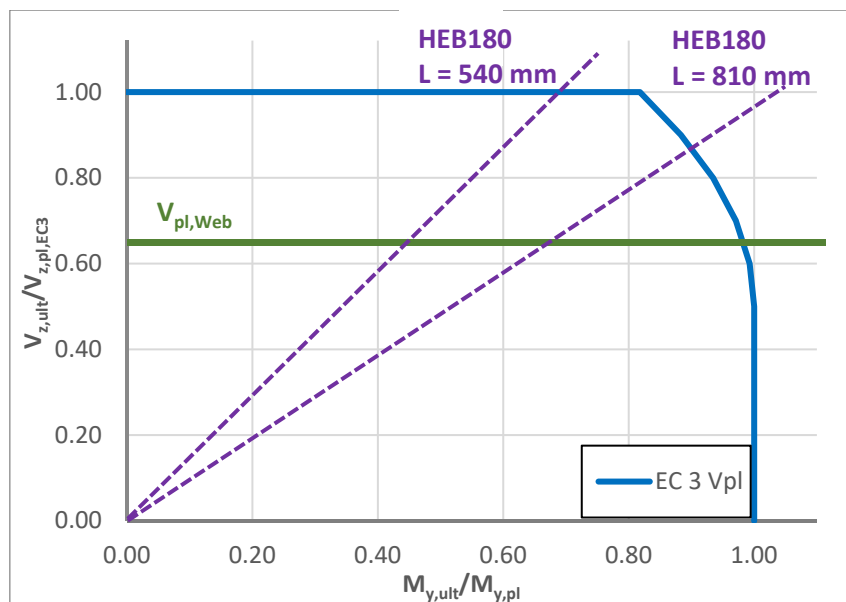


Figure 4-24: Laboratory tests for HEB 180 in the interaction diagram

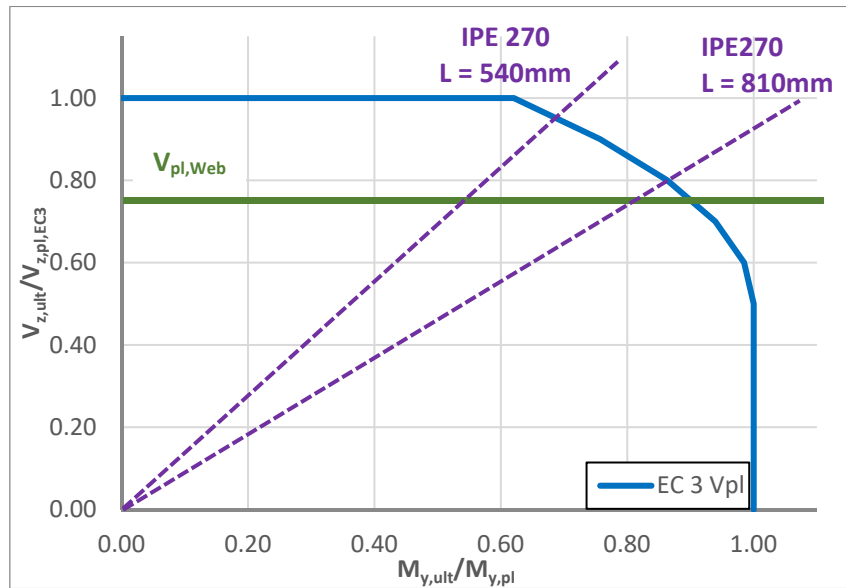


Figure 4-25: Laboratory tests for IPE 270 in the interaction diagram

As the shear strength reserve is sometimes attributed to strain hardening, it is also interesting to study its influence by testing the two steel grades S235 and S355 possessing a ratio between the ultimate strength f_u and the yield strength f_y of f_u/f_y of 1,53 and 1,44 respectively. Consequently, strain hardening is less pronounced in case of S355.

Table 4-9 summarizes the specimen tested in the laboratory of University of Applied Sciences of Western Switzerland in Fribourg.

Table 4-9: Summary of test specimen

Designation	Cross-section	Nominal yield stress [MPa]	Member length [mm]	Web height h_w [mm]	Web thickness t_w [mm]	$h_w/t_w \epsilon$
HEA220_S235_L420	HEA 220	235	420	188,0	7,0	26,9
HEA220_S235_L840			840			
HEA220_S355_L420		355	420			33,0
HEA220_S355_L840			840			
HEB180_S235_L540	HEB 180	235	540	152,0	8,5	17,9
HEB180_S235_L810			810			
HEB180_S355_L540		355	540			22,0
HEB180_S355_L810			810			
IPE270_S355_L540	IPE 270	355	540	257,8	6,6	48,0
IPE270_S355_L810			810			

4.3.3 Test set-up

As mentioned before, three point bending tests are performed in order to characterize the interaction behaviour and shear resistance of the studied specimen. The tested members are placed on a trolley in a reaction frame (see Figure 4-26). The trolley is used to simplify the exchange of the specimen at the end of each test.

The theoretical simple support conditions are realized in the laboratory tests by three elements (see Figure 4-27):

- U composed of three steel plates used to adjust the position of the steel plate in contact with the specimen before the start of the test;
- Steel cylinder free to move;
- Steel plate in contact with the test specimen uniformly introducing the load.

At mid-span the test specimen is in contact with the reaction frame via a semi-cylindrical steel element. The tests are performed under displacement control and the load is introduced by a hydraulic jack situated beneath the trolley. The test layout is represented in Figure 4-26 and Figure 4-27 showing an ongoing laboratory test.

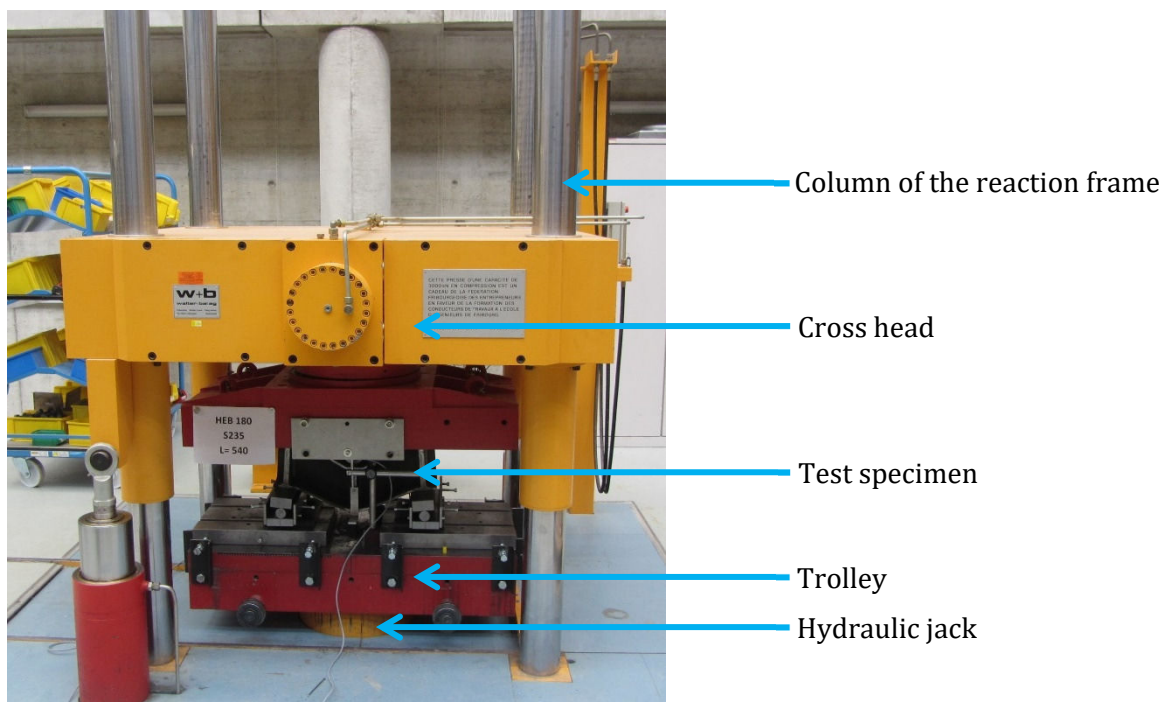


Figure 4-26: Test set up - General view

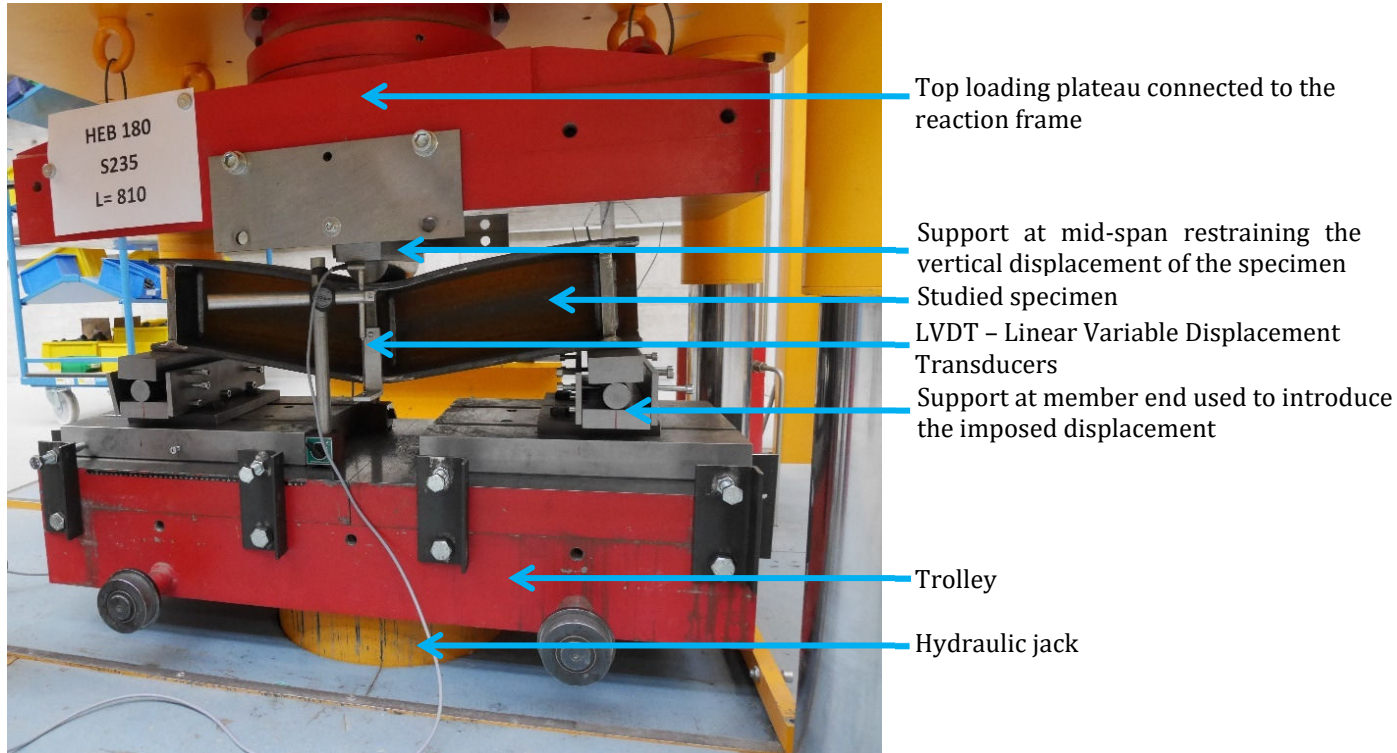


Figure 4-27: Test set up - Detailed view

Figure 4-26 and Figure 4-27 also show that stiffeners are applied at the member ends (at the theoretical support) and at mid-span in order to avoid local buckling at the supports. During the test the displacement of the hydraulic jack as well as the displacements of two LVDTs are measured. The LVDTs are applied at mid-span on both sides of the member. Figure 4-28 shows a front view of an ongoing test with the LVDT.

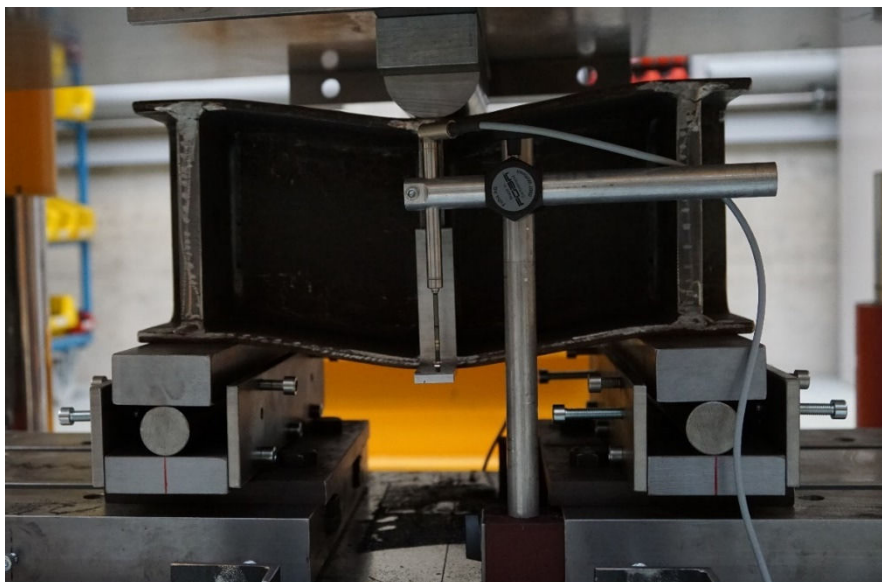


Figure 4-28: Test set up - Detailed view of supports and LVDT

4.3.4 Preparatory measurements

4.3.4.1 General

So as to interpret the results of the laboratory tests correctly, it is necessary to possess knowledge of the parameters influencing these results. In case of the tests presented next, the resistance is in particular influenced by the real yield strength and the material behaviour as well as the real geometry of the cross-section. In order to determine these parameters, preparatory measurements of the cross-section geometry and the material behaviour have been performed.

4.3.4.2 Dimensions of the cross-sections

The geometric dimensions of the cross-sections have been measured with an electronic slide gauge. The position of the measurements along the cross-section and the member are represented in Figure 4-29. As can be seen the dimensions have been determined for three intermediate sections along the member. For each intermediate section, the thickness has been measured twice for the upper flange, the lower flange and the web, respectively. In addition to the thicknesses, the height of the cross-section and the width of the flanges have been measured for each intermediate section.

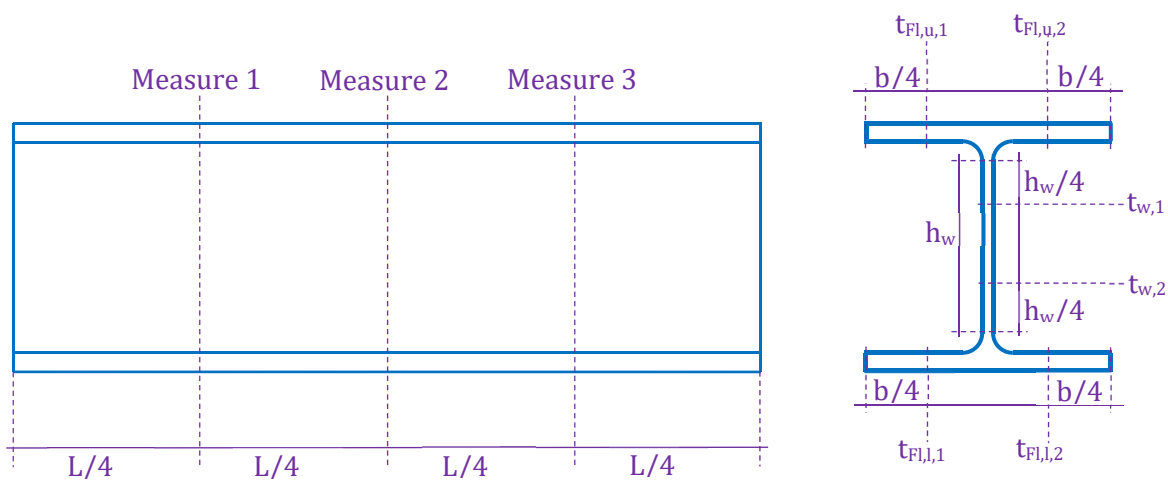


Figure 4-29: Measurements of cross-section dimensions

The following tables show examples for the obtained dimensions. The other measurements are summarized in Annex C. Table 4-10, Table 4-11 and Table 4-12 show that the fabrication tolerances defined in EN 10034 (CEN 2011) are respected. Additionally, it can be seen that the dimensions exceed in general the nominal values except for the thickness of the flanges that is lower than its nominal value for the studied sections.

Table 4-10: Measured dimensions for test HEA220_S235_L420

	Measure 1	Measure 2	Measure 3	Mean value	Nominal value (Tolerance)
$b_{F1,u}$ [mm]	221,20	220,29	220,54	220,67	220,00 (+4;-2)
$t_{f1,u1}$ [mm]	10,68	10,80	10,43	10,62	11,00 (+2.5;-1.5)
$t_{f1,u2}$ [mm]	10,77	10,47	10,56		
$b_{F1,l}$ [mm]	220,60	220,25	220,73	220,53	220,00 (+4;-2)
$t_{f1,l1}$ [mm]	10,73	10,88	10,80	10,82	11,00 (+2.5;-1.5)
$t_{f1,l2}$ [mm]	11,00	10,93	10,82		
h [mm]	210,26	211,47	210,8	210,84	210,00 (+3;-2)
$t_{w,1}$ [mm]	7,17	7,17	7,35	7,24	7,00 (+0.7;-0.7)
$t_{w,2}$ [mm]	7,22	7,20	7,31		

Table 4-11: Measured dimensions for test HEB180_S355_L540

	Measure 1	Measure 2	Measure 3	Mean value	Nominal value (Tolerance)
$b_{F1,u}$ [mm]	180,39	179,91	179,72	180,01	180,00 (+4;-2)
$t_{f1,u1}$ [mm]	13,59	13,70	13,51	13,62	14,00 (+2.5;-1.5)
$t_{f1,u2}$ [mm]	13,72	13,59	13,61		
$b_{F1,l}$ [mm]	180,25	180,10	179,92	180,09	180,00 (+4;-2)
$t_{f1,l1}$ [mm]	13,46	13,59	13,58	13,57	14,00 (+2.5;-1.5)
$t_{f1,l2}$ [mm]	13,62	13,58	13,57		
h [mm]	180,40	180,33	180,44	180,39	180,00 (+3;-2)
$t_{w,1}$ [mm]	8,31	8,15	8,23	8,27	8,50 (+1;-1)
$t_{w,2}$ [mm]	8,35	8,19	8,38		

Table 4-12 : Measured dimensions for test IPE270_S355_L540

	Measure 1	Measure 2	Measure 3	Mean value	Nominal value (Tolerance)
$b_{F,u}$ [mm]	135,20	135,12	135,31	135,21	135,00 (+4;-2)
$t_{f,u1}$ [mm]	9,63	9,63	9,41	9,55	10,20 (+2.5;-1.5)
$t_{f,u2}$ [mm]	9,57	9,51	9,57		
$b_{F,l}$ [mm]	135,16	135,17	135,49	135,27	135,00 (+4;-2)
$t_{f,l1}$ [mm]	9,64	9,59	9,53	9,65	10,20 (+2.5;-1.5)
$t_{f,l2}$ [mm]	9,72	9,56	9,84		
h [mm]	270,57	270,24	270,39	270,40	270,00 (+4;-2)
$t_{w,1}$ [mm]	6,90	6,70	6,85	6,81	6,60 (+0.7;-0.7)
$t_{w,2}$ [mm]	9,62	6,74	6,72		

4.3.4.3 Tensile tests characterizing the material behaviour

The stress strain-behaviour of the material was determined for each studied member by tensile tests. So as to obtain precise results representing the entire cross-section, one necked coupon was cut out of each plated part of the section as shown in Figure 4-30 (left and right part of the upper and lower flange and web). Consequently, five coupon tests were performed for each specimen. In order to determine the Young’s modulus of the specimen the coupons were loaded until they reached approximatively the middle of the plastic plateau. Then they were released and loaded again. The initial inclination associated with this second load step corresponds to the Young’s modulus. After the determination of the Young’s modulus, the load is increased up to failure with a constant strain rate of 0,045%/s.

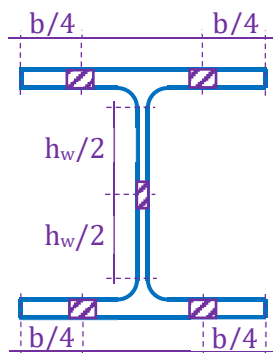


Figure 4-30: Position of the coupons

Figure 4-31 and Figure 4-32 show the obtained material law for the HEB 180 section fabricated from steel S235 and S355, respectively. The results are represented in terms of engineering stresses and engineering strains, i.e. both are calculated with reference to the initial cross-section area of the coupon specimen.

The two following figures show that the material behaves homogeneously as the curves practically overlap for each specimen up to the initiation of failure. With the initiation of failure, however, the curves diverge. Yet, the divergence starts at very high strain levels that may not be attained in the laboratory tests of the entire members. The figures also show that, for both steel grades, the nominal yield strength is largely exceeded (35% in case of S235 and 16% in case of S355). Also, it may be observed that the steel used respects the minimum total strain at failure of 15% defined in reference (CEN 2005a) and the minimum ratio between the yield strength and the ultimate strength of 1,1 defined in the same reference. The results of the tensile tests are summarized in Table 4-13. The values given in this table represent the mean value of the five tensile tests performed for each section.

Table 4-13: Results of tensile tests

Section and steel grade	Young's modulus E (MPa)	Yield strength f_y (MPa)	Tensile strength f_u (MPa)	f_u/f_y (-)
HEA 220 S235	191118	315,07	447,43	1,42
HEA 220 S355	190882	412,79	518,29	1,26
HEB 180 S235	191554	302,56	435,90	1,44
HEA 180 S355	181900	409,32	509,11	1,24
IPE 270 S355	186144	408,48	497,98	1,22

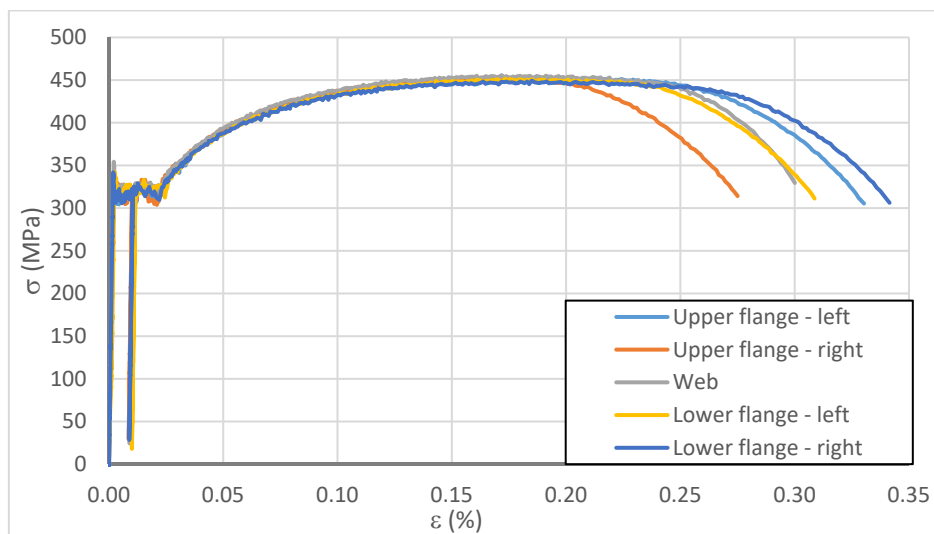


Figure 4-31: HEB 180 - L = 810 mm - S235

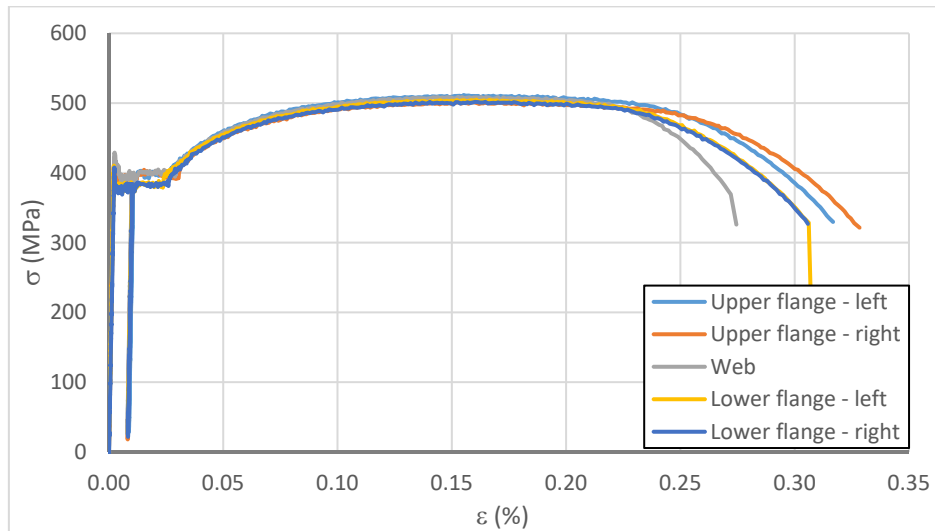


Figure 4-32: HEB 180 - L = 810 mm – S355

4.3.5 Three point bending laboratory tests

Table 4-14 summarizes the ultimate loads obtained in the laboratory tests. The failure of the specimen was characterized by local buckling of the web in the plastic range as represented in Figure 4-33 and Figure 4-34. Especially in Figure 4-33, one may also identify the formation of four plastic hinges (marked by the orange circles) indicating that a certain post buckling reserve has been activated in the tests (see also paragraph 4.3.6.3).

Table 4-14: Peak loads obtained in the laboratory tests

Cross-section	Measured yield strength (mean value) (MPa)	Member length (mm)	Maximum load (kN)
HEA 220	302,6 (S235)	420	1147,6
		840	884,2*
	398,0 (S355)	420	1297,2
		840	1021,0
HEB 180	316,0 (S235)	540	1156,4*
		810	885,8
	369,0 (S355)	540	1262,2
		810	998,8*
IPE 270	380,0 (S355)	540	1140,4
		810	963,8

*Peak load not attained due to displacement limits of the hydraulic jack

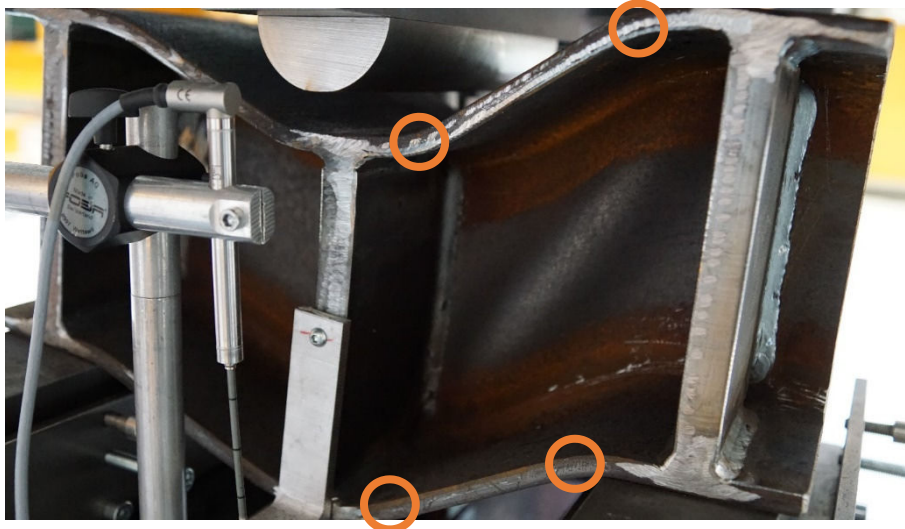


Figure 4-33: Failure of test HEA 220_S235_L420 by local buckling of the web



Figure 4-34: Failure of test IPE 270_S355_L810 by local buckling of the web

It should be noted that the tests HEA 220_S235_L840, HEB 180_S235_L540 and HEB 180_S355_L810 could not be conducted up to the peak load as the displacements exceeded the capacity of the hydraulic jack. The deformed specimen of test HEB 180_S235_L540 is represented in Figure 4-35. It may be observed that local buckling may not be identified visually when the test had to be aborted.

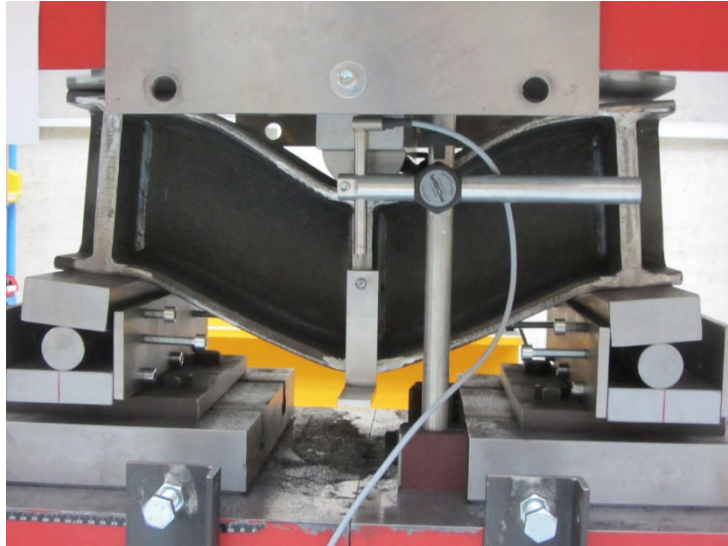


Figure 4-35: Specimen HEB 180 in S235 of 540 mm of length at abort of the test

4.3.6 Numerical simulations of the laboratory tests

4.3.6.1 Presentation of the numerical model

In order to recalculate the laboratory tests numerically, the finite element model detailed in Chapter 3 is slightly adapted. The whole member is modelled with ANSYS solid element “Solid 185”. The metal plates serving as supports and the stiffeners are modelled with the same finite element. The imposed displacement is introduced linearly below the metal plates as illustrated schematically by the blue triangles in Figure 4-36. The plates are free to rotate about the point of application of the imposed displacements. The rigid support created by the metal demi-sphere at mid-span in the laboratory test is represented in the numerical model by blocking the vertical displacement of the upper flange at mid-span.

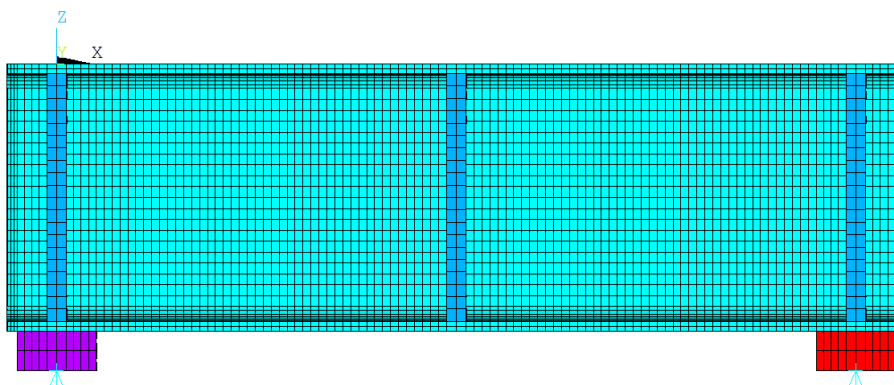


Figure 4-36: Numerical simulation of the laboratory tests – Side view

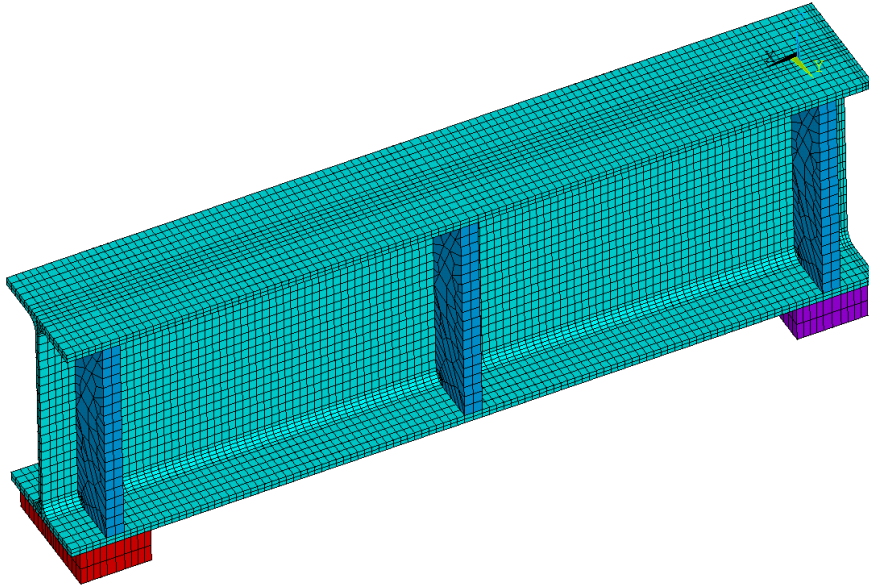


Figure 4-37: Numerical simulation of the laboratory tests – Isometric view

It should be noted that the classical residual stress pattern is included into the numerical model of the member and that the measured stress-strain behaviour is adopted as material law in the numerical GMNIA simulations. As the initial plate imperfection has not been measured, the numerical simulations include a sine shaped plate imperfection with varying amplitude. The influence of the amplitude of the imperfection is highlighted in the following paragraph.

4.3.6.2 Comparison between numerical model and laboratory tests

Table 4-15 presents the comparison of the GMNIA results and the laboratory tests. As stated previously, the plate imperfection has not been measured. Therefore, the laboratory tests are recalculated based on a sine shape imperfection introduced to the web. The amplitude of this imperfection is varied between $h_w/50000$ and $h_w/500$ as shown in Table 4-15 and Figure 4-38. It may be observed that, independently from the applied local imperfection, the numerical results are rather close to the laboratory tests. Yet, with increasing amplitude of the imperfection, the simulations become more and more safe-sided. Consequently, it appears that the tested members were only subject to very low imperfections and in particular imperfections much lower than the tolerances authorized by the fabrication standard EN 1090-2 (CEN 2011).

When the load displacements curves obtained with the numerical simulations are studied, one may observe that the amplitude of the imperfection does not influence the pre-buckling zone. Yet, with increasing amplitude, local buckling is initiated at lower load levels. Also, after buckling, the load decreases less abruptly for higher amplitudes of the imperfection than in the case of small imperfections (compare curves associated with $h_w/500$ and $h_w/50000$ in Figure 4-38). This is not surprising as the webs affected by a higher imperfection are also subject to higher out-of-plane bending before local buckling affects the resistance of the member. In case of webs with low imperfection, the out-of-plane bending moments increase abruptly with the initiation of local buckling generating an abrupt decrease of the load with increasing applied displacements.

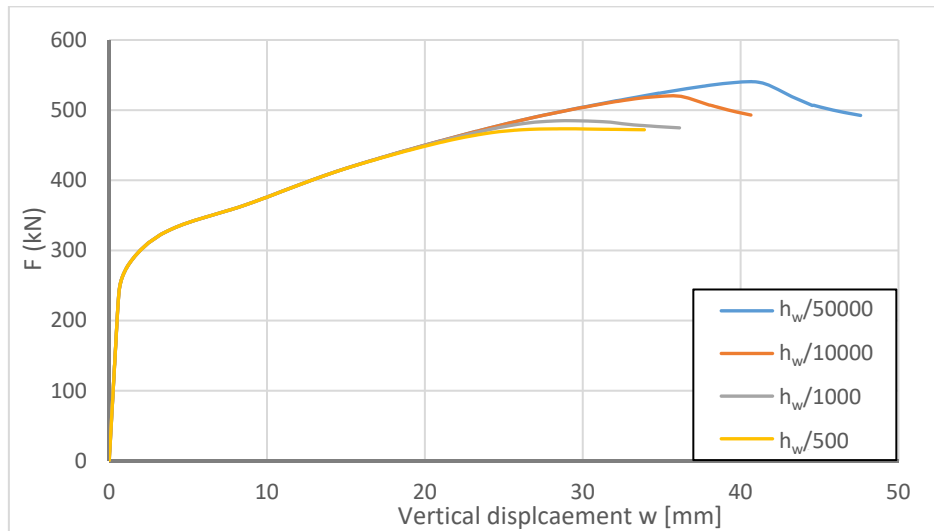


Figure 4-38: Load-displacement curve obtained numerically for test HEA220_S235_L420

Table 4-15: Comparison between test results and GMNIA simulations

Designation	Peak load Laboratory $F_{ult,Lab}$ (kN)	Peak load GMNIA – $h_w/50000$ (kN)	Peak load GMNIA – $h_w/10000$ (kN)	Peak load GMNIA – $h_w/1000$ (kN)	Peak load GMNIA – $h_w/500$ (kN)
HEA220_S235_L420	1147,6	1081,2	1041,1	970,00	946,76
HEA220_S235_L840	884,2*	855,95	849,72	827,61	817,45
HEA220_S355_L420	1297,2	1293,7	1252,8	1180,2	1153,4
HEA220_S355_L840	1021,0	1036,3	1033,0	1011,5	999,54
HEB180_S235_L540	1156,4*	1085,9	1069,0	1032,4	1016,8
HEB180_S235_L810	885,8	872,77	872,7	869,47	866,4
HEB180_S355_L540	1262,2	1200,6	1193,6	1153,7	1139,9
HEB180_S355_L810	998,8*	975,76	975,65	975,51	975,05
IPE270_S355_L540	1140,4	1128,7	1089,1	1018,7	990,96
IPE270_S355_L810	963,8	1001,2	989,0	944,79	924,52
Mean value $F_{ult,GMNIA}/F_{ult,Lab}$		0,979	0,964	0,929	0,916
Standard deviation $F_{ult,GMNIA}/F_{ult,Lab}$		0,033	0,039	0,058	0,065

* Peak load not attained due to displacement limits of the hydraulic jack

By observing the results given in Table 4-15 in more detail, it may seem surprising that the numerical simulations are safe-sided for the tests HEA220_S235_L840, HEB180_S235_L540 and HEB180_S355_L810 even if they do not attain their peak load in the laboratory. However, the load displacement curves show that these tests are very close to their ultimate load in the laboratory as represented in Figure 4-39. In Figure 4-39, one may also recognize that the load-displacement curve obtained by the GMNIA simulation has a slightly different shape than the one obtained by

the laboratory tests. In fact, one may distinguish four phases in the load-displacement curve of the numerical simulation corresponding respectively to 1) linear elastic behaviour, 2) the start of yielding and the passage through the yield plateau, 3) strain hardening up to plastic shear buckling and 4) finally the decrease of load in the post buckling stage. Especially, for loads corresponding to the beginning of yielding, the real behaviour of the specimen seems to be smoother. Indeed, the passage through the yield plateau cannot be clearly identified in the laboratory test. It should be noted that the numerical simulations are based on the material behaviour obtained by **uni-axial tensile** tests. For the compact members failing in shear it seems that the tensile tests may not exactly represent the material behaviour. However, even if there are some differences in the load displacement curves, Figure 4-40 and Figure 4-41 show that the deformed shape of the physical member corresponds very well to the numerical simulation. It can be seen that a plastic hinge (again marked with an orange circle) is formed near the stiffener at mid-span.

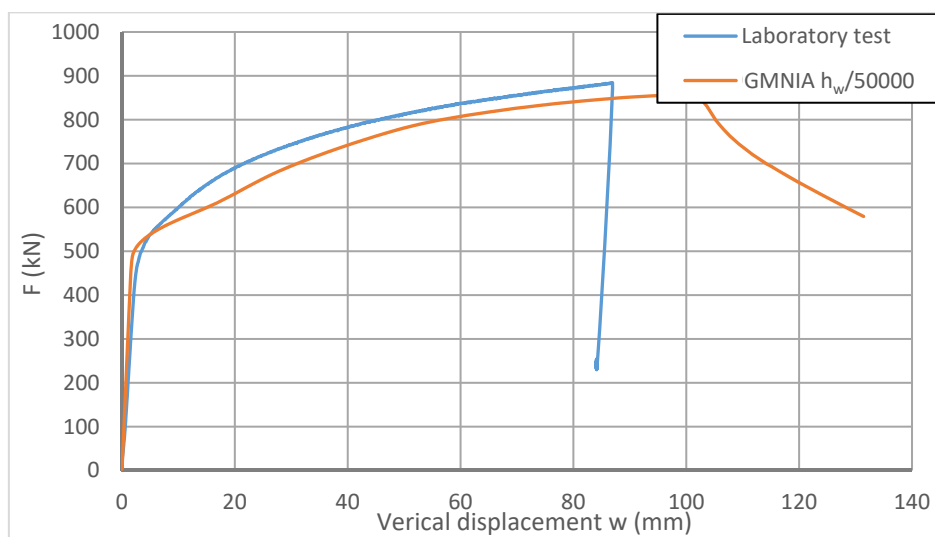


Figure 4-39: Load-displacement curve for test HEA220_S235_L840



Figure 4-40: Photo for test HEA220_S235_L840

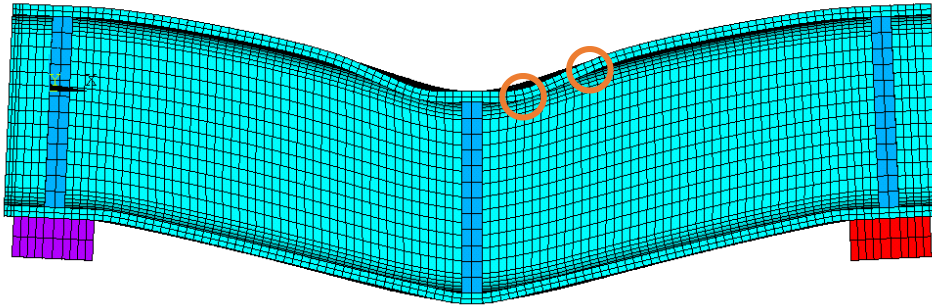


Figure 4-41: GMNIA for test HEA220_S235_L840 – $u_z = 87\text{mm}$

The numerical simulation of this test has been conducted further on up to the formation of local buckling under a high shear force (in the plastic domain) as shown in Figure 4-42 and Figure 4-43.

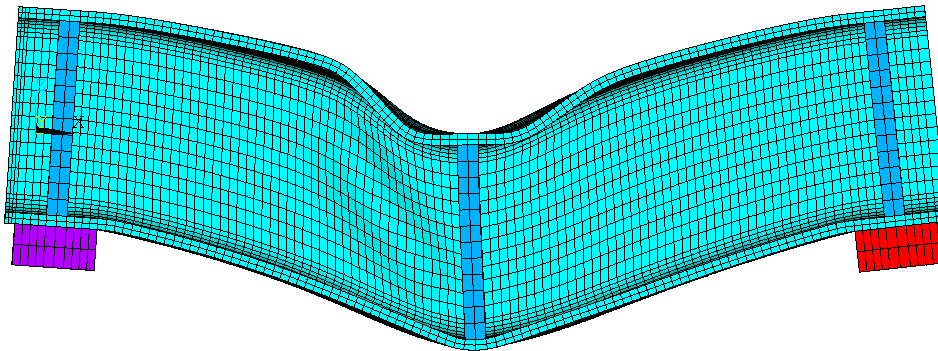


Figure 4-42: GMNIA for test HEA220_S235_L840 – $u_z = 115\text{ mm}$

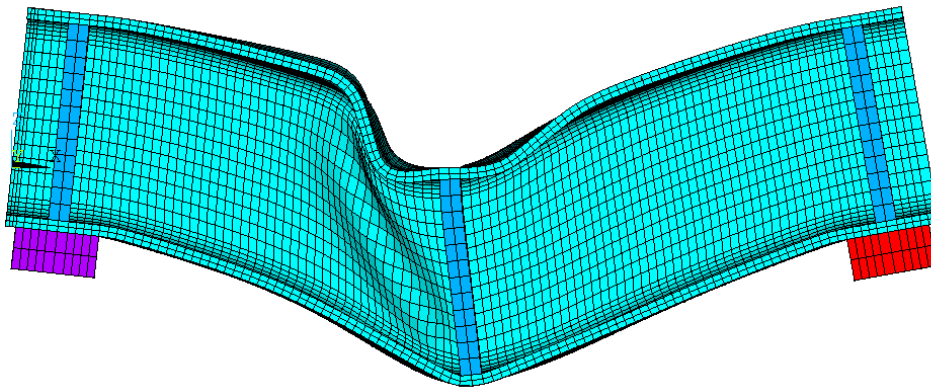


Figure 4-43: GMNIA for test HEA220_S235_L840 – $u_z = 148\text{ mm}$

Last, Figure 4-44 compares the deformed shape obtained in the numerical simulations and the laboratory test HEA220_S355_L420. Obviously, the results correspond very well.

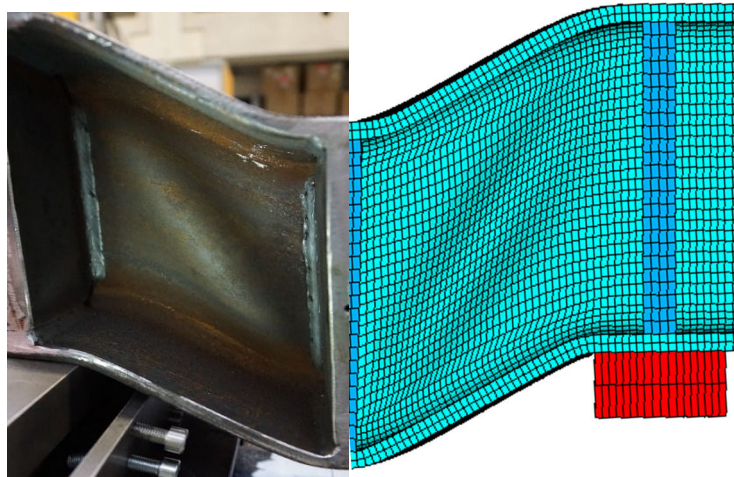


Figure 4-44: Deformed shape at ultimate end of the test HEA220_S355_L420

This paragraph presented a comparison between the laboratory tests characterizing the major-axis bending-shear force interaction and the corresponding numerical simulations. It could be shown that the GMNIA calculations represent very well the obtained results in terms of peak load, failure mode and deformed shape. However, in some cases the load-displacement curve is slightly smoother at the beginning of yielding for the laboratory tests than for the simulations. Yet, this does not alter the quality of the GMNIA results. Therefore, it may be concluded that the numerical model is capable to correctly simulate the real behaviour of the member and it is consequently be used for the parametric study presented paragraph 4.4.

4.3.6.3 Comparison between laboratory tests and resistance models

Hereafter, the ultimate resistance obtained in the laboratory is compared to different resistance models. The proposals of Eurocode 3 Part 1-1 (CEN 2005a) and AS 4100 (Standard Australia 1998) are recalled in Table 4-16.

Table 4-16: Major-axis bending - shear interaction proposed in EN 1993-1-1 and AS 4100

Standard	Interaction formula	Shear area
EN 1993-1-1	$M_{y,Rd} = M_{y,c,Rd} \quad \text{if } \frac{V_{Ed}}{V_{pl,Rd}} \leq 0,5$ $M_{y,Rd} = \left[W_{pl,y} - \frac{\rho A_w^2}{4t_w} \right] f_y \leq M_{y,c,Rd} \quad \text{elsewise}$ <p>and:</p> $\rho = \left[\frac{2V_{Ed}}{V_{pl,Rd}} - 1 \right]^2 \leq 1,0$	$A_v = A - 2bt_f + (t_w + 2r)t_f$
AS 4100	$M_{y,V,Rd} = \left(\frac{11}{8} - \frac{V_{Ed}}{1,6V_{pl,Rd}} \right) M_{y,Rd} \leq M_{y,Rd}$	$A_v = A - 2bt_f$

Recently, the strain based Continuous Strength Method (CSM) has been developed in order to consider especially the strain hardening and deformation capacity of compact stainless steel cross-sections (Gardner et al. 2013). It has been extended to sections made from structural steel (noted as S...) in bending and combined bending and compression (Liew et al. 2015) and to stainless steel sections in combined bending and shear (Saliba et al. 2014). Hereafter, it is evaluated for the cross-sections tested here. The applied method is recalled in Table 4-17 to Table 4-19.

Table 4-17: CSM for major-axis bending resistance

Calculation steps	Expression
Cross-section slenderness	$\bar{\lambda}_p = \sqrt{\frac{f_y}{\sigma_{cr}}}$
CSM axial deformation capacity	$\varepsilon_{CSM} = \frac{0,25}{\lambda_p^{3,6}} \leq 15\varepsilon_y$
Strain hardening modulus	$E_{sh} = 0,015 \frac{f_u/f_y - 1}{1,3 - 1,0} E \quad \text{for } f_u/f_y \leq 1,3$ $E_{sh} = 0,015E \quad \text{for } f_u/f_y > 1,3$
CSM axial stress	$\sigma_{CSM} = f_y + E_{sh}(\varepsilon_{CSM} - \varepsilon_y)$
CSM Bending resistance	$M_{CSM} = M_{pl} \left[1 + \frac{E_{sh}}{E} \frac{W_{el}}{W_{pl}} \left(\frac{\varepsilon_{CSM}}{\varepsilon_y} - 1 \right) - \left(1 - \frac{W_{el}}{W_{pl}} \right) \right] / \left(\frac{\varepsilon_{CSM}}{\varepsilon_y} \right)^2$

Table 4-18: CSM for shear resistance

Calculation steps	Expression
Web slenderness	$\bar{\lambda}_w = \sqrt{\frac{\tau_y}{\tau_{cr}}}$
CSM deformation capacity in shear	$\gamma_{CSM} = \frac{0,62}{\bar{\lambda}_w^{2.56}} \leq \text{Min} \begin{cases} 15\gamma_y \\ 0,1 \frac{\gamma_u}{\gamma_y} \end{cases}$
Shear strain hardening modulus	$G_{sh} = \frac{E_{sh}}{2(1 + \nu)}$
CSM shear stress	$\tau_{CSM} = \tau_y + G_{sh}(\gamma_{CSM} - \gamma_y)$
Shear resistance of the web	$V_{w,CSM} = \tau_{CSM} A_v^*$
Contribution of the flanges	$V_{bf,CSM} = \left(\frac{b_f t_f^2 \sigma_{CSM}}{c} \right) \left(1 - \left(\frac{M_{Ed}}{M_{f,CSM}} \right) \right)$ and $M_{f,CSM} = b_f t_f \sigma_{CSM} (h_w + t_f)$
Overall shear resistance of the cross-section	$V_{CSM} = V_{w,CSM} + V_{bf,CSM}$

Table 4-19: Major-axis bending – shear interaction based on CSM resistances

Calculation steps	Expression
Bending resistance	$\eta_1 = \frac{M_{Ed}}{M_{CSM}}$
Shear resistance	$\eta_3 = \frac{V_{Ed}}{V_{CSM}}$
Interaction	if $\eta_3 > 0,5$ and $\eta_1 > \frac{M_{f,CSM}}{M_{CSM}}$ then $\frac{M_{Ed}}{M_{CSM}} + \left(1 - \frac{M_{f,CSM}}{M_{CSM}} \right) \left(2 \frac{V_{Ed}}{V_{w,CSM}} - 1 \right)^2 \leq 1,0$

It should be noted that the CSM procedure for the shear resistance and the major-axis bending shear interaction has been developed based on physical tests of welded plate girders (Saliba et al. 2015). Consequently, the shear area considered in that study has been set equal to the area of the web. For the comparison represented in Table 4-21, it is considered that the shear area is again equal to the area of the web not including the fillets of the studied hot-rolled cross-sections. Therefore, it may be notably smaller than the shear area defined in EN 1993-1-1 as summarized in Table 4-20. The influence of the definition of the shear area is discussed further in paragraph 4.3.7 and 4.4.2.

Table 4-20: Comparison between Eurocode 3 and AS 4100 shear area and area of the web

Cross-section	$A_{v,EC3}$ (cm ²)	$A_{v,AS4100}$ (cm ²)	$A_{v,EC3}/A_{v,AS4100}$ (-)	$A_w = h_w \times t_w$ (cm ²)	$A_{v,EC3}/A_w$ (-)
HEB 180*	20,00	14,73	1,36	12,92	1,55
HEA 220*	21,14	16,49	1,28	13,16	1,61
IPE 270*	22,55	19,01	1,19	16,47	1,37

*nominal section dimensions are used

Obviously, the application of CSM to the major-axis bending-shear interaction leads to a slightly increased calculation effort especially in order to determine the deformation capacities. Yet, as it considers explicitly the effect of strain hardening, one might suppose that it yields more precise results compared to laboratory tests and numerical calculations. Table 4-21 presents the comparison between the laboratory tests and the ultimate resistance obtained when the different resistance models are applied.

Table 4-21: Comparison between laboratory tests and resistance models

Laboratory test	$V_{ult,EC3}/V_{ult,Lab}$	$V_{ult,AS4100}/V_{ult,Lab}$	$V_{ult,CSM}/V_{ult,Lab}$	$V_{ult,CSM}/V_{ult,Lab}$ without γ_{lim}
HEB180_S235_540	0,629	0,463	0,558	0,807
HEB180_S235_810	0,773	0,605	0,669	0,907
HEB180_S355_540	0,748	0,552	0,635	0,813
HEB180_S355_810	0,886	0,697	0,740	0,926
HEA220_S235_420	0,644	0,502	0,589	0,697
HEA220_S235_840	0,821	0,651	0,672	0,751
HEA220_S355_420	0,776	0,608	0,692	0,754
HEA220_S355_840	0,967	0,772	0,741	0,813
IPE270_S355_540	0,924	0,786	0,770	0,820
IPE270_S355_810	0,896	0,814	0,826	0,858
Mean	0,807	0,645	0,689	0,815
Standard deviation	0,115	0,121	0,083	0,070

Table 4-21 shows that the method used in the Australian standard AS 4100 is clearly the least precise one of the approaches studied here. Especially, the ultimate resistance obtained for the very compact HEB 180 and HEA 220 sections are overly safe-sided compared to the physical tests. Also, the standard deviation confirms the poor quality of this proposal.

The strength predictions obtained with Eurocode 3 Part 1-1 seem satisfactory. Only, for tests HEB180_S235_540 and HEA220_S235_420 the provisions seem to be too safe-sided. However, these tests concern very compact sections that additionally possess an important strain hardening reserve. Indeed, the measured ratios f_u/f_y are equal to 1,44 and 1,42, respectively.

The Continuous Strength Method, used with a shear area equal to $h_w t_w$, yields conservative results if the strain limitation γ_{Lim} of 15% is considered. Nonetheless, it appears that the standard deviation is very satisfactory. As tensile tests have been performed the real strain limit is known. Hence, it is possible to neglect the limitation of 15%. If this is done, CSM gives even better results. Especially, the low standard deviation of 7% for this complex interaction problem seems very satisfying. In order to evaluate the proposal further on, supplementary calculations are presented in the following paragraph.

4.3.7 Complementary numerical simulations and comparison to resistance models

In the previous paragraph, the laboratory tests have been compared to design models proposed in standards and in the literature. Obviously, this comparison cannot be considered as complete because of the limited number of physical tests. Also, the tests have been designed in order to study very compact sections fabricated from steel with considerable strain hardening reserve. Hereafter, some complementary numerical simulations are presented with the objective to extend the comparisons. In particular, the cross-section compactness (sensitivity to shear buckling) and the influence of the ratio f_u/f_y (strain hardening reserve) are studied. Additionally, the influence of the fillets on the shear resistance is of special interest. The calculations are performed with the same model as before. In paragraph 4.3.6.2 it has been shown that the amplitude of the plate imperfection was very low for the studied members. Yet, for the following simulations the amplitude is chosen to be equal to $h_w/200$ as recommended in reference (CEN 2007a). This is justified here as the execution standard EN 1090-2 authorizes this value as out-of-plane tolerance for the web. Consequently, sections may possess this high amplitudes of geometric imperfection in practice.

The parameters of the complementary simulations are summarized in Table 4-22 and Table 4-23. First, the compact sections HEA220 and the IPE270 section are re-examined considering steel S460 and steel S690 in order to quantify the influence of the strain hardening reserve for compact sections (see Table 4-22). After this, supplementary hot-rolled sections (HR) with invented dimensions are studied. The dimensions are chosen so that the web slenderness is close to the limit of shear buckling, i.e. 72ε following the provisions of Eurocode 3 Part 1-1. In order to quantify the influence of the fillets for slender sections, they are studied considering the fillets (HR11-HR31) and without fillets (HR12-HR32) (see Table 4-22). Finally, the influence of strain hardening on the ultimate bending moment resistance is investigated for the compact sections

HEA 100, HEB 220 and HEA 280 (see Table 4-23). Inversely to the other tests, the shear force is rather low for these last three simulations and should, in theory, not reduce the major-axis bending resistance. In order to study exclusively the cross-section resistance, without the influence of lateral torsional buckling, the out-of-plane displacements are restrained at the intersection between the web and the two flanges.

Table 4-22: Complementary simulations – compact sections

Designation	Cross-section	Yield stress/Tensile strength (MPa)	Member length (mm)	$h_w/t_w \varepsilon$ (-)
HEA220_S460_L420	HEA220	460/570	420	37,58
HEA220_S460_L840			840	
HEA220_S690_L420		690/770	420	46,02
HEA220_S690_L840			840	
IPE270_S460_L540	IPE 270	460/570	540	52,91
IPE270_S460_L810			810	
IPE270_S690_L540		690/770	540	64,80
IPE270_S690_L810			810	
HR11_S355_L874	HR.437.7,5.135,9.6.15*	355/470	847	69,99
HR11_S355_L1311			810	
HR21_S460_L780	HR.390.7,5.135,9.6.15*	460/570	780	70,02
HR21_S460_L1170			1170	
HR31_S460_L654	HR.327.7,5.135,9.6.0*	690/770	654	69,90
HR31_S460_L981			981	
HR12_S355_L874**	HR.437.7,5.135,9.6.0*	355/470	847	68,47
HR12_S355_L1311**			810	
HR22_S460_L780**	HR.390.7,5.135,9.6.0*	460/570	780	69,17
HR22_S460_L1170**			1170	
HR32_S460_L654**	HR.327.7,5.135,9.6.0*	690/770	654	70,32
HR32_S460_L981**			981	

* HR.A.B.C.D.E = Hot-rolled cross-section h = A; t_w = B; b_f = C; t_f = D; r_f = E

** Hot-rolled cross-section without fillets

Table 4-23: Supplementary calculations - compact section under predominant bending

Designation	Cross-section	Yield stress/Tensile strength (MPa)	Member length (mm)	$h_w/t_w \varepsilon$ (-)
HEA100_S235_L1440*	HEA100	235/360	1440	16,00
HEB220_S235_L3300*	HEB220	235/360	3300	19,79
HEA280_S235_L4050*	HEA280	235/360	4050	30,50

*with nominal section dimensions

The results obtained for the complementary calculations are given in Table 4-24 and Table 4-25. Table 4-24 represents the members failing predominantly due to the shear force and Table 4-25 represents the members failing in bending.

Regarding Table 4-24 it seems interesting to note that:

- The fillets have only negligible influence on the shear resistance. Indeed, the obtained resistance is only of about 5%-10% higher for sections HR11-HR31 (with fillets) whereas their shear area (Eurocode 3) exceeds the shear area of sections HR12-HR32 (without fillets) by approximately 18%-24%.
- The Eurocode 3 strength predictions are safe-sided on average. Additionally, the low standard deviation seems satisfying. However, for high strength steels the predicted resistance becomes unsafe.
- The Australian steel construction standard as well as CSM yield very similar results in terms of mean value and standard deviation. Also, both methods are generally safe-sided.

Table 4-24: Results of complementary calculations – Major-axis bending – Shear force interaction

Test	$V_{ult,GMNIA}$ (kN)	$V_{ult,EC3}/V_{ult,GMNIA}$ (-)	$V_{ult,AS4100}/V_{ult,GMNIA}$ (-)	$V_{ult,CSM}/V_{ult,GMNIA}$ (-)
HEA220_S460_L420	629,00	0,892	0,696	0,791
HEA220_S460_L840	539,57	<u>1,024</u>	0,812	0,780
HEA220_S690_L420	859,18	0,988	0,773	0,809
HEA220_S690_L840	734,64	<u>1,133</u>	0,904	0,811
IPE270_S460_L540	589,58	<u>1,015</u>	0,856	0,840
IPE270_S460_L810	551,92	0,881	0,801	0,808
IPE270_S690_L540	793,20	<u>1,133</u>	0,955	0,896
IPE270_S690_L810	741,38	0,983	0,894	0,864
HR11_S355_L874	641,71	0,983	0,952	0,956
HR11_S355_L1311	491,32	0,989	0,960	<u>1,030</u>
HR21_S460_L780	752,11	<u>1,019</u>	0,979	0,943
HR21_S460_L1170	622,26	0,957	0,919	0,940
HR31_S690_L654	975,93	<u>1,072</u>	<u>1,012</u>	0,935
HR31_S690_L981	853,96	0,963	0,908	0,888
HR12_S355_L874	623,43	0,905	0,931	0,935
HR12_S355_L1311	472,13	0,952	0,950	0,983
HR22_S460_L780	738,16	0,917	0,943	0,931
HR22_S460_L1170	594,84	0,917	0,911	0,923
HR32_S690_L654	958,35	0,940	0,960	0,942
HR32_S690_L981	814,47	0,907	0,896	0,881
Mean value $V_{ult,Method}/V_{ult,GMNIA}$		0,979	0,901	0,894
Standard deviation $V_{ult,Method}/V_{ult,GMNIA}$		0,073	0,078	0,069

In order to analyse the results further on, Figure 4-45 and Figure 4-46 show the stress distribution at ultimate limit state for the tests HEA220_S460_L420 (Eurocode 3 is safe-sided) and HR31_S690_L654 (Eurocode 3 is unsafe). It may be observed that the stress distribution is very similar for both sections. Indeed, the web has yielded in shear between the fillets. Moreover, in both cases the stresses nearly attain the ultimate strength of steel due to the high influence of strain hardening (570 MPa for S460Q and 770 MPa for S690Q). It should be noted that Figure 4-45 and Figure 4-46 represent “true stresses” and not “engineering stresses” ($\sigma_{Eng} = \sigma_{True}/(1+\epsilon_{Eng})$).

The shear strains attain high values of 12% and 6% for tests HEA220_S460_L420 and HR31_S690_L654. However, the strains respect the minimum strain capacity defined in Eurocode 3 Part 1-1.

Figure 4-45 and Figure 4-46 show that the stresses are nearly uniform over the web. Yet, they decrease rapidly at the connection of the web with the flanges. It seems that plasticity is not capable to spread into the fillets and the flanges as supposed by the shear area defined by Eurocode 3. Consequently, it becomes obvious that the safety margin of the shear strength prediction directly depends on the level of strain hardening attained by the cross-section. It has been shown that strain hardening leads generally to safe-sided results for the shear strength predicted by Eurocode 3. However, for less compact sections and steel grades possessing only limited strain hardening reserve (S460 and S690) the results may become unsafe.

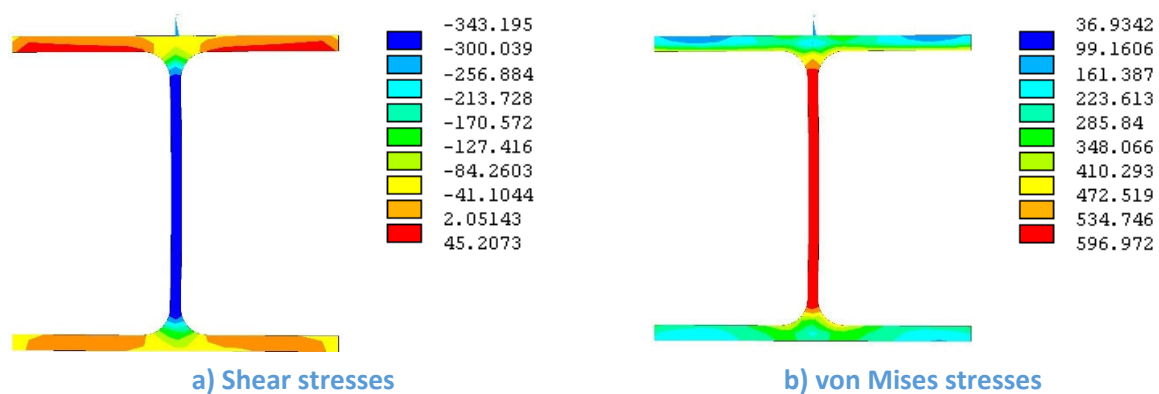


Figure 4-45: Distribution of a) shear stresses and b) von Mises stresses at the ultimate limit state for test HEA220_S460_L420

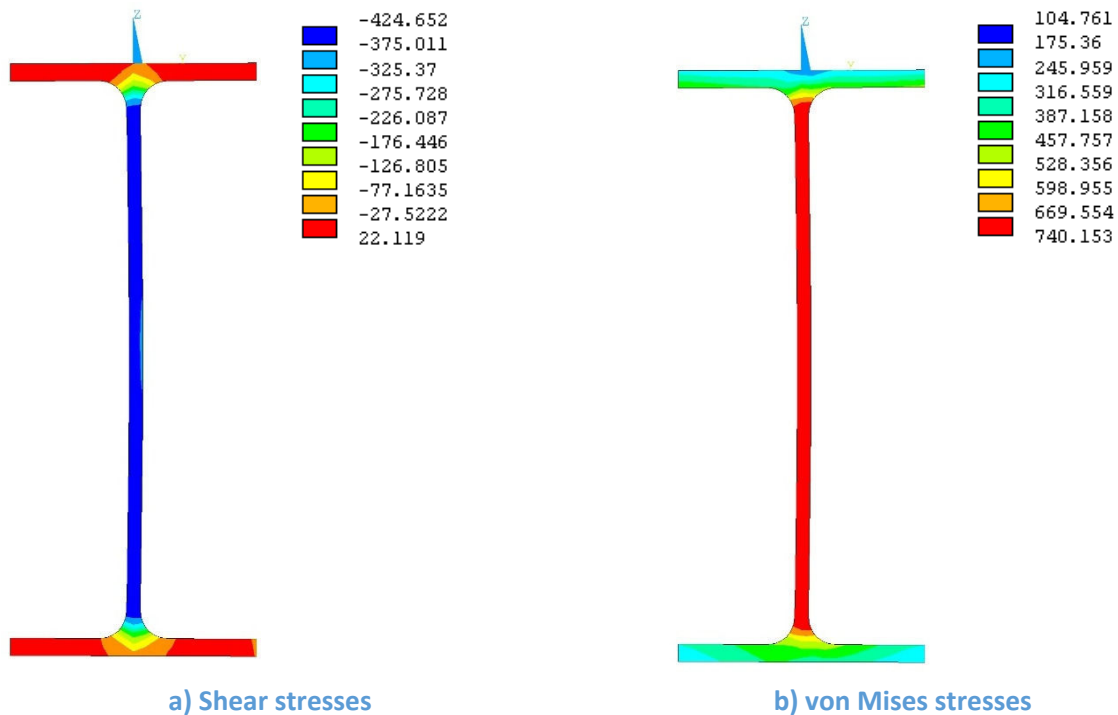


Figure 4-46: Distribution of a) shear stresses and b) von Mises stresses at the ultimate limit state for test HR31_S690_L654

Table 4-25 represents the results of the compact members failing predominantly in bending ($V_{z,ult}/V_{z,pl} < 0,5$). For the three members, the ultimate limit state is characterized by local buckling in the plastic range of the compressed flange at mid-span as shown for test HEA280_S235_L4050 in Figure 4-47.

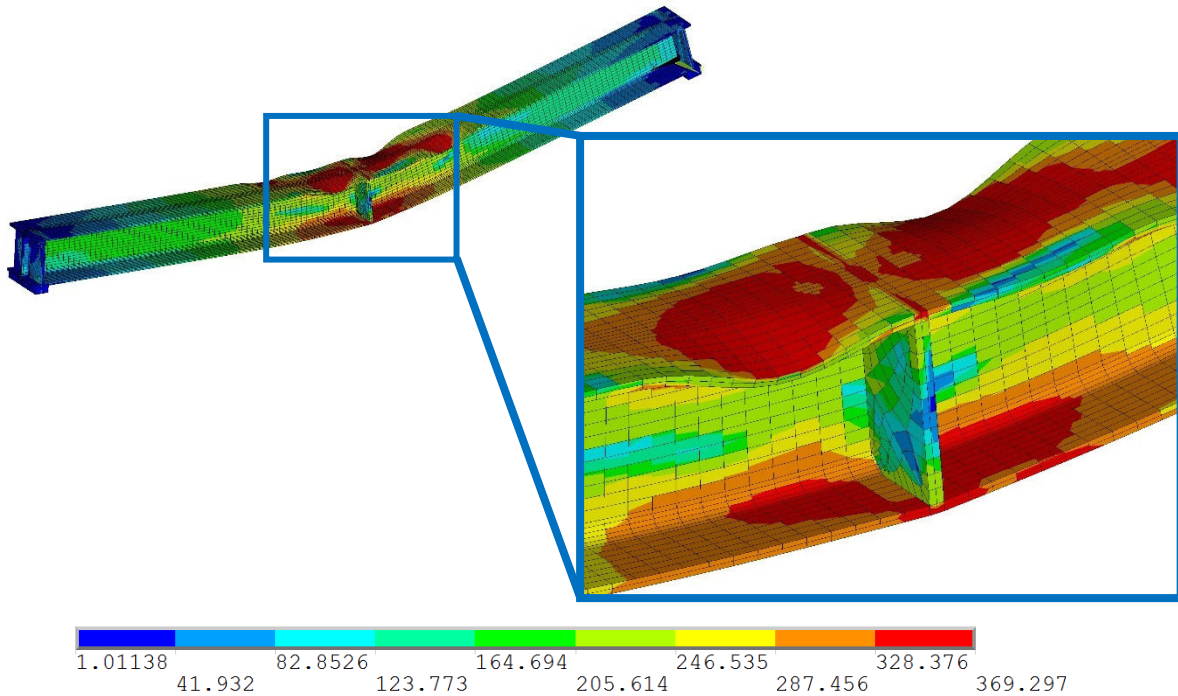


Figure 4-47: von Mises stress distribution and local buckling at ULS for HEA280_S235_L4050

These last tests are performed in order to quantify the influence of strain hardening on the major-axis bending resistance. Table 4-25 clearly shows that strain hardening highly influences the resistance not only in case of shear but also for bending. Only CSM considers this influence and consequently yields more economic results than Eurocode 3 and the Australian steel standard. These standards are limited to the plastic bending moment resistance and therefore give very conservative results compared to the simulations.

Table 4-25: Major-axis bending resistance of very compact sections

Test	$M_{ult,GMNIA}$ (kN)	$M_{ult,EC3}/M_{ult,GMNIA}$ (-)	$M_{ult,AS4100}/M_{ult,GMNIA}$ (-)	$M_{ult,CSM}/M_{ult,GMNIA}$ (-)
HEA100_S235_L1440	43,46	0,625	0,625	0,738
HEB220_S235_L3300	172,00	0,685	0,685	0,813
HEA280_S235_L4050	180,30	0,716	0,716	0,739
Mean value $M_{ult,Method}/M_{ult,GMNIA}$		0,676	0,676	0,763
Standard deviation $M_{ult,Method}/M_{ult,GMNIA}$		0,046	0,106	0,043

4.3.8 Conclusions

The objective of the laboratory tests was to validate the numerical model used for the parametric study and to obtain more insights into the real interaction between major-axis bending and the shear force. It has been shown that the numerical model is satisfactory as it predicts the ultimate limit load as well as the failure mode obtained by the laboratory tests.

The laboratory tests as well as the supplementary calculations and comparisons to code provisions have shown that:

- Strain hardening highly influences the ultimate resistance of compact sections failing in shear and bending.
- Generally, the strength predictions of Eurocode 3, AS 4100 and CMS are safe-sided. However, Eurocode 3 may become unsafe for cross-sections close to the limit of shear buckling and/or high strength steels. It has been shown that the Eurocode 3 safety problem is linked to the definition of the shear area as it implicitly includes a minimum level of strain hardening. Yet, if this level of strain hardening cannot be attained by the cross-section, Eurocode 3 becomes unsafe.

Obviously, in today's practice, compact sections are generally not used with steels S460 and S690, in particular when they are subject to bending. However, provisions given in standards should be safe in their field of application. Consequently, a reduction of the shear area may be justified, especially as it has also been shown that the fillets do not have a considerable influence on the shear resistance. By reducing the shear area to the area of the web (without fillets), the Eurocode 3 provisions of the shear resistance of welded and hot-rolled sections would be unified and the application would be simpler for the engineer. Nevertheless, strain hardening does have an important impact on the major-axis bending-shear force interaction (see also paragraph 4.4.1.3) and should therefore be considered in order to obtain an economic design. This can be done if the over strength factor η (see paragraph 4.2.1.2.1) is applied to welded **and** hot-rolled sections and if it is linked to the available strain hardening reserve (for example ratio f_u/f_y).

CSM proposes to introduce explicitly the influence of strain hardening into the design equations. Admittedly, this leads to more complex interaction equations. Yet, it also leads to less scattered results than considering strain hardening implicitly by increasing the shear resistant area. It is recalled again that the shear area to be used in combination with CSM is the area of the web without the fillets ($= (h - 2t_f) \cdot t_w$). The slight increase of the resistance due to the presence of fillets is taken into account through the critical shear stress τ_{cr} that is used as key parameter to determine the shear strain capacity in CSM.

Finally, it should be noted that even if the Eurocode shear area for hot-rolled sections was limited to the area of the web, the design would not become non-economic as only very compact sections are highly impacted. Yet, these sections are in general not used when the shear resistance becomes determining for the design.

4.4 Parametric study and resistance model

4.4.1 General remarks

4.4.1.1 *Studied cross-sections*

Hereafter, the plastic cross-section resistance of I and U sections is studied based on an extensive parametric study. This study is based on FEM calculation taking into account a bilinear elastic-perfectly plastic material law excluding local buckling and member second order effects (MNA calculations - see paragraph 4.4.1.3).

In order to account for the influence of the section geometry, the compactness as well as the ratio h/b_f are varied. The studied cross-sections are represented in Figure 4-48. In addition, mono-symmetric I sections are considered by reducing/increasing the width of the flanges of the double symmetric I sections. It is considered that the mono-symmetric sections are always welded and hence do not possess fillets.

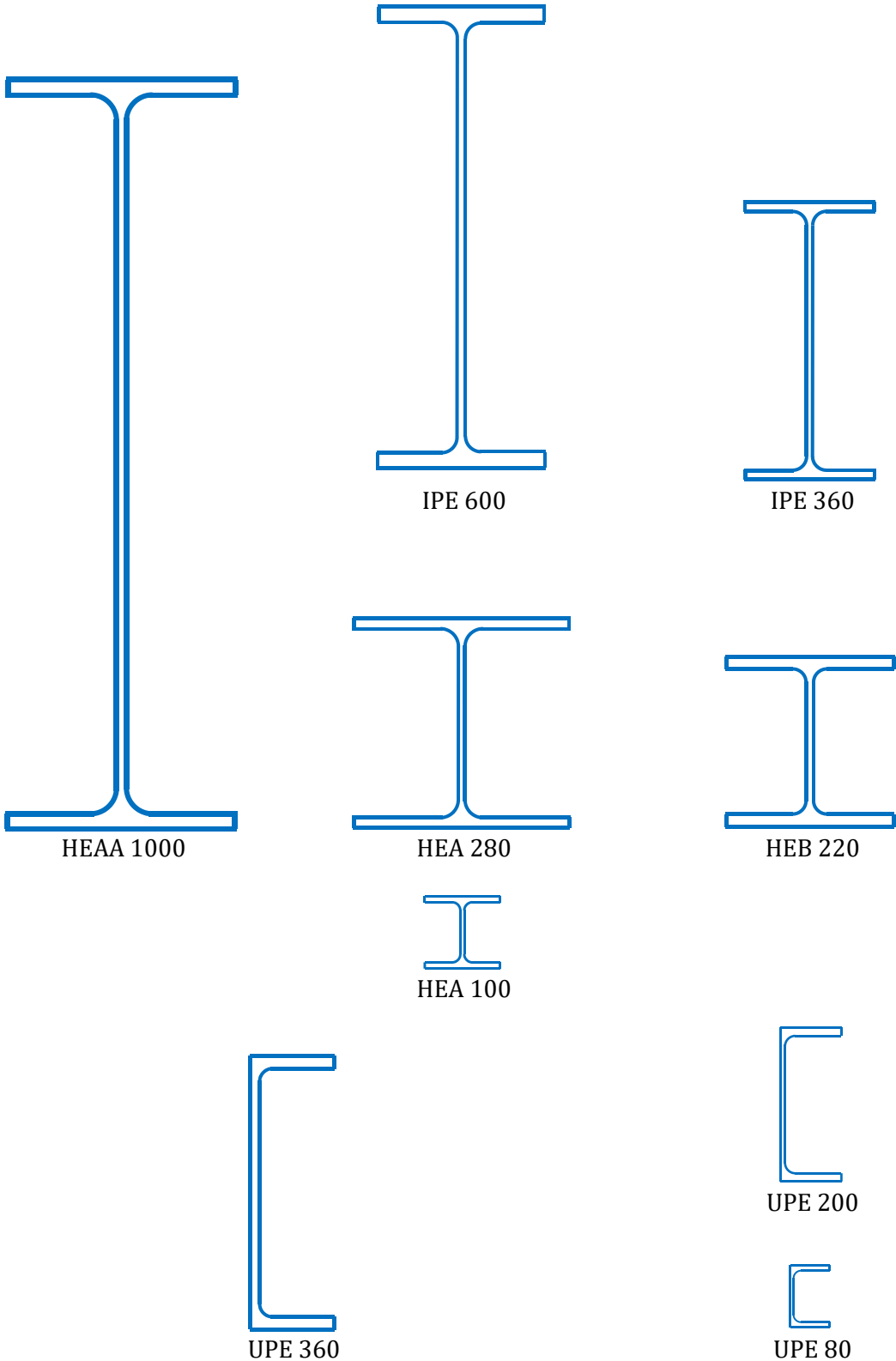


Figure 4-48: Cross-sections considered for the parametric study

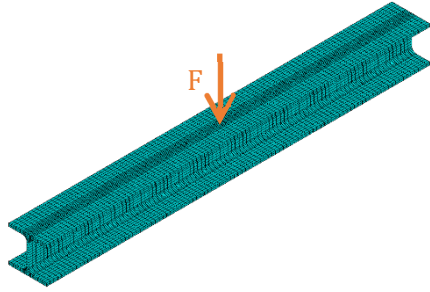

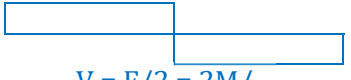
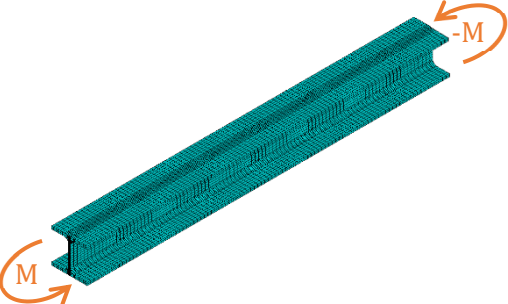
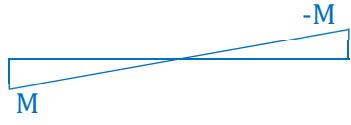
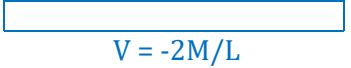
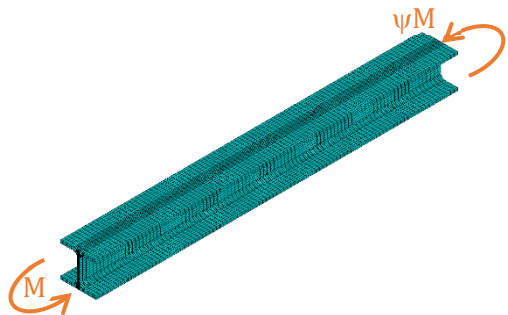
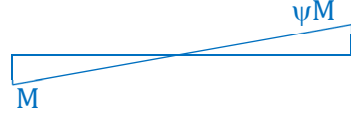
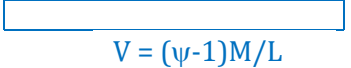
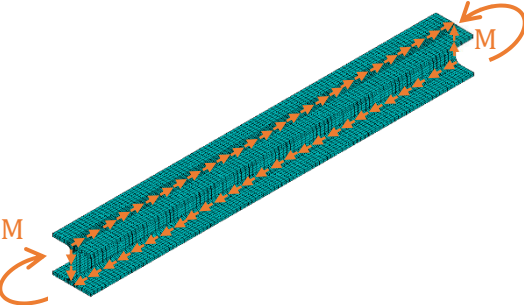
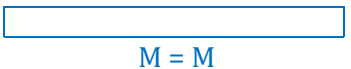

4.4.1.2 *Load cases*

Throughout the present paragraph, the **plastic interaction** between internal forces and moments creating exclusively axial stresses (N , M_y , M_z , B) and internal force and moments creating shear stresses (V_z , V_y , $M_{x,ST,V}$, $M_{x,w}$) is of special interest. In fact, the interaction behaviour between internal forces and moments creating exclusively axial stresses may be treated quasi-analytically. Conversely, the interaction between axial stresses and shear stresses can only be treated “analytically” based on some **key assumption** as the definition of a shear area or the form of the plastic distribution of shear stresses. As has been shown previously, these key assumption may differ greatly from one standard to another. Therefore, it is absolutely necessary to investigate the bending moment-shear force interaction. For double symmetric I sections, this study has already been advanced greatly owing to the laboratory tests and complementary simulations presented in paragraph 4.3. Hereafter, the investigations on bending moment-shear force interaction are completed for U and mono-symmetric I sections based on numerical analyses. Moreover, the influence of torsion on the resistance of the cross-section is studied in detail. However, it has to be noted that this study is much more delicate as a study on the interaction behaviour between axial force and (bi-axial) bending as the shear stresses, resulting from the shear force, are always linked to the variation of the internal moments along the member length. Consequently, it is practically inevitable to perform the numerical simulation on the whole member subject to variable bending or torsion. On the first sight, this fact may seem insignificant but it has a major influence on the interpretation of the obtained results. Indeed, as the whole member is modelled and the internal forces vary along its length, the plasticity spreads along the member accordingly to plastic zone theory. Due to the spreading of plasticity, the member possesses a certain plastic reserve. Also, it has been shown in reference (Gonçalves et al. 2014) and in Chapter 3 that the load introduction may create a complex stress field combining in-plane and through thickness stresses that are generally neglected in the interaction. These secondary stresses may have a beneficial effect on the von Mises yield criterion leading to resistances exceeding the theoretical plastic cross-section resistance. Inversely, it is much less delicate to study the interaction between axial force and bending as the forces and moments may be introduced as constant along the member. Consequently, all sections yield simultaneously and the member does not have any supplementary reserve (or only numerical reserve due the simulation precision). The maximum loads therefore correspond (quasi) exactly to the analytical values. Hence, in this case the interaction can be evaluated very precisely. However, in case of, for example, bending shear interaction, the influence of plastic zones somewhat disturbs the theoretical cross-section interaction behaviour. Also, it should be noted that if torsion is applied, the bi-moment, the warping torsional moment and the Saint Venant’s torsional moment always interact as recalled in Chapter 2. In fact, it is not possible to apply one of the previous moments independently from the others. Hence, it becomes even more delicate (or nearly impossible) to study the individual influence of one of the torsional components on the interaction. Nevertheless, in case of torsion the maximum respective torsional moments are generally not located at the same abscissa of the member. Additionally, it is shown that the warping torsional moment is insignificant and may be neglected when the interaction is studied (see paragraph 4.4.4).

So as to limit the influence of the exact form of the bending moment distribution and load introduction on the numerical results, different load cases are studied hereafter (see Table 4-26). The member is always considered to possess fork supports at its ends. Load cases LC2 and LC3 resemble, however, for load case LC2 **the member length is varied** to obtain different values of the shear force, whereas, for load case LC3, **the ratio between the end moments is varied** to obtain different values of the shear force. Load case LC4 consists in the application of a constant bending moment combined with pure shear. Admittedly, this load case is not of practical interest, yet, it permits to study the interaction behaviour without the influence of yield zones (as both internal forces are constant). It therefore yields a lower bound of the interaction. Hereafter, it is only used when the bending shear force interaction is studied and it is not used in case of applied torsion.

For hot-rolled cross-sections the fillets may have a certain influence on the interaction behaviour in presence of shear stresses. Yet, for the case of major-axis bending – shear force interaction, it has been shown in paragraph 4.3.7 that the fillets do not increase considerably the shear force resistance. Nevertheless, it seems important to include the fillets explicitly in the simulations in order to predict as precisely as possible the interaction behaviour especially in presence of torsion.

Table 4-26: Load cases studied for the characterisation of the M_y - V_z cross-section interaction

Load case		Distribution of bending moment and shear force
LC 1		 $M = FL/4$
		 $V = F/2 = 2M/L$
LC 2		
		 $V = -2M/L$
LC 3		
		 $V = (\psi-1)M/L$
LC 4		 $M = M$
		 $V = V$

4.4.1.3 Material model

The results presented in paragraph 4.3.7 imply that the plastic shear resistance of hot-rolled I sections should be limited to the plastic shear resistance of the web only in order to be consistent with the resistances obtained for predominant bending and for the resistances of welded sections. However, it has been shown that strain hardening may increase the shear resistance considerably. Hereafter, the influence of strain hardening is highlighted again for the major-axis bending – shear force interaction curve. The numerical analyses are performed without considering geometric

second order effects and geometric imperfection (MNA). The calculation is stopped when the limit strain (von Mises) of 15% is exceeded.

The results are given for two examples in Figure 4-49 and Figure 4-50. Obviously, as before strain hardening increases the shear resistance notably. Yet, one may observe again that even with strain hardening the Eurocode 3 plastic shear resistance is not attained for all calculations. It might however be acceptable to use the Eurocode 3 plastic shear resistance for very compact sections. Nevertheless, one should also observe that the obtained bending resistance exceeds the theoretical plastic moment resistance by up to 65%! It is recalled again, that neither Eurocode 3 nor other international standards consider this strain hardening reserve for the bending resistance. Therefore, in order to be consistent with the definition of the plastic bending moment resistance, the following simulations are based on an elastic-perfectly plastic material law. Obviously, it is not possible to consider strain hardening only for the shear stresses and not for the axial stresses in the numerical simulations. However, the influence of strain hardening may be introduced by simply changing the reference resistance for the individual internal force (for example accept a bending moment resistance higher than the plastic bending moment or a shear resistance equal to Eurocode 3 shear resistance). The resistance may for example be based on the strain capacity of the section as rigorously done by the Continuous Strength Method presented in paragraph 4.3.6.3. The general aspect of the interaction curve is not influenced by the reference resistance.

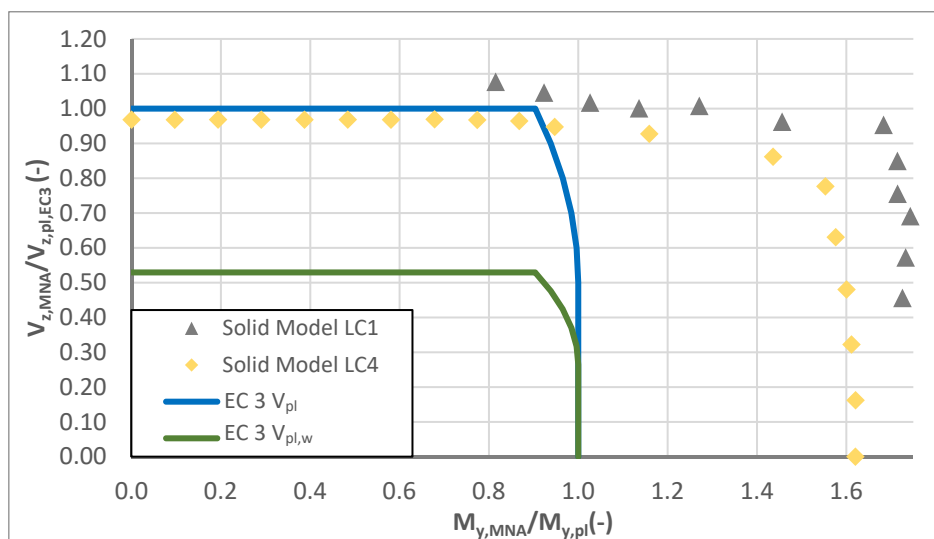


Figure 4-49: M_y - V_z plastic cross-section interaction diagram for HEA 100 with strain hardening

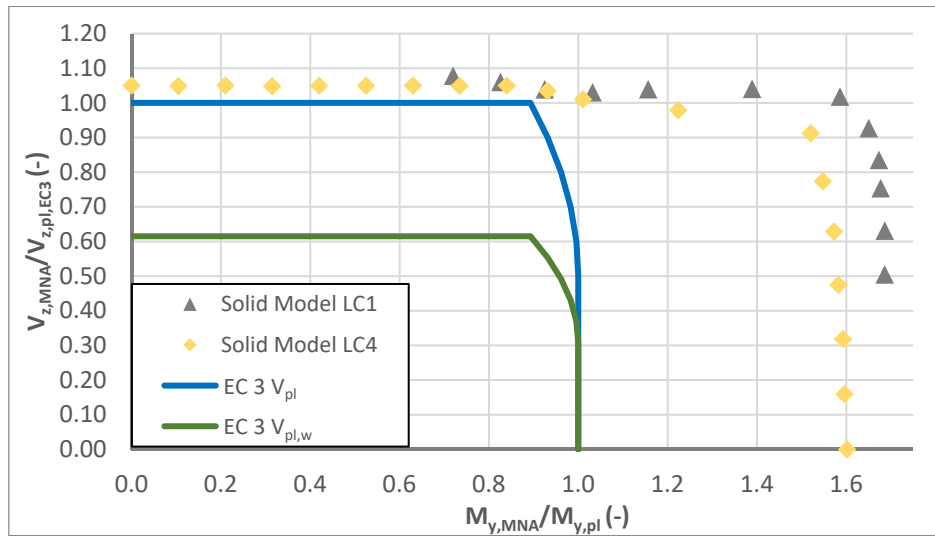


Figure 4-50: M_y - V_z plastic cross-section interaction diagram for HEA 280 with strain hardening

In the following, the cross-sections represented in Figure 4-48 are studied for combined loading. Step by step, the interaction behaviour of double and mono-symmetric I sections and U sections are evaluated for the load cases of:

- Major axis bending and associated shear force
- Minor axis bending and associated shear force
- Bending, shear force and torsion
- Complex interaction including bi-axial bending, shear forces, axial forces and torsion

4.4.2 Interaction between major-axis bending and shear force

4.4.2.1 Double symmetric I sections

Through paragraph 4.3 the interaction between major-axis bending and the shear force has been studied in detail for double symmetric I sections in three point bending. A series of ten laboratory tests as well as several supplementary GMNIA calculation led to the conclusion that the Eurocode 3 shear area may be unsafe in some conditions. Hereafter, several complementary MNA calculations are performed in order to confirm these calculations for a greater variety of cross-sections. Additionally, the influence of the load case is studied based on the following examples.

First, the section HEA 280 is studied. The numerical results are given in Figure 4-51. Figure 4-51 also gives the interaction curve provided by Eurocode 3 Part 1-1 (EC 3 V_{pl}) and the interaction curve EC 3 $V_{pl,w}$ based on the provisions of Eurocode 3 but considering a shear area A_{vz} equal to the area of the web ($h_w \times t_w$).

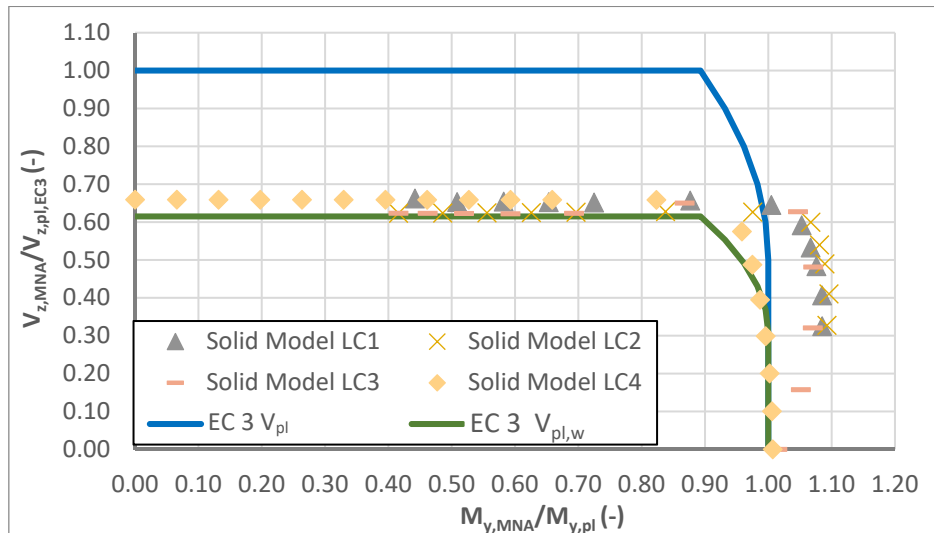


Figure 4-51: M_V cross-section interaction diagram for HEA 280

As can be seen, the numerical results are rather close for load cases LC1 to LC3. One may also recognize the influence of the yield zones and complex stress interaction. In fact, for load cases LC1 to LC3, the maximum bending moment of the member exceeds the plastic bending moment ($M_{MNA} > M_{pl}$) even if the simulations do not include the effect of strain hardening. Inversely, for load case 4 (constant bending moment + pure shear) the maximum bending moment is always less (or equal) than the plastic moment resistance as all sections of the member yield simultaneously. Additionally, Figure 4-51 confirms that Eurocode 3 seems to overestimate the **plastic** shear resistance. It can be observed that the numerically obtained shear resistance only attains the shear resistance of the web.

In order to compare the results obtained for the different load cases further on, the following figures show the stress distributions at plastic limit state for the members subject to approximately $0,5V_{pl}$ at their PLS. Consequently, the failure occurs in the interaction zone between major-axis bending and the shear force. It may be observed that the stress distribution is similar for LC1 to LC3 in the vicinity of the plastic hinge explaining again why the results are nearly identical.

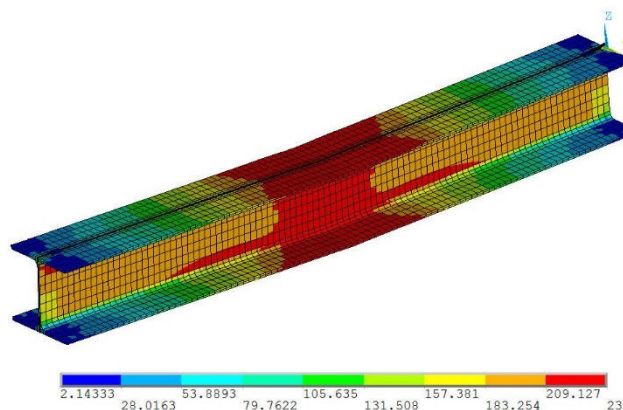


Figure 4-52: HEA 280 subject to point load at mid-span (LC1)

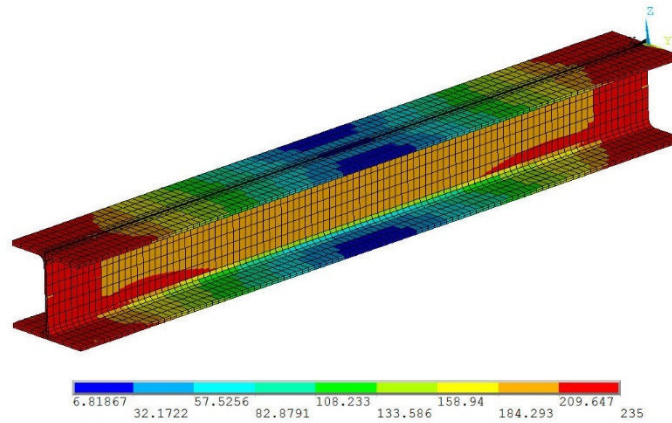


Figure 4-53: HEA 280 subject to inverse moments at member ends (LC2)

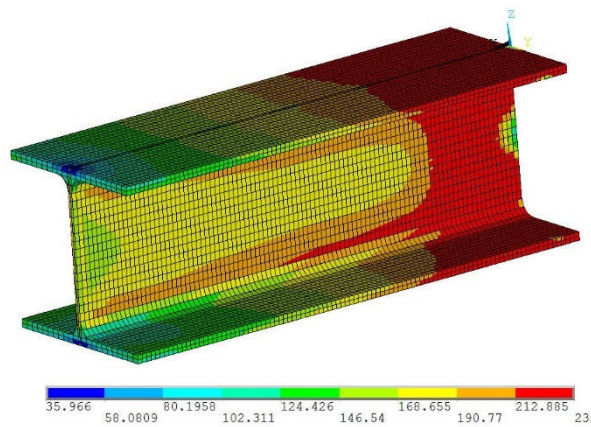


Figure 4-54: HEA 280 subject to moments at member ends – $\psi = 0,4$ (LC3)

The results obtained for the other cross-sections are given next. However, as it has been shown that the load case possesses only insignificant influence on the obtained results, hereafter load cases LC2 and LC3 are not considered anymore. LC4 is kept for the comparison as it represents the lower bound of the resistance.

Figure 4-55 to Figure 4-58 clearly confirm the conclusions obtained for the cross-section HEA 280. In particular, it is observed that:

- Due to the spreading of plasticity and complex stress interaction in the yield zone the ultimate moment obtained by MNA calculations may exceed the theoretical plastic moment resistance of the cross-section.
- The **plastic** shear resistance of the cross-section is overestimated by Eurocode 3 Part 1-1. It is recalled again that the influence of strain hardening, not considered here, may increase the **ultimate** shear resistance.

Also, it is interesting to note that the shear resistance may be more or less close to the shear resistance of the web depending on the cross-section geometry. For compact cross-sections, for which the fillet area is rather tall the numerically obtained shear resistance exceeds the shear

resistance of the web by approximately 10 to 20% (HEA 100, HEB 220, HEA 280). However, for cross-sections with smaller fillets compared to the cross-section geometry, the shear resistance coincides practically with the shear resistance of the web (IPE 360, IPE 600).

The present paragraph confirms the conclusions concerning the plastic major-axis bending shear force interaction obtained based on the laboratory tests. Additionally, it has been shown that the load case has only an insignificant influence on the obtained resistance (apart from load case 4 that is only of theoretical nature). In the following paragraphs the study concerning the plastic cross-section resistance is extended to U sections and mono-symmetric I sections.

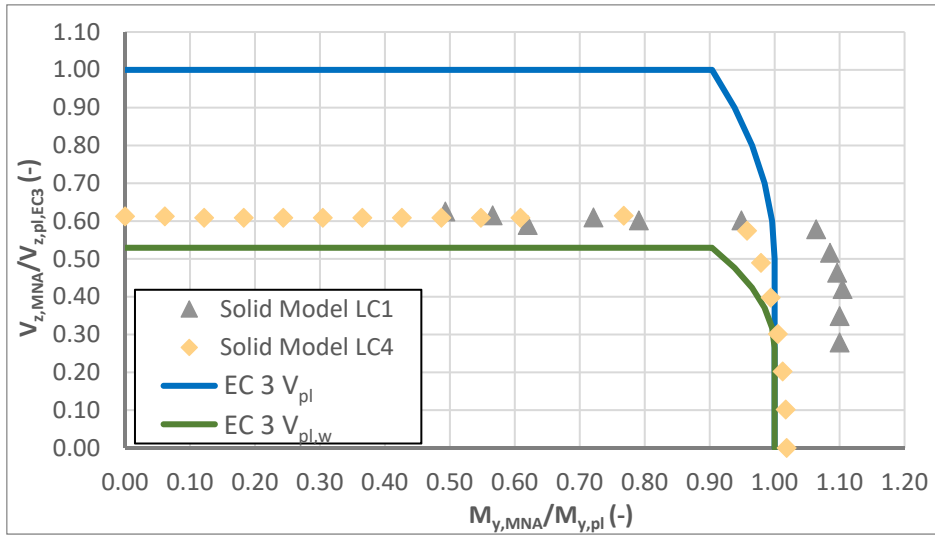


Figure 4-55: M_y - V_z plastic cross-section interaction diagram for HEA 100

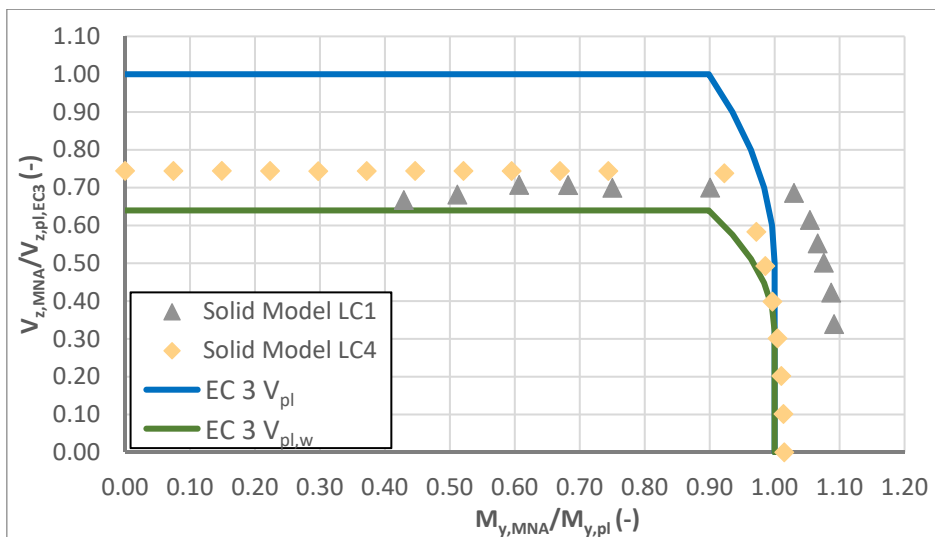


Figure 4-56: M_y - V_z plastic cross-section interaction diagram for HEB 220

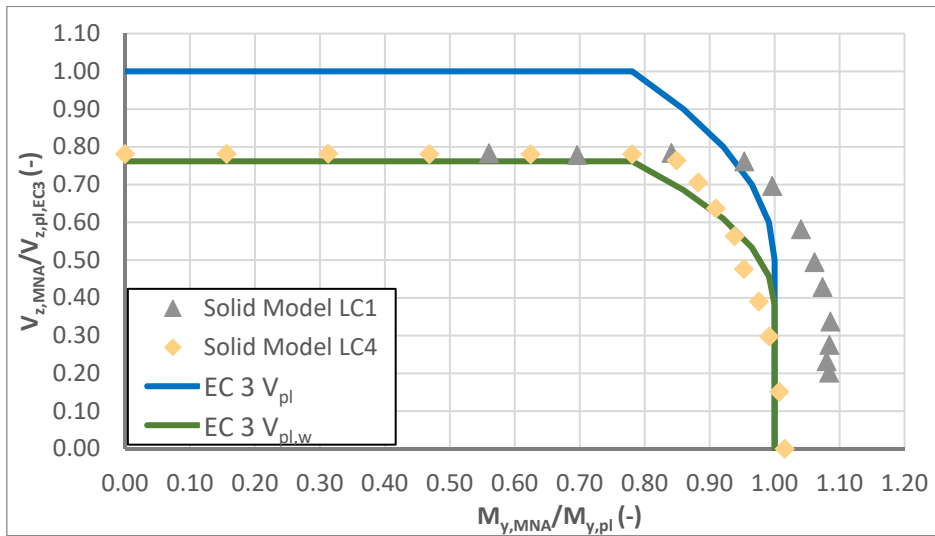


Figure 4-57: M_y - V_z plastic cross-section interaction diagram for IPE 360

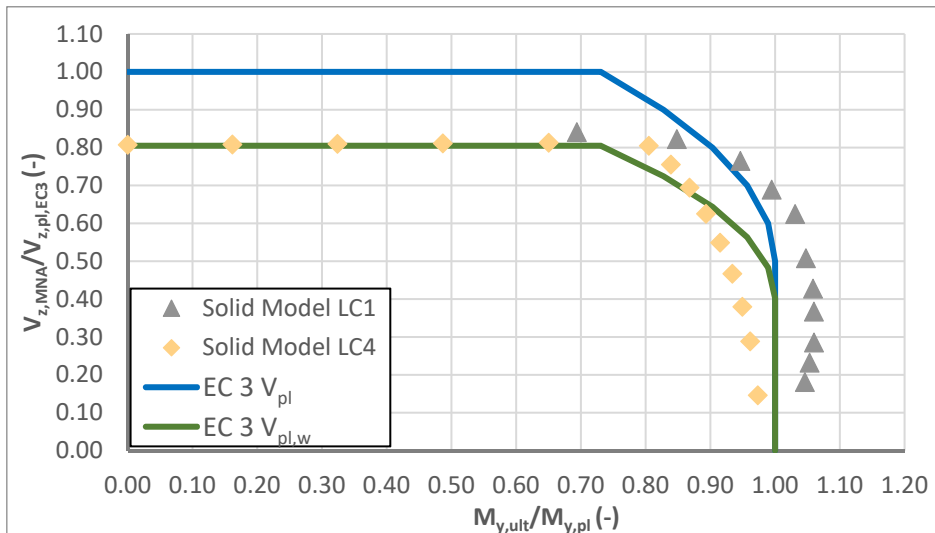


Figure 4-58: M_y - V_z plastic cross-section interaction diagram for IPE 600

4.4.2.2 *U sections*

Before the major-axis bending-shear force interaction is addressed, it seems necessary to review essential points concerning the resistance of U sections subject to major-axis bending only. In paragraph 4.2.2.3, it has been shown that the definition of the plastic major-axis bending resistance is much more delicate than for I sections as illustrated by the discussion published in references (Kindmann et al. 1999b), (Rubin 2000) and (Rubin 2005). In order to recall the problem Figure 4-59 represents the elastic and plastic stress distribution for a UPE section under major-axis bending as well as the warping function of a UPE 200 cross-section without fillets.

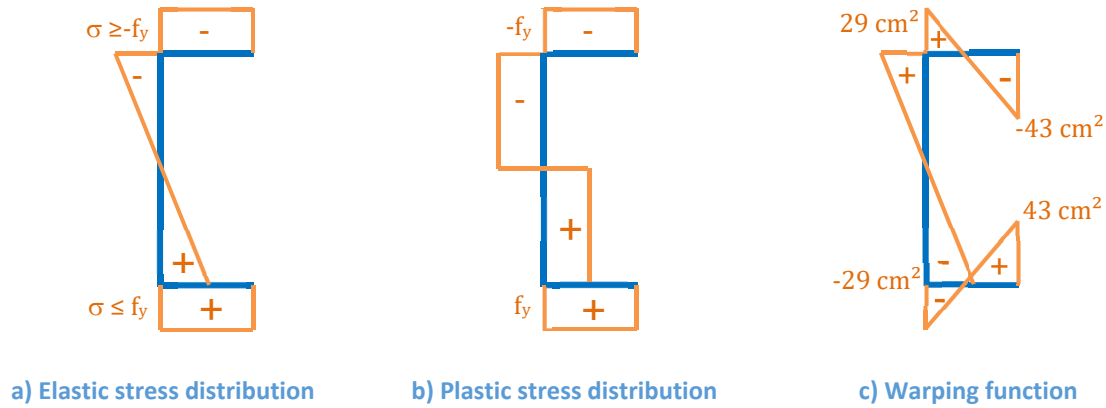


Figure 4-59: Representation of a) elastic and b) plastic stress distribution and c) the warping function

The theoretical elastic and plastic moment resistance can be obtained by integrating the stresses over the section. For a UPE 200 section without fillets fabricated from steel S235 ($f_y = 235$ MPa), one obtains:

$$M_{y,el} = 43,60 \text{ kNm}$$

$$M_{y,pl} = 50,25 \text{ kNm}$$

However, if the stresses are integrated over the cross-section, one also obtains the bi-moments:

$$B_{My,el} = 0 \text{ kNcm}^2 \quad (\text{associated with the elastic moment resistance } M_{y,el})$$

$$B_{My,pl} = -1321,13 \text{ kNcm}^2 \quad (\text{associated with the plastic moment resistance } M_{y,pl})$$

It should be noted that the elastic stress distribution does not generate a bi-moment as the “partial” bi-moments resulting from the stress distribution in the flanges are equilibrated by the “partial” bi-moment resulting from the stress distribution along the web. It is possible to determine an analytical expression of the stress induced bi-moment as given in Eq. (4.70).

$$B_{My,pl} = -f_y \left[\frac{(h-t_f)^2 t_w}{4} y_{s,w} + \frac{(h-t_f)t_f}{2} y_{s,w}^2 - \frac{\left(b_f - \frac{t_w}{2} - y_{s,w}\right)^2}{2} (h-t_f)t_f \right] \quad (4.70)$$

$$y_{s,w} = \frac{3\left(b - \frac{t_w}{2}\right)^2 t_f}{6\left(b - \frac{t_w}{2}\right)t_f + (h-t_f)t_w} \quad (4.71)$$

The distance $y_{s,w}$ is equal to the distance along the y-axis between the shear centre and the plane of the web. One may note that $y_{s,w}$ is also equal to the distance between the plane of the web and the zero of the warping function. Table 4-27 gives the value of the stress induced bi-moment for three U sections (fillets are included into the calculation of $y_{s,w}$). These stress induced bi-moments induce a torsional twist to the member even if it is subject to major-axis bending only (see Chapter

5). Yet, it is recalled that the bi-moment is linked to the second derivative of the torsional twist. Consequently, the resulting torsional twist is low especially for short member that may attain their full plastic resistance. Obviously, longer members under bending are sensitive to lateral-torsional buckling (if there are not restrained) and may therefore not attain the full plastic major-axis bending moment. It should be noted that it is not necessary to consider the stress induced bi-moment in the interaction between major-axis bending and the shear force as it directly yields from the stress distribution and consequently does not lead to a strength reduction.

Table 4-27: Stress induced bi-moments associated with plastic moment resistance for U sections

Cross-section	Stress induced bi-moment associated with $M_{y,pl}$ (kNcm ²)
UPE 80	-87,51
UPE 200	-1321,13
UPE 360	-10357,79

For the interaction between major-axis bending and the associated shear force, it may be supposed that U sections behave similarly as double symmetric I sections as only the lateral position of the flanges changes. However, neither of the standards studied in paragraph 4.2 explicitly treat the case of U-sections. Hereafter, the results of the calculations performed on sections UPE 80, UPE 200 and UPE 360 are represented. In paragraph 4.4.2.1 it has been demonstrated that the load case does not have any significant influence on the plastic interaction behaviour. Therefore, only load cases LC1 and LC4 are kept for the analysis. It is recalled that the members are supposed to possess end fork supports and the material is supposed to behave elastic – perfectly plastic (no strain hardening).

Figure 4-60 to Figure 4-62 confirm that the Eurocode 3 plastic interaction formula, recalled hereafter, may be safely applied to U sections if it is based on the plastic shear resistance of the web.

$$M_{y,Rd} = \left[W_{pl,y} - \frac{\rho A_w^2}{4t_w} \right] f_y \leq M_{y,c,Rd} \quad \text{if } \frac{V_z}{V_{z,pl}} \leq 0,5 \quad (4.72)$$

$$\rho = \left[\frac{2V_z}{V_{z,pl}} - 1 \right]^2 \leq 1,0 \quad \text{elsewise} \quad (4.73)$$

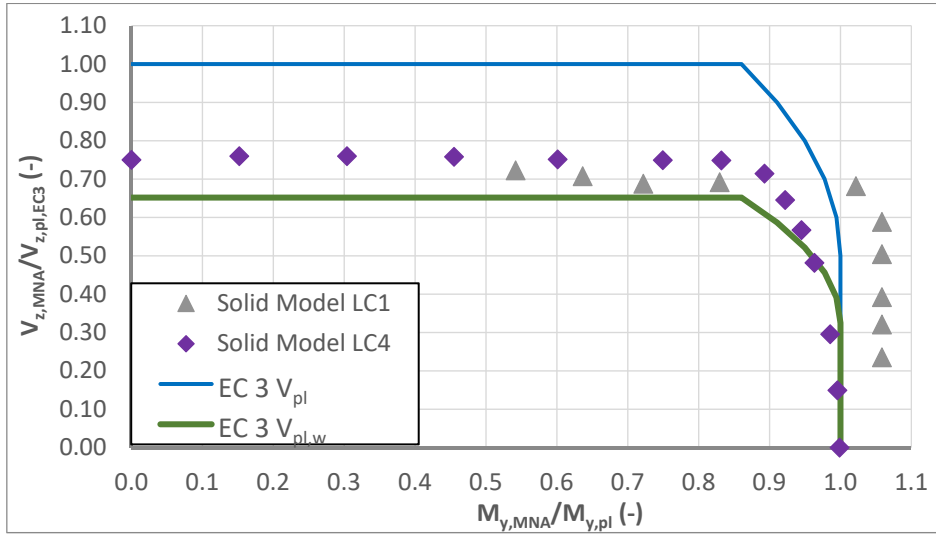


Figure 4-60 : M_y - V_z plastic cross-section interaction diagram for UPE 80

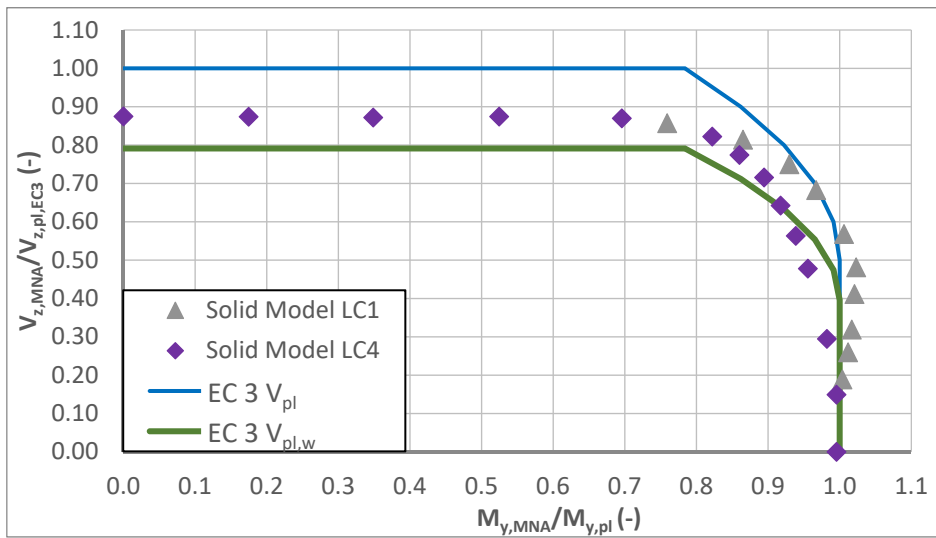


Figure 4-61 : M_y - V_z plastic cross-section interaction diagram for UPE 200

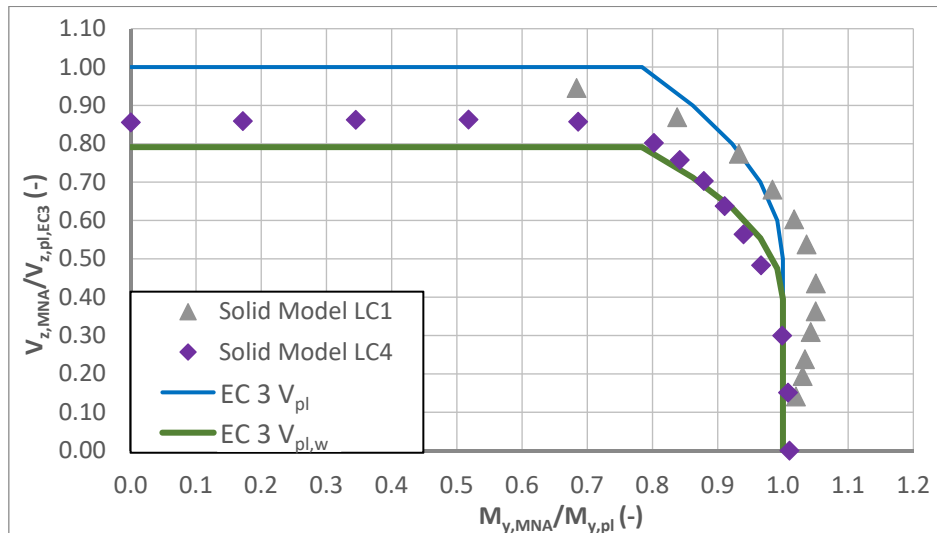


Figure 4-62 : M_y - V_z plastic cross-section interaction diagram for UPE 360

4.4.2.3 Mono-symmetric I sections

Hereafter, the interaction behaviour of mono-symmetric I sections is studied. It is supposed that the sections are welded. Consequently, fillets are not accounted for. Accordingly to the conclusions of paragraph 4.4.1.3 the MNA calculations are based on an elastic-perfectly plastic material law neglecting strain hardening. It has been shown that the shell model represents very well the plastic interaction for welded cross-sections without fillets. Therefore, the following calculations are performed exclusively with the shell model. As the load case does not have any significant influence either, it is supposed that the studied members possess fork supports at their ends and that they are subject to a point load applied at mid-span.

As before several section geometries are studied to characterize the M_y - V_z plastic cross-section interaction. The cross-section geometries are based on 4 cross-sections:

- HEA 100
- IPE 360
- IPE 600
- W 1450.12.300.25

The mono-symmetry of the cross-section is obtained by varying the flanges' widths. The thickness of the flanges is kept constant for all calculations. The mono-symmetry is characterizes hereafter by the parameter ψ_{mono} defined by equation (4.74).

$$\psi_{mono} = \frac{I_{z,cFl} - I_{z,TF}}{I_{z,cFl} + I_{z,TF}} \tag{ 4.74 }$$

It should be noted that:

- For double symmetric cross-section $\psi_{mono} = 0$;

- For mono-symmetric sections whose tension flange's second moment of area is greater than the compression flange's second moment of area $\psi_{mono} < 0$;
- For mono-symmetric sections, whose compression flange's second moment of area is greater than the tension flange's second moment of area $\psi_{mono} > 0$ (common case).

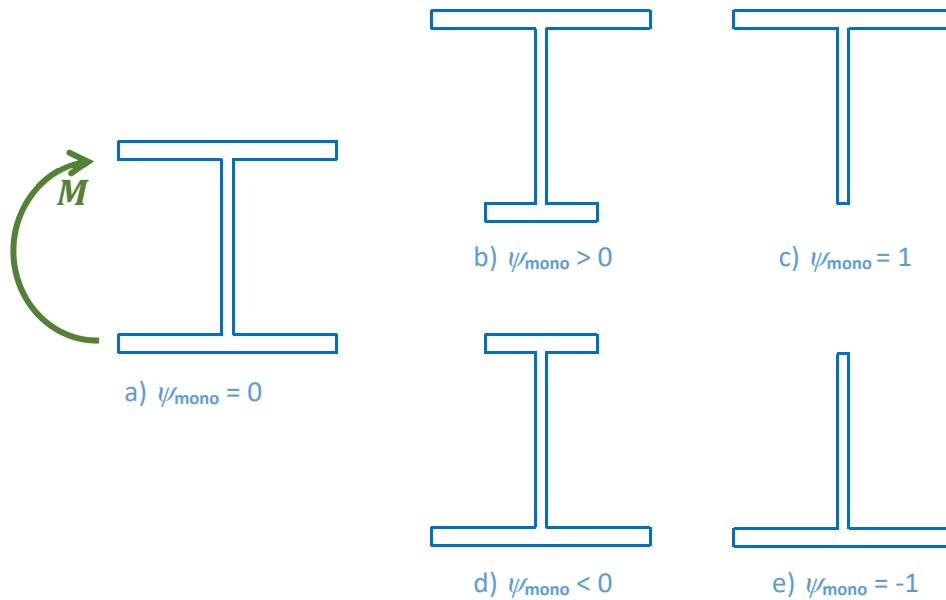


Figure 4-63: Derivation of mono-symmetric cross-section from their double symmetric original

So as to illustrate the influence of the mono-symmetry parameter ψ_{mono} , Figure 4-64 represents the IPE 600 section and its mono-symmetric derivatives.

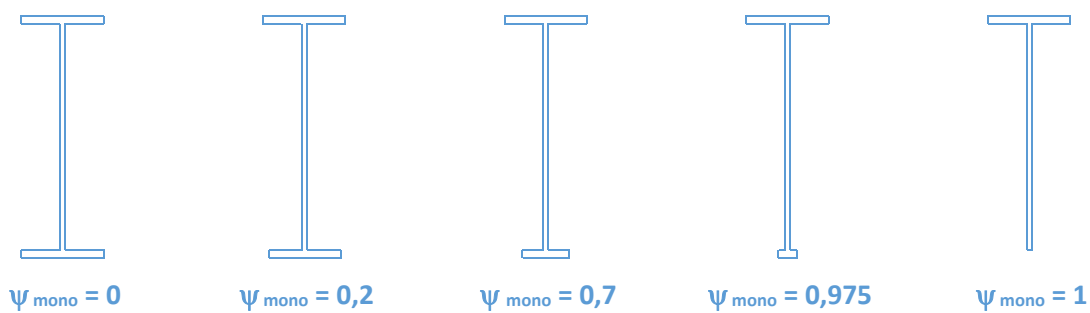


Figure 4-64: Geometry of IPE 600 section and of its mono-symmetric derivatives

First, the results obtained for the HEA 100 cross-section and its mono-symmetric derivatives are given in Figure 4-65. The results for all cross-sections are represented in the same diagram. For a given section, the obtained resistance is given with reference to its own theoretical plastic resistance. Consequently, if two different cross-sections possess a ratio $M_{ult,i}/M_{pl,i}$ of 1,0 they do not possess the same value of the ultimate moment but they attain their respective plastic moment resistance at plastic limit state. Also, Figure 4-65 shows the standardized interaction curves based on the plastic moment resistance of each cross-section and the plastic shear resistance of the web.

It is proposed here to apply the same simplified interaction equation as used for double symmetric I sections again.

It may be observed that, for the plastic cross-section interaction, it has no influence whether the smaller flange is in compression or in tension. In fact, the results obtained for the same absolute value of ψ_{mono} practically overlap. Additionally, it can be seen that the results are grouped. A major difference can only be observed for the T cross-section ($\psi_{mono} = \pm 1$). Nevertheless, it seems that the general form of Eurocode 3 plastic cross-section interaction yields safe-sided results, if it is based on the shear resistance of the web and the plastic moment resistance of the cross-section.

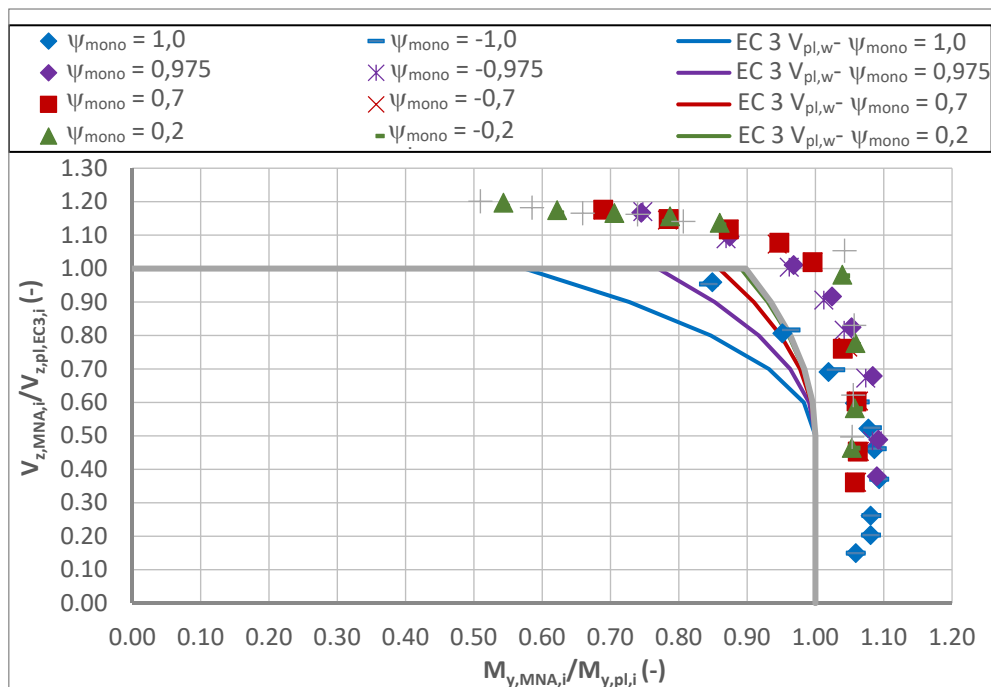
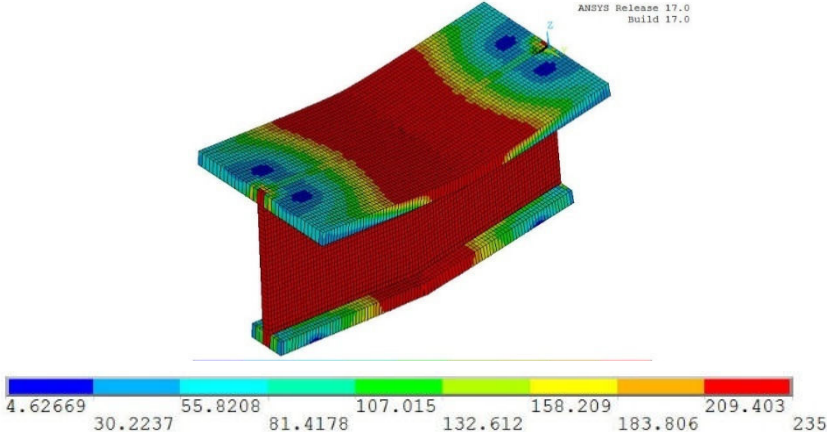


Figure 4-65: Numerical M_y - V_z plastic cross-section interaction for HEA 100 and its mono-symmetric derivatives

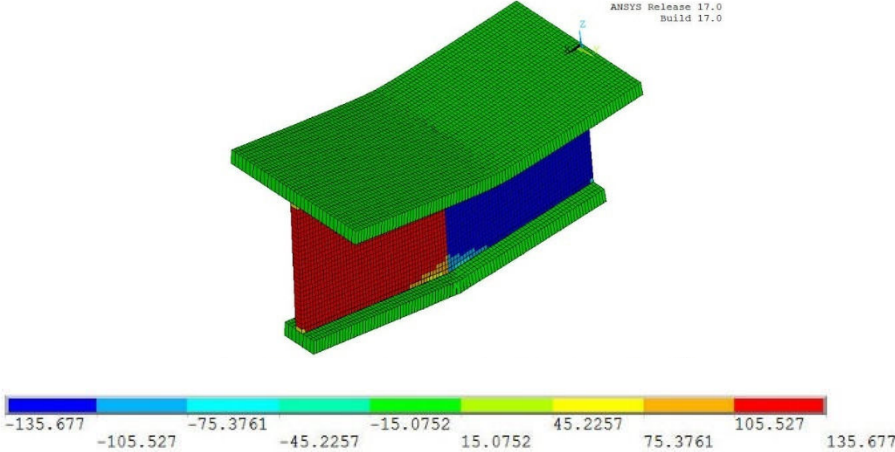
In addition to the interaction curve, it seems interesting to study the stress distribution over the cross-section, especially for the case of high mono symmetry and high shear forces. Figure 4-66 and Figure 4-67 show the results obtained for the cross-section of $\psi_{mono} = 0,975$ and $\psi_{mono} = 1,0$ and a shear force at the plastic limit state of $1,1 V_{pl,w,0,975}$ and $0,95 V_{pl,w,1,0}$, respectively. For a better representation, the stiffener and the force applied at mid-span are not represented.

It can be seen that, at the plastic limit state, the cross-section at mid-span has entirely yielded. Also, one may observe the influence of plastic zones, leading to a spreading of plasticity along the member. For both cases, the compressed flange and the lower part of the cross-section yields due to axial stresses at mid-span. However, the shear stress distribution in the web differs. In fact, Figure 4-66 shows that the total height of the web yields due to shear for the mono-symmetric section with $\psi = 0,975$. Contrariwise, in the case of the T section, the shear stresses only lead to yielding of the upper part of the web as the axial stresses already utilize completely the lower part. Consequently, it seems not astonishing that the major-axis bending moment resistance suffers a higher strength reduction at a given load level of the shear force for T sections than for mono-

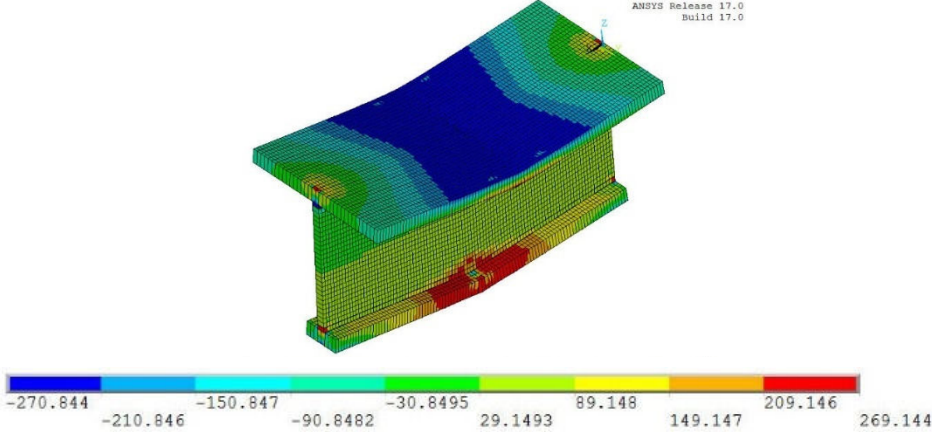
symmetric sections possessing two flanges. Obviously, the interaction formula given for double symmetric sections is not fully consistent in the case of mono-symmetric I sections as the plastic neutral axis in bending is not located at mid-height of the web. However, its application leads to safe results. Consequently, its application may be accepted. Also, applying the same interaction equation contributes to the unification of the design formulae.



a) Distribution of von Mises stresses



b) Distribution of shear stresses in the web



c) Distribution of axial stresses

Figure 4-66: Stress distribution for $\psi_{mono} = 0,975$ and $L = 2h$ at PLS

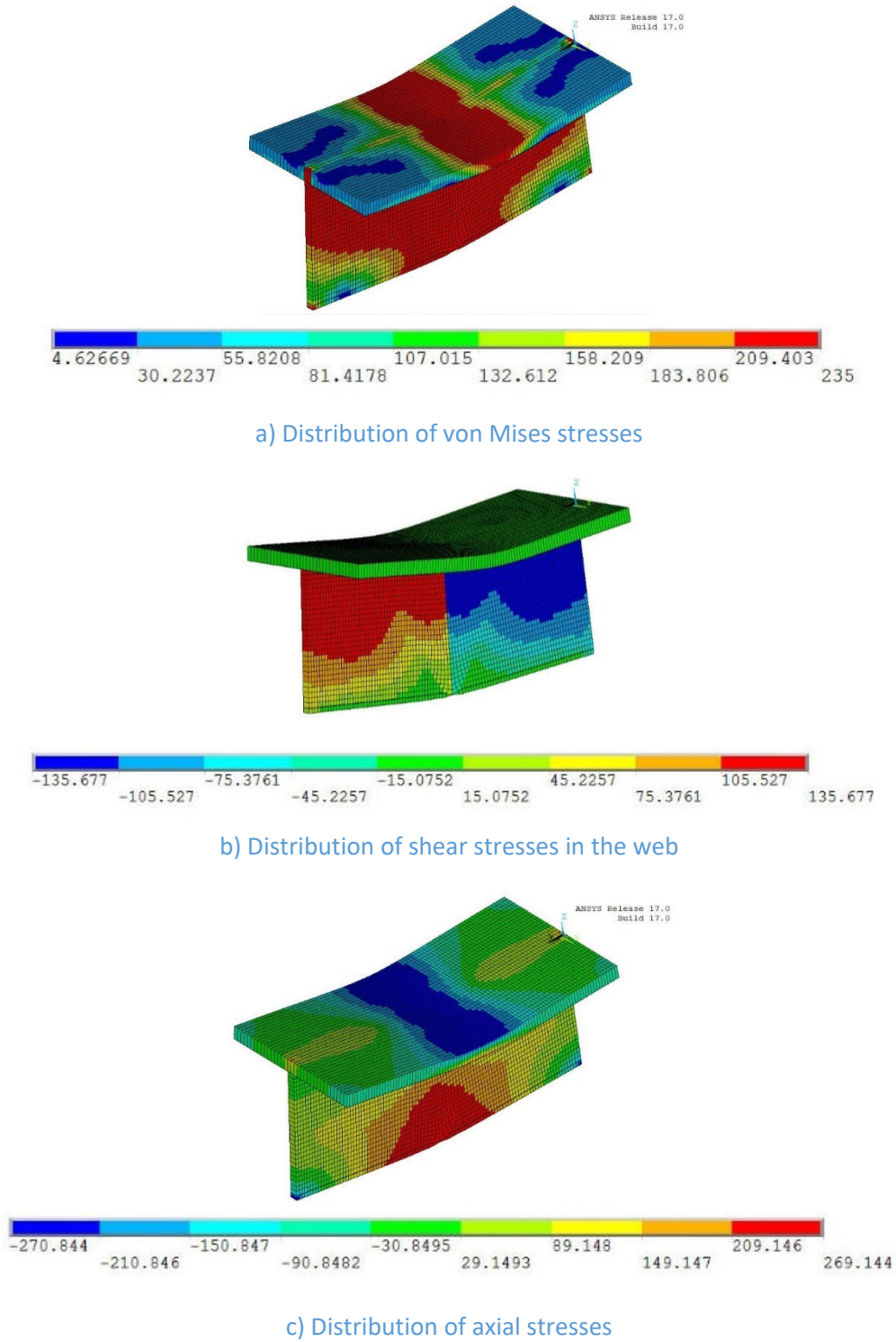


Figure 4-67: Stress distribution for $\psi_{mono} = 1,0$ and $L = 2h$ at PLS

Hereafter, the results obtained for other section geometries are represented. As it has no influence whether the tension flange is the smallest or not, only results corresponding to a positive value of the factor ψ_{mono} are given.

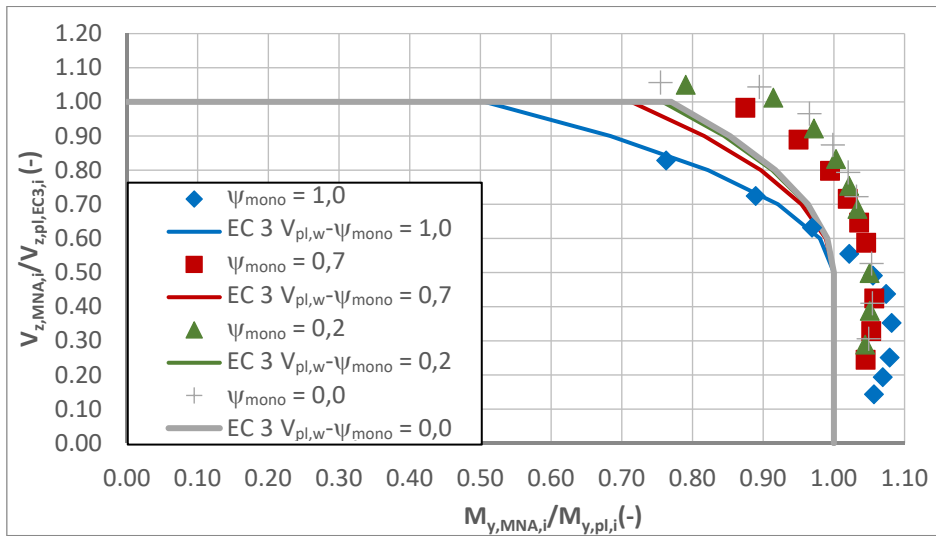


Figure 4-68: Numerical M_y-V_z plastic cross-section interaction for IPE 360 and its mono-symmetric derivatives

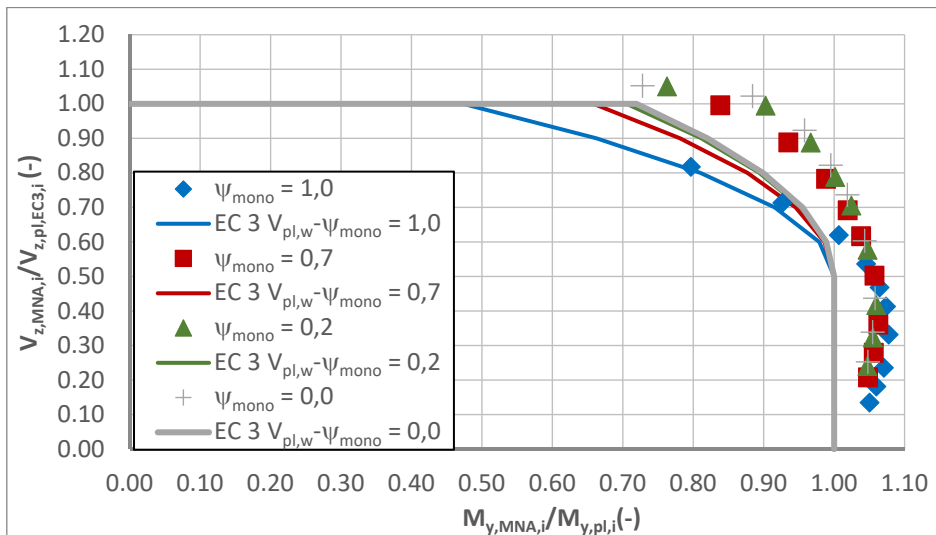


Figure 4-69: Numerical M_y-V_z plastic cross-section interaction for IPE 600 and its mono-symmetric derivatives

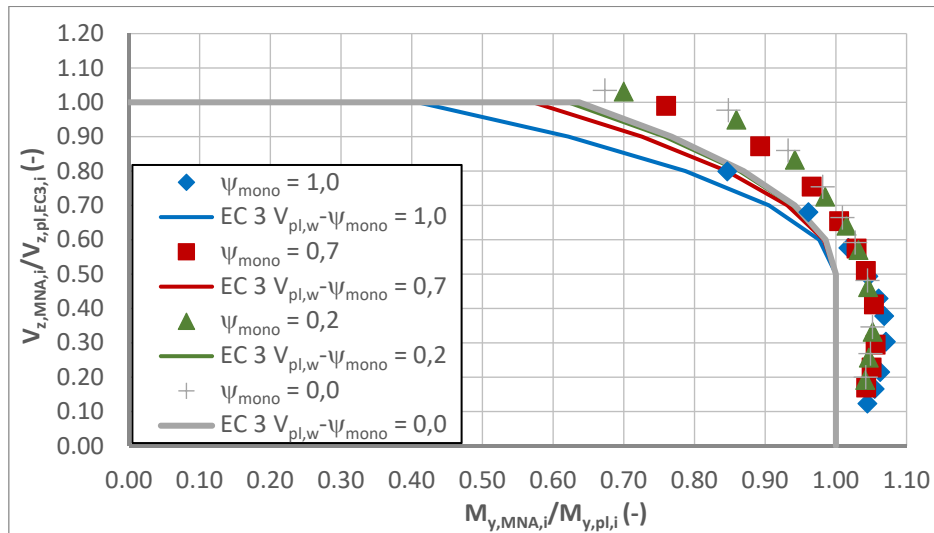


Figure 4-70: Numerical M_y - V_z plastic cross-section interaction for W 1450.12.300.25 and its mono-symmetric derivatives

Figure 4-68 to Figure 4-70 confirm the conclusions obtained for the cross-section HEA 100 and its derivatives. The interaction formula yields only one slightly unsafe result in case of the T section based on IPE 360. Yet, the member length is equal to 1,5 times the section height and consequently at the very lower bound of practical interest. Hence, it is concluded that the Eurocode 3 interaction formula may be applied if it is based on the shear resistance of the web and the plastic moment of the cross-section. It seems also justified to neglect the influence of the shear force on the plastic moment resistance if the ratio $V_z/V_{z,pl}$ is less than or equal to 0,5.

4.4.3 Interaction between minor-axis bending and shear force

4.4.3.1 Double symmetric I sections

In the following, the interaction between minor-axis bending and the associated shear force is studied. Admittedly, the interaction is of less practical interest as the interaction between major-axis bending and the associated shear force because the shear force acting parallel to the flanges is even less important than the shear force acting parallel to the web in practical cases. Yet, Eurocode 3 does not propose any provisions and therefore, it seems necessary to study this load case. For I sections, the M_z - V_y plastic interaction may be assimilated to the interaction for a simple plate as the shear stresses only transit through the flanges. However, in order to evaluate the influence of the fillets and the web on the resistance of the cross-section, three different section geometries are studied. As before, the member is supposed to possess end fork supports and the material is supposed to follow an elastic perfectly plastic material law. The results are represented in Figure 4-71 to Figure 4-73. Also, the interaction curve resulting from the application of Eqs. (4.75) and (4.76) is represented.

$$M_{z,pl,V} = M_{z,pl} - \frac{b_f^2 t_f}{2} \rho f_y \quad (4.75)$$

$$\rho = 0 \quad \text{for } V_y \leq 0,5V_{y,pl}$$

$$\rho = \left(\frac{2V_y}{V_{y,pl}} - 1 \right)^2 \quad (4.76)$$

Figure 4-71 to Figure 4-73 show again that load cases LC1 and LC2 yield very similar results. Yet, LC4 leads to rather conservative results, especially for shear forces less than 70% of the plastic shear resistance defined by Eurocode 3. This can again be explained as LC4 supposes that shear force and bending moment are completely independent. Therefore, the beneficial influence of the variation of the bending moment is not considered.

On Figure 4-71 to Figure 4-73, one may observe that there is a plateau on the interaction curve for low values of the bending moment. This plateau is especially pronounced for the cross-section HEAA 1000. In fact, if the applied bending moment M_z is less than the minor-axis bending moment resistance of the web (and of the fillets), there is no interaction as the shear stresses only transit in the flanges. Admittedly, the plateau is not of practical interest as the shear force cannot attain high values if the bending moment tends to 0. Also, the strains necessary to mobilize the yielding of the web are very high and, depending on the cross-section, may exceed the minimum strain at failure of 15% defined by Eurocode 3 Part 1-1.

The following figures clearly show that the interaction between minor-axis bending and the associated shear force may be neglected. Indeed, it should be noted that shear forces exceeding the value of $0,5V_{pl}$ are linked to very short members with lengths of about 1,5 times the flanges width.

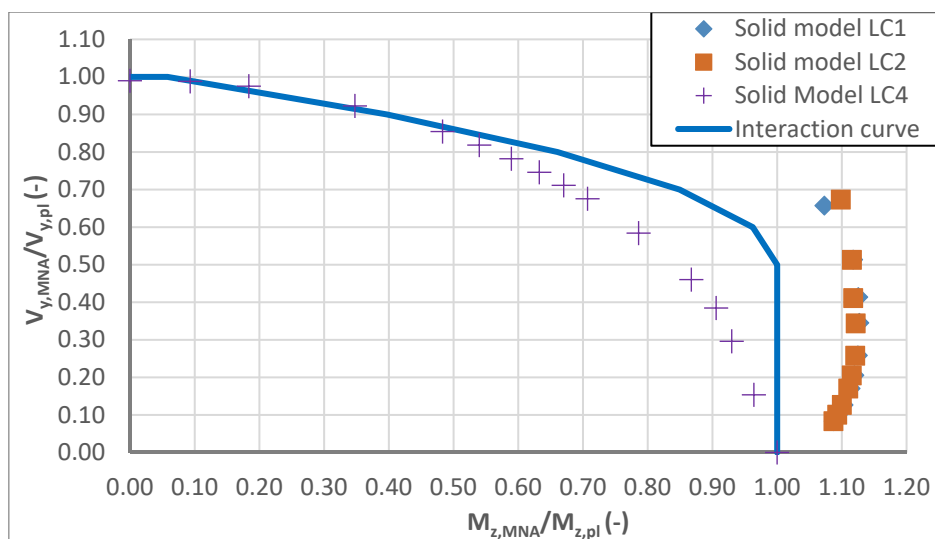


Figure 4-71 : M_z - V_y plastic cross-section interaction diagram for HEM 100

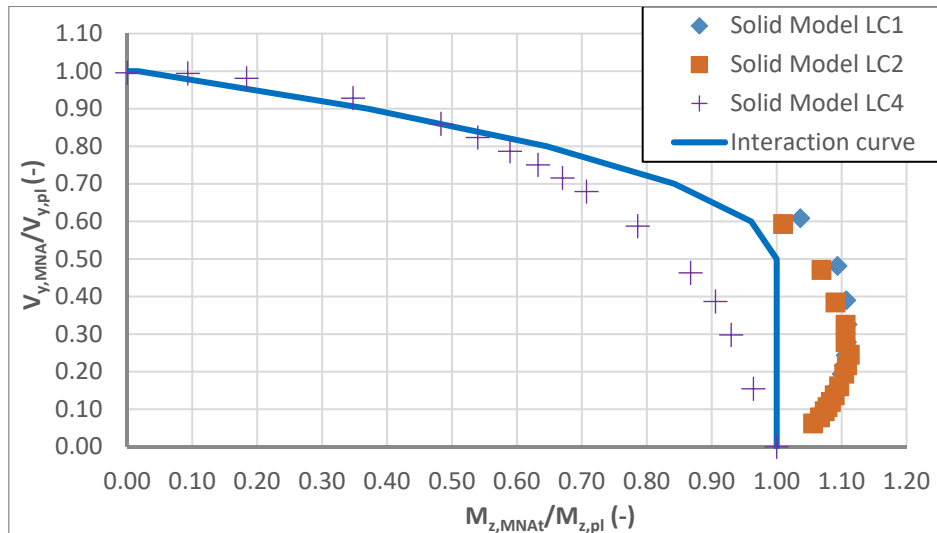


Figure 4-72: M_z - V_y plastic cross-section interaction diagram for HEA 280

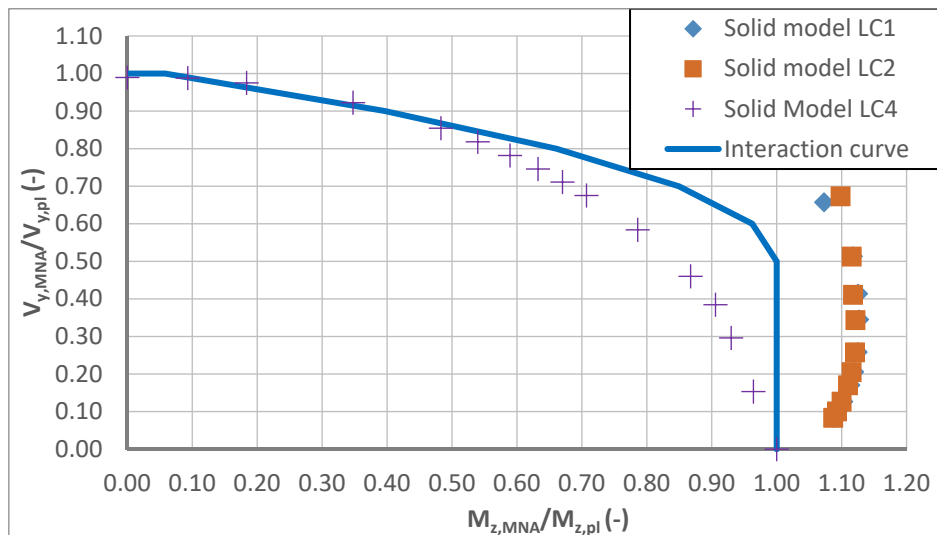


Figure 4-73: M_z - V_y plastic cross-section interaction diagram for HEAA 1000

4.4.3.2 U sections

The following figures represent the results obtained for the three U sections UPE 80, UPE 200 and UPE 360. For the UPE 80 section the results for load cases LC1 and LC2 are represented. For the other sections only LC1 is considered as the load case has again only insignificant influence on the results. Figure 4-74 to Figure 4-76 also represent the quadratic interaction curve given in Eq. (4.79) and Eq. (4.80).

$$M_{z,pl,V} = M_{z,pl}(1 - \rho) \tag{4.77}$$

$$\rho = 0 \quad \text{for } V_y \leq 0,5V_{y,pl} \tag{4.78}$$

$$\rho = \left(\frac{2V_y}{V_{pl,y}} - 1 \right)^2 \quad \text{elsewise}$$

The figures given hereafter, show that the interaction curve is safe-sided. It may even be considered that the interaction is negligible as before for I sections. Only for shortest member of UPE 80 section this would be unsafe. However, the member length is of only once the member height. Obviously, such short members are again out of the range of practical interest.

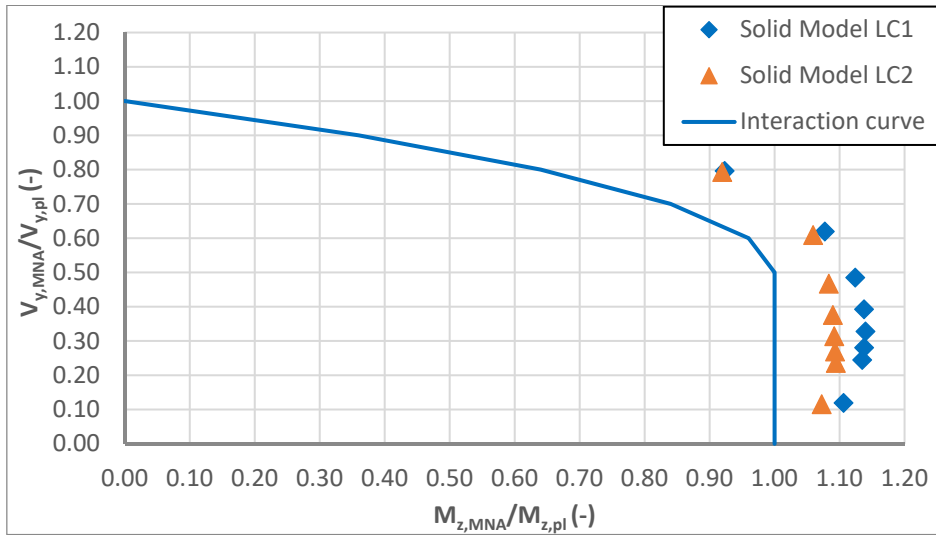


Figure 4-74 : M_z - V_y plastic cross-section interaction diagram for UPE 80

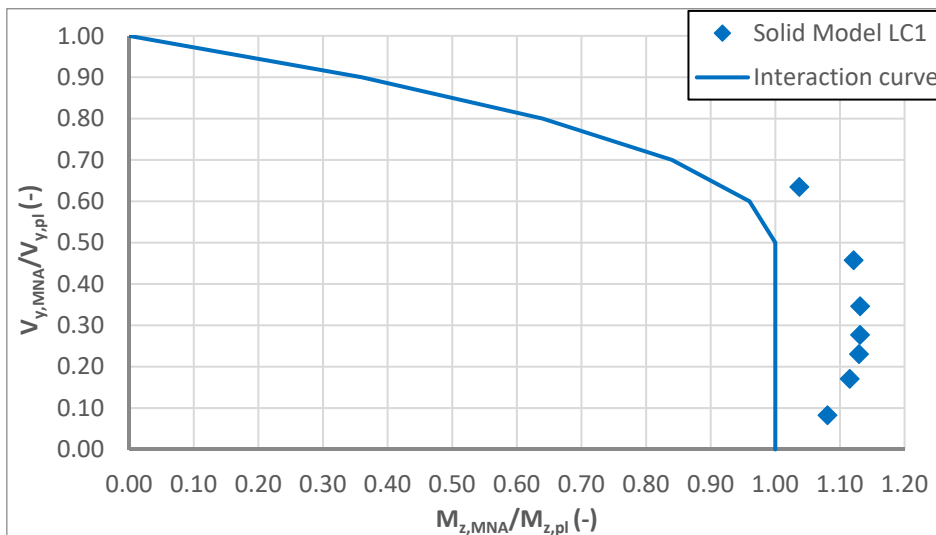


Figure 4-75 : M_z - V_y plastic cross-section interaction diagram for UPE 200

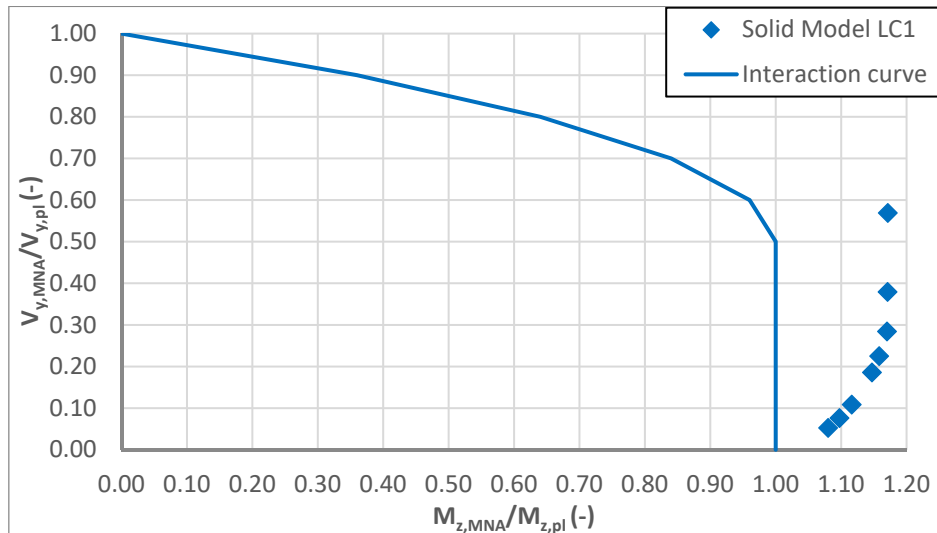


Figure 4-76 : M_z - V_y plastic cross-section interaction diagram for UPE 360

4.4.3.3 Mono-symmetric I sections

Last the interaction between minor-axis bending and the shear force V_y is studied for mono-symmetric I sections. Before the interaction behaviour is addressed, it is necessary to go back to the plastic minor-axis bending moment. In fact, as for U sections under major-axis bending, mono-symmetric I section cannot entirely yield under applied minor-axis bending without stress induced bi-moments as may be observed in Figure 4-77. By integrating the plastic stress distribution over the cross-section one obtains the plastic minor-axis bending moment of:

$$M_{z,pl} = M_{z,pl,uf} + M_{z,pl,lf} = \frac{b_{uf}^2 t_{uf}}{4} f_y + \frac{b_{lf}^2 t_{lf}}{4} f_y \quad (4.79)$$

The resulting bi-moment is given in Eq. (4.84).

$$B_{Mzpl} = -\left(z_{S,uf} M_{z,pl,uf} - z_{S,lf} M_{z,pl,lf} \right) \quad (4.80)$$

The sign “-” in Eq. (4.80) directly results from the sign convention used in the framework of this thesis. The distances $z_{S,uf}$ and $z_{S,lf}$ represent the distances between the shear centre and the upper flange and the shear centre and the lower flange, respectively. The same expression has also been derived in reference (Glitsch 2008). Obviously, the bi-moment vanishes for double symmetric I sections, as the distances $z_{S,uf}$ and $z_{S,lf}$ are equal, and for T sections as they do not possess a second flange. Between these two extrema and depending on the cross-section geometry the stress induced bi-moments develops. Yet, as before these stress induced bi-moments do not decrease the plastic section resistance to minor-axis bending moments.

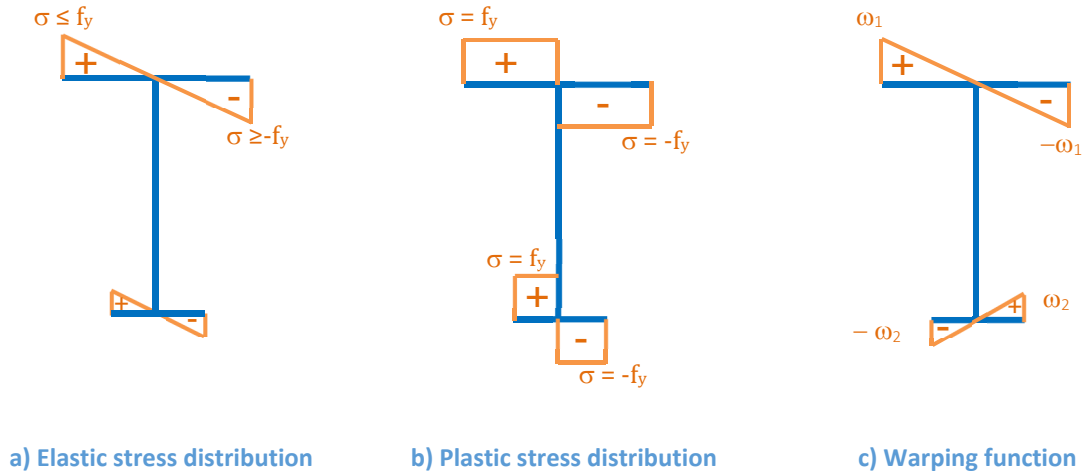


Figure 4-77: Elastic and plastic stress distribution and warping function for a mono-symmetric I section

The two following figures represent the interaction behaviour for sections HEA 100 and its mono-symmetric derivatives as well as section IPE 600 and its mono-symmetric derivatives. The length of the members is varied between twice the section height and 8 times the section height. Figure 4-78 and Figure 4-79 show that even for the shortest members the shear force is rather low. Moreover, it may be observed again, that the shear force does not reduce the plastic minor-axis bending moment. Also, as stated before, the stress induced bi-moment develops in all cases and allows the cross-section to attain its theoretical plastic resistance.

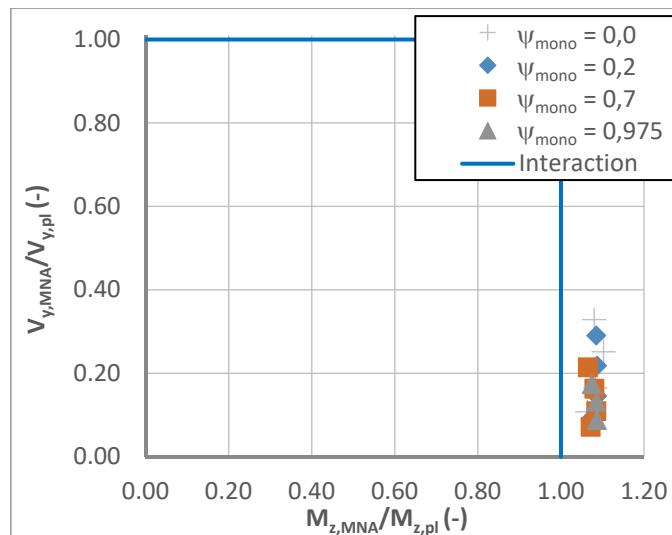


Figure 4-78: M_z - V_y plastic cross-section interaction diagram for HEA 100 and its mono-symmetric derivatives

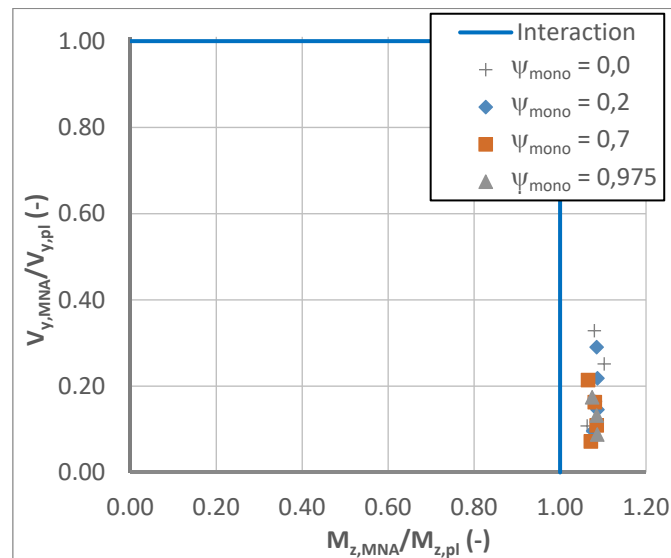


Figure 4-79: M_z - V_y plastic cross-section interaction diagram for IPE 600 and its mono-symmetric derivatives

4.4.3.4 Conclusions

Before the case of applied torsion is studied in detail it seems necessary to summarize the results obtained here before for the interaction between major-axis bending and shear forces as well as minor-axis bending and shear forces. The numerical study based on MNA simulations has shown that:

- Complex 3 dimensional stress fields developing at the plastic hinge as well as the spreading of plasticity along the member have a beneficial effect on the cross-section resistance leading to bending moments at plastic limit state that exceed the theoretical plastic bending moment resistance in case of low shear forces.
- In practice, the load case has only insignificant influence on the generation of these 3 dimensional stress fields or the spreading of plasticity. The cross-section interaction behaviour is therefore independent from the load case.
- The Eurocode 3 plastic interaction formula for combined major-axis bending and shear force given for double symmetric I sections may also be applied for U sections and mono-symmetric I sections.
- For practical cases, the minor-axis bending moment is not reduced by the influence of shear forces. Consequently, it is recommended to neglect the interaction.
- Stress induced bi-moments are necessary for mono-symmetric I sections to yield entirely under minor-axis bending and for U sections to entirely yield under major-axis bending.
- These stress induced bi-moments do not influence the cross-section interaction behaviour as they directly result from the stress distribution. However, they

induce a torsional twist to the member. Nevertheless, the torsional twist is low for members sufficiently short to attain their plastic resistance without lateral-torsional buckling (see Chapter 5).

- The shear resistance $V_{y,pl}$ may be based on the shear area equal to the area of the two flanges.

Hereafter the study is extended to the case of applied torsion.

4.4.4 Interaction between bending, shear force and torsion

4.4.4.1 *Influence of the plastic torsional system reserve of the member*

The study of the interaction behaviour presented in the previous paragraphs has been based on MNA calculations and hence plastic analysis of the studied members. For statically determined structures, as the members studied here, this is generally not remarkable as the internal forces and moments evolve linearly with the applied loads up to the formation of the first plastic hinge. Inversely, for statically non-determined structures, the internal forces and moments do not increase linearly with the applied loads due to plastic redistribution after formation of the first plastic hinge. For members subject to torsion, a certain parallelism to statically non-determined structures may be observed as shown in Figure 4-80. This figure compares the ratio between the major-axis bending moment and the bi-moment obtained by plastic analysis (MNA) and their values obtained by linear elastic analysis (LA) of the same member (UPE 200 with a length of 1 m subject to a point load with an eccentricity y_F of approx. 14 cm). It can be seen that plastic and elastic analysis yield the same value for the major-axis bending moment. However, for load factors greater than 0,65, the difference between the bi-moment determined by plastic and elastic analysis increases rapidly. In fact, due to yielding of the cross-section at mid-span, the warping stiffness decreases locally. This leads to the formation of a “warping hinge” at mid-span. Yet, the plastic limit state is not attained as the cross-section has not fully yielded and the additional torsional moment may be carried by shear stresses resulting from Saint Venant’s torsion. In order to illustrate this observation, Figure 4-81 shows the von Mises stress distribution for the studied member for a load factor of 0,80 and 1,00 (corresponding to points I and II in Figure 4-80). In Figure 4-81a), it may be seen that the flanges of the cross-section have entirely yielded leading to an important loss of warping stiffness at mid-span. However, the web is able to carry supplementary stresses as it has not yielded over its total height. Therefore, the load may be increased further on and the supplementary torsional moment is carried through shear stresses generated by Saint Venant’s torsion developing between the warping hinge and the supports of the member.

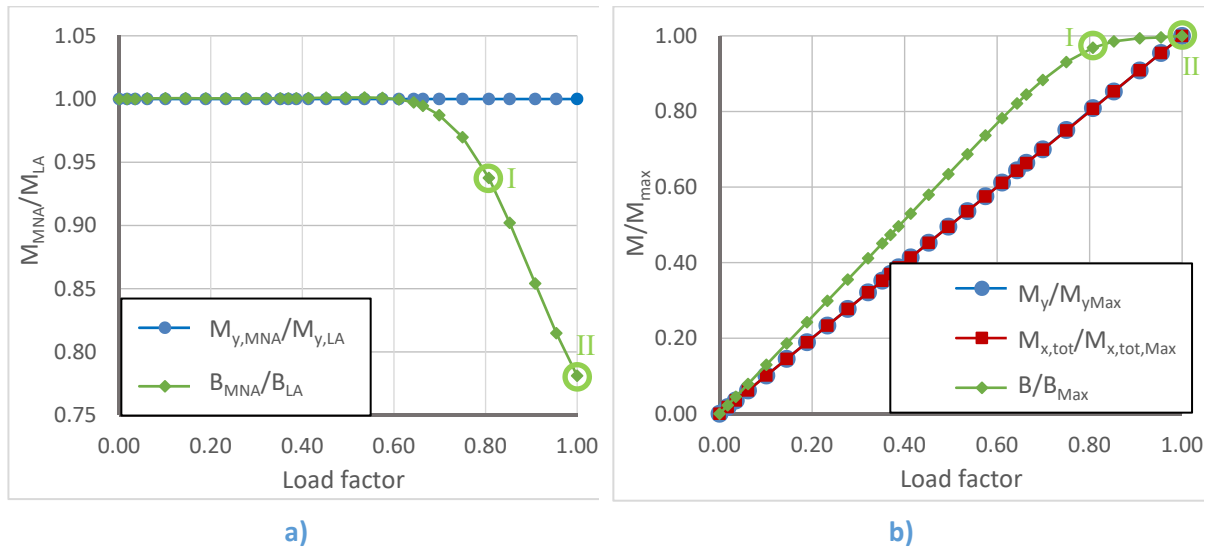


Figure 4-80: a) Ratio between internal moments obtained by plastic and elastic analysis at mid-span and b) Evolution of the internal moments with the load factor

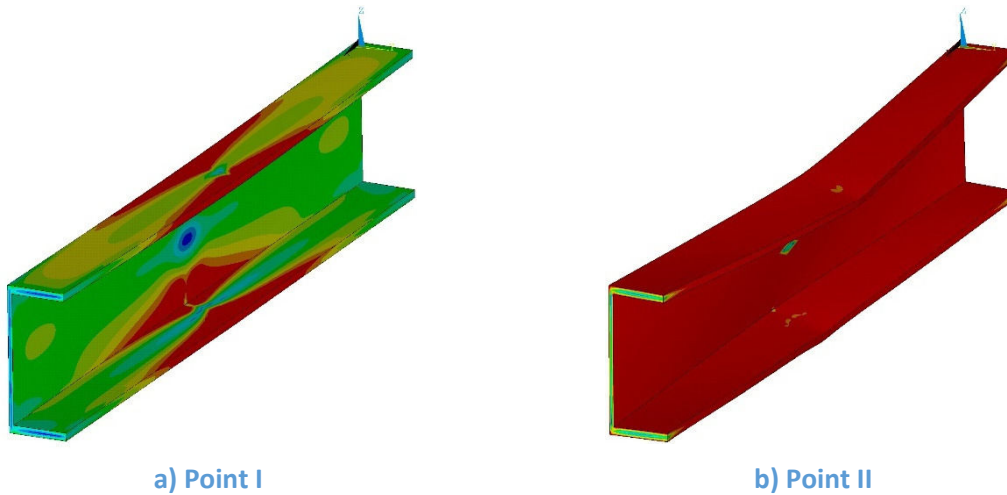


Figure 4-81: Von Mises stresses at a) point I and b) point II of Figure 4-80

The torsional system reserve described here before is not specific to U sections but to all open sections possessing a considerable warping stiffness. Inversely, as the warping constant of T sections is close to zero, axial stresses due to warping do not develop (this is discussed in more detail in 4.4.4.3) and hence even before yielding is initiated, the torsional moment is carried through Saint-Venant's torsional shear stresses. Consequently, this type of section does not possess any supplementary reserve.

The torsional system reserve may lead to a considerable increase of the load that may be carried by the member. However, it should be noted that the torsional twist also highly increases compared to an elastic analysis as the member loses its warping stiffness. If the torsional system reserve is implicitly included in the design method, as has been done for example in reference (Glitsch 2008) (see paragraph 5.4.4), the designer completely loses the control about the torsional twist of the member at failure. Hence, the engineer is not capable to verify whether the deformations of the member are compatible with its position in the real structure (stiffness,

rotation capacity and resistance of the joints and connected members and equipment). Additionally, it has been shown in Figure 4-81 that important Saint-Venant's torsional moments develop that lead to yielding of the member over its length. These Saint-Venant's torsional moments may obviously not be determined with an elastic analysis based on the initial warping stiffness of the member. However, they should be accounted for if the torsional system reserve is exploited. It may therefore be concluded that:

- Members of open cross-section that have a considerable warping stiffness (I and U sections but not T sections) possess a certain plastic torsional system reserve that leads to the complete yielding of the whole member and not only to yielding of the most loaded cross-section.
- The plastic torsional system reserve is mobilised after the creation of a warping hinge and leads to a considerable increase of the loads that may be carried by the member.
- After formation of the warping hinge, the torsional behaviour of the member has completely changed; additional torsional moments are not carried principally through warping torsion but exclusively by Saint-Venant's torsion. Due to the small Saint-Venant's torsional stiffness (GI_t) of members with open cross-section the torsional twists highly increase after formation of the warping hinge.
- For simplified design based on an elastic analysis of the member the plastic torsional system reserve should be neglected. Yet, it may be accounted for when the member is analysed plastically.

A simplified method to account for the torsional plastic system reserve may be developed based on the equivalence between the second order (in-plane) equilibrium of members under combined axial tension forces and bending and the behaviour of members of open section subject to torsion as has been discussed for the case of elastic analysis in paragraph 2.4. This equivalence can be extended into plasticity. So as to illustrate this fact, a member of IPE 500 section with a length of 5,4 m is studied. The member, fabricated from steel S235, is subject to a vertical point load at mid-span. Finally, it is supposed that the member possess simple supports at its ends that are **both restrained against axial displacement**. The static system of the member is represented in Figure 4-82.

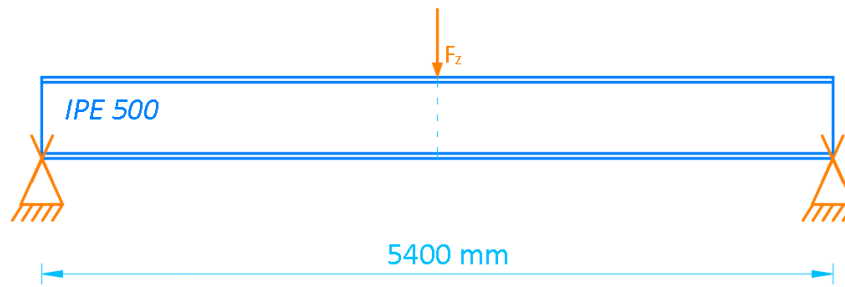


Figure 4-82 : Studied member

It is supposed to be restrained against lateral displacement and torsional twist along its total length to prevent the member from lateral-torsional buckling. The member is analysed through second order plastic analysis but without imperfection (GMNA). The material is supposed to follow an elastic-perfectly plastic law. The second order effects have to be accounted for to represent the equivalence of a member in bending to members under torsion. Finally, it should be noted that the member is modelled with beam elements in order to avoid local plate instability before the formation of the plastic hinge. As the shear force is low the interaction with the major-axis bending moment can be neglected and consequently, the beam elements can be used.

The obtained load displacement curve is shown in Figure 4-83. It may be observed that it is characterised by five sections:

- A nearly linear part up to a vertical displacement of approximately 12 mm: in this section of the load displacement diagram the member attains the elastic major-axis bending moment at a load level of $P_{My,el} = 248$ kN. With starting yielding the stiffness of the member decreases but less as would be expected for members in bending due to the beneficial second order effects arising from the tension axial force.
- At a mid-span vertical displacement of approximately 27 mm the plastic hinge in bending is formed and the member therefore loses its total bending stiffness.
- After the formation of the plastic bending hinge the applied load continues to increase due to the catenary effect. Also, the stiffness of the member increases as the catenary effect is amplified with increasing vertical displacement.
- At a vertical mid-span displacement of approximately 275 mm, the section located at mid-span starts to be highly used by the increasing axial force and consequently the stiffness decreases again up to the complete transformation of the plastic bending hinge into a plastic axial displacement hinge.
- Finally, after the formation of the plastic axial displacement hinge the load cannot increase anymore and the peak load is therefore attained at a vertical mid-span displacements of approximately 370 mm.

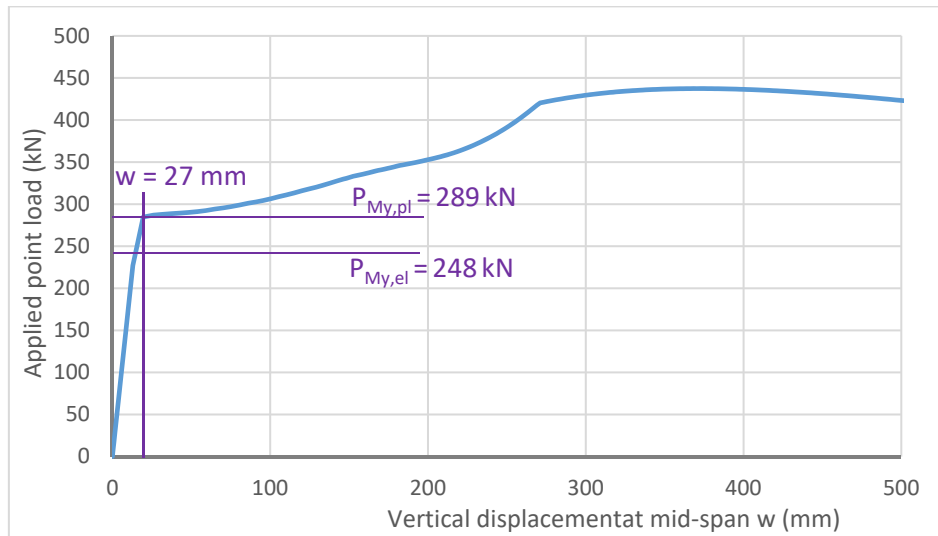


Figure 4-83 : Load displacement curve

It seems also interesting to compare the evolution of major-axis bending moment as well as the evolution of the axial force with the vertical displacement at mid-span. In Figure 4-84, one may clearly identify the catenary effect. Indeed, the axial force is practical equal to zero up to a vertical mid-span displacement of 12 mm. At this point, the member starts to yield at mid-span as the elastic major-axis bending moment is attained. Due to spreading of yielding, the vertical displacements increase rapidly and consequently, the axial force as well as the catenary effect increase. The plastic bending hinge is generated at a vertical displacement of 27 mm (Point A of Figure 4-84). As the member is statically determined (for vertical loads), the bending moment cannot be redistributed. Moreover, the bending moment at mid-span reduces and practically vanishes when the axial force attains its maximum value for a vertical displacement of 370 mm (Point B of Figure 4-84).

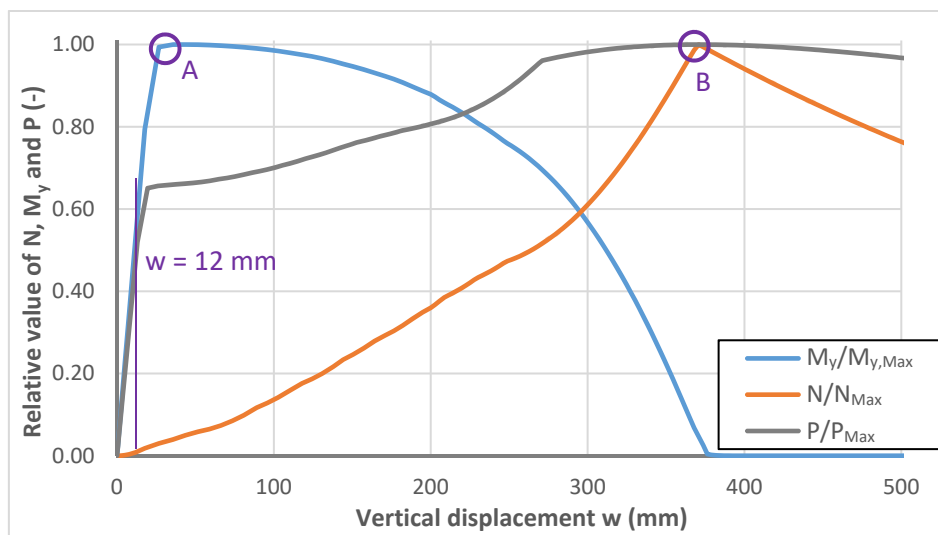


Figure 4-84 : Evolution of the major-axis bending moment and the axial force with the load factor

The axial stress distribution for the member is represented in Figure 4-85 for point A of Figure 4-84. The plastic hinge generated by the major-axis bending moment may be easily identified.

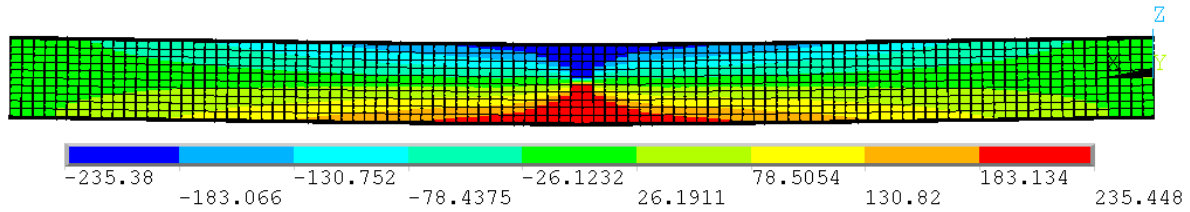


Figure 4-85 : Axial stress distribution for load level corresponding to $M_{y,pl}$

Due to the increasing axial force, the major-axis bending moment has to decrease at mid-span and this is possible as the member does not possess any global bending stiffness after the formation of the plastic bending hinge. The supplementary load is transferred to the supports by the axial force and the member consequently behaves similarly to a cables. Finally, Figure 4-86 presents the distribution of axial stresses at mid-span at B of Figure 4-84 (the deformed shape is not represented). The observed stress distribution clearly indicates yielding under the tension axial force at mid-span. It should be noted that the maximum value of the axial stress exceeds 235 MPa as “real” stresses are represented and not “engineering stresses”. For high strains the differences between both become relevant ($\sigma_{real} = \sigma_{engin}(1+\epsilon)$).

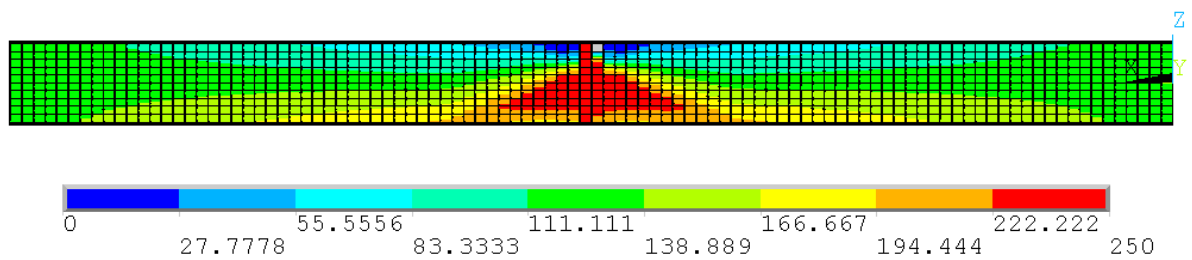


Figure 4-86: Axial stress distribution at the peak load level

The example treated above reveals that the plastic torsional system reserve of members of open cross-section subject to torsion is similar to the catenary effect for members subject to bending. For members in bending the catenary effect is exploited in particular in fire design situations and for structures subject to blast loads (FABIG 2002). Indeed, in this design situation one can accept the failure of the structural element accompanied with high displacements. For other design situations, this is generally not acceptable. Consequently, the catenary effect is not accounted for for the design of members in non-accidental design situations. If the plastic torsional system reserve is exploited the torsional twist also increases highly. Yet, for short members it may be economic to account for the plastic warping hinge, as the torsional twist does not attain unacceptable high values in all cases. Here, it is proposed to allow for the plastic torsional system reserve in the analysis of the member and hence for the determination of the internal forces and moments but only in cases where the torsional twist is not incompatible with the deformation capacity of the possible structural elements attached to the member, i.e. especially for short members that are not sensitive to the effect of elasto-plastic member instability.

Anyhow, it appears that a completely analytical method cannot be developed as members subject to torsion are generally also subject to a complex interaction with over internal forces and

moments as for example major-axis and minor-axis bending and consequently it is not possible to determine exactly the load factor linked to the creation of the warping hinge. In fact, the plastic warping hinge is generated when yielding of a given cross-section along the member leads to a significant loss of the warping stiffness at this location. Still, first, it is difficult to define exactly what is “significant” and second, even if “the significant loss” may be quantified it seems even more difficult to determine the load combination that leads to this loss. In general, one may determine the load that leads to the elastic limit state and the load that leads to the plastic limit state of a section with a sufficient precision. Inversely, a load combination that results in a given reduction of the stiffness of a given section cannot be obtained easily.

As a simplified approach one could envisage to perform the analysis of the member in two steps:

- In a first step, the loads are increased up to complete yielding of the cross-section along the member that is subject to the maximum combination of major-axis bending, minor-axis bending, vertical shear force, axial force and **the bi-moment**. It is considered that the plastic warping hinge is generated at this load level.
- In a second step, the static system is transformed by generating a warping hinge at the location determined in the first step. The loads are then increased up to yielding of the member under the combination of major-axis bending, minor-axis bending, vertical shear force, axial force and **the Saint-Venant’s torsional moment**.

Obviously, depending on the boundary conditions, intermediate restraints and applied loads, several plastic warping may be generated before the plastic resistance of the member as a whole is attained. These more complex situations should only be treated by rigorous plastic analysis if it is intended to account for the torsional plastic system reserve.

So as to illustrate the possible procedure, the following example is treated:

- The member is of HEB 200 section (without fillets) subject to a constant major-axis bending moment of 119,6 kNm and a torsional moment applied at mid-span of 21,8 kNm.
- The length of the member is equal to 1,1 m.
- The member possess fork end support.
- The member is fabricated from steel S235.

Admittedly, this example may not be very current in practice (especially concerning the loading conditions) but it is used here for the ease of representation of the effects to be studied. The first order elastic analysis of this member leads to the following maximum internal forces and moments:

$$M_{y,Max} = 119,6 \text{ kNm}$$

$$M_{x,St.V,max} = 1,577 \text{ kNm}$$

$$M_{x,w,max} = 10,9 \text{ kNm}$$

$$M_{x,tot,max} = 10,9 \text{ kNm}$$

$$B_{max} = 5,41 \text{ kNm}^2$$

The distributions of the internal forces and moments linked to torsion are represented in Figure 4-87 and Figure 4-88. Due to the short length and consequently the low value of the warping decay factor ϵ_t , the member is principally subject to warping torsion and major-axis bending. The part of Saint-Venant's torsion is nearly negligible.

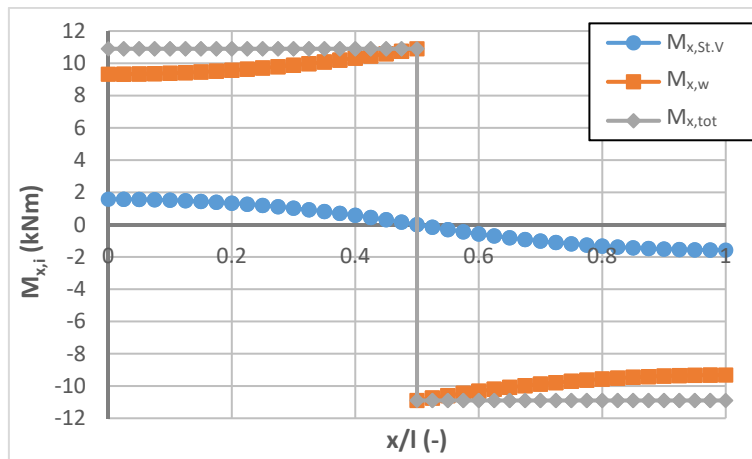


Figure 4-87: Distribution of the internal torsional moments

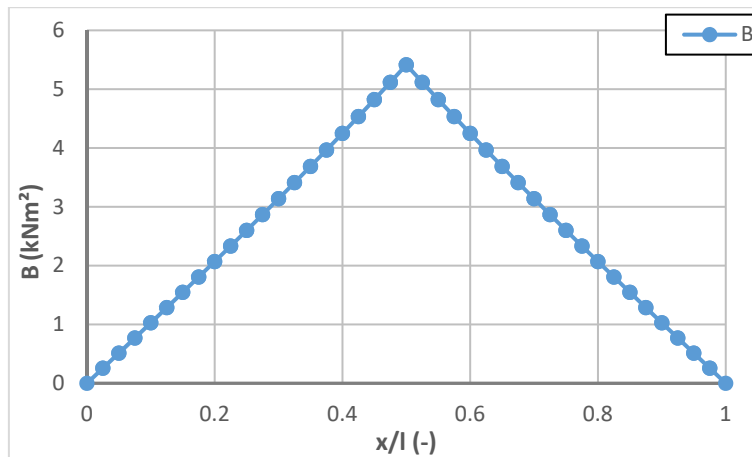


Figure 4-88: Distribution of the bi-moment

Based on the method that is developed in the following paragraphs (adaption of PIFM), it is possible to determine a plastic load amplification factor for the given load combination. It should be noted that only the bi-moment and the major-axis bending moment are considered because only these two act simultaneously at mid-span. The warping torsional moment is shown to be negligible in all cases in the following paragraphs.

The load factor linked to the plastic warping hinge ($R_{pl,wh}$) is obtained with the adapted PFIM (validated in paragraphs 4.4.4 to 4.5):

$$R_{pl,wh} = 0,777$$

The obtained result indicates that the plastic warping hinge is generated at load level corresponding to 78% of the applied loads. Nevertheless, the member may resist additional loads owing to the plastic torsional system reserve. The static system of the member is transformed and a warping hinge is introduced at mid-span. The new member is loaded with a constant major-axis bending moment of 26,67 kNm $((1-0,777)M_{y,max})$ and a torsional moment of 4,86 kNm applied at mid-span $(2*(1-0,777)M_{x,tot,max})$. The distribution of the obtained internal moments linked to torsion are again represented in Figure 4-89 (only the additional moments are represented). The additional torsional moment is carried exclusively through Saint-Venant's torsion as a result of the formation of the plastic warping hinge and consequently, neither an additional warping torsional moment nor an additional bi-moment are generated.

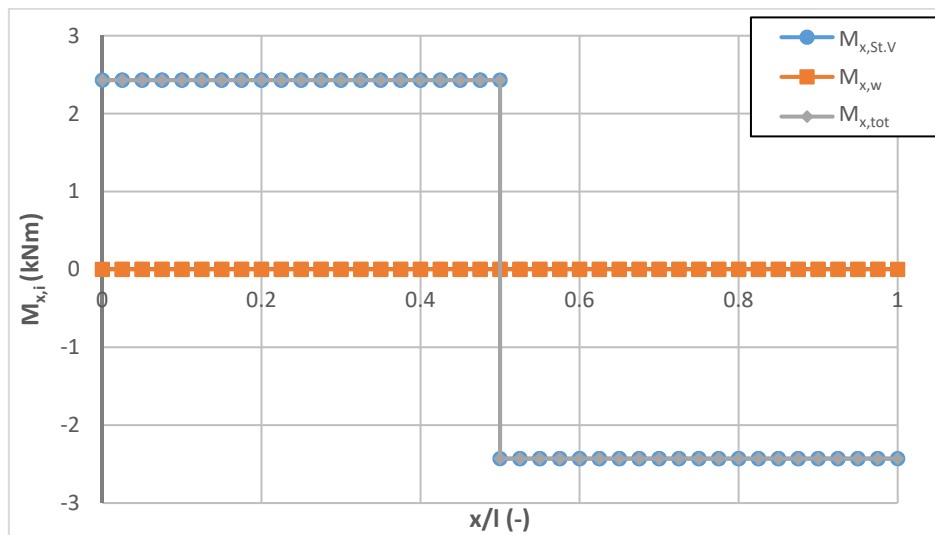


Figure 4-89: Distribution of the internal torsional moments for the member with warping hinge

The resulting internal forces and moments necessary to check the resistance of the member can be obtained as the sum of the internal forces and moments determined at the load level corresponding to the formation of the warping hinge and those determined by elastic analysis of the member possessing the warping hinge. Consequently, one obtains:

$$M_{y,Max} = 119 \text{ kNm} (= 0,777*119 \text{ kNm} + 26,67 \text{ kNm})$$

$$M_{x,St,V,max} = 3,66 \text{ kNm} (= 0,777*1,577 \text{ kNm} + 2,43 \text{ kNm})$$

$$M_{x,w,max} < 8,39 \text{ kNm}$$

$$M_{x,tot,max} = 10,9 \text{ kNm} (= 0,777*10,9 \text{ kNm} + 2,43 \text{ kNm})$$

$$B_{max} < 4,16 \text{ kNm}^2$$

It should be noted that neither the bi-moment nor the warping torsional moment, which act in the member at its plastic limit state, can be determined exactly. Obviously, the bi-moment has to decrease in order to allow the major-axis bending moment to increase at mid-span. At this location the member has entirely yielded when it attains the load level corresponding to the assumed plastic warping hinge and it stays entirely yielded up to the plastic limit state of the member. Consequently, the bi-moment at mid-span is always just equal to the bi-moment resistance of the section reduced by the influence of the major-axis bending moment.

The plastic resistance of the member can be checked based on the internal forces and moments determined after the second calculation step. For the example, the plastic interaction of the HEB 200 section subject to a Saint-Venant's torsional moment of 3,66 kNm and a major-axis bending moment of 119 kNm is checked. The adapted PIFM is again applied to obtain:

$$R_{pl} = 1,00$$

The member consequently just attains its plastic limit load.

So as to analyse the obtained result the member is calculated numerically with a MNA simulation based on the solid model of the studied member. The numerical results are represented in Figure 4-90 and Figure 4-91. Figure 4-90 represents the evolution of the major-axis bending moment, the total torsional moment and the bi-moment with the vertical displacement at mid-span. The reference values ($M_{y,max}$, $M_{x,tot,max}$ and B_{max}) are those obtained at the supposed plastic limit state of the member that has been determined here before.

In Figure 4-90, one may easily recognize the creation of the warping hinge for a vertical displacement of 2,4 mm. At this point the bi-moment attains its maximum. As the member has not completely yielded (also see Figure 4-93), the load can increase further on. Hence, the bi-moment has to decrease in order to allow an augmentation of the major-axis bending moment. The total torsional moment however increases further on (in Figure 4-90 the curves associated with $M_{x,tot}$ and M_y are superposed) and the additional torsion is carried by the Saint-Venant's torsional moment creating shear stresses over the member. The maximum load is attained for a vertical displacement of approximately 25 mm. At this point the member has (nearly) completely yielded (also see Figure 4-95) and does therefore not possess any additional stiffness (the material is supposed to behave elastic-perfectly plastic here). As the member has lost its complete stiffness the displacement increases without an increase of neither the major-axis bending moment nor the total torsional moment. Therefore the bi-moment stays constant, too. It is however to be noted that the major-axis bending moment does not completely attain the maximum value predicted by the simplified analysis method. The difference is of about 6%.

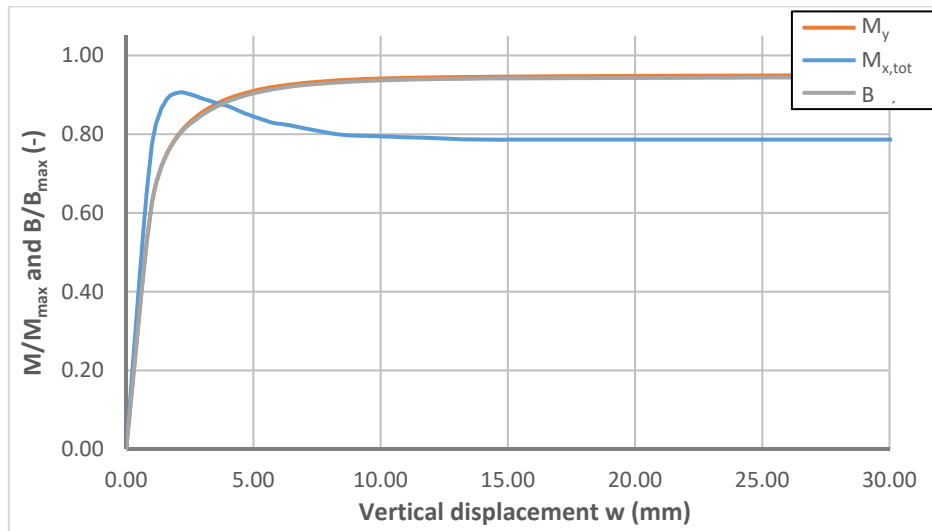


Figure 4-90: Evolution of the internal moments with the vertical displacement

Figure 4-91 represents the evolution of the major-axis bending moment and the bi-moment as a function of the load factor. Again, a load factor of 1,0 corresponds to the plastic limit state predicted by the simplified two step analysis method. Also, the load level corresponding to the predicted generation of the warping hinge (noted as $R_{pl,wh}$) as well as the load factor corresponding to first yield are represented. One may observe that the load level corresponding to the theoretical generation of the warping hinge is close to the load level linked to the maximum value of the bi-moment. Yet, it is to be noted that the evolution of the bi-moment is non-linear before the warping hinge is created. In fact, one may observe that the evolution of the bi-moment starts to be non-linear at a load level situated between first yield and the assumed generation of the warping hinge (point A of Figure 4-91). This indicates that the torsional load starts already to be carried by an increasing part of Saint-Venant's torsion at a lower load level than assumed by the simplified analysis. The Saint-Venant's torsional moment in the member is consequently higher than predicted and hence the plastic limit state is attained at a lower load level than the one obtained with the simplified method. This leads to the unsafe strength prediction observed for the simplified analysis method.

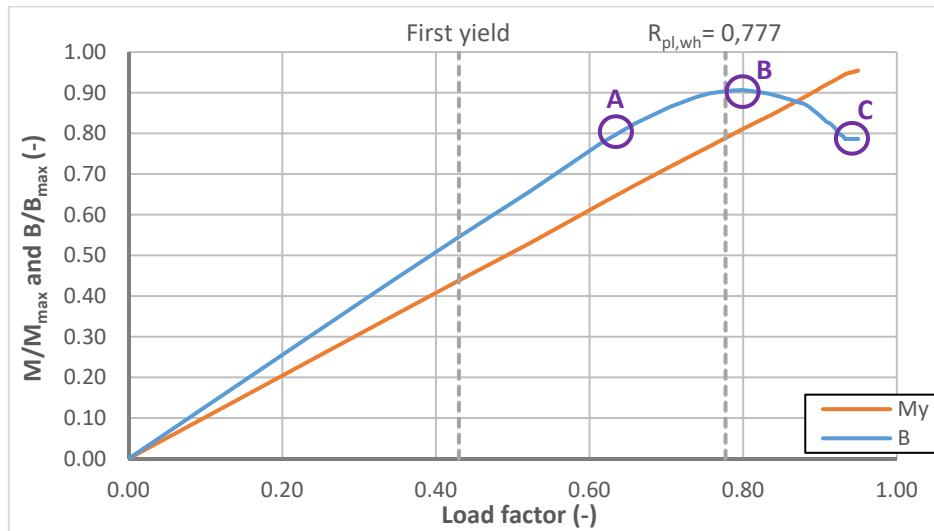


Figure 4-91 : Evolution of the internal moments with the load factor

Figure 4-92 shows the von Mises stress distribution over the member at the load level corresponding to point A of Figure 4-91. At this point the evolution of the bi-moment with the load factor becomes non-linear. Clearly, the member has already yielded in the flanges over an important part of its length. Yet, the web stays nearly completely elastic.

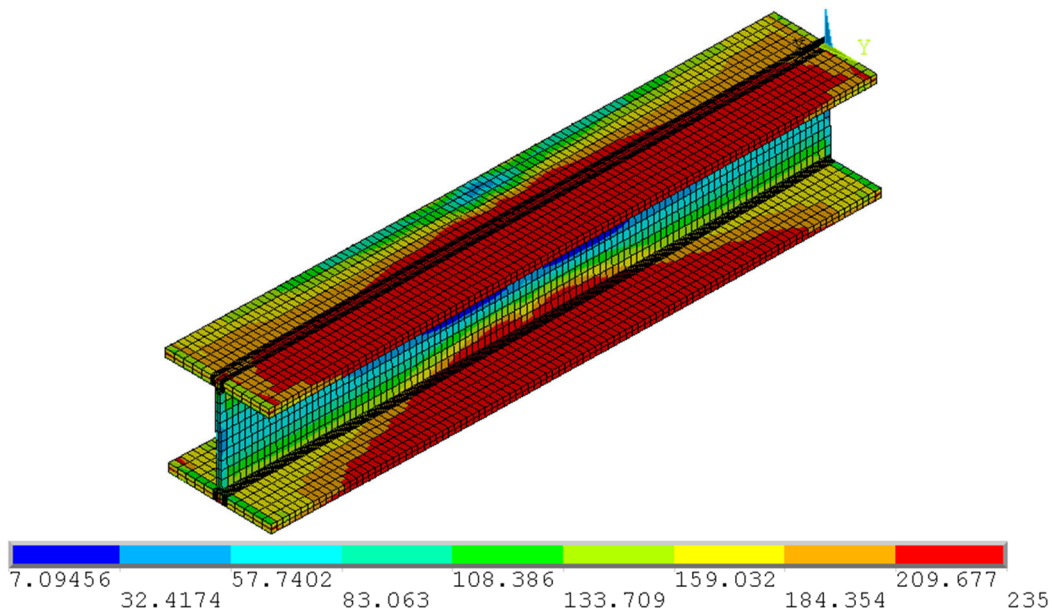


Figure 4-92 : Von Mises stresses at point A of Figure 4-91

Figure 4-93 and Figure 4-94 show the von Mises stress distribution as well as the distribution of the shear stresses over the member when it attains the load level corresponding to point B of Figure 4-91. Obviously, yielding has continued to spread over the member. Indeed, at this load level the flanges have nearly completely yielded over their total length. It is shown in Figure 4-94 that the flanges do not yield exclusively under axial stresses resulting from the major-axis bending moment but also due to the shear stresses resulting from Saint-Venant’s torsion. Additionally, the von Mises stresses have increased in the web of the member.

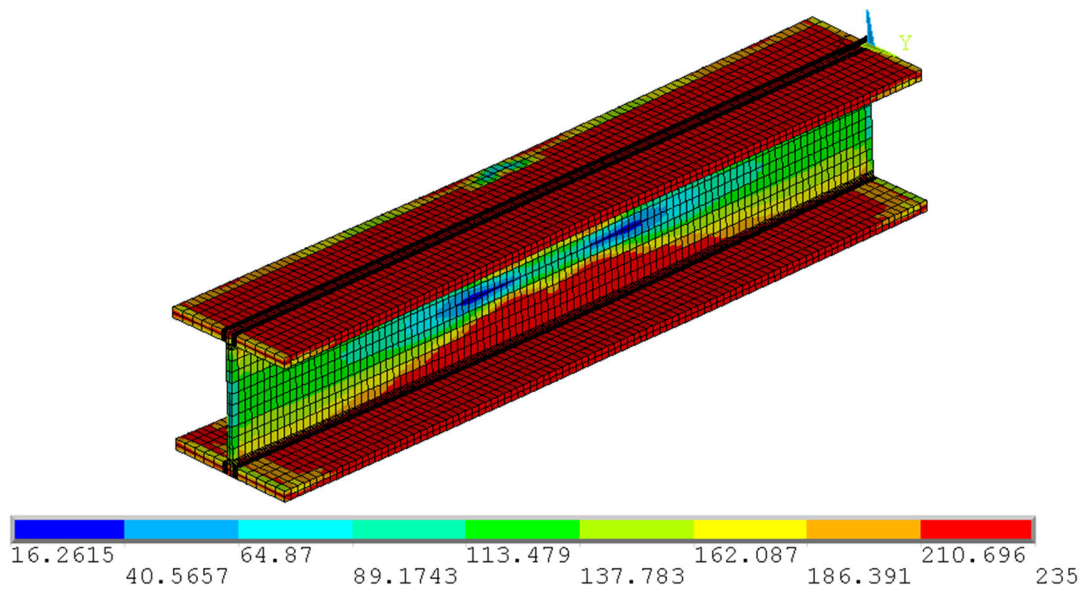


Figure 4-93: Von Mises stresses at point B of Figure 4-91

As the member is subject to a constant bending moment, the shear stresses represented in Figure 4-94 result from the Saint-Venant's torsional moment (the shear stresses resulting from the warping torsional moment are nearly negligible due to the high corresponding resistance of the section). Also, they are much higher than expected based on the Saint-Venant's torsional moment determined with the elastic analysis. At the shown load level $M_{x,StV}$ is equal to 1,22 kNm following and elastic analysis. Consequently, the shear stresses should be equal to:

$$\tau_{web} = \frac{M_{x,StV}}{I_t} t_w = \frac{1,22kNm}{48,01cm^4} 0,9cm = 23,0MPa \quad (4.81)$$

$$\tau_{flange} = \frac{M_{x,StV}}{I_t} t_w = \frac{1,22kNm}{48,01cm^4} 1,5cm = 38,3MPa \quad (4.82)$$

Obviously, the results indicate that the Saint-Venant's torsional moment is already much higher than predicted by the elastic analysis (the shear stresses attain nearly 3 times the value of Eqs (4.81) and (4.82)).

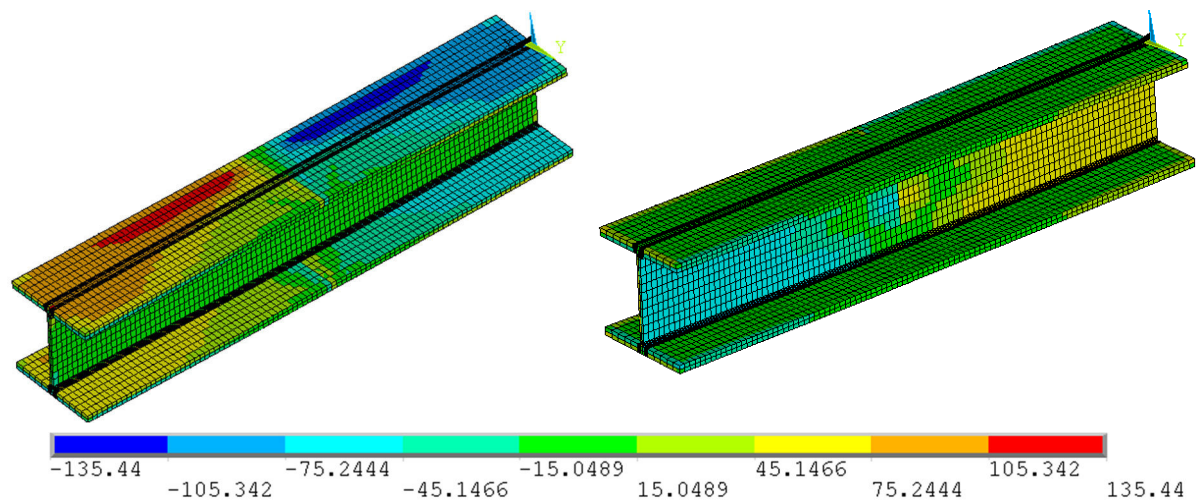


Figure 4-94: Shear stresses at point B of Figure 4-91

Finally, Figure 4-95 represents the von Mises stress distribution at the plastic limit state of the member. One may easily observe that the member has practically completely yielded due to the arising Saint-Venant's torsional moment. Additionally, it is clear that the torsional twist is rather important and in particular much higher than at points A and B of Figure 4-91 (the displacement of the members are represented in Figure 4-92, Figure 4-93, Figure 4-94 and Figure 4-95 in true scale).

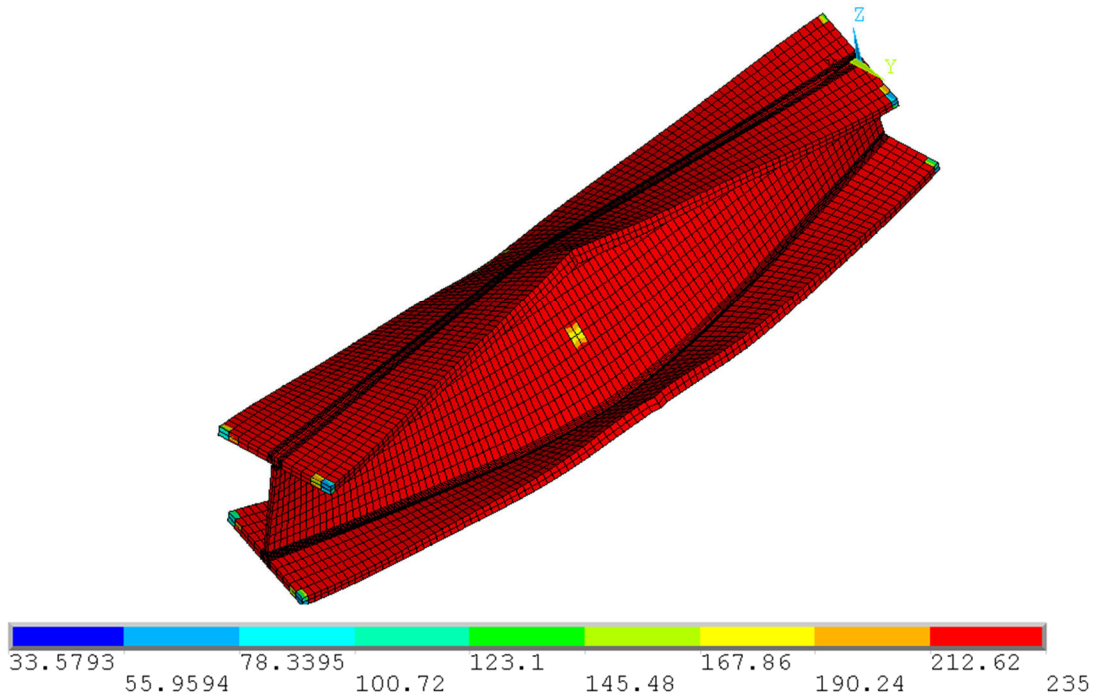


Figure 4-95: Von Mises stress distribution at the plastic limit state

The results represented above show that a simplified two step elastic analysis may approximately represent the complex plastic behaviour of members subject to torsion. In order to ensure a sufficient level of safety, the creation of the warping hinge should however be considered before the plastic limit state of the most loaded section under the combination of the bi-moment and other internal forces and moments is obtained. At this point of the thesis, the proportion of the plastic load amplification factor that should be associated with the creation of the plastic warping hinge is not determined. Before this is done, the interaction between the bi-moment and the other internal forces and moments is studied in detail in paragraphs 4.4.4.2, 4.4.4.3 and 4.4.4.4. These investigations are based on MNA simulations of the members under combined bending, shear force and torsion. Consequently, the plastic limit state of these members is always linked to complete yielding over their total lengths owing to the generation of the plastic warping hinge and the resulting Saint-Venant's torsional moment. Nonetheless, at the location of the plastic warping hinge, yielding is due to the combination of the bi-moment with the other internal forces and moments acting in the same section. Consequently, the plastic interaction behaviour can be studied at this location even if the ratio between the bi-moment and the other internal forces and moments is not the one predicted by an elastic analysis. Anyhow, it is to be noted that the internal forces and moments are determined by integrating the stresses over the

section. Therefore, the interaction diagrams, presented in the following, are always based on the real internal forces and moments acting in the studied section (if not otherwise indicated).

Last, it should be noted that the design methods and interaction equations developed hereafter remain valid if the internal forces and moments are determined based on an elastic analysis of the member as the bi-moment is overestimated in this case. Consequently, an elastic analysis is always safe-sided, as is also shown in the following paragraphs.

4.4.4.2 Double symmetric I sections

4.4.4.2.1 Plastic reference resistances to torsion

The plastic bi-moment is one of the reference values that is used hereafter. However, its value is not defined in any standard. For double symmetric I sections it may be determined by integrating the plastic stress distribution of the section. One obtains the following expression:

$$B_{pl} = \frac{b_f^2 t_f}{4} (h - t_f) f_y = \frac{M_{pl,z}}{2} (h - t_f) \quad (4.83)$$

In Chapter 2, it has been recalled that the bi-moment is associated with the warping torsional moment that attains its maximum at the same location as the bi-moment. Hence, one might suppose that an interaction between warping torsional moment and bi-moment is necessary. As shown by Eq. (4.84), the plastic warping torsional moment is equal to the plastic shear force resistance of one flange multiplied with the lever arm between the flanges. Anyhow, the resistance to the warping torsional moment is very high compared to the value of the warping torsional moment that may act on the members in practice. Consequently, it has no influence on the resistance of the cross-section (see paragraph 4.4.4.2.2).

$$M_{x,w,pl} = b_f t_f (h - t_f) \frac{f_y}{\sqrt{3}} = \frac{V_{pl,y}}{2} (h - t_f) \quad (4.84)$$

4.4.4.2.2 Interaction between major-axis bending, torsion and shear force

As for the case of interaction between bending and shear force, the following figures represent interaction diagrams obtained based on numerical MNA simulations of members subject to LC1 (point load applied at mid-span). Obviously, as three internal forces and moments interact (neglecting the warping torsional moment and the Saint Venant's torsional moment that do not influence the interaction), the representation of the results is more complex than before. Indeed, it is necessary to show two interaction diagrams that represent respectively the V_z - M_y plane and the B - M_y plane of the interaction space.

Additionally to the numerical results, the Eurocode 3 Part 1-1 interaction curve for the major-axis bending shear force interaction (without torsion) and an analytical interaction curve between the bi-moment and the major-axis bending moment (without shear forces) are represented in the

diagrams. The analytical interaction curve $B - M_y$ is based on the same hypothesis concerning the distribution of stresses as the interaction curve proposed by Mirambell (see paragraph 4.2.1.2.3), i.e. the bi-moment is distributed over the flanges as flange bending moment and the bending moment is distributed to the web and the flange. In the flange, the bending moment induces an axial force. The equation representing this interaction is:

$$M_{y,B,pl} = M_{y,pl} - \left[1 - \sqrt{1 - \left(\frac{B}{B_{pl}} \right)} \right] M_{y,pl,fl} \quad (4.85)$$

Eq. (4.85) may also be expressed as resistance criterion as follows:

$$\frac{B}{B_{pl}} \leq 1,0 \quad \text{if } M_y \leq M_{y,pl,web} = M_{y,pl} - M_{y,pl,fl} \quad (4.86)$$

$$\left(\frac{M_y - M_{y,pl,web}}{M_{y,pl,fl}} \right)^2 + \frac{B}{B_{pl}} \leq 1,0 \quad \text{if } M_y > M_{y,pl,web} \quad (4.87)$$

Eq. (4.86) to (4.87) may be easily adapted for the case of applied shear:

$$M_{y,V,pl} = \left(W_{pl,y} - \frac{\rho A_w^2}{4t_w} \right) f_y \quad \text{if } \frac{V_z}{V_{z,pl}} > 0,5 \quad (4.88)$$

$$\text{and } \rho = \left(\frac{2V_z}{V_{pl,z}} - 1 \right)^2$$

$$M_{y,B,V,pl} = M_{y,V,pl} - \left[1 - \sqrt{1 - \left(\frac{B}{B_{pl}} \right)} \right] M_{y,pl,fl} \quad (4.89)$$

Or as interaction equations:

$$\frac{B}{B_{pl}} \leq 1,0 \quad \text{if } M_y \leq M_{y,V,pl,web} = M_{y,V,pl} - M_{y,pl,fl} \quad (4.90)$$

$$\left(\frac{M_y - M_{y,V,pl,web}}{M_{y,pl,fl}} \right)^2 + \frac{B}{B_{pl}} \leq 1,0 \quad \text{if } M_y > M_{y,V,pl,web} \quad (4.91)$$

The presentation of the interaction formula (4.85) is slightly different from the one used by Mirambell recalled in Eq. (4.92) **Erreur ! Source du renvoi introuvable.** It should be noted that the notations used in this thesis are introduced into Eq. (4.85). Also, the partial factor γ_{M0} is omitted here. The main difference between Eq. (4.92) and Eq. (4.85) is the factor considering the influence of the bi-moment. In fact, Mirambell only considers partial plasticity by the reference resistance of $1,25f_y$ (for full plasticity the factor should be $1,5f_y$ - see paragraph 4.2.1.2.3).

$$M_{y,B,pl} = \left(\sqrt{1 - \left(\frac{\sigma_B}{1,25f_y} \right)^2} \right) M_{y,pl} = \rho_B M_{y,pl} \quad (4.92)$$

Also, Eq. (4.92) does **not** consider that the interaction may be neglected if the major-axis bending moment is less than the major-axis bending resistance of the web. Admittedly, this case is obviously of less practical interest. In case of high shear forces Mirambell proposes the following adaption, equivalent to Eq. (4.95). Again, he considers a reduction of the web resistance due to the bi-moment.

$$M_{y,B,V,Rd} = M_{web,Rd} (1 - \rho_{Vz}) \rho_B + \rho_B M_{f,Rd} \quad (4.93)$$

In the following, the numerical results are represented. First, Figure 4-96 and Figure 4-97 give the results obtained for the section HEB 220. The influence of the bi-moment may be easily identified. Regarding Figure 4-96, it is clear that the major-axis bending - shear resistance of a member with a given length is reduced by the action of the bi-moment. For very short members (L = 3h) however, it is not the bi-moment that leads to failure but the shear resistance as shown in Figure 4-98 and Figure 4-99.

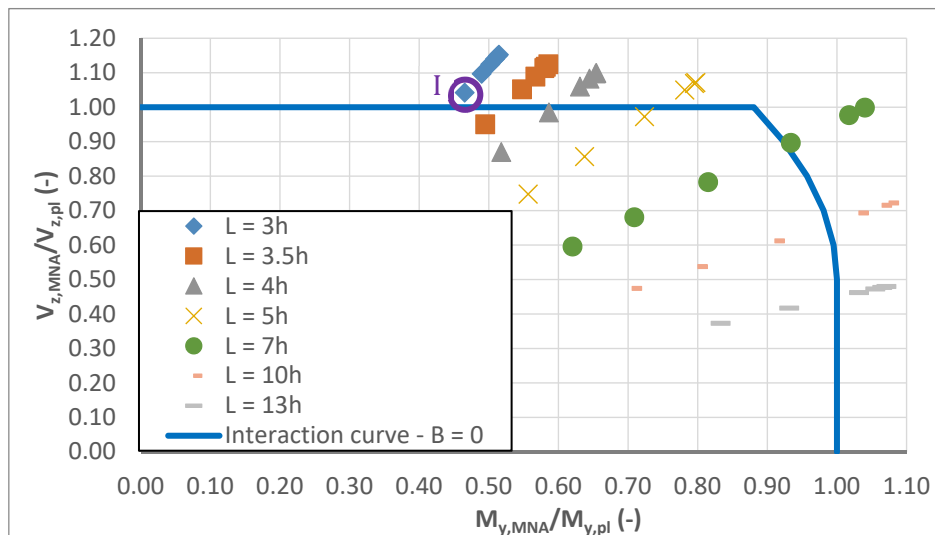


Figure 4-96 : M_y - V_z - B plastic interaction for HEB 220 – V_z - M_y plane

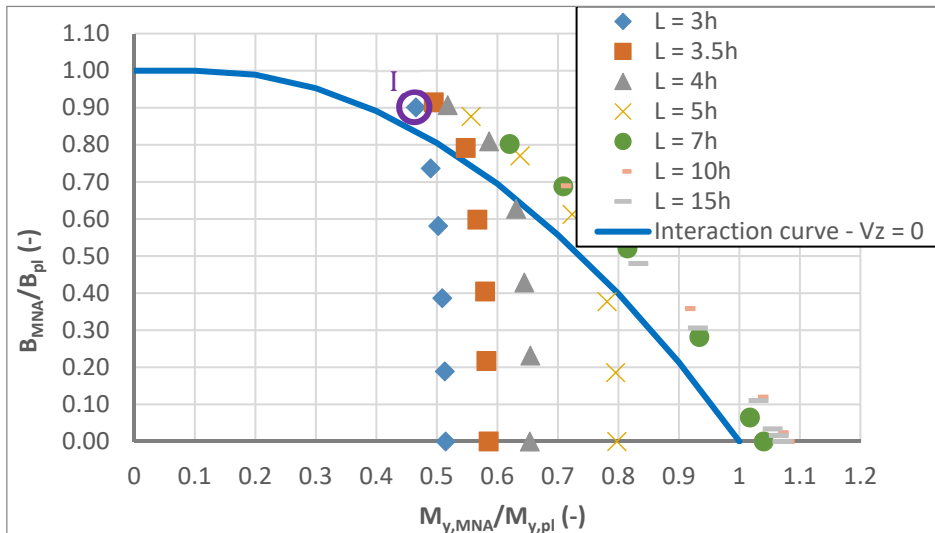


Figure 4-97 : M_y - V_z - B plastic interaction for HEB 220 – B - M_y plane

In Figure 4-98, the axial stress distribution shows the interaction between the bi-moment and the major-axis bending moment in the flanges. It should be noted again that the axial stresses exceed the yield stress of 235 MPa due to a 3 dimensional stress field created at the plastic hinge. Consequently, a supplementary resistance reserve is mobilized explaining why the numerical results exceed the analytical plastic resistance. In Figure 4-98 one may also observe that the axial stresses do not transit through the web, as it is entirely utilized by the shear force as shown in Figure 4-99. In this figure one may recognize that the shear stresses are constant through the thickness of the web. Hence, they are not resulting from Saint Venant's torsion (creating shear stresses varying linearly over the thickness – see Chapter 2) but from the shear force V_z as indicated.

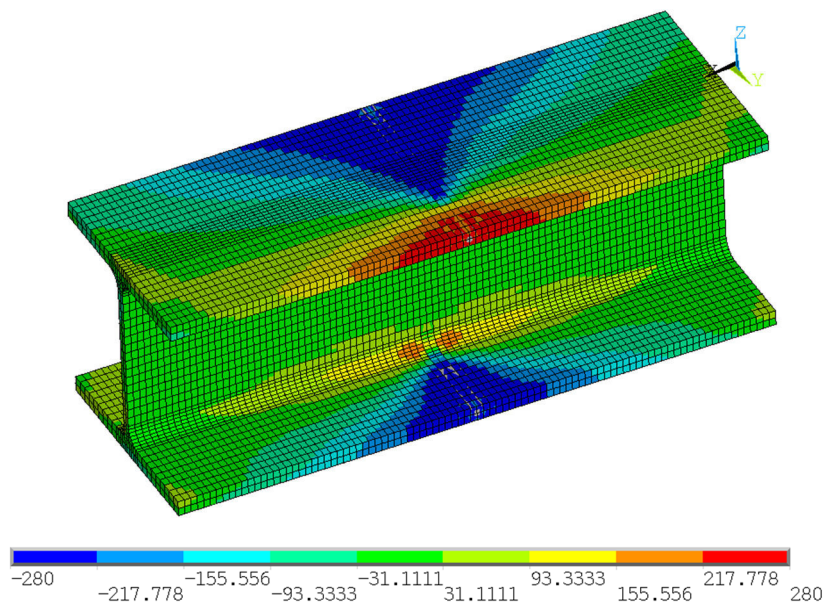


Figure 4-98: Axial stress distribution at PLS for section HEB 220 under combined M_y - B - V_z – Case I of Figure 4-96

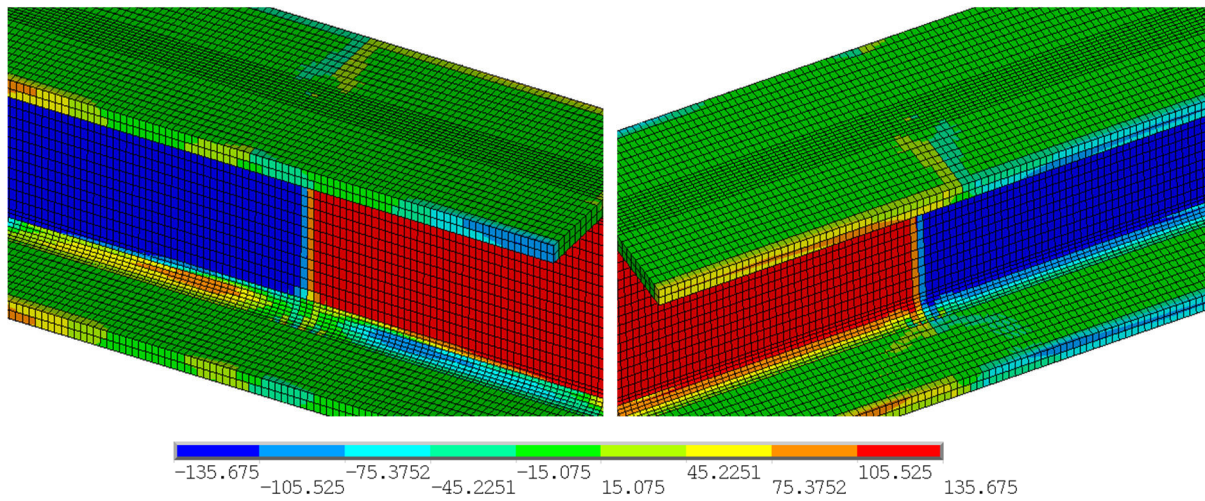


Figure 4-99: Shear stress distribution at PLS for section HEB 220 under combined M_y -B- V_z – Case I of Figure 4-96

Figure 4-100 to Figure 4-103 present the results obtained for section IPE 600 and HEA 100. As before the influence of the bi-moment and the shear force may be easily identified. Also, the interaction curves applicable for the extreme cases of respectively zero shear force and zero bi-moment represent very well the interaction behaviour.

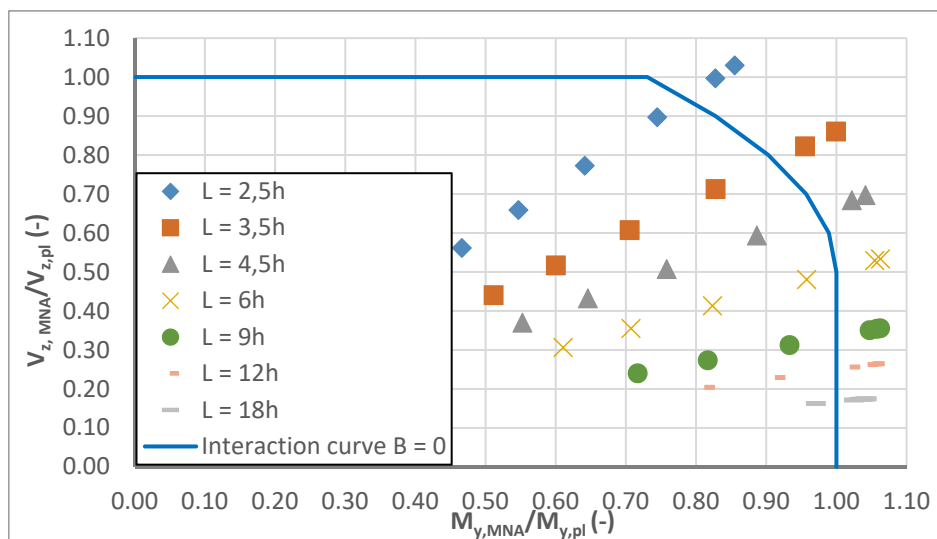


Figure 4-100 : M_y - V_z -B plastic interaction for IPE 600 – V_z - M_y plane

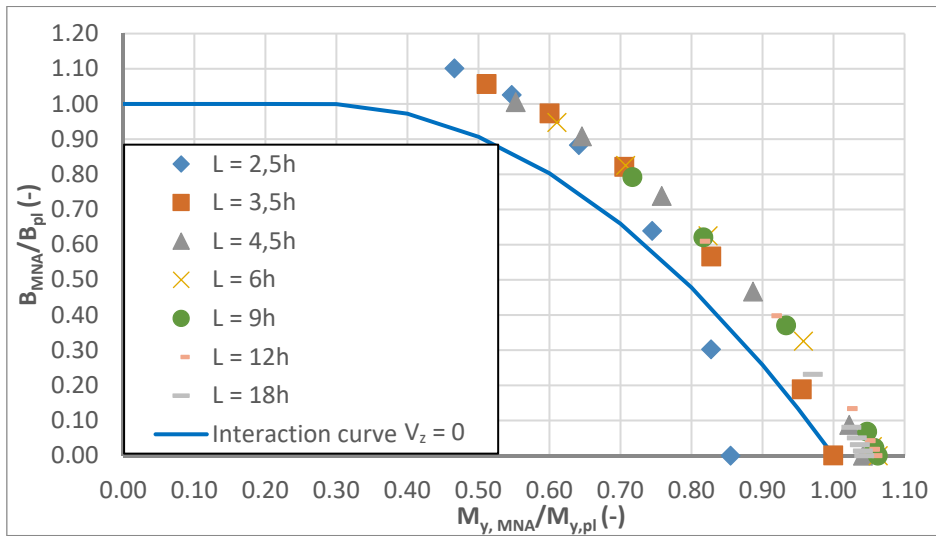


Figure 4-101 : M_y - V_z - B plastic interaction for IPE 360 – B - M_y plane

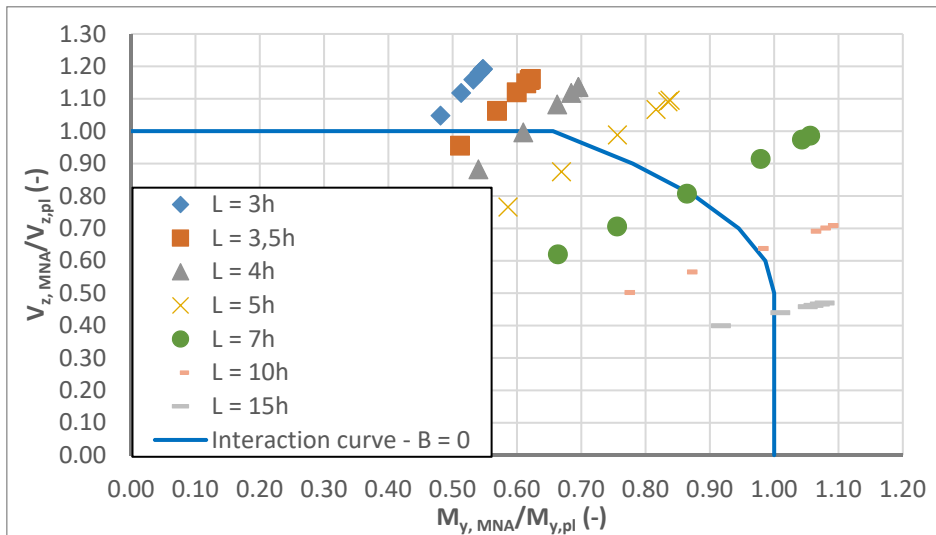


Figure 4-102 : M_y - V_z - B plastic interaction for HEA 100– V_z - M_y plane

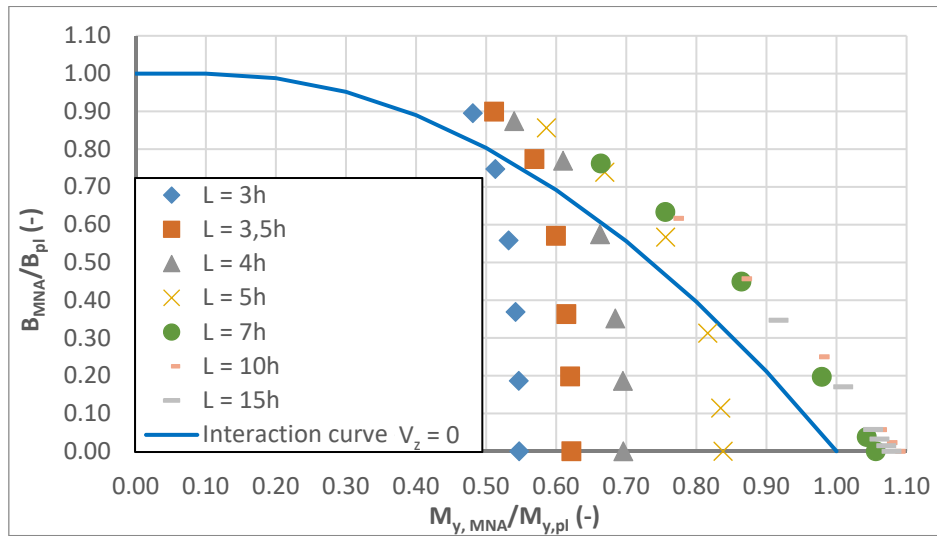


Figure 4-103 : M_y-V_z-B plastic interaction for HEA 100 – B- M_y plane

The previous figures have shown that the proposed interaction corresponds very well to the numerically determined resistances for selected examples. Hereafter, the interaction conditions are compared to the totality of the numerical simulations performed for the characterization of the plastic major-axis bending-shear force-bi-moment interaction.

Figure 4-104 presents the comparison between the MNA simulations and the interaction conditions defined by Eq. (4.89). Obviously, the results are very satisfactory both in terms of scatter and in terms of precision. Yet, for some simulations of the IPE 360 section, the proposal seems to be slightly unsafe. In order to explain this, the example of a member with a length of 1260 mm is studied in more detail. The member is made of IPE 360 section and it is subject to a point load applied at mid-span at the upper flange's tip (Point I in Figure 4-104).

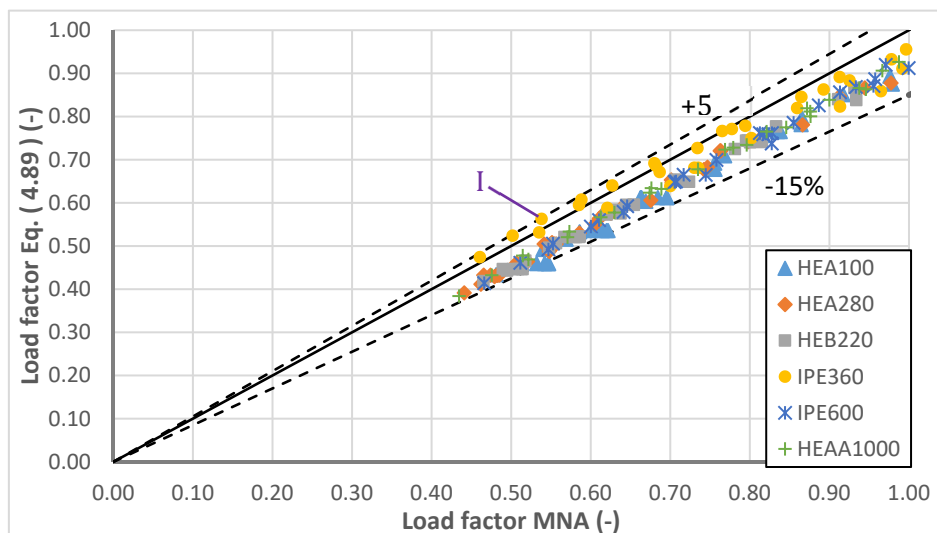


Figure 4-104: Comparison between MNA simulations and interaction curve of Eq. (4.89)

Figure 4-105 shows the evolution of the major-axis bending M_y and of the total torsional moment $M_{x,tot}$ as well as of the bi-moment B with the applied loads for the example I of Figure 4-104. Again,

one may observe the specific behaviour of members with open sections subject to torsion that has been discussed in detail in paragraph 4.4.4.1. Indeed, the bending moment and the total torsional moment increase linearly with the load factor whereas the bi-moment attains its maximum at a given load level and then decreases due to the formation of a plastic warping hinge. After the formation of this warping hinge the applied load may increase further on. However, it is recalled that the supplementary torsional load is exclusively carried by Saint-Venant's torsion leading to yielding of the member over its total length. For the studied example Figure 4-106 illustrates the von Mises stress distribution at the plastic limit state.

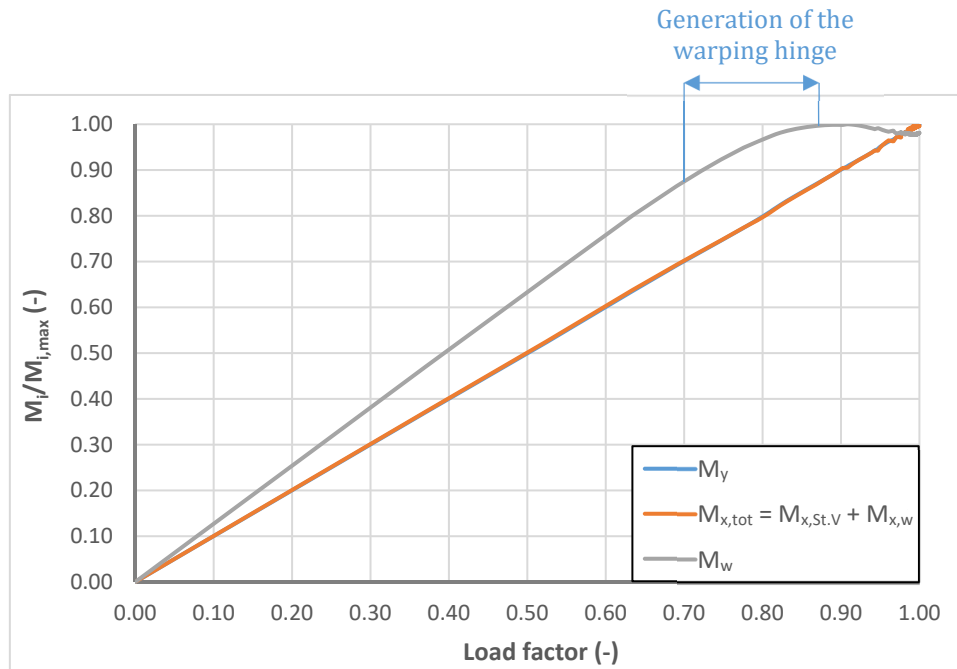


Figure 4-105: Evolution of the internal forces with the applied load

The von Mises stress distribution represented in Figure 4-106 clearly shows that the member has yielded over its total length. At mid-span, the member yields predominantly under combined major-axis bending, bi-moment and the shear force (see Figure 4-107). Inversely, at its ends, the member yields under shear stresses resulting from the Saint Venant's torsional moment that highly increases after the formation of the plastic warping hinge as shown by the representation of the shear stress distribution in Figure 4-108.

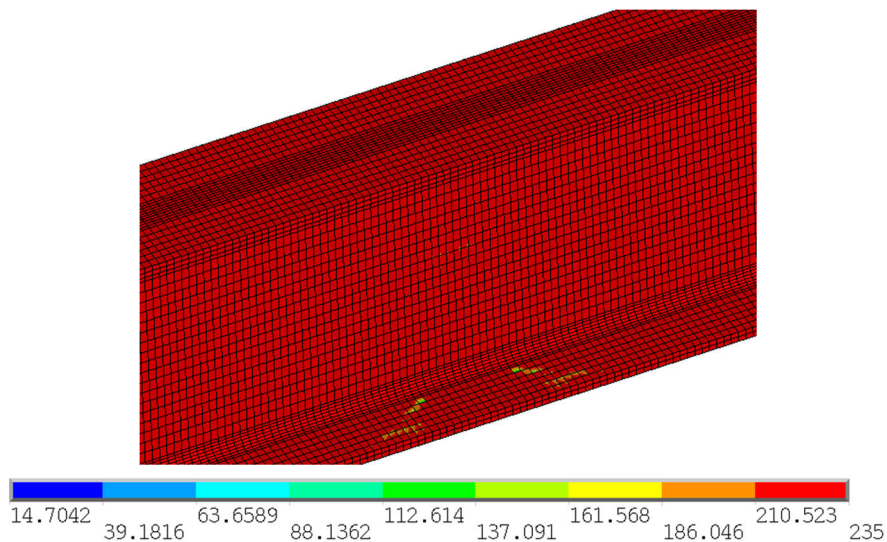


Figure 4-106: Distribution of von Mises stresses at plastic limit state for example I of Figure 4-104

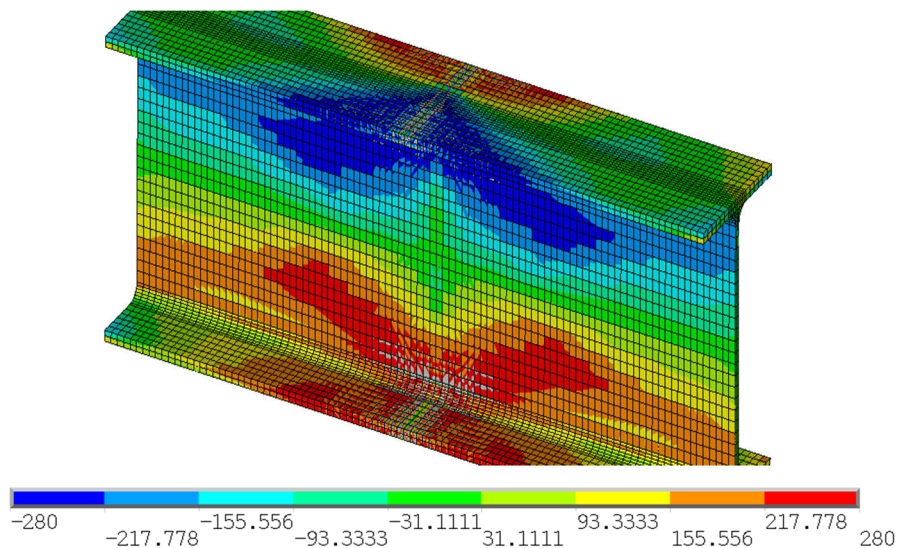


Figure 4-107: Distribution of axial stresses at plastic limit state for example I of Figure 4-104

Especially, the shear stress distribution in the flanges given in Figure 4-108 b) clearly indicates the presence of high Saint Venant's torsional moments. This example confirms, once more, the conclusions of paragraph 4.4.4.1 dedicated to the plastic behaviour of members in torsion. Moreover, it appears that, depending on the case, there can be a slight interaction between the Saint-Venant's torsional moment arising between the supports and the plastic warping hinge and the internal forces and moments acting in the plastic warping hinge itself. Nonetheless, the interaction leads only to a small supplementary reduction of the plastic section resistance. Hence, the influence of the Saint-Venant's torsional moment can be neglected for the interaction between the internal forces and moments acting in the warping hinge.

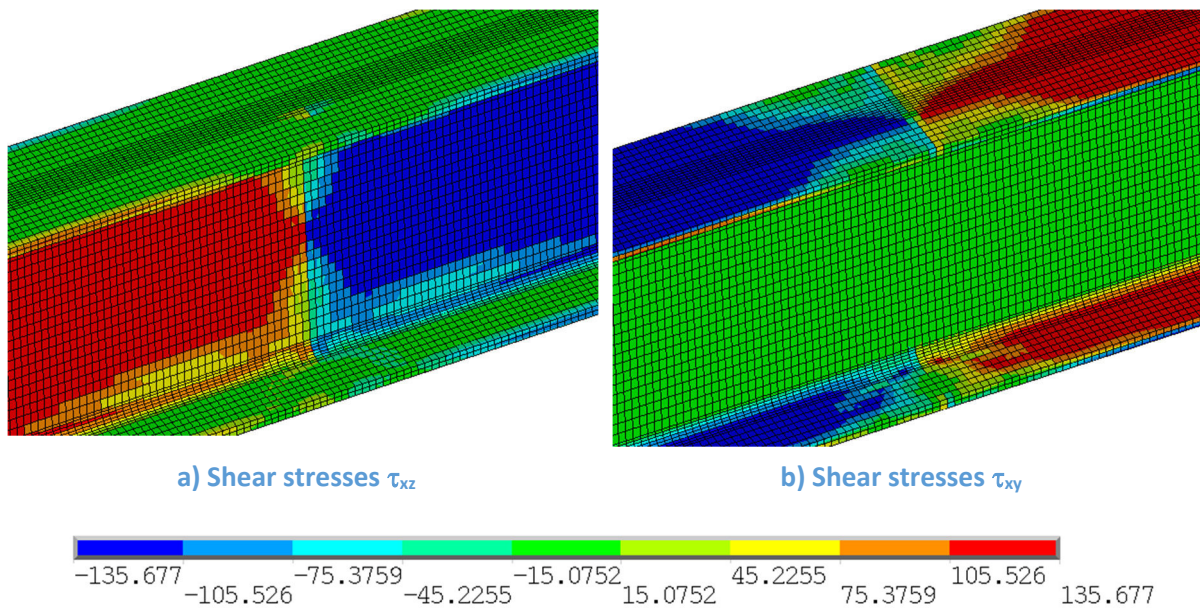


Figure 4-108: Distribution of shear stresses at plastic limit state for example I of Figure 4-104

It should again be emphasized that the objective of the present paragraph is not the development of a design method describing the plastic resistance of a member as a whole, i.e. including the plastic system reserve resulting from the formation of plastic warping hinge, but rather the development of a design method (interaction equations) that describes the plastic interaction that leads to the formation of the plastic warping hinge in the first place. The supplementary plastic system reserve should be covered in the analysis as described in paragraph 4.4.4.1. Consequently, it is not unsafe to accept the provisions of the current version of Eurocode 3 Part 1-1 that indicate that the influence of the Saint Venant's torsional moment may be neglected for members of open section (§6.2.7 of (CEN 2005a)). In fact, these provisions are, implicitly, based on **elastic** analysis and hence they do not consider the formation of a warping hinge leading to higher resistances. In order to underline this fact Figure 4-109 represents the comparison of the MNA results to the interaction curve again. Yet, hereafter, it is considered that the internal forces and moments used in the interaction equation have been determined based on an elastic analysis of the member. Obviously, the results obtained with the interaction formulae are less precise as before because the bi-moment used in the formulae is not the bi-moment really acting in the studied section. Indeed, the elastic analysis overestimates the bi-moment. Also, due to this fact the scatter of the results is increased. Nevertheless, it seems that the results are still acceptable. Additionally, it is shown that neither the Saint Venant's torsional moment nor the warping torsional moment need to be accounted for (as the results do not become unsafe if both are neglected). Hence, the verification is simplified.

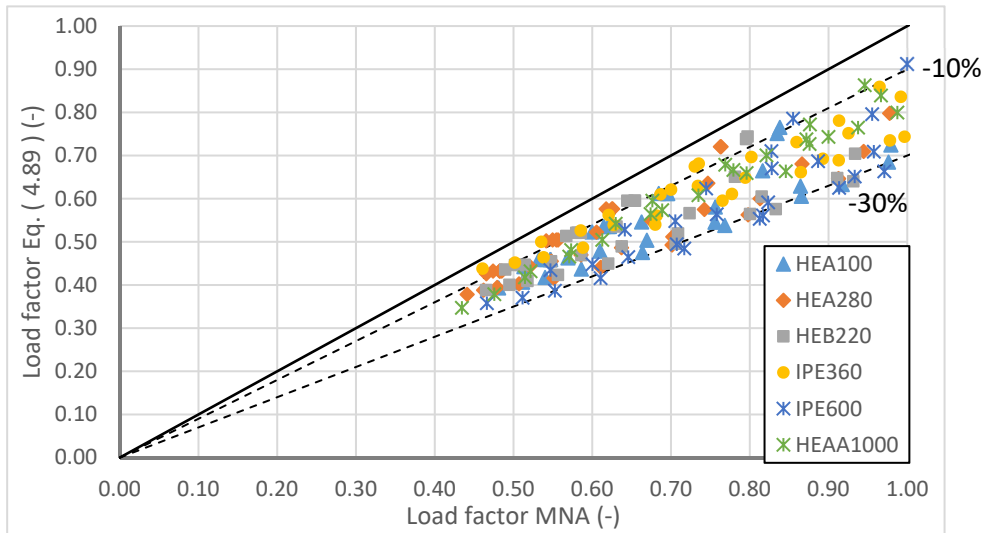


Figure 4-109: Comparison between MNA simulations and interaction curve of Eq. (4.89) used with elastic analysis

Last, the proposal of Mirambell is compared to the MNA simulations. As before two diagrams present the comparisons. In Figure 4-110 the internal forces and moments used in the interaction formulae are those obtained by the MNA simulations and in Figure 4-111 the internal forces and moments are determined by elastic analysis. For both cases the proposal of Mirambell is less precise than the interaction formulae defined in Eq. (4.89). Especially, if the design is based on an elastic analysis, the precision is poor and the scatter is important for Mirambell’s proposal. Yet, it should however be noted that, by introducing a plastic adaption factor equal to 1,25 (and not equal to analytical factor of 1,50) Mirambell seems to accept this scatter

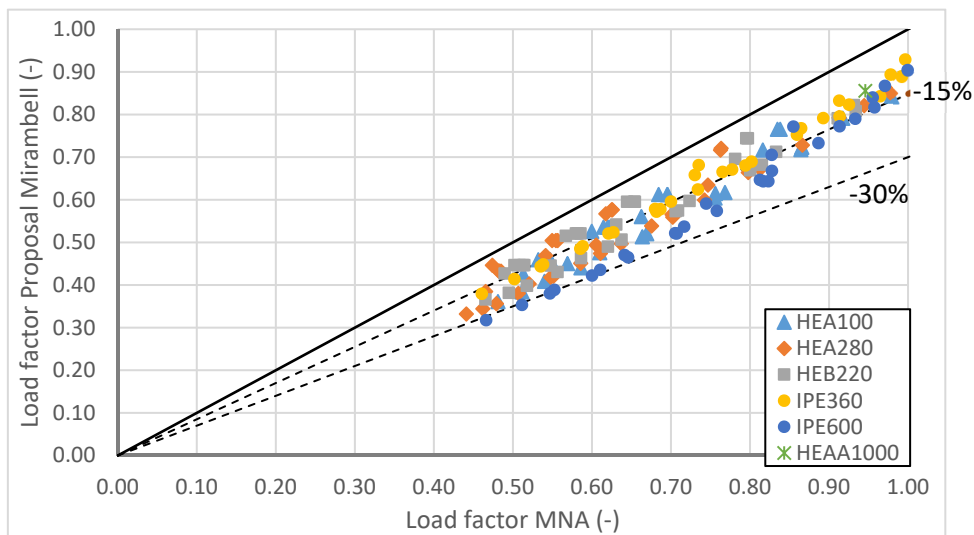


Figure 4-110: Comparison between MNA simulations and proposal Mirambell – Eq. (4.93) used with plastic analysis

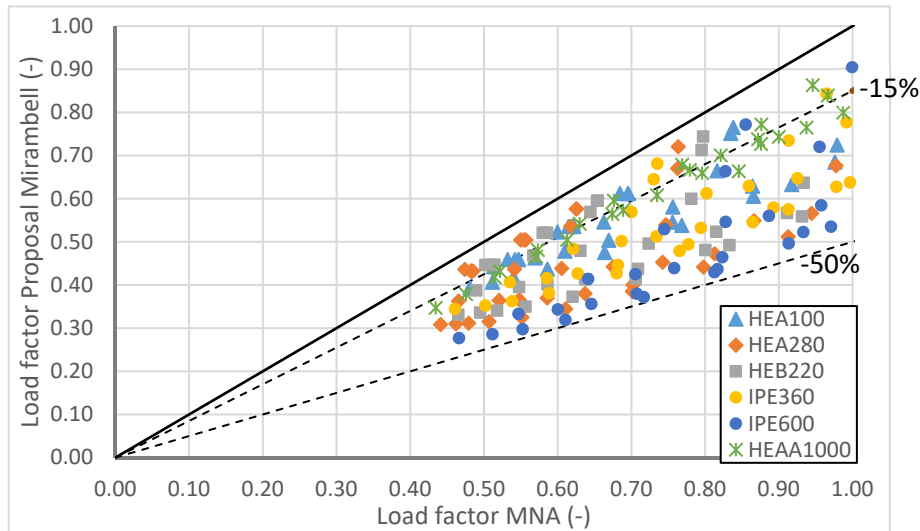


Figure 4-111: Comparison between MNA simulations and proposal Mirambell – Eq. (4.93) used with elastic analysis

4.4.4.2.3 Interaction between minor-axis bending, torsion and shear force

In paragraph 4.4.3.1 it has been shown that the interaction between the shear force and the minor-axis bending moment may be neglected. It is shown hereafter that this hypothesis may also be considered in case of the more complex interaction including torsion.

It is recalled that the stresses resulting from the minor-axis bending moment and the bi-moment are affine in the flanges. Yet, depending on the sign of bending moment and the bi-moment, the stresses may add in the upper flange and neutralise in the lower flange or inversely (see Chapter 2 for stresses resulting from the bi-moment). Anyhow, owing to the distribution of the stresses in the flange a linear interaction may be considered. Hereafter, the example of the HEA 280 section is studied. Again, two diagrams are given in order to characterize the interaction behaviour. Figure 4-112 represents the V_y - M_z plane of the interaction space and Figure 4-113 represents the B - M_z plane. As before, one may observe that the shear force parallel to the flanges does generally not influence the plastic minor-axis bending resistance. Only for extremely short members, outside of the practical range, the shear force slightly reduces the resistance.

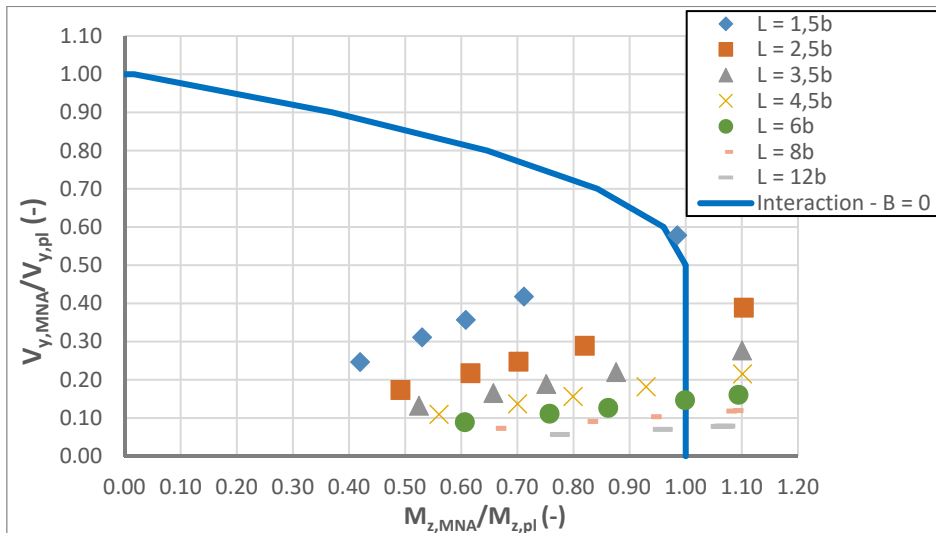


Figure 4-112: M_z - V_y - B plastic interaction for HEA 280 – V_y - M_z plane

Figure 4-113 shows that the linear interaction fits very well the real interaction behaviour of the section. It should however be recalled that the internal forces used in Figure 4-112 and Figure 4-113 are those obtained by the MNA analysis and hence the real internal forces and moments acting in the plastic warping hinge. Here, it is shown again that, conversely to the hypothesis done by certain authors, the bi-moment does not vanish entirely after the formation of the warping hinge (see reference (Glitsch 2008) and Chapter 5). Indeed, after the formation of the warping hinge, the plastic failure of the member is always due to the Saint Venant’s torsional moment leading to the yielding of the member over its total length. Depending on the case, the failure of the member may occur before the minor-axis bending moment is close to the plastic minor-axis resistance of the section at mid span.

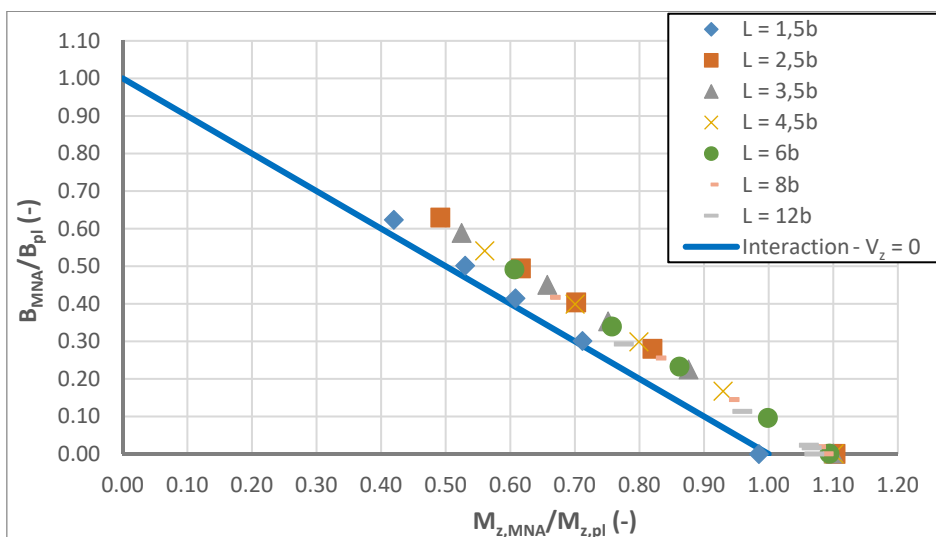


Figure 4-113: M_z - V_y - B plastic interaction for HEA 280 – B - M_z plane

If the interaction is based on elastic analysis the results become, in some cases, very conservative as shown in Figure 4-114.

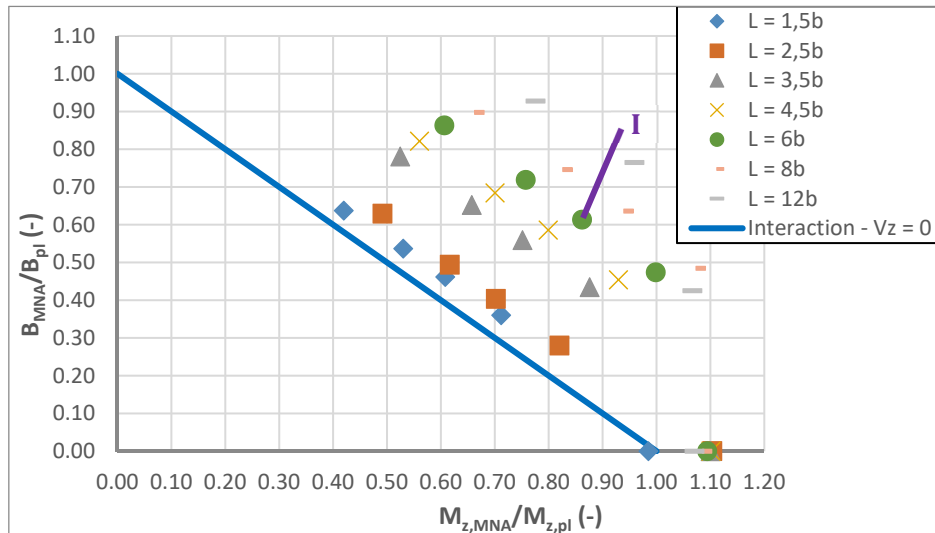


Figure 4-114: M_z - V_y - B plastic interaction for HEA 280 – B - M_z plane – internal forces and moments obtained by elastic analysis

The pronounced difference between elastic and plastic analysis may be explained with Figure 4-115 showing the evolution of the internal forces with the applied loads of case I of Figure 4-114. It can be seen that the bi-moment decreases highly after the formation of the warping hinge. Consequently, the plastic system reserve is even more pronounced than in the case of combined major-axis bending and torsion. In fact, as the web of the I section is not utilized by the stresses resulting from minor-axis bending and the corresponding shear force, it may be entirely used by the shear stresses resulting from the arising Saint Venant’s torsional moment. In case of combined major-axis bending, shear force and torsion the web is already utilized by the shear stresses resulting from the shear force and the axial stresses generated by the major-axis bending moment. Hence, the plastic system reserve is generally less pronounced than for combined minor-axis bending, torsion and shear force.

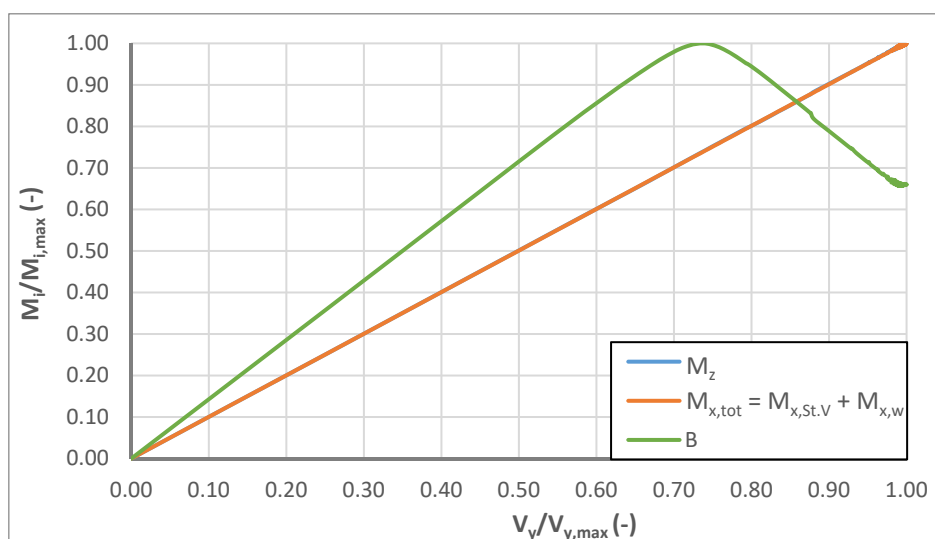


Figure 4-115: Evolution of the internal moments with the applied loads

4.4.4.2.4 Conclusions

Through the present paragraph the interaction between bending, torsion and the shear force has been investigated in detail for double symmetric I sections. It has been shown that the torsional plastic system reserve highly influences the member behaviour. In fact, owing to the formation of a plastic warping hinge the torsional load is redistributed and carried through a Saint Venant's torsional moment that is negligible before yielding of the member is initiated. This system reserve may highly increase the resistance of the member compared to an elastic analysis. Yet, after the formation of the warping hinge, the torsional twist may also highly increase. Therefore, the torsional plastic system reserve should only be accounted for if the torsional twist is not incompatible with the member in the structure. Generally, the internal forces and moment are determined by an elastic analysis in practice. Consequently, the interaction equations, that precisely predict the cross-section resistance based on the real internal forces acting in the section, may be rather conservative. However, this conservatism has to be accepted as it ensures that the torsional twist does not increase excessively.

4.4.4.3 Mono-symmetric I sections

4.4.4.3.1 Plastic bi-moment resistance

In paragraph 4.4.3.3 it has been shown that the mono-symmetric I sections can only fully yield under minor-axis bending if a stress-induced bi-moment arises. The numerical simulation have indicated that the stress-induced bi-moment is generated and consequently full yielding of the mono-symmetric I section under M_z may be attained. If the section is subject to a bi-moment, the problematic is similar. In fact, the section can only entirely yield if a minor-axis bending moment M_z arises as represented in Figure 4-116. However, due to the static equilibrium conditions, a minor-axis bending moment can only be induced by an external load.

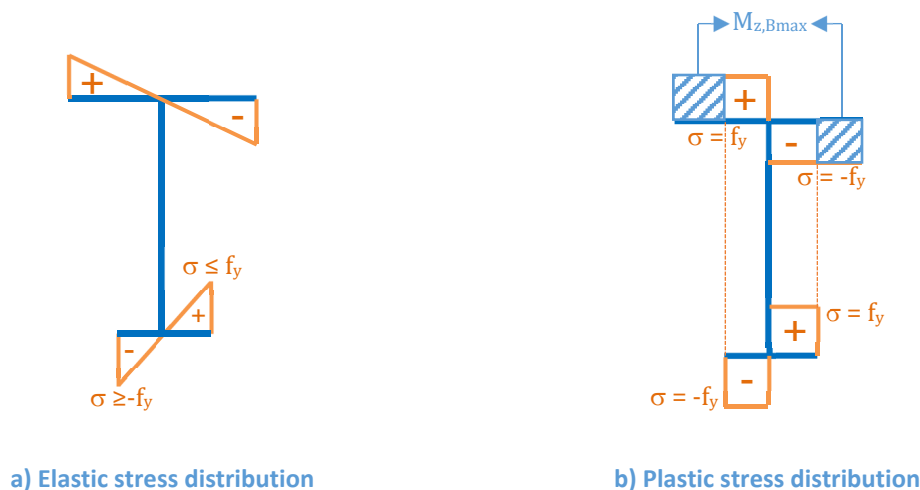


Figure 4-116: Elastic and plastic stress distribution for a mono-symmetric I section subject to a bi-moment

In presence of an externally applied minor-axis bending moment, the bi-moment resisted by the cross-section may therefore exceed the plastic bi-moment resistance determined under a sole bi-

moment. The minor-axis bending moment leading to the maximum bi-moment can be determined with Eq. (4.94). It should be noted, that following the sign convention used in this thesis $M_{z,B_{\max}}$ and the corresponding maximum bi-moment B_{\max} are of the same sign.

$$M_{z,B_{\max}} = \left(\frac{b_{uf}^2 t_{uf}}{4} - \frac{b_{lf}^2 t_{lf}}{4} \right) f_{y,y} \quad (4.94)$$

The expression of the corresponding maximum bi-moment may be derived based on the stress distribution given in Figure 4-116b).

$$B_{\max} = \left(\frac{b_{uf}^2 t_{uf}}{4} z_{S,uf} + \frac{b_{lf}^2 t_{lf}}{4} z_{S,lf} \right) f_y \quad (4.95)$$

In Eq. (4.95), $z_{S,uf}$ and $z_{S,lf}$ correspond to the distance between the shear centre and the centroid of the upper and lower flange, respectively.

The plastic bi-moment may also be obtained based on the stress distribution shown in Figure 4-116b) and by neglecting the stresses associated with $M_{z,B_{\max}}$ represented in light blue. One obtains:

$$B_{pl} = \text{Min} \left[\frac{b_{uf}^2 t_{uf}}{4}; \frac{b_{lf}^2 t_{lf}}{4} \right] \left(h - \frac{t_{uf}}{2} - \frac{t_{lf}}{2} \right) f_y \quad (4.96)$$

Depending on the cross-section dimensions the upper or the lower flange may be determining for the value of the plastic bi-moment. Nevertheless, it is to be noted that the plastic bi-moment should only be considered as a reference value as the real plastic stress distribution under an applied bi-moment is obviously not the one represented in orange in Figure 4-116b). Indeed, in any case the yielding of the flanges starts from the flange's tips and evolves to the centre of the flanges. Yet, the numerical simulations presented in the following paragraphs justify that the expression given in Eq. (4.98) is acceptable.

4.4.4.3.2 Interaction between major-axis bending, torsion and shear force

First, the interaction between major-axis bending, the associated shear force and the bi-moment is studied. As before, the mono-symmetry is introduced by reducing the width of the lower flange. The following figures represent the results obtained for the modified IPE 600 section. Additionally, the interaction curves applicable for the extreme cases of respectively negligible bi-moment and negligible shear force are represented. For the major-axis bending-bi moment interaction, the interaction curve used for double symmetric sections is used again. Yet, the value of $M_{y,pl,fl}$ is calculated based on the weaker of the two flanges (see Eq. (4.98)) and the plastic bi-moment is obtained with Eq. (4.96).

$$M_{y,B,V,pl} = M_{y,V,pl} - \left[1 - \sqrt{1 - \left(\frac{B}{B_{pl}} \right)} \right] M_{y,pl,fl} \quad (4.97)$$

$$\text{and } M_{y,pl,\eta} = \text{Min}\left[b_{uf}t_{uf}; b_{lf}t_{lf}\right] \left(h - \frac{t_{uf}}{2} - \frac{t_{lf}}{2} \right) f \quad (4.98)$$

In the following, the mono-symmetry parameter ψ is varied between 0,2 (slightly mono-symmetric) and 0,975 (highly mono-symmetric). Figure 4-117 and Figure 4-118 show that the proposed interaction curves are in good agreement with the numerical results and may therefore considered as satisfying.

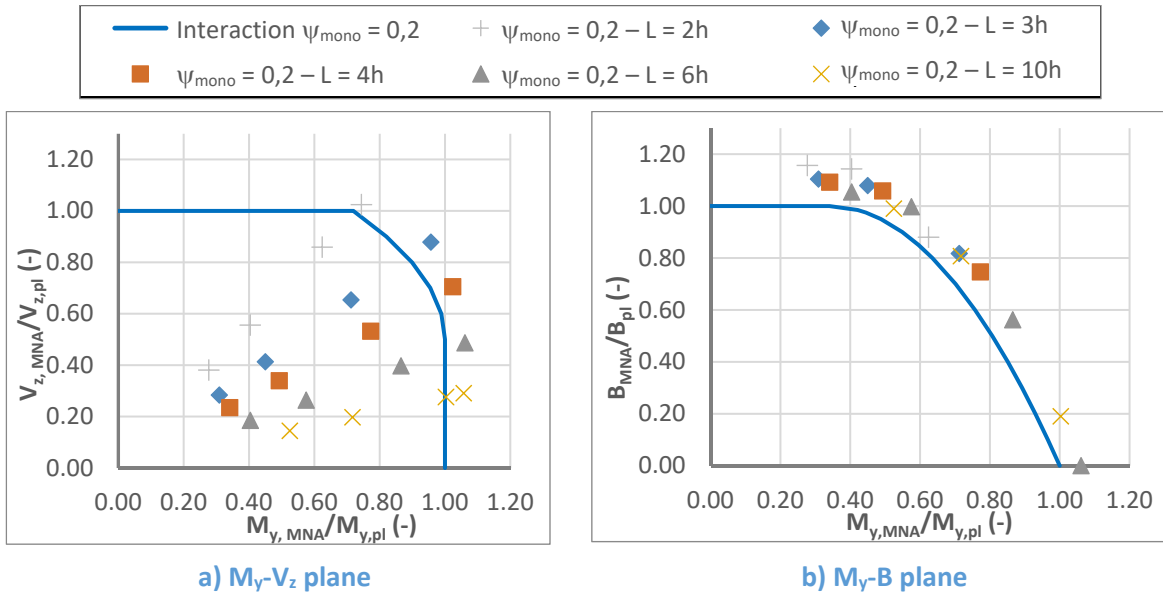


Figure 4-117: Major-axis bending - shear force - bi-moment interaction for IPE 600m $\psi_{\text{mono}} = 0,2$

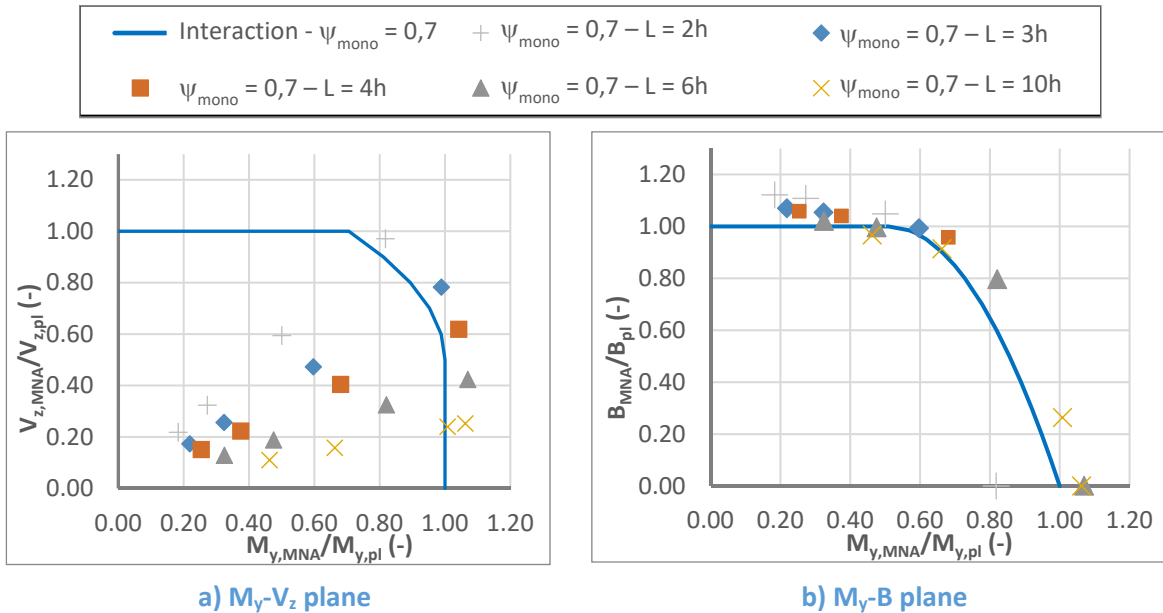


Figure 4-118: Major-axis bending - shear force - bi-moment interaction for IPE 600m $\psi_{\text{mono}} = 0,7$

On the contrary, to the case of slightly and medium mono-symmetric sections, the results obtained for the highly mono-symmetric section seem to be much less satisfying especially if one observes the M_y - B plane represented in Figure 4-119. Obviously, the plastic bi-moment resistance is much higher than predicted with Eq. (4.97).

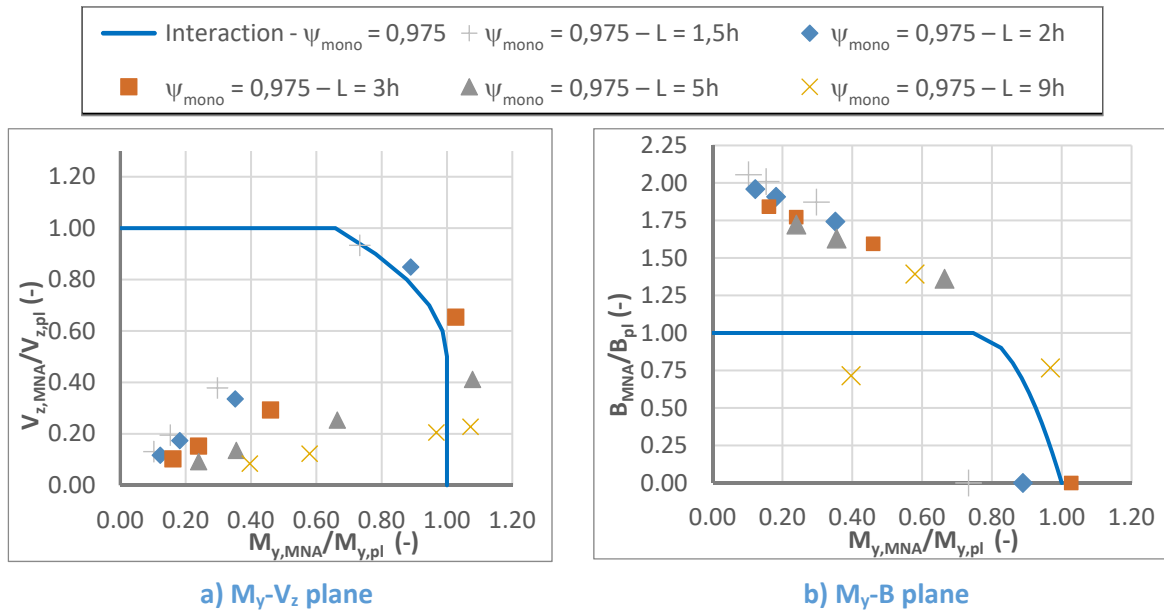


Figure 4-119: Major-axis bending - shear force - bi-moment interaction for IPE 600m $\psi_{mono} = 0,975$

So as to highlight the reason of this surprising results, Figure 4-120 represents the stress distribution for a IPE 600m section possessing a ψ_{mono} value of 0,975. The section is subject to a vertical point load applied at mid-span at the upper flange’s tip. For the represented load step, the bi-moment just attains the value of the plastic bi-moment defined in Eq. (4.96). It may be observed that the lower flange has yielded due to the influence of the bi-moment. Contrariwise, the upper flange has not reached the yield stress in any point. However, it can also be observed that the axial stresses vary through the upper flange from approximately -90 MPa to 150 MPa at the right tip and from -150 MPa to 90 MPa at the left tip. This indicates that the local warping stiffness and associated resistance is mobilised (see Chapter 2). It is evident that the supposed stress distribution shown in Figure 4-116 is not valid anymore for highly mono-symmetric sections.

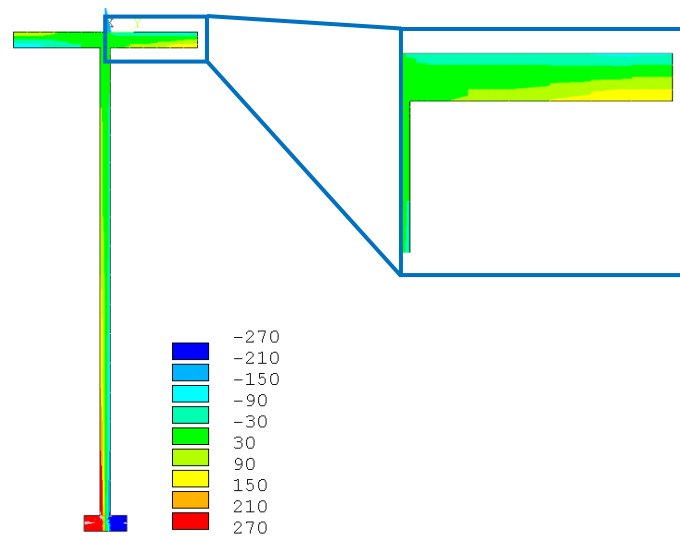


Figure 4-120: Plastic stress distribution for IPE 600m $\psi_{mono} = 0,975$ at load factor corresponding to B_{pl}

The stress distribution at the plastic limit state is represented in Figure 4-121. Especially, the distribution of axial stresses in the upper flange indicates clearly the mobilisation of the local warping resistance. In fact, after the yielding of the lower flange the mono-symmetric section acts like a T section whose behaviour is prescribed by local warping.

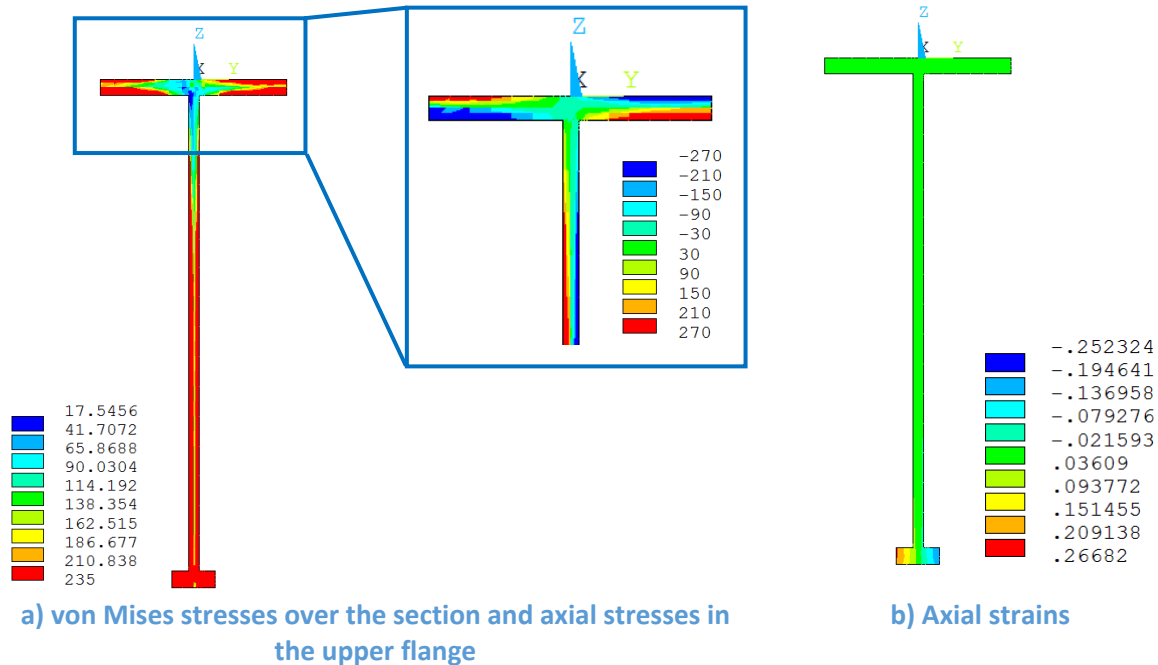


Figure 4-121: Stress and strain distribution for IPE 600m $\psi_{\text{mono}} = 0,975$ at plastic limit state

Also, it should be noted that inversely to double and slightly or medium mono-symmetric sections the reduction of the warping stiffness due to yielding of the lower flange appears to be insufficient to generate a real warping hinge. Consequently, the bi-moments continues to increase in the most loaded section at mid-span. Indeed, the diagram represented in Figure 4-122, gives the ratio between the initial warping constant I_w of the section and the effective warping constant of the section with yielded lower flange (T section $I_w = 10320 \text{ cm}^4$). Figure 4-122 points out that the decrease of the warping constant for the highly mono-symmetric IPE 600m $\psi_{\text{mono}} = 0,975$ section is much less pronounced than for the less mono-symmetric sections.

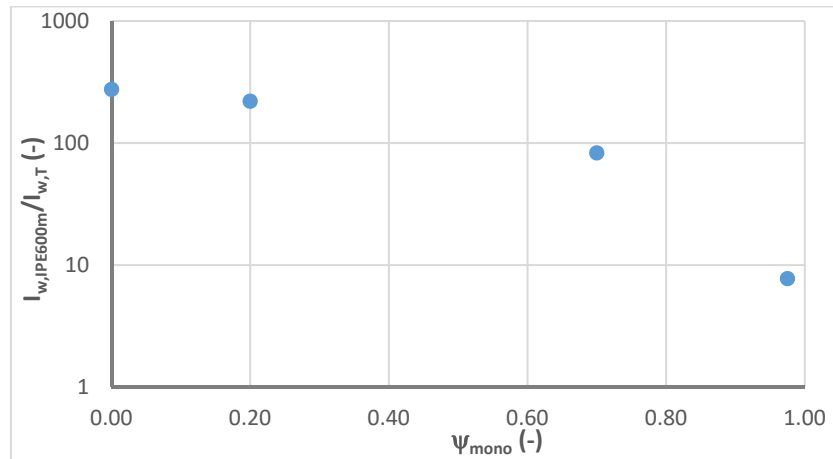


Figure 4-122: Ratio between warping constant for the mono-symmetric I section and warping constant of the associated T section for different ψ_{mono} values

Additionally, it seems interesting to represent the influence of the local bi-moment resistance on the overall bi-moment resistance. The overall plastic bi-moment including the local warping has been determined numerically. By observing Figure 4-123 it becomes obvious that for mono-symmetric sections the local effects leading to an increased plastic bi-moment can be neglected in general. However, for highly mono-symmetric sections, as the IPE 600m $\psi_{mono} = 0,975$, the local effects are nearly as important as the global plastic bi-moment.

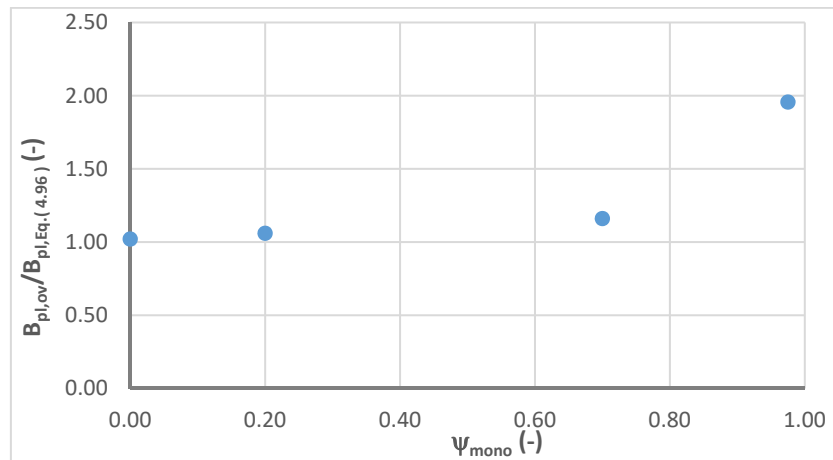


Figure 4-123: Ratio between total plastic bi-moment including local effects and plastic bi-moment obtained with Eq. (4.96) for different ψ_{mono} values

It is obvious that the local bi-moment influences considerably the behaviour of highly mono-symmetric I sections. However, Figure 4-121b) also shows that the yielding may be accompanied by very high axial strains depending on the exact geometry of the section. Therefore, the local effects are not accounted for and the observed conservatism is accepted here for the resistance model.

4.4.4.3.3 Interaction between minor-axis bending, torsion and shear force

The plastic interaction curve for combined minor-axis bending torsion and the shear force is derived based on the assumed distribution of axial stresses represented in Figure 4-116. In

particular, the local effects leading to an increased plastic bi-moments are not considered hereafter. Again, this leads to certain conservatism for highly mono-symmetric sections.

It should be recalled that the interaction between the shear force V_y and the minor-axis bending moment has been shown to be negligible. Also, as the minor-axis bending moment and the bi-moment are affine in the flanges a linear interaction may be considered again. Yet, due to the mono-symmetry of the section this linear interaction possesses two special features as discussed in paragraph 4.4.4.3.1:

- In presence of a minor-axis bending moment, the maximum bi-moment that can be resisted by the section is higher than the theoretical plastic bi-moment (not considering local effects).
- A stress induced bi-moment is necessary for the complete yielding of the section subject to minor-axis bending only.

As the interaction behaviour is not symmetric it has to be distinguished between the two cases that the bi-moment and the minor-axis bending moment are of the same sign and that the minor-axis bending moment and the bi-moment are of opposite sign. The following interaction equations may be applied:

M_z and B are of the same sign:

$$B_{pl,Mz} = B_{\max} \left[1 - \frac{M_z - M_{z,B\max}}{M_{z,B,pl} - M_{z,B\max}} \right] \quad \text{if: } M_z \geq M_{z,B\max} \quad (4.99)$$

$$B_{pl,Mz} = B_{pl} + (B_{\max} - B_{pl}) \frac{M_z}{M_{z,B\max}} \quad \text{if: } M_z < M_{z,B\max} \quad (4.100)$$

M_z and B are of opposite sign:

$$B_{pl,Mz} = B_{pl} - (B_{pl} - B_{Mzpl}) \left(\frac{M_z}{M_{z,pl}} \right) \quad \text{if: } M_z \geq M_{z,B\max} \quad (4.101)$$

It should be noted that the absolute values should be used for all quantities used in Eqs. (4.99) to (4.101). The quality of the proposed interaction curve is presented in Figure 4-124 giving the results obtained for a modified HEA 100 section whose lower flange is reduced to a width of 87 mm ($\psi_{\text{mono}} = 0,2$). Obviously, the interaction curve is in in good agreement to the MNA results. Yet, it might be confusing for the engineer that the bi-moment resistance exceeds the plastic bi-moment when the minor-axis bending moment is increased up to $M_{z,B\max}$. For simplified desing it seems more appropriate to consider a plateau for the plastic bi-moment up to the value of $M_{z,B\max}$.

Also, it seems more convenient to present the interaction formulae as a function of the bi-moment. The proposed interaction formulae for simplified design are given in Eqs. (4.102) to (4.104).

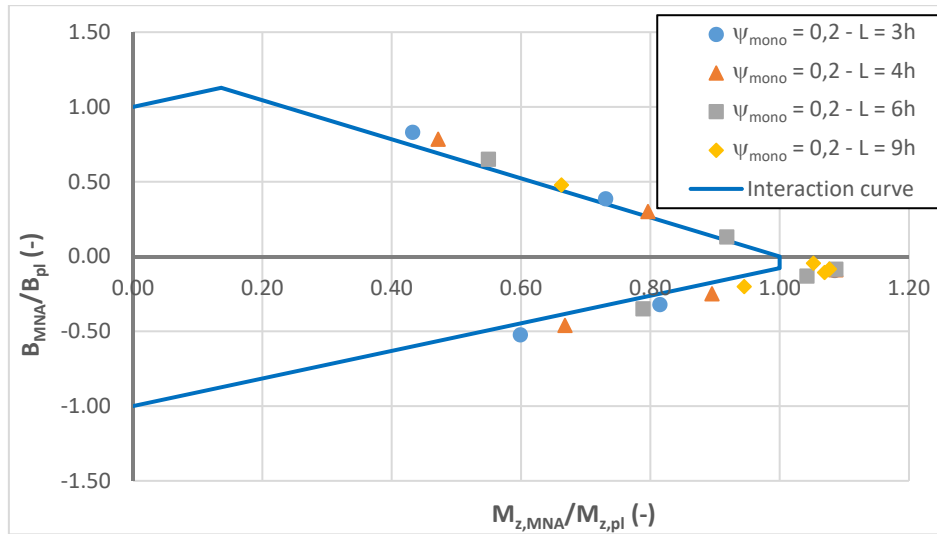


Figure 4-124 : Minor-axis bending - bi-moment interaction for HEA 100m $\psi_{mono} = 0,2$

M_z and B are of the same sign:

$$M_{z,B,pl} = M_{z,pl} - \left(M_{z,pl} - M_{z,Bmax} \right) \frac{B}{B_{pl}} \quad (4.102)$$

M_z and B are of opposite sign:

$$M_{z,B,pl} = M_{z,pl} \quad \text{if: } B \leq B_{Mz,pl} \quad (4.103)$$

$$M_{z,B,pl} = M_{z,pl} \left(1 - \frac{B - B_{Mz,pl}}{B_{pl} - B_{Mz,pl}} \right) \quad \text{if: } B > B_{Mz,pl} \quad (4.104)$$

The proposed interaction curve is compared to the MNA results in the following figures. Again, one may observe that the proposal represents well the interaction behaviour for slightly and medium mono-symmetric sections. However, it becomes rather conservative for highly mono-symmetric members as shown in Figure 4-127 as the local warping effects become relevant in this case.

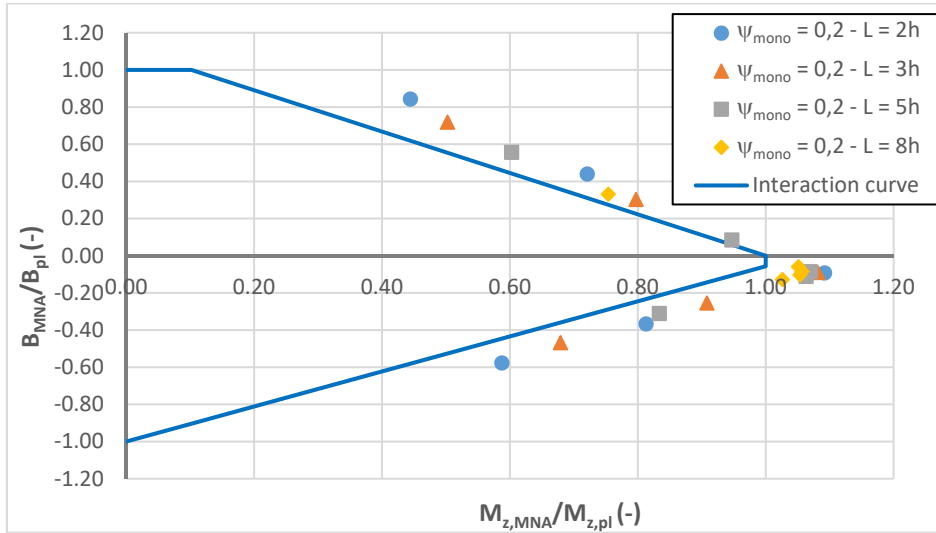


Figure 4-125: Minor-axis bending - bi-moment interaction for IPE 600 m $\psi_{mono} = 0,2$

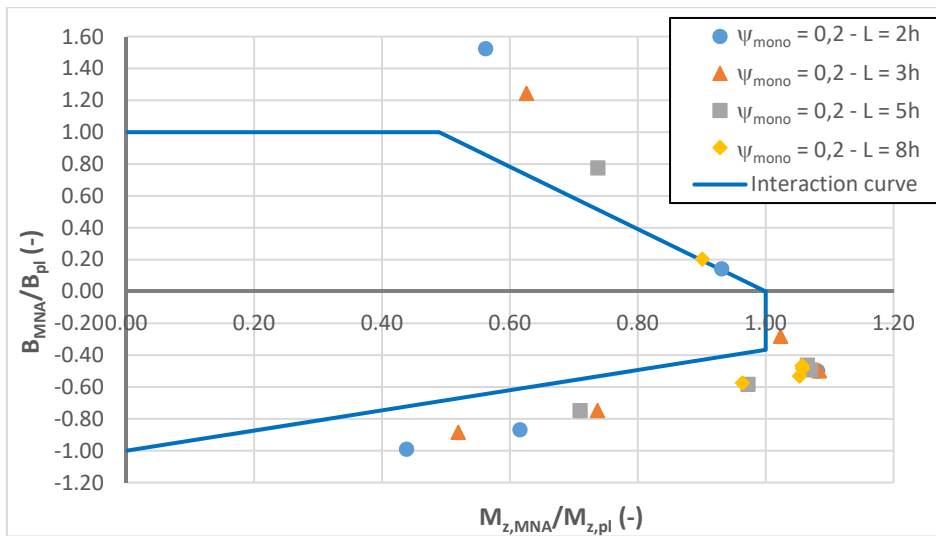


Figure 4-126: Minor-axis bending - bi-moment interaction for IPE 600 m $\psi_{mono} = 0,7$

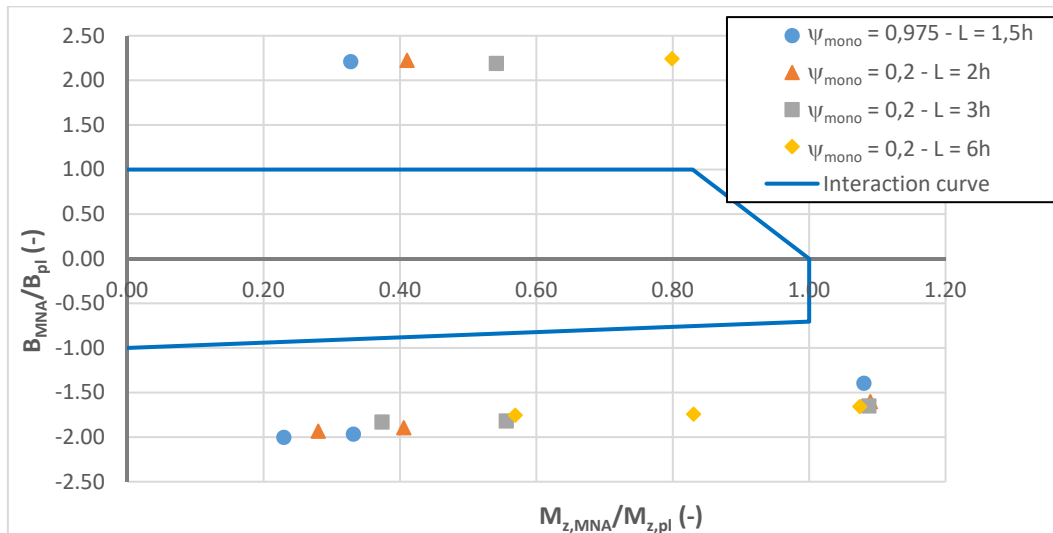


Figure 4-127: Minor-axis bending - bi-moment interaction for IPE600 m $\psi_{mono} = 0,975$

The study on mono-symmetric I sections presented throughout the three previous paragraphs shows that simplified interaction formulae may be derived based on a presumed plastic stress distribution. However, for highly mono-symmetric cross-sections the supposed stress distribution is not valid anymore due to local warping effects that increase the plastic bi-moment. These local effects may attain approximatively the same magnitude as the “global” plastic bi-moment. Yet, for simplified design they are not considered.

4.4.4.4 U sections

4.4.4.4.1 Plastic bi-moment

Before interaction equations are developed for U sections under combined bending, torsion and shear forces, it seems interesting to determine an expression of the plastic bi-moment resistance that is used as reference value in the interaction formulae. It is possible to calculate the plastic bi-moment resistance based on the plastic stress distribution represented in Figure 4-128. In order to obtain the plastic bi-moment, the position of the neutral axis should be determined. The horizontal neutral axis has to be located at the mid-height of the cross-section for symmetry reasons. The position of the vertical neutral axis, characterized by the distance noted as $y_{B,pl}$ in Figure 4-128 a), is not known a priori. It can be calculated based on the assumption that the major-axis bending moment vanishes as expressed by Eq. (4.105) (due to the form of the plastic stress distribution, the axial force and the minor-axis bending moment vanish independently from the value of $y_{B,pl}$). Consequently, the position of the vertical neutral axis is given by Eq. (4.106).

$$M_y = 0 = \left[\frac{h^2 t_w}{4} + \left(y_{B,pl} - \frac{t_w}{2} \right) t_f (h - t_f) - \left(b - \frac{t_w}{2} - y_{B,pl} \right) t_f (h - t_f) \right] f \quad (4.105)$$

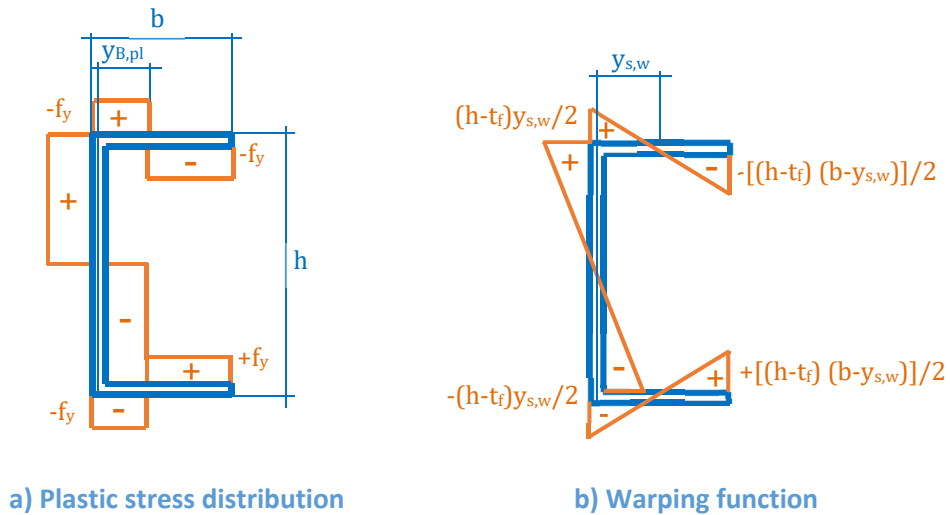


Figure 4-128: a) Plastic stress distribution for a U section subject to a positive bi-moment and b) warping function

$$y_{B,pl} = \frac{b}{2} - \frac{1}{8} \frac{h^2}{(h-t_f)} \frac{t_w}{t_f} \quad (4.106)$$

$$y_{s,w} = \frac{3 \left(b - \frac{t_w}{2} \right)^2 t_f}{6 \left(b - \frac{t_w}{2} \right) t_f + (h-t_f) t_w} \quad (4.107)$$

The position of the vertical plastic neutral axis allows the determination of the plastic bi-moment as given by Eq. (4.108) and Eq. (4.109).

$$B_{pl} = W_{B,pl} f_y \quad (4.108)$$

$$W_{B,pl} = \frac{(h-t_f)^2 t_w}{4} y_{s,w} + 2(h-t_f) t_f y_{s,w} y_{B,pl} \left(1 - \frac{y_{B,pl}}{2y_s} \right) + (h-t_f) \left(b - \frac{t_w}{2} \right) \left(\frac{b-t_w}{2} - y_{s,w} \right) t_f \quad (4.109)$$

It should be noted that, as the vertical plastic neutral axis is not located at the same point as the zero of the warping function in the flanges (distance $y_{s,w}$ – see Table 4-28), the cross-section may resist a slightly higher bi-moment than the plastic bi-moment resistance if the section is also subject to a certain major-axis bending moment $M_{y,Bmax}$.

Table 4-28: Comparison of $y_{B,pl}$ and $y_{s,w}$

Cross-section	$y_{B,pl}$ (mm)	$y_{s,w}$ (mm)
UPE 80	18,74	20,96
UPE 200	25,57	31,48
UPE 360	21,66	37,46

Table 4-29 gives the value of the plastic bi-moment B_{pl} and the maximum bi-moment B_{max} that the cross-section can resist in presence of the major-axis bending moment $M_{y,Bmax}$. Again, it is supposed that the cross-section is fabricated from steel grade S235.

Table 4-29: Plastic and maximum bi-moment (Steel grade S235)

Cross-section	B_{pl} (kNm ²)	B_{max} (kNm ²)	$M_{y,Bmax}$ (kNm)
UPE 80	0,0966	0,09716	0,535
UPE 200	1,1372	1,1540	5,771
UPE 360	6,8998	7,2323	43,309

The expressions of the maximum bi-moment B_{max} and the associated major-axis bending moment $M_{y,Bmax}$ are given in Eqs. (4.110) and (4.111).

$$B_{max} = -\frac{1}{2} \left[\frac{(h-t_f)^2 t_w y_{s,w}}{2} + (h-t_f) y_{s,w}^2 t_f + (h-t_f) \left(b - \frac{t_w}{2} - y_{s,w} \right)^2 t_f \right] f_y \quad (4.110)$$

$$M_{y,Bmax} = 2(y_{s,w} - y_{pl}) (h-t_f) t_f f_y \quad (4.111)$$

Here, it should be noted that, contrarily to the case of major-axis bending (see paragraph 4.4.2.2), the maximum bi-moment B_{max} is not considered as plastic bi-moment as the major-axis bending moment $M_{y,Bmax}$, necessary to attain this bi-moment does not develop naturally for a U section subject to torsion only. Indeed, it cannot develop as static equilibrium would not be respected. Inversely, the stress-induced bi-moment $B_{My,pl}$ necessary to attain $M_{y,pl}$ results directly from the stress distribution and develops even if the cross-section is subject to major-axis bending only.

4.4.4.4.2 Interaction between major-axis bending, torsion and shear force

The following figures represent the results of the numerical simulations. The internal forces and moments at the plastic limit state are, as before, determined according to the stress distribution in the cross-section. Consequently, these internal forces and moments correspond exactly to the internal forces acting in the most loaded section.

In Figure 4-129, the influence of the shear force and the bi-moment on the plastic major-axis bending resistance may be easily identified again. If the cross-section is subject to combined major-axis bending and shear force the interaction curve applicable to double symmetric I sections may be safely applied as has already been shown in paragraph 4.4.2.2. When a torsional load is applied to the member, the cross-section is subject to an additional bi-moment reducing the combined major-axis bending-shear resistance. Consequently, with increasing bi-moments the numerically determined resistances tend to zero in the M_y - V_z interaction diagrams for the members of a given length.

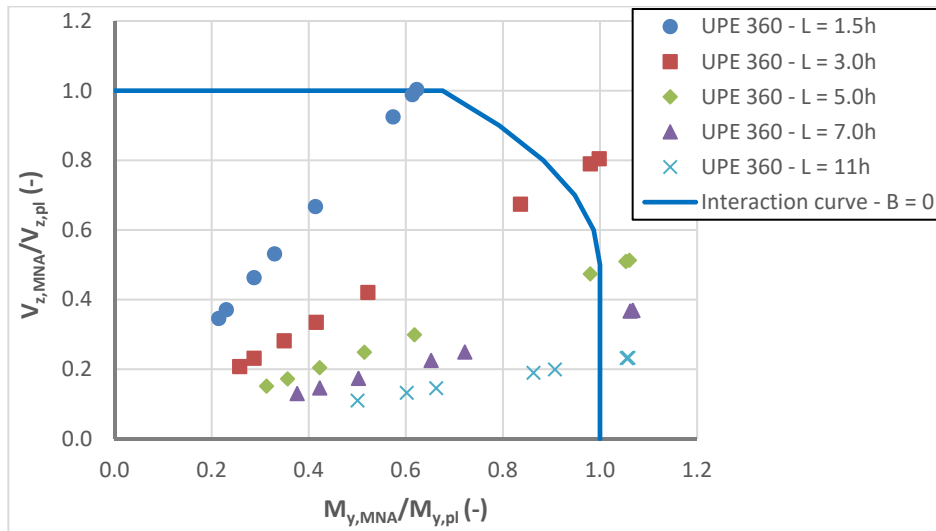


Figure 4-129 : M_y - V_z - B interaction diagram for UPE 360 – M_y - V_z -plane

The interaction diagram given here before in the M_y - V_z plane resembles to the interaction diagram obtained for double symmetric I sections. However, it should be noted that the interaction diagram is not symmetric in the B - M_y plane as, depending on the sign of the bi-moment and major-axis bending moment the axial stresses may add or neutralise in the web as recalled in Figure 4-130.



a) Elastic stress distribution due to $M_y > 0$

b) Elastic stress distribution due to $B > 0$

Figure 4-130: Elastic stress distribution due to a) positive major-axis bending and b) positive bi-moments

The results of the MNA simulations performed for three UPE sections are represented in Figure 4-131. In order to simplify the lecture, the following diagrams contain only the cases not affected by a strength reduction due to the shear force. Observing Figure 4-131, one may recognize the mentioned asymmetry of the interaction curve.

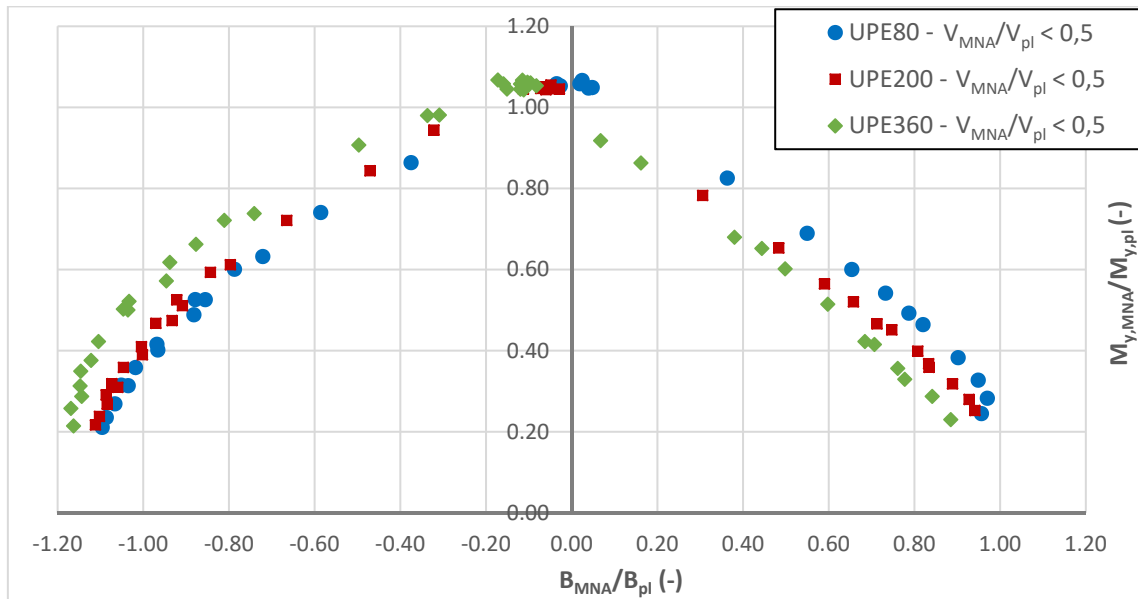


Figure 4-131: M_y - B interaction curve for UPE sections obtained by MNA calculations

Hereafter, interaction equations are based on the stress distribution and the position of the plastic neutral axis.

First, the case of interaction between a bi-moment and a major-axis bending moment of the same sign (both either positive or negative) is investigated. If both internal moments are of the same sign, the axial stresses neutralise in the web. The vertical plastic neutral axis may therefore be situated in the web or in the flanges as shown for the case of a UPE 200 section subject to a low bi-moment (Figure 4-132) and to a high bi-moment (Figure 4-133). In the flange the position of the vertical neutral axis varies between $y_{B,pl}$ and the edge of the web.

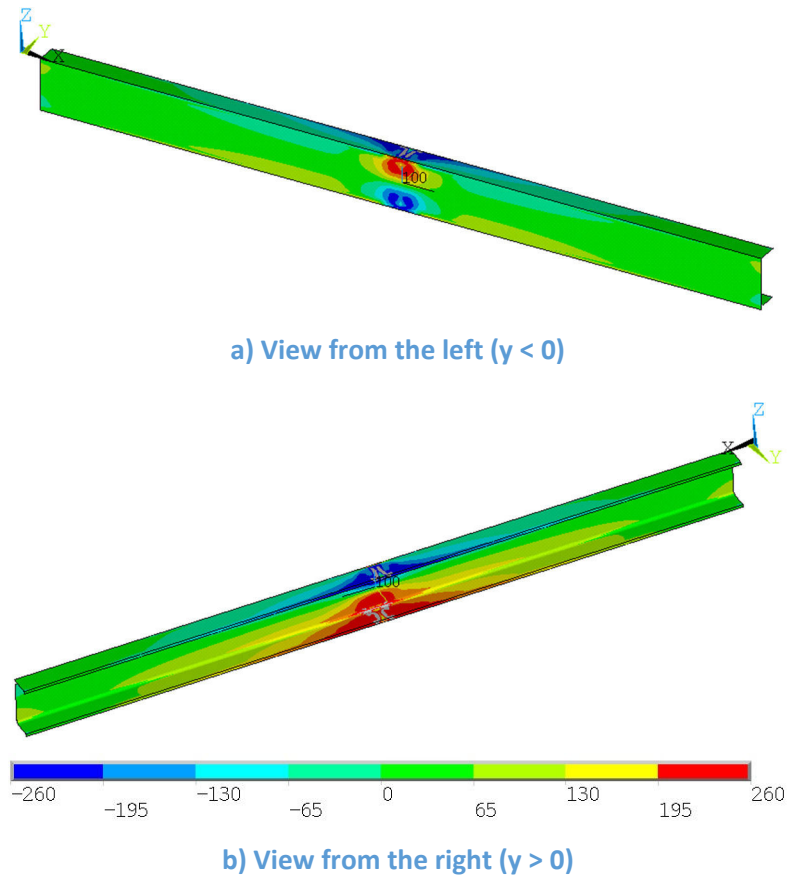


Figure 4-132: Plastic stress distribution for low bi-moments and high major-axis bending moments – vertical plastic neutral axis in the web

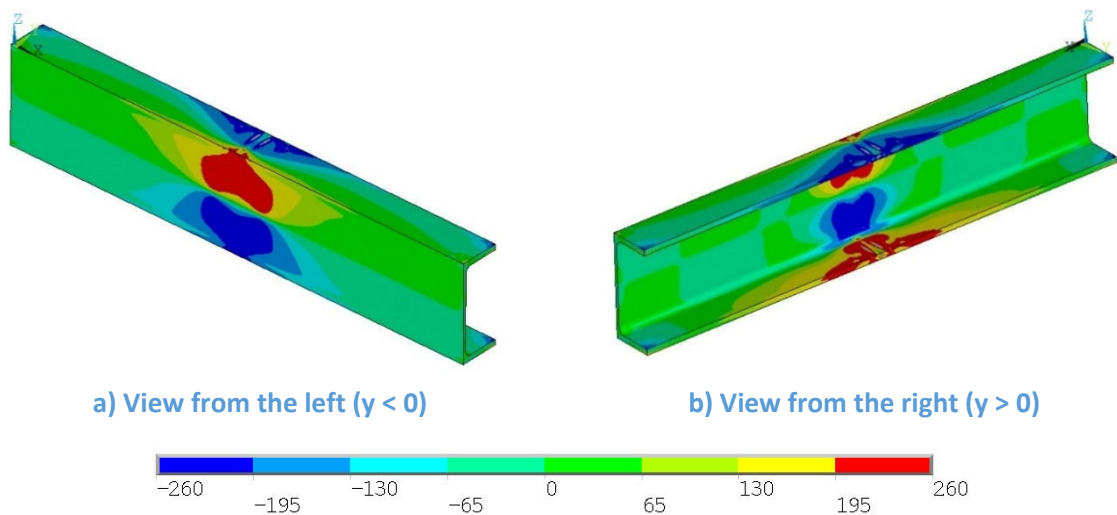


Figure 4-133: Plastic stress distribution for high bi-moments and low major-axis bending moments – vertical plastic neutral axis in the flange

The vertical plastic neutral axis is situated in the web in case of high major-axis bending moments and low bi-moments. Eq. (4.112) gives the limit bi-moment that leads to a plastic vertical neutral axis that is just located at the edge between the web and the flange. Condition (4.112) expresses that the vertical plastic neutral axis is located in the web if the bi-moment is less than **twice** the

bi-moment resistance of the web. The factor of “2” may be explained as follows: In absence of a bi-moment, the positive major-axis bending moment creates compression stresses at the upper part of the web and tension stresses at the lower part of the web. It has been shown that the positive bi-moment creates stresses with of opposite sign in the web. Consequently, in order to “push” the vertical plastic neutral axis into the flange, the bi-moment has to **inverse** the stresses created by the major-axis bending moment and hence it has to be twice the resistance of the web.

$$B_{Ed} \leq \frac{1}{2} (h - t_f)^2 t_w y_{s,w} f_y = 2B_{pl,web} \quad (4.112)$$

It is considered that the position of the vertical neutral axis varies linearly through the web with increasing bi-moment. Hence, one may determine the moment resistance in presence of a bi-moment by Eq. (4.113).

$$M_{y,B,pl} = M_{y,pl} - \frac{h^2 t_w}{2} \left(\frac{B_{Ed}}{2B_{pl,web}} \right) f_y \quad (4.113)$$

For bi-moments exceeding the value of $2B_{pl,web}$ the vertical plastic neutral axis transits through the flange up to its position $y_{B,pl}$ obtained under the sole influence of a bi-moment. Compared to the numerical simulation a slightly non-linear variation is justified for the variation of the position of the vertical plastic neutral axis. The moment resistance may therefore be obtained with Eq. (4.114) if the vertical plastic neutral axis passes through the flange.

$$M_{y,B,pl} = M_{y,pl} - \frac{h^2 t_w}{2} f_y - 2t_f (h - t_f) \left(y_{B,pl} - \frac{t_w}{2} \right) \left(\frac{B_{Ed} - 2B_{pl,web}}{B_{pl} - 2B_{pl,web}} \right)^{1.5} f_y \quad (4.114)$$

The **absolute values** should be used for of all the quantities in Eqs.(4.112) to (4.114). The interaction curve is compared to the numerical results in Figure 4-134. It appears that the interaction curve corresponds rather well to the numerical results.

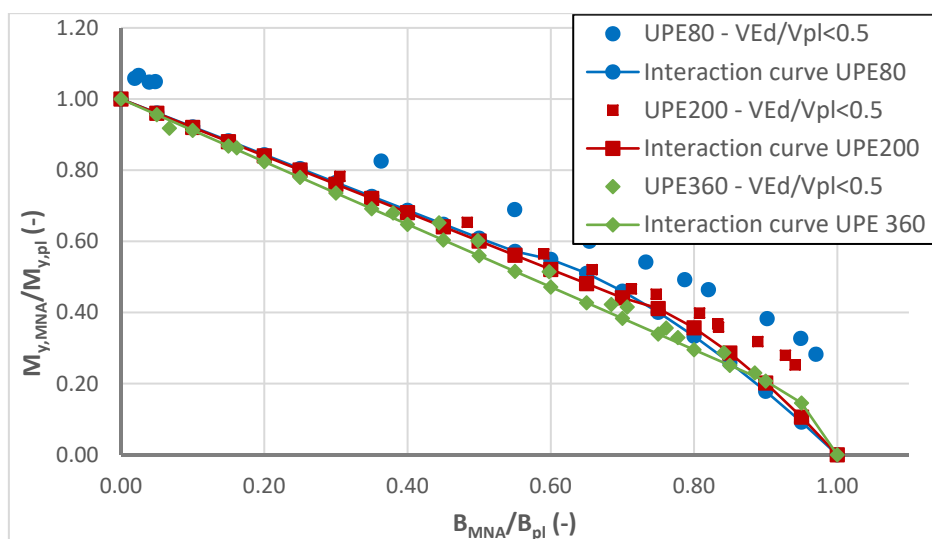


Figure 4-134: Comparison between numerical results and interaction curve

In the following the interaction curve is developed for the case that the major-axis bending moment and the bi-moment are of opposite sign. In this case, the axial stresses sum up in the web of the cross-section. Consequently, the vertical neutral axis only transits through the flange and its position varies between the tips of the flanges and $y_{B,pl}$. Even if the location of vertical plastic neutral stays in the flange two specific features of the interaction behaviour lead to its complexification as may be observed in Figure 4-131:

- For small bi-moments the major-axis bending moment resistance is not reduced. The plateau length is equal to the value of the bi-moment that is necessary for full yielding of the section under an applied moment M_y ($B_{My,pl}$ – Eq. (4.70)).
- The maximum bi-moment that may be resisted by the cross-section exceeds the plastic bi-moment (B_{max} – Eq. (4.110)).

For simplicity it is considered that the interaction curve is constituted by two plateaus – one horizontal corresponding to $B_{My,pl}$ and one vertical corresponding to twice the bending moment leading to B_{max} . The two plateaus are linked by a slightly non-linear curve that considers approximatively the interaction behaviour. The interaction curve may consequently be expressed by Eq. (4.115) and Eq. (4.116).

$$M_{y,B,Rd} = M_{y,pl} \quad \text{if } B \leq B_{My,pl} \quad (4.115)$$

$$M_{y,B,Rd} = M_{y,pl} - \left(M_{y,pl} - 2M_{y,Bmax} \right) \left(\frac{B_{Ed} - B_{My,pl}}{B_{pl} - B_{My,pl}} \right)^{1.5} \quad \text{elsewise} \quad (4.116)$$

The interaction curve is compared to the numerical results in Figure 4-135. The proposed equations are satisfactory again.

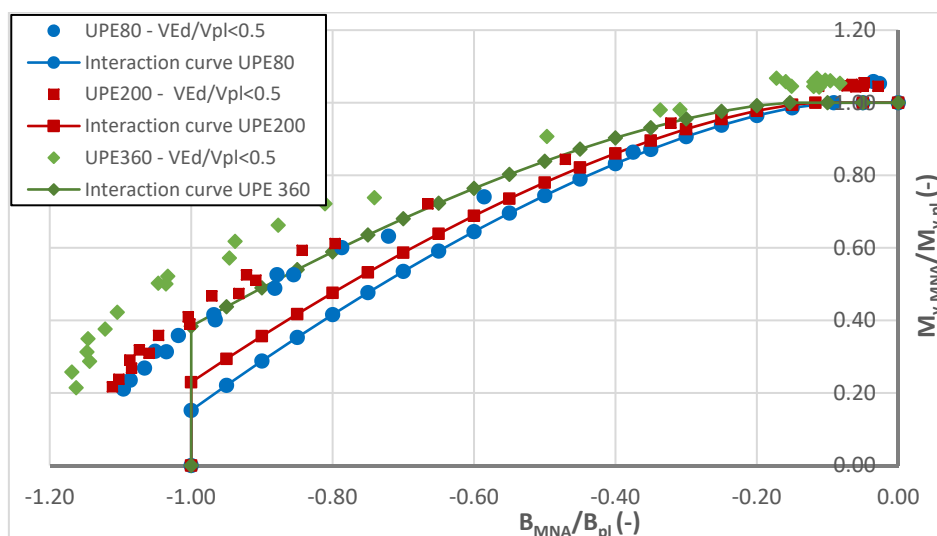


Figure 4-135: Comparison between numerical results and interaction curve

Before, only cases with low shear force have been treated. If the shear force exceeds the value of 0,5, its influence on the resistance should be accounted for. Here, it is proposed to consider its influence by reducing the thickness of the web as shown in Eq. (4.117).

$$t_{w,V} = (1 - \rho)t_w \tag{ 4.117 }$$

The reduction factor ρ can be determined with the expression given in Eurocode 3 Part 1-1 recalled in Eq. (4.15). This reduced web thickness $t_{w,V}$ is introduced into Eq. (4.70), (4.106), (4.107), (4.109), (4.111) and (4.112) to obtain the corresponding values of $B_{My,pl,V}$, $y_{B,pl,V}$, $y_{s,w,V}$, $W_{B,pl,V}$, $M_{y,Bmax,V}$, $B_{pl,web,V}$. The interaction equations developed in this paragraph may then be applied with these reduced quantities. In order to visualize the quality of the proposed interaction equations, Figure 4-136 represents the ratio between the resistance predicted by the interaction equations and the resistance obtained numerically by MNA calculations. It may be observed that the results are very satisfactory for the studied cross-sections. It seems that the interaction equations yield more precise results for tall sections than for small sections. This is due to the fact that the influence of the fillets on the warping characteristics, as for example $y_{B,pl}$, are not included in the derivation of the formulae. Indeed, their relative influence decreases with the height of the cross-section. Nevertheless, the results are in the large majority of cases safe-sided and sufficiently precise. A higher precision may only be obtained if the interaction equations that are already rather complex, include additional parameters. Last, it should be noted that, for simplicity, a linear interaction may always be considered between the major-axis bending moment and the bi-moment.

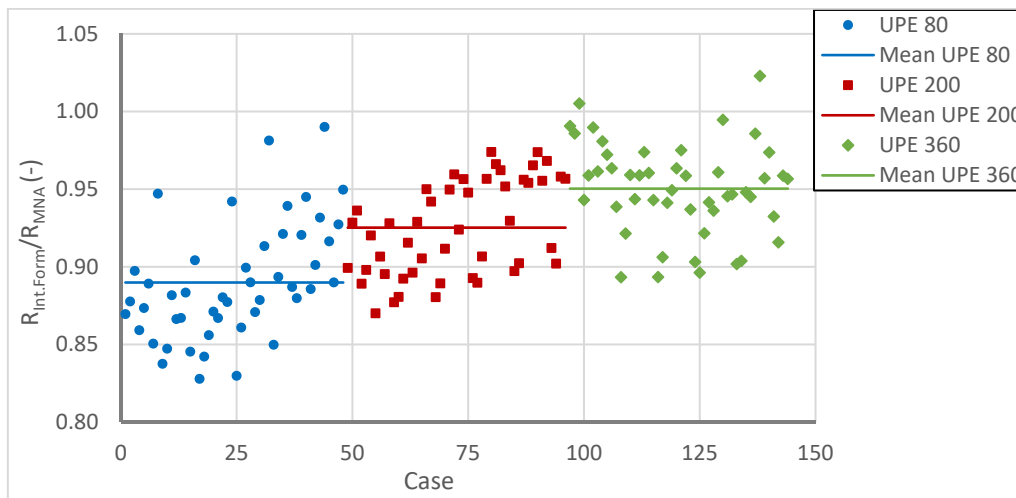


Figure 4-136: Ratio between resistance predicted by proposed interaction equations and resistance obtained by MNA

4.4.4.4.3 Interaction between minor-axis bending, torsion and shear force

Figure 4-137 and Figure 4-138 represent the results obtained for the interaction between minor-axis bending, shear force and the bi-moment. Again, it may be observed in Figure 4-137 that the bi-moment may highly reduce the cross-section capacity under combined shear and bending moments. Inversely, the influence of the shear force is negligible. It should be noted that, even for

the shortest member ($L = 1,5h$), the shear force does not exceed 50% of the plastic shear force resistance that is supposed to be equal to:

$$V_{y,pl} = 2bt_f \frac{f_y}{\sqrt{3}} \quad (4.118)$$

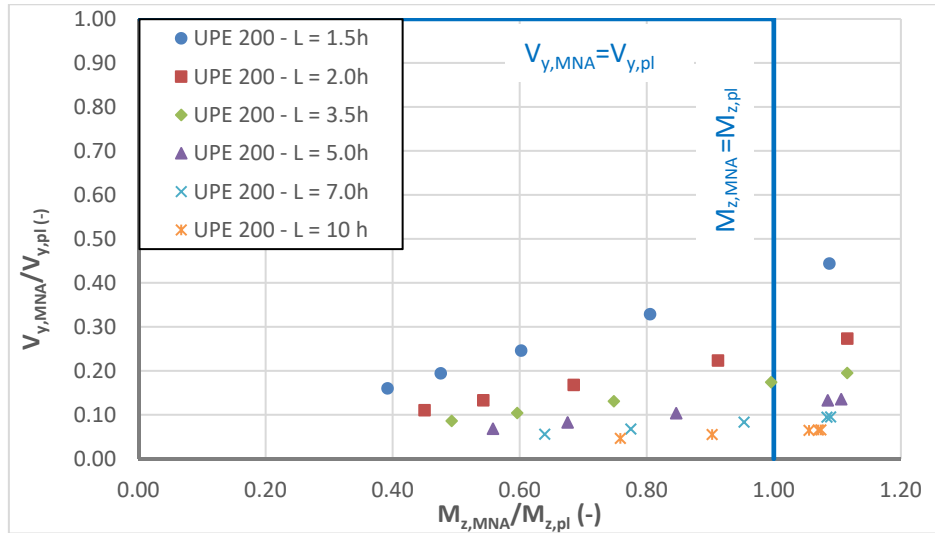


Figure 4-137: M_z - V_y - B interaction diagram for UPE 200 – M_z - V_y -plane

Figure 4-138 characterizes very clearly the interaction behaviour between minor-axis bending and the bi-moment. In particular, it is shown that:

- The interaction behaviour between minor-axis bending and bi-moments is symmetric,
- For low levels of minor-axis bending or bi-moments, it may be admitted that the corresponding plastic resistance is not reduced (plateau length = $0,1M_{z,pl}$ and $0,1B_{pl}$, respectively),
- The interaction curve linking both plateaus may be linear.

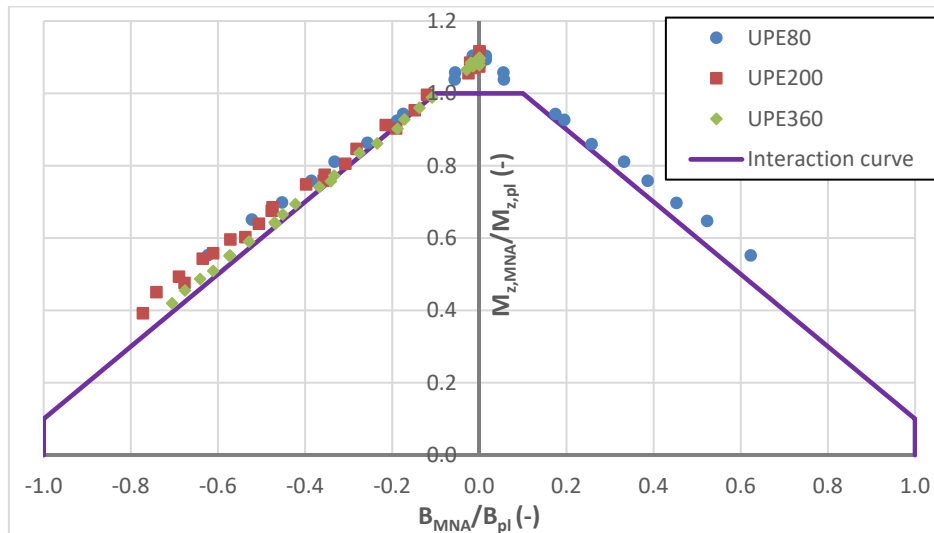


Figure 4-138: M_z - V_y - B interaction diagram for all studied sections – M_z - B -plane

The interaction curve represented in Figure 4-138 may be expressed by Eq. (4.119).

$$M_{z,B,pl} = M_{z,pl} \left(1, 1 - \frac{B}{B_{pl}} \right) \leq M_{z,pl} \quad (4.119)$$

4.4.5 Other selected load cases

4.4.5.1 General

In the following, two specific load cases are treated in order to highlight the complexity of the interaction behaviour in some cases. First, the interaction equations applicable for the case of combined major-axis bending, shear force and torsion are extended to the case of an applied axial force ofr double symmetric I sections. Then the case of a U section subject to combined axial force and major-axis bending is treated. This load combination may seem trivial on a first sight, but it is shown that due to the mono-symmetry of the U section, the interaction is again complex even for simple load combinations.

4.4.5.2 Combined axial force, bending and torsion for double symmetric I sections

In many cases I sections are subject to an axial force (even if rather small) additionally to bending and torsion. Consequently, this load case is of practical interest and should be treated. It is proposed to extend the interaction equations introduced in paragraph 4.4.4.2.2 for the case of combined major-axis bending, shear force and bi-moment to the case of an additional axial force. The equations not considering the axial force are recalled hereafter:

$$M_{y,V,pl} = \left(W_{pl,y} - \frac{\rho A_w^2}{4t_w} \right) f_y \quad \text{if } \frac{V_z}{V_{z,pl}} > 0,5$$

$$\text{and } \rho = \left(\frac{2V_z}{V_{pl,z}} - 1 \right)^2$$

$$M_{y,B,V,pl} = M_{y,V,pl} - \left[1 - \sqrt{1 - \left(\frac{B}{B_{pl}} \right)} \right] M_{y,pl,fl}$$

Depending on the relative importance of the axial force and the shear force, the axial force may only reduce the bending moment resistance of the web (relatively small axial force) or it may contribute to the reduction of the major-axis bending moment resistance of the flange. Several cases should be distinguished as shown in the following table. Clearly, the interaction conditions become rather complex. They are based on the assumption that the combined action of the axial force and the shear force is, in priority, resisted by the web of the section; the bi-moment is only resisted by the flange. Consequently, the major-axis bending moment resistance is the sum of the residual plastic bending moment of the web (for combined action “N+V_z” lower than the resistance of the web) and the residual bending moment resistance of the flange (reduced by the bi-moment and by the axial force that may not be carried by the web).

Table 4-30: Interaction between major-axis bending, shear force, axial force and bi-moment

Value of the shear force	Value of the axial force	Value of the major-axis bending moment resistance
$\frac{V_z}{V_{z,pl}} \leq 0,5$	$\frac{N}{h_w t_w f_y} \leq 1,0$	$M_{y,N,pl} = \left(W_{pl,y} - \frac{\rho A_w^2}{4 t_w} \right) f_y$ <p>with: $\rho = \left(\frac{N}{h_w t_w f_y} \right)^2$</p> <p>and: $M_{y,N,B,pl} = M_{y,N,pl} - \left[1 - \sqrt{1 - \left(\frac{B}{B_{pl}} \right)} \right] M_{y,pl,fl}$</p>
	$\frac{N}{h_w t_w f_y} > 1,0$	$M_{y,N,B,pl} = M_{y,pl,fl} - \left[1 - \sqrt{1 - \left(\frac{B}{B_{pl}} \right)} \right] \left(1 - \frac{N_{fl}}{2 b_f t_f f_y} \right) M_{y,pl,fl}$ <p>with: $N_{fl} = N - h_w t_w f_y$</p>
$\frac{V_z}{V_{z,pl}} > 0,5$	$\rho \leq 1,0$	$M_{y,N,V,pl} = \left(W_{pl,y} - \frac{\rho A_w^2}{4 t_w} \right) f_y$ <p>with: $\rho = \left(\frac{2V_z}{V_{pl,z}} - 1 + \frac{N}{h_w t_w f_y} \right)^2$</p> <p>and: $M_{y,N,V,B,pl} = M_{y,N,V,pl} - \left[1 - \sqrt{1 - \left(\frac{B}{B_{pl}} \right)} \right] M_{y,pl,fl}$</p>
	$\rho > 1,0$	$M_{y,N,V,B,pl} = M_{y,pl,fl} - \left[1 - \sqrt{1 - \left(\frac{B}{B_{pl}} \right)} \right] \left(\frac{N_{fl}}{2 b_f t_f f_y} \right) M_{y,pl,fl}$ <p>with: $N_{fl} = N - \left(2 - \frac{2V_z}{V_{z,pl}} \right) h_w t_w f_y$</p>

It should be noted that for the studied load case of combined major-axis bending, shear force, axial force and bi-moment other proposals exist as the one published in (Ludwig 2014) that has been derived based on the PIFM (see 4.2.2.3.1). However, the obtained equations are obviously not simpler to apply than the ones proposed in Table 4-30 (see 4.2.2.3.1). Clearly, the interaction

behaviour between more than two or three internal forces and moments may not be treated by a simple equation even in the case of double symmetric sections. Through the next paragraph it is demonstrated that the interaction behaviour of U sections is even more complex although, on the first sight, the rather simple interaction of combined major-axis bending and axial force is studied.

4.4.5.3 Combined axial force and major-axis bending for U sections

The interaction between major-axis bending and the axial force has also been discussed in reference (Kalameya 2008). Based on some numerical simulations the author showed that the interaction may be treated as for I sections. Indeed, so as to obtain the interaction equation the following stress distribution is supposed (see Figure 4-139).

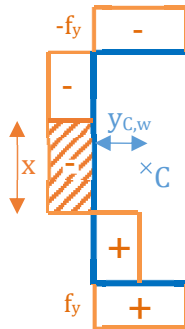


Figure 4-139: Supposed plastic stress distribution under combined major-axis bending and axial force for U sections

However, one may observe that the proposed plastic stress distribution also leads to a resulting minor-axis bending moment equal to:

$$M_z = N \times y_{C,w} \quad (4.120)$$

Consequently, this stress distribution is not valid, as, due to the condition of static equilibrium, the minor-axis bending moment cannot be generated without an external load. In fact, in case of combined major-axis bending and axial force the plastic neutral axis cannot be horizontal as this would always lead to a resulting minor-axis bending moment. So as to obtain a valid plastic stress distribution the neutral axis has to be inclined crossing one flange and the web as shown in Figure 4-140.

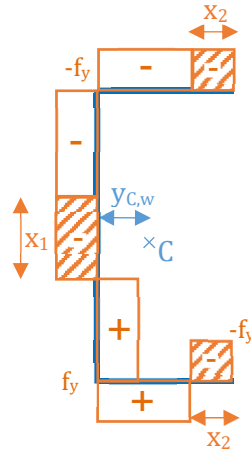


Figure 4-140: Valid plastic stress distribution for U sections under combined major-axis bending and axial force

The axial force creating this stress distribution is given in Eq. (4.121).

$$N = f_y (x_1 t_w + 2x_2 t_f) \quad (4.121)$$

Based on this stress distribution it is also possible to determine the major-axis bending moment resistance as shown in Eq. (4.122).

$$M_{y,N,pl} = \left[\frac{(h - t_f - x_1)^2 t_w}{4} + (h - t_f) (b - t_w - x_2) t_f \right] f_y \quad (4.122)$$

So as to obtain the value of the major-axis bending moment resistance given in Eq. (4.122), it is necessary to determine the distances x_1 and x_2 first. One condition is expressed by Eq. (4.121). The second condition needed for the calculation of x_1 and x_2 may be expressed by Eq. (4.123) indicating that the plastic stress distribution should not generate a minor-axis bending moment. Here, it should be noted that no condition is used concerning the bi-moment as it may arise from the stress distribution as for the case of the plastic major-axis bending moment (stress induced bi-moment).

$$M_z = 0 = \left[x_1 t_w y_{c,w} - 2x_2 t_f \left(b - \frac{t_w}{2} - \frac{x_2}{2} - y_{c,w} \right) \right] f_y \quad (4.123)$$

Based on Eq. (4.121) and (4.123), one obtains the following expressions for the distances x_1 and x_2 .

$$x_2 = b - \frac{t_w}{2} - \sqrt{\left(b - \frac{t_w}{2} \right)^2 - \frac{N y_{c,w}}{t_f f_y}} \quad (4.124)$$

$$x_1 = 2 \frac{t_f x_2}{t_w y_{c,w}} \left(b - \frac{t_w}{2} - \frac{x_2}{2} - y_{c,w} \right) \quad (4.125)$$

Observing Eqs. (4.124) and (4.125), one may remark that they represent very well the extreme cases of zero axial force and an axial force equal to the plastic axial force N_{pl} of the section. Indeed, if the axial force is zero the distances x_1 and x_2 become zero, too. Consequently, the plastic neutral axis passes through the web at mid-height. Hence, the major-axis bending resistance is not reduced. If the axial force equals N_{pl} the distance x_2 is equal to $b-t_w/2$ and x_1 is equal to $h-t_f$. Following the mid-line model of the cross-section considered for the determination of x_1 and x_2 , the plastic neutral axis is tangential to the theoretical intersection between one flange and the web but passes just outside the section. Obviously, Eqs. (4.124) and (4.125) are rather complex to use in the practice. However, they describe the interaction behaviour as shown based on the following example of a UPE 200 section subject simultaneously to a major-axis bending moment and a compression axial force. The plastic stress distribution is represented for the case of a section subject to a compression axial force of 350 kN and a major-axis bending moment of 27 kNm in Figure 4-141. Depending on this axial force, it is possible to determine the position of the plastic neutral axis with Eqs. (4.124) and (4.125). One obtains:

$$x_1 = 160,3mm$$

$$x_2 = 23,98mm$$

In Figure 4-141 one may recognize that there is slight difference between the results of Eqs. (4.124) and (4.125) and the MNA simulations. In fact, the plastic neutral axis crosses the web at a higher level than predicted by Eq. (4.124). However, this may also be explained based on the plastic stress distribution resulting from the MNA simulation. Indeed, Eqs. (4.124) and (4.125) have been derived based on the assumption that the stresses are constant through the thickness. Yet, in Figure 4-141 one may observe that the neutral axis is inclined in the lower flange. Consequently, the lower flange carries more compression stresses and hence the web has to carry less compression stresses to ensure static equilibrium. This leads to differences observed for the position of the plastic neutral axis. Yet, the major-axis bending moment resistance obtained based on the calculated values of x_1 and x_2 is equal to 24,7 kNm and hence close to the value obtained by the MNA simulations (\approx difference 10%).

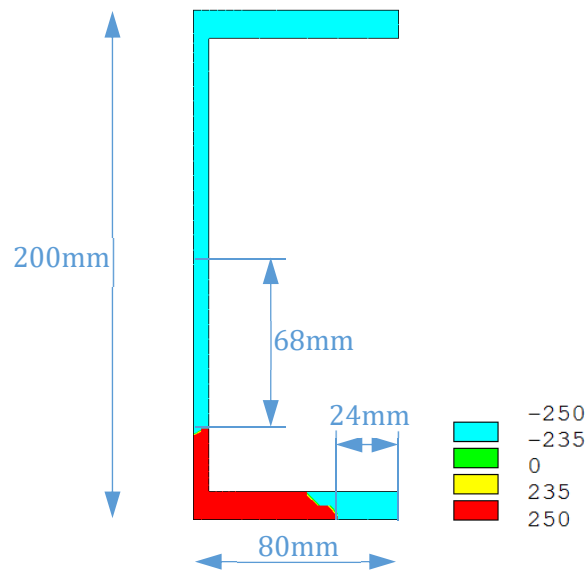


Figure 4-141: Stress distribution at plastic limit state - UPE200 under combined compression and major-axis bending

Nevertheless, it has to be noted that for high axial forces the differences may be greater as the plastic neutral axis crosses only the flange as shown in Figure 4-142. In this case Eqs. (4.124) and (4.125) may obviously not be applied. Yet, here it seems not straightforward to develop supplementary analytical interaction equations that cover this case. Indeed, this would lead even to equations that are more complex. Rather, it seems preferable to apply the adapted version of PIFM (see paragraphs 4.2.2.3.2 and 4.5). The resulting interaction curve is compared to the MNA results in Figure 4-143.

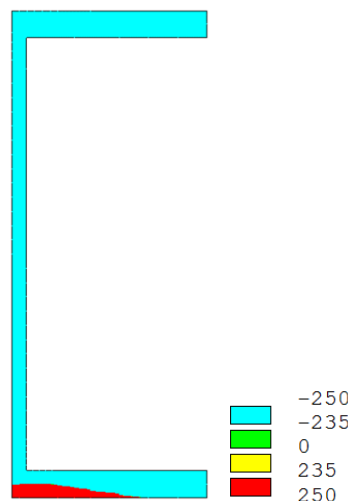


Figure 4-142: Stress distribution at plastic limit state – UPE200 under combined compression and major-axis bending – High axial force

Figure 4-143 clearly shows that the adapted PIFM may predict well the complex interaction. Also, it is recalled that PIFM has been derived in reference (Kindmann et al. 1999b) based on

equilibrium conditions on the cross-section. Therefore, it respects the stress distribution at the plastic limit state discussed here before. Yet, as it is based on the mid-line model, PIFM cannot represent exactly the stress distribution obtained for high axial forces illustrated in Figure 4-143. Nevertheless, the adapted PIFM leads to very satisfactory results.

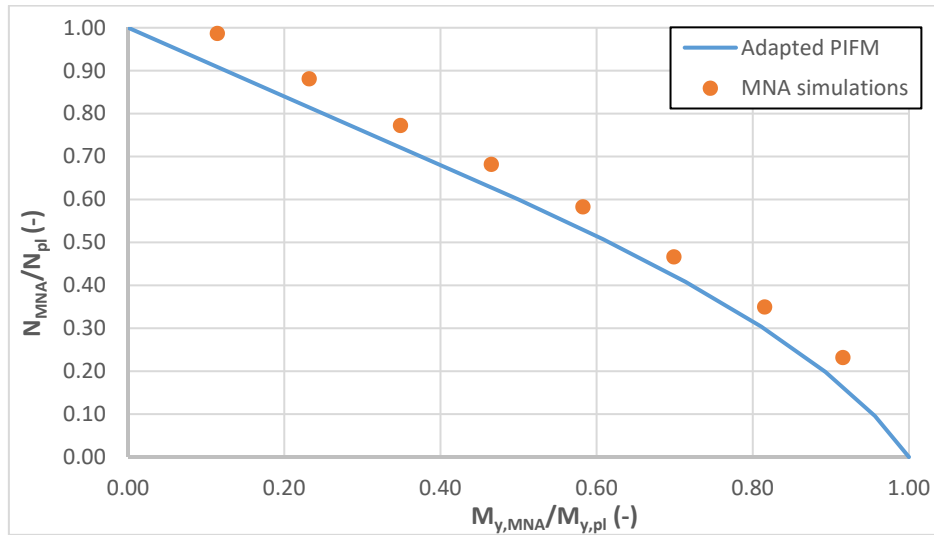


Figure 4-143: UPE200 under combined compression and major-axis bending – Comparison between MNA and adapted PIFM

4.4.5.4 Conclusions

In this section, two different interaction cases have been studied. First the rather complex load case of combined major-axis bending-shear force-axial force-bi-moment has been treated for the rather simple double symmetric I section. Then the “simple” interaction between axial force and major-axis bending has been studied for the rather complex U section. In both cases, it has been shown that analytically derived interaction equations are complex and difficult to apply in the practice. As practical engineers use more and more numerical tools, it may be considered that an analytical method implemented numerically is acceptable for the practice as resistance model. The Partial Internal Force Method PIFM developed by Kindmann is derived analytically based on some key assumptions. Throughout the present Chapter, some of the assumptions have been shown to be too conservative (see stress induced bi-moments). Also, owing to the extensive experimental and numerical study on the plastic interaction including shear forces and torsional actions the PIFM is adapted to the observed “real” behaviour. The adaptations are summarized the following paragraph. Additionally, the proposed method is again validated with reference to the totality of the performed MNA simulations.

4.5 Proposed resistance model

Throughout the present Chapter the plastic interaction has been studied for double and mono-symmetric I sections as well as for U sections subject to complex load cases including applied torsion. Several interaction equations have been proposed that yield precise results. However, with increasing complexity of the specific case (cross-section and load combination) the interaction equations became also more complex. Consequently, it did not seem straightforward to develop interaction equations that cover all possible cases. Rather, it has been shown that an adaption of the PIFM method proposed by Kindmann may lead to safe-sided and economical results. The introduced adaptations are summarized hereafter:

- The stress induced bi-moment that is, in some cases, necessary for the complete yielding of cross-section is determined iteratively.
- The influence of the fillets on the cross-section resistance is considered. The fillets are used to carry internal forces and moments in the following order of priority:
 1. Major-axis bending moment
 2. Minor axis bending moment
 3. Axial force

Consequently, a completely continuous interaction space is ensured.

- The interaction between the shear force V_y and the other internal forces and moments is neglected.
- The interaction between the shear force V_z and the other internal forces is adapted to the results of the experimental and numerical studies performed in this Chapter:
 1. A cut-off limit equal to $0,5V_{z,pl}$ is taken into account.
 2. The shear area is equal to the area of the web.
 3. If the shear force exceeds the cut-off limit, the yield stress of the web is reduced by the factor ρ given in Eq. (4.6).

Again, the importance of the stress induced bi-moment has to be highlighted. However, up to this point it has not been detailed how the stress induced bi-moment interact with an externally applied bi-moment in the framework of the adapted PIFM. In order to explain this problematic Figure 4-144 shows major-axis bending-bi-moment interaction diagram for UPE sections again.

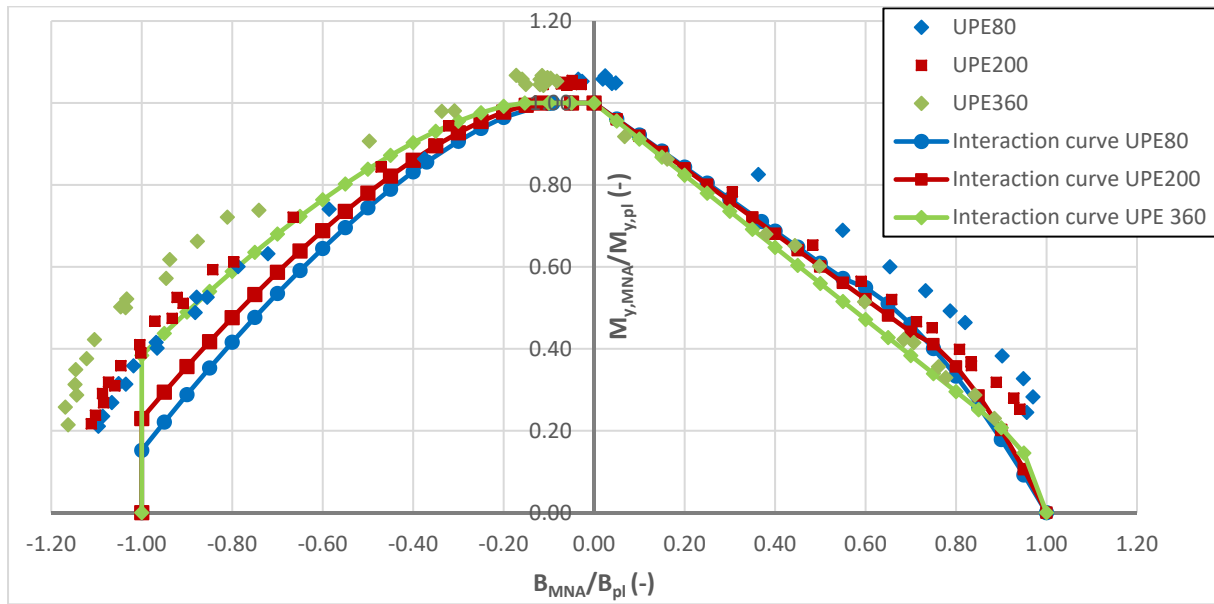


Figure 4-144: Major-axis bending-bi-moment interaction diagram for UPE sections

It should be recalled that a negative bi-moment (following the sign conventions used here) is necessary for the full yielding of the cross-section under major-axis bending only. Figure 4-145 represents the results obtained for the UPE 200 section again as well as the interaction curve obtained with the originally proposed PIFM.

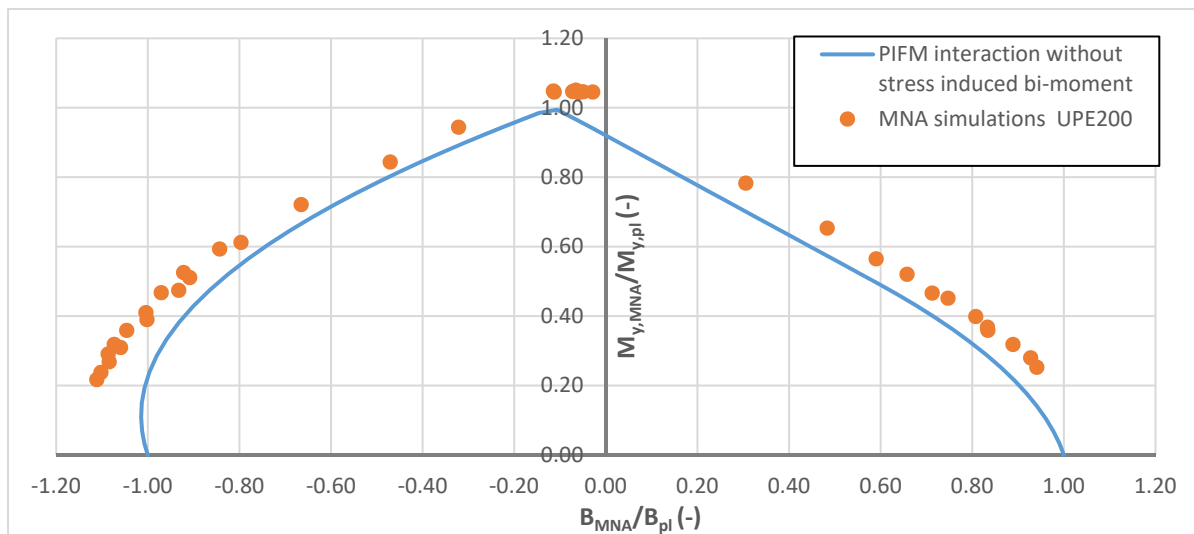


Figure 4-145: Major-axis bending-bi-moment interaction diagram for UPE sections

In Figure 4-145, it may be observed that the interaction behaviour is in general very well represented by PIFM. However, for low bi-moments considerable differences may be recognized, too. Obviously, the problem is that the original PIFM does not consider the stress induced bi-moment. The MNA results clearly indicated that the major-axis bending moment is not reduced until the externally applied bi-moment B_{ext} exceeds the value of the stress induced bi-moment ($B < 0$). For higher negative bi-moments the PIFM is in very good accordance to the numerically determined resistances. On the other side of the interaction diagram PIFM leads to a non-

negligible strength reduction even for small bi-moments. So as to obtain a continuous interaction curve, it is considered that the stress induced bi-moment B_{SI} influences the resistance even for small positive values of the externally applied bi-moment B_{ext} . However, in case of high externally applied bi-moments the stress induced bi-moment has obviously no importance. Consequently, the value of B_{ext} is modified for the calculation as follows:

$$B_{ext,PIFM} = B_{ext} + \left(1 - \frac{B_{ext}}{B_{pl}}\right) B_{SI} \quad (4.126)$$

Eq. (4.126) is applied if the stress induced bi-moment and the externally applied bi-moment are of opposite sign. If both are of the same sign the bi-moment $B_{ext,PIFM}$ is determined by Eq. (4.127).

$$\begin{aligned} B_{ext,PIFM} &= B_{SI} && \text{if } abs(B_{ext}) \leq abs(B_{SI}) \\ B_{ext,PIFM} &= B_{ext} && \text{elsewise} \end{aligned} \quad (4.127)$$

The value of $B_{ext,PIFM}$ is then used for the design with the adapted Partial Internal Force Method. Admittedly, the proposed procedure is of empirical and phenomenological nature. Nevertheless, it represents very well the interaction behaviour observed in the extensive numerical study presented throughout this Chapter. In order to validate the approach, the case of the UPE 200 section subject to combined major-axis bending and bi-moments is considered again. The interaction curve obtained by the adapted PIFM as well as the MNA results are represented in Figure 4-146. This figure clearly shows that the adapted PIFM represents closely the interaction behaviour of the UPE 200 section obtained by the MNA simulations.

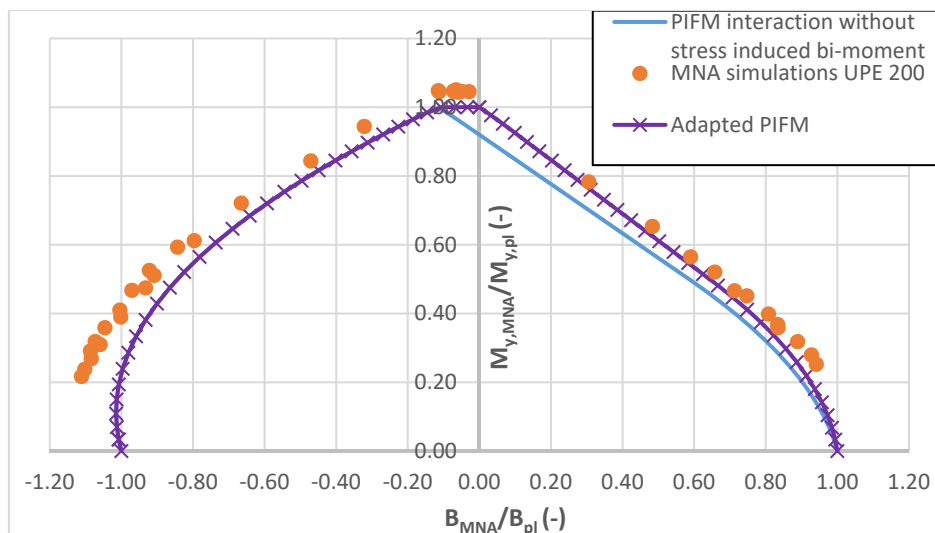


Figure 4-146: Major-axis bending-bi-moment interaction curve – MNA simulations and design model

In Figure 4-146 the proposed design approach has been validated for the example of a UPE 200 sections under major-axis bending and a bi-moment. Hereafter, it is validated with reference to the totality of MNA simulations performed in the framework of this thesis. These simulations contain the calculations presented throughout this Chapter as well as the MNA calculations performed in Chapter 5 for the characterisation of the member behaviour. The simulations comprise a large domain including 29 sections presented in Figure 4-48 and Annex C. These sections have been subject to combined axial force, bi-axial bending, shear forces and torsion of variable relative importance leading to a total number of nearly 10000 MNA simulations. The scope of the numerical study is summarized in Table 4-31. It should be noted that the fabrication process, welded or hot-rolled, does not influence the plastic cross-section resistance but only the member resistance studied in Chapter 5. Also, one may remark that several sections given in Table 4-31 are not compact (or of class 1 or class 2 in the terminology of EN 1993-1-1). Yet, as the MNA simulations performed to characterize the plastic cross-section resistance do not consider second order effects, they also attain their plastic limit state in simple and combined loading.

Table 4-31: Scope of the parametric study on plastic cross-section resistance

Cross-section	Combination of internal forces and moments										
	M_y V_z	M_z V_y	M_y V_z B	M_z V_y B	M_y M_z	M_y M_z B	M_y V_z M_z B	M_y M_z N	M_y M_z V_z N	M_y M_z V_z B	M_y M_z V_z N B
HEAA 1000	x	x									
HEAA 800	x	x	x	x	x	x	x	x	x	x	x
IPE 600	x	x	x	x							
IPE 500	x	x	x	x	x	x	x	x	x	x	x
IPE 360	x	x	x	x							
HEA 280	x	x	x	x							
HEB 220	x	x	x	x							
HEB 200	x	x	x	x	x	x	x	x	x	x	x
HEA 100	x		x								
HEM 100		x		x							
HR 290.3.300.14 ¹					x	x		x			x
HR 500.4.300.20 ¹	x	x	x	x	x	x	x	x	x	x	x
HR 770.5.400.17 ¹	x	x	x	x	x	x	x	x	x	x	x
W 1330.10.280.15 ²	x	x	x	x	x	x	x	x	x	x	x
W 850 5,5.300.12 ²					x	x		x			x
W 850.5,5.200.14 ²					x	x		x			x
W 650.5.180.10 ²	x	x	x	x	x	x	x	x	x	x	x
IMS 1500.12.300.25.262,1.25 ³ - $\psi_{mono} = 0,2$	x										
IMS 1500.12.300.25.168,3.25 ³ - $\psi_{mono} = 0,7$	x										
IMS 1500.12.300.25 ³ - $\psi_{mono} = 1,0$	x										
IMS 600.12.220.19.192,2.19 ³ - $\psi_{mono} = 0,2$	x	x	x	x							
IMS 600.12.220.19.123,4.19 ³ - $\psi_{mono} = 0,7$	x	x	x	x							
IMS 600.12.220.19.51,3.19 ³ - $\psi_{mono} = 0,975$	x	x	x	x							
IMS 600.12.220.19 ³ - $\psi_{mono} = 1,0$	x										
IMS 500.10,2.200.16.125.16 ³ - $\psi_{mono} = 0,61$	x	x	x	x	x	x	x	x	x	x	x
IMS 500.10,2.200.16.75.16 ³ - $\psi_{mono} = 0,9$	x	x	x	x	x	x	x	x	x	x	x
IMS 200.9.200.15.150.15 ³ - $\psi = 0,41$	x	x	x	x	x	x	x	x	x	x	x
IMS 200.9.200.15.125.15 ³ - $\psi_{mono} = 0,61$	x	x	x	x	x	x	x	x	x	x	x
IMS 96.5.100.8.87.8 ³ - $\psi_{mono} = 0,2$	x	x	x	x							
IMS 96.5.100.8.56.8 ³ - $\psi_{mono} = 0,7$	x	x	x	x							
IMS 96.5.100.8.23,3.8 ³ - $\psi_{mono} = 0,975$	x	x	x	x							
IMS 96.5.100.8 ³ - $\psi_{mono} = 1,0$	x										
UPE 80	x	x	x	x	x	x	x	x	x	x	x
UPE 200	x	x	x	x	x	x	x	x	x	x	x
UPE 360	x	x	x	x	x	x	x	x	x	x	x

¹Hot-rolled section with inverted dimensions – HR h.t.w.b.f.t.f

²Welded section – W h.t.w.b.f.t.f

³Mono-symmetric I section – IMS h.t.w.b.m.t.f.u.b.f.t.f

Figure 4-147 shows that the results are very satisfying. In case of high shear forces V_z , the results are slightly more safe-sided than the mean value as the plastic shear force resistance is limited to the shear force resistance of the web for all types of cross-section (hot-rolled and welded double symmetric I sections, mono-symmetric I sections and U sections). However, the maximum deviation on the safe side is only of approximately 25%. This seems acceptable. Nevertheless, it should be noted that highly mono-symmetric cross-sections ($\psi_{\text{mono}} = 0,975$) are not considered in the following figure. For these section the adapted PIFM may be up to 50% safe-sided as the assumptions concerning the plastic stress distribution are not valid anymore as the local warping resistance is mobilised.

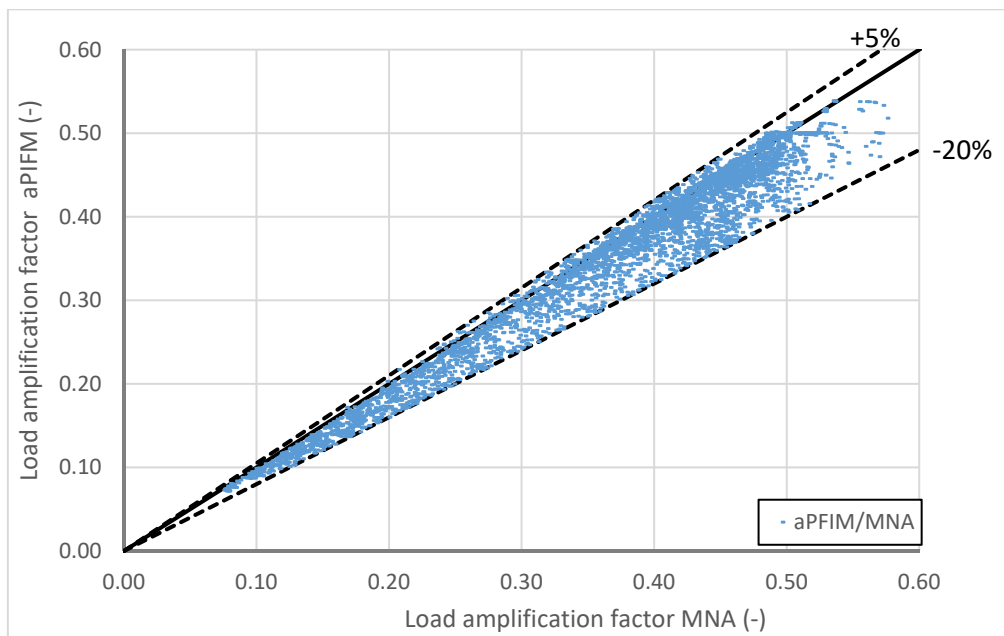


Figure 4-147: Comparison between MNA results and plastic resistance predicted by adapted PIFM

It should be noted again, that the load amplification factor obtained with the adapted PIFM is based on **the internal forces and moments calculated through MNA simulations**. Consequently, the results consider the real internal forces and moments acting in the member. Yet, it has been shown that the MNA simulations lead to the creation of a warping hinge for members subject to torsion and hence high Saint Venant's torsional moments may arise along the member. Therefore, the plastic failure of the member is always linked to the interaction between the Saint-Venant's torsional moment with the other internal forces and moments. It is recalled that if the internal forces and moments are determined by an elastic analysis, it is generally not necessary to consider the Saint Venant's torsional moment in the verification of resistance of I and U sections. Indeed, the interaction including the bi-moment is always design relevant because the bi-moment is overestimated by this type of analysis as shown in Figure 4-148. The difference between Figure 4-148 and Figure 4-147 is the type of analysis performed to obtain the internal forces and moments. In Figure 4-147 the internal forces and moments are determined with plastic analysis (MNA) whereas they are determined with elastic analysis in Figure 4-148. Consequently, the high Saint-Venant's torsional moments arising after the formation of the plastic warping hinge are not considered in Figure 4-148. Nonetheless, one may observe that the strength predictions

are generally safe-sided and even more conservative than the results shown in Figure 4-147. This observation has already been confirmed throughout paragraph 4.4.4 dedicated to plastic interaction including torsion. Again, the results of highly mono-symmetric I sections are not represented. Obviously, the results would be even more conservative in case of interaction including torsion.

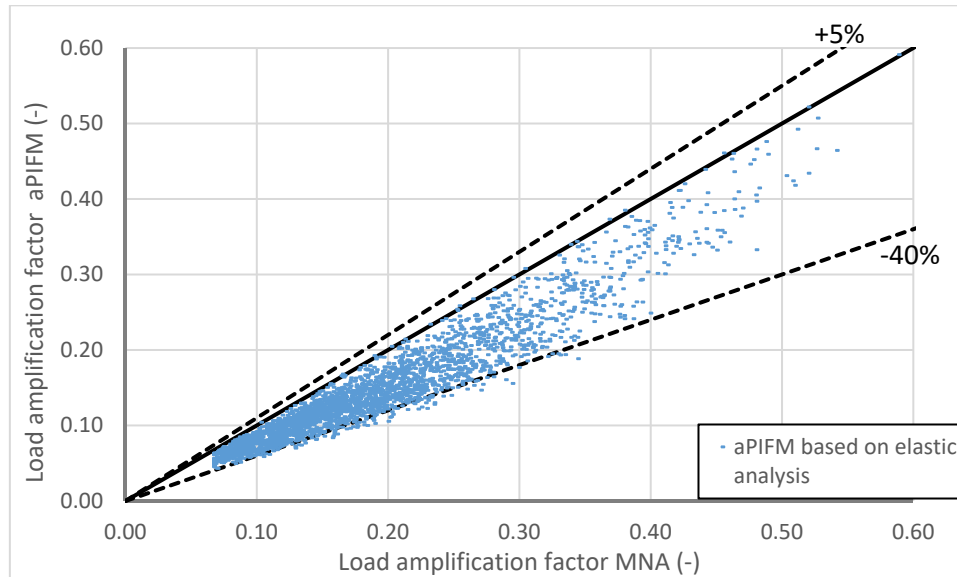


Figure 4-148: Comparison between MNA results and plastic resistance predicted by adapted PIFM based on elastically determined internal forces and moments

Figure 4-148 shows that an elastic analysis may lead to rather conservative results for the plastic cross-section interaction that is a practical failure mode for short members of compact section. In these cases it could be economically interesting to account for the plastic torsional system reserve. Inversely, for longer members the effect of elasto-plastic instability, discussed in Chapter 5, leads to failure taking place before the plastic limit state is attained.

The plastic torsional system reserve may obviously be accounted for in rigorous MNA simulations as performed in this Chapter. Nonetheless, in practice the software necessary to perform these type of analysis is not widespread. In paragraph 4.4.4.1 a two-step elastic analysis method has been proposed to take benefit of the plastic behaviour of members subject to torsion. It has however been shown that the Saint-Venant's torsional moments start to increase over proportionally before the plastic warping hinge is completely created (yielding of the complete section at mid-span for example). As a simplified method, it is proposed here to consider that an applied torsional load is carried exclusively through Saint-Venant's torsional moments when the internal forces and moments attain a load level corresponding to 80% of the plastic resistance of the most loaded cross-section.

In order to illustrate this analysis procedure, the example treated in paragraph 4.4.4.1 is studied again:

- The member is of HEB 200 section (without fillets) subject to a constant major-axis bending moment of 119,6 kNm and a torsional moment applied at mid-span of 21,8 kNm.
- The length of the member is equal to 1,1 m.
- The member possess fork end support.
- The member is fabricated from steel S 235.

The first order elastic analysis of this member leads to the following maximum internal forces and moments:

$$M_{y,Max} = 119,6 \text{ kNm}$$

$$M_{x,St.V,max} = 1,577 \text{ kNm}$$

$$M_{x,w,max} = 10,9 \text{ kNm}$$

$$M_{x,tot,max} = 10,9 \text{ kNm}$$

$$B_{max} = 5,41 \text{ kNm}^2$$

The load factor linked to the plastic warping hinge ($R_{pl,LA}$) is obtained with the adapted PFIM:

$$R_{pl,LA} = 0,777$$

Therefore, it is considered that the torsional load is exclusively carried by Saint-Venant's torsion starting from a load factor of $0,8 * 0,777 = 0,622$.

The static system of the member is transformed and a warping hinge is introduced at mid-span. The new member is loaded with a constant major-axis bending moment of 42,26 kNm $((1-0,622)M_{y,max})$ and a torsional moment of 8,25 kNm applied at mid-span $(2*(1-0,622)M_{x,tot,max})$. The member is analysed elastically a second time with these loads.

The resulting internal forces and moments necessary to check the resistance of the member can be obtained as the sum of the internal forces and moments determined at the load level corresponding to the formation of the warping hinge and those determined by elastic analysis of the member possessing the warping hinge. Consequently, one obtains:

$$M_{y,Max} = 119 \text{ kNm} (= 0,622*119 \text{ kNm} + 45,26 \text{ kNm})$$

$$M_{x,St.V,max} = 5,11 \text{ kNm} (= 0,622*1,577 \text{ kNm} + 4,13 \text{ kNm})$$

$$M_{x,tot,max} = 10,9 \text{ kNm} (= 0,622*10,9 \text{ kNm} + 4,13 \text{ kNm})$$

It is recalled that neither the bi-moment nor the warping torsional moment, which act in the member at its plastic limit state, can be determined exactly.

The plastic resistance of the member can be checked based on the internal forces and moments determined after the second calculation step. For the example, the plastic interaction of the

HEB 200 section subject to a Saint-Venant's torsional moment of 5,11 kNm and a major-axis bending moment of 119 kNm is checked. The adapted PIFM is again applied to obtain:

$$R_{pl} = 0,877$$

The rigorous MNA analysis of this member leads to a load factor at the plastic limit state of $R_{pl,MNA} = 0,94$.

The example studied above shows that the proposed procedure may be sufficiently precise for one example. Figure 4-149 shows a more global evaluation of the two-step analysis method applied to members of double symmetric I and U section subject a combination of internal forces and moments including torsion. The procedure is not applied to members of mono-symmetric section due to the effect of local warping. Also, members failing predominantly by the shear force V_z are not studied as they do not possess a significant plastic torsional system reserve. Figure 4-149 indicates that the proposed two-step analysis procedure may be globally satisfactory. Indeed, the obtained results are comparable to those represented in Figure 4-147 (the internal forces and moments are obtained by MNA). Figure 4-150 shows a statistical evaluation of the two-step elastic analysis method in order to quantify its accuracy further on.

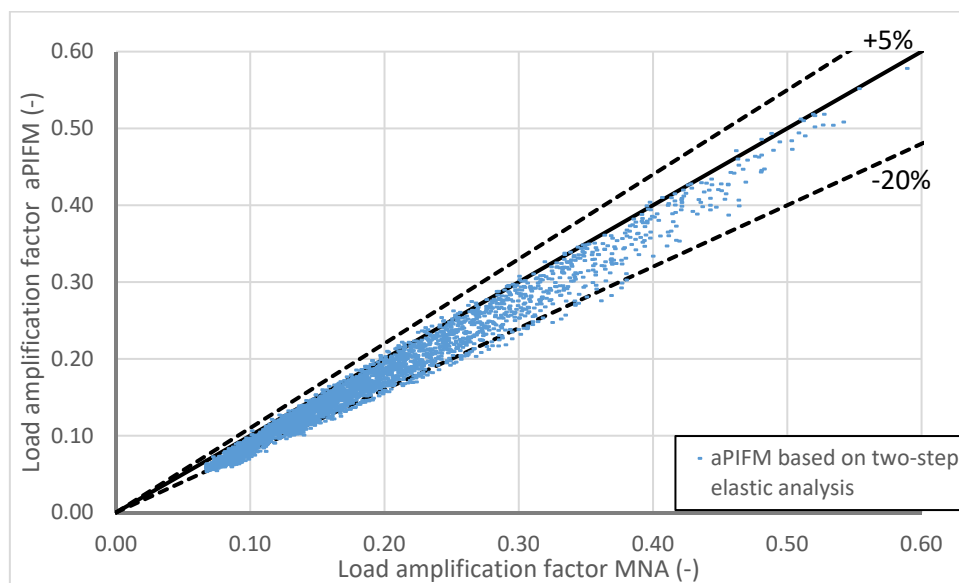


Figure 4-149: Comparison between MNA results and plastic resistance predicted by adapted PIFM based on two-step elastic analysis

In Figure 4-150, one may observe that the number of unsafe results is rather low and that the obtained strength predictions are very precise for the majority of cases. Indeed, the strength predictions attains between 0,8 and 1,0 of the numerically obtained resistance for approximately 85% of the studied cases. Also, the proposed method is obviously much more precise than the design method based on a simple elastic analysis (compare Figure 4-149 and Figure 4-148).

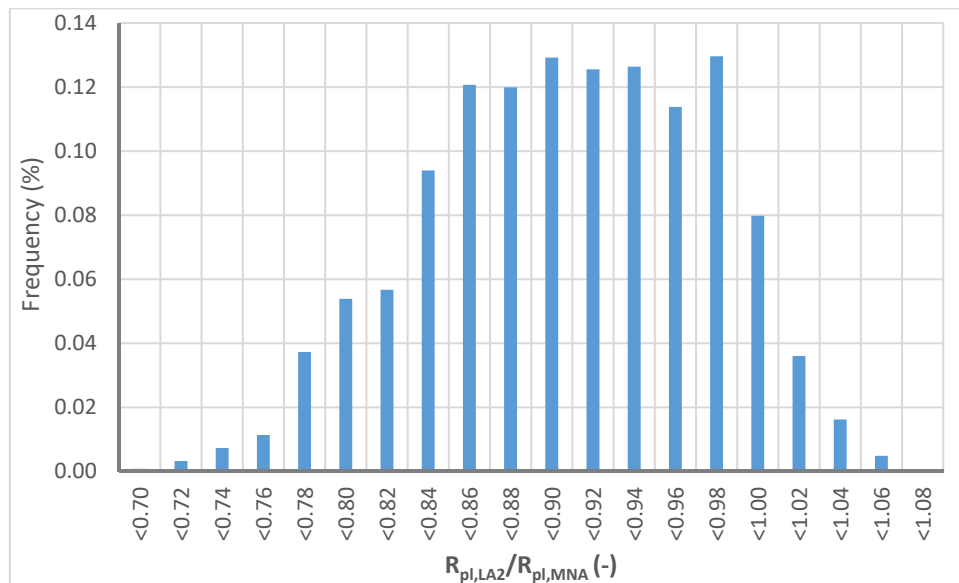


Figure 4-150 : Ratio between plastic load amplification factor obtained with two-step elastic analysis and plastic load amplification factor obtained with plastic analysis of the members

4.6 General conclusions concerning the plastic cross-section resistance

Chapter 4 has concerned the plastic cross-section resistance of double and mono-symmetric I sections as well as of U sections under complex combination of internal forces and moments including torsion. The literature review presented in paragraph 4.2 has shown that major international standards do not propose any comprehensive design approach for open sections subject to a combination between the axial force, bi-axial bending and torsion. Additionally, it has been shown that there are high discrepancies in the definition of the resistance to the shear force acting parallel to the web. In order to verify the shear force resistance predictions given in the three major standards AISC 360-10, AS 4100:1998 and Eurocode 3 Part 1-1 ten laboratory tests have been performed and presented in paragraph 4.3. These tests as well as supplementary numerical simulations revealed that:

- The definition of the plastic shear force $V_{z,pl}$ given in Eurocode 3 may be safely applied for compact sections ($h_w \ll 72\varepsilon/\eta$) and sections fabricated from steel grades up to S355.
- However, the shear resistance cannot be linked to a shear area exceeding the area of the web but it is directly associated with the level of strain hardening that may be attained by the cross-section.
- For slender cross-sections ($h_w \approx 72\varepsilon/\eta$) and cross-sections fabricated from steel grades higher than S355, especially the strength prediction of Eurocode 3 may become unsafe.

- Yet, as the strain hardening is of importance it should be accounted for. Comparisons between the Continuous Strength Method (explicitly considering strain hardening) and the numerical simulations showed good agreement.

The laboratory tests have also been used to validate the numerical model that has been employed in paragraph 4.4 to study the interaction between, in particular, bending, shear forces and torsion. More than 10000 MNA simulations have been performed. For “simple” load combination analytical interaction formulae have been derived based on the MNA results. However, for more complex load cases and mono-symmetric sections, analytical interaction formulae, based on a presumed plastic stress distribution, may become very complex and difficult to use in the practice. Additionally, they are not consistent in all cases with the real physical interaction behaviour of the sections. Therefore, it seemed more convenient to adapt the Partial Internal Force Method PIFM to the results obtained through the laboratory tests and those obtained by the numerical simulations. In particular the following ameliorations have been introduced:

- The stress induced bi-moment, in some cases necessary for the complete yielding of the cross-section, is accounted for.
- The influence of the fillets is considered.
- The PIFM strength predictions are adapted to the real interaction behaviour; in particular the cut-off limits observed in the MNA simulations are introduced.

In order to predict the strength of members reliably in the whole slenderness range, it was absolutely necessary to study the plastic cross-section resistance as it represents the ultimate resistance of short members (of compact cross-section) not sensitive to member instability and member second order effects. The following Chapter concerns the resistance of longer specimen whose resistance is reduced due to the effect of member instability.

5 MEMBER RESISTANCE

5.1	Introduction	260
5.2	Numerical study – Particular modelling aspects	262
5.2.1	Influence of assumed imperfections on the ultimate member resistance	262
5.2.1.1	General	262
5.2.1.2	Residual stresses for double symmetric I sections	262
5.2.1.3	Residual stresses for welded mono-symmetric I sections	267
5.2.1.4	Equivalent geometric member imperfection for I sections	270
5.2.1.5	Residual stresses for U sections	271
5.2.1.6	Equivalent geometric member imperfection for U sections	285
5.2.1.7	Equivalent geometric plate imperfection	301
5.2.2	Influence of loading sequence	305
5.2.3	Influence of local plate instability on ultimate member resistance	308
5.2.3.1	General	308
5.2.3.2	Calibration of rigid beam elements	309
5.3	Design proposals for the resistance of members subject combined axial force and bi-axial bending without torsion	314
5.3.1	General	314
5.3.2	Double symmetric members	314
5.3.3	Extension of the Eurocode 3 Part 1-1 interaction equations to mono-symmetric I and U sections	318
5.4	Review of design proposals for members with open section subject to combined axial compression, bending and torsion	321
5.4.1	General	321
5.4.2	Great Britain: BS 5950-1:2000 and SCI Publication 057	322
5.4.3	Design rules proposed at RWTH Aachen	326
5.4.3.1	General	326
5.4.3.2	Proposal RWTH Aachen I	326
5.4.3.3	Proposal RWTH Aachen II	331
5.4.3.4	Proposal RWTH Aachen III	340
5.4.3.5	Summary of design proposal made at RWTH Aachen	344
5.4.4	Design rule proposed at TU Berlin	345
5.4.5	Design rule proposed at Eindhoven University of Technology	347
5.4.6	Summary of the proposals and comparison to physical tests	352
5.4.7	Conclusion	358
5.5	Analytical solutions	359
5.5.1	General	359
5.5.2	Assumptions	359

5.5.3	System of axis and kinematics	360
5.5.4	Energy method, equilibrium of the member and critical loads	361
5.5.4.1	General	361
5.5.4.2	Energy method	363
5.5.4.3	Differential equation characterizing the second order static equilibrium of the member	365
5.5.4.4	Elastic stability and state of indifferential equilibrium	367
5.5.5	Determination of the critical loads for I-shaped members	372
5.5.5.1	Common approach neglecting pre-buckling displacements	372
5.5.5.2	Influence of pre-buckling displacements	376
5.5.5.3	Conclusions	381
5.5.6	Determination of critical loads for U-shaped members	382
5.5.6.1	Common approach neglecting pre-buckling displacements	382
5.5.6.2	Influence of the pre-buckling displacements	383
5.5.7	Elastic second order equilibrium of the member	400
5.5.7.1	General	400
5.5.7.2	Members of double symmetric I section subject to constant major-axis bending	402
5.5.7.3	Members of double symmetric I section subject to major-axis bending and axial force	407
5.5.7.4	Members subject bending and torsion	416
5.5.7.5	Members subject to combined bi-axial bending, axial force and torsion	430
5.5.7.6	Conclusions	433
5.6	Numerical parametric study	435
5.6.1	General	435
5.6.2	Scope of the parametric study	436
5.6.2.1	Representation of the results	436
5.6.2.2	Cross-sections	438
5.6.2.3	Load cases	439
5.6.2.4	Influence of the steel grade on the ultimate member resistance	444
5.6.3	Overall results	447
5.6.4	Design based on interaction formulae	452
5.6.4.1	General	452
5.6.4.2	Members with double symmetric I sections	455
5.6.4.3	Members with mono-symmetric I sections	491
5.6.4.4	Members with U sections	500
5.6.4.5	Summary of the design of members subject to torsion based on interaction equations	518
5.6.5	Design based on OIC approach – Double symmetric I sections	523
5.6.5.1	General requirements for the OIC approach to be developed	523
5.6.5.2	OIC approach for lateral-torsional buckling	525
5.6.5.3	OIC approach for flexural buckling under combined minor-axis bending and axial force	535
5.6.5.4	OIC approach for lateral-torsional buckling under combined major- and minor-axis bending	543
5.6.5.5	OIC approach for combined major-axis bending and axial force	551
5.6.5.6	OIC approach for combined bi-axial bending and axial force	559
5.6.5.7	Extension of the OIC approach to torsion	568
5.6.5.8	Summary of the OIC approach for the resistance of members of double symmetric I section	578

5.1 Introduction

Figure 5-1 shows again the ultimate resistance curve describing the general behaviour of an arbitrary member subject to an arbitrary combination of internal forces. The plastic resistance of short members not sensitive to member instability has been studied in Chapter 4 and a design approach has been proposed. In Chapter 5, the member resistance is studied and a resistance model is proposed covering double symmetric and mono-symmetric I sections as well as U sections. The resistance model is based on an extensive numerical study presented in paragraph 5.6. This study is performed with the numerical model presented and validated in Chapter 3. It is recalled that it has been shown that the member resistance can be evaluated with the “Shell” model whereas the plastic section resistance has been studied with a “Solid” model in order to take accurately into account the possible influence of the fillets.

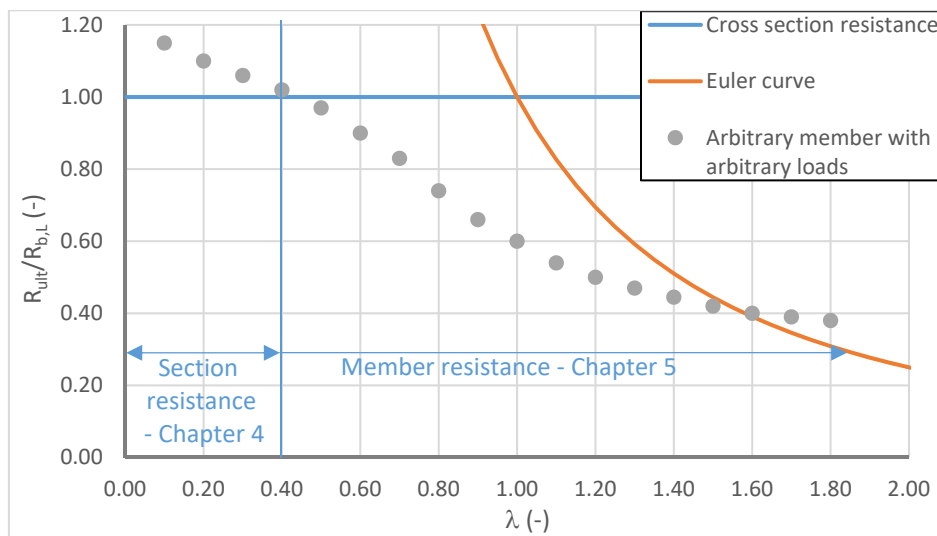


Figure 5-1: Ultimate resistance curve of an arbitrary member subject to an arbitrary combination of loads

So as to obtain reliable numerical results, the geometrical and material imperfections that highly influence the member resistance should be accounted for. The real physical imperfections are of random nature and cannot be reproduced in a parametric study. Consequently, it is absolutely necessary to replace the random imperfections by equivalent calculation imperfections that reproduce safe-sided strength predications. However, the strength prediction should not be non-economic. Therefore, the calculation imperfections should only be as severe as necessary. Hence, before the parametric study leading to the resistance model is performed, the influence of assumed calculation imperfections is studied in paragraph 5.2. Additionally, this paragraph presents a study on the influence of loading sequence. Indeed, it is not possible to justify a priori that a proportional increase of the loads leads to the same ultimate resistance as a sequential loading increase (for example: the member is loaded by a bending moment first and a torsional moment is applied in a second load step). As the numerical model is used in selected cases to highlight problems and inconsistencies linked to design models proposed in the past, the

calibration of the numerical model has to be done before the proposals on the design of members subject to combined axial force, bending and torsion are discussed in detail in paragraph 5.4.

Paragraph 5.5 then presents a theoretical study addressing the elastic critical loads and second order equilibrium of members with open cross-section. This study is performed in order to obtain a theoretical background on the behaviour of members with open cross-sections subject to an arbitrary combination of internal forces and moments. The theoretical basis obtained in paragraph 5.5 is then used to develop the resistance model in the last paragraph of this Chapter.

It is recalled that one of the objectives of this thesis is the development of a simple design method that may be easily accepted in the practice. This simple design method should therefore not significantly change the habit of practical engineers and consequently an extension of the well accepted Eurocode 3 Part 1-1 interaction equations addressing member stability is intended. Yet, it has to be noted that these interaction equations possess inherent limitations and approximations leading to a certain scatter of results even in their initial field of application (in particular members subject to combined axial force and bi-axial bending - see paragraph 5.3). A simple extension of these interaction equations to an even more complex load case including torsion is therefore susceptible to increase the scatter of results and it may lead to less precise results. Yet, this is explicitly accepted here in order to propose a simple and safe design method. Nonetheless, reasons leading to an increased scatter are discussed and quantified in paragraph 5.6. Additionally to the extension of the Eurocode 3 Part 1-1 interaction equations, a second design method based on the OIC format is proposed in the last part of this thesis with the objective to eliminate some of the reasons linked to the limited precision of the extended interaction equations. However, the proposed OIC is only developed for double symmetric I sections.

5.2 Numerical study – Particular modelling aspects

5.2.1 Influence of assumed imperfections on the ultimate member resistance

5.2.1.1 *General*

In order to predict the ultimate resistance of members by means of numerical simulations (GMNIA – geometric and material non-linear analysis with imperfection), it is indispensable to realistically assume physical imperfections of the studied member. It is possible to distinguish between geometric imperfections, i.e. initial member/plate out-of-straightness, and material imperfection, i.e. residual stresses. Especially, for double symmetric I sections residual stress distributions are well known and typical stress distributions are accepted for long time (see paragraph 5.2.1.2 and references (Tebedge 1973), (Young 1975), (ECCS 1976), (ECCS 1984)). Yet, for welded double symmetric I sections research is going on up to present days so as to account realistically for the influence of the fabrication process (Thiébaud 2014). Moreover, to the author's knowledge no results for the residual stress pattern of hot-rolled U sections have been published so far. This lack of information for U sections should therefore be closed in order to reliably simulate the behaviour of U-shaped members. Additionally, it is shown in paragraph 5.2.1.6 that there is certain lack of knowledge concerning the equivalent geometric imperfection to be used when U-shaped members are analysed.

In any case, it is indispensable to ensure that the assumed geometric imperfection represent the real behaviour of the physical member. Hence, it seems inevitable to study the influence of assumed imperfections on the ultimate resistance in detail. It is highlighted that existing recommendations for I-shaped members may not be applied directly to U-shaped members.

5.2.1.2 *Residual stresses for double symmetric I sections*

Due to the fabrication process, steel sections are subject to an initial state of stresses. These stresses, generally referred to as residual stresses, are auto-equilibrated and depend essentially on the fabrication process itself, the form of the section and post fabrication heat treatment. Post fabrication heat treatment can highly reduce the amount of residual stresses. However, members used for buildings are generally not treated with the objective to reduce residual stresses. Therefore, the potential beneficial effect of heat treatment is not considered in the following.

For hot-rolled I sections basically two shapes of distribution of residual stresses may be found in the literature as show in Figure 5-2: the triangular shape and the parabolic shape (see references (Young 1975), (ECCS 1976), (ECCS 1984), (Lindner et al. 1998)). The amplitude of the residual stresses is generally fixed depending on the section geometry. In (ECCS 1984) the triangular shape of Figure 5-2a) is proposed. The lower value of $0,3f_y$ is applicable to sections for which the ratio between the height of the section and the width of the flanges exceeds 1,2. A more complex parabolic shape has been proposed in (Young 1975) and adopted in (ECCS 1976) as shown in Figure 5-2b). Similar patterns are proposed in (Lindner et al. 1998) and (Boissonnade 2012). The distribution of residual stresses used in this last reference is given in Figure 5-3.

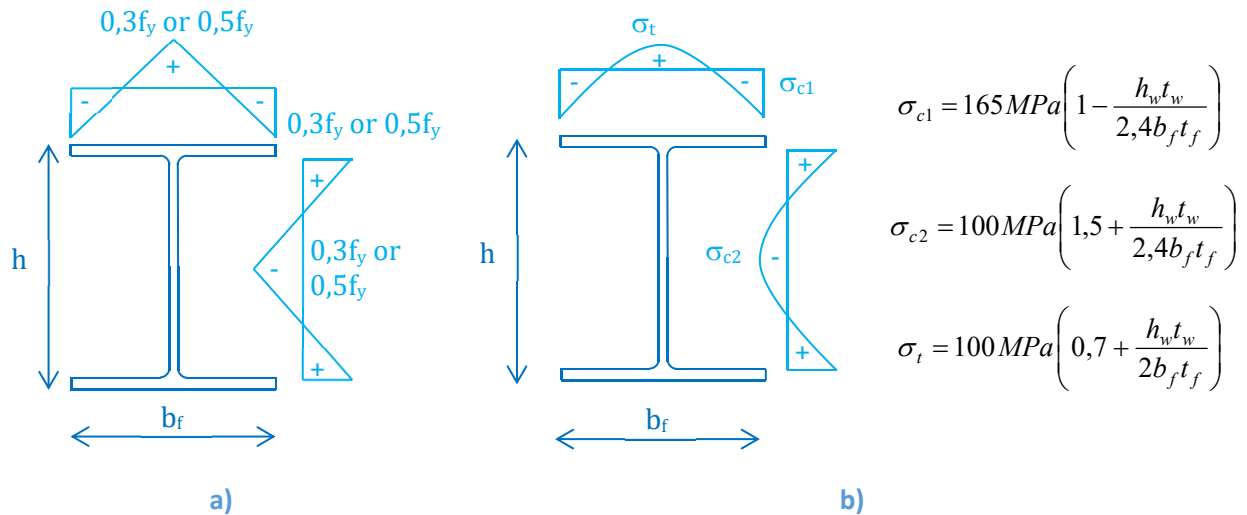


Figure 5-2: Possible distributions for residual stresses of I sections a) (ECCS 1984) and b) (Young 1975)

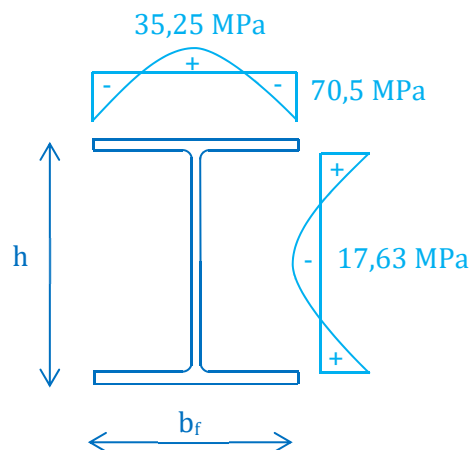


Figure 5-3: Possible distributions for residual stresses of I sections (Boissonnade et al. 2012)

The residual stress patterns proposed in Figure 5-3 and Figure 5-2b) are similar. However, depending on the form of the section the amplitudes of the maximum stresses may be different. For example, based on the geometry of an IPE 500 section, the stresses σ_{c1} , σ_{c2} and σ_T used in (Young 1975) are equal to:

$$\sigma_{c1} = -62,4 \text{ MPa}$$

$$\sigma_{c2} = -212 \text{ MPa}$$

$$\sigma_T = 145 \text{ MPa}$$

In order to evaluate the influence of the residual stress pattern on the ultimate resistance, it is proposed to study a member of IPE 500 sections made of S 235 and subject to constant major-axis bending. It should be noted that the residual stresses proposed in (Young 1975) (see above) are neither auto-equilibrated over the section nor over the plates. Additionally, the amplitudes of the

residual stresses (compression and tension) appear to be higher than measured in the past (see (Tebedge et al. 1974) – and paragraph 5.2.1.5). The ultimate resistance factor obtained for the three different residual stress shapes are given in Figure 5-4.

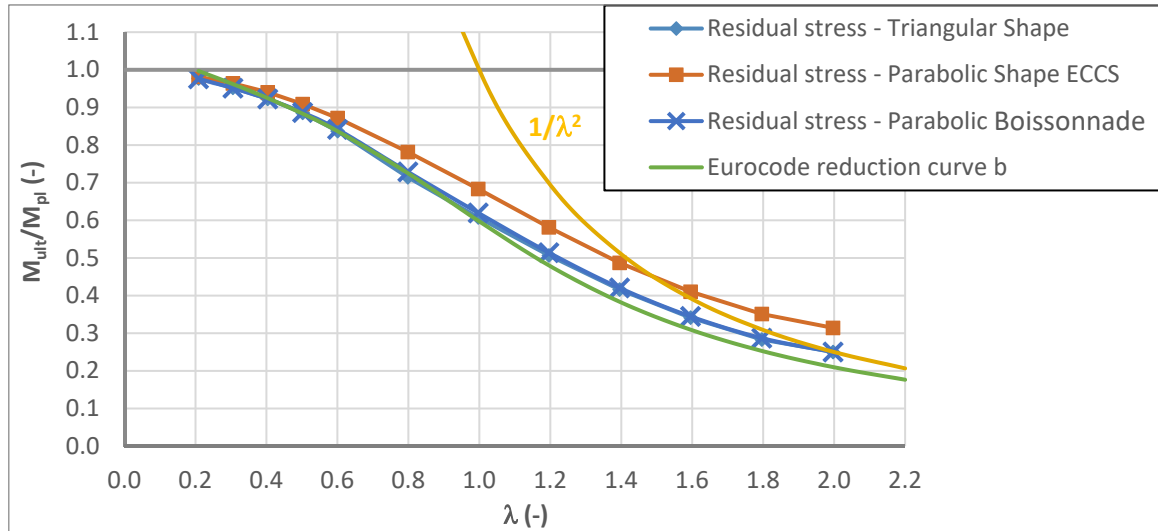
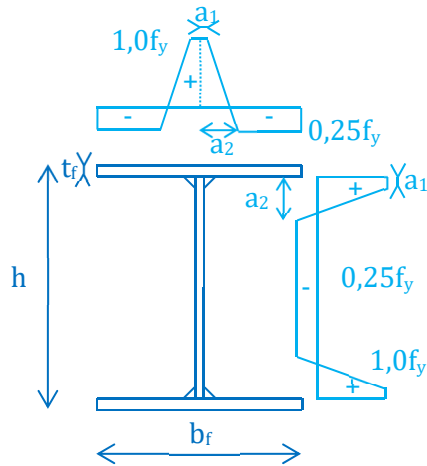


Figure 5-4: Ultimate resistance depending on the distribution of residual stresses for IPE 500

In Figure 5-4, one can observe that the results obtained on the basis of the triangular shape are practically identical with the results obtained based on the parabolic shape proposed in (Boissonnade 2012). Conversely, the use of the parabolic residual stress pattern proposed in (Young 1975) leads to more favourable results. As the amplitude of tensile stresses in the flanges is higher than for the other proposals this finding does not seem surprising. In fact, the ultimate resistance related to lateral instability of a member depends highly on its lateral stiffness. This lateral stiffness is reduced due to the yielding of the compressed flange. Thanks to higher tensile residual stresses the lateral stiffness of the member possessing the residual stress pattern proposed in (Young 1975) is less reduced for the same applied bending moment. Consequently, it is understandable that this member obtains the highest ultimate resistance.

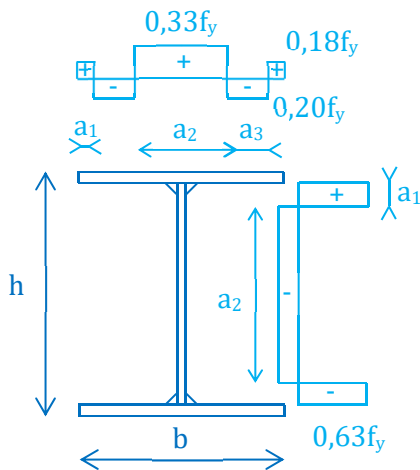
However, as stated above, measurements imply that this residual stress pattern is too favourable. Therefore, the triangular residual stress pattern is used for numerical studies of hot-rolled sections as proposed in (ECCS 1984).

For welded sections one may distinguish between sections fabricated from hot-rolled or flame cut plates. Depending on the fabrication process of the plates, two different shapes can be found in the literature as shown in Figure 5-5 and Figure 5-6.



	Flange	Web
a_1	$0,075b_f$	$0,075(h-2t_f)$
a_2	$0,125b_f$	$0,125(h-2t_f)$

Figure 5-5: Residual stress distribution for welded sections made of rolled plates (ECSS 1984)



	Flange	Web
a_1	$b_f/20$	$(h-2t_f)/10$
a_2	$9b_f/20$	$8(h-2t_f)/10$
a_3	$9b_f/40$	-

Figure 5-6: Residual stress distribution for welded sections made of flame cut plates (Chacon et al. 2009)

Figure 5-7 shows how the residual stress pattern for welded profiles influences their ultimate resistance. Again, an IPE 500 section is studied. Yet, it is supposed to be subject to the welded residual stress patterns.

It can be seen that the ultimate resistance of members is generally higher if the section is fabricated from flame cut plates. For this example the difference attains 16% for a slenderness of 1,0. As the amplitude of the residual stresses is less than for sections made of hot-rolled plates, this result is not surprising. Also, it can be observed that the ultimate resistance curve of the member made of flame cut plates crosses the Euler curve at a slenderness of about 1,6 (member length is 990 cm). Obviously, this slenderness is rather high, but it can be considered at the upper bound of the practical range. For this case the load displacement curves are given in Figure 5-8 to Figure 5-10. It can be seen that the displacements and the torsional twist are not out of practical limits.

Up to date the favourable influence of the residual stress pattern for flame cut plates is not accounted for in the Eurocode provisions. However, it appears that the gain of resistance may be non-negligible at least in some cases. A larger study would be necessary to confirm the results and to propose an amelioration of the current provisions. Yet, this study is not performed in the framework of the present thesis.

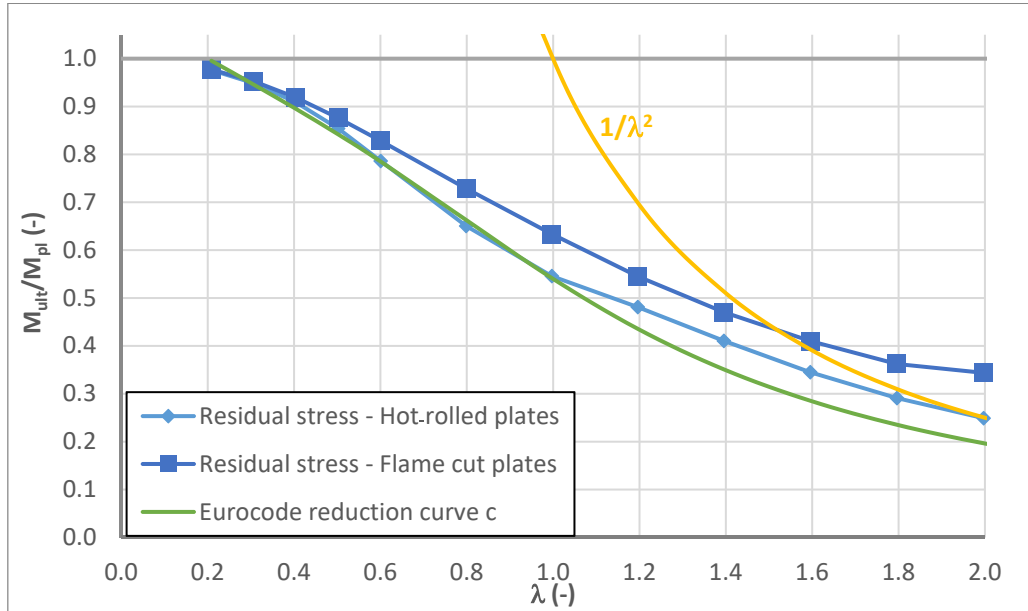


Figure 5-7: Influence of residual stress pattern on the ultimate resistance of welded sections

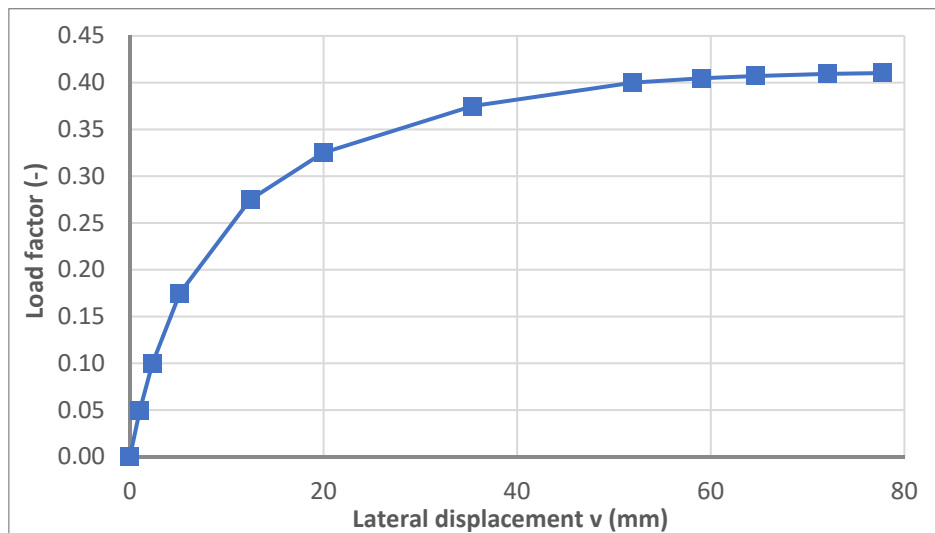


Figure 5-8: Load – Lateral displacement curve for the member made of flame cut plates at a slenderness of 1,6

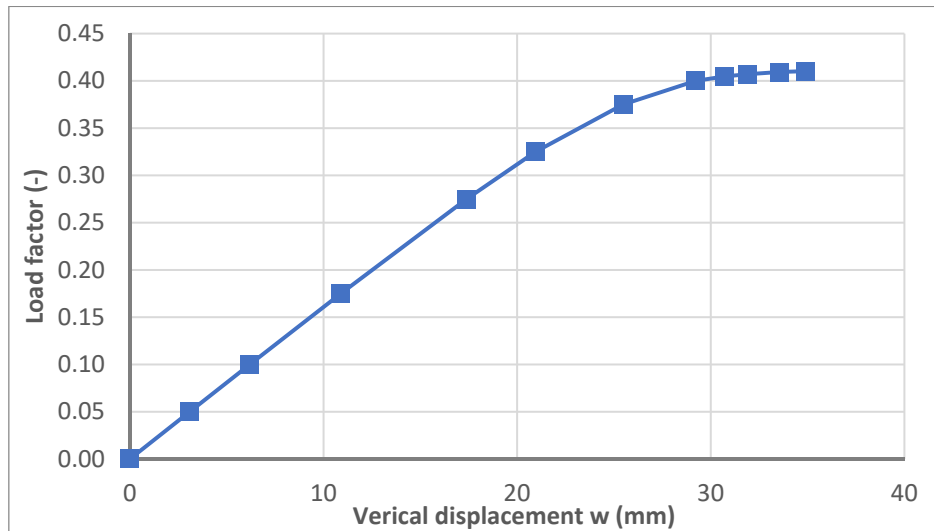


Figure 5-9: Load – Vertical displacement curve for the member made of flame cut plates at a slenderness of 1,6

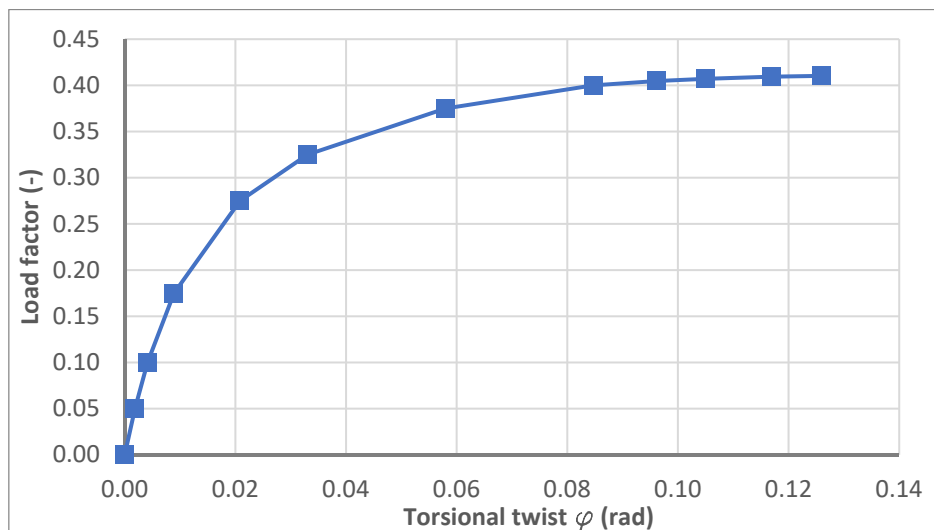
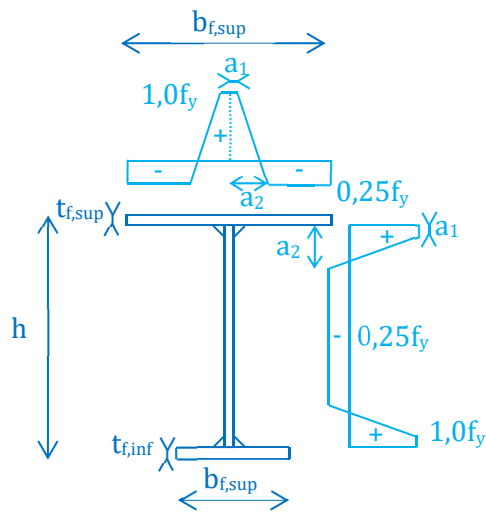


Figure 5-10: Load – Torsional twist curve for the member made of flame cut plates at a slenderness of 1,6

5.2.1.3 Residual stresses for welded mono-symmetric I sections

In this paragraph the residual stress pattern of welded mono-symmetric I sections is of interest. To the authors knowledge neither physical measurements nor numerical simulations concerning the residual stress distribution of mono-symmetric I sections have been published up to date. So as to obtain a realistic residual stress distribution it might be envisaged to perform thermo-mechanical analyses as done for U-shaped members in paragraph 5.2.1.5.3. Yet, it seems that the simulation of the welding process is even more delicate than the simulation of the cooling of hot-rolled members. Obviously, simple cooling of a steel member is a much simpler process than welding that is influenced by the welding speed, the number of layers, the type of welding process etc.. Therefore, it does not seem usefull to perform sophisticated thermo-mechanical analyses based on (too) simplified assumptions concerning the process. Rather it is proposed to determine

the residual stress pattern numerically on the basis of the residual stress distribution for welded sections fabricated from hot-rolled plates as represented in Figure 5-11. The adaption concerns the width of a_1 and a_2 at the lower flange and the lower part of the web.



	a_1	a_2
Upper Flange	$0,075b_{f,sup}$	$0,125b_{f,sup}$
Lower Flange	$0,075b_{f,inf}$	$0,125b_{f,inf}$
Web	$0,075(h-2t_f)$	$0,125(h-2t_f)$

Figure 5-11 : Assumed residual stress distribution for welded mono-symmetric I sections

An auto-equilibrated stress distribution is then calculated iteratively based on the finite (shell) element model used in the framework of this thesis. The calculation is performed as long as the equilibrium conditions represented in Eqs. (5.1) to (5.4) are not respected.

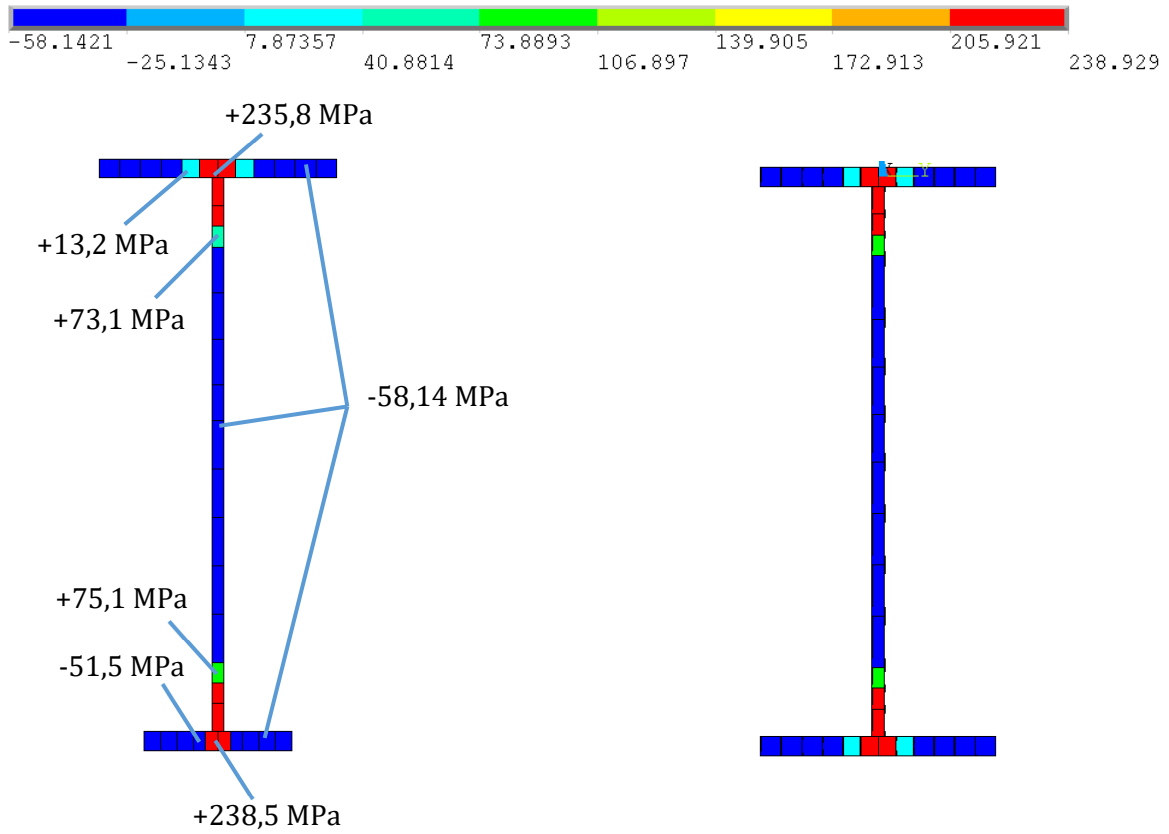
$$N = \int \sigma dA = 0 \quad (5.1)$$

$$M_y = \int \sigma z dA = 0 \quad (5.2)$$

$$M_z = \int \sigma y dA = 0 \quad (5.3)$$

$$B = \int \sigma \alpha dA = 0 \quad (5.4)$$

In Figure 5-12a) the results of this procedure are represented for a welded mono-symmetric section section W478.10,2.200.16.125.16 ($W \cdot h_w \cdot t_w \cdot b_{f,sup} \cdot t_{f,sup} \cdot b_{f,inf} \cdot t_{f,inf}$) fabricated from S235. The residual stress distribution is represented for a similar welded double symmetric section W478.10,2.200.16. For both members the residual stresses are symmetrical about the z-axis. Yet, whereas the residual stresses are also distributed symmetrically about the y-axis for the double symmetric section, one may observe differences concerning the residual stresses in the mono-symmetric I section. Indeed, one may observe that the width of the upper flange in tension is greater than in the lower part. Nonetheless, this difference is already partially imposed by the assumed residual stress distribution given in Figure 5-11. Also, one may observe that the amplitude of the tension residual stresses exceed the yield stress of 235 MPa. Yet, physically it seems questionable that the residual stresses exceed the yield stress of the steel but the applied procedure needs to increase the amplitude of the residual stresses to obtained an auto-equilibrated distribution.



a) Welded mono-symmetric I section

b) Welded double symmetric I section

Figure 5-12 : Residual stress distribution for welded sections of hot-rolled plates

Figure 5-13 representst the deformed shape of the member at the end of the applied procedure. If the deformed shape is shown in “true scale” the displacements are not visible. Only after an amplification by a factor of 2200, the displacements can be observed. They are concentrated at the member ends and only of local nature. One may therefore conclude that a global equilibrium is respected.

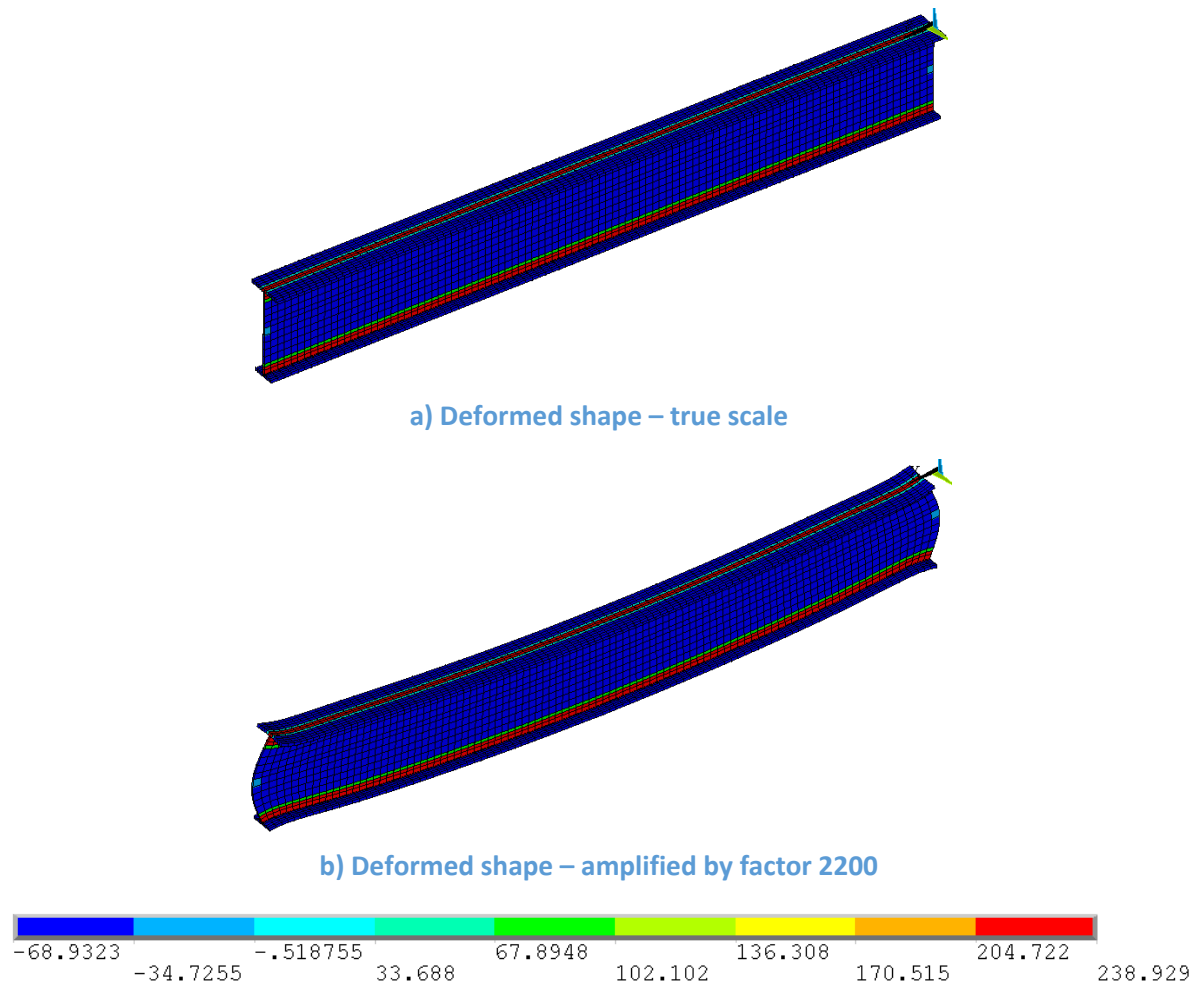


Figure 5-13: Deformed shape of the member with residual stresses

In this paragraph the residual stress distribution for welded mono-symmetric I sections is studied. A simplified procedure is applied so as to obtain an auto-equilibrated distribution based on an assumed distribution similar to welded double symmetric I sections. Admittedly, this procedure is not fully consistent as an initial distribution is imposed. A more detailed study based on physical measurements and possibly numerical simulations would be desirable to get a clearer idea on residual stress pattern and the amplitudes. Yet, this study is not the priority of the present thesis and is therefore not performed in the following.

5.2.1.4 Equivalent geometric member imperfection for I sections

Member geometric imperfections should account for the out-of-straightness of the member along its length. Due to the fabrication process the member is not perfectly straight. Generally, it has an initial in- and out-of-plane deflection and an initial twist. These “real” geometric imperfections are generally not known. In order to simulate the behaviour of the member realistically, a practical hypothesis for the form of the geometric imperfection has to be made. Most numerical studies are based on eigenmode affine imperfections with an amplitude of $L/1000$ as recommended in (CEN 2007a). For I-shaped members, one may find a detailed analysis that confirms these recommendations in reference (Boissonnade et al. 2012). Consequently, the parametric study is based on this assumption for the geometric member imperfection.

5.2.1.5 Residual stresses for U sections

5.2.1.5.1 Form and amplitude

Physical tests on residual stresses could not be found in the literature for U sections. Previous research projects concerning stability of U sections are based on a residual stress distribution similar to I sections as in (FOSTA 2004) and (de Louw 2007). This distribution is represented in Figure 5-14. However, it can be shown that the residual stresses are not equilibrated. In fact, an axial force and a minor-axis bending moment results from this distribution.

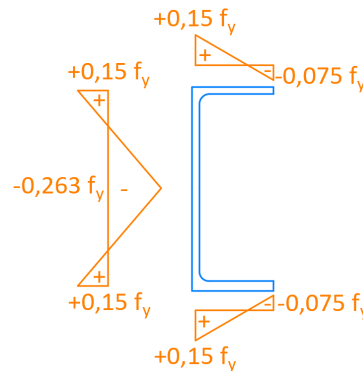


Figure 5-14: Distribution of residual stresses for U sections used in the literature (see (FOSTA 2004), (de Louw 2007))

Hereafter, the equilibrium conditions represented by Eqs. (5.1) to (5.4) as well as the general form of the residual stress pattern shown in Figure 5-15 are used to determine an auto-equilibrated residual stress distribution. Since U sections are generally symmetric about their major-axis, conditions (5.2) and (5.4) are automatically respected. Conversely, the conditions represented by Eqs. (5.1) and (5.3) depend on the residual stress pattern and is applied hereafter. Following Figure 5-15, the stresses along the web (only one half of the web is considered) can be expressed Eq. (5.5).

$$\sigma = 1 + 2 \left(\frac{x_1 - 1}{h_w} \right) z \tag{ 5.5 }$$

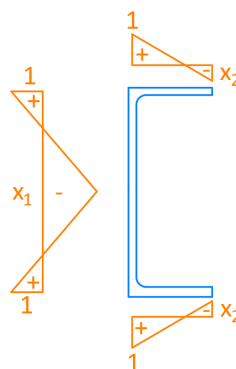


Figure 5-15: General form of residual stresses

The distribution of the residual stresses over the flange width can be expressed by:

$$\sigma = 1 + \left(\frac{x_2 - 1}{b} \right) y \quad (5.6)$$

Introducing Eqs. (5.5) and (5.6) in the conditions represented by Eqs. (5.1) and (5.3) results in:

$$N = 2 \int_0^{h_w/2} 1 + 2 \left(\frac{x_1 - 1}{h_w} \right) z dA + 2 \int_0^{b_f} 1 + \left(\frac{x_2 - 1}{b_f} \right) y dA = 0 \quad (5.7)$$

$$M_z = 2 \int_0^{h_w/2} y_c \left[1 + 2 \left(\frac{x_1 - 1}{h_w} \right) z \right] dA + 2 \int_0^{b_f} \left[1 + \left(\frac{x_2 - 1}{b_f} \right) y \right] [y_c - y] dA = 0 \quad (5.8)$$

Solving the integrations of Eqs. (5.7) and (5.8) and reorganising the resulting expressions lead to the value of the unknown x_1 and x_2 given in Eqs. (5.9) and (5.10).

$$x_1 = - \frac{bt_f + h_w t_w}{h_w t_w} = - \left(1 + \frac{bt_f}{h_w t_w} \right) \quad (5.9)$$

$$x_2 = -0,5 \quad (5.10)$$

One notices that the value of x_2 does not depend on the cross-section dimensions and that it is equal to the value used in Figure 5-14. However, the value of x_1 depends on the cross-section dimensions and is only equal to the value of Figure 5-14, if the product bt_f is equal to $0,74h_w t_w$. The following table gives the value of x_1 for various U sections.

Table 5-1: Amplitude of residual stresses depending on the cross-section

Section	$bt_f/h_w t_w$	x_1
UPE80	1,326	-2,326
UPE120	0,923	-1,923
UPE160	0,858	-1,858
UPE200	0,824	-1,824
UPE270	0,704	-1,704
UPE330	0,513	-1,513
UPE400	0,421	-1,421

The value of x_1 following Figure 5-14 is -1,74 and therefore corresponds to a medium sized U section. It should be noted that the values of x_1 and x_2 are non-dimensional and have to be scaled. The influence of the amplitude of the residual stresses is studied hereafter.

5.2.1.5.2 Sensitivity study

In the framework of the research project FOSTA P554, addressing the influence of torsion on the resistance of steel sections, several laboratory tests have been performed and documented in reference (FOSTA 2004). Next, laboratory tests on U-shaped members is utilized to calibrate the residual stress model. The tests were performed on a UPE 200 cross-sections loaded at mid-span. The tests are summarized in Table 5-2. One may note that an eccentricity of 68,5 mm corresponds to a load applied through the centroid of the flanges. The eccentricities of 18,5 mm to 38,5 mm correspond to loads applied in the vicinity of the web (distance between the shear centre and the web plane is 28,5 mm).

Table 5-2: Tests performed on UPE 200 sections

Name of the test	Length of the member (mm)	Yield stress (MPa)	Lateral eccentricity of the force // shear centre (mm)	Ultimate load (kN)
BE-3-1	2800	409	68,5	43,0
BE-3-22	2800	400	18,5	57,4
BE-3-3	4000	392	38,5	31,8
BE-3-41	4000	409	28,5	34,5
BE-3-42	4000	389	68,5	30,4

The tests are recalculated numerically based on measured geometric imperfections and four different amplitudes of the residual stresses. The residual stress at the intersection between the web and the flange for each residual stress model tested is equal to:

- 0 MPa – without residual stresses
- 35,25 MPa
- 117,5 MPa
- 235 MPa

Figure 5-16 shows the ratio between the ultimate resistance obtained by the numerical simulations and the ultimate resistance obtained in the laboratory tests. One notices in particular that, surprisingly, increasing the amplitude of the residual stresses increases the ultimate resistance in all cases.

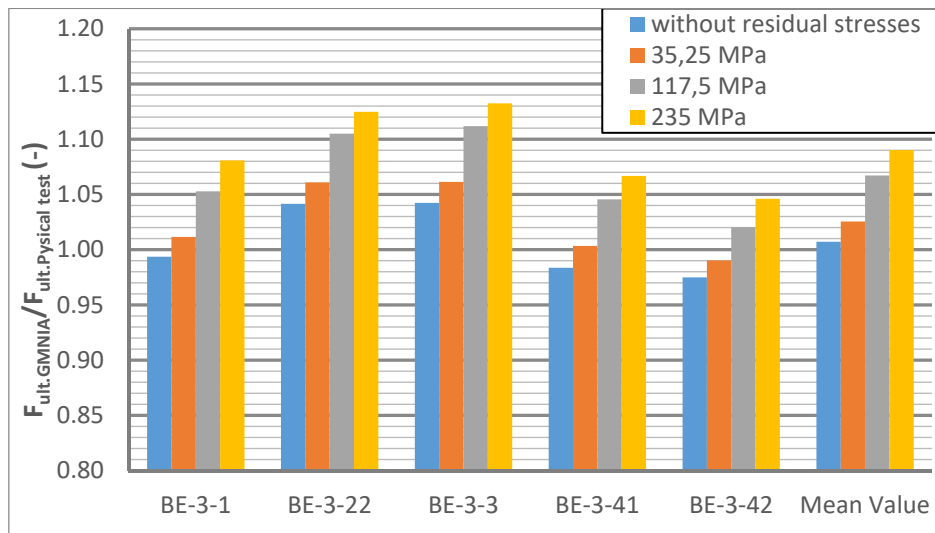


Figure 5-16: Comparison between ultimate resistance obtained through GMNIA to by physical tests

In order to understand this behaviour, one should keep in mind the distribution of stresses due to the major-axis bending and the bi-moment, recalled in Figure 5-17 (see also Chapter 4).

As can be seen in Figure 5-17 and Figure 5-15 the maximum compression residual stress is situated at the neutral axis of the section under combined major-axis bending and bi-moment (in the web). Additionally, the stresses due to major-axis bending are partially reduced by the residual stresses in the compressed flange and in the upper part of the web. The compression stresses are increased only in a small zone near the flange’s tip. Globally, the residual stresses decrease the stresses induced by the loading and consequently, if residual stresses are included into the analysis, the results become more favourable.

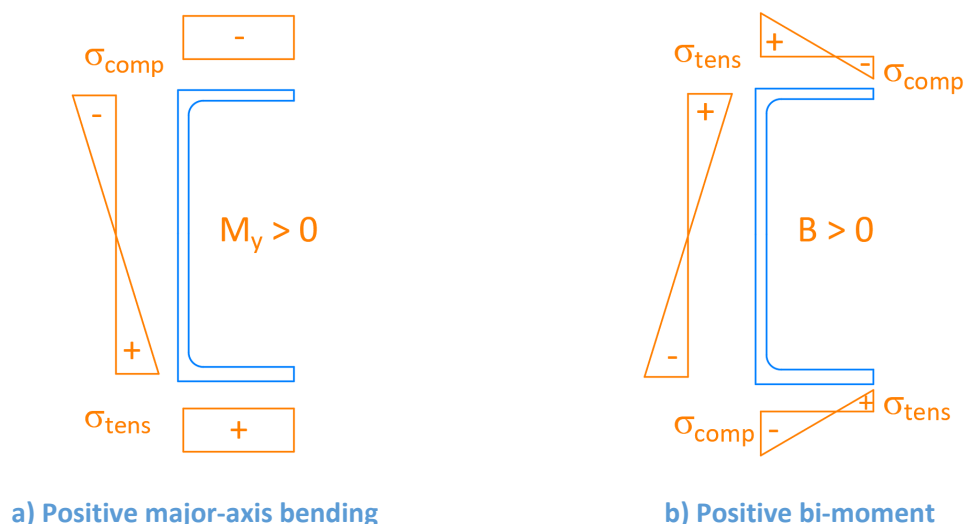


Figure 5-17: Distribution of axial stresses due to a) the major-axis bending moment and b) the bi-moment

The results shown above may have convinced some authors to neglect residual stresses in order to avoid their favourable effect on the ultimate resistance (see for example (la Poutré 1999) and (Kalameya 2008)). However, as shown in Figure 5-18, the conclusion given above is not true for all load cases. In fact, in case of U sections subject to an axial force, the results show that considering residual stresses lead to a lower ultimate resistance. Obviously, the maximum residual compression stress situated in the centre of the web increases the compression stresses induced by the axial force. In case of U sections this superposition unfavourably affects the lateral stiffness of the member and therefore leads to a lower ultimate resistance (see paragraph 5.5.6.2).

One may therefore conclude that the amplitude of the residual stresses cannot be chosen only by considering the least favourable value, as it depends on the loading situation. It should rather be calibrated with reference to physical tests and measurements of residual stresses. Unfortunately, to the author's knowledge no residual stress measurements have been published up to now. In order to validate the residual stress model developed based on equilibrium conditions and comparison to physical tests further on, it is therefore proposed to simulate the cooling process of hot-rolled sections by a thermo-mechanical analysis in the following paragraph.

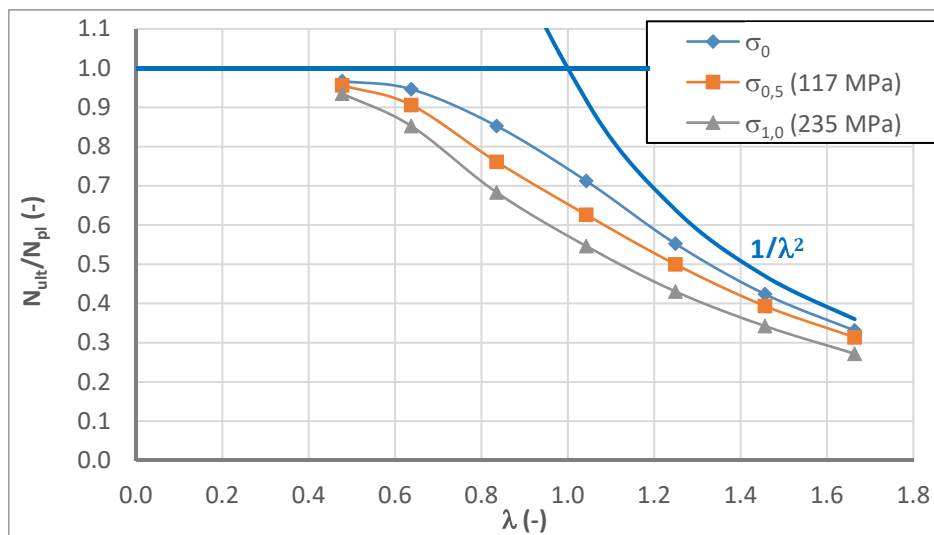


Figure 5-18: Influence of the residual stress amplitude on the ultimate resistance of a member subject to compression

5.2.1.5.3 Thermo-mechanical simulations of the cooling process of hot-rolled sections

So as to obtain the residual stress distribution for hot-rolled sections thermo-mechanical simulations are performed hereafter. For similar analysis, concerning residual stresses resulting from welding or flame cutting (see references (Li et al. 2012) and (Thiébaud 2014)), it has however been shown that the studied problem may be considered as uncoupled. Consequently, it is possible to treat the thermal and the mechanical analysis separately. Indeed, in a first step the temperature distribution over the cooling time and across the section is determined by a thermal analysis. This analysis is performed based on the thermal properties of steel defined in Eurocode 3 Part 1-2 (CEN 2005b), an emissivity ϵ of 0,55 and a convection coefficient h of

7 W/m²K. The thermal properties are represented in Figure 5-19. In a second step, the temperature history obtained at each node of the finite element model is introduced as nodal load into the mechanical model.

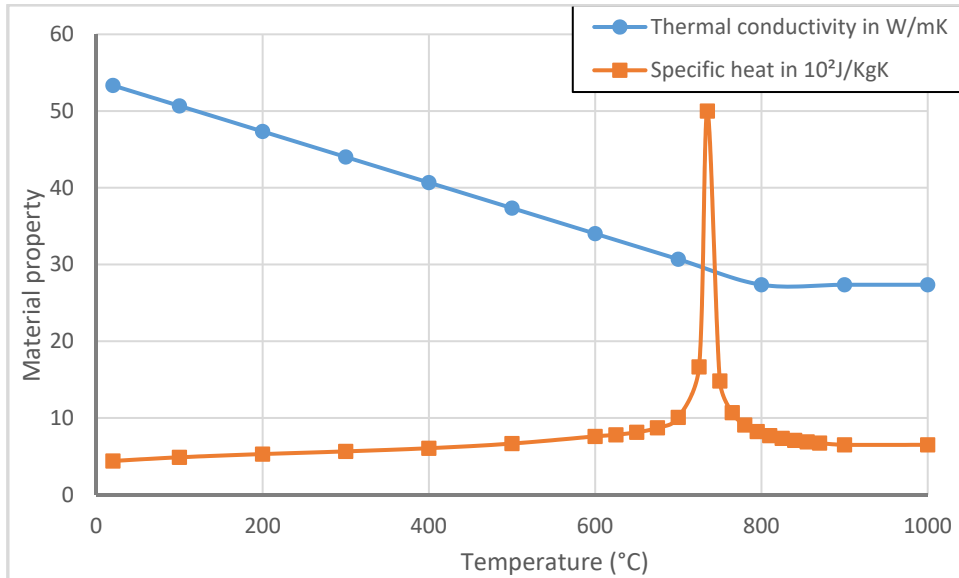


Figure 5-19 : Thermal properties of steel following Eurocode 3 Part 1-2

The values of the emissivity and the convection coefficient have been calibrated in order to obtain a temperature evolution close to measurements performed during the cooling process of a HEB 200 section published in references (Alpsten 1968) and (Alpsten 1972). The points of measurement are shown in Figure 5-20 and the obtained evolution of the temperature is given in Figure 5-21.

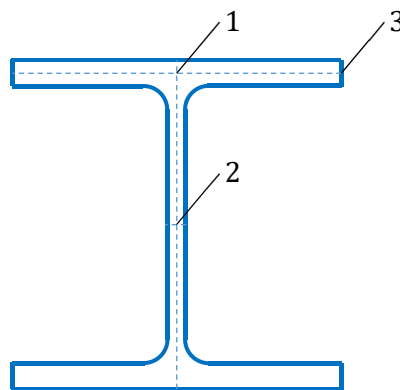


Figure 5-20 : Points of temperature measurements as published in reference (Alpsten 1968)

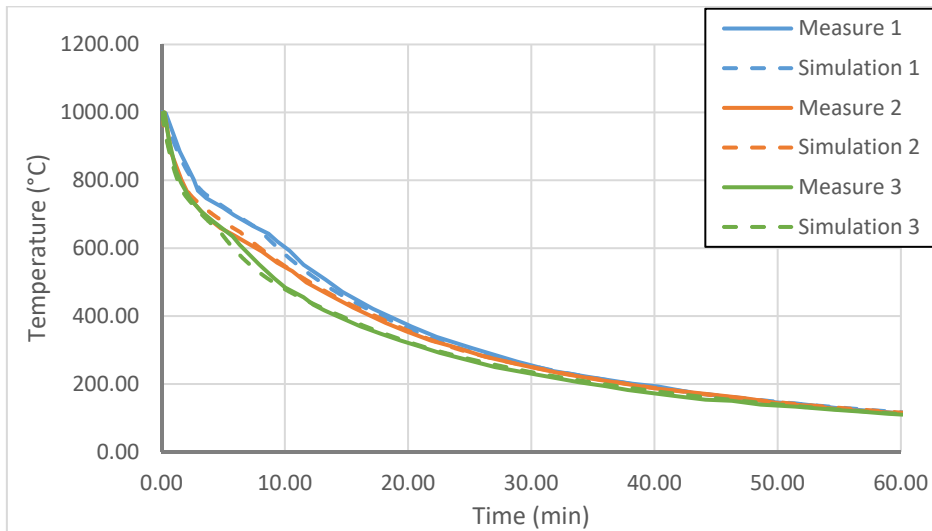


Figure 5-21 : Evolution of the temperature during cooling of a HEB 200 section

Figure 5-21 shows that the simulation is in good agreement with the measurements. Also, it may be noted that the temperature gradient through the section is highest in the first fifteen minutes of the cooling process. It is recalled that the residual stresses result from the temperature strains caused by the stress gradient over the section. Therefore, it appears that the first phase of cooling is most important for creation of the residual stresses.

As mentioned, the second step of the calculation is purely mechanical based on temperature depending material properties. These material properties are represented in Figure 5-22. The curves have been determined by measurements and the results have been published in references (Alpsten 1968) and (Lee et al. 2012).

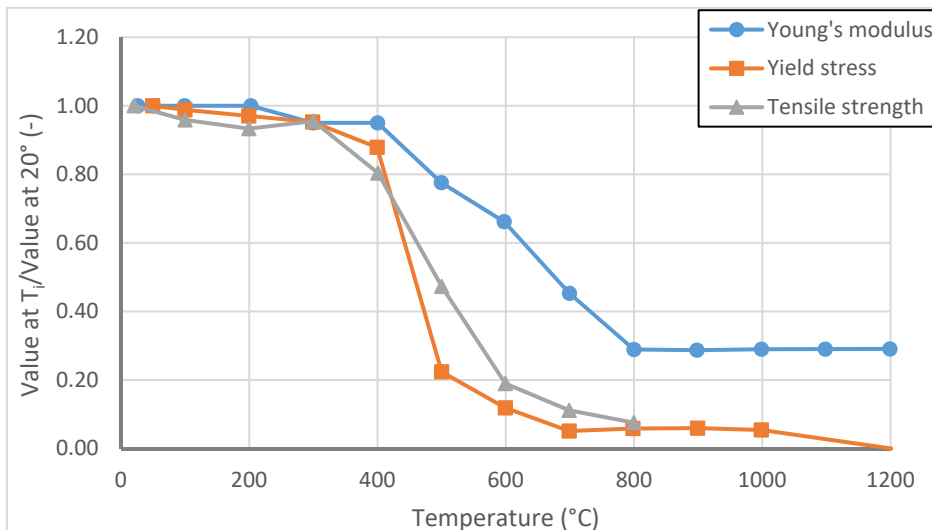


Figure 5-22: Temperature depending mechanical properties of steel

In order to validate the applied procedure for the determination of the residual stresses, the example of a double symmetric H section is studied first. The obtained results are compared to physical measurements published in reference (Alpsten 1972).

As the studied section is double symmetric, it is possible to perform the simulation on one quarter of a section. This quarter model is meshed with solid elements of type Solid 185 (from ANSYS element library). The finite element model is represented in Figure 5-23. The length of the model is equal to $4h$. Due to symmetry conditions the vertical displacement is restrained at the bottom of the model, representing the mid-height of the physical section and lateral displacement is restrained at the outer face of the model representing the mid-plane of the web of the physical section. These boundary conditions are also represented schematically in Figure 5-23. Additionally, the axial displacement of the whole section is restrained on one member extremity.

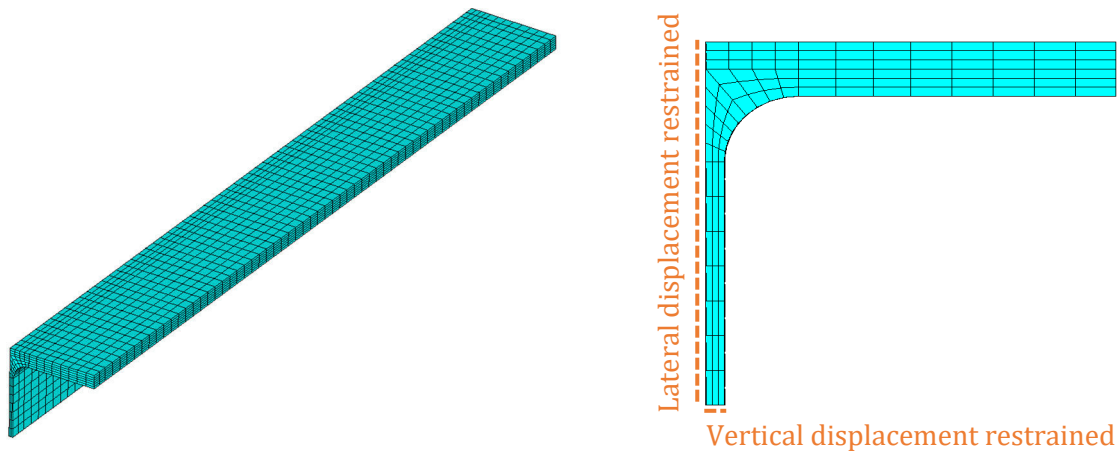


Figure 5-23: Quarter model of HEB200 section

The residual stresses obtained with the FEM simulations are compared to those determined by Alpsten in Figure 5-24. Obviously, the agreement is very satisfying, both in terms of the amplitude and distribution of the residual stresses. Consequently, the procedure described here before, is used next to determine the residual stresses for hot-rolled U sections.

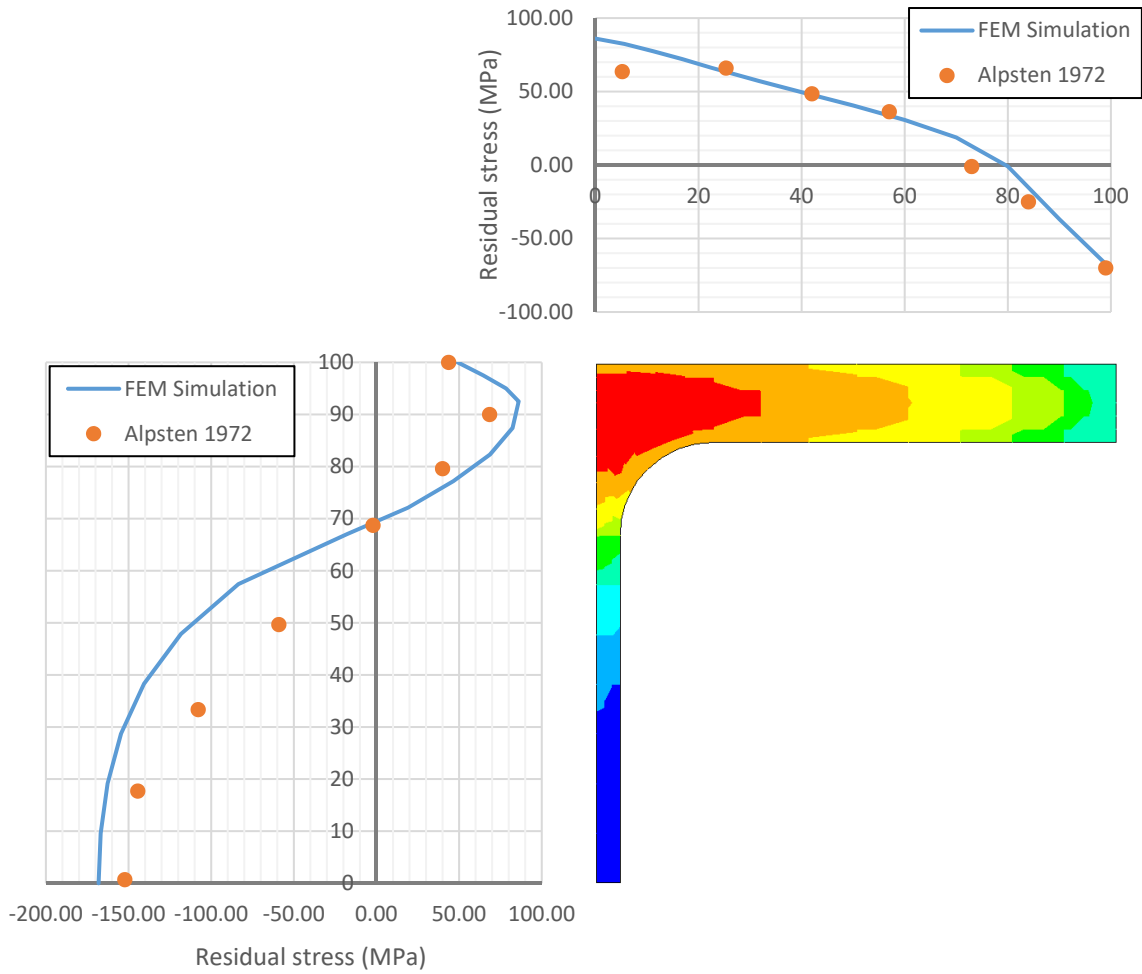


Figure 5-24: Residual stresses obtained by FEM simulation compared to residual stresses determined in (Alpsten 1972)

As before, the symmetry of the section is used to reduce the problem. Again, one extremity of the section is entirely restrained against axial displacements. Also, the vertical displacement at mid-height of the web is restrained along the whole member. Yet, as the cross-section is only mono-symmetric the lateral displacements are not restrained over the entire height of the model but only at mid-height (but as before over the total length) as schematically represented in Figure 5-25.

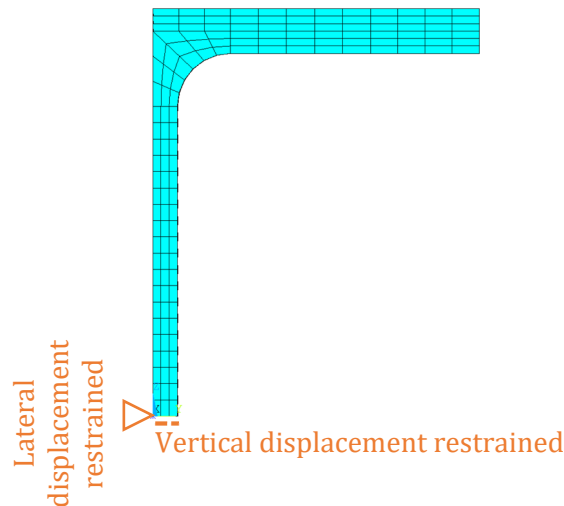


Figure 5-25: Boundary conditions for U section

The results of the thermal simulation are represented in Figure 5-26. When the results are compared to the thermal analysis of the HEB section (see Figure 5-21), one may remark that the temperature difference between the tip of the flange and the fillet zone is highly reduced. Indeed, over the total time range, the temperature is nearly identical in Points 1 and 3 for the UPE 200 section. This observation may be understood easily as the fillet zone is less insulated because the second part of the flange is missing compared to I sections. Consequently, the fillet zone is closer to the air and cools down as rapidly as the tip of the flange. The temperature gradient between Points 1 and 2 is similar to the case of I sections.

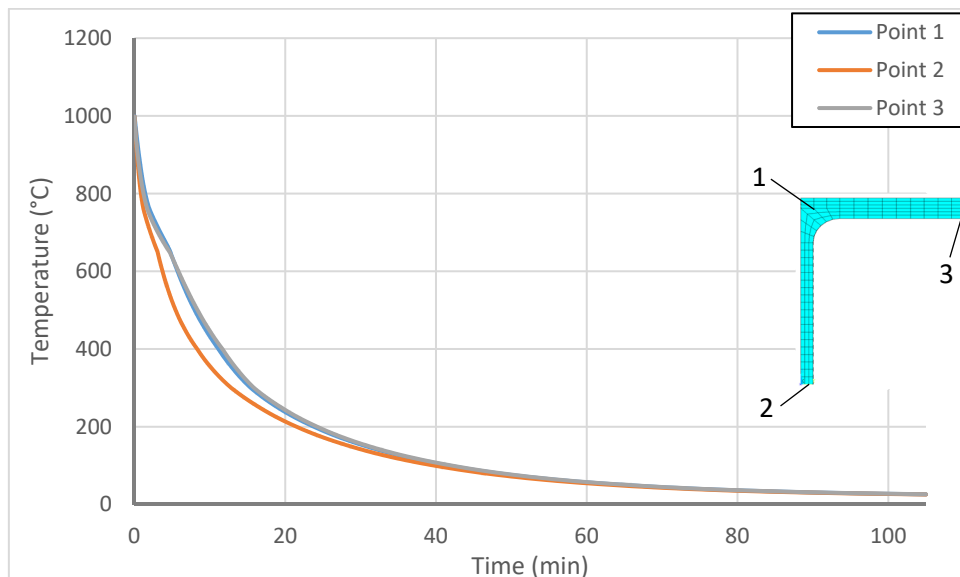


Figure 5-26 : Evolution of the temperature during cooling for UPE 200 section

In order to visualize the thermal results further on, Figure 5-27 and Figure 5-28 show the temperature distribution over the cross-section at 48,5s and 284s after the start of the cooling process.

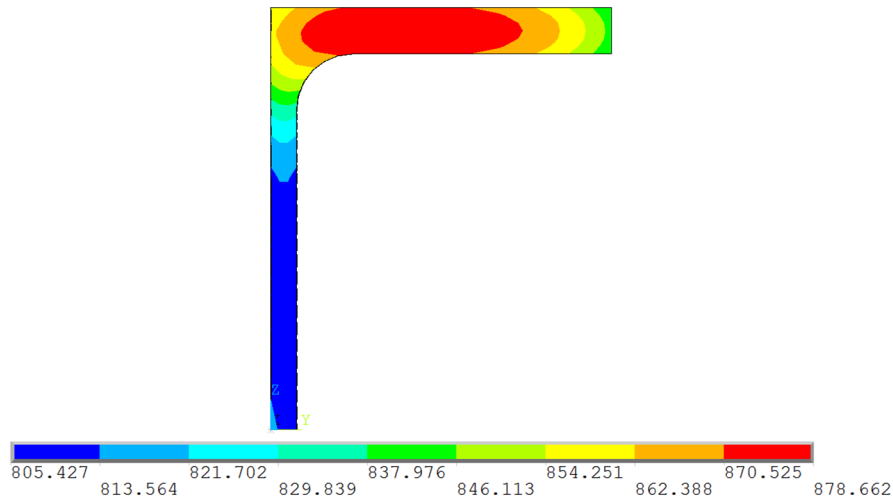


Figure 5-27: Temperature distribution over UPE section at 48,5s – T in °C

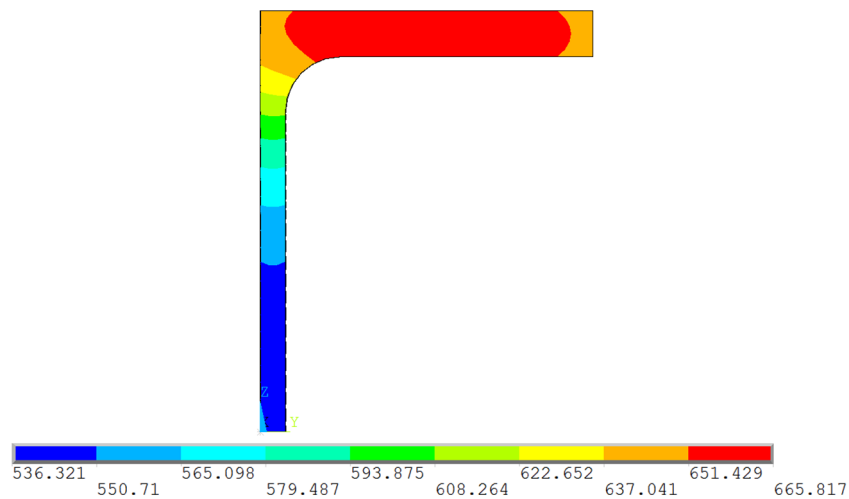


Figure 5-28: Temperature distribution over UPE section at 284s – T in °C

Observing Figure 5-27 and Figure 5-28, it becomes obvious that the section cools down the slowest approximatively at the middle of the flange. The flange's tip and the fillet zone cools faster. However, the temperature gradient over the flange is less pronounced as for I sections of similar shape. Since the web's thickness is much less than the flange's thickness ($t_w = 6$ mm and $t_f = 11$ mm for UPE 200), it is not surprising to observe that the web cools much faster than the flanges.

The temperature history obtained by the thermal analysis is now introduced as nodal loads into the mechanical model. The residual stress distribution obtained at the end of the mechanical analysis is represented in Figure 5-29. It may be observed that the stress distribution is approximatively constant up to the middle of the flange. Then it decreases and the stresses become negative (compression) near the flange's tip. Additionally, one may remark that the maximum tensile stress is not situated in the fillet zone but in the flange. This seems consistent with the results of the thermal analysis as the section cools down less rapidly at this point (see Figure 5-27). The variation of the residual stresses seem also to be slightly different than supposed

in paragraph 5.2.1.5.1. Indeed, they are constant over nearly half of the web and then vary linearly. This result may also be explained with reference to thermal analysis that shows homogenous cooling for the zones of the web that are far from the flange. Last, one should note that the maximum value of the tensile residual stress is approximately equal to 80 MPa. The maximum compression stress is slightly higher and attains approximately 105 MPa.

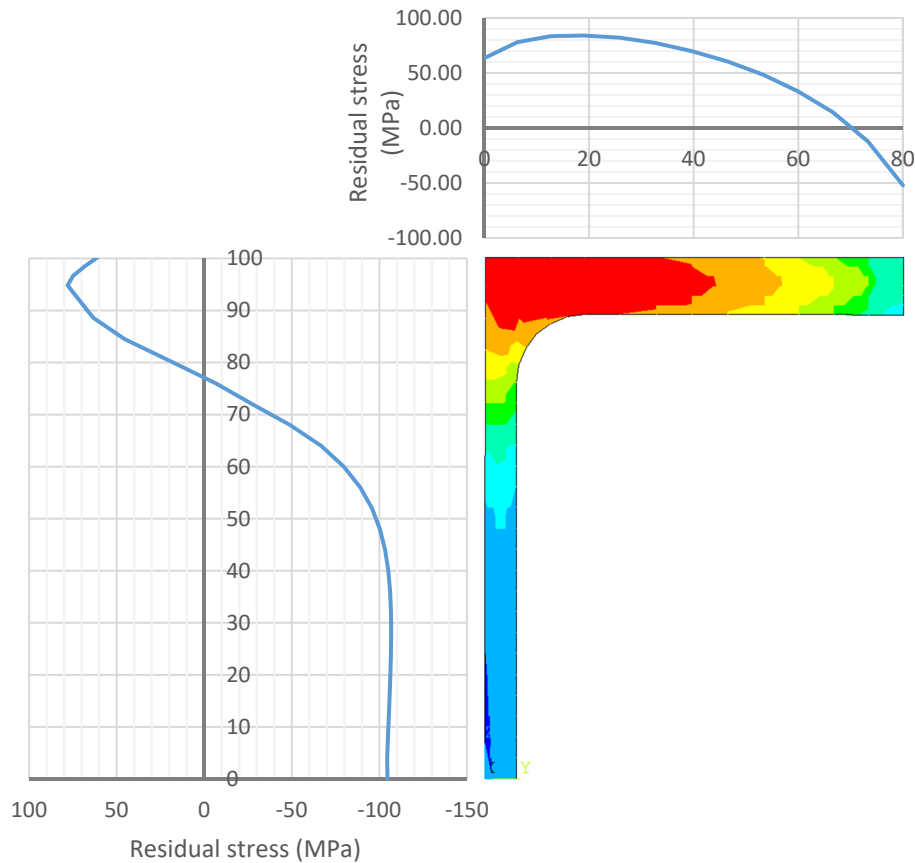


Figure 5-29: Residual stress distribution for UPE 200 obtained by FEM simulation

Last, the results determined for a more compact UPE 80 are represented in Figure 5-30. The distribution of the residual stresses over the flange is very similar to what has been obtained for the UPE 200 section. Conversely, the residual stresses vary over the total height of the web because of the proportion of the section. Indeed, the ratio between the web height and the flanges width is rather low compared to the UPE 200 section (1,6 compared to 2,5). Therefore, the temperature varies over the total height of web during cooling as represented in Figure 5-31 and Figure 5-32 whereas it attains a nearly constant value over half of the web for the UPE 200 section (see Figure 5-27 and Figure 5-28).

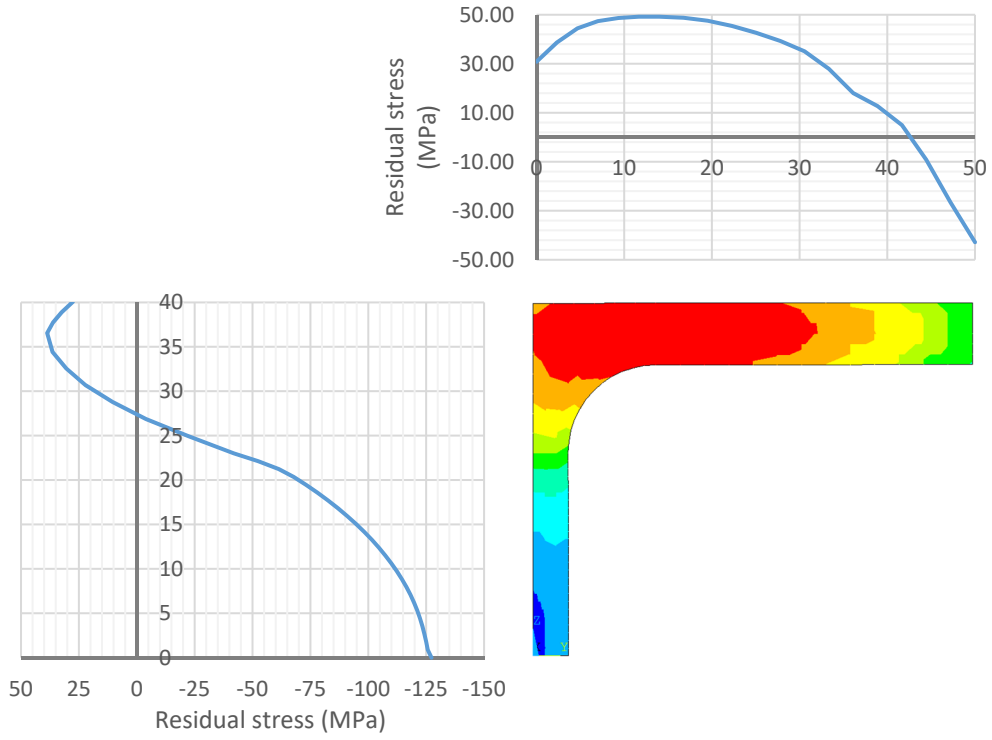


Figure 5-30: Residual stress distribution for UPE 80 obtained by FEM simulation

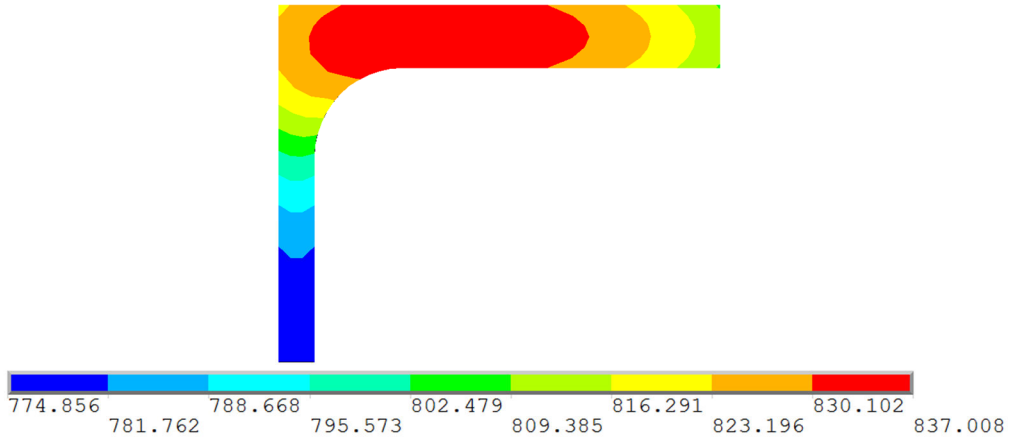


Figure 5-31: Temperature distribution over UPE section at 43,5s – T in °C

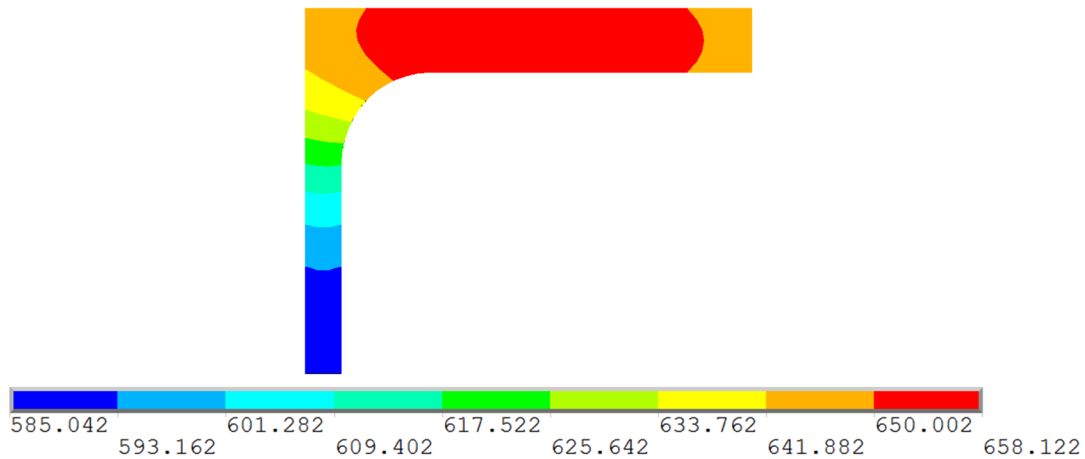


Figure 5-32: Temperature distribution over UPE section at 187s – T in $^{\circ}\text{C}$

Regarding the results obtained for the two U sections studied here before, it may be concluded that the simplified residual stress distribution of paragraph 5.2.1.5.1 is not exactly identical to the finite element simulations. Indeed, the stresses do not vary linearly over the flange and the web.

The influence of the distribution on the resistance of a U-shaped member is quantified based on the following three examples:

- Member of UPE 200 section subject to constant major-axis bending (noted as UPE200_M);
- Member of UPE 80 sections subject to constant major-axis bending (noted as UPE 80_M);
- Member of UPE 80 section subject to an axial compression force (noted as UPE 80_N).

All members are supposed to possess fork end supports.

Figure 5-33 represents the ultimate resistance curves for the three examples and compares the results obtained based on residual stress obtained by the thermo-mechanical simulations (noted as `_ResStrThermoMech`) with the results obtained based on the residual stress model determined in paragraph 5.2.1.5.1 with a value of the residual stress at the intersection between the flanges and the web of 80 MPa (noted as `_ResStrModel`). It can be easily observed that, even if the residual stress model developed in paragraph 5.2.1.5.1 on the basis of equilibrium conditions is not exactly identical to the results obtained through the thermo-mechanical simulations, the GMNIA simulations yield very close results for all three cases. One may therefore conclude that the simplified residual stress model can be applied to simulate the ultimate resistance of U-shaped members. This is done in the framework of this thesis. It would also be possible to use directly the residual stress pattern determined by the thermo-mechanical analysis. Nonetheless, this study has been performed in order to obtain general information on the distribution and amplitude of the residual stresses. A deeper investigation might be necessary to determine the residual stresses

more precisely based on the exact thermal conditions of the hot-rolling and cooling processus (including exact initial temperature, etc.).

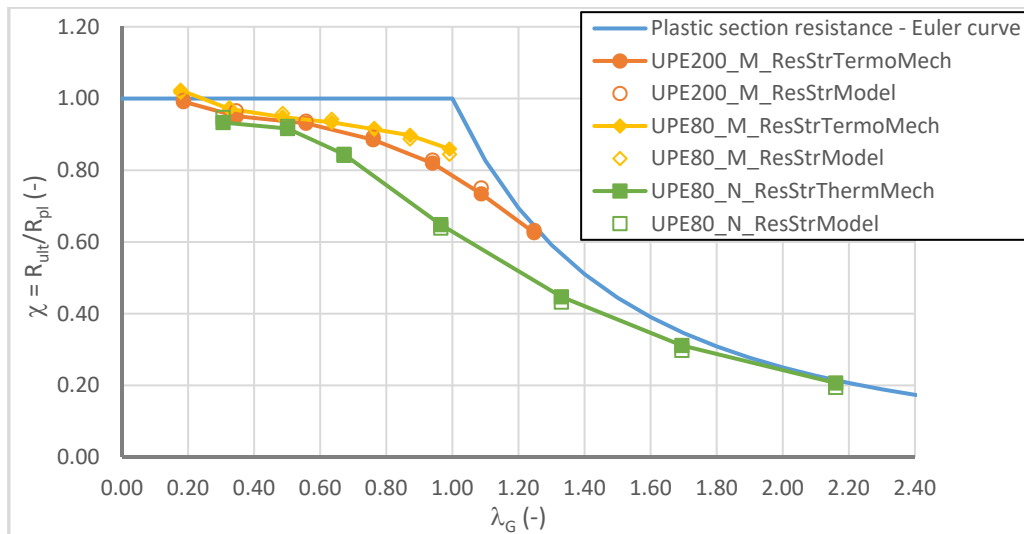


Figure 5-33: Ultimate resistance curve of UPE 200 subject to axial compression and major-axis bending

5.2.1.6 Equivalent geometric member imperfection for U sections

5.2.1.6.1 Form and amplitude

Several numerical studies concerning the stability of U-shaped members have been performed in the past as for example in (de Louw 2007), (la Poutrée 1999), (FOSTA 2004) and (Kalameya 2008). Even if the previous mentioned authors studied the same type of member, the applied geometric member imperfection differs from one author to the other. Table 5-3 summarizes the geometric member imperfection used in the mentioned studies. Each of the authors claims to have used the form of the imperfection leading to a lower bound value of the resistance, i.e. that the chosen imperfection is safe-sided compared to other possible imperfections. As obviously no general agreement exists on the geometric member imperfection to be used for U-shaped members, it seems inevitable to check which assumption is valid. Various shapes of imperfection are studied hereafter. They are presented in Figure 5-34.

Table 5-3: Geometric member imperfection used in previous studies

Reference	Form of the imperfection	Amplitude of the imperfection	Load case considered
(FOSTA 2004) and (de Louw 2007)	Eigenmode affine in the positive direction (EM+)	L/1000	$M_y + M_x$
(la Poutrée 1999)	Lateral imperfection directed to the flange's tip (v+)	L/1000	$M_y + M_x$
(Kalameya 2008)	Lateral imperfection directed to the flange's web (v-)	L/400	$M_y + M_z + N$

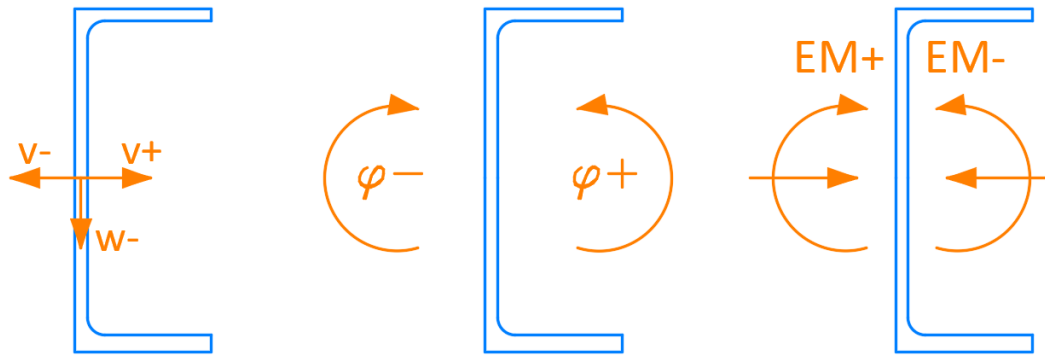


Figure 5-34: Possible forms of geometric member imperfection used for GMNIA

The numerical simulations performed in the following do not include the residual stresses in order to quantify the sole effect of the geometric member imperfections.

5.2.1.6.2 Sensitivity study

5.2.1.6.2.1 Member subject major-axis bending

First, the load case of constant major-axis bending is considered. The following comparisons are based on a member of UPE 200 section with fork supports at both ends. The amplitude of the imperfections is varied between $L/2000$ and $L/500$. Figure 5-35 to Figure 5-37 show the “ultimate resistance curves” representing the ratio between the bending moment at ultimate limit state and the plastic bending moment resistance.

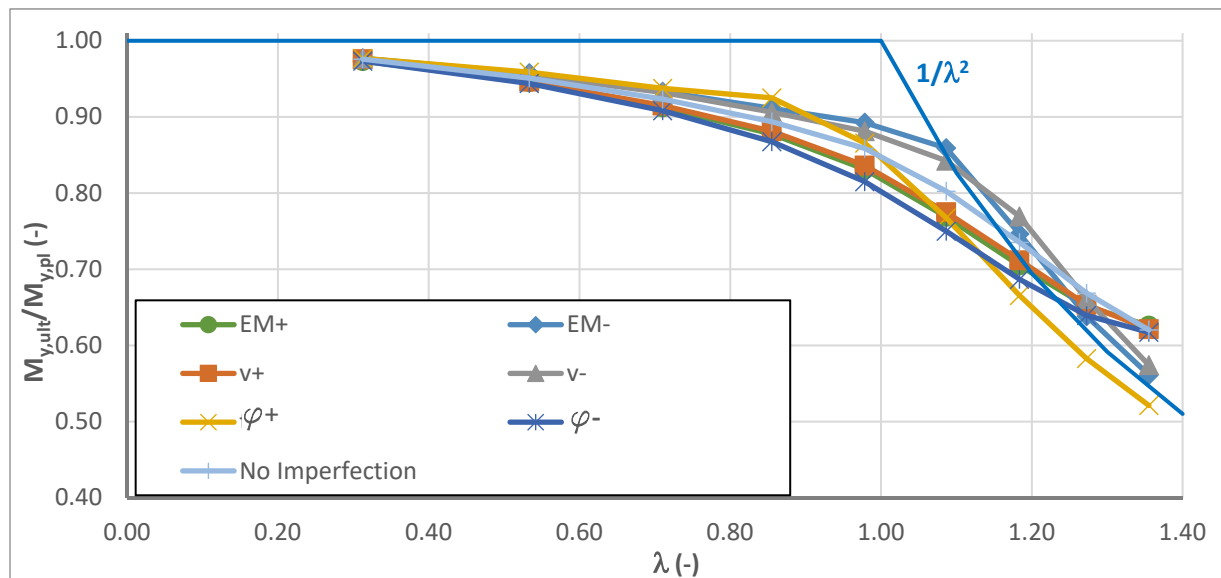


Figure 5-35: Ultimate resistance curve for imperfection amplitude of $L/2000$

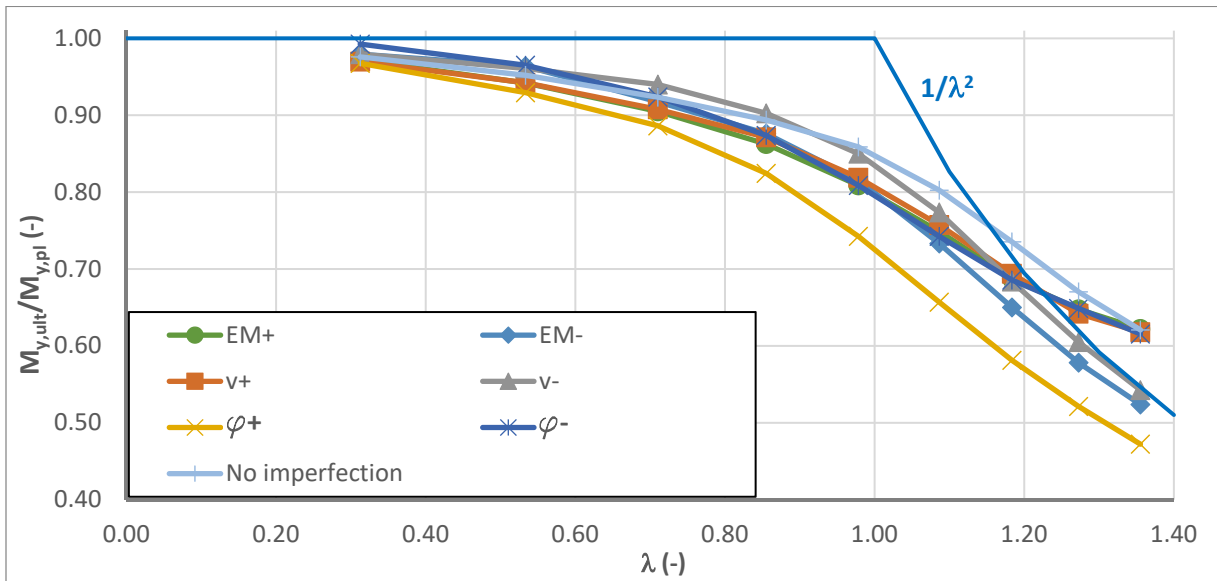


Figure 5-36: Ultimate resistance curve for imperfection amplitude of L/1000

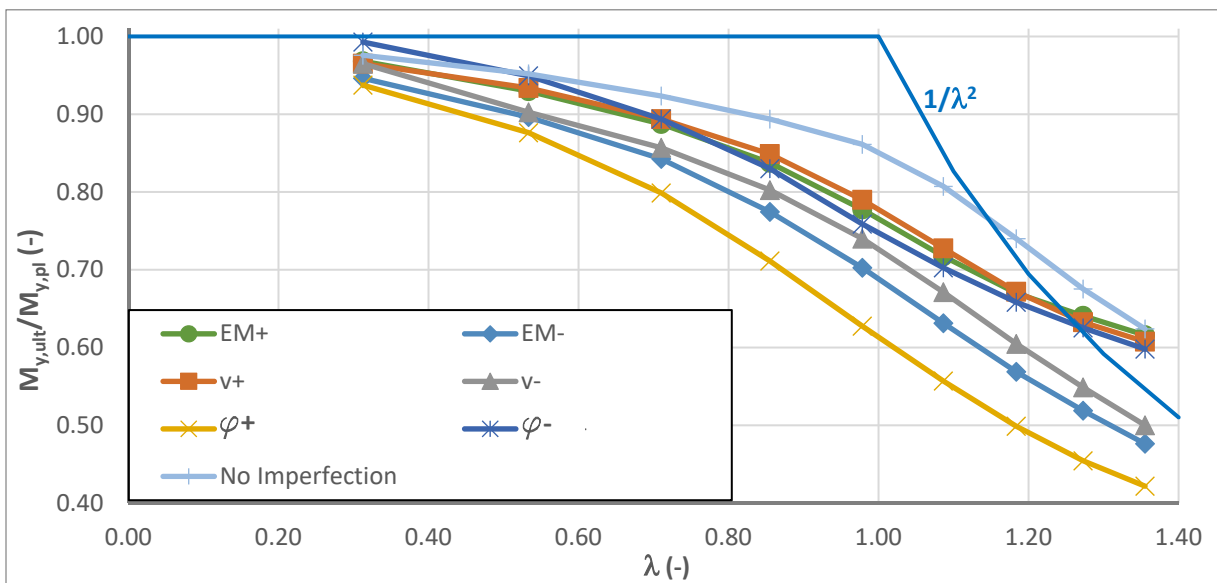


Figure 5-37: Ultimate resistance curve for imperfection amplitude of L/500

The previous figures reveal several interesting points. First of all, it seems somewhat astonishing that even the perfectly straight member (noted as “No Imperfection”) suffers a reduction of its ultimate resistance depending on the relative lateral-torsional buckling slenderness. In order to explain this behaviour it is necessary to return to the question of the section resistance (see also Chapter 4).

Figure 5-38 recalls the elastic and plastic stress distribution for a U section subject to positive-major-axis bending. Also, the distribution of the warping function ω is given. The elastic and plastic major-axis bending moments can be determined by integrating the corresponding stress distribution over the section. In paragraph 4.4.2.2 it has been shown that the plastic stress

distribution under major-axis bending is linked to a stress induced bi-moment (negative following the sign conventions used here).

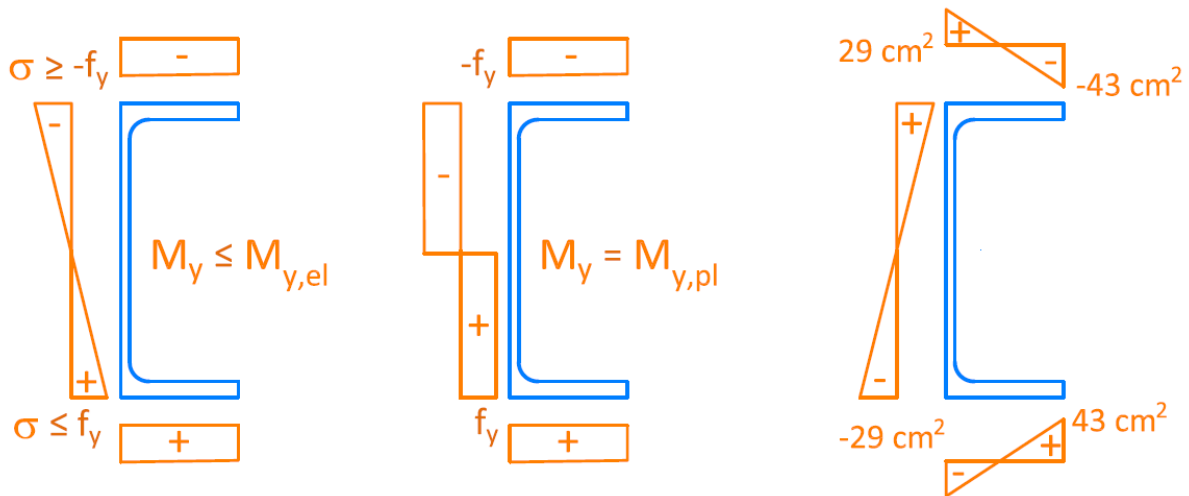


Figure 5-38: Elastic and plastic stress distribution and warping function for a UPE 200 section

The influence of these resulting bi-moments, on the cross-section resistance has been discussed in Chapter 4. Here, Figure 5-35 to Figure 5-37 clearly show their influence on the resistance for the perfectly straight member. In fact, the stress induced bi-moment and the associated torsional rotation create out-of-plane second order effects leading to the observed reduction. It is also interesting to show the displacements at the ultimate limit state. Figure 5-39 shows this result for member possessing a lateral-torsional buckling slenderness of approximately 1,0. As can be seen the member has mainly rotated about its longitudinal axis and, in a less important amount, laterally displaced.

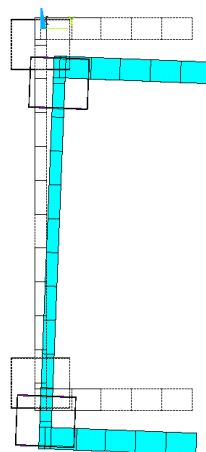


Figure 5-39: Displaced shape of the section at mid-span at the ultimate limit state for the perfectly straight member

In order to fully understand the results shown in Figure 5-35 to Figure 5-37, it is also of interest to recall the stresses induced by the different internal moments and depending on the sense of the deformation.

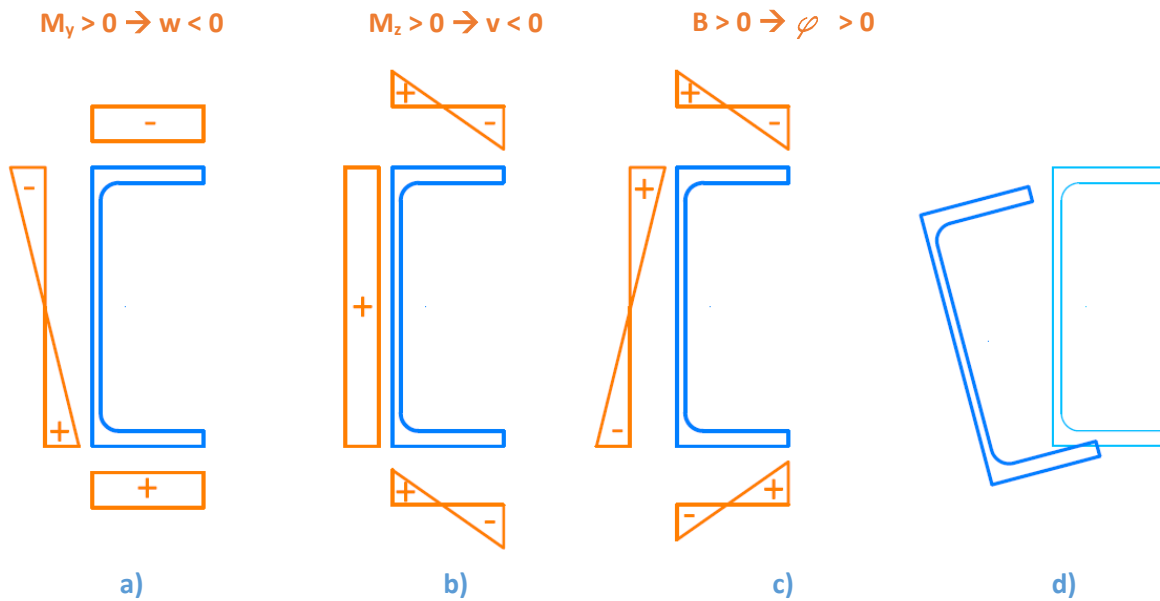


Figure 5-40: Elastic stress distribution for a U section under a) major-axis bending, b) minor-axis bending and c) the bi-moment and d) resulting deformed shape

It is recalled that compression stresses are defined as negative. Figure 5-40 shows that if all internal moments are positive:

- The maximum (compression) normal stress results at the tip of the upper flange;
- The stresses due to minor-axis bending and the bi-moment counterbalance at a certain degree at the upper flange;
- The stresses due to major-axis bending and the bi-moment counterbalance at a certain degree along the web;
- A positive bi-moment is associated with a positive torsional twist.

Consequently, the displaced shape, represented in Figure 5-39 is consistent with the stress-induced bi-moment (negative stress induced bi-moment generates negative torsional twist).

In Figure 5-35 to Figure 5-37, it can be seen that the form of the ultimate resistance curves resulting from the imperfections $v+$, $EM+$ and $\varphi-$ are similar. Also, the resulting ultimate resistances for these imperfections are, for all values of the relative slenderness and amplitudes of the imperfection, less than the ultimate resistance of the perfectly straight member. As these imperfections amplify the effect of the stress induced bi-moment, this result is not astonishing. Moreover, by increasing the amplitude of the imperfection the difference with respect to the perfectly straight member increases, too. It should be noted that the absolute value of the imperfection also increases with the member slenderness (member length).

The form of the ultimate resistance curves associated with imperfections $\varphi+$, $EM-$ and $v-$ may be more surprising. It can be seen that, depending on their absolute amplitude, these imperfections may lead to higher or lower resistances than those obtained for the perfectly straight member and for the members subject to imperfections $\varphi-$, $EM+$ and $v+$. In order to understand these results

Figure 5-39 and Figure 5-40 should be studied again. It may be observed that imperfections generating a positive torsional rotation ($\varphi+$, EM- and v-) lead to a reduction of the torsional twist generated by the stress induced bi-moment. Hence, these imperfections may have a stabilizing effect. In order to illustrate this observation, it is interesting to compare the stress distribution and the deformed shape at the ultimate limit state for the case of the perfectly straight member and a member subject to an imperfection $\varphi+$. Figure 5-41 and Figure 5-42 show the results for a member possessing a relative slenderness of 0,85.

In Figure 5-42 one may observe that the deformed shape of the perfectly straight member is characterized by the in-plane displacement and a non-negligible torsional rotation. Contrariwise, it may be seen in Figure 5-41 that the imperfection $\varphi+$ nearly completely counterbalance the effect of the stress induced bi-moment. Consequently, in this case the imperfection has a favourable effect on the behaviour of the member leading to a higher member resistance.

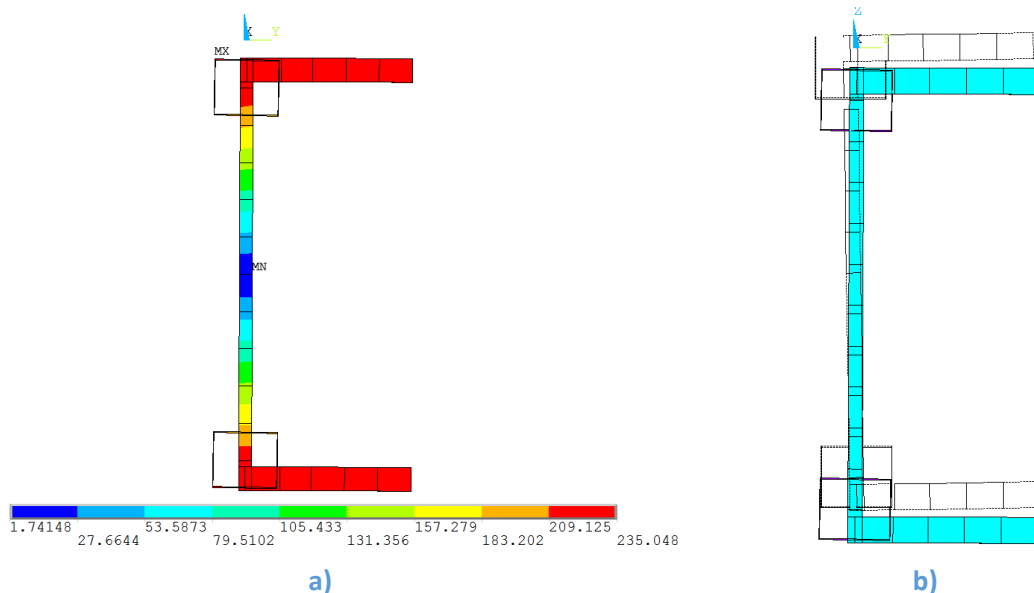


Figure 5-41: a) Von Mises stress and b) deformed shape at mid span for the member of 2,9 m length subject to imperfection $\varphi+$ of $L/2000$

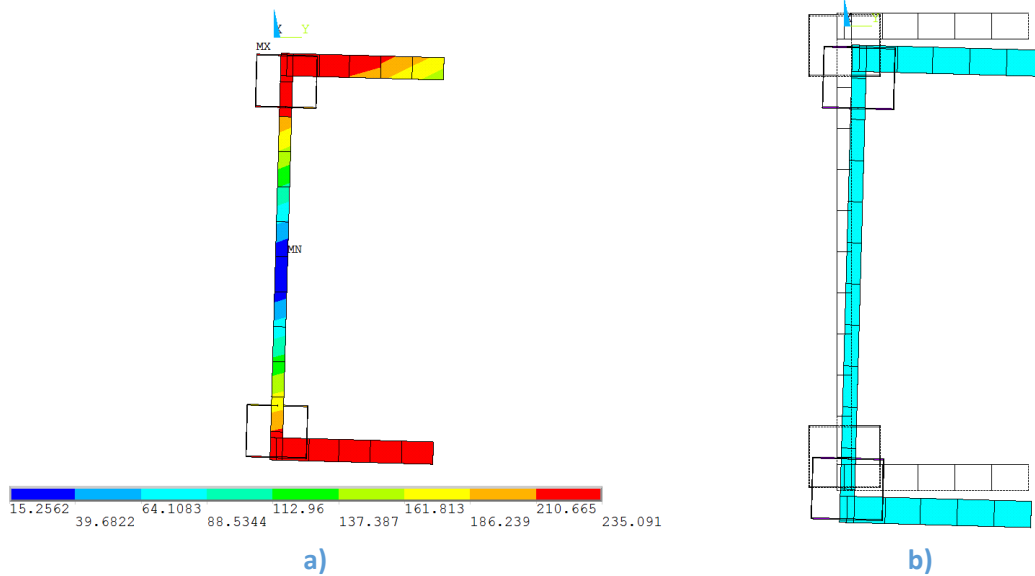


Figure 5-42: a) Von Mises stress and b) deformed shape at mid span for the perfectly straight member of 2,9 m length

Moreover, for higher absolute amplitudes, these imperfections may even lead to a greater strength reduction than the imperfections amplifying the effect of the stress induced bi-moments. This may again be explained based on the stress distribution and deformed shape obtained at the ultimate limit state. Figure 5-43 shows the result calculated for the imperfection $\varphi+$ and an out-of-straightness of the compressed flange of $L/500$. As in Figure 5-41 and Figure 5-42 the member length is 2,9 m.

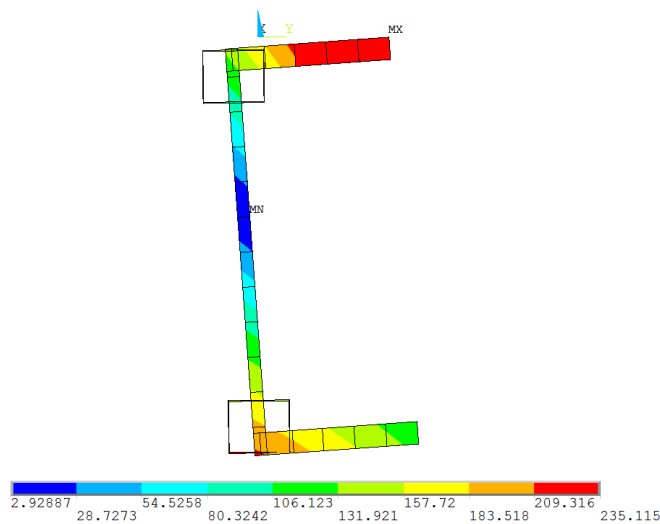


Figure 5-43: Von Mises stresses at mid span for the member of 2,9 m length subject to imperfection $\varphi+$ of $L/500$

It may be observed that the amplitude of the imperfection is high enough to counterbalance entirely the effect of the stress induced bi-moment and to reverse the torsional twist. In the chosen system the torsional twist is positive indicating a positive bi-moment. Also, the lateral displacement directed to the web indicates a positive minor-axis bending moment. Consequently,

the configuration represented in Figure 5-40 is obtained and the maximum compression stress is situated at the tip of the upper flange. Conversely, the maximum tension stress is obtained at the intersection between upper flange and the web in case of the perfectly straight member. It should be mentioned that positive minor-axis bending, as obtained for the configuration represented in Figure 5-40, has a negative effect on the (elastic) stability of U-shaped members as is shown in paragraph 5.5.6.2. Therefore, this member fails at a lower load level than the members subject to a negative minor-axis bending moment.

Finally, it should be mentioned that the imperfections v^- and EM^- have less tendency to counterbalance the effect of the stress induced bi-moment than the imperfection φ^+ as they obviously have a smaller (EM^-) torsional rotation component or no torsional rotation component at all (v^-).

One may summarize the results obtained for the case of constant major-axis bending, as follows:

- Due to the stress induced bi-moment even the perfectly straight member suffers a reduction of its ultimate resistance;
- Imperfections that possess displacement components directed in the same sense as the displacements created by the stress induced bi-moment (v^+ , EM^+ and φ^-) lead always to ultimate resistances that are lower than the one obtained for the perfectly straight member;
- Imperfections that possess displacement components directed in the opposite sense than the displacements created by the stress induced bi-moment (v^- , EM^- and φ^+) may lead to higher or lower ultimate resistances than the one obtained for the perfectly straight member depending on the absolute amplitude of the imperfection;
- The obtained resistance based on the imperfection v^- , EM^- and φ^+ are higher than the ultimate resistance of the perfectly straight member, if they do not result in an unfavourable deformed shape (= unfavourable combination of M_y , M_z and B), i.e. if they do not entirely counterbalance the effect of the stress induced bi-moment;
- If the imperfections v^- , EM^- and φ^+ generate a positive torsional twist and a lateral displacement directed to the web (positive minor-axis bending moment) at the ultimate limit state, they lead to resistances lower than those obtained for the perfectly straight member.

5.2.1.6.2.2 Member subject to combination of major-axis bending and torsion

Next, it is shown that the previous conclusions depend on the applied loads. We might now consider the case of a U-shaped member loaded by a vertical point load at mid-span applied at the intersection between the web and the upper flange. Consequently, the applied load induces a rotation in the negative direction (φ^-). The following figures give the ultimate resistance curves depending on the form of the imperfection and its amplitude for a member of UPE 200 section made of S235.

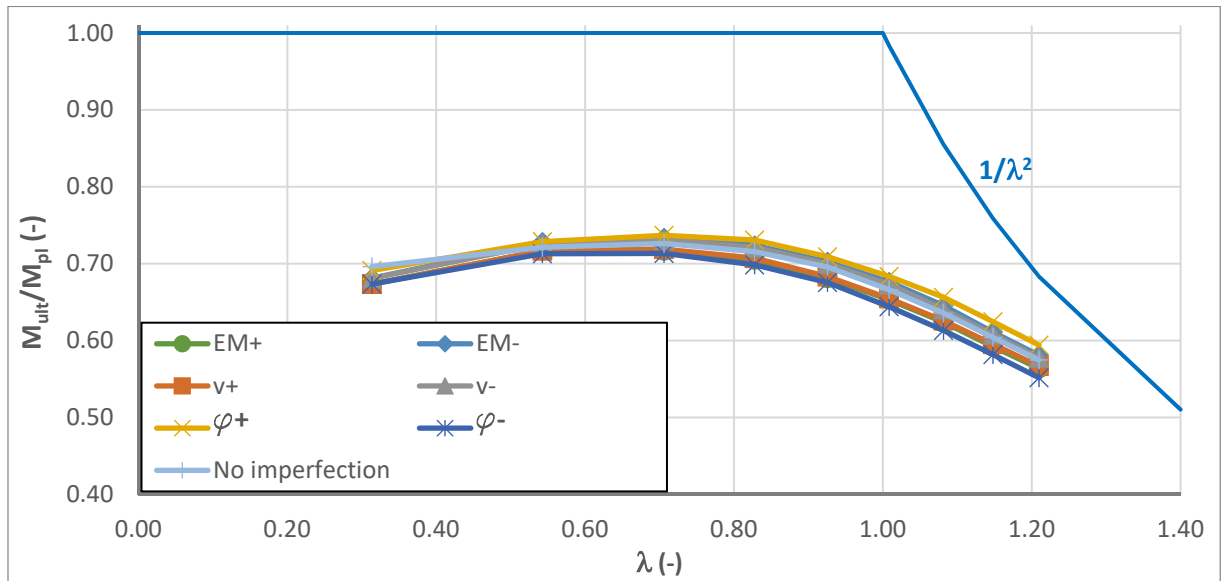


Figure 5-44: Ultimate resistance curve for imperfection amplitude of L/2000

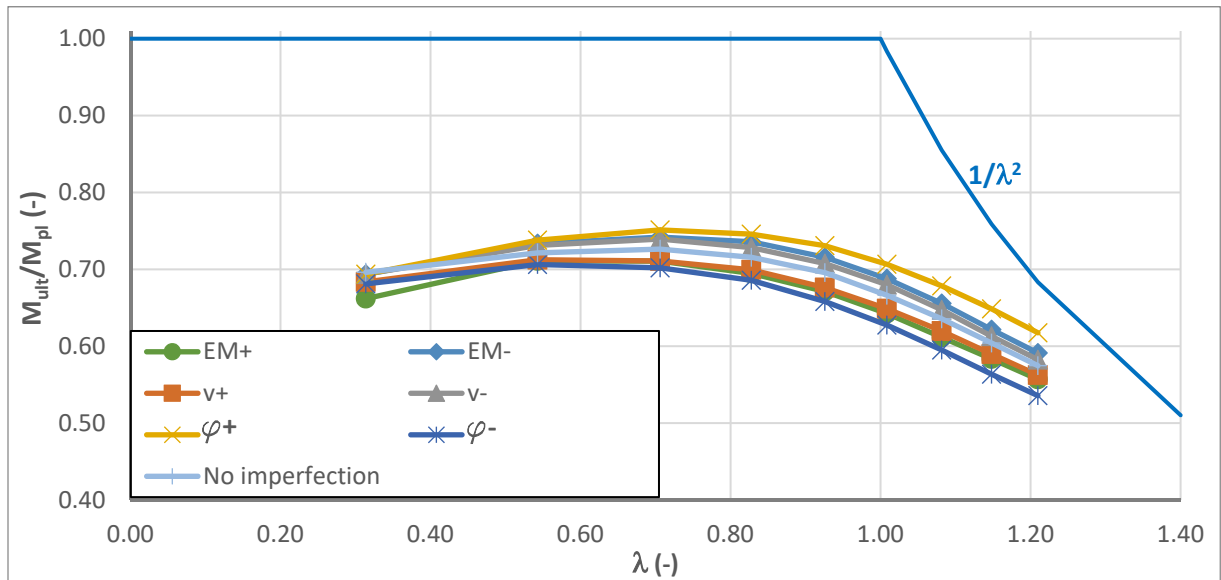


Figure 5-45: Ultimate resistance curve for imperfection amplitude of L/1000

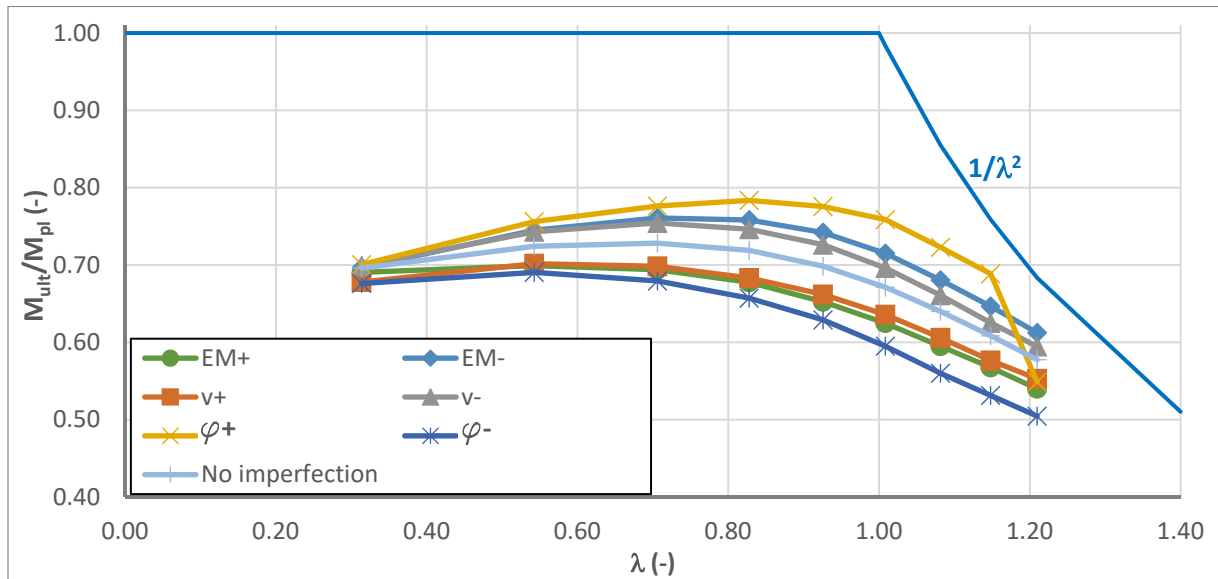


Figure 5-46: Ultimate resistance curve for imperfection amplitude of L/500

As before, Figure 5-44 to Figure 5-46 show that the curves associated with the different forms of imperfection move from each other with increasing amplitude. Also, it can be seen that the differences between the curves are higher for high values of the relative slenderness. Again, this can be explained based on the behaviour of the perfectly straight member. In fact, for small amplitudes of the applied geometric imperfection, the first order torsional twist created by the applied torsional moment (and – in a less important amount – by the stress induced bi-moment) predominates the behaviour of the member. The imperfections directed in the same direction as the first order torsional twist amplify the effect only by small amounts and the imperfections directed in the other sense stabilize the member only slightly. When the amplitude of the imperfection is increased, both effects, destabilizing and stabilizing, are amplified. Therefore, the curves move from each other. The same is true for higher values of the relative slenderness and hence longer members. In fact, as the torsional load is introduced by an eccentrically applied point load, the value of the torsional moment decreases for longer members (the point load necessary to attain the same value of the major-axis bending moment for longer members is lower than for short members). Additionally, it can be seen that the effect of a sole torsional imperfection is again more pronounced than the effect of an imperfection in form of lateral displacement or in form of the eigenmode. For a high amplitude of the imperfection $\varphi+$ and a sufficiently high relative slenderness (in this case $>1,2$) and thus small values of torsional moments, the imperfection $\varphi+$ may even fully counterbalance the applied torsional moment and lead to an unfavourable deformed shape (see also Figure 5-43). In this case the imperfection $\varphi+$ becomes most unfavourable again. The previous observations lead to the following conclusions:

- The applied torsional moment creates a first order torsional twist inducing second order effects and instability;

- The imperfections v^- , EM^- and φ^+ may be favourable, if they do not counterbalance entirely the first order displacements and the effect of the stress induced bi-moment;
- If the amplitude of the imperfections v^- , EM^- and φ^+ is high enough to counterbalance the first order displacements and the effect of the stress induced bi-moment fully, they are unfavourable as they then lead to unfavourable displacements and associated internal moments (see paragraph 5.2.1.6.2.1);
- The imperfections v^+ , EM^+ and φ^- are always unfavourable compared to the perfectly straight member, as they amplify the first order displacements;
- The effect of a torsional imperfection is higher than the effect of lateral imperfection.

Last, the following paragraph studies members subject to an axial compression force.

5.2.1.6.2.3 Member subject to compression

Hereafter, the influence of the form of the imperfection for a member subject to axial compression is evaluated. Again, the imperfection forms used in 5.2.1.6.2.1 and 5.2.1.6.2.2 are studied. Additionally, a pure vertical imperfection w^- is tested. As before, members of UPE 200 section are studied.

The results, represented in Figure 5-47 to Figure 5-49, show that, conversely to the load cases of pure major-axis bending and a combination of major-axis bending and torsion, the perfectly straight member follows the curve describing the theoretical behaviour (section resistance up to a relative slenderness of 1,0 and elastic buckling for higher values of the slenderness). Obviously, the load case of an axial compression force does not create stress induced bi-moments and associated torsional twist or any other effect susceptible to generate second order effects.

The imperfection w^- is the most favourable one. As the major-axis second moment of area I_y of the section equals approximatively 10 times the minor-axis second moment of area I_z , second order effects arising from in-plane displacements are much less important than the second order effects resulting from lateral displacements.

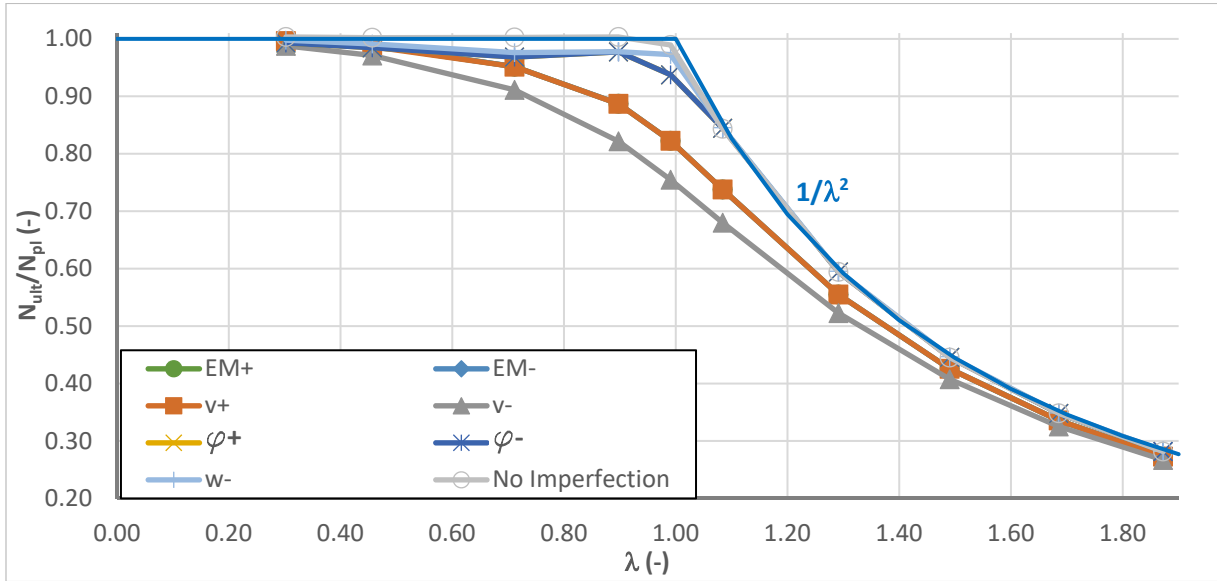


Figure 5-47: Ultimate resistance curve for imperfection amplitude of $L/2000$

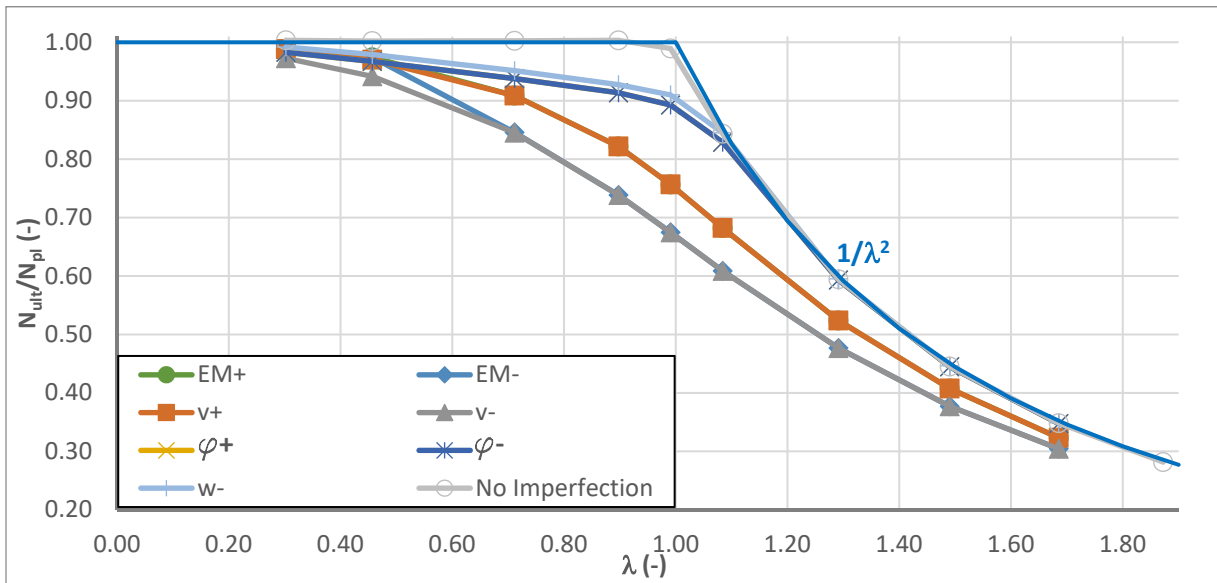


Figure 5-48: Ultimate resistance curve for imperfection amplitude of $L/1000$

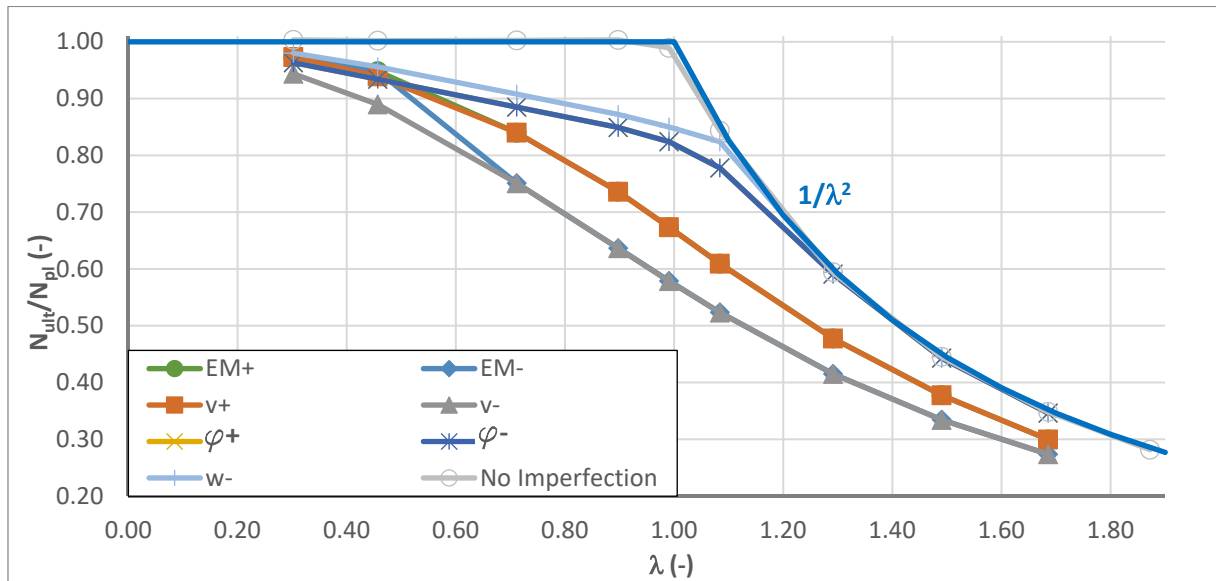


Figure 5-49: Ultimate resistance curve for imperfection amplitude of L/500

It can also be seen that the vertical imperfections w- leads to results close to the ultimate resistances obtained when a torsional imperfection is applied (the curves associated with $\phi+$ and $\phi-$ are superposed). This can be explained on behalf of Figure 5-50 to Figure 5-52. In fact, all three imperfections lead to a similar deformed shape at the ultimate limit state that is characterized by a torsional rotation of the section. Also, one may observe that the stress distribution is similar. In fact, for both torsional imperfections one of the flanges tips (upper in case of $\phi+$ and lower in case of $\phi-$) and the intersection of the other flange with the web have yielded at mid-span. The imperfection w- leads to yielding at the intersection between the upper flange and the lower flange. This yielding seems to be more pronounced than in case of the torsional imperfection. Conversely, the lower flange's tip stays elastic, even if the stresses are close to the yield strength. Additionally, it can be seen from Figure 5-51 and Figure 5-52 why the ultimate resistance curves associated with the imperfection $\phi+$ and $\phi-$ literally overlay. In fact, both imperfections lead to (exactly) the same ultimate limit state, however symmetrically inversed.

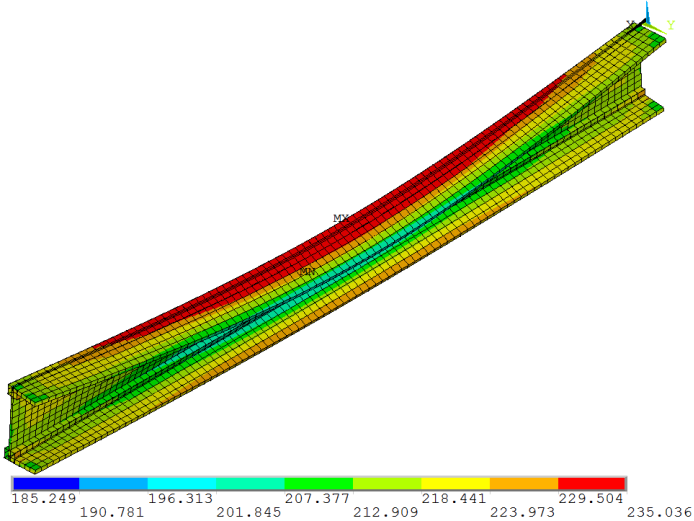


Figure 5-50: von Mises stresses and deformed shape at the ULS for the member subject to imperfection w -

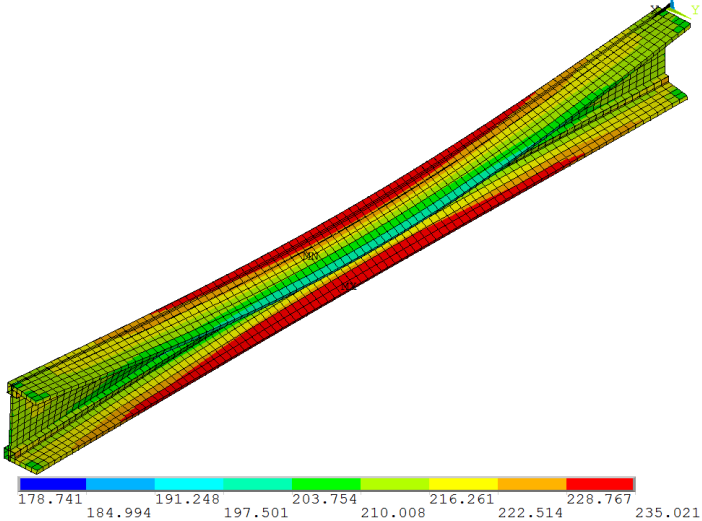


Figure 5-51: von Mises stresses and deformed shape at the ULS for the member subject to imperfection φ -

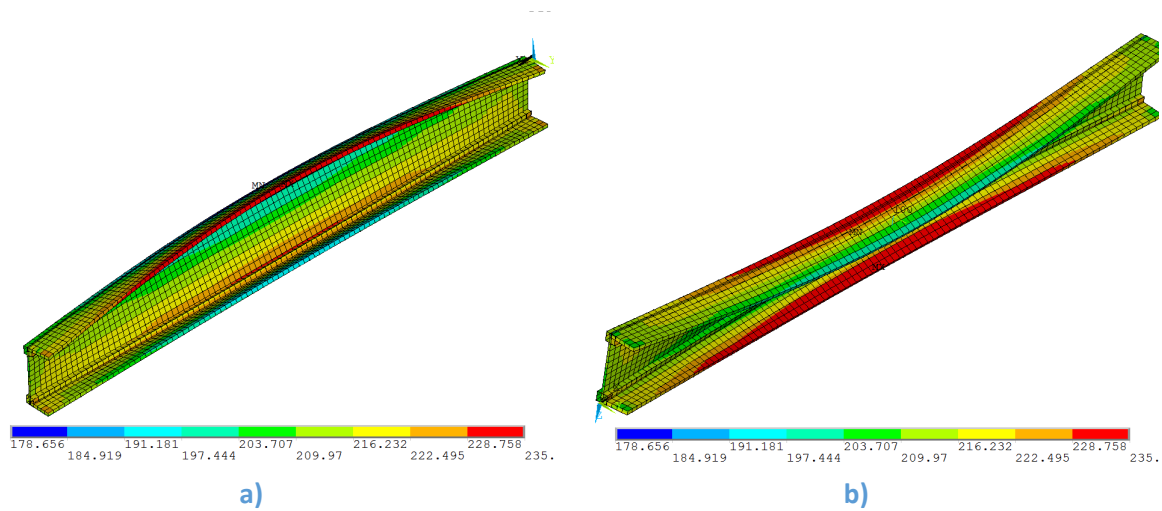


Figure 5-52: von Mises stresses and deformed shape at the ULS for the member subject to imperfection $\varphi+$ - a) view from above and b) view from below

The ultimate resistance curves, represented in Figure 5-47 to Figure 5-49, also show that the effect of an imperfection $v+$ is not the same as the effect of the imperfection $v-$. In order to understand this difference, Figure 5-53 represents the stress distribution and the (amplified) deformed shape at the ultimate limit state for both forms of the imperfection for an amplitude of $L/1000$ and a member length of 2600 mm. Obviously, both imperfections lead to a failure characterized by lateral instability. In case of the imperfection $v-$ a positive minor-axis bending moment, compressing the flanges tips, results from the displacements. It is shown in paragraph 5.5.6.2, that positive minor-axis bending has a destabilizing effect on the stability of U sections whereas negative minor-axis bending tends to stabilize the member. This effect explains the (rather important) difference between an applied positive respectively negative lateral imperfection.

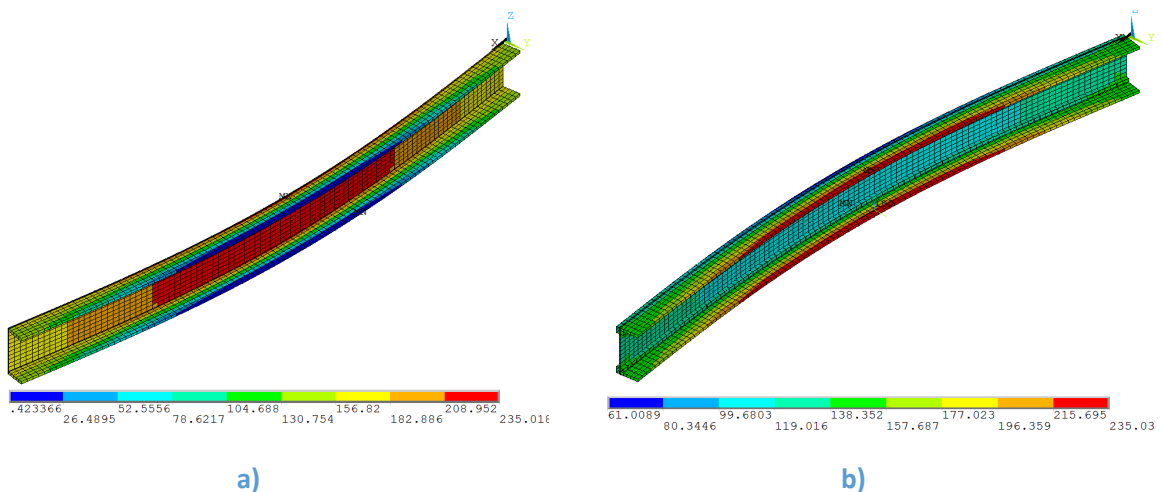


Figure 5-53: von Mises stresses and deformed shape at the ULS for the member subject to a) imperfection $v+$ and b) imperfection $v-$

Last, it should be noted, that the ultimate resistance curves associated with the imperfections $v+$ and $EM+$ as well as $v-$ and $EM-$ overlay for a wide range of the relative slenderness. Only, for small values of the relative slenderness the results differ (compare especially $v-$ and $EM-$ in Figure 5-48

and Figure 5-49). For these short members the first eigenmode corresponds to a combination of vertical displacement and torsional rotation. For longer members the first eigenmode is characterized by a sole lateral displacement. Consequently, the applied imperfection $EM+$ and $EM-$ are equal to the applied imperfection $v+$ and $v-$, respectively.

The results presented in this paragraph lead to the conclusions that in case of axial compression:

- The vertical imperfection leads to the highest ultimate resistance (apart from the perfectly straight member);
- The lateral imperfections ($v-$ and $v+$) are more unfavourable than only torsional imperfection;
- The lateral imperfection $v-$ creating a positive minor-axis bending moment leads to the most unfavourable result.

Also, through the entire paragraph 5.2.1.6.2 it has been shown that there is no single form of the geometric imperfection that always leads to a lower bound for the ultimate resistance. Sometimes it is argued that a geometric imperfection based on the deformation of the perfect structure at ultimate limit state leads to the most unfavourable result (Peer et al. 2015). However, in paragraphs 5.2.1.6.2.1 and 5.2.1.6.2.2, one may observe that this is not always true. In fact, it has been shown that an imperfection directed in the opposite direction to the first order displacements under the applied loads can lead to a lower ultimate resistance than other imperfections as it creates the most unfavourable combination of internal forces and moments. Consequently, in order to determine the most critical form of geometric imperfection, it would be necessary to first calculate (elastically) the internal forces and moments under the applied loads and different forms of the geometric imperfection and then determine which geometric imperfection creates the most unfavourable combination of internal forces and moments. However, even this procedure may not generally lead to a certain lower bound for ultimate resistance as, for hyperstatic structures, a redistribution of internal forces due to plasticity may lead to more favourable results than expected. One may also argue that the real geometric imperfection is completely independent from the applied loads and that the equivalent geometrical imperfection is a concept to reproduce realistic ultimate resistances. Based on the previous study it seems therefore justified to perform GMNIA calculations of U-shaped members based on an equivalent geometric member imperfection affine to the first member eigenmode provided that it is directed in the same sense as the first order displacements. An amplitude of $L/1000$ seems justified. If the first member eigenmode is not directed in the same sense as the first order displacements, an amplitude of $-L/1000$ should be applied.

5.2.1.7 Equivalent geometric plate imperfection

5.2.1.7.1 Form and amplitude

As for the member itself, its constituting plates possess a certain degree of out of straightness. The influence of this geometric imperfection should be accounted for in GMNIA simulations in order to capture the behaviour of the member at its section level (local instability). As these imperfections concern the plates not the member or the cross-section as a whole the obtained conclusions does not depend on the form of the cross-section (I- or U-shaped section). Therefore, the study is based on I sections hereafter.

Different recommendations concerning the inclusion of local geometric imperfection exist. Eurocode 3 Part 1-5 (CEN 2007a) recommends scaling the local buckling eigenmode to 80% of the fabrication tolerances. The resulting amplitudes are given in Table 5-4.

Table 5-4: Local geometric imperfection based on fabrication tolerances

Web	$\frac{h_w}{t_w} \leq 80 \quad \rightarrow e_0 = \frac{h_w}{250}$ $80 < \frac{h_w}{t_w} \leq 200 \quad \rightarrow e_0 = \frac{h_w^2}{20000 t_w} > \frac{h_w}{125}$ $\frac{h_w}{t_w} > 200 \quad \rightarrow e_0 = \frac{h_w}{125}$ <p>and $e_0 > t_w$</p>
Flange	$\frac{b_f}{t_f} \leq 20 \quad \rightarrow e_0 = \frac{b_f}{187,5}$ $\frac{b_f}{t_f} > 20 \quad \rightarrow e_0 = \frac{b_f^2}{3750 t_f}$

For sake of simplicity reference (CEN 2007a) recommends in the same section the values of Table 5-5.

Table 5-5: Simplified local geometric imperfection

Web	$e_0 = \text{Min} \left(\frac{h_w}{200}; \frac{L}{200} \right)$
Flange	$e_0 = \text{Min} \left(\frac{b_f/2}{200}; \frac{L}{200} \right)$

However, some doubts concerning the safe-sided character of eigenmode affine imperfection may arise if one argues in the following way: Local buckling modes may be concentrated in the zone of maximum loading. If a member is subject to end moments only, the maximum loading lies near a restraint. Yet, if the **member** is slender enough, it may also be sensitive to global (member) buckling. Therefore, the maximum amplitude of the displacement at the ultimate limit state of the

member is in the span. If the local imperfection only affects the zone near the restraints, the critical section, leading to the failure of the member, may not be affected by the local imperfection. In order to avoid this shortcoming, Boissonnade proposes to include local imperfections independently from the local eigenmode by modifying the node coordinates of the FEM model (Boissonnade et al. 2012). This author introduced a sine shaped local imperfection with a wave length $l_{wave/2}$ equal to the depth of the considered plate ($b_f/2$ for the flanges and h_w for the web) with an amplitude of $l_{wave/2} / 400$. This approach has been investigated further on in (Nseir 2015). This last author investigated, amongst others, whether the wave length should be chosen independently for the flange and the web, or if the local imperfection of the web and the flange should possess the same wave length. The numerical simulations performed in (Nseir 2015) permitted the conclusion that the use of a common wavelength equal to the medium width of the flange and the web leads to reasonable results. As this study only concerned closed sections, these conclusions are validated in the next paragraph for open sections.

5.2.1.7.2 Sensitivity study

Hereafter four different configurations for the application of the local imperfection are studied:

- The half wave lengths of the sine shaped local imperfection are independent and equal to approximately the panel width “a” (height of the web or width of half a flange for I sections – noted as “Independent wave lengths” hereafter)
- The half wave lengths are equal to h_w for both, the web and the flanges (noted as “Wave length of web” hereafter)
- The half wave lengths are equal to $b_f/2$ for both, the web and the flanges (noted as “Wave length of flange” hereafter)
- The half wave lengths are equal to the average value of the independent wave lengths of the first configuration as represented by Eq. (5.11) (noted as “Medium wavelength” hereafter).

$$l_{wave / 2} = \left(\frac{b_f - t_w}{2} + h_w \right) / 2 \quad (5.11)$$

For all configurations the amplitude is chosen to be the panel width divided by 200 as proposed in Eurocode 3 Part 1-5.

The geometries of the eighteen (nine sections per load case) studied sections are given in Table 5-6. The dimensions of the different plates are chosen so that sections 1 to 3 are class 4 sections due to their web, sections 4 to 6 are class 4 sections due to their flanges and sections 6 to 9 are class 4 sections due to web and flanges (section classes according to Eurocode 3 Part 1-1 (CEN 2005a)). The results are given in Figure 5-54 and Figure 5-55.

Table 5-6: Geometry of studied sections

Section	Geometry for load case M_y		Geometry for load case N	
1	h_w (mm)	475	h_w (mm)	475
	t_w (mm)	3,83	t_w (mm)	11,3
	b_f (mm)	200	b_f (mm)	200
	t_f (mm)	12,5	t_f (mm)	12,5
2	h_w (mm)	475	h_w (mm)	475
	t_w (mm)	3,17	t_w (mm)	9,5
	b_f (mm)	200	b_f (mm)	200
	t_f (mm)	12,5	t_f (mm)	12,5
3	h_w (mm)	475	h_w (mm)	475
	t_w (mm)	2,38	t_w (mm)	6,33
	b_f (mm)	200	b_f (mm)	200
	t_f (mm)	12,5	t_f (mm)	12,5
4	h_w (mm)	473,0	h_w (mm)	486,8
	t_w (mm)	7,00	t_w (mm)	15
	b_f (mm)	200	b_f (mm)	200
	t_f (mm)	6,89	t_f (mm)	6,61
5	h_w (mm)	476,1	h_w (mm)	489,7
	t_w (mm)	7,00	t_w (mm)	15
	b_f (mm)	200	b_f (mm)	200
	t_f (mm)	5,36	t_f (mm)	5,14
6	h_w (mm)	479,1	h_w (mm)	492,6
	t_w (mm)	7,00	t_w (mm)	15
	b_f (mm)	200	b_f (mm)	200
	t_f (mm)	3,86	t_f (mm)	3,7
7	h_w (mm)	486,0	h_w (mm)	486,5
	t_w (mm)	3,83	t_w (mm)	11,3
	b_f (mm)	200	b_f (mm)	200
	t_f (mm)	7,00	t_f (mm)	6,74
8	h_w (mm)	489,1	h_w (mm)	489,4
	t_w (mm)	3,17	t_w (mm)	9,5
	b_f (mm)	200	b_f (mm)	200
	t_f (mm)	5,47	t_f (mm)	5,29
9	h_w (mm)	492,1	h_w (mm)	492,3
	t_w (mm)	2,38	t_w (mm)	6,33
	b_f (mm)	200	b_f (mm)	200
	t_f (mm)	3,95	t_f (mm)	3,87

The resistance predicted by the effective width method proposed in of Eurocode 3 Part 1-5 is chosen as reference results. Figure 5-54 and Figure 5-55 show that, depending on the chosen configuration for the local imperfection the ultimate resistance may vary of about 5%. Also, one notices that the Eurocode provisions are not always safe-sided compared to the numerical calculation. Especially, in case of compression, the Eurocode effective width method (EWM) is unsafe in the majority of cases and it is more unsafe for sections situated at the limit between class 3 and class 4 (sections 1, 4 and 7). However, it is recalled that the numerical calculation performed here cannot be used to conclude on the safe-sided nature of the EWM as the results of the

numerical calculation depend on the applied hypotheses. Only an extensive numerical study accompanied by physical tests would yield satisfying conclusions.

Also, concerning the choice of an equivalent geometric imperfection, it seems difficult to draw a general conclusion. However, it can be observed that using independent wavelengths and the wavelength of the web for both, the web and the flange, leads in the majority of the cases to the most favourable results. This tendency may be explained as follows: When using independent wavelengths the interaction between flange and web local buckling is disturbed by the difference of the wavelengths. In order to illustrate this statement Figure 5-56 shows the displacement (scaling factor 15) of section 8 subject to major-axis bending. It can be observed that the two wavelengths interference for the local buckling of the flange. This interference might be a reason for the generally higher ultimate resistance. When the wavelength of the web is used, it can be argued that the curvature of the plates is lower at ultimate limit state as in case of medium or flange (shorter) wavelengths. Therefore, the stresses in the plate due to plate flexure become higher and influence in a more important amount the ultimate resistance of the section.

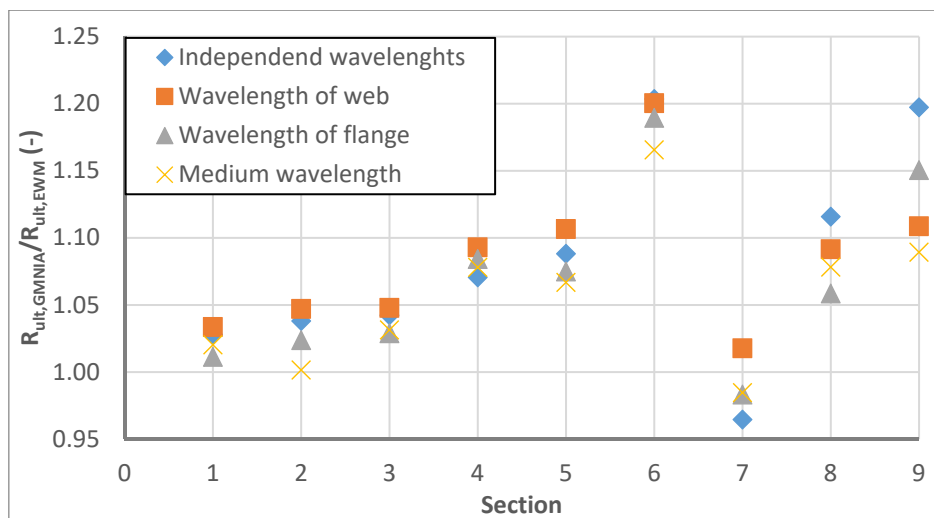


Figure 5-54: Comparison of ultimate resistance of members with local imperfection subject to major-axis bending

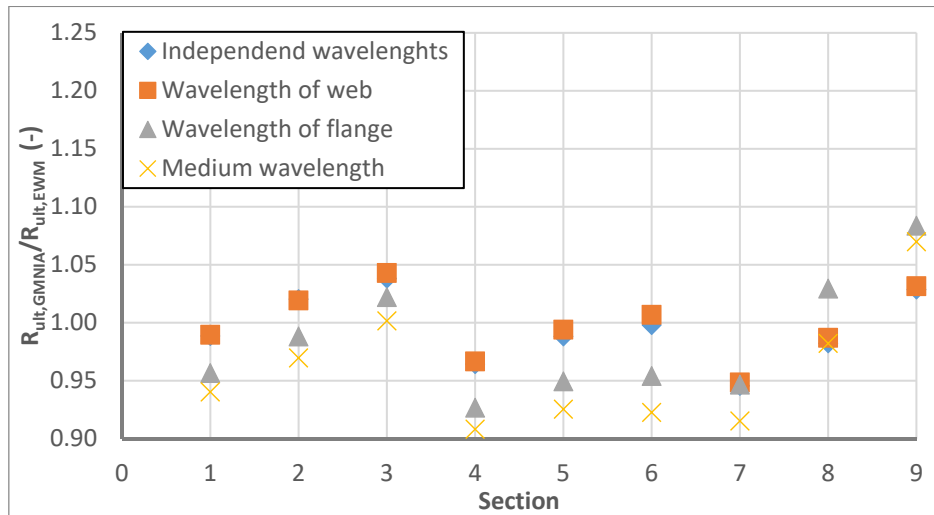


Figure 5-55: Comparison of ultimate resistance of members with local imperfection subject to compression

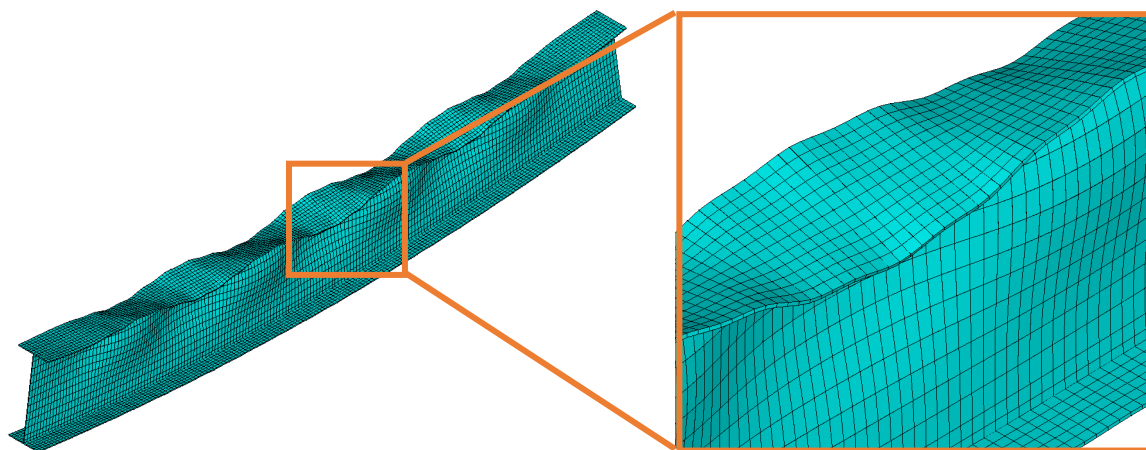


Figure 5-56: Deformed shape at ultimate limit state of section 8 subject to major-axis bending

On the basis of the simulations performed here and on the basis of the conclusions obtained by other authors (see especially (Nseir 2015)), it is proposed to use, for the flanges and the web, sine shaped local imperfections possessing the average wavelength defined by Eq. (5.11).

5.2.2 Influence of loading sequence

For combined axial force and bending, it has been shown that the loading sequence has only little influence on the ultimate member resistance (see for example (Taras 2012)). Contrariwise, no study exists that confirms this conclusion for applied torsion. It seems therefore necessary to study the influence of the loading sequence on the ultimate member resistance for the case of torsional loads.

Hereafter, a torsional moment is introduced by an eccentrically applied vertical load as shown in Figure 5-57. Consequently, the value of the applied torsional moment depends directly on the value of the maximum bending moment as shown in Eq. (5.12).

$$M_T = 2M_y \frac{e}{L} \quad (5.12)$$

Obviously, the value of the torsional moment is greater for shorter members and higher eccentricities, for given value of the major-axis bending moment.

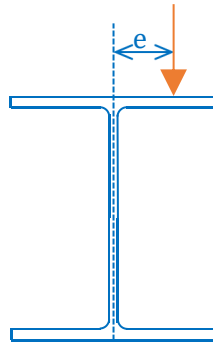


Figure 5-57: Introduction of torsion by an eccentrically applied vertical load

Hereafter, the example of a member of IPE 500 cross-section is studied. The load is supposed to be applied at one flanges tip. Consequently, the eccentricity e is equal to 100 mm. The length of the studied member is 2520 mm. In order to obtain the ultimate resistance of the member, GMNIA calculations are performed. In Figure 5-58, the resulting load-displacement curves correspond to:

1. Proportional loading: M_y and M_T are applied simultaneously up to failure. The resulting moments are noted as M_{y0} and M_{T0} .
2. Priority M_y : M_y is applied first up to a given value M_{y0} and then M_T is applied up to failure.
3. Priority M_T : M_T is applied first up to a given value M_{T0} and then M_y is applied up to failure.

The values of M_{T0} and M_{y0} correspond to the major-axis bending moment and the torsional moment obtained at failure for the case of proportional loading. For load cases 2 and 3, the torsional moment cannot be introduced by the vertical load. In these cases, the vertical load is applied without an eccentricity and an additional torsional moment is applied.

In Figure 5-58, it can be observed that the obtained ultimate resistances are very close for the three cases. In fact, the differences are less than 0,1%. The discontinuity in the curves associated with load cases “Priority M_y ” and “Priority M_T ” correspond to the application of the second load component. For the case “Priority M_y ”, it can be seen that the torsional twist increases very little up to the point of introduction of the torsional moment. The small torsional rotation developing before the introduction of the torsional moment is due to the applied geometrical member imperfection.

For the case of “Priority M_T ”, one notices that the torsional twist developing during the first step of loading (only M_T) is greater than the one obtained for proportional loading. As the torsional moment corresponding to the same load factor is greater in this case than in the case of

proportional loading this observation is not surprising. After introducing the major-axis bending moment, the torsional twist continues to increase, however not as rapidly as before. At this point the torsional twist increases only due to second order effects (the externally applied torsional moment is not increased anymore). These second order effects become important near the limit point and therefore lead to an acceleration of the increase rate of the torsional twist.

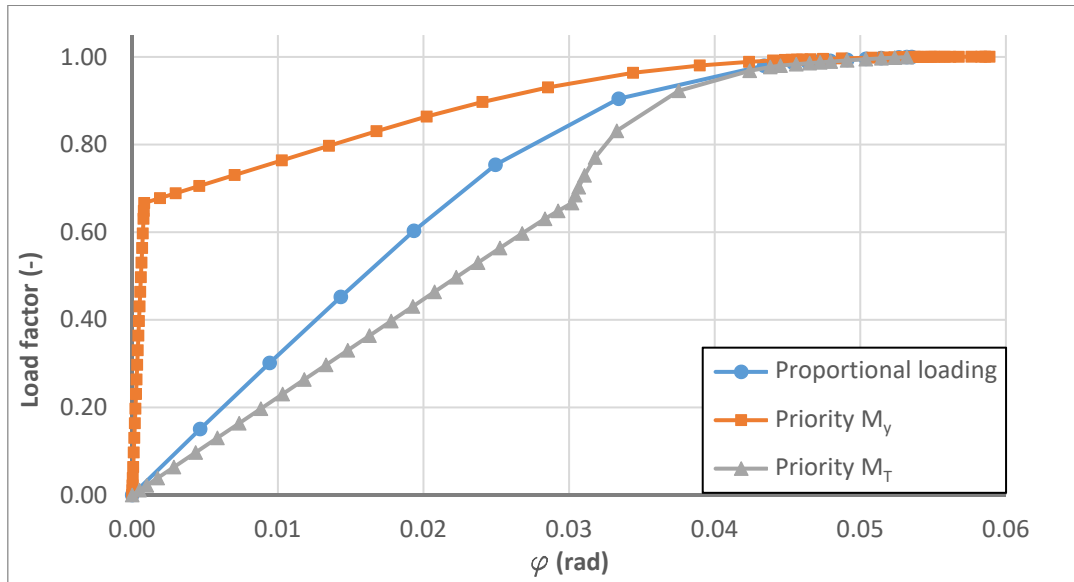


Figure 5-58: IPE 500 - L = 2520 mm - e = 100 mm

Figure 5-59, Figure 5-60 and Figure 5-61 compare the von Mises stress distribution at the ultimate limit state for the three cases. Obviously, there is no noticeable difference. It can therefore be concluded that the load sequence has only negligible influence on the behaviour of the member if torsion is introduced by an eccentrically applied vertical force.

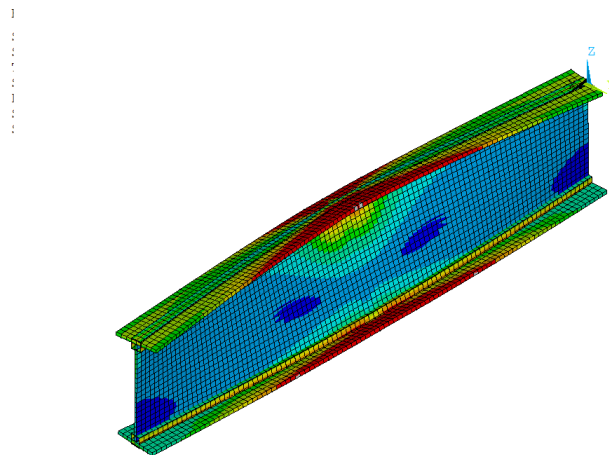


Figure 5-59: Von Mises stress distribution at ultimate limit state for proportional loading

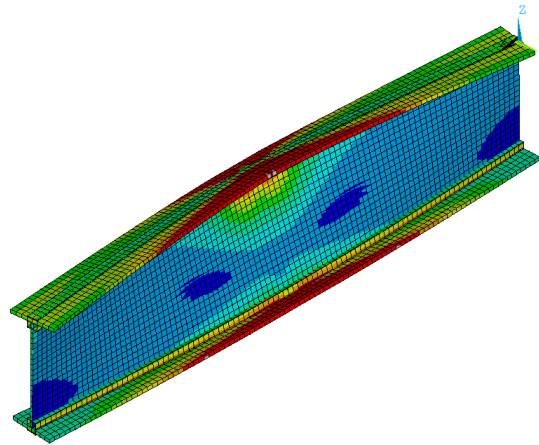


Figure 5-60: Von Mises stress distribution at ultimate limit state – priority M_t

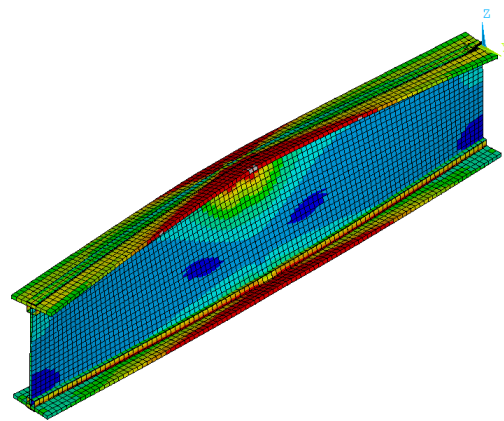


Figure 5-61: Von Mises stress distribution at ultimate limit state – priority M_y

5.2.3 Influence of local plate instability on ultimate member resistance

5.2.3.1 *General*

Depending on the cross-section and member slenderness, local buckling may more or less affect the ultimate resistance of the member. The numerical simulations performed in the framework of the parametric study accounts for the influence of local instability by introducing a plate imperfection in form of sine waves as discussed in paragraph 5.2.1.7. Nevertheless, it seems also interesting to determine the ultimate resistance of members made of slender cross-sections without the influence of local instability. Indeed, this helps to quantify the exact influence of the local instability on the overall member resistance. Additionally, as two simulations on the whole member are performed, the data basis of results is enlarged. Consequently, the developed resistance model can be validated on the basis of a greater number of tests. The first simulation is performed on the member subject to plate and member imperfection without any further preconisation. The second simulation is performed on a “locally restrained” model excluding local buckling by creating rigid cross-section along the member with beam elements. This principle is

shown in Figure 5-62. The beam elements (Beam4 of the ANSYS element library – see (ANSYS 2016)) are directly defined by their mechanical characteristics (A , I_y , I_z , I_t , I_w). The geometrical dimensions are only used for the visualisation and do not influence the calculation. The used beam elements are supposed to possess only bending stiffness corresponding to out-of-plane bending of the restrained plate. The other mechanical characteristics are negligible small. The necessary out-of-plane bending stiffness of these beam elements is determined in the next paragraph.

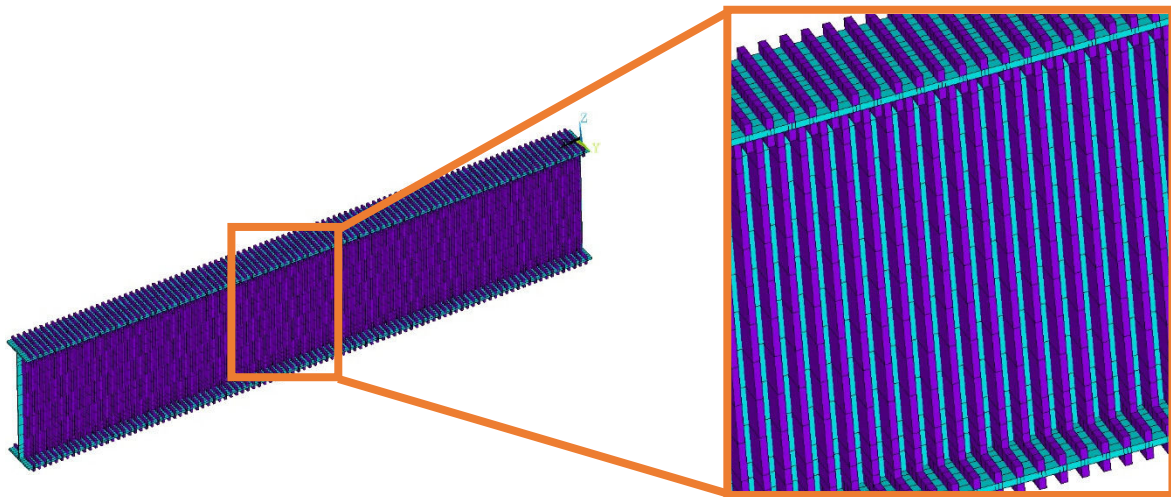


Figure 5-62: Locally restrained model of an I-shaped member

5.2.3.2 Calibration of rigid beam elements

Hereafter, the minimum stiffness of the beam elements is determined based on two examples. The two cross-sections given in Table 5-7 are studied. Section 1 is of class 4 due to the slenderness of the web and Section 2 is of class 4 due to the slenderness of its flanges (section classification according to Eurocode 3 Part 1-1).

Table 5-7: Studied cross-sections

Parameter	Section 1	Section 2
Height (mm)	500	290
Thickness of the web (mm)	3	10
Width of the flanges (mm)	300	300
Thickness of the flanges (mm)	20	7
Relative plate slenderness of the web (CEN 2007a)	2,758	0,365
Relative plate slenderness of the flange (CEN 2007a)	0,352	1,112
$A_{\text{eff}}/A_{\text{brut}}$ following (CEN 2007a)	0,873	0,852

The stiffness of the beam elements is determined based on the out-of-plane bending stiffness of the restrained plate (web or flange) supposed to be of class 1 in compression. The corresponding limit width to thickness ratios defined in (CEN 2005a) are recalled hereafter.

$$\text{Web in compression} \quad (h_w/t)_{\text{lim}} = 33\varepsilon$$

$$\text{Flange in compression} \quad (b/2t)_{\text{lim}} = 9\varepsilon$$

Depending on the previous values and the height of the web and the width of the flanges, fictitious web and flange thicknesses are determined. The class 1 out-of-plane bending stiffnesses D of the flanges and the web may consequently be determined with Eq. (5.13).

$$D = \frac{Et^3}{12(1-\nu^2)} \quad (5.13)$$

This value is then multiplied by the length l_{Shell} of the shell element (dimension along the x-axis of the member). Consequently, the reference stiffness of the beam elements is given by Eqs. (5.14) and (5.15).

$$\text{For the web} \quad EI_{\text{beam,web}} = \frac{Et_{\text{Cl,web}}^3}{12(1-\nu^2)} l_{\text{Shell}} \quad (5.14)$$

$$\text{For the flange} \quad EI_{\text{beam,flange}} = \frac{Et_{\text{Cl,flange}}^3}{12(1-\nu^2)} l_{\text{Shell}} \quad (5.15)$$

The minimum stiffness EI_{min} necessary to restrain the cross-section is determined as an integer multiple of these reference stiffnesses. The factor applied to the reference stiffness is noted as “a” in Figure 5-63 and Figure 5-64. These two figures represent the results obtained for the two cross-sections defined in Table 5-7 subject to an axial compression force, a plate imperfection as defined in paragraph 5.2.1.7 and a member imperfection affine to the first member eigenmode (flexural buckling about the minor-axis). Both members are fabricated from steel S235. The relative slenderness given along the abscissa of the following diagrams is calculated based on gross section properties.

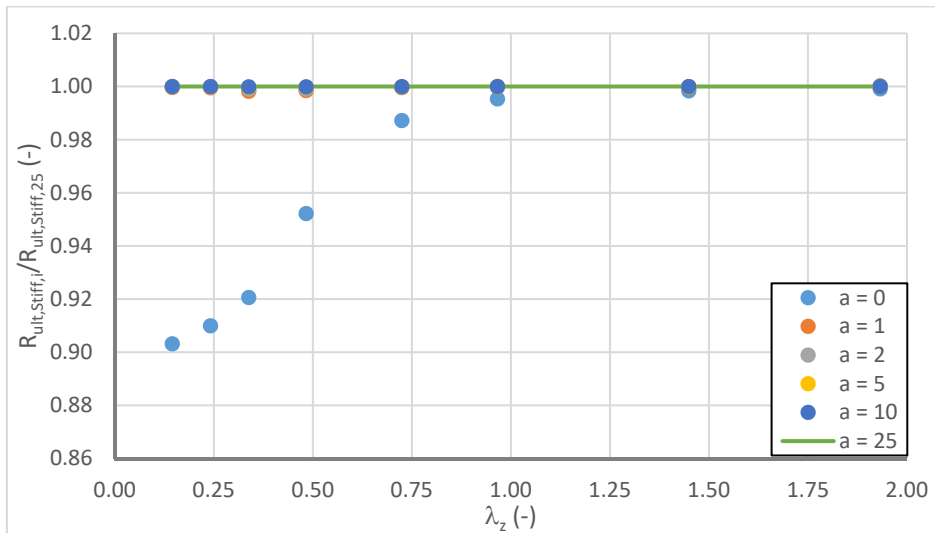


Figure 5-63: Ultimate member resistance obtained with restrained section 1

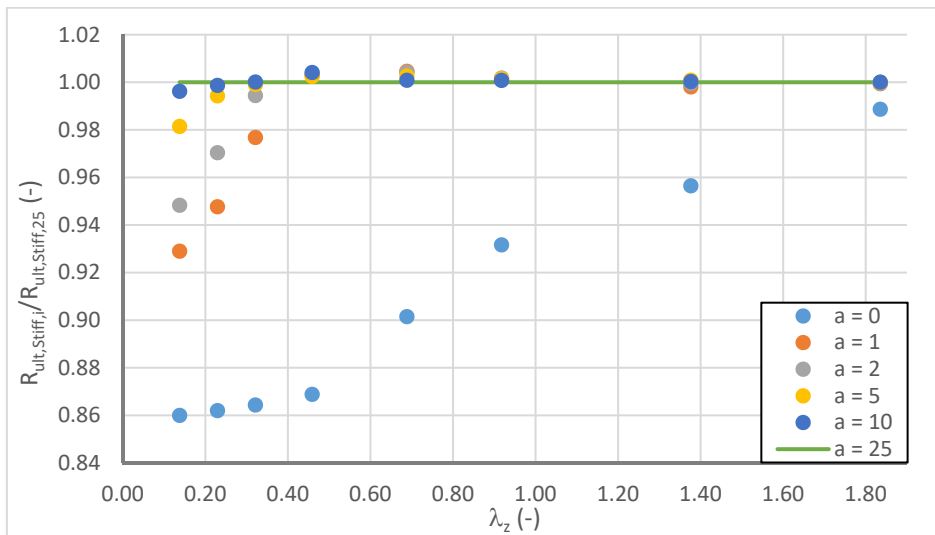


Figure 5-64: Ultimate member resistance obtained with restrained section 2

By observing the two previous figures, one may note that the numerically obtained strength reduction due to local buckling (ratio between ultimate load factor of the non-restrained model $R_{ult,Stiff,0}$ and the restrained model $R_{ult,Stiff,25}$) corresponds very well to the strength reduction predicted by Eurocode 3 Part 1-5 (CEN 2007a). Consequently, the numerical results seem consistent for both cases. One may observe that the minimum stiffness necessary to restrain the web of the cross-section is much less than the stiffness needed for the flanges. In fact, it seems sufficient to use the reference stiffness given in Eq. (5.14) to prevent local buckling of the web. On the contrary, it is necessary to apply at least ten times the reference stiffness of equation (5.15) to the beam elements to restrain the flanges. Also, the influence of local buckling on the member resistance is of importance over a greater range if the flanges are sensitive to local buckling. As the local buckling of the flanges not only affects the cross-section resistance but also the lateral stiffness against flexural buckling, this observation does not seem surprising.

In order to visualize the obtained results further on Figure 5-65 represents the load-displacement curves for the member made of Section 1. The lateral displacement is measured at the intersection between the upper flange and the web.

It can be seen that the curves corresponding to the stiffness multiplier “a” greater than zero are practically superposed, and this not only in the pre-buckling range but also in the post-buckling range. Contrariwise, the member, whose intermediate sections are not restrained, fails at a lower axial compression level due to local instability of its slender web.

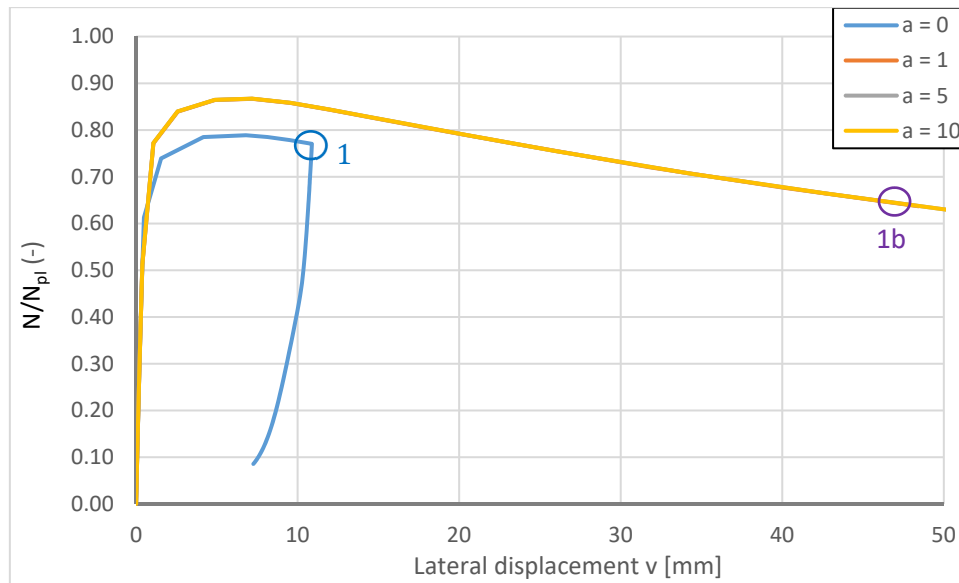


Figure 5-65: Load-displacement curve – Section 1 – L = 2500 mm

Last, Figure 5-66 and Figure 5-67 represent the von Mises stress distribution and deformed shape at the ultimate limit state (maximum load) and for the points noted as 1a and 1b in Figure 5-65 for the unrestrained model and the restrained one ($a = 10$). Both figures clearly confirm that the unrestrained model fails in predominant local buckling whereas the restrained model attains the elasto-plastic lateral buckling load. Especially, Figure 5-67 shows that even far behind the ultimate limit state local buckling does not occur for the restrained model.

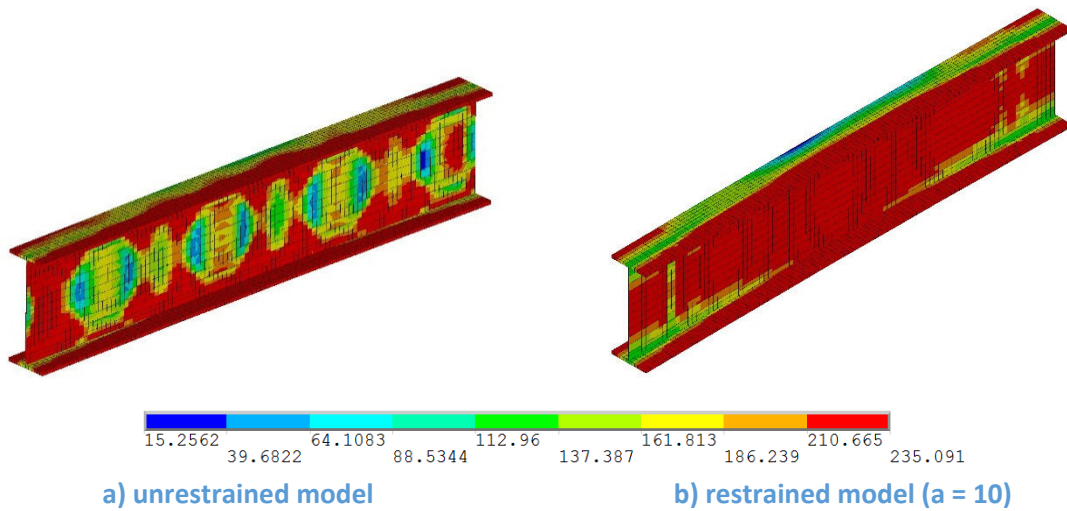


Figure 5-66: Von Mises stresses and deformed shape at ultimate limit state - Section 1 - L = 2500 mm

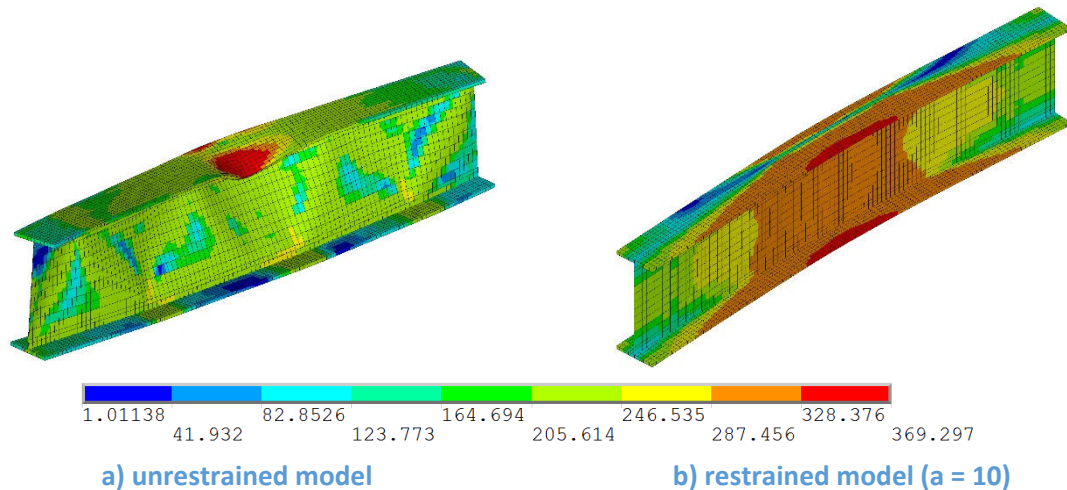


Figure 5-67: Von Mises stresses and deformed shape at point 1a and 1b - Section 1 - L = 2500 mm

The present paragraph has shown that rigid beam elements may be applied to prevent local buckling. The rigid beam elements are applied at each longitudinal element division of the member. It has been shown that the stiffness of the beam elements restraining the flanges of the cross-section should be at least ten times the reference stiffness given in Eq. (5.15). For the beam elements restraining the web, the stiffness may be less. However, in order to be homogenous a stiffness multiplier of 10 is applied for both cases as shown in Eqs. (5.16) and (5.17). It is recalled that the cross-section characteristics (A, I_z, I_t, I_w), other than the second moment of area associated with out-of-plane bending of the restrained plate, are set to 0.

For the web

$$EI_{beam, flange} = 10 \frac{Et_{Cl1, flange}^3}{12(1 - \nu^2)} I_{Shell} \quad (5.16)$$

$$\text{For the flange} \quad EI_{beam, flange} = 10 \frac{Et_{CI1, flange}^3}{12(1-\nu^2)} I_{Shell} \quad (5.17)$$

5.3 Design proposals for the resistance of members subject combined axial force and bi-axial bending without torsion

5.3.1 General

One of the main objectives of this thesis is to propose an extension of the Eurocode 3 interaction equations for members subject to combined axial force and bi-axial bending to the case of applied torsion. Therefore, only these provisions are detailed further more in the following paragraphs. Other international steel design standards contain different approaches to address the member resistance under complex load combinations. However, the vast majority proposes the design based on interaction equations as done in Eurocode 3. The design equations given in AISC 360-10 have been presented rapidly in Chapter 1. However, as it does not account for the cross-section dimensions, this approach may be rather safe-sided as has already shown in Chapter 4 for the resistance of the section.

In the following, the Eurocode 3 Part 1-1 interaction equations are detailed in their original field of application. Then two extensions proposed for mono-symmetric I sections and U sections published in references (Kaim 2004) and (Kalameya 2008) are presented.

5.3.2 Double symmetric members

The interaction equations proposed in paragraph 6.3.3 of Eurocode 3 Part 1-1 are recalled in Eqs. (5.18) and (5.19). In case of slender sections, the moments $\Delta M_{y,Ed}$ and $\Delta M_{z,Ed}$ should be included because they account for the possible shift between the gravity centre of the effective section and the gravity centre of the gross section. As stated in Chapter 1, the interaction factors k_{ij} can be obtained with Annex A or B of Eurocode 3 Part 1-1. In general, Annex A, developed on a theoretical basis (see reference (Boissonnade et al. 2002)) leads to more precise results compared to numerical simulations as shown in reference (ECCS 2006). Yet, due to its complexity, this approach is much less used in the design practice. Moreover, it can be noted that the difference between both methods is less than 10% in average.

$$\frac{N_{Ed}}{\chi_y \frac{N_{Rk}}{\gamma_{M1}}} + k_{yy} \frac{M_{y,Ed} + \Delta M_{y,Ed}}{\chi_{LT} \frac{M_{y,Rk}}{\gamma_{M1}}} + k_{yz} \frac{M_{z,Ed} + \Delta M_{z,Ed}}{\gamma_{M1}} \leq 1,0 \quad (5.18)$$

$$\frac{N_{Ed}}{\chi_z \frac{N_{Rk}}{\gamma_{M1}}} + k_{zy} \frac{M_{y,Ed} + \Delta M_{y,Ed}}{\chi_{LT} \frac{M_{y,Rk}}{\gamma_{M1}}} + k_{zz} \frac{M_{z,Ed} + \Delta M_{z,Ed}}{\gamma_{M1}} \leq 1,0 \quad (5.19)$$

The expressions of the interaction factors of Annex B of Eurocode 3 Part 1-1 (CEN 2005a) are recalled in Table 5-8.

Annex B has been criticised in the past for two main reasons. First, the empirical calibration of the interaction coefficients leads to rather pronounced discontinuity between the member resistance, determined with Eqs. (5.18) and (5.19) and the plastic cross-section resistance. Yet, it is obvious that with simplified interaction equations the complex plastic cross-section behaviour discussed in Chapter 4 cannot be represented precisely. It seems that only global methods as OIC can ensure a complete continuity.

A second point of criticism that is sometimes pointed out is linked to the expressions of the equivalent uniform moment factor $C_{m,i}$ recalled in Figure 5-68 (see reference (Villette 2004)). In fact, the equivalent uniform moment factor should account for the influence of the bending moment diagram on the second order effects resulting from the axial force. This is considered in Annex A of the current version of Eurocode 3 Part 1-1 (CEN 2005a) by introducing the term $N_{Ed}/N_{cr,i}$ as shown in Figure 5-69. Consequently, the second order effects are very well represented in the elastic case by the Annex A expressions. Yet, regarding Figure 5-68, one may easily remark that the axial force is not included into the expression of the Annex B $C_{m,i}$ factors. Nevertheless, one should keep in mind that the Annex B approach has been developed empirically based on physical tests and numerical simulations. Moreover, the expressions of interaction factors k_{ij} have been derived based on the assumption that the factors $C_{m,i}$ are correct and consequently the possible lack of precision of the equivalent uniform moment factors is compensated by the expression of the interaction factors. Also, these last contain the term $N_{Ed}/N_{cr,i}$ and consequently consider empirically its effect on the second order amplification of the bending moments.

Table 5-8: Annex B interaction factors for members sensitive to lateral-torsional buckling

Interaction factor	Class 1 and Class 2 sections	Class 3 and Class 4 sections
k_{yy}	$\bar{\lambda}_y < 1,0:$ $k_{yy} = C_{my} \left(1 + (\bar{\lambda}_y - 0,2) \frac{N_{Ed}}{\chi_y N_{Rk}} \right)$ $\bar{\lambda}_y \geq 1,0:$ $k_{yy} = C_{my} \left(1 + 0,8 \frac{N_{Ed}}{\chi_y N_{Rk}} \right)$	$\bar{\lambda}_y < 1,0:$ $k_{yy} = C_{my} \left(1 + 0,6 \bar{\lambda}_y \frac{N_{Ed}}{\chi_y N_{Rk}} \right)$ $\bar{\lambda}_y \geq 1,0:$ $k_{yy} = C_{my} \left(1 + 0,6 \frac{N_{Ed}}{\chi_y N_{Rk}} \right)$
k_{yz}	$k_{yz} = 0,6 k_{zz}$	$k_{yz} = k_{zz}$
k_{zy}	$\bar{\lambda}_z < 0,4:$ $k_{zy} = \bar{\lambda}_z + 0,6$ $0,4 \leq \bar{\lambda}_z < 1,0:$ $k_{zy} = 1 - \frac{0,1 \bar{\lambda}_z}{C_{mLT} - 0,25} \frac{N_{Ed}}{\chi_z N_{Rk}}$ $\bar{\lambda}_z \geq 1,0:$ $k_{zy} = 1 - \frac{0,1}{C_{mLT} - 0,25} \frac{N_{Ed}}{\chi_z N_{Rk}}$	$\bar{\lambda}_z < 1,0:$ $k_{zy} = 1 - \frac{0,05 \bar{\lambda}_z}{C_{mLT} - 0,25} \frac{N_{Ed}}{\chi_z N_{Rk}}$ $\bar{\lambda}_z \geq 1,0:$ $k_{zy} = 1 - \frac{0,05}{C_{mLT} - 0,25} \frac{N_{Ed}}{\chi_z N_{Rk}}$
k_{zz}	$\bar{\lambda}_z < 1,0:$ $k_{zz} = C_{mz} \left(1 + (2 \bar{\lambda}_z - 0,6) \frac{N_{Ed}}{\chi_z N_{Rk}} \right)$ $\bar{\lambda}_z \geq 1,0:$ $k_{zz} = C_{mz} \left(1 + 1,4 \frac{N_{Ed}}{\chi_z N_{Rk}} \right)$	$\bar{\lambda}_z < 1,0:$ $k_{zz} = C_{mz} \left(1 + 0,6 \bar{\lambda}_z \frac{N_{Ed}}{\chi_z N_{Rk}} \right)$ $\bar{\lambda}_z \geq 1,0:$ $k_{zz} = C_{mz} \left(1 + 0,6 \frac{N_{Ed}}{\chi_z N_{Rk}} \right)$

Moment diagram	range		C_{my} and C_{mz} and C_{mLT}		
			uniform loading	concentrated load	
	$-1 \leq \psi \leq 1$		$0,6 + 0,4\psi \geq 0,4$		
	$0 \leq \alpha_s \leq 1$	$-1 \leq \psi \leq 1$	$0,2 + 0,8\alpha_s \geq 0,4$	$0,2 + 0,8\alpha_s \geq 0,4$	
	$-1 \leq \alpha_s < 0$	$0 \leq \psi \leq 1$	$0,1 - 0,8\alpha_s \geq 0,4$	$-0,8\alpha_s \geq 0,4$	
	$\alpha_h = M_h/M_s$	$-1 \leq \psi < 0$	$0,1(1-\psi) - 0,8\alpha_s \geq 0,4$	$0,2(-\psi) - 0,8\alpha_s \geq 0,4$	
		$0 \leq \alpha_h \leq 1$	$-1 \leq \psi \leq 1$	$0,95 + 0,05\alpha_h$	$0,90 + 0,10\alpha_h$
		$0 \leq \psi \leq 1$	$0,95 + 0,05\alpha_h$	$0,90 + 0,10\alpha_h$	
	$-1 \leq \alpha_h < 0$	$-1 \leq \psi < 0$	$0,95 + 0,05\alpha_h(1+2\psi)$	$0,90 - 0,10\alpha_h(1+2\psi)$	
For members with sway buckling mode the equivalent uniform moment factor should be taken $C_{my} = 0,9$ or $C_{mz} = 0,9$ respectively.					
C_{my} , C_{mz} and C_{mLT} should be obtained according to the bending moment diagram between the relevant braced points as follows:					
moment factor	bending axis	points braced in direction			
C_{my}	y-y	z-z			
C_{mz}	z-z	y-y			
C_{mLT}	y-y	y-y			

Figure 5-68: Annex B equivalent uniform moment factors

Moment diagram	$C_{mi,0}$
	$C_{mi,0} = 0,79 + 0,21\psi_i + 0,36(\psi_i - 0,33) \frac{N_{Ed}}{N_{cr,i}}$
	$C_{mi,0} = 1 + \left(\frac{\pi^2 EI_i \delta_x }{L^2 M_{i,Ed}(x) } - 1 \right) \frac{N_{Ed}}{N_{cr,i}}$ $M_{i,Ed}(x)$ is the maximum moment $M_{y,Ed}$ or $M_{z,Ed}$ $ \delta_x $ is the maximum member displacement along the member
	$C_{mi,0} = 1 - 0,18 \frac{N_{Ed}}{N_{cr,i}}$
	$C_{mi,0} = 1 + 0,03 \frac{N_{Ed}}{N_{cr,i}}$

Figure 5-69: Annex A equivalent uniform moment factors

Last, it has to be underlined that for the design practice, it is absolutely of no interest how a resistance model has been developed (empirically or analytically). Conversely, it is of importance that the resistance model is generally safe but not non-economic. Therefore, both approaches, analytical and empirical based design models, are valid in general provided that they result in an adequate level of precision.

In the next paragraph, extensions to mono-symmetric I and U sections proposed in references (Kaim 2004) and (Kalameya 2008) are presented. Both have been developed mostly empirically on the basis of numerical simulations.

5.3.3 Extension of the Eurocode 3 Part 1-1 interaction equations to mono-symmetric I and U sections

First, the extension to U-shaped members is presented. In reference (Kalameya 2008) the following interaction equation is proposed:

$$\frac{N_{Ed}}{\text{Min}(\chi_z, \chi_{TF}) \frac{N_{Rk}}{\gamma_{M1}}} + k_{zy} \frac{M_{y,Ed} + \Delta M_{y,Ed}}{\chi_{LT} \frac{M_{y,Rk}}{\gamma_{M1}}} + k_{zz} \frac{M_{z,Ed} + \Delta M_{z,Ed}}{\frac{M_{z,Rk}}{\gamma_{M1}}} \leq 1,0 \quad (5.20)$$

The U sections considered in the present thesis are always compact. Consequently, the terms $\Delta M_{y,Ed}$ and $\Delta M_{z,Ed}$ vanish. It should be noted that only the equation considering the out-of-plane second order effects is proposed by Kalameya. Following his research, interaction between in-plane buckling and lateral-torsional buckling does not occur for U-shaped members. This, however, is only true if one considers members that are not restrained laterally along the span. If the member possesses lateral restraints the relative slenderness associated with buckling about the major-axis may become relevant and in this case the member may fail by interaction between in-plane buckling and lateral-torsional buckling. Therefore, the proposal of Kalameya should only be applied for laterally unrestrained members.

Kalameya proposes and validates the use of the interaction factors used in Annex B. Only, the specific expression for the factor k_{zy} for members of class 1 and class 2 sections with a relative slenderness λ_z lower than 0,4 is suppressed. Also, he recommends to limit the minor-axis bending resistance to $1,25M_{el,Rk}$ so as to avoid to favourable results compared to the numerical simulations.

Using the same interaction factors for I and U sections is clearly advantageous and leads to simple and uniform design equations. Yet, it should be noted that it is not completely mechanically consistent as the cross-section interaction is obviously different and, in some cases, more complex than for I sections (see Chapter 4). However, as stated previously, for a practical design approach a certain lack of mechanical consistency may be accepted. The proposal of Kalameya is studied further on in paragraph 5.6.4.4.

Next, the proposed extension to mono-symmetric I sections is presented. In references (Kaim 2008) and (Greiner et al. 2011) the following interaction equations are given:

$$\frac{N_{Ed}}{\chi_y \frac{N_{Rk}}{\gamma_{M1}}} + k_{yy} \frac{M_{y,Ed}}{\chi_{LT,cf} \frac{M_{y,Rk,cf}}{\gamma_{M1}}} \leq 1,0 \quad (5.21)$$

$$\frac{N_{Ed}}{\chi_{TF} \frac{N_{Rk}}{\gamma_{M1}}} + k_{zy} \frac{M_{y,Ed}}{\chi_{LT,cf} \frac{M_{y,Rk,sf}}{\gamma_{M1}}} \leq 1,0 \quad (5.22)$$

$$\frac{N_{Ed}}{\chi_z \frac{N_{Rk}}{\gamma_{M1}}} - k_{zy} \frac{M_{y,Ed}}{\chi_{LT,cf} \frac{M_{y,Rk,lf}}{\gamma_{M1}}} \leq 1,0 \quad (5.23)$$

where:

$\chi_{LT,cf}$: is the reduction factor for lateral-torsional buckling calculated with reference to the compressed flange (the flange that is compressed by the major-axis bending moment);

$M_{y,Rk,cf}$: is the bending moment resistance associated with the compression flange;

$M_{y,Rk,lf}$: is the bending moment resistance associated with the larger flange;

$M_{y,Rk,sf}$: is the bending moment resistance associated with the smaller flange.

Eq. (5.21) represents the interaction between in-plane buckling and lateral-torsional buckling. In this formula it is not distinguished between the sign of the bending moment. The absolute value of the major-axis bending moment should be used. However, the reduction factor χ_{LT} is to be calculated with reference to the compression flange (based on a relative slenderness calculated with $M_{y,Rk,cf}$).

For the out-of-plane instability, two interaction formulae are proposed in order to account for the pronounced difference between the case of the smaller flange in compression and the larger flange in compression. It should be noted that the signed values of the bending moment has to be introduced into Eqs. (5.22) and (5.23). Following reference (Kaim 2004) **a positive bending moment compresses the smaller flange** and **a negative bending moment compresses the larger flange**. In case of elastic design the bending moment resistance used in Eqs. (5.21) to (5.23) should be calculated with reference to the compression flange.

If the larger flange is in compression the effect tensions flange yielding has to be considered for sections of class 3 and class 4. In reference (Kaim 2004), the application of the conditions given in Eq. (5.24) is proposed and validated.

$$\frac{N_{Ed}}{\chi_y \frac{N_{Rk}}{\gamma_{M1}}} \left(\frac{1}{\chi_y} - 2 + \bar{\lambda}_y \right) + \frac{M_{y,Ed}}{\chi_{LT,cf} \frac{M_{y,Rk,tf}}{\gamma_{M1}}} \leq 1,0 \quad \text{for } \bar{\lambda}_y \leq 1,0$$

$$\frac{N_{Ed}}{\chi_y \frac{N_{Rk}}{\gamma_{M1}}} \left(\frac{1}{\chi_y} - 1,5 + 0,5 \bar{\lambda}_y \right) + \frac{M_{y,Ed}}{\chi_{LT,cf} \frac{M_{y,Rk,tf}}{\gamma_{M1}}} \leq 1,0 \quad \text{for } \bar{\lambda}_y > 1,0$$

The interaction factors used in Eqs. (5.21) to (5.23) are given in Table 5-9. It may be noted that for the factor k_{zy} the expressions used for double-symmetric sections are again utilized. Conversely, specific expressions are given for the factor k_{yy} .

Table 5-9: Interaction factors for mono-symmetric I sections

Interaction factor	Class 1 and Class 2	Class 3 and Class 4
k_{yy}	$\bar{\lambda}_y < 1,0:$ $k_{yy} = C_{my} \left(1 + 2(\bar{\lambda}_y - 0,2) \frac{N_{Ed}}{\chi_y N_{Rk}} \right)$ $\bar{\lambda}_y \geq 1,0:$ $k_{yy} = C_{my} \left(1 + 1,6 \frac{N_{Ed}}{\chi_y N_{Rk}} \right)$	$\bar{\lambda}_y < 1,0:$ $k_{yy} = C_{my} \left(1 + \bar{\lambda}_y \frac{N_{Ed}}{\chi_y N_{Rk}} \right)$ $\bar{\lambda}_y \geq 1,0:$ $k_{yy} = C_{my} \left(1 + \frac{N_{Ed}}{\chi_y N_{Rk}} \right)$
k_{zy}	$\bar{\lambda}_z < 1,0:$ $k_{zy} = 1 - \frac{0,1\bar{\lambda}_z}{C_{mLT} - 0,25} \frac{N_{Ed}}{\chi_z N_{Rk}}$ $\bar{\lambda}_z \geq 1,0:$ $k_{zy} = 1 - \frac{0,1}{C_{mLT} - 0,25} \frac{N_{Ed}}{\chi_z N_{Rk}}$	$\bar{\lambda}_z < 1,0:$ $k_{zy} = 1 - \frac{0,05\bar{\lambda}_z}{C_{mLT} - 0,25} \frac{N_{Ed}}{\chi_z N_{Rk}}$ $\bar{\lambda}_z \geq 1,0:$ $k_{zy} = 1 - \frac{0,05}{C_{mLT} - 0,25} \frac{N_{Ed}}{\chi_z N_{Rk}}$

As for U section relatively simple design equations are proposed. However, the case of an applied minor-axis bending moment has not been addressed. This certainly is a limitation especially for crane girders that are often mono-symmetric and subject to a minor-axis bending moment that results from the operation of the crane.

Here before, the extensions of the Eurocode 3 interaction equations for the resistance of U-shaped members and members of mono-symmetric I section have been presented. Rather simple design expressions based on Annex A are proposed in references (Kalameya 2008), (Kaim 2004) and (Greiner et al. 2011). Nevertheless, the extensions contain still some limitations. In particular, the proposal of Kalameya can only be applied to U sections without lateral restraints as buckling about the major-axis is not accounted for. The proposal made for mono-symmetric I sections is limited to the case of combined major-axis bending and axial force. Consequently, it cannot be applied to crane girders. Yet, these members are always subject to additional torsion as the minor-axis bending moment is introduced through point load applied with an eccentricity to the shear centre. In paragraph 5.6, the proposals are evaluated in their field of application and possible extensions to the case of applied torsion are presented. Additionally, it is investigated if the proposal for mono-symmetric I sections can be easily extended to applied minor-axis bending and if the proposal for U sections may be safely adapted to the case of laterally restrained members for which the interaction between flexural buckling about the major-axis and lateral-torsional buckling may become relevant.

5.4 Review of design proposals for members with open section subject to combined axial compression, bending and torsion

5.4.1 General

Hereafter, the main design models proposed in the past for the resistance of members subject to combined axial force, (bi-axial) bending and torsion are discussed. Table 5-10 recalls the field of application as well as the limitations of the design approaches proposed in the past. It appears, that none of these design models has a field of application covering I and U sections subject to all internal forces and moments. Nevertheless, it seems interesting to study these proposals in detail in order to verify their consistency in their specific field of application and to judge whether they may be extended to be more general cases.

Table 5-10: Summary of design approaches for the resistance of members subject to torsion

Proposal (Reference)	Field of application		Limitation
	Form of the section	Load case	
BSI and Nethercott (Nethercott et al. 1989)	I and U sections	M_y, M_z, M_T	No axial force N
Aachen I (FOSTA 2004)	I sections	N, M_y, M_z, M_T	May not be applied to U sections
Aachen II (Stangenberg 2007)	I and U sections	N (for I sections), M_y, M_z, M_T	No axial force in case of mono-symmetric sections
Aachen III (Naumes 2009)	I	N, M_y, M_z, M_T	May not be applied to U sections
Berlin* (Glitsch 2008)	I sections	M_y, M_z, M_T	No axial force May not be applied to U sections
Eindhoven (de Louw 2007)	U sections	M_y, M_T – loads applied in the web plane	No axial force and minor axis bending May not be applied to I sections

*included in Annex E of EN 1993-6 (CEN 2007b)

In order to unify the presentation of the design approaches Eurocode 3 notations are used as much as possible.

5.4.2 Great Britain: BS 5950-1:2000 and SCI Publication 057

In BS 5950-1:2000 (BSI 2000) no specific information is given on the design of members subject to torsion. However, the former national British standard refers to SCI Publication 057 (Nethercot et al. 1989) for the design criteria covering members in this situation. According to this publication, the two following design criteria (Eqs. (5.25) and (5.27)) should be satisfied at the ultimate limit state for I- and U-shaped members.

$$\frac{C_{mLT,BS} M_{y,Ed}}{\chi_{LT} \frac{M_{y,Rk}}{\gamma_M}} + \frac{C_{mz,BS} M_{z,Ed}}{\frac{M_{z,el}}{\gamma_M}} + \frac{(\sigma_{z,T,Ed} + \sigma_{w,Ed})}{\frac{f_y}{\gamma_M}} k_T \leq 1,0 \quad (5.25)$$

$$k_T = 1 + 0,5 \frac{C_{mLT,BS} M_{y,Ed}}{\chi_{LT} \frac{M_{y,Rk}}{\gamma_M}} \quad (5.26)$$

$$\sigma_{y,Ed} + \sigma_{z,Ed} + \sigma_{z,T,Ed} + \sigma_{w,Ed} \leq \frac{f_y}{\gamma_M} \quad (5.27)$$

where:

$C_{mLT,BS}$: is the equivalent uniform moment factor for lateral-torsional buckling defined in (BSI 2000);

$C_{mz,BS}$: is the equivalent uniform moment factor for minor-axis bending defined in (BSI 2000);

$\sigma_{z,T,Ed}$: is the design axial stress due to “indirect” minor-axis bending resulting from torsional rotations (see Eq. (5.28));

$\sigma_{w,Ed}$: is the design axial stress due to the bi-moment.

The equivalent uniform moment factors $C_{mLT,BS}$ and $C_{mz,BS}$ consider the influence of the distribution of the bending moment on the ultimate resistance of the member. Since $C_{mLT,BS}$ also applies in case of major-axis bending only, the proposed approach ensures continuity (see (BSI 2000)). Nonetheless, in this case, the resistance is limited to the theoretical resistance of the most loaded section $M_{y,Rk}$.

It is to be noted that the factors $C_{mLT,BS}$ and $C_{mz,BS}$ should not be confounded with the equivalent uniform bending moment factors used in Eurocode 3 Part 1-1 that account for the influence of the form of the bending moment diagram on the second order effects created by an axial compression force.

The first criterion represents the member resistance including the second order effects and instability. The second criterion is used to verify that the cumulated stresses resulting from the different internal forces and moments do not exceed the yield stress f_y . For this second design check, the second order effects are only included partially. Indeed, second order effects are not considered for the stresses resulting from the minor-axis bending moment and the bi-moment. On the contrary, the term $\sigma_{z,T,Ed}$ represents the stresses resulting from the major-axis bending moment acting on the twisted member. Due to the twist the principal axis of the rotated member are not identical anymore to the axis of the loads. The resulting stresses $\sigma_{z,T,Ed}$ may be determined with Eq. (5.28). Eq. (5.29) gives the expression proposed in reference (Nethercott et al. 1989) for the determination of the stresses resulting from the bi-moment.

$$\sigma_{z,T,Ed} = \frac{\varphi M_{y,Ed}}{W_{el,z}} \quad (5.28)$$

$$\sigma_{w,Ed} = E\omega\varphi_{,xx} = \frac{B_{Ed}}{I_w}\omega \quad (5.29)$$

As the second interaction criterion limits the design to the elastic resistance, this approach may obviously be rather conservative, especially for short members and compact sections.

In reference (Nethercott et al. 1989), the expression of the interaction factor k_T is justified with reference to the one used in the interaction formula between axial force and major-axis bending provided in (BSI 2000) and represented by Eqs. (5.30) and (5.31), for members non-susceptible of lateral-torsional buckling.

$$\frac{N_{y,Ed}}{\chi \frac{N_{Rk}}{\gamma_M}} + \frac{M_{y,Ed}}{\frac{M_{y,Rk}}{\gamma_M}} k_{yy} \leq 1,0 \quad (5.30)$$

$$k_{yy} = C_{my} \left(1 + 0,5 \frac{N_{Ed}}{\chi \frac{N_{Rk}}{\gamma_M}} \right) \quad (5.31)$$

Also, the similitude to the corresponding interaction factor given in Annex B of Eurocode 3 Part 1-1 cannot be overseen:

$$k_{yy} = C_{my} \left(1 + (\bar{\lambda}_y - 0,2) \frac{N_{Ed}}{\chi \frac{N_{Rk}}{\gamma_M}} \right) \leq C_{my} \left(1 + 0,8 \frac{N_{Ed}}{\chi \frac{N_{Rk}}{\gamma_M}} \right) \quad (5.32)$$

It is recalled that the interaction factor considers the influence of second order effects and the influence of the cross-section interaction. Consequently, using the same factor for the interaction between axial force and major-axis bending and for the interaction between major-axis bending and the bi-moment, by simply replacing the term N_{Ed}/N_{Rk} by $M_{y,Ed}/M_{y,Rk}$, does not seem

mechanically consistent a priori. Nevertheless, for a simple and practical design approach some mechanical inconsistencies could possibly be accepted if they contribute to the simplification of the design approach without losing the safe-sided character.

In paragraph 5.5.7 addressing the elastic second order equilibrium of the member, the case of a double symmetric I section subject to bi-axial bending and torsion is treated and the elastic interaction formula given in Eq. (5.33) is obtained (see (Stangenberg 2007) and paragraph 5.5.7 for more details). As the former British standard limits the design to the elastic resistance it seems completely consistent to compare the interaction criterion represented by Eq. (5.25) to the analytically derived condition given in Eq. (5.33). Yet, it is to be noted that the following interaction criterion does not take into account the form of the bending moment diagram considered through the factors $C_{mLT,BS}$ and $C_{mz,BS}$ in Eq. (5.25).

$$\begin{aligned} & \frac{M_y}{M_{y,Rd}} + \frac{M_y}{M_{z,Rd}} \frac{1}{1 - \frac{M_y}{M_{y,cr}}} \left(1 + \frac{N_{cr,z}}{M_{y,cr}} \frac{M_{z,Rd}}{B_{Rd}} \frac{I_w}{I_z} \right) \varphi_0 + \frac{M_z^I}{M_{z,Rd}} \frac{1}{1 - \frac{M_y^2}{M_{y,cr}^2}} \\ & + \frac{M_y \varphi^I}{M_{z,Rd}} \frac{1}{1 - \frac{M_y^2}{M_{y,cr}^2}} + \frac{B^I}{B_{Rd}} \frac{1}{1 - \frac{M_y^2}{M_{y,cr}^2}} + \frac{M_y \frac{v^I}{\delta_T}}{B_{Rd}} \frac{1}{1 - \frac{M_y^2}{M_{y,cr}^2}} = 1 \end{aligned} \quad (5.33)$$

In order to eliminate the equivalent geometric imperfection φ_0 , it is generally replaced by (see for example (Greiner 2001) and (Stangenberg 2007)):

$$\frac{M_{z,Rd}}{M_{y,Rd}} \left(1 + \frac{N_{cr,z}}{M_{y,cr}} \frac{M_{z,Rd}}{B_{Rd}} \frac{I_w}{I_z} \right) \varphi_0 = \eta = \frac{1}{\chi_{LT}} - 1 - \bar{\lambda}^2 + \chi_{LT} \bar{\lambda}^2 \quad (5.34)$$

After some reorganisation, one obtains an analytical interaction formula of equivalent format as the one given in Eq. (5.25).

$$\frac{M_y}{\chi M_{y,Rd}} + \left(\frac{M_z^I + M_y \varphi^I}{M_{z,Rd}} + \frac{B^I + M_y \frac{v^I}{\delta_T}}{B_{Rd}} \right) k_T = 1 \quad (5.35)$$

$$k_T = \frac{1}{\left(1 + \frac{M_y}{M_{y,Rd}} \bar{\lambda}^2 \right) \left(1 - \frac{M_y}{M_{y,Rd}} \chi \bar{\lambda}^2 \right)} \quad (5.36)$$

Some differences between the two formulae might be observed. The analytic interaction formula shows that the first order minor-axis bending moment should also be multiplied by the interaction factor taking into account second order effects (here the term multiplied is used rather than “amplified” as k_T may be less than 1,0 as shown later). Also, the supplementary bi-moment

resulting from first order lateral displacement (M_{yV}/δ_T) is not taken into account by the British approach. Finally, the proposed interaction factor does not correspond exactly to the one derived analytically. The two interaction factors are compared in Figure 5-70 supposing that the applied bending moment just reaches the lateral-torsional buckling resistance $\chi M_{y,Rd}$ and that the member is subject to constant bending. Obviously, the interaction factor proposed in reference (Nethercott et al. 1989) is constant for a given ratio between the applied bending moment and the lateral-torsional buckling resistance moment. The maximum value is 1,5. On the contrary, the analytical interaction factor varies depending on the relative slenderness and can even reach values lower than 1,0. As explained in (Greiner 2001) for the case of interaction between axial force and major-axis bending, the reason for this surprising behaviour is purely mathematic. In fact, by replacing the equivalent imperfection η with Eq. (5.34) the part of the major-axis bending moment is overestimated (as the factor χ partially considers second order effects already). In order to keep the equivalence, the interaction factor has to compensate this effect. Consequently, it is not surprising that the interaction factor proposed in (Nethercott et al. 1988) is highly conservative with regard to the analytical one.

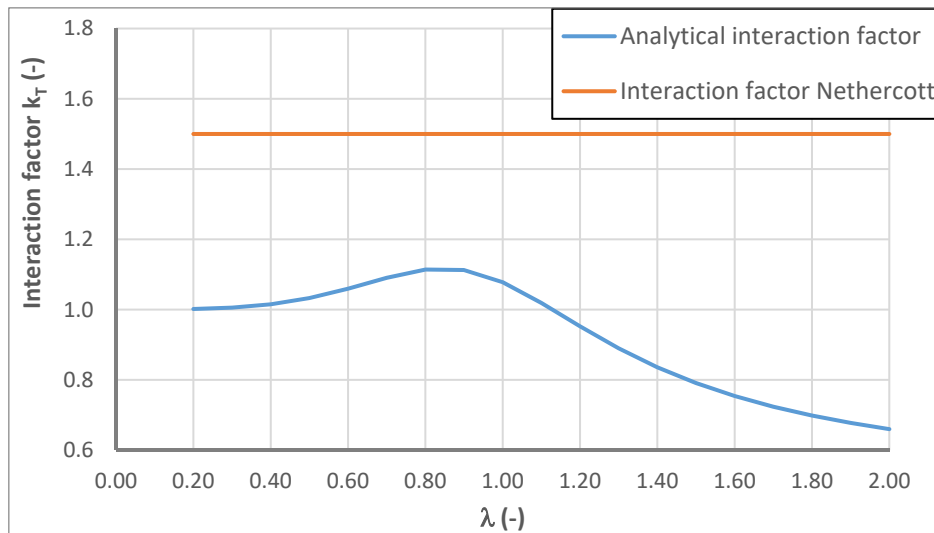


Figure 5-70: Comparison of interaction factors

It has been shown that the proposal of Nethercott may be conservative for I sections compared to the analytical solution.

5.4.3 Design rules proposed at RWTH Aachen

5.4.3.1 General

At the German university RWTH Aachen three distinct design proposals have been published by Sedlacek in 2004 (FOSTA 2004), Stangenberg in 2007 (Stangenberg 2007) and Naumes in 2009 (Naumes 2009). Principally, they are all based on the same mechanical background, i.e. interaction between second order internal forces. For an I section, they can be determined analytically for simple load cases (see paragraph 5.5.7). For constant bending moments they are given in Eqs. (5.37) to (5.39). The influence of member imperfection is not accounted for at this stage.

$$M_{y,Ed}^{II} = \frac{M_{y,Ed}^I}{1 - \frac{N_{Ed}}{N_{cr,y}}} \quad (5.37)$$

$$M_{z,Ed}^{II} = \left(M_{z,Ed}^I - M_{y,Ed}^I \varphi \frac{1}{1 - \frac{N_{Ed}}{N_{cr,T}}} \right) \frac{1}{1 - \frac{N_{Ed}}{N_{cr,z}}} \frac{1}{1 - \frac{M_{y,Ed}^2}{M_{y,cr,N}^2}} \quad (5.38)$$

$$B_{Ed}^{II} = \left(B_{Ed}^I - \frac{M_{y,Ed}^I v}{\delta_T} \frac{1}{1 - \frac{N_{Ed}}{N_{cr,T}}} \right) \frac{1}{1 - \frac{N_{Ed}}{N_{cr,T}}} \frac{1}{1 - \frac{M_{y,Ed}^2}{M_{y,cr,N}^2}} \quad (5.39)$$

Based on the second order moments, the design approaches presented at RWTH Aachen are developed and discussed hereafter.

5.4.3.2 Proposal RWTH Aachen I

The first proposal was published in 2004 in (FOSTA 2004). The second order internal forces and moments are introduced in the quadratic interaction between major-axis bending and combined minor-axis bending and the bi-moment given in Eq. (5.40). Figure 5-72 compares different forms of interaction equations and shows that the quadratic interaction can be very conservative if no cut-off limit is introduced. It is recalled that the major-axis bending does not interact with the bi-moment and the minor-axis bending moment if its value is less than the major-axis bending moment resistance of the web (see Chapter 4).

$$\left(\frac{M_{y,Ed}^{II}}{M_{y,Rd}^{II}} \right)^2 + \frac{M_{z,Ed}^{II}}{M_{z,Rd}} + \frac{B_{Ed}^{II}}{B_{Rd}} \leq 1 \quad (5.40)$$

Introducing the second order moments and the imperfections, represented by the factor η (see Eq. (5.34), into the interaction equation leads to:

$$\left(\frac{M_{y,Ed}^I}{M_{y,Rd}}\right)^2 + \frac{1}{M_{z,Rd}} \left(M_{z,Ed}^I + M_{y,Ed}^I \varphi\right) \frac{1}{1 - \frac{M_{y,Ed}^2}{M_{y,cr}^2}} + \frac{1}{B_{Rd}} \left(B_{Ed}^I + \frac{M_{y,Ed}^I \nu}{\delta_T}\right) \frac{1}{1 - \frac{M_{y,Ed}^2}{M_{y,cr}^2}} \leq 1$$

$$+ \frac{M_{y,Ed}^I}{M_{y,Rd}} \eta \frac{1}{1 - \frac{M_{y,Ed}}{M_{y,cr}}} \leq 1 \quad (5.41)$$

In order to obtain a design criterion, the equivalent imperfection η is again replaced by the expression given in Eq. (5.42).

$$\eta = \frac{1}{\chi_{LT}} - 1 - \bar{\lambda}_{LT}^2 + \chi_{LT} \bar{\lambda}_{LT}^2 \quad (5.42)$$

Introducing Eq. (5.42) into Eq. (5.41) leads to the following interaction criterion.

$$\frac{M_{y,Ed}^I}{\chi_{LT} M_{y,Rd}} + \frac{1}{M_{z,Rd}} \left(M_{z,Ed}^I + M_{y,Ed}^I \varphi\right) \frac{1}{1 + \frac{M_{y,Ed}}{M_{y,cr}}} + \frac{1}{B_{Rd}} \left(B_{Ed}^I + \frac{M_{y,Ed}^I \nu}{\delta_T}\right) \frac{1}{1 + \frac{M_{y,Ed}}{M_{y,cr}}} \leq 1$$

$$+ \left(\left(\frac{M_{y,Ed}^I}{M_{y,Rd}}\right)^2 - \left(\frac{M_{y,Ed}^I}{M_{y,Rd}}\right)^3 \bar{\lambda}_{LT}^2 - \frac{M_{y,Ed}^I}{M_{y,Rd}} + \frac{M_{y,Ed}^I}{M_{y,Rd}} \chi_{LT} \bar{\lambda}_{LT}^2 - 1 \right) \leq 1 \quad (5.43)$$

As the last term of Eq. (5.43) is always less than 1,0, it is neglected in reference (FOSTA 2004). Here, it should be mentioned that, owing to this simplification, the interaction becomes linear again. Consequently, the benefit of the quadratic interaction used in equation (5.40) is lost. Additionally, the bi-moment created by the lateral displacement is neglected. After reorganising, Sedlacek presents the following interaction formula:

$$\frac{M_{y,Ed}^I}{\chi_{LT} \frac{M_{y,Rk}}{\gamma_{M1}}} + C_{zw} \left(\frac{M_{z,Ed}^I}{\gamma_{M1}} + \frac{M_{y,Ed}^I \varphi}{\gamma_{M1}} + \frac{B_{Ed}^I}{\gamma_{M1}} \right) \leq 1 \quad (5.44)$$

$$C_{zw} = \frac{1 - \frac{M_y}{M_{cr,y}}}{1 - \frac{M_y}{M_{cr,y}} \frac{M_y - C_1 N_{cr,z} \frac{8}{\pi^2} z_F}{M_{cr,y} - C_1 N_{cr,z} \frac{8}{\pi^2} z_F}} \quad (5.45)$$

The factor C_{zw} introduces the influence of second order effects. However, it is not clear how this factor has been derived. Again, it may be astonishing that the factor C_{zw} is less than one. Yet, one should remember that the term $M_y/\chi_{LT}M_{y,Rd}$ already contains an important part of the second order effects and therefore overestimates the influence of major-axis bending. The factor C_{zw} has to counterbalance this overestimation by reducing the influence of the other internal moments.

Sedlacek extends his proposal by the influence of the axial force using the same hypotheses as before. The resulting interaction criterion is represented in Eq. (5.46).

$$\chi_{LT,N} \frac{M_{y,Ed}^I}{\gamma_{M1} M_{y,Rk,N}} + C_{zw,N} \left(\frac{M_{z,Ed}^I}{\gamma_{M1} M_{z,Rk}} + \frac{M_{y,Ed}^I \varphi}{\gamma_{M1} M_{z,Rk}} \right) + C_{zw,N} \left(\frac{B_{Ed}^I}{\gamma_{M1} B_{Rk}} \varpi_N \left(1 - \frac{N}{N_{cr,z}} \right) \right) \leq 1 \quad (5.46)$$

$$C_{zw,N} = \frac{1 - \frac{M_y}{M_{y,cr,N}}}{1 - \frac{M_y \left[M_y - C_1 N_{cr,z} \frac{8}{\pi^2} z_F \left(1 - \frac{N}{N_{cr,z}} \right) \right]}{M_{y,cr,N} \left[M_{y,cr,N} - C_1 N_{cr,z} \frac{8}{\pi^2} z_F \left(1 - \frac{N}{N_{cr,z}} \right) \right]}} \frac{1}{1 - \frac{N}{N_{cr,z}}} \quad (5.47)$$

$$\varpi_N = \frac{1 + \frac{G I_T L^2}{E I_w \pi^2}}{1 + \frac{G I_T L^2}{E I_w \pi^2} - \frac{N_{Ed} j_s^2 L^2}{E I_w \pi^2}} \quad (5.48)$$

where:

$M_{y,Rk,N}$: is the characteristic value of the moment resistance for major axis bending reduced in the presence of an axial force (see Eq. (5.52));

$\chi_{LT,N}$: is the reduction factor due to lateral-torsional buckling, reduced in the presence of an axial force;

$C_{zw,N}$: is a factor accounting for second order effects for out-of-plane displacements;

ϖ_N : is a factor accounting for the influence of torsional buckling on the second order effects.

Observing Eq. (5.46), one notices that the axial force is not considered explicitly. In fact, its influence is accounted for by reducing the major-axis bending resistance and the reduction factor for lateral-torsional buckling. Its influence concerning second order effects is accounted for in the interaction coefficients $C_{zw,N}$ and ϖ_N and the factor $1 - N/N_{cr,z}$.

The first term of the interaction formula, $M_{y,Ed}/\chi_{LT,N}M_{y,Rd,N}$, can be compared to the criterion given in §6.3.4 of Eurocode 3 Part 1-1 recalled in Eq. (5.49).

$$\frac{\chi_{op} \alpha_{ult,Rk}}{\gamma_{M1}} \geq 1,0 \quad (5.49)$$

When in-plane second order effects and the equivalent geometric imperfection are not considered $\alpha_{ult,Rk}$ corresponds to the amplification factor applied to major-axis bending and the axial force to attain the section resistance. Consequently, one may introduce the equality given in Eq. (5.50). It should however also be noted that the amplification factor $\alpha_{ult,Rk}$ considers a proportional increase of both the major-axis bending moment and the axial force, whereas $M_{y,Rk,N}$ is calculated based on a constant value of the axial force. Yet, the main principle is identical.

$$\frac{1}{\alpha_{ult,Rk}} \approx \frac{M_{y,Ed}^I}{M_{y,Rk,N}} \quad (5.50)$$

To determine the reduction factor $\chi_{LT,N}$, (or χ_{op} with Eurocode notation), in reference (FOSTA 2004), it is proposed to use the reduction curve of paragraph 6.3.2.2 of (CEN 2005a) based on the relative slenderness for out-of-plane instability $\lambda_{LT,N}$ (λ_{op}) and by increasing the imperfection factor α by the influence of the axial force as shown in Eq. (5.51).

$$\alpha_N = \alpha \frac{1}{1 - \frac{N_{Ed}}{N_{cr,z}}} \leq 0,76 \quad (5.51)$$

It should be noted that Eq. (5.51) may lead to imperfection factors that are even more unfavourable than the ones for lateral buckling under axial compression only, especially for hot-rolled I sections whose flanges' thickness is less than 100 mm (applicable buckling curve for minor-axis buckling is c or better). It would certainly be more consistent to limit the imperfection factor to the one applicable for the case of flexural buckling under the axial force.

For the reduction of the major-axis bending moment resistance, a simplified approach is given by Eq. (5.52).

$$M_{y,N,Rk} = M_{y,Rk} \frac{1 - \frac{N_{Ed}}{N_{pl,Rk}}}{1 - \frac{A_w}{A}} \leq M_{y,Rk} \quad (5.52)$$

It should be noted that the interaction formula (5.52) is unsafe compared to the interaction formula of EN 1993-1-1 and compared to the analytical solution as shown in Figure 5-71 for the section IPE 200 ($\frac{A_w}{A} = 0,4035$). Figure 5-71 also shows the results obtained by applying the interaction provided in Eurocode 3 Part 1-1.

$$M_{y,N,Rk} = M_{y,Rk} \frac{1 - \frac{N_{Ed}}{N_{pl,Rk}}}{1 - 0,5 \frac{A_w}{A}} \leq M_{y,Rk} \quad (5.53)$$

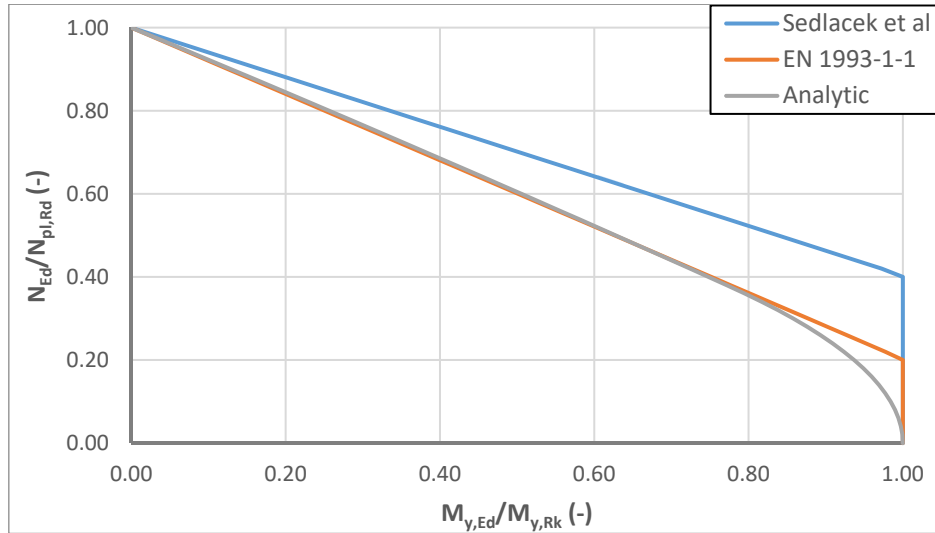


Figure 5-71 : Interaction between major axis bending and axial force for the section IPE 200

The proposed interaction may be highly unsafe, especially for low and medium axial forces (15-20% for IPE 200). The unsafe character of the proposed interaction is mainly due to the omission of the factor 0,5 associated with the web area in Eq. (5.52). Whether or not this factor is deliberately omitted or if the omission is only due to oblivion is not clear.

Finally, some comments concerning the factor ϖ_N should be made. Its formulation appears rather complicated and its actual meaning is not obvious. Yet, it may be rewritten as follows:

$$\varpi_N = \frac{1 + \frac{G I_T L^2}{E I_w \pi^2}}{1 + \frac{G I_T L^2}{E I_w \pi^2} - \frac{N_{Ed} j_s^2 L^2}{E I_w \pi^2}} = \frac{1}{1 - \frac{N_{Ed}}{N_{cr,T}}} \quad (5.54)$$

Regarding Eq. (5.54), it is obvious that the factor ϖ_N accounts for second order effects resulting from torsional buckling modes.

In summary, it has been shown that, despite of the analytical derivation of the proposal, some inconsistencies remain. Also, the continuity between section resistance and member resistance is abandoned. Last, the rather complex presentation of the proposal may certainly lead to difficulties, if one intends to apply the method by hand. A less complex and more comprehensive representation of the proposal may be given by the equations Eqs. (5.55) to (5.57).

$$\frac{1}{\chi_{op} \frac{\alpha_{ult,k}}{\gamma_{M1}}} + C_{zw,N} \left(\frac{M_{z,Ed}^I}{\gamma_{M1}} + \frac{M_{y,Ed}^I \varphi}{\gamma_{M1}} \right) + C_{ww,N} \frac{B_{Ed}^I}{B_{Rk}} \leq 1 \quad (5.55)$$

$$C_{zw,N} = \frac{1 - \frac{M_y}{M_{y,cr,N}}}{1 - \frac{M_y \left[M_y - C_1 N_{cr,z} \frac{8}{\pi^2} z_F \left(1 - \frac{N}{N_{cr,z}} \right) \right]}{M_{y,cr,N} \left[M_{y,cr,N} - C_1 N_{cr,z} \frac{8}{\pi^2} z_F \left(1 - \frac{N}{N_{cr,z}} \right) \right]}} \frac{1}{1 - \frac{N}{N_{cr,z}}} \quad (5.56)$$

$$C_{ww,N} = \frac{1 - \frac{M_y}{M_{y,cr,N}}}{1 - \frac{M_y \left[M_y - C_1 N_{cr,z} \frac{8}{\pi^2} z_F \left(1 - \frac{N}{N_{cr,z}} \right) \right]}{M_{y,cr,N} \left[M_{y,cr,N} - C_1 N_{cr,z} \frac{8}{\pi^2} z_F \left(1 - \frac{N}{N_{cr,z}} \right) \right]}} \frac{1}{1 - \frac{N}{N_{cr,T}}} \quad (5.57)$$

Eqs. (5.55) to (5.57) represent the exact same method but written in a more comprehensive way. Of course, the discontinuity between section resistance and member resistance and the previously mentioned inconsistencies are maintained. Additionally, it seems questionable whether or not this method is applicable to mono-symmetric I and U sections as the effects of their mono-symmetry is not accounted for.

5.4.3.3 Proposal RWTH Aachen II

In 2007, Stangenberg published a new method based on a similar mechanical background as the proposal Aachen I. Stangenberg introduces the second order internal moments in the modified linear interaction of Eq. (5.58).

$$\frac{M_{y,Ed}^{II}}{M_{y,Rd}} + \frac{2}{3} \frac{2 - 2a_w}{2 - a_w} \left(\frac{M_{z,Ed}^{II}}{M_{z,Rd}} + \frac{B_{Ed}^{II}}{B_{Rd}} \right) \leq 1 \quad (5.58)$$

$$\text{and: } a_w = \frac{h_w t_w}{A}$$

The proposed interaction equation is compared to the analytical results obtained with the adapted PIFM (se Chapter 4) in Figure 5-72. Also, the quadratic interaction proposed in (FOSTA 2004) is represented. As stated before, the quadratic interaction may be rather conservative and does not represent precisely the interaction behaviour. The proposal introduced by Stangenberg is more precise.

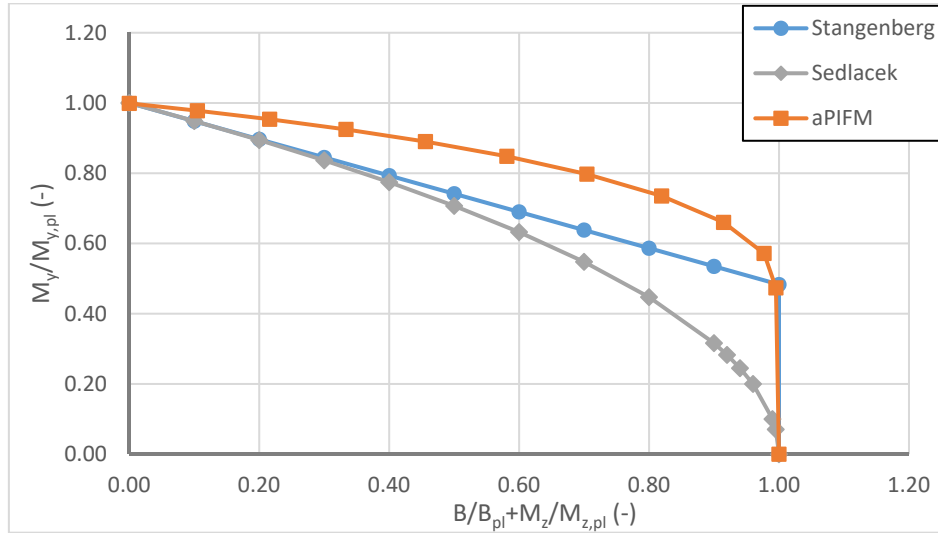


Figure 5-72: Plastic M_y - M_z - B interaction for an IPE 300 section

After introducing the expressions of the internal moments and the expression of the generalized imperfection η , Stangenberg obtains:

$$\frac{M_{y,Ed}^I}{\chi_{LT} M_{y,Rd}} + \frac{2}{3} \frac{2 - 2a_w}{2 - a_w} \left(\frac{M_{z,Ed}^I + M_{y,Ed}^I \varphi}{M_{z,Rd}} + \frac{B_{Ed}^I + \frac{M_{y,Ed}^I v}{\delta_T}}{B_{Rd}} \right) \frac{1}{1 + \frac{M_{y,Ed}}{M_{y,cr}}} + \left(\frac{M_{y,Ed}^I}{M_{y,Rd}} \chi_{LT} \bar{\lambda}_{LT}^2 - \left(\frac{M_{y,Ed}^I}{M_{y,Rd}} \bar{\lambda}_{LT} \right)^2 \right) \leq 1 \quad (5.59)$$

Stangenberg expresses the first order lateral displacement and torsional twist by:

$$\frac{v}{\delta_T} = \frac{M_z^I}{M_{cr,y}} \frac{I_w}{c I_z} \quad (5.60)$$

$$\varphi = \frac{B^I}{M_{cr,y}} \frac{I_z}{I_w} c \quad (5.61)$$

Introducing Eqs. (5.60) and (5.61) into Eq.(5.59), he obtains:

$$\frac{M_{y,Ed}^I}{\chi_{LT} M_{y,Rd}} + \left(\frac{M_{y,Ed}^I}{M_{y,Rd}} \chi_{LT} \bar{\lambda}_{LT}^2 - \left(\frac{M_{y,Ed}^I}{M_{y,Rd}} \bar{\lambda}_{LT} \right)^2 \right) + \frac{2}{3} \frac{2 - 2a_w}{2 - a_w} \left(\frac{B_{Ed}^I + \frac{M_{y,Ed}^I}{M_{y,Rd}} \bar{\lambda}_{LT}^2 \frac{B_{Ed}^I}{M_{z,Rd}} \frac{I_z}{I_w} c}{+ \frac{M_{z,Ed}^I}{M_{z,Rd}} + \frac{M_{y,Ed}^I}{M_{y,Rd}} \bar{\lambda}_{LT}^2 \frac{M_{z,Ed}^I}{B_{Rd}} \frac{I_w}{I_z} \frac{1}{c}} \right) \frac{1}{1 + \frac{M_{y,Ed}}{M_{y,cr}}} \leq 1 \quad (5.62)$$

As the factor $1/(1+M_{y,Ed}/M_{y,cr})$ is always less than 1, Stangenberg neglects it in the following. Also, the second term of Eq. (5.62) is neglected. Here it should be noted that this term, noted as η^1 hereafter, is not always less than 0. Obviously, the term is equal to 0, if the value of major-axis bending moment just reaches the resistance to lateral-torsional buckling of the member, $\chi_{LT}M_{y,Rd}$. The following figures show the evolution of the term with the slenderness and the load factor $\alpha_L=M_{y,Ed}/\chi M_{y,Rd}$. Figure 5-73 shows that it has its maximum for a relative slenderness of about 1,0.

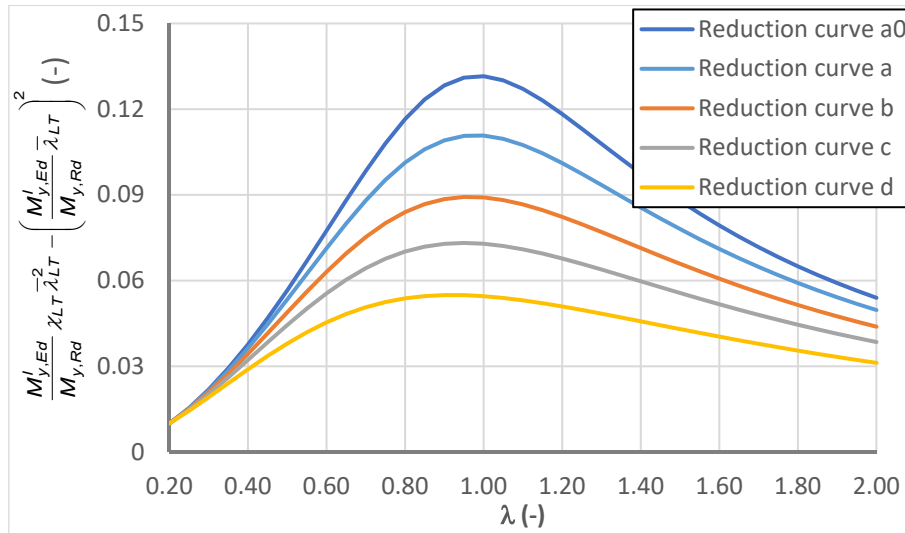


Figure 5-73: Evolution of η_1 with the slenderness – $\alpha_L = 0,5$

Depending on the reduction factor, the slenderness λ_{opt} maximizing η^1 , is given in Table 5-11.

Table 5-11: Slenderness maximizing η_1 depending on the reduction curve

Reduction curve	Slenderness λ_{opt}
a ₀	0,987
a	0,979
b	0,965
c	0,950
d	0,921

Figure 5-74 shows that the load factor maximizing η_1 is equal to 0,5. This value does not depend on the reduction curve. Both, Figure 5-73 and Figure 5-74, demonstrate that the maximum value of η_1 increases when the imperfection factor α , associated with the reduction curve (of Eurocode 3 Part 1-1), decreases. Anyhow, η_1 does not exceed the value of 0,13 ($\alpha_L = 0,5$ and reduction curve a₀). Even if the value of η_1 is not important, neglecting it is not justified a priori. However, as the factor $1/(1+M_{y,Ed}/M_{y,cr})$, being always less than 1,0, is neglected and as other empirical factors considering the variability of the moments and cross-section characteristics are introduced, the safety margin may be sufficient.

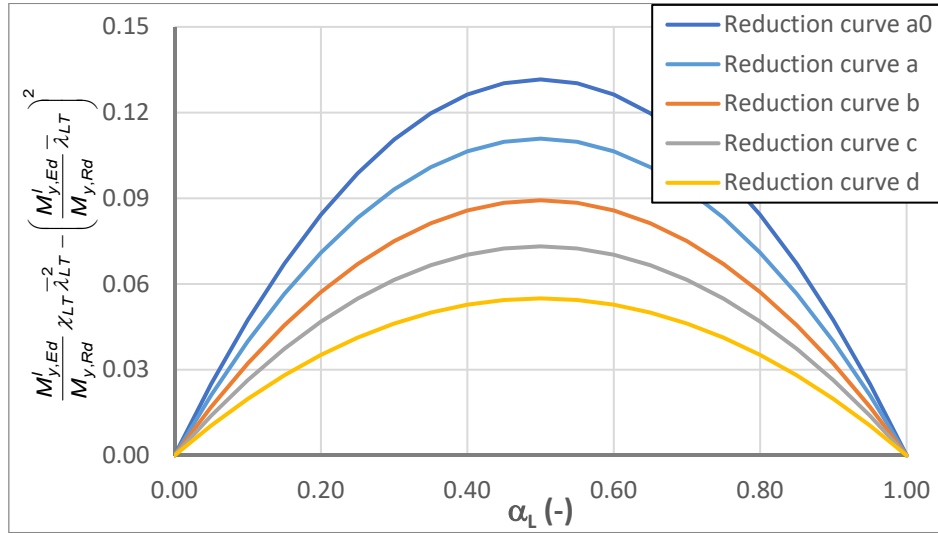


Figure 5-74: Evolution of η_1 with the load factor – slenderness equals λ_{opt}

Eq. (5.63) shows the final proposal for I sections subject to bi-axial bending and torsion.

$$\begin{aligned} \frac{M_{y,Ed}^I}{\chi_{LT} M_{y,Rd}^I} + \frac{2}{3} \frac{2 - 2a_w}{2 - a_w} \frac{B_{Ed}^I}{B_{Rd}^I} \left(1 + \frac{C_1}{C_{1,\eta} k_{\delta,\theta}} \frac{M_{y,Ed}^I}{M_{y,Rd}^I} \bar{\lambda}_{LT}^{-2} \sqrt{\frac{I_z}{I_w}} c_r \right) \\ + \frac{2}{3} \frac{2 - 2a_w}{2 - a_w} \frac{M_{z,Ed}^I}{M_{z,Rd}^I} \left(1 + \frac{C_1 C_{1,E}}{k_{\delta,z}} \frac{M_{y,Ed}^I}{M_{y,Rd}^I} \bar{\lambda}_{LT}^{-2} \sqrt{\frac{I_w}{I_z}} \frac{1}{c_r} \right) \leq 1 \end{aligned} \quad (5.63)$$

The coefficient C_1 represents the variability of the bending moment diagram. The coefficient $C_{1,\eta}$ is introduced in order to correct the ratio between the lateral displacement component and the torsional twist component of the eigenmode as it is not equal to c_r (see also paragraph 5.5.7) in case of variable bending moments. However, Stangenberg does not provide a literal expression for the correction factor $C_{1,\eta}$. Consequently, a numerical determination of this parameter is necessary based on the definition of Eq. (5.64).

$$\frac{v_{cr}}{\varphi_{cr}} = C_{1,\eta} c_r \quad (5.64)$$

The coefficient $C_{1,E}$ considers the ratio between the minor-axis bending moment and bi-moment of the imperfect member considering second order effects:

$$\frac{M_{z,Ed,imp}}{B_{Ed,imp}} = C_{1,E} \frac{I_z}{I_w} c_r \quad (5.65)$$

Finally, the coefficients $k_{\delta,\theta}$ and $k_{\delta,z}$ take into account the influence of variable minor-axis and bi-moments. Yet, again no literal expressions are provided for $C_{1,E}$, $k_{\delta,\theta}$ and $k_{\delta,z}$. However, it seems understandable that the literal expressions of $C_{1,E}$, $C_{1,h}$, $k_{\delta,\theta}$ and $k_{\delta,z}$ are omitted. Indeed, depending on the cross-section geometry, the exact shape of the moment diagrams, the support conditions and the torsional characteristics the parameters may vary highly.

Following the same reasoning as before, Stangenberg proposes a design criterion for U sections under bi-axial bending and torsion:

$$\frac{M_{y,Ed}^I}{\chi_{LT} M_{y,Rd}} + 2 \frac{3 - 2\beta_w^2}{7 - 4\beta_w^2} \frac{B_{Ed}^I}{B_{Rd}} \left(1 + \frac{C_1}{C_{1,\eta} k_{\delta,\theta}} \frac{M_{y,Ed}^I}{M_{y,Rd}} \bar{\lambda}_{LT}^{-2} \frac{B_{Rd}}{M_{z,Rd}} \frac{I_z}{I_w} c_r \right) + \frac{5}{3} \frac{2 - \beta_z^2}{5 - 3\beta_z^2} \frac{M_{z,Ed}^I}{M_{z,Rd}} \left(1 + \frac{C_1 C_{1,E}}{k_{\delta,z}} \frac{M_{y,Ed}^I}{M_{y,Rd}} \bar{\lambda}_{LT}^{-2} \frac{M_{z,Rd}}{B_{Rd}} \frac{I_w}{I_z} \frac{1}{c_r} \right) \leq 1 \quad (5.66)$$

The coefficients β_z and β_w consider the form of the plastic cross-section interaction. They are given in Eqs. (5.67) and (5.68).

$$\beta_z = 1 - \frac{a_w}{2a_f} \quad (5.67)$$

$$\beta_w = 1 - \frac{a_w}{4a_f} \quad (5.68)$$

It can be noted that the slight non-symmetry in the interaction between the major-axis and the bi-moment is neglected in Eq. (5.66) (see Chapter 4). The linearized cross-section interaction is compared to the values obtained with the adapted PIFM (noted as aPIFM in the following diagrams). Figure 5-77 also represents the interaction curve proposed in Chapter 4 of this thesis.

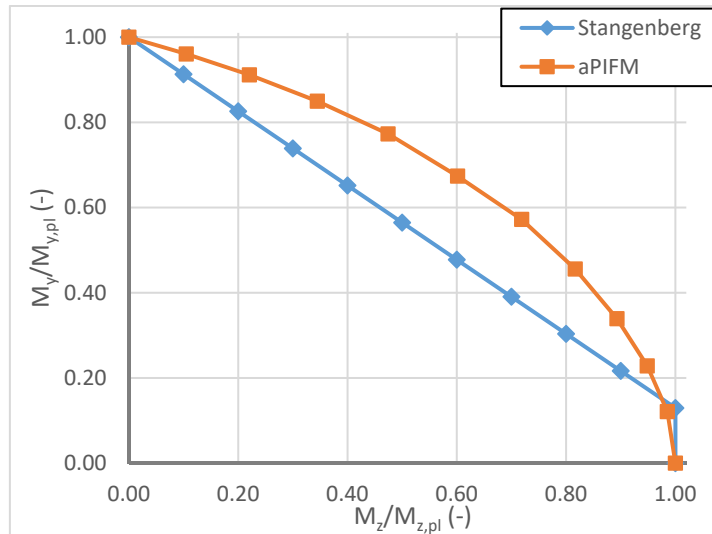


Figure 5-75: Plastic M_y - M_z interaction for UPE 220

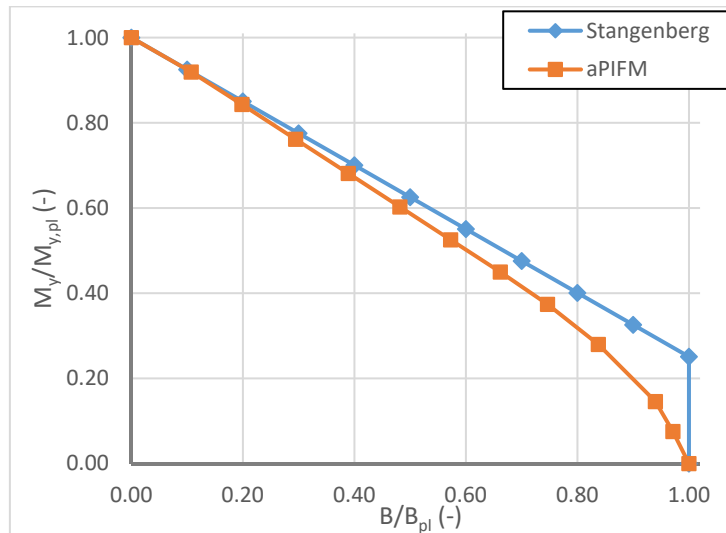


Figure 5-76: Plastic M_y -B interaction for UPE 220

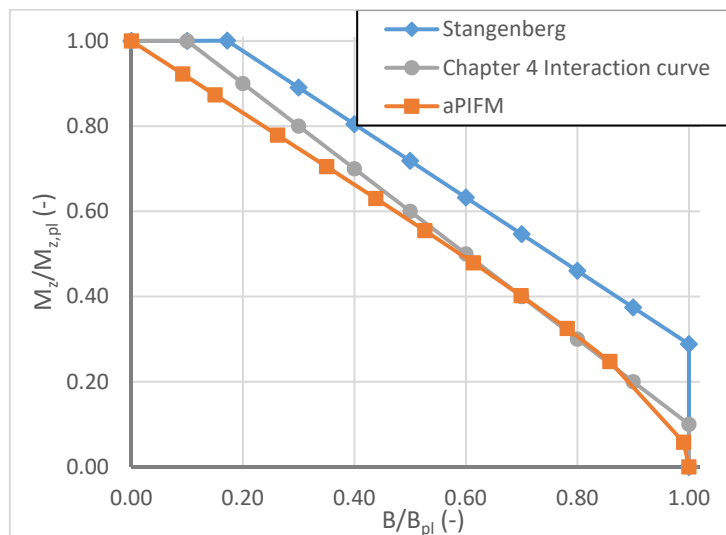


Figure 5-77: Plastic M_z -B interaction for UPE 220

The previous figures show that the linearized interaction curves proposed by Stangenberg can only roughly represent the complex interaction behaviour of U sections. In fact, the major-axis bending-minor-axis bending interaction is rather safe-sided and only slightly more economic than a linear interaction. Conversely, the interaction between major-axis bending and the bi-moment as well as minor-axis bending and the bi-moment seem to be slightly unsafe. Especially, for the minor-axis bending-bi-moment interaction, it has to be recalled that the numerical results have shown that the cut-off limits should not exceed ten percent of both ratios $M_z/M_{z,pl}$ and B/B_{pl} . Also, it should be noted that the plastic interaction may obviously only be applied if the studied member is of compact cross-section and not too slender in order to attain a failure mode characterised by complete yielding of the most loaded section. This problem is highlighted based on the example of the cross-section given in Table 5-12. Hereafter, the hot-rolled cross-section with invented dimensions is studied. This section is also used in the parametric study presented in paragraph 5.6 (the choice of the dimensions is discussed in paragraph 5.6). The section is of class 4 due to its

slender web. The flanges are of class 3. The studied member is subject to a point load applied at mid-span at the upper flange's tip.

Table 5-12: Studied cross-section

Cross-section	HR770.5.400.17*
A	172,8 cm ²
I _z	18134 cm ⁴
I _y	209428 cm ⁴
I _t	131,01 cm ⁴
I _w	25705928 cm ⁶
Class	4**
M _{y,pl} (S235)	1362,4 kNm
M _{y,eff} (S235)	1233,9 kNm
M _{z,pl} (S235)	320,3 kNm
M _{z,eff} = M _{z,el} (S235)	213,08 kNm
B _{pl} (S235)	120,34 kNm ²
B _{eff} = B _{el} (S235)	80,00 kNm ²

* Hot-rolled section HR.h.t.w.b.t_f

** Web of class 4 and flanges of class 3

The results are presented in form of the ultimate resistance curve given in Figure 5-78. The relative slenderness is determined based on the critical load amplification factor and the load amplification factor leading to the plastic cross-section resistance as defined by Eq. (5.69).

$$\bar{\lambda} = \sqrt{\frac{R_{pl}}{R_{cr,G}}} \quad (5.69)$$

Figure 5-78 clearly highlights that the resistance model proposed by Stangenberg may be very unsafe for members of slender cross-section. Obviously, a linear interaction should apply in these cases. For longer members the results may seem more surprising. Indeed, the proposal approaches the results obtained numerically and may even become safe-sided, although a non-linear interaction is applied. Here, two main factors may explain these results:

- For longer members the influence of section slenderness (and therefore local buckling) becomes negligible.
- The favourable factor $1/(1+M_{y,Ed}/M_{y,cr})$ is neglected by Stangenberg in order to simplify his proposal (compare Eqs. (5.62) and (5.63)).

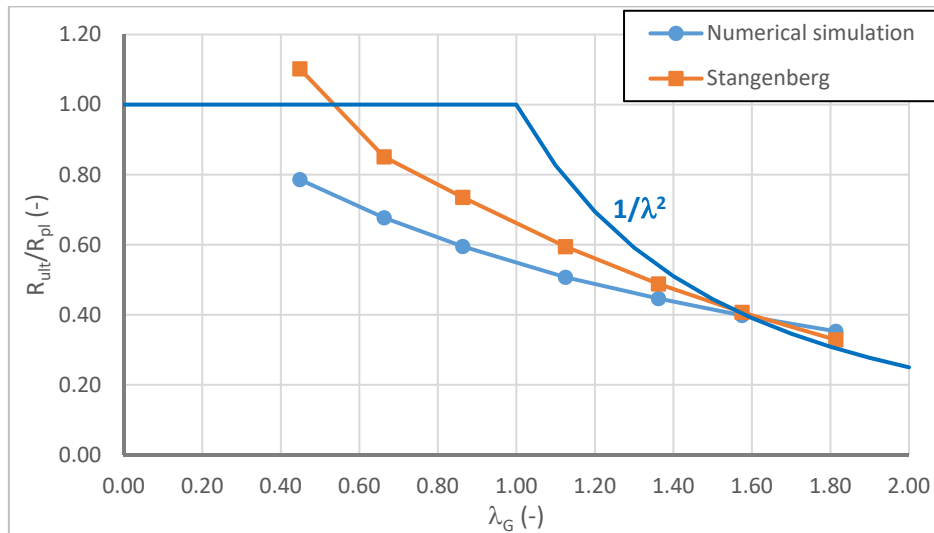


Figure 5-78: Ultimate resistance curve of the studied member

The first point may be highlighted based on the deformed shape and von Mises stress distribution for the two members of a length of 4,0 m and 10,8 m represented in Figure 5-79 (the load introduction as well as the stiffener at mid-span are not represented). Figure 5-79 a) clearly shows the formation of local buckles in the flange at mid-span indicating a failure caused by interaction between local and member instability. Conversely, the longer member fails predominantly by elasto-plastic member instability as indicated by yielding of the upper flange at mid-span. One may note that the two members are also calculated with the restrained model (see paragraph 5.2.3). These supplementary calculations allow the quantification of the influence of local buckling on the member resistance. Indeed, for the two members, one obtains the following ratios between the calculation considering local buckling (linked to the load amplification factor $R_{ult,NR}$) and the calculation not considering the influence of local buckling (linked to the load amplification factor $R_{ult,R}$):

Member of 4,4 m of length:
$$\frac{R_{ult,NR}}{R_{ult,R}} = 0,768$$

Member of 10,8 m of length:
$$\frac{R_{ult,NR}}{R_{ult,R}} = 0,966$$

The ratios obtained for the two members confirm the conclusions concerning the failure mode influenced by local plate instability.

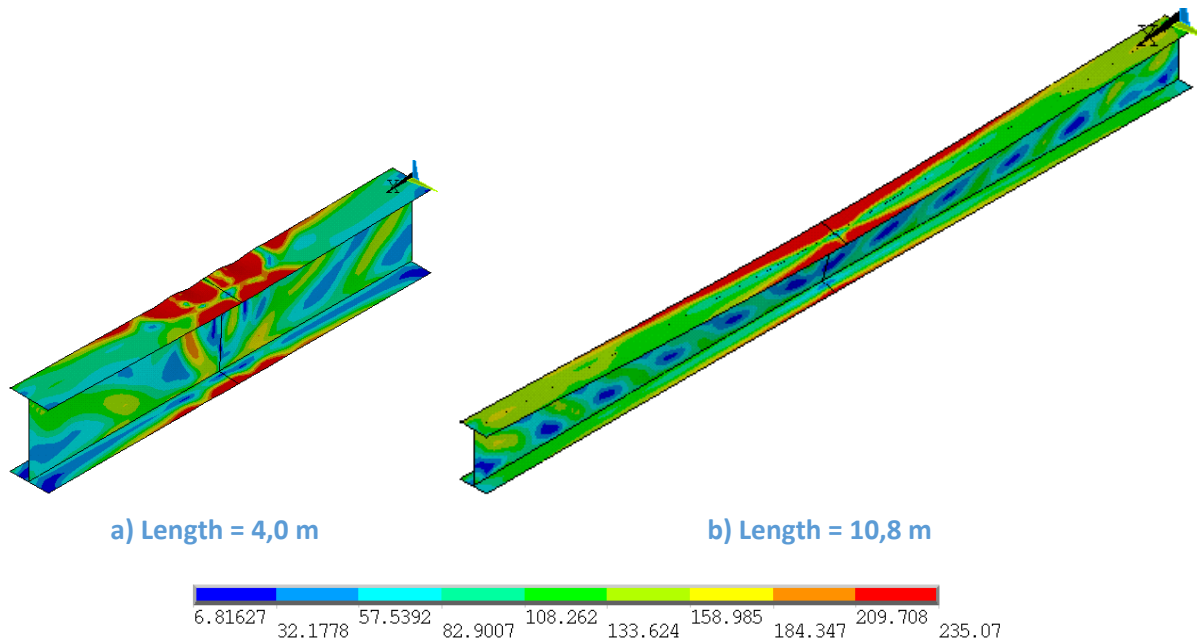


Figure 5-79: Deformed shape and residual stress distribution

Additionally, it may be shown that the omission of the factor $1/(1+M_{y,Ed}/M_{y,cr})$ may be rather conservative as highlighted in Figure 5-80. It is recalled that this factor is linked to the ratio B_{Ed}/B_{Rd} . Consequently, the possible reduction of up to 30% for the working ratio of the bi-moment is neglected leading to less unsafe results when the proposal of Stangenberg is applied to long members.

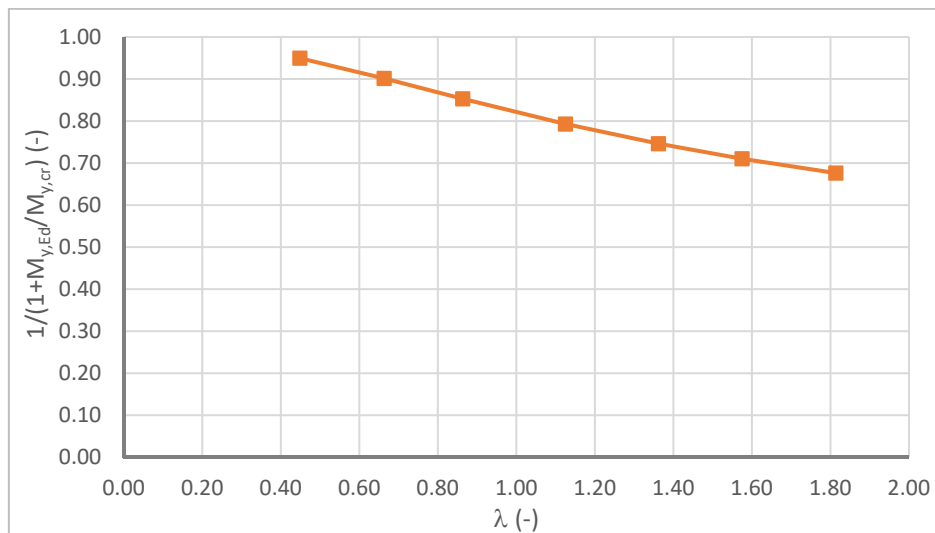


Figure 5-80: Evolution of the factor $1/(1+M_{y,Ed}/M_{y,cr})$

Last, for I sections, Stangenberg proposes an extension of Eq. (5.63) to an additional axial force as shown in Eq. (5.70).

$$\begin{aligned} & \frac{1}{\chi_{op} \alpha_{ult,Rd}} + \chi_{op}^2 \bar{\lambda}_{op}^2 \left(\frac{1}{\chi_{op} \alpha_{ult,Rd}} - \left(\frac{1}{\chi_{op} \alpha_{ult,Rd}} \right)^2 \right) \frac{N_{Ed}}{N_{Rd}} \alpha_{ult,Rd} \\ & \frac{2}{3} \frac{B_{Ed}^I}{B_{Rd}} \frac{C_{mT}}{1 - \frac{N_{Ed}}{N_{cr,T}}} \left(1 + \frac{C_1}{C_{1,\eta}} \frac{1}{k_{\delta,\theta}} \frac{1}{\alpha_{ult,Rd}} \bar{\lambda}_{LT}^2 \frac{B_{Rd}}{M_{z,Rd}} \frac{I_z}{I_w} c_\alpha \frac{C_{mz}}{1 - \frac{N_{Ed}}{N_{cr,z}}} \right) \\ & + \frac{2}{3} \frac{M_{z,Ed}^I}{M_{z,Rd}} \frac{C_{mz}}{1 - \frac{N_{Ed}}{N_{cr,z}}} \left(1 + \frac{C_1 C_{1,E}}{k_{\delta,z}} \frac{1}{\alpha_{ult,Rd}} \bar{\lambda}_{LT}^2 \frac{M_{z,Rd}}{B_{Rd}} \frac{I_w}{I_z} \frac{1}{c_\alpha} \frac{C_{mT}}{1 - \frac{N_{Ed}}{N_{cr,T}}} \right) \leq 1 \end{aligned} \quad (5.70)$$

Eq. (5.70) represents several disadvantages. The first one is certainly the complexity of the presentation that leads to an unreadable design criterion. Additionally, it should be noticed that if the axial force tends to zero, Eq. (5.70) does not tend to the proposal for bi-axial bending and torsion without axial force due to the difference in the cross-section interaction. Also, for the case of an additional axial force, the term introducing the influence of the imperfection is kept (second term of Eq. (5.70)) whereas it has been neglected for combined bi-axial bending and torsion. The resulting discontinuity may be confusing for potential users. Moreover, the proposed non-linear interaction dismisses the proposal again for slender sections (class 3 or class 4) and for slender members attaining a purely elastic limit state.

5.4.3.4 Proposal RWTH Aachen III

A last proposal developed at RWTH Aachen is made by Naumes in 2009. He proposed the following format based on a linear interaction between internal forces and moments:

$$\frac{1}{\chi_{op} \alpha_{ult,Rd}} + \frac{M_{z,Ed}^I}{M_{z,Rd}} (1 - q_{Mz}) + \frac{B_{Ed}^I}{B_{Rd}} (1 - q_B) \leq \Delta n_R \quad (5.71)$$

$$\Delta n_R = 1 - \chi_{op}^2 \bar{\lambda}_{op}^2 \left(\frac{1}{\chi_{op} \alpha_{ult,Rd}} - \left(\frac{1}{\chi_{op} \alpha_{ult,Rd}} \right)^2 \right) \quad (5.72)$$

where:

q_{Mz} and q_B : are coefficients taking into account the shape of the minor axis bending/ bi-moment diagram

Compared to the previous design methods proposed at RWTH Aachen, the present proposal has the advantage of being much more compact even if it has been developed based on the same mechanical background. As Stangenberg, Naumes proposes to keep the influence of the imperfection in the design concept through the term Δn_R . Additionally, one notices that out-of-plane second order effects created by axial forces are not accounted for, conversely to the two

previous design proposals. This omission might lead to unsafe results in cases of high axial forces and interaction with a minor-axis bending moment. Moreover it is not clear whether the first order minor-axis bending moment and first order bi-moment include the components created by the first order displacements ($M_z = M_y\varphi$; $M_w = M_yv/\delta_T$ – see Eqs. (5.60) and (5.61)).

Naumes gives an analytic expression for the factors q_{Mz} and q_{Mw} :

$$q_{mz} = \frac{1}{\alpha_{ult,Rd}} \bar{\lambda}^{-2} \left(1 - \frac{M_{z,m}}{M_{z,0}} \right) \quad (5.73)$$

$$q_B = \frac{1}{\alpha_{ult,Rd}} \bar{\lambda}^{-2} \left(1 - \frac{B_m}{B_0} \right) \quad (5.74)$$

where:

$M_{z,m}$ and B_m : are the modal minor-axis bending moment and bi-moments (resulting from the eigenmode)

$M_{z,0}$ and B_0 : are the maximum first order minor-axis bending and bi-moments

In order to facilitate the determination of the factor q_{Mz} , Naumes provides literal expressions so that $(1-q_{mz})$ is equivalent to the C_{mz} factor given in Annex A of Eurocode 3 Part 1-1 (CEN 2005a). However, no expression is given for q_B . Yet, one might argue that, as the warping moment is certainly not the predominant component for the resistance of the member, it is not necessary to account for the influence of the form of the bi-moment. In some situations, especially for members with high warping decay factors ε_T (and therefore bi-moments concentrated in small zones), neglecting the form of the warping moment may be conservative.

So as to highlight the problem linked to the omission of the out-of-plane second order effects arising from the axial force, it is proposed to study the example of a member made of HEB 200 section fabricated from steel S235. The member is subject to an axial compression force and a lateral point load applied at mid-span generating a minor-axis bending moment but no torsion (it is applied through the shear centre). The loads are increased proportionally and the ratio between the minor-axis bending moment and the axial force is equal to 7,35 cm. The results obtained by the numerical simulations as well as by the application of the proposal from Naumes are given in Figure 5-81. Additionally, the strength prediction obtained with the Eurocode 3 interaction formulae and Annexe B of the same standard are represented.

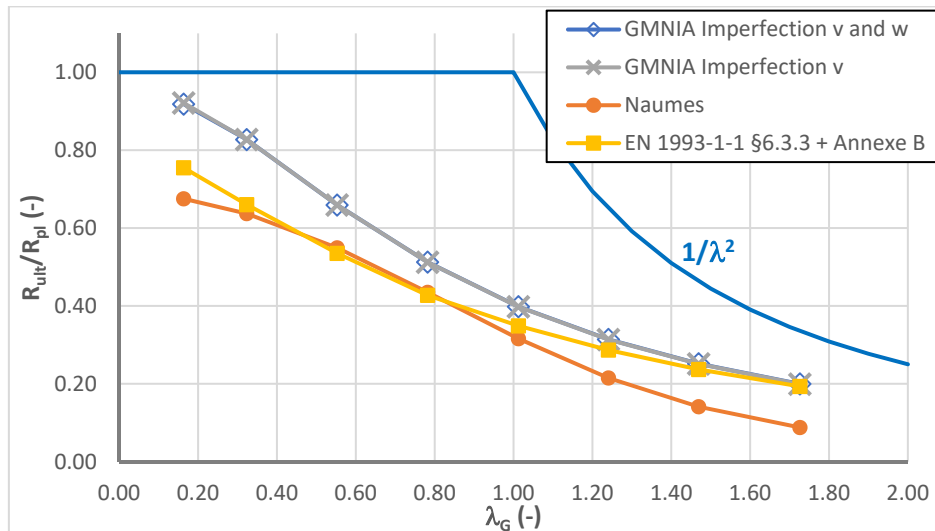


Figure 5-81: Ultimate resistance curves for a member of HEB 200 section subject to combined minor-axis bending and compression force

It may seem astonishing that the proposal of Naumes is safe-sided over the whole range of the slenderness. For short members, this seems natural as Naumes supposes a linear interaction between the minor-axis bending moment and the axial force. Obviously, this is rather conservative. On the contrary, for longer members sensitive to second order effects the safe-sided nature of the proposal seems more surprising as the amplification factor $1/(1-N_{Ed}/N_{cr,z})$ is omitted for the minor-axis bending moment. Yet, it should be noted that the parameter $\alpha_{ult,k}$ representing the working degree of the member about its major-axis **includes second order effects and the member imperfection**. For the studied case the proposal may therefore be rewritten as shown in Eq. (5.75).

$$\frac{N_{Ed}}{\chi_y \chi_z N_{Rd}} + \frac{M_{z,Ed}}{M_{z,Rd}} + \chi_z^2 \bar{\lambda}_z^2 \left(\frac{N_{Ed}}{\chi_y \chi_z N_{Rd}} - \left(\frac{N_{Ed}}{\chi_y \chi_z N_{Rd}} \right)^2 \right) \leq 1 \quad (5.75)$$

The last term at the left-hand side of Eq. (5.75) varies between approximately 0,01 and 0,05. Consequently, it is nearly negligible for the studied case. Contrarywise, it may be seen that the first term representing the working degree of the member with respect to the axial force includes the in-plane **and** the out-of-plane buckling reduction factor. The reduction factor χ_y varies between 1,0 for the shortest member to 0,34 for the longest member. Hence, it contributes highly to the strength reduction and counterbalances the omission of the amplification factor $1/(1-N_{Ed}/N_{cr,z})$ that should theoretically be associated with the minor-axis bending moment. It should however be noted that this is not conceptually correct as shown by the two curves linked to the numerical simulations, GMNIA Imperfection v and GMNIA Imperfection v and w, including respectively a sole lateral imperfection of amplitude $L/1000$ and a combination of lateral and vertical Imperfection both of amplitude $L/1000$. As can be seen the vertical imperfection has no effect on the member strength. Indeed, the failure is characterized by flexural buckling about the minor-axis in both cases. The second order effects arising from the vertical imperfection are negligible.

Additionally, depending on the member geometry, the results of the Eq. (5.71) may become unsafe. Indeed, if the sensitivity of the member for in-plane and out-of-plane buckling is very different (if $I_y \gg I_z$), the omission of the out-of-plane second order effects cannot be covered anymore by the in-plane reduction factor. So as to illustrate this problem a member of HEAA 800 section is studied. This member is subject to constant minor-axis bending and an axial compression force. The values of the axial force and the minor axis-bending moment is chosen to obtain a ratio $(M_z/M_{z,pl})/(N/N_{pl}) = 6,7$ (if the minor-axis bending moment attains the value of $M_{z,pl}$, the axial force attains $0,15N_{pl}$). Figure 5-82 shows that the studied proposal may be unsafe for this member. Conversely, the Eurocode 3 Part 1-1 interaction equations represent very well the behaviour of the member as the second order effects amplifying the minor-axis bending moment are accounted for. For short members the interaction equations as well as the proposal of Naumes become more conservative as the exact plastic cross-section interaction is not represented.

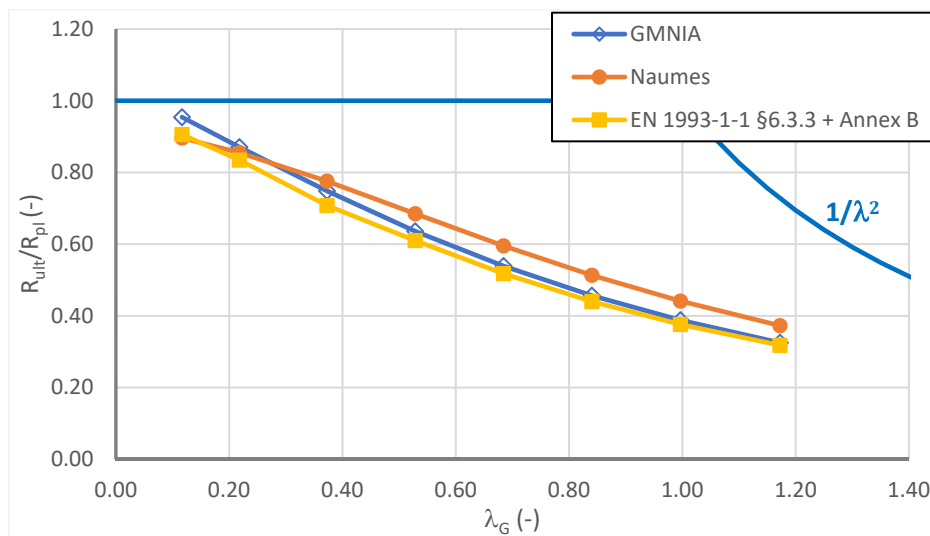


Figure 5-82: Ultimate resistance curves for a member of HEAA 800 section subject to combined minor-axis bending and compression force

It can be concluded that Naumes' proposal for the extension of the "General Method" of §6.3.4 of the current version of Eurocode 3 Part 1-1 may or may not be safe-sided depending on the member geometry and depending on the relative importance of the in- and out-of-plane second order effects.

Last, one may note that the domain of application of the proposed method is extended to U sections without any modification. Consequently, additionally to the problems highlighted here before, the flexural-torsional buckling mode is not accounted for. As, for U-shaped members, this mode combines in- and out-of-plane displacements, the separate treatment of both (as done through the introduction of the term $1/(\alpha_{ult,k}\chi_{op})$) seems delicate.

5.4.3.5 Summary of design proposal made at RWTH Aachen

Through the previous paragraphs the design proposals made at RWTH Aachen have been discussed. It may be noted that they can be rewritten in a very similar format as shown in Eqs. (5.76) to (5.78). The main differences between the three proposals are associated with the hypothesis concerning the cross-section interaction (non-linear or linear). Additionally, proposals Aachen I and Aachen II include the effect of the member displacements on the internal moments. In fact, Aachen I includes explicitly the complementary term $M_{y,Ed}\varphi$ and Aachen II the effects linked to the displacements φ and v but the explicit values of the displacement components are replaced by analytical expressions. Yet, this leads to an increased complexity for the presentation of proposal Aachen II. Moreover, it seems obvious that the “analytical” expressions used are only approximate for complex load combinations. Therefore, it seems more convenient to keep the displacements explicitly in the interaction equations (if necessary). Also, in practice the analysis of the structure is done by a numerical simulation in nearly every case. Consequently, the engineer possesses directly the information of the torsional twist and the displacements. In proposal Aachen III the additional minor-axis bending moment arising from the torsional twist and the additional bi-moment arising from lateral displacements seem to be neglected. In paragraph 5.6, it is investigated, based on comparisons to GMNIA simulations, whether or not it is necessary to consider the displacements.

Proposal Aachen I:

$$\frac{1}{\chi_{op}\alpha_{ult,Rd}} + C_{zw,N} \left(\frac{M_{z,Ed}^I + M_{y,Ed}^I \varphi}{M_{z,Rd}} \right) + C_{ww,N} \frac{B_{Ed}^I}{\frac{B_{Rk}}{\gamma_{M1}}} \leq 1$$

$$C_{zw,N} = \frac{1 - \frac{M_y}{M_{y,cr,N}}}{1 - \frac{M_y \left[M_y - C_1 N_{cr,z} \frac{8}{\pi^2} z_F \left(1 - \frac{N}{N_{cr,z}} \right) \right]}{M_{y,cr,N} \left[M_{y,cr,N} - C_1 N_{cr,z} \frac{8}{\pi^2} z_F \left(1 - \frac{N}{N_{cr,z}} \right) \right]}} \frac{1}{1 - \frac{N}{N_{cr,z}}} \quad (5.76)$$

$$C_{ww,N} = \frac{1 - \frac{M_y}{M_{y,cr,N}}}{1 - \frac{M_y \left[M_y - C_1 N_{cr,z} \frac{8}{\pi^2} z_F \left(1 - \frac{N}{N_{cr,z}} \right) \right]}{M_{y,cr,N} \left[M_{y,cr,N} - C_1 N_{cr,z} \frac{8}{\pi^2} z_F \left(1 - \frac{N}{N_{cr,z}} \right) \right]}} \frac{1}{1 - \frac{N}{N_{cr,T}}}$$

Proposal Aachen II:

$$\begin{aligned}
 & \frac{1}{\chi_{op} \alpha_{ult,Rd}} + \frac{2}{3} \frac{M_{w,Ed}^I}{M_{w,Rd}} C_{zw,N} + \frac{2}{3} C_{ww,N} \frac{M_{z,Ed}^I}{M_{z,Rd}} \\
 & + \chi_{op}^2 \bar{\lambda}_{op}^{-2} \left(\frac{1}{\chi_{op} \alpha_{ult,Rd}} - \left(\frac{1}{\chi_{op} \alpha_{ult,Rd}} \right)^2 \right) \frac{N_{Ed}}{N_{Rd}} \alpha_{ult,Rd} \leq 1 \\
 \\
 & C_{zw,N} = \frac{C_{mT}}{1 - \frac{N_{Ed}}{N_{cr,T}}} \left(1 + \frac{C_1}{C_{1,\eta} k_{\delta,\theta}} \frac{1}{\alpha_{ult,Rd}} \bar{\lambda}_{LT}^{-2} \frac{M_{w,Rd}}{M_{z,Rd}} \frac{I_z}{I_w} c_\alpha \frac{C_{mz}}{1 - \frac{N_{Ed}}{N_{cr,z}}} \right) \\
 \\
 & C_{ww,N} = \frac{C_{mz}}{1 - \frac{N_{Ed}}{N_{cr,z}}} \left(1 + \frac{C_1 C_{1,E}}{k_{\delta,z}} \frac{1}{\alpha_{ult,Rd}} \bar{\lambda}_{LT}^{-2} \frac{M_{z,Rd}}{M_{w,Rd}} \frac{I_w}{I_z} \frac{1}{c_\alpha} \frac{C_{mT}}{1 - \frac{N_{Ed}}{N_{cr,T}}} \right)
 \end{aligned} \tag{5.77}$$

Proposal Aachen III:

$$\begin{aligned}
 & \frac{1}{\chi_{op} \alpha_{ult,Rd}} + \frac{M_{z,Ed}^I}{M_{z,Rd}} (1 - q_{Mz}) + \frac{M_{w,Ed}^I}{M_{w,Rd}} (1 - q_{Mw}) \\
 & + \chi_{op}^2 \bar{\lambda}_{op}^{-2} \left(\frac{1}{\chi_{op} \alpha_{ult,Rd}} - \left(\frac{1}{\chi_{op} \alpha_{ult,Rd}} \right)^2 \right) \leq 1
 \end{aligned} \tag{5.78}$$

It is recalled that all three proposal may be unsafe in certain conditions even if they appear to be rather complex.

5.4.4 Design rule proposed at TU Berlin

In the framework of the German national research project P554 (FOSTA 2004) that involved three universities (TU Berlin, RWTH Aachen and RU Bochum), several design proposals were developed. The proposal developed by RWTH has already been presented as proposal Aachen I in paragraph 5.4.3.2. The design proposal of TU Berlin, presented in (Glitsch 2008) is detailed hereafter. It should be noticed that this proposal has been adopted in Eurocode 3 Part 6 – Crane Supporting Structures (CEN 2007b) for double and slightly to medium mono symmetric I sections (mono symmetric sections for which the ratio between the second moment of area of the flanges about their major-axis is not less than 0,2 – $-0,67 \leq \psi_{mono} \leq 0,67$). Yet, it is invalidated by the French National Annex (CEN 2011b). As the proposals of Nethercot and Naumes, Glitsch proposes the linear interaction between major-axis bending, minor-axis bending and the bi-moment represented in Eq. (5.79). This proposal has been derived empirically based on numerical simulations conversely to the proposals made by RWTH Aachen that are based on a theoretical

basis. Consequently, the empirical interaction factors k_w , k_{zw} and k_α are used to adapt the model to the observed resistances.

$$\frac{M_{y,Ed}}{\chi_{LT} \frac{M_{y,Rk}}{\gamma_{M,1}}} + \frac{C_{mz} M_{z,Ed}}{\frac{M_{z,Rk}}{\gamma_{M,1}}} + \frac{k_w k_{zw} k_\alpha B_{Ed}}{\frac{B_{Rk}}{\gamma_{M,1}}} \leq 1,0 \quad (5.79)$$

where:

k_w, k_{zw}, k_α : are interaction factors given in Eqs. (5.80) to (5.82)

$$k_w = 0,7 - \frac{0,2B_{Ed}}{\frac{B_{Rk}}{\gamma_{M1}}} \quad (5.80)$$

$$k_{zw} = 1 - \frac{M_{z,Ed}}{\frac{M_{z,Rk}}{\gamma_{M1}}} \quad (5.81)$$

$$k_\alpha = \frac{1}{1 - \frac{M_{y,Ed}}{M_{y,cr}}} \quad (5.82)$$

The bi-moment is multiplied by three coefficients given by the expressions of Eqs (5.80) to (5.82). Obviously, the factor k_α accounts for the influence of second order effects. As the interaction factor used in paragraph 5.4.2, k_α overestimates the second order effects on the bi-moment arising from the major-axis bending moment compared to an elastic analysis. It is recalled that these second order effects are already partially included in the reduction factor χ_{LT} (the analytically determined amplification factor is used in Eq. (5.62) and it is equal to $1/(1+M_y/M_{y,cr})$).

The factor k_{zw} is supposed to represent the modification of the torsional behaviour of the member and in particular the effect of the warping hinge. It can be observed that if the minor-axis bending moment $M_{z,Ed}$ equals the moment resistance for minor-axis bending $M_{z,Rk}$ (omitting γ_{M1} as it is 1,0 according to (CEN 2005a)) the factor k_{zw} equals 0, i.e. the member may always attain the plastic minor-axis bending resistance in case of combined minor-axis bending and torsion (without M_y). Yet, it has been shown in Chapter 4 that this is not true. In particular, it has been shown that, if the warping hinge is accounted for, high Saint-Venant's torsional moments may arise. The failure of short moments is then always associated with complete yielding over their total length. Additionally, for relatively long members susceptible to fail by instability, the torsional modification of the member leads to a high increase of the torsional twist that may not be acceptable in practice. The effect of this factor on the safety level of this proposal is evaluated further on in paragraph 5.6.4.2.

Following the explanations given in reference (Glitsch 2008) the last component of the interaction factors, k_w , is supposed to account for the interaction between major-axis bending and the bi-moment. However, it appears that its expression given in Eq. (5.80) can absolutely not ensure the continuity of the design approach for members subject to low major-axis bending moments. Also, it should be noted that the factor k_w has been calibrated supposing that the other factors are valid. Consequently, it seems that this factor rather compounds for uncertainties of the design approach. Figure 5-83 shows the calibration of the factor based on a limited number of numerical simulations. This figure, taken from reference (Glitsch 2008), gives the value of k_w necessary to yield the same strength prediction with the model as the one obtained numerically. Obviously, there is a high scatter. The expression of k_w is calibrated in order to obtained safe-sided lower bound strength predictions. Anyhow, it can be observed that the factor k_w only varies between 0,7 and 0,5. Moreover, Glitsch recommends the use of his proposal only if the ratio B_{Ed}/B_{Rk} is less than 0,5. Consequently, the factor k_w varies only in the range of 10% to 15% and hence, the need to introduce a purely empirical factor that varies this slightly is not obvious here.

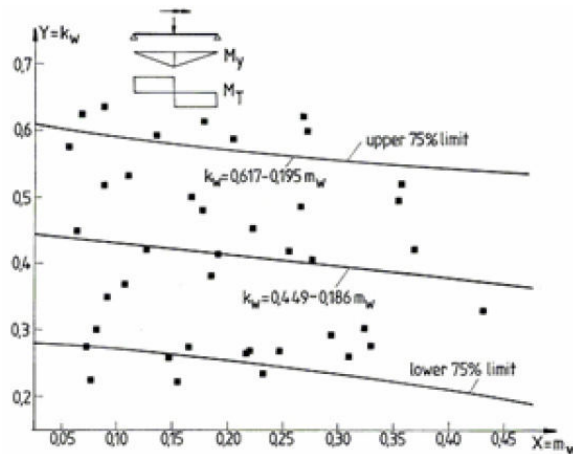


Figure 5-83 : Calibration of the factor k_w – Figure taken from reference (Glitsch 2008)

5.4.5 Design rule proposed at Eindhoven University of Technology

In 1999 and 2007 two research reports concerning lateral-torsional buckling of U-shaped members subject to major-axis bending and torsion were published at Eindhoven University of Technology ((La Poutrée 1999) and (De Louw 2007)). In order to conclude on a design rule four experimental and approximately 350 numerical tests were conducted. Finally, both projects propose a design formula introducing the effect of torsion by a modified relative slenderness for lateral-torsional buckling. A similar approach has been proposed by (Kindmann et al. 2002). However, it is based on lateral-torsional buckling curve of DIN 18800-2 (DIN 1990). As these three approaches are similar, only the most recent proposition published in references (De Louw 2007) and (Snijder et al. 2008) is presented in the following. The proposed design approach is given Eqs. (5.83) to (5.88).

$$\frac{M_{y,Ed}}{\chi_{LT} \frac{M_{y,Rk}}{\gamma_{M,1}}} \leq 1,0 \quad (5.83)$$

$$\chi_{LT} = \frac{1}{\phi_{LT} + \sqrt{\phi_{LT}^2 + \bar{\lambda}_{MT}^2}} \quad (5.84)$$

$$\phi_{LT} = 0,5 \left(1 + 0,21 \left(\bar{\lambda}_{MT} - 0,2 \right) + \bar{\lambda}_{MT}^2 \right) \quad (5.85)$$

$$\bar{\lambda}_{MT} = \bar{\lambda}_{LT} + \bar{\lambda}_T \quad (5.86)$$

$$\bar{\lambda}_T = 1 - \bar{\lambda}_{LT} \quad \text{if: } 0,5 \leq \bar{\lambda}_{LT} < 0,8$$

$$\bar{\lambda}_T = 0,43 - 0,29 \bar{\lambda}_{LT} \quad \text{if } 0,8 \leq \bar{\lambda}_{LT} < 1,5 \quad (5.87)$$

$$\bar{\lambda}_T = 0 \quad \text{if } 1,5 \leq \bar{\lambda}_{LT}$$

$$\bar{\lambda}_{LT} = \sqrt{\frac{M_{y,Rk}}{M_{y,cr}}} \quad (5.88)$$

where:

$\bar{\lambda}_{MT}$: is the ideal relative slenderness accounting for the influence of torsion on lateral-torsional buckling

$\bar{\lambda}_T$: is the ideal relative slenderness accounting for torsion

For a better understanding of the method, the buckling curve resulting from the design proposal is shown in Figure 5-84.

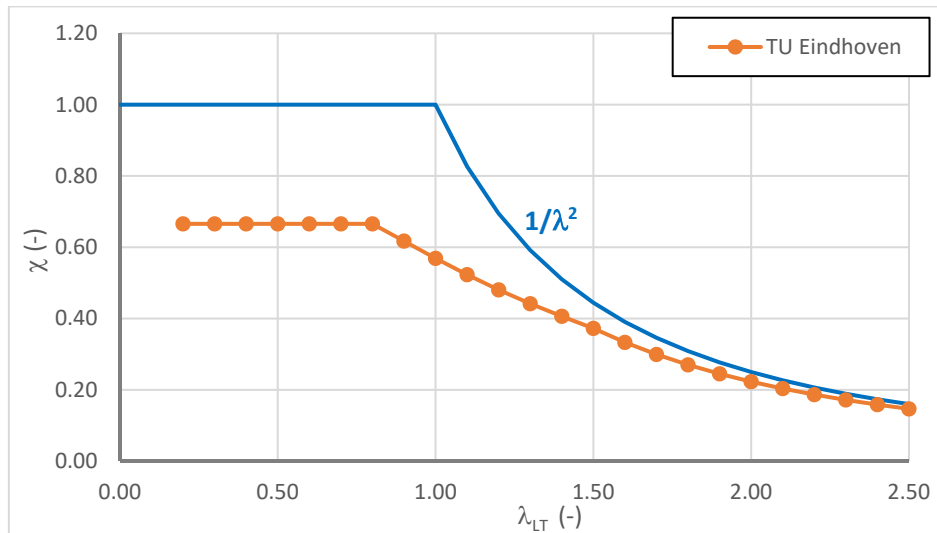


Figure 5-84 : Reduction curve for lateral-torsional buckling of channel section

Figure 5-84 clearly shows the plateau of the reduction factor up to a relative slenderness of 0,8. The corresponding reduction factor is equal to 0,67. For high slendernesses exceeding 1,5 the reduction of the lateral-torsional buckling resistance due to torsion may be neglected.

In (De Louw 2007), the plateau value of 0,67 for the reduction factor is explained on the basis of the GMNIA numerical results. Figure 5-85 presents the example of a member of UPE 80 section subject to a uniformly distributed load applied in the plane of the web at the upper flange.

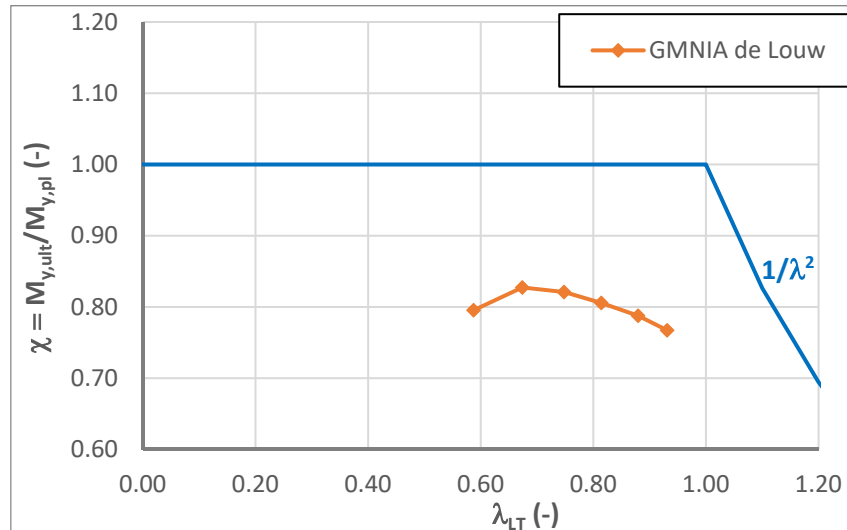


Figure 5-85 : Reduction factor calculated with the reference to bending moment resistance of the section

It seems that the reduction factor does not approach a value of 1,0 for small values of the relative slenderness. It even decreases after passing through a maximum value of approximately 0,83 for a relative slenderness of 0,67. However, this behaviour can be easily explained by the fact that de Louw proposes to apply the reduction factor to the bending moment only. Obviously, the reduction factor cannot tend to 1 for zero slenderness (representing the case of cross-section resistance) in this situation as the bi-moment (and minor-axis bending due to torsional rotation)

is not included explicitly. Moreover, in case of variable bending, the shear force may also cause the failure of the member. Besides the restricted domain of application, the fixed plateau value for the reduction factor is a clear disadvantage of de Louw's proposal as it may lead to highly conservative results for small slendernesses, especially in cases where only a small amount of torsion is applied.

It may be recalled that global design approaches as OIC refer the reduction factor to the cross-sectional resistance under combined loading. If this is done for the present case, the reduction factor χ should tend to 1,0 (cross-section resistance) for short members as shown in Figure 5-86 (curve "GMNIA global") for the example of the UPE 80 member of Figure 5-85. This figure also represents the results of de Louw with reference to the plastic bending moment resistance $M_{y,pl}$.

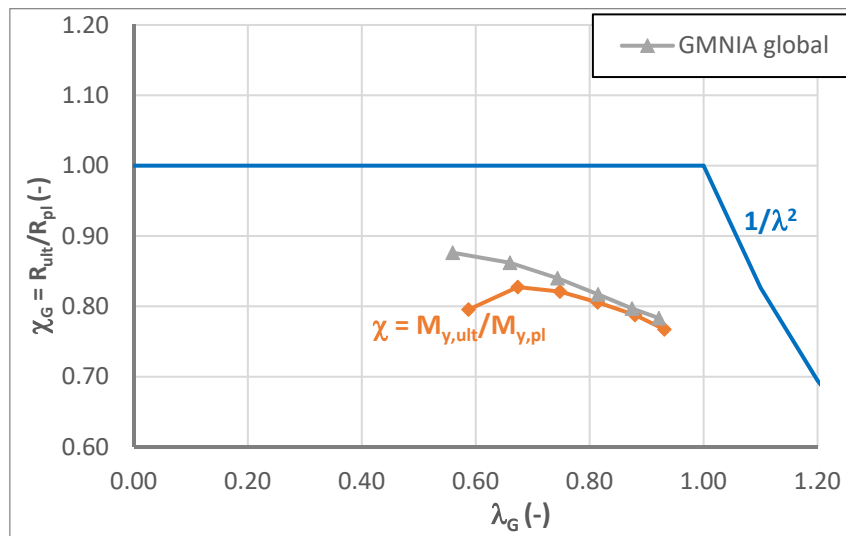


Figure 5-86 : Reduction factor calculated with the reference to bending moment resistance of the section and global section resistance

The grey curve of Figure 5-86 is obtained by the application of Eqs. (5.89) and (5.90) to the numerical results obtained by de Louw.

$$\bar{\lambda}_G = \sqrt{\frac{R_{pl}}{R_{cr,G}}} \quad (5.89)$$

$$\chi_G = \frac{R_{ult,GMNIA}}{R_{pl}} \quad (5.90)$$

The section resistance is calculated numerically with the adapted PIFM considering the full plastic limit state (based on first order internal forces and moments). Yet, it should be kept in mind that the formation of the plastic warping hinge (see Chapter 4) somewhat disturbs the theoretical approach as the bi-moment does not increase proportionally with the major-axis bending moment. Consequently, the ultimate resistance curve linked to "GMNIA Global" does not seem to tend to unity for zero slenderness neither. This problematic is not treated further on in this paragraph. Rather, it is addressed in paragraph 5.6.5 when the possibility of OIC based design is studied for members under torsion.

Nevertheless, Figure 5-87, representing the totality of the GMNIA results used in reference (De Louw 2007), shows that a reduction curve based on the principles of a global concept can be appropriate for the design of members subject to a combination of internal forces, in the present case major-axis bending and bi-moments.

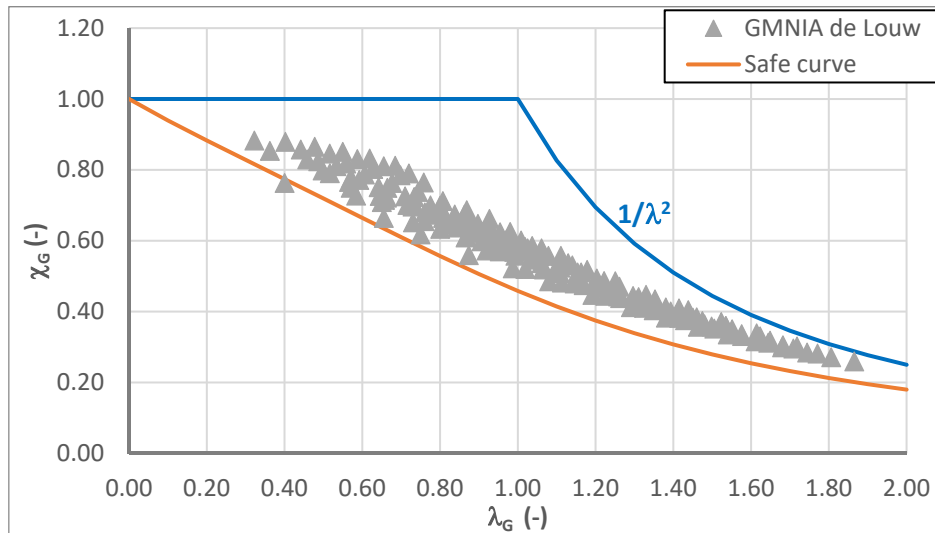


Figure 5-87: Introduction of a global reduction curve for U-shaped members

The “safe curve” represented in Figure 5-87 is defined in Eqs. (5.91) and (5.92). This simple design expressions yields results that capture the tendencies of the GMNIA calculations well. Compared to the reduction curves for flexural and lateral-torsional buckling, the proposed “safe curve” does not include a plateau for a small relative slenderness. Additionally, it is clear that the natural scatter of the results due to the complex configuration of a mono-symmetric section under combined bending and torsion cannot be covered precisely. Anyhow, it is obvious that with one single expression containing only two parameters, i.e R_{pl} and $R_{cr,G}$ the complexity of the load case cannot be treated in detail.

$$\phi = 0,5 \left(1 + 0,64(\bar{\lambda}_G) + \bar{\lambda}_G^2 \right) \quad (5.91)$$

$$\chi_G = \frac{1}{\phi + \sqrt{\phi^2 - \bar{\lambda}_G^2}} \quad (5.92)$$

Nonetheless, Eqs. (5.91) and (5.92) should not be understood as design proposal but as an indication that a global concept can lead to satisfactory strength prediction. Consequently, global methods seem worth to be studied in more detail also for complex load cases. However, it should also be noted that the case studied here does not include many parameters. Indeed, only U-shaped members are addressed. Additionally, torsion is introduced by a vertical load applied through the web of the member. This is obviously of practical interest. Yet, the importance of the torsional moment is directly linked to the major-axis bending moment and, due to the small eccentricity

between the shear centre and the applied load, it is rather low. If the torsional moment is introduced independently from major-axis bending, the design curve would not be applicable anymore. So as to propose a more general design approach the influence of the torsional moment should certainly be accounted for (see paragraph 5.6).

5.4.6 Summary of the proposals and comparison to physical tests

Table 5-13 presents a summary of the proposals discussed here before. It is clear that the majority of the approaches consist in interaction formulae. As shown in the corresponding paragraphs, their main difference is the form of the cross-section interaction (linear or non-linear). On the contrary, TU Eindhoven proposes a simplified and conservative method that consists in modifying the lateral-torsional buckling (ltb) slenderness of the member to account for the influence of torsion. However, due to its calibration it is the most restrictive method.

Table 5-13: Summary of the proposal presented in paragraph 5.4

Proposal (Reference)	Form	Domain of application	
		Form of the section	Load case
BSI and Nethercott (Nethercott et al. 1989)	linear interaction formula	I and U sections	M_y, M_z, M_T
Aachen I (FOSTA 2004)	linear interaction formula	I sections	N, M_y, M_z, M_T
Aachen II (Stangenberg 2007)	non-linear interaction formula	I and U sections	N (for I sections), $M_y,$ M_z, M_T
Aachen III (Naumes 2009)	linear interaction formula	I and U sections	N, M_y, M_z, M_T
Berlin (Glitsch 2008)	linear interaction formula	I sections	M_y, M_z, M_T
Eindhoven (de Louw 2007)	modified relative ltb slenderness	U sections	M_y, M_T – loads applied in the web plane

In order to facilitate the evaluation of the methods, it is proposed to compare them to physical tests. In the literature only a limited number of tests on members subject to a combination of flexure, axial force and torsion can be found. The following comparisons are based on the tests performed during the research project P554 (FOSTA 2004). The physical tests are summarized in Table 5-14. More details on the load introduction, support conditions and realisation of the tests are given in (FOSTA 2004) and Chapter 3 addressing the numerical model used in the framework of this thesis.

Table 5-14: Physical tests performed in the framework of research project P554

Name of the test	Cross-section	Member length (cm)	Load case
BE-1-1	IPE 200	280	M_y+M_T
BE-1-21	IPE 200	280	$M_y+ M_z+M_T$
BE-1-22	IPE 200	280	$M_y+ M_z+M_T$
BE-1-3	IPE 200	280	$M_y+ M_z+M_T$
BE-1-4	IPE 200	400	M_y+M_T
BE-1-51	IPE 200	400	$M_y+ M_z+M_T$
BE-1-52	IPE 200	400	$M_y+ M_z+M_T$
BE-1-6	IPE 200	400	$M_y+ M_z+M_T$
BE-2-1	HEB 200	400	M_y+M_T
BE-2-21	HEB 200	400	$M_y+ M_z+M_T$
BE-2-22	HEB 200	400	$M_y+ M_z+M_T$
BE-2-3	HEB 200	400	$M_y+ M_z+M_T$
BE-2-4	HEB 200	560	M_y+M_T
BE-2-51	HEB 200	560	$M_y+ M_z+M_T$
BE-2-52	HEB 200	560	$M_y+ M_z+M_T$
BE-2-6	HEB 200	560	$M_y+ M_z+M_T$
BE-3-1	UPE 200	280	M_y+M_T
BE-3-21	UPE 200	280	M_y+M_T
BE-3-22	UPE 200	280	M_y+M_T
BE-3-3	UPE 200	400	M_y+M_T
BE-3-41	UPE 200	400	M_y+M_T
BE-3-42	UPE 200	400	M_y+M_T
BO-I-1	UPE 200	400	M_y+N+M_T
BO-I-2	UPE 200	400	M_y+N+M_T
BO-I-3	UPE 200	400	M_y+N+M_T
BO-I-4	UPE 200	400	M_y+N+M_T
BO-I-5	UPE 200	600	M_y+N+M_T
BO-I-6	UPE 200	600	M_y+N+M_T
BO-I-7	UPE 200	600	M_y+N+M_T
BO-I-8	UPE 200	600	M_y+N+M_T
BO-II-1	HEB 200	500	M_y+N+M_T
BO-II-1a	HEB 200	500	M_y+N+M_T
BO-II-2	HEB 200	500	M_y+N+M_T
BO-II-3	HEB 200	800	M_y+N+M_T
BO-II-4	HEB 200	800	M_y+N+M_T
BO-II-5	HEB 200	500	M_z+N+M_T
BO-II-6	HEB 200	500	M_z+N+M_T
BO-II-7	HEB 200	800	M_z+N+M_T
BO-II-8	HEB 200	800	M_z+N+M_T

It is recalled that most of the presented methods are limited in their field of application. Nevertheless, it is interesting to evaluate the proposed design methods outside the initial field of application in order to judge whether an extension may be envisaged. The results of the comparisons are given in Table 5-15. In this table the light green background colour indicates that the evaluated physical tests lie in the field of application of the method. Conversely, the orange background colour shows that the physical test is out of scope of the method. In order to apply the methods outside their initial field of applications the following extensions are introduced:

- Aachen I and Aachen III: extension to U sections without any modification of the method.
- Aachen II: extension to U sections with compression without any modification of the method.
- Berlin : extension to the case of compression axial force by applying the Eurocode 3 interaction criteria (6.61 and 6.62) and Eurocode 3 Annexe B for the determination of the interaction coefficients.
- Eindhoven: extensions to I sections without any modification and extension to applied compression axial force and minor-axis bending by applying the Eurocode 3 interaction criteria (6.61 and 6.62) and Eurocode 3 Annexe B for the determination of the interaction coefficients.

Also, it should be recalled that the proposal Aachen I introduces the influence of an axial force to the major-axis bending resistance. Therefore, it cannot be modified to members subject to an axial force but not subject to major-axis bending. As the proposal BSI/Nethercott is based on the interaction formula provided in the former British standard and not based on the principles of Eurocode 3, no extension to the case of axial compression is applied.

Last, it has to be recalled that the proposals Aachen II and Aachen III use coefficients that are not literally defined. These coefficients are set to 1,0 for the comparison. This is surely representative of what would be done in the practice if no other information is available.

Table 5-15: Comparison of test results and proposed methods

Name of the test	BSI $R_{ultBSI}/R_{ultTest}$	Aachen I $R_{ultAaI}/R_{ultTest}$	Aachen II $R_{ultAaII}/R_{ultTest}$	Aachen III $R_{ultAaIII}/R_{ultTest}$	Berlin $R_{ultBer}/R_{ultTest}$	Eindhoven $R_{ultEind}/R_{ultTest}$
BE-1-1	0,730	0,937	0,969	0,969	0,908	1,208
BE-1-21	0,532	0,694	0,850	0,682	0,829	0,960
BE-1-22	0,496	0,657	0,811	0,650	0,801	0,941
BE-1-3	0,372	0,442	0,589	0,405	0,482	0,487
BE-1-4	0,789	0,939	0,931	0,978	0,896	1,105
BE-1-51	0,562	0,703	0,793	0,695	0,775	0,874
BE-1-52	0,565	0,707	0,797	0,698	0,779	0,879
BE-1-6	0,395	0,464	0,592	0,421	0,474	0,480
BE-2-1	0,582	0,853	0,863	0,848	0,866	0,905
BE-2-21	0,522	0,818	0,889	0,759	0,894	0,902
BE-2-22	0,513	0,804	0,874	0,746	0,879	0,886
BE-2-3	0,330	0,584	0,600	0,496	0,585	0,606
BE-2-4	0,620	0,852	0,829	0,858	0,850	0,875
BE-2-51	0,520	0,776	0,803	0,718	0,814	0,814
BE-2-52	0,391	0,634	0,659	0,603	0,696	0,729
BE-2-6	0,390	0,632	0,656	0,601	0,693	0,727
BE-3-1	0,358	0,579	0,507	0,574	0,548	1,192
BE-3-21	0,376	0,573	0,488	0,566	0,511	1,001
BE-3-22	0,359	0,535	0,453	0,529	0,470	0,893
BE-3-3	0,415	0,596	0,483	0,601	0,513	0,922
BE-3-41	0,397	0,560	0,453	0,564	0,490	0,839
BE-3-42	0,375	0,564	0,460	0,570	0,499	0,952
BO-I-1	n.a.	0,532	0,431	0,523	0,468	0,781
BO-I-2	n.a.	0,594	0,477	0,581	0,541	0,977
BO-I-3	n.a.	0,545	0,672	0,481	0,524	0,712
BO-I-4	n.a.	0,625	0,725	0,545	0,604	0,869
BO-I-5	n.a.	0,569	0,461	0,584	0,494	0,758
BO-I-6	n.a.	0,577	0,453	0,590	0,507	0,824
BO-I-7	n.a.	0,585	0,586	0,596	0,546	0,767
BO-I-8	n.a.	0,602	0,566	0,599	0,559	0,840
BO-II-1	n.a.	1,059	0,997	1,001	1,057	1,113
BO-II-1a	n.a.	1,043	0,905	0,934	1,003	1,047
BO-II-2	n.a.	1,031	0,824	0,879	0,964	0,997
BO-II-3	n.a.	0,938	0,797	0,892	0,915	0,935
BO-II-4	n.a.	0,940	0,593	0,772	0,905	0,900
BO-II-5	n.a.	n.a.	1,050	0,799	0,944	0,986
BO-II-6	n.a.	n.a.	0,917	0,761	0,846	0,886
BO-II-7	n.a.	n.a.	1,040	0,843	0,942	0,972
BO-II-8	n.a.	n.a.	1,066	0,802	0,894	0,923
Maximum	0,789	1,059	1,066	1,001	1,057	1,208
Minimum	0,330	0,442	0,431	0,405	0,468	0,480
Mean value	0,481	0,701	0,716	0,685	0,723	0,884
Standard deviation	0,125	0,175	0,198	0,159	0,190	0,156

Regarding Table 5-15, it may again be observed that the proposal “Eindhoven” is the most restrictive one. However, in combination with the Eurocode 3 interaction formulae, it yields rather satisfactory results. In fact, the mean value and the standard deviation of the results are clearly better than for the other proposals. Since, this proposal is the simplest one, this observation is even more remarkable. Nevertheless, in some cases, outside its initial range of application, the proposal may be too unsafe. Especially in case of torsional loads higher than the ones used to calibrate the method, as for the tests BE-1-1 (IPE 200 – point load applied at the mid of one flanges cantilever), BE-1-3 (as BE-1-1), BE-3-1 (UPE 200 – point load applied on the flange through the gravity centre of the section), BO-II-1 (HEB 200 – point load applied at one flange’s tip) and BO-II-2 (as BO-II-1), the proposal yields to optimistic values. Conversely, if the member is subject to bi-axial bending and torsion with high proportion of minor-axis bending, the modified proposal is very conservative (BE-1-3, BE-1-6). This last observation is also true for the other proposals.

The proposal “BSI/Nethercott” is also rather simple to apply. However, one may observe that most of the results are very conservative. This is certainly due to the limitation to the elastic resistance for the effects of torsion (stresses created by indirect minor-axis bending and the bi-moment). Also, it has been shown in paragraph 5.4.2 that the interaction factor considering the interaction between bending and torsion is rather conservative.

The proposal “Berlin” currently adopted in Eurocode 3 Part 6 (CEN 2007b) yields rather satisfactory results in its initial field of application. As mentioned the proposal seems however to be highly conservative in case of combination between major-axis bending, high minor-axis bending and torsion (tests BE-1-3 and BE-1-6). Additionally, the proposal seems to be very conservative in case of U sections (BE-3-x and BO-I-x). This is most likely due to the form of interaction between the internal forces. Obviously, the mono-symmetry of U sections leads to a more complex interaction behaviour as shown in Chapter 4 presenting the study on the plastic cross-section resistance. In order to account for this complexity in more detail, proposal Aachen II introduces a specific interaction formula for U sections. Consequently, the results are slightly closer to the tests for U sections. However, the difference is only of about 10%. This also indicates that the simplified cross-section interaction formulae do not fully account for the complex interaction behaviour of U sections. For I sections, the proposal Aachen II yields rather satisfactory and safe-sided results certainly due to the consistent mechanical background. Yet, in case of combined minor-axis bending, axial force and torsion (tests BO-II-5 – BO-II-8) the proposal seems to lead to too optimistic values. Here, the exact determination of the (non-literally defined) interaction factors may lead to an amelioration. Nonetheless, for practical engineers, the determination of these interaction coefficients is impossible due to the lack of literal expressions. The method “Aachen I” yields in most cases similar results as the proposal “Aachen II” despite of the inconsistencies discussed in paragraph 5.4.3.2. As for the proposals “Berlin” and “Aachen II”, the proposal “Aachen I” is very conservative for U sections. Conversely, in case of I sections subject to combined axial force, major-axis bending and torsion, proposal “Aachen I” may be slightly too

favourable, especially for short members (member length = 5 m for tests BO-II-1 – BO-II-2 and 8 m for BO-II-3 and BO-II-4).

Last, it is interesting to discuss method Aachen III. It can be seen that all results are safe-sided, accepted for the case BO-II-1 that is (very) slightly un-conservative. As for the other proposals provided by the researches from RWTH Aachen and the proposal “Berlin”, the method is very conservative for U sections. Again, the form of the cross-section interaction may be contested. Also, in presence of combined major-and high minor-axis bending the proposal seems to be too conservative (tests BE-1-3 and BE-1-6). Nevertheless, this proposal leads in general to satisfactory results, as reflected by the standard deviation of 0,159. Yet, the results are in the majority of cases very safe-sided. The safe-sided nature of the proposal may be explained by the fact that the interaction factor for the bi-moment is always taken to one. This is certainly very conservative for most cases. Also, it should be noted that none of the tested U-shaped members failed in a flexural-torsional buckling mode that is not considered in approach Aachen III. Yet, the high conservatism of the approach observed for U-shaped members may cover the conceptual problems.

The results may be summarized as follows:

- The proposal calibrated for I sections (all except Eindhoven) are very conservative for U sections;
- Proposals Aachen I, Aachen II and Berlin yield very similar, mostly very safe-sided, results;
- Proposal BSI/Nethercott is too safe-sided and yields non-economic results due to the limitation to elastic resistance for the effects of torsion;
- Proposal Aachen III yields satisfactory results, especially for I sections;
- Proposal Eindhoven combined with the Eurocode 3 Part 1-1 interaction formulae yields the most economic results. Yet, in some cases, outside its initial scope, the method may be too unsafe as the influence of the relative importance of torsion is not considered directly.

Finally, it should be noted that the results obtained in physical tests always contain a certain amount of incertitude partially explaining the scatter of the resistances predicted by the design models. It should also be recalled that U-shaped members currently lie outside of the scope of the Eurocode 3 interaction formulae. Therefore, the extension of certain methods to U sections subject to axial force by applying these interaction formulae is certainly discussable. However, this extension has been performed here for comparison.

5.4.7 Conclusion

The present paragraph has given a review of design methods proposed for the verification of the stability behaviour of members made of open cross-sections subject to a combination of internal forces and moments including torsion. Most of the design proposals are based on simplified interaction of quasi analytically determined 2nd order internal forces (the second order internal forces are analytically determined for a reference load case and empirical parameters are introduced to account for differences to other load cases). The differences in these interaction formulae are mainly due to the factors accounting for second order effects, especially on minor-axis bending and the bi-moment. It has been shown in the previous paragraph that these interaction formulae might be very conservative for U-shaped members.

A different approach has been used at TU Eindhoven for U sections subject to vertical loads applied in the plane of the web. It is proposed to modify the relative lateral-torsional buckling slenderness empirically to account for the effect of torsion. By comparison to physical tests, it has been shown that this method might be introduced to the Eurocode 3 interaction formulae. However, in this case some modifications should be included in order to account for the form of the cross-section and the relative importance of torsion (bi-moment) on the cross-section resistance. It is recalled that the method has only been calibrated for U-shaped members subject to a uniformly distributed load or a point load applied through the web. Also, it is recalled that this method may be highly conservative for short member due to the plateau value for the reduction factor χ_{LT} of 0,67. As the influence of torsion is exclusively accounted for by increasing the relative slenderness for lateral-torsional buckling, this method cannot be applied to members without major-axis bending.

In the following paragraphs the theoretical basis necessary to develop the simplified design approach is presented. In particular, the elastic critical loads and the elastic second order equilibrium is of interest. This theoretical study is performed in order to get more insights into the behaviour of members under complex combination of internal forces and moments.

5.5 Analytical solutions

5.5.1 General

Paragraphs 5.3 and 5.4 gave a review of existing provisions for the design of members subject to a complex load combination including applied torsion. Several times, it has been made reference to analytically derived second order internal forces and moments in order to highlight the development of the proposed design approaches. Consequently, it seems of interest to dedicate the following section to the theoretical analysis of members with open sections subject to complex load combinations. After the recall of the theoretical basis necessary for the following developments in paragraphs 5.5.2 to 5.5.4, paragraphs 5.5.5 and 5.5.6 address the problem of elastic member instability and finally paragraph 5.5.7 concerns the second order equilibrium of the member. Admittedly, the analytical solutions cannot directly be transposed as design model for steel members as these always experience at least partial yielding even if the section is slender. Moreover, it is shown in the following that analytical solutions can only be obtained based on some key assumptions especially concerning the deformed shape of the member and that these key assumptions are contradictory in some cases. Therefore, the analytical solutions diverge in any case from the real behaviour of the member. Nevertheless, the theoretically derived results give relevant information about the parameters influencing the second order effects and member instability. Additionally, when the analytical solutions are compared to existing design models, it can be highlighted which effects are already covered and which effects have to be included in order to extend them to more complex cases.

5.5.2 Assumptions

In the framework of the theoretical study, the following assumptions are considered:

- The material is homogenous and isotropic.
- The material behaves linearly elastic (in this paragraph only elastic instability and elastic second order equilibrium is of interest).
- The cross-section is rigid and not prone to local instability or distortion.
- The cross-section is constant along the member.
- The cross-sections of the deformed member stays plane (warping is accepted).

5.5.3 System of axis and kinematics

It is recalled that the developments presented in this thesis are based on the system of axis shown in Figure 5-88.

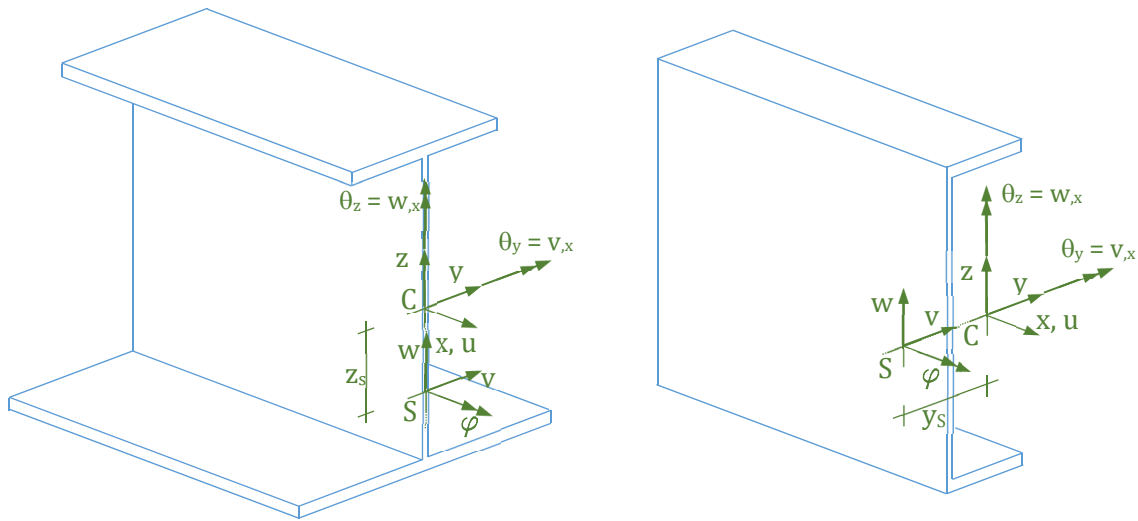


Figure 5-88: Reference system

Also, it is recalled that positive bending moments and a positive bi-moment generate compression axial stresses for positive ordinates y and z , i.e. at the right tip of the upper flange (and at the left tip of the lower flange for the bi-moment). Consequently, the positive moments are oriented as shown in Figure 5-89. It is to be noted that tension stresses are defined as positive. In order to respect common convention compression axial force is considered to be positive.

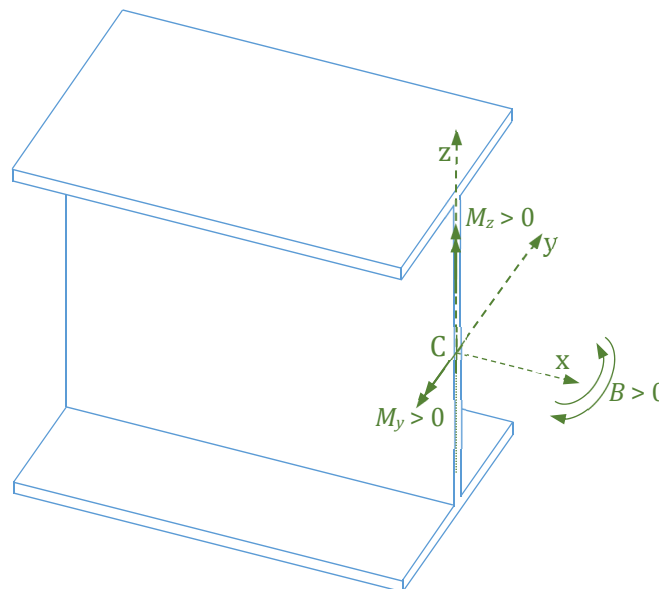


Figure 5-89: Definition of positive internal moments

As can be seen in Figure 5-88, it is supposed that the torsional twist acts about the shear centre. Consequently, the displacements of an arbitrary point of the cross-section can be determined with Eq. (5.93).

$$\begin{aligned}
 U(x) &= u - y(v_{,x} \cos(\varphi) + w_{,x} \sin(\varphi)) - z(w_{,x} \cos(\varphi) - v_{,x} \sin(\varphi)) - \omega \varphi_{,x} \\
 V(x) &= v - (z - z_S) \sin(\varphi) - (y - y_S)(1 - \cos(\varphi)) \\
 W(x) &= w + (y - y_S) \sin(\varphi) - (z - z_S)(1 - \cos(\varphi))
 \end{aligned} \tag{ 5.93 }$$

If one assumes that the torsional twist is small and consequently that the trigonometric functions may be approximated by $\sin(\varphi) = \varphi$ and $\cos(\varphi) = 1$, the displacement field can be simplified to (de Ville de Goyet 1989):

$$\begin{aligned}
 U(x) &= u - y(v_{,x} + w_{,x} \varphi) - z(w_{,x} - v_{,x} \varphi) - \omega \varphi_{,x} \\
 V(x) &= v - (z - z_S) \varphi \\
 W(x) &= w + (y - y_S) \varphi
 \end{aligned} \tag{ 5.94 }$$

Generally, the displacement field given in Eq. (5.94) is simplified rather on by neglecting the higher order terms $w_{,x} \varphi$ and $v_{,x} \varphi$. It yields the linearized displacement field of Eq. (5.95).

$$\begin{aligned}
 U(x) &= u - yv_{,x} - zw_{,x} - \omega \varphi_{,x} \\
 V(x) &= v + (z - z_S) \varphi \\
 W(x) &= w - (y - y_S) \varphi
 \end{aligned} \tag{ 5.95 }$$

The choice of the displacement field may have a non-negligible influence on the equilibrium equation of the member and especially on the critical loads if pre-buckling deflections are considered (see paragraph 5.5.4.4 for more details). Hereafter, critical loads for elastic member instability as well as differential equations describing the second order equilibrium of the member are developed based on the energy method.

5.5.4 Energy method, equilibrium of the member and critical loads

5.5.4.1 General

Throughout paragraph 5.5.4 the theoretical background necessary for the development of the critical loads as well as the second order equilibrium of the member is compiled. In the first part of this paragraph the potential energy of the member is developed. Then the system of differential equations describing the second order static equilibrium is determined based on the first variation of the potential energy. Finally, paragraph 5.5.4.4 presents the determination of the second variation of the potential energy of the member that is used to develop the critical loads. In particular, it is shown that, if the influence of pre-buckling displacements is considered, many additional terms influencing the critical loads arise compared to the classical approach neglecting first order displacements.

5.5.4.2 Energy method

Hereafter, the energy method is used to determine the equilibrium of the member and the critical loads. The total potential energy of a member is the sum of the strain energy Π_i and the work of the applied loads Π_e as shown in Eq. (5.96).

$$\Pi = \Pi_i + \Pi_e = \int \int \bar{\sigma} dE dV - \int F_z W dV - \int F_y V dV - \int F_x U dV \quad (5.96)$$

In the following, it is supposed that the influence of the work of an axial force is negligible due to the high axial stiffness of steel members.

As mentioned previously, the material is supposed to be linear elastic. Therefore, the stress tensor can be expressed as a linear function of the strain tensor:

$$\bar{\sigma} = K \bar{E} \quad (5.97)$$

Hence, the strain energy is given by:

$$\Pi_i = \frac{1}{2} K \int \bar{E}^2 dV \quad (5.98)$$

The elastic strain tensor is defined by Eq. (5.99).

$$\bar{E} = \begin{bmatrix} E_{xx} & 2E_{yx} & 2E_{xz} \\ 2E_{yx} & E_{yy} & 2E_{yz} \\ 2E_{xz} & 2E_{yz} & E_{zz} \end{bmatrix} \quad (5.99)$$

In the framework of the theory of beams the strains along the y- and z-axis E_{yy} and E_{zz} and the associated shear strain in the plane y-z are neglected. Thus, the strain tensor simplifies to:

$$\bar{E} = \begin{bmatrix} E_{xx} & 2E_{yx} & 2E_{xz} \\ 2E_{yx} & 0 & 0 \\ 2E_{xz} & 0 & 0 \end{bmatrix} \quad (5.100)$$

Following theory of small strains (Cauchy strain tensor), the different components $E_{\alpha\beta}$ of the strain tensor are defined by Eq. (5.101).

$$E_{\alpha\beta} = \frac{1}{2} (R_{,\alpha}^T R_{,\beta} - r_{,\alpha}^T r_{,\beta}) \quad (5.101)$$

Here, R and r are the vectors defining the position of an arbitrary point of the undeformed member (r) and the deformed member (R). They are given in Eqs. (5.102) and (5.103).

$$r = \begin{pmatrix} x \\ y \\ z \end{pmatrix} \quad (5.102)$$

$$R = r + \begin{pmatrix} U \\ V \\ W \end{pmatrix} \quad (5.103)$$

By introducing the displacement field given in Eq. (5.94), one may express the strains as shown in Eq.(5.104).

$$\begin{aligned} E_{xx} &= u_{,x} - y(v_{,xx} + w_{,xx}\varphi) - z(w_{,xx} - v_{,xx}\varphi) - \omega\varphi_{,xx} + \frac{1}{2}(v_{,x}^2 + w_{,x}^2 + \rho^2\varphi_{,x}^2) \\ &+ z_s\varphi_{,x}v_{,x} - y_s\varphi_{,x}w_{,x} \\ 2E_{xy} &= -(z - z_s)\varphi_{,x} - \omega_{,y}\varphi_{,x} \\ 2E_{xz} &= (y - y_s)\varphi_{,x} - \omega_{,z}\varphi_{,x} \end{aligned} \quad (5.104)$$

The state of equilibrium of the member is characterized by the condition that the first variation of the potential energy of the member vanishes:

$$\begin{aligned} \delta\Pi = 0 \longrightarrow \int E\delta E_{xx}E_{xx} + 4G(\delta E_{xz}E_{xz} + \delta E_{xy}E_{xy})dVol - \int F_z\delta WdVol \\ - \int F_y\delta VdVol = 0 \end{aligned} \quad (5.105)$$

The member is in a critical state representing elastic instability if the second variation of the potential energy vanishes, too as given in Eq. (5.108).

$$\begin{aligned} \delta\delta\Pi = 0 \longrightarrow \int E(\delta^2 E_{xx}E_{xx} + (\delta E_{xx})^2)dVol \\ + \int 4G(\delta^2 E_{xz}E_{xz} + (\delta E_{xz})^2 + \delta^2 E_{xy}E_{xy} + (\delta E_{xy})^2)dVol \\ - \int F_z\delta^2 WdVol - \int F_y\delta^2 VdVol = 0 \end{aligned} \quad (5.106)$$

Both, conditions (5.105) and (5.106), are used in the following paragraphs to determine the second order equilibrium of the member and then its critical loads linked for a given load case.

5.5.4.3 *Differential equation characterizing the second order static equilibrium of the member*

The differential equation characterizing the second order equilibrium of the member may be determined based on the first variation of the total potential energy given in Eq. (5.105). Eq. (5.107) presents the first variation of the elastic strains necessary for the following developments.

$$\begin{aligned} \partial E_{xx} = & \partial u_{,xx} - y(\partial v_{,xx} + \partial w_{,xx} \varphi + w_{,xx} \partial \varphi) - z(\partial w_{,xx} - \partial v_{,xx} \varphi - v_{,xx} \partial \varphi) - \omega \partial \varphi_{,xx} \\ & + v_{,x} \partial v_{,xx} + w_{,x} \partial w_{,xx} + \left((z - z_s)^2 + (y - y_s)^2 \right) \varphi_{,x} \partial \varphi_{,xx} + z_s (\partial \varphi_{,xx} v_{,xx} + \varphi_{,xx} \partial v_{,xx}) \\ & - y_s (\partial \varphi_{,xx} w_{,xx} + \varphi_{,xx} \partial w_{,xx}) \end{aligned} \quad (5.107)$$

$$\partial E_{xy} = -\frac{1}{2} \left[(z - z_s) + \omega_{,y} \right] \partial \varphi_{,x}$$

$$\partial E_{xz} = \frac{1}{2} \left[(y - y_s) - \omega_{,z} \right] \partial \varphi_{,x}$$

In order to obtain the first variation of the total energy of the member, the variation of the lateral and vertical displacements V_F and W_F of the load application point given in Eq. (5.108) are also needed.

$$\partial W_F = \partial w + (y_F - y_S) \partial \varphi \quad (5.108)$$

$$\partial V_F = \partial v - (z_F - z_S) \partial \varphi$$

Eqs. (5.107) and (5.108) are introduced in the expression of the first variation of the total potential energy of the member as shown in Eq. (5.109).

$$\begin{aligned} \partial \Pi = & \int_x \left[-N \partial u_{,xx} - N v_{,x} \partial v_{,xx} - N w_{,x} \partial w_{,xx} - N r_{yz}^2 \varphi_{,x} \partial \varphi_{,xx} \right. \\ & \left. - N z_s (\partial \varphi_{,xx} v_{,xx} + \varphi_{,xx} \partial v_{,xx}) - N y_s (\partial \varphi_{,xx} w_{,xx} + \varphi_{,xx} \partial w_{,xx}) \right] dx \\ & + \int_x \left[M_y (\partial w_{,xx} - \partial v_{,xx} \varphi - v_{,xx} \partial \varphi) - 2 M_z \beta_y^2 \varphi_{,x} \partial \varphi_{,xx} \right] dx \\ & + \int_x \left[M_z (\partial v_{,xx} + \partial w_{,xx} \varphi + w_{,xx} \partial \varphi) - 2 M_z \beta_y^2 \varphi_{,x} \partial \varphi_{,xx} \right] dx \quad (5.109) \\ & + \int_x B \partial \varphi_{,xx} dx + \int_x G I_t \partial \varphi_{,xx} dx - \int_x F_z [\partial w + (y_F - y_S)] \partial \varphi dx \\ & - \int_x F_y [\partial v - (z_F - z_S)] \partial \varphi dx \end{aligned}$$

The system of differential equations describing the static equilibrium of the member is determined by integrating Eq. (5.109) has to be integrated by parts so that the terms in the integral are only linked to first variations of the displacement functions u, v, w, φ (and not to their derivatives as in Eq. (5.109)). The detail is omitted again. The result is given directly in Eq. (5.110).

$$\begin{aligned}
 \delta\Pi = & \int_x \left[+ N_{,x} \delta u + (Nv_{,x})_{,x} \delta v + (Nw_{,x})_{,x} \delta w + (Nr_{yz}^2 \varphi_{,x})_{,x} \delta \varphi \right. \\
 & \left. + (Nz_s v_{,x})_{,x} \delta \varphi + (Nz_s \varphi_{,x})_{,x} \delta v - (Ny_s w_{,x})_{,x} \delta \varphi - (Ny_s \varphi_{,x})_{,x} \delta w \right] dx \\
 & + \int_x \left[M_{y,xx} \delta w - (M_y \varphi)_{,xx} \delta v - M_y v_{,xx} \delta \varphi + 2\beta_z (M_y \varphi_{,x})_{,x} \delta \varphi \right] dx \\
 & + \int_x \left[M_{z,xx} \delta v + (M_z \varphi)_{,xx} \delta w + M_z w_{,xx} \delta \varphi + 2\beta_y (M_z \varphi_{,x})_{,x} \delta \varphi \right] dx \\
 & + \int_x B_{,xx} \delta \varphi dx - \int_x (GI_t \varphi_{,x})_{,x} \delta \varphi dx \\
 & - \int_x q_z [\delta w + (y_F - y_S) \delta \varphi] dx - \int_x q_y [\delta v - (z_F - z_S) \delta \varphi] dx \\
 & - N \delta u|_0^L - Nv_{,x} \delta v|_0^L - Nw_{,x} \delta w|_0^L - Nr_{yz} \varphi_{,x} \delta \varphi|_0^L - Nz_s v_{,x} \delta \varphi|_0^L - Nz_s \varphi_{,x} \delta v|_0^L \\
 & + Ny_s w_{,x} \delta \varphi|_0^L - Ny_s w_{,x} \delta v|_0^L + M_y \delta w_{,x}|_0^L - M_{y,x} \delta w|_0^L - M_y \varphi \delta v_{,x}|_0^L + (M_y \varphi)_{,x} \delta v|_0^L \\
 & - 2\beta_z M_y \varphi_{,x} \delta \varphi|_0^L + M_z \delta v_{,x}|_0^L - M_{z,x} \delta v|_0^L + M_z \varphi \delta w_{,x}|_0^L + (M_z \varphi)_{,x} \delta w|_0^L \\
 & - 2\beta_y M_z \varphi_{,x} \delta \varphi|_0^L + B \delta \varphi_{,x}|_0^L - B_{,x} \delta \varphi|_0^L + GI_t \varphi_{,x} \delta \varphi|_0^L
 \end{aligned} \tag{5.110}$$

The same result has been obtained for example in reference (de Ville de Goyet 1989). The system of differential equations is now obtained by considering that the terms linked to the variations of the displacement functions vanish in the integrals. The terms outside the integral represent the boundary conditions. The resulting system of differential equations is given in Eqs. (5.111) to (5.114).

$$[N_{,x}] \delta u = 0 \tag{5.111}$$

$$[(Nw_{,x})_{,x} - (Ny_s \varphi_{,x})_{,x} + M_{y,xx} + (M_z \varphi)_{,xx} - q_z] \delta w = 0 \tag{5.112}$$

$$[(Nv_{,x})_{,x} + (Nz_s \varphi_{,x})_{,x} + M_{z,xx} - (M_y \varphi)_{,xx} - q_y] \delta v = 0 \tag{5.113}$$

$$\left[\begin{aligned}
 & (Nr_{yz}^2 \varphi_{,x})_{,x} + (Nz_s v_{,x})_{,x} - (Ny_s w_{,x})_{,x} - M_y v_{,xx} + 2\beta_z (M_y \varphi_{,x})_{,x} \\
 & M_z w_{,xx} + 2\beta_y (M_z \varphi_{,x})_{,x} + B_{,xx} - GI_t \varphi_{,xx} - q_z (y_F - y_S) + q_y (z_F - z_S)
 \end{aligned} \right] \delta \varphi = 0 \tag{5.114}$$

Hereafter, it is considered that the axial force is constant along the member length. Consequently, Eq. (5.111) may be omitted hereafter. Also, the definition of the internal moments given in (5.115) to (5.117) may be introduced into the system of differential equations. By doing so, the system used in paragraph 5.5.7 is obtained as shown in Eqs. (5.118) to (5.120).

$$M_y = EI_y w_{,xx} \tag{5.115}$$

$$M_z = EI_z v_{,xx} \quad (5.116)$$

$$B = -EI_w \varphi_{,xx} \quad (5.117)$$

$$EI_y w_{,xxxx} + (M_z \varphi)_{,xx} + N w_{,xx} - N y_s \varphi_{,xx} = q_z \quad (5.118)$$

$$EI_z v_{,xxxx} - (M_y \varphi)_{,xx} + N v_{,xx} + N z_s \varphi_{,xx} = q_y \quad (5.119)$$

$$\begin{aligned} N r_{yz}^2 \varphi_{,xx} + N z_s v_{,xx} - N y_s w_{,xx} - M_y v_{,xx} + 2\beta_z (M_y \varphi_{,x})_{,x} \\ M_z w_{,xx} + 2\beta_y (M_z \varphi_{,x})_{,x} + EI_w \varphi_{w,xxxx} - GI_t \varphi_{,xx} = q_z (y_F - y_S) - q_y (z_F - z_S) = m_x \end{aligned} \quad (5.120)$$

5.5.4.4 Elastic stability and state of indifferent equilibrium

In order to obtain the elastic critical loads it is necessary to determine the second variation of the total potential energy of the member. So as to facilitate the lecture of the development, the expression of the axial strain is split in two parts: $\epsilon_{xx,1}$ and $\epsilon_{xx,2}$.

$$E_{xx} = \epsilon_{xx,1} + \epsilon_{xx,2} \quad (5.121)$$

$$\epsilon_{xx,1} = u_{,x} - y(v_{,xx} + w_{,xx}\varphi) - z(w_{,xx} - v_{,xx}\varphi) - \omega\varphi_{,xx} \quad (5.122)$$

$$\epsilon_{xx,2} = \frac{1}{2}(v_{,x}^2 + w_{,x}^2 + \rho^2 \varphi_{,x}^2) + z_s \varphi_{,x} v_{,x} - y_s \varphi_{,x} \quad (5.123)$$

Eqs. (5.121) to (5.123) are introduced into the condition represented by Eq. (5.106) so as to obtain:

$$\begin{aligned} \delta^2 \Pi = \int_{Vol} E \left(\delta^2 \epsilon_{xx,1} \epsilon_{xx,1} + \delta^2 \epsilon_{xx,2} \epsilon_{xx,2} + \delta^2 \epsilon_{xx,1} \epsilon_{xx,2} + \delta^2 \epsilon_{xx,2} \epsilon_{xx,1} \right) dVol \\ + \int_{Vol} 4G \left(\delta^2 E_{xz} E_{xz} + (\delta E_{xz})^2 + \delta^2 E_{xy} E_{xy} + (\delta E_{xy})^2 \right) dVol \\ - \int_{Vol} (F_z \delta^2 W + F_y \delta^2 V + F_x \delta^2 U) dVol \end{aligned} \quad (5.124)$$

The second variations of $\epsilon_{xx,1}$ and $\epsilon_{xx,2}$ as well as the second variations of E_{xy} and E_{xz} are given in Eqs. (5.125) to (5.128).

$$\begin{aligned} \delta^2 \epsilon_{xx,1} = \delta^2 u_{,x} - y \left(\delta^2 v_{,xx} + \delta^2 w_{,xx} \varphi + 2\delta w_{,xx} \delta \varphi + w_{,xx} \delta^2 \varphi \right) \\ - z \left(\delta^2 w_{,xx} - \delta^2 v_{,xx} \varphi - 2\delta v_{,xx} \delta \varphi - v_{,xx} \delta^2 \varphi \right) - \omega \delta^2 \varphi_{,xx} \end{aligned} \quad (5.125)$$

$$\begin{aligned} \partial^2 \varepsilon_{xx,2} = & v_{,x} \partial^2 v_{,x} + (\partial v_{,x})^2 + w_{,x} \partial^2 w_{,x} + (\partial w_{,x})^2 \\ & + \left((z - z_s)^2 + (y - y_s)^2 \right) \left(\varphi_{,x} \partial^2 \varphi_{,x} + (\partial \varphi_{,x})^2 \right) \\ & + z_s \left(\partial^2 \varphi_{,x} v_{,x} + 2 \partial \varphi_{,x} \partial v_{,x} + \varphi_{,x} \partial^2 v_{,x} \right) - y_s \left(\partial^2 \varphi_{,x} w_{,x} + 2 \partial \varphi_{,x} \partial w_{,x} + \varphi_{,x} \partial^2 w_{,x} \right) \end{aligned} \quad (5.126)$$

$$\partial^2 E_{xy} = -\frac{1}{2} \left[(z - z_s) + \omega_{,y} \right] \partial^2 \varphi_{,x} \quad (5.127)$$

$$\partial^2 E_{xz} = \frac{1}{2} \left[(y - y_s) - \omega_{,z} \right] \partial^2 \varphi_{,x} \quad (5.128)$$

Hereafter, it is considered that the terms containing second variations ∂^2 are negligible compared to terms containing only first variations. Consequently, the previous equations simplify and one obtains Eqs. (5.129) to (5.132).

$$\partial^2 \varepsilon_{xx,1} = -2y \partial w_{,xx} \partial \varphi + 2z \partial v_{,xx} \partial \varphi \quad (5.129)$$

$$\partial^2 \varepsilon_{xx,2} = (\partial v_{,x})^2 + (\partial w_{,x})^2 + \left((z - z_s)^2 + (y - y_s)^2 \right) (\partial \varphi_{,x})^2 + 2z_s \partial \varphi_{,x} \partial v_{,x} - 2y_s \partial \varphi_{,x} \partial w_{,x} \quad (5.130)$$

$$\partial^2 E_{xy} = 0 \quad (5.131)$$

$$\partial^2 E_{xz} = 0 \quad (5.132)$$

Eqs. (5.129) to (5.132) as well as the expressions of the strains $\varepsilon_{xx,1}$ and $\varepsilon_{xx,2}$ are introduced into Eq. (5.124). It should be noticed that the term $(\partial \varepsilon_{xx,2})^2$ is of higher order than the other terms. Its influence is therefore neglected in the following. The expression of the second variation of the total potential energy of the member is given in Table 5-16.

Table 5-16 : Second variation of the total potential energy of the member

$\int E(\partial \varepsilon_{xx,1})^2 dVol =$	$\begin{aligned} & \int EI_y \partial w_{,xx}^2 + EI_z \partial v_{,xx}^2 + EI_w \partial \varphi_{,xx}^2 dx \\ & + \int EI_y \varphi^2 \partial v_{,xx}^2 + EI_z \varphi^2 \partial w_{,xx}^2 - 2(EI_y + EI_z) \varphi \partial v_{,xx} \partial w_{,xx} dx \\ & + \int \left(\frac{I_y}{I_z} \frac{M_z^2}{EI_z} + \frac{I_z}{I_y} \frac{M_y^2}{EI_y} + \frac{M_y^2 \varphi^2}{EI_y} + \frac{M_z^2 \varphi^2}{EI_z} + 2 \frac{M_z \varphi}{EI_z} M_y - 2 \frac{M_y \varphi}{EI_y} M_z \right) \partial \varphi^2 dx \\ & + \int \left(2M_y \varphi^2 + 2 \frac{I_y}{I_z} M_z \varphi + 2 \frac{I_z}{I_y} M_y - 2M_z \varphi \right) \partial \varphi \partial v_{,xx} dx \\ & + \int \left(-2M_z \varphi^2 + 2 \frac{I_z}{I_y} M_y \varphi - 2 \frac{I_y}{I_z} M_z - 2M_y \varphi \right) \partial \varphi \partial w_{,xx} dx \end{aligned}$
$2 \int E \partial \varepsilon_{xx,1} \partial \varepsilon_{xx,2} dVol =$	0
$\int E \partial^2 \varepsilon_{xx,1} \varepsilon_{xx,1} dVol =$	$\begin{aligned} & 2 \int \left(-M_y - M_z \varphi - \frac{I_z}{I_y} M_y \varphi^2 + \frac{I_y}{I_z} M_z \varphi \right) \partial \varphi \partial v_{,xx} dx \\ & + 2 \int \left(M_z - M_y \varphi + \frac{I_y}{I_z} M_z \varphi^2 + \frac{I_z}{I_y} M_y \varphi \right) \partial \varphi \partial w_{,xx} dx \\ & + \int \left(-\frac{M_z^2}{EI_z} - \frac{M_y^2}{EI_y} - 2 \frac{M_z M_y \varphi}{EI_y} + 2 \frac{M_z M_y \varphi}{EI_z} - \frac{I_z}{I_y} \frac{M_y^2 \varphi^2}{EI_y} - \frac{I_y}{I_z} \frac{M_z^2 \varphi^2}{EI_z} \right) \partial \varphi^2 dx \end{aligned}$
$\int E \partial^2 \varepsilon_{xx,2} \varepsilon_{xx,2} dVol =$	0
$\int E \partial^2 \varepsilon_{xx,1} \varepsilon_{xx,2} dVol =$	0
$\int E \partial^2 \varepsilon_{xx,2} \varepsilon_{xx,1} dVol =$	$\begin{aligned} & 2 \int \left(-\beta_y M_z - \beta_y \frac{I_z}{I_y} M_y \varphi - \beta_z M_y - \beta_z \frac{I_y}{I_z} M_z \varphi \right) \partial \varphi_{,x}^2 dx \\ & - \int N (\partial v_{,x}^2 + \partial w_{,x}^2 + r_{yz}^2 \partial \varphi_{,x}^2) dx \\ & - 2 \int N z_c (\partial \varphi_{,x} \partial v_{,x} + \varphi \partial \varphi_{,x} \partial w_{,x} + w_{,x} \partial \varphi \partial \varphi_{,x} + \varphi_{,x} \partial \varphi \partial w_{,x}) dx \\ & - 2 \int N y_c (-\partial \varphi_{,x} \partial w_{,x} + \varphi \partial \varphi_{,x} \partial v_{,x} + v_{,x} \partial \varphi \partial \varphi_{,x} + \varphi_{,x} \partial \varphi \partial v_{,x}) dx \end{aligned}$
$4 \int \left(\begin{array}{c} (\partial E_{xz})^2 \\ + (\partial E_{xy})^2 \end{array} \right) Vol =$	$\int GI_T \partial \varphi_{,x}^2 dx$
$- \int \left(\begin{array}{c} F_z \partial^2 W \\ + F_y \partial^2 V \end{array} \right) dVol =$	$\begin{aligned} & - \sum F_z (e_z \partial \varphi^2 - e_y \varphi \partial \varphi^2) - \sum F_y (e_y \partial \varphi^2 + e_z \varphi \partial \varphi^2) - \sum \int q_z (e_z \partial \varphi^2 - e_y \varphi \partial \varphi^2) dx \\ & - \sum \int q_y (e_y \partial \varphi^2 + e_z \varphi \partial \varphi^2) dx \end{aligned}$

If one considers that the pre-buckling displacements are negligible, the second variation of the total potential energy becomes:

$$\begin{aligned}
 \partial^2 \Pi = & \int [EI_y \partial w_{,xx}^2 + EI_z \partial v_{,xx}^2 + EI_w \partial \varphi_{,xx}^2 + GI_T \partial \varphi_{,x}^2] dx \\
 & - 2 \int [M_y \partial \varphi \partial v_{,xx} + \beta_z M_y \partial \varphi_{,x}^2] dx + 2 \int [M_z \partial \varphi \partial w_{,xx} - \beta_y M_z \partial \varphi_{,x}^2] dx \\
 & - \int N (\partial v_{,x}^2 + \partial w_{,x}^2 + r_{yz}^2 \partial \varphi_{,x}^2 + 2z_c \partial \varphi_{,x} \partial v_{,x} - 2y_c \partial \varphi_{,x} \partial w_{,x}) dx \\
 & + \sum F_z e_z \partial \varphi^2 + \sum F_y e_y \partial \varphi^2 + \sum \int q_z e_z \partial \varphi^2 dx + \sum \int q_y e_y \partial \varphi^2 dx
 \end{aligned} \tag{5.133}$$

Eq. (5.133) corresponds to the classical approach previously developed various times. It should be noted that the supplementary terms given in Table 5-16 do not appear if the development is based on the linearized displacement field of Eq. (5.95) as the coupled terms $w_{,x}\varphi$ and $v_{,x}\varphi$ are neglected.

By reorganising the terms given in Table 5-16 it is possible to highlight terms linked to the classical approach neglecting the influence of pre-buckling displacements and terms linked to pre-buckling vertical and lateral displacements and pre-buckling torsional twist as shown in Table 5-17.

It has already been stated that the elastic critical load is a key parameter to evaluate the sensitivity of a member to second order effects and to elastic instability. It is used in all current design standards to assess the member resistance. Therefore, the next paragraph is dedicated to the development of the elastic critical loads. Also, the influence of pre-buckling displacements is highlighted.

Table 5-17: Summary of the second variation of the total potential energy of the member

<p>Classical terms not linked to pre-buckling displacements</p>	$\begin{aligned} \partial\partial\Pi_1 = & \int EI_y \partial w_{,xx}^2 + EI_z \partial v_{,xx}^2 + EI_w \partial \varphi_{,xx}^2 + GI_T \partial \varphi_{,x}^2 dx \\ & - 2 \int M_y \partial \varphi \partial v_{,xx} + \beta_z M_y \partial \varphi_{,x}^2 dx + 2 \int M_z \partial \varphi \partial w_{,xx} - \beta_y M_z \partial \varphi_{,x}^2 \\ & - \int N (\partial v_{,x}^2 + \partial w_{,x}^2 + r_{yz}^2 \partial \varphi_{,x}^2 + 2z_c \partial \varphi_{,x} \partial v_{,x} - 2y_c \partial \varphi_{,x} \partial w_{,x}) dx \\ & - \sum F_z e_z \partial \varphi^2 - \sum F_y e_y \partial \varphi^2 - \sum \int q_z e_z \partial \varphi^2 dx - \sum \int q_y e_y \partial \varphi^2 dx \end{aligned}$
<p>Terms linked to pre-buckling flexure</p>	$\begin{aligned} \partial\partial\Pi_2 = & - \int \frac{M_z^2}{EI_z} \left(1 - \frac{I_y}{I_z}\right) \partial \varphi^2 - \frac{M_y^2}{EI_y} \left(1 - \frac{I_z}{I_y}\right) \partial \varphi^2 dx \\ & + \int \left(2 \frac{I_z}{I_y} M_y\right) \partial \varphi \partial v_{,xx} dx + \int \left(-2 \frac{I_y}{I_z} M_z\right) \partial \varphi \partial w_{,xx} dx \\ & - 2 \int Nz_c (w_{,x} \partial \varphi \partial \varphi_{,x}) dx - 2 \int Ny_c (v_{,x} \partial \varphi \partial \varphi_{,x}) dx \end{aligned}$
<p>Terms linked to pre-buckling torsional twist</p>	$\begin{aligned} \partial\partial\Pi_3 = & \int EI_y \varphi^2 \partial v_{,xx}^2 + EI_z \varphi^2 \partial w_{,xx}^2 - 2(EI_y + EI_z) \varphi \partial v_{,xx} \partial w_{,xx} dx \\ & + \int \left(\frac{M_y^2 \varphi^2}{EI_y} \left(1 - \frac{I_z}{I_y}\right) + \frac{M_z^2 \varphi^2}{EI_z} \left(1 - \frac{I_y}{I_z}\right) + 4 \frac{M_z M_y \varphi}{EI_z} - 4 \frac{M_y M_z \varphi}{EI_y} \right) \partial \varphi^2 dx \\ & + 2 \int \left(M_y \varphi^2 \left(1 - \frac{I_z}{I_y}\right) - 2 M_z \varphi \left(1 - \frac{I_y}{I_z}\right) \right) \partial \varphi \partial v_{,xx} dx \\ & + 2 \int \left(-M_z \varphi^2 \left(1 - \frac{I_y}{I_z}\right) - 2 M_y \varphi \left(1 - \frac{I_z}{I_y}\right) \right) \partial \varphi \partial w_{,xx} dx \\ & 2 \int \left(-\beta_y \frac{I_z}{I_y} M_y \varphi - \beta_z \frac{I_y}{I_z} M_z \varphi \right) \partial \varphi_{,x}^2 dx \\ & - 2 \int Nz_c (\varphi \partial \varphi_{,x} \partial w_{,x} + \varphi_{,x} \partial \varphi \partial w_{,x}) dx - 2 \int Ny_c (\varphi \partial \varphi_{,x} \partial v_{,x} + \varphi_{,x} \partial \varphi \partial v_{,x}) dx \\ & - \sum F_z e_y \varphi \partial \varphi^2 + \sum F_y e_z \varphi \partial \varphi^2 - \sum \int q_z e_y \varphi \partial \varphi^2 dx + \sum \int q_y e_z \varphi \partial \varphi^2 dx \end{aligned}$

5.5.5 Determination of the critical loads for I-shaped members

5.5.5.1 Common approach neglecting pre-buckling displacements

5.5.5.1.1 Members under major-axis bending

The expressions for the critical bending moment developed in this paragraph are known for a long time and are partially included in the European standard (see for example (CEN 2014)). However, in order to illustrate the approach used in the following paragraphs for more complex cases, it seems justified to treat the well-known problem of elastic lateral-torsional buckling of I-shaped members again.

For the case of double symmetric I sections subject to constant major axis bending, expression (5.133) reduces to:

$$\partial\partial\Pi_1 = \int EI_z \partial v_{,xx}^2 + EI_w \partial \varphi_{,xx}^2 + GI_T \partial \varphi_{,x}^2 dx - 2 \int M_y \partial \varphi \partial v_{,xx} dx = 0 \quad (5.134)$$

Supposing that the member possesses end fork conditions, the variations of the displacements may be expressed by sine functions as given in Eqs. (5.135) and (5.136).

$$\partial v = \underline{v} \sin\left(\frac{\pi x}{L}\right) \quad (5.135)$$

$$\partial \varphi = \underline{\varphi} \sin\left(\frac{\pi x}{L}\right) \quad (5.136)$$

By solving the integral of Eq. (5.134) and deriving with reference to the unknowns of the displacement functions, the following system is obtained:

$$\begin{aligned} \frac{\pi^4}{L^4} EI_z \underline{v} + \frac{\pi^2}{L^2} M_y \underline{\varphi} &= 0 \\ \frac{\pi^2}{L^2} M_y \underline{v} + \frac{\pi^2}{L^2} \left(GI_T + EI_w \frac{\pi^2}{L^2} \right) \underline{\varphi} &= 0 \end{aligned} \quad (5.137)$$

The elastic critical moment resulting from Eq. (5.137) is:

$$M_{y,cr} = EI_z \frac{\pi^2}{L^2} \sqrt{\frac{I_w}{I_z} + \frac{GI_T}{EI_z} \frac{L^2}{\pi^2}} \quad (5.138)$$

Other authors use different formats for the obtained solution. In (FOSTA 2004), (Stangenberg 2007) and (Naumes 2009), the elastic critical moment is expressed by:

$$M_{y,cr} = N_{cr,z} \sqrt{\frac{I_w}{I_z} \left(1 + \frac{GI_T}{EI_w} \frac{L^2}{\pi^2} \right)} = N_{cr,z} c_r \quad (5.139)$$

Using this format, the elastic critical moment is shown to be equal to the critical axial force for lateral buckling multiplied by a distance (or radius) c_r .

Based on Eq. (5.139), the lateral displacement at the critical state can be expressed as a function of the torsional twist at the critical state and the distance c_r :

$$v_{cr} = -\frac{M_{cr,y}\varphi_{cr}}{N_{cr,z}} = -\varphi_{cr}\sqrt{\frac{I_w}{I_z}\left(1 + \frac{GI_T}{EI_w}\frac{L^2}{\pi^2}\right)} = -\varphi_{cr}c_r \quad (5.140)$$

It is recalled that v_{cr} corresponds to the lateral displacement component of the eigenmode and φ_{cr} corresponds to the torsional twist component of the eigenmode. The sign “-” yields directly from the definition of the system of axis (also see Figure 5-90).

The distance c_r depends on the torsional behaviour of the member. In fact, if the torsion constant I_t becomes negligible (supposing that the length and the 2nd moment of area do not change), the torsional twist component of the first eigenmode of the member is predominant. Hence, the distance c_r tends to:

$$c_r = \sqrt{\frac{I_w}{I_z}} = \frac{h}{2} \quad (5.141)$$

Consequently, the lower flange does not displace laterally and the whole section rotates about the intersection between lower flange and web. If, however, the torsion constant I_t is very high the distance c_r also attains high values. In these cases the eigenmode is characterised by a low torsional twist component. Figure 5-90 shows the displaced member for the two extreme cases.

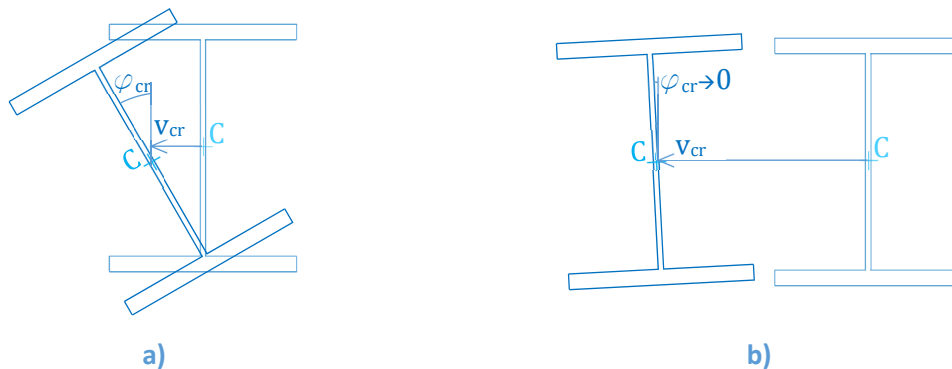


Figure 5-90: Shape of the eigenmode for a) a section with low torsional stiffness and b) as section with high torsional stiffness

Obviously, open sections, as I and U sections, possess a rather low torsional stiffness. Therefore, their behaviour is closer to the one shown in Figure 5-90a) than to the one shown in Figure 5-90b). The behaviour in Figure 5-90b) is representative for closed sections.

Similarly to the development of the critical major-axis bending moment, one may determine a critical minor-axis bending moment. Its expression is given in Eq. (5.142). Nevertheless, it is shown in paragraph 5.5.5.2 that, if pre-buckling displacements are taken into account, the elastic instability under minor-axis bending does not have a physical meaning for I sections.

$$M_{z,cr} = EI_y \frac{\pi^2}{L^2} \sqrt{EI_w \frac{\pi^2}{L^2} + GI_T} \quad (5.142)$$

In steel construction, beams are very often subject to varying bending moments. Moreover, so as to optimize their use, I sections may be mono-symmetric. It seems therefore interesting to redevelop the critical major-axis bending moment for this slightly more complex configuration. In this case, the Wagner constant β_z does not vanish (compare Eqs. (5.143) and (5.134)). Consequently, the second variation of total internal energy Π of the member becomes:

$$\begin{aligned} \partial\delta\Pi = & \int EI_z \partial v_{,xx}^2 + EI_w \partial \varphi_{,xx}^2 + GI_T \partial \varphi_{,x}^2 dx \\ & - 2 \int M_y \partial \varphi \partial v_{,xx} + \beta_z M_y \partial \varphi_{,x}^2 dx + \int q_z e_z \partial \varphi^2 dx \end{aligned} \quad (5.143)$$

Considering the case of a uniformly distributed vertical load and using the sine approximation of the displacement functions, the following expression is obtained for the critical bending moment:

$$M_{y,cr} = C_1 EI_z \frac{\pi^2}{L^2} \left(\sqrt{\frac{I_w}{I_z} \left(1 + \frac{GI_T}{EI_w} \frac{L^2}{\pi^2} \right) + (C_2 z_q + C_3 \beta_z)^2} - (C_2 z_q + C_3 \beta_z) \right) \quad (5.144)$$

The analytical expressions of the constants C_1 , C_2 and C_3 are given in Eqs. (5.145) to (5.147).

$$C_1 = \frac{3\pi^2}{2(\pi^2 + 3)} = 1,15 \quad (5.145)$$

$$C_2 = \frac{6}{(\pi^2 + 3)} = 0,47 \quad (5.146)$$

$$C_3 = \frac{\pi^2 - 3}{\pi^2 + 3} = 0,534 \quad (5.147)$$

It is obvious that the expression is more complex than the one developed for the case of double symmetric I sections under constant bending. The factors C_1 , C_2 and C_3 introduce the influence of the bending moment diagram, the effect of the vertical eccentricity of an applied load with respect to the shear centre and the influence of the mono-symmetry of the section. The precision of the analytical values given in Eqs. (5.145) to (5.147) depend on the mechanical characteristics I_z , I_w , I_t and β_z as well as on the distance z_q and the form of the bending moment diagram. Indeed, these parameters influence the exact form of the eigenmode and consequently the precision of the sine approximation. In order to take account of the influence of, especially the mono-symmetry of the section characterized by the Wagner constant, reference (CEN 2007c) defines the constants C_1 , C_2 and C_3 depending on the sign of the maximum bending moment, the form of the bending moment diagram and the value ψ that is representative of the mono-symmetry of the cross-section (see Chapter 4).

The distance from the centre of torsional twist to the shear centre of the section is in this case given by Eq. (5.148).

$$c_r = C_1 \left(\sqrt{\frac{I_w}{I_z} \left(1 + \frac{GI_T}{EI_w} \frac{L^2}{\pi^2} \right) + (C_2 z_q + C_3 \beta_z)^2} - (C_2 z_q + C_3 \beta_z) \right) \quad (5.148)$$

Hereafter, the development is extended to the case of combined major-axis bending and axial forces.

5.5.5.1.2 Members under combined major-axis bending and compression

Here, it is supposed that both axial force and major-axis bending moment may be amplified proportionally. The expression of the second variation of potential energy of a double symmetric member subject to a constant bending moment is given by Eq. (5.149).

$$\begin{aligned} \delta^2 \Pi = & \int \left[EI_z \delta v_{,xx}^2 + EI_w \delta \varphi_{,xx}^2 + GI_T \delta \varphi_{,x}^2 \right] dx \\ & - 2 \int \alpha_{cr} M_y \delta \varphi \delta v_{,xx} dx - \int \alpha_{cr} N \left(\delta v_{,x}^2 + r_{yz}^2 \delta \varphi_{,x}^2 \right) dx \end{aligned} \quad (5.149)$$

Again, the integration is performed to obtain the system given in Eq. (5.150).

$$\begin{aligned} \left(\frac{\pi^4}{2L^3} EI_z - \frac{\pi^2}{2L} N \alpha_{cr} \right) \underline{v} + \frac{\pi^2}{2L} \alpha_{cr} M_y \underline{\varphi} &= 0 \\ \frac{\pi^2}{2L} \alpha_{cr} M_y \underline{v} + \frac{\pi^2}{2L} \left(GI_T + EI_w \frac{\pi^2}{L^2} \right) \underline{\varphi} - \frac{\pi^2}{2L} N \alpha_{cr} r_{yz}^2 \underline{\varphi} &= 0 \end{aligned} \quad (5.150)$$

After various reorganisation steps, the critical amplification factor is obtained as follows:

$$\alpha_{cr} = \frac{1}{2} \sqrt{\frac{4 \frac{M_y^2}{M_{y,cr}^2} + \left(\frac{N}{N_{cr,z}} - \frac{N}{N_{cr,T}} \right)^2 - \left(\frac{N}{N_{cr,z}} + \frac{N}{N_{cr,T}} \right)}{\frac{M_y^2}{M_{y,cr}^2} - \frac{N^2}{N_{cr,z} N_{cr,T}}} \quad (5.151)$$

For the more complex case of a member subject to a variable bending moment and possessing a mono-symmetric cross-section (symmetric with respect to its minor-axis) the critical amplification factor is directly given in Eqs. (5.152) and (5.153).

$$\alpha_{cr} = \frac{1}{2} \sqrt{\frac{4 \frac{M_y^2}{M_{y,cr}^2} + \left(\frac{N}{N_{cr,z}} + \frac{N}{N_{cr,T}} - C_4 \right)^2 - 4 \frac{N^2}{N_{cr,z} N_{cr,T}} + 4 C_4 \frac{N}{N_{cr,z}} - \left(\frac{N}{N_{cr,z}} + \frac{N}{N_{cr,T}} \right) + C_4}{\frac{M_y^2}{C_1^2 M_{y,cr,u}^2} + C_4 \frac{N}{N_{cr,z}} - \frac{N^2}{N_{cr,z} N_{cr,T}}} \quad (5.152)$$

$$C_4 = 2 \frac{M_y N_{cr,z} (C_3 \beta_z + C_2 z_F)}{C_1 M_{y,cr,u}^2} \quad (5.153)$$

The former expression for the critical amplification factor has been presented in a similar way in (Stangenberg 2007). It is obvious that Eq. (5.153) is not suitable for hand calculation. Also, its precision depends, even more than for the “simple case” of mono-symmetric I sections subject to variable bending, on the mechanical characteristics, the exact form of the bending moment diagram and additionally it depends on the ratio between the major-axis bending moment and the axial force. In order to obtain precise values of the load amplification factor it seems therefore more convenient to use specialised programs as, for example, *LTBeamN* presented in reference (Beyer et al. 2015).

5.5.5.2 Influence of pre-buckling displacements

5.5.5.2.1 General

Throughout the previous paragraph, it has been considered that pre-buckling (or first order) displacements are negligible. Yet, it can be shown that their influence may be rather important. If first order displacements are taken into account, the second variation of the total potential energy becomes:

$$\begin{aligned} \delta\delta\Pi = & \int EI_y \delta w_{,xx}^2 + EI_z \delta v_{,xx}^2 + EI_w \delta \varphi_{,xx}^2 + GI_T \delta \varphi_{,x}^2 dx \\ & - 2 \int M_y \left(1 - \frac{I_z}{I_y} \right) \delta \varphi \delta v_{,xx} + \beta_z M_y \delta \varphi_{,x}^2 dx + 2 \int M_z \delta \varphi \delta w_{,xx} \left(1 - \frac{I_y}{I_z} \right) dx \\ & - \int \frac{M_z^2}{EI_z} \left(1 - \frac{I_y}{I_z} \right) \delta \varphi^2 - \frac{M_y^2}{EI_y} \left(1 - \frac{I_z}{I_y} \right) \delta \varphi^2 dx \\ & - \int N \left(\delta v_{,xx}^2 + \delta w_{,xx}^2 + r_{yz}^2 \delta \varphi_{,x}^2 + 2z_c \delta \varphi_{,x} \delta v_{,xx} \right) dx \\ & - 2 \int Nz_c \left(w_{,xx} \delta \varphi \delta \varphi_{,x} \right) dx - 2 \int Ny_c \left(v_{,xx} \delta \varphi \delta \varphi_{,x} \right) dx \\ & + \sum F_z e_z \delta \varphi^2 + \sum F_y e_y \delta \varphi^2 + \sum \int q_z e_z \delta \varphi^2 dx + \sum \int q_y e_y \delta \varphi^2 dx \end{aligned} \quad (5.154)$$

Obviously, the expression given in Eq. (5.154) is much more complex than the classical expression not accounting for first order displacements. For the general case of combined flexure and compression the analytical derivation of the critical loads leads to highly complex formulations. Therefore, only the case of a double symmetric I section subject to constant mono-axial bending is treated hereafter.

5.5.5.2.2 I-shaped member subject to constant major-axis bending

If pre-buckling displacements are considered one obtains the following second variation of the total potential energy of the member for the case of a double symmetric I section under constant bending:

$$\begin{aligned} \delta\delta\Pi = & \int \left[EI_z \delta v_{,xx}^2 + EI_w \delta \varphi_{,xx}^2 + GI_T \delta \varphi_{,x}^2 \right] dx \\ & - 2 \int M_y \left(1 - \frac{I_z}{I_y} \right) \delta \varphi \delta v_{,xx} dx - \int \frac{M_y^2}{EI_y} \left(1 - \frac{I_z}{I_y} \right) \delta \varphi^2 dx \end{aligned} \quad (5.155)$$

Again, it is supposed that the buckling displacements $\delta\varphi$ and δv are of sinusoidal form. After solving the integration and deriving with respect to the unknown displacements, one obtains the following system:

$$\begin{aligned} N_{cr,z} v + M_y \left(1 - \frac{I_z}{I_y} \right) \varphi &= 0 \\ M_y \left(1 - \frac{I_z}{I_y} \right) v + GI_T \varphi + EI_w \left(\frac{\pi}{L} \right)^2 \varphi - \frac{M_y^2}{N_{cr,y}} \left(1 - \frac{I_z}{I_y} \right) \varphi &= 0 \end{aligned} \quad (5.156)$$

Hence, the critical major axis bending moment for lateral-torsional buckling reads:

$$M_{y,cr} = \frac{N_{cr,z}}{\sqrt{1 - \frac{I_z}{I_y}}} \sqrt{\frac{I_w}{I_z} \left(1 + \frac{GI_T L^2}{EI_w \pi^2} \right)} = f_{zy} N_{cr,z} \sqrt{\frac{I_w}{I_z} \left(1 + \frac{GI_T L^2}{EI_w \pi^2} \right)} \quad (5.157)$$

The previous expression has been derived several times in the past (see for example (de Ville de Goyet 1989), (Vinnakota et al. 1975)). Compared to Eq. (5.139) giving the expression of the critical moment when pre-buckling deflections are neglected, Eq. (5.158) contains the supplementary factor f_{zy} . If the minor-axis second moment of area I_z is negligible compared to the second moment of area I_y , the factor f_{zy} tends to unity. This assumption is generally considered for I-shaped members. Figure 5-91 shows the evolution of the factor f_{zy} for commonly used I sections. One notices that the pre-buckling flexure has an influence especially on the elastic critical moment for small H sections. In fact, up to a height of approximately 300 mm, the consideration of pre-buckling deflection leads to a critical moment that is up to 20% higher than the value calculated without the influence of pre-buckling displacements. For greater H sections the influence decreases rapidly as the flanges' width stays approximately constant and consequently the minor-axis second of area stays approximately constant, too.

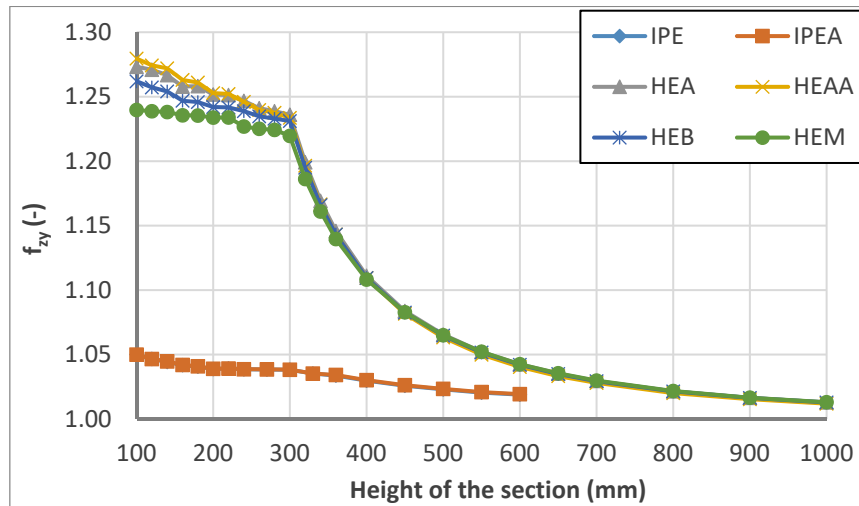


Figure 5-91: Factor f_{zy} for commonly used I sections

Even if the difference between the critical moment calculated with the common formula of Eq. (5.139) and the formula (5.157) may seem very important for some sections, it should be noted that it is not an error to use Eq. (5.139) combined with the methods assessing member stability given in Eurocode 3, as these methods have been calibrated based on the value predicted by Eq. (5.139). However, it might be necessary to include the effects of pre-buckling displacements for global methods as OIC. This can be shown directly, based on the next load case.

We consider an I-shaped member subject to minor-axis bending. For this configuration, one obtains Eq. (5.158) for the critical bending moment about the minor-axis.

$$M_{z,cr} = \frac{N_{cr,y}}{\sqrt{1 - \frac{I_y}{I_z}}} \sqrt{\frac{I_w}{I_y} \left(1 + \frac{GI_T L^2}{EI_w \pi^2} \right)} = f_{yz} N_{cr,y} \sqrt{\frac{I_w}{I_y} \left(1 + \frac{GI_T L^2}{EI_w \pi^2} \right)} \quad (5.158)$$

As the major-axis second moment of area I_y is always greater than the minor-axis second moment of area I_z the factor $1 - I_y/I_z$ is always negative. Consequently, equation (5.158) does not yield a numerical value and it may therefore be concluded that the phenomenon of elastic instability of I sections under minor-axis bending is not physical. Contrariwise, if the critical moment is calculated with the expression represented by Eq. (5.142), i.e. without considering the influence of pre-buckling displacements, a numerical value of the critical minor-axis bending moment is obtained (even if rather high) and consequently, in some case erroneous conclusions could be obtained concerning the sensitivity to instability of I sections under minor axis bending.

Current steel design standards as reference (CEN 2005a) consider implicitly the influence of pre-buckling displacements as they suppose that a member subject to minor-axis bending only can always attain the resistance of its most loaded section without any reduction due to member instability.

5.5.5.2.3 Consideration of pre-buckling flexure and pre-buckling torsional twist

If a member is subject to additional first order torque, it might be necessary to consider the resulting twist for the determination of the critical load. For a double-symmetric I section the second variation of the total potential energy becomes in this case:

$$\begin{aligned}
 \partial\partial\Pi = & \int [EI_z \partial v_{,xx}^2 + EI_w \partial \varphi_{,xx}^2 + GI_T \partial \varphi_{,x}^2] dx \\
 & - 2 \int [M_y \partial \varphi \partial v_{,xx} + \beta_z M_y \partial \varphi_{,x}^2] dx + \int \frac{M_y^2}{EI_y} \left(1 - \frac{I_z}{I_y}\right) \partial \varphi^2 dx + \int \left(2 \frac{I_z}{I_y} M_y\right) \partial \varphi \partial v_{,xx} dx \\
 & + \int [EI_y \varphi^2 \partial v_{,xx}^2 + EI_z \varphi^2 \partial w_{,xx}^2 - 2(EI_y + EI_z) \varphi \partial v_{,xx} \partial w_{,xx}] dx \\
 & + \int \left[\frac{M_y^2 \varphi^2}{EI_y} \left(1 - \frac{I_z}{I_y}\right) \partial \varphi^2 + 2M_y \varphi^2 \left(1 - \frac{I_z}{I_y}\right) \partial \varphi \partial v_{,xx} - 2M_y \varphi \left(1 - \frac{I_z}{I_y}\right) \partial \varphi \partial w_{,xx} \right] dx
 \end{aligned} \quad (5.159)$$

Eq. (5.159) leads to the system represented in Eq. (5.162) for the determination of the critical bending moment $M_{y,cr}$.

$$\begin{aligned}
 (N_{cr,y} + N_{cr,z} \varphi^2) \underline{w} + (N_{cr,z} - N_{cr,y}) \varphi \underline{v} + \left(1 - \frac{I_z}{I_y}\right) M_y \varphi \underline{\varphi} &= 0 \\
 (N_{cr,z} - N_{cr,y}) \varphi \underline{w} + (N_{cr,y} \varphi^2 + N_{cr,z}) \underline{v} + \left[\left(1 - \frac{I_z}{I_y}\right) M_y - M_y \varphi^2 \right] \underline{\varphi} &= 0 \\
 \left(1 - \frac{I_z}{I_y}\right) M_y \varphi \underline{w} + \left[\left(1 - \frac{I_z}{I_y}\right) M_y - M_y \varphi^2 \right] \underline{v} + \left[EI_w \frac{\pi^2}{L^2} + GI_T + \frac{M_y^2}{N_{cr,y}} \varphi^2 - \left(1 - \frac{I_z}{I_y}\right) \frac{M_y^2}{N_{cr,y}} \right] \underline{\varphi} &= 0
 \end{aligned} \quad (5.160)$$

It is recalled that the pre-buckling torsional twist is noted φ whereas the amplitudes of the buckling displacements are noted \underline{w} , \underline{v} and $\underline{\varphi}$. The solution of (5.160) leads to expression (5.161) for the critical moment accounting for pre-buckling flexure and torsional twist:

$$M_{y,cr} = \frac{1 + \varphi^2}{\sqrt{1 - \frac{I_z}{I_y} (1 + \varphi^4 + \varphi^2)}} N_{cr,z} \sqrt{\frac{I_w}{I_z} + \frac{GI_T}{EI_w} \frac{L^2}{\pi^2}} = f_{zy,\varphi} N_{cr,z} \sqrt{\frac{I_w}{I_z} + \frac{GI_T}{EI_w} \frac{L^2}{\pi^2}} \quad (5.161)$$

One may observe that expression (5.161) respects the continuity with the common expression of the critical moment not accounting for pre-buckling displacements (Eq. (5.139)) and the expression of the critical moment only accounting for pre-buckling flexure (Eq. (5.157)).

It should be recalled that Eq. (5.161) has been developed based on the assumption of small torsional twist φ ($\sin(\varphi) = \varphi$ and $\cos(\varphi) = 1$). This condition may be accepted for rotations less than 20° or 0,3 rad. If the torsional twist is greater, it would be necessary to develop the angular functions more accurately, for example by $\cos(\varphi) = 1 - \varphi^2/2$. However, in practice, the condition of

small twist may certainly be considered as respected because higher twist would not be compatible with the boundary conditions.

In order to illustrate the influence of the pre-buckling displacements on the critical moment, Figure 5-92 represents the evolution of the factor $f_{zy,\varphi}$ for the torsionally compact section HEM 160 (high torsional stiffness compared to other open sections) and the rather slender section IPE 550.

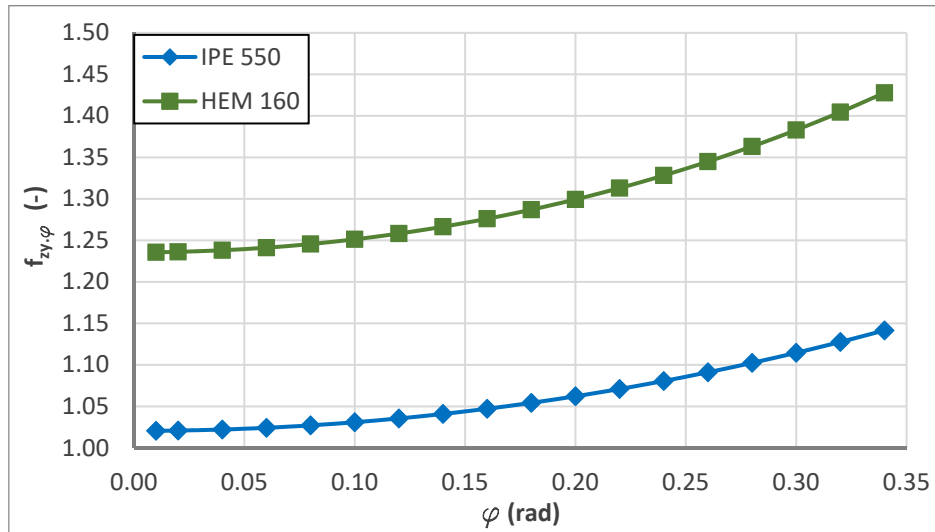


Figure 5-92: Influence of the pre-buckling displacements on the critical moment

It can be seen that pre-buckling displacements may increase the critical moment of about 15% to 45% depending on the form of the section. Obviously, the highest increase is reached for high pre-buckling twist. However, it has to be noticed that Figure 5-92 includes the influence of both, pre-buckling flexure and torsional twist. So as to identify the sole influence of torsional twist, Figure 5-93 shows the evolution of the ratio $f_{zy,\varphi}/f_{zy}$ (f_{zy} representing the influence of pre-buckling flexure).

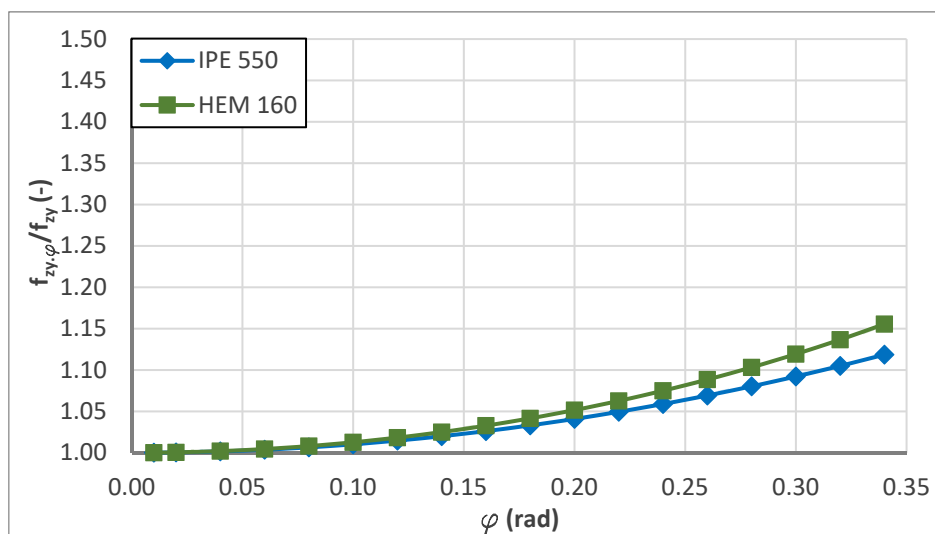


Figure 5-93: Influence of pre-buckling torsional twist on the critical moment

Figure 5-93 shows that the pre-buckling torsional twist has much less influence on the critical moment than pre-buckling flexure for compact sections. In fact, for the section HEM 160 the factor f_{zy} , characterizing the influence of pre-buckling flexure, is equal to 1,23. Even for very high pre-buckling torsional twist the ratio $f_{zy,\varphi}/f_{zy}$ does not exceed this value. Also, up to a value of 0,2 rad the ratio $f_{zy,\varphi}/f_{zy}$ does not exceed 1,05, signifying that pre-buckling twist has an influence of less than 5% on the value of the critical moment. In case of the torsionally slender IPE 550 section, important pre-buckling twist may influence the value of the critical moment more than pre-buckling flexure. Nevertheless, the influence remains rather small with a maximum value of 12%. Also, it should be noted again, that a pre-buckling torsional twist of 0,3 rad seem rather excessive for practical cases. Consequently, it seems justified to neglect its influence on elastic stability hereafter.

5.5.5.3 Conclusions

Paragraph 5.5.5 presented a discussion on the critical loads for I-shaped members. First, the well-known expressions for the elastic critical bending moment have been redeveloped in order to illustrate the approach applied for more complex cases. It has been shown that the expression become rather complex especially for combined axial compression and major-axis bending. For these more complex cases the application of specialised programs as *LTBeamN* (see reference (Beyer et al. 2015)) is therefore recommended as they allow the practical engineer to determine rapidly precise values of the critical loads. In the last part of this paragraph the influence of pre-buckling displacements is quantified. Eqs. (5.157) and (5.158) describing respectively the major- and minor-axis critical bending moment including the influence of pre-buckling displacements. These expressions have also been developed previously. Here, it has been shown that for practically used I sections under major-axis bending the influence of pre-buckling displacements may attain about 30% for small and compact H sections. For section heights of more than 400 mm the difference is less than 10%. Also, the theoretical developments imply that I-shaped members are not sensitive to elastic instability if they are subject to minor-axis bending only. This finding is not surprising and has been accepted for a long time. Yet, it is only obtained if the pre-buckling displacements are considered. Therefore, it seems necessary to take them into account for global design models as OIC that use the critical load amplification factor as key parameter for the resistance predictions.

Last, an expression of the critical loads has been developed that takes into account the influence of pre-buckling torsional twist. To the author's knowledge, this expression has not been developed in this form previously. It has however been shown that the influence of pre-buckling torsional twist may be neglected for practical cases, i.e. for torsional twists less than 0,3 rad.

Next, the case of U-shaped members is treated and it is shown that the influence of pre-buckling displacements is even more pronounced than for I sections.

5.5.6 Determination of critical loads for U-shaped members

5.5.6.1 Common approach neglecting pre-buckling displacements

As for I sections, the critical loads are determined in a first step without considering the influence of pre-buckling displacements in this paragraph. In paragraph 5.5.6.2 the study is then extended to the effect of pre-buckling displacements.

If pre-buckling displacements are neglected, the second variation of the potential energy reduces to:

$$\begin{aligned} \delta^2 \Pi = & \int EI_y \delta w_{,xx}^2 + EI_z \delta v_{,xx}^2 + EI_w \delta \varphi_{,xx}^2 + GI_T \delta \varphi_{,x}^2 dx \\ & - 2 \int M_y \delta \varphi \delta v_{,xx} dx + 2 \int M_z \delta \varphi \delta w_{,xx} - \beta_y M_z \delta \varphi_{,x}^2 \\ & - \int N (\delta v_{,x}^2 + \delta w_{,x}^2 + r_{yz}^2 \delta \varphi_{,x}^2 - 2y_c \delta \varphi_{,x} \delta w_{,x}) dx \\ & + \sum F_z e_z \delta \varphi^2 + \sum F_y e_y \delta \varphi^2 + \sum \int q_z e_z \delta \varphi^2 dx + \sum \int q_y e_y \delta \varphi^2 dx \end{aligned} \quad (5.162)$$

At this point it should be noted that due to the form of the section some differences exist between the expression given here before and the one applicable for I sections: As hot-rolled U sections are always symmetric about their major-axis the parameter β_z vanishes. Conversely, the parameter β_y never vanishes as U sections are never symmetric about the minor-axis. These two points also imply that the axial force is linked to the term y_c (last term of the third line of Eq. (5.162)) that represents the lateral distance between the shear centre and the centroid.

Hereafter, critical loads are developed for some special cases as for I shaped sections. First, the case of major axis bending is studied. Supposing a uniformly distributed load applied at a vertical distance e_z from the shear centre the second variation of the potential energy becomes:

$$\delta^2 \Pi = \int EI_z \delta v_{,xx}^2 + EI_w \delta \varphi_{,xx}^2 + GI_T \delta \varphi_{,x}^2 dx - 2 \int M_y \delta \varphi \delta v_{,xx} dx + \int q_z e_z \delta \varphi^2 dx \quad (5.163)$$

Obviously, this expression is identical to the expression given for I sections. Hence the critical moment is identical and given by Eq. (5.164).

$$M_{y,cr} = C_1 EI_z \frac{\pi^2}{L^2} \left(\sqrt{\frac{I_w}{I_z} \left(1 + \frac{GI_T}{EI_w} \frac{L^2}{\pi^2} \right) + (C_2 e_z)^2} \pm (C_2 e_z) \right) \quad (5.164)$$

Similarly, the critical moment about the minor-axis may be expressed by Eq. (5.165).

$$M_{z,cr} = \pm C_1 EI_y \frac{\pi^2}{L^2} \left(\sqrt{\frac{I_w}{I_y} \left(1 + \frac{GI_T}{EI_w} \frac{L^2}{\pi^2} \right) + (C_2 e_y + C_3 \beta_y)^2} \mp (C_2 e_y + C_3 \beta_y) \right) \quad (5.165)$$

It is recalled that, in the reference system used here, the positive minor-axis-bending moment compresses the flanges tips and the negative minor-axis bending moment compresses the web of the U section. Due to the mono-symmetry about the z-axis the value of $M_{z,cz}$ is in an important range of member length less than $M_{y,cr}$ as shown in Figure 5-94 and Figure 5-95 for a UPE 120

section and a UPE 330 section made of S235. Also, the relative slenderness for lateral-torsional buckling under minor-axis bending seems to be non-negligible. In paragraph 5.5.5.2 it has been shown that I section are not sensitive to elastic instability when they are subject to minor-axis bending. Yet, this conclusion cannot be transferred directly to U sections as is shown in the following paragraphs.

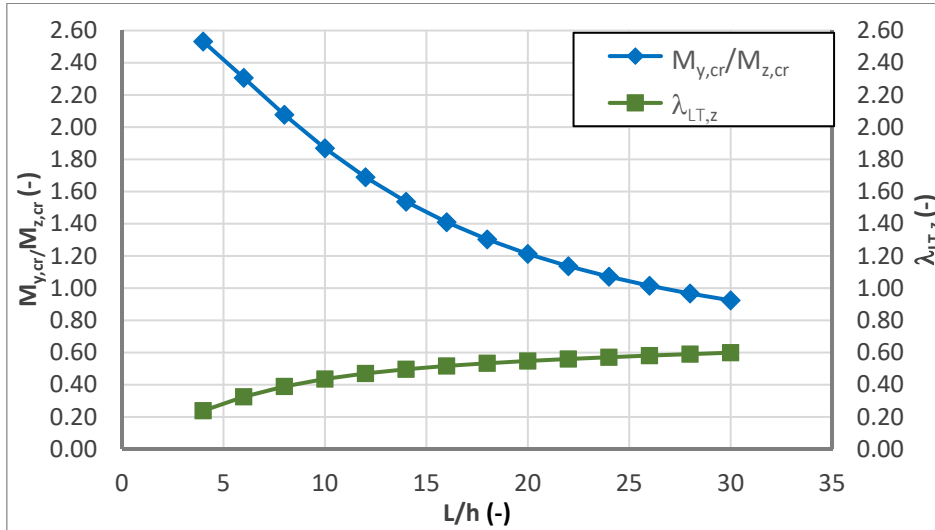


Figure 5-94: Comparison between critical major and minor axis moments for UPE 120 section

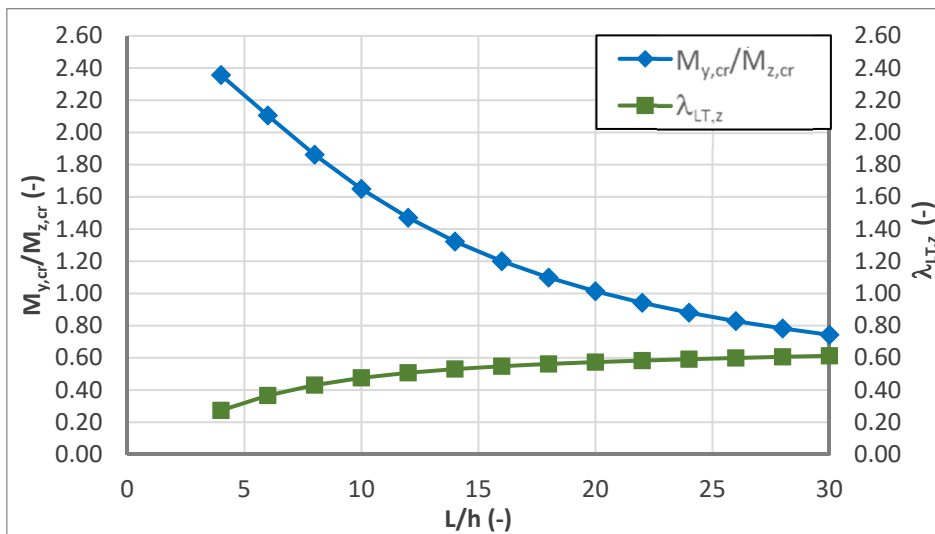


Figure 5-95: Comparison between critical major and minor axis moments for UPE 330 section

5.5.6.2 Influence of the pre-buckling displacements

5.5.6.2.1 General

It has been shown that pre-buckling displacements may have an important influence on the critical loads of a member. For I sections, this phenomenon has been studied several times in the past (for example in (de Ville de Goyet 1988), (Vinnakota et al. 1975)). However, the influence of pre-buckling displacements has not been studied explicitly for U sections before. In the previous paragraph, it has been shown that the critical moment $M_{z,cr}$ and the associated relative slenderness

may be in a practical range and not negligible. Therefore, it seems even more important to study the (theoretical) phenomenon of elastic instability under minor-axis bending in order to justify whether or not instability may occur for this load case. The second variation of the total potential energy of the member for the problem studied in the following is given by Eq. (5.166).

$$\begin{aligned}
 \delta\delta\Pi = & \int EI_y \delta w_{,xx}^2 + EI_z \delta v_{,xx}^2 + EI_w \delta \varphi_{,xx}^2 + GI_T \delta \varphi_{,x}^2 dx \\
 & - 2 \int M_y \delta \varphi \delta v_{,xx} dx + 2 \int M_z \delta \varphi \delta w_{,xx} - \beta_y M_z \delta \varphi_{,x}^2 \\
 & - \int \frac{M_z^2}{EI_z} \left(1 - \frac{I_y}{I_z}\right) \delta \varphi^2 - \frac{M_y^2}{EI_y} \left(1 - \frac{I_z}{I_y}\right) \delta \varphi^2 dx \\
 & + \int \left(2 \frac{I_z}{I_y} M_y\right) \delta \varphi \delta v_{,xx} dx + \int \left(-2 \frac{I_y}{I_z} M_z\right) \delta \varphi \delta w_{,xx} dx \\
 & - \sum F_z e_z \delta \varphi^2 - \sum F_y e_y \delta \varphi^2 - \sum \int q_z e_z \delta \varphi^2 dx - \sum \int q_y e_y \delta \varphi^2 dx
 \end{aligned} \tag{ 5.166 }$$

5.5.6.2.2 U-shaped members subject to constant major-axis bending

As before, the elastic critical major-axis bending moment can be obtained based on the second variation of the total potential energy represented in Eq. (5.166). Again, the displacement functions are supposed to be of sine shape. Consequently, one obtains the expression of the critical major-axis bending moment $M_{y,cr,II}$ taking into account the effect of pre-buckling displacements in Eq. (5.167). Additionally, Eq. (5.168) presents the expression for $M_{y,cr,I}$, obtained if pre-buckling displacements are neglected. Obviously, both expressions correspond to the solution obtained for I-shaped members.

$$M_{y,cr,II} = \frac{EI_z \frac{\pi^2}{L^2}}{\sqrt{1 - \frac{I_z}{I_y}}} \sqrt{\frac{I_w}{I_z} + \frac{GI_T}{EI_z} \frac{L^2}{\pi^2}} = f_{zy} M_{y,cr,I} \quad (5.167)$$

$$M_{y,cr,I} = EI_z \frac{\pi^2}{L^2} \sqrt{\frac{I_w}{I_z} + \frac{GI_T}{EI_z} \frac{L^2}{\pi^2}} \quad (5.168)$$

It can be observed that the influence of pre-buckling displacements is again introduced by the term $1 - I_z/I_y$. In order to highlight the influence of the pre-buckling displacements on the critical major-axis bending moment for U sections, Figure 5-96 gives the ratio between $M_{y,cr,II}$ and $M_{y,cr,I}$ for standard hot-rolled UPE sections.

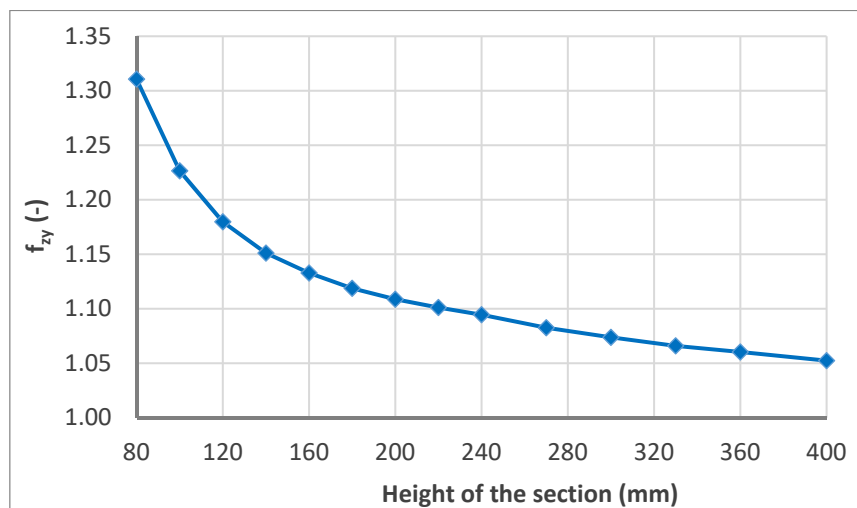


Figure 5-96 : Ratio between $M_{y,cr,II}$ and $M_{y,cr,I}$ for UPE sections

It may be observed that the difference is maximum for small UPE sections as the ratio between the second moments of area I_y and I_z is minimum. The maximum difference is of about 30% for UPE 80 cross-section. However, it reduces rapidly and falls below 10% for UPE cross-sections with heights greater than 200 mm often used for structural members in practice. The difference is therefore in the same range as for I-shaped members under major-axis bending. It is shown

next, that in case of minor-axis bending and bi-axial bending, U-shaped members show non-negligible differences compared to I-shaped members under minor-axis bending.

5.5.6.2.3 U-shaped members subject to constant minor-axis bending

First, the case of constant minor-axis bending is considered. The second variation of the potential energy reads:

$$\begin{aligned} \delta\delta\Pi = & \int EI_y \delta w_{,xx}^2 + EI_w \delta \varphi_{,xx}^2 + GI_T \delta \varphi_{,x}^2 dx + 2 \int M_z \delta \varphi \delta w_{,xx} - \beta_y M_z \delta \varphi_{,x}^2 dx \\ & - \int \frac{M_z^2}{EI_z} \left(1 - \frac{I_y}{I_z}\right) \delta \varphi^2 - 2 \frac{I_y}{I_z} M_z \delta \varphi \delta w_{,xx} dx \end{aligned} \quad (5.169)$$

Eq. (5.169) leads to the following system:

$$\begin{aligned} N_{cr,y} \underline{w} - M_z \left(1 - \frac{I_y}{I_z}\right) \underline{\varphi} &= 0 \\ -M_z \left(1 - \frac{I_y}{I_z}\right) \underline{w} + GI_T \underline{\varphi} + EI_w \left(\frac{\pi}{L}\right)^2 \underline{\varphi} - \frac{M_z^2}{N_{cr,z}} \left(1 - \frac{I_y}{I_z}\right) \underline{\varphi} - 2M_z \beta_y \underline{\varphi} &= 0 \end{aligned} \quad (5.170)$$

By solving (5.170), one obtains the expression of the critical minor-axis bending moment for elastic instability:

$$M_{z,cr,II,pos} = \frac{1}{1 - \frac{I_y}{I_z}} EI_y \frac{\pi^2}{L^2} \left[\sqrt{\left(\frac{I_w}{I_y} + \frac{GI_T L^2}{EI_y \pi^2}\right) \left(1 - \frac{I_y}{I_z}\right) + \beta_y^2} - \beta_y \right] \quad (5.171)$$

$$M_{z,cr,II,neg} = -\frac{1}{1 - \frac{I_y}{I_z}} EI_y \frac{\pi^2}{L^2} \left[\sqrt{\left(\frac{I_w}{I_y} + \frac{GI_T L^2}{EI_y \pi^2}\right) \left(1 - \frac{I_y}{I_z}\right) + \beta_y^2} + \beta_y \right] \quad (5.172)$$

Conversely, if the effect of the pre-buckling displacements is **neglected**, the expressions given in Eqs. (5.173) and (5.174) are obtained.

$$M_{z,cr,I,pos} = EI_y \frac{\pi^2}{L^2} \left(\sqrt{\left(\frac{I_w}{I_y} + \frac{GI_T L^2}{EI_y \pi^2}\right) + \beta_y^2} - \beta_y \right) \quad (5.173)$$

$$M_{z,cr,I,neg} = -EI_y \frac{\pi^2}{L^2} \left(\sqrt{\left(\frac{I_w}{I_y} + \frac{GI_T L^2}{EI_y \pi^2}\right) + \beta_y^2} + \beta_y \right) \quad (5.174)$$

Comparing Eqs. (5.171) and (5.172) to Eqs. (5.173) and (5.174), one may observe that the influence of pre-buckling displacements is represented by the term $1-I_y/I_z$. Consequently, as for major-axis bending, the ratio between the major- and the minor-axis second moment of area is the key parameter introducing the effect of pre-buckling displacements into the expression of elastic instability.

Also, it has to be distinguished between positive and negative minor-axis bending as the absolute values of the elastic critical loads are not identical for the two cases due to the mono-symmetry of the cross-section with respect to the minor-axis. It is recalled that positive minor-axis bending compresses the tips of the flanges. If expressions given in Eqs. (5.173) and (5.174) are compared to each other, one may recognise that the absolute value of the negative elastic critical moment is always greater than the positive one implying that U-shaped members are less sensitive to elastic instability in case of negative minor-axis bending than for positive minor-axis bending.

If pre-buckling displacements are considered, again two different expressions for the positive and negative elastic critical moment associated with minor-axis bending are obtained. However, analysing Eq. (5.172), one may observe that it always yields a positive result as the Wagner constant β_y is always positive in the reference system used here and the term $1-I_y/I_z$ is always negative as it is supposed that I_y is associated with the major-axis. Consequently, the analytical solution, taking into account the influence of pre-buckling displacements, implies that U-shaped members subject to **negative** minor-axis bending are **never** sensitive to elastic instability. Conversely, the expressions for the critical minor-axis bending moment can give a numerical value for members under positive moments M_z implying that U-shaped members can, in some conditions, be sensitive to elastic instability for this load case. As Eq. (5.172) always yields a greater value than Eq. (5.171), this last equation is kept hereafter.

It is interesting to note that Eq. (5.171) only yields a value for the critical minor-axis bending moment, if the radicand is positive. This may be expressed by Eq. (5.175).

$$\beta_y^2 > - \left(\frac{I_w}{I_y} + \frac{GI_T}{EI_y} \frac{L^2}{\pi^2} \right) \left(1 - \frac{I_y}{I_z} \right) \quad (5.175)$$

As the Wagner constant β_y is cross-section specific, it seems more convenient to express the condition expressed by Eq. (5.175) as a function of the member length as shown in Eq. (5.176).

$$L_{th,ltb,Mz} = \pi \sqrt{ \left(- \frac{\beta_y^2}{1 - \frac{I_y}{I_z}} - \frac{I_w}{I_y} \right) \frac{EI_y}{GI_T} } \quad (5.176)$$

Eq. (5.176) indicates that it exists a threshold value of the length $L_{th,ltb,Mz}$ that characterizes whether a U-shaped member is sensitive to elastic instability under minor-axis bending or not. In fact, if the **length of the member exceeds the threshold length $L_{th,ltb,Mz}$, the member is not**

sensitive to elastic instability under M_z and, contrariwise if the **length of the member is less than $L_{th,ltb,Mz}$** , the U-shaped member becomes sensitive to elastic instability under M_z ! This observation may seem contrary to the natural feeling that a long member of a given cross-section is more sensitive to elastic instability than a shorter one with the same cross-section.

Table 5-18 summarizes the resulting threshold lengths for different cross-sections. Also, the ratio between the threshold length and the height of the cross-section is given. It appears that the value of $L_{th,ltb,Mz}$ is small; nevertheless the lengths are still in the practical range.

Table 5-18: Threshold values $L_{th,ltb,Mz}$ for different hot-rolled U sections

Section	Threshold length $L_{th,ltb,Mz}$ (mm)	$L_{th,ltb,Mz}/h$
UPE 80	942,9	11,79
UPE 140	1246	8,90
UPE 200	1680	8,40
UPE 270	2146	7,95
UPE 400	2817	7,04

In order to study if elastic instability due to minor-axis bending is of interest, Figure 5-97 and Figure 5-98 show the evolution of the critical minor-axis bending moment and the relative slenderness over the length for a member of UPE 140 section and one of UPE 270 section. The two members are supposed to be fabricated from steel S235.

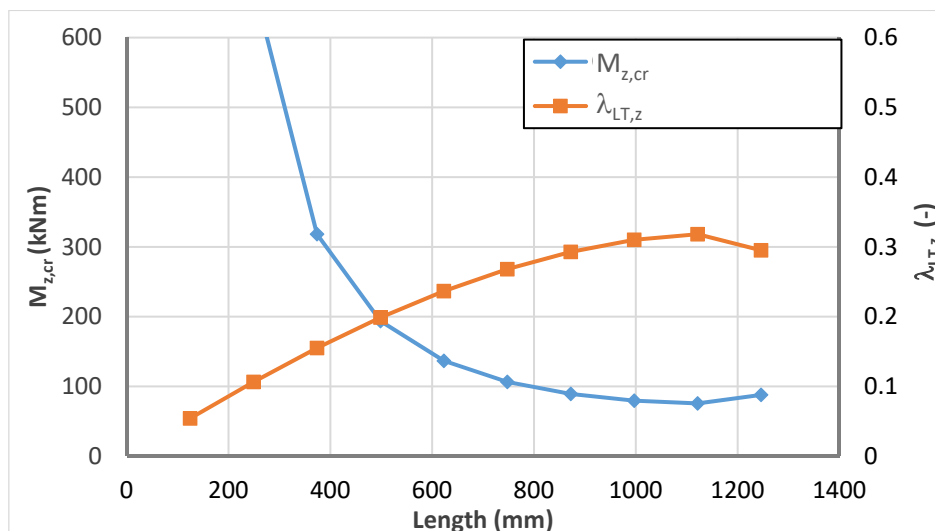


Figure 5-97: Critical moment $M_{z,cr}$ and relative slenderness for a member of UPE 140 section subject to constant minor axis bending

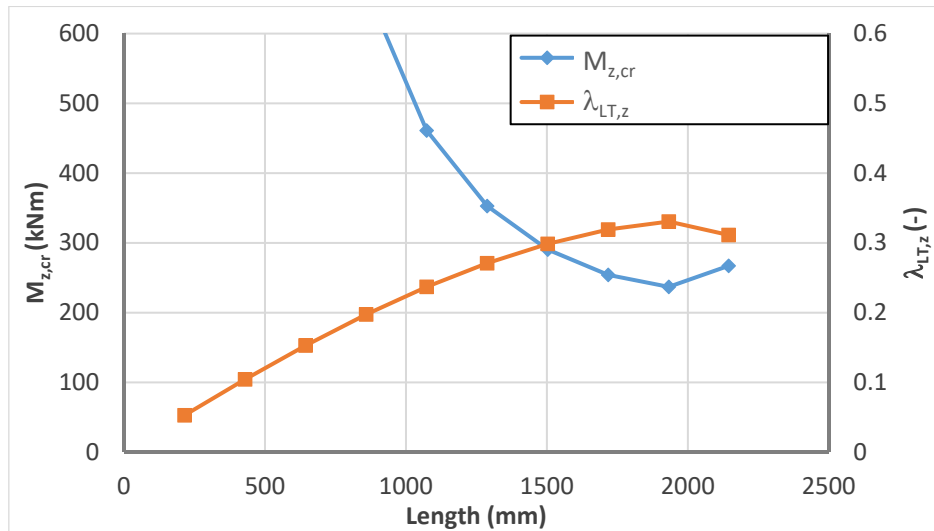


Figure 5-98: Critical moment $M_{z,cr}$ and relative slenderness for a member of UPE 270 section subject to constant minor axis bending

In Figure 5-97 and Figure 5-98, it can be seen that the relative slenderness for both members are very low. Also, one may note that the curves are represented up to the threshold length and consequently, the curves end abruptly at a given slenderness associated with the maximum length giving a numerical value of the critical moment. Yet, one may observe that the slenderness linked to the threshold length is not the maximum slenderness attained by a given member. Indeed, for both sections it appears that the curve representing the slenderness passes through a maximum and then slightly decreases. The length minimizing the critical minor-axis bending moment (and hence the maximizing the slenderness) can be obtained by deriving Eq. (5.171) with respect to the length L . The resulting expression is set equal to zero and then reorganised to isolate the length. The only admissible solution of the problem is given in Eq. (5.177).

$$L_{Mz,cr,max} = \pi \sqrt{-2 \frac{EI_w}{GI_t} \left(1 - \frac{\beta_y}{\sqrt{-\frac{I_w}{I_y} \left[1 - \frac{I_y}{I_z} \right]}} \right)} \quad (5.177)$$

The obtained results are compared for different U sections in Table 5-19.

Table 5-19: Member lengths minimising the critical minor-axis bending moment

Section	$L_{Mz,cr,max}$ (mm)	$\lambda_{Mz,cr,II}$ ($L_{Mz,cr,max}$) for S235
UPE 80	804,9	0,335
UPE 140	1132,8	0,318
UPE 200	1549,7	0,328
UPE 270	1987,9	0,331
UPE 400	2579,8	0,311

Table 5-19 highlights that the maximum relative slenderness linked to elastic instability under minor-axis bending is just above 0,3. It should be recalled that, if pre-buckling flexure is not considered, the maximum relative slenderness may attain 0,6 for practical cases (see Figure 5-94 and Figure 5-95).

In order to validate the analytical expression of the elastic critical minor-axis bending moment, elastic second order calculations (GNIA) including an imperfection about the z-axis (half sine wave; amplitude = $L/1000$) are performed. It is proposed to study a member of UPE 200 section subject to constant positive minor-axis bending (web is in tension). The load displacement curves obtained by the numerical simulation are plotted in Figure 5-99 and Figure 5-100.

It should be noted that the lateral displacement represented in Figure 5-99 refers to the node situated at the theoretical intersection between upper flange and web. Both figures suggest that the behaviour of the member may become highly non-linear for short lengths indicating the importance of second order effects. Conversely, for member lengths exceeding approximately 2000 mm the behaviour of the member is practically linear. Figure 5-99 and Figure 5-100 also represent the value of the critical minor-axis bending moment calculated with Eq. (5.171). It can be seen that the calculated values represent well the real behaviour of the member. Obviously, GNIA calculations may not yield a single value of the critical moment. Generally, it is accepted to consider the point of inflection of the load-displacement curve as done for example in reference (Erkmen et al. 2011). Based on this definition, it can be concluded that the given results are very satisfactory compared to the GNIA calculation.

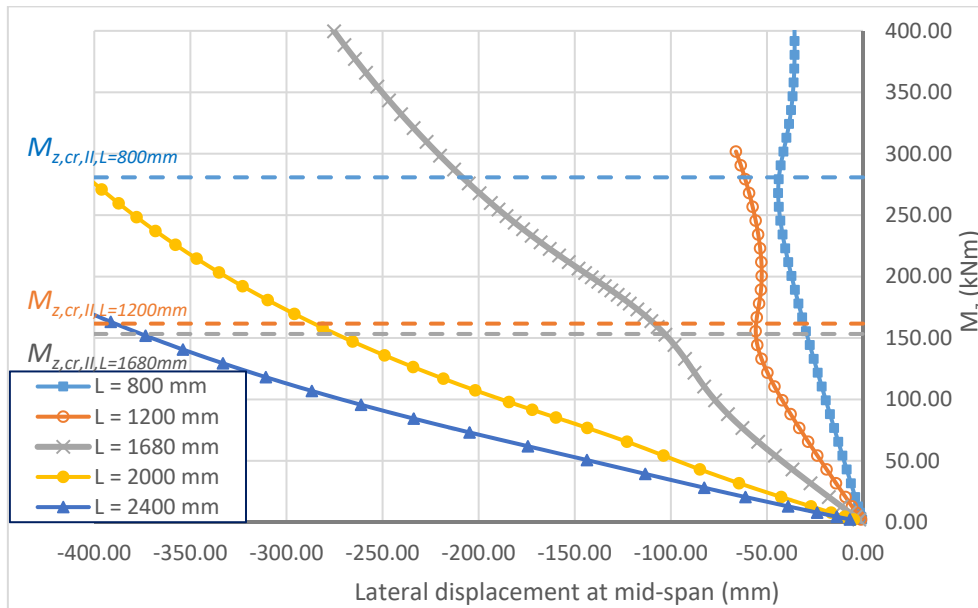


Figure 5-99: Load-displacement curve for member of UPE 200 section

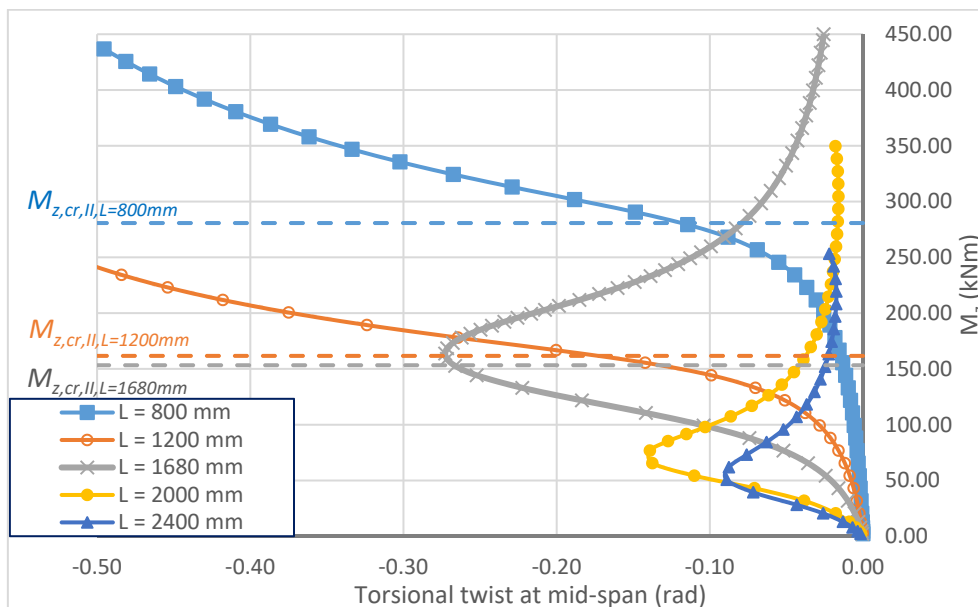


Figure 5-100: Load-displacement curve for member of UPE 200 section

The previous figures show that the member behaviour becomes non-linear at a certain value for the minor-axis bending moment for members whose lengths does not exceed 1680 mm. Conversely, for member lengths of 2000 mm and 2400 mm, the behaviour is nearly completely linear (see especially Figure 5-100). Hence, second order effects and instability may be considered negligible for these member lengths.

In order to permit an easier visualisation of the behaviour, Table 5-20 presents the mid-span displacement of the member possessing a length of 1200 mm.

Table 5-20 shows that the member displaces principally along the y-axis up to a certain value of the minor-axis bending moment. Starting from approximately 120 kNm the torsional twist of

the member increases rapidly. When the bending moment approaches the value of $M_{z,cr,II}$, the torsional twist becomes non-negligible (see displacement for $M_z = 153 \text{ kNm}$).

Table 5-20: Evolution of the displacement of the member with increasing minor-axis bending

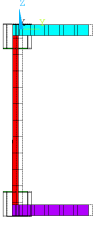
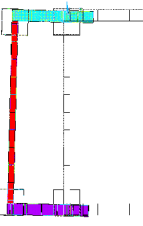
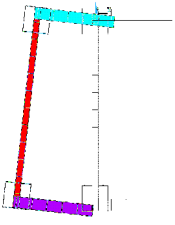
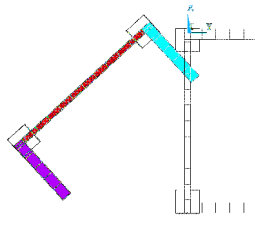
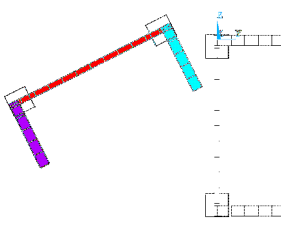
Applied bending moment M_z (kNm)	Deformed shape at mid-span
9,00	
120,0	
153,0	
285,2	
450,0	

Figure 5-101 presents the displacement of the entire member for $M_z = 450 \text{ kNm}$. One may easily observe that the deformation is principally characterized by an important torsional twist.

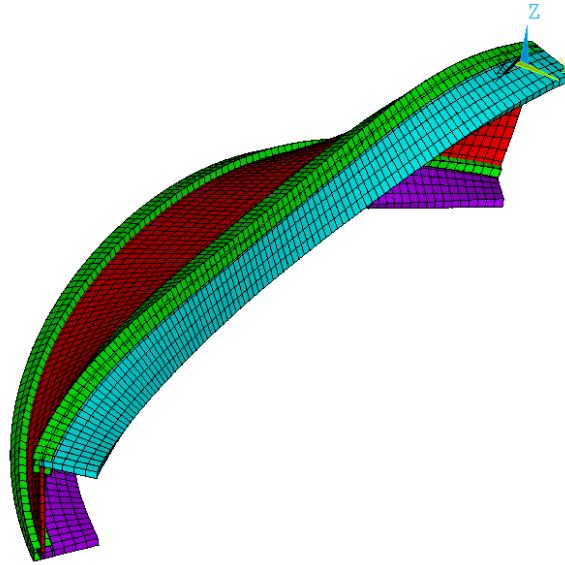


Figure 5-101: Deformed shape of the member for $M_z = 450$ kNm

It also seems interesting to compare the values of the critical moments $M_{z,cr,I}$ and $M_{z,cr,II}$ with increasing member length for the example given before (UPE 200 with fork supports subject to constant minor-axis bending). In Figure 5-102 one may observe that the difference between the two expressions of the critical minor-axis bending moment increases heavily with the member length. Near the threshold length ($L/h = 8,4$) the ratio between $M_{z,cr,II}$ and $M_{z,cr,I}$ exceeds the value of 2,0 indicating that the member is much less sensitive to elastic instability than predicted by the critical minor-axis bending moment $M_{z,cr,I}$, neglecting the influence of pre-buckling displacements. Also, it can be seen that the pre-buckling displacements have a greater influence on elastic stability of U-shaped members under minor-axis bending than for those subject to major-axis bending. For this load case the ratio $M_{y,cr,II}$ and $M_{y,cr,I}$ attains its maximum of approximately 1,3 for a UPE 80 cross-section (see Figure 5-96).

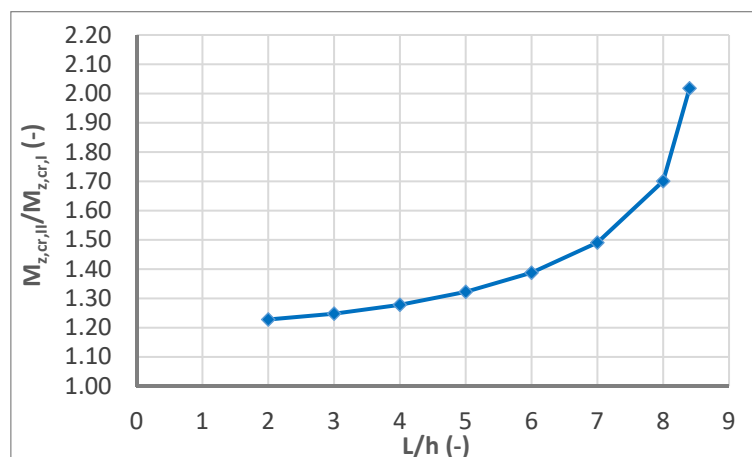


Figure 5-102: Difference between $M_{z,cr,II}$ and $M_{z,cr,I}$ for a UPE 200 section

It has been shown that it is crucial to consider the pre-buckling deflection for the determination of the elastic critical moment $M_{z,cr,z}$ for U sections. If they are not considered, the influence of elastic instability may be highly overestimated. Yet, conversely to the case of I-shaped members, U-shaped members might be sensitive to elastic member instability in some configurations even if they are subject to a sole minor-axis bending moment. Again, it appears that global design methods as OIC should be based on the elastic critical load considering the influence of pre-buckling displacements as, if this is not done, the behaviour of the member is not well represented by the critical load amplification factor.

5.5.6.2.4 U sections subject to bi-axial bending

Hereafter, it is proposed to study elastic instability in case of bi-axial bending. The second variation of the total potential energy of the member in case of constant bending moments is recalled in Eq (5.178). The terms linked to pre-buckling displacements are provided in the third line of Eq. (5.178).

$$\begin{aligned}
 \partial^2 \Pi = & \int \left[EI_y \partial w_{,xx}^2 + EI_z \partial v_{,xx}^2 + EI_w \partial \varphi_{,xx}^2 + GI_T \partial \varphi_{,x}^2 \right] dx \\
 & + 2\alpha_{cr} \int \left[M_z \partial \varphi \partial w_{,xx} - \beta_y M_z \partial \varphi_{,x}^2 - M_y \partial \varphi \partial v_{,xx} \right] dx \\
 & - \alpha_{cr}^2 \int \left[\frac{M_z^2}{EI_z} \left(1 - \frac{I_y}{I_z} \right) \partial \varphi^2 + \frac{M_y^2}{EI_y} \left(1 - \frac{I_z}{I_y} \right) \partial \varphi^2 \right] dx \\
 & - \alpha_{cr} \int \left[+ 2 \frac{I_y}{I_z} M_z \partial \varphi \partial w_{,xx} - \left(2 \frac{I_z}{I_y} M_y \right) \partial \varphi \partial v_{,xx} \right] dx
 \end{aligned} \tag{ 5.178 }$$

Based on the approximation of the displacements by a sine half wave, it is possible to determine the expressions of the critical load amplification factor. Again, the index “I” indicates that pre-buckling displacements are not considered and the index “II” indicates that pre-buckling displacements are accounted for.

$$\alpha_{cr,I} = \frac{\sqrt{\left(\frac{M_y^2}{N_{cr,z}} + \frac{M_z^2}{N_{cr,y}} \right) \left(GI_T + \frac{\pi^2}{L^2} EI_w \right) + M_z^2 \beta_y^2 - M_z \beta_y}}{\frac{M_y^2}{N_{cr,z}} + \frac{M_z^2}{N_{cr,y}}} \tag{ 5.179 }$$

$$\alpha_{cr,II} = \frac{\sqrt{\left[\frac{M_y^2}{N_{cr,z}} \left(1 - \frac{I_z}{I_y} \right) + \frac{M_z^2}{N_{cr,y}} \left(1 - \frac{I_y}{I_z} \right) \right] \left(GI_T + \frac{\pi^2}{L^2} EI_w \right) + M_z^2 \beta_y^2 - M_z \beta_y}}{\frac{M_y^2}{N_{cr,z}} \left(1 - \frac{I_z}{I_y} \right) + \frac{M_z^2}{N_{cr,y}} \left(1 - \frac{I_y}{I_z} \right)} \tag{ 5.180 }$$

One may note that Eq. (5.179) has also been derived in reference (Cheng et al. 2013) based on the assumption that pre-buckling displacements are negligible.

In order to visualize the differences between the two expressions, a U-shaped member of UPE 200 cross-section is studied again. The member is supposed to be subject to constant bi-axial bending and to possess a length of 4 m. As before, the member possesses fork supports at its ends. The obtained interaction curves are represented in Figure 5-103 for a value of the critical amplification factor α_{cr} of 2,0. Note again that positive minor-axis bending compresses the flanges' tips.

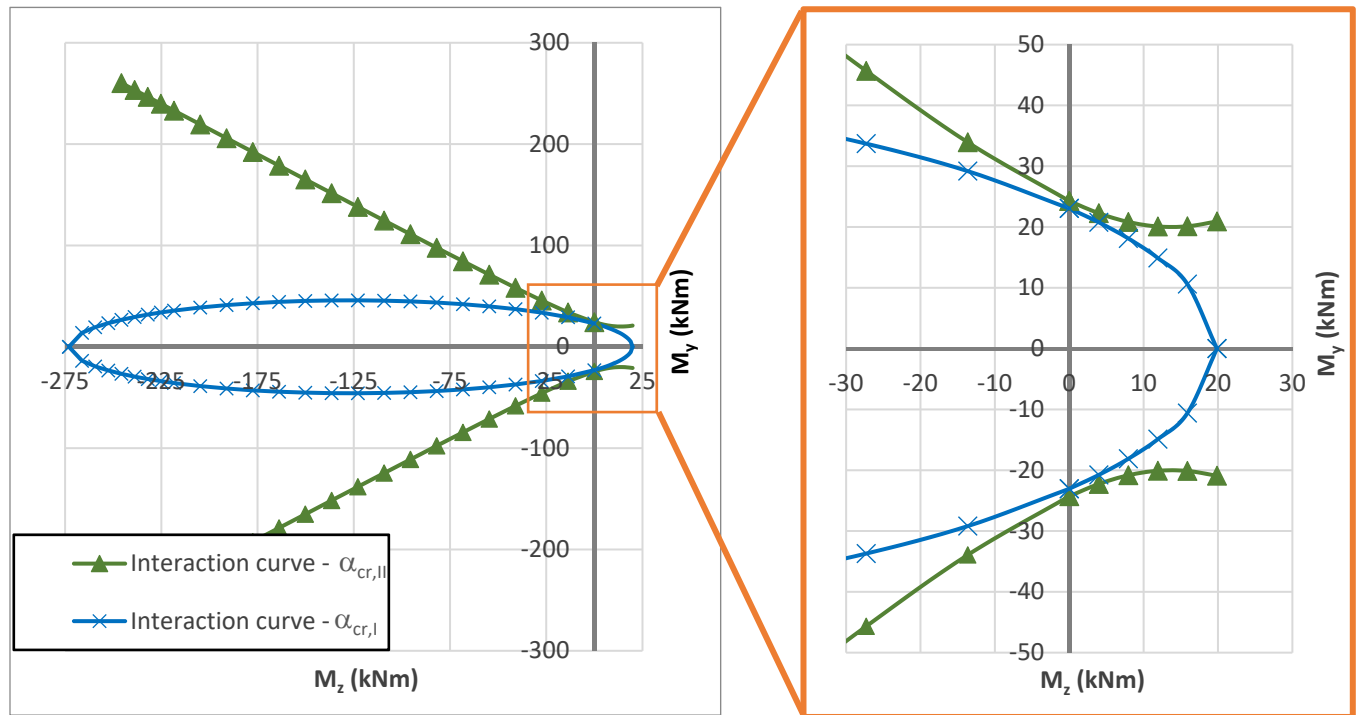


Figure 5-103: M_y - M_z interaction curve for elastic instability of the studied member – $\alpha_{cr} = 2.0$

Figure 5-103 clearly highlights the difference between the two formulations of the critical load amplification factor. The difference is maximum for negative minor-axis bending. It is recalled that for this load case the more precise approach considering pre-buckling displacements suggests that the member is not sensitive to elastic instability if it is only subject to minor-axis bending. Consequently, for bi-axial bending, the minor-axis bending moment possesses a stabilizing effect on the member. In fact, it can be seen that with increasing negative minor-axis bending (absolute value), the major-axis bending moment has to increase, too so as to obtain the same critical load amplification factor. This behaviour is not well represented by the approach that neglects pre-buckling displacements.

For the case of positive minor-axis bending one may also observe considerable differences. It can be seen that the curve associated with the expression $\alpha_{cr,II}$ does not cross the abscissa indicating that the member is not sensitive to elastic instability for positive minor-axis bending only. This observation may be confirmed by recalling that the threshold length for the UPE 200 cross-section is less than the length of the member: $L_{th,ltb,Mz} = 1680$ mm. Again, this behaviour is not correctly represented by the approach neglecting the influence of pre-buckling displacements because the corresponding curve crosses the abscissa at $M_{z,cr,I}/\alpha_{cr} = 19,86$ kNm. Even if the studied member is not sensitive to elastic instability under minor-axis bending only, a positive moment M_z has a

slightly negative effect on elastic instability as is shown by the interaction curve linked to $\alpha_{cr,II}$. Indeed, the minimum is obtained for a positive value of the moment M_z whose value may be obtained with Eq. (5.181). The corresponding value of the major-axis bending moment is given in Eq. (5.182).

$$M_z (M_{y,cr,min,II}) = - \frac{N_{cr,y}}{\left(1 - \frac{I_y}{I_z}\right) \alpha_{cr}} \beta_y \quad (5.181)$$

$$M_{y,cr,min,II} = \pm \frac{1}{\alpha_{cr}} \sqrt{\frac{M_{y,cr,0}^2}{1 - \frac{I_z}{I_y}} + \frac{N_{cr,z} N_{cr,y} \beta_y^2}{\left(1 - \frac{I_z}{I_y}\right) \left(1 - \frac{I_y}{I_z}\right)}} \quad (5.182)$$

and

$$M_{y,cr,0} = N_{cr,z} \sqrt{\frac{I_w}{I_z} + \frac{GI_T}{EI_z} \frac{L^2}{\pi^2}}$$

Throughout the previous paragraphs, it has been shown that the problem of elastic instability is very complex for U-shaped members in bending. It has been highlighted that, in some cases, they may be sensitive to **elastic instability** when they are subject to minor-axis bending only. Consequently, second order effects may arise and potentially lead to a reduction of the member resistance. This result is in complete opposition to the general accepted theory for I-shaped members. However, if pre-buckling displacements are considered, it may be shown that the sensitivity to elastic instability under minor-axis bending is much less pronounced as might be concluded if pre-buckling displacements are not considered in the derivation of the elastic critical load. Also, it is recalled again that the elastic critical loads do not directly represent the resistance of the member but they are only a parameter that enters the design model. Consequently, it seems interesting to study the ultimate resistance of U shaped members under minor-axis bending even if this somewhat forestall the parametric study presented in paragraph 5.6.

5.5.6.2.5 Elasto-plastic instability of U-shaped members subject to minor-axis bending

In order to evaluate the influence of elastic instability under minor-axis bending moments on the ultimate resistance of U-shaped members the example of a UPE 200 section is studied. In the previous paragraph, it has been shown that members possessing lengths greater than the threshold length $L_{th,ltb,Mz}$ are not sensitive to **elastic instability** under minor-axis bending. However, for shorter members elastic instability may occur. Yet, the slenderness of members made from steel S235 is rather low for these lengths. Therefore, different steel grades are studied. For the example, it is supposed that the member is subject to constant minor-axis bending compressing the tips of the flanges and that it possesses fork supports at its ends. The GMNIA simulations are performed including the residual stress pattern for the UPE 200 section determined in paragraph 5.2.1.5 and an equivalent imperfection along the z-axis with an amplitude of $L/1000$. Additionally, it is to be noted that rigid beam elements are applied along the

member so as to avoid local instability and distortion (see paragraph 5.2.3). Consequently, the failure of the member is caused by elasto-plastic instability or by exceeding the ultimate section resistance characterized by the strain limit of 15%.

The obtained ultimate resistances are represented in the following figures. In Figure 5-104 the ultimate resistance is given as a function of the relative slenderness calculated with the value of $M_{z,cr,I}$. Conversely, Figure 5-105 represents the results as a function of the relative slenderness determined with $M_{z,cr,II}$ considering the influence of pre-buckling displacements. Both figures show that U-shaped members may be sensitive to elasto-plastic instability. In fact, it may be observed that some members do not attain the full plastic section resistance. Nevertheless, the maximum strength reduction is only of about 10%. By comparing Figure 5-104 and Figure 5-105, one may again recognize the influence of the pre-buckling displacements on the critical moment about the minor-axis (that enters the relative slenderness). If they are not included calculation of $M_{z,cr}$, the relative slenderness does not well represent the behaviour of U-shaped members as shown in Figure 5-104. This figure seems to indicate that the ultimate resistance first decreases with the relative slenderness and then increases again. The increase of the resistance after passing through a minimum is directly linked to the influence of the pre-buckling displacements on the critical moment. Indeed, it has been shown in the previous paragraphs that U-shaped members are not sensitive to elastic member instability if their length exceeds the threshold length. Figure 5-105 confirms this theoretical result. For members whose length exceeds the threshold length, a critical minor-axis bending moment cannot be calculated. Consequently, their slenderness is defined as zero and their ultimate resistance is represented on the axis of ordinates. Obviously, these members always attain at least their plastic section resistance. It may be noted that the longer specimen may attain a higher resistance as the strain hardening can spread to a greater extend through the section before the maximum accepted strain is attained in the numerical simulations. Members that are shorter than the threshold length may be sensitive to elasto-plastic instability. Figure 5-105 represents this fact well as the ultimate resistance of a given member decreases with its slenderness. For relative slendernesses higher than 0,4 elasto-plastic instability can reduce the resistance of the member. Yet, even in Figure 5-105 it seems that the resistance may increase close to the threshold length. This can be explained based on the precision of the analytical result. In fact, in paragraph 5.5.6.2.3, it has been shown that the theoretical developments become less precise for members whose length is close to the threshold limit. Nevertheless, it is shown that the critical moment considering the effect of pre-buckling displacements represents well the behaviour of the member. However, it can also be seen that a relative slenderness of 0,4 can only be attained for members of high strength steel. For the widely used steel grades S235 and S355 the relative slenderness cannot exceed 0,4 due to the short threshold lengths. Therefore, it does not seem necessary to consider member instability in case of U-shaped members subject to minor-axis bending in today's practice.

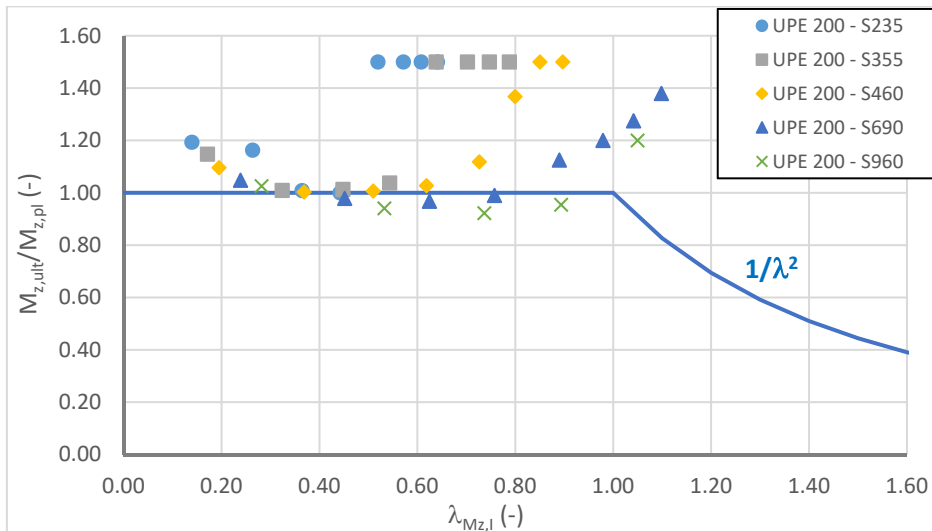


Figure 5-104: Ultimate resistance of a member of UPE 200 section under minor-axis bending – reduced slenderness based on $M_{z,cr,I}$

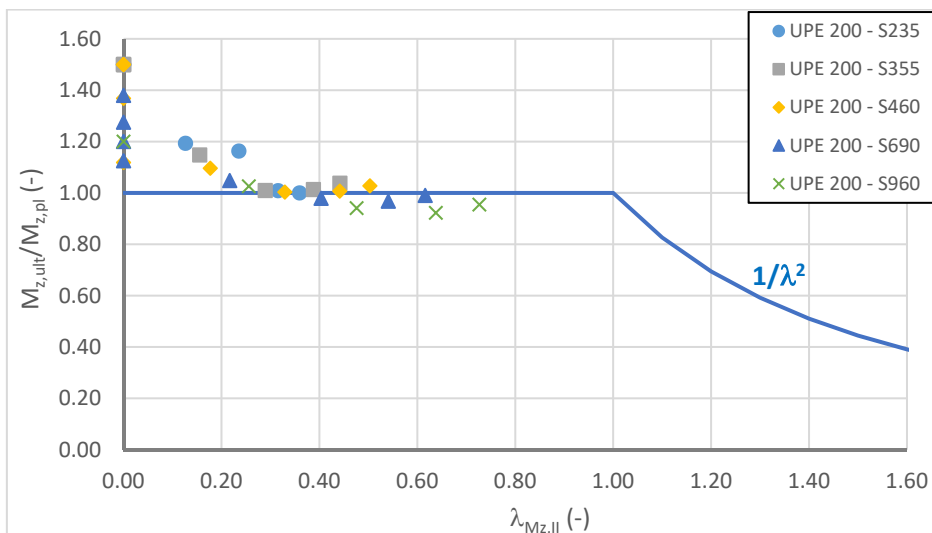


Figure 5-105: Ultimate resistance of a member of UPE 200 section under minor-axis bending – reduced slenderness based on $M_{z,cr,II}$

5.5.6.2.6 Conclusion

This paragraph presented a theoretical study concerning elastic instability of I- and U-shaped members. The well-known expressions of the critical major-axis bending moment applicable to I- and U- shaped members are developed. Yet, the classical expressions do not account for first order pre-buckling displacements. In order to evaluate their influence, a second series of equations for the elastic critical loads including the effect of pre-buckling displacements has been determined. In particular, it has been shown that:

- For I-shaped members under major-axis bending the difference between $M_{y,cr,I}$ and $M_{y,cr,II}$ is about 30% in case of compact H sections and less for more slender H and I sections;

- For I-shaped members under minor-axis bending, the consideration of pre-buckling displacements proves that this type of members is never sensitive to elastic instability under M_z ;
- For U-shaped members, it has been shown that the influence of pre-buckling displacements highly influences the elastic critical loads especially in case of minor-axis bending and bi-axial bending;
- U-shaped members are not sensitive to elastic instability under minor-axis bending if the bending moment leads to a compression of the web (negative minor-axis bending);
- U-shaped members under positive minor-axis bending may be sensitive to elastic instability if their length is **less** than a threshold value (see Eq. (5.176))!;
- The threshold value of the member length depends on the cross-section characteristics;
- The GMNIA analyses performed on U-shaped members under minor-axis bending have shown that for steel grades up to S460 the influence of member instability does not reduce the theoretical plastic resistance $M_{z,pl}$. For steel grades between S690 and S960 the maximum reduction due to member instability is of about 10%. Hence, it is not necessary to consider member instability under M_z for U section for the current design practice. Yet, if UPE section (or U section of similar form) are utilized with steel grades higher than S460 a reduction might be considered. Again, for steel construction this not of practical interest today, but for other industrial fields (crane construction), it might be necessary to account for a resistance reduction. Also, local and distortional buckling modes may then influence the member behaviour.

This paragraph has shown that the pre-buckling (or first order displacements) may have a non-negligible influence on the elastic critical loads, especially for U-shaped members. However, this does not imply that the use of the classical expressions not considering the pre-buckling displacements leads to erroneous results when they are used with the reduction curves as the ones of Eurocode 3 Part 1-1. Indeed, these curves have been calibrated based on the elastic critical loads not including pre-buckling displacements. Therefore, these last should be applied in the framework of the member stability checks of Eurocode 3. Additionally, as resistance models in current standards are based on interaction equations, it is possible to determine are “partial resistance” with reference to each individual internal force and moment. Consequently, one may directly account for the fact that members are generally not sensitive to instability when they are subject to minor-axis bending only. Yet, the OIC resistance model is based on global load amplification factors associated with plastic section resistance and elastic instability. The previous paragraphs have shown that, for U-shaped members, the relative slenderness may become rather high for members under minor-axis bending. However, their resistance should only be reduced in special cases. Consequently, a future reduction curve calibrated for this load case might be rather complex if it is based on the classical approach for the critical loads.

Conversely, if pre-buckling displacements are considered for the determination of the elastic critical loads the reduction curve could be given in the Eurocode format. Therefore, it is recommended here to use a critical load amplification factor including the influence of pre-buckling displacements when a global design concept is used, at least in case of open sections.

It should be noted that only selected load cases have been studied. Obviously, a general expression covering all configurations of members with arbitrary open section subject to a complex combination of loads would not be practical anymore. Even, the expressions developed before are already complex. Yet, their precision is affected when the shape of the bending moment diagrams are not uniform but variable. Consequently, it seems more straightforward to use numerical programs for the determination of critical loads (for example *LTBeamN*). Nevertheless, the analytical approach concerning the problem of elastic stability has given relevant information especially on the influence of pre-buckling displacements. Additionally, it has been recalled that the form of the eigenmode can be described by the parameter c_r representing the ratio between the modal lateral displacement and the modal torsional twist. This result are used in the next paragraphs concerning the elastic second order equilibrium of the imperfect member under the applied loads. It is assumed that the imperfections are affine to the first eigenmode and that it is consequently characterised by an amplitude v_0 or φ_0 and the ratio of v_0 to φ_0 defined by the parameter c_r .

5.5.7 Elastic second order equilibrium of the member

5.5.7.1 *General*

After the study concerning the elastic critical loads presented in the previous paragraphs, the second order equilibrium of the member is of interest. The second order internal forces and moments are derived for the imperfect member based on elastic theory. The member imperfection is chosen affine to the eigenmode that has been determined throughout paragraphs 5.5.5 and 5.5.6. The following study is performed in order to get more insights into the non-linear behaviour of members subject to torsion in view to develop a consistent design model for the member stability. Nevertheless, due to the limitation to elastic theory, the obtained results cannot be transferred directly to the ultimate member resistance. A certain empirical calibration is necessary as has been done in the past for the elaboration of the interaction formulae addressing the case of members subject to combined bi-axial bending and axial forces. This calibration is done in paragraph 5.6.

The determination of the second order internal forces and moments is based on the system represented in (5.183). This system of differential equations governs the elastic behaviour of a member with open cross-section that is subject to an arbitrary combination of loads. Again, it is supposed that the axial force is constant and consequently, the differential equation linked to the axial displacement of the centroid can be omitted.

$$EI_y w_{,xxxx} + (M_z \varphi)_{,xx} + N w_{,xx} - N y_s \varphi_{,xx} = q_z$$

$$EI_z v_{,xxxx} - (M_y \varphi)_{,xx} + N v_{,xx} + N z_s \varphi_{,xx} = q_y \quad (5.183)$$

$$N r_{yz}^2 \varphi_{,xx} + N z_s v_{,xx} - N y_s w_{,xx} - M_y v_{,xx} + 2\beta_z (M_y \varphi_{,x})_{,x}$$

$$M_z w_{,xx} + 2\beta_y (M_z \varphi_{,x})_{,x} + EI_w \varphi_{,xxxx} - GI_t \varphi_{,xx} = q_z (y_F - y_S) - q_y (z_F - z_S) = m_x$$

In general, system (5.183) cannot be solved analytically. In order to approximate the solution, suitable functions have to be used for the displacements v , φ , w . For the case of a member subject to a sinusoidal torsional load and to bi-axial bending whose distribution is affine to a sine half wave the displacements may be approximated by sine half waves as before provided that the member possess fork end conditions:

$$w = \underline{w} \sin\left(\frac{\pi x}{L}\right) \quad w_{,xx} = -\frac{\pi^2}{L^2} \underline{w} \sin\left(\frac{\pi x}{L}\right) \quad w_{,xxxx} = \frac{\pi^4}{L^4} \underline{w} \sin\left(\frac{\pi x}{L}\right)$$

$$v = \underline{v} \sin\left(\frac{\pi x}{L}\right) \quad v_{,xx} = -\frac{\pi^2}{L^2} \underline{v} \sin\left(\frac{\pi x}{L}\right) \quad v_{,xxxx} = \frac{\pi^4}{L^4} \underline{v} \sin\left(\frac{\pi x}{L}\right) \quad (5.184)$$

$$\varphi = \underline{\varphi} \sin\left(\frac{\pi x}{L}\right) \quad \varphi_{,xx} = -\frac{\pi^2}{L^2} \underline{\varphi} \sin\left(\frac{\pi x}{L}\right) \quad \varphi_{,xxxx} = \frac{\pi^4}{L^4} \underline{\varphi} \sin\left(\frac{\pi x}{L}\right)$$

For more complicated cases (cantilever beam, more complicated moment distributions), an analytical determination of the second order internal forces becomes nearly impossible (at least for hand calculations) as the displacements functions have to account of the greater complexity of the configuration. Consequently, it would be necessary to use serial functions of higher degree. So as to simplify the presentation, it is proposed to keep the reference case as simple as possible.

System (5.183) is used hereafter in order to determine the internal forces and moments considering second order effects and imperfection. These internal forces and moments are used to verify the resistance of the critical, i.e. most loaded, section.

In the following, system (5.183) is solved for I- and U- shaped section for selected load cases. In a first step, solutions are detailed for simple load cases in order to allow the full understanding of the approach. In a second step, more complex load cases, including torsion and axial forces are considered.

5.5.7.2 *Members of double symmetric I section subject to constant major-axis bending*

In order to illustrate the adopted method, it is proposed to determine the second order internal forces and moments for the very simple case of members with double symmetric I section subject to constant major-axis bending. The development shown hereafter has been used, in a more or less similar way by several authors as in references (FOSTA 2004), (Stangenberg 2007), (Naumes 2009) and (Taras 2011).

In case of constant major-axis bending, system (5.183) simplifies to:

$$EI_z v_{,xxxx} - M_y (\varphi_{,xx} + \varphi_{0,xx}) = 0 \quad (5.185)$$

$$-M_y (v_{,xx} + v_{0,xx}) + EI_w \varphi_{,xxxx} - GI_t \varphi_{,xx} = 0$$

Eq. (5.185) assumes that the member is subject to a geometrical imperfection composed of a torsional twist φ_0 and a lateral displacement of the centroid v_0 . As stated above, it is considered hereafter that imperfection is affine to the eigenmode. For the studied case, the eigenmode is of sine shape. As shown in paragraph 5.5.5, the modal lateral displacement of the centroid can be expressed as a function of the modal torsional twist. Consequently, it may be written:

$$v_0 = v_0 \sin\left(\frac{\pi x}{L}\right) = -\varphi_0 \sqrt{\frac{I_w}{I_z} \left(1 + \frac{GI_T}{EI_w} \frac{L^2}{\pi^2}\right)} \sin\left(\frac{\pi x}{L}\right) \quad (5.186)$$

The imperfection and the approximation of the displacement functions are introduced into Eq. (5.185) to obtain:

$$EI_z \frac{\pi^4}{L^4} \underline{v} + M_y \frac{\pi^2}{L^2} \underline{\varphi} = -\frac{\pi^2}{L^2} M_y \underline{\varphi}_0 \quad (5.187)$$

$$M_y \frac{\pi^2}{L^2} \underline{v} + EI_w \frac{\pi^4}{L^4} \underline{\varphi} + GI_t \frac{\pi^2}{L^2} \underline{\varphi} = M_y \underline{\varphi}_0 \frac{\pi^2}{L^2} \sqrt{\frac{I_w}{I_z} \left(1 + \frac{GI_T}{EI_w} \frac{L^2}{\pi^2}\right)} \quad (5.188)$$

Based on Eq. (5.187), one may determine the amplitude of the lateral displacement:

$$\underline{v} = -\frac{M_y (\underline{\varphi} + \underline{\varphi}_0)}{EI_z \frac{\pi^2}{L^2}} \quad (5.189)$$

The lateral displacement obtained in Eq. (5.189) is introduced in Eq. (5.188). After several intermediate steps, one obtains an expression of the torsional twist represented in Eq. (5.190).

$$\underline{\varphi} = \frac{M_y}{M_{cr}} \frac{1}{\left(1 - \frac{M_y}{M_{y,cr}}\right)} \underline{\varphi}_0 \quad (5.190)$$

The second order lateral displacement may therefore be expressed as a function of the torsional twist as shown in Eq. (5.191).

$$\underline{v} = -\frac{\frac{M_y}{M_{y,cr}} \sqrt{\frac{I_w}{I_z} \left(1 + \frac{GI_T L^2}{EI_w \pi^2}\right)}}{1 - \frac{M_y}{M_{y,cr}}} \underline{\varphi} = -\frac{M_y}{N_{cr,z}} \frac{1}{1 - \frac{M_y}{M_{y,cr}}} \underline{\varphi}_0 \quad (5.191)$$

Consequently, the second order moments are:

$$M_z = EI_z v_{,xx} = -EI_z \frac{\pi^2}{L^2} \underline{v} = \frac{M_y}{1 - \frac{M_y}{M_{y,cr}}} \underline{\varphi}_0 \quad (5.192)$$

$$\begin{aligned} B = -EI_w \varphi_{,xx} &= EI_w \frac{\pi^2}{L^2} \underline{\varphi} = \frac{M_y}{\sqrt{\frac{I_z}{I_w} \left(1 + \frac{GI_T L^2}{EI_w \pi^2}\right)}} \frac{1}{1 - \frac{M_y}{M_{y,cr}}} \underline{\varphi}_0 \\ &= M_y \frac{N_{cr,z}}{M_{y,cr}} \frac{I_w}{I_z} \frac{1}{1 - \frac{M_y}{M_{y,cr}}} \underline{\varphi}_0 \end{aligned} \quad (5.193)$$

At this point the second order internal moments are introduced into a cross-section resistance interaction formula. Consequently, a form of interaction between the bending moments and the bi-moment has to be chosen. The analytical developments presented here suppose a linear elastic material behaviour. Therefore, a linear interaction is adopted and the resistance of the section is checked using the criterion represented by Eq. (5.194).

$$\frac{M_y^H}{M_{y,R}} + \frac{M_z^H}{M_{z,R}} + \frac{B^H}{B_R} \leq 1 \quad (5.194)$$

Introducing Eqs. (5.192) and (5.193) into Eq. (5.194), one obtains:

$$\frac{M_y}{M_{y,R}} + \frac{M_y}{1 - \frac{M_y}{M_{y,cr}}} \frac{1}{M_{z,R}} \underline{\varphi}_0 + M_y \frac{N_{cr,z}}{M_{cr,y}} \frac{I_w}{I_z} \frac{1}{1 - \frac{M_y}{M_{y,cr}}} \frac{1}{M_{w,R}} \underline{\varphi}_0 \leq 1 \quad (5.195)$$

One may note that the second and first order major-axis bending moments are identical based on the assumptions of small displacements (and especially small torsional twist). This assumption is generally respected for the case of lateral-torsional buckling under major-axis bending only.

Eq. (5.195) may be simplified as follows.

$$\frac{M_y}{M_{y,R}} + \frac{M_y}{M_{z,R}} \frac{1}{1 - \frac{M_y}{M_{y,cr}}} \left(1 + \frac{M_{z,R}}{B_R} \frac{I_w}{I_z} \frac{N_{cr,z}}{M_{y,cr}} \right) \varphi_0 \leq 1 \quad (5.196)$$

For double symmetric I sections, the bi-moment resistance and the minor axis bending moment resistance are proportional as shown in Eq. (5.197).

$$B_R = M_{z,R} \sqrt{\frac{I_w}{I_z}} \quad (5.197)$$

Introducing Eq. (5.197), the literal expressions of the critical moment and the critical axial force into Eq. (5.196) leads to:

$$\frac{M_y}{M_{y,R}} + \frac{M_y}{M_{z,R}} \frac{1}{1 - \frac{M_y}{M_{y,cr}}} \left(1 + \frac{1}{\sqrt{\left(1 + \frac{GI_T}{EI_w} \frac{L^2}{\pi^2} \right)}} \right) \varphi_0 \leq 1 \quad (5.198)$$

In order to transform this interaction formula into the commonly used format of the reduction curve, the reduction factor χ_{LT} and lateral-torsional buckling slendernesses λ_{LT} are introduced:

$$\chi_{LT} = \frac{M_{b,R}}{M_{y,R}} \quad (5.199)$$

$$\bar{\lambda}_{LT} = \sqrt{\frac{M_{y,R}}{M_{y,cr}}} \quad (5.200)$$

At ultimate limit state, the applied bending moment is just equal to the bending moment resistance and the criterion consequently equals 1,0. Hence, one obtains:

$$\chi_{LT} + \chi_{LT} \frac{1}{1 - \chi_{LT} \bar{\lambda}_{LT}^{-2}} \frac{M_{y,R}}{M_{z,R}} \left(1 + \frac{1}{\sqrt{\left(1 + \frac{GI_T}{EI_w} \frac{L^2}{\pi^2} \right)}} \right) \varphi_0 = 1 \quad (5.201)$$

At this stage, the generalized imperfection η is defined as proposed and justified by (Rondal and Maquoi 1979) for the case of flexural buckling.

$$\eta = \frac{M_{y,R}}{M_{z,R}} \left(1 + \frac{1}{\sqrt{\left(1 + \frac{GI_T L^2}{EI_w \pi^2} \right)}} \right) \varphi_0 = \alpha \left(\bar{\lambda} - \bar{\lambda}_0 \right) \quad (5.202)$$

It should be noted that the expression of the generalized imperfection has been empirically justified and calibrated with physical tests and numerical simulations for flexural buckling. The resulting expression of the reduction factor χ represents very well the flexural buckling behaviour of members. Yet, in case of lateral-torsional buckling the reduction curve is of slightly different form than in case of flexural buckling. Consequently, the possibility of introducing a modified form for the reduction curve has been discussed several times as for example in (Villette 2004). However, in order to keep a similar form for reduction curves for the cases of flexural buckling and lateral-torsional buckling, many authors followed the proposal of Rondal and Maquoi as for example (Stangenberg 2007), (Naumes 2009) and (Taras 2011). If this is accepted, one obtains the expressions of the “lateral-torsional buckling curve” proposed in paragraph 6.3.2.2 of Eurocode 3 Part 1-1 (CEN 2005a), i.e. the “Lateral-torsional buckling curves – General case”:

$$\chi_{LT} + \chi_{LT} \frac{1}{1 - \chi_{LT} \bar{\lambda}_{LT}^2} \alpha \left(\bar{\lambda} - \bar{\lambda}_0 \right) = 1 \quad (5.203)$$

$$\chi_{LT} = \frac{1}{\phi + \sqrt{\phi^2 - \bar{\lambda}_{LT}^2}} \quad (5.204)$$

$$\phi = 0,5 \left(1 + \alpha \left(\bar{\lambda}_{LT} - \bar{\lambda}_{LT,0} \right) + \bar{\lambda}_{LT}^2 \right) \quad (5.205)$$

In order to obtain accurate results, the combination of the imperfection factor α and the limit slenderness $\bar{\lambda}_{LT,0}$ should obviously depend on the residual stress pattern (as it is not accounted for explicitly in the given solution), i.e. the section geometry, and additionally on the torsional characteristics of the member expressed by the factor ε_T .

$$\delta_T = \sqrt{\left(1 + \frac{GI_T L^2}{EI_w \pi^2} \right)} = \frac{M_{y,cr}}{N_{cr,z}} \sqrt{\frac{I_z}{I_w}} \quad (5.206)$$

Some researchers, (Stangenberg 2007), (Naumes 2009) and (Taras 2011), decided not to introduce the torsional behaviour of the member in the imperfection but to keep it explicitly in the expression of the reduction curve. Their approach leads to the following expression of the resistance criterion.

$$\chi_{LT} + \chi_{LT} \frac{\bar{\lambda}_{LT}^2}{\bar{\lambda}_z^2} \frac{1}{1 - \chi_{LT} \bar{\lambda}_{LT}^2} \frac{N_R}{M_{z,R}} \varphi_0 = 1 \quad (5.207)$$

The previously cited authors (Stangenberg, Naumes and Taras) chose to introduce the generalized imperfection of Eq. (5.208).

$$\eta = \alpha \left(\bar{\lambda} - \bar{\lambda}_0 \right) = \frac{N_R}{M_{z,R}} v_{0,CF} \quad (5.208)$$

By introducing this expression of the generalized imperfection η into Eq. (5.207) one obtains:

$$\chi_{LT} + \chi_{LT} \frac{\bar{\lambda}_{LT}^2}{\bar{\lambda}_z^2} \frac{1}{1 - \chi_{LT} \bar{\lambda}_{LT}^2} \alpha \left(\bar{\lambda}_{LT} - \bar{\lambda}_{LT,0} \right) = 1 \quad (5.209)$$

The solution of the second order Eq. (5.209) is given in Eqs. (5.210) and (5.211).

$$\chi_{LT} = \frac{1}{\phi + \sqrt{\phi^2 - \bar{\lambda}_{LT}^2}} \quad (5.210)$$

$$\phi = 0,5 \left(1 + \alpha \frac{\bar{\lambda}_{LT}^2}{\bar{\lambda}_z^2} \left(\bar{\lambda}_{LT} - \bar{\lambda}_{LT,0} \right) + \bar{\lambda}_{LT}^2 \right) \quad (5.211)$$

This solution is also given in (Stangenberg 2007) and (Naumes 2009). Contrarily, Taras chose to replace the generalized imperfection by:

$$\eta = \alpha \left(\bar{\lambda}_z - \bar{\lambda}_{z,0} \right) \quad (5.212)$$

Independently of the chosen expression of the generalized imperfection, the difference between Eqs. (5.210) and (5.211) and the current Eurocode provision (see Eqs. (5.204) and (5.205), cannot be overseen. In fact the torsional behaviour of the member is directly accounted for in Eqs. (5.211) by the ratio of the squares of the slendernesses λ_{LT} and λ_z and indirectly (and very roughly) in Eq. (5.204) by the imperfection factor and limit slenderness, α and $\lambda_{LT,0}$. Obviously, replacing the influence of the torsional behaviour, depending not only on the cross-section but also on the member length, by a constant value for the imperfection factor α leads to a loss of accuracy. However, a more simple expression of the reduction curve is obtained. Yet, if both methods (Eqs. (5.204) and (5.205) and Eqs. (5.210) and (5.211)) are equally well calibrated (for example by defining an imperfection factor depending on the torsional behaviour of the member for the Eurocode reduction curve), they should be equally accurate as the same theoretical background is used.

In this paragraph, the determination of the second order internal forces and moments has been presented for a very simple load case in order to facilitate the understanding of the following developments. Hereafter, the influence of the axial force is introduced. Then, an additional minor-axis bending moment is studied. For both load cases, Eurocode 3 Part 1-1 proposes resistance models. The assumptions necessary to obtain the Eurocode design equations are presented and discussed. Then the study is extended to the case of an applied torque and a simplified design

equation is derived based on similar assumptions. Also, it is shown how the OIC approach may be derived for selected load cases including torsional loads.

5.5.7.3 Members of double symmetric I section subject to major-axis bending and axial force

Before addressing the case of combined internal forces and moments including torsion, it seems interesting to address the complex cases of combined major-axis bending and axial force and combined bi-axial bending and axial force. The following developments recall the scientific background of the Eurocode 3 Part 1-1 interaction formulae. Consequently, the two following paragraphs are helpful for the discussion on how the existing interaction formulae may be extended to the case of applied torsion.

It is assumed that the major-axis bending moment and the axial force are amplified simultaneously. The ratio of the lateral displacement and the torsional twist at the point of elastic out-of-plane instability is therefore given by Eq. (5.213).

$$\frac{v}{\varphi} = \frac{\alpha_{cr} M_y}{N_{cr,z} - \alpha_{cr} N} = -c_r \quad (5.213)$$

If the member is subject to major-axis bending only, the ratio between lateral displacement and torsional twist is equal to the ratio between the elastic critical bending moment and the elastic critical force for flexural buckling about the minor-axis. This result has already been used in the previous paragraphs. If, however, the bending moment M_y becomes negligible compared to the axial force, the product $\alpha_{cr} N$ tends to the critical lateral buckling force $N_{cr,z}$. In this case the ratio v/φ tends to infinity. Consequently, eigenmode is characterised by a sole lateral displacement v ; hence, the extreme cases of a member subject to an axial force or a major-axis bending moment only are well represented. It may be noted that Eq. (5.213) has also been used in (Stangenberg 2007).

As before, it is considered that the member possesses an eigenmode affine imperfection. For the studied case the governing system of differential equations is given in Eqs. (5.214) and (5.215) (the displacement functions have already been introduced).

$$N_{cr,z} v + M_y (\varphi + \varphi_0) - N(v + v_0) = 0 \quad (5.214)$$

$$-Nr_{yz}^2 (\varphi + \varphi_0) + M_y (v + v_0) + \frac{\pi^2}{L^2} EI_w \varphi + GI_t \varphi = 0 \quad (5.215)$$

Based on Eq. (5.214), it is possible to determine the amplitude of the lateral displacement as provided by Eq. (5.216).

$$v = -\frac{M_y (\varphi + \varphi_0) - N c_r \varphi_0}{N_{cr,z} - N} \quad (5.216)$$

Eq. (5.216) is introduced into Eq. (5.215). After some calculation steps not described here, the following expression is obtained:

$$\underline{\varphi} = \frac{\frac{M_y^2}{M_{y,cr}^2} + \frac{N_{cr,z}c_r M_y}{M_{y,cr}^2} + \frac{N}{N_{cr,T}} \left(1 - \frac{N}{N_{cr,z}}\right)}{\left(1 - \frac{N}{N_{cr,z}}\right) \left(1 - \frac{N}{N_{cr,T}}\right) - \frac{M_y^2}{M_{y,cr}^2}} \underline{\varphi}_0 \quad (5.217)$$

Here, it is recalled that a compression axial force is considered positive. Introducing Eq. (5.217) into (5.216) leads to the following expression of the lateral displacement.

$$\underline{v} = \frac{\frac{M_y^2}{M_{y,cr}^2} + \frac{N}{N_{cr,z}} \left(\frac{M_y}{Nc_r} + 1 - \frac{N}{N_{cr,T}}\right)}{\left(1 - \frac{N}{N_{cr,z}}\right) \left(1 - \frac{N}{N_{cr,T}}\right) - \frac{M_y^2}{M_{y,cr}^2}} c_r \underline{\varphi}_0 \quad (5.218)$$

The second order minor-axis bending moment as well as the second order bi-moment can now be determined based on the expressions of the lateral displacement and the torsional twist.

$$EI_z \frac{\pi^2}{L^2} \underline{v} = -EI_z v_{,xx} = -M_z = N_{cr,z} \frac{\frac{M_y^2}{M_{y,cr}^2} + \frac{N}{N_{cr,z}} \left(\frac{M_y}{Nc_r} + 1 - \frac{N}{N_{cr,T}}\right)}{\left(1 - \frac{N}{N_{cr,z}}\right) \left(1 - \frac{N}{N_{cr,T}}\right) - \frac{M_y^2}{M_{y,cr}^2}} c_r \underline{\varphi}_0 \quad (5.219)$$

$$EI_w \frac{\pi^2}{L^2} \underline{\varphi} = -EI_w \varphi_{,xx} = B = N_{cr,z} \frac{I_w}{I_z} \frac{\frac{M_y^2}{M_{y,cr}^2} + \frac{N_{cr,z}c_r M_y}{M_{y,cr}^2} + \frac{N}{N_{cr,T}} \left(1 - \frac{N}{N_{cr,z}}\right)}{\left(1 - \frac{N}{N_{cr,z}}\right) \left(1 - \frac{N}{N_{cr,T}}\right) - \frac{M_y^2}{M_{y,cr}^2}} \underline{\varphi}_0 \quad (5.220)$$

In order to validate the previous development, it is proposed to compare the second order internal forces and moments and second order displacements obtained by application of Eqs. (5.217) to (5.220) to finite element results (GNIA simulations). The studied member is of IPE450 section. It is subject to an axial force of 100 kN and a constant major-axis bending moment of 50 kNm. Also, the member is supposed to possess an eigenmode affine imperfection with an amplitude of 0,01 rad for the torsional twist component. This choice is arbitrary and only used for the validation of the expressions developed here before. The lateral displacement component is calculated following Eq. (5.218). The results are represented in Table 5-21.

Table 5-21: Comparison of analytically and numerically determined second order quantities

Length (mm)	Second order quantity	Analytical result	Finite element result	Analytic/FE
2700	φ (rad)	0,000644	0,000644	1,00
	v (cm)	-0,0171	-0,0171	1,00
	M_z (kNm)	-0,8151	-0,8165	0,998
	B (kNm ²)	0,1447	0,1447	1,00
3600	φ (rad)	0,00112	0,00112	1,00
	v (cm)	-0,03292	-0,03292	1,00
	M_z (kNm)	-0,8822	-0,8837	0,998
	B (kNm ²)	0,1421	0,1421	1,00
4500	φ (rad)	0,00173	0,00173	1,00
	v (cm)	-0,05654	-0,05654	1,00
	M_z (kNm)	-0,9699	-0,9710	0,999
	B (kNm ²)	0,1400	0,1400	1,00
5400	φ (rad)	0,00248	0,00248	1,00
	v (cm)	-0,09076	-0,09076	1,00
	M_z (kNm)	-1,0811	-1,0830	0,998
	B (kNm ²)	0,1392	0,1392	1,00
6750	φ (rad)	0,00392	0,00392	1,00
	v (cm)	-0,1709	-0,1709	1,00
	M_z (kNm)	-1,3029	-1,3030	1,00
	B (kNm ²)	0,1410	0,1410	1,00

In order to analyse the results more easily, they are also represented graphically in Figure 5-106. As can be seen all analytically determined second order quantities practically coincide with the numerical calculation.

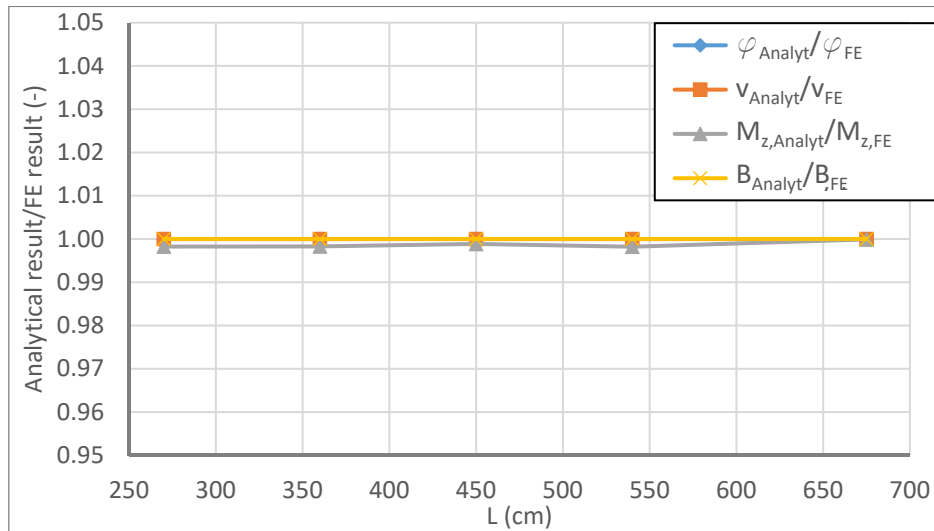


Figure 5-106: Comparison of analytically and numerically determined second order quantities

Next, it is proposed to study the example of a member subject to a uniformly distributed vertical load applied on the upper flange of a HEB 260 cross-section and directed downwards. The value of the applied axial force is 800 kN and the maximum major-axis bending moment is 150 kNm. The results are represented in Figure 5-107.

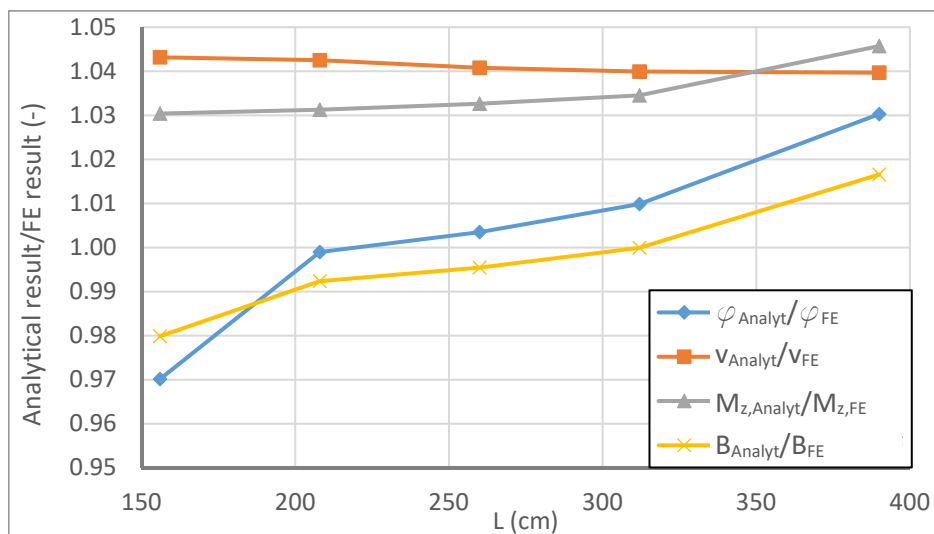


Figure 5-107: Comparison of analytically and numerically determined second order quantities

Clearly, the analytically determined solutions are less precise in case of variable bending than for constant bending. Nonetheless, the maximum deviation is only of about 4,5%.

Several reasons for the differences may be given. First, the assumption of a sine shaped eigenmode does not hold anymore in case of variable bending. Also, the value of the ratio v/φ has to be corrected. For example, if the HEB 260 member of 390 cm of length is considered, the value of $c_r = v/\varphi$ calculated analytically is equal to - 13,70 cm. The numerical calculation yields of value of - 12,11 cm. Nevertheless, the differences are still acceptable.

As before, the previously determined second order internal moments M_z and B are introduced in the linear cross-section interaction formula. One obtains:

$$\frac{N}{N_R} + \frac{M_y}{M_{y,R}} + \frac{N_{cr,z}}{M_{z,R}} \frac{\frac{M_y^2}{M_{y,cr}^2} + \frac{N}{N_{cr,z}} \left(\frac{M_y}{Nc_r} + 1 - \frac{N}{N_{cr,T}} \right)}{\left(1 - \frac{N}{N_{cr,z}} \right) \left(1 - \frac{N}{N_{cr,T}} \right) - \frac{M_y^2}{M_{y,cr}^2}} c_r \varphi_0 +$$

$$\frac{N_{cr,z}}{B_R} \frac{I_w}{I_z} \frac{\frac{M_y^2}{M_{y,cr}^2} + \frac{N_{cr,z} c_r M_y}{M_{y,cr}^2} + \frac{N}{N_{cr,T}} \left(1 - \frac{N}{N_{cr,z}} \right)}{\left(1 - \frac{N}{N_{cr,z}} \right) \left(1 - \frac{N}{N_{cr,T}} \right) - \frac{M_y^2}{M_{y,cr}^2}} \varphi_0 = 1 \quad (5.221)$$

It should be noted that in-plane second order effects and imperfection are not accounted for in Eq. (5.221). If one intends to include in-plane imperfection, one obtains the additional second order major-axis bending moment given in Eq. (5.222).

$$EI_y \frac{\pi^2}{L^2} w = EI_y w_{,xx} = M_y = \frac{Nw_0 + M_y}{1 - \frac{N}{N_{cr,y}}} \quad (5.222)$$

If the in-plane second order effects are introduced into the linear interaction formulae, one obtains Eq. (5.223).

$$\frac{N}{N_R} + \frac{Nw_0 + M_y}{\left(1 - \frac{N}{N_{cr,y}} \right) M_{y,R}} + \frac{N_{cr,z}}{M_{z,R}} \frac{\frac{M_y^2}{M_{y,cr}^2} + \frac{N}{N_{cr,z}} \left(\frac{M_y}{Nc_r} + 1 - \frac{N}{N_{cr,T}} \right)}{\left(1 - \frac{N}{N_{cr,z}} \right) \left(1 - \frac{N}{N_{cr,T}} \right) - \frac{M_y^2}{M_{y,cr}^2}} c_r \varphi_0 +$$

$$\frac{N_{cr,z}}{B_R} \frac{I_w}{I_z} \frac{\frac{M_y^2}{M_{y,cr}^2} + \frac{N_{cr,z} c_r M_y}{M_{y,cr}^2} + \frac{N}{N_{cr,T}} \left(1 - \frac{N}{N_{cr,z}} \right)}{\left(1 - \frac{N}{N_{cr,z}} \right) \left(1 - \frac{N}{N_{cr,T}} \right) - \frac{M_y^2}{M_{y,cr}^2}} \varphi_0 \leq 1 \quad (5.223)$$

Obviously, Eq. (5.223) resembles very few to the Eurocode 3 interaction formula applicable for the studied case. In order to obtain the expression proposed in the European standard, it is necessary to take a step backwards and consider separately in-plane second order effects created by the axial force and out-of-plane second order effects created by the major-axis bending moment.

If one neglects the out-of-plane second order effects in a first step, Eq. (5.224) is obtained as design criterion:

$$\frac{N}{N_R} + \frac{N \underline{w}_0}{\left(1 - \frac{N}{N_{cr,y}}\right) M_{y,R}} + \frac{M_y}{M_{y,R}} \leq 1 \quad (5.224)$$

In order to develop the Eurocode 3 interaction formulae, it is now supposed that the equivalent geometric imperfection is expressed by the buckling curve as shown in Eq. (5.225). Thus, one also respects continuity with the buckling check for a member only subject to axial compression only.

$$\underline{w}_0 = \frac{(1 - \chi) \left(1 - \chi \frac{N_R}{N_{cr,y}}\right) M_{y,R}}{\chi N_R} \quad (5.225)$$

When Eq. (5.225) is introduced into Eq. (5.224), it is possible to obtain the format used by Annex A of Eurocode 3 Part 1-1 (see references (Boissonnade et al. 2002), (Boissonnade et al. 2004) and (Villette 2004):

$$\frac{N}{\chi_y N_R} + \mu_y \frac{M_y}{\left(1 - \frac{N}{N_{cr,y}}\right) M_{y,R}} \leq 1 \quad (5.226)$$

$$\mu_y = \frac{1 - N/N_{cr,y}}{1 - \chi N/N_{cr,y}}$$

It should be noted that Eq. (5.226) can only be derived if the resistance criterion represented in Eq. (5.224) is strictly equal to 1,0. Consequently both, Eq. (5.224) and Eq. (5.226), only yield the same result at the ultimate limit state.

In the next step, the second order effects created by the major-axis bending moment are introduced by the reduction factor χ_{LT} as defined by Eq. (5.204). It yields:

$$\frac{N}{\chi_y N_R} + k_{yy} \frac{M_y}{\chi_{LT} M_{y,R}} \leq 1 \quad (5.227)$$

$$k_{yy} = \frac{\mu_y}{\left(1 - \frac{N}{N_{cr,y}}\right)} C_{my} C_{mLT}$$

The factor C_{my} considers the influence of variable bending moments. The factor C_{mLT} has to account for the difference between the analytically derived design expression given in Eq.(5.223) and the Eurocode 3 format given in Eq. (5.227). Obviously, a purely analytical expression for C_{mLT} cannot be envisaged and therefore it has been calibrated empirically to consider implicitly the effect of the coupling terms not included in Eq. (5.227). It is to be noted that, whereas Eq. (5.223) takes

into account the out-of-plane second order effects created by the axial force (minor-axis bending moment due to v_0), Eq. (5.227) does not. Consequently, Eurocode 3 introduces a second verification criterion derived similarly as Eq. (5.227) but based on an out-of-plane imperfection v_0 . One obtains:

$$\frac{N}{\chi_z N_R} + k_{zy} \frac{M_y}{\chi_{LT} M_{y,R}} \leq 1$$

$$k_{zy} = \frac{\left(1 - \frac{N}{N_{cr,z}}\right)}{\left(1 - \chi_z \frac{N}{N_{cr,z}}\right)} \frac{1}{\left(1 - \frac{N}{N_{cr,y}}\right)} C_{my} C_{mLT} = \frac{\mu_z}{\left(1 - \frac{N}{N_{cr,y}}\right)} C_{my} C_{mLT} \quad (5.228)$$

The derived solution may seem mechanically consistent at first view. However, the supposed equivalent imperfections do not have a strictly physical sense as in Eq. (5.228) the member is supposed to be subject to an initial imperfection of v_0 and pure compression on one hand for the determination of the reduction factor χ_z and the interaction factor k_{zy} and, on the other hand, the same member is supposed to be subject to an imperfection affine to the first member eigenmode and pure bending leading to the reduction factor χ_{LT} . Obviously, the real member cannot be subject to two different forms of member imperfections simultaneously. Physically, it seems much more consistent to suppose that the member possesses one single imperfection (that should be a combination of lateral and vertical displacements and a torsional twist leading to the resistance criterion of Eq. (5.223)). Nevertheless, the exact form and amplitude of this geometrical equivalent imperfection would still be conceptual. Therefore, in order to obtain simple solutions it may certainly be admitted that for calculation purposes the member is treated independently for the case of buckling under axial force and lateral-torsional buckling under the major-axis bending moment. Here, it should be recalled that, up to this point, only elastic interaction has been considered. Annexe A of Eurocode 3 Part 1-1 introduces the influence of plasticity by the factors C_{ij} .

Last, it should be noted that Annex B of Eurocode 3 Part 1-1 proposes different formulations for the interaction factors k_{ij} (see Table 5-8). Yet, these last have been calibrated on a pure numerical and experimental basis and consequently they cannot be derived analytically as shown here before. Still, it is recalled again that even the interaction factors in the format of Annex A of Eurocode 3 Part 1-1 need empirical calibration.

As an alternative to the interaction equation, Eurocode 3 proposes a second design method that might be applied in case of combined bending and axial force. The so called "General method" of paragraph 6.3.4 of (CEN 2005a) is expressed by the condition given in Eq. (5.229).

$$\frac{\alpha_{ult,k} \chi_{op}}{\gamma_{M1}} \geq 1,0 \quad (5.229)$$

As Annex B, this method proposed and developed in (Müller 2003) cannot be derived by a strictly analytical approach. However, it follows the principle of the derivation leading to Eq. (5.223). In fact, the term α_{ult} represents the in-plane behaviour of the member and may consistently be defined by the first two terms of Eq. (5.223) as follows:

$$\frac{1}{\alpha_{ult,k}} = \frac{N}{N_R} + \frac{Nw_0 + M_y}{\left(1 - \frac{N}{N_{cr,y}}\right)M_{y,R}} \quad (5.230)$$

Eq. (5.230) supposes that the bending moment diagram is affine to a sine half wave. Elsewise, an equivalent sinusoidal moment factor has to be introduced to account for the influence of the bending moment diagram on the second order amplification.

The factor χ_{op} represents the reduction of the in-plane resistance of the member due to out-of-plane second order effects. In order to be consistent to the analytical solution of Eq. (5.223), it should therefore be equal to:

$$\chi_{op,analyt} = 1 - \left[\frac{N_{cr,z} \frac{M_y^2}{M_{y,cr}^2} + \frac{N}{N_{cr,z}} \left(\frac{M_y}{Nc_r} + 1 - \frac{N}{N_{cr,T}} \right)}{M_{z,R} \left(1 - \frac{N}{N_{cr,z}} \right) \left(1 - \frac{N}{N_{cr,T}} \right) - \frac{M_y^2}{M_{y,cr}^2}} c_r \right. \\ \left. + \frac{N_{cr,z} \frac{I_w}{B_R} \frac{M_y^2}{M_{y,cr}^2} + \frac{N_{cr,z} c_r M_y}{M_{y,cr}^2} + \frac{N}{N_{cr,T}} \left(1 - \frac{N}{N_{cr,z}} \right)}{\left(1 - \frac{N}{N_{cr,z}} \right) \left(1 - \frac{N}{N_{cr,T}} \right) - \frac{M_y^2}{M_{y,cr}^2}} \right] \frac{\varphi_0}{\varphi_0} \quad (5.231)$$

Eq. (5.231) shows that if the ratio between internal loads and critical loads is important the second term of this equation tends to 0 and the reduction factor tends to 1,0. This obviously respects the physical background as in this case second order effects are negligible. However, it does not seem evident to link Eq. (5.231) to the well-known format of the buckling curves. Yet, if the key parameters of the buckling curve (factor α and plateau length λ_0) are well calibrated, the general method may lead to satisfactory results. One may note that the “General method” is based on a purely empirical calibration of the reduction factor. The interaction between axial force and bending moment on the instability is roughly taken into account by a linear interpolation between the reduction curves for lateral and lateral-torsional buckling. Additionally, it is recalled that the general method may lead to rather conservative strength predictions in some cases as in- and out-of-plane second order effects are both included in the approach. Nonetheless, it seems interesting to compare the results obtained by the general method to a genuine elastic second order calculations and to the analytically obtained “general method” characterized by the reduction factor $\chi_{op,Analyt}$. It is proposed to consider the example of a member made of IPE 300 cross-section fabricated of steel S235. The member is supposed to be subject to a constant major-axis bending moment of 92,64 kNm and a compression axial force of 358 kN. Under this load combination the

first fibre of the cross-sections attains the yield stress and consequently the studied combination corresponds to the elastic limit load. In order to compare the general method proposed by Müller (general method – EC3/Müller’s approach) it is necessary to recalculate the applied imperfection φ_0 entering the genuine second order calculation and the analytically derived “general method”. The imperfection φ_0 is determined based on Eq. (5.232) recalled hereafter:

$$\eta = \frac{M_{y,R}}{M_{z,R}} \left(1 + \frac{1}{\sqrt{\left(1 + \frac{GI_T L^2}{EI_w \pi^2} \right)}} \right) \varphi_0 = \alpha(\bar{\lambda}_{op} - 0,2) \quad (5.232)$$

Depending on the member length, the torsional twist component of the imperfection may therefore be determined with Eq. (5.233).

$$\varphi_0 = \alpha(\bar{\lambda}_{op} - 0,2) \frac{M_{z,R}}{M_{y,R}} \left(1 + \frac{1}{\sqrt{\left(1 + \frac{GI_T L^2}{EI_w \pi^2} \right)}} \right)^{-1} \quad (5.233)$$

Following Eurocode 3, the imperfection factor “ α ” should be set to 0,21 corresponding to buckling curve a. The second order calculations are performed based on an eigenmode affine imperfection whose torsional twist component possesses the amplitude calculated with Eq. (5.233). Additionally, a sine shaped vertical imperfection corresponding to the in-plane buckling curve “a” is introduced. It should be recalled that the same imperfection has been used to determine the analytically based general method. Also, one should note that the factor $\alpha_{ult,k}$ used in the general method is calculated based on the elastic resistance of the member so that the obtained results are comparable.

Figure 5-108 shows the elastic ultimate resistance curve determined for the three studied approaches. It may be observed that the analytical approach and the elastic second order calculation yield identical results. The percentage difference, also represented in Figure 5-108 by the green curve, is generally less than 1%. The general method of Eurocode 3 Part 1-1, noted as EC3-Müller, also yields satisfactory results. Yet, for longer members the EC3 general method seems to loose precision. In fact, the difference between this approach and elastic second order calculation attains approximatively 10% as shown by the blue curve represented in Figure 5-108. Nevertheless, if one considers the simplicity of the Eurocode 3 general method compared to the analytical solution, the precision is very satisfactory.

Last, it should though be pointed out that the general method is not entirely consistent in case of U-shaped members as in and out-of-plane behaviour are coupled and consequently cannot be separated as shown in this approach. Yet, again an empirical calibration might lead to satisfactory

results and may avoid overly complex design equations. Nonetheless, it is recalled that the simple extension to minor-axis bending proposed by Naumes in reference (Naumes 2009) by simply adding the working degree of the member with reference to minor-axis bending can be unsafe as shown in 5.4.3.4.

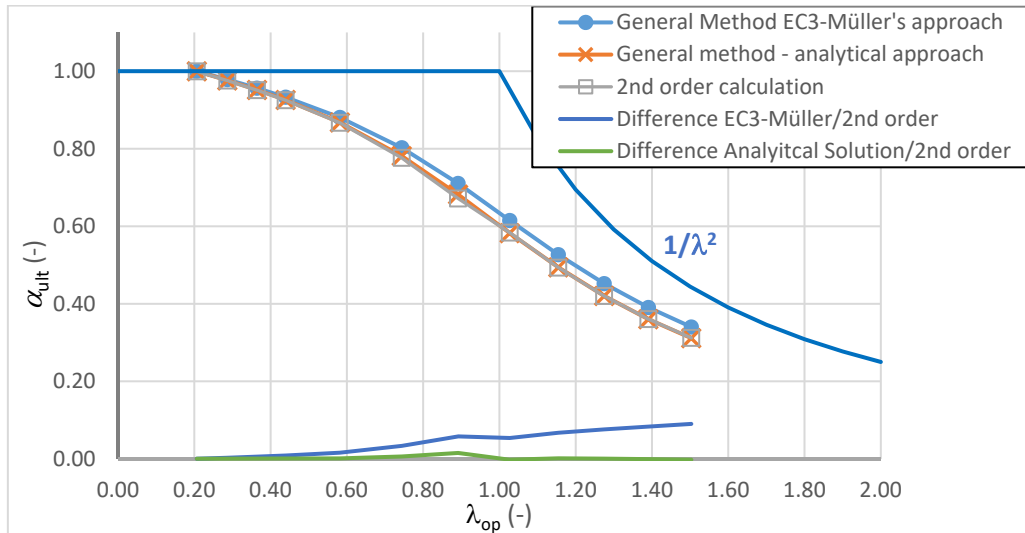


Figure 5-108: Comparison between the general method and genuine second order calculations

The present paragraph has shown that a purely analytical approach addressing the stability of members subject to major-axis bending and axial force is possible for the elastic case. Yet, the obtained design expression is rather complex even for the simple configuration of constant bending and a double symmetric I section. It has then been discussed rapidly how the complex analytical solution is adapted to obtain the design equations in the Eurocode 3 format. This format is not fully consistent from a mechanical point of view but as a certain empirical calibration is necessary to adapt the resistance model to plasticity and the influence of variable bending, the lack of consistency can be accepted in order to obtain simple and sufficiently precise design expressions.

In the following the influence of an applied torque is studied from a theoretical point of view.

5.5.7.4 Members subject bending and torsion

Hereafter, it is considered that the member is subject to a constant major-axis bending moment and a distributed torsional load. So as to develop analytical expressions it is supposed that the distribution of the torque follows a sinusoidal shape. Also, it is supposed that the member possesses an initial geometric imperfection affine to the first eigenmode. The governing system of differential equations is given in Eq. (5.234). The amplitude of the torsional load is noted as m_x .

$$EI_z \frac{\pi^2}{L^2} \underline{v} + M_y \underline{\varphi} = -M_y \underline{\varphi}_0 \quad (5.234)$$

$$M_y \underline{v} + \left(EI_w \frac{\pi^2}{L^2} + GI_T \right) \underline{\varphi} = M_y \underline{\varphi}_0 c_r + \frac{L^2}{\pi^2} m_x$$

In a first step, the system (5.234) is treated without the influence of the imperfection. The reduced system is given in Eq. (5.235).

$$EI_z \frac{\pi^2}{L^2} \underline{v} + M_y \underline{\varphi} = 0 \tag{ 5.235 }$$

$$M_y \underline{v} + \left(EI_w \frac{\pi^2}{L^2} + GI_T \right) \underline{\varphi} = \frac{L^2}{\pi^2} m_x$$

The lateral displacement can be expressed as a function of the torsional twist by:

$$\underline{v} = - \frac{M_y}{EI_z \frac{\pi^2}{L^2}} \underline{\varphi} = - \frac{M_y}{N_{cr,z}} \underline{\varphi} \tag{ 5.236 }$$

Eq. (5.236) is introduced in the system (5.235). After some reorganisation, the expression of the second order torsional twist is obtained as shown in Eq. (5.237).

$$\underline{\varphi}^{II} = m_x \frac{L^2}{\pi^2} \frac{1}{M_{y,cr} c_r \left(1 - \frac{M_y^2}{M_{y,cr}^2} \right)} \tag{ 5.237 }$$

The torsional load m_x can be replaced by the first order torsional twist given in Eq. (5.238).

$$\underline{\varphi}^I = m_x \frac{L^2}{\pi^2} \frac{1}{\left(EI_w \frac{\pi^2}{L^2} + GI_T \right)} = m_x \frac{L^2}{\pi^2} \frac{1}{M_{y,cr} c_r} \tag{ 5.238 }$$

If Eq. (5.238) is introduced into Eq. (5.237) a new expression of the second order torsional twist is obtained.

$$\underline{\varphi}^{II} = \underline{\varphi}^I \frac{1}{1 - \frac{M_y^2}{M_{y,cr}^2}} \tag{ 5.239 }$$

The following expression of the second order lateral displacement is determined by introducing Eq. (5.239) into Eq. (5.236).

$$\underline{v}'' = -\underline{\varphi}' \frac{M_y}{N_{cr,z}} \frac{1}{1 - \frac{M_y^2}{M_{y,cr}^2}} \quad (5.240)$$

As before, the second order minor-axis bending moment and the second order bi-moment are determined.

$$M_z'' = EI_z v_{,xx} = -EI_z \frac{\pi^2}{L^2} \underline{v} = M_y \underline{\varphi}' \frac{1}{1 - \frac{M_y^2}{M_{y,cr}^2}} \quad (5.241)$$

$$B'' = -EI_w \varphi_{,xx} = EI_w \frac{\pi^2}{L^2} \underline{\varphi} = EI_w \frac{\pi^2}{L^2} \underline{\varphi}' \frac{1}{1 - \frac{M_y^2}{M_{y,cr}^2}} = B^I \frac{1}{1 - \frac{M_y^2}{M_{y,cr}^2}} \quad (5.242)$$

The previous results have also been obtained in (FOSTA 2004), (Stangenberg 2007) and (Naumes 2009). The second order minor-axis bending moment and the second order bi-moment resulting from the imperfection have been determined in 5.5.7.2 (see Eqs. (5.192) and (5.193)). They are introduced into Eq. (5.241) and (5.242) and the final expressions of the M_z'' and B'' are obtained as provided in Eqs. (5.243) and (5.244).

$$M_z = M_y \left(\frac{\frac{\varphi_0}{1 - \frac{M_y}{M_{y,cr}}} + \frac{\varphi^I}{1 - \frac{M_y^2}{M_{y,cr}^2}} \right) \quad (5.243)$$

$$B = M_y \frac{N_{cr,z}}{M_{y,cr}} \frac{I_w}{I_z} \frac{1}{1 - \frac{M_y}{M_{y,cr}}} \varphi_0 + B^I \frac{1}{1 - \frac{M_y^2}{M_{y,cr}^2}} \quad (5.244)$$

It should be noted that the internal moments created by the imperfection are amplified by the factor $\alpha_{2nd,l} = 1/(1-M_y/M_{y,cr})$, whereas the internal forces due to first order torsion are amplified by the factor $\alpha_{2nd,q} = 1/(1-(M_y/M_{y,cr})^2)$. In order to illustrate the difference between both amplification factors, Figure 5-109 shows their evolution as a function of the ratio between the applied bending moment and the critical bending moment.

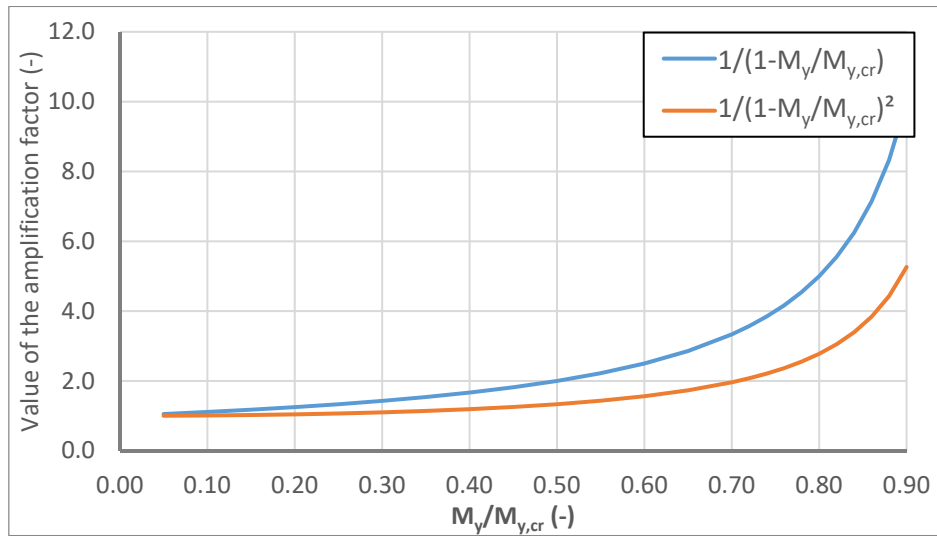


Figure 5-109: Comparison between amplification factors

As can be seen from Figure 5-109, the amplification of the internal moments due to the imperfection is obviously more severe than the amplification of the internal forces due to first order torsion. However, the difference becomes pronounced only if the major-axis bending moment is closed to the elastic critical moment ($M_y/M_{y,cr} > 0,70$).

In order to check the validity of the developed amplification factors, second order displacements are numerically calculated for the example of a member of IPE 300 section subject to major-axis bending and a sinusoidal distributed torsional load. The value of $\alpha_{cr} = M_{y,cr}/M_y$ is varied between 3 and 15. Table 5-22 summarizes the geometric and mechanical characteristics of the section and Table 5-23 gives the lengths of the studied members and the corresponding amplification factors.

Table 5-22: Section geometry and mechanical characteristics

Section	Geometry		Mechanical characteristics	
IPE 300	h (mm)	300	A (cm ²)	53,8
	t _w (mm)	7,1	I _y (cm ⁴)	8356
	b (mm)	150	I _z (cm ⁴)	604
	t _f (mm)	10,7	I _t (cm ⁴)	20,1
	r (mm)	15	I _w (cm ⁶)	12600

Table 5-23: Value of second order amplification factors for different member lengths

Length (mm)	α_{cr}	$\alpha_{2nd,l} = 1/(1-1/\alpha_{cr})$	$\alpha_{2nd,q} = 1/(1-1/\alpha_{cr}^2)$
915	15	1,071	1,004
1027	12	1,091	1,007
1192	9	1,125	1,012
1475	6	1,200	1,029
2153	3	1,500	1,125

First, the second order displacements are calculated with GNIA simulations for the member subject to the major-axis bending moment and the geometric imperfection only. The geometric imperfection is chosen to be affine to the first eigenmode. The amplitudes of the torsional twist component of the eigenmode is chosen to be equal to 0,1 rad. The corresponding amplitudes for the lateral displacement of the imperfection can be calculated depending on the member length with Eq. (5.186). The values are given in Table 5-24.

Table 5-24: Second order minor axis displacement and torsional twist – only geometrical imperfection

Length (mm)	$\alpha_{2nd,l}$	v_0 (cm)	Analytical Results		Numerical Results	
			v^{II} (cm)	φ^{II} (rad)	v^{II} (cm)	φ^{II} (rad)
915	1,071	1,482	0,105	0,0071	0,105	0,0071
1027	1,091	1,491	0,135	0,0091	0,135	0,0091
1192	1,125	1,507	0,188	0,0125	0,188	0,0126
1475	1,200	1,530	0,307	0,0200	0,307	0,0201
2153	1,500	1,640	0,816	0,0500	0,820	0,0505

Table 5-24 shows that the analytical and the numerical results are in excellent agreement in case of the imperfect member subject to major-axis bending only.

Next, the member subject to a combination of major-axis bending and a sinusoidal torsional load is studied. Here, the member is supposed to be **perfectly straight**, i.e. without any geometric imperfection. The torsional load is calibrated so as to obtain a first order torsional twist of 0,1 rad at mid span.

Table 5-25: Second order minor axis displacement and torsional twist – only torsional load

Length	$\alpha_{2nd,q}$	m_x (kNm/m)	Analytical Results		Numerical Results	
			φ^{II} (rad)	v^{II} (cm)	φ^{II} (rad)	v^{II} (cm)
915	1,004	383,07	0,099	0,1004	0,099	0,1005
1027	1,007	244,46	0,125	0,1007	0,125	0,1007
1192	1,012	137,59	0,169	0,1012	0,169	0,1013
1475	1,029	61,210	0,263	0,1029	0,263	0,1029
2153	1,125	15,302	0,612	0,1125	0,613	0,1126

As before the analytical and numerical solutions are in excellent agreement. Finally, Table 5-26 considers the **imperfect** member subject to a sinusoidal torsional load and major-axis bending. The imperfection is the one considered in Table 5-24 and the torsional load is the one considered in Table 5-25.

Table 5-26: Second order minor axis displacement and torsional twist – combination of geometrical imperfection and torsional load

Length	v ₀ (cm)	m _x (kNm/m)	Analytical Results		Numerical Results	
			φ ^{II} (rad)	v ^{II} (cm)	φ ^{II} (rad)	v ^{II} (cm)
915	1,482	383,07	0,204	0,1075	0,204	0,1077
1027	1,491	244,46	0,260	0,1098	0,260	0,1099
1192	1,507	137,59	0,357	0,1154	0,357	0,1141
1475	1,530	61,210	0,570	0,1229	0,570	0,1230
2153	1,640	15,302	1,428	0,1625	1,433	0,1631

Again, Table 5-26 shows the excellent agreement between theory and numerical calculation. It should be noted that, if the member is subject to a torsional load and geometrical imperfection, the second order lateral displacement and torsional twist correspond to the sum of the same second order displacements for the individual cases represented in Table 5-24 (only geometric imperfection) and Table 5-25 (only torsional load).

As the analytical results are validated by numerical calculation, the second order moments are introduced in the linear interaction formula as shown in Eq. (5.245).

$$\frac{M_y}{M_{y,R}} + \frac{M_y}{M_{z,R}} \frac{1}{1 - \frac{M_y}{M_{y,cr}}} \left(1 + \frac{N_{cr,z}}{M_{cr,y}} \frac{M_{z,R}}{B_R} \frac{I_w}{I_z} \right) \varphi^I + \frac{M_y}{M_{z,R}} \frac{\varphi^I}{1 - \frac{M_y^2}{M_{y,cr}^2}} + \frac{B^I}{B_R} \frac{1}{1 - \frac{M_y^2}{M_{y,cr}^2}} = 1 \quad (5.245)$$

So as to obtain a design equation, the imperfection has to be replaced. It would obviously be possible to replace it by a numerical value. Nonetheless, the geometric imperfection is replaced by the generalised imperfection η again (see Eq. (5.202) again for the definition of η).

$$\frac{M_y}{M_{y,R}} + \frac{M_y}{M_{y,R}} \frac{1}{1 - \frac{M_y}{M_{y,cr}}} \eta + \frac{M_y}{M_{z,R}} \frac{\varphi^I}{1 - \frac{M_y^2}{M_{y,cr}^2}} + \frac{B^I}{B_R} \frac{1}{1 - \frac{M_y^2}{M_{y,cr}^2}} = 1 \quad (5.246)$$

In paragraph 5.5.7.2, it has been shown that the lateral-torsional buckling curve can be expressed by Eq. (5.247). If Eq. (5.247) is exactly equal to 1,0, an expression of the generalised imperfection can be determined as represented in Eq. (5.248).

$$\chi_{LT} + \chi_{LT} \frac{1}{1 - \chi_{LT} \bar{\lambda}_{LT}^2} \eta \leq 1 \quad (5.247)$$

$$\eta = \frac{1}{\chi_{LT}} - 1 - \bar{\lambda}_{LT}^2 + \chi_{LT} \bar{\lambda}_{LT}^2 \quad (5.248)$$

By introducing Eq. (5.248) into Eq. (5.246) one obtains:

$$\frac{M_y}{M_{y,R}} + \frac{M_y}{M_{y,R}} \frac{1}{1 - \frac{M_y}{M_{y,cr}}} \left(\frac{1}{\chi_{LT}} - 1 - \bar{\lambda}_{LT}^2 + \chi_{LT} \bar{\lambda}_{LT}^2 \right) + \frac{M_y}{M_{z,R}} \frac{\varphi^I}{1 - \frac{M_y^2}{M_{y,cr}^2}} + \frac{B^I}{B_R} \frac{1}{1 - \frac{M_y^2}{M_{y,cr}^2}} \leq 1 \quad (5.249)$$

Eq. (5.249) is now reorganised using Eq. (5.250).

$$1 - \frac{M_y^2}{M_{y,cr}^2} = \left(1 - \frac{M_y}{M_{y,cr}} \right) \left(1 + \frac{M_y}{M_{y,cr}} \right) = \left(1 - \frac{M_y}{M_{y,R}} \bar{\lambda}_{LT}^2 \right) \left(1 + \frac{M_y}{M_{y,cr}} \right) \quad (5.250)$$

The resulting interaction formula is given in Eq. (5.251).

$$\frac{M_y}{\chi_{LT} M_{y,R}} + \frac{M_y}{M_{z,R}} \frac{\varphi^I}{1 + \frac{M_y}{M_{y,cr}}} + \frac{B^I}{B_R} \frac{1}{1 + \frac{M_y}{M_{y,cr}}} + \chi_{LT} \bar{\lambda}_{LT}^{-2} \left(\frac{M_y}{\chi_{LT} M_{y,R}} - \left[\frac{M_y}{\chi_{LT} M_{y,R}} \right]^2 \right) \leq 1 \quad (5.251)$$

It is recalled that the same procedure has been applied in references (Stangenberg 2007) and (FOSTA 2004) (see paragraph 5.4.3 describing the design proposals made at RWTH Aachen). The resulting expression may seem again somewhat surprising as the factor introducing second order effects to the first order torsional twist and the bi-moment is always less than 1 and even decreases if the applied major-axis bending moment approaches the critical bending moment. Yet, this directly results from the substitution of the generalised imperfection by Eq. (5.248). Again, it is to be noted that this substitution is only completely consistent if the member reaches its ultimate limit state by pure lateral-torsional buckling under major-axis bending only, i.e. if Eq. (5.247) is strictly equal to 1,0. Assuming that this is true, the member would obviously not be able to carry an additional bi-moment. Therefore, the derived interaction equation is not completely consistent from a mechanical point of view as the replacement of the generalised imperfection overestimates the working degree of the member under M_y . Also, it is recalled that a similar approach has been used to derive the axial force – major-axis bending interaction formulae in the Eurocode 3 format. In order to cover the lack of consistency empirically calibrated interaction factors have been introduced.

Based on Eq. (5.245), it is possible to derive a design concept with a different approach. To do so Eq. (5.245) is rewritten as shown hereafter:

$$\frac{M_y}{M_{y,R}} + \frac{M_y}{M_{z,R}} \frac{1}{1 - \frac{M_y}{M_{y,cr}}} \left[\left(1 + \frac{N_{cr,z}}{M_{y,cr}} \frac{M_{z,R}}{B_R} \frac{I_w}{I_z} \right) \varphi_0 + \frac{1}{1 + \frac{M_y}{M_{y,cr}}} \left(\varphi^I + \frac{B^I}{B_R} \frac{M_{z,R}}{B_R} \right) \right] = 1 \quad (5.252)$$

As in paragraph 5.5.7.2 the non-dimensional parameters χ and λ are introduced and one obtains Eq. (5.253).

$$\chi + \chi \frac{1}{1 - \chi \bar{\lambda}^2} \left[\left(1 + \frac{N_{cr,z}}{M_{y,cr}} \frac{M_{z,R}}{B_R} \frac{I_w}{I_z} \right) \phi_0 + \frac{1}{1 + \frac{M_y}{M_{y,cr}}} \left(\frac{M_y \phi^I}{M_{z,R}} + \frac{B^I}{B_R} \right) \right] = 1 \quad (5.253)$$

At this point the new form of the generalized “imperfection” of Eq. (5.254) is introduced to obtain the equation of second degree that may be used to determine the resistance of the member.

$$\eta = \left(1 + \frac{N_{cr,z}}{M_{y,cr}} \frac{M_{z,R}}{B_R} \frac{I_w}{I_z} \right) \phi_0 + \frac{1}{1 + \frac{M_y}{M_{y,cr}}} \left(\frac{M_y \phi^I}{M_{z,R}} + \frac{B^I}{B_R} \right) \quad (5.254)$$

$$\chi + \chi \frac{1}{1 - \chi \bar{\lambda}^2} \eta \leq 1 \quad (5.255)$$

Here, it may be argued that the designation “imperfection” is not suited anymore as η considers, in addition to the geometrical imperfection, the influence of the ratio between first order major-axis bending and the bi-moment and the influence of first order torsional twist. However, the designation of “generalized imperfection” is kept hereafter, since the function of this term is the same as the one in the classical design concept of buckling curves, i.e. reduce the resistance with respect to the theoretical case of the perfect member.

The equation of second degree is solved so as to determine the reduction factor χ :

$$\phi = 0,5 \left(1 + \eta + \bar{\lambda}^2 \right) \quad (5.256)$$

$$\chi = \frac{1}{\phi^2 + \sqrt{\phi^2 - \bar{\lambda}^2}} \quad (5.257)$$

This is exactly the same format as the classical buckling curve given in §6.3.1.2 of Eurocode 3 Part 1-1 (CEN 2005a) for the case of flexural buckling and in §6.3.2.2 of the same standard for the case of lateral-torsional buckling.

If one intends to keep the classical formulation of the generalized imperfection, the influence of the minor axis bending moment due to the torsional twist and the influence of the first order bi-moment can be considered in the format of the reduction curve as shown in Eq. (5.258) to (5.261).

$$\chi = \frac{r_m}{\phi^2 + \sqrt{\phi^2 - \bar{\lambda}^2} r_m} \quad (5.258)$$

$$r_m = 1 - \frac{1}{1 + \frac{M_y}{M_{y,cr}}} \left(\frac{M_y \phi^I}{M_{z,R}} + \frac{B^I}{B_R} \right) \geq 0 \quad (5.259)$$

$$\phi = 0,5 \left(1 + \eta + \bar{\lambda}^2 \right) \quad (5.260)$$

$$\eta = \frac{M_{y,R}}{M_{z,R}} \left(1 + \frac{N_{cr,z}}{M_{y,cr}} \frac{M_{z,R}}{B_R} \frac{I_w}{I_z} \right) \phi_0 = \alpha (\bar{\lambda} - \bar{\lambda}_0) \quad (5.261)$$

The form of the factor r_M is due to the hypothesis of linear interaction behaviour between the internal moments. It describes the reduction of the major-axis bending moment resistance reduced by the influence of minor-axis bending and the bi-moment. The given solution represents well the extreme cases: if the member is not subject to torsion the solution given in paragraph 5.5.7.2 is obtained and if the section resistance of the member is attained by the sole influence of the bi-moment, the reduction factor is 0, even for small slendernesses. It would be possible to introduce a non-linear interaction so as to account for the possible plastic reserve. Here, this is not done as the theoretical development shown in this paragraph is not intended to lead to a precise design model.

The developed reduction curve may directly be compared to the design method proposed at TU Eindhoven (see references (de Louw 2007) and (Snijder et al. 2008)) for U-shaped members subject to loads applied through the plane of the web. It may be observed that the reduction curve developed here confirms the tendencies included into the empirically determined reduction curve proposed by de Louw. In fact, the reduction factor χ does not tend to unity for small slendernesses as the member is subject to the bi-moment. For long members and hence high values of the relative slenderness the influence of torsion is neglected by de Louw. This is also shown to be right by the theoretical developments as, for the studied case of U-shaped members loaded through the web, the applied torsional moment and the resulting bi-moment tend to zero for long members. Consequently, the theoretical derived factor r_m tends to 1,0 and the design reduction curve becomes identical to the reduction curve applicable to lateral-torsional buckling of members subject to a sole major-axis bending moment.

If the same approach is applied to members under torsion and bi-axial bending the interaction formulae given in Eq. (5.264) can be derived (see Stangenberg 2007).

$$\frac{M_y}{M_{y,R}} + \frac{M_y}{M_{y,R}} \frac{1}{1 - \frac{M_y}{M_{y,cr}}} \left(1 + \frac{N_{cr,z}}{M_{y,cr}} \frac{M_{z,R}}{B_R} \frac{I_w}{I_z} \right) \frac{M_{y,R}}{M_{z,R}} \varphi_0 + \frac{M_y \varphi^I + M_z}{M_{z,R}} \frac{1}{1 - \frac{M_y^2}{M_{y,cr}^2}} + \frac{B^I + M_y \frac{v^I}{\delta_T}}{B_R} \frac{1}{1 - \frac{M_y^2}{M_{y,cr}^2}} = 1 \quad (5.262)$$

and

$$\delta_T = 1 + \frac{GI_t}{EI_w} \frac{L^2}{\pi^2} \quad (5.263)$$

As before the generalized imperfection η is introduced and then replaced by Eq. (5.248). Consequently, the new form of the interaction formula given in Eq. (5.264) is obtained.

It may be recalled that an equivalent interaction equation is derived by Stangenberg as presented in paragraph 5.4.3.3. Conversely to Eq. (5.264), he proposes a non-linear interaction between the second order internal forces and moments and he replaces the first order torsional twist and first order lateral displacement by analytical expressions. Additionally, Stangenberg neglects the term in the second line of Eq. (5.264) and the factor $1/(1+M_y/M_{y,cr})$. His proposal is recalled in Eq. (5.265). It is also recalled that the factors $C_1, C_{1,h}, C_{1,E}, k_{\delta,\theta}$ and $k_{\delta,z}$ introduce the influence of variable moment distribution.

$$\frac{M_y}{\chi_{LT} M_{y,pl}} + \left(\frac{M_y \varphi^I + M_z}{M_{z,pl}} + \frac{B^I + M_y \frac{v^I}{\delta_T}}{B_{pl}} \right) \frac{1}{1 + \frac{M_y}{M_{y,cr}}} + \chi_{LT} \bar{\lambda}_{LT}^2 \left(\frac{M_y}{\chi_{LT} M_{y,pl}} - \left[\frac{M_y}{\chi_{LT} M_{y,pl}} \right]^2 \right) \leq 1 \quad (5.264)$$

$$\frac{M_{y,Ed}^I}{\chi_{LT} M_{y,Rd}} + \frac{2}{3} \frac{2 - 2a_w}{2 - a_w} \frac{B_{Ed}^I}{B_{Rd}} \left(1 + \frac{C_1}{C_{1,\eta} k_{\delta,\theta}} \frac{M_{y,Ed}^I}{M_{y,Rd}} \bar{\lambda}_{LT}^{-2} \sqrt{\frac{I_z}{I_w}} c_r \right) + \frac{2}{3} \frac{2 - 2a_w}{2 - a_w} \frac{M_{z,Ed}^I}{M_{z,Rd}} \left(1 + \frac{C_1 C_{1,E}}{k_{\delta,z}} \frac{M_{y,Ed}^I}{M_{y,Rd}} \bar{\lambda}_{LT}^{-2} \sqrt{\frac{I_w}{I_z}} \frac{1}{c_r} \right) \leq 1 \quad (5.265)$$

Obviously, the expression given in Eq. (5.265) seems less readable than Eq. (5.264). Again, one may state that it seems more advantageous to keep the values of the first order displacement and the first order torsional twist directly in the interaction equation as these values can be determined easily with current design software.

Similarly to the case of combined major-axis bending and torsion, the design model can be represented in form of a buckling curve. The interaction equation of the second order internal

forces and moments is given in Eq. (5.266). Here, a more complex linearized interaction is supposed to account more precisely for plasticity. Consequently, interaction factors k_{My} , k_{Mz} and k_B are introduced.

$$k_{My} \frac{M_y}{M_{y,pl}} + k_{Mz} \frac{M_y}{M_{z,pl}} \frac{\varphi_0}{1 - \frac{M_y}{M_{y,cr}}} + k_{Mz} \frac{M_z + M_y \frac{\varphi^I}{M_{y,cr}^2}}{1 - \frac{M_y}{M_{y,cr}^2}} + k_B \frac{M_y}{B_{pl}} \frac{N_{cr,z}}{M_{y,cr}} \frac{I_w}{I_z} \frac{1}{1 - \frac{M_y}{M_{y,cr}}} \varphi_0 + k_B \frac{1}{B_{pl}} \frac{B^I + M_y \frac{v^I}{\delta_T}}{1 - \frac{M_y}{M_{y,cr}^2}} \leq 1 \quad (5.266)$$

Eq. (5.265) is rewritten as follows:

$$k_{My} \frac{M_y}{M_{y,pl}} + \frac{M_y}{M_{y,pl}} \frac{1}{1 - \frac{M_y}{M_{y,cr}}} (\eta_{imp} + k_{Mz} \eta_{Mz} + k_B \eta_B) \leq 1 \quad (5.267)$$

and:

$$\eta_{imp} = \left(k_{Mz} + k_B \frac{N_{cr,z}}{M_{cr,y}} \frac{M_{z,R}}{B_R} \frac{I_w}{I_z} \right) \frac{M_{y,R}}{M_{z,R}} \varphi_0 = \alpha (\bar{\lambda} - \bar{\lambda}_0) \quad (5.268)$$

$$\eta_{Mz} = \left(m_{zy} + \frac{M_{y,pl} \varphi^I}{M_{z,pl}} \right) \frac{1}{1 + \frac{M_y}{M_{y,cr}}} \quad \text{and} \quad m_{zy} = \frac{M_z}{M_{z,pl}} \frac{M_{y,pl}}{M_y} \quad (5.269)$$

$$\eta_B = \left(m_{by} + \frac{M_{y,pl} \frac{v^I}{\delta_T}}{B_{pl}} \right) \frac{1}{1 + \frac{M_y}{M_{y,cr}}} \quad \text{and} \quad m_{by} = \frac{B}{B_{pl}} \frac{M_{y,pl}}{M_y} \quad (5.270)$$

It can be observed that the generalized imperfection contain the interaction factors k_{Mz} and k_B . However, they are neglected in this expression in order to ensure the continuity with the load case of pure major-axis bending. In fact, it is the form of the reduction curve itself that already accounts for the influence of the non-linear interaction. Consequently, the generalised imperfection takes its usual form.

Again, Eq. (5.267) is transformed into the buckling curve format as shown by Eq. (5.271).

$$k_{My} \chi_{My} + \chi_{My} \frac{1}{1 - \chi_{My} \bar{\lambda}_{My}^2} (\eta_{imp} + k_{Mz} \eta_{Mz} + k_B \eta_B) = 1 \quad (5.271)$$

The solution of the previous equation of the second degree is given in Eqs. (5.272) and (5.273).

$$\chi_{My} = \frac{1}{\phi + \sqrt{\phi^2 - k_{My} \bar{\lambda}_{My}^2}} = 1 \quad (5.272)$$

$$\phi = 0,5 \left(k_{My} + k_{Mz} \eta_{Mz} + k_{Mb} \eta_B + \eta_{imp} + \bar{\lambda}_{My}^2 \right) \quad (5.273)$$

Here, the buckling curve is given with reference to the major-axis bending moment resistance. Yet, it may be more convenient to determine a reduction factor that is applied to the complete loading. To do so, the plastic load amplification factor is first expressed by Eqs. (5.274) and (5.275).

$$R_{pl} \left(k_{My} \frac{M_y}{M_{y,pl}} + k_{Mz} \frac{M_z}{M_{z,pl}} + k_B \frac{B}{B_{pl}} \right) = 1 \quad (5.274)$$

$$R_{pl} = \frac{1}{\left(k_{My} + k_{Mz} \frac{M_z}{M_{z,pl}} \frac{M_{y,pl}}{M_y} + k_B \frac{B}{B_{pl}} \frac{M_{y,pl}}{M_y} \right) \frac{M_y}{M_{y,pl}}} \quad (5.275)$$

The global reduction factor χ_G can be expressed based on the plastic load amplification factor R_{pl} and the load amplification factor leading to the failure of the member R_{ult} as given in Eq. (5.276).

$$\chi_G = \frac{R_{ult}}{R_{pl}} \quad (5.276)$$

Obviously, the factor R_{ult} is also equal to the ratio of the applied bending moment and the bending moment resistance reduced by the influence of buckling. One may therefore write:

$$R_{ult} = \frac{\chi_{My} M_{y,pl}}{M_y} \quad (5.277)$$

At this point, it is possible to combine Eqs. (5.276) and (5.277) so as to express the reduction factor χ_{My} as a function of χ_G :

$$\chi_{My} = \chi_G R_{pl} \frac{M_{y,pl}}{M_y} \quad (5.278)$$

Next, the relative slenderness linked to the major-axis bending moment has to be replaced by a global slenderness associated with the global load combination. Consequently, the critical load amplification factor is expressed with Eq. (5.279).

$$R_{cr,G} = \frac{M_{cr,y}}{M_y} = \frac{M_{y,pl}}{M_y} \frac{M_{cr,y}}{M_{y,pl}} = \frac{M_{y,pl}}{M_y} \frac{1}{\bar{\lambda}_{My}^2} \quad (5.279)$$

The global slenderness is defined with Eq. (5.280).

$$\bar{\lambda}_G = \sqrt{\frac{R_{pl}}{R_{cr,G}}} = \bar{\lambda}_{My} \sqrt{R_{pl} \frac{M_{y,pl}}{M_y}} \quad (5.280)$$

Eqs. (5.278) and (5.280) are now introduced into Eqs. (5.272) and (5.273) to rewrite the global buckling curve as shown in Eqs. (5.281) and (5.282).

$$\chi_G = \frac{1}{R_{pl} \frac{M_y}{M_{y,pl}} \phi + \sqrt{\phi^2 - \bar{\lambda}_G^2 \frac{M_{y,pl}}{R_{pl} M_y}}} \quad (5.281)$$

$$\phi = 0,5 \left(k_{My} + k_{Mz} \eta_{Mz} + k_B \eta_B + \eta_{imp} + \bar{\lambda}_G^2 \frac{1}{R_{pl} \frac{M_y}{M_{y,pl}}} \right) \quad (5.282)$$

The expressions of the terms η_{imp} , η_{Mz} and η_B are recalled in Eqs. (5.283) to (5.285).

$$\eta_{imp} = \alpha (\bar{\lambda}_G - \bar{\lambda}_0) \quad (5.283)$$

$$\eta_{Mz} = \left(m_{zy} + \frac{M_{y,pl} \phi^I}{M_{z,pl}} \right) \frac{1}{1 + \frac{M_y}{M_{y,cr}}} \quad (5.284)$$

$$\eta_B = \left(m_{by} + \frac{M_{y,pl} \frac{v^I}{\delta_T}}{B_{pl}} \right) \frac{1}{1 + \frac{M_y}{M_{y,cr}}} \quad (5.285)$$

One may note that equations (5.281) and (5.282) are fully continuous to the reduction curve that applies for members under major-axis bending if the interaction factor k_{My} becomes 1,0. Obviously, this should be the case. Additionally, the terms η_{Mz} and η_B vanish and the ratio between the plastic load amplification factor R_{pl} and $M_y/M_{y,pl}$ equals 1,0 for members subject to a sole moment M_y . For combined load cases the interaction factors k_{My} , k_{Mz} and k_B account for the interaction behaviour between the internal forces and moments. Yet, they also account for the influence of elasto-plastic instability as for longer member, the plastic interaction supposed in Eq. (5.266) is not valid anymore. For these members the interaction factors should tend to the ratio between the plastic resistance and the elastic resistance of the individual internal moment. Also, the moment distribution influences the importance of second effects. Consequently, a correction

factor might be necessary comparable to the equivalent (uniform or sinusoidal) moment factor C_m used in case of axial-force – major-axis bending moment interaction.

The calibration of the different factors necessary to account as precisely as possible for the effects not considered in the analytical development is not done in this paragraph. Nevertheless the derived global reduction curve allows the identification of several key parameters (additionally to R_{pl} and R_{cr}) that should probably be considered for the proposal of a global design buckling curve:

- The relative ratio between major-axis bending and minor-axis bending introduced by the factor m_{zy} ;
- The relative ratio between major-axis bending and the bi-moment introduced by the factor m_{by} ;
- The importance of first order displacements \underline{v}^I and $\underline{\varphi}^I$;
- The ratio between the plastic load amplification factor R_{pl} and the utilization grade of the member with respect to the major-axis bending moment only (or more generally the utilization grade of the member to the internal forces and moments generating second order effects).

It should be noted that a similar approach has been applied in reference (Taras 2011) to derive a global reduction curve for in-plane buckling of members subject to combined axial force and mono-axial bending. He obtained the following expressions:

$$\chi_G = \frac{c_0}{\phi + \sqrt{\phi^2 - \bar{\lambda}_G^2 c_0}} \quad (5.286)$$

$$\phi = 0,5 \left(k_{ni}^* + k_{mi}^* C_{ms} \eta_0 + \eta_{imp} + \bar{\lambda}_G^2 c_0 \right) \quad (5.287)$$

In Eqs. (5.286) and (5.287):

- The factor c_0 represents the ratio between R_{pl} and the utilisation grade of the member with respect to the axial force N/N_{pl} (generating second order effects);
- The factors k_{ni}^* and k_{mi}^* represents the plastic interaction behaviour between the axial force and the bending moment and the transition behaviour from plastic interaction to elastic interaction with increasing member slenderness (only compact sections are treated);
- The factor C_{ms} represents the influence of the bending moment diagram on the second order effects;
- The factor η_0 is equal to the ratio $(M/M_{pl})/(N/N_{pl})$ and consequently represents the relative importance between the bending moment (about the major- or minor-axis) and the axial force.

Obviously, the expression proposed in (Taras 2011) accounts for the same influences as the expressions proposed here for the interaction between major- and minor-axis bending and the bi-moment.

Before the design model is calibrated, in paragraph 5.6 based on an extensive numerical study, the theoretical developments is extended to combined torsion and axial forces in the next paragraph.

5.5.7.5 Members subject to combined bi-axial bending, axial force and torsion

The system of differential equations given in Eq. (5.235) is extended to the case of an applied axial force and bi-axial bending. Hereafter, only the case of a double symmetric I section is treated. For the studied configuration, the system of differential equations is given in Eq. (5.288).

$$EI_y w_{,xxxx} + (M_z \varphi)_{,xx} + N w_{,xx} = q_z + N w_0 + M_z \varphi_0$$

$$EI_z v_{,xxxx} - (M_y \varphi)_{,xx} + N v_{,xx} = q_y + M_y \varphi_0 + N v_0 \quad (5.288)$$

$$N r_{yz}^2 \varphi_{,xx} - M_y v_{,xx} + M_z w_{,xx} + EI_w \varphi_{,xxxx} - GI_t \varphi_{,xx} = m_x + M_y v_0 + M_z w_0 + N r_{yz}^2 \varphi_0$$

As before, the system of Eq. (5.288) can only be solved supposing appropriate approximations of the displacement functions and the imperfection. Again, a sine half wave is assumed. Hence, so as to obtain consistent results the externally applied loads q_z , q_y and m_x as well as the resulting bending moments should also respect the shape of a sine half wave in order to generate the assumed displacements. Consequently the loads q_z and q_y can be replaced by the bending moments following Eqs. (5.289) and (5.290).

$$M_y = \iint q_z(x) dx dx = -\frac{L^2}{\pi^2} q_z \sin\left(\pi \frac{x}{L}\right) \quad (5.289)$$

$$M_z = \iint q_y(x) dx dx = -\frac{L^2}{\pi^2} q_y \sin\left(\pi \frac{x}{L}\right) \quad (5.290)$$

As for the case of combined major-axis bending and torsion, it has to be noted that there is a certain inconsistency concerning the shape of the bending moment diagram supposed for the analytical developments. Again, to account for the influence for the eigenmode affine imperfection, it has to be supposed that the bending moment is constant leading to the amplification factor $1/(1-M_y/M_{y,cr})$. Contrariwise, to account for the effect of the applied torsional load the bending moment diagrams are supposed to be affine to a half sine wave leading to the amplification factor $1/(1-M_y^2/M_{y,cr}^2)$. Yet, this inconsistency has to be accepted so as to obtain relatively simple expressions of the second order displacements and the resulting second order internal forces and moments. In order to account for the influence of the bending moment diagram

correction factors have to be introduced (equivalent moment factors). This is not done at this point of the developments so as to keep the expressions simple. Additionally, to simplify the lecture of the second order major-and minor axis bending moment as well as the second order bi-moment given in Eqs. (5.291)to (5.293), the quantities defined in Eqs. (5.294) to (5.297) are introduced. It should be noted that the expressions given in Eqs. (5.291)to (5.293) have been derived several times in the past (see for example (Kaim 2004)).

$$M_y^{\text{II}} = N_{cr,y} w^{\text{II}} = \frac{M_y + Nw_0 + M_z \phi_0}{D_y} - \frac{M_y M_z^2}{D_M D_y M_{y,cr,N}^2} - \frac{M_z \phi^I}{D_M D_T D_y} + \frac{M_z M_y (Nv_0 + M_z \phi_0)}{D_M D_y M_{y,cr,N}^2} + \frac{D_z M_z N_{cr,z} (Ni_p^2 \phi_0 + M_z w_0 + M_y v_0)}{D_M D_y M_{y,cr,N}^2} \quad (5.291)$$

$$M_z^{\text{II}} = N_{cr,z} v^{\text{II}} = \frac{Nv_0 + M_z + M_y \phi_0}{D_M D_z} + \frac{M_y \phi^I}{D_M D_z D_T} + N_{cr,z} \frac{M_y (Ni_p^2 \phi_0 + M_y v_0 + M_z w_0)}{D_M M_{y,cr,N}^2} + \frac{N_{cr,z} M_z M_y (Nw_0 + M_y + M_z \phi_0)}{N_{cr,y} D_M D_y M_{y,cr,N}^2} \quad (5.292)$$

$$B^{\text{II}} = N_{cr,z} \frac{I_w}{I_z} \phi^{\text{II}} = \frac{B^I}{D_T D_M} + N_{cr,z} \frac{I_w}{I_z} \left[\frac{M_y (Nv_0 + M_y \phi_0 - M_z)}{D_M M_{y,cr,N}^2} + \frac{D_z N_{cr,z} M_y (Ni_p^2 \phi_0 + M_y v_0 + M_z w_0)}{D_M M_{y,cr,N}^2} + \frac{D_z M_z N_{cr,z} (Nw_0 + M_y + M_z \phi_0)}{D_M D_y M_{y,cr,N}^2 N_{cr,y}} \right] \quad (5.293)$$

$$D_y = \frac{1}{1 - \frac{N}{N_{cr,y}}} \quad (5.294)$$

$$D_z = \frac{1}{1 - \frac{N}{N_{cr,z}}} \quad (5.295)$$

$$D_T = \frac{1}{1 - \frac{N}{N_{cr,t}}} \quad (5.296)$$

$$D_M = \frac{1}{1 - \frac{M_y}{M_{y,cr,N}}} \quad (5.297)$$

In order to obtain an interaction equation that may be applied to the member design the explicit values of the imperfections have to be replaced. It may be accepted that out-of-plane (here combination of v_0 and φ_0) and in-plane imperfection (w_0) need not be applied simultaneously. Consequently, one might consider to study two sets of second order internal moments, one exclusively containing the influence of in-plane imperfection and the other containing only out-of-plane imperfection. However, it should be noted that this approach could not lead to the Eurocode 3 Part 1-1 interaction formulae. Admittedly, these last treat independently the reduction for in-plane and out-of-plane buckling (introduced by the factors χ_y and χ_z , respectively) but the reduction factor introducing the effect of lateral-torsional buckling and the corresponding out-of-plane imperfection is considered in both interaction equations. Therefore, it appears that the interaction formulae proposed in Eurocode 3 Part 1-1 are partially inconsistent as they assume, for the same member, an out-of-plane imperfection only for the major-axis bending moment and they consider that second order effects do not arise from the combination of the out-of-plane imperfection and the axial force. Nonetheless, observing the second order internal moments derived before for the case of combined axial force, bi-axial bending and torsion, it seems evident that a completely consistently derived analytical design approach is impossible to develop for an arbitrary combination of loads.

It is recalled that one of the objectives of this thesis is to propose a simple extension of the interaction formulae provided in Eurocode 3 Part 1-1 to members subject to additional torsional loads. The interaction formulae have been derived based on the works of several researches based on extensive analytical and numerical studies as well as physical tests. They have proven to be sufficiently safe and economic to be applied in the practice to members subject to combined axial force and bi-axial bending. Therefore, it is admitted hereafter that all effects and terms included in the second order internal moments not linked to an applied torsional load are already considered in the interaction factors k_{ij} of the Eurocode 3 interaction formulae. Conversely, the influence of the terms linked to an applied torsional load should be quantified in the following. These terms are recalled in Eqs. (5.298) to (5.300). One may note that the torsional load generates a bi-moment that is amplified through the influence of torsional (D_T) and lateral-torsional (D_M) buckling. Also, the torsional load induces a twist φ^t . As the first order bi-moment, the twist is amplified by the factors $1/D_M$ and $1/D_T$. Additionally, as the principal axis of the twisted member are not aligned anymore with the axis of the load supplementary bending moments $M_{y,Mx}$ and $M_{z,Mx}$ arise and they are amplified by the effect of flexural buckling about the respective axis. It should be noted here that the bi-moment generated by lateral displacement (see Eq. (5.270) for example) is not influenced by the torsional load and is consequently supposed to be accounted for by the Eurocode 3 interaction factors as stated above for all other effects not linked to first order torsion.

$$M_{y,Mx}^{II} = -\frac{M_z \varphi^I}{D_y D_M D_T} \quad (5.298)$$

$$M_{z,Mx}^{II} = \frac{M_y \varphi^I}{D_z D_M D_T} \quad (5.299)$$

$$B_{Mx}^{II} = \frac{B^I}{D_T D_M} \quad (5.300)$$

In paragraph 5.5.7.4, it has been shown that if the equivalent geometric imperfections is replaced by the generalized imperfection η , the bi-moment is not associated with the factor $1/D_M$ anymore but with the factor $1/(1 + M_y/M_{y,cr})$ (compare Eqs. (5.252)and (5.253)). Consequently, the bi-moment is not amplified but reduced if the major-axis bending moment approaches the critical moment. The reason leading to this surprising observation has been discussed in paragraph 5.5.7.4. The numerical study presented in paragraph 5.6 is therefore very helpful to verify if a second order amplification of the bi-moment by the factor $1/D_M$ is necessary or not.

5.5.7.6 Conclusions

In paragraph 5.5.7 the elastic second order equilibrium of the member was of special interest. In particular, it was intended to develop analytical expressions of the second order internal forces and moments as well as analytical interaction equations in order to facilitate the comparison to the existing design models and to highlight the main parameters influencing the member resistance.

First, the well-known lateral-torsional buckling curves of Eurocode 3 Part 1-1 (CEN 2005a) have been re-derived as reference case. Also, the amelioration of the reduction curve developed by several researchers (see references (Stangenberg 2007), (Naumes 2009) and in particular (Taras 2011)) has been presented and compared to the existing design approach for lateral-torsional buckling of I-shaped members. It has been shown that the main difference between the currently standardised reduction curve and the proposals consist in the consideration of the torsional behaviour of the member that is only roughly approximated by the imperfection factor α in Eurocode 3 Part 1-1 and more precisely considered by the ratio between λ_{LT}^2 and λ_z^2 in the proposals. Here, it should be noted that the proposal made by Taras is accepted as amendment to the current version of Eurocode 3 Part 1-1 and is therefore provided in the future version of this standard.

After the treatment of the reference case, the investigations have been extended to members under combined axial force and major-axis bending, major-axis bending and torsion, axial force and bi-axial bending and finally to combined axial force, bi-axial bending and torsion. For the case of combined axial force and major-axis bending, it has been shown that the Eurocode 3 interaction formulae can only be derived if a certain inconsistency is accepted for the applied geometric imperfections. It is recalled that the development supposes that the member is subject to the entire lateral imperfection leading the reduction factor χ_z for the axial force and in the same time

to an imperfection affine to the first member eigenmode for lateral-torsional buckling leading to the reduction factor χ_{LT} . Obviously, this assumption is not physical but it allows the development of relatively simple design expressions. The interaction formulae account empirically for their inconsistency by the calibration of the interaction factors, in particular the calibration of the factor k_{zy} . For the same load case Eurocode 3 Part 1-1 proposes the “general method” in its paragraph 6.3.4. This method replaces the influence of the equivalent geometric imperfection and the resulting second order internal forces and moments by a global reduction factor χ_{op} for out-of-plane instability. It has been shown that this approach, despite of its empirical nature, can give rather satisfactory results compared to elastic second order calculations (GNIA) in its field of application. In paragraph 5.4.3.4, it has however already been shown that an extension to minor-axis bending moments as proposed in reference (Naumes 2009) may lead to unsafe results.

The analytical developments for combined major-axis bending and torsion were of interest as they have shown that the empirically developed design proposal of (de Louw 2007) and (Snjider et al. 2008) can be justified analytically. The extension to the case of bi-axial bending and torsion clearly pointed out that, even if the proposal of Stangenberg included a plastic interaction, the introduction of simplifying assumptions and empirical factors accounting for different effects as the bending moment diagram leads to a loss of precision.

The load case of combined bi-axial bending and torsion has also been used as example to demonstrate how a global reduction curve following the principles of the OIC approach can be derived. Several terms and influences that may be accounted for have been highlighted.

Last, the case of combined axial force and bi-axial bending as well as axial force, bi-axial bending and torsion have been treated. Again, it has been demonstrated that certain inconsistencies have to be accepted when the Eurocode 3 interaction equations are developed for combined axial force and bi-axial bending. In the past, these inconsistencies have been covered by an empirical calibration of the interaction factors. It appeared absolutely necessary to study these last both cases from a theoretical point of view so as to emphasise which effects are already empirically covered by the current interaction formulae and which terms should additionally be included if the Eurocode 3 design method is extended to applied torsion.

In the following paragraph, the member resistance is addressed based on an extensive numerical study. A database of numerically determined member resistances is constituted and used to develop a simple and practical design approach.

5.6 Numerical parametric study

5.6.1 General

The following paragraphs present a numerical study performed to develop a simple and practical design approach for I- and U-shaped members subject to an arbitrary combination of loads. The previous paragraph presented a detailed theoretical study that has been performed in order to highlight the key parameters of the studied problem. Consequently, the results of the theoretical study represent the framework of the resistance model and the following numerical study is used to adjust and validate the design approach.

The numerical study consists in over 10 000 GMNIA calculations. This high number of simulations has been carried out so as to cover a sufficiently wide range of cross-sections and load cases as detailed in paragraph 5.6.2. The numerical calculations are realised with the model validated in Chapter 3. Additionally, the conclusions of paragraph 5.2, concerning particular modelling aspects, are considered. Therefore, the following simulations are based on:

- A shell model not considering the fillets of hot-rolled sections according to the investigations of paragraph 3.3.5;
- A residual stress pattern for I sections according to reference (ECCS 1984);
- A residual stress pattern for U sections according to the investigations of paragraph 5.2.1.5;
- An equivalent member imperfection affine to the first member eigenmode directed in the appropriate direction (see paragraph 5.2.1.6) and with an amplitude of $L/1000$;
- An equivalent sinusoidal plate imperfection with an amplitude of $h_w/200$ for the web and $b_f/400$ for the flange and a half wave length of $l_{wave}/2 = (h_w + (b_f - t_w))/2$ according to paragraph 5.2.1.7;
- A multi-linear material law following the recommendations of reference (ECCS 1984) with a yield stress of 235 MPa if not indicated otherwise (the influence of the yield stress is also studied in paragraph 5.6.2.4);
- A proportional increase of the applied loads according to paragraph 5.2.2.

It should also be noted that members of slender cross-section are analysed twice: first they are calculated without considering the influence of local plate instability (see paragraph 5.2.3) and then a second calculation is performed on the model not containing the rigid beam elements applied to avoid local buckling. The first simulation allows the treatment of a greater variety of cross-section geometries without the influence of local buckling. Moreover, by comparing the results obtained by both simulations it is possible to quantify the influence of local buckling on the member resistance.

The next paragraph details the choices concerning the parametric field of the numerical study.

5.6.2 Scope of the parametric study

5.6.2.1 *Representation of the results*

Hereafter, the results obtained with the GMNIA simulations are presented in form of ultimate resistance curves as schematically represented in Figure 5-110. This choice is somewhat different of what has been done in numerous research works studying the member resistance in the past (see for example references (Ofner 1997), (Villette 2004), (Kaim 2004) and (Kettler 2008)). In fact, the mentioned authors chose a representation in form of interaction curves as for example shown in Figure 5-111 (member of IPE 500 section subject bending moment varying from M_y to 0 – data obtained from reference (Ofner 1997)). However, the cited research works concerned interaction between not more than three internal forces and moments. In the framework of the present thesis at least four internal forces and moments can act simultaneously in the member (N , M_y , M_z , B). For short members the additional shear force may also influence the member resistance. Consequently, it appears to be unpractical to represent the results in form of interaction diagrams hereafter. Additionally, the interaction diagrams do only roughly give information about the member behaviour in terms of sensitivity to elasto-plastic instability. Conversely, the ultimate resistance curve of Figure 5-110 clearly highlights several zones: short members can attain the theoretical (plastic) section resistance and are not much influenced by the effect of member instability whereas longer members suffer from an important strength reduction due to their sensitivity to imperfections and second order effects. Finally, the failure of members possessing high values of the relative slenderness may be highly influenced by the effect of elastic instability. For members in bending, a certain post buckling reserve due to torsional rotations may also be observed leading to an ultimate resistance curve crossing the Euler curve. Finally, in order to represent the results in form of interaction curves at least six to eight points per curve are necessary. Consequently, many authors chose to study only three to four different values of the member slenderness. In the framework of this thesis, at least eight member lengths are studied to cover the whole range of the ultimate resistance curve. Therefore, the numerical simulations presented hereafter also contribute to extend the database of member resistances obtained in the past.

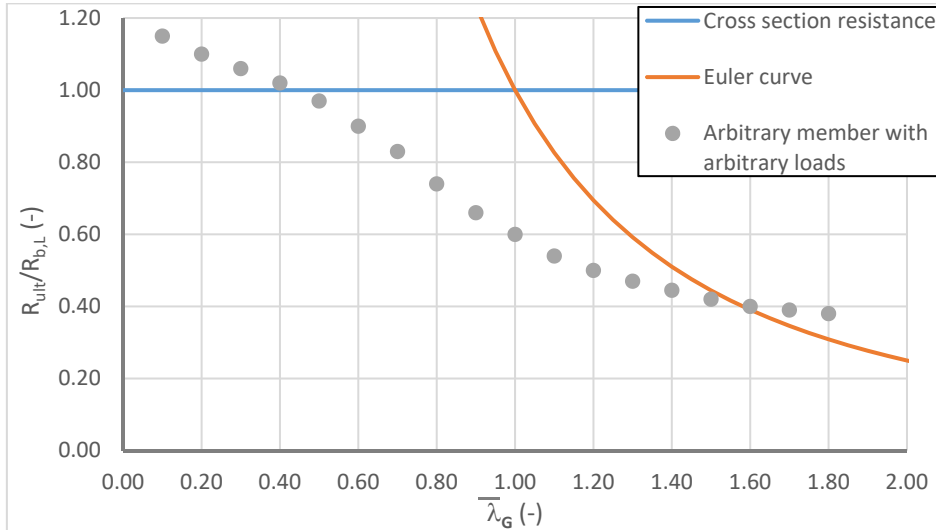


Figure 5-110: Schematic representation of an ultimate resistance curve

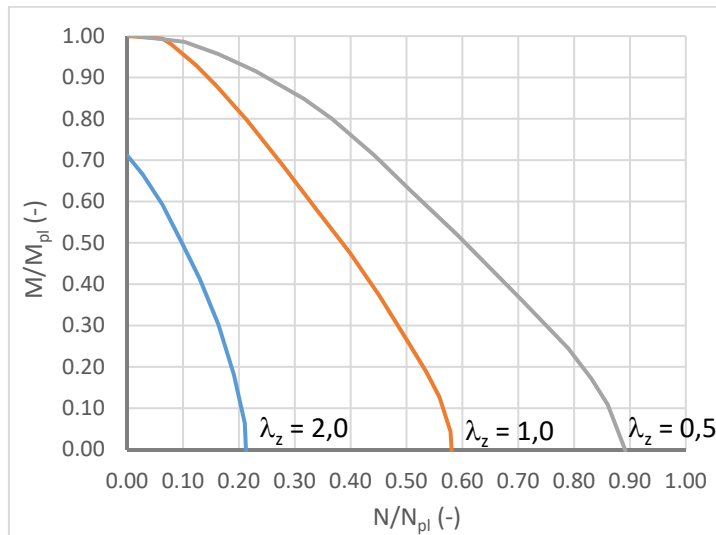


Figure 5-111: Representation of member resistance in form of interaction diagram

5.6.2.2 Cross-sections

Table 5-27 summarises the dimensions of the studied sections. The sections are chosen to obtain a sufficient variety in terms of:

- Ratio h/b representing the sensitivity to lateral-torsional buckling (with increasing ratio h/b sections become more sensitive to lateral-torsional buckling in practice);
- Web slenderness varying from compact (class 1) to slender (class 4);
- Flange slenderness varying from compact (class 1) to semi-compact (class 3);
- Ratio between web and flange slenderness representing the restraining effect from the flange to the web that reduces the local buckling sensitivity of the web in practice;
- Warping decay factor ε_T .

Table 5-27: Dimensions of studied sections

Cross-section type	Notation	h (mm)	t_w (mm)	b (mm)	t_f (mm)	
U	UPE 80	80	4	50	7	
	UPE 200	200	6	80	11	
	UPE 360	360	12	110	17	
Double symmetric I	HEB 200	200	9	200	15	
	IPE 500	500	10,2	200	16	
	HEAA 800	770	14	300	18	
	HR290.3.300.14	290	3	300	14	
	HR500.4.300.20	500	4	300	20	
	HR770.5.400.17	770	5	400	17	
	W650.5.180.10	650	5	180	10	
	W1330.10.280.15	1330	10	280	15	
	W850.6.300.12	850	6	300	12	
	W850.5,5.200.14	850	5,5	200	14	
Mono-symmetric I	Notation	h (mm)	t_w (mm)	b_{fsup} (mm)	b_{finf} (mm)	t_f (mm)
	IMS1	200	9	200	150	15
	IMS2	200	9	200	125	15
	IMS3	500	10,2	200	125	16
	IMS4	500	10,2	200	75	16

Figure 5-112 illustrates the ratios between the slenderness of the web and the flanges. Additionally, the section are represented in Annex C.

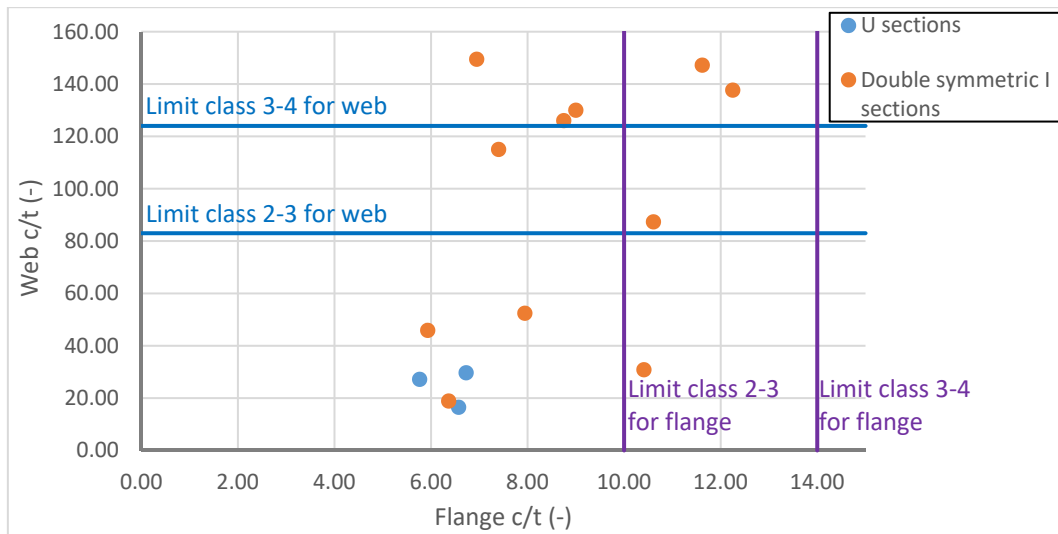


Figure 5-112 : Web and plate slenderness of studied sections in bending

It should be noted that the parametric study does not contain sections that are of class 4 due to their flanges as these sections are of less practical interest, especially for the field of building construction that is covered in the framework of this thesis.

5.6.2.3 Load cases

In this thesis members subject to combined axial force, bi-axial bending and torsion are studied. Consequently, the resistance is influenced by the degree of bi-axiality, and the relative importance of internal forces and moments to each other. Moreover, the form of the bending moment diagram influences the ultimate resistance. Here, it is considered that the members are mainly subject to bending. This certainly covers practical cases in particular for members subject to torsion. Consequently, the following rather low utilisation degrees are considered systematically for the axial force:

- $N/N_{pl} = 0$ noted as "N0";
- $N/N_{pl} = 0,15$ noted as "N15";
- $N/N_{pl} = 0,30$ noted as "N30".

However, in order to validate the obtained solution, a certain number of members are studied under predominant axial force. It is recalled that the loads are increased proportionally. Therefore, the axial force attains the given reference value only if the member attains its full plastic section resistance.

The bi-axiality of bending is characterised by an angle in the M_y - M_z interaction diagram. In the following five angles are chosen as represented in Figure 5-113 for an IPE 500 section. It may be noted that the members are in most cases subject to predominant major-axis bending because this corresponds to the mechanical performance of I and U sections and therefore matches to the

practical habit. The bi-axiality is noted as MyMz0, MyMz15, MyMz30, MyMz60 and MyMz90 in the following depending on the studied angle.

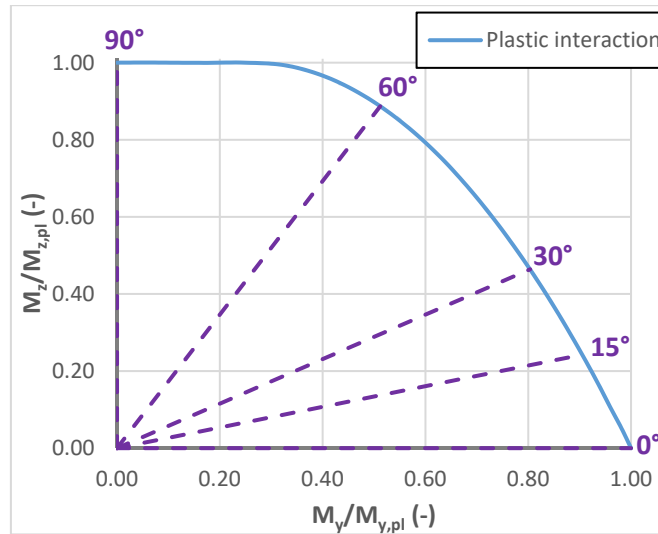


Figure 5-113: Definition of bi-axiality

Throughout this paragraph the three load case of Table 5-28 are studied. Load cases P1 and P2 correspond to point loads applied at mid-span. In case of load case P1 it is considered that the member possesses simple supports at its ends and for load case P2 the member is supposed to possess fixed ends (yet, warping is not restrained). Load case M corresponds to a constant bending moment distribution. Even for this load case, the torsional moment M_T is introduced as point moment depending on the value of the major-axis bending moment. Its value is calculated by Eq. (5.301). The introduced torsional moment is therefore equal to the torsional moment that would be introduced by a point load applied at mid-span creating the same maximum bending moment M for a member on fork supports (depending on the bi-axiality, the major- or minor-axis bending moment is considered).

$$M_T = 2M_{x,tot} = 4M \frac{e}{L} \tag{ 5.301 }$$

Table 5-28: Distribution of moments My, Mz and Mx along the member

Notation	Distribution of bending moments M_y and M_z	Distribution of torsional moment $M_{x,tot} = M_{x,StV} + M_{x,w}$
M		
P1		
P2		

Eq. (5.301) shows that the applied torsional moment is proportional to the maximum bending moment and the eccentricity e . Different eccentricities are studied as defined in Table 5-29, Table 5-30 and Table 5-31.

Table 5-29: Lateral load eccentricities for I sections

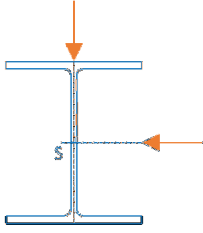
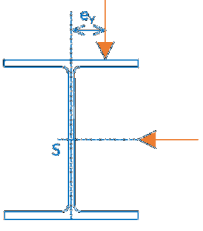
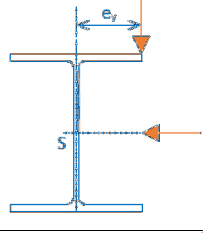
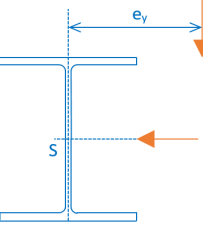
Load eccentricity	Representation	
Ecc0		
EccY1		
EccY2		
EccY3		

Table 5-30: Lateral load eccentricities for U sections

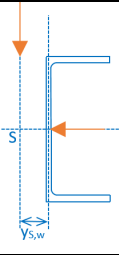
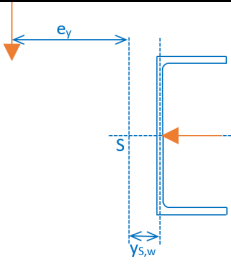
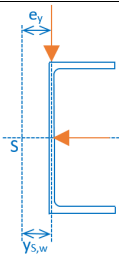
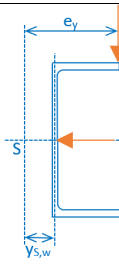
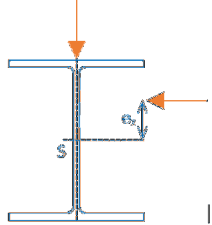
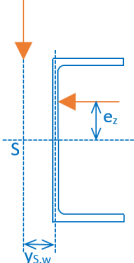
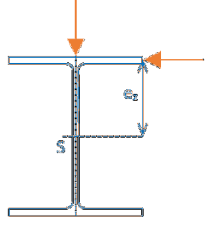
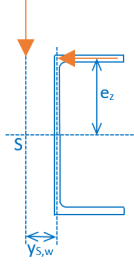
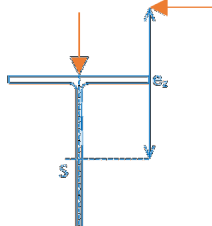
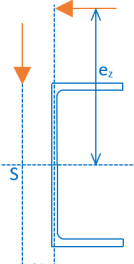
Load eccentricity	Representation	
Ecc0		$e_y = 0$ $e_z = 0$
EccY1		$e_y = 3y_{s,w}$ $e_z = 0$
EccY2		$e_y = y_{s,w}$ $e_z = 0$
EccY3		$e_y = b_f t_w / 2 + y_{s,w}$ $e_z = 0$

Table 5-31: Vertical load eccentricities for I and U sections

Load eccentricity	Representation		
EccZ1			$e_y = 0$ $e_z = (h-t_f)/4$
EccZ2			$e_y = 0$ $e_z = (h-t_f)/2$
EccZ3			$e_y = 0$ $e_z = (h-t_f)$

It should be noted that the load eccentricities have not been chosen to represent necessarily the most practical configurations but rather to modify the relative importance of the applied torsional moment compared to the bending moments.

Finally, Table 5-32 represents the field of the systematic parametric study. So as to vary the slenderness of the member, eight lengths are studied included in the interval of $5,5b_f$ and $60b_f$ ($70b_f$ for some members without torsion and for low bi-axiality of bending). Also, it is recalled that additional simulations are performed in order to study the influence of high axial compression forces and the influence of the steel grade.

Table 5-32: Field of the parametric study for I sections

Load case	Cross-section	Axial force	Bi-axiality	Eccentricity
M	HEB 200 IPE 500 HEAA 800 HR290.3.300.14 (HR1) HR500.4.300.20 (HR2) HR770.5.400.17 (HR3) W650.5.180.10 (W1) W1330.10.280.15 (W2) W850.6.300.12 (W3) W850.5,5.200.14 (W4) IMS1 IMS2 IMS3 IMS4	N0 N15 N30	MyMz0 MyMz15 MyMz30 MyMz60	Ecc0, EccY1, EccY2, EccY3
			MyMz90	Ecc0, EccZ1, EccZ2, EccZ3
P1 P2	HEB 200 IPE 500 HR500.4.300.20 (HR2) HR770.5.400.17 (HR3) W650.5.180.10 (W1) W1330.10.280.15 (W2) IMS1 IMS2 IMS3 IMS4	N0 N30	MyMz0 MyMz30	Ecc0, EcY1, EccY3
			MyMz60	Ecc0, EcZ1, EccY3

Table 5-33: Field of the parametric study for U sections

Load case	Cross-section	Axial force	Bi-axiality	Eccentricity
M P1 P2	UPE80 UPE200 UPE360	N0 N15 N30	MyMz0 MyMz15 MyMz30	Ecc0, EccY1, EccY2, EccY3
			MyMz60	Ecc0, EccZ1, EccZ2, EccY3
			MyMz90	Ecc0, EccZ1, EccZ2, EccZ3

5.6.2.4 *Influence of the steel grade on the ultimate member resistance*

In paragraph 5.6.1, it is stated that the members studied in the framework of the parametric study are supposed to be fabricated from steel S235. The investigations performed on U-shaped members under high minor-axis bending in paragraph 5.5.6.2.5 indicated that the steel grade may have an influence as it can increase the member slenderness (associated with elastic instability under M_z) above 0,4 leading to a certain strength reduction due to elasto-plastic instability. Nonetheless, the effect of elasto-plastic member instability only influences U-shaped members subject to minor-axis bending for steel grades higher than S460. This seems out of the field of application of today's practice. The influence of the steel grade on the ultimate resistance of

members subject to other load cases is quantified in this paragraph on the basis of three different members under complex loading. The examples are represented in Table 5-34. In this table the notations introduced in paragraph 5.6.2 are used. The GMNIA calculations are performed including geometric member and plate imperfection as well as the appropriate residual stress pattern. It is recalled that the amplitude of the residual stresses is considered as constant and not as proportional to the yield stress.

Table 5-34: Members studied to characterize the influence of the steel grade on the member resistance

Example	Section	Load Case	Axial force	Bi-axiality	Eccentricity	Steel grade
IPE500_P1_N30_MyMz30_EccY1	IPE500	P1	0,3N _{pl}	30°	EccY1	S235 S355 S460
W2_P1_N30_MyMz0_EccY1	W1330.10.280.15	P1	0,3N _{pl}	0°	EccY1	S235 S355 S460
UPE200_P1_N0_MyMz15_EccY2	UPE200	P1	0	15°	EccY2	S235 S355 S460

The ultimate resistance curves are given in Figure 5-114, Figure 5-115 and Figure 5-116 for the three studied cases. The global slenderness used along the abscissa is calculated in the OIC format by Eq. (5.303). For the following examples, the effect of local buckling is excluded as described in 5.2.3.

$$\bar{\lambda}_G = \sqrt{\frac{R_{pl}}{R_{cr,G}}} \quad (5.302)$$

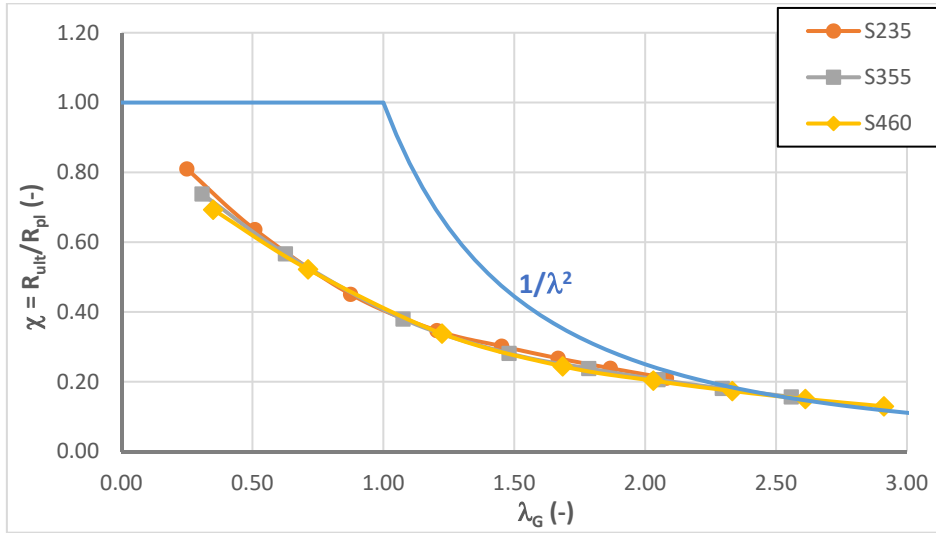


Figure 5-114: Ultimate resistance curves for IPE 500_P1_N30_MyMz30_EccY1

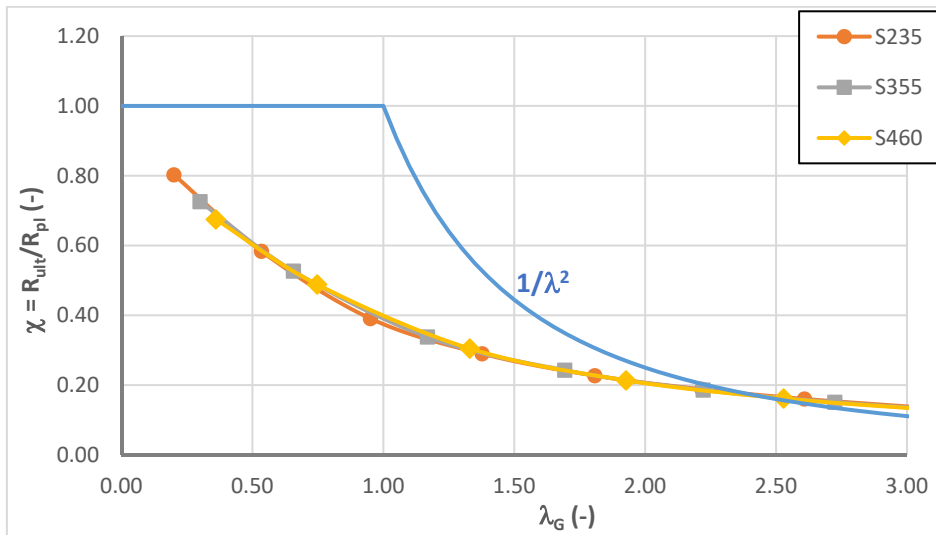


Figure 5-115: Ultimate resistance curves for W2_P1_N30_MyMz0_EccY1

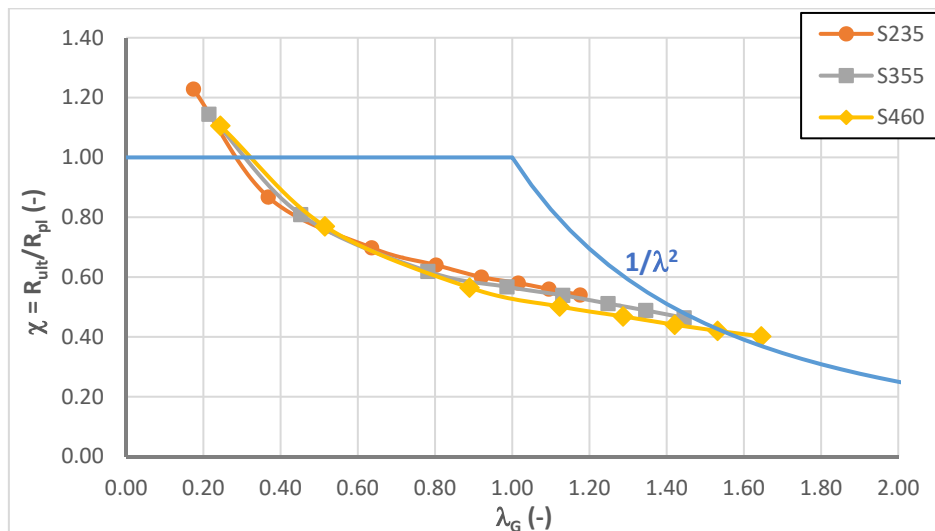


Figure 5-116: Ultimate resistance curves for UPE200_P1_N0_MyMz15_EccY2

Figure 5-114 to Figure 5-116 clearly indicate that the influence of the steel grade can be neglected in the framework of the parametric study. For both I sections the ultimate resistance curves associated with the different steel grades overlay nearly perfectly over the whole range of the relative slenderness. For the U-shaped member slight differences may be observed in Figure 5-116. It may seem somewhat surprising that the resistance linked to steel grade S460 is less than for the other steel grades for medium to high values of the slenderness even if the relative influence of the residual stresses is lower. Yet, it is recalled that the residual stresses may have a favourable effect on the member resistance for certain load cases and in particular for major-axis buckling (see paragraph 5.2.1.5). Anyhow, the differences are less than 5% and can be neglected hereafter.

5.6.3 Overall results

In paragraphs 5.6.4 and 5.6.5 design methods for the resistance of members subject to a combination of a compression axial force, bi-axial bending and torsion is developed. Before this is done it seems interesting to represent a global view of the results obtained through the parametric study. In Figure 5-117 all numerically determined resistances for members possessing compact section (or sections treated as compact as discussed in paragraph 5.2.3) are represented. The results obtained for members of non-compact and slender cross-section are not given so as to facilitate the interpretation of Figure 5-117.

In Figure 5-117 one may observe a very high scatter of the numerically obtained resistances. For example, depending on the configuration (load case, cross-section) a member possessing a relative slenderness of 0,5 may attain between 55% and, at least, 150% of its numerically determined plastic resistance (calculated with MNA simulation). It should be noted that the GMNIA simulations are stopped when the member attains 150% of its plastic resistance as this high resistance reserve is, in particular, linked to the effect of strain hardening. Since the objective of this thesis is not the quantification of the strain hardening reserve on the member resistance the simulations have not been carried on with higher loads so as to limit the calculation time. In

any case, the high scatter of the results seems consistent with the wide range of the parametric study. Nonetheless, some of the results should be studied in more detail. In fact, it appears that even for rather high values of the relative slenderness (0,8...1,0), many members exceed their numerically determined plastic resistance.

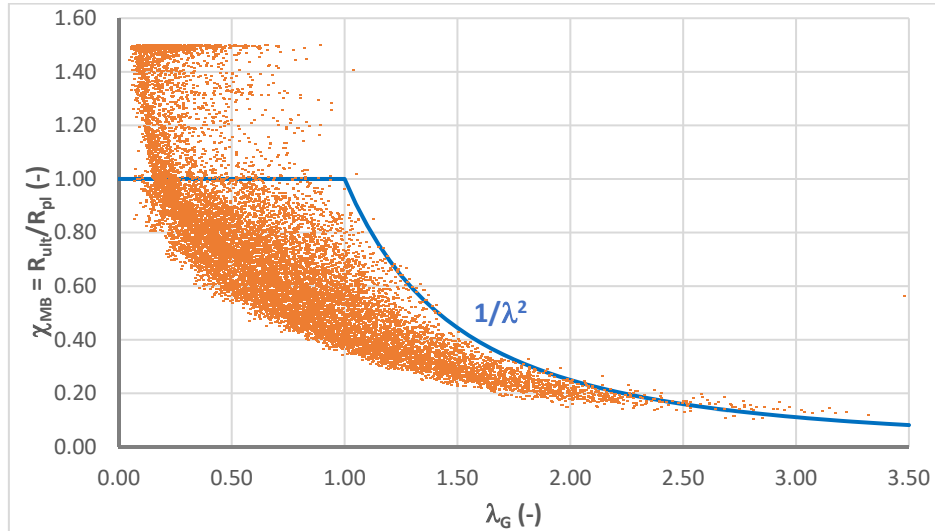


Figure 5-117: Global view of the results of the parametric study

In order to understand this surprising observation, a member of HR.290.3.300.14 section is studied. The section is prevented from local plate instability as discussed in paragraph 5.2.3. The member possesses a length of 8,1 m and fork supports at its ends. It is subject to a constant major-axis bending moment and a torsional moment applied at mid-span corresponding to the case EccY3. Consequently, it is subject to rather high torsion. The resulting member slenderness is equal to 0,6.

Figure 5-118 represents the evolution of the load factor with the torsional twist of the member at mid-span. One may observe that the member resistance exceeds the load factor of 1,0 associated with the plastic resistance of the members. The load displacement curve is characterised by three stages: first, the member behaves linearly in the elastic range, for a load factor of approximately 0,60 the stiffness of the member decreases due to initiation of yielding but the member does not fail by elasto-plastic instability. In fact, starting from a torsional twist of 1,00 the stiffness of the member increases again. Finally, the member attains its ultimate resistance for a load factor of 1,10. Obviously, the value of the torsional twist is extremely high as also represented in Figure 5-119.

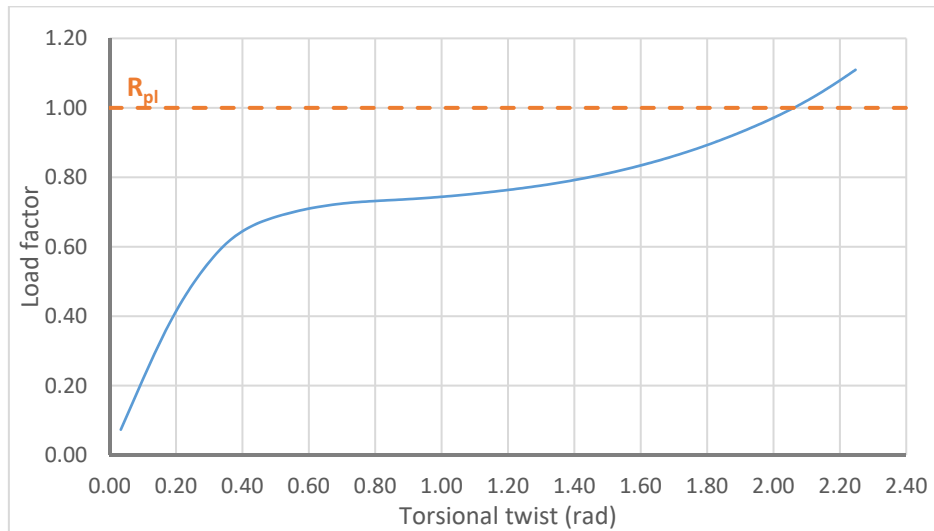


Figure 5-118 : Lpad displacement curve for member HR290.3.300.14_M_N0_MyMz0_EccY3_L8100

Figure 5-119 shows the von Mises stress distribution for the studied member as well as its deformed shape at ULS. One may easily observe that the member has yielded over practically its total length and it has even attained the strain hardening in the flanges and at the supports. Most importantly, it appears that the member undergoes an extremely high torsional twist that is certainly not acceptable in practice, even at ULS.

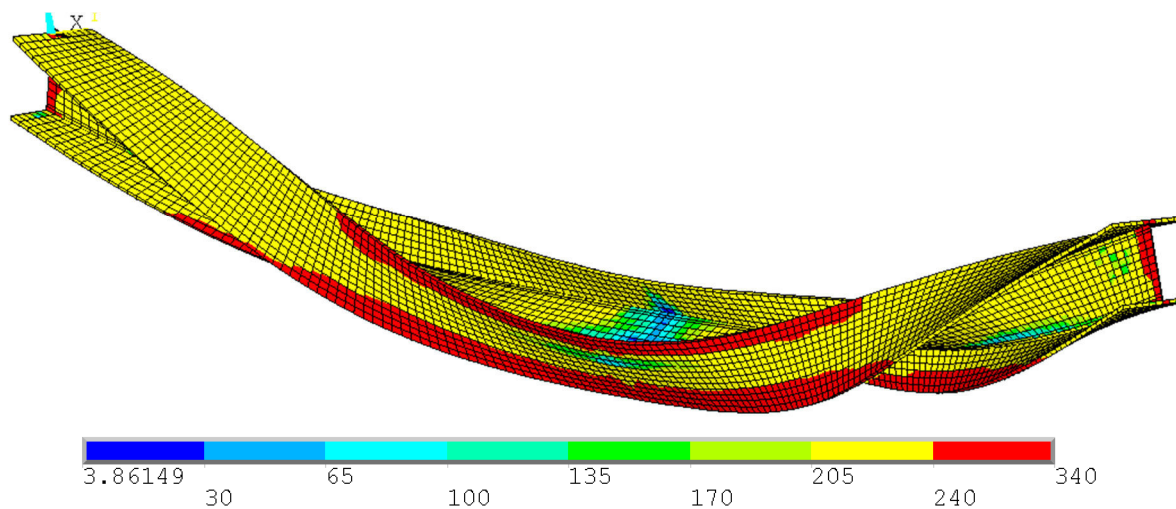


Figure 5-119 : Von Mises stress distribution and deformed shape of member HR290.3.300.14_M_N0_MyMz0_EccY3_L8100 at its Ultimate Limit State

It seems that it is necessary to define a limit torsional twist that could be accepted at ULS. Nonetheless, the torsional twist that can be accepted at ULS, i.e. that does endanger the structural elements attached to the studied member, highly depends on the design of the structure, and in particular, it depends on the deformation capacity of the secondary members and joints. Rather than to define a limit torsional twist based on the design of the structure and its joints, it is proposed to define a limit torsional twist based on experience. In fact, even members not subject to torsion may endure rather high values of the torsional twist at ULS. Since, the research projects that led to the development of the Eurocod 3 Part 1-1 interaction equations did not include any

limit concerning the maximum torsional twist of the member, it seems that these values are acceptable (see (Offner 1997), (Müller 2003), (Boissonnade et al. 2004) and (ECCS 2008)). In the framework of this thesis approximately 5000 members only subject to a combination of bi-axial bending and compression axial force have been treated. Figure 5-120 represents the maximum torsional twist obtained for these members as a function of the ratio L/b_f . It should be noted that members possessing a ratio L/b_f of 70 are not subject to high degrees of bi-axial bending (only 15°). Therefore, the maximum torsional twist is less than for shorter members.

It seems that very long members subject to high degrees of bi-axiality (60°) may also experience very high mid-span torsional twists. Yet, these members are at the limit of the practical range.

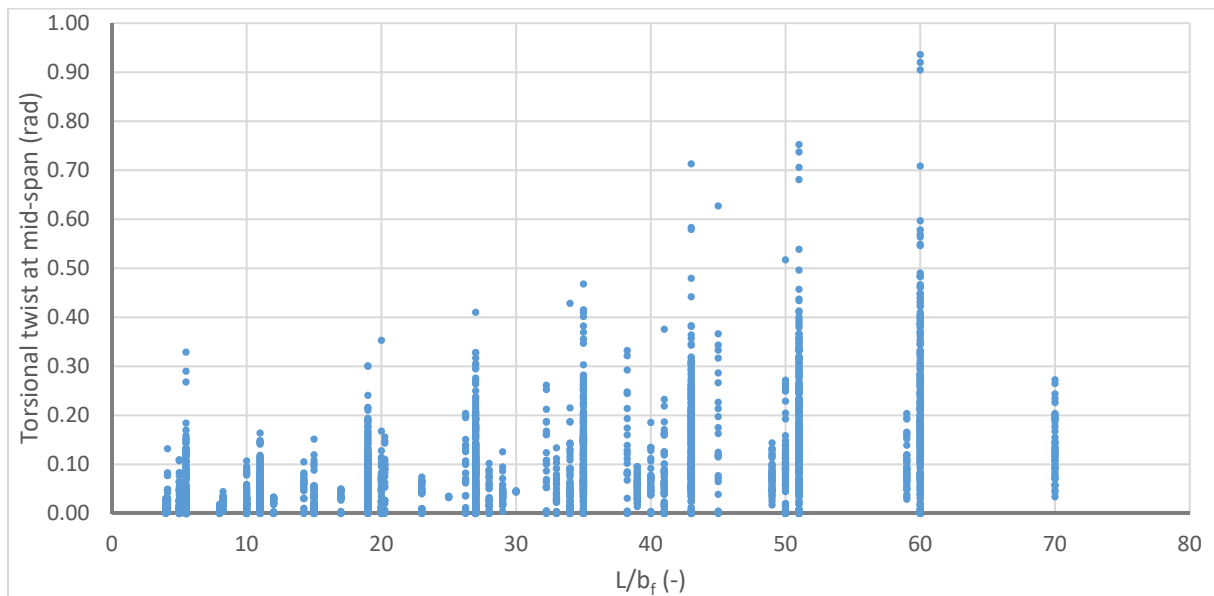


Figure 5-120 : ULS maximum torsional twist at mid-span for members under bi-axial bending and compression axial force

Globally, the maximum torsional twist that is not exceeded by the majority of the studied members is of about 0,5 rad to 0,6 rad. Therefore, it is proposed to limit the torsional twist to 0,6 rad even for members subject to torsion. One might argue that in case of applied torsion a higher maximum twist should be accepted. Nonetheless, the maximum acceptable torsional twist does obviously not depend on the applied loads but on the design of the structure. Hence, the same maximum value should be considered for members not subject to torsion and members subject to torsion.

If the torsional twist limit of 0,6 rad is introduced, the ultimate resistance of many members reduces. For the example studied above (see HR.290.3.300.14_M_N0_MyMz0_EccY3_L8100 Figure 5-118) the global reduction factor χ_{MB} reduces from 1,1 to 0,7. Figure 5-121 shows the global view of the results including the limit of $\varphi \leq 0,6$ rad.

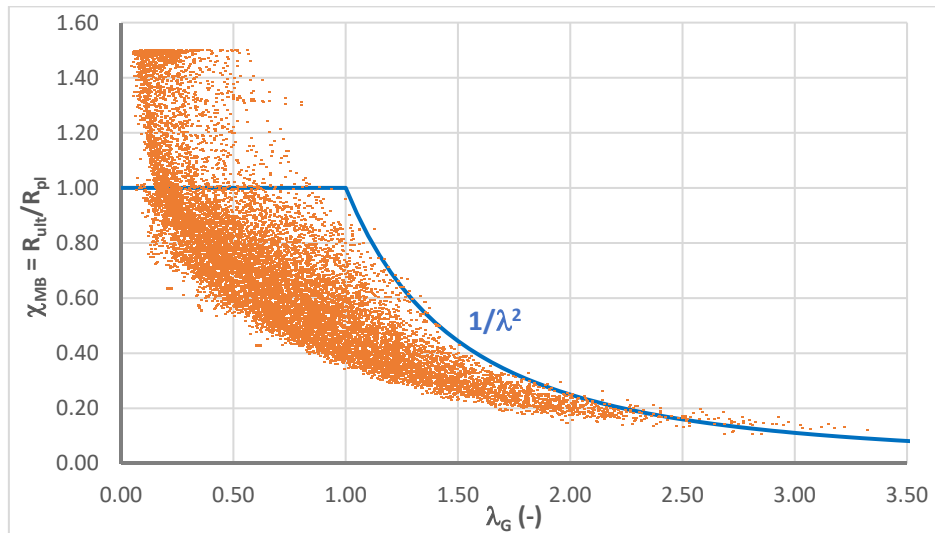


Figure 5-121: Global view of the results of the parametric study – Maximum torsional twist is limited to 0,6 rad

It appears that even with the introduced limit torsional twist, some members attain very high resistances in the slenderness range of 0,8 to 1,0. At this point, the theoretical study performed on U-shaped members in paragraph 5.5.6.2.5 may be recalled. Indeed, it has been shown that the value of the critical load amplification factor is highly influenced by the first order displacements, especially in presence of high minor-axis bending moments. The influence of first order (or pre-buckling) displacements is much less pronounced for I-shaped members. If the first order displacements are accounted for for the calculation of the critical loads, the global view of the results changes again as represented in Figure 5-122. The differences are visible for U-shaped members under high minor-axis bending and for I- and U-shaped members under minor-axis bending only. Indeed, for these last members, the relative slenderness becomes zero. The results obtained for these members are consequently aligned on the axis of ordinates. Nonetheless, there are still some members that attain a surprisingly high resistance. These members may mobilise a significant level of strain hardening before they fail by elasto-plastic instability as is discussed in detail in paragraph 5.6.4.2.1.

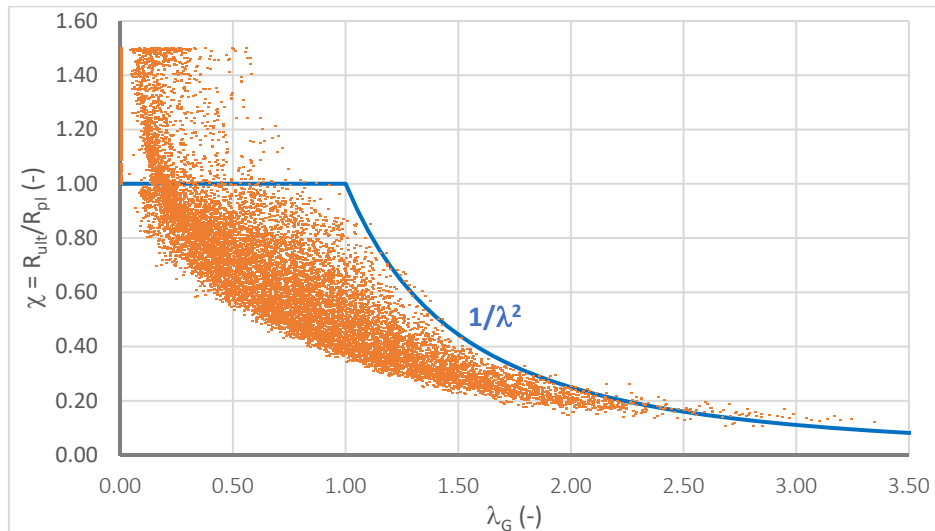


Figure 5-122: Global view of the results of the parametric study – Maximum torsional twist is limited to 0,6 rad

In this paragraph a global view on the results has been presented. The observations led to the definition of a maximum torsional twist that is accepted at ULS. Even if the numerical simulations indicate that a given member may carry higher loads, the load level corresponding to its Ultimate Limit State is considered for a maximum torsional twist of $\varphi = \mathbf{0,6 \text{ rad}}$ for the development of the design model.

5.6.4 Design based on interaction formulae

5.6.4.1 General

In paragraph 5.4 several methods proposed for the design of members subject to combined bi-axial bending, axial forces and torsion have been presented and discussed in detail. It has been shown that some of these proposals are highly complex and not suited for the design practice. Additionally, most of the proposals are limited in their field of application concerning for example the load combination and form of the cross-section. Therefore, these proposals is not evaluated in detail in the following. Hereafter, it is proposed to evaluate the design method developed at TU Berlin, presented in paragraph 5.4.4 and recalled in Eqs. (5.303) to (5.305).

$$\frac{M_{y,Ed}}{\chi_{LT}M_{y,R}} + \frac{C_{mz}M_{z,Ed}}{M_{z,R}} + \frac{k_w k_{zw} k_{\alpha} B_{Ed}}{B_R} \leq 1,0 \quad (5.303)$$

$$k_w = 0,7 - \frac{0,2B_{Ed}}{B_R} \quad (5.304)$$

$$k_{zw} = 1 - \frac{M_{z,Ed}}{M_{z,R}} \quad (5.305)$$

$$k_{\alpha} = \frac{1}{1 - \frac{M_{y,Ed}}{M_{y,cr}}} \quad (5.306)$$

It is recalled that this proposal is also limited as the axial force is not considered. Nevertheless, if this proposal ensures a sufficient safety level for bi-axial bending and torsion, it may be envisaged to extend it to an additional axial compression force.

In addition, a very simple extension of the Eurocode 3 Part 1-1 interaction equations is studied in the following. It is proposed to simply add the utilisation ratio of the bi-moment to the interaction equations.

$$\frac{N_{Ed}}{\chi_y N_R} + k_{yy} \frac{M_{y,Ed}}{\chi_{LT} M_{y,R}} + k_{yz} \frac{M_{z,Ed}}{M_{z,R}} + k_{yw} \frac{B_{Ed}}{B_R} \leq 1,0 \quad (5.307)$$

$$\frac{N_{Ed}}{\chi_z N_R} + k_{zy} \frac{M_{y,Ed}}{\chi_{LT} M_{y,R}} + k_{zz} \frac{M_{z,Ed}}{M_{z,R}} + k_{zw} \frac{B_{Ed}}{B_R} \leq 1,0 \quad (5.308)$$

The interaction factors k_{yw} and k_{zw} are intended to account for several effects:

- The form of the (plastic) cross-section interaction;
- The transition effect between plastic and elastic failure for compact sections;
- The second order effects arising from axial force and major-axis bending.

In Chapter 4, it has been shown that the bi-moment and the minor-axis bending moment are affine and transit only through the flanges for double symmetric I sections. The plastic cross-section interaction with other internal forces and moments is therefore identical. Also, the study on U sections under combined minor-axis bending and bi-moments revealed that a linear interaction between both can be considered safely and with acceptable precision. For simplicity, the proposed cut-off lengths for the interaction are not considered for the member resistance hereafter (see paragraph 4.4.4). Admittedly, this leads to a certain discontinuity between member and section resistance but this has to be accepted here in order to obtain sufficiently simple design equations. Also, this does not increase significantly the discontinuity between member and section resistance that already exists for members under combined bi-axial bending and axial forces.

The second order effects influencing the bi-moment are linked to the critical major-axis bending moment and the critical axial force for torsional buckling as represented in Eq. (5.312). It is recalled that the amplification factors can be derived analytically but only based on certain hypotheses concerning the equivalent imperfection that in some cases are contradictory (see paragraph 5.5.7.5). Paragraphs 5.5.7.4 and 5.5.7.5 revealed that the second order amplification of the bi-moment and the minor-axis bending moment arising from major-axis bending are identical. Conversely, the second order amplification arising from the axial force is linked to the critical axial force for flexural buckling about the minor-axis for the minor-axis bending moment. For members of I and U sections without intermediate restraints or members with intermediate restraints against torsional twist **and** lateral displacements, the critical axial force for minor-axis bending is

generally lower than the critical axial force for torsional buckling. Only, for short members the torsional buckling mode may be relevant but in this case the second order amplification of the bending moments and the bi-moment is rather low. With the objective of a simple design approach, it is therefore proposed to consider that the second order amplification of the bi-moment can be safely linked to the critical axial force for minor-axis buckling. Based on the assumptions discussed here before, it may be considered that the interaction factors k_{yw} and k_{zw} can be expressed similarly to the interaction factors k_{yz} and k_{zz} . The proposed expressions are summarised in Table 5-35. Additionally, it is proposed to use the expressions of Annex B for the determination of the equivalent uniform moment factor C_{mw} . For the studied cases of a torsional moment applied at mid-span the factor C_{mw} is consequently equal to 0,9. On the safe-side a value of 1,0 could also be used. Admittedly, the proposal made here is empirically and in some points not fully mechanically consistent. Nevertheless, a fully consistent design method based on analytical expressions seems neither envisagable nor practical as highlighted in paragraphs 5.5.7.4 and 5.5.7.5 as well as in paragraph 5.4.3.3. Therefore, a certain empiricism has to be accepted. The precision as well as the level of safety is studied in paragraphs 5.6.4.2, 5.6.4.3 and 5.6.4.4.

Table 5-35 : Definition of interaction factors k_{yw} and k_{zw}

Interaction factor	Class 1 and Class 2 sections	Class 3 and Class 4 sections
k_{yw}	$k_{yw} = 0,6k_{zw}$	$k_{yw} = k_{zw}$
k_{zw}	$\bar{\lambda}_z < 1,0 :$ $k_{zw} = C_{mw} \left(1 + (2\bar{\lambda}_z - 0,6) \frac{N_{Ed}}{\chi_z N_R} \right)$ $\bar{\lambda}_z \geq 1,0 :$ $k_{zw} = C_{mw} \left(1 + 1,4 \frac{N_{Ed}}{\chi_z N_R} \right)$	$\bar{\lambda}_z < 1,0 :$ $k_{zw} = C_{mw} \left(1 + 0,6\bar{\lambda}_z \frac{N_{Ed}}{\chi_z N_R} \right)$ $\bar{\lambda}_z \geq 1,0 :$ $k_{zw} = C_{mw} \left(1 + 0,6 \frac{N_{Ed}}{\chi_z N_R} \right)$

Finally, it was shown in paragraph 5.5.7.5 that several terms arise from the effect of an applied torsional moment. They are recalled in Eqs. (5.309) to (5.315).

$$M_{y,Mx}'' = - \frac{M_z \varphi^I}{D_y D_M D_T} \quad (5.309)$$

$$M_{z,Mx}'' = \frac{M_y \varphi^I}{D_z D_M D_T} \quad (5.310)$$

$$B_{Mx}'' = \frac{B^I}{D_T D_M} \quad (5.311)$$

and

$$D_y = \frac{1}{1 - \frac{N}{N_{cr,y}}} \quad (5.312)$$

$$D_y = \frac{1}{1 - \frac{N}{N_{cr,z}}} \quad (5.313)$$

$$D_T = \frac{1}{1 - \frac{N}{N_{cr,t}}} \quad (5.314)$$

$$D_M = \frac{1}{1 - \frac{M_y}{M_{cr,y,N}}} \quad (5.315)$$

The necessity to consider these terms is also investigated when the possible design models are compared to the numerical results of the parametric study.

5.6.4.2 Members with double symmetric I sections

5.6.4.2.1 Double symmetric I-shaped members of compact section subject to combined bi-axial bending and torsion

Through this paragraph the two design approaches recalled and presented in paragraph 5.6.4.1 are investigated. It should be noted that the numerical results, that are the basis for the following comparisons, are obtained for members fabricated from steel S235 and possessing fork end supports. The influence of the yield stress has been shown to be negligible for practical cases in paragraphs 5.5.6.2.5 and 5.6.2.4. Also, all members considered here may attain the full plastic resistance of their most loaded section as local plate instability is prevented (see paragraph 5.2.3).

The cases studied in this paragraph are in the field of application of the design model noted as TU Berlin and proposed in references (FOSTA 2004) and (Glitsch 2008). First, this design method is evaluated with reference to the parametric study. The design approach is compared to the totality of numerical results in Figure 5-123. It appears that the results possess a very important scatter (the standard deviation equals 0,31) that cannot be accepted even for the complex cases tested here. It seems that some of the results obtained with this method are very unsafe with ratios attaining 2,00 and more for individual cases and many results exceed the value of 1,10 for the

ratio $\chi_{\text{Method}}/\chi_{\text{GMNIA}}$. The observed results somewhat confirm the interrogations concerning method TU Berlin summarised in paragraph 5.4.4.

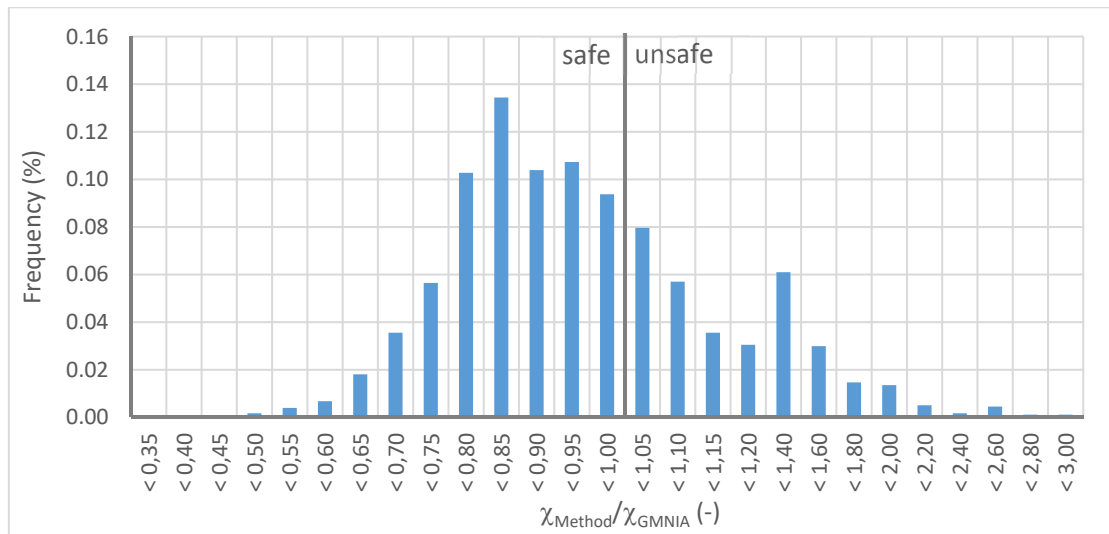


Figure 5-123: Ratio between predicted resistance by approach TU Berlin and numerically obtained resistance

In order to highlight the problem linked to method TU Berlin again, Figure 5-124 represents the minor-axis bending moment at the predicted ultimate limit state for this method. The studied member is subject to combined minor-axis bending and torsion. Following the conventions introduced in paragraph 5.6.2 the studied case is noted as IPE500_M_N0_MyMz90_EccZ2 (constant minor-axis bending and a torsional moment applied at mid-span equal to $2M_z h/L$).

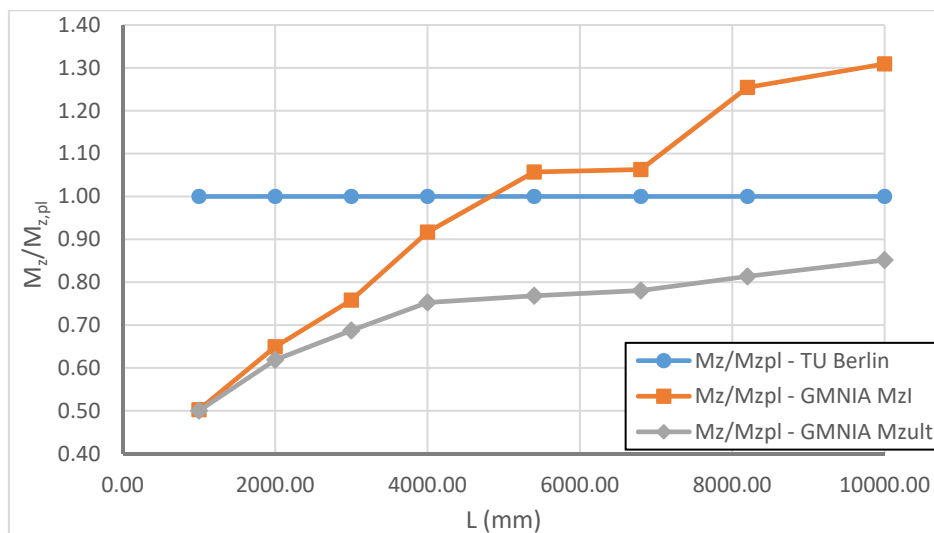


Figure 5-124: Evolution of the predicted and calculated minor-axis bending moment at limit load

The predicted minor-axis bending moment at the ultimate limit state (represented by the ratio $M_z/M_{z,pl}$ - TU Berlin) is compared to:

- The minor-axis bending moment obtained through the GMNIA simulations ($M_z/M_{z,pl}$ - GMNIA M_{ult});

- The minor-axis bending moment that is obtained when the member is subject to the loads corresponding to the GMNIA peak load but when it is calculated with a first order elastic analysis ($M_z/M_{z,pl} - \text{GMNIA } M_{zI}$).

Obviously, when the member is designed with the method proposed by TU Berlin, it always attains the plastic minor-axis bending moment resistance owing to the factor $k_{z,w}$ that becomes equal to 0 in these cases. The results of the GMNIA simulations indicate however that the plastic minor-axis bending moment is not attained, especially for short members. Indeed, Figure 5-125 shows that the member with a length of 1000 mm does not fail through elasto-plastic instability but rather by complete yielding along its length due to the combined influence of the internal forces and moments and, in particular, due to the Saint-Venant's torsional moment arising after the formation of the warping hinge.

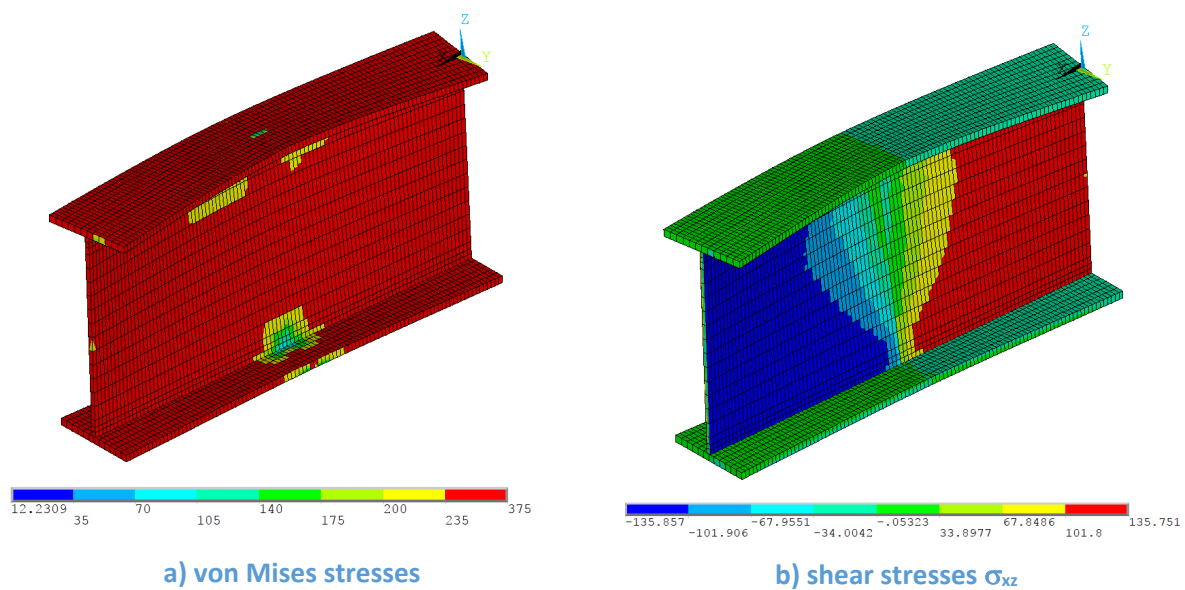


Figure 5-125 : Failure of the member of 1000 mm of length

Even if the member does not attain its full plastic minor-axis bending moment resistance, the formation of the warping has a beneficial effect on the obtained resistance as a redistribution of the torsion takes place. Nonetheless, it should be noted that yielding of the member leads to a non-negligible increase of the torsional twist. So as to study this increase Table 5-36 gives the values of the torsional twist at the ultimate limit state (ULS) and at the serviceability limit state (SLS) obtained by the GMNIA simulation and compares the values to these torsional twists obtained by linear elastic analysis of the member at the corresponding load levels. For simplicity, it is considered that the ratio between the loads at ULS and SLS is equal to 1,5 (this value corresponds to the factor of combination of a variable action for a ULS load combination according to (CEN 2003)). Table 5-36 shows that the difference between the respective torsional twists at the ULS load level attains a value of 15,26. As expected this ratio is rather high due to yielding and the corresponding loss of stiffness. Yet, generally it is not necessary to check the displacements at the ULS load level and therefore this ratio has no particular interest for the practice. Conversely, the displacements should be checked at the SLS load level in order to ensure the functioning of the structure, the comfort of people and/or the appearance of the structure (CEN 2003). Obviously,

in order to verify the serviceability limit states reliably, the calculated displacements should correspond to the real displacements taken by the structure and consequently, the ratio between φ_{pl} and φ_{el} should be close to 1,0 (as generally the analysis of the structure is performed elastically). Though, in Table 5-36, one may observe that even for the SLS load level the ratio is rather high and attains 5,80. The elastic serviceability limit check would therefore highly underestimate the real torsional twist. Nevertheless, the torsional twist obtained by the member may be still acceptable. Contrariwise, for longer member this may not be the case anymore.

Table 5-36: Torsional twist obtained by elastic and plastic analysis of the studied member of 1,0 m of length

Load level	Torsional twist obtained by GMNIA simulation φ_{pl} (rad)	Torsional twist obtained by linear elastic analysis φ_{el} (rad)	$\varphi_{pl}/\varphi_{el}$
ULS: R_{ult}	0,1143 ($\approx 6,5^\circ$)	0,00749	15,26
SLS: $R_{ult}/1,5$	0,0289 ($\approx 1,6^\circ$)	0,00498	5,80

In order to illustrate the issue of the torsional twist at the serviceability limit state the specimen of 8,2 m of Figure 5-124 is considered hereafter. It is recalled that, owing to the warping hinge and strain hardening, the member attains and exceeds its theoretical plastic minor-axis bending moment resistance. Hereafter, the ULS load level is limited to the plastic minor-axis bending moment resistance as also predicted by the design model of TU Berlin. The resulting torsional twists are given in Table 5-37. One may observe that the ratios between the torsional twist determined by plastic and by elastic analysis are lower than for the case of the short member as the load level is limited to $M_{z,pl}$ and consequently the spreading of yielding is limited, too. Nevertheless, the ratio between the torsional twist at SLS load level obtained by plastic analysis and elastic analysis attains still 1,34. Moreover, the obtained torsional twist of approximately 0,3 rad seems rather high and may probably not be accepted in all practical cases at the serviceability limit state.

Table 5-37: Torsional twist obtained by elastic and plastic analysis of the studied member of 8,2 m of length

Load level	Torsional twist obtained by GMNIA simulation φ_{GMNIA} (rad)	Torsional twist obtained by linear elastic analysis φ_{el} (rad)	$\varphi_{GMNIA}/\varphi_{el}$
ULS: $M_{z,pl}$	0,584 ($\approx 33,5^\circ$)	0,328	1,78
SLS: $M_{z,pl}/1,5$	0,293 ($\approx 16,8^\circ$)	0,219	1,34

Finally, it seems interesting to study the difference between the curves linked to $M_{z,l}$ (minor-axis bending moment obtained through elastic analysis) and to $M_{z,ult}$ (minor-axis bending moment obtained through GMNIA simulations). In case of members subject to an axial force or a major-

axis bending moment it is not astonishing to observe differences between the internal forces and moments determined through first order elastic and through second order plastic analysis. Yet, for the studied case second order effects (amplification of moments) do not exist as has been demonstrated in paragraph 5.5.5.2.3 concerning the elastic critical loads (and consequently the influence of second order amplification) for I-shaped members under minor-axis bending. The difference between both minor-axis bending moments has to be attributed to the high torsional twist to which the member is exposed. The minor-axis bending moment acting initially in the principal system of axis of the member acts on the rotated member at the ultimate limit state. In most practical cases, the torsional twist is rather low and consequently the effect is neglected (for example for lateral-torsional buckling problems). However, for members subject to torsion the twist may increase highly leading to a reduction of the effective minor-axis bending moment acting in the member. Obviously, this reduction is accompanied with a creation of a major-axis bending moment. Anyhow, it is clear that the design model proposed at TU Berlin does not capture the described behaviour and it cannot ensure that the member failure is not produced by yielding of the cross-section at the supports due to the Saint-Venant's torsional moment that arises after the formation of the warping hinge. Again, this highlights that the effect of the warping hinge should be considered in the analyses and for the determination of the internal forces and moments but not directly in the design equation. Indeed, if the proposed two-step elastic analysis performed (see paragraph 4.5).

It should however be noted that the bi-moment (determined by a first order elastic analysis of the tested members) may attain rather high values and in particular exceed the value of 50% of the plastic bi-moment resistance of the tested members. It is recalled that Glitsch recommends to apply the proposed design model only up to the limit of $0,5B_{pl}$. If this limit is explicitly introduced as a supplementary design check combined with Eq. (5.303) the method TU Berlin highly reduces its unsafe character as shown in Figure 5-126. It is clear that the method becomes much safer but the scatter continues to be at the upper bound of what can be accepted (standard deviation of 0,20). If the bi-moment is limited to $0,5B_{pl}$ the factor k_w (see Eq. (5.304)) only varies between 0,7 and 0,6 and consequently the product $k_w B_{Ed}/B_{pl}$ varies only between 0,35 and 0,30. One might argue again that a constant value of 0,7 for k_w could be acceptable especially with regard to the rather important scatter of the results obtained with this design model.

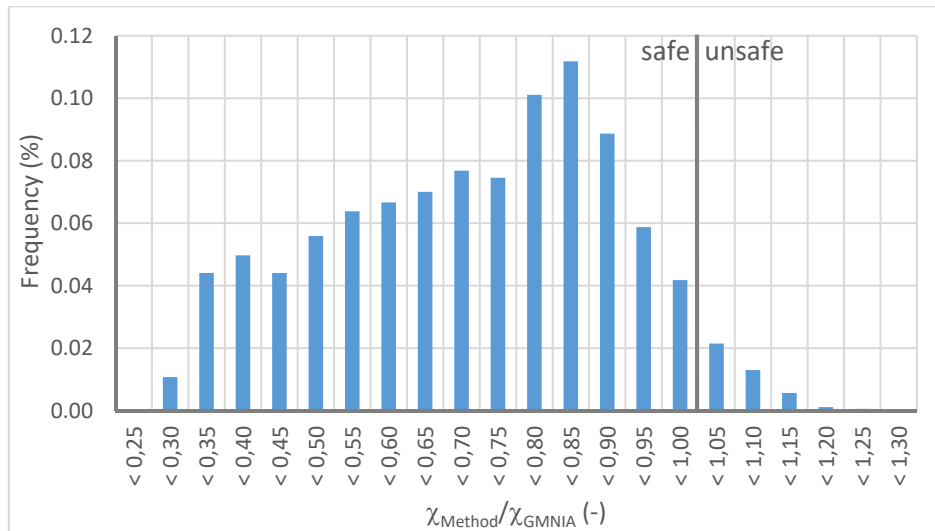


Figure 5-126: Ratio between predicted resistance by approach TU Berlin + limitation of the bi-moment and numerically obtained resistance

Figure 5-126 shows that, despite the introduction of the limitation of the bi-moment, some of the results are still rather unsafe. As an example, a member of HR770.5.400.17 (HR3) section is considered. It is subject to constant bi-axial bending with $M_y M_z 60$ and a torsional moment corresponding to case EccY2. Figure 5-127 shows that the member attains its full plastic cross-section resistance for low values of the slenderness and even more due to the effect of strain hardening. For values of the relative member slenderness exceeding 0,2 the strength is reduced due to the effect of elasto-plastic instability. For higher values of the relative member slenderness the decrease of strength reduction appears to decelerate and finally to stop at a relative slenderness of about 0,9. It should be noted that the resistance of the member possessing the highest relative slenderness is not limited by the effect of elasto-plastic instability but by the torsional twist (the limit has been defined at 0,6 rad $\approx 35^\circ$ - see paragraph 5.6.3).

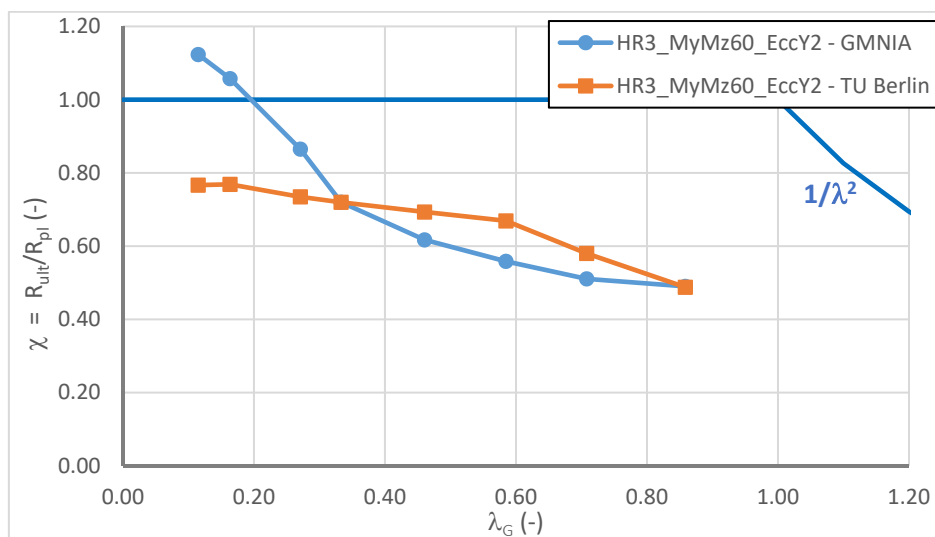


Figure 5-127: Ultimate resistance curve for a member of HR770.5.400.17 section subject to bi-axial bending and torsion

In Figure 5-127 one may observe that the design model proposed at TU Berlin is unsafe compared to the numerical results for intermediate values of the member slenderness. For low to intermediate values (0,1 ... 0,6) of the relative slenderness the resistance obtained with the design model is limited by the condition $B_{Ed} \leq 0,5B_{pl}$. For longer members the bi-moment becomes less than the defined limit. The pronounced kink in the curve associated with the design model can be explained based on the combined influence of the factors k_w , k_{zw} and k_α . In fact, Figure 5-128 shows that the product of these factors increases only slightly for small values of the relative slenderness but starting from a relative slenderness of 0,60 the increase is accelerated. This acceleration is, in particular, due to the factor k_α that introduces the second order amplification $1/(1-M_y/M_{y,cr})$. The other two factors are nearly constant especially for a relative slenderness up to 0,60 owing to the limitation of the bi-moment to $0,5B_{pl}$. Consequently, the factor k_α seems to counterbalance the too optimistic values of the factors k_{zw} and k_w for the studied case if the relative slenderness is sufficiently high.

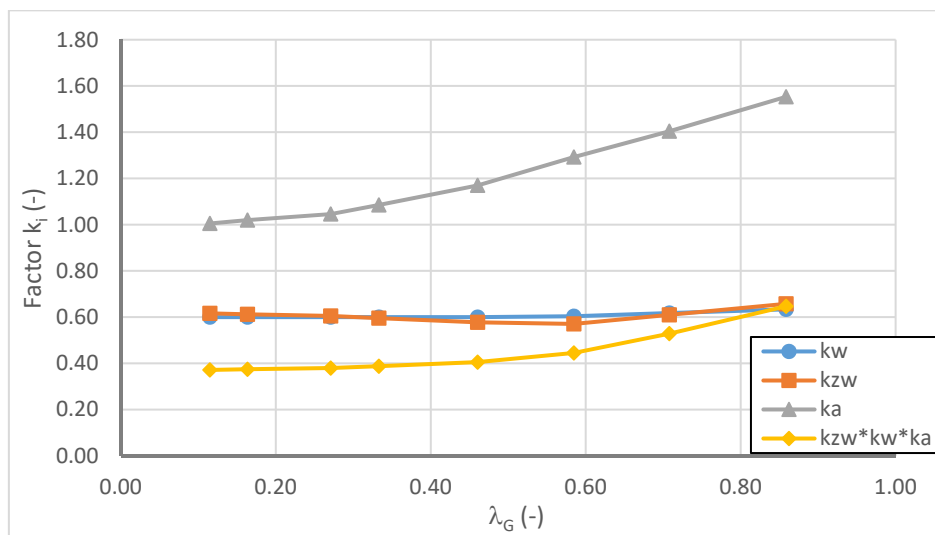


Figure 5-128: Evolution of the factor k_i of design model TU Berlin with the relative slenderness

On the basis of the comparisons presented here before it is recommended to modify the design model proposed initially at TU Berlin as follows:

- The factor k_{zw} should be considered equal to 1,0 at least for members exceeding a given length/relative slenderness;
- If the factor k_{zw} is considered less than 1,0 the resistance of the member to the arising Saint-Venant's torsional moment has to be checked (verification of the cross-section resistance at the supports under combined bi-axial bending, shear forces and Saint-Venant's torsional moment). It is emphasized that the Saint-Venant's torsional moment used for this design check cannot be obtained by a simple elastic analysis because the effect of the plastic warping hinge is not considered in this type of analysis;

- Additionally to the design formula represented by Eq. (5.303) it should be checked that the bi-moment is less than 50% of the (plastic) bi-moment resistance of the member.

Up to this point of the present paragraph the proposal of TU Berlin has been evaluated and it has been shown that several points should be amended so as to ensure a sufficient level of safety with reference to the numerical simulations performed here. It appears again that the reduction of the bi-moment by the factors k_{zw} and k_w may lead to unsafe results as the failure due to the Saint-Venant's torsional shear stresses of the sections at the supports is not checked. It is recalled that the necessity to verify the cross-section with reference to the Saint-Venant's torsional moment is not in contradiction with the conclusions of Chapter 4 and the common habit. Indeed, generally the Saint-Venant's torsional is neglected for the design of members of open cross-section. This is acceptable if the member is analysed through elastic analysis that does not consider the formation of the warping hinge. The high Saint-Venant's torsional moments arising after the formation of the warping should however not be neglected (as done by method TU Berlin) if the plastic redistribution of the torsional moment is accounted for (see paragraph 4.4.4.1 again).

Hereafter, the proposal introduced in Eqs. (5.307) and (5.308) of this thesis are evaluated. It is recalled that these equations represent a very simple extension of the Eurocode 3 Part 1-1 interaction formulae and could therefore easily be introduced in a future version of the European standard for the design of steel structures.

Figure 5-129 shows a statistical evaluation of the proposal. Clearly, it appears that a sufficient level of safety may be ensured. Only 4% of the results are unsafe and the maximum unsafe result attains a ratio of approximately 1,09. This seems acceptable. The scatter of the results appears to be rather high but for the totality of all studied members the standard deviation is of 16%, but, regarding the complexity of the studied cases, this value could be accepted. Nevertheless, one may observe that an important number of case is very safe-sided. In fact, 33% of the strength predictions are less than 70% of the value obtained through the GMNIA simulations. So as to analyse these results further on Figure 5-130 represents the ratio $\chi_{\text{Method}}/\chi_{\text{GMNIA}}$ depending on the relative lateral-torsional buckling slenderness of the members.

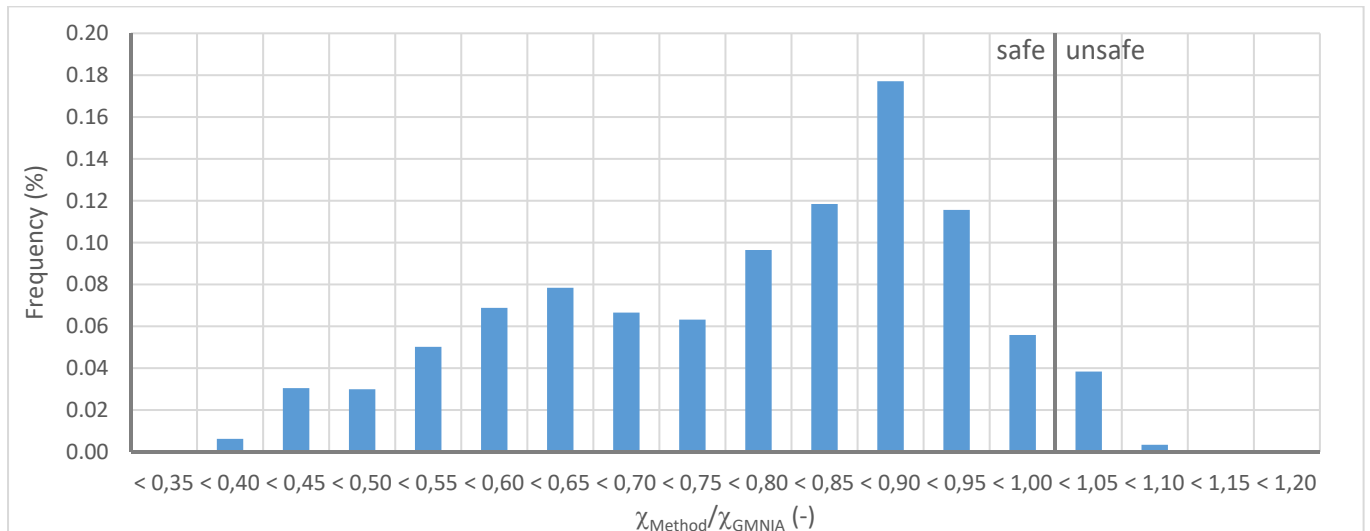


Figure 5-129: Ratio resistance obtained with Eqs. (5.307) and (5.308) and numerically obtained resistance

Figure 5-130 shows that the resistances predicted by Eqs. (5.307) and (5.308) are very conservative in particular for:

- Low values of the relative slenderness ($\lambda_{TL} = 0$ for combined minor-axis bending and torsion): for these cases the creation of the warping hinge leads to the observed conservatism; the precision of the results can be increased if the plastic torsional system reserve is considered in the analyses see paragraphs 4.4.4.1 and 4.5);
- For high values of the relative slenderness: these results are obtained for members of welded section that are somewhat disadvantaged by the attribution of a rather conservative reduction curve for lateral-torsional buckling;
- For intermediate values of the relative slenderness: in this case the results are obtained for members subject to high values of the applied torsional moment. Consequently, the resistance is influence partially by the torsional system reserve and partially by the effect of high torsional twist.

The two last points are discussed further on hereafter.

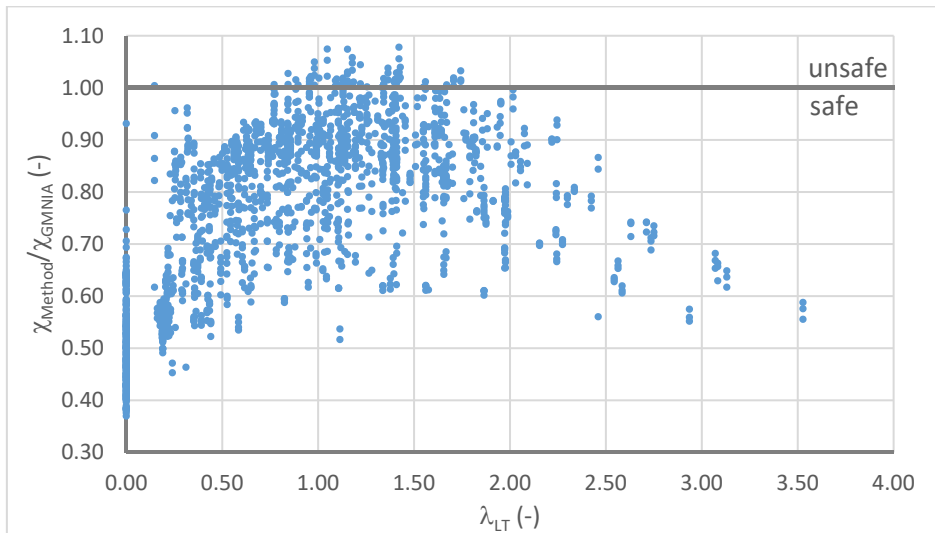


Figure 5-130 : Ratio between resistance obtained with interaction equations and the numerically obtained resistance depending on the relative member slenderness

Figure 5-131 represents the results obtained for the welded sections. Again, the safe-sided nature of the interaction equations (in fact, the conservatism should not be attributed to the interaction equations but rather to the elastic analysis performed to obtain the internal forces and moments) is easily observed for low values of the relative slenderness. For intermediate to high values of λ_{LT} one may remark two groups of results. The first group (encircled in orange) is arranged in form of an arc possessing the highest precision for a relative slenderness of approximately 1,00. For lower and higher values of λ_{LT} the obtained resistances recede from the numerical reference values. The second group (encircled in violet) is rather conservative independently from the relative slenderness.

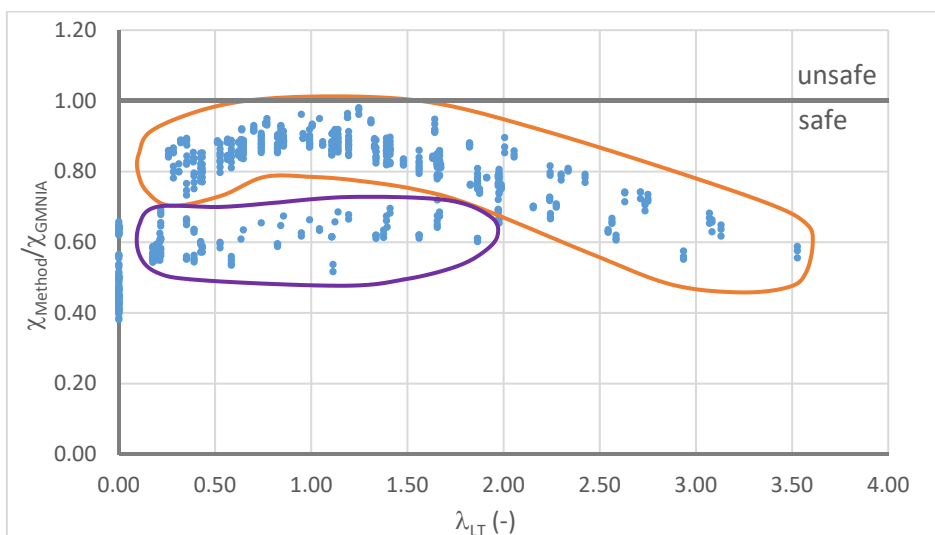


Figure 5-131: Ratio resistance obtained with interaction equations and numerically obtained resistance depending on the relative member slenderness – welded sections

The arrangement in form of an arc of the results for the welded members can be linked to the general shape of the reduction curve as shown in Figure 5-132. In fact, the typical shape of the

ultimate resistance curve for members of welded section subject to major-axis bending can be observed. In fact, this curve is characterised by 3 inversions of the sign of its curvature: for the given example it changes from concave to convex at relative slenderness of about 0,7 then it changes back to concave at a slenderness of about 1,2 and finally it changes again at a relative slenderness of about 1,6 from concave to convex. Contrariwise, the reduction curve proposed in Eurocode 3 Part 1-1 (§6.3.2.2 of (CEN 2005a)) does not possess the mentioned changes of the curvature. Consequently, the discrepancy between the predicted results and the numerically obtained resistances depend on the slenderness. In Figure 5-132, it can be seen that both curves approach for a slenderness λ_{LT} of about 0,70 explaining the arrangement of the results in form of an arc in Figure 5-131. Obviously, the exact difference between the numerical results and the predicted resistance depend on the relative importance of the major-axis bending moment in the global loading (Figure 5-131 presents results for members under combined bi-axial bending and torsion).

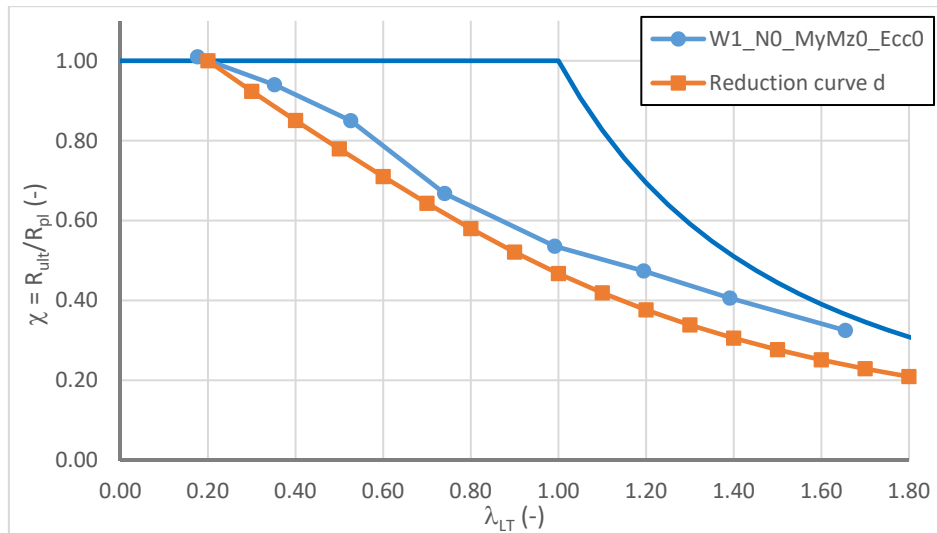


Figure 5-132 : Ultimate resistance curve for a member of W650.5.180.10 (W1) section under constant major-axis bending

So as to understand the difference observed for the two distinctive groups of results represented in Figure 5-131 the example of the member of welded section W650.8.180.10 (W1) is considered. This member is subject to constant bi-axial bending MyMz60 and it is subject to an intermediate value of the applied torsional moment (EccY2) in a first case and subject to a high torsional moment (EccY3) in a second case.

The results obtained for the first case, W1_NO_MyMz60_EccY2, are given in Figure 5-133 and Figure 5-134. Figure 5-133 shows the load displacement curve linking the torsional twist to the ratio between load factor R_{Load} and the plastic limit load amplification factor R_{pl} . Not surprisingly, the curve is characterised by a first linear part up to a torsional twist of 0,04 rad. The curve becomes than non-linear due to increasing yielding. The peak load is attained for a ratio R_{Load}/R_{pl} of 0,5. After passing through the peak load the curve descends. Figure 5-134 shows the von Mises stress distribution at the peak load level. It can be observed that the upper flange has yielded due to the combined influence of the applied loads and second order internal forces and moments. The

lateral stiffness of the upper flange tends consequently to 0 leading to failure by elasto-plastic instability. These observations do not seem astonishing and represent the expected failure mode for this member.

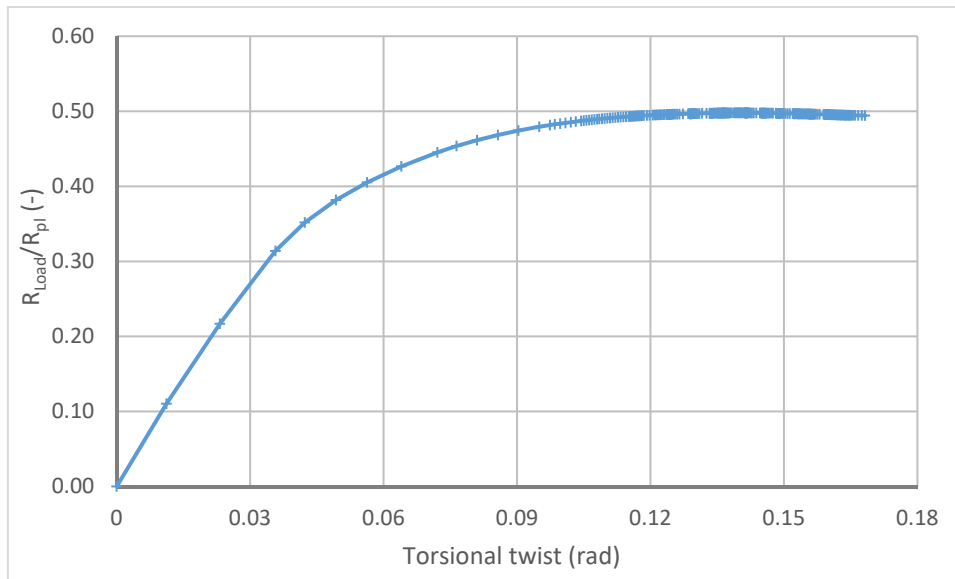


Figure 5-133 : Load-displacement curve for W1_N0_MyMz60_EccY2

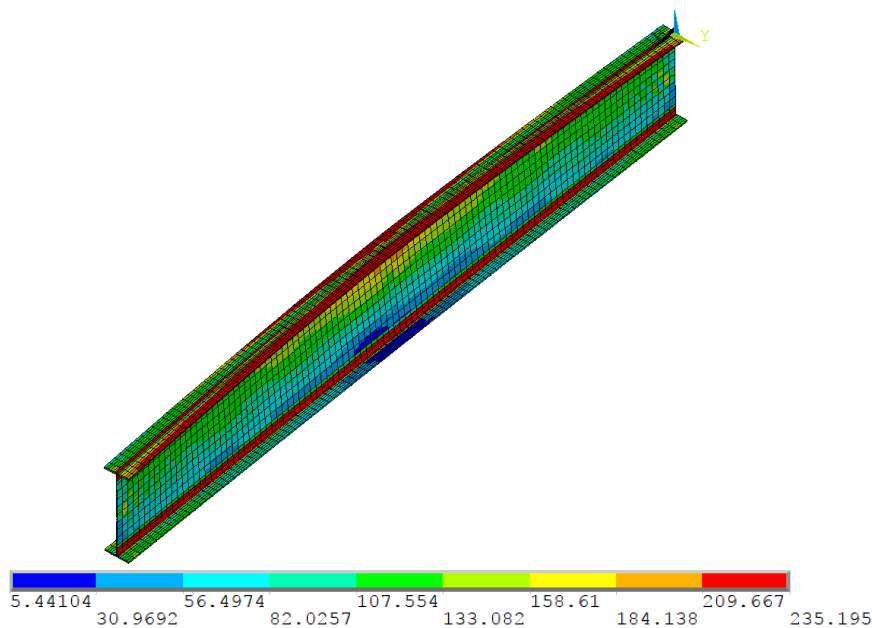


Figure 5-134: von Mises stresses for W1_N0_MyMz60_EccY2 at its peak load level

It is now interesting to compare the results obtained for the member subject to an intermediate torsional moment and for the member subject to high torsion. For this last member, the results are represented in Figure 5-135, Figure 5-136 and Figure 5-137. Figure 5-135 clearly shows that the behaviour of the two members are different. Indeed, the load-displacement curve of the second member is characterised by four parts: approximately linear behaviour up to a torsional twist of 0,07 rad; non-linear behaviour with decreasing stiffness up to a torsional twist of 0,16 rad; non-linear behaviour but with increased stiffness up to torsional twist of 0,35 rad and finally the

stiffness decreases a second time until the failure load is attained for a load ratio of $R_{Load}/R_{pl} = 0,7$. For this member the failure mode can also be characterised by elasto-plastic instability but at a higher level of yielding. Indeed, the increase of the stiffness after first yielding is due to the effect of strain hardening.

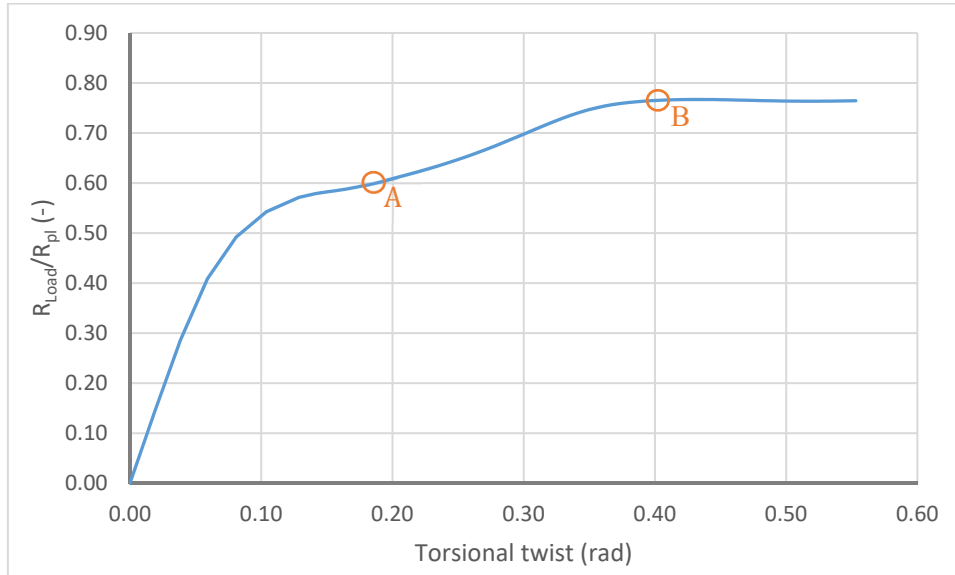


Figure 5-135: Load-displacement curve for W1_N0_MyMz60_EccY3

Figure 5-136 and Figure 5-137 represent the von Mises stress distribution at points A and B for the studied member. At point A (Figure 5-136), the upper flange has yielded approximatively as for the first member represented in Figure 5-134. Yet, it appears that the upper flange possesses still sufficient stiffness to avoid failure by elasto-plastic instability and to attain a strain level that is linked to starting strain hardening. With starting strain hardening the upper flange increases its stiffness according to the defined strain hardening modulus of the material.

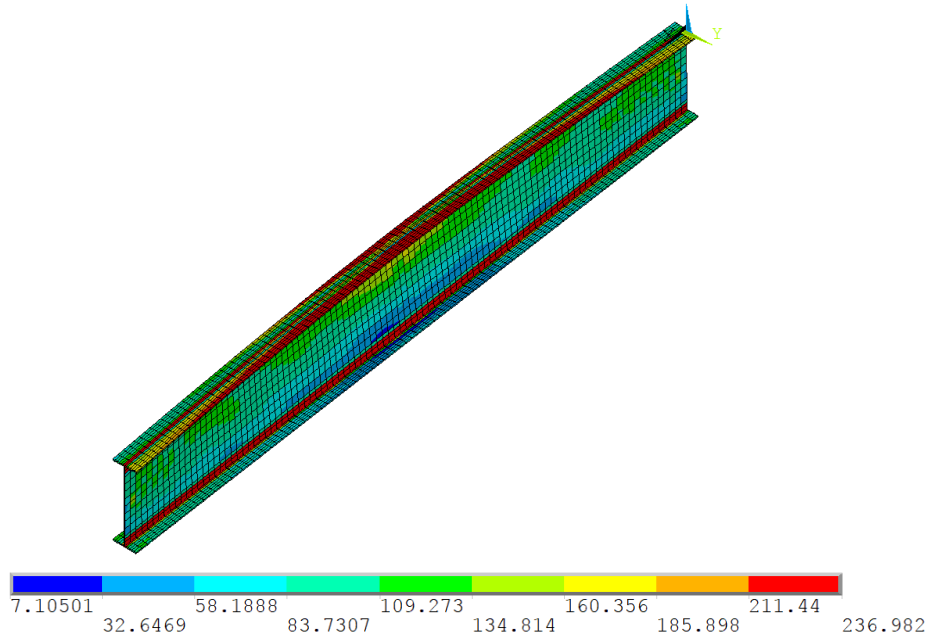


Figure 5-136: von Mises stresses for W1_N0_MyMz60_EccY3 at point A of the load-displacement curve

Finally, Figure 5-137 shows that the member has yielded over great parts of its length due to the applied minor-axis bending moment and to the Saint-Venant’s torsional moment that is generated after the formation of the warping hinge. At this point, nearly the whole flange attains a stress of 325 MPa and consequently has attained a significant level of strain hardening. Nonetheless, the effect of elasto-plastic instability leads to the failure of the member.

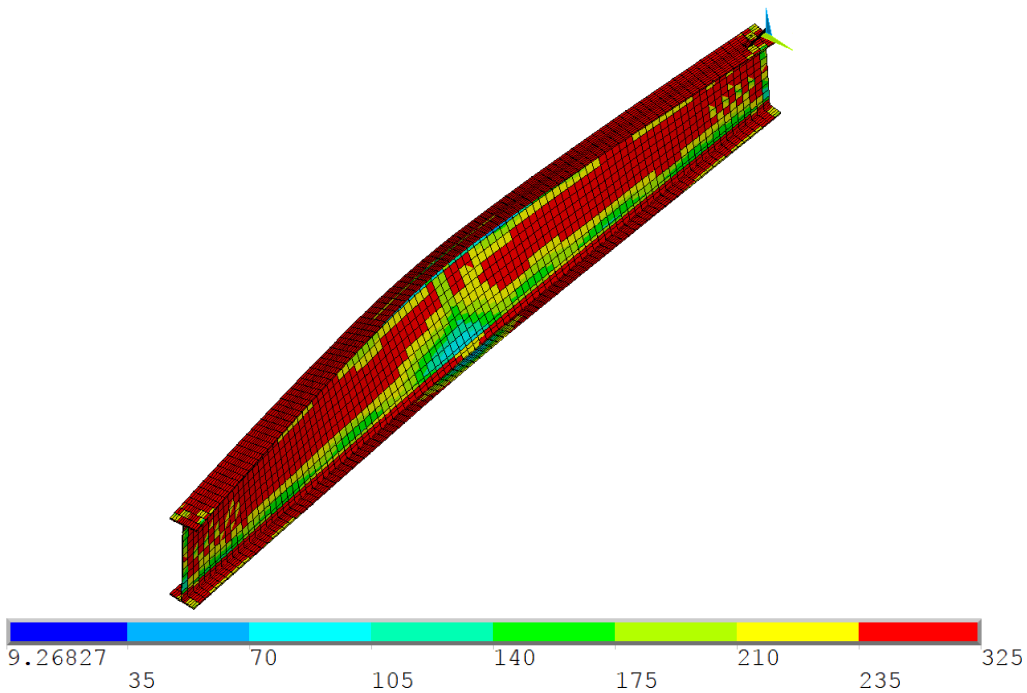


Figure 5-137: von Mises stresses for W1_N0_MyMz60_EccY3 at the peak load level – point B of the load-displacement curve

It has to be admitted that the results obtained for the two previous examples are certainly very sensitive to the practical design of the load introduction and the end supports. The design may enable the first member subject to intermediate torsional moments to attain strain hardening before it fails by elasto-plastic instability. Conversely, it cannot be excluded that the practical design may lead to failure by elasto-plastic instability of the second member before it reaches strain hardening. Also, it should be noted that the calculation options for the numerical simulations may influence the obtained resistances as well. If the calculation is continued for the first member, it might attain strain hardening after passing through a valley of the load-displacement curve. Here, the calculation was not pursued further on and it has been considered that the first limit point corresponds to the failure of the member, even if this may be discussable for the present case. Anyhow, it may be concluded that a lower bound of the resistance of the studied members in torsion is linked to elasto-plastic instability without significant strain hardening. This failure mode is well represented by the simplified interaction formulae proposed in Eqs. (5.307) and (5.308). Depending on the practical design, the member may attain strain hardening of the material leading to a failure obtained at a higher load level. This corresponds to an upper bound resistance. The interaction equations do not represent this failure mode and may therefore be rather conservative for these cases. Yet, it is also to be noted that the torsional twist linked to the upper bound resistance is rather high even if it seems still acceptable at the ultimate limit state (0,45 rad).

Last, it is recalled that the members evaluated up to this point were simulated without considering the influence of local plate instability (see paragraph 5.2.3). Consequently, they may always attain the strain level necessary for yielding and even for strain hardening. Yet, if local plate instability is not prevented the members may also fail before they form the warping hinge or attain the strain levels necessary for strain hardening. Consequently, depending on the slenderness of the section (class of the section in the terminology of Eurocode 3 Part 1-1), the resistance of the member may also be less than the upper bound resistance obtained for W1_N0_MyMz60_EccY3. So as to illustrate the influence of the plate slenderness on the resistance, this last member is studied again but without constraining the possibility of local plate instability. The obtained load-displacement curve is represented in Figure 5-138. It may be observed that the load-displacement curve is again characterised by four parts. Before yielding is initiated, the member behaves linearly up to a torsional twist of approximately 0,075 rad. Then yielding starts to spread throughout the member and reduces its stiffness significantly, but at a torsional twist of about 0,16 rad the stiffness of the member increases again due to strain hardening. The load can be increased further on and the peak load is attained for a torsional twist of approximately 0,31 rad.

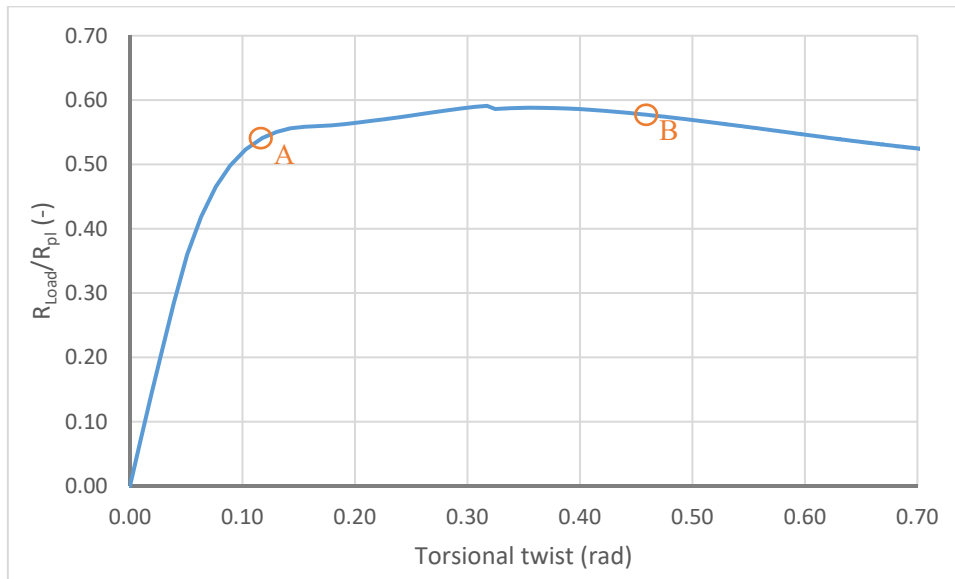


Figure 5-138: Load-displacement curve for W1_N0_MyMz60_EccY3 not restrained against local plate instability

The distribution of the von Mises stresses for the studied member is represented at point A of the load-displacement curve in Figure 5-139. As the flanges can be considered as compact (class 1), it is not surprising that they can yield over their total width. Yet, one may also remark that local plate instability starts to be induced. Indeed, owing to the upcoming out-of-plate flexure, the stress distribution is not uniform in the web along the member length. Finally, Figure 5-140 shows the von Mises stress distribution at point B of the load-displacement curve. At this point the member has passed its peak load and one may observe that local buckles have formed as indicated by the yield line pattern. Indeed, the yield lines pass through the valleys and summits of the local buckles. Due to the effect of local instability the member may not resist any supplementary load and, in particular, it cannot reach the load level obtained for the same member restrained from local buckling. A deeper evaluation of the resistance model for members of slender section is given in paragraph 5.6.4.2.3.

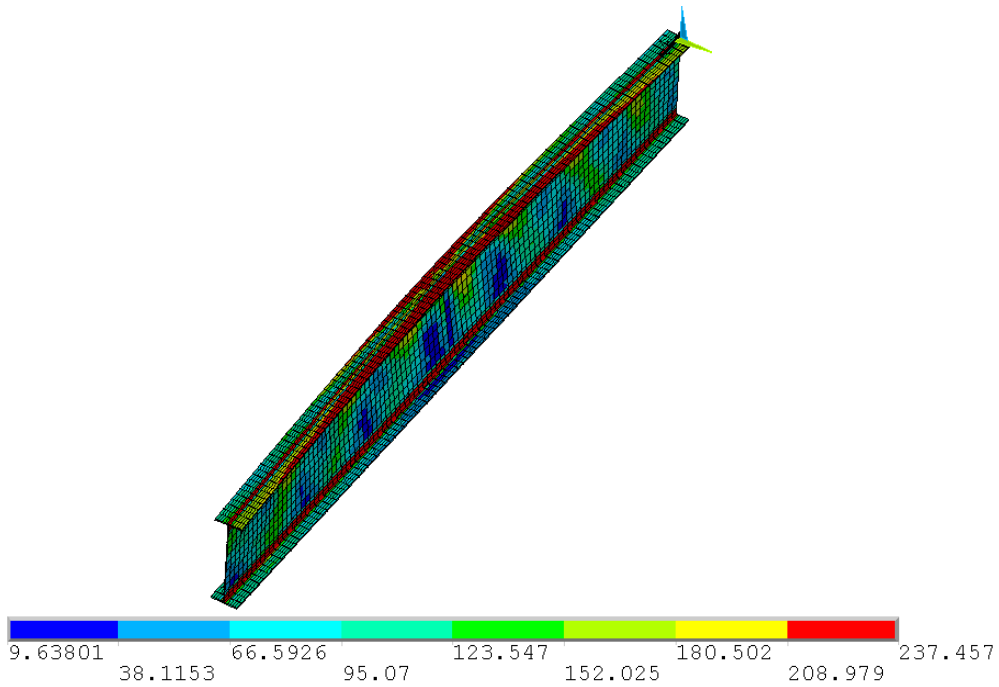


Figure 5-139: von Mises stresses for W1_N0_MyMz60_EccY2 not restrained against local plate instability at point A of the load-displacement curve

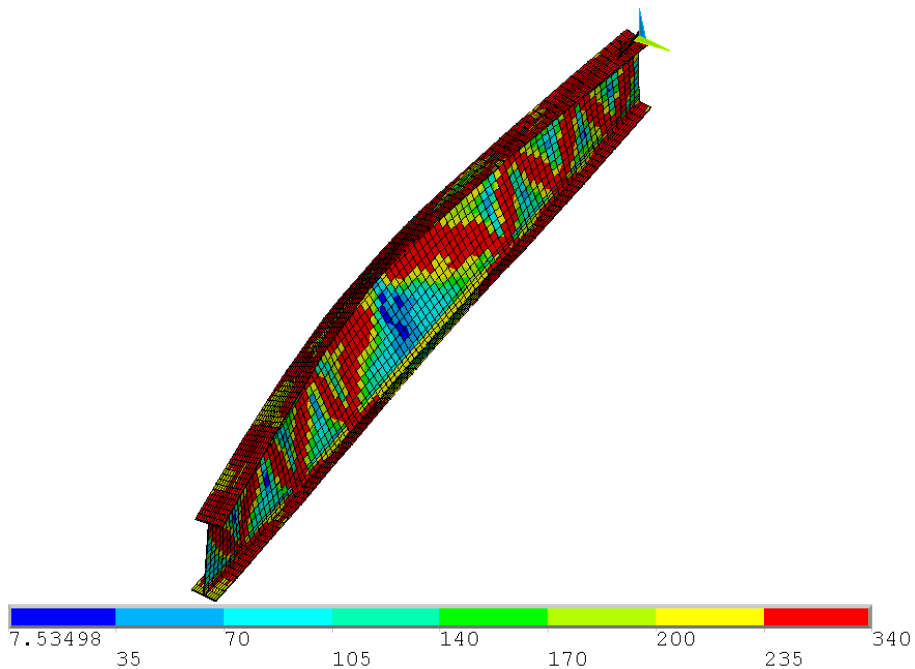


Figure 5-140: von Mises stresses for W1_N0_MyMz60_EccY3 not restrained against local plate instability at point B of the load-displacement curve

Last, it should be noted that some of the strength predictions obtained with the interaction formulae of Eqs. (5.307) and (5.308) are unsafe (see Figure 5-130). These unsafe results are obtained for rather long members. Two examples of the unsafe results are represented in Figure 5-141. The members are made of HR770.5.400.17 (HR3) and they are subject to bi-axial bending

and torsion. One may observe that the degree of bi-axiality only influences slightly the results. For short members the interaction equations are very conservative as the plastic cross-section interaction is not well represented. Also, the effect of the warping hinge is not considered at this stage of the study. With increasing relative slenderness, the strength predictions of the interaction equations approach the numerical results and become slightly unsafe. The maximum un-conservatism reaches 6,8% for the case HR3_N0_MyMz15_EccY2 with a length of 12,9 m. This may certainly be accepted in particular as the number of unsafe results is rather small as shown in Figure 5-130.

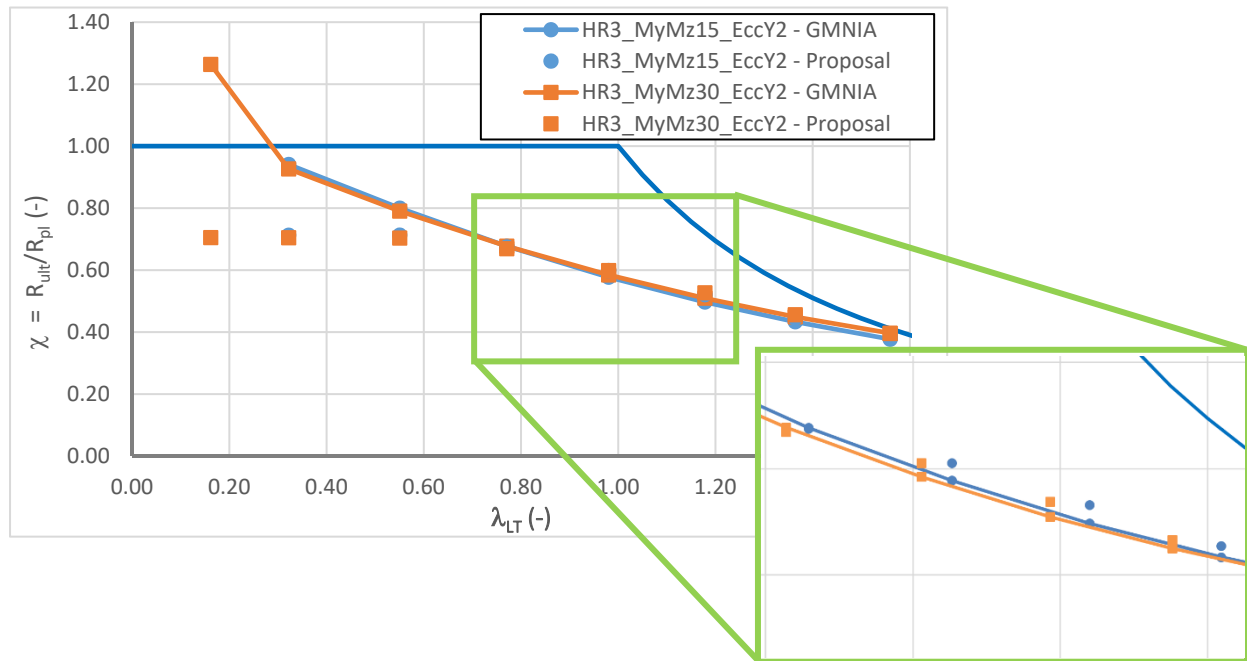


Figure 5-141: Ultimate resistance curves of member HR 770.5.400.17 subject to bi-axial bending and torsion

Additionally, it should be noted that the slight unsafe character of the proposal does not result from the applied torsional moment but is rather due to the interaction equations and interaction factors used for the case of combined bi-axial bending as shown in Figure 5-142. Figure 5-142 represents the results obtained for the members studied in Figure 5-141 but not subject to torsion. As before, one may observe that the resistance of short members is predicted rather safely but not as conservative as in case of applied torsion because the warping hinge does obviously not influence the member behaviour. It appears that the design model becomes unsafe (up to 14%) for members with intermediate slenderness (member length between 8,1 m and 12,9 m). The discrepancy between the numerical results and the interaction equations (combined with interaction factors of Annex B of (CEN 2005a)) appear to be even greater than in case of applied torsion. For longer members the results of the interaction equations approach the reference results again. Here, the maximum un-conservatism appears to be slightly higher than observed in the past when the interaction equations were evaluated for the case of combined bi-axial bending and axial force (see for example (Lindner 2001), (Villette 2004) and (ECCS 2006)). Indeed, in the mentioned references the maximum unsafe result was equal to approximately 1,10 (ratio

R_{Method}/R_{GMNIA}). Though, it seems that the case of bi-axial bending has not been of principal interest, at least in these references. Therefore, it may not be surprising to obtain slightly more unsafe results for individual cases.

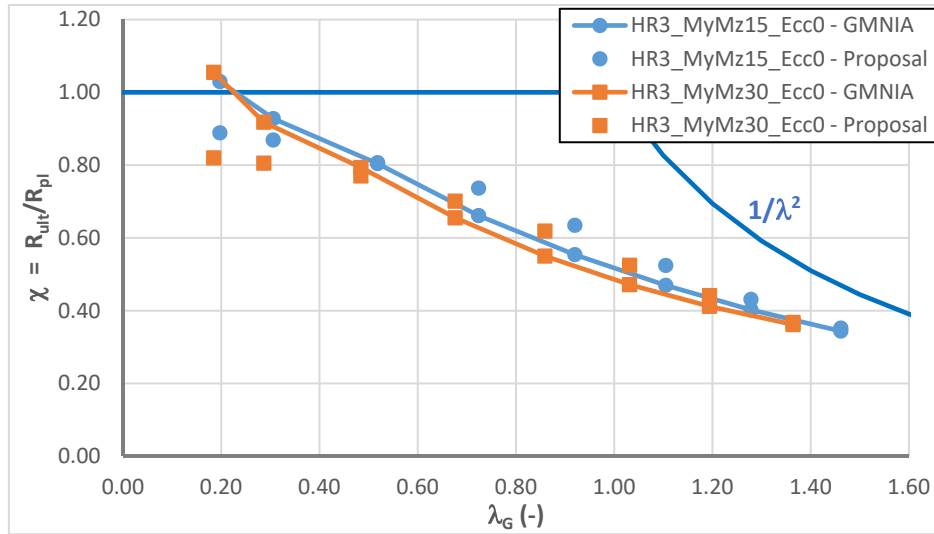


Figure 5-142: Ultimate resistance curves of member HR 770.5.400.17 subject to bi-axial bending without torsion

The reason for the unsafe results has not been discussed in detail before. It might possibly be linked to the interaction factors k_{zy} and k_{zz} recalled hereafter for the case of compact cross-sections that can potentially attain their plastic resistance.

$$k_{zz} = C_{mz} \left(1 + (2\bar{\lambda}_z - 0,6) \frac{N_{Ed}}{\chi_z N_R} \right) \leq C_{mz} \left(1 + 1,4 \frac{N_{Ed}}{\chi_z N_R} \right) \quad (5.316)$$

$$k_{yz} = 0,6k_{zz} \quad (5.317)$$

Eqs. (5.316) and (5.317) consider the second order effects and additionally the transition between plastic interaction for short members and elastic interaction for longer members (see paragraphs 5.6.5.1 and 5.6.5.4 for more details). Obviously, the interaction factors only depend on the axial force and not on the major-axis bending moment. In case of bi-axial bending the interaction factors are consequently equal to C_{mz} and $0,6C_{mz}$ ($k_{yz} = 1$ and $k_{zz} = 0,6$ for constant bending) and might therefore not entirely capture the mentioned effects (second order effects arising from major-axis bending). Nonetheless, the observed discrepancy for bi-axial bending is not studied further on as it is not the objective of this thesis. Here, the interaction equations are accepted as valid in their initial field of application.

Throughout the present paragraph members of compact section subject to combined bi-axial bending and torsion have been studied. In particular, it has been shown that:

- The design proposal of TU Berlin initially proposed in references (Glitsch 2008) and (FOSTA 2004) may be rather unsafe as the warping hinge is accounted for

without any verification of the resistance to the Saint-Venant's torsional moment that arises;

- The unsafeness of the proposal TU Berlin is reduced if the factor k_{zw} is considered equal to 1,0 and if the bi-moment is explicitly limited to $0,5B_{pl}$. Yet, in some cases the limitation of the bi-moment can lead to rather conservative results for the design practice;
- The proposed simple extension of the Eurocode 3 Part 1-1 interaction equations, currently applicable for the case of combined bi-axial bending and axial forces, has proven to be satisfactory for the case of bi-axial bending and torsion;
- The proposal may lead to rather safe-sided results for i) short members as the plastic cross-section interaction is only approximated, ii) for members of intermediate length if strain hardening is mobilised before the member fails by elasto-plastic instability and iii) for long members of welded sections due to the conservative attribution of reduction curve d ($h/b > 2$) for lateral-torsional buckling;
- In some cases the proposal may lead to slightly unsafe results but this is due to the definition of the interaction factors for the case of bi-axial bending (and axial force). Indeed, the interaction equations may be unsafe, in some cases, in their current field of application (in particular for bi-axial bending without axial force).

Based on the investigations and conclusions presented in this paragraph, the design method TU Berlin is not studied further on. Rather, the proposed extension of the interaction equations provided in Eurocode 3 Part 1-1 is privileged as design method. Hereafter, the proposal is studied further on for the case of combined axial compression force and bi-axial bending.

5.6.4.2.2 Double symmetric I sections subject to combined bi-axial bending, axial forces and torsion

Figure 5-143 represents the statistical evaluation of the proposed extension of the interaction formulae (Eqs. (5.307) and (5.308)). It may be observed that the design proposal may again be safely applied to check the resistance of members subject to a complex combination of axial compression force, bi-axial bending and torsion. Only, very few results are slightly unsafe (0,4% of the 3300 cases considered here). Also, it appears that the scatter of the results is even less than in case of members that are only subject to bi-axial bending and torsion. This may be understood as the supplementary axial compression forces induces additional second order effects. Therefore, the studied members are less capable of activating the plastic torsional system reserves. Nonetheless, it appears that the design approach is in general rather safe-sided. Indeed, the mean value of the ratio $\chi_{Method}/\chi_{GMNIA}$ is equal to 0,75.

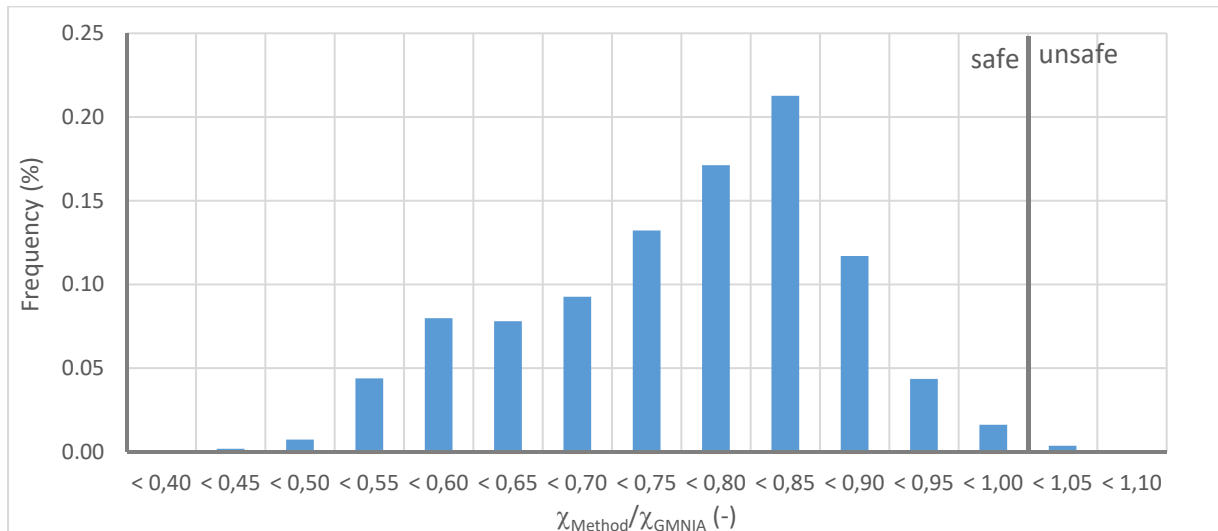


Figure 5-143: Ratio between resistance obtained with Eqs. (5.307) and (5.308) and numerically obtained resistance

It is again interesting to study the precision of the proposed design approach as a function of the relative slenderness. First, Figure 5-144 represents the results depending on the maximum value of the relative member slenderness. Depending on the case, the maximum slenderness may therefore correspond to flexural buckling about the minor-axis or to lateral-torsional buckling. Based on this representation of the results, it seems difficult to obtain a clear tendency. In fact, the scatter of the results is nearly independent from the maximum slenderness. Therefore, the results are represented again depending on the overall member slenderness λ_G in Figure 5-145.

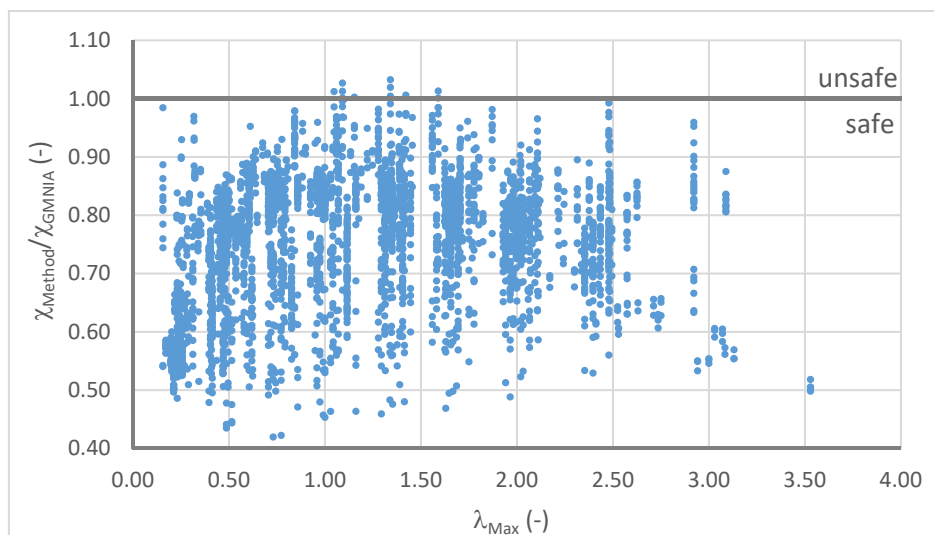


Figure 5-144: Ratio between resistance obtained with interaction equations and the numerically obtained resistance depending on the relative member slenderness

Figure 5-145 clearly indicates interesting tendencies. First, one may again remark that some results are rather safe-sided even for high values of the member slenderness. These cases, encircled in orange, concern welded section as in paragraph 5.6.4.2.1. In fact, the attribution of the buckling curves do not represent precisely the resistance for long welded specimen, in particular

if they are subject to significant major-axis bending. For the other members, it is possible to identify a clear tendency: The scatter of the results decreases with the member slenderness and the precision of the proposed design model increases with the member slenderness. This observation confirms once more the influence of the torsional plastic system reserve that allows members of low slenderness to attain rather high resistances. With increasing slenderness the plastic torsional system reserve loses its beneficial effect as failure by elasto-plastic instability becomes relevant before the warping hinge is generated through significant yielding of the most loaded section. Furthermore, the relative bi-moment reduces with the member length (hence with increasing warping decay factor) and consequently the potential plastic system reserve decreases, too. Moreover, it is recalled again that the plastic cross-section interaction is only roughly approximated by the interaction equations and consequently, their precision is decreased additionally for short members. This is, however, not a specific problem for members subject to torsional but a problem that is of general nature for (simplified) interaction equations.

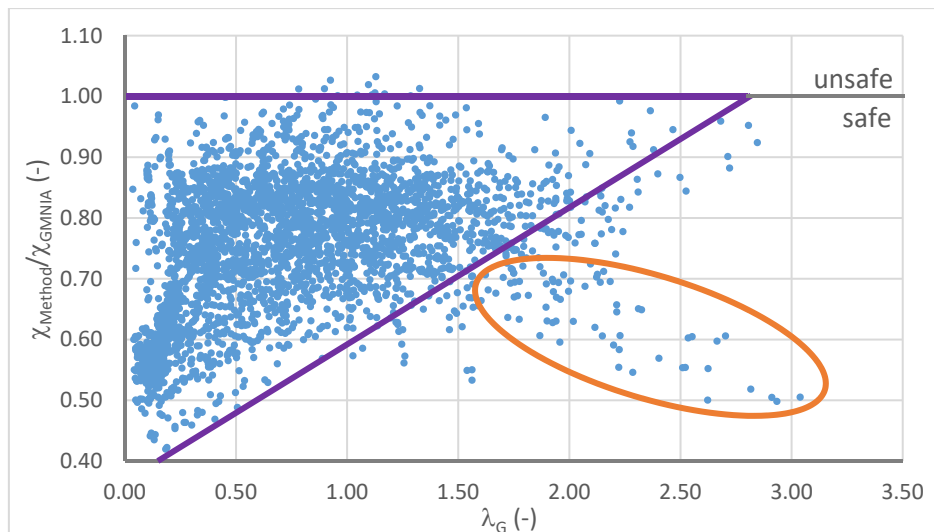


Figure 5-145: Ratio between resistance obtained with interaction equations and the numerically obtained resistance depending on the relative member slenderness

In order to illustrate the results of Figure 5-145 in more detail, Figure 5-146 represent the ultimate resistance curves for member of IPE 500 section subject to axial force, major-axis bending and torsion with different ratios m_y/n ($= (M_y/M_{y,pl}) / (N/N_{pl})$). First, one may observe that the curves are very close, both, for the numerically determined ultimate resistance curves and for the strength predictions obtained with the proposed interaction equations. As the sensitivity of the members to instability under axial force and to instability under a major-axis bending moment is similar, this result is not surprising. As the same reduction curves are attributed to the IPE 500 section for lateral-torsional buckling and for flexural buckling about the minor-axis, the interaction formulae are capable to reproduce the behaviour of the studied members. Though, it is obvious that the strength predictions do not tend to unity for zero slenderness as it should be in theory and consequently, the interaction equations may become very safe-sided for short members. The reason for the observed discrepancy has been discussed before (plastic cross-section interaction and plastic torsional system reserve). Nonetheless, it is clear that the results

of the interaction equations become closer to the numerical obtained results with increasing slenderness. This indicates that the second order effects are satisfactorily accounted for through the interaction factors k_{ij} . Last, it seems interesting to study the curve linked to $m_y/n = 0$ (only axial compression force and torsion) in more detail. It appears that this curve is the most favourable case if one considers the numerical results. Especially, for intermediate values of the relative slenderness, the results are up to 10% more favourable than the other cases. The observed difference can be attributed to the second order effects arising from the applied axial force and major-axis bending moments and the failure mode of the member. Indeed, the axial compression force induces, in particular, second order effects about the minor-axis. The critical axial force for torsional buckling is relatively high for the studied cases and consequently, the amplification of the torsional twist and consequently the bi-moment is relatively low. Conversely, the major-axis bending moment, applied for the other cases, induces a second order amplification of the torsional twist and the bi-moment. Consequently, the strength reduction is slightly more pronounced than in case of combined compression axial force and torsion only.

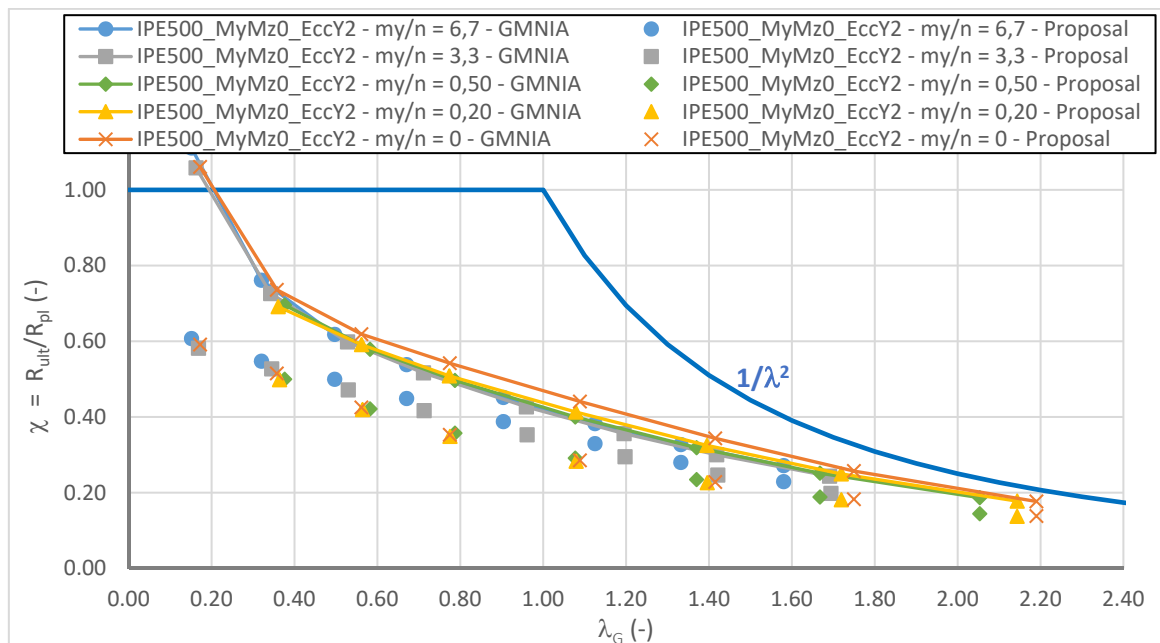


Figure 5-146: Ultimate resistance curves of member of IPE500 section subject to major-axis bending, axial force and torsion

A second example is given in Figure 5-147. The studied members of IPE 500 section are subject to bi-axial bending, torsion and a compression axial. Similarly, to the members treated in Figure 5-146, it is seen that the results predicted by the interaction curves are practically identical for a given slenderness, independently of the ratio between the major-axis bending moment and the axial force. The minor-axis bending moments does not significantly influence the obtained results compared to the members of Figure 5-146. Conversely, the difference between the numerically obtained ultimate resistance curves are more pronounced than for members not subject to minor-axis bending. It is recalled that, in the framework of this thesis, the value of the minor-axis bending moment is directly linked to the value of the major-axis bending moment through the degree of bi-axiality. Consequently, the members subject to low major-axis bending are also subject to

relatively low minor-axis bending ($m_y/n = 0,43$ and $m_y/n = 0,17$). Hence, the relative influence of the second order effects amplifying minor-axis bending is lower. Additionally, it is obvious that depending on the relative influence of the different internal forces and moments, the plastic cross-section interaction may be more or less non-linear. In paragraph 5.6.5 it is shown that the form of the plastic cross-section interaction possesses an influence on the member resistance even for intermediate values of the relative slenderness. Therefore, it appears that the combined influence of the second order effects and the form of the plastic cross-section interaction leads to the differences between numerically determined ultimate resistance curves. It seems that the simplified interaction equations do not cover precisely the mentioned influences, especially concerning the cross-section interaction.

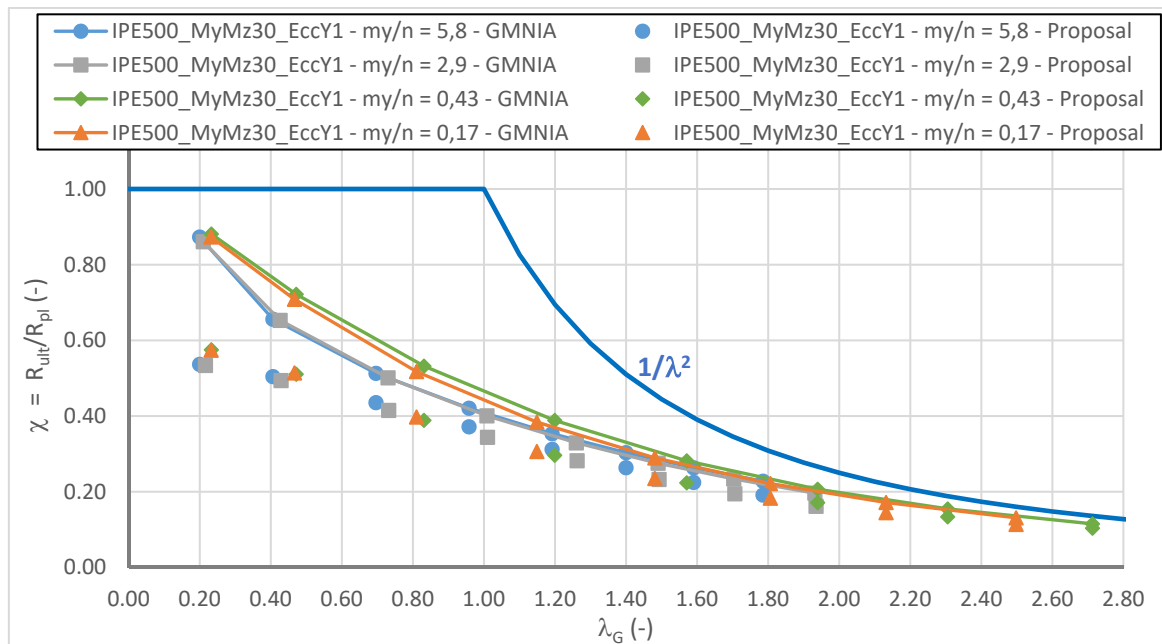


Figure 5-147: Ultimate resistance curves of member of IPE500 section subject to major-axis bending, axial force and torsion

Before the case of members with slender and semi-compact cross-section section is studied, it seems interesting to compare the precision of the proposed extension of the interaction equations to torsion with the precision of original interaction equations proposed in Eurocode 3 Part 1-1 in their field of application. The results are represented in Table 5-38. First, it appears that the results obtained for members not subject to torsion are somewhat more safe-sided in average and slightly less precise than shown in references (ECCS 2006) and (Lindner 2001). It should however be noted that the evaluations performed in the mentioned references concern a less extended number of cross-sections. Therefore, it does not seem surprising that the dispersion of the results is higher. One may also observe that the interaction equations may be unsafe, especially in case of bi-axial bending. As discussed in paragraph 5.6.4.2.1 the discrepancy may be linked to the interaction factors k_{zz} and k_{yz} . It can be noted that members under bi-axial bending without axial force are not treated in references (ECCS 2006) and (Lindner 2001). Due to the approximation of the plastic cross-section interaction the strength prediction may be rather safe-sided for the

interaction equations even for members not subject to torsion. For members subject to torsion the results represented Table 5-38 indicate that:

- The interaction equation are more conservative for members subject to torsion than for members not subject to torsion due to the plastic torsional system reserve that is not accounted for at this point. The results are most safe-sided for combined axial force, minor-axis bending and torsion as the plastic torsional system reserve is very pronounced for this load case;
- The standard deviation of the results for members subject to torsion is acceptable and close to the standard deviation of members not subject to torsion. Yet, in case of bi-axial bending the standard is rather high. This is due to two opposite tendencies: the results may be very safe-sided for short members subject to high minor-axis bending owing to the plastic torsional system reserve; conversely the results may be unsafe for long members due to the interaction factors k_{yz} and k_{zz} that do not account for the influence of the major-axis bending moment.
- The maximum un-conservatism of the results is of 10% and it is lower than for members not subject to torsion. As only few results are unsafe (see Figure 5-130 and Figure 5-145) the safety level seems acceptable.

Table 5-38: Evaluation of the interaction equations for members subject and not subject to torsion

Load case	Members subject to torsion – Ratio $\chi_{\text{Mehtod}}/\chi_{\text{GMNIA}}$				Members not subject to torsion – Ratio $\chi_{\text{Mehtod}}/\chi_{\text{GMNIA}}$			
	Mean	σ	Min	Max	Mean	σ	Min	Max
N+M _y (+M _x)	0,77	0,11	0,45	1,05	0,88	0,10	0,67	1,04
N+M _z (+M _x)	0,65	0,11	0,42	1,04	0,88	0,12	0,48	1,11
M _y +M _z (+M _x)	0,77	0,16	0,37	1,10	0,86	0,11	0,52	1,17
N+M _y +M _z (+M _x)	0,76	0,10	0,43	1,09	0,84	0,10	0,50	1,13
Overall	0,75	0,13	0,37	1,10	0,86	0,11	0,48	1,17

It is also interesting to represent the results of Table 5-38 depending on the (overall) member slenderness as shown in Table 5-39. Obviously, the scatter of the results is rather homogenous for the chosen slenderness ranges even if all load cases are considered together. For the shortest members the scatter is maximum as the importance of the plastic torsional system reserve depends on the load case. Nonetheless, the value of 0,135 is acceptable for the complex load combinations studied here. Additionally, one may observe that the mean value of the ratio $\chi_{\text{Mehtod}}/\chi_{\text{GMNIA}}$ is most safe-sided for short members and then increases. For members with values of relative slenderness exceeding 1,50 the mean value decreases again as the strength predictions become safe-sided due to the attribution of the reduction curves especially for welded members as already shown in Figure 5-145.

Table 5-39: Evaluation of the interaction equations for members subject to torsion

Member slenderness	Members subject to torsion – Ratio $\chi_{\text{Method}}/\chi_{\text{GMNIA}}$	
	Mean	Standard deviation σ
$\lambda \leq 0,30$	0,640	0,135
$0,30 < \lambda \leq 0,60$	0,764	0,117
$0,60 < \lambda \leq 1,00$	0,807	0,100
$1,00 < \lambda \leq 1,50$	0,814	0,091
$1,50 < \lambda$	0,775	0,105

The statistical evaluation of the proposal represented by Eqs. (5.307) and (5.308) as well as the detailed comparison to the numerical results shows that the design method is globally satisfying, yet somewhat conservative. The conservatism is, in particular, due to the plastic torsional system reserve that is not exploited here. It has already been shown that the plastic torsional system reserve can be compared to the catenary effect for members in bending that is generally not accounted for for the design in non-accidental situations. Nevertheless, this membrane effect is beneficial even if the failure of the member is caused by instability as shown by this last example treated for members of compact double symmetric I section. The following member is considered:

- The member is of IPE 500 section (without fillets) subject to a vertical point load of applied at mid-span at the theoretical intersection between the upper flange and the web. Consequently, it is subject to major-axis bending only;
- The length of the member is equal to 5,4 m;
- The member possess fork end support;
- The member is fabricated from steel S 235.

Hereafter, two cases are considered: First, the member is treated including the membrane effect by restraining the axial displacement at its two ends (member A). Then the axial displacement is liberated at one of the ends (member B).

Figure 5-148 shows the evolution of the axial tension force in the two members. Obviously, the catenary effect as well as the axial force do not develop if the member does not possess axial displacement restraints at both ends. On the contrary, owing to the boundary conditions an axial tension force arises in member A leading to a higher peak load as shown in Figure 5-149.

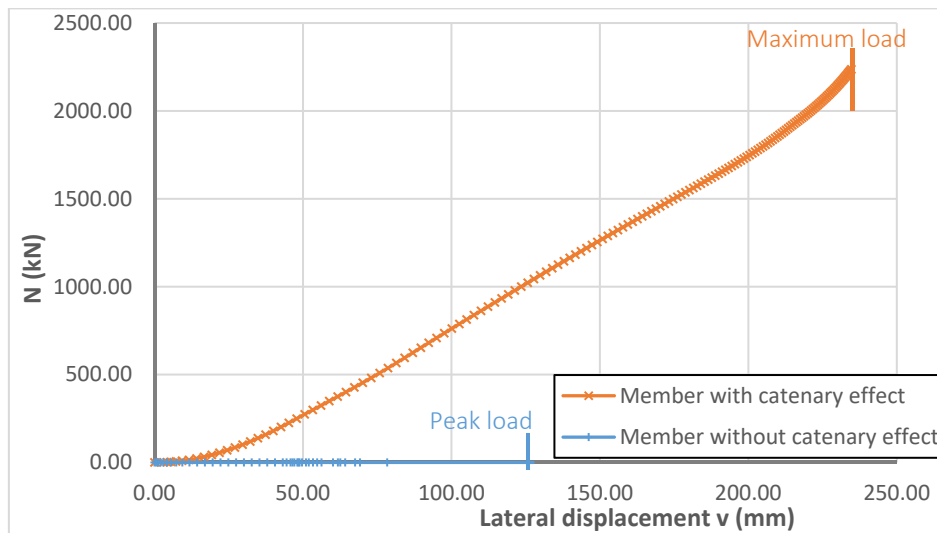


Figure 5-148: Evolution of the axial tension force for member with and without catenary effect

Figure 5-149 represents the load displacement curves for the two members (the lateral displacement is measured at the theoretical intersection between the upper flange and the web). Additionally, the value of a point load leading to the plastic major-axis bending moment ($P(M_{y,pl})$) and of a point load leading to the lateral-torsional buckling resistance obtained with §6.3.2.2 of Eurocode 3 Part 1-1 (CEN 2005a). It may be observed that the member B not developing the catenary effect exceeds the predicted resistance and then fails by elasto-plastic instability. The peak load of approximately 200 kN may be easily identified as the load-displacement curve for member B possesses a clear maximum. Conversely, member A developing the catenary action does not possess a maximum load as pronounced as for member B. In fact, one may observe that the two members behave similarly up to a lateral displacement of approximately 20 mm. It appears that member B possesses a higher stiffness in this first part of the diagram. This might be surprising at first sight but one should keep in mind that the catenary action leads to an axial tension force that, combined with the applied loads, induces yielding earlier than in case of member B not developing catenary action and the associated tension force. However, at a displacement of approximately 20 mm, member B loses rapidly its stiffness and attains its peak load of 200 kN for a lateral displacement of 22 mm. Owing to the catenary action, member A may resist additional loads and attains its first limit point for a lateral displacement of 58 mm. The point load attains approximately 220 kN at this point. The increase represents roughly 10%. However, after passing through the first limit point the applied load may again rise owing to the catenary action that becomes more pronounced with increasing displacements. Nonetheless, the attained displacements are high and may be incompatible with the design leading possibly to localised failure of the structure. For non-accidental design situation, this would not be acceptable and consequently the increase of the peak load of 71% (!) could not be exploited in practice. Nonetheless, the increase of the peak load of 10% associated with the first limited point attained by member A developing the catenary action could potentially be accounted for even in non-accidental design situations as it is not associated with excessive displacements as shown in Figure 5-151.

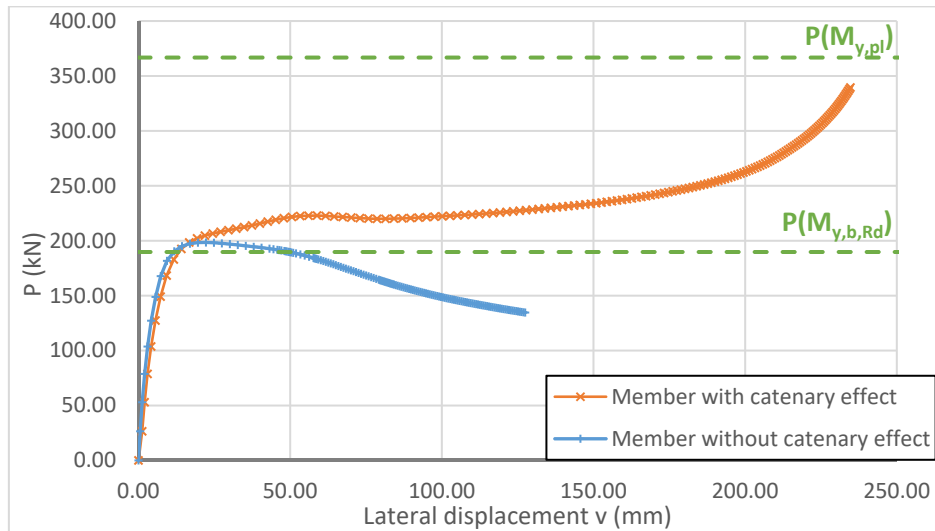


Figure 5-149: Load displacement curves for member with and without catenary effect

The obtained results may be analysed further on with the aid of Figure 5-150, Figure 5-151 and Figure 5-152. Figure 5-150 represents the von Mises stress distribution for member when it reaches its peak load. Clearly, the displacements are rather low and yielding is concentrated at mid-span over half of the flange. Additionally, it can be seen that the stresses in the other parts of the member are rather low (observe stresses in the web near the member ends).

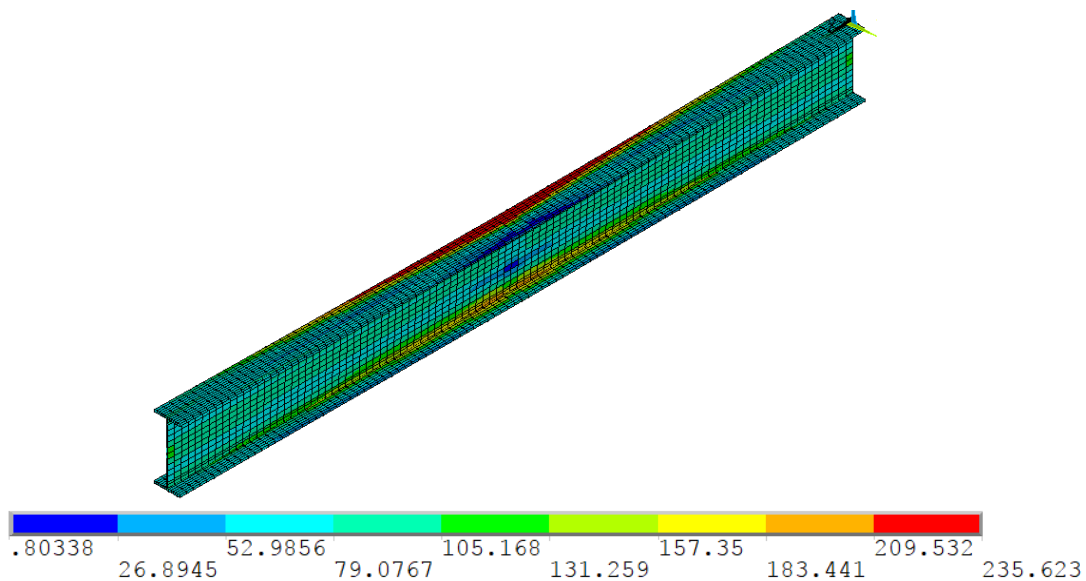


Figure 5-150: von Mises stresses and deformed shape of the member without catenary action at peak load level

Figure 5-151 represents the von Mises stress distribution and the deformed shape of the member A when it attains its first limit point. Compared to the member B represented in Figure 5-150, one may observe that the stresses along member A are higher. The increase of the stresses obviously results from the increased load and second order effects (2nd order minor-axis bending moment and 2nd order bi-moment) but also from the axial tension force that develops owing to the catenary action (observe again the stresses in the web near the member ends). One may also observe that

the displacements linked to the first limit point are not excessive and can be accepted at ultimate limit state. Figure 5-152, representing the von Mises stress distribution as well as the displacements of member A when it attains its peak load, indicates that the member has (nearly) completely yielded over its total length due to the axial tension force (von Mises stresses between 235 MPa and 250 MPa). Moreover, it can be observed that a certain strain hardening reserve is activated as the stresses exceed 235 MPa. Additionally, the displacements become very high at this point (torsional twist attains 1 rad at mid-span!) and cannot be accepted for a non-accidental design situation.

This last example treated here does not concern the proper objective of the present thesis but it is used to emphasize that the interaction equations and other provisions given in Eurocode 3 Part 1-1 explicitly neglect certain strength reserves (catenary action) that may potentially attain about 10% and more. The increased conservatism of the proposed extension of the Eurocode 3 Part 1-1 interaction equations to the case of applied torsion is due to the specific torsional behaviour of members with open cross-section (generation of a warping hinge) that is comparable (qualitatively and quantitatively) to the catenary action explicitly neglected by the currently available Eurocode 3 provisions. Therefore, it seems acceptable to neglect the plastic torsional system reserve as well for the simplified resistance model as the observed increase of the conservatism for members subject to torsion is only of theoretical (numerical) nature as the plastic system reserve cannot be excluded in the numerical simulations contrariwise to the catenary action. Indeed, if the catenary action was accounted for in case of members subject to combined axial force and bi-axial bending the average value of the Eurocode 3 strength predictions would be approximatively equal to the average value obtained for members additionally subject to torsion.

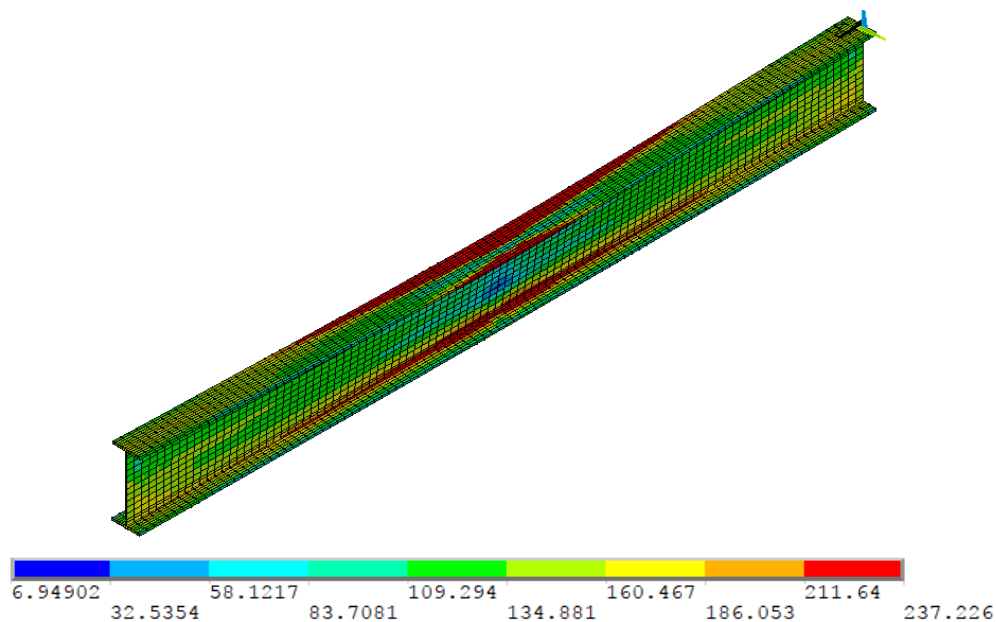


Figure 5-151: von Mises stresses and deformed shape of the member with catenary action at first limit point

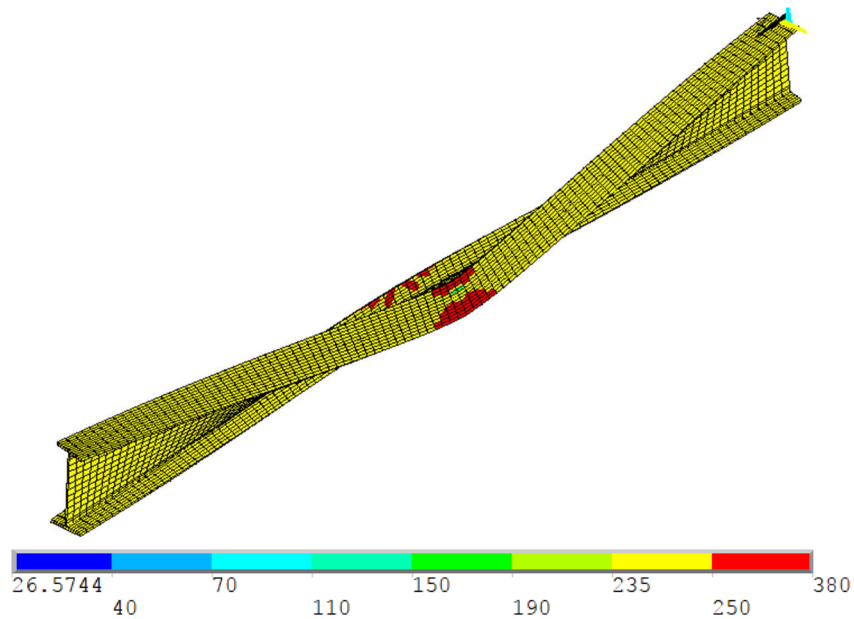


Figure 5-152 : von Mises stresses and deformed shape of the member with catenary action at peak load level

Throughout the present paragraph, the proposed extension of the Eurocode 3 Part 1-1 interaction formulae, applicable to the design of members under combined bi-axial bending and axial force, are evaluated and it is shown that satisfactory results are obtained. The reasons for very conservative as well as for unsafe strength predictions have been discussed in detail. Also, it appears that it is not necessary to account for neither the minor-axis bending moment that results from the torsional twist and major-axis bending nor the major-axis bending moment that results from the torsional twist and minor-axis bending (φM_y and φM_z – derived in the theoretical study presented in paragraph 5.5.7.5). In fact, even without this term sufficient safety is ensured and the scatter of the results is satisfactory.

In the following the resistance model is evaluated for members of slender and semi-compact cross-section (class 3 and class 4 sections in the terminology of Eurocode 3 Part 1-1).

5.6.4.2.3 Double symmetric I sections subject to combined bi-axial bending, axial forces and torsion –
Sections of class 3 and 4

Up to this point, local plate buckling has been prevented in the numerical simulations by the application of rigid beam elements over the sections of the members as described in paragraph 5.2.3. Consequently, all members could attain the plastic resistance of their most loaded section if the effect of member instability was negligible. In the present paragraph the influence of local plate instability is studied and the comparisons are therefore based on the numerical simulations performed without the rigid beam elements. It is to be noted that only members whose cross-sections are slender or semi-compact are considered hereafter. These sections are recalled in Figure 5-40.

Table 5-40: Studied slender and semi-compact cross-sections

Section	Web slenderness h_w/t_w	Flange slenderness $(b_f-t_w)/(2t_f)$
HR290.3.300.14	87,3	10,6
HR500.4.300.20	115,0	7,4
HR770.5.400.17	147,2	11,6
W650.5.180.10	126,0	8,8
W850.6.300.12	137,7	12,3
W850.5,5.200.14	149,5	6,9
W1330.10.280.15	130,0	9,0

So as to account for the effect of local plate instability the effective width method proposed in paragraph 4 of Eurocode 3 Part 1-5 (CEN 2007a) is applied for slender cross-sections (class 4). For semi-compact sections (class 3) the plastic reference resistances ($M_{y,pl}$, $M_{z,pl}$, B_{pl}) are replaced by the elastic reference resistances ($M_{y,el}$, $M_{z,el}$, B_{el}). Owing to the stiffener applied at mid-span and to the modelling of the support conditions, local buckling resulting from an applied point load has not to be checked. Conversely, due to the slenderness of the web all sections considered here are sensitive to shear buckling. In case of high shear forces the provisions given in paragraph 5 and 7 of EN 1993-1-5 are applied. They are recalled in Table 5-41. The last calculation step represents the interaction between the shear force and the bending moment. If an axial force is applied, the plastic bending moment resistance of the section as a whole $M_{y,pl}$ as well as the plastic bending moment resistance linked to the flanges only $M_{f,Rd}$ should be reduced. In the framework of this thesis, the members may also be subject to significant minor-axis bending moments and bi-moments that can, potentially, also reduce the major-axis bending moment resistance. Their influence is accounted for by calculating analytically $M_{y,pl}$ and $M_{f,Rd}$ in presence of the bi-moment and the minor-axis bending moment (and the axial force).

Table 5-41 : Resistance of the section to shear buckling

Calculation step	Expressions to be used
Shear buckling coefficient	$k_{\tau} = 5,34 + 4\left(\frac{h_w}{a}\right)^2 \text{ if } \frac{a}{h_w} \geq 1$ $k_{\tau} = 4 + 5,34\left(\frac{h_w}{a}\right)^2 \text{ if } \frac{a}{h_w} < 1$
Relative slenderness of the web	$\bar{\lambda}_w = \frac{h_w}{37,4t\varepsilon\sqrt{k_{\tau}}}$
Reduction factor	$\chi_w = \frac{0,83_w}{\bar{\lambda}_w}$
Shear resistance of the web*	$V_{b,Rd} = V_{bw,Rd} = \frac{\chi_w f_y h_w t}{\sqrt{3}\gamma_{M1}}$
Working degree with respect to shear force	$\bar{\eta}_3 = \frac{V_{Ed}}{V_{b,Rd}}$
Working degree with respect to bending moment	$\bar{\eta}_1 = \frac{M_{y,Ed}}{M_{pl,Rd}}$
Interaction between bending and shear force	<p>if $\bar{\eta}_3 \geq 0,5$ and $\bar{\eta}_1 \geq \frac{M_{f,Rd}}{M_{pl,Rd}}$:</p> $\bar{\eta}_1 + \left(1 - \frac{M_{f,Rd}}{M_{pl,Rd}}\right) \left(2\bar{\eta}_3 - 1\right)^2 \leq 1,0$

*The contribution of the flange is neglected here.

First, the results obtained for members that are not subject to torsion are represented in Figure 5-153 in order to evaluate the precision of the original interaction equations for class 3 and class 4 sections. It may be observed that the precision as well as the scatter of the results is very similar to the case of compact sections. Indeed, the obtained mean value of the ratio $\chi_{\text{Method}}/\chi_{\text{GMNIA}}$ is equal to 0,84 (=0,86 for members of compact section) and the standard deviation of the same ratio is equal to 0,12 (=0,11 for members of compact section).

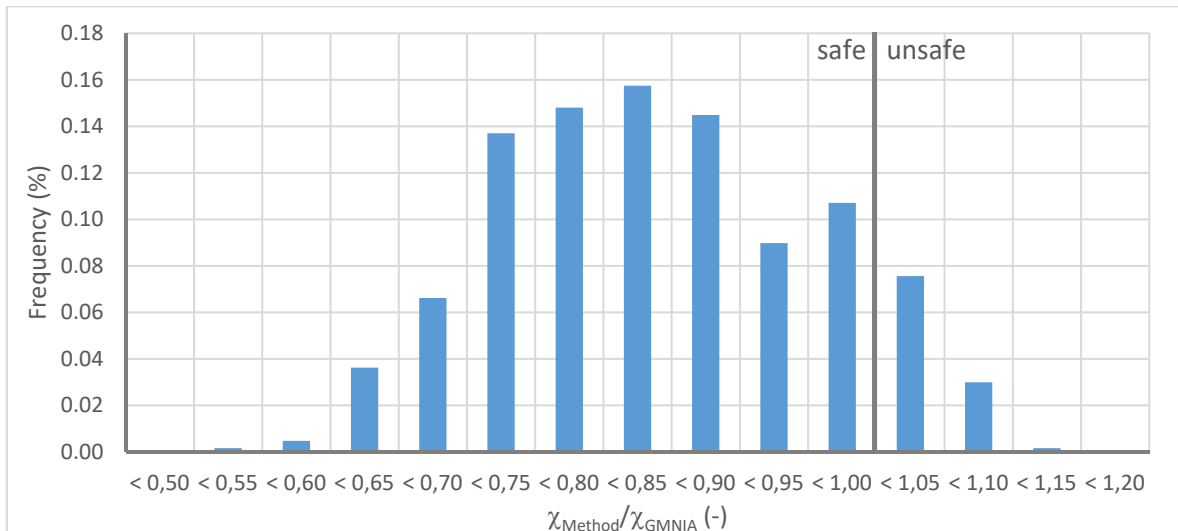


Figure 5-153: Ratio between resistance obtained with Eqs. (5.307) and (5.308) and numerically obtained resistance – members not subject to torsion

Figure 5-153 shows that some of the results may be rather conservative. In the majority of cases very safe-sided results are linked to high minor-axis bending moments as shown in Figure 5-154 that represents the results depending on the degree of bi-axiality. It is clearly shown that the results become more and more safe-sided with increasing minor-axis bending moment. The very safe-sided nature of the Eurocode 3 Part 1-5 effective width method in case of minor-axis bending has been discussed in references (Brune 1998) and (Rusch et al. 2004). It appears that the effective width determined with the Eurocode 3 Part 1-1 provisions is too conservative for flanges in bending (see in particular (Brune 1998)).

Figure 5-154 also shows that the scatter of the results seems to be more pronounced for longer members that are sensitive to member instability. Here, it appears that the interaction equations combined with the effective width method only covers roughly the interaction between member instability (flexural buckling, lateral-torsional buckling) and local plate instability especially in case of combined bi-axial bending and compression axial forces. For combined compression axial force and minor-axis bending however, it appears that the interaction between member instability and local plate instability is more precisely accounted for. In fact, in Figure 5-154 one may observe that the results are very conservative for low values of the relative slenderness as the member is not sensitive to lateral-torsional or flexural buckling. Consequently, the failure is mainly due to local plate instability and hence the conservatism of the effective width method causes the observed discrepancy. For longer members the sensitivity to lateral-torsional and flexural buckling increases and the failure of the member is caused by interaction between local plate instability and member instability. For these case the strength predictions approach the numerically obtained results.

Finally, it is observed that the unsafe results are linked to members subject to major-axis bending only and to combined axial force and major-axis bending. Additionally, the unsafe results are obtained for longer members for which the sensitivity to local plate instability decreases. Here, it seems that the attribution of the reduction curve for lateral-torsional buckling leads to the un-

conservatism of the design method. It may be noted that unsafe results, yet closer to the reference results, have been obtained for the same members prevented from local plate instability (studied in paragraph 5.6.4.2.2). Nonetheless, it is recalled that these members are made of hot-rolled sections but with “invented” dimensions (see Table 5-40) so as to increase the diversity of the studied sections. Obviously, the Eurocode 3 reduction curves have not been calibrated for these sections and therefore a slight unsafeness can be accepted.

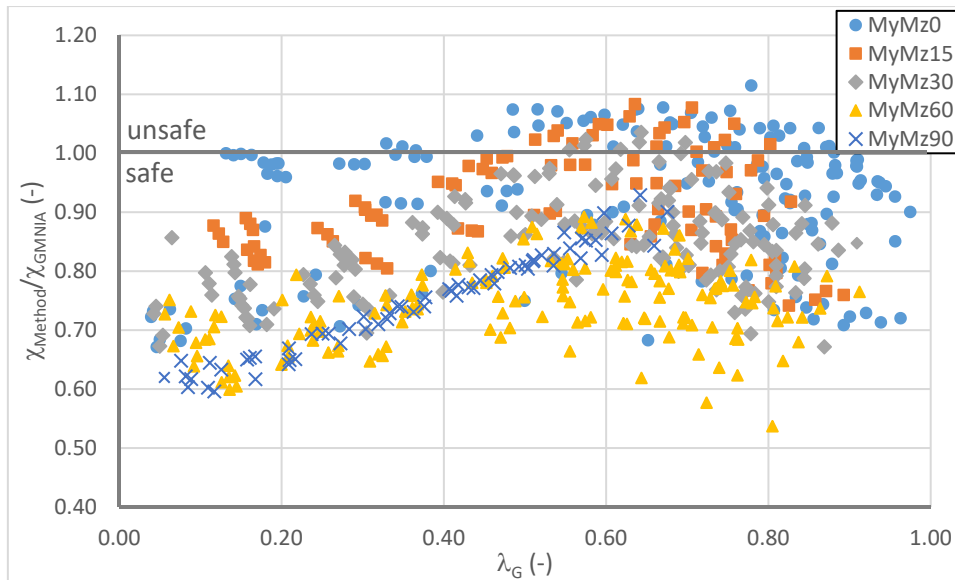


Figure 5-154: Ratio between resistance obtained with Eqs. (5.307) and (5.308) and numerically obtained resistance – members not subject to torsion

Here before, the design method has been evaluated for members not subject to torsion in order to obtain a clear idea of the precision of the interaction formulae combined with the effective width method in their original field of application. It has been shown and confirmed that the effective width method may be rather conservative for sections under minor-axis bending and hence flanges in bending.

Next, the proposed extension of the interaction equations is evaluated for members subject to combined axial compression force, bi-axial bending and torsion. Figure 5-155 indicates that the interaction equations may be safely applied. Nonetheless, it seems that the results are rather conservative again (mean value = 0,68). The conservative nature of the proposal may however be explained based on the results shown here before for members not subject to torsion and based on the conclusions of paragraph 5.6.4.2.2. Indeed, due to the bi-moment resulting from torsion the distribution of the axial stresses is non uniform in the flanges (flanges in bending). For this situation the effective width method proposed in Eurocode 3 Part 1-1 has been shown to be rather conservative (see reference (Brune 1998)). Additionally, for short members the effect of the warping hinge leads again to redistribution of the internal forces and moments resulting from torsion and consequently the safe-sided nature of the proposal is amplified.

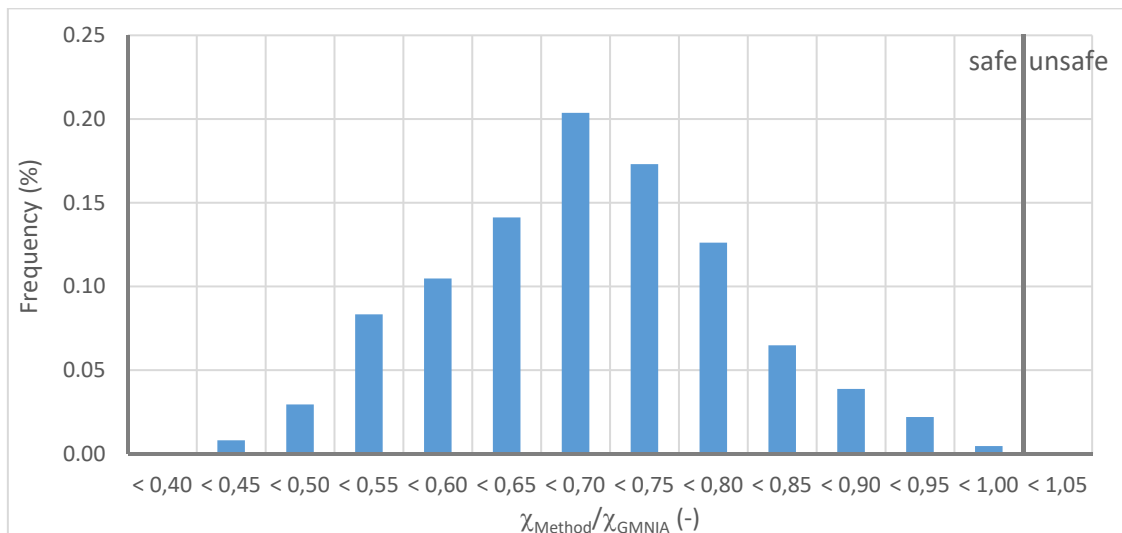


Figure 5-155: Ratio between resistance obtained with Eqs. (5.307) and (5.308) and numerically obtained resistance – members subject to torsion

If the results of Figure 5-155 are represented as function of the relative slenderness, one may easily recognize that the difference between the numerically obtained resistances and the design model decreases with increasing member slenderness. Nonetheless, in some cases the strength predicted by the design model are very conservative independently from the relative member slenderness (results encircled in orange in Figure 5-156). As before, these results are not principally due to the applied torsional moment but they may be explained based on the inherent limits of the Eurocode 3 design model in its initial field of application. In particular, one may cite again:

- The conservatism of the reduction curves for lateral-torsional buckling when they are applied to welded members of intermediate to high values of the relative slenderness;
- The conservatism of the effective width method for members under minor-axis bending;
- The roughly approximated interaction between local plate instability and member instability for members under bi-axial bending.

The mentioned reasons for the discrepancy between the design model and the numerical results are only slightly amplified by the applied torsional moment. As the objective of this thesis is not the amelioration of the Eurocode 3 Part 1-1 interaction equations themselves but their extension to the case of applied torsion the resulting conservatism has to be accepted.

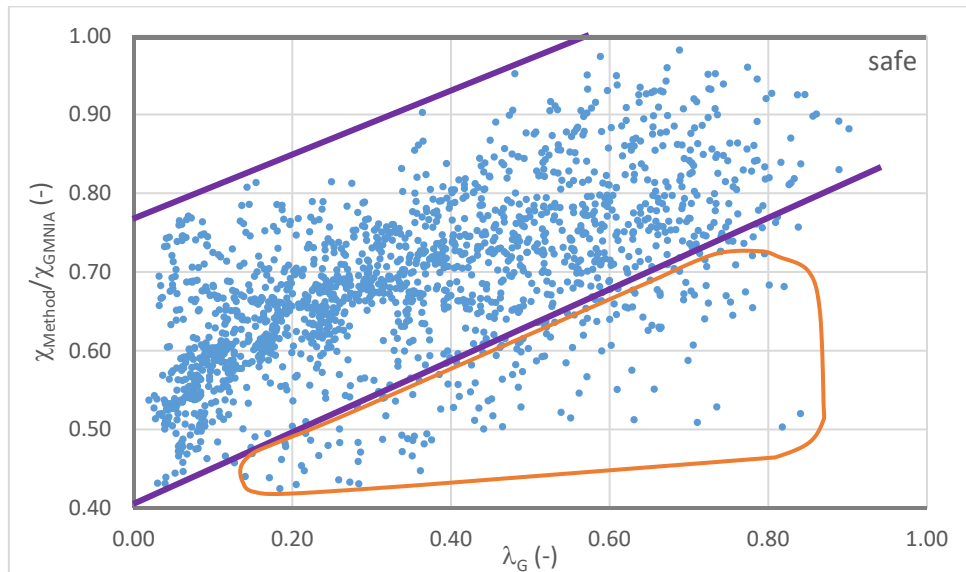


Figure 5-156: Ratio between resistance obtained with Eqs. (5.307) and (5.308) and numerically obtained resistance – members subject to torsion

5.6.4.2.4 Conclusions

Throughout paragraphs 5.6.4.2.1, 5.6.4.2.2 and 5.6.4.2.3 the resistance of members of double symmetric I section has been studied. Members of compact section as well as of semi-compact and slender section have been considered. In particular, it has been shown that:

- The design model initially proposed at TU Berlin may be very unsafe and leads to a significant scatter of the results. So as to obtain safe-sided strength predictions, the design model should be modified by adding the verification that the bi-moment is less than $0,5B_{pl}$. Additionally, the reduction of the bi-moment resulting from the factor k_{zw} should not be accounted for if the member exceeds a given length (length linked to the plateau of the reduction curve for lateral-torsional buckling could be used);
- The proposed simple extension of the Eurocode 3 Part 1-1 interaction equations (see §6.3.3 of (CEN 2005a)) leads to satisfactory results without a significant complexification of the design approach;
- The proposal leads, however, to rather conservative results for short members subject to high torsion due to the effect of the warping hinge and the resulting redistribution of torsion. This strength reserve can be compared (quantitatively and qualitatively) to the catenary action that develops for members in the structure but that is not accounted for in the current Eurocode 3 resistance model for non-accidental design situations;
- For members of slender cross-section the proposed extension of the interaction equations appears to be satisfying again but the conservatism is increased

especially for short members due to the combined effect of the specific torsional behaviour of members with open section and the conservatism of the effective width method of Eurocode 3 Part 1-1 (CEN 2005a).

In the following, it is investigated if the design models, proposed for mono-symmetric sections in the past, (see paragraph 5.3) can also be extended to the case of applied torsion. First, 5.6.4.3 concerns mono-symmetric I sections. Paragraph 5.6.4.4 is then dedicated to U sections.

5.6.4.3 Members with mono-symmetric I sections

5.6.4.3.1 General

In paragraph 5.3.3 a proposal for the extension of the Eurocode 3 interaction formulae to mono-symmetric I sections has been presented (see also reference (Kaim 2004)). The interaction equations are recalled hereafter:

$$\frac{N_{Ed}}{\chi_y \frac{N_{Rk}}{\gamma_{M1}}} + k_{yy} \frac{M_{y,Ed}}{\chi_{LT,cf} \frac{M_{y,Rk,cf}}{\gamma_{M1}}} \leq 1,0 \quad (5.318)$$

$$\frac{N_{Ed}}{\chi_{TF} \frac{N_{Rk}}{\gamma_{M1}}} + k_{zy} \frac{M_{y,Ed}}{\chi_{LT,cf} \frac{M_{y,Rk,sf}}{\gamma_{M1}}} \leq 1,0 \quad (5.319)$$

$$\frac{N_{Ed}}{\chi_z \frac{N_{Rk}}{\gamma_{M1}}} - k_{zy} \frac{M_{y,Ed}}{\chi_{LT,cf} \frac{M_{y,Rk,lf}}{\gamma_{M1}}} \leq 1,0 \quad (5.320)$$

Additionally, tension flange yielding should be checked with Eq. (5.321).

$$\frac{N_{Ed}}{\chi_y \frac{N_{Rk}}{\gamma_{M1}}} \left(\frac{1}{\chi_y} - 2 + \bar{\lambda}_y \right) + \frac{M_{y,Ed}}{\frac{M_{y,Rk,tf}}{\gamma_{M1}}} \leq 1,0 \quad \text{for } \bar{\lambda}_y \leq 1,0 \quad (5.321)$$

$$\frac{N_{Ed}}{\chi_y \frac{N_{Rk}}{\gamma_{M1}}} \left(\frac{1}{\chi_y} - 1,5 + 0,5 \bar{\lambda}_y \right) + \frac{M_{y,Ed}}{\frac{M_{y,Rk,tf}}{\gamma_{M1}}} \leq 1,0 \quad \text{for } \bar{\lambda}_y > 1,0$$

It is clear, that the proposal can only be used to check the resistance of members that are not subject to an additional minor-axis bending moment or to additional torsion. Hereafter, it is therefore checked first if the interaction equations may be extended to the case of applied minor-axis bending moments (paragraph 5.6.4.3.2) and then the extension to an applied torsional moment is investigated in paragraph 5.6.4.3.3. It should be noted that only members of compact cross-section are studied hereafter.

5.6.4.3.2 Mono-symmetric I sections under combined bi-axial bending and axial forces

Before the extension to bi-axial bending is studied, it seems necessary to obtain a clear idea on the precision of the design proposal of Kaim in its initial field of application. Therefore, the interaction equations are evaluated first for mono-symmetric members only subject to a compression axial force and a major-axis bending moment in Figure 5-157. It appears that the interaction equations are rather conservative. Indeed the mean value of the ratio $\chi_{Method}/\chi_{GMNIA}$ is equal to 0,71. Nonetheless, the scatter of the results seems to be acceptable as the standard deviation is only of about 9%.

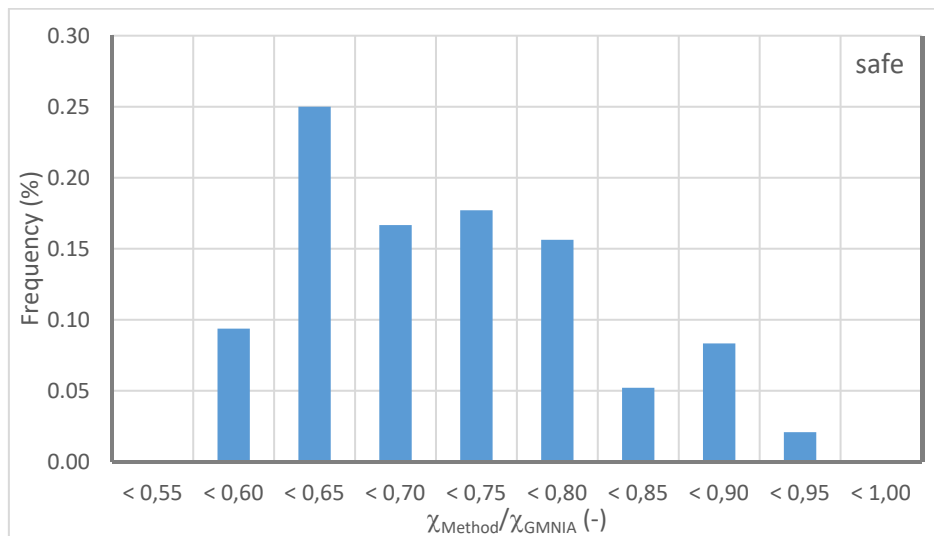


Figure 5-157: Ratio between resistance obtained with Eqs. (5.307) and (5.308) and numerically obtained resistance – members subject to combined axial force and major-axis bending

In order to analyse the obtained results further on, Figure 5-158 represents the ultimate resistance curves of members of section IMS500.10,2.200.16.125.16 (IMS3) subject to combined axial force and major-axis bending. The load cases M (constant bending), P1 (point load applied at mid-span – simple supports at member ends) and P2 (point load at mid-span – fixed supports at member ends) are studied. Figure 5-158 confirms the conservatism of the design approach over the total range of the member slenderness. Nonetheless, it seems that the overall tendencies of the member behaviour are captured by the interaction equations. In fact, one may observe that both, the GMNIA simulations and the interaction equations, predict that members subject to load case P2 possess a higher resistance up to a relative slenderness of approximately 1,40. For higher values of the member slenderness the difference between the load cases becomes negligible. It should be noted that the shortest member subject to load case P2 fails by shear buckling in the plastic range. Consequently, a significant resistance reserve can be mobilised by strain hardening and the member attains a very high load level. The resistance model does not consider this strain hardening reserve and hence the predicted resistance cannot exceed the theoretical plastic resistance (obtained through MNA simulations). Nonetheless, one may observe that the strength prediction is close to the plastic resistance of the most loaded section. Additionally, for load cases P1 and M, the interaction equations are rather safe-sided even for the shortest members. Again, the reason for this conservatism is the approximation of the cross-

section interaction. This conservatism has also been observed in reference (Kaim 2004). In order to ameliorate the strength predictions of the interaction formulae a large study seems to be necessary. Yet, hereafter this conservatism is accepted and the extension to bi-axial bending and torsion is studied in priority.

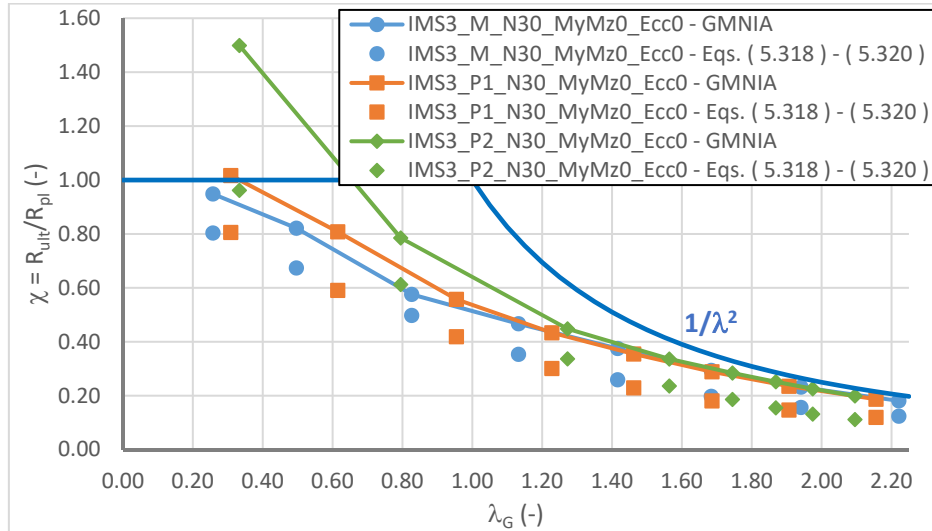


Figure 5-158: Ultimate resistance curves for members of section IMS3 subject to combined axial compression force and major-axis bending

It is proposed to extend the interaction equations to an applied minor-axis bending moment as provided in Eqs. (5.322) to (5.324) (the partial factor γ_{M1} is omitted here). For simplicity, the expressions of the interaction factors k_{zy} and k_{zz} used for double symmetric sections are used again. Admittedly, these interaction factors do not exactly cover the behaviour of mono-symmetric members as both the plastic cross-section interaction and the second order effects arising from the axial force are somewhat different than for double symmetric members. This inconsistency is however accepted here.

$$\frac{N_{Ed}}{\chi_y N_R} + k_{yy} \frac{M_{y,Ed}}{\chi_{LT,cf} M_{y,R}} + k_{yz} \frac{M_{z,Ed}}{M_{z,R}} \leq 1,0 \quad (5.322)$$

$$\frac{N_{Ed}}{\chi_{TF} N_R} + k_{zy} \frac{M_{y,Ed}}{\chi_{LT,cf} M_{y,R}} + k_{zz} \frac{M_{z,Ed}}{M_{z,R}} \leq 1,0 \quad (5.323)$$

$$\frac{N_{Ed}}{\chi_z N_R} - k_{zy} \frac{M_{y,Ed}}{\chi_{LT,cf} M_{y,R}} + k_{zz} \frac{M_{z,Ed}}{M_{z,R}} \leq 1,0 \quad (5.324)$$

Figure 5-159 shows the evaluation of the interaction equations extended to the case of bi-axial bending. It appears that the design model is again rather safe-sided but the conservatism is not increased. Indeed, it appears that the resistance model is even more precise if an additional minor-axis bending moment is applied. In Table 5-42, gives a quantitative evaluation of Eqs. (5.322) to (5.324).

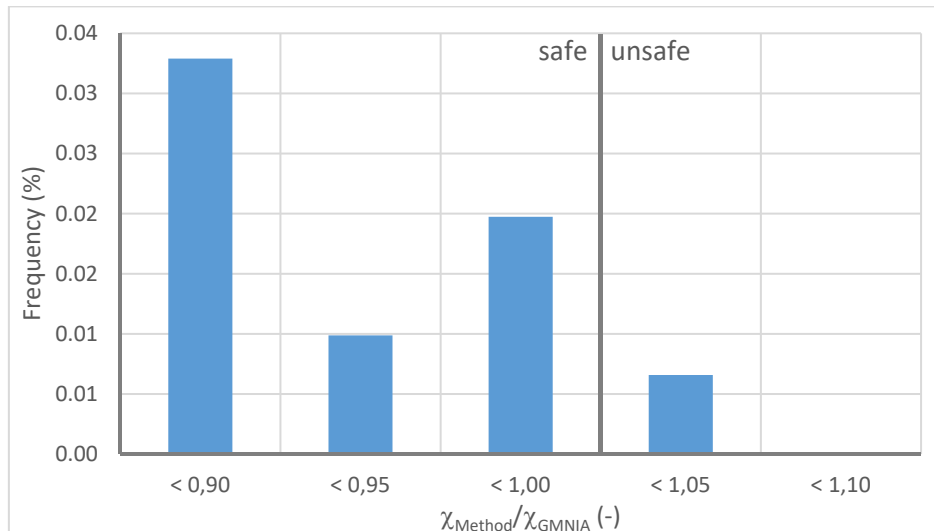


Figure 5-159: Ratio between resistance obtained with Eqs. (5.322) to (5.324) and numerically obtained resistance – members subject to combined axial force and bi-axial bending

Table 5-42 indicates that Eqs. (5.322) to (5.324) lead to satisfying strength predictions for mono-symmetric members and, in particular, it confirms that the precision is higher for member subject to bi-axial bending and an axial force than for those only subject to combined major-axis bending and axial forces.

Table 5-42 : Precision of interaction equations for mono- and double symmetric members

$\chi_{Method}/\chi_{GMNIA}$	Eqs. (5.322) to (5.324) for mono-symmetric sections under $N + M_y + M_z$	Eqs. (5.322) to (5.324) for mono-symmetric sections under $N + M_y$
Mean	0,79	0,72
Standard deviation σ	0,08	0,09
Mean + 2σ	0,95	1,00
Maximum	1,09	0,94
Minimum	0,56	0,55

So as to analyse the global results in more detail, Figure 5-160 represents the ultimate resistance curves of members of section IMS500.10.2.200.16.125.16 (IMS3). As before, the results are rather conservative for short members whose resistance is influenced by the plastic cross-section resistance. Yet, for longer members the strength predictions obtained with Eqs. (5.322) to (5.324) become closer to the numerically determined ultimate resistance curves. Especially, for members under a combination of minor-axis bending and axial compression forces the design model yields very precise results. It appears that the precision of the interaction equations improves with the relative importance of the minor-axis bending moment. Indeed, an increase of the minor-axis bending moments also increases the tendency of the member to fail by flexural buckling about the minor-axis rather than by lateral-torsional buckling. Since the failure mode of

minor-axis flexural buckling appears to be covered more precisely by the interaction equations their precision is ameliorated for longer members if a minor-axis bending moment is applied.

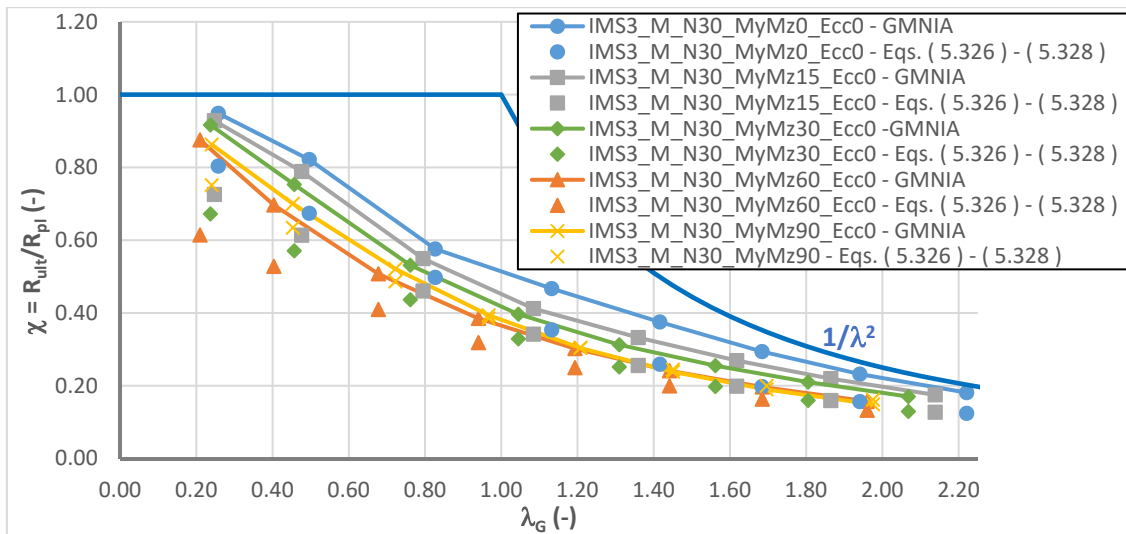


Figure 5-160: Ultimate resistance curves for members of section IMS3 subject to combined axial compression force and bi-axial bending

The present paragraph evaluated the proposal of reference (Kaim 2004) for mono-symmetric members subject to a combination of an axial compression force and a major-axis bending moments. It has been shown that the design approach is conservative. Then an extension in the Eurocode 3 format is proposed in order to cover mono-symmetric member that are also subject to an additional minor-axis bending moment. Again, the results are rather conservative especially for short members as the complex cross-section interaction is only roughly approximated. In the following paragraph an extension to applied torsion is studied.

5.6.4.3.3 I Mono-symmetric I sections under combined bi-axial bending, axial forces and torsion

Similarly to the case of members of double symmetric I section, the interaction equations are extended by the term linked to the bi-moment as shown in Eqs. (5.325) to (5.327). One should note that this extension is only partially justified. Indeed, the bi-moment and the minor-axis bending moment are affine in the flanges as for double symmetric I sections but, conversely to these last sections, the interaction is not linear as discussed in Chapter 4. For a simplified design model the resulting discontinuity between cross-section and member resistance is however accepted.

$$\frac{N_{Ed}}{\chi_y N_R} + k_{yy} \frac{M_{y,Ed}}{\chi_{LT,cf} M_{y,R}} + k_{yz} \frac{M_{z,Ed}}{M_{z,R}} + k_{yw} \frac{B_{Ed}}{B_R} \leq 1,0 \quad (5.325)$$

$$\frac{N_{Ed}}{\chi_{TF} N_R} + k_{zy} \frac{M_{y,Ed}}{\chi_{LT,cf} M_{y,R}} + k_{zz} \frac{M_{z,Ed}}{M_{z,R}} + k_{zw} \frac{B_{Ed}}{B_R} \leq 1,0 \quad (5.326)$$

$$\frac{N_{Ed}}{\chi_z N_R} - k_{zy} \frac{M_{y,Ed}}{\chi_{LT,cf} M_{y,R}} + k_{zz} \frac{M_{z,Ed}}{M_{z,R}} + k_{zw} \frac{B_{Ed}}{B_R} \leq 1,0 \quad (5.327)$$

Figure 5-161 represents a statistical evaluation of the design model. Obviously, the interaction equations are very conservative. Also, the scatter appears to be higher ($\sigma = 0,14$) than the one obtained for mono-symmetric members not subject to torsion ($\sigma = 0,08$).

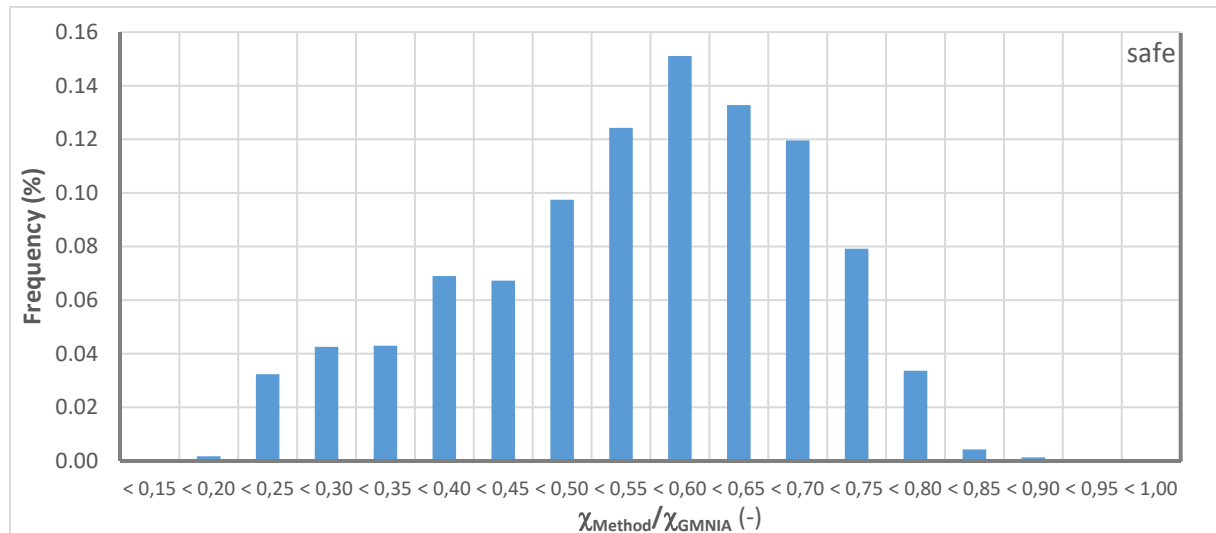


Figure 5-161: Ratio between resistance obtained with Eqs. (5.325) to (5.327) numerically obtained resistance

In order to understand the reasons for this high conservatism, Figure 5-162 first represents the obtained ratio $\chi_{Method} / \chi_{GMNIA}$ depending on the relative member slenderness. One may observe a clear tendency in Figure 5-162. Indeed, the results are highly (over) conservative for short members and become less safe-sided for longer ones. Starting for a member slenderness of approximately 1,1, the accuracy of the interactions equations is comparable to the precision obtained for members not subject to torsion. This has been expected because the plastic cross-section resistance is only roughly approximated.

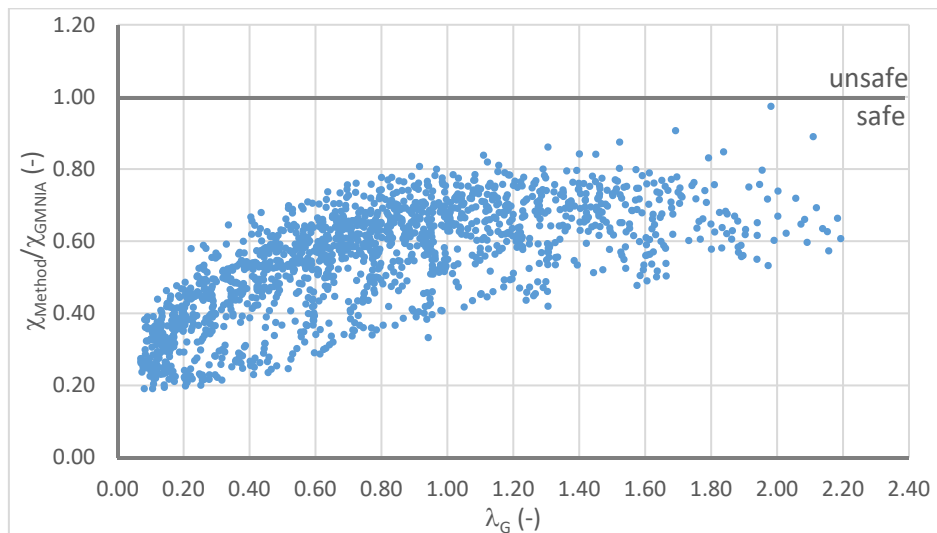


Figure 5-162: Ratio between resistance obtained with Eqs. (5.325) to (5.327) numerically obtained resistance depending on the member slenderness

Figure 5-163 represents the obtained results for the example of members of IMS3 section subject to constant bi-axial bending moments, a compression axial force and a torsional moment applied at mid-span. Again, it is obvious that the results are highly safe-sided for short members. As the importance of the torsional moment decreases with the member length, it is not surprising that the interaction equations become more accurate for relatively high values of the member slenderness ($> 1,2$). Additionally, Figure 5-163 highlights that there is an important difference between members subject to torsion ($EccY1$, $EccY2$ and $EccY3$) and members that are not subject to torsion. Even if the plastic cross-section interaction between the axial force and the bending moments is not precisely predicted, the accuracy of the interaction equations is much higher for short members not subject to torsion. This difference may be attributed to the more complex interaction, especially between the minor-axis bending moment and the bi-moment and additionally to the plastic torsional system reserve. It should be noted that the plastic load amplification factor used as reference in Figure 5-163 is the one obtained by MNA simulations ($R_{pl,MNA}$) and it is consequently linked to the plastic limit state of the member as a whole and not to the creation of the warping hinge ($R_{pl,LA}$). The difference between both factors, $R_{pl,MNA}$ and $R_{pl,LA}$, is illustrated in Figure 5-164.

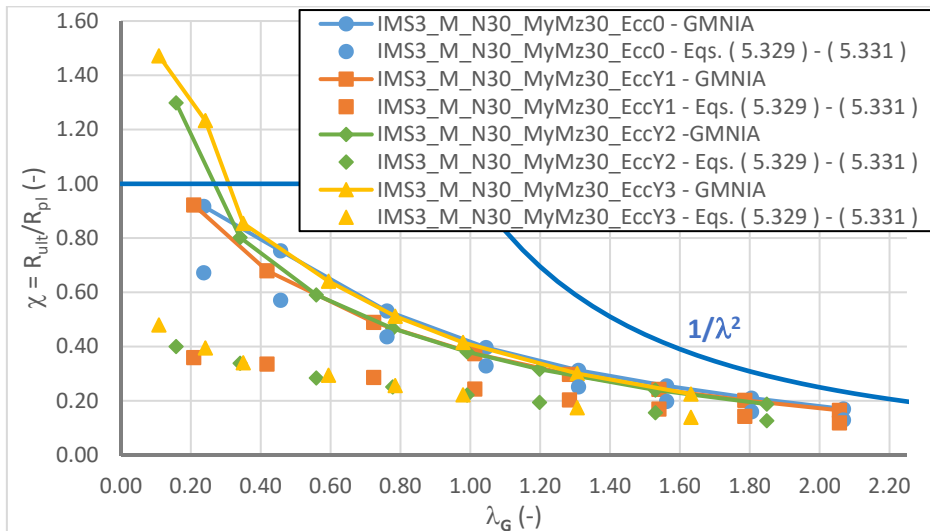


Figure 5-163: Ultimate resistance curves for members of IMS3 section subject to combined bi-axial bending, axial compression forces and torsion

Figure 5-164 clearly shows that the plastic torsional system reserve has a huge effect on the plastic resistance of the member in case of mono-symmetric members. Indeed, the effect of the plastic redistribution of the stresses resulting from torsion is even higher than for members of double symmetric section. In fact, the ratio $R_{pi,MNA}/R_{pi,LA}$ attains approximatively 1,30 in average for double symmetric sections. For mono-symmetric sections it appears that the difference between the two plastic load amplification factors can attain much higher values. Yet, this is understandable because the warping hinge is generated when the warping stiffness of the yielded section is sufficiently low compared to the initial warping stiffness. For mono-symmetric sections subject to warping, the lower flange generally yields rapidly and the cross-section consequently loses its warping stiffness faster than double symmetric sections as represented in Figure 5-165 (se also paragraph 4.4.4.3).

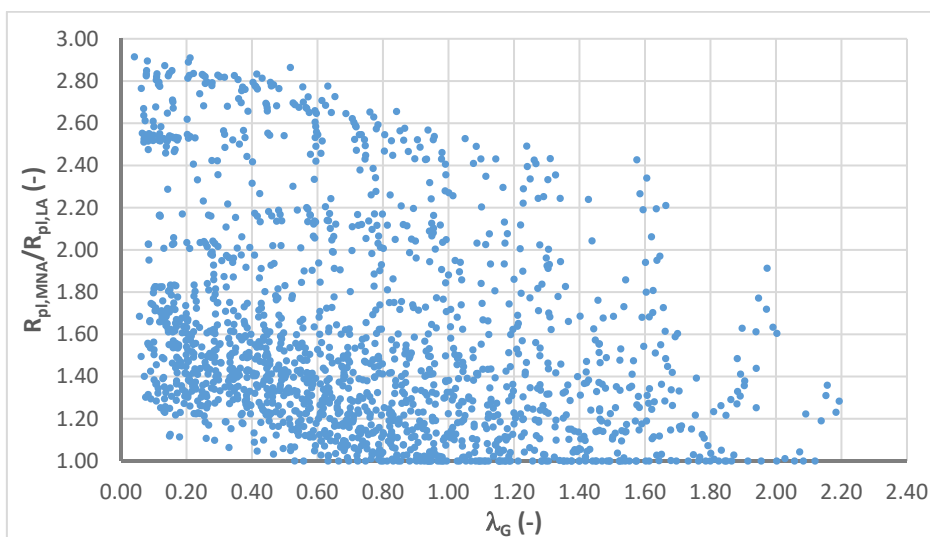


Figure 5-164: Difference between $R_{pi,MNA}$ and $R_{pi,LA}$ depending on the member slenderness

Figure 5-165 shows that the warping hinge is generated for a load factor corresponding to 62,5% of the plastic limit load of the member obtained through MNA simulations. It is recalled that, depending on the load case, the warping hinge is generated at load levels corresponding to 75%-90% of $R_{pI,MNA}$ in case of double symmetric I sections (see paragraph 4.4.4.2). The pronounced plastic torsional system reserve leads to the observed high conservatism for short members of mono-symmetric I section. Again, it is emphasized that the torsional system reserve may be included in the analysis for the determination of the internal forces and moments. Yet, in this case the torsional twist of the member should not be limited by Serviceability Limit State criteria. Indeed, the simplified plastic analysis method proposed in the framework of this thesis is obviously not capable to predict the torsional twist after yielding has initiated. Generally, the member has already started to yield at the load level corresponding to the Serviceable Limit State if the plastic torsional system reserve is accounted for as discussed in paragraph 5.6.4.2.1 for members of double symmetric section. As the torsional system reserve is even more pronounced for member of mono-symmetric section, the problematic of the determination of the torsional twist at Serviceability Limit State seems even more critical.

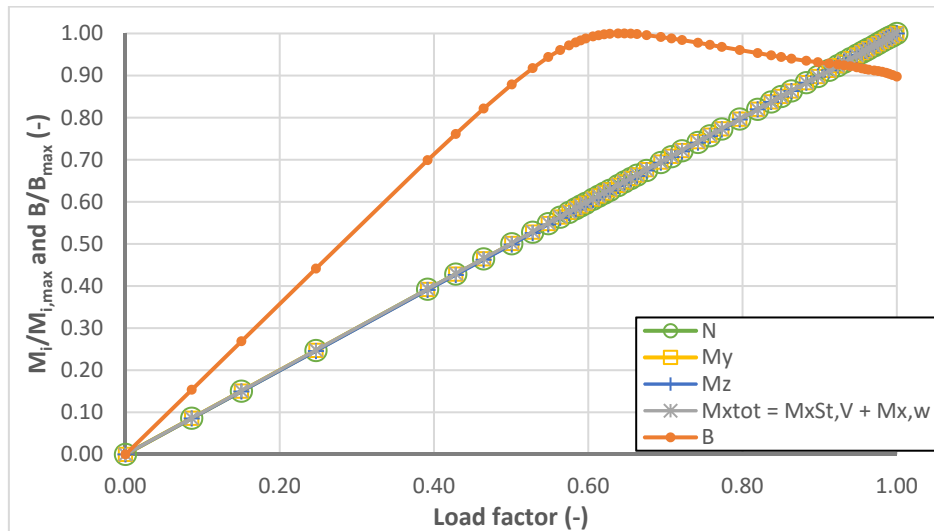


Figure 5-165: Evolution of the internal forces and moments with the load factor – MNA simulation of IMS3_M_N30_MyMz30_EccY2_L2200

Paragraph 5.6.4.3 addressed the resistance of mono-symmetric I sections subject to combined axial forces, bi-axial bending and torsion. First, the proposal of Kaim published in reference (Kaim 2004) has been extended to applied minor-axis bending moments. It has been shown that the resulting interaction equations may be safely applied even if they are conservative due to the approximation of the plastic cross-section interaction. Then the extension to applied torsion is studied. The proposed simplified interaction equations are even more conservative than for members without torsion as the plastic torsional system reserve possesses a huge influences on the resistance. Nonetheless, it seems that the conservatism has to be accepted if the member is analysed elastically (elastic determination of internal forces and moments). In fact, due to the pronounced plastic reserve of the member, the torsional twist at the Serviceability Limit State cannot be reliably determined in general. In practice, torsional loads on members of mono-

symmetric I section often result from their use as crane girders. In these cases the Serviceability Limit State criteria are very strict and the beneficial effect of the plastic torsional system reserve should not be considered.

5.6.4.4 Members with U sections

5.6.4.4.1 General

The research on the resistance of members fabricated from compact U sections has been of much less interest in the past than research of cold-formed slender U sections or the resistance on I sections. Especially, lateral-torsional buckling has not been investigated sufficiently. This lack of information led to the attribution of the most severe lateral-torsional buckling curve (curve d) to U-shaped members in Eurocode 3 Part 1-1 (Maquoi 2015). Recent research on members fabricated from U sections has been published in (Kalameya 2008). Nevertheless, it has been shown in paragraph 5.2.1.6 that the numerical simulations performed in this reference are based on very severe geometrical imperfection. Therefore, it seems necessary to reinvestigate the resistance of U-shaped members to lateral-torsional buckling based on the geometrical imperfections and residual stresses determined in paragraphs 5.2.1.5 and 5.2.1.6.

5.6.4.4.2 Lateral-torsional buckling resistance

First, the load case of constant major-axis bending is studied. The obtained results are represented for different hot-rolled U sections in Figure 5-166.

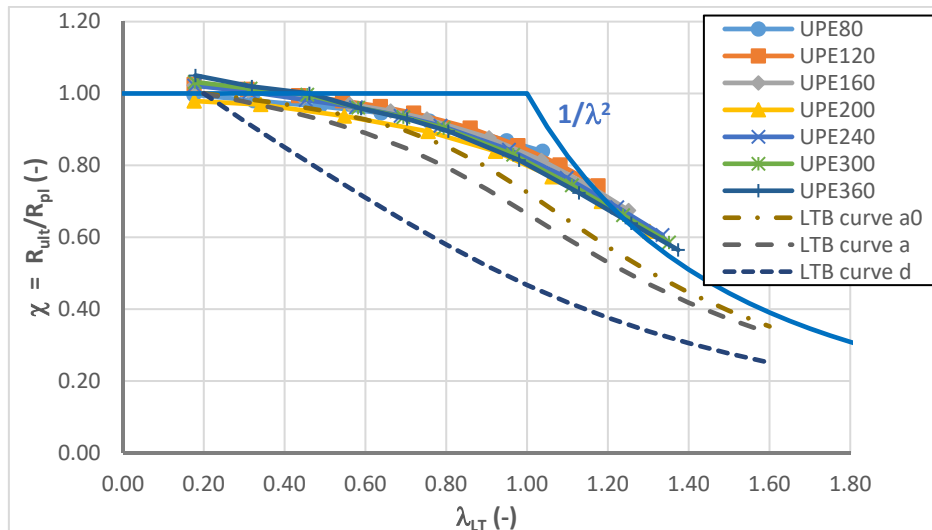


Figure 5-166: Ultimate resistance curve for U-shaped members subject to constant major-axis bending

Obviously, the numerically obtained ultimate resistance curves are very close for all examples independently of the cross-section. For a relative slenderness of about 1,0 the maximum difference between the curves is approximatively 6% and therefore nearly negligible from a practical point of view. Also, it is obvious that the studied U-shaped members are not very sensitive to lateral-torsional buckling. Indeed, even for a slenderness of 1,0, the strength reduction

due to instability is at maximum 20%. Moreover, for a slenderness of approximately 1,2 the ultimate resistance curves cross the Euler curve linked to elastic instability.

Additionally, to the numerically obtained ultimate resistance curves Figure 5-166 represents possible reduction curves for lateral-torsional buckling. It is recalled that the current version of Eurocode 3 Part 1-1 imposes the use of reduction curve d. Clearly, this choice is highly safe-sided in case of constant bending. Also, one may observe that the shape of this buckling curve does not at all represent the behaviour of the studied U-shaped members. It appears that at least the lateral-torsional buckling curve “a” could be applied. One might even consider to apply the reduction curve a_0 even if this curve is only defined for buckling of members subject to an axial force.

Next, it is shown that, conversely to the case of an I section, the load case of an applied point load at mid-span can be unfavourable for U sections compared to constant bending. Figure 5-167 represents the obtained ultimate resistance curves with reference to the ratio $M_{y,ult}/M_{y,pl}$ and to the relative slenderness λ_{LT} . The numerical results are compared to the Eurocode 3 Part 1-1 (lateral-torsional) buckling curve c and d. Observing Figure 5-167, it may seem astonishing that the members of UPE 240 and UPE 300 section do not attain the full plastic major-axis bending moment resistance for small values of the relative slenderness. One should note that these members do not fail under the sole influence of major-axis bending but rather under combined shear force and major-axis bending. The shortest members fail under a predominant shear force even before the major-axis bending moment leads to yielding of the flanges. For longer members the shear force decreases and the plastic major-axis bending moment resistance is not affected anymore. Therefore, the ultimate resistance curves increase up to the value of the relative slenderness from which elasto-plastic instability influences the resistance of the member. Short members of sections UPE 80 and UPE 120 also fail in predominant shear. However, owing to their compact webs significant strain hardening is mobilised and consequently, the influence of the shear force on the major-axis bending moment cannot be represented in the chosen reference system of Figure 5-167.

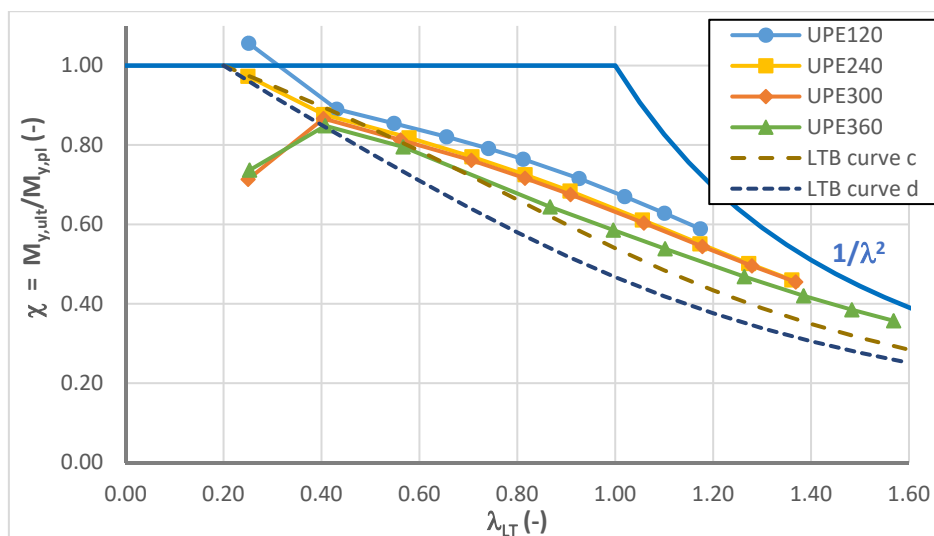


Figure 5-167: Ultimate resistance curve for U-shaped members subject to a constant point load applied at mid-span through the shear centre

It seems that a more convenient representation of the results is the one of Figure 5-168. In this figure the resistance of the member is expressed by the ratio R_{ult}/R_{pl} . Consequently, one may easily identify the failure mode of the members. Indeed, for low values of the relative slenderness, all members attain the plastic resistance of the most loaded section ($R_{ult} \geq R_{pl}$); longer members fail by elasto-plastic instability. For the studied members, the plateau length, defining the limit between failure by plastic section resistance and failure by elasto-plastic instability, is approximatively equal to 0,3.

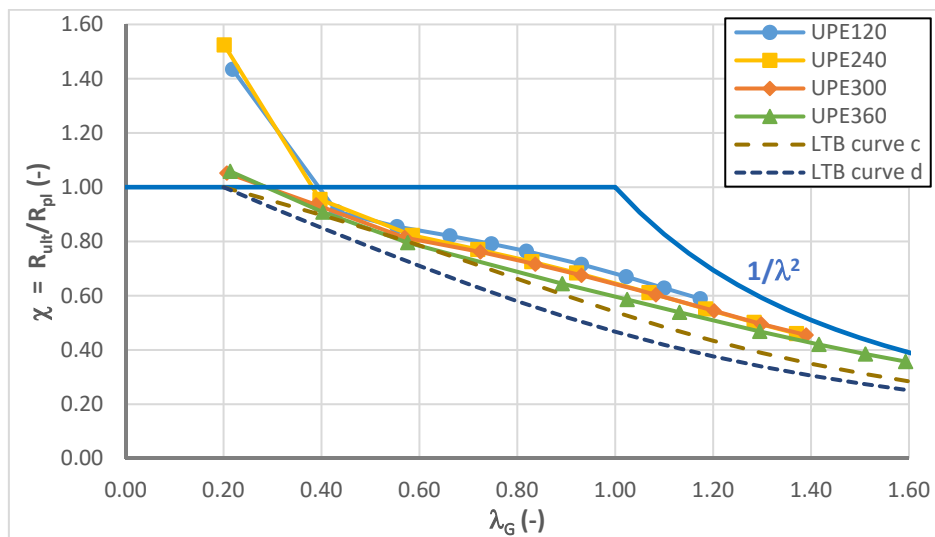


Figure 5-168: Ultimate resistance curves with reference to R_{ult}/R_{pl} – Load case P1

Both, Figure 5-167 and Figure 5-168, show that the resistance of U-shaped members subject to a point load at mid-span is much more effected by elasto-plastic instability than the resistance of the same members subject to constant bending. The reason for this astonishing result may be attributed to the imperfection sensitivity of the mono-symmetric U sections. In paragraph 5.2.1.6, it has been shown that the choice of the shape of the equivalent imperfection as well as the direction may heavily influence the resistance of the member. The results represented in Figure 5-167 and Figure 5-168 are based on an eigenmode affine imperfection possessing a lateral displacement component directed towards the tips of the flanges. The second order minor-axis bending moment consequently induces compression in the web. If the examples shown in Figure 5-168 are recalculated with an imperfection directed in the opposite sense the results of Figure 5-169 are obtained. Obviously, the results are much more favourable than those obtained previously. They are also more favourable than the results obtained for constant bending.

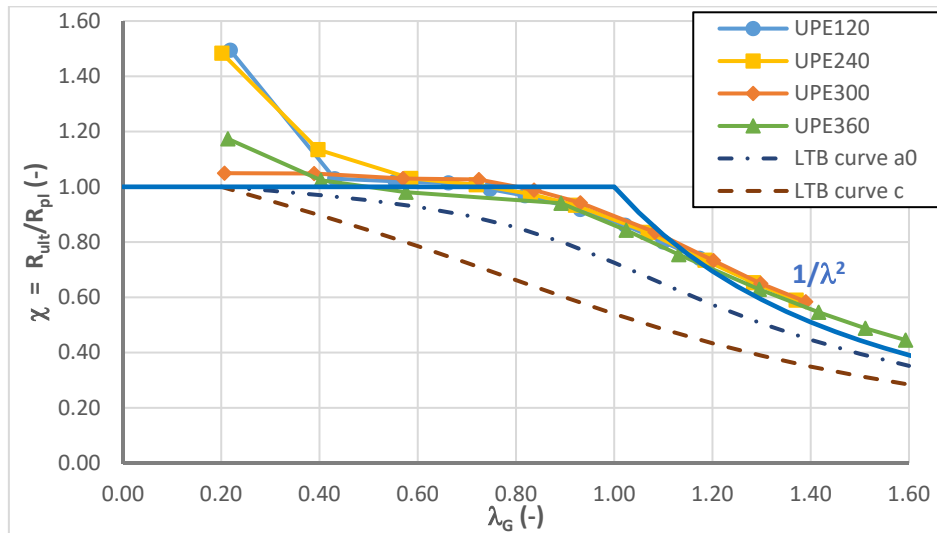


Figure 5-169: Ultimate resistance curves with reference to R_{uit}/R_{pl} – Load case P1

So as to analyse the results further on, Figure 5-170 shows the load-lateral displacement curve for two member of UPE 300 section possessing a length of 4 m. The curve in light blue shows the results obtained for the member subject to an imperfection with a lateral displacement component directed to the web (Eigenmode- - EM-) and the curve in orange represents the results of the same member but with an imperfection directed in the opposite sense (Eigenmode+ - EM+). It can be easily observed that the second order effects arise much faster for the member subject to EM-.

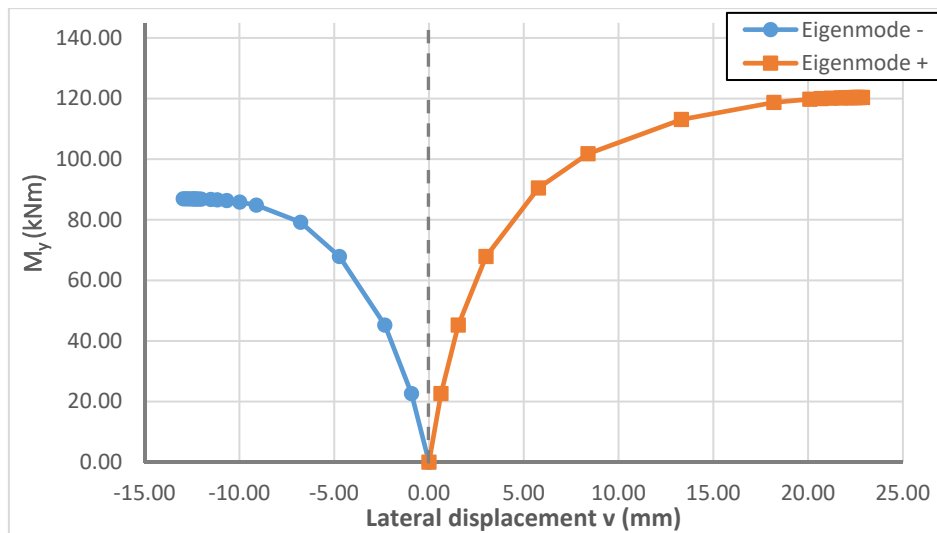


Figure 5-170: Load-displacement curve for member of UPE 300 section with a length of 4 m

Finally, Figure 5-171 shows the distribution of the von Mises stresses for the two members of Figure 5-170. For an easier visualisation of the results, the stiffener used for load introduction is not represented.

Comparing, Figure 5-171a) and b), one may easily observe that the member subject to imperfection EM+ attains a higher load level characterised by yielding that extends over a longer part of the member. In particular, this member yields under tension stresses at the bottom flange and under compression stresses at the intersection between the upper flange and the web. Conversely, the member subject to imperfection EM- yields only at the upper flange's tip under compression due to the combined action of major-axis bending introduced by the point load and second order minor-axis bending and the second order bi-moment. It has been shown in paragraph 5.5.6.2.4 that a positive minor-axis bending moment compressing the flange's tips can have a negative influence on elastic and elasto-plastic instability. This has also been confirmed in paragraph 5.2.1.6 (presenting a study on imperfection sensitivity). Consequently, the resistances of members subject to an imperfection EM- is significantly less than those of the members subject to EM+ for the studied load case of a point load applied at mid-span. It is recalled that this is not always the case for a constant major-axis bending moment due to the stress induced bi-moment that may counterbalance the effect of imperfection EM-. Therefore, the obtained results may be more favourable than those obtained with imperfection EM+ (see paragraph 5.2.1.6). As the stress induced bi-moment is concentrated at mid span for load case P1, it has much less effect than for constant major-axis bending moment and consequently has not the mentioned favourable effect on the member resistance.

Last, it should be mentioned that it seems justified here to base the choice of the lateral-torsional buckling curve on the results obtained with imperfection EM- not only as this ensures a lower bound solution but also as, due to the fabrication tolerances, it cannot be guaranteed that the point load is perfectly applied through the shear centre in practice. A slight eccentricity may have a huge effect on the resistance because it can lead to displacements generating a failure mode similar to the one represented in Figure 5-171a).

Finally, it can be concluded that the results represented in this paragraph justify the attribution of the **Eurocode 3 reduction curve c** for lateral-torsional buckling of U-shaped members. This choice covers the unfavourable failure mode leading to positive second order minor-axis bending moments compression the flanges' tips. Nevertheless, curve c is very safe-sided if the member fails under negative minor-axis bending (compressing the web). Consequently, it might be considered to authorize the use of reduction curve *a* in case of bi-axial bending with negative M_z . Yet, in practice, the definition of different reduction curves for major-axis bending only and for bi-axial bending seems to complicate the design and is therefore not pursued here.

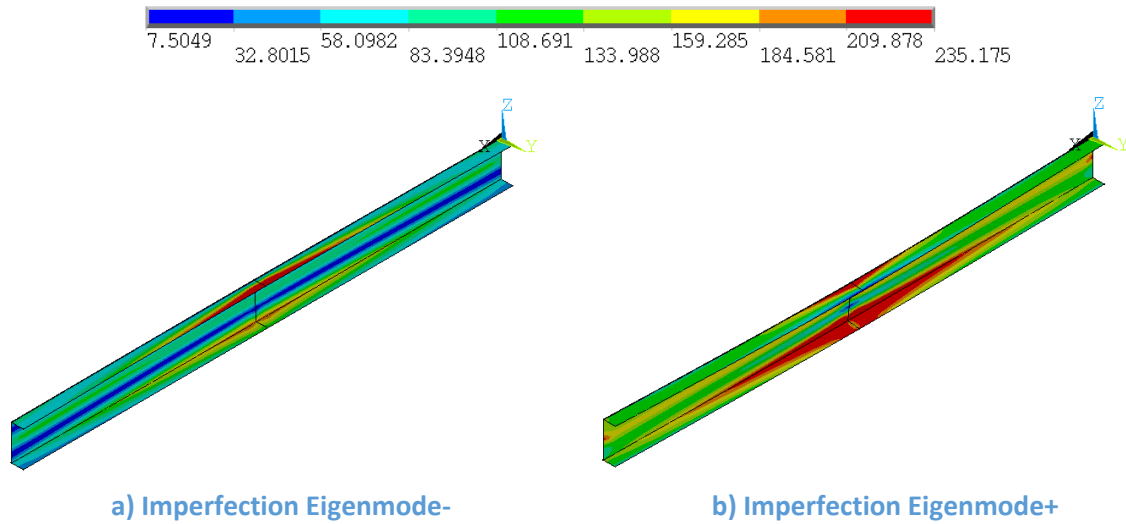


Figure 5-171: Distribution of von Mises stresses at the Ultimate Limit State for the member of UPE 300 section with a length of 4 m

5.6.4.4.3 Interaction between bi-axial bending and axial force

It is recalled that the current provisions given in Eurocode 3 Part 1-1 do not include interaction equations that can be applied to U-shaped members. In paragraph 5.3.3 an extension of the interaction equations proposed in reference (Kalameya 2008) has been presented. The interaction equations applicable to members of compact U sections are recalled in Eqs. (5.328) and (5.329).

$$\frac{N_{Ed}}{\text{Min}(\chi_y, \chi_{TF})N_R} + k_{yy} \frac{M_{y,Ed}}{\chi_{LT}M_{y,R}} + k_{yz} \frac{M_{z,Ed}}{1,25M_{z,el,R}} \leq 1,0 \quad (5.328)$$

$$\frac{N_{Ed}}{\text{Min}(\chi_z, \chi_{TF})N_R} + k_{zy} \frac{M_{y,Ed}}{\chi_{LT}M_{y,R}} + k_{zz} \frac{M_{z,Ed}}{1,25M_{z,el,R}} \leq 1,0 \quad (5.329)$$

The reduction factor linked to torsional-flexural buckling (χ_{TF}) is calculated based on the critical axial force $N_{cr,TF}$. Its expression is recalled in Eqs. (5.330) and (5.331).

$$N_{cr,TF} = \frac{I_0}{2(I_y + I_z)} \left(N_{cr,y} + N_{cr,T} - \sqrt{(N_{cr,y} + N_{cr,T})^2 - N_{cr,y}N_{cr,T} \frac{I_y + I_z}{I_0}} \right) \quad (5.330)$$

and

$$N_{cr,T} = \frac{1}{i_0^2} \left(GI_T + EI_w \frac{\pi^2}{L^2} \right) \quad (5.331)$$

$$I_0 = I_y + I_z + y_s^2 A \quad (5.332)$$

$$i_0^2 = \frac{I_y + I_z}{A} + y_s^2 \quad (5.333)$$

Also, it should be noted that the reduction factor χ_{TF} is calculated with the European buckling curve *c*.

It is recalled that Kalameya does not include Eq. (5.328) in his proposal as he considers buckling about the major- (*y*-) axis as negligible. Obviously, major-axis flexural buckling can take place if the member is sufficiently restrained against displacements along the minor-axis. So as to illustrate the influence of buckling about the major-axis, the example of a member of UPE 200 section is considered hereafter. The member is supposed to:

- possess fork supports at its end and to possess four equally spaced intermediate restraints;
- possess a total length of 4,6 m;
- be fabricated from S235;
- be subject to combined major-axis bending and axial force with a ratio $(M_y/M_{y,pl})/(N/N_{pl})$ equal to 0,5.

For the studied case, the first eigenmode is, not surprisingly, characterised by displacements along the *z*-axis only without torsional twist and displacements along the *y*-axis as shown in Figure 5-172 (the displacement boundary conditions as well as the applied loads are not represented).

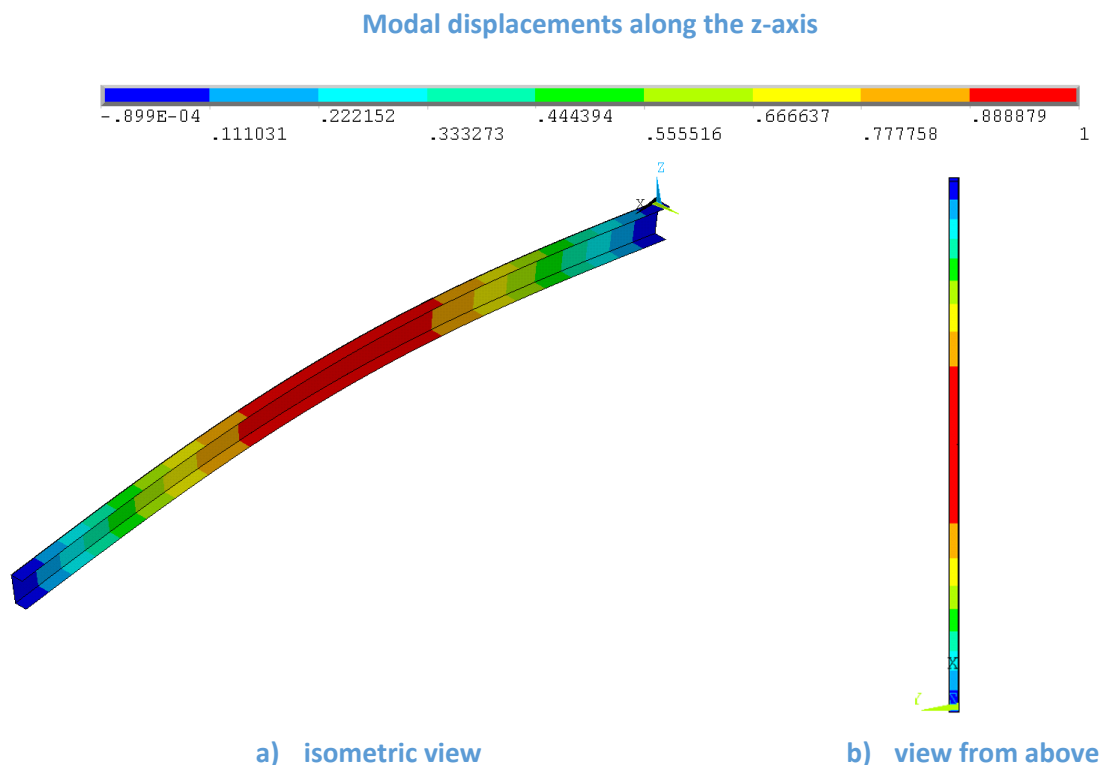


Figure 5-172: First eigenmode of the studied member

The member of Figure 5-172 is hereafter analysed through a GMNIA simulation including residual stresses, a geometric imperfection affine to the first eigenmode directed downwards with an amplitude of 4,6 mm ($L/1000$) and an additional geometric imperfection in the lateral direction with the same amplitude. Generally, it is not necessary to introduce this last supplementary

geometric imperfection but this done here in order to ensure that the lateral buckling mode may appear if it is relevant. Indeed, if the lateral imperfection is not introduced, lateral buckling is not always initiated even in cases where it is relevant (members without lateral restraints).

Figure 5-173 presents the load displacement curve of the member with reference to the axial compression force and the vertical displacement (here positive downwards). The numerical results represent a typical load displacement curve indicating failure by elasto-plastic instability. The peak load is obtained in point A and corresponds to an axial force of 410 kN and a major-axis bending moment of 17 kNm. The resulting ratio $(M_y/M_{y,pl})/(N/N_{pl})$ is equal to 0,54. It is slightly higher than the same ratio calculated for the applied loads due to the second order effects.

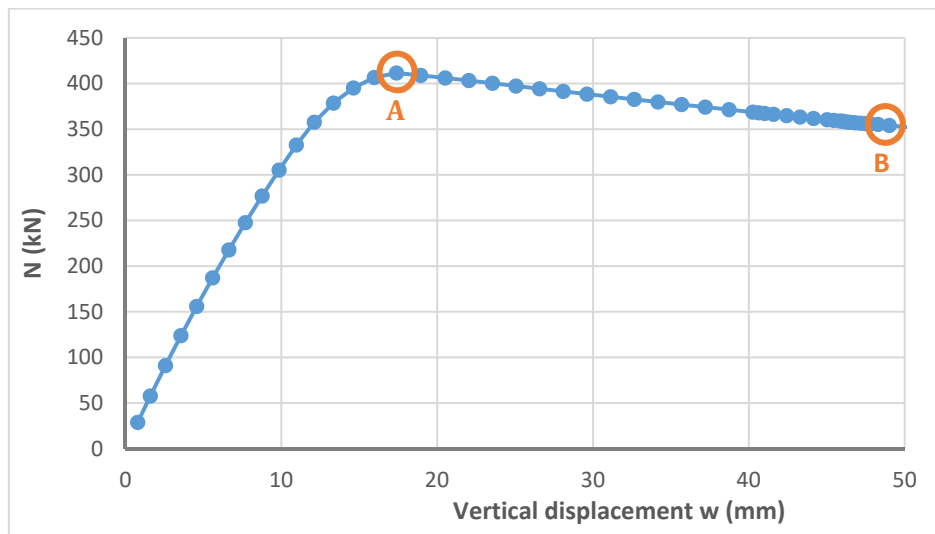


Figure 5-173: Load displacement curve of the studied member

Figure 5-174 and Figure 5-175 represent the von Mises stress distribution for the member at its ultimate limit state (Point A of Figure 5-173) and at Point B further downwards on the load-displacement curve. On may easily observe yielding of the member in its upper part due to the combined action of the axial force and the bending moments. Moreover, the deformed shape represented in Figure 5-175 suggests the failure mode of major-axis flexural buckling. Owing to the intermediate lateral restraints the member possesses practically no out-of-plane displacements (along the y-axis).

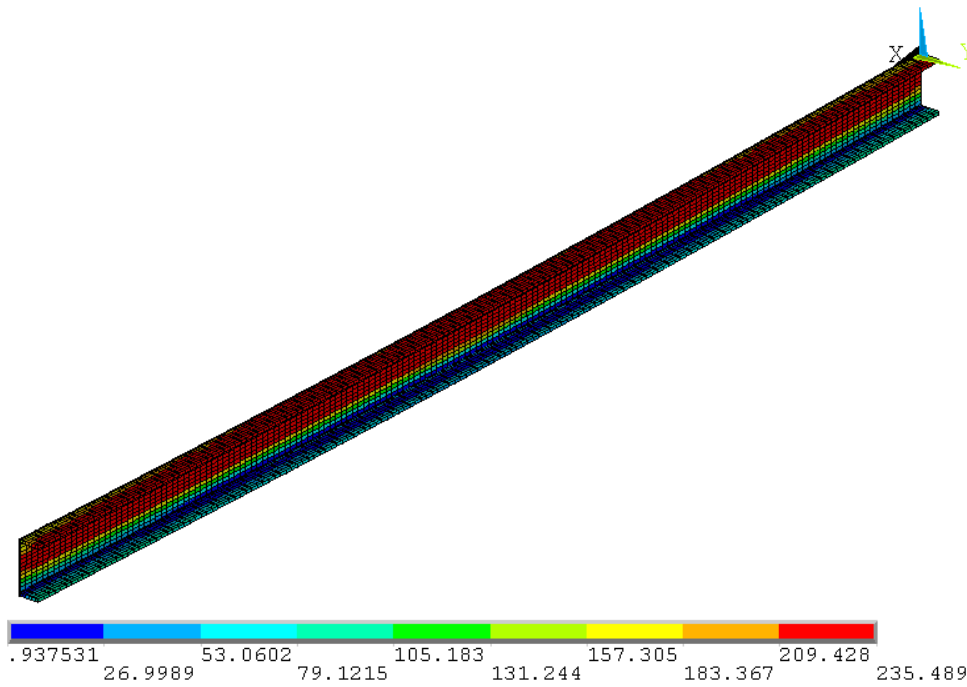


Figure 5-174: Von Mises stress distribution of the member at Point A of Figure 5-173

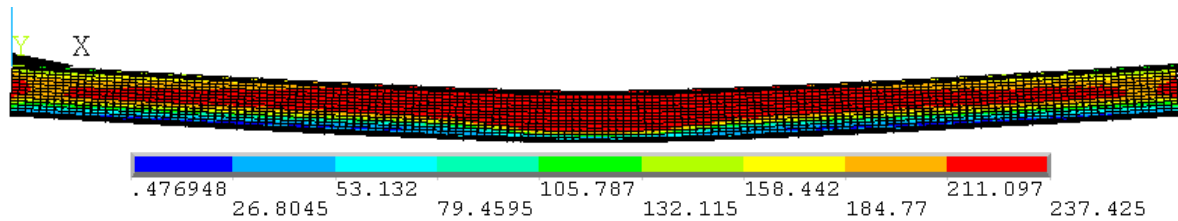


Figure 5-175: Von Mises stress distribution of the member at Point B of Figure 5-173

The example studied here before clearly indicated that major-axis flexural buckling is a relevant failure mode for U-shaped members. Admittedly, this failure mode only occurs if the member is sufficiently restrained against out-of-plan displacements. Still, in practice members often possess these restraints and therefore the failure mode of major-axis flexural buckling is also of practical interest.

It should however be noted that Eq. (5.329) also covers partially the failure mode of major-axis flexural buckling even if it is not intended to do so. Indeed, for the member studied before the critical axial force for minor-axis buckling $N_{cr,z}$ as well as for torsional buckling $N_{cr,T}$ are much higher than the critical axial force for major-axis buckling. The critical axial force for torsional-flexural buckling is calculated depending on $N_{cr,T}$ and the critical axial force for major-axis flexural buckling $N_{cr,y}$ with Eq. (5.344). If $N_{cr,T}$ is much higher than $N_{cr,y}$ the resulting critical axial force for torsional flexural buckling simply tends to $N_{cr,TF} = N_{cr,y}$. Consequently, the failure mode of major-axis flexural buckling is also introduced into Eq. (5.329) through the critical axial force $N_{cr,TF}$. Nonetheless, the second order effects linked to the major-axis bending moment are not covered completely by the interaction factor k_{zy} associated with M_y in Eq. (5.329) as this factor has been calibrated for combined minor-axis flexural buckling and lateral-torsional buckling. Therefore, it

seems more consistent to verify the resistance of U-shaped members with Eqs. (5.329) **and** (5.328) so as to ensure that all failure modes are covered. However, it may seem somewhat inconsistent to keep the reduction factor for torsional-flexural buckling in Eq. (5.329) as it represents rather an interaction between torsional buckling and buckling about the major-axis. Nonetheless, it is recalled that in case of failure by pronounced major-axis buckling, Eq. (5.328) becomes relevant for design. Additionally, as the interaction factor have not been calibrated for torsional buckling modes it is recommended here to keep the reduction factor χ_{TF} in Eqs. (5.329) and (5.328) so as to ensure the safeness of the strength predictions. The resulting inconsistency is accepted for the ease of application. Additionally, the objective of this thesis is not to develop a completely new set of interaction equations for U-shaped members but to extend existing proposal to the case of torsion, in particular if these proposal are already in the format of Eurocode 3 Part 1-1. Obviously, the extension can only be envisaged if sufficient safeness is given for members not subject to torsion. Therefore, both interaction equations (Eqs. (5.329) and (5.328)) are evaluated with reference to the numerical GMNIA simulations for members under combined axial force and bi-axial bending, including members subject to point loads (load cases P1 and P2).

First, the case of combined compression axial force and constant bending moments is investigated. It should be noted that this case has already been treated in reference (Kalameya 2008). So as to facilitate the interpretation of the cases studied in the previous paragraph, i.e. members under a sole major-axis bending moment, are not studied again.

Figure 5-176 represent a statistical evaluation of the interaction equations (5.328) and (5.329). It is clear that the approach may be safely applied. Indeed, no single result in unsafe. Additionally, the mean value of the results is approximatively equal to 0,85 and consequently rather satisfactory. Last, it should be noted that the standard deviation of 8% is also acceptable especially for the given complexity of the studied case.

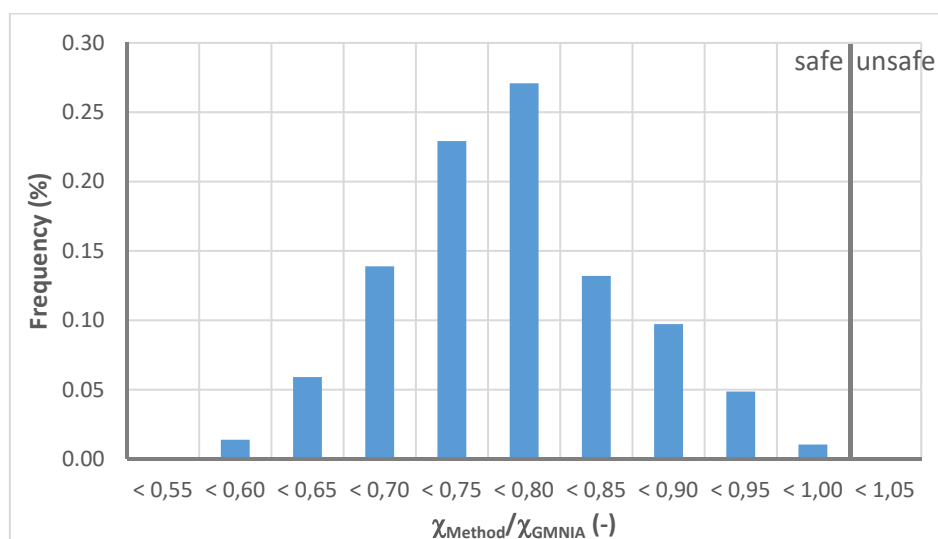


Figure 5-176: Ratio between predicted resistance and numerically obtained resistance

So as to analyse the results further on, Figure 5-177 shows the numerically obtained ultimate resistance curves as well as the strength predictions obtained with Eqs. (5.328) and (5.329) for the example of a member of UPE 200 section. Clearly, the results confirm the complexity of the studied case. In particular, one may observe that:

- There is an important gap between the curve linked to combined axial force and major-axis bending and the curves linked to combined axial force and bi-axial bending. This gap can be explained based on the failure mode as for the case of members under major-axis bending only. Indeed, the stress induced bi-moment leads to a favourable failure mode in case of constant major-axis bending. Conversely, the applied positive minor-axis bending moment induces compression in the flanges tips and consequently leads to an unfavourable failure mode causing the observed gap even if for low minor-axis bending;
- The curves linked to combined bi-axial bending and a compression axial force are very close, especially for in the low slenderness range. For higher values of the relative slenderness, the three curves seem to move from each other;
- The general shape of the ultimate resistance curves linked to the design model appears to correspond well to the GMNIA predicted ultimate resistance curves. The resistance predicted for the member subject to combined axial force and major-axis bending is obviously very safe-sided as the favourable effect of the stress induced bi-moment is not accounted for. The curves linked to bi-axial bending are also safe-sided but less. The limitation of the minor-axis bending resistance to $1,25M_{el,z}$ seems to be too conservative. The curve linked to combined axial force and minor-axis bending seems to be rather safe-sided, too. Again, the limitation to $M_R = 1,25M_{el,z}$ leads to the observed discrepancies as shown in Figure 5-178.

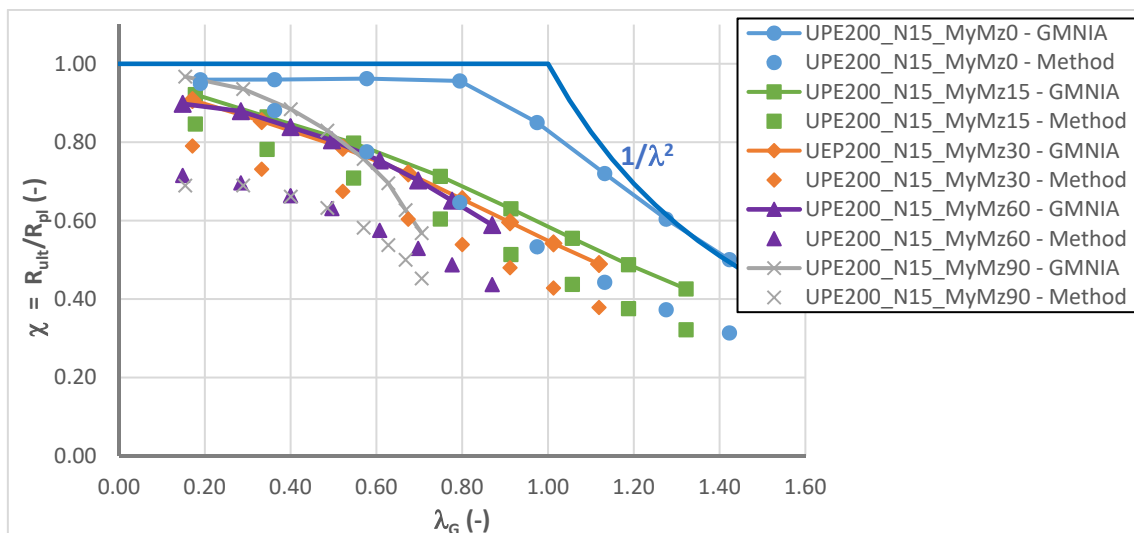


Figure 5-177: Ultimate resistance curves for a member of UPE 200 section subject to combined axial force and bi-axial bending

Figure 5-178 shows that it seems acceptable to use the full plastic minor-axis bending moment as reference value. Actually, the strength prediction obtained are very close to the numerical values especially for short members whose failure is characterised by important yielding. For longer members, the improvement of the precision through the introduction of $M_{z,pl}$ is also visible. Obviously, for these long members the precision of the results of the interaction equations is highly increased for the members subject to high minor-axis bending moments (UPE200_N15_MyMz60 and UPE200_N15_MyMz90) but it is much less increased for the cases subject to low minor-axis bending moments as they less influence the resistance of the member. Additionally, it has to be noted that the precision of the results also depend on the form of the plastic interaction between the internal forces and moments. In fact, for the more compact UPE 80 section, the strength predictions are less precise compared to the numerically determined reference values, even if the interaction equations (5.328) and (5.329) are based on the plastic minor-axis bending moment resistance.

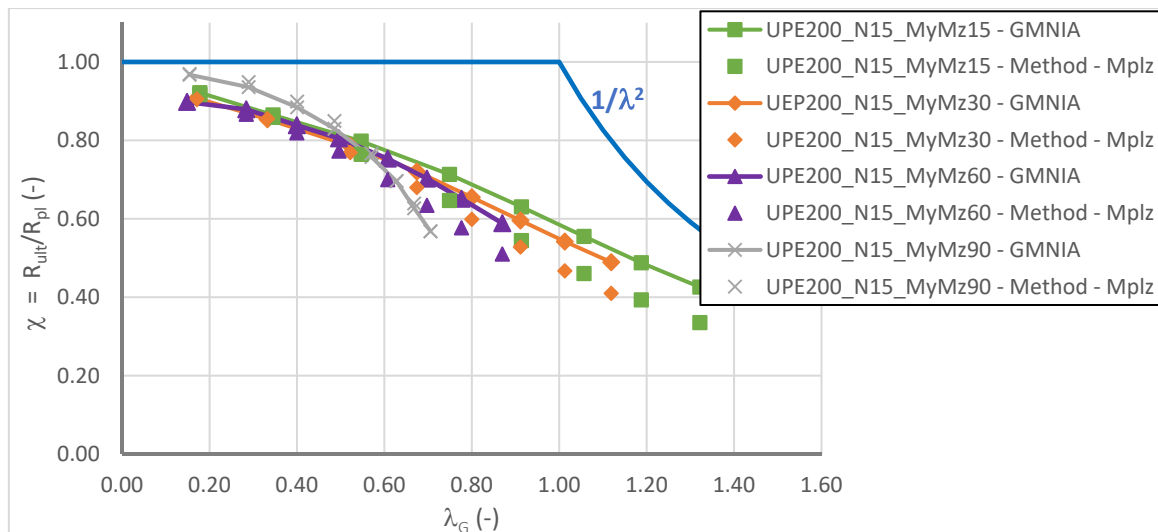


Figure 5-178: Ultimate resistance curves for a member of UPE 200 section subject to combined axial force and bi-axial bending

Figure 5-179 compares the numerically determined ultimate resistance curves to the strength predictions obtained with Eqs. (5.328) and (5.329) for members of UPE 80 section. Most obviously, the interaction equations are again highly safe-sided for members under combined axial force and major-axis bending as these members fail in a favourable mode owing to the stress induced bi-moment. For bi-axial bending, the strength predictions are also rather safe-sided and this not only for long members but also for very short members that do not fail by predominant instability but by yielding of the most loaded section. This seems surprising as the resistance of short members of UPE200 section has been predicted very precisely. Conversely to members under bi-axial bending and axial force, the case of combined axial force and minor-axis bending seems to be represented rather well, especially for long members. Clearly, the failure mode of flexural buckling, relevant for these members, is less complex than failure by combined flexural and lateral-torsional buckling relevant for members subject to a compression axial force and major-axis bending. Consequently, the simple interaction equations can capture the behaviour of

members subject to axial force and minor-axis bending very well. Nonetheless, if the relative slenderness decreases the precision of the design model decreases, too because the plastic cross-section interaction is not represented sufficiently precisely to obtain results that are closer to the numerically determined resistance. This is illustrated by Figure 5-180.

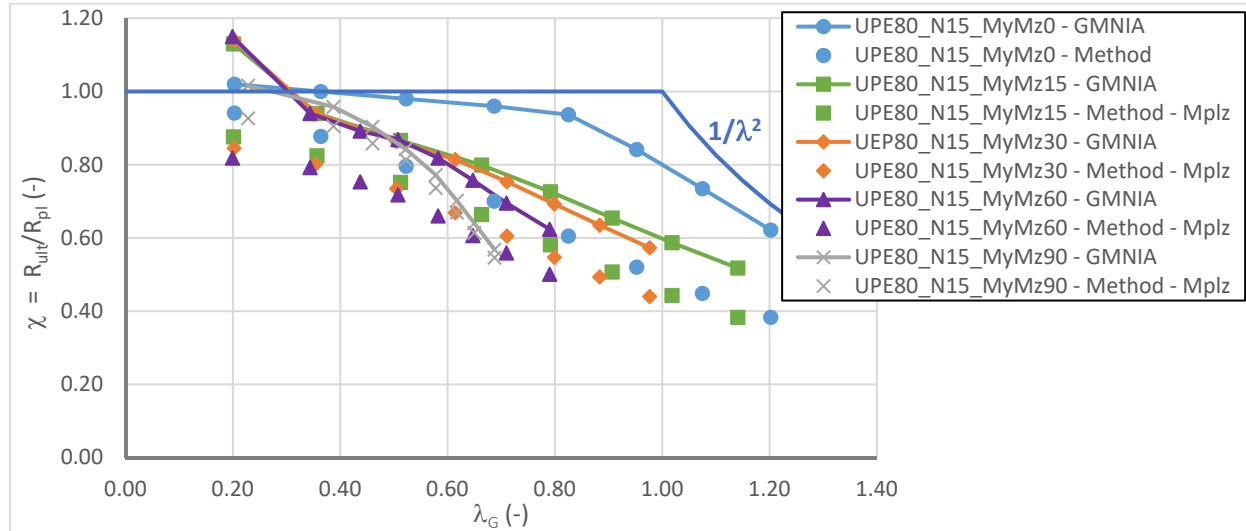


Figure 5-179: Ultimate resistance curves for a member of UPE 80 section subject to combined axial force and bi-axial bending

Figure 5-180 represents the ratio between the plastic load amplification factor determined through MNA calculations of the studied members and the plastic load amplification factor determined based on the plastic linear interaction of Eq. (5.334).

$$R_{pl,L} = \frac{1}{\frac{N_{Ed}}{N_{pl}} + \frac{M_{y,Ed}}{M_{y,pl}} + \frac{M_{z,Ed}}{M_{z,pl}}} \quad (5.334)$$

Figure 5-180 clearly indicates that the plastic cross-section interaction is significantly more non-linear for the UPE 80 section than for the UPE 200 section for the given load combinations. Indeed, the ratio between the non-linear plastic load amplification factor $R_{pl,MNA}$ and the linear one $R_{pl,L}$ attains 1,22 for the UPE 80 section whereas the difference between both amplification is only of about 10% for the UPE 200 section. Therefore, the simplified interaction used in Eqs. (5.328) and (5.329) is much more precise for short members of UPE 200 section than for the same members of UPE 80 section as shown in Figure 5-178 and Figure 5-179. In general, the precision of the interaction equations depends on the importance of the non-linearity of the plastic cross-section interaction. With the objective to propose a simple and safe-sided design method, it has to be accepted to loose precision in some cases. Additionally, it is recalled that the discrepancy for short U-shaped members is not significantly increased compared to short members of I section designed based on the interaction equations of Eurocode 3 Part 1-1. Here, it appears that only global design methods, as the Overall Interaction Concept (OIC), that are based on a precisely determined plastic load amplification factor could improve the strength prediction for short

members. The quality of the OIC approach is investigated in paragraph 5.6.5 for complex load combinations but only for I-shaped members.

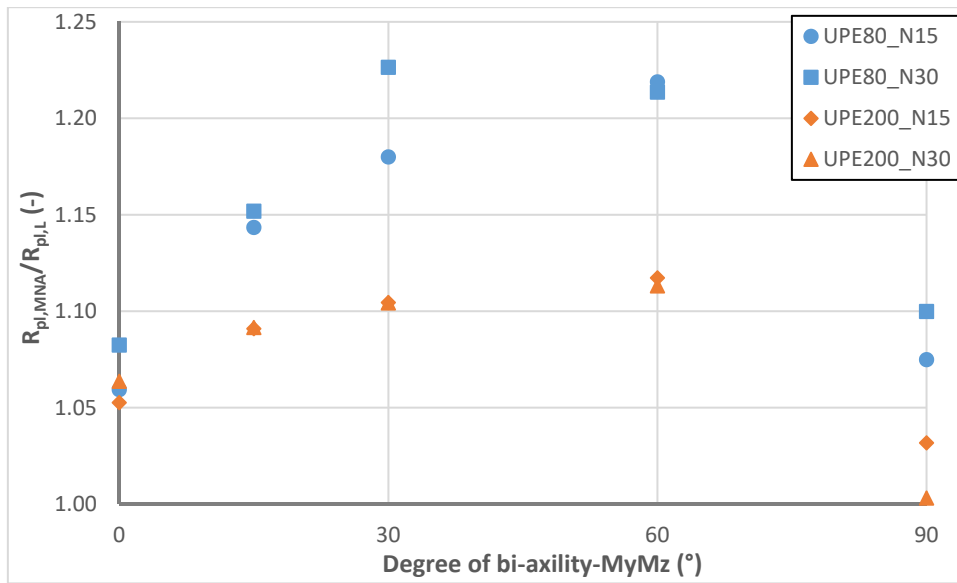


Figure 5-180: Importance of non-linearity on the plastic interaction of U section

Hereafter the load cases P1 and P2 are studied. It should be noted that these load case have not been considered in reference (Kalameya 2008).

First, Figure 5-181 represents a global evaluation of the interaction equation for load cases P1 and P2. It may be seen that the interaction equations are more conservative than in case of constant bending moments. The mean value of the ratio $\chi_{Method}/\chi_{GMNIA}$ is only of about 0,71 (0,85 for constant bending moments). Also, the scatter of the results is higher as represented by the standard deviation that attains 0,12 (0,08 for constant bending). Nonetheless, there only very few unsafe strength predictions and the design method can therefore be applied even for variable bending moments.

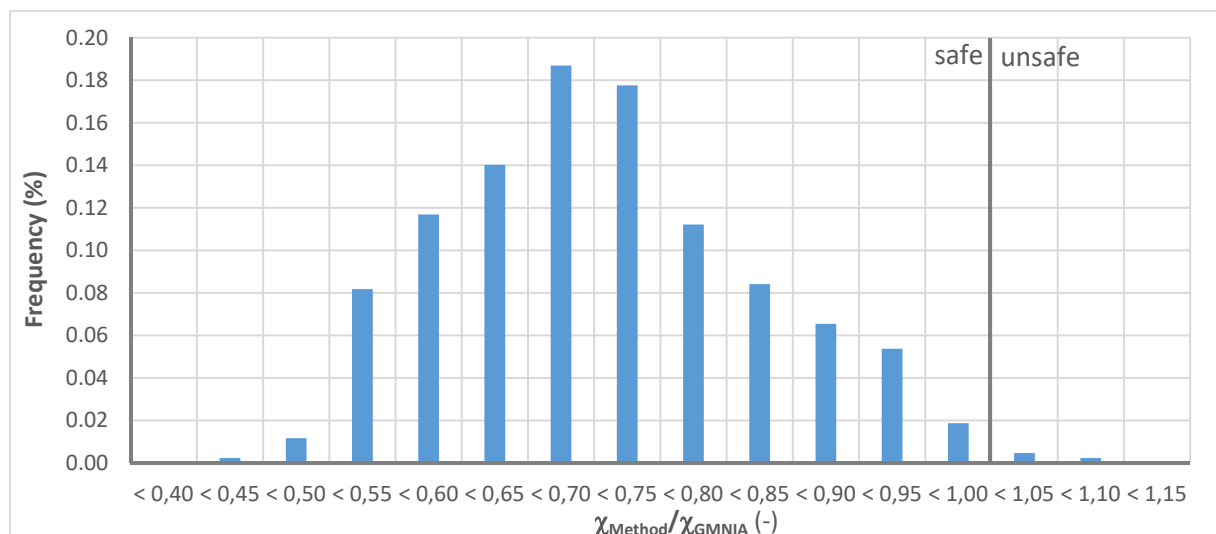


Figure 5-181: Ratio between predicted resistance and numerically obtained resistance

In order to get a clearer idea of the reasons leading to the conservatism of the design approach, the example of a UPE 200 section under combined axial force and bi-axial bending is studied in Figure 5-182. The numerical results show that short members may attain a significant level of strain hardening. In fact, the shortest specimen of case UPE200_N15_MyMz0 fails due to the high transversal shear force. As the member is short and the cross-section is compact, neither local nor member instability influences the resistance. Strain hardening may therefore be completely mobilised and increases the ultimate resistance by a ratio $f_u/f_y = 1,53$ compared to the plastic resistance of the member. The strain hardening reserve that can be mobilised by the most loaded section decreases with increasing value of the minor-axis bending moment as the shear force V_z , leading to yielding of the web, interacts with the minor-axis bending moment. In case of combined minor-axis bending and axial force, a higher level of the strain hardening reserve can be reached by the most loaded section as the interaction with the shear force V_z vanishes. For longer specimen the reduction due to elasto-plastic member instability can be easily observed. Figure 5-182 shows that the behaviour of the members subject to point loads applied at mid-span is similar to the members under constant bending moments. Again, the case of major-axis bending is much more favourable than the case of bi-axial bending. Nonetheless, the gap between the curve linked to MyMz0 and the other curves is less pronounced than in case of constant bending moments as the stress induced bi-moment loses its influence because it only acts in the proximity of the load application. As before, the curves linked to bi-axial bending are very close with a maximum difference of about 10% for intermediate and high values of the relative slenderness. For combined minor-axis bending and axial force, one may observe that the shape of the ultimate resistance curve is different than in case of constant bending moments (see Figure 5-177). In fact, the reduction is much less pronounced for the longer specimen. This difference results certainly from the shape of the bending moment diagram because for the bi-triangular moment distribution, introduced by the point load, the second order effects are less important. Nonetheless, the second order effects appear to be well accounted for by the interaction equations, both, in case of constant minor-axis bending as shown in Figure 5-177 and in case of variable bending as represented in Figure 5-182. Yet, for shorter specimen the strength predictions of the interaction equations become rather conservative. This is the case, not only for minor-axis bending and axial force, but also for combined bi-axial bending and axial force. For the cases studied here, it seems that the discrepancy results not from the approximation of the cross-section interaction but rather from the influence of strain hardening. In fact, Figure 5-178, treating the same members subject to constant bending moments, show that the plastic cross-section resistance is sufficiently approximated for this combination of internal forces and moments (owing to the higher degree of non-linearity of the interaction, this is not the case for the UPE 80 section studied in Figure 5-180).

For longer members the effect of elasto-plastic instability seems to be overestimated again by the interaction equations leading to rather conservative results in the range of intermediate to high values of the relative slenderness. The differences are in the same range as for constant bending moment diagrams.

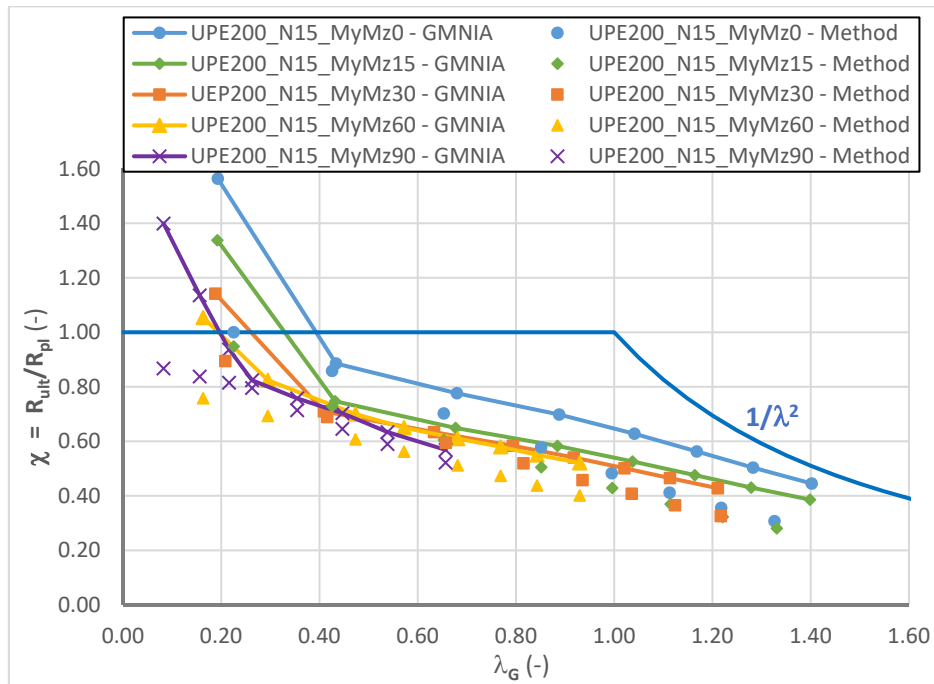


Figure 5-182: Ultimate resistance curves for a member of UPE 200 section subject to combined axial force and bi-axial bending – Load case P1

Up to this point, it has been shown that:

- Eqs. (5.328) and (5.329) can be safely applied to design U-shaped members subject to combined compression and bi-axial bending;
- The interaction equations are, however, very conservative if they are used with the limitation of the minor-axis bending moment resistance to $1,25 M_{el,z}$. If this limitation is abandoned the design model becomes more precise, especially for short members subject to constant bending moments. For members under variable bending, the influence of strain hardening leads again to rather conservative results for short members;
- Additionally, depending on the degree of non-linearity of the plastic-cross-section interaction for a given combination of internal forces and moments and a given section, the interaction equations may be rather safe-sided for short members;
- For longer members the strength predictions obtained with the interaction equations become conservative. It appears that the influence of elasto-plastic instability is overestimated for intermediate to high values of the relative member slenderness.

The investigations presented throughout this paragraph revealed that the interaction equations are in general conservative. In average the interaction equations are 21% safe-sided (all load cases; 15% safe-sided for constant bending moments and 28% safe-sided for variable bending moments). It is recalled that the average value of the resistance predictions is 14% safe-sided in case of double symmetric I sections. Consequently, the conservatism of the interaction equations is increased, yet this may be acceptable considering the complexity of the studied case and the

simplicity of the applied interaction equations. It seems necessary to enlarge the study in order to ameliorate the precision of the design approach. Nonetheless, this is not done here. Rather, it is studied if the interaction equations may be extended to the case of an applied torsional moment as done in paragraphs 5.6.4.2 and 5.6.4.3 for double and mono-symmetric I sections.

5.6.4.4.4 Interaction between bi-axial bending, axial force and torsion

Hereafter, the extension of the interaction equations to the load case of an applied additional torsional moment is studied. As for I sections, it is supposed that the expression of the interaction factor k_{yz} and k_{zz} can be applied to the bi-moment. It should however be recalled that this may be discussable for U sections because, contrariwise to I sections, the bi-moment and the minor-axis bending moment are not affine in the section. Nonetheless, it has been shown that the plastic interaction between the bi-moment and the minor-axis bending moment may be described by a interaction but it possesses two cut-off limits ($M_z = M_{z,pl}$ if $B \leq 0,1 B_{pl}$ and $B = B_{pl}$ if $M_z \leq 0,1 M_{z,pl}$). Moreover, the interaction between major-axis bending and the bi-moment has been shown to be slightly un-symmetric. Yet, for the ease of application, these special features of the plastic cross-section interaction are not accounted for in the interaction equations describing the member resistance. In any case, for longer members, the effect of elasto-plastic instability leads to failure before the most loaded section of the member attains complete yielding and hence the cross-section interaction becomes more and more linear with the member length (see paragraph 5.6.5.3 for a deeper discussion). Therefore, only the resistance prediction for short members is affected. Since the torsional plastic system reserve has even a higher influence on the member behaviour than the assumed shape of the plastic cross-section interaction curve, it seems acceptable to neglect its cited specific features. For very short members, this simplification leads again to a discontinuity in the design method. But, this discontinuity is not higher than the existent one for members not subject to torsion.

In the following, the majority of the members have to be considered as sensitive to elasto-plastic instability (minimum relative member slenderness is always higher than 0,2, i.e. the assumed plateau length linked to the respective failure modes of flexural, flexural-torsional and lateral-torsional buckling). Yet, some members are only subject to combined minor-axis bending and torsion, and hence, they are not sensitive to elasto-plastic instability.

Figure 5-183 represents a global evaluation of the results obtained with the interaction equations. Again, it appears that the design model is rather conservative. In particular, the conservatism is increased compared to members not subject to torsion. Indeed, the mean value of the ratio $\chi_{Method}/\chi_{GMNIA}$ decreases from 0,79 for members not subject to torsion to approximately 0,70 for members subject to torsion and the standard deviation increases from 0,08 to 0,13. Nonetheless, this loss of precision of the interaction equations is partially due to some very safe-sided results obtained for short members with values of the overall member slenderness lower than 0,2 as shown in Figure 5-184. If these short members possessing an overall slenderness of less than 0,2 are not accounted for, the mean value of the ratio $\chi_{Method}/\chi_{GMNIA}$ is equal to 0,73 and the standard deviation reduces slightly to 0,12. The resistance of the shortest members is again highly

influenced by the plastic torsional system reserve that is not considered in the interaction equations. Yet, it is recalled that a simplified method has been proposed to account for this supplementary strength reserve during the analysis of the member. In any case, it seems that a reduction of 6% (or even of 9% if short members are considered) is acceptable for the more complex load case of an applied torsional moment.

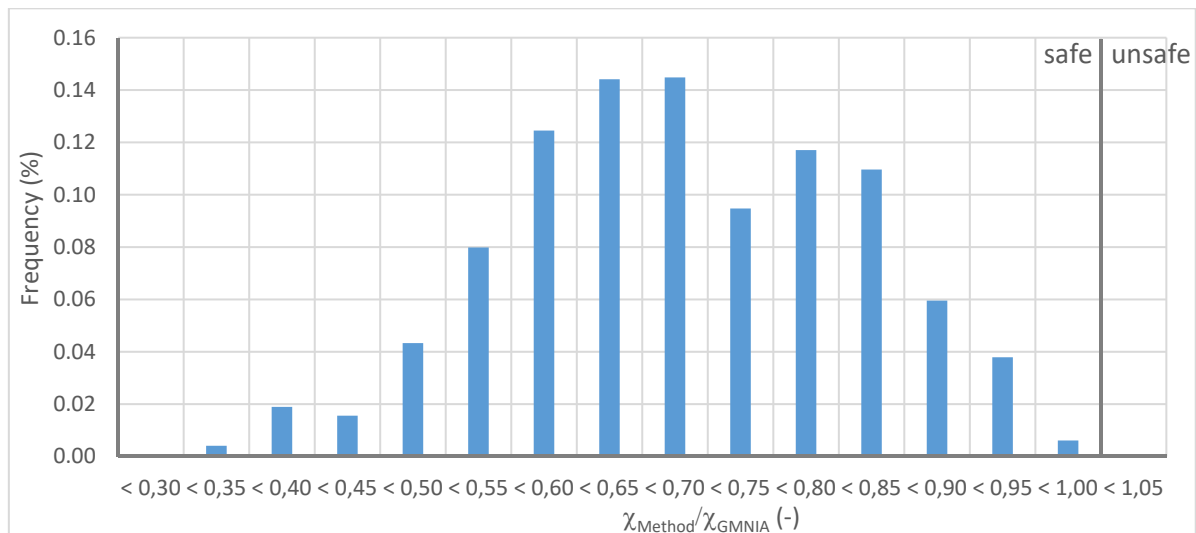


Figure 5-183: Ratio between predicted resistance and numerically obtained resistance

In Figure 5-184, the ratio $\chi_{Method}/\chi_{GMNIA}$ is represented as a function of the relative slenderness λ_G . As mentioned above, very conservative results are obtained for short members and members not sensitive to elasto-plastic instability (only subject to M_z and B). For these last members the plastic torsional system reserve is at the only origin of the observed discrepancy. Indeed, if the members are subject to a combination of minor-axis bending and bi-moments only, the plastic-cross-section interaction is applied and not the interaction formulae of Eqs. (5.328) and (5.329). Since the applied adapted PIFM leads to very precise results for the plastic cross-section interaction, it is clear that the generation of the warping hinge and consequently the supplementary system reserve leads to very conservative results, as this effect is not considered in the interaction equations. For members that are also subject to minor-axis bending and/or to an axial force, the approximation of the plastic interaction between the bi-moment and the other internal forces and moments on the cross-section level also contributes to the loss of precision of the interaction equations. At this point it appears that only a more precise approximation of the shape of the plastic cross-section interaction between the **four** internal forces and moments (M_y , M_z , N, B) may ameliorate the precision of the results.

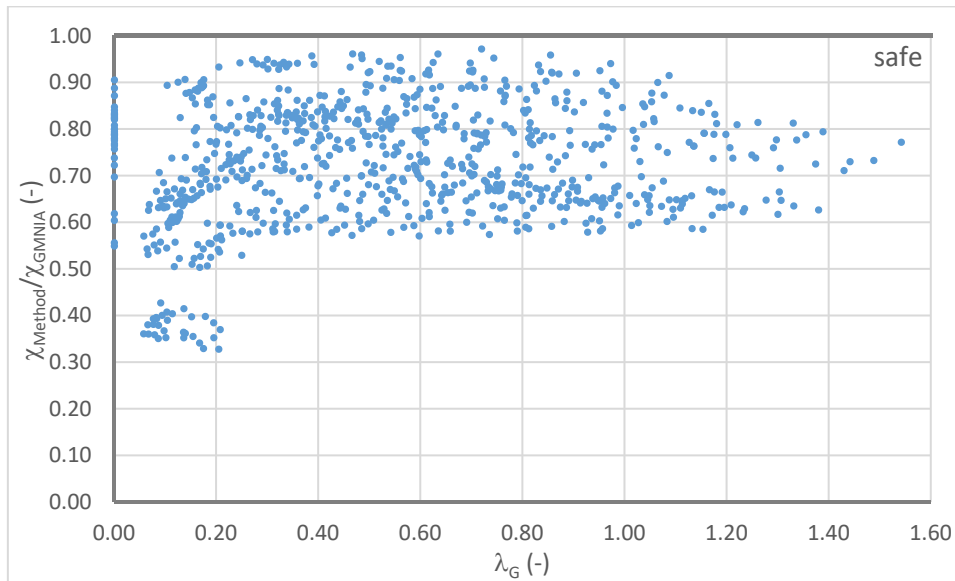


Figure 5-184: Ratio between resistance obtained with Eqs. (5.328) and (5.329) and numerically obtained resistance

It is recalled that the design method presented in reference (Stangenberg 2007) and in paragraph 5.4.3.3 considers a specific cross-section interaction for U-shaped members. This design approach has been validated in (Stangenberg 2007) for combined bi-axial bending and torsion but, despite the more precise approximation of the plastic cross-section interaction, this author obtains a mean value of the ratio $\chi_{Method}/\chi_{GMNIA}$ of 0,75. Consequently, the specific interaction leads only to an increase of about 5% of the precision compared to the simplified interaction equations proposed here and only in a more restrained field of application (Stangenberg does not include a compression axial force for U-shaped members). It appears that only a significant increase of the complexity of the interaction factors could lead to an appreciable amelioration of the precision of the interaction factors. Therefore, the conservatism of the interaction equations is accepted here for the complex combination of internal forces and moments including torsion.

5.6.4.5 Summary of the design of members subject to torsion based on interaction equations

Hereafter, the design proposals developed and validated in paragraph 5.6.4 are summarised. For double symmetric I sections the current Eurocode 3 Part 1-1 interaction equations provided for the member design are extended as shown in Eqs. (5.335) and (5.336) (the partial factors γ_{M1} are omitted here). The interaction factors k_{ij} are based on the Annex B expressions of Eurocode 3 Part 1-1 (CEN 2005a). They are recalled in Table 5-45.

$$\frac{N_{Ed}}{\chi_y N_R} + k_{yy} \frac{M_{y,Ed}}{\chi_{LT} M_{y,R}} + k_{yz} \frac{M_{z,Ed}}{M_{z,R}} + k_{yw} \frac{B_{Ed}}{B_R} \leq 1,0 \quad (5.335)$$

$$\frac{N_{Ed}}{\chi_z N_R} + k_{zy} \frac{M_{y,Ed}}{\chi_{LT} M_{y,R}} + k_{zz} \frac{M_{z,Ed}}{M_{z,R}} + k_{zw} \frac{B_{Ed}}{B_R} \leq 1,0 \quad (5.336)$$

Table 5-43 : Interaction factors k_{ij} for double symmetric I sections

Interaction factor	Class 1 and Class 2 sections	Class 3 and Class 4 sections
k_{yy}	$\bar{\lambda}_y < 1,0:$ $k_{yy} = C_{my} \left(1 + (\bar{\lambda}_y - 0,2) \frac{N_{Ed}}{\chi_y N_R} \right)$ $\bar{\lambda}_y \geq 1,0:$ $k_{yy} = C_{my} \left(1 + 0,8 \frac{N_{Ed}}{\chi_y N_R} \right)$	$\bar{\lambda}_y < 1,0:$ $k_{yy} = C_{my} \left(1 + 0,6 \bar{\lambda}_y \frac{N_{Ed}}{\chi_y N_R} \right)$ $\bar{\lambda}_y \geq 1,0:$ $k_{yy} = C_{my} \left(1 + 0,6 \frac{N_{Ed}}{\chi_y N_R} \right)$
k_{yz}	$k_{yz} = 0,6 k_{zz}$	$k_{yz} = k_{zz}$
k_{zy}	$\bar{\lambda}_z < 0,4 :$ $k_{zy} = \bar{\lambda}_z + 0,6$ $0,4 \leq \bar{\lambda}_z < 1,0 :$ $k_{zy} = 1 - \frac{0,1 \bar{\lambda}_z}{C_{mLT} - 0,25} \frac{N_{Ed}}{\chi_z N_R} :$ $\bar{\lambda}_z \geq 1,0 :$ $k_{zy} = 1 - \frac{0,1}{C_{mLT} - 0,25} \frac{N_{Ed}}{\chi_z N_R}$	$\bar{\lambda}_z < 1,0 :$ $k_{zy} = 1 - \frac{0,05 \bar{\lambda}_z}{C_{mLT} - 0,25} \frac{N_{Ed}}{\chi_z N_R}$ $\bar{\lambda}_z \geq 1,0 :$ $k_{zy} = 1 - \frac{0,05}{C_{mLT} - 0,25} \frac{N_{Ed}}{\chi_z N_R}$
k_{zz}	$\bar{\lambda}_z < 1,0 :$ $k_{zz} = C_{mz} \left(1 + (2\bar{\lambda}_z - 0,6) \frac{N_{Ed}}{\chi_z N_R} \right)$ $\bar{\lambda}_z \geq 1,0 :$ $k_{zz} = C_{mz} \left(1 + 1,4 \frac{N_{Ed}}{\chi_z N_R} \right)$	$\bar{\lambda}_z < 1,0 :$ $k_{zz} = C_{mz} \left(1 + 0,6 \bar{\lambda}_z \frac{N_{Ed}}{\chi_z N_R} \right)$ $\bar{\lambda}_z \geq 1,0 :$ $k_{zz} = C_{mz} \left(1 + 0,6 \frac{N_{Ed}}{\chi_z N_R} \right)$
k_{yw}	$k_{yw} = 0,6 k_{zw}$	$k_{yw} = k_{zw}$
k_{zw}	$\bar{\lambda}_z < 1,0 :$ $k_{zw} = C_{mw} \left(1 + (2\bar{\lambda}_z - 0,6) \frac{N_{Ed}}{\chi_z N_R} \right)$ $\bar{\lambda}_z \geq 1,0 :$ $k_{zw} = C_{mw} \left(1 + 1,4 \frac{N_{Ed}}{\chi_z N_R} \right)$	$\bar{\lambda}_z < 1,0 :$ $k_{zw} = C_{mw} \left(1 + 0,6 \bar{\lambda}_z \frac{N_{Ed}}{\chi_z N_R} \right)$ $\bar{\lambda}_z \geq 1,0 :$ $k_{zw} = C_{mw} \left(1 + 0,6 \frac{N_{Ed}}{\chi_z N_R} \right)$

So as to adapt the interaction equations to the case of U-shaped members, the torsional flexural buckling mode should be accounted for as shown in Eqs. (5.337) and (5.338). It may be noted that the interaction coefficients k_{ij} given in Table 5-45 may be used.

$$\frac{N_{Ed}}{\text{Min}(\chi_y, \chi_{TF})N_R} + k_{yy} \frac{M_{y,Ed}}{\chi_{LT}M_{y,R}} + k_{yz} \frac{M_{z,Ed}}{M_{z,R}} + k_{yw} \frac{B_{Ed}}{B_R} \leq 1,0 \quad (5.337)$$

$$\frac{N_{Ed}}{\text{Min}(\chi_z, \chi_{TF})N_R} + k_{zy} \frac{M_{y,Ed}}{\chi_{LT}M_{y,R}} + k_{zz} \frac{M_{z,Ed}}{M_{z,R}} + k_{zw} \frac{B_{Ed}}{B_R} \leq 1,0 \quad (5.338)$$

Finally, the resistance of mono-symmetric I sections can be verified with the interaction formulae given in Eqs. (5.339) to (5.341). The specific interaction factors k_{yy} and k_{zy} of Table 5-44 should be used as recommended by Kaim in reference (Kaim 2004). The interaction factors k_{yz} , k_{yw} , k_{zz} and k_{zw} may be used as provided in Table 5-43.

$$\frac{N_{Ed}}{\chi_y N_R} + k_{yy} \frac{M_{y,Ed}}{\chi_{LT,cf}M_{y,R}} + k_{yz} \frac{M_{z,Ed}}{M_{z,R}} + k_{yw} \frac{B_{Ed}}{B_R} \leq 1,0 \quad (5.339)$$

$$\frac{N_{Ed}}{\chi_{TF}N_R} + k_{zy} \frac{M_{y,Ed}}{\chi_{LT,cf}M_{y,R}} + k_{zz} \frac{M_{z,Ed}}{M_{z,R}} + k_{zw} \frac{B_{Ed}}{B_R} \leq 1,0 \quad (5.340)$$

$$\frac{N_{Ed}}{\chi_z N_R} - k_{zy} \frac{M_{y,Ed}}{\chi_{LT,cf}M_{y,R}} + k_{zz} \frac{M_{z,Ed}}{M_{z,R}} + k_{zw} \frac{B_{Ed}}{B_R} \leq 1,0 \quad (5.341)$$

Table 5-44: Specific interaction factors for mono-symmetric I sections

Interaction factor	Class 1 and Class 2	Class 3 and Class 4
k_{yy}	$\bar{\lambda}_y < 1,0 :$ $k_{yy} = C_{my} \left(1 + 2(\bar{\lambda}_y - 0,2) \frac{N_{Ed}}{\chi_y N_R} \right)$ $\bar{\lambda}_y \geq 1,0 :$ $k_{yy} = C_{my} \left(1 + 1,6 \frac{N_{Ed}}{\chi_y N_R} \right)$	$\bar{\lambda}_y < 1,0 :$ $k_{yy} = C_{my} \left(1 + \bar{\lambda}_y \frac{N_{Ed}}{\chi_y N_R} \right)$ $\bar{\lambda}_y \geq 1,0 :$ $k_{yy} = C_{my} \left(1 + \frac{N_{Ed}}{\chi_y N_R} \right)$
k_{zy}	$\bar{\lambda}_z < 1,0 :$ $k_{zy} = 1 - \frac{0,1\bar{\lambda}_z}{C_{mLT} - 0,25} \frac{N_{Ed}}{\chi_z N_R}$ $\bar{\lambda}_z \geq 1,0 :$ $k_{zy} = 1 - \frac{0,1}{C_{mLT} - 0,25} \frac{N_{Ed}}{\chi_z N_R}$	$\bar{\lambda}_z < 1,0 :$ $k_{zy} = 1 - \frac{0,05\bar{\lambda}_z}{C_{mLT} - 0,25} \frac{N_{Ed}}{\chi_z N_R}$ $\bar{\lambda}_z \geq 1,0 :$ $k_{zy} = 1 - \frac{0,05}{C_{mLT} - 0,25} \frac{N_{Ed}}{\chi_z N_R}$

The investigations presented in paragraph 5.6.4 revealed in particular that:

- A very simple extension of the Eurocode 3 Part 1-1 interaction equations may be sufficiently precise for the case of members of double symmetric I section subject to a complex combination of compression axial force, bi-axial bending and torsion. For short members, the extended interaction equations appear to be rather conservative mainly due to the plastic torsional system reserve. Its influence has been discussed in this paragraph and it is concluded that one may optionally take benefit of the creation of the warping hinge. However, this should be done in the analysis and not directly in the interaction equations;
- The proposed extension of the interaction equations may also be applied to double symmetric sections of semi-compact or slender section (class 3 and class 4 sections in the terminology of Eurocode 3 Part 1-1). Nonetheless, the conservatism is increased due to the inherent conservatism of the design approach of Eurocode 3 Part 1-1 (discontinuity between class 2 and class 3 sections, conservatism of the effective width method) and due to the plastic torsional system reserve that may in some cases be mobilised even for short members of semi-compact and slender section;
- The interaction equations proposed by Kaim in reference (Kaim 2004) for mono-symmetric I sections may be extended to members subject to minor-axis bending and torsion. For members subject to a combination of axial force and bi-axial bending the approach is satisfactory and leads to rather precise results. However, the interaction equations become very conservative for applied torsion due to the pronounced plastic torsional system reserve that influences the member resistance even for intermediate to high values of the member slenderness. However, if the plastic torsional system reserve is accounted for yielding is initiated for load levels lower than the one corresponding to the Serviceability Limit State. Consequently, the torsional twist determined by elastic analysis does not correspond to the real torsional twist experienced by the member. The plastic torsional system reserve should therefore not be accounted for in the simplified design method if Serviceable Limit State criteria are formulated for the studied member;
- The Eurocode 3 Part 1-1 reduction curve c may be applied to verify the resistance of U-shaped members to lateral-torsional buckling. Also, it has been shown that the interaction equation proposed in reference (Kalameya 2008) should be extended to capture the effect of flexural buckling about the minor-axis. Depending on the degree of non-linearity of the cross-section interaction, the simplified interaction equations may be rather conservative. Additionally, the interaction equations become even more conservative for short members subject to torsion due to the plastic torsional system reserve and the increased non linearity of the plastic cross-section interaction.

Throughout this paragraph it has also been shown that the interaction equations may be rather conservative even if the plastic torsional system reserve is not pronounced as for members subject to low torsional loads or for members not subject to torsion at all. The observed conservatism for these cases is due to the simplified approximation of the cross-section interaction between the internal forces and moments. In order to improve the precision the complexity of the interaction equations had be significantly increased. In recent years, the ongoing research on the OIC design model has shown that a continuous strength prediction is possible based on a globalised reduction curve (see for example references (Taras 2011)). Nonetheless, the cited works concentrate on members of hollow sections or members of open section not sensitive to lateral-torsional buckling. As the OIC approach appears to be promising it is studied hereafter for the case of members of double symmetric I section subject to compression axial forces, bi-axial bending and torsion. The interaction between flexural buckling and lateral-torsional buckling is studied. However, only members of compact section are considered and consequently, the interaction between local buckling and member instability is not accounted for.

5.6.5 Design based on OIC approach – Double symmetric I sections

5.6.5.1 *General requirements for the OIC approach to be developed*

In the previous paragraph, a design approach based on interaction equations has been proposed covering members of double and mono-symmetric I sections as well as of U sections. The proposal can be considered as simple extension of the well accepted Eurocode 3 interaction equations. Nonetheless, it can be stated again that the interaction equations have certain disadvantages, linked for example to the discontinuity between section and member resistance. The OIC approach introduced in references (Boissonnade et al. 2013) and (Boissonnade et al. 2017) aims to overcome these limitations by defining a continuous reduction curve. Also, in paragraph 5.5.7.4 it has been shown that the OIC approach may be derived quasi-analytically even for complex load cases including torsion. Therefore, the present paragraph tempts to introduce an analytically derived OIC reduction equation that may be applied to members of double symmetric I section under combined axial force, bi-axial bending and torsion. It is intended that the proposal represents as much as possible the currently available design approaches for the extreme case of:

- Flexural buckling addressed currently by the European buckling curves;
- Lateral-torsional buckling addressed by the lateral-torsional buckling curve introduced by Taras in reference (Taras 2011);
- Instability under combined axial force and minor-axis bending addressed by the OIC approach proposed by Taras in reference (Taras 2011).

The generalised form of the analytically derived reduction formula considered as basis for the following development is given in Eqs. (5.342) and (5.343).

$$\chi_G = \frac{R_{pl,MyN}}{R_{pl,ov}} \frac{1}{\phi + \sqrt{\phi^2 - \lambda_G^2 \frac{R_{pl,MyN}}{R_{pl,ov}}}} \quad (5.342)$$

$$\phi = 0,5 \left(f_{Instab} + \eta_{imp} + \lambda_G^2 \frac{R_{pl,MyN}}{R_{pl,ov}} \right) \quad (5.343)$$

In Eqs. (5.342) and (5.343) several new notations have been introduced to generalise the reduction formula presented in paragraph 5.5.7.4. In particular:

- $R_{pl,MyN}$ represents the plastic load amplification factor for the section subject only to combined major-axis bending and axial force;
- $R_{pl,ov}$ represents the plastic load amplification factor for the section subject to the all present internal forces and moments;

- f_{instab} represents the transition between failure mode characterized by the plastic cross-section resistance and a failure mode characterized by elasto-plastic instability.

The ratio between both factors, $R_{pl,MyN}$ and $R_{pl,ov}$, indicates the importance of the major-axis bending moment and the axial force to the total loading. Obviously, if the member is exclusively subject to an axial force, a major-axis bending moment or a combination of both, the ratio between $R_{pl,MyN}$ and $R_{pl,ov}$ becomes 1,0. Also, if the member is not subject, neither to major-axis bending nor to an axial force, $R_{pl,MyN}$ tends to infinity. Indeed, in this case the strength of the member is not reduced as the other internal forces and moments do not induce member instability. It should be noted that, if the member is restrained against torsional twist, the major-axis bending moment does not induce instability anymore. In this case, the M_y should not be considered in the factor $R_{pl,MyN}$. Yet, in the framework of the following study, restrained members are not considered.

The aspect of the reduction formula given in Eqs. (5.342) and (5.343) is rather simple and it is intended to keep the proposal developed hereafter as simple as possible. Consequently, the goal of the present paragraph is to introduce an OIC approach that includes as few parameters as possible and the parameters included should be provided by numerical tools as far as possible. In particular, the key parameters R_{pl} and $R_{Stab,MB}$ can be determined numerically by the adapted PIFM introduced in Chapter 4 and *LTBeamN* (including an extension accounting for first order displacements), respectively.

It should be noted that the investigations presented in the following do not include the influence of the interaction between plate instability and member instability. Therefore, only the results obtained based on the “locally restrained” (see paragraph 5.2.3) model are exploited hereafter. Additionally, only the load case of constant bending moments is considered in the framework of the following study.

The generalised form of the proposed OIC approach is slightly different from the approaches representing the extreme cases. Hence, before the complex load cases including interaction between flexural and lateral-torsional buckling are studied, it is necessary to examine if and how the existing proposals for lateral-torsional buckling and flexural buckling under combined axial force and minor-axis bending have to be adapted to respect the format chosen here.

5.6.5.2 OIC approach for lateral-torsional buckling

For double symmetric I sections a precise reduction formula has been proposed by Taras in reference (Taras 2011). It is recalled that this proposal is introduced into the future version of Eurocode 3 Part 1-1. Consequently, it seems desirable to develop the OIC approach as a continuous extension of this design method for lateral-torsional buckling. The proposal is recalled in Eqs. (5.344) and (5.345). The factor f used in these equations considers the influence of the variable bending moment diagram on the ultimate resistance. As stated previously, only constant bending is of interest hereafter and consequently the factor f can be omitted in the framework of the current study.

$$\chi_{LT} = \frac{f}{\phi + \sqrt{\phi^2 - f \bar{\lambda}_{LT}^2}} \quad (5.344)$$

$$\phi = 0,5 \left(1 + f \left[\alpha \frac{\bar{\lambda}_{LT}^2}{\bar{\lambda}_z^2} (\bar{\lambda}_z - 0,2) + \bar{\lambda}_{LT}^2 \right] \right) \quad (5.345)$$

Depending on the geometry of the section and the fabrication process Taras proposes the imperfection factors given in Table 5-45. The factor β_{LT} introduced in Table 5-45 is defined in Eq. (5.346).

$$\beta_{LT} = \sqrt{\frac{W_{y,el}}{W_{z,el}}} \quad (5.346)$$

Table 5-45: Imperfection factors to be used with Eqs. (5.344) and (5.345)

Case	Imperfection factor α
Hot-rolled section $h/b > 1,2$	$0,12\beta_{LT} \leq 0,34$
Hot-rolled section $h/b \leq 1,2$	$0,16\beta_{LT} \leq 0,49$
Welded section	$0,21\beta_{LT} \leq 0,64$

The analytical development of the proposal given in Eqs. (5.344) and (5.345) has been re-demonstrated in paragraph 5.5.7.2. It is recalled that the ratio $\lambda_{LT}^2/\lambda_z^2$ considers the torsional characteristics of the member explicitly in the reduction formula. Also, the term $(\lambda_z-0,2)$ has been considered to increase the precision of the proposal. However, for the development of the OIC approach it seems somewhat inconvenient to use several different types of member slenderness to characterise the failure mode. In reference (Naumes 2007), it is proposed to replace the ratio $\lambda_{LT}^2/\lambda_z^2$ by the ratio $\alpha_{cr}^*/\alpha_{cr}$ where α_{cr}^* represents the load amplification factor leading to elastic instability supposing that the torsion constant I_t is equal to 0 and α_{cr} represents the load

amplification factor considering the real torsional constant of the cross-section. In order to be consistent with the OIC notations, α_{cr} is denoted as R_{cr} and α_{cr}^* is denoted as R_{cr}^* in the following.

These both factors may be obtained easily with numerical tools. Yet, it should be noted that both ratios are not identical. Indeed, for double symmetric I sections subject to constant major-axis bending the ratio $R_{cr,G^*}/R_{cr,G}$ ($\alpha_{cr}^*/\alpha_{cr}$) is equal to:

$$\frac{R_{cr}^*}{R_{cr}} = \frac{1}{\sqrt{1 + \frac{GI_t}{EI_w} \frac{L^2}{\pi^2}}} \quad (5.347)$$

Conversely, the ratio between squares of the lateral-torsional and the flexural slenderness is equal to:

$$\frac{\lambda_{LT}^{-2}}{\lambda_z^2} = \frac{W_y}{A \sqrt{\frac{I_w}{I_z}}} \frac{1}{\sqrt{1 + \frac{GI_t}{EI_w} \frac{L^2}{\pi^2}}} \quad (5.348)$$

For the sections studied here, the ratio between both types of slenderness is smaller than the ratio between the load amplification factors. Consequently, if the same imperfection factor α is used, the results become **safe-sided**. Yet, in Taras' the term $(\lambda_z-0,2)$ contains the relative slenderness for flexural buckling about the minor-axis that is always higher than the lateral-torsional buckling slenderness for the same member under constant major-axis bending. If the slenderness λ_z is replaced by the lateral-torsional buckling slenderness the use of the same imperfection factor α would therefore lead to **unsafe** results compared to the reference method represented by Eqs. (5.344) and (5.345). Hence, so as to rewrite the reference design model in the intended OIC format the imperfection factor α has to be calibrated again. Indeed, Figure 5-185 shows that the proposed OIC approach seems slightly too unsafe if the imperfection factors α proposed by Taras is used directly without any adaption. It is recalled that paragraph 5.5.6.2 emphasized that pre-buckling displacement may have a significant influence on the stability of U-shaped members subject to minor-axis bending moments. It has been concluded that the pre-buckling displacements should be accounted for if a global method as OIC is developed for these sections. In order enable a continuity, it is therefore proposed to include the effect of pre-buckling displacements also for the I-shaped members considered here.

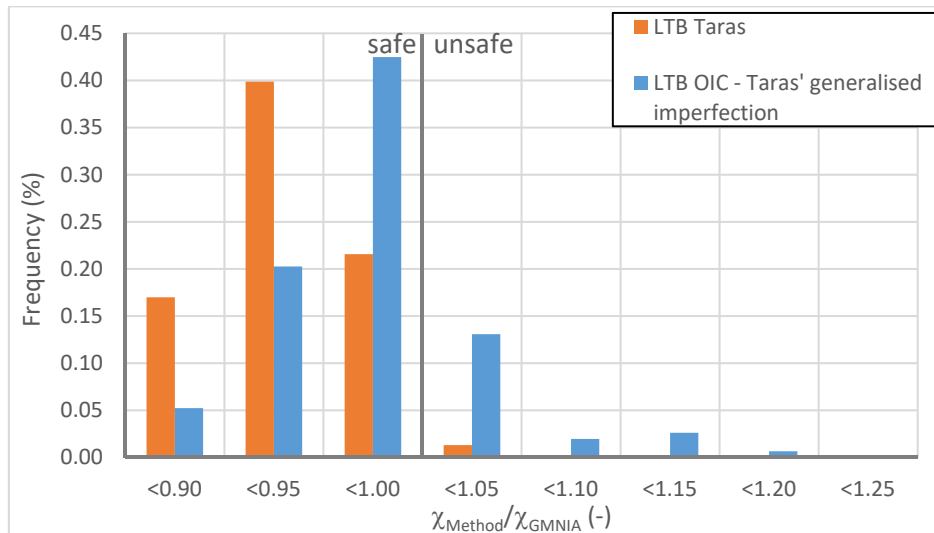


Figure 5-185: Ratio between predicted resistance and numerically obtained resistance

For the calibration of the generalised imperfection the studied cross-sections are divided into the three classes given in Table 5-45 as in case of the reference method. First, the case of welded sections is studied.

Figure 5-186 represents the exact imperfection factor α that should be used with the proposed OIC format to obtain the same ultimate resistance as the one obtained numerically. It is shown that the imperfections to be used are very similar for the four studied sections. It can be observed easily that the value of the imperfection factor increases up to a relative slenderness of about 0,9 and the decreases independently of the cross-section. The maximum value of the imperfection factor to be used is of about 0,60 and 0,66.

The observed evolution of the imperfection factor represents well the importance of the equivalent imperfection on the behaviour of members, i.e.:

- For low values of the relative slenderness the member failure is characterised by resistance of the most loaded section – the geometric imperfection does not highly influence the resistance;
- For high values of the relative slenderness the member failure is characterised by elastic instability – again, the geometric imperfection influences the resistance only slightly;
- For intermediate values of the relative slenderness the member failure is characterised by elasto-plastic instability – the geometric imperfection highly influences the resistance of the member.

Here, one might consider to link the value of the imperfection factor α to the relative slenderness so as to account its evolution. Yet, in the framework of the present thesis this is not investigated further on in order to keep simple expressions of the generalised imperfection. Moreover, other influences not studied in this paragraph, as the form of the bending moment diagram, may have an influence on the evolution of the value of the imperfection factor to be used.

It should be noted that the maximum value of the imperfection factor of 0,66 is close to the imperfection factor obtained when the provisions of Table 5-45 are applied. Indeed, as the ratio between the section modulus for major-axis bending and the section modulus for minor-axis bending is rather high, the limit value of the imperfection factor of 0,64 is always applicable. For practically used welded sections, these high ratios of the section moduli seem rather usual. However, in order to verify whether lower values of the imperfection factor may be accepted (and hence a variation of the imperfection factor α with the ratio $W_{y,el}/W_{z,el}$) according to Table 5-45 the less commonly welded sections of Table 5-46 are studied additionally.

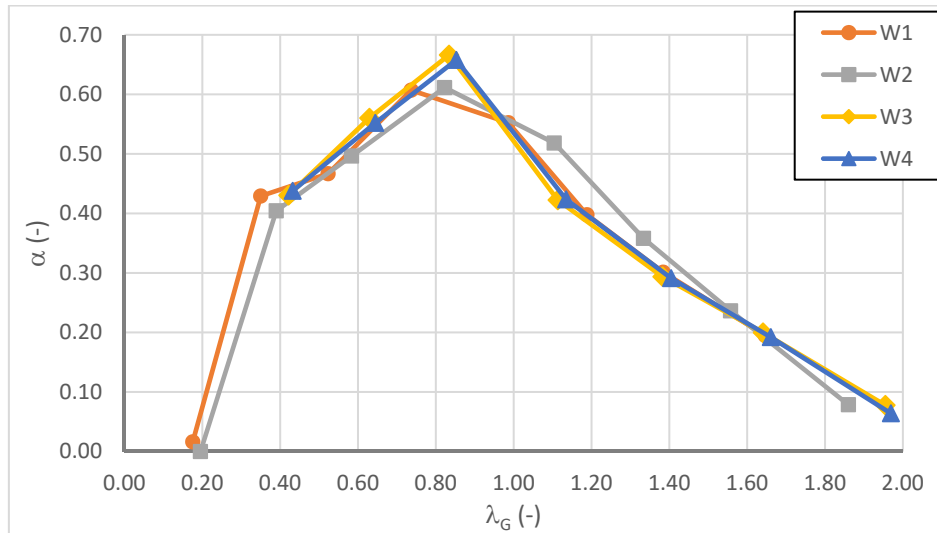


Figure 5-186 : Evolution of the imperfection factor α for welded sections

Table 5-46: Complementary welded sections used to calibrate generalised imperfection

Section	$W_{y,el}$	$W_{z,el}$	β_{LT}	α
W200.9.200.15	596,05	200,1	1,73	0,36
W390.11.300.19	2332,1	570,26	2,02	0,42
W500.4.300.20	3091,6	600,0	2,27	0,48
W330.7,5.160.11,5	699,85	98,27	2,67	0,56

Figure 5-187 confirms the observations of Figure 5-186 concerning the imperfection factor α . In particular, it can be noticed that the maximum value of the imperfection factor α is obtained for intermediate values of the relative slenderness of about 0,8 to 0,9. However, conversely to the other sections, W330.7,5.160.11,5 and W500.4.300.20 do not possess a pronounced summit but rather a plateau that extends from a relative slenderness of 0,6 to approximatively 1,1. It might be interesting to investigate this difference in more detail. Yet, this is not done here, as it does not contribute to an appreciable increase of the precision of the simple design approach. Additionally, it may be observed that the imperfection factor to be used in the proposed OIC format does not noticeably depend on the ratio between both section moduli $W_{y,el}$ and $W_{z,el}$. In fact, following the provisions of Table 5-45 sections W200.9.200.15 and W390.11.300.19 should possess

imperfection factors that are lower than for sections W500.4.300.20 and W330.7,5.160.11,5. Yet, somewhat surprisingly this not the case here. Nevertheless, this may be understood and explained based on the difference between the critical loads that are used in the reference approach and the proposed OIC approach. It is recalled that the OIC approach proposed here is based on the critical load considering pre-buckling displacements. For the compact cross-sections W200.9.200.15 and W390.11.300.19 this leads to a distinct increase of the critical moment and consequently a reduction of the relative slenderness compared to the one used in the reference approach. Hence, in order to obtain the same reduction factor χ for the same member the imperfection factor has to be higher for the OIC approach than for the reference model. Nevertheless, the increase of the imperfection factor α for compact sections leads to more uniform distribution its value.

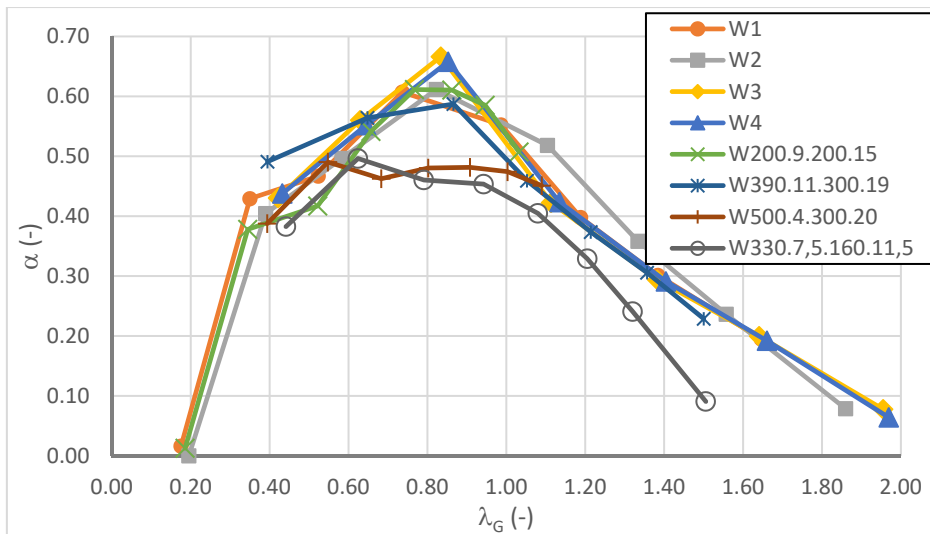


Figure 5-187: Evolution of the imperfection factor α for welded sections

For sake of simplicity, it is proposed to apply a value of 0,58 for the imperfection factor. This value is shown to lead to satisfactory results in terms of precision of the OIC resistance model as represented in Figure 5-188.

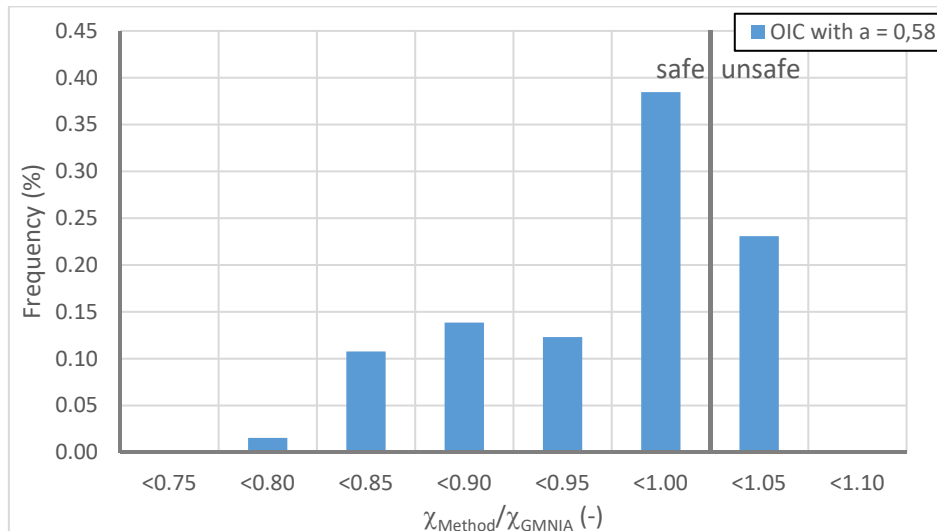


Figure 5-188: Ratio between predicted resistance and numerically obtained resistance – OIC $\alpha = 0,58$

Next, members fabricated from hot-rolled sections are studied. Again, so as to increase the variety of section geometries used for the calibration of the imperfection factor, additional sections are included into the following study. The imperfection proposed by the reference model for lateral-torsional buckling are given for all studied hot-rolled sections in Table 5-47. It is recalled again that sections noted as HR possess inverted dimensions and that the fillets are not included in the numerical simulations (and, of course, in the calculation of the cross-section characteristics).

One may note that the sections are chosen so as to represent, as much as possible, the whole range of the imperfection factor α . Table 5-47 shows that, in practice, the upper and the lower bound of the imperfection factor cannot be attained for hot-rolled sections with a ratio h/b smaller than 1,2 due to their geometry. It seems that the variation is limited between 0,24 and 0,32 (yet, the influence of the fillets increases the variation of the imperfection factor in practice). Additionally, one may observe in Table 5-47 that the value of α is in the same range for both classes of hot-rolled sections ($h/b \leq 1,2$ and $h/b > 1,2$). Nevertheless, the deeper sections with $h/b > 1,2$ – IPE 500, HEAA 800 and HEAA 1000 – attain the limit value of 0,34 for the imperfection factor due to their high section modulus about the major-axis compared to the section modulus about their minor-axis.

Table 5-47: Hot-rolled sections used for the calibration of the imperfection factor α

h/b	Section	$W_{y,el}$	$W_{z,el}$	β_{LT}	α
$\leq 1,2$	HR450.15.600.30	7926	3600,4	1,48	0,24
	HEB 200	596,05	200,1	1,69	0,27
	HEA 360	1903,9	525,2	1,73	0,28
	HR1200.15.1000.20	26909,2	6667,3	1,90	0,30
	HR290.3.300.14	1192,8	420,0	2,01	0,32
$> 1,2$	HEM 340	4575,7	1274,6	1,89	0,23
	HR500.4.300.20	3016,9	600,0	2,24	0,27
	HR770.5.400.17	5562,5	906,8	2,48	0,30
	IPE 500	1909,4	213,8	2,99	0,34
	HEAA 800	5288,6	541,1	3,13	0,34
	HEAA 1000	8225,4	632,1	3,61	0,34

The evolution of the imperfection factor to be applied with the proposed OIC approach is first represented in Figure 5-189.

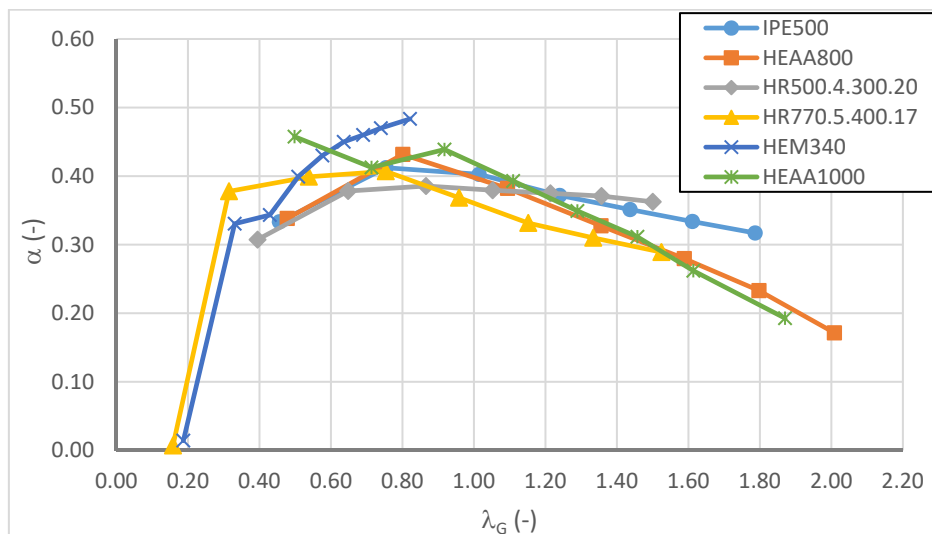


Figure 5-189: Evolution of the imperfection factor for hot-rolled sections with $h/b > 1,2$

As for the welded section one may observe that the imperfection factor tends to zero for low values of the slenderness, then it increases and reaches its maximum for a relative slenderness of about 1,0 and finally its value decreases. However, it seems that the curves for the studied hot-rolled sections do not possess a clear peak for an intermediate slenderness but rather a plateau. Also, the decrease of the necessary value of the imperfection factor is much slower than observed for the welded sections. Here, it is proposed again to introduce a constant value of the imperfection factor for simplicity. A value of $\alpha = 0,42$ seems reasonable as shown by the diagram of Figure 5-190 representing the distribution of the ratio χ_{Method} to χ_{GMNIA} . It is clear that the

proposed approach is very precise as none of the predictions is more than 2% unsafe and more than 8% conservative.

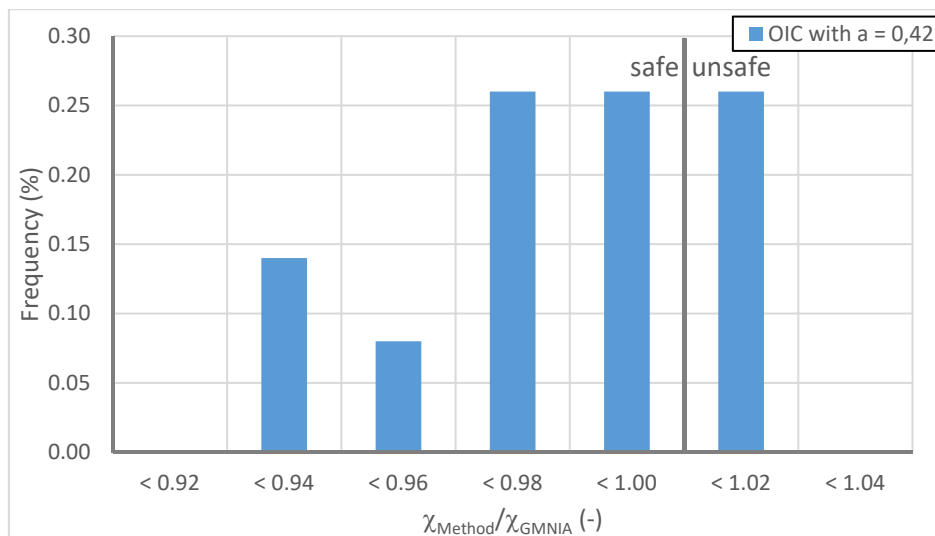


Figure 5-190: Ratio between predicted resistance and numerically obtained resistance – OIC $\alpha = 0,42$ for hot-rolled sections with $h/b > 1,2$

Last, hot-rolled sections possessing a ratio smaller than 1,2 between their height and the width of their flanges are studied. As before, the evolution of the imperfection factor that has to be applied so that the OIC predicted resistance just equals the numerically determined resistance is represented in Figure 5-191. It should be noted that the studied range of the relative slenderness is much more limited than before due to the section geometry. Indeed, as has been stated in paragraph 5.6.2, the length of the members is limited to approximately 50 to 60 times the width of the flanges (depending on the load case). This leads to a rather small maximum relative slenderness for the compact section whose results are represented in Figure 5-191. Nevertheless, one may again easily observe that shape of curves linked to the evolution of the imperfection factor α with the relative slenderness is similar as for the case of the welded sections and hot-rolled sections with $h/b > 1,2$. In particular, it is shown that the maximum value of α is attained for a relative slenderness of approximately 0,8 to 1,0. Yet, the variation of the curves is much higher than for the sections studied before. Additionally, it does not seem evident to highlight one single parameter that could explain the order of the different curves of Figure 5-191. In fact, neither the ratio $W_{el,y}$ to $W_{el,z}$ nor the ratio I_y/I_z . It seems that a complex interaction between several parameters leads to the discrepancies that are perceived in Figure 5-191. Consequently, a deeper investigation with supplementary numerical simulations appears necessary to give a clear explanation of the results. However, at this study is not performed hereafter. In order to keep the design approach simple, it is rather chosen to propose again a sufficiently safe-sided constant value of the imperfection factor α . Here, the value of 0,75 seems acceptable as it only leads to slightly unsafe resistance predictions for members at the extreme limit of the practical range. For example the resistance is overestimated by 4% for a member with a length of 12 m (without any intermediate restraint!) fabricated from a HEB 200 section.

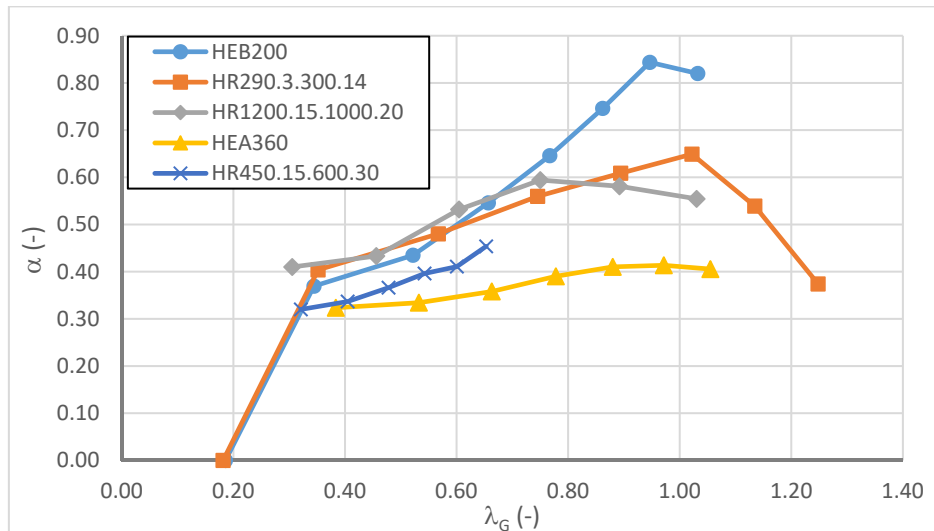


Figure 5-191: Evolution of the imperfection factor for hot-rolled sections with $h/b \leq 1,2$

The quality of the proposal is shown again with the diagram given in Figure 5-192. It can be observed that, even if there is a rather important variation of the imperfection factor in Figure 5-191, the precision of the OIC approach seems satisfactory if it is based on a constant value of 0,75 for α . Yet, it is to be noted that the approach is more conservative as for the cases of welded sections and hot-rolled sections with $h/b > 1,2$). Nonetheless, a mean value of 0,94 and a standard variation of 0,42 seems to be acceptable.

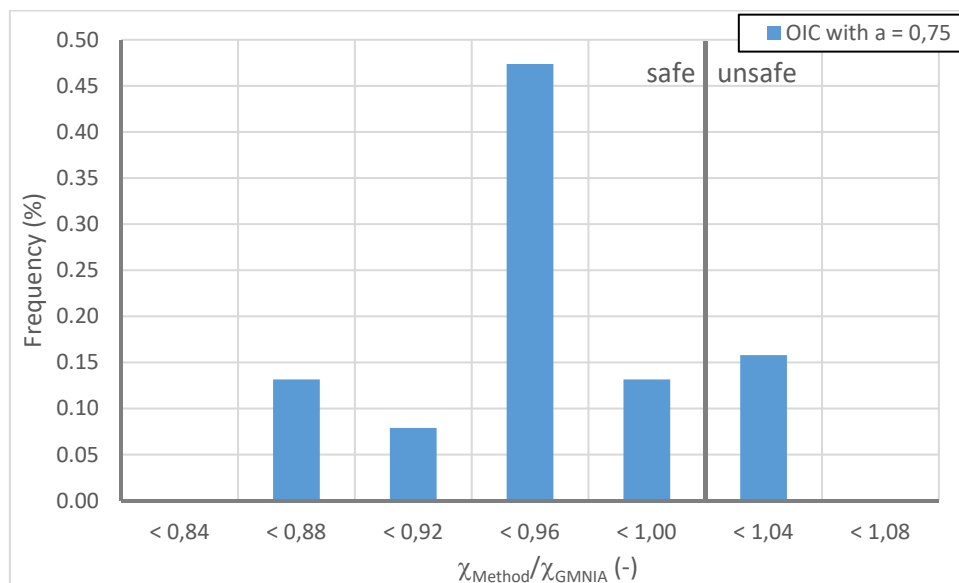


Figure 5-192: Ratio between predicted resistance and numerically obtained resistance – OIC $\alpha = 0,42$ for hot-rolled sections with $h/b \leq 1,2$

Finally, Figure 5-193 compares the overall results of the proposed OIC approach to the resistance model proposed in reference (Taras 2011) and to the design rule provided in the current version of Eurocode 3 Part 1-1 (CEN 2005a). First, it is clear that the European provisions for the lateral-torsional buckling of I sections are not very satisfactory compared to the two other proposals. Especially, for welded sections the applied lateral-torsional buckling curve is too safe-sided as has

already been shown rapidly in paragraph 5.2.1.2. In some cases the design approach may also be rather unsafe. Yet, the unsafe cases concern members at the limit of the practical range as the member with a length of 12 m fabricated from HEB 200 section. The proposal of Taras is also unsafe for these cases but only of about 10%. It is recalled that an increased imperfection factor is used for the proposed OIC approach in order to reduce the un-conservatism for this and other extreme cases. Consequently, the proposal introduced here is less unsafe (only of about 4%). Additionally, one may remark that the scatter of the results obtained with the proposed OIC approach is very small. So as to evaluate the approaches further on, Table 5-48 summarizes the mean value and the standard deviation as well as the maximum and minimum value of the ration $\chi_{Method}/\chi_{GMNIA}$ for the three design models.

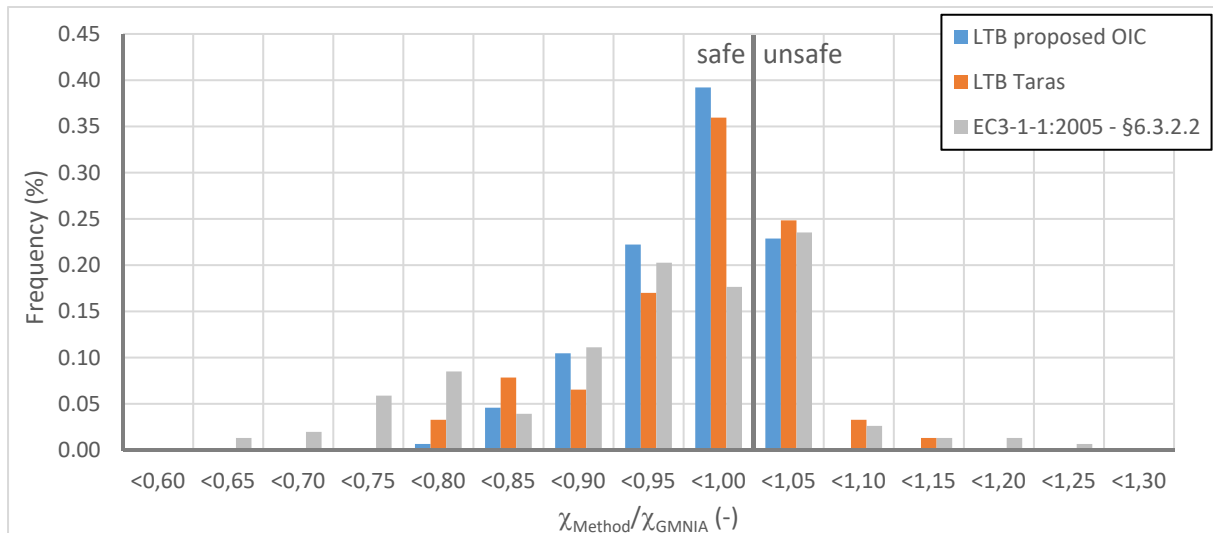


Figure 5-193: Ratio between predicted resistance and numerically obtained resistance

Table 5-48 validate the quality of the proposed design model. The approach proposed by Taras yields results that are very close to the proposal. Yet, the standard deviation is slightly higher and in some cases Taras' approach is more unsafe (the unsafe cases have been described before). Finally, the statistical evaluation confirms the poor quality of the Eurocode 3 provisions for the tested members. The lateral-torsional buckling curve provided in its paragraph 6.3.2.2 may yield very safe as well as rather unsafe results. Nevertheless, it should be noted that the field of application of §6.3.2.2 of Eurocode 3 Part 1-1 is very large as it may be applied to all types of open sections with arbitrary boundary conditions and constant or variable bending. Hence, it may be accepted that the precision for a special case is less than the precision of the proposals that have been calibrated explicitly for double symmetric I sections. The field of application of Taras' proposal includes double symmetric I sections subject to constant or variable bending. Consequently, it also exceeds the domain of the study presented here. Therefore, the evaluation of the different approaches does not strictly imply the general superiority of the proposed OIC approach over the other design models but only a higher quality in its field of application studied here: Double symmetric I sections under constant major-axis bending. Nonetheless, owing to the generalised formulation of the OIC approach the extension to other load cases and cross-sections seems feasible. Hereafter, the OIC format is, in a first step, applied and calibrated for buckling

under combined compression axial force and minor-axis bending and in paragraphs 5.6.5.4, 5.6.5.5, 5.6.5.6 it is extended step-by-step to combined minor- and major-axis bending, combined major-axis bending and axial force and combined minor-and major-axis and axial force. Finally, paragraph 5.6.5.7 concerns the extension of the OIC approach to applied torsion.

Table 5-48: Evaluation of different approaches for lateral-torsional buckling of double-symmetric I sections

$\chi_{\text{Method}}/\chi_{\text{GMNIA}}$	Proposed OIC format	LTB Taras	Eurocode 3 Part 1-1 - §6.3.2.2
Mean value	0,955	0,959	0,926
Standard deviation	0,054	0,070	0,110
Maximum value	0,792	0,764	0,636
Minimum value	1,047	1,122	1,201

5.6.5.3 OIC approach for flexural buckling under combined minor-axis bending and axial force

Hereafter, the OIC approach proposed in (Taras 2011) for the studied load case is transformed into the chosen format. First, Taras' proposal is recalled in Eqs. (5.349) and (5.350).

$$\chi_G = \frac{c_0}{\phi + \sqrt{\phi^2 - \bar{\lambda}_G^2 c_0}} \quad (5.349)$$

$$\phi = 0,5 \left(k_{ni}^* + k_{mi}^* C_{ms} \eta_0 + \eta_{imp} + \bar{\lambda}_G^2 c_0 \right) \quad (5.350)$$

The different parameters that are included in this approach are defined in Eqs. (5.351) to (5.355).

$$\eta_0 = \frac{M_y / M_{y,pl}}{N / N_{pl}} \quad (5.351)$$

$$c_0 = k_{ni} + \eta_0 k_{mi} \quad (5.352)$$

$$k_{ni}^* = k_{ni} + (1 - k_{ni}) \rho \bar{\lambda}_G C_{ms} \leq 1,0 \quad (5.353)$$

$$k_{mi}^* = k_{mi} + \left(\frac{W_{pl,z}}{W_{el,z}} - k_{mi} \right) \rho \bar{\lambda}_G C_{ms} \leq \frac{W_{pl,z}}{W_{el,z}} \quad (5.354)$$

$$\eta_{imp} = \alpha \left(\bar{\lambda}_G - 0,2 \right) \quad (5.355)$$

Regarding the definitions of the parameters, it is recalled that:

- c_0 represents the importance of the axial force in the overall loading and is consequently equal to the ratio $R_{pl,MyN}/R_{pl,ov}$ (even if the major-axis bending moment is not considered in the paragraph the notation $R_{pl,MyN}$ is conserved to keep the presentation uniform) ;
- k_{ni} and k_{mi} are the interaction factors of a simplified (multi-linear) plastic interaction between minor-axis bending and axial force;
- k_{ni}^* and k_{mi}^* represent the transition behaviour between plastic interaction for short members and elastic interaction for long members, the factor ρ introduces the influence of the form of the section ($\rho = 0,6$ for the studied case);
- η_{imp} introduces the effect of the equivalent imperfection; it is linked to the slenderness for flexural buckling determined based on $N_{cr,z}$ and N_{pl} .

Consequently, it appears that several parameters can be replaced easily to be rewritten in the OIC format chosen here as shown in Eqs. (5.356) and (5.357). If the function f_{Instab} , representing the effect of instability and consequently the transition between plastic and elastic cross-section interaction, is equal to $k_{ni}^* + k_{mi}^* C_{mS} \eta_0$, Eqs. (5.356) and (5.357) are identical to the approach proposed in reference (Taras 2011). However, in the framework of the current study, it is intended to use numerical obtained values of the plastic load amplification factor and consequently to base the proposed OIC approach on the analytical non-linear plastic cross-section interaction. This is also advantageous because for more complex load cases including up to five internal and moments a simple linearized interaction forces (N, M_y, M_z, B, V_z) does not seem practical (see also Chapter 4).

$$\chi_G = \frac{R_{pl,MyN}}{R_{pl,ov}} \frac{1}{\phi + \sqrt{\phi^2 - \bar{\lambda}_G^2 \frac{R_{pl,MyN}}{R_{pl,ov}}}} \quad (5.356)$$

$$\phi = 0,5 \left(f_{Instab} + \alpha \left(\frac{\bar{\lambda}_G}{\sqrt{\frac{R_{pl,MyN}}{R_{pl,ov}}}} - 0,2 \right) + \bar{\lambda}_G^2 \frac{R_{pl,MyN}}{R_{pl,ov}} \right) \quad (5.357)$$

The numerical simulations presented hereafter have shown that the precision of the approach is increased if the parameter ϕ is rewritten in the following form.

$$\phi = 0,5 \left(f_{Instab} + \frac{\alpha}{\sqrt{\frac{R_{pl,MyN}}{R_{pl,ov}}}} \left(\bar{\lambda}_G - 0,2 \right) + \bar{\lambda}_G^2 \frac{R_{pl,MyN}}{R_{pl,ov}} \right) \quad (5.358)$$

Obviously, if the member is subject to a sole axial force (or a sole major-axis bending moment), f_{instab} should be equal to 1,0 as recalled through the analytical developments represented in paragraph 5.5.7.2. For combined load cases, it has been shown in paragraph 5.5.7.4 that the parameter f_{instab} should tend to $R_{pl,MyN}/R_{pl,ov}$ for short members that are not sensitive to second order effects. Evidentially, this ratio tends to 1,0 if the minor-axis bending moment vanishes and hence a continuous transition from members under axial force and members subject to combined axial force and minor-axis bending is ensured. For longer member that are sensitive to instability the resistance cannot be expressed by a plastic interaction between the internal forces and moments at the most loaded section (including second order effects). Indeed, the member fails by elasto-plastic instability before the cross-section has entirely plastified and this even for compact sections as shown in Figure 5-194 for a member of HEB 200 section subject to combined axial force and minor-axis bending and possessing a length of 7,0 m. On may clearly observe that only the tips of the flanges plastify whereas the web and the centre part of the flanges stay completely elastic. So as to account for this difference the value of f_{instab} has to depend on the member slenderness. However, f_{instab} should again be equal to 1,0 if the member is only subject to an axial force even for long members because the form of the reduction curve itself describes the transition behaviour for simple load cases.

It should be noted that Annex A of the current version of Eurocode 3 Part 1-1 (CEN 2005a) explicitly considers the transition behaviour by the factors C_{ij} (see Annex A). Yet, the provided expressions are very complex and unpractical for the use in engineering offices. Hereafter, it is rather intended to adopt a similar approach as the one proposed by Taras through Eqs. (5.353) and (5.354). Key parameters are consequently the relative slenderness λ , the cross-section specific factor ρ and the equivalent sinusoidal moment factor C_{ms} .

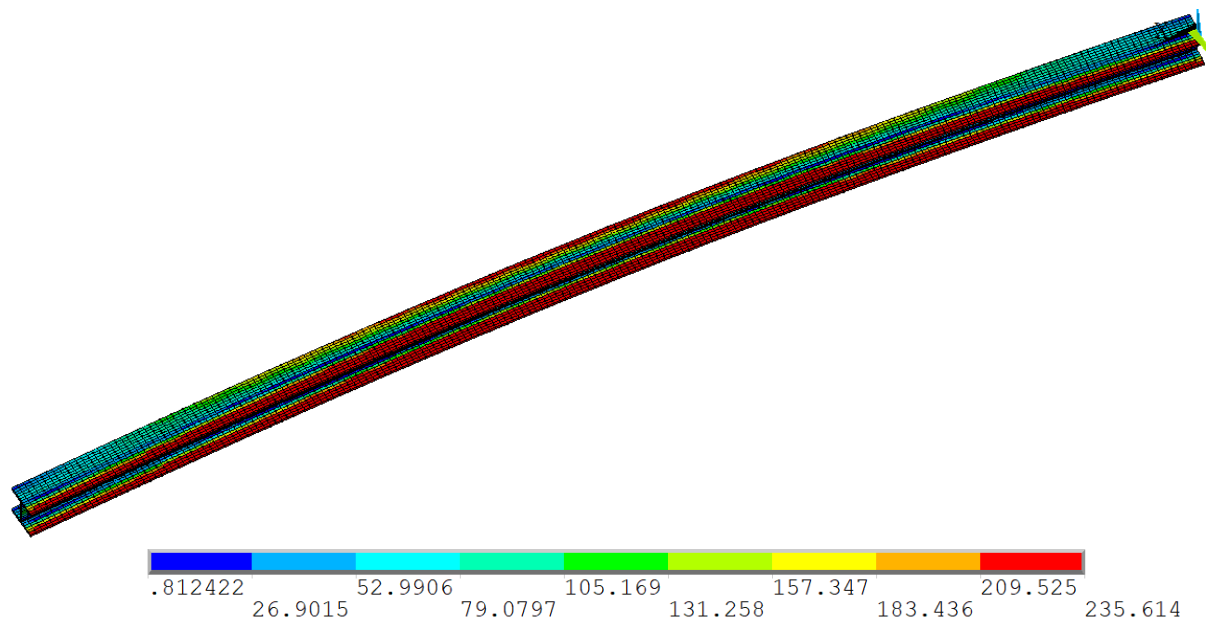


Figure 5-194: Member of HEB 200 section failing by elasto-plastic instability

It is recalled that only constant bending moments are of interest and consequently, the equivalent sinusoidal moment factor becomes (see (Taras 2011)):

$$C_{ms,z} = 1 + 0,27 \frac{N}{N_{cr,z}} \quad (5.359)$$

The index z in Eq. (5.359) indicates that the equivalent sinusoidal moment factor is related to the behaviour about the minor-axis.

The proposed expression for the parameter f_{Instab} is given in Eq. (5.360).

$$f_{Instab} = \frac{R_{pl,MyN}}{R_{pl,ov}} - \left(\frac{R_{pl,MyN}}{R_{pl,ov}} - \frac{R_{el,MyN}}{R_{el,ov}} \right) C_{ms,z} \rho \bar{\lambda}_G \leq \frac{R_{el,MyN}}{R_{el,ov}} \quad (5.360)$$

Eq. (5.360) represents a linear transition from a plastic interaction to an elastic interaction. The elastic interaction is characterised by the ratio $R_{el,MyN}$ to $R_{el,ov}$. Similarly, to the case of plastic interaction $R_{el,MyN}$ is the load factor leading the elastic limit state of the member under combined major-axis bending and axial force only whereas $R_{el,ov}$ is the load amplification factor that leads to the elastic limit state of the member considering all internal forces and moments. The speed of this transition between plastic and elastic interaction is modulated with the product $C_{ms,z} \rho \bar{\lambda}_{MB}$. Additionally, a cut-off value of $R_{el,MyN}/R_{el,ov}$ is introduced as, obviously, the elastic interaction is the limit case for long members. The numerical study revealed that a value of 0,8 for the factor ρ leads to sufficiently precise results as presented in the following. This limit value is attained for values of the relative slenderness of about 1,25 (depending on the value of the factor $C_{ms,z}$ the value varies).

For the studied load case the two elastic load amplification factors are defined as follows:

$$R_{el,MyN} = \frac{N_{pl}}{N} \quad (5.361)$$

$$R_{el,ov} = \frac{1}{\left(\frac{N}{N_{pl}} + C_{ms,z} \frac{M_z}{M_{z,el}} \right)} \quad (5.362)$$

It should be noted that the equivalent sinusoidal moment factor $C_{ms,z}$ introduced in Eq. (5.362) so as to account for the influence of the bending moment diagram on the second order amplification. The amplification factor itself is not accounted for in Eq. (5.362). It is shown by comparisons to the GMNIA results that the second order amplification is already sufficiently included in the design model through the shape of the reduction curve. Yet, in case of long members sensitive to flexural buckling it is necessary to include the influence of the bending moment diagram that is not accounted for in the original form of the reduction curve. This is done here by the introduction of the equivalent sinusoidal moment factor into the expression of $R_{el,ov}$.

Figure 5-195, Figure 5-196 and Figure 5-197 present the ultimate resistance curves obtained for members fabricated from sections HEB 200, IPE 500 and W850.6.300.12, respectively. All figures show that the OIC predicted resistance is in very good agreement with the numerical results. It is

shown that the relative importance between the axial force and the minor-axis bending moment (represented by the ratio $m_z/n = (M_z/M_{z,pl})/(N/N_{pl})$) has a great influence on the form of the ultimate resistance curve. It may be observed that the reduction of the member resistance increases with the relative importance of the minor-axis bending moment. This reduction is already very pronounced for relative small minor-axis bending moments ($m_z/n = 0,2$). It appears that a lower bound of the reduction curve is attained for a ratio $m_z/n = 3,3$ (the exact value is not determined here). Observing the curves linked to high values of the minor-axis bending moment ($m_z/n_z = 3,3$ and $m_z/n_z = 6,7$), it seems somewhat surprising that, between both curves, it is the curve linked to lower minor-axis bending moments ($m_z/n_z = 3,3$) that leads to a (slightly) higher strength reduction. This finding seems to be in opposition to what has been observed for the curves linked to lower values of the minor-axis bending moment. Yet, this observation respects the general tendencies for the behaviour of members under combined major-axis bending and axial force:

- The applied minor-axis bending moment decreases the relative slenderness as it does not affect the critical load amplification factor $R_{cr,G}$ but reduces the plastic load amplification factor $R_{pl,ov}$ (observe that end of the ultimate resistance curves for a given section are not located at the same value of the relative slenderness even if the member length is the same independently from the value of the minor-axis bending moment);
- For the same member slenderness an increased minor-axis bending moment has generally a negative effect on the member resistance as it leads to more pronounced second order effects;
- For very high values of the minor-axis bending moment, and consequently **low values of the axial force**, the influence of second order effects decreases and the influence of the minor-axis bending moment becomes favourable. Indeed, if the member is subject only to minor-axis bending, the reduction factor tends to 1,0 (omitting the influence of strain hardening) and the relative slenderness tends to 0 as minor-axis bending moments do not induce elastic instability for double symmetric I sections (see paragraph 5.5.5.2).

The interaction between these tendencies is rather complex and depends on the geometry of the cross-section. Nevertheless, it appears that the proposed OIC format represents very well the resistance of members under combined axial force and minor-axis bending. For the studied examples the highest difference between the ultimate resistance and the resistance predicted through the OIC approach is only of about 10% (safe-sided) obtained for a member of IPE 500 section of 2 m of length subject to combined axial force and minor-axis bending with a ratio m_z/n of 0,5 (see Figure 5-196).

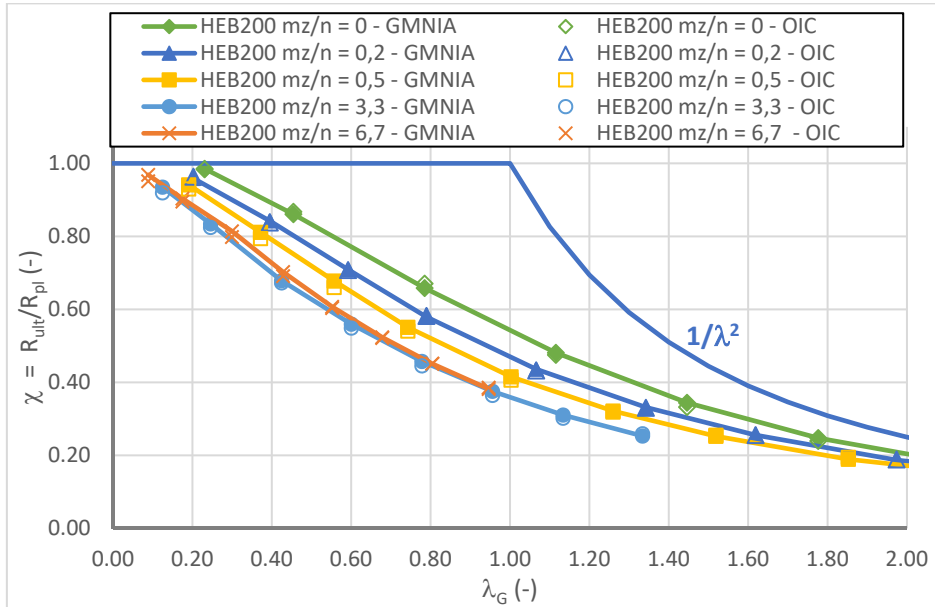


Figure 5-195: Ultimate resistance curves for a member of HEB 200 section subject to combined axial force and minor-axis bending

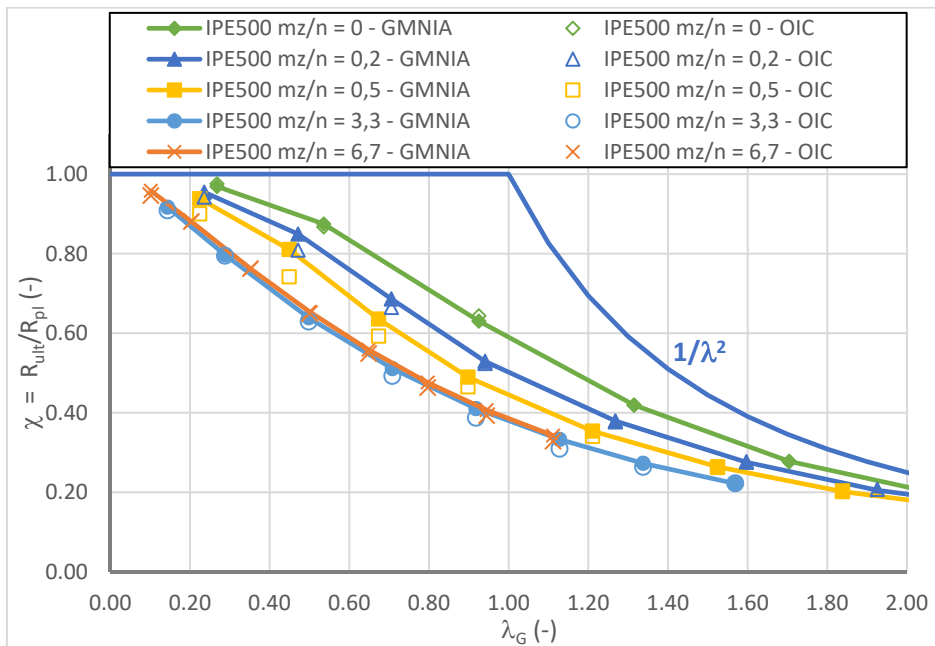


Figure 5-196: Ultimate resistance curves for a member of IPE 500 section subject to combined axial force and minor-axis bending

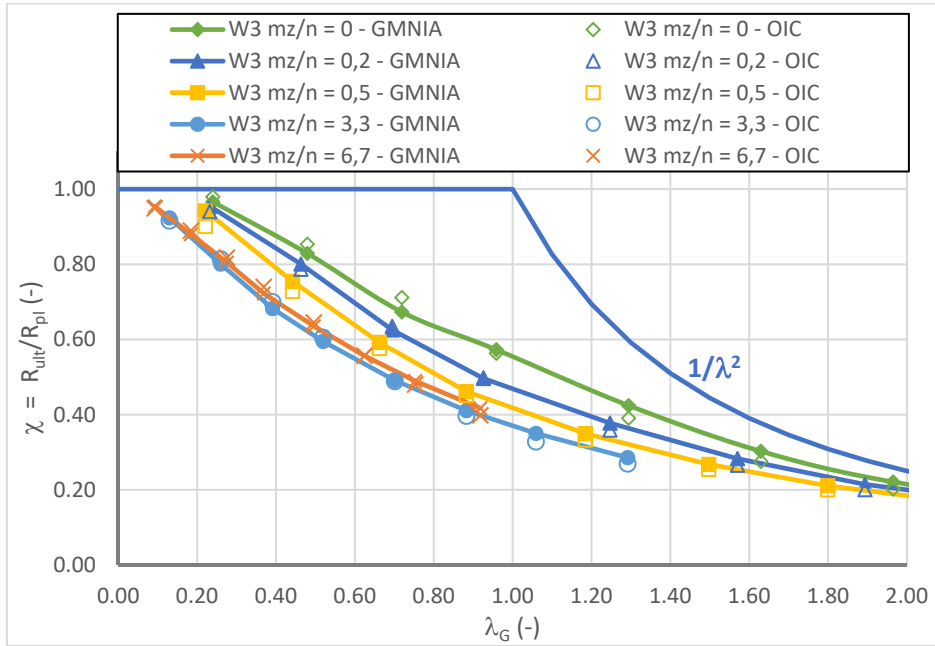


Figure 5-197: Ultimate resistance curves for a member of W850.6.300.12 (W3) section subject to combined axial force and minor-axis bending

Finally, Figure 5-198 and Figure 5-199 represent a statistical evaluation of the proposed OIC approach. Obviously, the vast majority of the predicted resistances is situated in the interval of $0,9\chi_{GMNIA} \dots 1,05\chi_{GMNIA}$. However, these cases concern two very short members subject to high major-axis bending. For these two examples, the numerically determined resistances attain $1,23R_{pl}$ and $1,31R_{pl}$ whereas the OIC predicted resistances only attain 0,951 and 0,965, respectively. As the OIC model is explicitly limited to a maximum value of 1,0 for the “reduction” factor χ it seems reasonable to limit the GMNIA strength to the theoretical plastic resistance of the most loaded cross-section **for the comparison**. If this is done the results represented in Figure 5-199 are obtained and confirm the quality of the proposal in terms of precision.

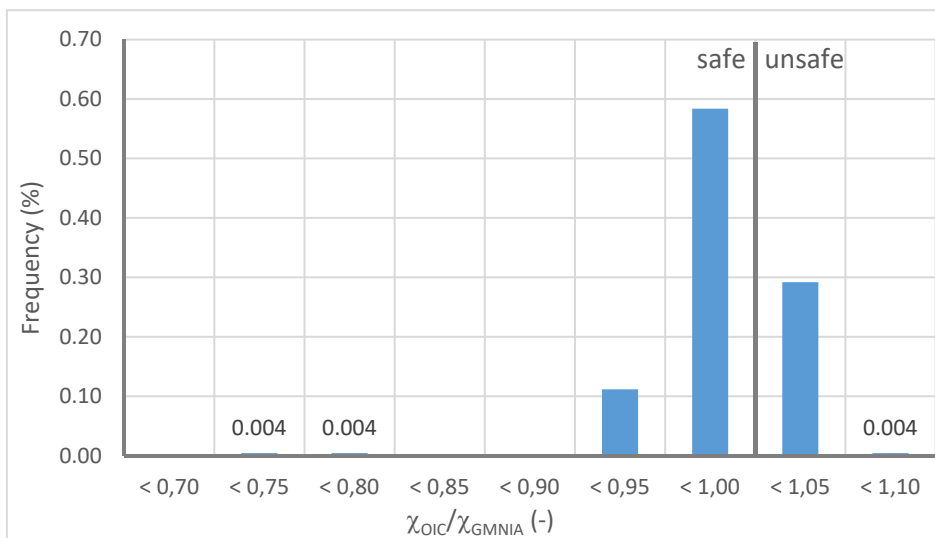


Figure 5-198: Ratio between OIC predicted resistance and numerically obtained resistance

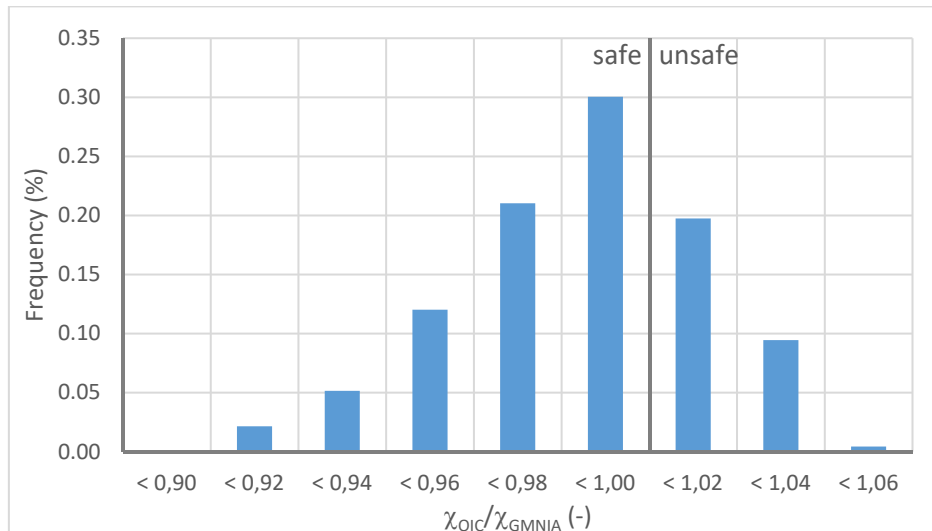


Figure 5-199: Ratio between OIC predicted resistance and numerically obtained resistance – not considering case exceeding the plastic cross-section resistance

Last, Table 5-49 compares the proposed OIC approach with the OIC proposal of Taras and the provisions given in Eurocode 3 Part 1-1. All methods yield a mean value of the ratio $\chi_{Method}/\chi_{GMNIA}$ close to 1,0. Yet, the standard deviation of the results determined with the Eurocode 3 Part 1-1 interaction equations (with Annex B for the interaction coefficients k_{ij}) is slightly higher than for both OIC proposals. Despite the (slight) differences between the design models it may be concluded that all three approaches are satisfactory to predict the resistance of I shaped members under combined axial force and minor-axis bending.

Table 5-49: Evaluation of different approaches for flexural buckling of double-symmetric I sections under combined axial force and minor-axis bending

$\chi_{Method}/\chi_{GMNIA}$	Proposed OIC format	Taras' OIC proposal	Eurocode 3 Part 1-1 - §6.3.3 + Annex B
Mean value	0,984	0,990	0,977
Standard deviation	0,027	0,025	0,052
Maximum value	0,911	0,912	0,841
Minimum value	1,057	1,060	1,028

Through the two previous paragraphs the OIC format has been calibrated to the case of lateral-torsional buckling in presence of major-axis bending only and flexural buckling in presence of combined axial force and minor-axis bending. It has been shown that a strength prediction in the OIC format may be very precise even if it is based only on a few parameters that may be determined with straightforward and easy to apply numerical tools. Nonetheless, it has to be admitted that the proposal can only be considered as an adaption of existing design provisions as the OIC design model proposed in reference (Taras 2011). Hereafter, the OIC approach is extended to load cases that are not covered yet by the Overall Interaction Concept.

5.6.5.4 OIC approach for lateral-torsional buckling under combined major- and minor-axis bending

The proposed OIC format is recalled again for the studied load case in Eqs. (5.363), (5.364) and (5.365).

$$\chi_G = \frac{R_{pl,MyN}}{R_{pl,ov}} \frac{1}{\phi + \sqrt{\phi^2 - \bar{\lambda}_G^2 \frac{R_{pl,MyN}}{R_{pl,ov}}}} \quad (5.363)$$

$$\phi = 0,5 \left(f_{Instab} + \frac{\alpha}{\sqrt{\frac{R_{pl,MyN}}{R_{pl,ov}}}} \left(\bar{\lambda}_{MB} - 0,2 \right) + \bar{\lambda}_G^2 \frac{R_{pl,MyN}}{R_{pl,ov}} \right) \quad (5.364)$$

$$f_{Instab} = \frac{R_{pl,MyN}}{R_{pl,ov}} - \left(\frac{R_{pl,MyN}}{R_{pl,ov}} - \frac{R_{el,MyN}}{R_{el,ov}} \right) C_{ms,z} \bar{\rho} \bar{\lambda}_G \leq \frac{R_{el,MyN}}{R_{el,ov}} \quad (5.365)$$

The main parameters included in Eqs. (5.363), (5.364) and (5.365) are defined for the load case of combined major-axis and minor-axis bending in Eqs. (5.366) to (5.369).

$$R_{pl,MyN} = \frac{M_{y,pl}}{M_y} \quad (5.366)$$

$$R_{pl,ov} = f(M_y, M_z) \quad (5.367)$$

$$R_{el,MyN} = \frac{M_{y,el}}{M_y} \quad (5.368)$$

$$R_{el,ov} = \frac{1}{\frac{M_y}{M_{y,el}} + \frac{M_z}{M_{z,el}}} \quad (5.369)$$

Obviously, the factor $R_{pl,ov}$ given in Eq. (5.367) cannot be expressed by an analytical expression due to the highly non-linear character of the major-axis – minor-axis bending interaction. For the application of the design model it is determined based on the adapted PIFM presented in Chapter 4. Additionally, it is to be noted that the cross-section shape factor ρ is equal to 0,8 and that, in absence of an axial force, the equivalent uniform moment $C_{ms,z}$ becomes 1,0. Depending on the form and the fabrication process, the imperfection factor has been calibrated in paragraph 0. The obtained values are recalled in Table 5-50. Note again that the factor R_{cr}^* is calculated without considering the Saint-Venant's torsional stiffness of the member ($I_t = 0$).

Table 5-50: Imperfection factor α for lateral-torsional buckling

Cross-section	Imperfection factor α
Hot-rolled sections $h/b \leq 1,2$	$\alpha = 0,75 \frac{R_{cr}^*}{R_{cr}}$
Hot-rolled sections $h/b > 1,2$	$\alpha = 0,42 \frac{R_{cr}^*}{R_{cr}}$
Welded sections	$\alpha = 0,58 \frac{R_{cr}^*}{R_{cr}}$

As before, the numerically obtained ultimate resistance curves are compared to the proposed design model for three examples. Figure 5-200 shows the results for the welded section W850.5,5.200.14, Figure 5-201 shows the results for the hot-rolled section IPE 500 ($h/b > 1,2$) and Figure 5-202 shows the results for the hot-rolled section HEB 200 ($h/b < 1,2$). The results are represented as a function for the degree of bi-axiality given by the ratio $m_z/m_y = M_z/M_{z,pl}/(M_y/M_{y,pl})$.

For the welded section the simple OIC design approach is shown to be rather satisfying as for the majority of the case the results are very close to the reference values obtained numerically. Yet, in some cases the proposal is slightly unsafe (maximum ratio $R_{ult,OIC}/R_{ult,GMNIA} \approx 1,055$). In Figure 5-200, it may also be observed that the OIC approach seems the least well suited for the welded members under major-axis bending only. The discrepancy is mainly due to the shape of the reduction curve itself because it does not well represent the changes of the curvature present in the numerically obtained ultimate resistance curve. It may be recalled that the typical shape of the ultimate resistance curve of welded members in major-axis is characterised by three inversions of the sign of the curvature. For given example (observe the green curve in Figure 5-200) it changes from concave to convex at relative slenderness of about 0,85 then it changes back to concave at a slenderness of about 1,14 and finally it changes again at a relative slenderness of about 1,5 from concave to convex.

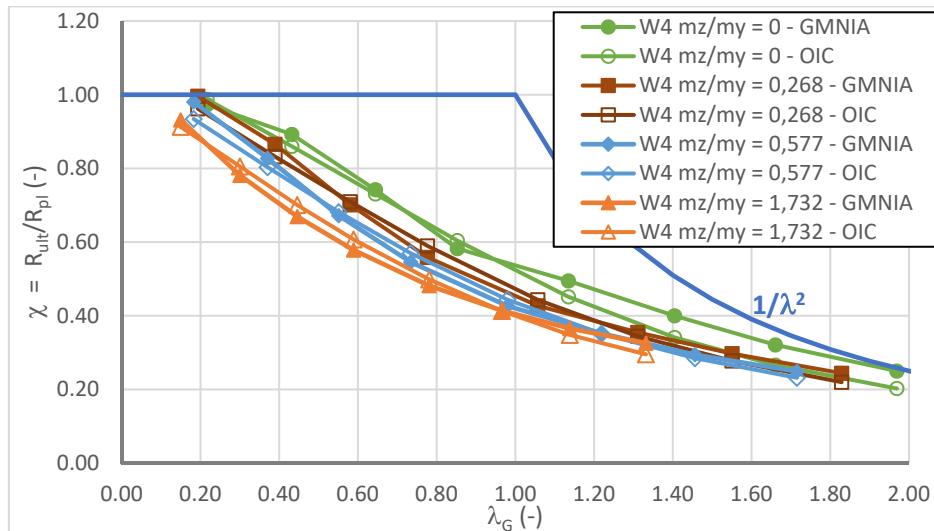


Figure 5-200: Ultimate resistance curves for a member of W850.5,5.200.14 (W4) section subject to combined major-axis and minor-axis bending

The complex form of the ultimate resistance curve for welded members under major-axis bending has been discussed extensively in reference (Villette 2004) and led this last author to propose special reduction curves for welded sections. Nevertheless, for sake of simplicity this is not done here and the same format for the reduction curve is applied for members of welded and of hot-rolled sections. Hence a certain conservatism is accepted for welded sections.

Figure 5-201 shows that the proposed OIC approach is again very satisfactory when it is applied to members of IPE 500 section. Conversely to the case of the welded member studied before the reduction curve practically overlaps the ultimate resistance curve associated with the member subject to major-axis bending only. For high minor-axis bending moments ($m_z/m_y = 1,732$) the proposed approach loses its precision. Nonetheless, the difference is of about 20% (safe-sided) obtained for a member with a length of 12 m. This member seems to be at the limit of the practical range (or even beyond) and consequently the discrepancy certainly acceptable.

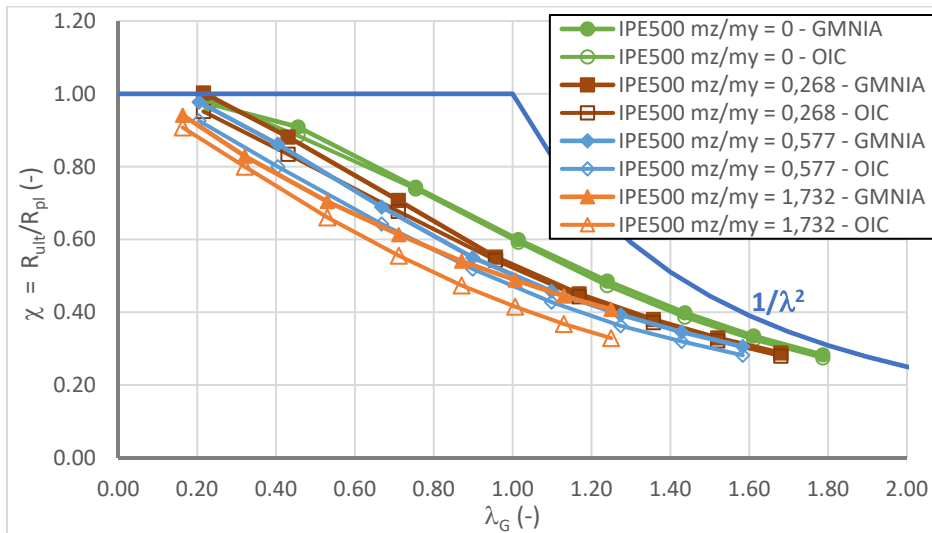


Figure 5-201: Ultimate resistance curves for a member of IPE 500 section subject to combined major-axis and minor-axis bending

Finally, Figure 5-201 represents the results of members fabricated from HEB 200 section. For this compact section ($h/b < 1,2$) one may observe many differences compared to the two sections studied before. First, obviously the ultimate resistance curves obtained numerically are very close to each other independently of the degree of bi-axiality. This may be understood as both, the ratio between the bending moment resistances $M_{y,pl}/M_{z,pl}$ and the ratio between the second moment of area about the major- and the minor-axis, are much lower than the same ratios for sections IPE 500 and W850.5,5.200.14. Consequently, it seems that the initiation of instability is not as much affected by an increase of the minor-axis bending moment as for the less compact sections (in terms ratio h/b) studied Figure 5-200 and Figure 5-201. Still, one may note that the maximum safety margin is only of about 25% for the extreme case of a member of HEB 200 section with a length of 12 m subject to bi-axial bending with a ratio m_z/m_y equal to 1,732.

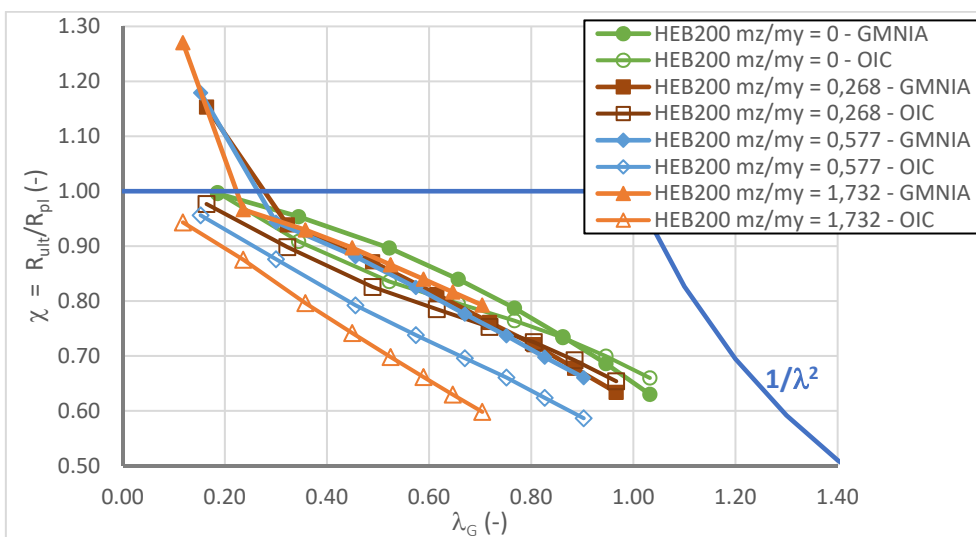


Figure 5-202: Ultimate resistance curves for a member of HEB 200 section subject to combined major-axis and minor-axis bending

In order to improve the design model for compact hot-rolled sections a modification of the transition function is proposed. Indeed, it seems that the transition from plastic to elastic cross-section interaction is modified as, with increasing minor-axis bending, instability is initiated differently for these compact sections. Consequently, the several requirements concerning the modification may be formulated:

- The resistance prediction for compact sections ($h/b < 1,2$) should be ameliorated;
- The resistance prediction for other types of sections should not be deteriorated;
- The resistance prediction for the previously studied load cases should not be affected (combined axial force and minor-axis bending as well as only major-axis bending).

These requirements indicate that the modification should be a function of the bi-axiality and should vanish if the member is subject to major-axis bending only. Therefore, it is obviously necessary to include the parameter m_y/m_z . Also, the modification should be a function of the geometry of the cross-section and vanish for sections that possess a tall ratio h/b . The comparison to numerical simulations has highlighted that the ratio I_z/I_y leads to more precise results than a modification based on the ratio h/b or (b/h) . In order to consider the specific behaviour of compact sections, it is proposed to adapt the transition function f_{Instab} as follows:

$$f_{Instab,2} = \frac{R_{pl,MyN}}{R_{pl,ov}} - \left(\frac{R_{pl,MyN}}{R_{pl,ov}} - \frac{R_{el,MyN}}{R_{el,ov}} \right) C_{ms,z} \mathcal{F}_{yz} \bar{\lambda}_G \leq \frac{R_{el,MyN}}{R_{el,ov}} \quad (5.370)$$

and:

$$f_{yz} = \max \left(0; 1 - 3,9 \frac{m_z}{m_y} \left(\frac{I_z}{I_y} \right)^2 \right) \quad (5.371)$$

Admittedly, the factor f_{yz} is of purely empirical nature. Yet, it represents well the tendencies observed Figure 5-200, Figure 5-201 and Figure 5-202. In particular the precision of the proposed OIC approach is highly improved for compact sections as shown in Figure 5-203.

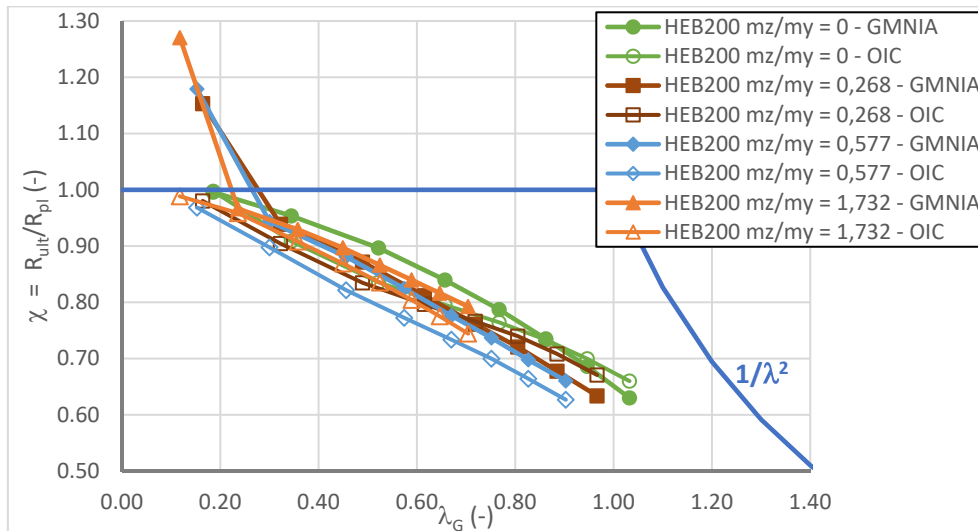


Figure 5-203: Ultimate resistance curves for a member of HEB 200 section subject to combined major-axis and minor-axis bending – modified function $f_{Instab,2}$

So as to highlight the quality of the proposed design model further on, Table 5-51 represents a comparison of its precision to the results obtained with the Eurocode 3 Part 1-1 interaction equations. Table 5-51 clearly shows that:

- The modification of the function f_{Instab} increases the precision of the proposal for compact sections without deteriorating the results for other types of sections;
- The scatter as well as the mean value of the results obtained with the OIC approach combined with the modified function $f_{Instab,2}$ is very homogenous for all section types;
- If the initial expression of the function f_{Instab} is applied the OIC approach is slightly more conservative and the standard deviation of the ratio χ_{OIC}/χ_{GMNIA} is increased. Nonetheless, the even the OIC approach without the modified function $f_{Instab,2}$ seems to be less conservative than the interaction equations proposed in Eurocode 3 Part 1-1;
- The standard deviation of the results obtained with the interaction equations proposed in Eurocode 3 Part 1-1 is significantly higher for all section types than the one obtained with the OIC approach (combined with the modified function $f_{Instab,2}$);
- The standard deviation and especially the mean value of the results obtained with the interaction equations proposed in Eurocode 3 Part 1-1 varies significantly depending on the type of the cross-section.

Table 5-51: Statistical evaluation of OIC approach and Eurocode 3 Part 1-1 interaction formulae

		OIC with modification of f_{instab}	OIC without modification of f_{instab}	EC 3-1-1 Interaction formulae
Welded sections	Mean value χ_{OIC}/χ_{GMNIA}	0,988	0,988	0,899
	Standard deviation χ_{OIC}/χ_{GMNIA}	0,048	0,048	0,071
HR sections $h/b > 1,2$	Mean value χ_{OIC}/χ_{GMNIA}	0,945	0,942	0,956
	Standard deviation χ_{OIC}/χ_{GMNIA}	0,055	0,057	0,100
HR sections $h/b < 1,2$	Mean value χ_{OIC}/χ_{GMNIA}	0,954	0,888	0,843
	Standard deviation χ_{OIC}/χ_{GMNIA}	0,053	0,096	0,092
Overall	Mean value χ_{OIC}/χ_{GMNIA}	0,964	0,950	0,911
	Standard deviation χ_{OIC}/χ_{GMNIA}	0,055	0,073	0,097

Globally, the comparison shows that the OIC approach seems to better represent the behaviour of the tested members under combined major-axis and minor-axis bending. Nevertheless, this cannot be understood as final conclusion on the superiority of the OIC approach over the interaction equations as they possess a larger field of application. Still, it seems remarkable that the rather simple OIC format is capable to represent precisely the complex interaction of major-axis and minor-axis bending for members of open sections.

Finally, Figure 5-204 and Figure 5-205 illustrate again the particular problem linked to the interaction equations of Eurocode 3 Part 1-1. In fact, they represent rather well the behaviour of slender members. On the contrary, the resistance of shorter specimen is not well represented as the plastic interaction is approximated only roughly by the interaction equations. This results in a safety margin of over 20% for short members subject to combined major-axis and minor-axis bending.

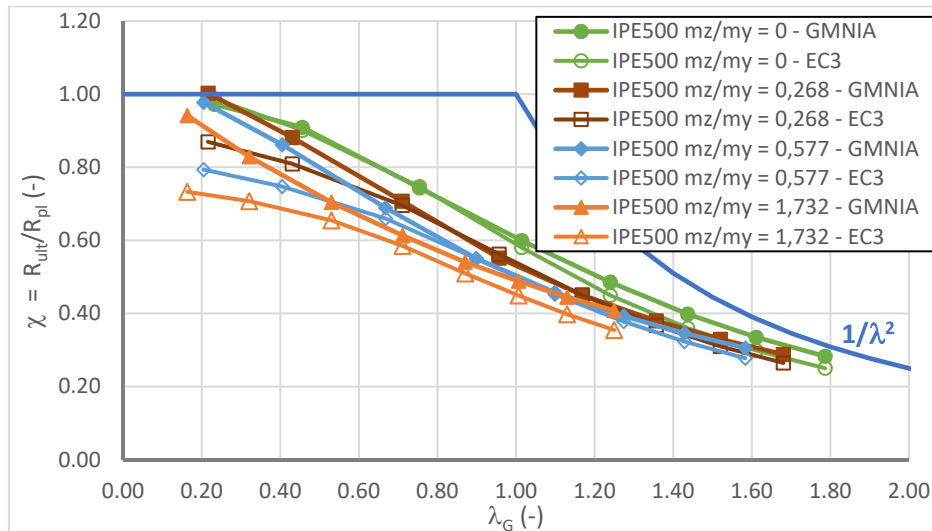


Figure 5-204: Ultimate resistance curves for a member of IPE 500 compared to strength predictions obtained with Eurocode 3 Part 1-1 interaction formulae

In addition to what has been observed in Figure 5-204, Figure 5-205 shows that the strength prediction of Eurocode 3 Part 1-1 may be rather conservative for long members of compact section as the interaction factors k_{ij} determined with Annex B (CEN 2005a) do not seem to include the specific transition behaviour between plastic and elastic interaction for compact sections possessing a ratio h/b inferior to 1,2 (this is also the case for the OIC approach based on the initial formulation of the function f_{Instab}).

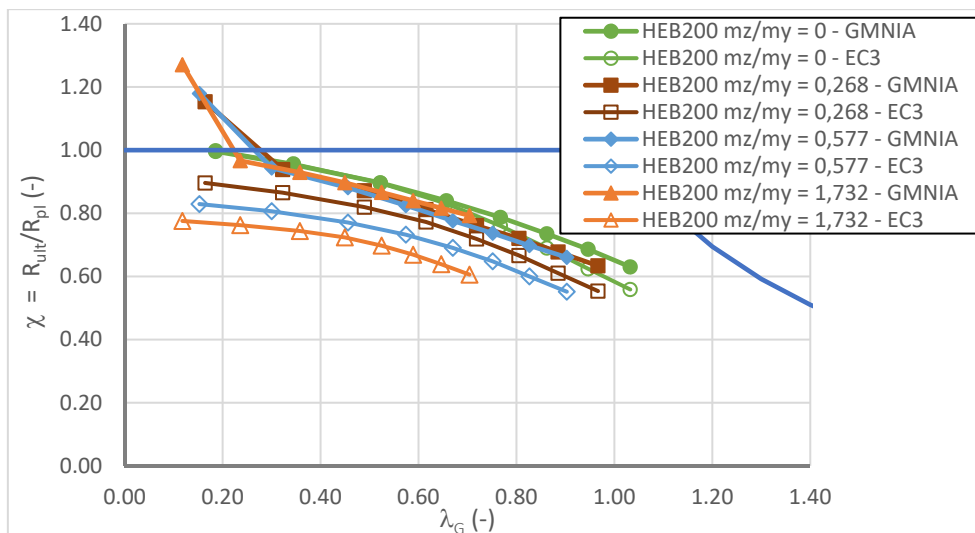


Figure 5-205: Ultimate resistance curves for a member of HEB 200 compared to strength predictions obtained with Eurocode 3 Part 1-1 interaction formulae

Up to this point, the load cases of uniform major-axis bending, combined axial force and minor-axis bending as well as combined major-axis and minor-axis bending have been studied. For these load cases, it has been shown that the OIC approach, even if it is based on very few parameters, is capable to predict rather precisely the behaviour of members of double symmetric I sections. In particular, it has been shown that the precision is comparable to the most straightforward design

methods proposed in the recent past and its precision even higher than the one of the currently applicable Eurocode 3 Part 1-1 interaction equations (applied with the Annex B interaction factors). Nonetheless, it should be noted, that the load cases studied before have the common particularity that only one of the internal forces and moments generates second order effects and instability (major-axis bending **or** axial force). Indeed, the minor-axis bending moment applied in the last two paragraphs is amplified by the effect of instability but does not generate second order effects itself. Consequently, minor-axis bending does not interact with the instability mode of flexural buckling if it is combined with an axial force and it does not interaction with the instability mode of lateral-torsional buckling if it is combined with the major-axis bending moment. In the next paragraph, the resistance of members subject to combined major-axis bending and axial compression forces is studied. For this load combination both internal forces and moments generate second order effects and instability. Therefore, a certain interaction between both modes of instability is expected. Moreover, due to the in-plane displacements the major-axis bending moment is amplified by the axial force. Hence, the load case studied next is of much higher complexity as the ones previously investigated.

5.6.5.5 OIC approach for combined major-axis bending and axial force

Before the OIC approach is compared to the numerical results, it seems interesting to analyse the member behaviour depending on the cross-section. In the following, three sections are considered: the compact HEB 200 section, the IPE 500 section sensitive to lateral-torsional buckling and the welded section W850.6.300.12 that is also sensitive to lateral-torsional buckling. In all cases the results are represented as a function $m_y/n = (M_y/M_{y,pl})/(N/N_{pl})$.

First, Figure 5-206 represents the ultimate resistance curves obtained for the members of HEB 200. It is recalled that the same range of member lengths is studied (5b ... 55b) but the resulting range of relative slenderness obviously depends on the sensitivity of the member for the given mode of instability (flexural buckling, lateral-torsional buckling or combination of both). When one observes the ultimate resistance curves for the members of HEB 200 section, one identifies several interesting points:

- Obviously, the members are less sensitive to lateral-torsional buckling than to flexural buckling. In fact, one easily observes that the curve linked to $m_y/n = \infty$ ($N = 0$) is much higher in the diagram than the curve linked to $m_y/n = 0$ ($M_y = 0$). Nonetheless, this result is expected as the HEB 200 section is rather compact and not very sensitive to lateral-torsional buckling as is also suggested by the association of the Eurocode 3 Part 1-1 reduction curves: curve *a* for lateral-torsional buckling and curve *c* for minor-axis buckling;
- With increasing axial force, the ultimate resistance curves descend in the diagram and approach the curve associated with the case of buckling under a sole axial force. But the decrease of the resistance with increasing axial force is not linear;
- For very low values of the axial force (up to $m_y/n = 20$) the influence of the axial force seems to be negligible. For low values of the relative slenderness the

resistance of the member with $m_y/n = 0,05$ is even slightly higher than the resistance of the member under pure major-axis bending. Yet, the difference is very low (<1%) and may simply be due to the numerical calculation tolerances;

- The influence of the axial force becomes visible for a ratio m_y/n of about 6,7. However, the decrease of the ultimate resistance curves appear to stop up to a ratio $m_y/n = 0,2$ as both curves (as well as all intermediate curves that are not represent to facilitate the lecture of the diagram) practically overlap;
- When the axial force is increased further on ($m_y/n = 0,05$), the ultimate resistance curve approaches the curve linked to a sole axial force again.

Globally, one may conclude that the ultimate resistance curves follow the expected scheme. Indeed, all curves are situated between the curves linked to the extreme load cases of major-axis bending only and axial force only.

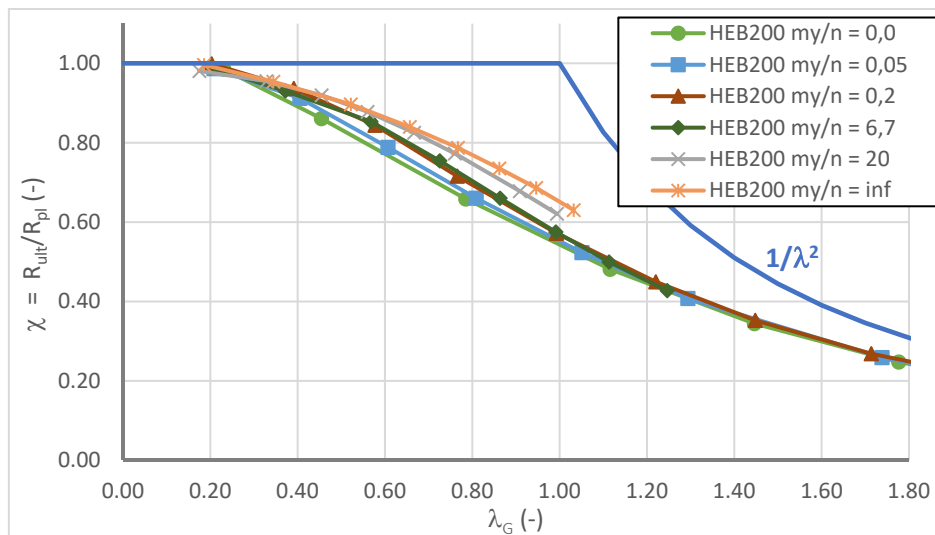


Figure 5-206 : Ultimate resistance curves for members of HEB 200 section under combined major-axis bending and axial force

Next, Figure 5-207 shows the results obtained for the members of IPE 500 section. One may observe that:

- The ultimate resistance curves are much closer to each other than for the members of HEB 200 section. Again, this does not seem surprising as members of IPE 500 section appear to be equally sensitive to flexural buckling and lateral-torsional buckling as suggested by the attribution of reduction curve *b* for both flexural buckling about the minor-axis and lateral-torsional buckling;
- For longer members the results obtained for the member subject to a sole axial compression force become more favourable than the results linked to the member under uniform major-axis bending. This may again be attributed to the favourable effect of the torsional twist that can even lead to ultimate resistance curves crossing the Euler curve (see for example paragraph 5.2.1.2);

- If one observes the ultimate resistance curves in more detail, it appears that the curves linked to combined major-axis bending and axial forces lie beneath the curves linked to the extreme cases of $m_y/n = 0$ and $m_y/n = \infty$. For these cases, there seems to be a noticeable interaction between both modes of instability.

Based on the observation, one may conclude that the behaviour of members of IPE 500 section seems to be more complex than the behaviour of members fabricated from more compact sections as for example HEB 200.

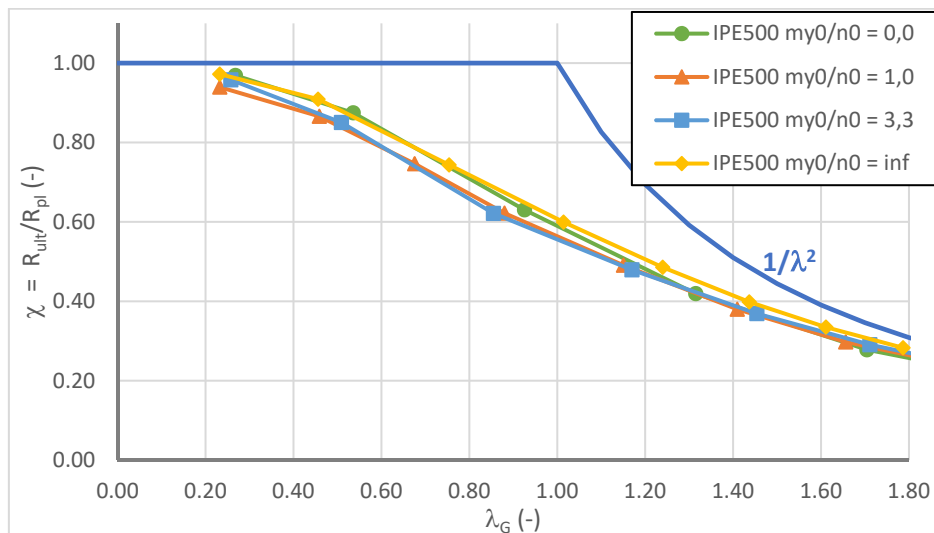


Figure 5-207 : Ultimate resistance curves for members of IPE 500 section under combined major-axis bending and axial force

Last, the case of the welded section W850.6.300.12 (W3) is studied. Here, it is recalled that local instability is not accounted for in the numerical simulations in the framework of OIC (see paragraph 5.2.3). Figure 5-208 shows in particular that:

- The ultimate resistance curves are again rather close, but less than for the members of IPE 500 section. This seems somewhat in contrary to what is predicted by Eurocode 3 Part 1-1 (buckling curve *c* and lateral-torsional buckling curve *d*) but it is recalled that the provisions given in the European standard for lateral-torsional buckling of members of welded section appear to be conservative (see paragraphs 5.2.1.2 and 5.6.4.2);
- Also, as for the members of IPE 500 section the curves for intermediate values of the ratio m_y/n do not lie between the curves associated with the extreme values $m_y/n = 0$ and $m_y/n = \infty$. But, it seems that the behaviour of the members represented in Figure 5-208 is even more complex because the curve associated with combined major-axis bending and **low** axial force ($m_y/n = 3,3$) lies **above** the curve of the member subject to a sole major-axis bending moment and the curve associated with combined major-axis bending and **high** axial force lies **below** the curve linked to the member subject to a sole axial force. Based on the observations of the members of IPE 500 section it could have been expected that the interaction

between flexural and lateral-torsional buckling decreases the resistance of the members. Yet, a low axial force ($m_y/n = 3,3$) seems to possess a favourable effect;

- The favourable effect of a low axial force can be explained based on the specific lateral-torsional buckling behaviour of welded members. Indeed, in Figure 5-208 on may again observe that the ultimate resistance curves of the members subject to major-axis bending possesses a different shape, characterised by three changes of the curvature (concave to convex at $\lambda_G \approx 0,8$; convex to concave at $\lambda_G \approx 1,1$; again concave to convex at $\lambda_G \approx 1,4 \dots 1,5$) than the curves associated with an axial force. Due to the several changes of the curvature, the ultimate resistance curves of welded sections under major-axis bending only possesses a certain notch for values of the relative slenderness between 0,6 and 1,1. A low axial force seems to straighten the curve and consequently leads to higher results for intermediate values of the relative slenderness;
- For relative high values of the axial force ($m_y/n = 1,0$), the interaction between flexural buckling and lateral-torsional buckling leads again to a descend of the ultimate resistance curve beneath the curve associated with the extreme case $m_y/n = 0$.

It appears that the behaviour of welded members is even more complex than the behaviour observed for the members of IPE 500 section. Nonetheless, in paragraph 0 it has already been accepted to apply the same form of the reduction curve for welded members and for members of hot-rolled section for the case of lateral-torsional buckling. The slight loss of precision can be accepted. For the development of the OIC approach for interaction between flexural buckling and lateral-torsional buckling it is not intended to obtain a higher precision than for the case of the individual instability modes but to develop a **sufficiently precise** approach that ensures a necessary level of safety.

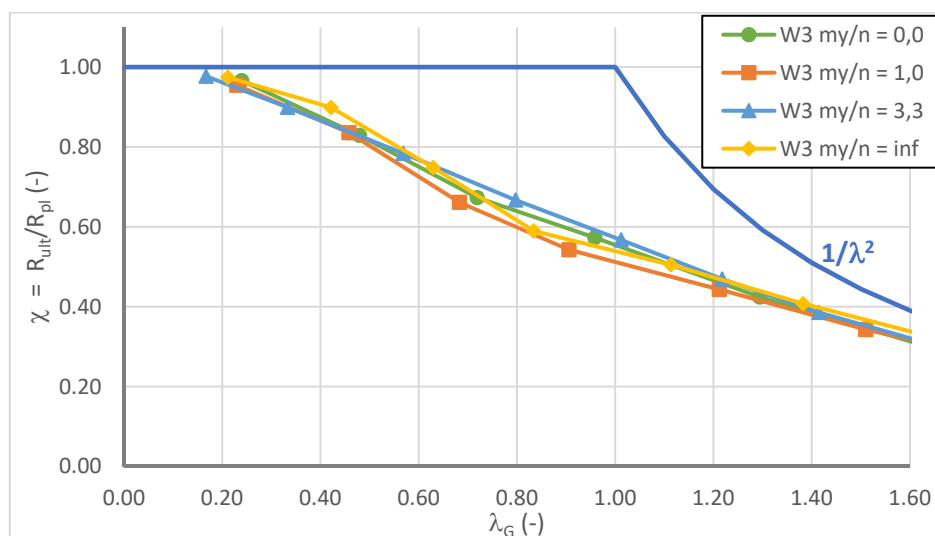


Figure 5-208 : Ultimate resistance curves for members of W850.6.300.12 section under combined major-axis bending and axial force

The study of the ultimate resistance curves represented in Figure 5-206, Figure 5-207 and Figure 5-208 has highlighted that the key factor for the development of the OIC design method is the determination of a suitable imperfection factor that i) should tend to the value of the imperfection factor applicable for the extreme cases of $m_y/n = 0$ and $m_y/n = \infty$ and ii) should represent sufficiently precisely the interaction between flexural buckling and lateral-torsional buckling. Depending on the cross-section, the imperfection factors for the proposed OIC approach are recalled in Table 5-52. It is also recalled that the critical load amplification factor R_{cr} is calculated based on the gross section characteristics and that R_{cr}^* is calculated neglecting the Saint-Venant's torsional stiffness of the member ($I_t = 0$). In case of combined major-axis bending and axial force, both factors are calculated for the studied load combination. As the major-axis bending moment is constant along the member the analytical expressions derived in paragraph 5.5.5.2 can be applied.

Table 5-52: Imperfection factors for the proposed OIC approach

Cross-section	Imperfection factor for minor-axis flexural buckling α_N	Imperfection factor for lateral-torsional buckling α_{My}
Hot-rolled $h/b \leq 1,2$	0,49	$0,75 \frac{R_{cr}^*}{R_{cr}}$
Hot-rolled $h/b > 1,2$	0,34	$0,42 \frac{R_{cr}^*}{R_{cr}}$
Welded	0,49	$0,58 \frac{R_{cr}^*}{R_{cr}}$

Here, it is proposed to define the interaction of the imperfection factors based on the critical loads of the individual instability mode as follows:

$$\alpha_{MyN} = \frac{\left(\alpha_N \frac{N}{N_{cr,z}} + \alpha_{My} \frac{M_y}{M_{y,cr}} + f_{interact} \right)}{\frac{N}{N_{cr,z}} + \frac{M_y}{M_{y,cr}}} \quad (5.372)$$

Eq. (5.372) represents a simple linear interaction between the imperfection factors but with the addition of a function $f_{interact}$ that increases the imperfection factor to account for the interaction between flexural buckling and lateral-torsional buckling. Obviously, this function should vanish if the member is subject to an axial force only or to major-axis bending only. Additionally, it should affect less the resistance of short members, which are not sensitive to instability, than the resistance of the longer counterparts. Finally, it seems justified to consider that the interaction is more pronounced if the amplification factors for the individual imperfection mode of flexural and lateral-torsional buckling are close.

A very simple expression of the interaction function f_{interact} respecting these three criteria is given in Eq. (5.373).

$$f_{\text{interact}} = \alpha_{\text{interact}} \bar{\lambda}_G \text{Min} \left(\begin{array}{l} \frac{N}{N_{cr,z}} ; \frac{M_y}{M_{y,cr}} \\ \frac{M_y}{M_{y,cr}} ; \frac{N}{N_{cr,z}} \end{array} \right) \quad (5.373)$$

The third factor of Eq. (5.373) represents the sensitivity of a given member under a given load combination to the interaction between the two studied mode of instability. It varies between 0 and 1,0. The specific imperfection factor α_{interact} introduces the influence of the imperfection on the interaction and the factor $\bar{\lambda}_G$ translates the transition between short and long members. This factor has to be calibrated. As, depending on the form of the cross-section and the fabrication process, the interaction between the modes of instability is more or less pronounced it is proposed to determine a specific factor α_{interact} for welded sections, hot-rolled sections with $h/b < 1,2$ and hot-rolled sections with $h/b > 1,2$. The calibration is performed with the objective to determine a design model that ensures at least the level of safety and precision of the Eurocode 3 Part 1-1 interaction formulae. When these interaction equations (together with Annex B of Eurocode 3 Part 1-1) are applied to the studied examples, the statistical values of Table 5-53 are obtained.

Table 5-53: Statistical evaluation of Eurocode 3 interaction equations

Mean $\chi_{\text{EC3}}/\chi_{\text{GMNIA}}$	0,918
Standard deviation $\sigma \chi_{\text{EC3}}/\chi_{\text{GMNIA}}$	0,076
Mean + 2 σ	1,071
Maximum $\chi_{\text{EC3}}/\chi_{\text{GMNIA}}$	1,109
Minimum $\chi_{\text{EC3}}/\chi_{\text{GMNIA}}$	0,730

The calibration of the imperfection interaction factor α_{interact} represents an optimisation problem. As optimisation criterion it is chosen to minimize the standard deviation of the results. Additionally, a boundary value of Mean + 2 σ of 1,08 is introduced in order ensure a sufficient level of safety. The results of the optimisation problem are given in Table 5-54. It is shown that the proposed OIC approach yields results that are at least equally precise as the Eurocode 3 interaction equations. Especially, the results of the compact hot-rolled sections ($h/b < 1,2$) are very precise. Admittedly, the interaction between the instability modes is the least pronounced for these sections. The precision for members of hot-rolled sections with $h/b > 1,2$ and welded members is somewhat less but still very acceptable compared to the provision given in Eurocode 3 Part 1-1.

Table 5-54 : Evaluation of the imperfection factor $\alpha_{interact}$

Section	$\alpha_{interact}$	Mean χ_{OIC}/χ_{GMNIA}	σ χ_{OIC}/χ_{GMNIA}	Mean + 2 σ	Maximum χ_{OIC}/χ_{GMNIA}	Minimum χ_{OIC}/χ_{GMNIA}
Hot-rolled h/b<1,2	0,07	0,962	0,026	1,015	1,021	0,912
Hot-rolled h/b>1,2	0,18	0,958	0,050	1,057	1,042	0,861
Welded	0,30	0,900	0,089	1,079	1,036	0,744
Overall	-	0,939	0,068	1,075	1,042	0,744

Figure 5-209 and Figure 5-210 compare the strength prediction obtained with the proposed OIC approach and the provisions given in Eurocode 3 Part 1-1 to the numerically determined ultimate resistance curves. Clearly, the OIC approach proposed here provides very precise results for the members of IPE 500 section over the whole range of the relative slenderness. For the extreme cases of $m_y/n = 0$ and $m_y/n = \infty$ the difference is negligible between the numerical results and the strength predictions. In case of interaction between flexural and lateral-torsional buckling one may observe slight differences but the proposal is close to the reference results and only slightly safe-sided.

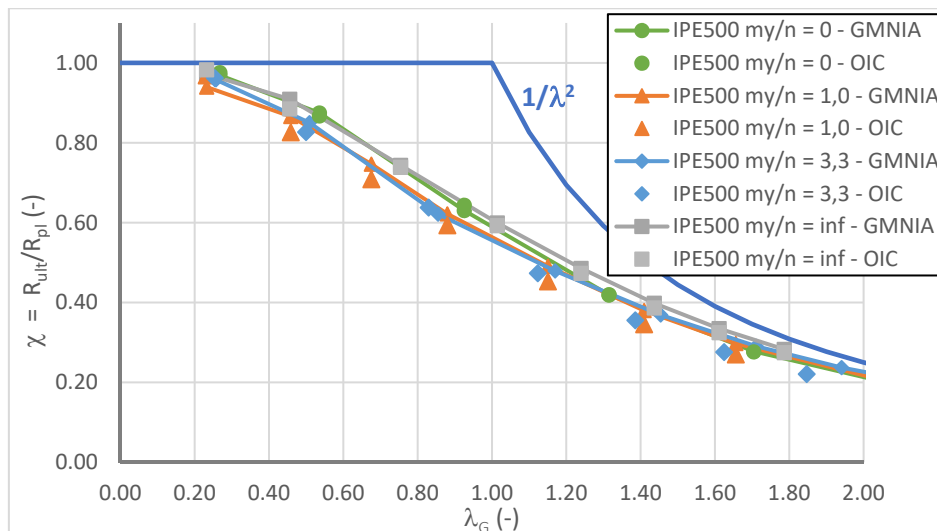


Figure 5-209: Ultimate resistance curves for members of IPE 500 section compared to OIC strength prediction

Figure 5-210 shows that the Eurocode 3 interaction equations together with the Annex B interaction factors represent well the resistance of the members, too. Nevertheless, it appears that for longer members the strength predictions deviate from the reference results and this even for the member subject to major-axis bending only. For members subject to major-axis bending only,

the factor R_{cr}^*/R_{cr} linked to the imperfection factor α_{My} in the OIC approach appears to be beneficial again.

Figure 5-210 also shows that the Eurocode 3 strength predictions derive from the reference results for short members under combined major-axis bending and torsion. For these cases the difference between the results can be explained based on the simplified approximation for the cross-section interaction in the interaction equations.

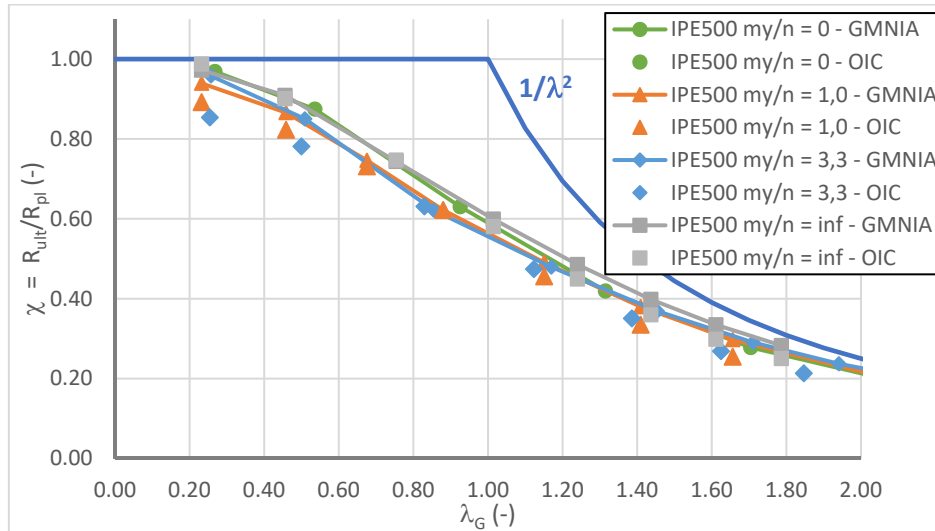


Figure 5-210: Ultimate resistance curves for members of IPE 500 section compared to OIC strength prediction

The developments and comparisons presented in this paragraph have shown that the OIC resistance model is capable to represent reliably the strength of members under combined axial force and major-axis bending even if this load case is highly complex and leads to interaction between the instability modes of minor-axis flexural and lateral-torsional buckling. The OIC approach leads to results that appear to be even more precise than the Eurocode 3 strength predictions especially for short members thanks to the continuous transition between the exact plastic cross-section resistance and failure by elasto-plastic instability. In the next paragraph, the OIC approach is applied to members subject to combined bi-axial bending and compression axial force. Consequently, paragraph 5.6.5.6 evaluates the OIC resistance model for a combination of the cases studied in the four previous paragraphs: 0 – OIC for members under major-axis bending only; 5.6.5.3 – OIC for members under combined axial compression force and major-axis bending; 5.6.5.4 – OIC for members under bi-axial bending; 5.6.5.5 – OIC for members under combined axial compression force and major-axis bending.

5.6.5.6 OIC approach for combined bi-axial bending and axial force

Hereafter, the OIC approach developed in the previous paragraphs is evaluated for combined axial compression forces and bi-axial bending. It is recalled that the bending moments as well as the axial force are constant along the member. Also, all sections can be considered as class 1 (in the terminology of Eurocode 3 Part 1-1) as local plate instability is excluded in the numerical simulations (see paragraph 5.2.3). Before the proposed design model is applied, it seems necessary to recall the calculation steps for combined bi-axial bending and axial forces. This is done in Table 5-55.

Table 5-55: OIC calculation steps for combined axial compression force and bi-axial bending

Calculation steps	Detail
(Numerical) Determination of key factors	$R_{pl,ov}$: Load amplification factor to attain the plastic limit state of the most loaded section considering all internal forces and moments
	$R_{pl,MyN}$: Load amplification factor to attain the plastic limit state of the most loaded section considering only major-axis bending and the axial compression force
	$R_{el,ov}$: Load amplification factor to attain the elastic limit state of the most loaded section considering all internal forces and moments
	$R_{el,MyN}$: Load amplification factor to attain the elastic limit state of the most loaded section considering only major-axis bending and the axial compression force
	$R_{cr,G}$: Load amplification factor to attain the elastic critical load of the member subject to all loads (considering the influence of first order displacements)
	$R_{cr,G}^*$: Load amplification factor to attain the elastic critical load of the member without its Saint-Venant's torsional stiffness subject to all loads (considering the influence of first order displacements)
	$N_{cr,z}$: Elastic critical axial force for minor-axis flexural buckling
	$M_{y,cr}$: Elastic critical moment for lateral-torsional buckling
$\bar{\lambda}_G$: Global relative member slenderness	

<p>Determination of imperfection factors</p>	$\alpha_{MyN} = \frac{\left(\alpha_N \frac{N}{N_{cr,z}} + \alpha_{My} \frac{M_y}{M_{y,cr}} + f_{interact} \right)}{\frac{N}{N_{cr,z}} + \frac{M_y}{M_{y,cr}}}$ $f_{interact} = \alpha_{interact} \bar{\lambda}_G \text{Min} \left(\frac{\frac{N}{N_{cr,z}}}{\frac{M_y}{M_{y,cr}}}; \frac{\frac{M_y}{M_{y,cr}}}{\frac{N}{N_{cr,z}}} \right)$ <table border="1" data-bbox="564 645 1390 987"> <thead> <tr> <th>Section</th> <th>α_N</th> <th>α_{My}</th> <th>$\alpha_{Interact}$</th> </tr> </thead> <tbody> <tr> <td>Welded sections</td> <td>0,49</td> <td>$0,58 \frac{R_{cr}^*}{R_{cr}}$</td> <td>0,30</td> </tr> <tr> <td>Hot-rolled sections $h/b > 1,2$</td> <td>0,34</td> <td>$0,42 \frac{R_{cr}^*}{R_{cr}}$</td> <td>0,18</td> </tr> <tr> <td>Hot-rolled sections $h/b \leq 1,2$</td> <td>0,49</td> <td>$0,75 \frac{R_{cr}^*}{R_{cr}}$</td> <td>0,07</td> </tr> </tbody> </table>	Section	α_N	α_{My}	$\alpha_{Interact}$	Welded sections	0,49	$0,58 \frac{R_{cr}^*}{R_{cr}}$	0,30	Hot-rolled sections $h/b > 1,2$	0,34	$0,42 \frac{R_{cr}^*}{R_{cr}}$	0,18	Hot-rolled sections $h/b \leq 1,2$	0,49	$0,75 \frac{R_{cr}^*}{R_{cr}}$	0,07
Section	α_N	α_{My}	$\alpha_{Interact}$														
Welded sections	0,49	$0,58 \frac{R_{cr}^*}{R_{cr}}$	0,30														
Hot-rolled sections $h/b > 1,2$	0,34	$0,42 \frac{R_{cr}^*}{R_{cr}}$	0,18														
Hot-rolled sections $h/b \leq 1,2$	0,49	$0,75 \frac{R_{cr}^*}{R_{cr}}$	0,07														
<p>Determination of transition function</p>	$f_{Instab} = \frac{R_{pl,MyN}}{R_{pl,ov}} - \left(\frac{R_{pl,MyN}}{R_{pl,ov}} - \frac{R_{el,MyN}}{R_{el,ov}} \right) C_{ms,z} \rho f_{yz} \bar{\lambda}_G \leq \frac{R_{el,MyN}}{R_{el,ov}}$ <p>$\rho = 0,8$</p> $f_{yz} = \max \left(0; 1 - 3,9 \frac{m_z}{m_y} \left(\frac{I_z}{I_y} \right)^2 \right)$ <p>$C_{ms,z} = 1 + 0,27 \frac{N}{N_{cr,z}}$ (equivalent sinusoidal moment factor for constant bending moments)</p>																
<p>Determination of the reduction factor</p>	$\phi = 0,5 \left(f_{Instab} + \frac{\alpha_{MyN}}{\sqrt{\frac{R_{pl,MyN}}{R_{pl,ov}}}} \left(\bar{\lambda}_G - 0,2 \right) + \bar{\lambda}_G^2 \frac{R_{pl,MyN}}{R_{pl,ov}} \right)$ $\chi_G = \frac{R_{pl,MyN}}{R_{pl,ov}} \frac{1}{\phi + \sqrt{\phi^2 - \bar{\lambda}_G^2 \frac{R_{pl,MyN}}{R_{pl,ov}}}}$																

The elastic load amplification factors can be easily determined with the literal expressions given in Eqs. (5.374) and (5.375). One may notice that the equivalent sinusoidal moment factor is only linked to the minor-axis bending moment. Due to the geometry of the studied sections the critical axial force for major-axis buckling is always rather high and consequently the sinusoidal moment factor $C_{ms,y}$ is always close to one. Consequently, the present study cannot conclude on the necessity to apply $C_{ms,y}$ in Eqs. (5.374) and (5.375). In the future, other bending moment distributions and members with lateral restraints should be studied in order to check whether or not to use it is necessary to use $C_{ms,y}$ linked to M_y .

$$R_{el,MyN} = \frac{1}{\left(\frac{N}{N_{pl}} + \frac{M_y}{M_{y,el}} \right)} \quad (5.374)$$

$$R_{el,ov} = \frac{1}{\left(\frac{N}{N_{pl}} + \frac{M_y}{M_{y,el}} + C_{ms,z} \frac{M_z}{M_{z,el}} \right)} \quad (5.375)$$

At this point, no specific factor has been introduced for the load case of combined bi-axial bending and axial force. The design approach presented in Table 5-55 corresponds to a simple combination of the developments presented in the previous paragraphs.

The precision of the proposed OIC approach is compared to the Eurocode 3 Part 1-1 interaction formulae in Figure 5-211 (only examples including bi-axial bending and axial compression forces are evaluated). It may be observed that the OIC approach seems to be slightly too unsafe in case of combined bi-axial bending and axial compression. Nonetheless, the general shape of the distribution is satisfactory. It should be noted that the numerically obtained resistances exceeding the theoretical plastic resistance of the member are again limited to the plastic limit state of the member for the comparison because the OIC approach developed here explicitly excludes the influence of strain hardening. Anyhow, only the results of very short members are affected.

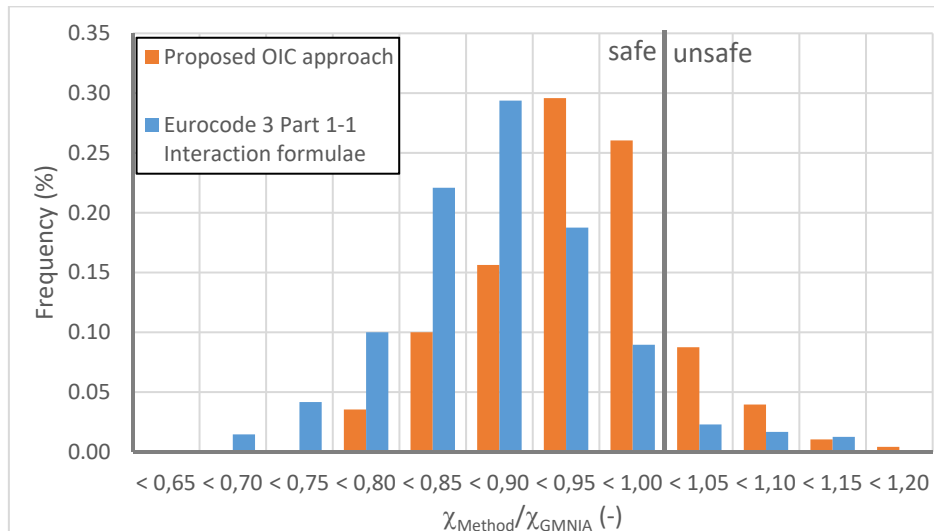


Figure 5-211: Ratio between OIC predicted resistance and numerically obtained resistance – not considering cases exceeding the plastic cross-section resistance

In order to analyse the unsafe results Figure 5-212 represents the ultimate resistance curves as well as the OIC approach for a member of HEB 200 section subject to bi-axial bending and an axial force. The GMNIA results are also represented for the extreme cases of an axial force combined with major-axis bending (MyMz0) and with minor-axis bending (MyMz90), respectively. So as to facilitate the lecture of the diagram the OIC approach is not represented for these case. A comparison has already been made in the previous paragraphs.

In Figure 5-212, one may easily identify the transition between the extreme cases MyMz0 and MyMz90. Again, it can be observed that small minor-axis bending moments only influence slightly the major-axis bending resistance (compare curves linked to MyMz0, MyMz15 and MyMz30). However, whereas all curves were very close for all degrees of bi-axiality in absence of an axial force, it is clear that the axial force causes a significant descent of the ultimate resistance curve linked to MyMz60 in the diagram. The proposed OIC approach represents well the resistance of the members with minor-axis bending moments of low and medium importance (MyMz15 and MyMz30). The maximum discrepancy is of about 15% (safe-sided) for these cases and intermediate values of the relative slenderness. The resistance of members under bi-axial bending with a predominant minor-axis bending moment is however not well represented. Indeed, it appears that the unsafe nature of the proposed OIC approach increases with the slenderness. It is recalled that the specific factor f_{zy} has been calibrated in paragraph 5.6.5.4 to account for the specific plastic-elastic transition behaviour for members of compact section ($h/b \leq 1,2$). It seems that this factor is too favourable in case of a supplementary applied axial compression force. It is therefore proposed to modify this factor to ensure a sufficient level of safety.

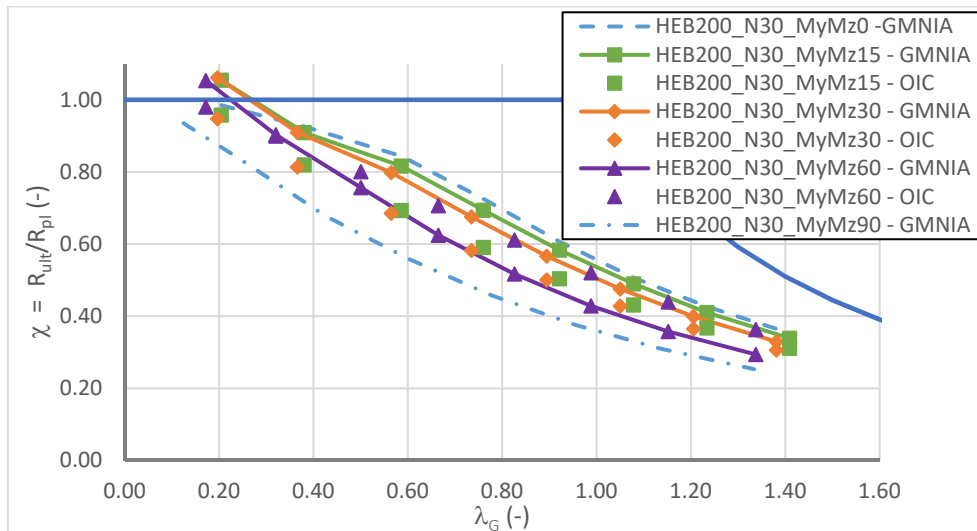


Figure 5-212: Ultimate resistance curves and OIC approach for a member of HEB 200 section under combined major-axis bending and axial force

The modification of the factor f_{zy} should not affect the load cases studied before. Additionally, the new formulation of the factor f_{zy} should represent the following tendencies:

- f_{zy} should decrease with decreasing ratio m_y/n . In particular: if the axial force vanishes it should be equal to the case of bi-axial bending only and if the bending moment M_y vanishes it should be 0 to represent the plastic-elastic transition behaviour for case of combined axial force and minor-axis bending ;
- f_{zy} should decrease with increasing sensitivity to flexural buckling of the member, i.e. with the ratio $N/N_{cr,z}$.

Both points represent well the physical meaning of the factor f_{zy} that is intended to reproduce the slower transition between plastic and elastic interaction for members of compact section sensitive to instability under bi-axial bending with a high minor-axis bending moment. Again, it is proposed to introduce a formulation that is as simple as possible to ensure a sufficient level of safety. Therefore, it is proposed to modify the factor f_{zy} as follows.

$$f_{yz} = 1 - f_{MyN} \frac{m_z}{m_y} \left(\frac{I_z}{I_y} \right)^2 \geq 0 \quad (5.376)$$

and

$$f_{MyN} = \left(1 - \frac{1}{\sqrt{\frac{m_y}{n}}} \right) \cdot \left(1 - \frac{N}{N_{cr,z}} \right) \geq 0 \quad (5.377)$$

The amelioration of the results is represented in Figure 5-213. By comparing Figure 5-212 and Figure 5-213, one may easily identify the improvement of the results for the case

HEB 200_N30_MyMz60. Over the whole range of the relative slenderness the results are safe-sided. Yet, it is also clear that the relative difference between the numerically obtained ultimate resistance curves linked to the cases HEB200_N30_MyMz15 and HEB200_N30_MyMz30 and to the case HEB200_N30_MyMz60 is not completely obtained by the OIC resistance model.

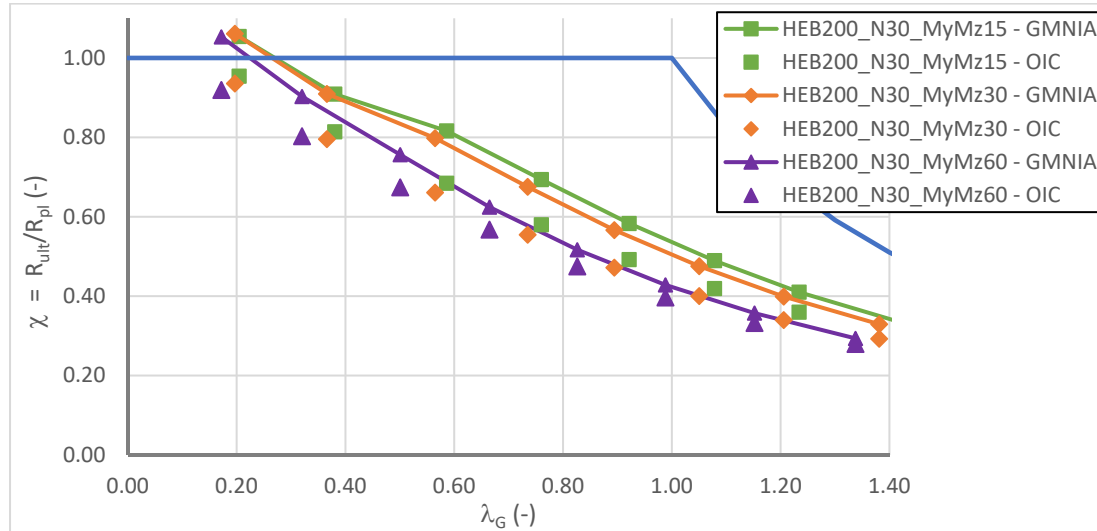


Figure 5-213: Influence of the modified factor f_{zy} on the precision of the proposed OIC approach

It seems also interesting to compare the numerical results to the resistances predicted by the Eurocode 3 interaction equations as shown in Figure 5-214. As for the load cases studied before, it is obvious that the interaction equations are very safe-sided for short to intermediate long members due to the roughly approximated plastic-cross-section interaction. The strength predictions become closer to the reference values for longer members as the cross-section interaction becomes linear and it is therefore better represented by the Eurocode design model. Nonetheless, it appears that the proposed OIC approach possesses a better precision for this specific case of the member of HEB 200 section subject to bi-axial bending and a compression axial force.

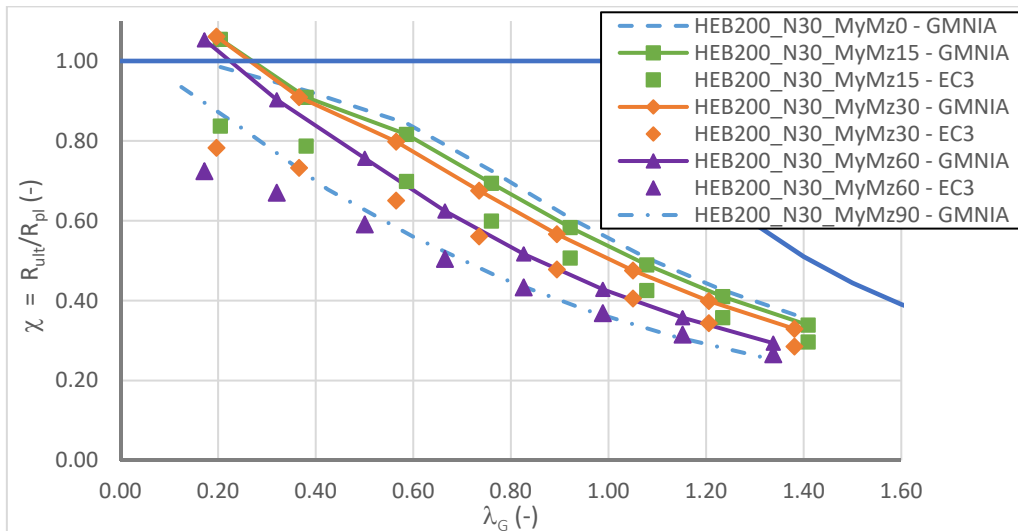


Figure 5-214: Ultimate resistance curves and EC3-Part 1-1 interaction equations for a member of HEB 200 section under combined major-axis bending and axial force

Next, members of IPE 500 section are studied in Figure 5-215. Again, the GMNIA results are represented for all degrees of “bi-axiality” (0° ... 90°) but in order to simplify the comparison the OIC predicted resistance are only represented for the members that are subject to bi-axial bending. It should be noted that the factor f_{zy} is approximately equal to 1,0 for all cases due to the high value of ratio I_y/I_z for the IPE 500 section.

Figure 5-215 shows that the proposed OIC approach leads to very precise results for all cases. Additionally, the relative difference between the ultimate resistance curves is very well represented by the design model. The maximum difference is only of about 10% (safe-sided) and hence completely acceptable and even more as no result is unsafe.

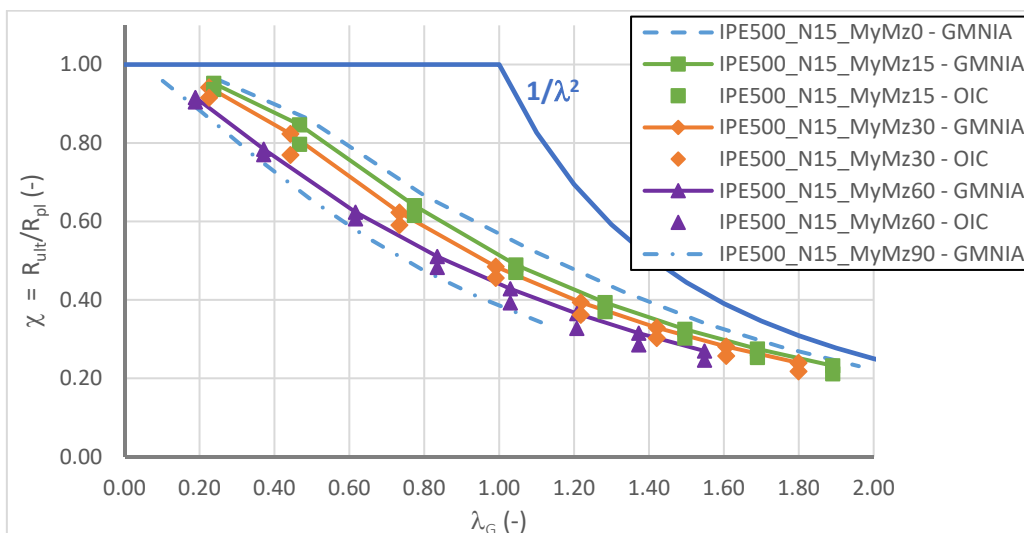


Figure 5-215: Ultimate resistance curves and OIC approach for a member of IPE 500 section under combined major-axis bending and axial force

As before, the results obtained by the Eurocode 3 Part 1-1 interaction equations are compared with the numerical results, too. Not surprisingly, one may observe that the resistance is not well

represented for short members because the plastic interaction is not well represented. For longer members the results become satisfactory again as the cross-section interaction becomes simpler. For intermediate to long members the precision of both design models studied here is therefore comparable.

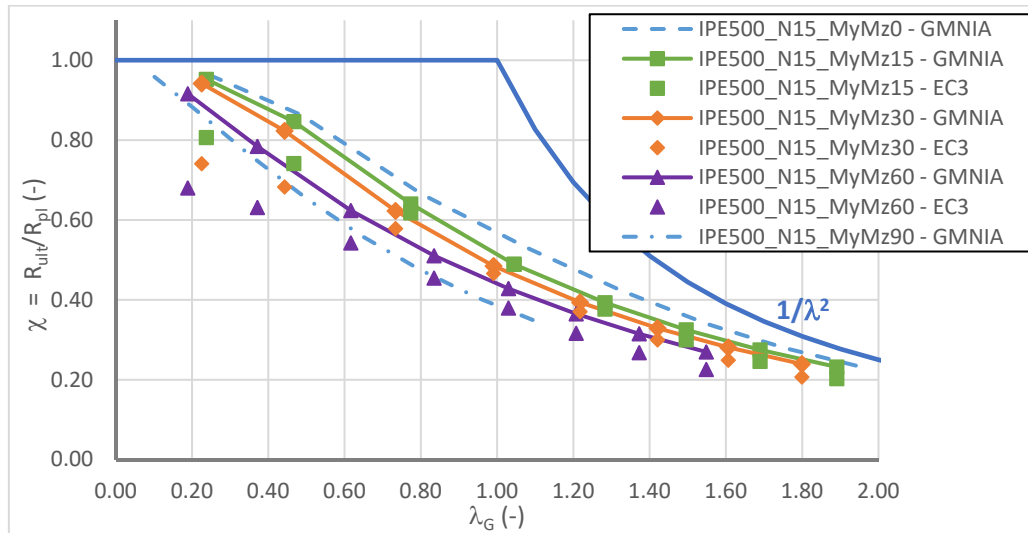


Figure 5-216: Ultimate resistance curves and EC3-Part 1-1 interaction equations for a member of IPE 500 section under combined major-axis bending and axial force

Last, members fabricated from the welded section W1330.10.280.15 (W2) are studied in Figure 5-217. It is recalled that local plate instability is excluded in the numerical calculations and that hence the resistance of the shortest members tends to the plastic resistance of the most loaded section. Figure 5-217 highlights again the good precision of the proposed OIC approach even for the members of the welded section W2 that are very sensitive to lateral-torsional buckling. For longer members however, the proposed design model seems to move slightly away from the reference results. Nevertheless the maximum difference is approximately of 18% (safe-sided) for the longest member. For the shorter members, the design model is very precise as it tends to the non-reduced plastic cross-section resistance. One may observe one unsafe result obtained for the case W2_N15_MyMz60 with a length of 1,12 m. Still, the difference is only of 5% and hence acceptable. Moreover, it should be noted that this is the most unsafe result of all studied members. This underlines again the good quality of the proposed OIC approach.

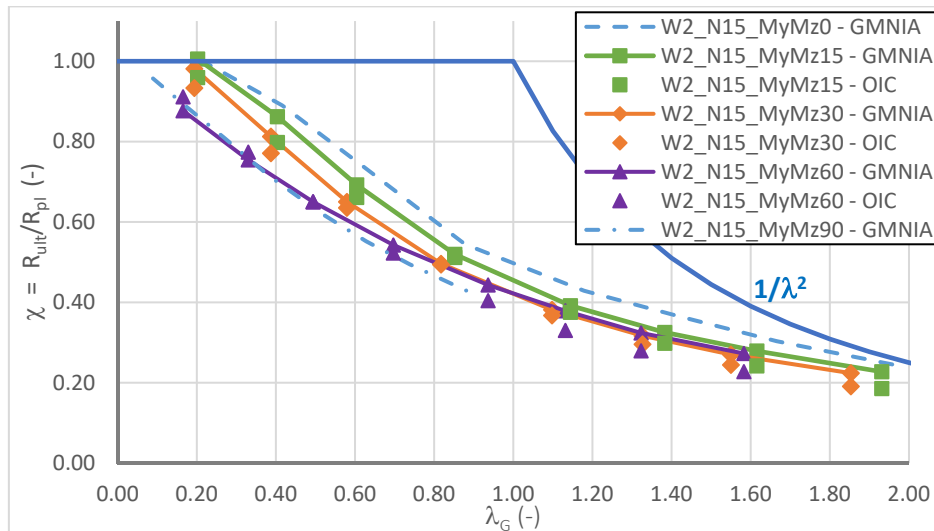


Figure 5-217: Ultimate resistance curves and OIC approach for a member of W1330.10.280.15 (W2) section under combined major-axis bending and axial force

The Eurocode 3 interaction equations are not compared in detail for this welded sections. Rather, it is proposed to evaluate statistically the OIC approach for all cases and to compare the results the Eurocode 3 Part 1-1 interaction equations. This is done in Table 5-56 and Figure 5-218. Both clearly indicate that the OIC approach ensures a safety level that is very similar to the Eurocode 3 Part 1-1 interaction formulae for the tested members. Furthermore, it appears that the OIC approach is even slightly more precise than the current European design model for members under combined bi-axial bending and compression axial forces. In particular, one should observe that the standard deviation of the results is smaller for the OIC approach and that the most unsafe result predicted by the OIC approach is much closer to the reference value than in case of the interaction equations (see Table 5-56).

Table 5-56: Statistical evaluation of studied design models

$\chi_{\text{Method}}/\chi_{\text{GMNIA}}$	OIC approach	Eurocode 3 Part 1-1 interaction equations
Mean	0,907	0,873
Standard deviation σ	0,067	0,079
Mean + 2 σ	1,041	1,031
Maximum	1,056	1,135
Minimum	0,728	0,662

Figure 5-218 represents graphically the statistical evaluation. It can be observed that the scatter is rather low and, in particular, lower than the one obtained for the interaction equations as also indicated in Table 5-56.

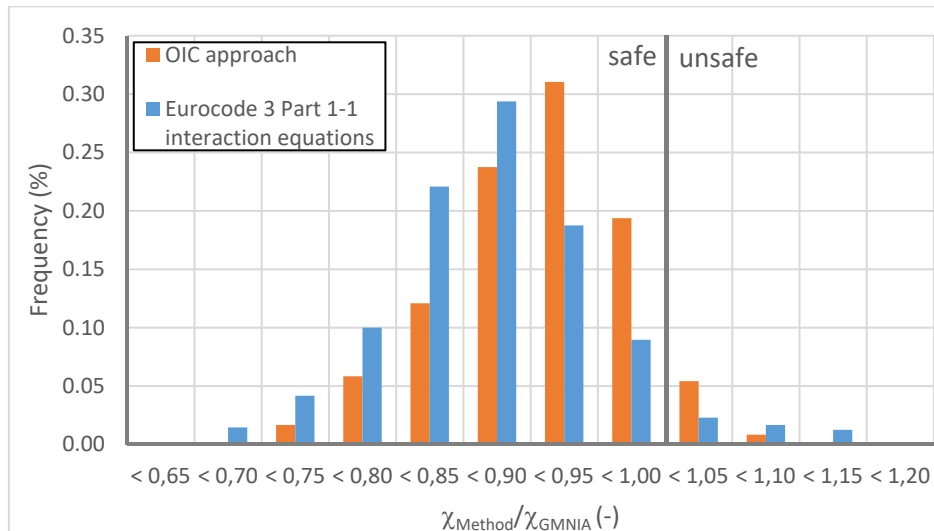


Figure 5-218: Ratio between predicted resistance and numerically obtained resistance

This paragraph presented the development of the OIC approach for I-shaped members under combined compression axial forces and bi-axial bending. It has been shown that a sufficient level of safety and precision can be attained. In particular, the OIC design model possess the advantage that the level of precision is homogenous over the whole range of the relative slenderness as the resistance is predicted continuously through the reduction curve. The (slightly) higher standard deviation of the Eurocode 3 Part 1-1 interaction equations results from the roughly approximated plastic cross-section interaction for members of short and intermediate length.

Finally, it is recalled that a supplementary empirical calibration of the factor f_{zy} had to be done for the OIC approach to cover safely the resistance of compact sections ($h/b \leq 1,2$). Obviously, this calibration is strictly valid only for the cases tested here and should therefore be validated for a greater number of cross-sections. This cannot be done in the framework of the present thesis. Rather, it is proposed to evaluate the developed OIC approach for an applied torsional moment. Obviously, the specific behaviour of members of open section (creation of the warping hinge) may possibly lead to a higher scatter of the results again. Yet, this has to be accepted as only a plastic analysis of the member could capture precisely this effect.

5.6.5.7 Extension of the OIC approach to torsion

Hereafter, the OIC approach developed in paragraphs 0, 5.6.5.3, 5.6.5.4, 5.6.5.5 and 5.6.5.6 is extended to the case of an applied torsional moment. As before, the bending moments as well as the axial compression forces are constant along the member length. The OIC approach presented in Table 5-55 is applied together with Eq. (5.376) for the factor f_{zy} . It should be noted that no modification is introduced at this point to account for the case of an applied torsional moment. Indeed, the value of the bi-moment enters directly into the calculation of the plastic load amplification factor $R_{pl,ov}$.

First, Figure 5-219 shows a statistical evaluation of the results obtained with the proposed OIC approach. The plastic load amplification factor used as a key factor of the design method is directly

determined by a MNA simulation. Consequently, the plastic torsional system reserve is accounted for in all cases. Nonetheless, it appears that the scatter of the results is slightly higher and the precision of the strength predictions is slightly lower than for members under combined bi-axial bending and compression axial forces. Yet, the results are certainly acceptable, especially when they are compared to the strength predictions obtained with the method introduced in paragraph 5.6.4.2 as shown in Table 5-57.

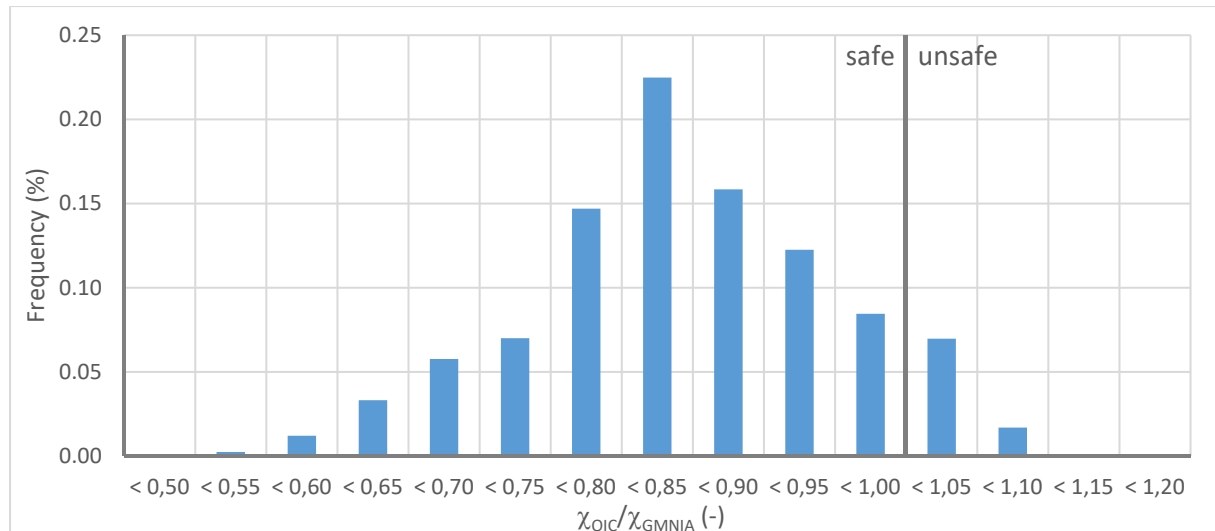


Figure 5-219: Ratio between OIC predicted resistance and numerically obtained resistance – $R_{pl,ov,MNA}$

Table 5-57 represents a comparison of the precision obtained by the OIC approach and the design method proposed in paragraph 5.6.4.2 for double symmetric I sections. Additionally, the statistical evaluation of the Eurocode 3 Part 1-1 interaction equations is represented. This last method is only applied to members (of the parametric study) subject to bi-axial bending (constant bending moments) and axial forces but not subject to torsion.

Table 5-57 confirms that the proposed OIC approach is rather satisfying. In particular, one observes that OIC approach applied to members subject to a compression axial force, bi-axial bending and torsion is only slightly less precise than the strength predictions obtained with the Eurocode 3 Part 1-1 interaction equations applied to members not subject to torsion. Also, Table 5-57 shows that the OIC approach appears to yield more precise results than the proposed extension of the Eurocode 3 Part 1-1 interaction equations owing to the continuous strength prediction starting from the exact plastic cross-section interaction up to a failure characterised by elasto-plastic instability.

The obtained results are analysed further on based on selected examples.

Table 5-57: Statistical evaluation of different design approaches

$\chi_{\text{Method}}/\chi_{\text{GMNIA}}$	OIC approach	Extension of interaction formulae (Eqs. (5.307) and (5.308))	Eurocode 3 interaction equations without torsion
Mean	0,84	0,75	0,87
Standard deviation σ	0,11	0,11	0,08
Mean + 2 σ	1,06	0,97	1,03
Maximum	1,12	1,03	1,13
Minimum	0,52	0,42	0,66

Table 5-57 as well as Figure 5-219 have shown that some of the strength predictions of the OIC approach may be unsafe. A majority of these unsafe results is obtained for welded members of rather low relative slenderness as shown for the examples of Figure 5-220. This figure represents the results obtained for a member of welded section W650.5.180.10 (W1) subject to an axial compression force, bi-axial bending (degree of bi-axiality = 60°) and different levels of torsion. The numerically determined ultimate resistance curves are of very similar shape. Indeed, the resistance of very short members may exceed the plastic resistance obtained with MNA calculations (considering the effect of the plastic warping hinge). The resistance decreases rapidly for values of the relative slenderness between 0,15 and 0,40. In this range of the slenderness the OIC approach seems to be too favourable. Nonetheless, on the unsafe side, the maximum discrepancy is of approximatively 12%. This difference is lower than the maximum unsafe strength prediction of the Eurocode 3 Part 1-1 interaction equations in their initial field of application (13% - see Table 5-57) and seems therefore acceptable.

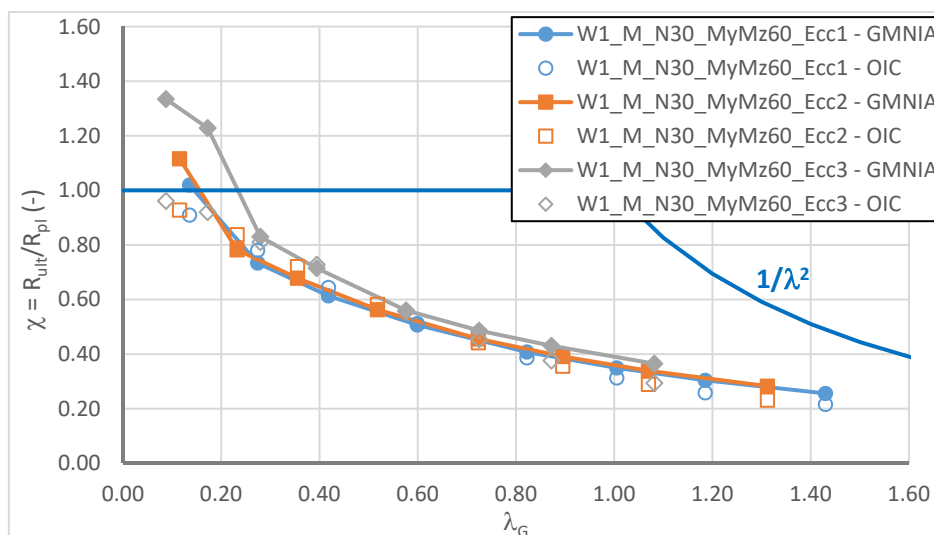


Figure 5-220: Ultimate resistance curves for a member of welded section W650.5.180.10 (W1) subject to combined axial compression force, bi-axial bending and torsion

The statistical evaluation of the proposed OIC approach has also revealed that some of the obtained results are very safe, even if the approach evaluated here is based on the plastic load

amplification factor determined numerically by MNA simulations. In order to understand the observed discrepancy a member of IPE500 section subject to combined axial force, minor-axis bending and torsion is studied in Figure 5-221. This Figure also represents the results obtained for the members not subject to torsion as reference case. In fact, one may observe again that the OIC approach is very precise for combined compression axial force and minor-axis bending (see paragraph 5.6.5.3). The strength predictions are practically identical to the numerical results for this load case. Conversely, one may observe rather important discrepancies if an additional torsional moment is applied. For very short members, the difference may attain up to 50% on the safe-side due to the strain hardening reserve of the member. Nonetheless, strain hardening is explicitly not accounted for in the proposed design model. The difference observed for very short members is hence not of the most interest. Contrariwise, it seems interesting to study the differences for values of the relative slenderness in the range between 0,2 and 0,8. It appears that the members subject to torsion attain a significantly higher resistance in this slenderness range than the members not subject to torsion. The OIC approach, however, predicts resistances that are less for members subject to torsion than for the members only subject to an axial force and minor-axis bending. Obviously, strain hardening possesses a non-negligible influence on the member resistance even for intermediate values of the relative slenderness as represented in Figure 5-222, Figure 5-223, Figure 5-224 and Figure 5-225.

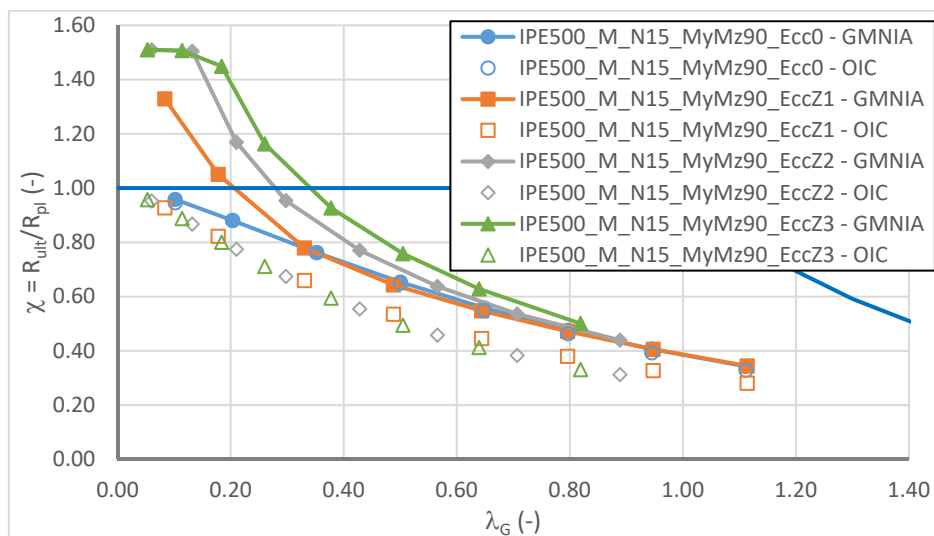


Figure 5-221: Ultimate resistance curves for a member of welded section IPE500 subject to combined axial compression force, bi-axial bending and torsion

The following figures clearly indicate that the members subject to torsion attain a strain level corresponding to strain hardening whereas the member that is only subject to an axial compression force and minor-axis bending, fails before strain hardening is initiated. In fact, Figure 5-222 shows that the flanges of this member have yielded over nearly their total length but the stresses do not exceed the yield stress of the material. Conversely, observing Figure 5-223, Figure 5-224 and Figure 5-225 one may remark that the maximum stress attained by the members increases with the relative importance of the applied torsional moment. This supplementary strain hardening reserve is not well captured by the OIC design model. Here, one

might consider to introduce a supplementary parameter considering the possible strain hardening reserve in case of applied torsional moments for certain sections. It is recalled that welded members appear to fail at a lower stress level for intermediate and high values of the relative slenderness (see Figure 5-220). A deeper investigation is necessary in order to capture precisely this resistance reserve. Yet, other parameters as the bending moment diagram also influence significantly the member resistance and should therefore be studied as well. In the framework of the present thesis, this is not done.

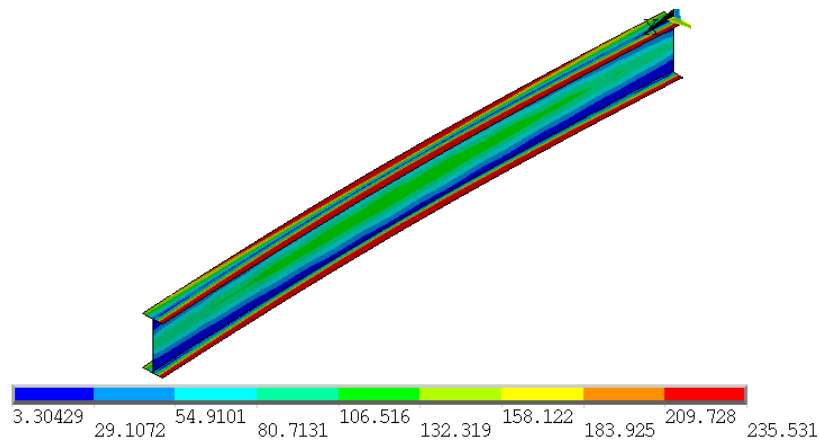


Figure 5-222 : Von Mises stresses and deformed shape for IPE500_M_N15_MyMz90_Ecc0

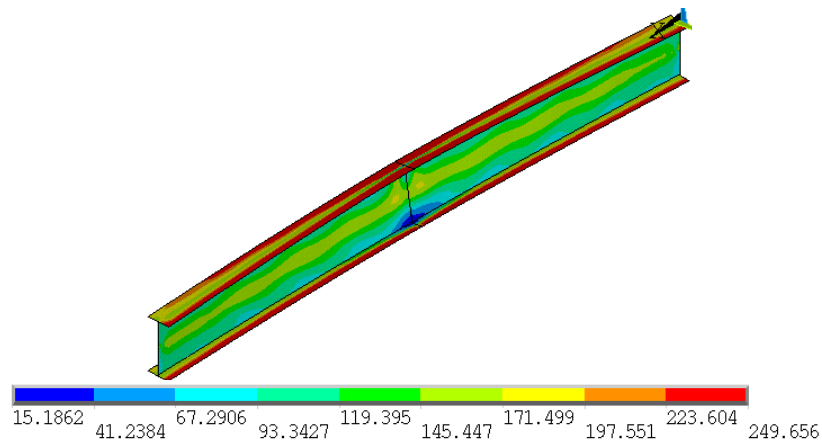


Figure 5-223: Von Mises stresses and deformed shape for IPE500_M_N15_MyMz90_EccZ1

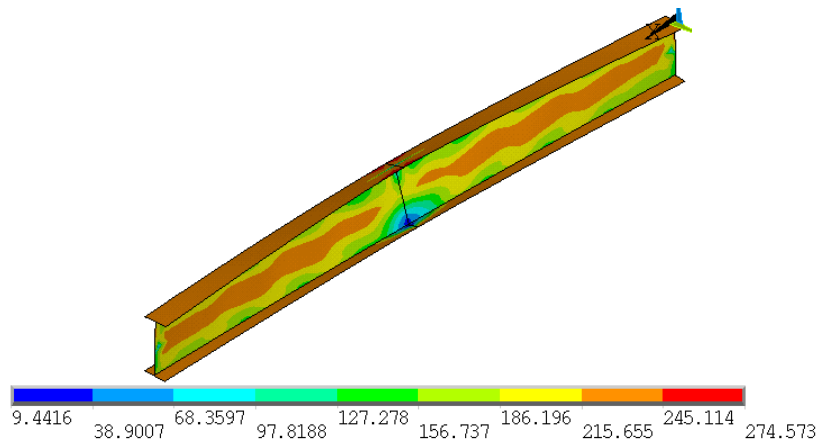


Figure 5-224: Von Mises stresses and deformed shape for IPE500_M_N15_MyMz90_EccZ2

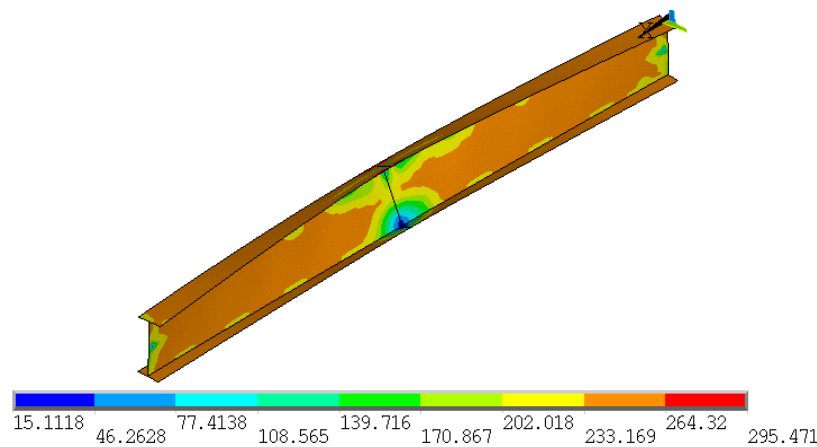


Figure 5-225: Von Mises stresses and deformed shape for IPE500_M_N15_MyMz90_EccZ3

Up to this point the OIC approach is applied with the plastic load amplification factor $R_{pl,ov}$ obtained with MNA calculations ($R_{pl,ov,MNA}$) performed on the whole member. In practice, the internal force and moments, acting in the structure and its constituting members, are, in most cases, determined through elastic analysis. Consequently, the plastic torsional system reserve cannot be accounted for directly. The plastic load amplification factor determined based on the elastically calculated internal forces and moments ($R_{pl,ov,LA}$) corresponds therefore to the formation of the (first) plastic warping hinge. Hence, the value of the plastic load amplification factor $R_{pl,ov,LA}$ is lower than the value of $R_{pl,ov,MNA}$ and, accordingly, the ratio $R_{pl,MyN}/R_{pl,ov}$ is overestimated. Nevertheless, underestimating the plastic load amplification factor $R_{pl,ov}$ should lead to more conservative results than in case of the exactly determined factor $R_{pl,ov,MNA}$, especially for short members. Figure 5-226 shows a statistical evaluation of the OIC approach when it is applied with the plastic load amplification factor corresponding to the formation of the plastic warping hinge. As expected the results are more conservative and the scatter is slightly higher. Nonetheless, differences to the OIC approach applied with $R_{pl,ov,MNA}$ are rather low.

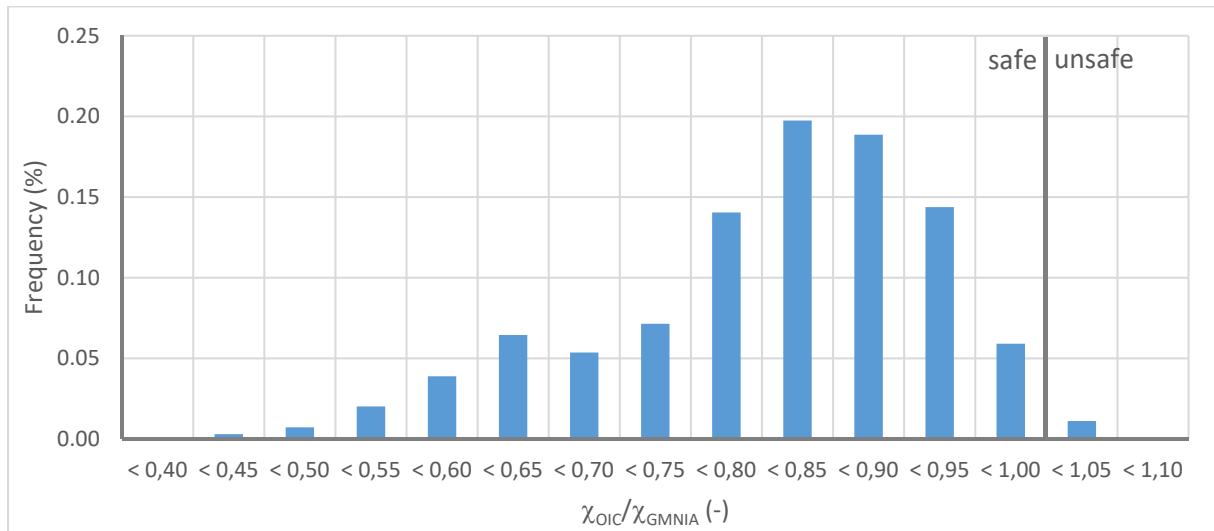


Figure 5-226: Ratio between OIC predicted resistance and numerically obtained resistance – $R_{pl,ov,LA}$

It is to be noted that the results obtained based on $R_{pl,ov,LA}$ are more conservative compared to the results obtained based on $R_{pl,ov,MNA}$, especially for short members as shown in Figure 5-227 and Figure 5-228. Nonetheless, the difference is only of about 10 to 20% in average for members possessing a relative slenderness lower than 0,6. Additionally, one may observe that for longer members the results are identically. This observation is not surprising as the plastic load amplification factor $R_{pl,ov}$ has only very few influence on the obtained global reduction factor starting from a relative slenderness of approximately 1,25 ($=1/(0,8C_{ms,z}f_{yz}$ – see Eq. (5.370) and Table 5-55 for the definition of the transition function f_{instab}). In fact, for a higher value of the relative slenderness the function f_{instab} is equal to the ratio $R_{el,MyN}/R_{el,tot}$. In this slenderness range $R_{pl,ov}$ is only used to determine the relative slenderness itself. Also, one may observe that the approach based on $R_{pl,ov,LA}$ is less unsafe for intermediate values of the relative slenderness. This seems also understandable as the plastic torsional system reserve is only mobilised for short members or if the member is subject to high torsion as the members of Figure 5-224 and Figure 5-225.

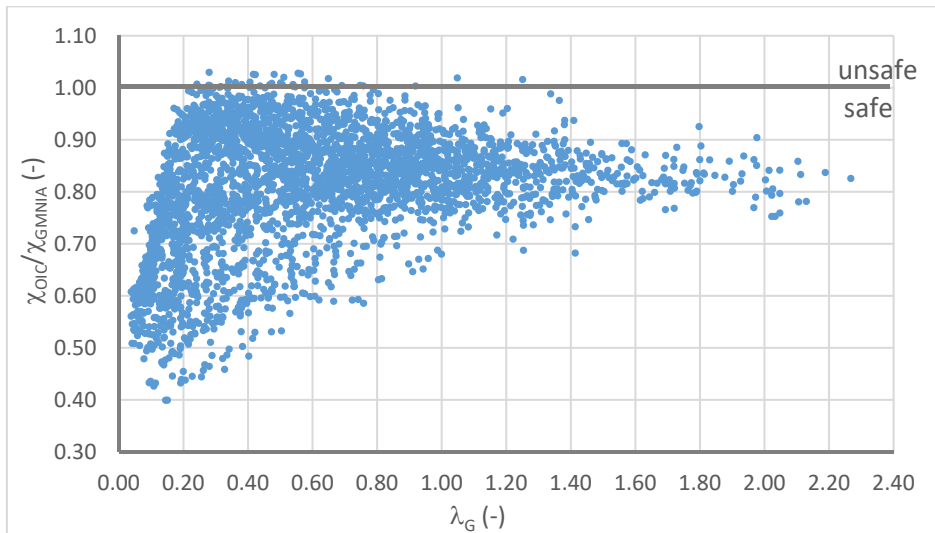


Figure 5-227: Ratio between OIC predicted resistance and numerically obtained resistance – $R_{pl,ov,LA}$

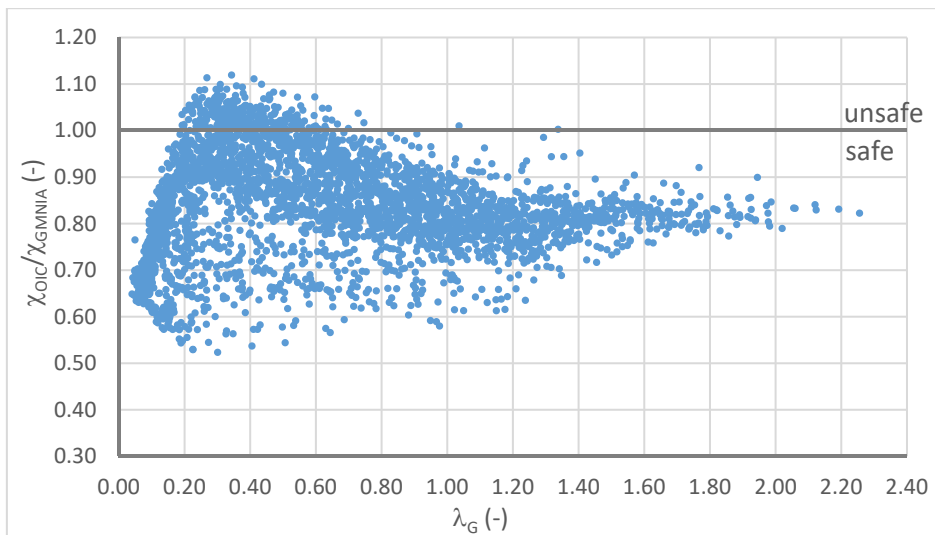


Figure 5-228: Ratio between OIC predicted resistance and numerically obtained resistance – $R_{pl,ov,MNA}$

The comparison presented above allows the conclusion that the OIC approach may be applied based on the plastic amplification factor $R_{pl,ov,LA}$ determined with the internal forces and moments obtained with an elastic analysis. The loss of precision with respect to the OIC approach based on $R_{pl,ov,MNA}$ is not significant. Moreover, it appears that the OIC approach should not be based on the value of $R_{pl,ov,MNA}$ (considering the formation of the plastic warping hinge) over the total range of the relative slenderness but only up to a limit slenderness. Indeed, Figure 5-228 shows unsafe OIC strength predictions for values of the relative slenderness between 0,2 and 0,6.

It is proposed here to determine a plastic load amplification factor to be used with the OIC approach as follows:

$$R_{pl,ov} = R_{pl,ov,MNA} \quad \text{if} \quad \bar{\lambda}_G \leq 0,2 \quad (5.378)$$

$$R_{pl,ov} = R_{pl,ov,MNA} - \frac{(R_{pl,ov,MNA} - R_{pl,ov,LA})}{0,2} (\bar{\lambda}_G - 0,2) \quad \text{if} \quad 0,2 < \bar{\lambda}_G \leq 0,4 \quad (5.379)$$

$$R_{pl,ov} = R_{pl,ov,LA} \quad \text{if} \quad \bar{\lambda}_G > 0,4 \quad (5.380)$$

It should be noted that an iteration has to be performed to determine the factor $R_{pl,ov}$ with Eq. (5.379) as the value of the relative slenderness λ_G depends itself on the factor $R_{pl,ov}$. Nonetheless, it has been shown that the application of $R_{pl,ov,LA}$ over the total range of the relative slenderness does not lead to a significant loss of precision. Consequently, the OIC approach may always be based on $R_{pl,ov,LA}$ for simplicity.

Finally, it is obvious that the determination of the factor $R_{pl,ov,MNA}$ seems delicate in practice because the software necessary to perform elasto-plastic analysis of a member considering its torsional characteristics including the warping stiffness is not widespread in the present practice. Additionally, this type of software is usually capable to account for geometric second order effects and imperfections. Consequently, the member resistance could directly be checked through a GMNIA simulation without significant supplementary effort compared to a MNA simulation. Therefore, it is certain that the factor $R_{pl,ov,MNA}$ is practically never determined in practice (here it is emphasized again that $R_{pl,ov,MNA}$ is determined through a MNA simulation of the **member** as a whole and not only by a plastic calculation of the most loaded section). In paragraphs 4.4.4.1 and 4.5 a simplified method for the plastic analysis of the member has been introduced. It is recalled that this method consists in the following steps:

- 1) Linear elastic analysis performed for the determination of the load factor corresponding to the generation of the plastic warping hinge ($=R_{pl,ov,LA}$) and of the internal forces and moments acting in the member at this load level;
- 2) Introduction of a warping hinge into the numerical model of the member;
- 3) Application of the loads corresponding to $0,9R_{pl,ov,LA}$;
- 4) Linear elastic analysis performed up to complete yielding of the member ends under the combination of the possible axial force, shear force, major- and minor-axis bending moment as well as the Saint-Venant's torsional moment (including the Saint-Venant's torsional moment corresponding to $0,8R_{pl,ov,MNA}$). The limit load can be determined with the adapted Partial Internal Force Method (aPIFM) introduced in Chapter 4.

This simplified "plastic" analysis may be applied to obtain an approximate value of $R_{pl,ov,MNA}$. The OIC approach can then be used as before including Eqs. (5.378) to (5.380) for the determination of the "effective" plastic load amplification factor. Table 5-58 represents the statistical evaluation of the developed OIC approach based on the plastic load amplification factor linked to the generation of the plastic warping hinge ($R_{pl,ov,LA}$) and the OIC approach based on the plastic load amplification factor obtained with the simplified elastic analysis. Eqs. (5.378) to (5.380) are only

applied in the second case. One may observe that the precision is slightly increased if the second approach is applied. Additionally, it is shown that the conservatism is highly reduced for short members thanks to the better approximation of the real plastic load amplification factor. This is also graphically shown in Figure 5-229.

Table 5-58: Statistical evaluation of OIC design approach

χ_{OIC}/χ_{GMNIA}	OIC approach - $R_{pl,ov,LA}$	OIC approach - $R_{pl,ov,LA,II}$ with simplified plastic analysis
Mean	0,805	0,813
Standard deviation σ	0,116	0,098
Mean + 2σ	1,038	1,008
Maximum	1,030	1,051
Minimum	0,399	0,483

Figure 5-229 represents the ratio χ_{OIC}/χ_{GMNIA} as a function of the relative member slenderness. The results represented in this Figure are obtained with the load amplification factor $R_{pl,ov}$ determined with the simplified “plastic” analysis. For short members, the obtained strength predictions are very close to the results determined based on the factor $R_{pl,ov,MNA}$. Additionally, thanks to the introduction of Eqs. (5.378) to (5.380) only very few results are unsafe ($\approx 2\%$). For the longer members the results are obviously identical to those presented in Figure 5-228 based on $R_{pl,ov,LA}$. Nonetheless, it appears that many results are still rather conservative. So as to get a clearer idea, Figure 5-230 represents the results of the OIC approach again but considering the maximum reduction factor χ_{GMNIA} equal to 1,0, i.e. if the numerically determined factor χ_{GMNIA} exceeds 1,0 it is artificially set equal to 1,0 for the comparison.

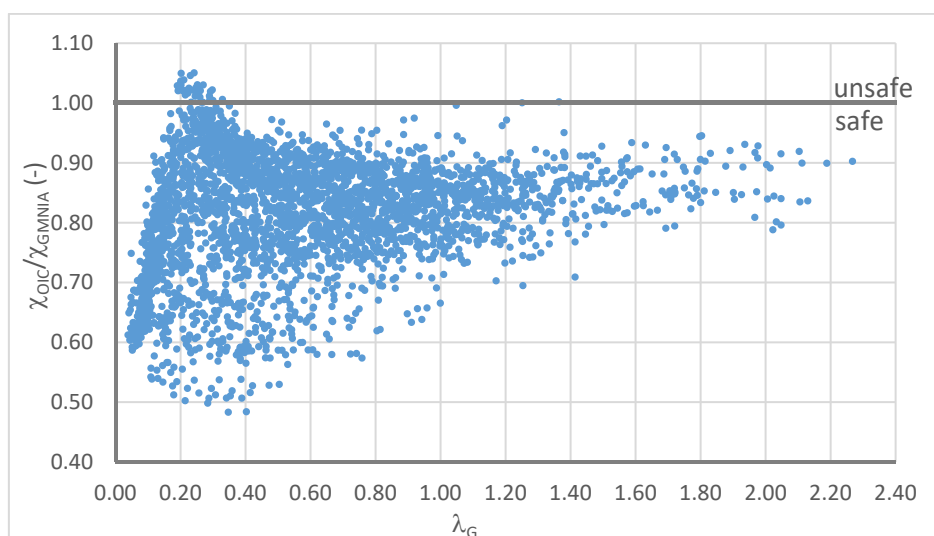


Figure 5-229: Ratio between OIC predicted resistance and numerically obtained resistance – $R_{pl,ov}$ obtained with simplified plastic analysis

Figure 5-230 indicates that the proposed OIC approach is very conservative for members of intermediate relative slenderness whose resistance is influenced by the effect of strain hardening even if they fail by elasto-plastic instability as for the examples given in Figure 5-223, Figure 5-224 and Figure 5-225. In order to ameliorate the strength prediction for these members, “encircled” in orange in Figure 5-230, it might be necessary to modify the plateau length in case of high torsional loads. This is not done here, but may be in the centre of interest of future research projects that should also introduce the effect of variable bending moment diagrams in the OIC approach.

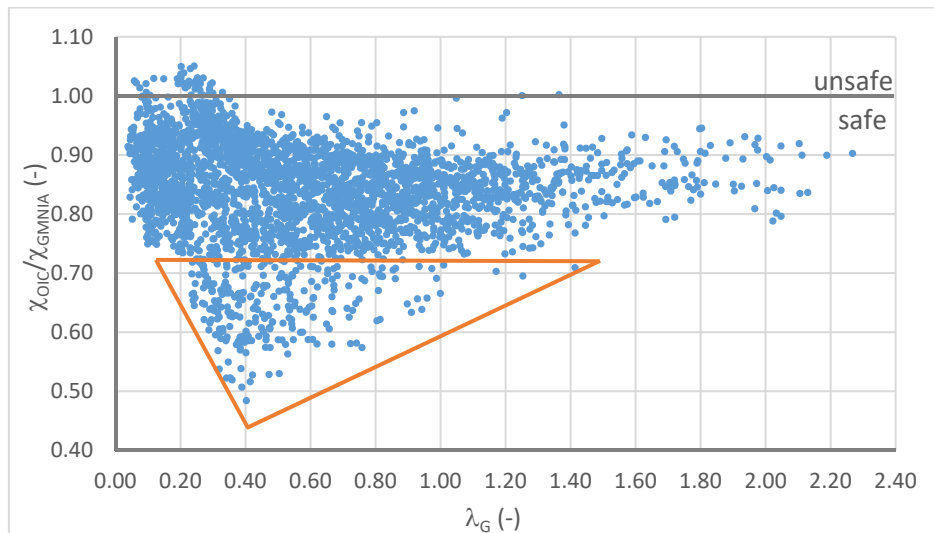


Figure 5-230: Ratio between OIC predicted resistance and numerically obtained resistance – $R_{pl,ov}$ obtained with simplified plastic analysis – χ_{GMNIA} considered equal to 1,0 at maximum

5.6.5.8 Summary of the OIC approach for the resistance of members of double symmetric I section

In paragraph 5.6.5 an OIC approach for the resistance of members of double symmetric I sections subject to combined axial compression force, bi-axial bending and torsion has been developed based on a simplification of the analytical developments presented in paragraph 5.5.7.4. Also, it was intended to propose an OIC approach that may be continuously linked to design methods developed in the past in the OIC format as done in reference (Taras 2011). So as to obtain a sufficiently precise approach covering the complex situation studied here, several parameters had to be calibrated empirically based on the numerical data basis. In particular:

- The imperfection factor α_{My} for lateral-torsional buckling;
- The imperfection factor α_{MyN} considering the interaction between minor-axis flexural buckling and lateral-torsional buckling;
- The transition function f_{Instab} considering the influence of elasto-plastic instability on the cross-section interaction of the most loaded section (transition between plastic and elastic interaction) and the factor f_{zy} considering specifically the influence of the minor-axis bending moment on the transition behaviour of compact section ($h/b < 1,2$);

- The effective plastic load amplification factor for short members subject to torsion considering the influence of the possible plastic torsional system reserve.

The obtained design model is summarised in Table 5-59.

Table 5-59: OIC calculation steps for combined axial compression force and bi-axial bending

Calculation steps	Detail
(Numerical) Determination of key factors	$R_{pl,ov}$: Load amplification factor to attain the plastic limit state of the most loaded section considering all internal forces and moments (in case of an applied torsional moment it should be distinguished between $R_{pl,MB,MNA}$ and $R_{pl,MB,LA}$)
	$R_{pl,MyN}$: Load amplification factor to attain the plastic limit state of the most loaded section considering only major-axis bending and the axial compression force
	$R_{el,ov}$: Load amplification factor to attain the elastic limit state of the most loaded section considering all internal forces and moments
	$R_{el,MyN}$: Load amplification factor to attain the elastic limit state of the most loaded section considering only major-axis bending and the axial compression force
	$R_{cr,G}$: Load amplification factor to attain the elastic critical load of the member subject to all loads (considering the influence of first order displacements)
	$R_{cr,G}^*$: Load amplification factor to attain the elastic critical load of the member without its Saint-Venant's torsional stiffness subject to all loads (considering the influence of first order displacements)
	$N_{cr,z}$: Elastic critical axial force for minor-axis flexural buckling
	$M_{y,cr}$: Elastic critical moment for lateral-torsional buckling
	$\bar{\lambda}_G$: Global relative member slenderness
	If the plastic torsional system reserve is accounted for: $\bar{\lambda}_G \leq 0,2$: $R_{pl,ov} = R_{pl,ov,MNA}$ $0,2 < \bar{\lambda}_G \leq 0,4$: $R_{pl,ov} = R_{pl,ov,MNA} - \frac{(R_{pl,ov,MNA} - R_{pl,ov,LA})}{0,2}(\bar{\lambda}_G - 0,2)$

	$\bar{\lambda}_G > 0,4 : \quad R_{pl,ov} = R_{pl,ov,LA}$															
Determination of imperfection factors	$\alpha_{MyN} = \frac{\left(\alpha_N \frac{N}{N_{cr,z}} + \alpha_{My} \frac{M_y}{M_{y,cr}} + f_{interact} \right)}{\frac{N}{N_{cr,z}} + \frac{M_y}{M_{y,cr}}}$															
	$f_{interact} = \alpha_{interact} \bar{\lambda}_G \text{Min} \left(\frac{\frac{N}{N_{cr,z}}}{\frac{M_y}{M_{y,cr}}}; \frac{\frac{M_y}{M_{y,cr}}}{\frac{N}{N_{cr,z}}} \right)$															
	<table border="1"> <thead> <tr> <th>Section</th> <th>α_N</th> <th>α_{My}</th> <th>$\alpha_{Interact}$</th> </tr> </thead> <tbody> <tr> <td>Welded sections</td> <td>0,49</td> <td>$0,58 \frac{R_{cr}^*}{R_{cr}}$</td> <td>0,30</td> </tr> <tr> <td>Hot-rolled sections h/b > 1,2</td> <td>0,34</td> <td>$0,42 \frac{R_{cr}^*}{R_{cr}}$</td> <td>0,18</td> </tr> <tr> <td>Hot-rolled sections h/b ≤ 1,2</td> <td>0,49</td> <td>$0,75 \frac{R_{cr}^*}{R_{cr}}$</td> <td>0,07</td> </tr> </tbody> </table>	Section	α_N	α_{My}	$\alpha_{Interact}$	Welded sections	0,49	$0,58 \frac{R_{cr}^*}{R_{cr}}$	0,30	Hot-rolled sections h/b > 1,2	0,34	$0,42 \frac{R_{cr}^*}{R_{cr}}$	0,18	Hot-rolled sections h/b ≤ 1,2	0,49	$0,75 \frac{R_{cr}^*}{R_{cr}}$
Section	α_N	α_{My}	$\alpha_{Interact}$													
Welded sections	0,49	$0,58 \frac{R_{cr}^*}{R_{cr}}$	0,30													
Hot-rolled sections h/b > 1,2	0,34	$0,42 \frac{R_{cr}^*}{R_{cr}}$	0,18													
Hot-rolled sections h/b ≤ 1,2	0,49	$0,75 \frac{R_{cr}^*}{R_{cr}}$	0,07													
Determination of transition function	$f_{Instab} = \frac{R_{pl,MyN}}{R_{pl,ov}} - \left(\frac{R_{pl,MyN}}{R_{pl,ov}} - \frac{R_{el,MyN}}{R_{el,ov}} \right) C_{ms,z} \rho f_{yz} \bar{\lambda}_G \leq \frac{R_{el,MyN}}{R_{el,ov}}$ <p>$\rho = 0,8$</p> $f_{yz} = \max \left(0; 1 - 3,9 \frac{m_z}{m_y} \left(\frac{I_z}{I_y} \right)^2 \right)$ <p>$C_{ms,z} = 1 + 0,27 \frac{N}{N_{cr,z}}$ (equivalent sinusoidal moment factor for constant bending moments)</p>															
Determination of the reduction factor	$\phi = 0,5 \left[f_{Instab} + \frac{\alpha_{MyN}}{\sqrt{\frac{R_{pl,MyN}}{R_{pl,ov}}}} \left(\bar{\lambda}_G - 0,2 \right) + \bar{\lambda}_G^2 \frac{R_{pl,MyN}}{R_{pl,ov}} \right]$ $\chi_G = \frac{R_{pl,MyN}}{R_{pl,ov}} \frac{1}{\phi + \sqrt{\phi^2 - \bar{\lambda}_G^2 \frac{R_{pl,MyN}}{R_{pl,ov}}}}$															

The design model presented in Table 5-59 has proven to be very satisfactory and it appears to be even more precise than the well accepted Eurocode 3 Part 1-1 interaction equations in their original field of application (without torsion). Especially the continuous strength prediction from short members, attaining the plastic resistance of their most loaded section, to long members, failing by elasto-plastic instability, is a very beneficial feature of the OIC approach. Yet, it should be noted that the study presented before was limited to members of double symmetric I section subject to constant bending moments and a constant axial force. In many situations the axial force can be considered as constant in practice. Conversely, the bending moments generally vary over the member length. Consequently, it is of great practical interest to pursue the investigations to include the effect of variable bending moments. Additionally, the following points merit further research:

- The developed OIC approach is based on the critical amplification factor considering first order displacements. Yet, the determination is delicate in practice and requires generally specific software that is not widespread today. An alternative might be the calculation of a critical amplification factor for the member only subject to loads generating axial forces and major-axis bending. Consequently, the disturbing influence of minor-axis bending (and torsion) on the critical loads is eliminated (as is also done if the critical loads are calculated through GNIA simulations);
- In case of relatively high torsion, members may mobilize a certain level of strain hardening reserve leading to increased resistances that are not precisely predicted by the developed OIC approach. It might be investigated if an increased plateau length can be applied for these situations. However, it seems necessary to ensure that yielding is not initiated at Serviceability Limit State, because the torsional twist (as well as the other displacements of the member) can not be determined through elastic analysis in this case anymore;
- The strain hardening reserve may be very beneficial for short members (or members possessing sufficient restraints against instability) and may therefore lead to more economic design. A possible design approach considering strain hardening is CSM as presented in Chapter 4. It may be interesting to couple the OIC design model with CSM;
- The effects of lateral restraints have not been investigated. The restraints may increase heavily the member resistance due to the stabilizing effect of member segments that are less loaded than their neighbour segments. For a practical design approach the influence of the lateral restraints should therefore be investigated.

5.7 Conclusions

Chapter 5 investigated the resistance of members subject to compression axial forces, bi-axial bending and torsion. The design models developed in the last part of this Chapter have been calibrated based on an extensive numerical study. Obviously, the results of the GMNIA simulations depend highly in the assumed imperfections. Consequently, it appeared necessary to study the influence of these imperfections on the numerically determined resistance in paragraph 5.2 before the parametric study has been performed. It has been shown that the influence of the imperfections have been studied in detail for double symmetric I sections. Conversely, for mono-symmetric sections and especially for U sections, it existed an important lack of information concerning geometric imperfections and residual stresses to be used for GMNIA simulations. Therefore, specific studies have been presented in paragraph 5.2.1 with the objective to get more detailed insights on assumed calculation imperfections. In particular, it has been shown that:

- The recommendations for I-shaped members concerning geometric imperfection cannot be transposed to U-shaped members without any preconisation;
- The residual stress pattern used in previous studies for U section should be modified. A more precise residual stress distribution has been developed based on the internal equilibrium conditions of a U section and thermo-mechanical simulations of the cooling process after hot-rolling.

One of the objectives of this thesis was the development of a design approach for members subject to torsion in the format of the Eurocode 3 Part 1-1 design models and in particular in the format of the interaction equations. Consequently, the initial field of application of these interaction equations is recalled in paragraph 5.3. It has also been recalled that the field of application is rather restrained especially concerning the type of the section. In particular, mono-symmetric I sections and U sections are not covered. Two extension of the interaction equations presented in references (Kaim 2004) and (Kalameya 2008) addressing mono-symmetric I sections and U sections have then been presented. Nonetheless, both proposals possess certain limitations even for members not subject to torsion. Consequently, it was necessary to complete these two design models before an extension to applied torsion could be envisaged.

In paragraph 5.4 design approaches proposed in the past for I- and U-shaped members subject to torsion have been discussed in detail. It has been shown that:

- The design proposals are either based on theoretical studies or based on purely empirical investigations;
- The theoretically based design models may be very complex and still inconsistent or incomplete in some conditions leading to very unsafe results as has been revealed by comparison to selected GMNIA simulations.;
- The empirically developed design models may also be very unsafe if they are applied outside the scope of the parametric study they are based on;

- Only the proposal “TU Berlin” published in reference (Glitsch 2008) discussed the plastic torsional system reserve rapidly, even if it highly influences the behaviour of members of open section subject to torsion. This last design approach considers the beneficial effect of the formation of the plastic warping hinge but it does not ensure neither that the member does not fail under the Saint-Venant’s torsional moment that arises in consequence of the warping hinge nor it ensures that the torsional twist does not attain excessively high values.

Nonetheless, it is certain that all of the design approaches developed in the past contributed to a better understanding of the behaviour of members subject to torsion.

So as to develop a simplified design model in the framework of this thesis paragraph 5.5 addressed the theoretical basis of the member behaviour. First, elastic instability has been studied and, in particular, the influence of the first order displacements on the critical loads of U-shaped members has been highlighted. In fact, it appears that if pre-buckling displacements are not considered the critical loads imply that U-shaped members are sensitive to elastic instability under minor-axis bending in many cases. However, if the pre-buckling displacements are included, it is shown that elastic instability under minor-axis bending is only of interest in certain conditions. These conditions have been discussed. Moreover, it has been shown that, in today’s practice, the resistance of hot-rolled U-shaped members is not affected by elasto-plastic instability if they are only subject to minor-axis bending moments as the relative slenderness cannot attain sufficiently high values. Indeed, only for members made of high strength steel ($> S460$) a noticeable strength reduction due to elasto-plastic instability is observed.

In the framework of the study concerning elastic instability it was possible to obtain the eigenmode that is used as form of the equivalent geometric imperfection introduced into the system of differential equations describing the second order equilibrium of the member. The system is solved for special cases in order to determine the parameters influencing the second order amplification of the internal forces and moments. It has been shown that it is possible to obtain analytical solutions for simple load cases as for example members under major-axis bending. The obtained solutions have also been developed in the past in several references (see (Stangenberg 2007), (Naumes 2009) and (Taras 2011)). Nevertheless, it appears that a complete (simple) analytical solution is not possible anymore for complex load cases including combined axial force and bi-axial bending or even combined axial force, bi-axial bending and torsion. Indeed, in these cases the displacement functions cannot be approximated by simple sine half waves. Also, some contradictory hypotheses are necessary for the approximation of the distribution of the bending moments and torsion. Moreover, even if it would be possible to obtain analytical second order internal forces and moments for complex load cases, they have to be introduced into an approximation of the interaction for the most loaded section. Consequently, it became obvious that a completely analytically based design model cannot be developed and therefore some inconsistencies had to be accepted in the following. Anyhow, the analytical developments revealed which second order effects are already included in the Eurocode 3 Part 1-1 interaction equations and the empirically determined Annex B (CEN 2005a) interaction factors and consequently it has

been pointed out which additional parameters and effects might additionally influence the behaviour of members subject to torsion. Also, an analytically based OIC approach has been developed for the case of combined bi-axial bending and torsion.

In paragraph 5.6 the database of numerically determined ultimate resistances is then used to calibrate and simplify the analytical OIC design approach. Additionally, this design model is extended to other load cases including combined major-axis bending and axial force. The proposed OIC approach is able to capture sufficiently precisely the behaviour of members under complex load combinations owing to the continuous strength prediction over the total range of relative member slenderness. Nonetheless, significant research effort has to be made in the future in order to extend the proposal to members under variable bending moments, members of non-compact and slender cross-section and members with lateral restraints. For these more complex cases, an extension of the Eurocode 3 Part 1-1 interaction equations to torsion is proposed in the framework of this thesis. This proposal may however be rather conservative as the plastic cross-section interaction is not well approximated. Yet, the conservatism is not significantly increased compared to the initial field of application of the interaction equations for members of double symmetric I section or members of U section. Indeed, in average the difference is of about 10%. In order to ameliorate the precision of the interaction equations for short members, a simplified plastic analysis of members subject to torsion is proposed. Yet, this approach should only be applied if the members do not possess a specific limitation of the torsional twist at the Serviceability Limit State. For members of mono-symmetric I section the proposed extension of the interaction equations may however be very conservative in the low slenderness range owing to the pronounced plastic torsional system reserve. Due to their structural use, Serviceability Limit State criteria are generally formulated for members of mono-symmetric I section. Therefore, the plastic torsional system reserve should not be accounted for by simplified analysis because the torsional twist cannot be determined reliably at the Serviceability Limit State.

6 GENERAL CONCLUSIONS

6.1	Summary and conclusions	586
6.2	Original contributions of the present thesis	591
6.3	Future research	593
6.4	Publications	595

6.1 Summary and conclusions

The three main objectives of the present thesis directly resulted from the limitations of the currently available design rules provided in the European standard for the design of steel structures, in particular Eurocode 3 Part 1-1 (CEN 2005a), for members with open cross-section subject to torsion. Indeed, it appears this standard does not give any design rule addressing the **resistance of members** of I and U sections subject to a combination of an axial compression force, bi-axial bending and torsion. For the **section resistance**, the current version of Eurocode 3 Part 1-1 does formulate limited design rules but these are partially inconsistent and contradictory. Therefore, this thesis intended to:

- Study the behaviour of members subject to combined axial compression forces, bi-axial bending and torsion.
- Derive design provisions addressing the plastic cross-section **resistance of open sections** subject to combined axial compression, bi-axial bending and torsion.
- Derive design provisions addressing the **resistance of members** subject to combined axial compression, bi-axial bending and torsion.

In order to achieve these, objectives the thesis has been structured in five main Chapters that may be summarised as follows:

- **Chapter 1** set the context of the present thesis and recalled the limitations of existing design rules for I- and U-shaped members. The main objectives of the thesis were formulated and the methodology used to attain these objectives was outlined.
- **Chapter 2** compiled the theoretical background necessary to understand the behaviour of members with open cross-section subject to torsion. In particular, the reasons for the sensitivity of open sections to torsion compared to closed sections are recalled. Additionally, the equivalence of the second order equilibrium of members under a tension axial force and bending to members under torsion was explained in the elastic domain. Throughout the thesis it was subsequently shown that this equivalence could be extended to the plastic behaviour.
- **Chapter 3** was dedicated to the construction and validation of a finite element model capable to predict reliably the section and member resistance studied in the following Chapters. The modelling of the fillets of hot-rolled sections was of special interest as these may highly influence the section resistance in case of applied torsion. It has been shown that only a solid model is capable to reproduce precisely the flow of the shear stresses over the cross-section containing fillets. The member resistance is also influenced by the presence of the fillets if an individual member is studied. Nonetheless, it could be demonstrated that, if the member resistance is normalised with reference to the real section characteristics (for example in a χ - λ diagram), the difference vanishes between sections with fillets and sections without fillets. Additionally, it has been shown that a shell model without fillets may yield equivalent

results as a solid model without fillets even for members subject to torsion. These two conclusions only allowed the construction of a database of member resistances containing approximately 10 000 configurations (combinations of cross-sections and load cases) that is used in Chapter 5 to develop a design model. Indeed, due to the calculation time, it would not have been possible to study such a high number of cases with the solid finite element model.

- **Chapter 4** addressed the plastic interaction between internal forces and moments including the effect of torsion. First, a review of the major international standards for the design of steel structures revealed several interesting points. In particular, it was shown that:
 - The precision of the Eurocode 3 Part 1-1 plastic cross-section interaction formulae for combined axial force and bi-axial bending is superior to the interaction formulae proposed in the North American Steel Design Standard AINSI/AISC 360-10 and the Australian Steel Design Standard AS 4100;
 - The shear area A_{vz} is defined differently for hot-rolled sections in the three cited standards leading to a non-negligible discrepancies in the obtained shear strength prediction;
 - None of the cited standards treats the effect of torsion on open sections satisfactorily.

In order to overcome the limitations of the standardised plastic cross-section interaction equations, two alternative design approaches have been presented. The first one is based on a presumed plastic distribution of the stresses resulting from the applied internal forces and moments. These stresses are iteratively increased up to complete yielding of the studied section. The second approach is the Partial Internal Force Method (PIFM) introduced by Kindmann (Kindmann et al. 1999a). The limitations of this second method were highlighted and an adaptation has been proposed. Nonetheless, all studied approaches are based on key assumptions based on the distribution of the stresses. Especially, the hypothesis concerning the plastic distribution of the shear stresses resulting from the transvers shear force V_z appeared to be critical. Therefore, it appeared of major-interest to study the strength of the section to this shear force before an extension/adaptation of the design rules to the case of torsion could be envisaged. This study was performed based on a campaign of laboratory tests and numerical simulations. It was shown that:

- The ultimate shear strength of compact H and I sections obtained by the laboratory tests and the numerical simulations is very high and exceeds even the shear strength predicted in Eurocode 3 Part 1-1;
- The shear resistance is however only slightly influenced by the presence of fillets. The difference between sections with fillets and equivalent sections without fillets is quite low and attains only of about 5%-10%;

- The “overstrength” predicted by Eurocode 3 Part 1-1 is linked to the effect of strain hardening and consequently the strength prediction may be unsafe if the level of strain hardening is insufficient (for high strength steels and/or if the web slenderness close to the limit for shear buckling);
- A design model explicitly considering the effect of strain hardening as the Continuous Strength Method (CSM) may increase the precision of the shear strength predictions.

The campaign of laboratory tests has also been used to validate the finite element model further on. This numerical model is then used to elaborate missing design rules, especially for mono-symmetric I and U sections under combined bending and shear force. After this, the investigations are extended to the plastic interaction including torsion. First, the influence of the type of analysis is discussed. Indeed, it is shown that the plastic torsional system reserve highly influences the Plastic Limit State of a member and that the generation of the plastic warping hinge leads inevitably to the yielding of the member along its whole length. The Plastic Limit State is therefore limited by the interaction between the Saint-Venant’s torsional moment with other internal forces and moments. Consequently, a simple elastic analysis followed by a cross-section verification is not capable to capture the plastic behaviour of members in torsion. Nonetheless, the cross-section resistance may be checked based on elastic analysis and without considering the Saint-Venant’s torsional moment as the obtained resistance is then linked to the creation of the warping hinge and hence always lower than the resistance associated with the Plastic Limit State of the member. In certain conditions, it may be interesting to account for the plastic torsional system reserve and therefore a simplified two-step elastic analysis procedure is proposed. Still, this method should only be applied to short members and if no particular Serviceability Limit State criteria are formulated for the studied member as the displacements and especially the torsional twist may be highly increased due to the formation of the plastic warping hinge. After the analysis of the plastic behaviour of members subject to torsion, the plastic cross-section interaction including the effect of the bi-moment was studied. Simplified plastic interaction equations were proposed for double and mono-symmetric I sections under bending moments, shear forces and bi-moments. It has however been shown that the complexity of this interaction equations is highly increased for mono-symmetric sections and for complex load combinations. Therefore, an adaptation of the PIFM appeared to be more constructive. The PIFM is consequently adapted to the results of the parametric study concerning the plastic cross-section and it is shown that the introduced adaptations may lead to very satisfactory results.

- **Chapter 5** concerned the resistance of members subject to torsion. As the development of the design models was based on an extensive numerical study, it was absolutely necessary to study the influence of assumed calculation imperfections on

the obtained results. It was shown that relevant information and guidelines exist for double symmetric I sections. Inversely, for mono-symmetric sections, in particular U sections, the existing habits and recommendations are partially contradictory. A comprehensive study of the influence of the calculation imperfections is therefore performed and this study yield the following results:

- The recommendations for equivalent member imperfection for members with I section cannot be directly transposed to U-shaped members. The resistance of U-shaped members may be determined numerically based on an Eigen mode affine geometric imperfection but it has to be ensured that the effect of the imperfection amplifies the first order displacements. Due to the effect of the stress induced bi-moment, this last remark is not self-evident.
- Local plate imperfection should be introduced with the same wave-length for the web and the flanges (in longitudinal direction of the member) as elsewhere the formation of local buckles may be disturbed by the interference between the different wave-lengths. The interference may lead (slightly) higher ultimate resistances.
- An auto-equilibrated residual stress pattern is proposed for U sections based on the internal equilibrium conditions of the section and thermo-mechanical simulations.

Following the study on calculation imperfections, different design approaches for the member resistance, particularly in presence of torsion, are discussed. With the help of the numerical model certain lacks and inconsistencies in these design models are highlighted and it is shown that none of them is complete. In order to get more insights into the behaviour of members with open cross-section subject to torsion a theoretical study is then performed.

The elastic critical loads are the basis of the assessment of the member stability. Therefore, they are studied again. In particular, the effect of pre-buckling displacements is highlighted and it is shown that they may have a considerable influence on the critical loads for U-shaped members under minor-axis bending. Indeed, only if pre-buckling displacements are accounted for, the critical loads may be representative of the member resistance for these cases. The study of the elastic instability also allowed the determination of the Eigen modes that are used subsequently as equivalent member imperfection for the theoretical study of the elastic second order equilibrium of the member. Different load cases are studied theoretically with the aim to outline the theoretical basis of the currently available design methods for the stability of members subject to a combination of axial compression force and bi-axial bending and to highlight the additional parameters arising if the member is subject to torsion. The theoretical study emphasized again that a completely analytical derived design method is not possible to the different assumptions that are necessary to obtain a closed form solution. In some cases, these

assumptions are contradictory and therefore, a certain degree of inconsistency has to be accepted. The last part of Chapter 5 was dedicated to the development of design rules. First, the design rules based on existing interaction equations are extended to the case of applied torsion. Also, it was necessary to close some lacks of the existing interaction equations for mono-symmetric sections. Indeed, the interaction equations for mono-symmetric I sections have been extended to applied minor-axis bending moments. For U-shaped member, the influence of in-plane buckling had to be quantified. For applied torsion it appeared that:

- The proposed simple extension to torsion appeared to be very satisfactory for double symmetric I sections with compact and non-compact or slender section. The loss of precision compared to the resistance predictions obtained for a member under a compression axial force and bi-axial bending has been shown to be negligible in practice.
- For U-shaped members, the interaction equations may be more conservative for short members, not only in case of applied torsion, due to the roughly approximated plastic cross-section interaction. Nonetheless, only an increased complexity would lead to an amelioration. So as to maintain the interaction equations simple for the practical application a higher conservatism is accepted for U-shaped members than for members of double symmetric I section.
- For members with mono-symmetric I section, the interaction equations may be even more conservative than for U-shaped members. In fact, it has been shown that the plastic torsional system reserve is very pronounced for members of mono-symmetric I section and consequently influences the resistance of these members even for intermediate values of the relative slenderness. It might be envisaged to apply the simplified two step elastic analysis method to account for the effect of the plastic torsional system reserve. However, this is not pursued further on in the framework of this thesis because the torsional twist may increase highly compared to the value obtained by an elastic analysis. Serviceable Limit State criteria could therefore not be checked reliably.

The conservatism of the interaction equations can be partially attributed to the approximate representation of the plastic cross-section interaction. This is a clear limitation of the design methods based on interaction equations. In order to obtain more precise and continuous strength predictions, global methods as the OIC approach have been introduced in the recent years. The OIC approach has been shown to be very promising especially for hollow sections and, consequently, it appeared to be interesting to investigate the possibility to extend this straightforward design method to members with open sections. Based on the database of numerical results a simple OIC approach has been proposed for members of double symmetric I section

subject to a combination of compression axial force, bi-axial bending and torsion. This design approach is, at least, as precise as the interaction equations and even more precise for low to intermediate values of the relative slenderness.

6.2 Original contributions of the present thesis

The original contributions of the present thesis may be summarised and categorised as follows:

Numerical simulations and influence of assumed calculation imperfections:

- Recommendations for equivalent geometric member imperfection have been derived for U-shaped members;
- A residual stress pattern has been developed for U sections based on equilibrium conditions and thermo-mechanical simulations;
- The influence of local plate imperfections have been studied for members with open section and recommendations on the shape to be used have been deduced.

Behaviour of members subject to torsion:

- In particular, the plastic behaviour of members subject to torsion has been studied and the influence of the plastic torsional system reserve on the section and the member resistance is highlighted;
- A simplified two-step elastic analysis method is proposed and shown to be sufficiently precise. However, it has to be emphasized here that this procedure should only be applied if the member is not subject to particular Serviceable Limit State criteria.

Plastic cross-section resistance:

- Based on laboratory tests, the shear resistance of hot-rolled members (with fillets) has been studied and it is shown that strain hardening has an important effect on the resistance;
- Numerical simulations have been performed to extend the results of the laboratory tests to welded sections, other steel grades and other section geometries. It could be concluded that the shear resistance is mainly linked to the strain hardening reserve of the studied section and that the fillets have only very little effect. It is shown that a design model considering explicitly the effect of strain hardening, as the Continuous Strength Method, is better suited to predict the shear resistance than the empirical increase of the shear area for hot-rolled sections as done in Eurocode 3 Part 1-1 (CEN 2005a);

- Based on MNA simulations the interaction between shear forces and bending moments is studied and it is shown that the shear force V_y may be neglected for mono- and double symmetric I and U sections in practice;
- “Simplified” interaction equations are developed for open sections subject to torsion but it is shown that the expressions may become very complex for mono-symmetric sections;
- An adaptation of the Partial Internal Force Method is proposed. In particular, the influence of the fillets for hot-rolled sections, the empirically observed shear force-bending moment interaction and the effect of the stress induced bi-moment are introduced.

Theoretical study of elastic buckling:

- The elastic critical loads represent an important factor to characterise the stability of members but only if they consider all relevant effects. In the framework of this thesis, it has been shown that it is necessary to account for the pre-buckling (or first order) displacements for U-shaped members under minor-axis bending and bi-axial bending. If this is not done, the sensitivity of these members to elasto-plastic instability is not reliably represented by the elastic critical loads.

Simplified design of members using interaction equations:

- An extension of the Eurocode 3 Part 1-1 interaction equations to the case of applied torsion is proposed. This extension is sufficiently precise and satisfactory for members with double symmetric I section;
- The resistance of U-shaped members is studied and the influence of in-plane buckling is introduced into an existing extension of the Eurocode 3 Part 1-1 interaction equations (see reference (Kalameya 2008)). This failure mode is shown to be relevant for members possessing intermediate lateral restraints;
- The interaction equations are subsequently extended to U-shaped members subject to torsion. The proposal is rather conservative for short members as the complex plastic cross-section interaction can only be roughly approximated with simplified interaction equations;
- An existing proposal for the resistance of members with mono-symmetric I section (see reference (Kaim 2004)) is extended to an applied minor-axis bending moment;
- The interaction equations applicable to members with mono-symmetric I section are extended further on to an applied torsional moment. The resulting expression are simple to use but very conservative. For members possessing low to intermediate values of the relative member slenderness, the approximation of the

plastic cross-section interaction and the high plastic torsional system reserve leads to the observed conservatism.

Straightforward design method based on OIC approach:

- A consistent OIC approach has been developed of members with double symmetric compact I section based on a theoretical basis and with the help of the database of numerical results.
- As far as possible, the OIC approach has been developed to continuously link existing design proposals for lateral-torsional buckling under major-axis bending and minor-axis flexural buckling for members subject to a combination of a compression axial force and a minor-axis bending moment.
- The interaction between flexural buckling and lateral-torsional buckling is studied and a specific imperfection factor α_{Interact} and an interaction function are proposed considering the specific interaction effect for members of different shape (ratio h/b) and different fabrication process (hot-rolled/welded).
- The OIC approach is extended to the load case of combined compression axial force, bi-axial bending and torsion. The resulting design model appears to be precise and even more precise than the well expected Eurocode 3 Part 1-1 interaction equations (even in their initial field of application) owing to the continuous strength prediction from short members, attaining the plastic limit state, to long members failing in a elasto-plastic buckling mode.

6.3 Future research

Obviously, this thesis could not respond to all problems that arise for members with open cross-section subject to torsion. Further research is necessary and in particular the following points merit deeper investigations:

Consolidation of the results and extension to other practical cases:

- The numerical parametric study comprises a totality of more than 10 000 configurations. However, it was not possible to study extensively the influence of the bending moment diagram and the distribution of the torsional moment. Only cases that appear to be common in practice have been treated. Therefore, other bending moment diagrams as well as other sources of torsional loads should be studied.
- In the framework of this thesis hot-rolled U-shaped members are studied. Today the use of cold formed channel sections become more and more frequent. Therefore, the study should be extended to cold formed sections. This also implies that the influence of distortion has to be characterised.

- Mono-symmetric I sections are also often slender. Their behaviour and resistance may thus be influenced by local plate instability. Consequently, additional mono-symmetric I sections should be studied.

Extension of OIC approach:

- The OIC approach developed in the framework of this thesis may be applied to members with compact double symmetric I section subject to a complex load combination including torsion. Yet, the approach is limited to constant bending moment diagrams. Consequently, the influence of the bending moment distribution should be investigated. Also, members with non-compact and slender section should be studied.
- The OIC approach should also be extended to members with mono-symmetric I section and U section. Due to the complex plastic cross-section interaction, simplified design methods based on interaction equations are rather conservative for short and intermediate member lengths. The OIC approach, based on the exact plastic cross-section interaction may possibly contribute to more economic design.
- For very short members with of compact cross-section, strain hardening increase the resistance. This beneficial effect may be accounted for by the Continuous Strength Method (CSM). It may therefore be of interest to study how the OIC approach could be coupled with CSM.
- In practice, members often possess intermediate restraints decreasing the sensitivity to instability. The influence of these intermediate restraints needs to be characterised in detail.

6.4 Publications

In the framework of the present thesis, the following papers have been published:

Journal

Beyer, A., Boissonnade, N., Khelil, A., Bureau, A. (2017), "Elastic stability of U-shaped members in bending considering pre-buckling displacements", *Journal of Constructional Steel Research* 135, 230-241.

Conference Proceedings

Beyer, A., Khelil, A., Boissonnade, N., Bureau, A. (2015), "Stability of I- and U-shaped members subjected to major-axis bending and torsion," Proceedings of the conference "1ère Conférence Internationale de Construction Métallique et Mixte – CICOMM'2015", Tlemcen, Algérie.

Beyer, A., Boissonnade, N., Khelil, A., Bureau, A. (2016), "Elastic stability of U-shaped members under bi-axial bending", Proceedings of the conference "The International Colloquium on Stability and Ductility of Steel Structures – SDSS 2016", Timisoara, Romania.

Beyer, A., Boissonnade, N., Khelil, A., Bureau, A. (2016), "Influence of geometric member imperfection on the ultimate resistance of U-shaped members", Proceedings of the conference "7th International Conference on Coupled Instabilities in Metal Structures – CIMS2016", Baltimore, United States of America.

Beyer, A., Khelil, A., Boissonnade, N., Bureau, A. (2017), "Plastic resistance of U sections under major-axis bending, shear force and bi-moments", Proceedings of the conference "EUROSTEEL 2017", Copenhagen, Denmark.

7 REFERENCES

Standards

1. ANSI (2010), "ANSI/AISC 360-10: Specification for Structural Steel Buildings".
2. BSI (2000). "Structural use of steelwork in building, Part 1: Code of practice for design – Rolled and welded sections".
3. Standards Australia (1998), "AS 4100-1998: Australian Standard – Steel structures".
4. CEN (1993), "EN 10034 – Structural steel I and H sections – Tolerances on shape and dimensions".
5. CEN (2003), "EN 1990 – Eurocode: Basis of structural design".
6. CEN (2005a), "EN 1993-1-1 – Eurocode 3: Design of steel structures, Part 1-1: General rules and rules for buildings".
7. CEN (2005b), "EN 1993-1-5 – Eurocode 3: Design of steel structures, Part 1-5: Design of plated structures". Changer 2007a
8. CEN (2005c), "EN 1993-1-2 – Eurocode 3: Design of steel structures, Part 1-2: General rules – Structural fire design".
9. CEN (2006), "EN 10210-2 – Hot finished structural hollow sections of non-alloy and fine grain steels – Part 2: Tolerances, dimensions and properties".
10. CEN (2007a), "EN 1993-6 – Eurocode 3: Design of steel structures, Part 6: Crane supporting structures".
11. CEN (2007b), "EN 1999-1-1 – Eurocode 9: Design of aluminium structures, Part 1-1: General structural rules".
12. CEN (2011a), "EN 1090-2 – Execution of steel structures and aluminium structures, Part 2: Technical requirements for steel structures".
13. CEN (2011b), "Eurocode 3: Design of steel structures, Part 6: Crane supporting structures – French national annex".
14. CEN (2014), "Eurocode 3: Design of steel structures, Part 1-1: General rules and rules for buildings – French national annex".
15. DIN (1990), "DIN 18800 Teil 2: Stahlbauten – Stabilitätsfälle, Knicken von Stäben und Stahlbauwerken".

Scientific publications

16. Alpsten, G. (1968), "Thermal residual stresses in hot-rolled steel members", Fritz Laboratory Reports, Paper 329.

17. Alpsten, G. (1972), "Prediction of thermal residual stresses in hot-rolled plates and shapes of structural steel", IABSE Ninth Congress - Volume 9 – 1a, 3-14.
18. Aswandy (2007), "Buckling behaviour of steel members with intermediate lateral restraints", Ph.D. Thesis, TU Graz.
19. Bazant, Z. P., Cedolin, L. (2010), "Stability of structures – Elastic, Inelastic, Fracture and Damage theories", World Scientific Publishing.
20. Beyer, A., Galéa, Y., Nguyen, T.M. (2015), "Déversement élastique des barres fléchies comprimées – Fondenement théorique et validation du logiciel LTBeamN", Revue Construction Métallique 3/2015, 25-42.
21. Boissonnade, N. (2002), "Mise au point d'un élément fini de type poutre à section variable et autres applications à la construction métallique", Ph.D. Thesis, University Blaise Pascal – Clermont II.
22. Boissonnade, N, Jaspar, J.-P., Muzeau, J.-P., Vilette, M. (2002), "Improvement of the interaction formulae for beam columns in Eurocode 3", Computers and Structures Vol.80, 2002.
23. Boissonnade, N, Jaspar, J.-P., Muzeau, J.-P., Vilette, M. (2004), "New interaction formulae for beam-columns in Eurocode 3: The French-Belgian approach", Journal of Constructional Steel Research Vol.60, 2004.
24. Boissonnade, N., Somja, H. (2012), "Influence of Imperfections in FEM Modelling of Lateral Torsional Buckling", Proceedings of the Annual Stability Conference – Structural Stability Research Council.
25. Boissonnade, N, Nseir, J., Saloumi, E. (2013). "The Overall Interaction Concept: an Alternative Approach to the Stability and Resistance of Steel Sections and Members". Proceedings of the Annual Stability Conference – Structural Stability Research Council.
26. Boissonnade, N., Hayeck, M., Saloumi, E., Nseir, J. (2017), "An Overall Interaction Concept for an alternative approach to steel members design", Journal of Constructional Steel Research 135, 199-212.
27. Brune, B. (1998), "Die dreisitig gelagerte Platte in der Methode der wirksamen Breiten", Stahlbau 11/1998, 851-863.
28. Chacón, R, Mirambell, E., Real, E. (2009), "Influence of designer-assumed initial conditions on the numerical modelling of steel plate girders subjected to patch loading", Thin-Walled Structures 47, 391-402.
29. Cheng, S.-S., Kim, B., Li, L.-Y. (2013), "Lateral-torsional buckling of cold-formed channel sections subject to combined compression and bending", Journal of Constructional Steel Research 80, 174-180.

30. De Louw, K. (2007). "Design rule for lateral torsional buckling of channel sections". Master Thesis TU Eindhoven.
31. De Ville de Goyet, V. (1989), "L'analyse statique non linéaire par la méthode des éléments finis des structures spatiales formées de poutres à section non symétrique", Ph.D. Thesis, University of Liège.
32. Djalaly, H. (1975), "Calcul de la résistance ultime des barres comprimées et fléchies", *Revue Construction Métallique*, 4/1975, 17-47.
33. ECCS TC 8 (1976), "Manual on Stability of Steel Structures", ECCS publication n°22.
34. ECCS TC 8 (1984), "Ultimate Limit State Calculation of Sway Frames with Rigid Joints", ECCS publication n°33.
35. ECCS TC 8 (2006), "Rules for Member Stability in EN 1993-1-1 – Background documentation and design guidelines", ECCS publication n°119.
36. Erkmen, R.E., Attard, M.M. (2011), "Lateral-torsional buckling analysis of thin-walled beams including shear and pre-buckling deformation effects", *International Journal of Mechanical Sciences* 53, 918-925.
37. FABIG (2002), "Technical Note And Worked Examples To Supplement The Interim Guidance Notes For The Design And Protection of Topside Structures Against Explosions And Fire – Technical Note 7", The Steel Construction Institute.
38. FOSTA (2004), "Forschungsvorhaben P 554 – Untersuchungen zum Einfluss der Torsionseffekte auf die plastische Querschnittstragfähigkeit und die Bauteiltragfähigkeit von Stahlprofilen", Verlag und Vertriebsgesellschaft mbH, Düsseldorf.
39. Friemann, H., Francke, W. (2005), "Schub und Torsion in geraden Stäben", Vieweg+Teubner Verlag.
40. Gardner, L., Afshan, S. (2013), "The continuous strength method for structural stainless steel design", *Thin-Walled Structures* 68, 42-49.
41. Glitsch, T. (2008). "Beitrag zur vereinfachten Bemessung von stabilitätsgefährdeten Stahlstäben mit offenen Profilen unter Quer- und Torsionsbelastung". Ph.D. Thesis, TU Berlin.
42. Gonçalves, R., Coelho, T., Camotim, D. (2014), "On the plastic moment of I-sections subjected to moderate shear forces", *Thin-Walled Structures* 78, 138-147.
43. Greiner, R. (2001), "Background Information on the Beam-Column Interaction Formulae at Level 1", ECCS TC8, non-numbered paper.
44. Greiner, R., Lindner, J. (2006), "Interaction formulae for members subjected to bending and compression in Eurocode 3 – the Method 2 approach", *Journal of Constructional Steel Research*, Vol. 62.

45. Greiner, R., Kaim, P., Taras, A. (2011), "Stabilitätsnachweis von Stäben mit einfachsymmetrischen Querschnitten – Eurocode-konforme Regelungen im österreichischen Nationalen Anhang zur EN 1993-1-1", *Stahlbau* 5/2011, 356-363.
46. Kaim, P. (2004), "Spatial buckling behaviour of steel members under bending and compression", Ph.D. Thesis, TU Graz.
47. Kalameya, J. (2008), "Zur Tragfähigkeit von druck- und biegebeanspruchten C-Profilen aus Stahl", Ph.D. Thesis, TU Dortmund.
48. Kettler, M. (2008), "Elastic-Plastic Cross-Sectional Resistance of Semi-Compact H-and Hollow Sections", Ph.D. Thesis, TU Graz.
49. Kindmann, R., Frickel, J. (1999a), "Grenztragfähigkeit von häufig verwendeten Stabquerschnitten für beliebige Schnittgrößen", *Stahlbau* 10/1999, 817-828.
50. Kindmann, R., Frickel, J. (1999b), "Grenztragfähigkeit von I-Querschnitten für beliebige Schnittgrößen", *Stahlbau* 4/1999, 290-301.
51. Kindmann, R., Frickel, J. (2002). "Resistance of U-sections subject to bending and torsion", *RUBSTAHL* 1-2002, RU Bochum.
52. Krüger, U. (1999), "1. Zuschrift zu: Grenztragfähigkeit von I-Querschnitten für beliebige Schnittgrößen", *Stahlbau* 10/1999, 852.
53. La Poutrée, D. B. (1999). "Strenght and stability of channel sections used as beam". Master Thesis TU Eindhoven.
54. Lee, C.K., Chiew, S.P., Jiang, J. (2012), "Residual stress study of welded high strength steel thin-walled plate-to-plate joints part 2: Numerical Modelling", *Thin-Walled Structures* 59, 120-131.
55. Li, G.-Q., Wang, Y.-B., Chen, S.-W. (2012), "Residual stresses in welded flame-cut high strength steel H-sections", *Journal of Constructional Steel Research* 79, 159-165.
56. Li, Y. (2014), "Extension of the Direct Strength Method to hot-rolled and welded H profile cross-sections", Ph.D. Thesis, University of Liège.
57. Liew, A., Gardner, L. (2015), "Ultimate capacity of structural steel cross-sections under compression, bending and combined loading", *Structures* 1, 2-11.
58. Lindner, J. (2001), "Evaluation of interaction formulae for level 1 approach with regard to ultimate load calculations and test results – flexural buckling and lateral torsional buckling", *ECCS TC8*, Paper No. TC8-2001-17.
59. Lindner, J., Scheer, J., Schmidt, H. (1998), "Stahlbauten – Erläuterungen zu DIN 18800 Teil 1 bis Teil 4", *Beuth-Kommentare*, Beuth Verlag GmbH, Berlin.
60. Ludwig, C. (2014), "Plastische Querschnittstragfähigkeit von doppelsymmetrischen I-Querschnitten – Tragfähigkeitsbedingungen, Genauigkeit, Nebeneffekte" Ph.D. Thesis, Ruhr-Universität Bochum.

61. Maquoi, R (2015), Personal communication.
62. Marques, L., da Silva, L. S., Rebelo, C., Santiago, A. (2014), "Extension of the EC3-1-1 interaction formulae for the stability verification of tapered beam-columns", *Journal of Constructional Steel Research* 100, 122-135.
63. Mirambell, E., Bordallo, J., Real, E. (2016), "Torsion and its interaction with other internal forces in EN 1993-1-1 – a new approach", *Steel Construction* 9/3, 240-248.
64. Müller, C. (2003), "Zum Nachweis ebener Tragwerke aus Stahl gegen seitliches Ausweichen", Ph.D. Thesis, RWTH Aachen.
65. Nadai, A (1923), "Der Beginn des Fließvorganges in einem tordierten Stab", *Zeitschrift für angewandte Mathematik und Mechanik* 3, 442-454.
66. Naumes, J. N. (2009), "Biegeknicken und Biegedrillknicken von Stäben und Stabsystemen auf einheitlicher Grundlage", Ph.D. Thesis, RWTH Aachen.
67. Nethercot, D.A., Salter, P.R., Malik, A.S. (1989), "Design of Members Subject to Combined Bending and Torsion", SCI Publication 057.
68. Nseir, J. (2015), "Development of a new design method for the cross-section capacity of steel hollow sections", Ph.D. Thesis, University of Liège.
69. RFCS (2009), "SEMI-COMP: Plastic member capacity of semi-compact steel sections – a more economic design", RFCS-CT-2004-00044, Final Report, Research Program of the Research Fund for Coal and Steel – RTD.
70. Offner, R. (1997); "Traglasten von Stäben aus Stahl bei Druck und Biegung", Ph.D. Thesis, TU Graz.
71. Peer, B., Axel, B., Hächel, M. (2015), "Stabilitätsnachweis für komplexe Blech- und Rohrkonstruktionen", *Stahlbau* 6/2015, 422-429.
72. Rondal, J., Maquoi, R. (1979), "Formulations d'Ayrton-Perry pour le Flambement des Barres Métalliques", *Revue Construction Métallique*, 4/1979, 41-53.
73. Rubin, H. (1978), "Interaktionsbeziehungen für doppelsymmetrische I- und Kasten-Querschnitte bei zweiachsiger Biegung und Normalkraft", *Stahlbau* 5/1978, 145-151.
74. Rubin, H. (1999), "3. Zuschrift zu: Grenztragfähigkeit von I-Querschnitten für beliebige Schnittgrößen", *Stahlbau* 10/1999, 853.
75. Rubin, H. (2000), "Grundlage für die N-My-Mz-Interaktionsbeziehungen von I-Querschnitten", *Stahlbau* 10/2000, 807-812.
76. Rubin, H. (2005), "Zur plastischen Tragfähigkeit von 3-Blech-Querschnitten unter Normalkraft, doppelter Biegung und Wölbkrafttorsion", *Stahlbau* 1/2005, 47-61.
77. Rusch, A., Lindner, J. (2004), "Application of level 1 interaction formulae to class 4 sections", *Thin-Walled Structures* 42, 279-293.

78. Saliba, N., Gardner, L. (2015), "Extension of the continuous strength method to the determination of the shear resistance", Proceedings of the Nordic Steel Construction Conference 2015.
79. Snijder, B., Hoenderkamp, H., Bakker, M., Steenbergen, H., de Louw, K. (2008). "Design rules for lateral torsional buckling of channel sections subject to web loading", *Stahlbau* 4/2008, 247-256.
80. Stangenberg, H. (2007). "Zum Bauteilnachweis offener, stabilitätsgefährdeter Stahlbauprofile unter Einbeziehung seitlicher Beanspruchung und Torsion". Ph.D. Thesis, RWTH Aachen.
81. Taras, A. (2011), "Contribution to the Development of Consistent Stability Design Rules for Steel Members", Ph.D. Thesis, TU Graz.
82. Tebedge, N., Tall, L. (1974), "Contraintes résiduelles dans les profiles en acier. Synthèse des valeurs mesurées", *Revue Construction Métallique* 2/1974, 37-48.
83. Thiébaud, R. (2014), "Résistance au déversement des poutres métalliques de pont", Ph.D. Thesis, Ecole Polytechnique Fédérale de Lausanne.
84. Timoshenko, S. P., Goodier, J. N. (1970), "Theory of Elasticity", McGraw-Hill Education.
85. Villette, M. (2004.), "Analyse critique du traitement de la barre comprimée et fléchie et propositions de nouvelles formulations", Ph.D. Thesis, University of Liège.
86. Vinnakota, S. , Badoux, J.-C., Yasuyuki, A. (1975), "Equations fondamentales du comportement des poutres-colonnes à section ouverte et parois minces", *Bulletin technique de la Suisse romande* 26/101, 437-
87. Vlassov, B.Z. (1962), "Pièces longues en voiles minces", Editions Eyrolles.
88. Werner, G. (1999), "2. Zuschrift zu: Grenztragfähigkeit von I-Querschnitten für beliebige Schnittgrößen", *Stahlbau* 10/1999, 852-853.
89. Wolf, C., Frickel, J. (2014), "Plastischer Querschnittstragfähigkeit für 3Blech-Querschnitte v10/14", RU Bochum.
90. Young, B.W. (1975), "Residual stresses in hot rolled members", IABSE: Proceedings of the International Colloquium on Columns Strength Volume 23, 25-38.

Programs

91. ANSYS® Mechanical, Release 17.0 (2016), "Help System - Mechanical APDL", ANSYS, Inc.

8 ANNEXES

8.1	Annex A: Recall of Annex A of EN 1993-1-1 :2005	606
8.2	Annex B: Measured geometry and material law for the laboratory tests performed at University of Applied Sciences of Western Switzerland	608
8.3	Annex C: Sections used for the parametric study concerning the member resistance	616

8.1 Annex A: Recall of Annex A of EN 1993-1-1 :2005

Hereafter, the expressions of the Annex A interaction factors of Eurocode 3 Part 1-1 (CEN 2005a) are recalled.

Interaction factors	Design assumptions	
	elastic cross-sectional properties class 3, class 4	plastic cross-sectional properties class 1, class 2
k_{yy}	$C_{my} C_{mLT} \frac{\mu_y}{1 - \frac{N_{Ed}}{N_{cr,y}}}$	$C_{my} C_{mLT} \frac{\mu_y}{1 - \frac{N_{Ed}}{N_{cr,y}}} \frac{1}{C_{yy}}$
k_{yz}	$C_{mz} \frac{\mu_y}{1 - \frac{N_{Ed}}{N_{cr,z}}}$	$C_{mz} \frac{\mu_y}{1 - \frac{N_{Ed}}{N_{cr,z}}} \frac{1}{C_{yz}} 0,6 \sqrt{\frac{W_z}{W_y}}$
k_{zy}	$C_{my} C_{mLT} \frac{\mu_z}{1 - \frac{N_{Ed}}{N_{cr,y}}}$	$C_{my} C_{mLT} \frac{\mu_z}{1 - \frac{N_{Ed}}{N_{cr,y}}} \frac{1}{C_{zy}} 0,6 \sqrt{\frac{W_y}{W_z}}$
k_{zz}	$C_{mz} \frac{\mu_z}{1 - \frac{N_{Ed}}{N_{cr,z}}}$	$C_{mz} \frac{\mu_z}{1 - \frac{N_{Ed}}{N_{cr,z}}} \frac{1}{C_{zz}}$
Auxiliary terms:		
$\mu_y = \frac{1 - \frac{N_{Ed}}{N_{cr,y}}}{1 - \chi_y \frac{N_{Ed}}{N_{cr,y}}}$ $\mu_z = \frac{1 - \frac{N_{Ed}}{N_{cr,z}}}{1 - \chi_z \frac{N_{Ed}}{N_{cr,z}}}$ $w_y = \frac{W_{pl,y}}{W_{el,y}} \leq 1,5$ $w_z = \frac{W_{pl,z}}{W_{el,z}} \leq 1,5$ $n_{pl} = \frac{N_{Ed}}{N_{Rk} / \gamma_{M1}}$ C_{my} see Table A.2 $a_{LT} = 1 - \frac{I_T}{I_y} \geq 0$	$C_{yy} = 1 + (w_y - 1) \left[\left(2 - \frac{1,6}{W_y} C_{my}^2 \bar{\lambda}_{max} - \frac{1,6}{W_y} C_{my}^2 \bar{\lambda}_{max}^2 \right) n_{pl} - b_{LT} \right] \geq \frac{W_{el,y}}{W_{pl,y}}$ with $b_{LT} = 0,5 a_{LT} \frac{\bar{\lambda}_0^2}{\chi_{LT}} \frac{M_{y,Ed}}{M_{pl,y,Rd}} \frac{M_{z,Ed}}{M_{pl,z,Rd}}$ $C_{yz} = 1 + (w_z - 1) \left[\left(2 - 14 \frac{C_{mz}^2 \bar{\lambda}_{max}^2}{W_z^5} \right) n_{pl} - c_{LT} \right] \geq 0,6 \sqrt{\frac{W_z}{W_y}} \frac{W_{el,z}}{W_{pl,z}}$ with $c_{LT} = 10 a_{LT} \frac{\bar{\lambda}_0^2}{5 + \bar{\lambda}_z^4} \frac{M_{y,Ed}}{C_{my} \chi_{LT} M_{pl,y,Rd}}$ $C_{zy} = 1 + (w_y - 1) \left[\left(2 - 14 \frac{C_{my}^2 \bar{\lambda}_{max}^2}{W_y^5} \right) n_{pl} - d_{LT} \right] \geq 0,6 \sqrt{\frac{W_y}{W_z}} \frac{W_{el,y}}{W_{pl,y}}$ with $d_{LT} = 2 a_{LT} \frac{\bar{\lambda}_0}{0,1 + \bar{\lambda}_z^4} \frac{M_{y,Ed}}{C_{my} \chi_{LT} M_{pl,y,Rd}} \frac{M_{z,Ed}}{C_{mz} M_{pl,z,Rd}}$ $C_{zz} = 1 + (w_z - 1) \left[\left(2 - \frac{1,6}{W_z} C_{mz}^2 \bar{\lambda}_{max} - \frac{1,6}{W_z} C_{mz}^2 \bar{\lambda}_{max}^2 \right) n_{pl} - e_{LT} \right] \geq \frac{W_{el,z}}{W_{pl,z}}$ with $e_{LT} = 1,7 a_{LT} \frac{\bar{\lambda}_0}{0,1 + \bar{\lambda}_z^4} \frac{M_{y,Ed}}{C_{my} \chi_{LT} M_{pl,y,Rd}}$	

Figure 8-1: Table A.1 of Eurocode 3 Part 1-1 (CEN 2005a)

$\bar{\lambda}_{\max} = \max \left\{ \begin{array}{l} \bar{\lambda}_y \\ \bar{\lambda}_z \end{array} \right.$	
$\bar{\lambda}_0 = \text{non-dimensional slenderness for lateral-torsional buckling due to uniform bending moment, i.e. } \psi_y = 1,0 \text{ in Table A.2}$	
$\bar{\lambda}_{LT} = \text{non-dimensional slenderness for lateral-torsional buckling}$	
<p>If $\bar{\lambda}_0 \leq 0,2\sqrt{C_1} \sqrt{\left(1 - \frac{N_{Ed}}{N_{cr,z}}\right) \left(1 - \frac{N_{Ed}}{N_{cr,TF}}\right)}$:</p>	$C_{my} = C_{my,0}$ $C_{mz} = C_{mz,0}$ $C_{mLT} = 1,0$
<p>If $\bar{\lambda}_0 > 0,2\sqrt{C_1} \sqrt{\left(1 - \frac{N_{Ed}}{N_{cr,z}}\right) \left(1 - \frac{N_{Ed}}{N_{cr,TF}}\right)}$:</p>	$C_{my} = C_{my,0} + (1 - C_{my,0}) \frac{\sqrt{\varepsilon_y} a_{LT}}{1 + \sqrt{\varepsilon_y} a_{LT}}$ $C_{mz} = C_{mz,0}$ $C_{mLT} = C_{my}^2 \frac{a_{LT}}{\sqrt{\left(1 - \frac{N_{Ed}}{N_{cr,z}}\right) \left(1 - \frac{N_{Ed}}{N_{cr,T}}\right)}} \geq 1$
$\varepsilon_y = \frac{M_{y,Ed}}{N_{Ed}} \frac{A}{W_{el,y}} \quad \text{for class 1, 2 and 3 cross-sections}$	
$\varepsilon_y = \frac{M_{y,Ed}}{N_{Ed}} \frac{A_{eff}}{W_{eff,y}} \quad \text{for class 4 cross-sections}$	
$N_{cr,y} = \text{elastic flexural buckling force about the y-y axis}$	
$N_{cr,z} = \text{elastic flexural buckling force about the z-z axis}$	
$N_{cr,T} = \text{elastic torsional buckling force}$	
$I_T = \text{St. Venant torsional constant}$	
$I_y = \text{second moment of area about y-y axis}$	

Figure 8-2: Table A.1 continued of Eurocode 3 Part 1-1 (CEN 2005a)

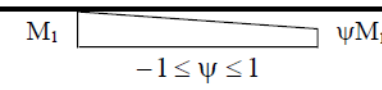
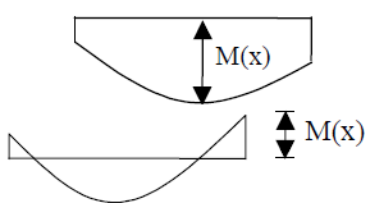
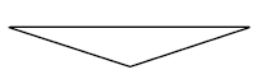

Moment diagram	$C_{mi,0}$
	$C_{mi,0} = 0,79 + 0,21\psi_i + 0,36(\psi_i - 0,33) \frac{N_{Ed}}{N_{cr,i}}$
	$C_{mi,0} = 1 + \left(\frac{\pi^2 EI_i \delta_x }{L^2 M_{i,Ed}(x) } - 1 \right) \frac{N_{Ed}}{N_{cr,i}}$ <p>$M_{i,Ed}(x)$ is the maximum moment $M_{y,Ed}$ or $M_{z,Ed}$ δ_x is the maximum member displacement along the member</p>
	$C_{mi,0} = 1 - 0,18 \frac{N_{Ed}}{N_{cr,i}}$
	$C_{mi,0} = 1 + 0,03 \frac{N_{Ed}}{N_{cr,i}}$

Figure 8-3: Table A.1 of Eurocode 3 Part 1-1 (CEN 2005a)

8.2 Annex B: Measured geometry and material law for the laboratory tests performed at University of Applied Sciences of Western Switzerland

Figure 8-4 recalls the points of measurements of the cross-section dimensions.

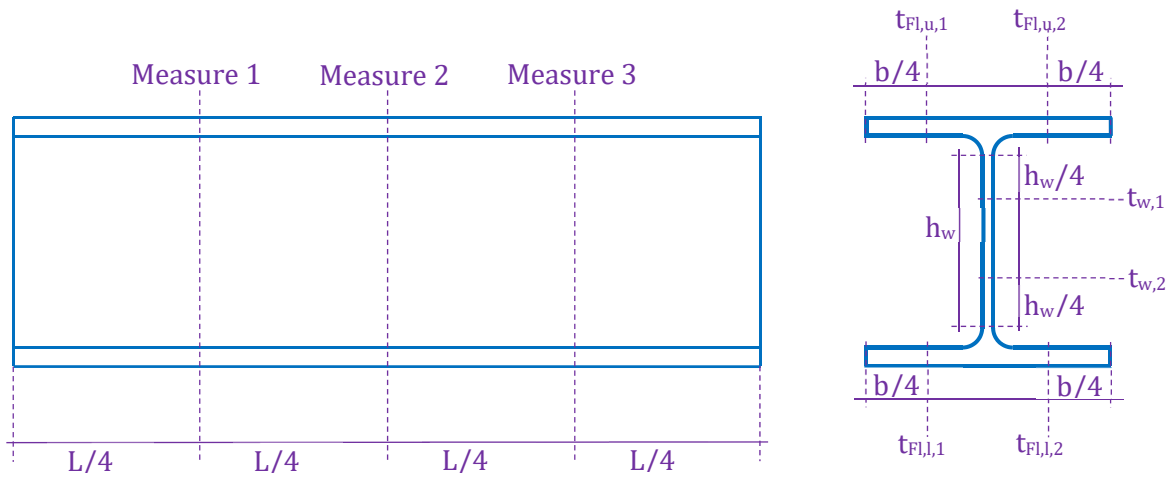


Figure 8-4: Measurements of cross-section dimensions

Table 8-1 to Table 8-10 represent the results of the measurements of the cross-section dimensions of the specimen tested in the laboratory.

Table 8-1: Measured dimensions for test HEA220_S235_L420

	Measure 1	Measure 2	Measure 3	Mean value	Nominal value (Tolerance)
$b_{Fl,u}$ [mm]	221,20	220,29	220,54	220,67	220,00 (+4;-2)
$t_{fl,u1}$ [mm]	10,68	10,80	10,43	10,62	11,00 (+2.5;-1.5)
$t_{fl,u2}$ [mm]	10,77	10,47	10,56		
$b_{Fl,l}$ [mm]	220,60	220,25	220,73	220,53	220,00 (+4;-2)
$t_{fl,l1}$ [mm]	10,73	10,88	10,80	10,82	11,00 (+4;-2)
$t_{fl,l2}$ [mm]	11,00	10,93	10,82		
h [mm]	210,26	211,47	210,8	210,84	210,00 (+3;-2)
$t_{w,1}$ [mm]	7,17	7,17	7,35	7,24	7,00 (+0.7;-0.7)
$t_{w,2}$ [mm]	7,22	7,20	7,31		

Table 8-2: Measured dimensions for test HEA220_S235_L840

	Measure 1	Measure 2	Measure 3	Mean value	Nominal value (Tolerance)
$b_{F,u}$ [mm]	221,52	220,72	220,35	220,53	220,00 (+4;-2)
$t_{f,u1}$ [mm]	10,75	10,72	10,81	10,62	11,00 (+2.5;-1.5)
$t_{f,u2}$ [mm]	10,52	10,41	10,52		
$b_{F,l}$ [mm]	220,42	220,75	221,09	220,75	220,00 (+4;-2)
$t_{f,l1}$ [mm]	10,65	10,91	10,71	10,74	11,00 (+4;-2)
$t_{f,l2}$ [mm]	10,59	10,72	10,85		
h [mm]	210,61	210,42	211,25	210,76	210,00 (+3;-2)
$t_{w,1}$ [mm]	7,14	7,19	7,20	7,23	7,00 (+0.7;-0.7)
$t_{w,2}$ [mm]	7,21	7,32	7,34		

Table 8-3: Measured dimensions for test HEA220_S355_L420

	Measure 1	Measure 2	Measure 3	Mean value	Nominal value (Tolerance)
$b_{F,u}$ [mm]	220,50	221,32	220,62	220,81	220,00 (+4;-2)
$t_{f,u1}$ [mm]	10,83	10,74	10,78	10,76	11,00 (+2.5;-1.5)
$t_{f,u2}$ [mm]	10,76	10,71	10,75		
$b_{F,l}$ [mm]	220,67	220,51	220,10	220,43	220,00 (+4;-2)
$t_{f,l1}$ [mm]	10,79	10,94	10,70	10,67	11,00 (+4;-2)
$t_{f,l2}$ [mm]	10,56	10,56	10,45		
h [mm]	211,97	211,90	212,18	212,02	210,00 (+3;-2)
$t_{w,1}$ [mm]	7,33	7,18	7,20	7,29	7,00 (+0.7;-0.7)
$t_{w,2}$ [mm]	7,23	7,37	7,45		

Table 8-4: Measured dimensions for test HEA220_S355_L840

	Measure 1	Measure 2	Measure 3	Mean value	Nominal value (Tolerance)
$b_{Fl,u}$ [mm]	220,42	221,19	220,98	220,86	220,00 (+4;-2)
$t_{fl,u1}$ [mm]	10,95	10,65	10,78	10,80	11,00 (+2.5;-1.5)
$t_{fl,u2}$ [mm]	10,82	10,89	10,71		
$b_{Fl,l}$ [mm]	220,53	220,75	220,25	220,51	220,00 (+4;-2)
$t_{fl,l1}$ [mm]	10,72	10,83	10,69	10,80	11,00 (+4;-2)
$t_{fl,l2}$ [mm]	10,92	10,79	10,82		
h [mm]	211,52	211,84	211,35	211,57	210,00 (+3;-2)
$t_{w,1}$ [mm]	7,19	7,12	7,35	7,24	7,00 (+0.7;-0.7)
$t_{w,2}$ [mm]	7,29	7,17	7,32		

Table 8-5: Measured dimensions for test HEB180_S235_L540

	Measure 1	Measure 2	Measure 3	Mean value	Nominal value (Tolerance)
$b_{Fl,u}$ [mm]	180,33	180,11	181,00	180,48	180,00 (+4;-2)
$t_{fl,u1}$ [mm]	13,85	13,88	13,86	13,81	14,00 (+2.5;-1.5)
$t_{fl,u2}$ [mm]	13,86	13,67	13,76		
$b_{Fl,l}$ [mm]	180,81	181,12	180,92	180,72	180,00 (+4;-2)
$t_{fl,l1}$ [mm]	13,75	13,71	13,74	13,76	14,00 (+2.5;-1.5)
$t_{fl,l2}$ [mm]	13,56	13,67	13,76		
h [mm]	180,26	181,17	180,93	180,79	180,00 (+3;-2)
$t_{w,1}$ [mm]	8,34	8,26	8,34	8,27	8,50 (+1;-1)
$t_{w,2}$ [mm]	8,34	8,41	8,42		

Table 8-6: Measured dimensions for test HEB180_S235_L810

	Measure 1	Measure 2	Measure 3	Mean value	Nominal value (Tolerance)
$b_{F,l,u}$ [mm]	180,25	180,34	179,93	180,17	180,00 (+4;-2)
$t_{fl,u1}$ [mm]	13,91	13,85	13,95	13,86	14,00 (+2.5;-1.5)
$t_{fl,u2}$ [mm]	13,78	13,87	13,82		
$b_{F,l}$ [mm]	180,59	180,72	180,21	180,51	180,00 (+4;-2)
$t_{fl,11}$ [mm]	13,62	13,71	13,82	13,76	14,00 (+2.5;-1.5)
$t_{fl,12}$ [mm]	13,85	13,72	13,83		
h [mm]	181,14	180,72	180,9	180,85	180,00 (+3;-2)
$t_{w,1}$ [mm]	8,25	8,19	8,29	8,26	8,50 (+1;-1)
$t_{w,2}$ [mm]	8,27	8,32	8,21		

Table 8-7: Measured dimensions for test HEB180_S355_L540

	Measure 1	Measure 2	Measure 3	Mean value	Nominal value (Tolerance)
$b_{F,l,u}$ [mm]	180,39	179,91	179,72	180,01	180,00 (+4;-2)
$t_{fl,u1}$ [mm]	13,59	13,70	13,51	13,62	14,00 (+2.5;-1.5)
$t_{fl,u2}$ [mm]	13,72	13,59	13,61		
$b_{F,l}$ [mm]	180,25	180,10	179,92	180,09	180,00 (+4;-2)
$t_{fl,11}$ [mm]	13,46	13,59	13,58	13,57	14,00 (+2.5;-1.5)
$t_{fl,12}$ [mm]	13,62	13,58	13,57		
h [mm]	180,40	180,33	180,44	180,39	180,00 (+3;-2)
$t_{w,1}$ [mm]	8,31	8,15	8,23	8,27	8,50 (+1;-1)
$t_{w,2}$ [mm]	8,35	8,19	8,38		

Table 8-8: Measured dimensions for test HEB180_S355_L810

	Measure 1	Measure 2	Measure 3	Mean value	Nominal value (Tolerance)
$b_{F,u}$ [mm]	180,21	180,75	180,31	180,42	180,00 (+4;-2)
$t_{f,u1}$ [mm]	13,51	13,82	13,76	13,72	14,00 (+2.5;-1.5)
$t_{f,u2}$ [mm]	13,62	13,79	13,82		
$b_{F,l}$ [mm]	180,59	180,72	180,21	180,51	180,00 (+4;-2)
$t_{f,l1}$ [mm]	13,91	13,65	13,79	13,76	14,00 (+2.5;-1.5)
$t_{f,l2}$ [mm]	13,85	13,72	13,66		
h [mm]	181,14	180,72	180,9	180,85	180,00 (+3;-2)
$t_{w,1}$ [mm]	8,25	8,19	8,29	8,26	8,50 (+1;-1)
$t_{w,2}$ [mm]	8,27	8,32	8,21		

Table 8-9 : Measured dimensions for test IPE270_S355_L540

	Measure 1	Measure 2	Measure 3	Mean value	Nominal value (Tolerance)
$b_{F,u}$ [mm]	135,20	135,12	135,31	135,21	135,00 (+4;-2)
$t_{f,u1}$ [mm]	9,63	9,63	9,41	9,55	10,20 (+2.5;-1.5)
$t_{f,u2}$ [mm]	9,57	9,51	9,57		
$b_{F,l}$ [mm]	135,16	135,17	135,49	135,27	135,00 (+4;-2)
$t_{f,l1}$ [mm]	9,64	9,59	9,53	9,65	10,20 (+2.5;-1.5)
$t_{f,l2}$ [mm]	9,72	9,56	9,84		
h [mm]	270,57	270,24	270,39	270,40	270,00 (+4;-2)
$t_{w,1}$ [mm]	6,90	6,70	6,85	6,81	6,60 (+0.7;-0.7)
$t_{w,2}$ [mm]	6,62	6,74	6,72		

Table 8-10 : Measured dimensions for test IPE270_S355_L810

	Measure 1	Measure 2	Measure 3	Mean value	Nominal value (Tolerance)
$b_{F,u}$ [mm]	135,21	135,19	135,44	135,28	135,00 (+4;-2)
$t_{f,u1}$ [mm]	9,43	9,61	9,55	9,56	10,20 (+2.5;-1.5)
$t_{f,u2}$ [mm]	9,52	9,59	9,63		
$b_{F,l}$ [mm]	135,35	135,17	135,41	135,31	135,00 (+4;-2)
$t_{f,l1}$ [mm]	9,96	9,82	9,73	9,82	10,20 (+2.5;-1.5)
$t_{f,l2}$ [mm]	9,83	9,65	9,92		
h [mm]	270,21	270,59	270,35	270,38	270,00 (+4;-2)
$t_{w,1}$ [mm]	6,85	6,63	6,71	6,70	6,60 (+0.7;-0.7)
$t_{w,2}$ [mm]	6,59	6,71	6,69		

In the following, the material behaviour represented by the stress-strain curves is shown. The position of the coupons are recalled in Figure 8-5

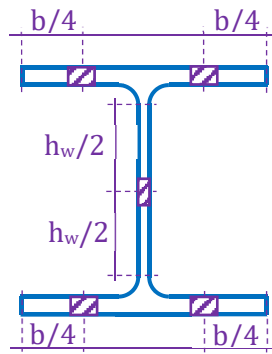


Figure 8-5: Position of the coupons

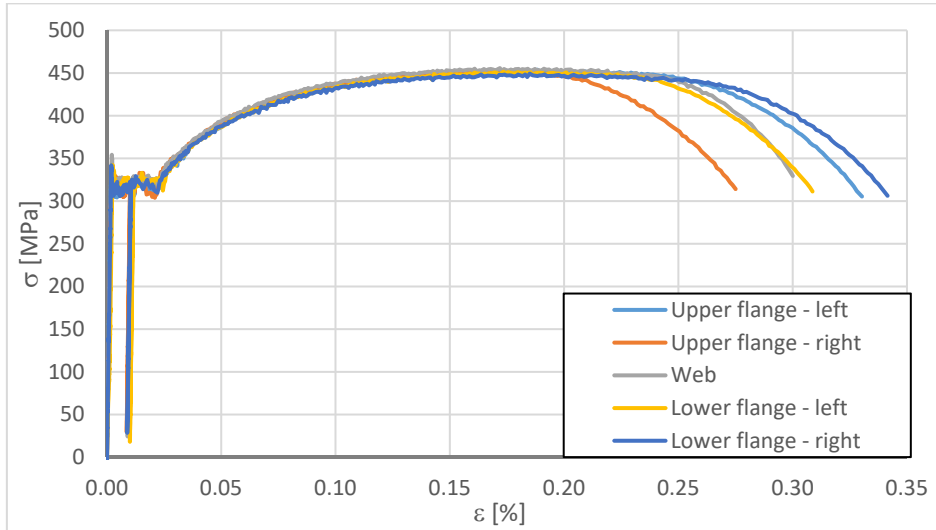


Figure 8-6: HEB 180 – S235

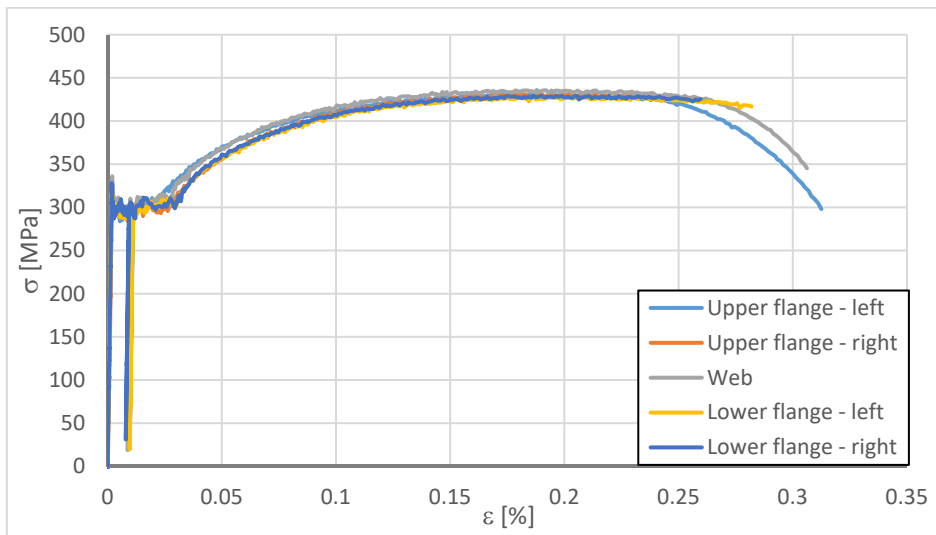


Figure 8-7: HEA 220 – S235

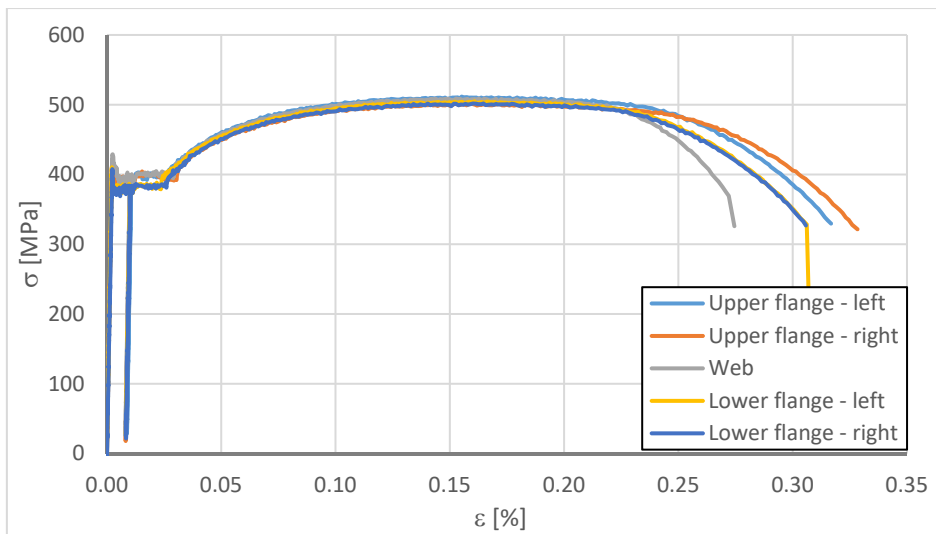


Figure 8-8: HEB 180 – S355

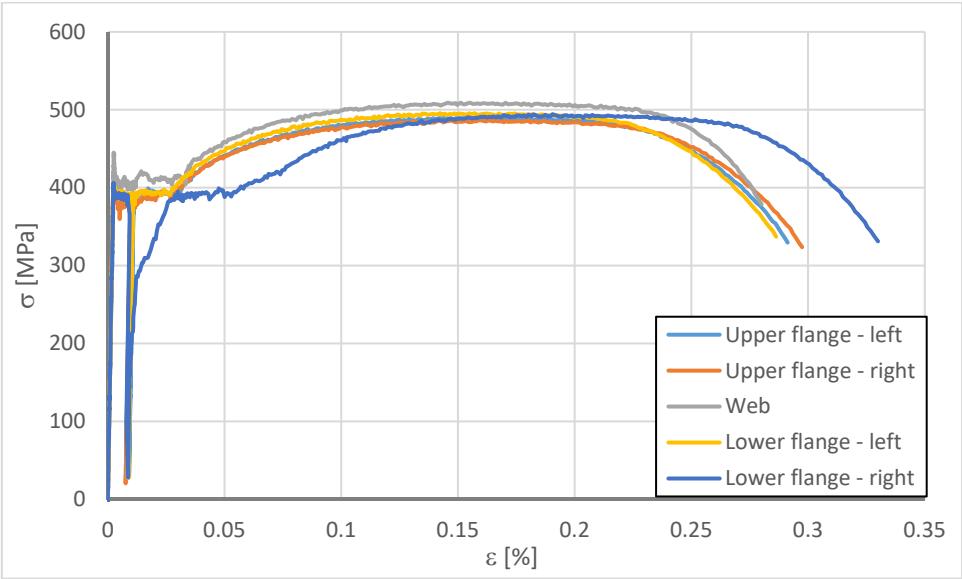


Figure 8-9: HEA 220 – S355

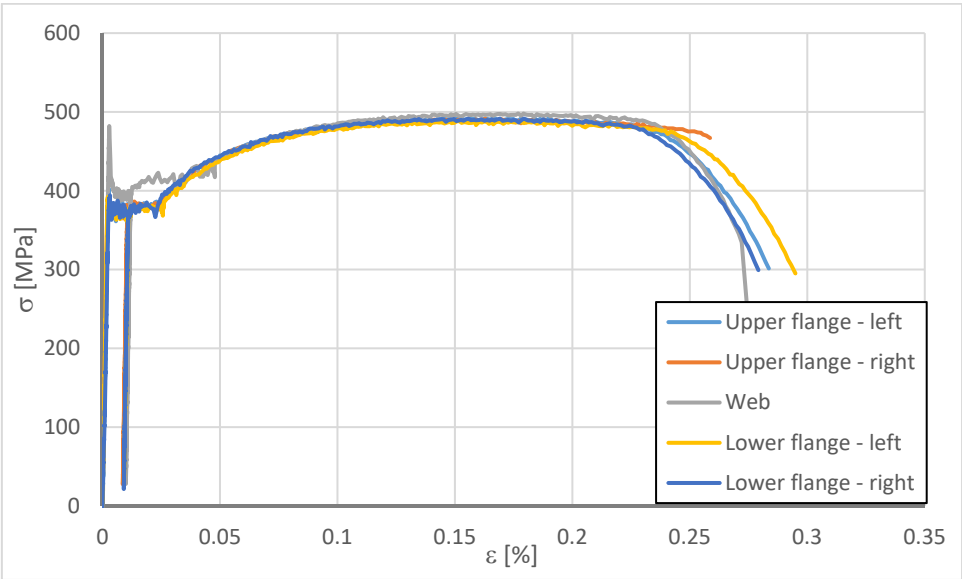


Figure 8-10: IPE 270 – L = 810 mm – S355

8.3 Annex C: Sections used for the parametric study concerning the member resistance

Hereafter, the sections used in the framework of the study concerning the member resistance are represented. In order to simplify the visualisation all sections are shown with the same scale. The dimensions of the sections are recalled in Table 8-11. It is recalled that the hot-rolled sections noted as HR possess inverted dimensions. Also, it is recalled that the fillets of hot-rolled sections are not included in the numerical simulations.

Table 8-11: Dimensions of studied sections

Cross-section type	Notation	h (mm)	t_w (mm)	b (mm)	t_f (mm)	
U	UPE 80	80	4	50	7	
	UPE 200	200	6	80	11	
	UPE 360	360	12	110	17	
Double symmetric I	HEB 200	200	9	200	15	
	IPE 500	500	10,2	200	16	
	HEAA 800	770	14	300	18	
	HR290.3.300.14	290	3	300	14	
	HR500.4.300.20	500	4	300	20	
	HR770.5.400.17	770	5	400	17	
	W650.5.180.10	650	5	180	10	
	W1330.10.280.15	1330	10	280	15	
	W850.6.300.12	850	6	300	12	
	W850.5,5.200.14	850	5,5	200	14	
Mono-symmetric I	Notation	h (mm)	t_w (mm)	b_{fsup} (mm)	b_{finf} (mm)	t_f (mm)
	IMS1	200	9	200	150	15
	IMS2	200	9	200	125	15
	IMS3	500	10,2	200	125	16
	IMS4	500	10,2	200	75	16

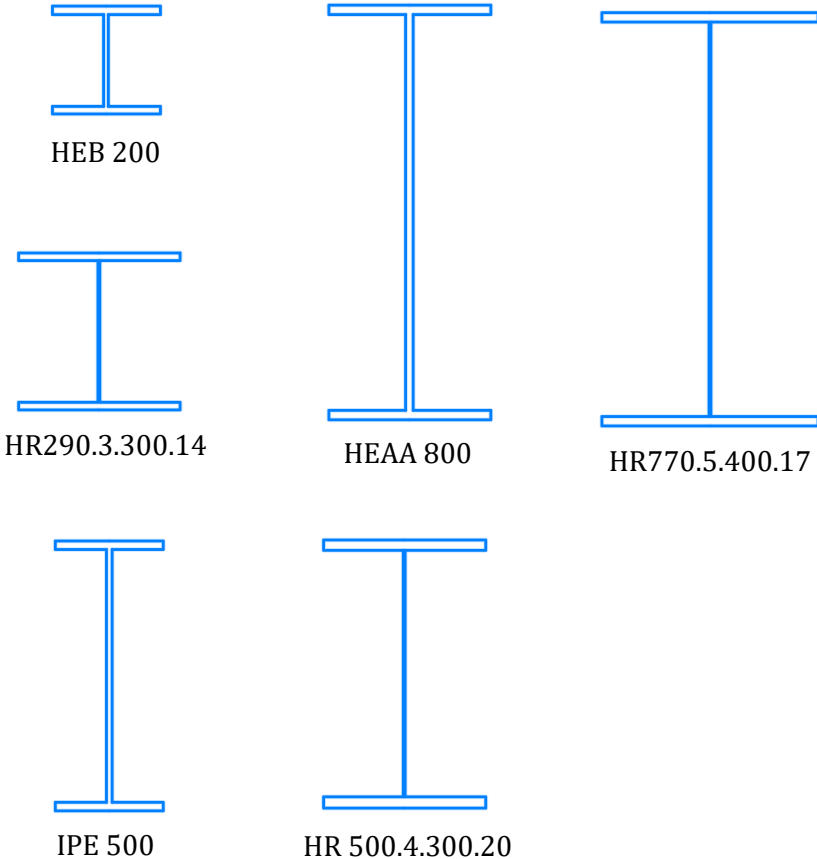


Figure 8-11 : Studied hot-rolled I sections

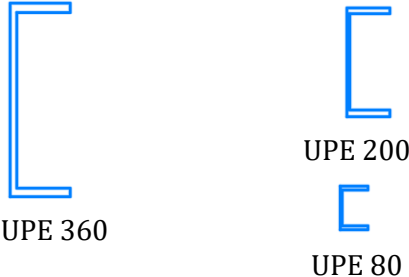


Figure 8-12 : Studied hot-rolled U sections

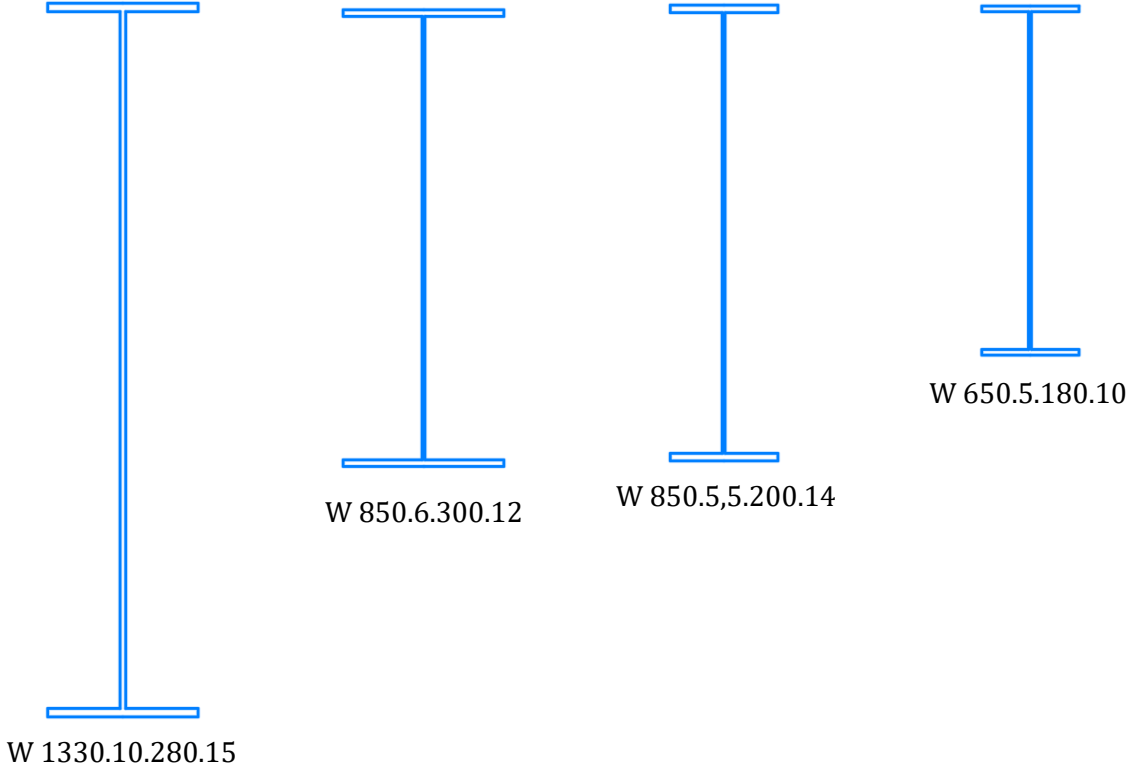


Figure 8-13 : Studied double symmetric welded sections

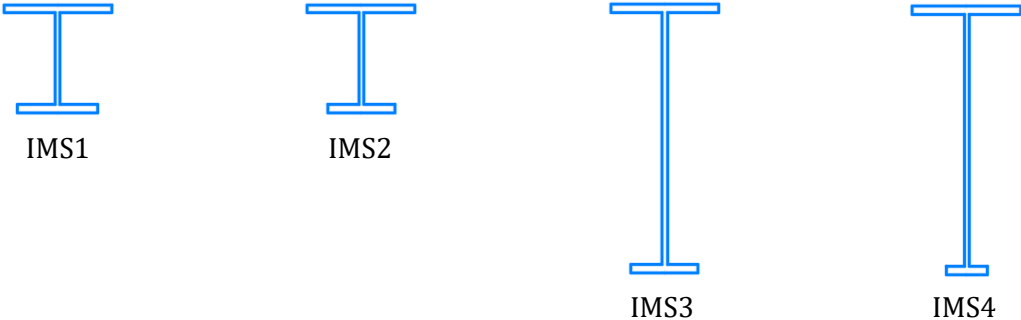


Figure 8-14 : Studied mono-symmetric welded sections

Résumé

Des barres en acier à section ouverte sont, dans la majorité des cas, soumises à une combinaison d'effort normal et de flexion bi-axiale. Cependant, en raison de leur utilisation elles peuvent également être soumises à un moment de torsion. Même si les barres à section ouverte peuvent être soumises à des charges de torsion en pratique, l'Eurocode 3, ne définit pas comment la résistance de la barre peut être déterminée dans ces conditions. Ce pourquoi, l'objectif principal de cette thèse est de remplir cette lacune. Pour atteindre cet objectif, le comportement des barres métalliques soumises à une combinaison complexe de charges est étudié par voie théorique, expérimentale et numérique. Tout d'abord, la résistance plastique des barres est étudiée. En cas de torsion, il a été montré que les barres à section ouverte possèdent une réserve plastique importante qui ne peut pas être mise en évidence à l'aide d'une simple analyse élastique. Afin de tenir compte de l'effet bénéfique de la réserve plastique en torsion, une méthode d'analyse simplifiée est développée et validée par des analyses numériques. Ensuite, l'interaction plastique entre les efforts internes est étudiée. Des essais en laboratoire ont été réalisés afin de caractériser l'interaction entre l'effort tranchant et le moment de flexion. L'étude est ensuite étendue à l'aide de simulations numériques sur des cas d'interaction plus complexes incluant notamment des moments de torsion. Les essais accompagnés par l'étude numérique ont permis de mettre au point un modèle de résistance basé sur la méthode « Partial Internal Force Method » développée dans le passé. La dernière partie de la thèse concerne la résistance des barres à l'instabilité. Un modèle de résistance incluant l'effet de l'instabilité élasto-plastique est développé pour les barres métalliques en présence de torsion. Cette méthode est basée sur une extension des formules d'interaction proposées dans l'Eurocode. Afin de franchir certaines limitations liées à cette méthode, un deuxième modèle de résistance est développé pour les barres en I dans le format du « Overall Interaction Concept ».

Abstract

Structural steel members with open cross-section are, in the majority of cases, subject to a combination of axial forces and mono- or bi-axial bending. Nonetheless, owing to specific use they may be subject to torsion as well. Even if torsional loads are of practical interest for steel members of open section, the European standard for the design of steel structures, Eurocode 3, does not contain a generally accepted design method addressing the resistance of these members. Consequently, the main objective of this thesis is to close the lack in the current standard. So as to attain this objective the behaviour of members of open section subject to a complex load combination has been studied theoretically, experimentally and numerically. First, the plastic resistance of steel members has been analysed. It has been shown that members subject to torsion may possess a high plastic system reserve that cannot be predicted by simple elastic analysis. So as to account for the beneficial effect of the plastic reserve, a simplified analysis method has been developed and validated with numerical simulations. After this, the plastic interaction between all internal forces and moments has been studied. Several laboratory tests have been performed to characterise the interaction between bending moments and the shear force. The study is then extended to more complex interaction cases including torsion by means of numerical simulations. The laboratory test and the numerical simulations allowed the development of a precise resistance model based on the "Partial Internal Force Method" developed in the past. The last part of this thesis was dedicated to the member resistance including instability. A resistance model has been developed based on the Eurocode 3 interaction equations. So as to overcome some of the limitations linked to this method, a second design approach is developed based on the "Overall Interaction Concept".